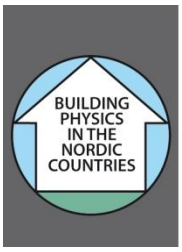

NSB2008

Nordic Symposium on Building Physics 2008

Proceedings of the 8th Symposium on Building Physics in the Nordic Countries

Volume 2

Tuesday, June 17

Copenhagen, June 16-18, 2008

Carsten Rode, editor

Department of Civil Engineering
Technical University of Denmark

The Danish Society of Engineers
Society for Building Physics

Danish Building Research Institute
Aalborg University

The Organizing Committee

Carsten Rode, Technical University of Denmark (chairman)
Svend Svendsen, Technical University of Denmark
Eva B. Møller, The Danish Society of Engineers, IDA, Society for Building Physics
Torben V. Rasmussen, Danish Building Research Institute, Aalborg University (since Dec. 2007)
Morten H. Hansen, Danish Building Research Institute, Aalborg University (until Dec. 2007)
Dan Kallehave, Technical University of Denmark (student help, secretary to the Committee)

Contact Address

Nordic Symposium on Building Physics 2008
Department of Civil Engineering
Brovej, Building 118
Technical University of Denmark
DK-2800 Kgs. Lyngby, Denmark

Phone: +45 45 25 17 00
Fax: +45 45 88 32 82
E-mail: byg@byg.dtu.dk
Web: www.byg.dtu.dk
www.nsb2008.org

Reference to papers

Author. Title. Proceedings of the 8th Symposium on Building Physics in the Nordic Countries (C. Rode, editor) , Report R-189, Dept. of Civil Engineering, Technical University of Denmark, Kgs. Lyngby, Denmark, 2008

DTU Byg Report R-189
ISBN 978-87-7877-265-7

Number of copies printed: 280
Printed by the Danish Society of Engineers, IDA
Copenhagen, Denmark, June, 2008

Foreword

The 8th Symposium on Building Physics in the Nordic Countries was held June 16-18, 2008 in Copenhagen, Denmark. The Symposium has been organized jointly by The Technical University of Denmark; The Danish Society of Engineers' Society for Building Physics; and the Danish Building Research Institute, Aalborg University.

The Symposium in Copenhagen invited contributions regarding:

Research results on

- *Energy performance*
- *Hygrothermal performance/moisture*
- *Air transport*

Covering building physical heat, air and moisture transfer in

- *Building materials*
- *Building envelopes*
- *Whole buildings*

With special emphasis on

- *Models*
- *Experiments*
- *Practice*

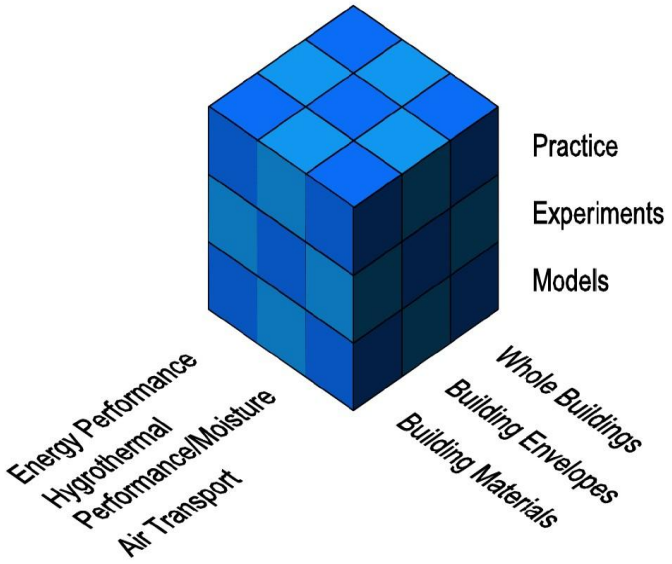

The Symposium was held in the format of two days as a traditional conference with oral presentations followed by brief discussions. The third day was devoted to the practical use of research results, and the programme on this day was laid such as to allow for more discussion of the presented results, not least with a scope to debate the practical implications.

The Symposium follows previous symposia held in Lund 1987, Trondheim 1990, Copenhagen 1993, Helsinki 1996, Gothenburg 1999, Trondheim 2002 and Reykjavik 2005. While the symposia are always arranged in one of the Nordic countries, they are increasingly attracting participants from other countries. Out of more than 250 abstracts, some 182 papers were eventually prepared for the 2008 Symposium in Copenhagen, half of them by researchers from other than the Nordic countries.

The venue of the Symposium was the meeting centre of the Danish Society of Engineers, IDA, on the harbour front of central Copenhagen. By providing this facility, IDA constituted the main sponsor of the Symposium, and their cooperation is gratefully acknowledged!

The organizers also would like to thank the participants of the scientific committee and people who have assisted in reviewing papers. Their contributions have been very important to ensure the quality of the Symposium.

Personally, I would like to thank my colleagues in the organizing committee for their true dedication to the project.

Copenhagen, June 2008

Carsten Rode
Chairman of the organizing committee

Scientific Committee

Prof. Anker Nielsen, Chalmers University of Technology
Dr. Berit Time, SINTEF Byggforsk
Prof. Carl-Eric Hagentoft, Chalmers University of Technology
Sen.Res.Fel. Chris Sanders, Glasgow Caledonian University
Prof. Georg-Wilhelm Mainka, University of Rostock
Prof. Gerd Hauser, Fraunhofer Institute for Building Physics
Prof. Gudni Johannesson, Royal Institute of Technology in Stockholm
Dr. Gulten Manioglu, Istanbul Technical University
Prof. Hugo Hens, Katholieke Universiteit Leuven
Prof. Ingemar Samuelson, SP Technical Research Institute of Sweden
Prof. Jan Carmeliet, Technische Universiteit Eindhoven
Prof. Jan Vincent Thue, Norwegian University of Science and Technology
Prof. Jesper Arfvidsson, Lund University
Prof. John Grunewald, Technische Universität Dresden
Prof. Kalema Timo, Tampere University of Technology
Prof. Klaus Sedlbauer, Fraunhofer Institute for Building Physics
Prof. Lars-Olof Nilsson,Lund University
Assoc. Prof. Maria Wall, Lund University
Dr. Miimu Airaksinen, Technical Research Centre of Finland
Dr. Monika Woloszyn,University of Science and Technology - INSA Lyon
Prof. Paul Fazio, Concordia University
Prof. Per Heiselberg, Aalborg University
Dr. Phalguni Mukhopadhyaya,National Research Council Canada
Prof. Shuichi Hokoi, Kyoto University
Sen.Res. Targo Kalamees, Tallinn University of Technology
Assoc. Prof. Dr. Thomas Bednar, Vienna University of Technology
Prof. Dr. Holger Wallbaum, Swiss Federal Institute of Technology - ETH Zürich
Prof. Arild Gustavsen, Norwegian University of Science and Technology
Dr. Juha Vinha, Tampere University of Technology
Dr. Morten Hjorslev Hansen, DUKO · Dansk Undertagsklassifikationsordning

Reviewers

The following experts have contributed to the review of papers. Their important contribution is gratefully acknowledged!

Hashem Akbari ; Steve Cornick; Andre Desjarlais; Heiko Fechner; Diana Fisler; Hua Ge; Stig Geving; William Healy; Bengt Hellström; Jonas Holme; Ronald Krpan; Mark Lawton; Qinru Li; Yang Li; Uwe Meinhold; Qian Mao; Wahid Maref; Andreas Nicolai; Mostafa Nofal ; Vildan Ok; Seyhan Onbaşıoğlu; Gul Koclar Oral; Anil Parekh; İsmail Cem Parmaksızoğlu; Hans Petzold; Jiwu Rao; Cynthia Howard Reed; Ian Ridley; Patrick Roppel; Madeleine Rousseau; Uli Ruisinger; Prabal Talukdar; Sergio Vera; Xiangjin Yang; Alpin Yener & Zerrin Yılmaz

Table of Contents

Monday, June 16

Session M1A – Energy Performance of Materials

Session M2A – Energy Performance of Constructions

Session M3A – Energy Performance of Windows

Session M4A – Air Flow in Windows

Session M1B – HVAC System Interaction

Session M2B – Exterior climate interaction

Session M3B – Exterior Climate Interaction / Durability of Surfaces

Session M4B – Thermal Conductivity / HM Salt

Session M1C – Air Flow Assessment

Session M2C – Air in Rooms

Session M3C – Air Flow in The Building Envelope / Air Flow Assessment

Session M4C – Insulation Materials

Tuesday, June 17

Session T1A – Ventilation and Heating of Buildings

Session T2A – Calculation of Thermal Performance of Buildings

Session T3A – Design and Optimization of Low Energy Buildings

Session T4A – Low Exergy Buildings

Session T1B – Mass Exchange 1

Session T2B – Mass Exchange 2 / Tools and Protocols

Session T3B – Building Envelope Issues

Session T4B – Indoor Humidity and Buffering

Session T1C – Silicate Materials and Structures 1

Session T2C – Silicate Materials and Structures 2 / Mould

Session T3C – Measuring Techniques / Wood Materials

Session T4C – Wood Constructions

Wednesday, June 18

Session W1A – Design and Development of Energy Efficient Buildings

Session W2A – Measured Energy Performance of Buildings

Session W3A – Energy Savings in Existing Buildings

Session W4A – Windows and Facades

Session W1B – Moisture Safety

Session W2B – Moisture Sensitive Construction

Session W3B – Building Envelope Issues and Innovation

Session W4B – Innovative Products

Session W1C – Energy Performance in Cold Climate

Session W2C – Heat Capacity and Energy Performance

Session W3C – Air Tightness and Building Envelope

Session W4C – Indoor Humidity in Practice

LIST OF AUTHORS

Saving energy for ventilation by careful selection of building materials

Pawel Wargocki, Ph.D.,
International Centre for Indoor Environment and Energy, Department of Civil Engineering, Technical University of Denmark;
pw@mek.dtu.dk; www.ie.dtu.dk

Henrik N. Knudsen, Ph.D.,
Danish Building Research Institute, Aalborg University;
hnk@sbi.dk; www.sbi.dk

KEYWORDS: *Building materials; Perceived air quality; Ventilation; Energy.*

SUMMARY:
The main objective of the research project described in this paper was to study the potential of reducing energy used for ventilating buildings by using low-polluting building materials, without compromising indoor air quality. To quantify this potential, the exposure-response relationships, i.e. the relationships between ventilation rate and the perceived indoor air quality (indoor air quality perceived by humans as opposed to indoor air quality evaluated by chemical measurements), were established for rooms furnished with different more or less polluting materials. Based on these results, simulations of energy used for ventilation were carried out for selected building scenarios. The results show that the exposure-response relationships vary between different building materials. Consequently, the ventilation required to achieve a certain level of perceived indoor air quality varies according to which building materials are used. Furthermore, the results show that the perceived air quality in rooms can be considerably improved when low-polluting building materials are selected and that the improvement is greater than a realistic increase of the ventilation rate. The energy simulations show that selecting low-polluting materials will result in a considerable energy saving as a result of reducing the ventilation rates without compromising indoor air quality. Halving the ventilation rate, which seem to be realistic when low-polluting building materials are used, can reduce the energy used for ventilation by up to 50%. However, the energy savings from using low-polluting building materials are limited by the extent to which ventilation is used to control the thermal environment, i.e. heating and/or cooling the supplied outdoor air.

1. Introduction

There is a need to reduce energy consumption worldwide. One initiative to reach this goal is the EU Directive 2002/91/EC Energy Performance of Buildings (2002) that makes it obligatory to reduce energy consumption in buildings while taking into account the indoor environment. For most buildings this can only be achieved if the energy used for ventilation is also reduced, because it constitutes about 20-30% of the total energy consumed in buildings today. This, however, may lead to reduced ventilation rates and increased levels of air pollution from buildings, people and their activities, and thus to poorer indoor air quality, which contradicts the requirements of the EU Directive. The obvious solution for these apparently opposing requirements would be to reduce the pollution sources indoors.

This paper describes the results of the research project called “Reduced energy use in buildings through selection of low-polluting building materials and furniture”. The main objective of the project was to quantify the extent to which reducing pollution sources indoors by selecting low-polluting building materials would reduce the energy used for ventilation of buildings, without compromising indoor air quality as it is perceived by humans and not as it is defined by the concentration of air pollutants measured using chemical methods. This objective was achieved by summarizing the existing data on the effects of emissions from building materials on perceived air quality, by carrying out experiments in which the effects of using low-polluting building materials on the perceived air quality were examined and related to ventilation requirements, and by performing energy simulations examining the extent to which reducing ventilation rates, as a consequence of using low-polluting building materials, will affect energy use.

2. The effects of using low-polluting materials on ventilation

Several studies have previously investigated the effects of pollution emitted by building materials on indoor air quality as it is perceived by people, and related these effects to ventilation requirements. In these studies, perceived air quality was generally measured by a group of untrained persons who were exposed to air polluted by emissions from building materials and /or rooms and assessed the quality of air immediately upon exposure by rating whether the air quality was acceptable or not acceptable. To examine the effect of ventilation on the perceived air quality when different building materials are selected, the exposure-response relationships between the acceptability of air quality and the dilution achieved by changing the ventilation are created by log-linear regression (Cain and Moskowitz 1974, Knudsen et al. 1998).

The data obtained in previous experiments was summarized and systematized by Knudsen et al. (2006). They concluded that the effect of changing the ventilation rate on the perceived quality of air polluted by different building materials can vary considerably. Consequently there are relatively large differences in the ventilation requirements needed to obtain a certain level of perceived air quality for emissions from different building products. There could be a number of factors causing the observed differences and may for example include: the type of pollution source; psychological factors such as context in which assessments are made (in laboratory vs. in real buildings); expectations and previous experience with odours; the information given concerning the pollution sources before assessments; physiological factors such as more or less adaptation to air pollution; perception of complex odour mixtures from e.g. combinations of building products; chemical/physical factors, e.g. how products interact when air pollution is adsorbed and/or desorbed on material surfaces; and reactive chemistry, e.g. when odorous secondary emissions are formed in reactions with for example ozone. All these factors should be taken into account when investigating the effects of using low-polluting materials on perceived air quality and ventilation requirements.

The summary of Knudsen et al. (2006) showed in addition that there is a lack of systematic experiments in which building materials are first ranked according to their pollution strength, e.g. by using methods applied in labelling schemes (Witterseh 2002) and then the effect on the indoor air quality of using these materials in real rooms is examined. Experiments were carried out to fill this gap (Wargocki et al. 2007). In these experiments a sensory panel assessed the air quality in full-scale test rooms ventilated with three different outdoor air supply rates and polluted by nine combinations of typical building materials including wall, floor and ceiling materials; the materials ranged from high- to low-polluting, and were ranked in this range using sensory assessments of air quality in small-scale glass chambers where they were tested individually following the principles of the Nordtest methods (Nordtest 1990, 1998). The results of this testing are shown in Figure 1 confirming that both high- and low-polluting materials were selected.

The materials tested individually in small-scale glass chambers were examined in combinations in the test rooms. The results of these experiments confirm that reducing pollution sources by selecting lower-polluting building materials, ranked by means of sensory assessments made in small-scale glass chambers, improves the perceived air quality in full-scale rooms where these materials are used. This is exemplified in Figure 2. It shows that the air quality improved when the high-polluting paint on gypsum board (Paint 2) was substituted with lower-polluting paint on gypsum board (Paint 1) or unpainted gypsum board (Gypsum board). The improvement was greater than that achieved by increasing the outdoor air supply rate in a realistic range: a sevenfold increase of the outdoor air supply rate improved acceptability of quality of air polluted by a combination of materials including plastic-coated gypsum ceiling (Ceiling 2), polyolefine flooring (Polyolefine) and paint on gypsum board (Paint 1) less than substituting Paint 1 in this combination with lower-polluting gypsum board (Gypsum board). Similar results were obtained for nearly all other substitutions with the lower-polluting building materials examined (Wargocki et al. 2007).

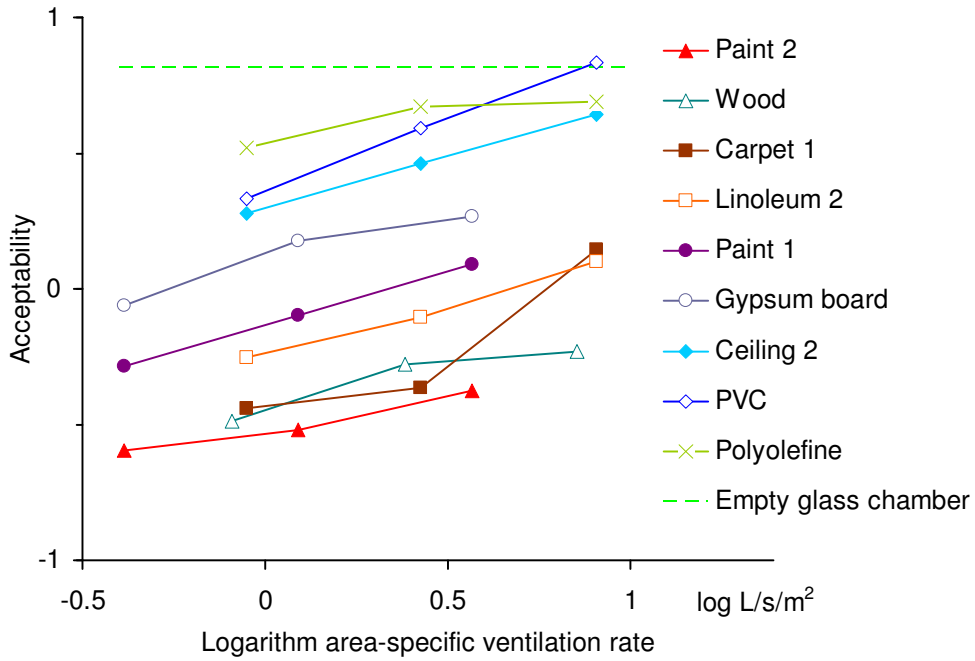

FIG 1: Acceptability of air quality as a function of the area-specific ventilation rate in small glass chambers containing the individual building materials that were examined in combinations in test rooms (Wargocki et al. 2007); the scale coding was as follows: -1=clearly not acceptable; 0=just not acceptable/just acceptable; +1=clearly acceptable

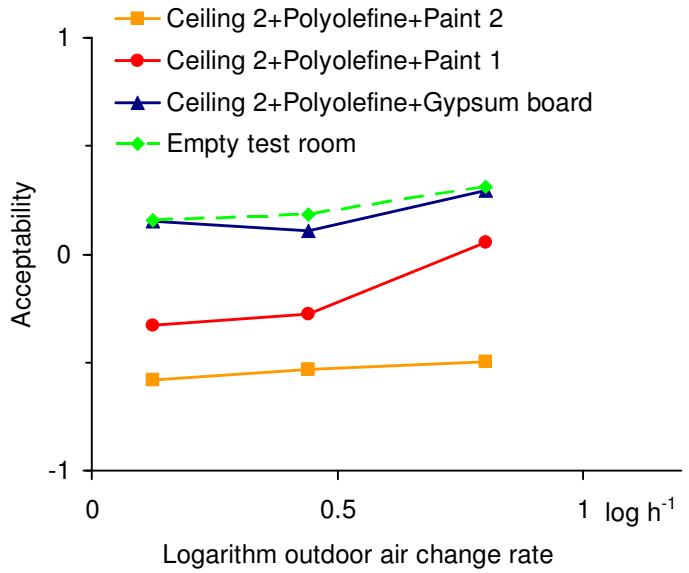

FIG 2: The effect of substituting high-polluting wall materials with lower-polluting materials on the air quality in the tests rooms (Wargocki et al. 2007); the scale coding was as follows: -1=clearly not acceptable; 0=just not acceptable/just acceptable; +1=clearly acceptable

3. The effects of using low-polluting materials on energy

The results presented in Fig. 2 show that reducing pollution sources by selecting lower-polluting building materials improved the perceived air quality and that this improvement was much greater than the improvement

of perceived air quality by increasing ventilation rates in a range realistic for indoor environments. To examine the consequences of selecting low-polluting building materials on energy used for ventilation, dynamic simulations were performed of annual energy used for ventilation of a single office room. Simulations of energy used for different ventilation rates in the office were performed. Because the ventilation rates are proportional to the pollution load at a constant air quality level, varying the ventilation rates during simulations was equivalent to changing the pollution load or simply selecting materials that were more polluting or less polluting. Simulations were performed for 19 different total outdoor air supply rates. The maximum ventilation rate was 117 L/s. It was selected with due consideration to the limitations regarding maximum air velocities in the room. It corresponds to an air change rate of 8 h^{-1} and it was assumed to be the highest possible ventilation rate that can be delivered to the room without causing any local discomfort due to draught. The lowest ventilation rate was 6 L/s. It is based on the minimum requirements of ASHRAE Standard-62 for the case of adapted occupants (ASHRAE, 2007), i.e. 3 L/s per person.

Different configurations of the office were simulated. The office had two different orientations (windows facing south or north) and three different methods of reducing heat loads: solar shading, cooling the air supplied to the office by the HVAC system and night cooling. In addition, the conditions with normal and reduced heat loads in the office were simulated. In total, 69 different simulations were performed.

The modelled office had a floor area of 19 m^2 and a height of 2.8 m (volume 53 m^3). It was situated in Copenhagen, Denmark. The office was occupied by 2 non-smoking persons and was equipped with 2 computers, 2 desk lamps and general lighting. The occupants were scheduled to work in the room from Monday to Friday between 8 am and 4 pm excluding public holidays.

The room's envelope was designed according to Addendum 12 to the Danish Building Regulations (BR95, 2005). The air was supplied to the room by mechanical ventilation and the heating in winter was provided by a radiator. The supply air to the room was provided by a constant air volume (CAV) ventilation system. The air was taken from outside the building and was treated in an air-handling unit consisting of heat recovery unit, heating coil and in some cases cooling coil. No humidification of the air took place. It was assumed that the outside air was clean and that full mixing in the room took place. The heat from the exhaust air was recovered in a heat exchanger with the efficiency of 0.6; no cold or moisture recovery took place. The ventilation system was started one hour prior to arrival of occupants of the office and it was in operation until the end of working hours. Additionally, when the night cooling was simulated, the ventilation system was also operated at night. Infiltration to the room during non–occupancy period was assumed to be 0.2 h^{-1}. During working hours it was increased to 0.4 h^{-1}. The windows could not be opened.

Simulation of annual energy use was carried out using a BSim simulation programme (Wittchen et al. 2005); the energy used for the heating, ventilation and air-conditioning (HVAC) system was calculated. The energy consumption of the HVAC system includes the energy used for transporting, heating and, when applicable, cooling the air. The energy used for heating comprises that used for radiators and for the heating coil in the air-handling unit. The energy consumption for cooling is the energy consumed by the cooling coil in the air-handling unit. The energy consumption of a fan is proportional to both the airflow and the pressure rise. In the simulations it was assumed that the supply and return fans had flat characteristics within the considered range of airflows. Therefore, the pressure rise was constant in all simulations and the energy consumption by a fan depended only on the airflow. While calculating the total energy consumption for a HVAC system, the weighting factors for different types of energy were used as prescribed in the Danish Building Regulations (BR95, 2005). Assuming an average coefficient of performance (COP) of 2.5 for the cooling system, the cooling energy and the heating energy had the same weight and were added without correction by any factor. The electrical energy for fans was multiplied by a factor of 2.5. The total energy consumption for the HVAC system was thus calculated by adding the cooling and heating energy, and the energy for operation of fans, multiplied by the factor of 2.5.

Figures 3 and 4 show the results of simulations for an office facing south and north, respectively, for the relationships between energy used by the HVAC system and the ventilation rate. Separate relationships are presented for the different conditions simulated. Both figures show that the energy used by the HVAC system can be assumed to increase linearly with the increased ventilation rate, independently of the room orientation and different means of reducing heat in the office. They show also that when night cooling and air cooling are applied, the energy used by the HVAC system increased, as expected.

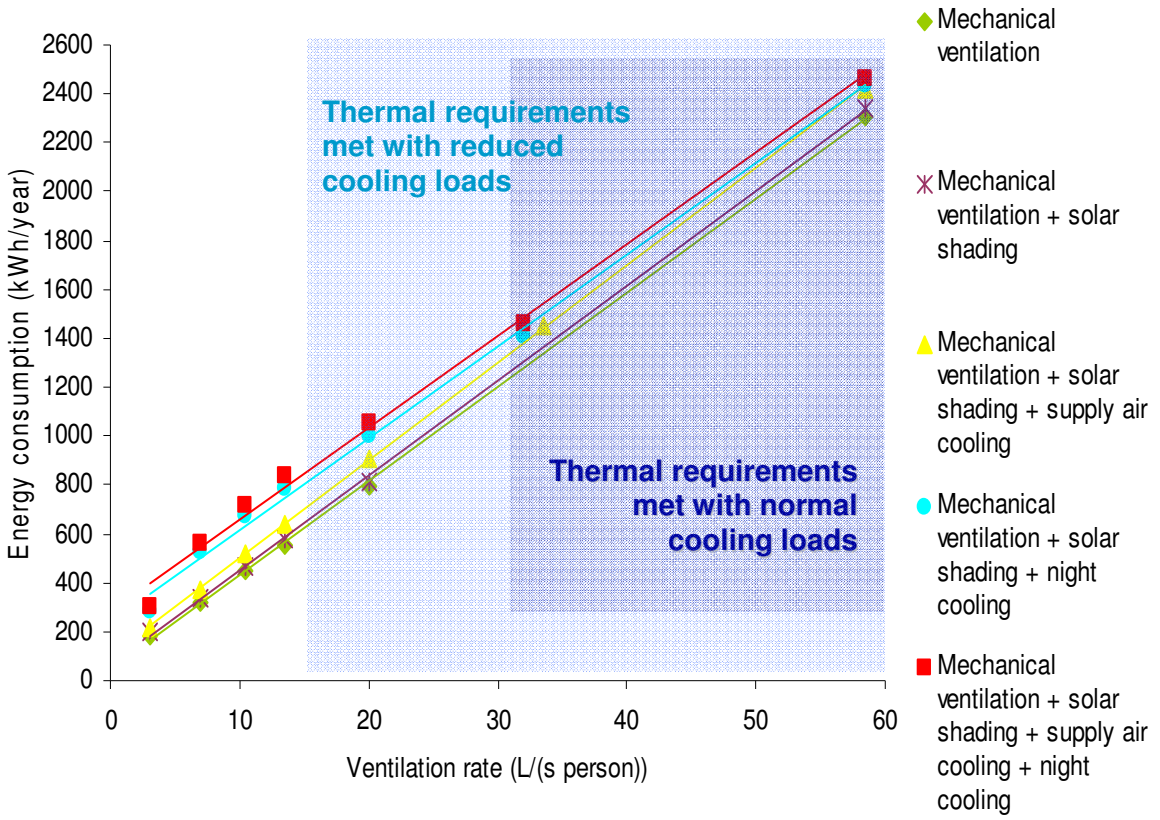

FIG 3: The relationships between energy used by the HVAC system and the ventilation rate for the room facing south for different simulated conditions

The results of simulations show that there is considerable potential for saving energy when low-polluting building materials are used. The ventilation rates can then be reduced significantly without compromising the perceived indoor air quality in the office. The greatest potential exists when ventilation is not used to cool the office to avoid overheating. The energy used by the HVAC system can then be reduced by about 90% when the ventilation rate is reduced to the minimum required by ASHRAE Standard 62 (ASHRAE, 2007) as a consequence of selecting low-polluting building materials (see the relationships in Figures 3 and 4 showing the results of simulations in the office ventilated by mechanical ventilation only and when the solar shading was applied). The potential for energy savings is lower when ventilation is used to cool the office so that it does not become overheated for longer periods than those specified in building regulations and standards. The maximum potential for energy savings in this case is illustrated in Figures 3 and 4 by the shaded areas, assuming that the periods with overheating are not longer than those specified by the Danish Standard DS 474 (DS 474, 1993); two cases are illustrated (1) for the office with normal heat loads and (2) when all efforts were made to reduce heat loads (by the application of energy-saving bulbs and low-energy PC monitors to reduce heat loads by 35% at their peak). In the office with normal heat loads, it was possible to decrease the ventilation rate to 32 L/(s•person) for the room with south orientation and 25 L/(s•person) for the room facing north when the supply air cooling, night cooling and solar shading were applied. This corresponds to about 50% reduction in energy use for the HVAC system, compared to the office ventilated with the maximum ventilation rate, but the minimum ventilation rates are still much higher than those prescribed by the current ventilation rates (ASHRAE, 2007; CEN CR 1752, 1998). In the office with reduced heat loads it was possible to reduce the ventilation rate to 16.5 L/(s•person) for the room with south orientation and 6.5 L/(s•person) for the room with north orientation without compromising the requirements of DS 474, the ventilation rates being similar to those specified by current ventilation standards. This corresponds to about 60% to 75% reduction in energy use for the HVAC system. It should be noted that when the office was ventilated by mechanical ventilation only, it was not possible to meet the requirements of DS 474 for either south or north orientation, even when solar shading was applied in the former case; the office was overheated for periods that were too long.

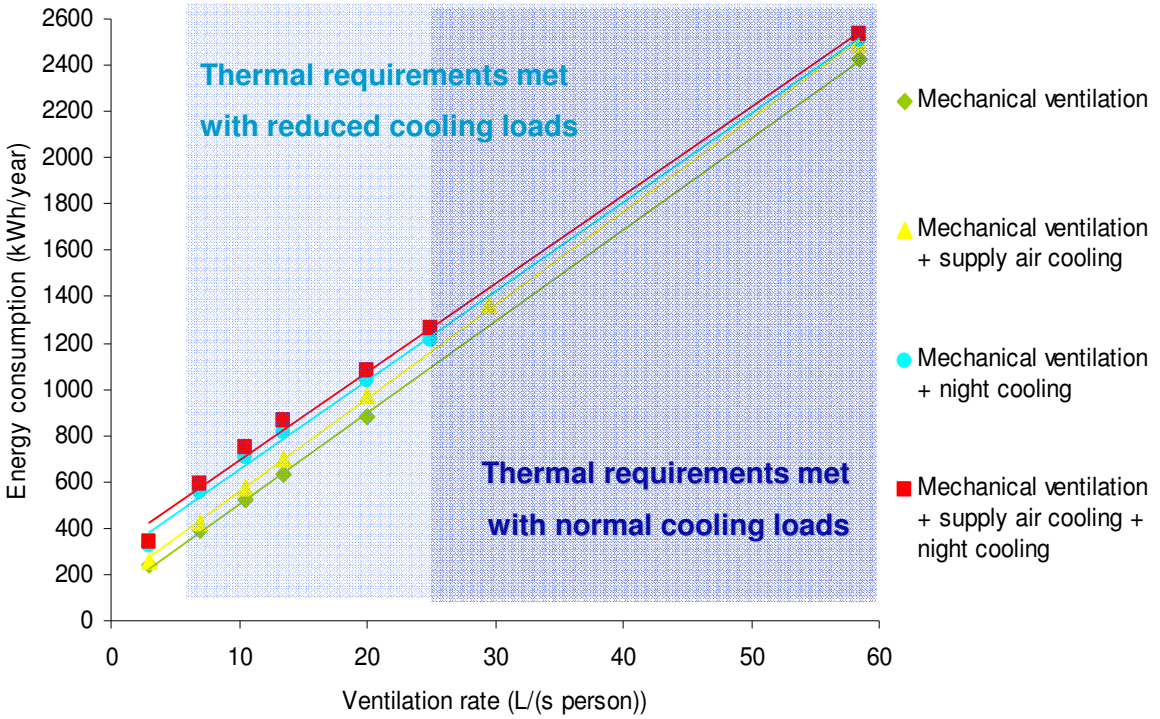

FIG 4. The relationships between energy used by the HVAC system and the ventilation rate for the room facing north for different simulated conditions

The results presented above show that when the supply air from the ventilation system is used to cool rooms, a great effort must be made to limit the heat gains in order to fully utilize the potential for energy saving when low-polluting building materials are used. This will lead to even higher energy savings as less energy will be used for light and equipment. At the same time, the requirements for both thermal climate and indoor air quality will not be compromised and the requirements of the EU Directive 2002/91/EC Energy Performance of Buildings will thus be met.

4. Conclusions

Data were summarized reporting the relationships between ventilation rate and perceived air quality when building materials are the main pollution sources. They show that these relationships vary for different building materials.

Substituting building materials with materials shown in small-scale chamber tests to be lower-polluting, improved the perceived air quality in full-scale tests.

The improvement of the perceived air quality was greater than the improvement obtained by increasing the outdoor air supply rate within a range that is realistic for indoor settings.

Simulations of the operation of HVAC systems showed that the energy used by a ventilation system for transporting, heating and cooling the air can be assumed to be linearly related to the ventilation rate, e.g. halving ventilation rates can result in up to 50% reduction in energy use.

Energy simulations showed that reducing the ventilation requirements when low-polluting materials are selected will result in potentially large energy savings. However, they also show that the potential for energy saving may be limited if ventilation is used to control thermal conditions, e.g. for cooling the supply air to rooms. In this case, all efforts must be made to minimize heat loads so that energy saving as a result of using low-polluting building materials will be fully utilized.

5. Recommendations for future studies

The exposure-response relationships used in the present work express the influence of pollution from combinations of different building materials and furniture on the perceived air quality. However, the indoor air is also polluted by human bioeffluents. It is therefore recommended to create exposure-response relationships for combinations of building materials and people and in this way investigate how the presence of people influences the ventilation required for acceptable indoor air quality and consequently the energy used for ventilation.

The impact of other methods of improving indoor air quality without unnecessary use of energy should be investigated. These methods include the use of active and passive air cleaners and air-cleaning building materials.

It would be useful to validate the present results obtained in laboratory experiments in existing buildings. Energy simulations for other climate zones would also be useful considering that the energy simulations in the present project were performed only for a hypothetical building located in a moderate climate.

6. Acknowledgments

The work was supported by the Danish Energy Authority through an EFP-05 project "Reduced energy use for ventilation in buildings through selection of low-polluting building materials and furniture", contract #33031-0048. The authors wish to thank Jana Vondruskova, Pawel Zuczek and Monika Frontczak who acted as research assistants in the laboratory experiments and during energy simulations described in the present report and gave an account of them in their M.Sc. theses. Thanks are due to Kjeld Johnsen from SBi for assistance and help during energy simulations, Gunnar Holm from SBi and Peter Simonsen from DTU for technical help during experimental work as well as Birgit Markfoged from SBi for help during recruitment of a sensory panel.

7. References

BR95. (2005). *Addendum 12 to BR 95* (Tillæg 12 til Bygningsreglement 1995), Erhvervs – og Byggestyrelsen.

ASHRAE (2007). *ANSI/ASHRAE Standard 62.1-2007. Ventilation for Acceptable Indoor Air Quality*, Atlanta: American Society of Heating and Air-Conditioning Engineers Inc.

Cain WS and Moskowitz HR. (1974). Psychophysical scaling of odor, *Human Responses to Environmental Odors*, New York, Academic Press, 1–32.

CEN CR 1752 (1998). *Ventilation for buildings – Design criteria for the indoor environment,* European Committee for Standardization. Brussels, Belgium

Dansk Standard 474. (1993). Norm for specifikation af termisk indeklima, Code for Indoor Thermal Climate.

Directive 2002/91/EC of the European Parliament and of the Council of 16 December 2002 on the energy performance of buildings.

Knudsen HN, Valbjørn O and Nielsen PA. (1998). Determination of Exposure-Response Relationships for Emissions from Building Products, *Indoor Air*, Vol. 8, 264-275.

Knudsen HN, Wargocki P and Vondruskova J. (2006). Effect of ventilation on perceived quality of air polluted by building materials – a summary of reported data, In: Oliveira Fernandes, E. de, Gameiro da Silva, M. and Rosado Pinto, J. (eds) *Proceedings of Healthy Buildings 2006*, Lisboa, Portugal, Vol. I, pp. 57-62.

Nordtest .(1990). *NT Build 358, Building materials: Emission of volatile compounds, chamber methods*, Esbo, Finland: Nordtest.

Nordtest. (1998). *Nordtest Method 1216-95, Building materials: Emission testing by CLIMPAQ chamber*, Esbo, Finland: Nordtest.

Wargocki P, Knudsen HN and Zuczek P.(2007). Effect of using low-polluting building materials and increasing ventilation on perceived indoor air quality, *Proceedings of CLIMA 2007*, Helsinki (on the CDROM).

Wittchen KB, Johnsen L and Grau K. (2005). *BSIM User's guide*, Danish Building Research Institute, Hørsholm, Denmark.

Witterseh T. (2002). Status of the indoor climate labelling system in Denmark, *Proceedings of Indoor Air 2002*, Monterey, USA, Vol. III, 612-614.

The influence of different sealing methods of window and door joints on the total air leakage of wood-frame buildings

Thor-Oskar Relander, Ph.D Student,
Department of Civil and Transport Engineering, Norwegian University of Science and Technology;
thor.oskar.relander@ntnu.no

Jan Vincent Thue, Professor,
Department of Civil and Transport Engineering, Norwegian University of Science and Technology;
jan.thue@ntnu.no

Arild Gustavsen, Professor,
Department of Architectural Design, History and Technology, Norwegian University of Science and Technology;
arild.gustavsen@ntnu.no

KEYWORDS: air change rate, window and door joints, sealing techniques

SUMMARY:
Air tightness is particularly important to achieve buildings with low energy demand. The air tightness requirements in the Norwegian technical regulations, TEK 2007, cause considerable concern for the building industry. Thus there is a growing interest of forecasting whole buildings' air tightness based on sealing techniques chosen.

In this paper the effects of different window and door sealing techniques on the total air leakage of buildings is investigated. The air change rate requirements investigated were passive house, low energy and according to TEK 2007, the building regulation of Norway 2007. From a selection of 7 different wood-frame standard houses of gross area around 175 m^2 an average building was formulated. For this building the effects of different sealing techniques and air change rate requirements were evaluated. This was also done for the most favourable and unfavourable building. This gave a conception of the deviations among the 7 different buildings.

For this selection of buildings, the calculations show that the effects of choosing a favourable building design can reduce the leakages from the windows and doors with about 24 % relative to the average of the 7 buildings. For the unfavourable building, the leakages can increase by about 16 % relative to the average of the 7 buildings. This effect is less notable for the tightest sealing techniques compared to the less air tight. Calculations also show that the choice of sealing methods has to be more thorough when the passive house standard is to be achieved compared to low-energy or TEK 2007

1. Introduction

The air change rate [h^{-1}] measured during blower door tests is of considerable concern for contractors responsible for the air tightness performance of buildings. To achieve air tight buildings, it is important to know what constructions and methods that are air tight and which are not. This can avoid costly repairs. Air leakages in buildings have many origins, e.g. windows, joints, walls etc. These leakages will depend on craftsmanship, materials and sealing technique to mention a few. An investigation of different sealing techniques of window and door joints was done by Proskiw (1994). Most of the sealing techniques tested were combined with mineral wool insulation in the joints. Proskiw also used interior casing and exterior battens in all measurements.

In addition to measuring different techniques, Proskiw examined the effects of different sealing techniques on a hypothetical 97 m^2 bungalow with an air change rate of 1.5 h^{-1} at 50 Pa. In this paper this procedure is repeated, with the addition of varying both the building *and* the air change rate requirement. As basis for these calculations, measurements done by Relander (2008) will be used. Compared to Proskiw, these measurements were performed *without* mineral wool in the joints and *without* interior casing and exterior battens as basis.

2. Method

2.1 Model description and corresponding assumptions

During blower door pressurization of buildings, a certain air leakage is measured q_{50} [m^3/h] at 50 Pa pressure difference. The air change rate n_{50} [h^{-1}] can be found with knowledge of q_{50} and the volume V, as seen in equation (1). Contrarily, if a building has a certain volume and is to satisfy a *given* air change rate requirement n_{50max}, it is possible to calculate the *maximum* air flow, $q_{50\,max}$ from the relation in equation (1). q_{50} must therefore not exceed q_{50max} for the building to fall within the air change rate requirement.

$$n_{50} = \frac{q_{50}}{V} \qquad \Rightarrow \qquad q_{50\max} = n_{50\max} V \tag{1}$$

The q_{50} value will be the sum of the different leakages of the entire building envelope and will depend on craftsmanship, materials and sealing methods, to mention a few. The importance of the sealing methods of windows and doors is now to be investigated. This is done by establishing the model in equation (2).

$$C_{wd} = \left(\frac{q_{\text{window joints+door joints}}}{q_{50\max}} \right) = \left(\frac{q_{\text{wd}}}{q_{50\max}} \right) \qquad C_{wd} \geq 0 \qquad \left[\frac{m^3/h}{m^3/h} \right] \tag{2}$$

The numerator can be interpreted as a completely air tight building with leakages from the window and door joints *only*. The denominator refers to the *same* building that just barely falls within the air change rate requirement. Thus C_{wd} can be used to evaluate the relative magnitude of the leakages from the window and door joints. If C_{wd} is zero, there are no leakages from the window and door joints. Consequently there is a *buffer* to allow for other leakages on the building envelope. Contrarily, if C_{wd} exceeds 1, there cannot be any other leakages on the building envelope for the building to fall within the air change rate requirement.

As can be seen by the numerator in equation (2), it is assumed that the sealing methods of all windows and doors are equal. This was also done by Proskiw (1994). Henceforth therefore *joints* refers to both window and door joints.

It is clear that the numerator in equation (2) will depend on the sealing technique chosen in the joints as well as the *total* length of the joints in the actual building. Taking this into consideration and using equation (1) in (2), equation (2) reduces to (3):

$$C_{wd}\left(q'_{\text{wd}}, n_{50\max}, L_{wd}, V\right) = \frac{q'_{\text{wd}}}{n_{50\max}} \cdot \left(\frac{L_{wd}}{V} \right) \qquad \left[\frac{m^3/h}{m^3/h} \right]$$

where

q'_{wd} = Air leakage for actual sealing technique at 50 Pa pressure difference $\left[m^3/hm \right]$ (3)

$\frac{L_{wd}}{V}$ = Total perimeter length of all joints in the building per volume $\left[m^{-2} \right]$

$n_{50\max}$ = Air change requirement for actual building $\left[h^{-1} \right]$

2.2 Overview and description of the parametrical variations in the model

Equation (3) shows that C_{wd} depends on 4 parameters. But for a specific building, L_{wd} and V reduces to one quantity. Therefore the parameters reduce to 3 for a specific building. This is emphasized using the parenthesis in equation (3). For this model, it is further clear that for a given n_{50max} and q'_{wd} it is the building with the highest L_{wd}/V that will get the highest C_{wd}. For evaluation of equation (3), the variations described in table 1 were done. Subsequent description of the parametric variations, are explained in the table's order below the table.

TABLE. 1: Parametrical variations used in accordance with equation (3).

Parametrical variation	Explanation
q'_{wd}	7 different sealing techniques. In all 19 variants.
n_{50max}	Air change rate requirements of 2.5, 1.0 and 0.6 representing conventional Norwegian building regulations 2007, low energy and passive house respectively
L_{wd}/V	Maximum, average and minimum values were investigated

The sealing techniques can be obtained from Relander (2008) or Proskiw (1994). The former is used in this paper, and a total of 7 different sealing techniques will be used. Totally this results in 19 variations. The calculations will be based on 50 Pa mean pressure difference. More detailed information about the measurements can be found in Relander (2008). It is important to notice that these are *one-layer* measurements. Each sealing method was tested *alone* without mineral wool or any other sealing technique.

In the second row of table 1, the air change rate requirements appear. 2.5 h^{-1} is for residential buildings only, and set by the Norwegian building regulation, TEK 2007. There exists no official requirement for low- energy buildings today, but it is common to use 1.0 h^{-1}. For passive houses the requirement is 0.6 h^{-1} (Feist, 2002).

As implied by equation (3), the L_{wd}/V is of importance for the C_{wd} ratio. For the case of L_{wd}/V, an *arbitrarily* building could be formulated with basis in assumptions of the geometry. This was done by Proskiw (1994). The disadvantage of this, is the consequences of the assumptions on the results since L_{wd}/V can vary among buildings. Alternatively, a statistical representative sample of various wood-frame buildings could have been picked out. From that sample the variation in the L_{wd}/V could be analyzed. Since this is a comprehensive procedure, a middle course was chosen. This was not a statistical representative method, but of interest for the building industry.

From 7 selected wood-frame buildings, L_{wd} and V were collected. First the average of L_w for all the 7 buildings was calculated. Secondly the average of V for all the buildings was calculated. The ratio of this gave an average L_{wd}/V belonging to the so-called *average building*. These 7 buildings were of approximately the same gross area, and are built by Mesterhus, a Norwegian wood-frame house contractor. The buildings had a gross area of around 175 m^2 and can say to indicate typical Norwegian building tradition of today's standard wood-frame houses.

The L_{wd}/V for the average building was compared with the one with the highest and the lowest L_{wd}/V of the 7 buildings. This was to see the effects on different buildings. Since the average building is a *result* of data collection, the definition of the average building will appear from subsequent chapters.

To evaluate variations among the 7 buildings, the empirical standard deviation and empirical relative standard deviation were used. They are referred to as σ and $\sigma_{relative}$. Since no attempt was made on picking a statistical representative sample, the sample standard deviation, S and $S_{relative}$ were not used.

3. Results

3.1 Variations among the 7 buildings

Before defining the average building, the 7 buildings forming the basis of the average building have to be investigated. The buildings with their respective values from the data collection are shown in ascending order by volume in table 2. The table presents the gross area, A_g of the buildings ranging from 172 m^2 to 179.60 m^2. The gross areas and volumes are indicated by columns 2 and 3 respectively. The number of windows and doors is

indicated in columns 4 and 5. In columns 6-8 the total lengths of window and door joints as well as their respective sum is indicated. Beneath the horizontal line in the middle of the table, the mean, maximum, minimum values and σ and $\sigma_{relative}$ are indicated.

TABLE. 2: Wood-frame buildings of gross area around 175 m^2 from Mesterhus sorted in ascending order by volume.

			Number of		Total lengths of		
Building	Gross area A_g [m^2]	Volume V [m^3]	Windows [-]	Doors [-]	Windows L_w [m]	Doors L_d [m]	L_{wd} [m]
Nelia	179.60	398	20	4	91.60	24.60	116.20
Mie	176.00	411	25	3	103.50	19.60	123.10
Karita	172.00	413	19	3	85.60	21.60	107.20
Miranda	173.00	416	32	4	115.40	24.80	140.20
Kirsten	176.00	423	24	4	111.20	28.80	140.00
Mina	172.00	477	20	4	79.80	26.00	105.80
Marion	176.00	493	28	4	127.00	24.60	151.60
Mean	174.94	432.90	24.00	3.71	102.01	24.29	126.30
Max	179.60	493	32	4	127.00	28.80	151.60
Min	172.00	398	19	3	79.80	19.60	105.80
σ	2.57	34	4.44	0.45	16.71	2.33	16.64
$\sigma_{relative}$	1 %	8 %	19 %	12 %	16 %	10 %	13 %

From table 2, it is seen that the number of doors differs less than the number of windows. Consequently the total lengths of the joints of doors differ less than for windows. The influences on the L_{wd}/V ratio is shown in figure 1. Figure 1 shows V, L_{wd}, L_{wd}/V and the sum of window and door area per gross area, A_{wd}/A_g . A_{wd}/A_g will have influence on L_{wd} and is therefore included in the figure. A_{wd}/A_g usually varies around 0.2 for residential buildings.

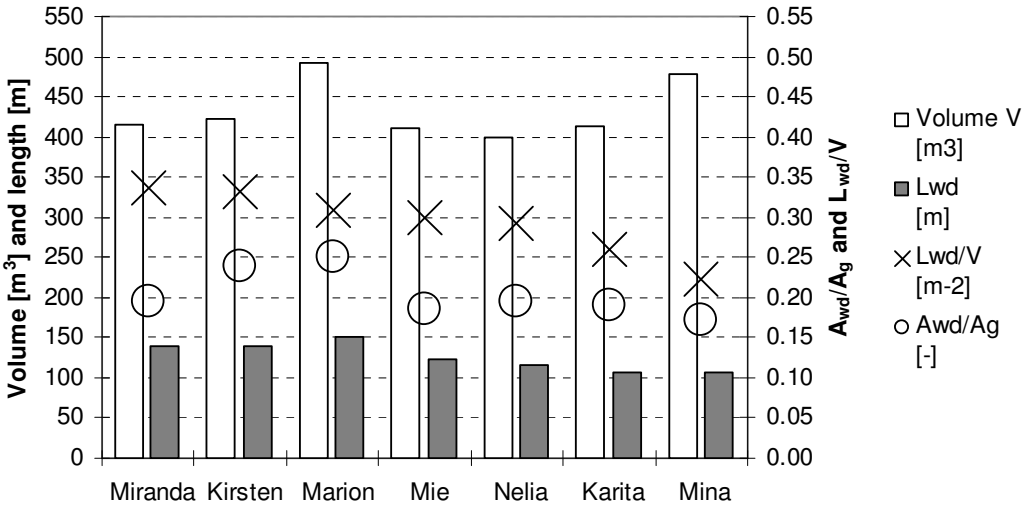

FIG. 1: For the 7 houses the figure shows the variation of V and L_{wd} on the primary axis and L_{wd}/V and A_{wd}/A_g on the secondary axis. The figure is sorted from left to right in descending order by the L_{wd}/V ratio.

Intuitively, one would believe a correlation between A_{wd}/A_g and L_{wd} to exist. This is true for some of the buildings in this selection. Mina and Marion have the smallest and highest values of A_{wd}/A_g. They also have the longest and shortest lengths of joints, respectively. From the same reasoning, one could expect the difference in L_{wd} for Nelia and Miranda to be negligible. Inspection of the figure shows that L_{wd} are different. For these two buildings the amounts of windows differs considerably as can be seen in table 2.

When it comes to the L_{wd}/V ratio, it is clear that the higher the L_{wd}, the higher the fraction L_{wd}/V. For this selection of buildings, it is Marion that has the highest L_{wd}, but the highest L_{wd}/V ratio is for Miranda. For Marion, it is clear that the higher volume causes the L_{wd}/V not to be the biggest for this selection of 7 buildings. The smallest L_{wd}/V is for Mina.

3.2 Defining the average building to be used for the prediction of C_{wd}

With basis in table 2, the average building is now defined as the ratio of the mean value of L_{wd} to the mean value of V. This appears from table 3. A discussion of the numbers and geometries of windows and doors for this non-physical building could have been done, but since this is beyond scope here, it is not included.

TABLE. 3: Description of the average building used for the prediction of C_{wd}.

Building	Volume V [m^3]	L_{wd} [m]	L_{wd}/V [m^{-2}]
Average building	432.90	126.30	0.29

For the average building, the L_{wd}/V will be 0.293 when defined as in the left hand side of equation (4), and 0.292 as in the right hand side. This difference is therefore negligible. For simplicity, and to match with equation (3), the right hand side of equation (4) is used henceforth.

$$Average\left[\frac{L_{wd}}{V}\right] \neq \frac{Average\left[L_{wd}\right]}{Average\left[V\right]} \tag{4}$$

3.3 The variation of C_{wd} depending on sealing technique, air change rate requirement and building

Figure 2 shows the C_{wd} ratio for the average building with different sealing techniques and air change rate requirements. Additionally the effects of choosing a building with favourable and unfavourable L_{wd}/V compared to the average building are indicated by variation bars. For all sealing techniques and air change rate requirements, the unfavourable building Miranda deviates from the average building upwards by 16 %. Correspondingly, Mina, which is the favourable building, deviates downwards by 24 %.

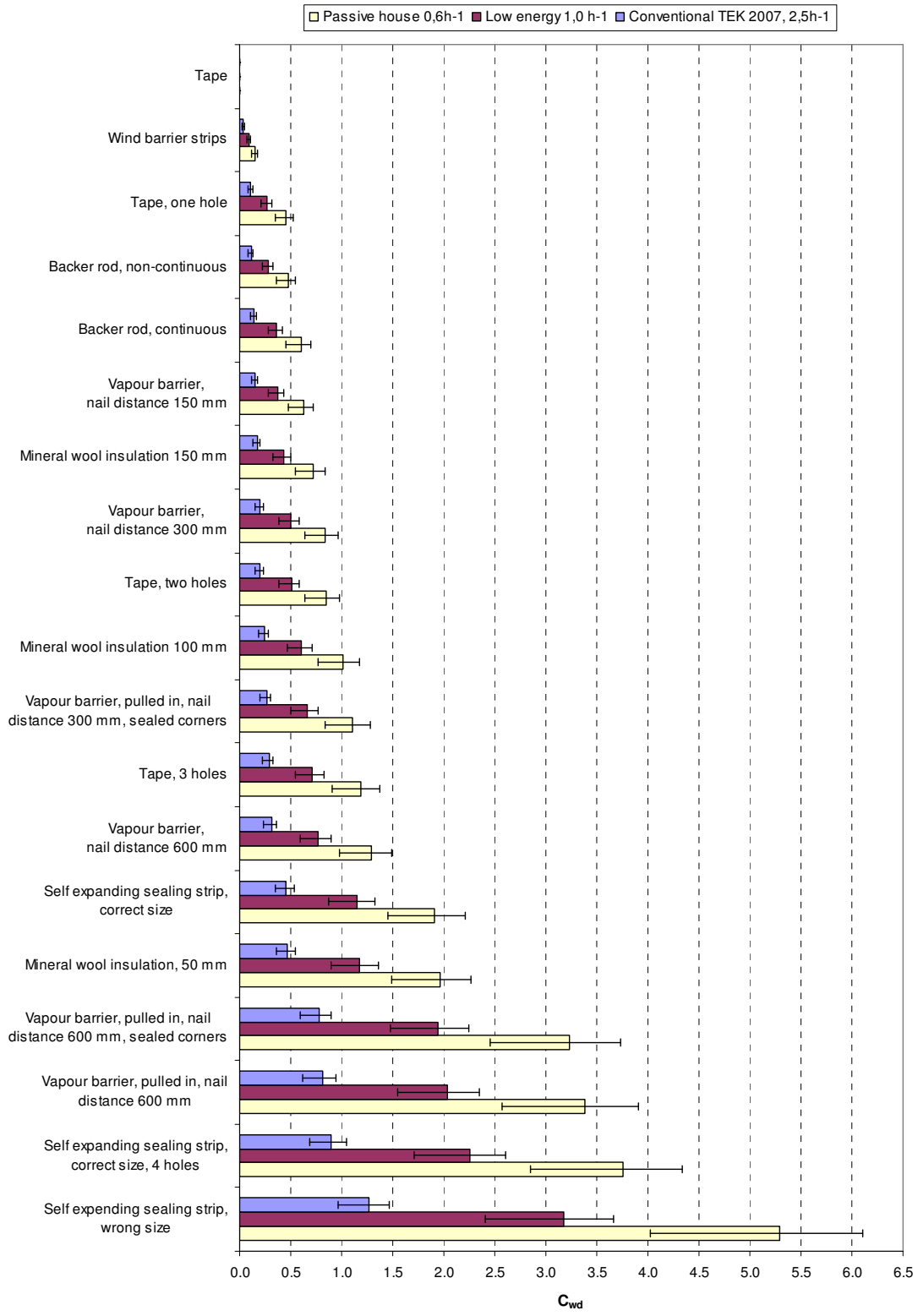

FIG. 2: The magnitude of C_{wd} depending on sealing technique, air change rate requirement and building. The variation bars indicates from the left the following 3 buildings: Mina, the average building and Miranda.

4. Discussion and conclusions

It is becoming customary to carry out blower door measurements during construction. Typically this is done as a first step when the wind barrier is finished, and secondly after completion. This can also be supplied with measurements after the vapour barrier is finished.

All values in figure 2 are for each sealing technique alone. Figure 2 is therefore best suited for discussing the effects of sealing techniques of joints when the air leakage of the building with wind barrier *only* is tested. For this case, the joints could be sealed with either tape, wind barrier strips, backer rod with mastic or self expanding sealing strips. These can be called outer sealing techniques among the ones tested.

For the measurement of backer rod, mastic was not included. With basis in figure 2, it is reason to believe that backer rod combined with mastic can give air tight joints. Similarly wind barrier strips or tape can be air tight and suitable sealing techniques also for passive houses. For the self expanding sealing strip, figure 2 shows that only TEK 2007 standard can be achieved for the first step blower door test of the wind barrier. When using tape, figure 2 indicates that this sealing technique can be sensible to workmanship. This is most notable when aiming at low energy or passive house standard for buildings with an unfavourable L_{wd}/V.

One can also imagine a practical case due to faulty workmanship. If neither mineral wool nor outer sealing is used, there is reason to believe that relying on the air tightness of the vapour barrier can be discussable, as implied by figure 2. This is more notable for buildings with unfavourable L_{wd}/V aiming at passive house standard.

In general figure 2 also shows that the effect of choosing a favourable sealing technique is more important for passive house and low-energy buildings compared to for TEK 2007. Further the figure implies that the geometry of the windows is more important during first step blower door test than for the final blower door test. For the final blower door test the joints should be sealed with mineral wool and inner sealing as well.

Additionally, the effect of unfavourable L_{wd}/V is more prominent for the less air tight sealing techniques. Figure 1 implies that there are deviations among the total lengths of joints of the various buildings, even though the gross area and A_{wd}/A_g are virtually the same. Although the data collection is scanty, it can to some extent illustrate the importance that the number of doors and windows can have on C_{wd}. From this it is seen that a certain prediction of L_{wd} cannot be done with basis in A_{wd}/A_g. One needs to know the geometry and numbers of the windows also. Big L_{wd}/V therefore is likely to be unfavourable. For a *given* A_{wd} therefore bigger windows should be chosen in preference to smaller.

From figure 1, the fact is illustrated that higher volume of a building reduces the C_{wd} ratio. Therefore a building with unfavourable number and geometries of windows can compensate by increasing the ceiling height. If the volume of Marion was reduced to similar values as for the other buildings, it would get the highest C_{wd}. This illustrates a possible conflict with energy efficient architecture. For design purposes a useful ratio taking this into consideration could be L_{wd}/A_g.

In practice there are many contributions to the total air leakage of a building. Air leakages from joints are only *one* of them. In order to forecast if a building will fall within the air change requirements in practice, one needs to know all the contribution coefficients C_i of the entire building envelope for the specific building. In sum these have to be less than 1 as stated in equation (5).

$$C_{50\max} = \frac{\sum_{\text{building envelope}} q_i}{n_{50\max} V} = \sum C_{walls} + C_{floor} + C_{roof} + \ldots + C_{wd} \leq 1 \qquad (5)$$

C_{wd} can theoretically be determined in a design phase of a specific building. But the magnitude of the other terms in equation (5) is unknown. Therefore C_{wd} cannot be used to forecast which buildings that will fall within the air change rate requirement and which that will not.

Finally, it should be mentioned that it is common to install mineral wool insulation in the joints. From figure 2 it is seen that this will contribute considerably to the air tightness. In low-energy and passive houses, the depth of the joints can exceed the ones in Relander (2008). It is therefore clear that this will reduce the air leakages from the joints.

5. Acknowledgements

This paper has been written within the ongoing SINTEF strategic institute project "Climate Adapted Buildings". The authors gratefully acknowledge the Research Council of Norway.

Thanks also Gjermund Grønhaug for data collection of great value.

6. References

Feist, W. (2002). Zertifikat – qualitätsgeprüftes Passivhaus, (Certificate – quality approved passive house), Passiv Haus Institut, Darmstadt, Germany (in German)

Proskiw, G. (1994). Air leakage characteristics of various rough-opening sealing methods for windows and doors, Energy Technology Branch, CANMET – Energy Sector, Department of Natural Resources Canada, Ottawa, Ontario

Relander, T.O. (2008). Air tightness performance of different jointing methods for windows in wood-frame buildings, submitted to Nordic Symposium on Building Physics 2008, Copenhagen

TEK (2007). Technical regulations under the planning and building act, 2007, National Office of Building Technology and Administration Norway

Manual for Improving the Energy Performance of Existing Buildings using Timber and Derived Timber Products

Dipl. -Ing. Michaela Hoppe, Architect
Lehrstuhl für Bauphysik, Technische Universtität München;
hoppe@tum.de, www.bp.bv.tum.de

KEYWORDS: *carbon dioxide emissions, building stock, design principles, energy consumption, manual, timber.*

SUMMARY:
Against a background of advancing climate change, brought about by CO_2 emissions, and rising energy prices, it becomes ever more important to use renewable energy sources and, above all, to improve the energy performance of existing buildings. A significant step in this connection is the introduction of energy certificates for buildings within the EU, which must be accompanied by recommendations for the cost-effective improvement of the building's energy performance.

The upcoming introduction of this Energy Performance Certificate was the key reason for a research project of the Department of Building Physics at the Technische Universität München. The project's primary aim is the development of design principles that will lead to a reduction of energy consumption and carbon dioxide emissions in the built stock, using renewable and sustainable materials such as timber and timber derived products. The resulting manual provides technical support for energy consultants in helping them to choose ecological and reasonable energy refurbishment measures. Technical drawings of the particular measures are rounded off with explanation of the main structural and physical aspects as well as cost-effectiveness.

1. Energy savings potential in existing buildings in Germany

In Germany around 30% of end-use energy consumption – and therefore approx. 20% of CO_2 emissions – is accounted for by private households. The main portion of this, at around 76%, falls on space heating (Figure 1).

Against a background of advancing climate change, brought about by CO_2 emissions, and rising energy prices, it becomes ever more important not only to use renewable energy sources and, above all, to improve the energy performance of existing buildings. A comparison between the energy savings that can be gained through targeted

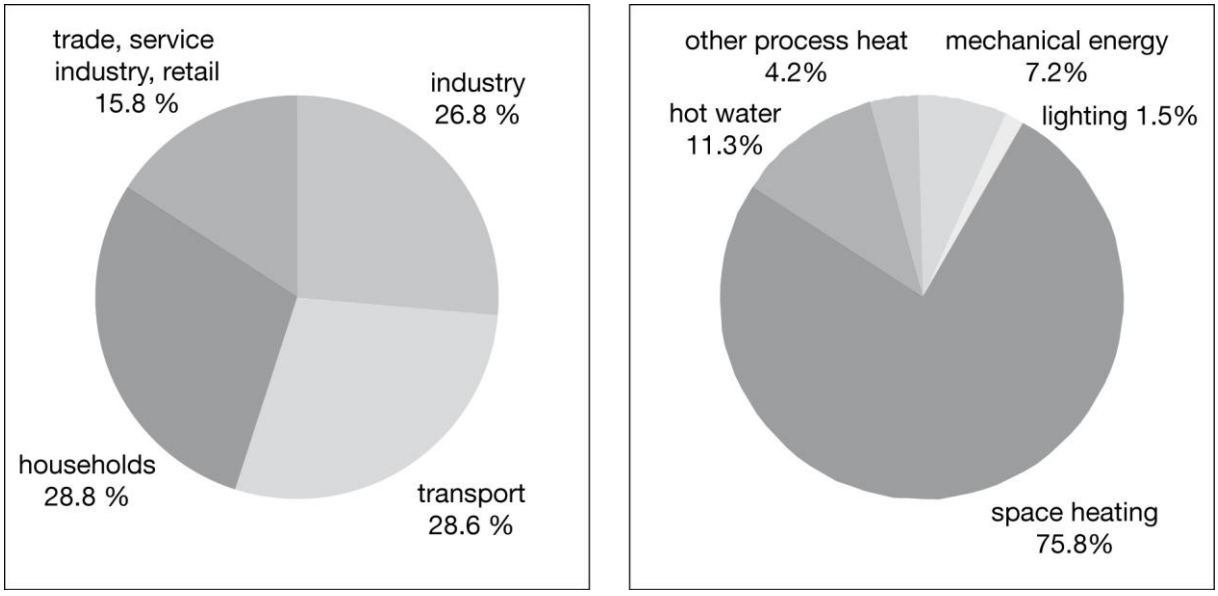

FIG. 1: Left: Breakdown of end-use energy consumption. Right: Breakdown of energy consumption in private households. Figures for 2005 [BMWi]

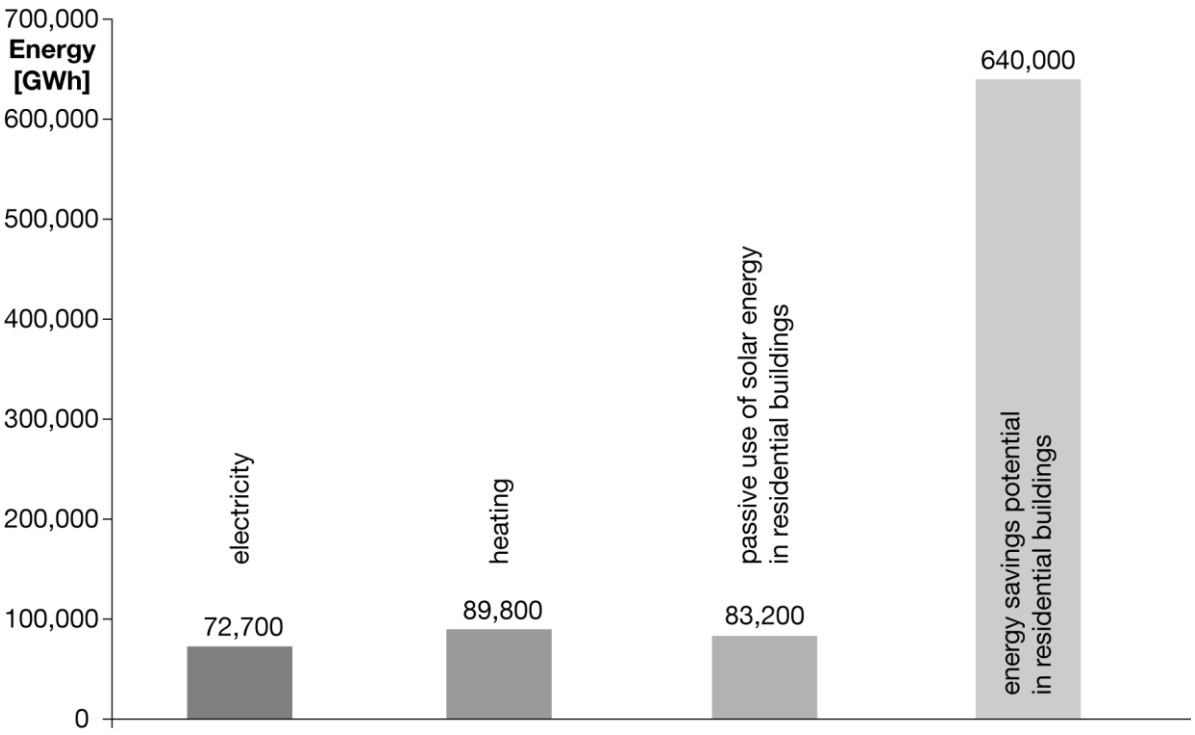

FIG. 2: Energy supplied from renewable sources in Germany in 2006 [BMU], compared to the energy savings achievable through improving the energy performance of existing residential building [Hauser G.]

improvements to existing buildings and the amount of energy currently generated from renewable sources illustrates the potential in this field. In 2006, for example, the estimates for residential buildings alone exceed many times the total figures for energy generated from renewable sources (Figure 2).

There is therefore tremendous potential for saving energy in buildings – primarily through improving thermal insulation, but also through a range of other targeted measures.

2. Energy performance certificates for buildings

A significant step in this connection is the introduction of energy certificates for buildings (Figure 3). Of interest to property owners, buyers and tenants, this certificate sets out in compact form the annual energy requirements of the building in question. It also comes with recommendations on how to modernise the building (structure and installations) with the aim of reducing energy consumption. One problem with this new system is that the persons involved in issuing these certificates come from a range of technical backgrounds, as provided for in the Energy Conservation Regulations 2007 (*Energieeinsparverordnung 2007)* [BMVBS]. An important aspect of the research was therefore not only to develop sensible eco-friendly improvement strategies as regards a building´s structure and physical properties, but also to produce a practical manual that would give professional support to those persons whose job it is to issue the energy certificates, but whose core competence does not lie directly in the field of construction (e.g. installations engineers, chimney sweeps etc.)

3. Manual of energy-efficiency improvements in buildings

Because of the above-mentioned issue of rising energy costs, many property owners are willing to undertake measures to reduce the energy consumption of their buildings. Yet often there is great uncertainty about what measures to take and how these changes will impact on the look of the building. Worries about possible complications, e.g. damp, also affect decisions, as do concerns about the actual cost-effectiveness of any measures taken.

This frequently leads to owners opting for conventional solutions, such as a composite thermal insulation system based on rigid foam polystyrene. A central aim of the study was to identify sensible alternatives to conventional

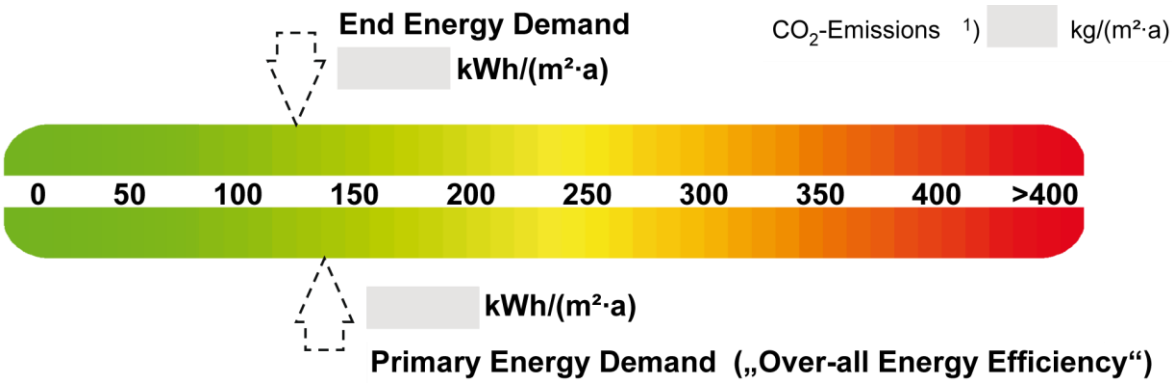

FIG. 3: Display of energy demand according to the energy certificate for residential buildings, ccording to the Energy Conservation Regulations 2007 (Energieeinsparverordnung 2007) *[BMVBS]*

modernisation approaches, alternatives that are based on the use of a material that has good ecological, structural and physical properties, is also easy to work and in addition offers great scope in terms of design such as timber and derived timber products.

Timber is an ideal construction material for energy refurbishment measures, not only for the positive carbon dioxide balance (Figure 4) and good recyclability but also for its technical qualities. As a lightweight but strong material, timber is an excellent material for facade cladding [Wegener G., Zimmer B.] [Herzog T., Krippner R., Lang W.].

The resulting manual takes a detailed look at the various options for modernisation, and as such is intended for both energy-certificate issuers and building owners who are interested in more in-depth information. The main aspects covered in the manual are: how to assess the energy performance of an existing building; a review of the requirements that have to be met; a presentation of the options for modernisation; the criteria for selecting options; an itemisation of the expected building costs; and an investigation of the cost-effectiveness of the individual measures.

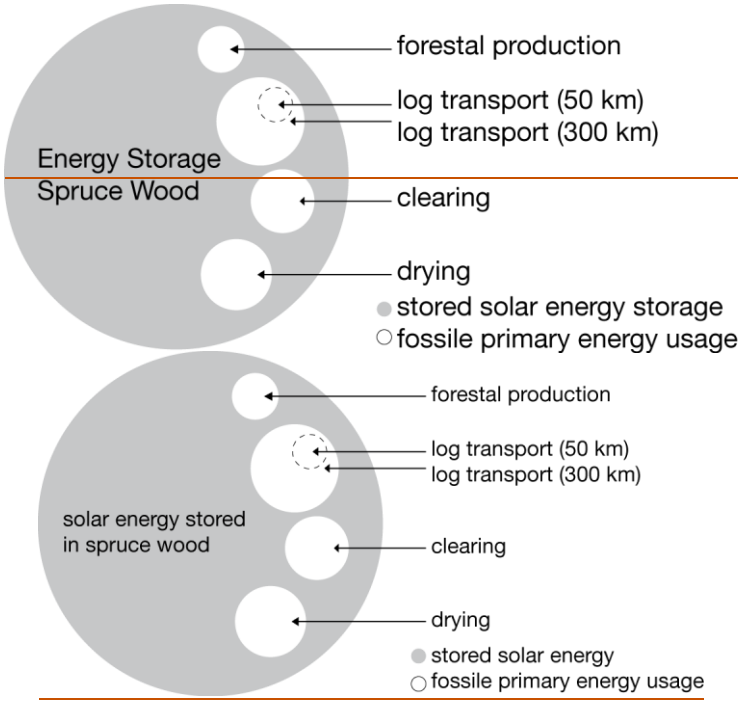

FIG. 4: Energy balance fortimber production, white circles showing the cumulated fossile energy demand in comparison to the amount of energy stored within the material (grey circle) [Wegener G., Zimmer B.]

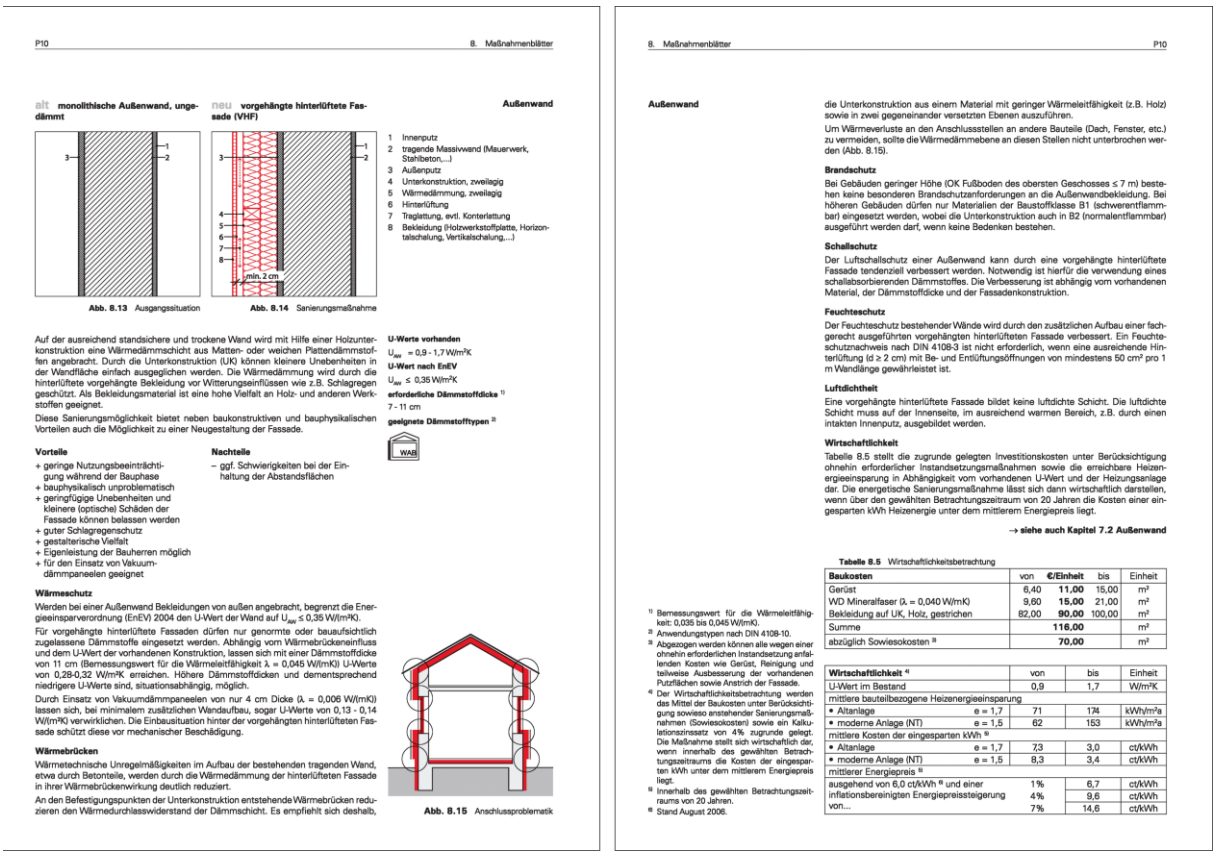

FIG. 5: Sample fact sheets: Insulating a monolithic exterior wall by fitting a ventilated façade. Each double page contains illustrations to represent the situation before and after measures are taken, a short description of the proposed measure, a summary of advantages and disadvantages, an explanation of the main structural and physical aspects and a cost-effectiveness table (see Table 1 for detailt).

4. Fact sheets

The manual is accompanied a series of fact sheets on the recommended measures (Figure 5) which set out, on a double page, what is involved in each case. They are directed primarily at the property owner and can be included with an energy certificate to provide further information on the recommended modernisation measures. The fact sheets contain a short description of the proposed measure, and illustrations to represent the situation before and after measures are taken. Plus a summary of the advantages and disadvantages, as well as an explanation of the main structural and physical aspects such as thermal insulation, thermal bridges, damp proofing, acoustic insulation and fire protection. To conclude the main parameters affecting the cost-effectiveness of the particular measures are set out in a table.

5. Cost-effectiveness analysis

The cost-effectiveness of each individual measure to improve energy efficiency is illustrated in the form of a table (Table 1) which compares the mean costs of carrying out building work to save one kilowatt-hour of heating energy with the mean energy costs to be expected in the future. A range of energy parameters (U-value in the existing building, heating system) is taken into account. An individual modernisation measure is thus only considered cost-effective when the costs for the kilowatt-hour saved lie below the mean energy costs in the time period. This table can help in the initial assessment of the cost-effectiveness of a particular modernisation measure.

6. Conclusion

As the investigation of the individual modernisation strategies showed, the cost-effectiveness of the individual measures varies considerably according to the particular situation of the building in question. Future developments in energy prices also play an important role. The investigation showed that it is certainly possible within the life cycle of the property (here: 20 years) to recoup the initial investment costs, even in difficult situations. This is only achievable, however, with proper professional advice and planning for property in question. Many modernisation strategies, however, such as insulating the uppermost floor, are so simple and cheap to carry out that they are always cost-effective. The resulting manual of energy-efficiency improvements in buildings will be published as soon as the research project is finished and accepted by the sponsor. It is also planned to make the study available for consultation in digital form on the website of 'Holzbau der Zukunft' (*Timber Structures for the Future*) (www.holzbauderzukunft.de).

TABLE. 1: Cost-effectiveness (sample table): Insulating a monolithic exterior wall by fitting a ventilated façade.

Building costs	from	**€/unit**	to	unit
Scaffolding	6.40	**11.00**	15.00	m^2
Mineral fibre insulation (λ = 0.040 W/mK)	9.60	**15.00**	21.00	m^2
Cladding on frame, wood, varnished	82.00	**90.00**	100.00	m^2
Total		**116.00**		m^2
minus base costs [1)]		**70.00**		m^2

Cost-effectiveness [2)]		from	to	unit
Existing U-value		0.9	1.7	W/m^2K
Mean savings in heating energy for building component				
• old system	e = 1.7	71	174	kWh/m^2a
• modern system	e = 1.5	62	153	kWh/m^2a
Mean costs per kWh saved [3)]				
• old system	e = 1.7	7.3	3.0	ct/kWh
• modern system	e = 1.5	8.3	3.4	ct/kWh
Mean energy price [3)]				
Assuming 6.0 ct/kWh [4)] and an inflation-adjusted rise in energy prices of...		1%	6.7	ct/kWh
		4%	9.6	ct/kWh
		7%	14.6	ct/kWh

1) Costs that would have been incurred anyway during necessary maintenance, e.g. scaffolding, cleaning and where needed renovation of existing render and painting the façade. These are deducted from the total.

2) The cost-effectiveness calculation is based on mean building costs, taking into account any costs that would in any case have been incurred on necessary maintenance (base costs), and an assumed interest rate on the loan of 4%. The measure is deemed to be cost-effective when within the chosen time period the costs of the kWh saved are below the mean energy price.

3) Within the chosen time period of 20 years.

4) Date: August 2006.

7. References

BKI = Baukosteninformationszentrum (Information Center for Building Costs) (2005). Objektdaten Altbau (Object Specification for Existing Buildings), BKI Baukosteninformationszentrum Stuttgart

BMWi = Bundesministerium für Wirtschaft und Technologie (Federal Ministry of Economics and Technology) (2006). Energiestatistiken, Endenergieverbrauch nach Anwendungsbereichen (Energy statistics, end-use energy consumption, according to areas of application), Date of publication: 30.05.2006

BMU = Bundesministerium für Umwelt, Naturschutz und Reaktorsicherheit (Federal Ministry for the Environment, Nature Conservation and Nuclear Society) (2007). Entwicklung der erneuerbaren Energien im Jahr 2006 in Deutschland (Development of renewable energy in 2006 in Germany), *Aktuelle Daten des Bundesumweltministeriums zur Entwicklung der erneuerbaren Energien in Deutschland im Jahr 2006 auf der Grundlage der Angaben der Arbeitsgruppe Erneuerbare Energien-Statistik (Current statistics from the Federal Ministry for the Environment on the development of renewable energy in Germany in 2006 based on information from the Working Group on Renewable Energies/Statistics)*, Date of publication: 21.02.2007

BMVBS = Bundesministerium für Verkehr, Bau und Stadtentwicklung (Federal Ministry of Transport, Building and Urban Affairs) (2007). Verordnung über energiesparenden Wärmeschutz und energiesparende Anlagentechnik bei Gebäuden (Regulations on energy-saving thermal insulation and energy-saving technical installations in buildings), *Energieeinsparverordnung 2007 – EnEV 2007 (Energy Conservation Regulations 2007)*

Hauser G. (2007). Energieeffizienz – der wesentliche Lösungsansatz (Energy efficiency – the best way forward), *wksb*, No. 58/2007, 31 – 35

Hauser G., Höttges K., Lüking R.-M., Maas A., Otto F. and Stiegel H. (2007). Energieeinsparung im Wohngebäudebestand (Saving Energy in Existing Residential Buildings), GRE - Gesellschaft für rationelle Energieverwendung Kassel

Herzog T., Krippner R. and Lang W. (2004). Fassadenatlas (Facade Construction Manual), Institut für Internationale Architekturdokumentation München, 125 – 133

Hoppe M. (2008). Energetische Sanierung von Bestandsgebäuden unter Einsatz von Holz und Holzwerkstoffen (Improving the Energy Performance of Existing Buildings using Timber and Derived Timber Products), *Holzbau der Zukunft (Timber Structures for the Future)*, to be published

Informationsdienst Holz (Timber Information Service) (2001). Modernisierung von Altbauten (refurbishment of Existing Buildings), *Holzbau Handbuch (Timber Construction Manual)*, No. 1.14.1

Wegener G. and Zimmer B. (2003). Bauen mit Holz ist zukunftsfähiges Bauen (Timber Construction means Sustainable Building), *Holzbau Atlas (Timber Construction Manual)*, Institut für Internationale Architekturdokumentation München, 47 – 49

Evaluation of a dynamic model for a cold climate counter flow air to air heat exchanger

Toke Rammer Nielsen, Associate Professor,
Department of Civil Engineering, Technical University of Denmark;
trn@byg.dtu.dk

Jesper Kragh, Assistant Professor,
Department of Civil Engineering, Technical University of Denmark;
jek@byg.dtu.dk

Svend Svendsen, Professor,
Department of Civil Engineering, Technical University of Denmark;
ss@byg.dtu.dk

KEYWORDS: *ventilation, heat exchanger, condensation, frost formation, modelling.*

SUMMARY:
This article presents measurements and calculations for a prototype counter flow heat exchanger designed for cold climates. A dynamic model of a counter flow air to air heat exchanger taking into account condensation and freezing and melting of ice has been developed and the results of the model are compared to measurements on a heat exchanger prototype. During the measurements freezing occurred in the heat exchanger and the measurements showed that the applied defrosting strategy worked. The calculations show no ice formation but the calculated temperatures are in general close to the measured values. The results show that further improvements in both the computational model and the measurements are necessary to improve the accuracy of the calculations.

1. Introduction

In cold climates heat recovery in the ventilation system is important to reduce heating energy demand in buildings. The efficiency of the heat exchanger is essential to achieve low energy demand and it is now possible to get commercial products for comfort ventilation with efficiencies close to 90%. Ventilation systems for comfort ventilation in houses remove air with a considerable content of water vapour. In Denmark a typical family of four people produces 10 kg of water vapour per day, which has to be removed through ventilation. In the heat exchanger, the exhaust air is often cooled below its dew-point temperature and water condenses. If the surface temperature is below the freezing point, the condensate freezes. Increased efficiency and application in cold climates results in temperatures below the freezing point in the heat exchanger. Frost formation typically reduces the efficiency; the heat transfer rate is reduced and the exhaust air side of the heat exchanger experiences increased pressure drops, as the frost growth blocks the air flow passage. Unless defrosting mechanisms are initialized at this point, the exhaust air flow is eventually blocked by ice. Therefore, there is a need to analyze the possibilities of efficient methods to avoid or remove frost in heat exchangers. In order to analyze the possibilities of avoiding/removing frost formation, models that can predict the dynamic performance of heat exchangers are necessary.

Condensation and frost formation in heat exchangers, with special focus on the heat transfer mechanisms that these phenomena imply, has been the subject of numerous investigations in the past. Heat and mass transfer in situations with condensation are described in Terekov et al. (1998), Jilek and Young (1993) and Brouwers and van der Geld (1996). Iragorry et al. (2004) published a review and comparative analysis of the different methods and approaches for frost formation put forth during the last 20 years of research in the field. Much of the research on condensation and frost formation is mainly focused on applications in the refrigeration industry and therefore previous findings are not necessarily applicable for air to air heat exchanges for comfort ventilation.

The purpose of the presented work is to show the validity of a computational model by comparison of measured and calculated temperature profiles for a prototype heat exchanger with a dynamic defrosting strategy for cold climates. Calculations are performed using a dynamic computational model of heat flow in counter flow air to air

heat exchangers taking into account condensation and frost formation. The model is developed to investigate defrosting strategies. The results show that the calculated temperatures in the heat exchanger are reasonable compared to the measured values, but also shows that further improvements are necessary.

2. Experimental heat exchanger

A new heat exchanger with continuous defrosting for cold climates has been developed and tests of the defrosting strategy shows promising results (Kragh et al., 2007). The heat exchanger consists of two identical sections for cyclic defrosting of one of the sections as shown in figure 1. This design ensures the possibility to remove frost from one section at a time by switching the airflows between the two sections. In that way one section is active and one section is passive regarding the heat exchange. Two electrical valves control the airflows to the two sections. The flow rate of extracted room air is adjusted so the flow through the active and passive section is 90% and 10% respectively. After an adjusted time interval the airflows switch. For the presented results the air flows switch by an interval of 56 minutes. The inlet airflow also switches between the two sections but is always 100% or 0%. The idea is that 10% of airflow of warm extracted air is used to defrost the passive part of the heat exchanger. In warm periods where no freezing occurs, both sections are used simultaneously, maximizing the heat transfer area and thereby the efficiency of the heat exchanger. The heat exchanger is designed for a typical single-family house with a floor area of 100 m² to 140 m². Fulfilling the demands of the Danish building code the necessary air change rate should be 0.5 h^{-1}, which is approximately 150 m³/h.

The heat exchanger made of 5 mm double polycarbonate plates with a wall thickness of 0.5 mm. The final heat exchanger was made of 10 plates placed with a distance of 4 mm as shown in figure 2. The inlet air (cold air) flows in rectangular ducts of the polycarbonate plate and the exhaust air (warm air) flows between the plates. The calculated values of heat transfer coefficients on the exhaust side (warm air) and inlet side (cold air) are 26.3 W/(m² K) and 22.9 W/(m² K) (Kragh et al., 2007). A prototype of the heat exchanger is tested in a test facility that is able to supply air at temperature approximately -10 °C in order to investigate the defrosting strategy. The layout of the test facility is shown in figure 3. Temperature, air flow and relative humidity are measured at inlet and outlet conditions for the two air streams. On the exhaust side temperature is measured five places inside the heat exchanger. Figure 3 shows the position of the thermocouples and measurement of the airflows.

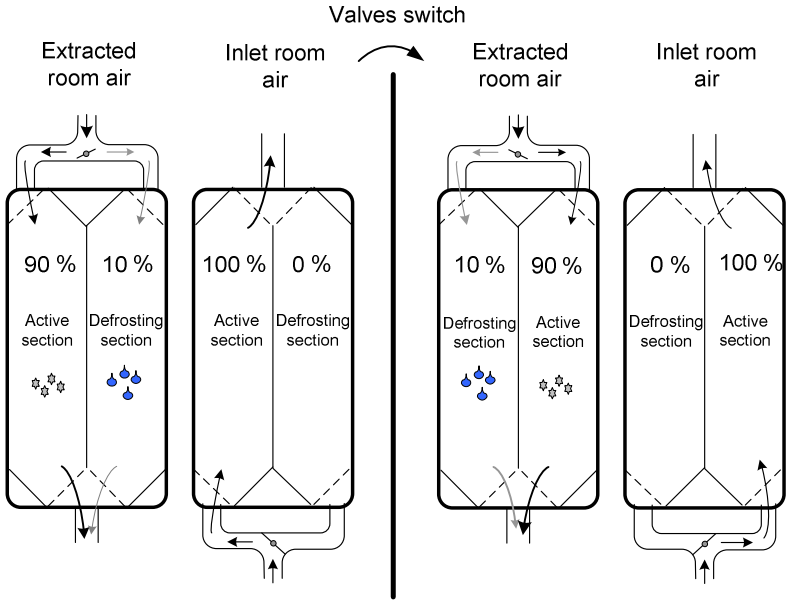

FIG. 1: Heat exchanger principle with defrosting strategy for cold climates

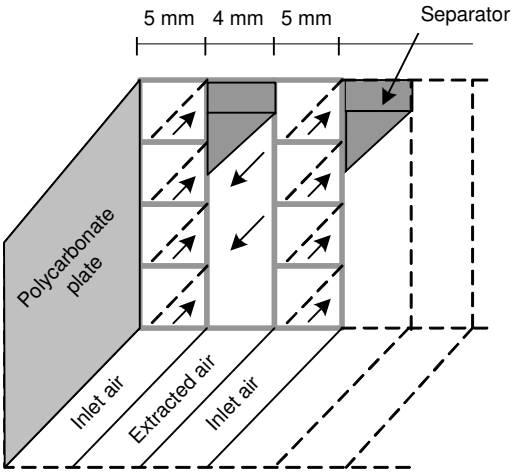

FIG. 2: Layers of 5mm double polycarbonate plates are placed with a distance of 4 mm to provide ducts for inlet and exhaust air. The final exchanger was made of 10 plates where the inlet air (cold air) flows in rectangular ducts of the polycarbonate plate and the exhaust air (warm air) flows between the plates

.

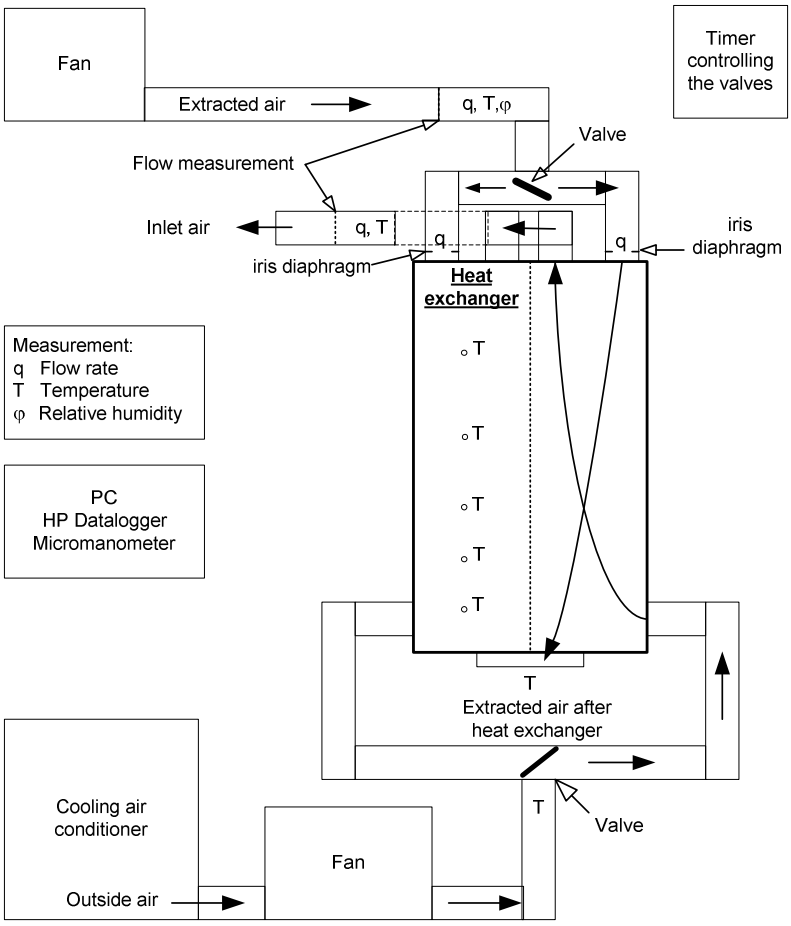

FIG. 3: Layout of prototype test facility. The positions for measurements of temperature, flow rate and relative humidity are indicated.

3. Heat exchanger model

A dynamic model of counter flow air to air heat exchangers for comfort ventilation taking into account condensation and freezing has been developed and implemented in Simulink (Nielsen et al., 2008). The heat exchanger model is developed in a 2-D time dependent formulation where the heat exchanger is divided into a number of control volumes as shown in figure 4. The heat exchanger is split into a finite number of segments perpendicular to the flow directions and each segment contain control volumes for the warm air stream, wall material and the cold air stream. The temperature nodes for the air streams are placed at the border where the air leaves the control volume and the temperature node for the heat exchanger wall material is placed in the centre of the wall material.

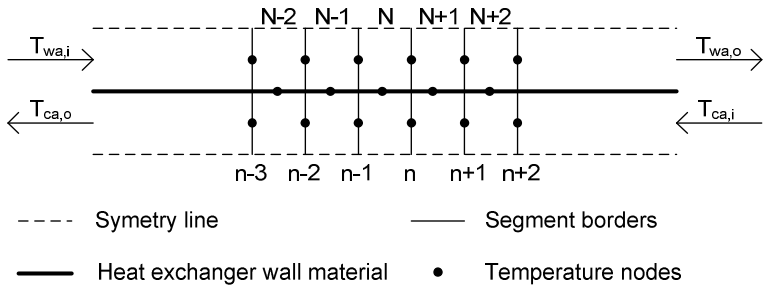

FIG. 4: Discretization of the heat transfer problem. Segments are indexed with capital letter N and segment borders are indexed with small letter n as shown.

The warm air side is characterized by an inlet temperature $T_{wa,n-1}$, inlet moisture content $x_{wa,n-1}$, outlet temperature $T_{wa,n}$, outlet moisture content $x_{wa,n}$, mass flow of dry air m_{wa}, and heat capacity of the control volume $C_{wa,N}$. The water (condensate and water from a previous control volume) is characterized by an inlet temperature $T_{w,n-1}$, inlet mass flow $m_{w,n-1}$, outlet temperature $T_{w,n}$, and outlet mass flow $m_{w,n}$. The mass flow of water leaving the control volume is calculated from a mass balance based on the moisture entering and leaving the control volume, the water that enters from the previous control volume and the rate of ice mass change, $\dot{M}_{ice,N}$, in the control volume. The ice in the control volume is characterized by the mass of ice $M_{ice,N}$. The heat capacity of water and ice is not taken into account. The heat exchanger wall material divides the two airstreams and is characterized by the wall temperature $T_{p,N}$, and wall heat capacity $C_{p,N}$. The cold air side is characterized by an inlet temperature $T_{ca,n}$, inlet moisture content $x_{ca,n}$, outlet temperature $T_{ca,n-1}$, outlet moisture content $x_{ca,n-1}$, mass flow of dry air m_{ca}, and heat capacity of the control volume $C_{ca,N}$. The heat transfer from wall material to the warm and cold air streams are given by the heat flows $\Phi_{wa,N}$ and $\Phi_{ca,N}$. The energy flows for each control volume in the segments and the mass balance for water are given by

$$C_{wa,N}\frac{dT_{wa,n}}{dt} = \left(h_{wa,n-1} - h_{wa,n}\right)\cdot m_{wa} + \Phi_{wa,N} + c_{pw}\cdot\left(m_{w,n-1}\cdot T_{w,n-1} - m_{w,n}\cdot T_{w,n}\right) \quad (1)$$

$$C_{ca,N}\frac{dT_{ca,n-1}}{dt} = \left(h_{ca,n} - h_{ca,n-1}\right)\cdot m_{ca} + \Phi_{ca,N} \quad (2)$$

$$C_{p,N}\frac{dT_{p,N}}{dt} = -\Phi_{wa,N} - \Phi_{ca,N} + H_{n-1}\cdot\left(T_{p,N-1} - T_{p,N}\right) + H_{n}\cdot\left(T_{p,N+1} - T_{p,N}\right) \quad (3)$$

$$0 = m_{w,n-1} - m_{w,n} + \left(x_{wa,n-1} - x_{wa,n}\right)\cdot m_{wa} - \dot{M}_{ice,N} \quad (4)$$

where h_{wa} and h_{ca} are the enthalpy of the moist air in the warm and cold air streams, H is the heat transfer coefficient for the heat flow in the wall material perpendicular to the air flows and c_{pw} is the heat capacity of water. Heat is transferred to the heat exchanger wall material by convection and phase changes and in the axial direction through the heat exchanger material. Phase changes only occur on the warm side of the heat exchanger where the air is cooled. It is assumed that the phase changes occur on the surface of the wall material and that the heat related to the phase change is absorbed directly in the wall material. Condensation occurs when the saturation moisture content of the air leaving the control volume is lower than the moisture content of the air entering the control volume. In this situation it is assumed that the air leaving the control volume is saturated

with moisture otherwise the moisture content is unchanged. Freezing takes place when the wall temperature is below 0 °C. During freezing it is assumed that all water flowing into the control volume and all condensate produced in the control volume freezes. During melting it is assumed that the temperature of the wall material is 0 °C until all the ice in the control volume is melted. Further details on the model and implementation in Simulink are described in Nielsen et al. (2008).

4. Results

Calculated and measured results are compared for two experiments where freezing was observed during the experiments. During the experiments the conditions of the air flows were very constant and the conditions for the simulations are based on average values from the experiments. The conditions used in the simulations for the two experiments are given in table 1. The heat exchanger is modelled using 10 segments. The segments are placed so the boundaries of five segments are located at temperature measurement points in the experimental setup. Table 2 summarises the size of each segment, their location from the top (where exhaust air enters the heat exchanger) and temperature measurement points. The segments are not of equal size. Condensation and frost will mainly occur in the bottom part of the exchanger and the heat exchanger is therefore divided into smaller segments in the lower part.

TABLE 1: Temperatures, moisture content and air flows used as input to the computational model for the two experiments.

	Ex. 1	Ex. 2
Indoor air temperature, °C	21.5	20.6
Indoor moisture content, kg/kg	0.0096	0.0076
Outdoor air temperature, °C	-6.0	-6.4
Air flow on exhaust (warm) air side, m³/s	0.0330	0.0222
Air flow on inlet (cold) air side, m³/s	0.0306	0.0218

TABLE 2: Size and location of each segment in the model of the heat exchanger. Distances are given from the top where exhaust air enters the heat exchanger. Points where temperatures are measured in the experimental setup are marked by X.

Segment nr.	Area, m²	Distance, m	Temperature measurement
		0	X (Extracted air)
1	0.5 · 2.18		
		0.22	X
2	1.98		
		0.42	
3	2.48		
		0.67	X
4	4.46		
		1.12	
5	2.97		
		1.42	X
6	1.49		
		1.57	
7	1.49		
		1.72	X
8	1.49		
		1.87	
9	1.49		
		2.02	X
10	0.5 · 2.18		
		2.24	X (Outlet air)

Only one section of the heat exchanger is modelled and the results show temperatures for both the active and inactive period. The air flow of exhaust air switches between 90% and 10% of the total flow given in table 1 during the active and inactive period. The air flow of inlet air switches between 100% and 0% of the total flow given in table 1 during the active and inactive period. The air flows switch with an interval of 56 minutes.

Figure 5 shows the measured and calculated temperature profiles through the heat exchanger at the end of the active period for the two experiments. The temperature at x = 0 m is the boundary condition of the exhaust air. The measured results are shown for three different active periods and are very similar. The calculations are performed with the moisture content from the experiments and for a case with no moisture in the exhaust air. It is seen that the moisture content of the exhaust air has a large influence on the temperature profiles. The calculated and measured temperature profiles in the heat exchanger are in good agreement but a large deviation is found for the outlet temperature at x = 2.24m in experiment 1. In both cases, the calculated outlet temperatures are higher than the measured values. During the experiment freezing was observed in the heat exchanger. The calculations at the other hand show no freezing in the heat exchanger at the given conditions.

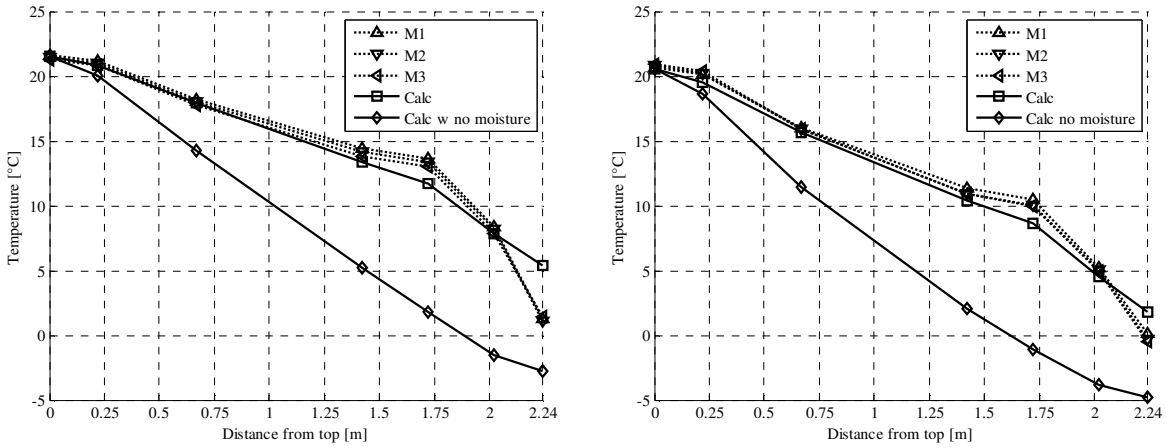

FIG. 5: Measured (dotted line) and calculated (full line) temperature profiles through heat exchanger on the exhaust side at the end of the active period. The calculated temperature development without condensation shows the significant influence of the moisture content. Left: Results for experiment 1. Right: Results for experiment 2.

The model calculates the dynamic development of temperatures in the heat exchanger as a function of time. The measured and calculated temperatures at the five measurement points inside the heat exchanger are shown in figure 6 for the two experiments. The figure starts with an active period and shows four periods of 56 minutes. During the active periods the calculated and measured temperatures are in good agreement. During the inactive periods the measured temperatures rise more rapidly than the calculated temperatures. At the end of the inactive period all the measured temperatures end up close to the temperature of the exhaust air with the exception of the lowest measured temperature. The calculated temperatures show a slower rise and are further from the exhaust conditions at the end of the inactive period. The results for experiment 1 in figure 6 (top) shows that all the calculated temperatures are close to the exhaust conditions at the end of the active period and a large deviation is found compared to the measured temperatures for the lowest point in the heat exchanger. The results for experiment 2 in figure 6 (bottom) shows that only the two top most calculated temperatures are close to the exhaust conditions at the end of the active period. The results show a larger deviation compared to the measured values in the middle of the heat exchanger, but for the lowest measurement point the calculated and measured values are in good agreement at the end of the inactive period.

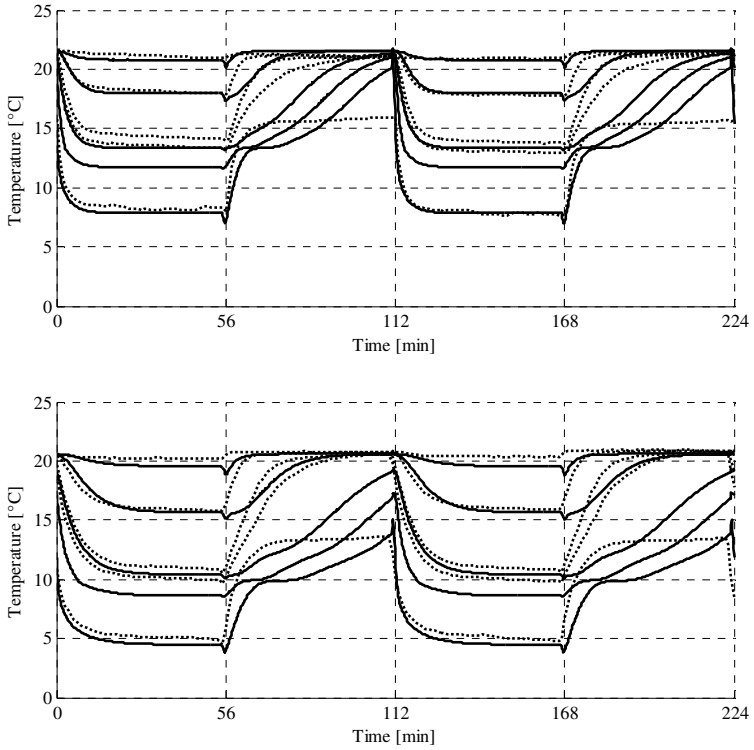

FIG. 6: Measured (dotted lines) and calculated (full lines) temperatures inside the heat exchanger. The curves show from the top down the exhaust air temperatures at distances 0.22m, 0.67m, 1.42m, 1.72m and 2.02m from the top of the heat exchanger. Top: Experiment 1. Bottom: Experiment 2.

During the inactive period there is no flow of inlet air (cold air) in the heat exchanger and in the model it is assumed that there is no heat transfer between the heat exchanger plate and the inlet air stream during this period. In the real situation heat transfer due to natural convection is present, which may account for some of the deviations between the measured and calculated temperatures during the inactive period.

Several of the measured values are uncertain. The measurement of temperatures on the exhaust side inside the heat exchanger is done by thermocouples on a string running through one duct. The distance between the plates in the duct is 4 mm and the thermocouples can be in more or less contact with the heat exchanger wall. In addition, the temperatures are only measured in one duct, so non uniform conditions in the heat exchanger may influence the results. The flow distribution of the exhaust air between the active and inactive side is approximately 90% versus 10%. The actual flows in the two directions are not measured. The influence of different flow distributions on the calculated temperatures is shown in figure 7 for experiment 2. Figure 7 (left) shows the temperature profile at the end of the active period and figure 7 (right) shows the temperature profile at the end of the inactive period for three different flow distribution situations where the total exhaust flow is distributed with 95%, 90% and 80% in the active side and respectively 5%, 10% and 20% in the inactive side. It is seen from figure 7 (left) that the flow distribution has only a small influence on the temperature profile in the active period. From figure 7 (right) it is seen that the flow distribution has a significant influence on the temperature profile at the end of the inactive period.

In general, the model shows reasonable agreement with the measured values. The largest errors are found during the inactive period and to further improve the calculations it is necessary with a better model of the inactive period. In order to improve the model it is necessary to have more controlled experiments for validation. The uncertainties regarding temperature and flow measurements are quite large and especially the flow distribution is important for the results during the inactive period.

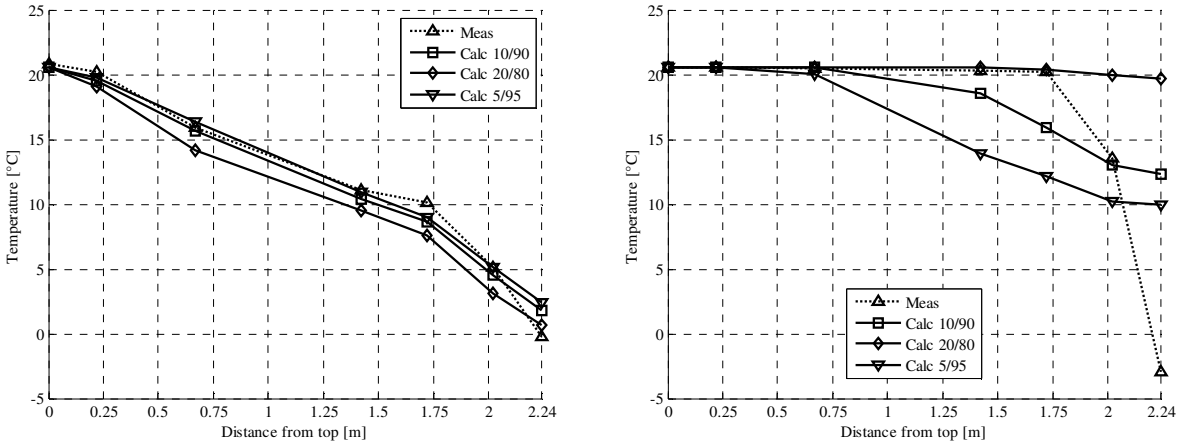

FIG. 7: Left: Measured (dotted line) and calculated (full line) temperatures inside the heat exchanger for experiment 2 at the end of the active period for different flow distrubutions between the active and inactive side. Right: Measured (dotted line) and calculated (full line) temperatures inside the heat exchanger for experiment 2 at the end of the inactive period for different flow distrubutions between the active and inactive side.

5. Conclusion

A dynamic computational model of heat flow in counter flow air to air heat exchangers taking into account condensation and frost formation is evaluated. The results of the model are compared with measured temperature profiles for a prototype heat exchanger with an active defrosting strategy for application in cold climates. The calculated results show reasonable agreement with the measured values considering large uncertainties on the measured values. The results also show that it is necessary to improve the calculation model for more precise estimation of temperatures and frost formation in the heat exchanger and that it is necessary with more controlled experiments in order to validate improvements in the model.

6. References

Brouwers H.J.H. and van der Geld C.W.M. (1996). Heat transfer, condensation and fog formation in crossflow plastic heat exchangers, *International Journal of Heat and Mass Transfer*,Vol. 39, No. 2, 391-405.

Iragorry J. and Tao Y.-X. (2004). A critical review of properties and models for frost formation analysis, *HVAC&R*, Vol. 10, No. 4, 393-420.

Jilek J. and Young J.H. (1993). Exergy efficiency of counterflow air/air heat exchanger with vapour condensation, *Wärme- und Stoffübertragung*, Vol. 28, 123-130.

Kragh J., Rose J., Nielsen T.R. and Svendsen S. (2007). New counter flow heat exchanger designed for ventilation systems in cold climates, *Energy and Buildings*, Vol. 39, p. 1151-1158.

Nielsen T.R., Rose J. and Kragh J. (2008). Dynamic model of counter flow air to air heat exchanger for comfort ventilation with condensation and frost formation, *Accepted for publication in Applied Thermal Engineering*. Online access: http://dx.doi.org/10.1016/j.applthermaleng.2008.03.006

Terekhov V.I., Terekhov V.V., and Sharov K.A. (1998). Heat and mass transfer in condensation of water vapor from moist air, *Journal of Engineering Physics and Thermophysics*, Vol. 71, No. 5, 771-777.

Self-Regulating Floor Heating Systems in Low Energy Buildings

Henrik Karlsson, Phd Student,
Chalmers University of Technology
Department of Civil and Environmental Engineering
henrik.karlsson@chalmers.se

KEYWORDS: low energy buildings, floor heating, numerical simulations, integrated design, control system.

SUMMARY:
The performance of an inexpensive floor heating system is studied by means of a numerical simulation tool. The study deals with an energy efficient detached single-family house. A building with such low space heating demand (25-30 kWh/m^2/year) yields a low floor surface temperature and this in turn means that the so-called self-regulating effect is significant. Initially, the design of the pipe circuits is studied. Especially the allocation of heat between different rooms are studied; the purpose is to find a design where the set-up of required fluid supply temperatures are as uniform as possible among the pipe circuits. Detailed simulations of the heating season is conducted for two simulation cases, one with a constant supply temperature, derived from the initial simulations; and a second case with a variable supply temperature. The results yield an apparent effect of self-regulation; the heat flux from the embedded floor heating pipes increases when the indoor air temperature declines and can be totally blocked when high indoor temperatures arise. Furthermore, excess heat is transferred from over-tempered zones towards the manifold assembly in the hydronic system. The occurrence of heat extraction trough floor heating pipes in certain zones has a levelling effect of the indoor temperature distribution.

1. Introduction

1.1 Background

This paper considers the combination of a hydronic floor heating system and a detached single-family house with a low energy demand for space heating. The idea is to explore the possibility to use an inexpensive and uncomplicated hydronic heat supply system that operates with as low supply temperature as possible. Heat losses from the building are kept down by means of a well-insulated building envelope and balanced mechanical ventilation system with an efficient air-to-air heat recovery unit.

Any floor, wall or similar low temperature heating system, that utilise large internal areas to supply space heating are influenced by the so-called self-regulating effect. The self-regulating quality of a low temperature heating system operates entirely without any active control system. A typical floor heating system today has a thermostatic control system that regulates the mass flow of warm water to each individual room. The control system consists of temperature sensors in each room and valves that are either fully open or fully closed. These valves are situated at the manifold assembly at the return side of the pipe circuits. The cost for temperature sensors, valves and so on are significant in comparison with the cost for the entire floor heating system. Thus, if thermostatic valves and temperature sensors were excluded in the design, the cost for floor heating would decrease. When the active control system is excluded, the self-regulating process would be the only instrument that in some sense regulates the rate of heat supply.

Low energy residential buildings have been an issue for research and a major concern for the construction industry for many years. In recent years, the so-called passive house concept was introduced in the Nordic countries. A number of passive house projects have been conducted. The cornerstone in the passive house concept is a very low space heating demand. Furthermore, the heat demand is entirely supplied by means of an electric or hydronic heat battery situated within the supply air duct. This supplementary heating of the supply air is preferred since the method is supposed to be the most cost-effective method to supply such small amount of heat into the building. Passive houses do not have any hydronic heating system or floor heating system. Extra costs for a supreme building envelope, which is necessary to lower conductive and air infiltration heat losses, is partly paired off against the fact that a traditional heat supply system is excluded.

Newly built detached single family houses in Sweden and Denmark are almost entirely designed with a floor heating system. In bathrooms, where bare feet are placed on top of a ceramic floor, the heated floor is necessary in order to ensure a comfortable contact temperature. Floor heating is preferred because of many subjective qualities, such as thermal comfort, aesthetic and fashion, rather than technical and economical qualities.

A low energy concept for a house equipped with an inexpensive floor heating system, combines costumer demands and the ambition to build energy efficient residential houses. By constructing the house with a genuine, but still inexpensive, space heating system ensures that the inhabitants can adjust the indoor temperature according to their preferences. Thus, a genuine space heating system will rule out the possibility that inhabitants e.g. set up electric heaters to uphold thermal comfort.

1.2 Self-regulation process

In the case of a floor heating system, heat conducts from embedded pipe circuits upwards through the concrete slab towards the floor surface. However, the heat balance at the surface will influence the upward heat flux from the pipe circuit towards the surface. The indoor temperature may deviate from the required indoor temperature due to time variations in heat gains and losses. The heat flux density at the floor surface changes instantly whenever the room conditions change. In essence, when the indoor temperature increase - the heat supply from the warm floor decreases; or the opposite, when the indoor temperature decrease - the heat supply increases. These backlash reactions indisputably control the heat supply from the floor heating system in accordance to the present conditions within the room. The surface heat flux density may change due to variations in solar radiation intensity at the floor surface, convective heat transfer between the indoor air volume and the floor surface or by means of long wave radiation exchange between internal surfaces within the room enclosure. These heat transfer modes are all transient and interconnected to each other.

A small total heat loss from a building with floor heating yields in a low supply temperature for all pipe circuits that runs all along the floor construction. Thus, the surface temperature of the heated floor is just a few °C above the desired room temperature. A small difference between floor surface and room temperature results in a large potential for self-regulation of the heat supply to the room. In the case of a residential building, the main advantage achieved by the self-regulation effect is to ensure that the heat supply to the room stops or decreases when high heat gains, such as solar radiation, are present.

2. Method

The concept of a low energy residential house with a simplified floor heating system is explored by means of numerical simulations. Karlsson (2006) developed a comprehensive numerical simulation model for embedded building integrated heating systems. The simulation model allows for a detailed thermal system analysis of a building equipped with building integrated heating, in this case floor heating. Especially the interior surface heat balance and the heat exchange process that takes place along embedded hydronic pipes is computed in detail. The net radiation exchange method (Hottel et al. 1967; Karlsson et al. 2005) allows for a transient computation of long wave radiation exchange within enclosures. The distribution of solar radiation within each zone is computed according to the method given by Judkoff (1995). All transmitted solar radiation hits initially the floor surface evenly. It is assumed that a diffuse reflection take place at the floor surface. Hence, the reflected part from the floor surface is allocated to walls, windows and to the ceiling. For the convective heat transfer at the heated floor surface, an empirical model derived by Awbi et al. (1999) is applied. In this paper, the model by Karlsson (2006) is developed further to comprise multi-zone simulations.

3. Description of the studied building

The plan of the building is inspired from a newly built existing detached single-family house. The total floor area is 105m^2. This building is broken up in seven rooms, see Figure 1. Based on the plan from the existing building, extra insulation is added in all parts of the building envelope, windows with lower U-values are also applied. Furthermore, the ventilation principle is changed from a mechanical exhaust air system with an exhaust air heat pump to a balanced mechanical ventilation system with air-to-air heat recovery. The building is located in Gothenburg at the south-west coast of Sweden, climate data with hourly resolution from the year of 1991 is applied in all simulation cases.

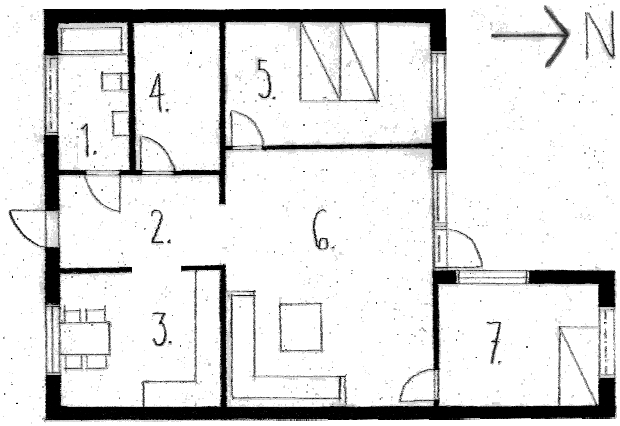

Figure 1 Plan of the studied building.

3.1 Building envelope

All external walls are made of a conventional wooden frame structure with thermal insulation, which are covered with internal gypsum boards and external wooden cladding. The U-value of the walls, roof and ground is 0.203, 0.101 and 0.117 W/m^2/K respectively. All U-values includes the effect of thermal bridges in the thermal envelope. The entire building envelope including windows has an average U-value of 0.196 W/m^2/K.

3.2 Windows and shading

Energy efficient windows with triple glazing panes, inert gas and a low emission layer are used; the U-value is 1.1 W/m^2/K for the entire window including thermal bridges. The simulation tool takes into account transmittance of solar heat trough windows according to orientation, tilt and transmittance of the windowpanes. The climate file includes both direct and diffuse solar radiation with one-hour resolution. The terrain around the building is considered not causing any shading of the façade at any time of the year. In order to estimate a realistically influence from solar heat gains, the use of shading devices such as blinds or curtains is included; the shading coefficient is set to 0.48 for all windows. All interior materials have a solar absorptivity of 0.6.

3.3 Mechanical ventilation, infiltration and cross ventilation

A mechanical ventilation system supply 40 l/s of air to the building. The heat recovery unit preheats the airflow before the supply air enters room 3, 5, 6 and 7. Exhaust air is taken from room 1, 3 and 4. The air-to-air heat recovery unit has a bypass function that is activated each time the common exhaust air temperature (before the heat recovery unit) exceeds +24°C. When the heat recovery unit is disabled, the supply air temperature equals the outdoor air temperature. The bypass function is enabled until the common exhaust air temperature has declined under +21°C. The heat recovery unit has a temperature efficiency equal to 0.85.

The assumed infiltration of outdoor air is 0.025h^{-1}. All leakage paths are distributed evenly within the building. The assumed air tightness represents a very well planed and skilfully constructed building. A correct operation of a balanced ventilation system is ensured when the building envelope is sufficiently airtight. It is important to reduce heat losses due to infiltration when low energy buildings are considered.

Controlled cross ventilation is assumed whenever heat gains give rise to high indoor air temperatures. Every time the air temperature exceeds +25°C, an extra outdoor airflow of 1 h^{-1} is supplied to a single room in the building. This extra airflow is supplied to the room until the air temperature has declined under +22°C.

3.4 Internal heat gains

A daily profile that takes into account daily variations in the use of household electricity is applied in order to estimate internal heat gains. Besides the daily profile, a yearly variation is also accounted for; Bagge et al. (2006) and Bennich (2008) give the applied yearly and daily profiles. The average supply of domestic electricity is 4.5 W/m^2 for the entire year, 70% of the electric energy is assumed to contribute to the heating of the building. The average heat supply from persons is estimated to 1.0 W/m^2.

4. Detailed description of floor heating system and studied simulation cases

4.1.1 Basic design of the floor heating system

An embedded hydronic floor heating system is installed in the lower part of a 100mm thick concrete slab foundation. The system is made of flexible cross linked polyethylene pipe loops were warm water is circulated. Over the entire concrete slab, the centre-to-centre distance between the pipes is 300mm. Each room is connected to a central manifold assembly with one or two pipe circuits, depending on the heat demand and the size of the room. Zone 3 and 4 have 12mm ceramic plates as floor covering, all other zones has 12mm parquet floor.

4.1.2 Allocation of heat between zones

Commonly, there are differences in heat demand between rooms in a building. The heat flux injected by the floor heating system in a certain room depends on the supply fluid temperature, the fluid flow rate in the pipe circuit and thermal properties of the floor heating construction. These parameters are adjusted during the design of the floor heating system in order to match the heat demand for each room. However, in practice only flow rate and thermal properties of the floor heating system, such as centre-to-centre distance between the pipes and floor covering, are adjustable on zone level. Since the design proposal does not permit thermostatic valves and the fact that the supply temperature is common for all pipe circuits, the variation in supply temperature demand between zones should be as homogeneous as possible. Otherwise, it is not possible to attain a uniform indoor temperature.

A potential problem is rooms where the heat demand is comparatively much higher (or lower) than the rest of the zones in the building. Although a high flow rate, tightly packed pipes and high conductive floor covering is applied, the needed supply temperature may still be too high in comparison to the supply temperature demand in other zones. A possible solution is to reduce the heat losses since these are the origin to the problem.

4.1.3 Finding a appropriate system design - simulation case 1, 2 and 3

Simulation case 1, 2 and 3 consider the month of February. The general design of the floor heating system and especially zone 7 is decided by means of a simplified steady-state calculation. The steady-state calculation is based on the thermal conductivity for a representative two-dimensional cross-section of the floor heating system, which is easily pre-calculated in a separate software, and the heat loss factor for of the building. For this steady-state calculation, the temperature decline that takes place along the pipe circuits is assumed linear. The choice of design parameters is afterwards verified by means of the detailed simulation tool.

The design procedure focus on the coldest month taking all climatic parameters as monthly average values; in February, the average outdoor temperature is -3.3°C and the average solar gain is 1.32 W/m^2 (floor area). The heat loss factor, 74 W/K, for the entire building and an assumed temperature decline of 0.75°C between supply and return fluid flows yields the total fluid flow (0.338 l/s). The total fluid flow is allocated between the zones in relation to the heat loss factors on zone level. The distribution of fluid flows is set to be constant throughout all simulation cases, see category axis within Figure 2.

For each zone, a simplified steady-state calculation yields the required ΔT_{supply} (difference between supply fluid temperature and indoor air temperature), see Figure 2. The common supply temperature for all zones is found by using the floor-area-weighted ΔT_{supply}, which equals +3.1°C for case 1. Thus, +23.1°C is selected as fluid supply temperature in simulation case 1-3.

The required ΔT_{supply} in zone 7 (case 1) is significantly higher than the mean ΔT_{supply}, see Figure 2. Therefore, the centre-to-centre distance between the pipe loops is tightened in zone 7. Thus, zone 7 is now heated with two evenly sized pipe circuits (centre-to-centre distance of 150mm). The new design (case 2) lowers the needed supply temperature by almost 1.0°C. However, in order to reduce the heat demand in zone 7, a final modification (case 3) is applied; the north-orientated window is excluded and the insulation of the exterior wall is improved. The enhanced wall has a U-value of 0.130 W/m^2/K. Finally, zone 3, 5 and 7 has a uniform supply temperature demand, see case 3 in Figure 2.

4.1.4 Study of the heating season – simulation case 4 and 5

The heating season is studied by means of two different control strategies. The heating season starts the 1st October and ends the 1st May. In case 4, the same configuration as in simulation case 3 is applied, only the

length of the simulation is changed. The supply temperature is still constant and based on the average conditions during the coldest month of the heating season.

In case 5, the concept of a constant supply temperature is changed in favour for a variable supply temperature. For each day throughout the heating season, the area-weighted ΔT_{supply} is pre-calculated in a similar manner as in case 1-4. The applied supply temperature curve is given by a running mean value, which is based on the past four days; see right-hand side in Figure 2. The selected period of the past four days is related to the intrinsic time-scale for the whole building, which is approximately 4 days.

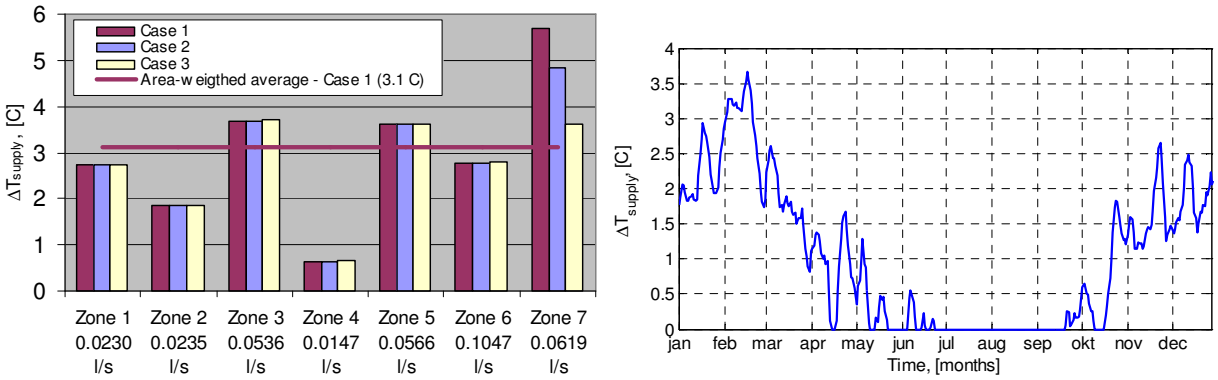

Figure 2 Left-hand side: Range of variation of ΔT_{supply} based on simplified steady-state calculations (average heat gains and losses throughout February). The horizontal line represents the area-weighted ΔT_{supply} from simulation case 1. The right-hand side illustrates conditions applied in simulation case 5; ΔT_{supply} for the area-weighted running mean (4 day period) during the entire year.

5. Results from detailed transient simulations

5.1 Study of zone 7 during February - case 1, 2 and 3

The simulation of case 1 yielded an indoor air temperature in zone 7 less than +20°C for approximately 88% of the time in February, see Figure 3. In comparison with case 1, the indoor air temperature in zone 7 increases with roughly 0.6°C for the entire period when case 2 is studied. The same observation is evident when the heat flux from the pipe circuit towards the concrete slab in case 2 is compared with case 1; see right-hand side in Figure 3. This increase is particularly obvious when conditions in zone 7 allows for the highest heat fluxes; when the heat flux is smaller the difference between case 1 and 2 is marginal. However, the heat flux from the pipe is still not enough to supply the room with the sufficient amount of heat; the indoor air temperature is less than +20°C for three quarters of the time in February. When the reduction of the transitive heat loss is applied in case 3; the indoor air temperature has evidently increased. The value of +20°C is exceeded for more than half the time. The minimum temperature is around +18°C during a very limited period. The heat flux density from the pipe circuit has simultaneously decreased; see Figure 3. While changing the construction in zone 7, the simulated indoor air temperature in the adjacent room (zone 6) is more or less unaffected, see left-hand side in Figure 3.

5.2 Study of the heating season with constant supply temperature – case 4

The simulation yielded a heat supply of 30.8 kWh/m^2 to the floor heating system. According to Figure 4, the indoor air temperature is above +20°C for all zones during approximately 80-95% of the heating season. Temperatures above +24°C occur rarely in all rooms. However, over-temperatures appear more frequent in zone 1, 3 and 7 mostly due to higher solar gains in these three rooms compared to zone 5 and 6. This is also the cause behind the fact that the embedded pipes extract heat from these three zones during approximately 7-10% of the period, see right-hand side of Figure 3.

The total heat flux, injected into the system at the manifold assembly, is studied in conjunction with the area-weighted indoor air temperature; see the left-hand side in Figure 6. The lower the indoor temperature is, the higher the heat flux rate is. During the heating season, the heat supply is occasionally blocked although the indoor air temperature is as low as +22°C. A similar relation is found when the outdoor temperature in conjunction with the heat flux is studied; see the right-hand side in Figure 6.

5.3 Study of the heating season with pre-calculated supply temperature – case 5

A heat supply of 24.9 kWh/m^2 is found when the heat fluxes are summed up. Compared to case 4, the indoor temperatures decrease in case 5, which is a patently obvious result due to the decreased supply temperature, see Figure 5. Furthermore, the heat exchange between pipe and concrete has manly decreased when the heat flux is relatively low; see right-hand side Figure 5. Heat is never supplied to the floor heating system when the outdoor temperature exceeds +13°C. In addition, the maximum heat supply occurs during the coldest day of the heating season; at the same time, the indoor air temperature is the lowest, see Figure 7.

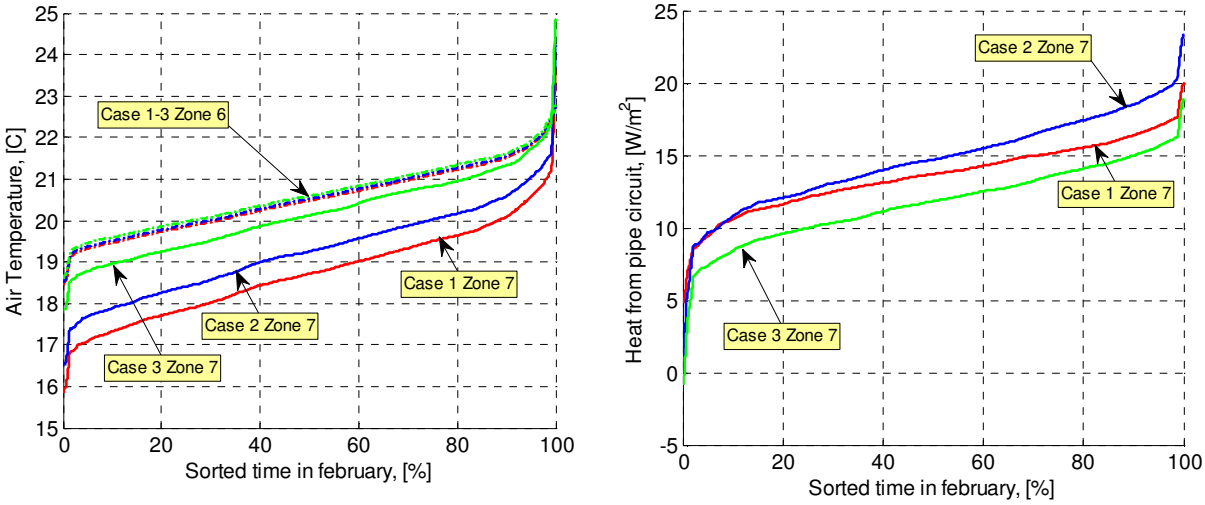

Figure 3 Duration diagrams illustrating differences in air temperature and heat flux density from the floor heating system (per m^2 floor) between the different simulation cases.

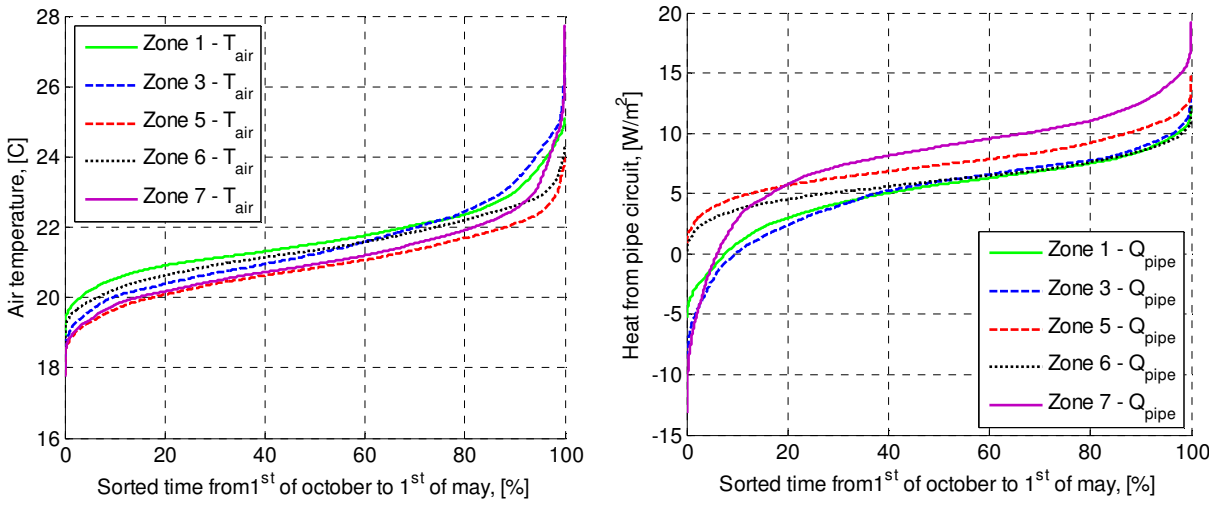

Figure 4 Duration diagrams for simulation case 4 during the entire heating season. On the left-hand side: Indoor air temperatures. On the right-hand side: Heat flux from the floor heating pipes towards the concrete slab.

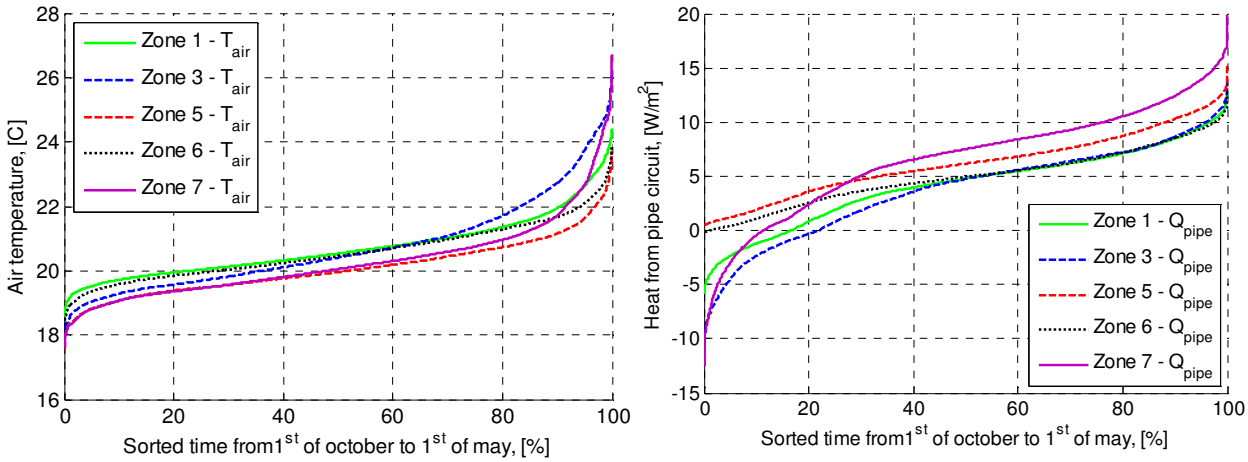

Figure 5 Duration diagrams for simulation case 5 during the entire heating season. On the left-hand side: Indoor air temperatures. On the right-hand side: Heat flux from the floor heating pipes towards the concrete slab.

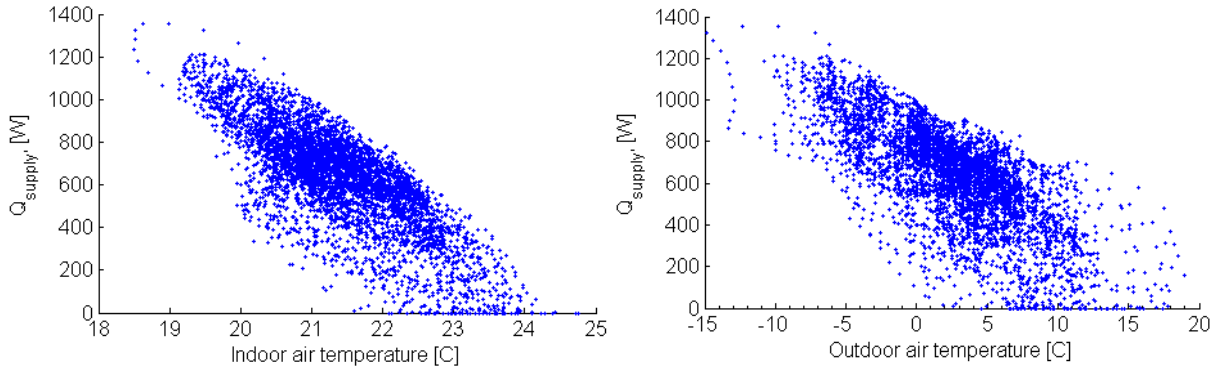

Figure 6 Point diagram illustrating the supplied heat flux to all pipe circuits and air temperatures. On the left-hand side is the area weighted indoor air temperature for the entire house applied. On the right-hand side is the outdoor air temperature applied. Each point represents the average conditions for one hour. The figure is valid for simulation case 4.

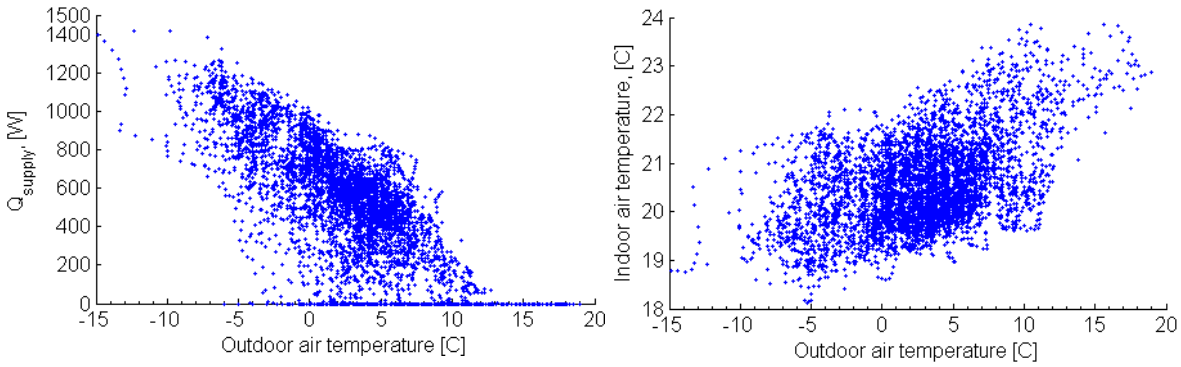

Figure 7 Point diagram of heat supply and indoor air temperature as a function of the outdoor temperature. The figure is valid for simulation case 5.

6. Discussion and conclusion

In simulation case 4 is the supply temperature not influenced by external climate variations; although, whenever the indoor temperature decline, the heat supply increases and vice versa, see Figure 6. It can be concluded that the heat extraction from the floor pipes is adapted to the heat demand of the building. Furthermore, the point diagram given by Figure 6 gives a clear illustration of the self-regulating quality of the studied building. The greater the slope of the scatter is the more significant is the self-regulation effect.

Variation of several factors in the design of the heating system is not included in this paper. Presumably are the thermal resistance and the heat capacity of the floor covering important quantities in the context of self-regulation. Another interesting factor is the area of the temperated building component in relation to the heat demand. The prospect to use internal walls as building integrated heating components is believed to contribute to a more significant self-regulation.

Another quality of a low temperature floor heating is the fact that a small heat flux can be extracted from over-tempered rooms. The peak value of the extracted heat flux is in the same range as the supplied heat flux; however, the duration of the heat extraction is relatively short. Thus, this quality contributes to an equalization of indoor temperatures. Furthermore, airflows between rooms that are driven by temperature differences are not included in the simulation model. Thus, the equalization of indoor air temperatures is actually more significant than the simulation results yields.

In simulation case 5 falls the indoor temperature below +20°C quite regularly despite the outdoor temperature, see right-hand side in Figure 7. The results indicate a problem with the selected control method. The more simple method in case 4 yields overall higher indoor temperatures. However, the supply temperature is too high in the beginning and the end of the heating season. An enhanced and simple control method is essential in order to apply the concept of a low temperature floor heating system in an existing building.

If the building concept includes a simplified low temperature floor heating system, engineers and architects must consider restrictions related to the heating system. For instance, simulation case 1-3 illustrate the importance of an integrated design process; the plan of the building cannot contain zones where the heat demand is significantly larger that the rest of the building. In addition, the choice of floor covering material is an aesthetic factor that strongly influences the function of the floor heating system.

7. References

Awbi H. B. and Hatton A. (1999). Natural convection from heated room surfaces. Energy and Buildings, 30(3).

Bagge H., Hiller C. and Sjögren J-U. (2006). Hushållsel i direktiv, beräkningar och verklighet. Seminar paper – Energy Performance of Buildings, Lund University, Sweden. http://www.byfy.lth.se/Publikationer/seminarieuppsatser2006.htm (2008-02-09)

Bennich P. (2008). Mätning av hushållsel i 400 bostäder. Swedish Energy Agency. http://www.energimyndigheten.se/WEB%5CSTEMFe01e.nsf/V_Media00/C12570D10037720FC125739200338F97/$file/M%E4tning%20av%20hush%E5llsel,%20Peter%20Bennich.pdf (2008-02-09)

Hottel H. and Sagofirm A. (1967). Radiative Transfer. McGraw-Hill, New York, United States.

Judkoff R. and Neymark J. (1995). ENVELOPE BESTEST: Building Energy Simulation Test and Diagnostic Method. International Energy Agency, Solar Heating and Cooling Program – Task 12 and Building and Community Systems Annex 21, NREL/TP-472-6231.

Karlsson H. and Hagentoft C-E. (2005). Modelling of Long Wave Radiation Exchange in Enclosures with Building Integrated Heating. Proceedings of the 7th Symposium on Building Physics in the Nordic Countries, Reykjavik, Iceland.

Karlsson H. (2006). Thermal system analysis of embedded building integrated heating- Numerical model and validation of hydronic heating systems. Thesis for the degree of licentiate of engineering. Chalmers University of Technology, Göteborg, Sweden.

Experimental Study on Crawl-Space Heating with Thermal Storage using Heat Pump

Koji Fujita, Graduate Student,
Graduate School of Science and Technology, Kobe University;
039d892n@stu.kobe-u.ac.jp

Atsushi Iwamae, Assoc. Professor,
Department of Architecture, School of Science and Engineering, Kinki University;
ai@arch.kindai.ac.jp

Takayuki Matsushita, Professor,
Department of Architecture, Graduate School of Engineering, Kobe University;
matusita@kobe-u.ac.jp

KEYWORDS*: Heating system, Crawl space, Thermal storage, Heat pump, Off-peak electricity.*

SUMMARY*:*
In the house that has a crawl space with the insulated foundation walls and non-insulated floor over the crawl space, if all the crawl space can be heated, then the entire floor will be heated, and as the result whole the space of the first floor will become the radiant heating environment. We call this heating system 'Crawl-space heating'. In this papar, the crawl-space heating system combined with the thermal storage using an air source heat pump as a heat source is introduced. To verify the efficiency of this heating system, field test was carried out in an experimental house and following facts were revealed. In the period from 23:00 to 7:00, that is off-peak electrical load period in Japan, the heat pump generates about 80 MJ heat and supplies the heat to the thermal storage equipments. In the same period, about 40 % of the supplied heat was stored in the thermal storage equipments and the balance 60 % was used to heat the crawl space. In the period from 7:00 to 23:00, that is peak period, the stored heat in the thermal storage equipments was released to the air coming from the fans and was used to heat the crawl space. Under the condition of the crawl-space heating, the radiant heating environment was obtained in the room. In the environment, vertical temperature distribution was small and floor-surface temperature was higher than the space. Furthermore, the difference between the room temperature in the first floor can be minimized as far as the adequate circulation of the warm air in the crawl space is secured and also the thermal conductivity of the floor material is good enough to transmit the heat in the crawl space to the above room.

1. Introduction

There are many ways for heating for detached houses. They can be divided into roughly two ways, one is convective air heating and the other is radiant heating. Convective air heating has some disadvantages compared with radiant heating. Convective air heating tends to make the temperature of the lower part of the room lower than that of the upper part. The moving dry air that blows to the body makes the people in the room uncomfortable. On the other hand, radiant heating does not have such disadvantages and it is becoming preferable.

As to the heating area of a house, there are roughly two ways. One is partial heating and the other is whole house heating. Partial heating has high risks of causing condensation and vascular disorders such as cerebrovascular disease, whereas whole house heating has low risks of them. To warm up whole house, it is needed to build well-insulated and highly airtight house and install the suitable heating system.

At the house that has a crawl space with the insulated foundation walls and non-insulated floor over the crawl space, if all the crawl space can be heated, then the entire floor will be heated, and as the result whole the space of the first floor will become the radiant heating environment. We call this heating system 'Crawl-space heating'. To make the same heating environment in the first floor using the general floor heating system, it is

needed to install the system in the whole floor of the first floor. On the other hand, in the case when using the crawl-space heating, it is only needed to install the heating system in the crawl space.

To heat the crawl space, several heat sources such as an electric-resistance heater or a gas boiler can be considered. If the climatic condition of the area is suitable for using a heat pump (Schibuola 2000), more efficient heating can be expected by using it because it has ability to output several times more thermal energy than the inputted electrical energy. The heat source the coefficient of performance (COP) of which is over 1 is only the heat pump. In Japan, which is comparatively warm climate, the heat pump can be used as a heat source for heating.

Furthermore, combining the crawl-space heating with the thermal storage would bring about some benefit in the countries where electrical energy consumption varies greatly during day and night. If some of the peak load could be shifted to the off-peak load period, better power generation management can be achieved. In order to narrow the gap between the peak and the off-peak electrical demand, the electric price in the peak load period is usually set higher than that in the off-peak load period in many countries. Then the shift of electrical consumption from the peak load period to the off-peak load period by using the thermal storage will provide significant economic benefit.

In this paper, the crawl-space heating system combined with the thermal storage using the air source heat pump for space heating as the heat source is presented. The schematic diagram of this heating system is shown in Fig. 1. A heat pump, a fun and thermal storage equipment are installed in the crawl space. The heat pump supplies heat to the thermal storage equipment by using cheep off-peak electricity. The thermal storage equipment consists of sensible thermal storage materials and spaces through which air from the heat pump or the fan flows exchanging the heat with the materials. At the off-peak period, some of the heat from the heat pump is stored in the thermal storage materials and the heat not stored is used to heat the crawl space. At the peak period, the stored heat in the thermal storage materials is released to the air coming from the fan and is used to heat the crawl space.

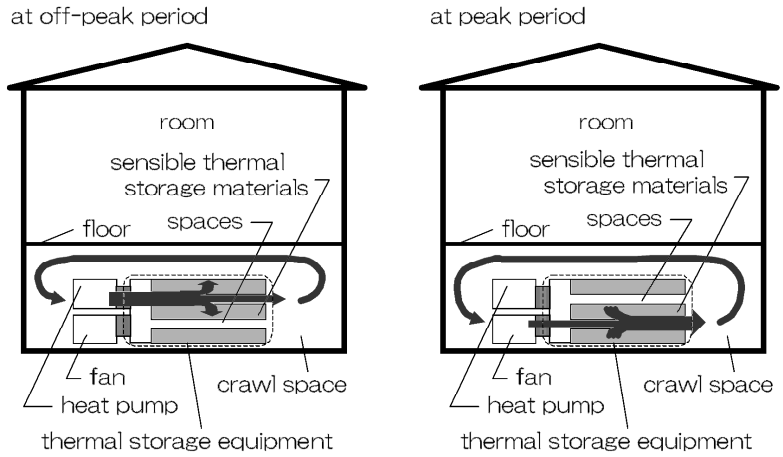

FIG. 1: Schematic diagram of crawl-space heating combined with thermal storage using heat pump as heat source. Left: at off-peak load period, Right: at peak load period.

There have been some studies of floor heating system combined with thermal storage (For example, Lin et al. 2005). However, heat pump has not been used as the heat source in those studies. There have been some studies of heat pump combined with thermal storage. Badescu (2003) used the thermal storage to store the collected solar energy that was used to operate a solar assisted heat pump system. Long and Zhu (2008) used the thermal storage in a heat pump water heater. Fujita (2007) developed a model to study the thermal performance of the crawl-space heating combined with thermal storage using a haet pump as a heat source. However, experimental study about the heating system has not appeared so far.

The objective of this work is to verify the efficiency of this heating system experimentally. Specifically, the indoor thermal environments such as vertical and horizontal temperature distributions were measured and the quantities of the stored and the released heat in the thermal storage equipment were estimated by the field tests that were carried out in an experimental house in Osaka, Japan.

2. Experimental Set-up

Field tests were carried out at the west end of an experimental house in Osaka, Japan from December 18 to 28, 2006. Figure 2 and Figure 3 show the foundation plan and the first-floor plan together with the temperature measurement points. Figure 4 shows a cross section.

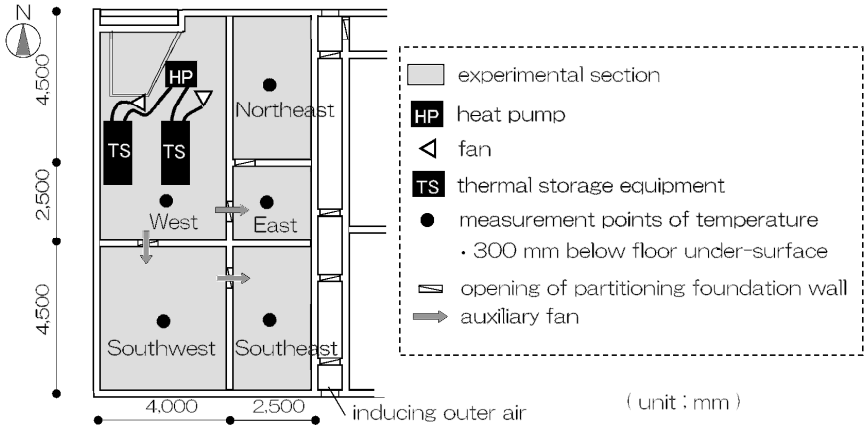

FIG. 2: Foundation plan showing measurement points.

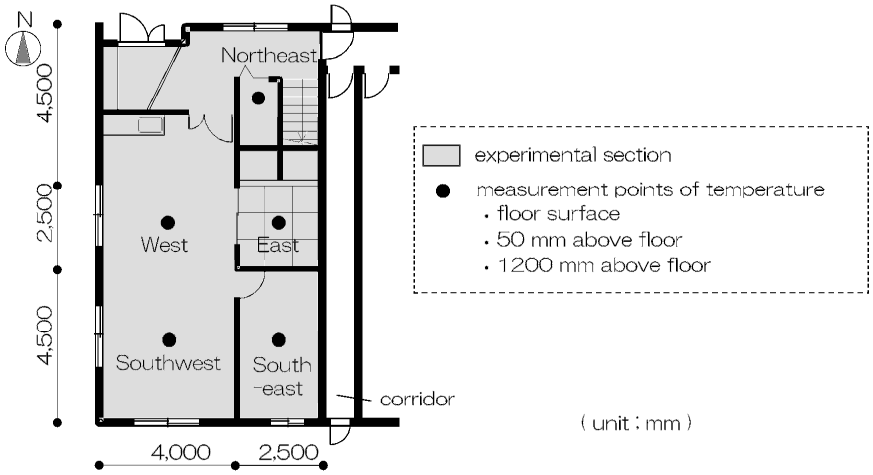

FIG. 3: First floor plan showing measurement points.

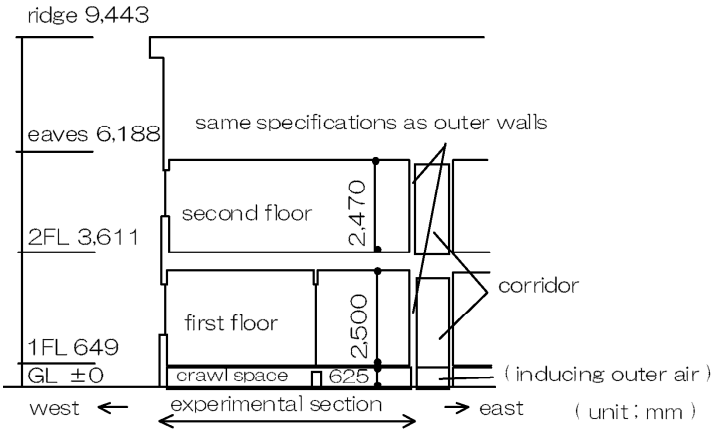

FIG. 4: Cross section.

The house was two-storied with other rooms to the east of the experimental section separated by a 1 m wide corridor running from north to south. The wall of the section facing the corridor had the same specifications as the outer walls. The crawl space of the corridor was connected with outdoor through openings of the foundation walls and the corridor was not heated. Therefore, the experimental section could be considered thermally as a detached house.

The floor of the experimental section consisted of sleepers, joists, plywood 12 mm thick, and wooden flooring 12 mm thick. The ground surface of the crawl space was covered with concrete 200 mm thick. The foundation walls of the crawl space were insulated by extruded polystyrene 100 mm thick. The edge parts of the slab concrete were insulated by extruded polystyrene of 50 mm thick and 500 mm width. The heat loss from the experimental section to the outdoor per floor area was estimated 2.3 W/m^{2}K.

A 6.0 kW heat pump was installed in the Northwest section of the crawl space. Two fans were installed also in the Northwest section of the crawl space. Two thermal storage equipments were installed in the west section of the crawl space and they were connected to the heat pump and also to each fan respectively by insulated ducts.

Figure 5 and Figure 6 show a horizontal cross section of the thermal storage equipment and a vertical cross section of that. The thermal storage equipments consist of sensible thermal storage materials and spaces through which air from the heat pump or the fan flows exchanging the heat with the materials. The physical properties of the materials are shown in Table 1.

The heat pump was set to 30 °C and operated from 23:00 to 7:00 that is off-peak period in Japan. The fans to promote the release of the stored heat were operated from 7:00 to 23:00.

Three auxiliary fans producing airflow 650 m^3/h respectively were operated to control the air current in the crawl space. As shown in Fig. 2, they were installed to move the air from the West to the Southwest, from the West to the East and from the Southwest to the Southeast respectively.

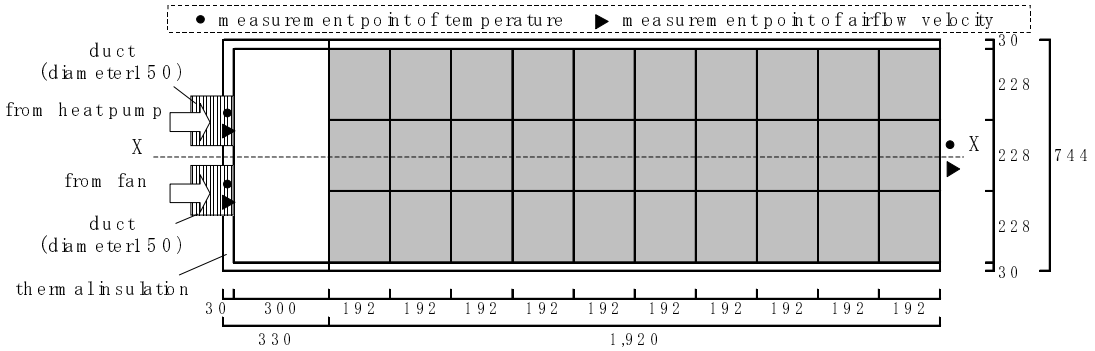

FIG. 5: Horizontal cross section of thermal storage equipment. (unit; mm)

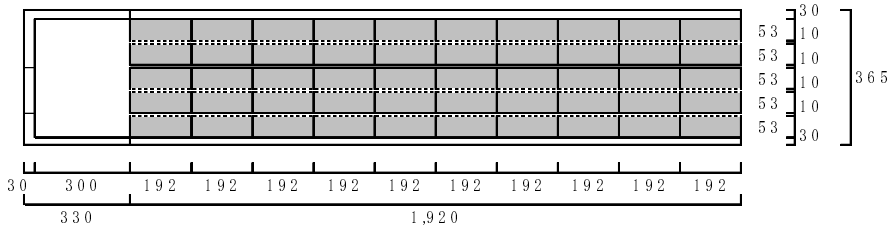

FIG. 6: Vertical cross section of thermal storage equipment. (unit; mm)

TABLE. 1: Physical properties of sensible thermal storage materials.

Specific heat	954 J/kgK
Density	3,750 kg/m^3
Thermal conductivity	2.7 W/mK

3. Results and discussions

Figure 7 shows the vertical temperature distributions at each point shown in Fig. 3 at 12/21 14:00. The temperatures at 50 mm and 1,200 mm above the floor were almost the same and the floor-surface temperatures were higher than the space temperatures. From these results, it was verified that the radiant heating environments were formed in the room by the crawl-space heating.

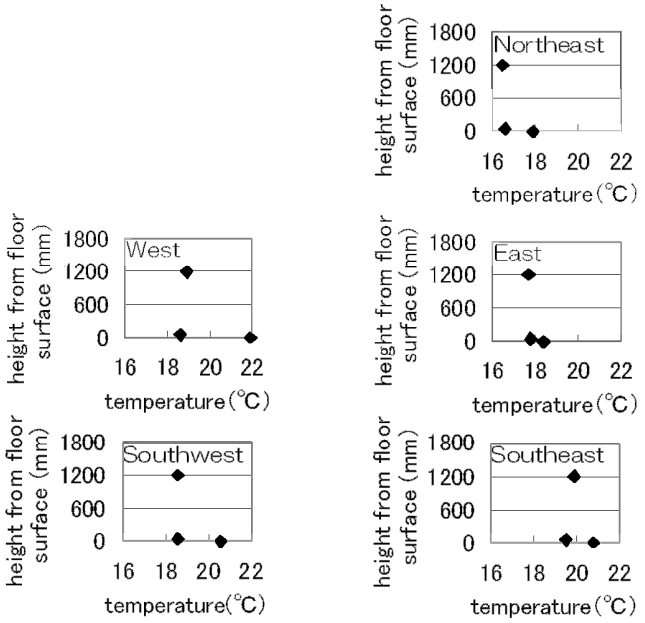

FIG. 7: Vertical temperature distributions at each point shown in Fig. 3.

Figure 8 shows the temperatures at 1,200 mm above the floor in the room on the respective points shown in Fig. 3. The differences between the temperatures of each measuring points were less than 2 °C except for the East and the Northeast. Figure 9 shows the temperatures of the respective points of the floor-surface. The temperatures were higher than 18 °C except for the East and the Northeast. The low temperatures at the East were due to the low thermal conductivity of the floor material, i.e. Japanese mat called 'tatami', the thickness of which was 50 mm and its thermal conductivity was about 0.1 W/mK. Figure 10 shows the crawl space temperatures at 300 mm below the floor under-surface in the crawl space on the respective points shown in Fig. 2. The temperatures of the Northeast were lower than the other points. Following reasons are considered. There was no auxiliary fan at the opening of the partitioning foundation wall between the East section and the Northeast section and there was no adequate opening in the partitioning foundation wall between the Northeast section and the Northwest section. Consequently, the warm air from the thermal storage equipment could not circulate to the heat pump or to the fans through the Northeast section.

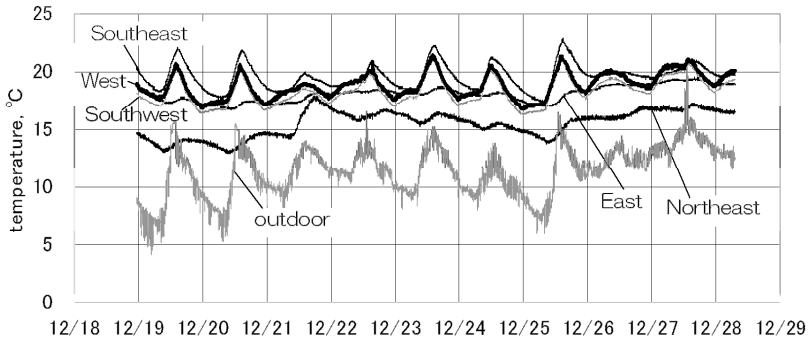

FIG. 8: Temperatures at 1,200 mm above floor in room on respective points shown in Fig. 3.

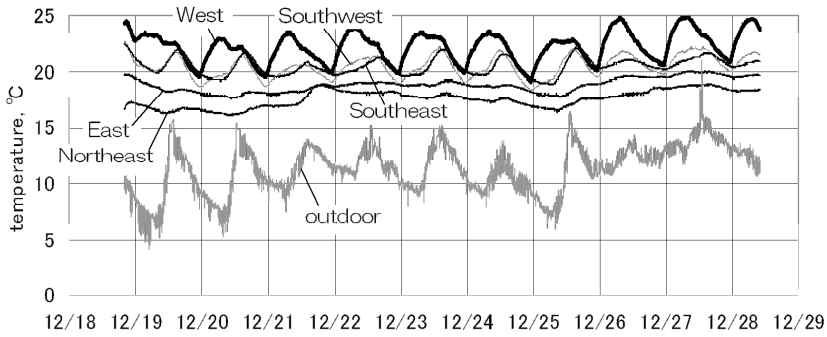

FIG. 9: Floor-surface temperatures on respective points shown in Fig. 3.

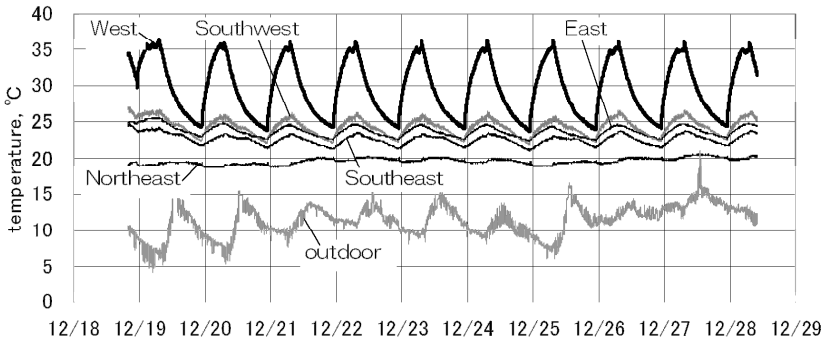

FIG. 10: Crawl space temperatures at 300 mm below floor under-surface in crawl space on respective points shown in Fig. 2.

These results prove that the difference between the room temperature in the first floor can be small by applying the crawl-space heating as far as the adequate circulation of the warm air in the crawl space is secured. Furthermore, the thermal conductivity of the floor material must be good enough to transmit the heat in the crawl space to the above room.

Table 2 shows the quantities of generated heat by the heat pump and those of stored and released heat in the thermal storage equipments.

The quantities of generated heat were estimated from the difference between the entering air temperature to the heat pump and the leaving air temperature from the heat pump with the specific heat of the air and the flowing air volume using the Equation (1).

$$Q_g = \sum_{t=y23}^{7} \left\{ \rho_a C_P V_a \left(T_{out,t}^{HP} - T_{in,t}^{HP} \right) \Delta t \right\} \quad (1)$$

where Q_g : quantity of generated heat by heat pump from 23:00 to 7:00 (J)

ρ_a : density of air (kg/m^3)

C_P : specific heat at constant pressure (J/kgK)

V_a : flowing air volume through heat pump and thermal storage equipments (m^3/s)

$T_{out,t}^{HP}$: leaving air temperature from heat pump (K)

$T_{in,t}^{HP}$: entering air temperature to heat pump (K)

Δt : measurement interval (s), (=300s)

and $\sum_{t=y23}^{7}$ means sum from 23:00 of previous day to 7:00

The quantities of stored and released heat were estimated from the difference between the entering air temperature to the thermal storage equipments and the leaving air temperature from the equipments with the specific heat of the air and the flowing air volumes using the Equations (2) and (3).

$$Q_S = \sum_{t=y23}^{7} \left\{ \rho_a C_P V_a \left(T_{in,t}^{TS} - T_{out,t}^{TS} \right) \Delta t \right\} \quad (2)$$

$$Q_R = \sum_{t=7}^{23} \left\{ \rho_a C_P V_a \left(T_{out,t}^{TS} - T_{in,t}^{TS} \right) \Delta t \right\} \quad (3)$$

where Q_s : quantity of stored heat in thermal storage equipments (J)

$T_{in,t}^{TS}$: entering air temperature to thermal storage equipments (K)

$T_{out,t}^{TS}$: leaving air temperature from thermal storage equipments (K)

Q_R : quantity of released heat in thermal storage equipment (J)

and $\sum_{t=7}^{23}$ means sum from 7:00 to 23:00

From 23:00 to 7:00, the quantity of generated heat was about 80 MJ and that of stored heat was about 30 MJ, and the balance 50 MJ was used to heat the crawl space. From 7:00 to 23:00, the heat pump was not in operation, and the stored heat of 30 MJ was released to the air coming from the fan in order to heat the crawl space. Figure 11 shows the quantities of released heat at each hour from 12/24 7:00 to 22:00. From these results, it was verified that about 40 % of the generated heat was stored in the thermal storage equipments from 23:00 to 7:00 and this stored heat could be used to heat the crawl space from 7:00 to 23:00.

TABLE. 2: Quantities of generated heat by heat pump and those of stored and released heat in thermal storage equipments.

Period	Generated heat (MJ)	Stored heat (MJ)	Released heat (MJ)
12/19 23:00 – 12/20 7:00	77	31	
12/20 7:00 – 12/20 23:00			28
12/20 23:00 – 12/21 7:00	78	31	
12/21 7:00 – 12/21 23:00			30
12/21 23:00 – 12/22 7:00	76	30	
12/22 7:00 – 12/22 23:00			30
12/22 23:00 – 12/23 7:00	76	30	
12/23 7:00 – 12/23 23:00			29
12/23 23:00 – 12/24 7:00	77	31	
12/24 7:00 – 12/24 23:00			30
12/ 24 23:00 – 12/25 7:00	79	32	
12/25 7:00 – 12/25 23:00			30
12/25 23:00 – 12/26 7:00	77	31	
12/26 7:00 – 12/26 23:00			29
12/26 23:00 – 12/27 7:00	75	30	
12/27 7:00 – 12/27 23:00			28

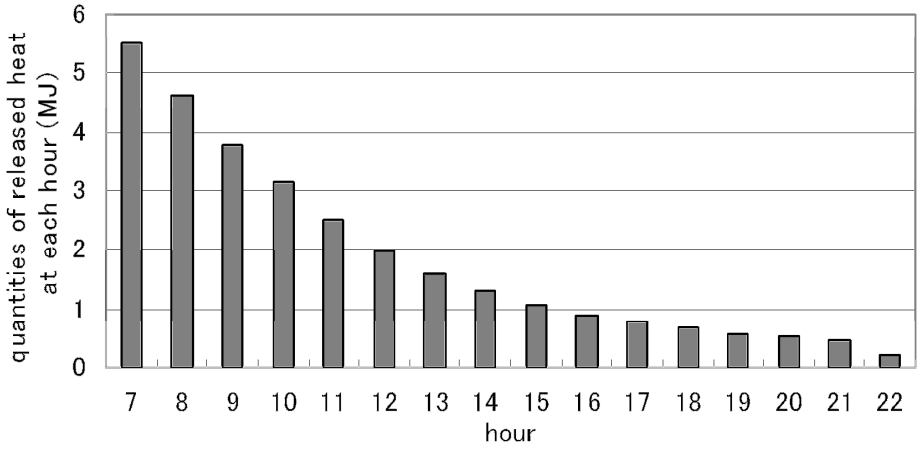

FIG. 11: Quantities of released heat at each hour from 12/24 7:00 to 22:00.

4. Summary and Conclusions

In the house that has a crawl space with the insulated foundation walls and non-insulated floor over the crawl space, if all the crawl space can be heated, then the entire floor will be heated, and as the result whole the space of the first floor will become the radiant heating environment. We call this heating system 'Crawl-space heating'.

A crawl-space heating system combined with the thermal storage using the air source heat pump as the heat source was introduced. To verify the efficiency of this heating system, field test was carried out in an experimental house in Osaka, Japan.

A heat pump, two funs and two thermal storage equipments were installed in the crawl space. In the period from 23:00 to 7:00, that is off-peak electrical load period in Japan, the heat pump generates about 80 MJ heat and supplies the heat to the thermal storage equipments. In the same period, about 40 % of the supplied heat was stored in the thermal storage equipments and the balance 60 % was used to heat the crawl space. In the period from 7:00 to 23:00, that is peak period, the stored heat in the thermal storage equipments was released to the air coming from the fans and was used to heat the crawl space.

Under the condition of the crawl-space heating, the radiant heating environment was obtained in the first floor. In the environment, vertical temperature distribution was small and floor-surface temperature was higher than the space. Furthermore, the difference between the room temperature in the first floor can be minimized as far as the adequate circulation of the warm air in the crawl space is secured and also the thermal conductivity of the floor material is good enough to transmit the heat in the crawl space to the above room.

5. References

Badescu V. (2003). Model of a thermal energy storage device integrated into a solar assisted heat pump system for space heating, *Energy conversion and management*, Vol 44, 1589-1604.

Fujita K., Iwamae A. and Matsushita T. (2007). A study on thermal performance of heat storage system connected with heat pump for residential houses, *Proceedings of Building Simulation 2007*, Tsinghua University, Beijing, China, 321-328

Lin K., Zhang Y., Xu X., Di H., Yang R. and Qin P. (2005). Experimental study of under-floor electric heating system with shape-stabilized PCM plates, *Energy and Buildings*, Vol 37, 215-220.

Long J. and Zhu D. (2008). Numerical and experimental study on heat pump water heater with PCM for thermal storage, *Energy and Buildings*, Vol 40, 666-672.

Schibuola L. (2000). Heat pump seasonal performance evaluation: a proposal for a European standard, *Applied thermal engineering*, Vol 20, 387-398.

Accuracy of the Calculation of Heating and Cooling Energy Needs in Nordic Conditions

Timo Kalema, professor,
Department of Mechanics and Design, Tampere University of Technology;
timo.kalema@tut.fi

Petri Pylsy, M. Sc. Student,
Department of Mechanics and Design, Tampere University of Technology;
petri.pylsy@tut.fi

KEYWORDS: Buildings, heating, cooling, energy, calculation.

SUMMARY:

In a joint Nordic research – Nordic Thermal Mass – it was compared calculation results for energy need obtained with six simulation programs and one program based on the monthly energy balance method of EN 832. The level of complexity of these programs was different. The calculations were made for a single-family house and for an apartment flat fulfilling the Finnish building regulations and using the weather data of Helsinki. The inaccuracy in the calculated needs for heating energy approximately was 5 kWh/m^2/a (8 %). In the cooling energy the inaccuracy was much higher, 5 kWh/m^2/a (50 %) for the single-family house and 20 kWh/m^2/a (45 %) for the apartment flat.

The monthly energy balance method ISO FDIS 13790 gives accurate results for heating energy when the building's time constant is at least approximately 50 h. For smaller time constants there is an error in the utilisation factor leading to too high heating energy needs. This error can be seen by comparing the utilisation factors of ISO FDIS 13790 with those calculated by the simulation programs of our study. On the other hand the utilisation factor of ISO FDIS 13790 seems to be correct, when the building's time constant is at least 50 h. This means that the building should include at least one massive surface, e.g. a massive floor.

1. Introduction

There are in principle two levels in the energy analysis of buildings. It can be used thermal simulation programs or calculation methods based on a monthly energy balance. A simulation program here means a program which uses a short time-step in calculations (typically one hour) and which calculates at the same time heating and cooling energy needs and the interior temperature. There are many buildings' thermal simulation programs having different principles and complexity e.g. in calculating convection, thermal radiation between rooms' surfaces and transient conduction. In this study six simulation programs were used.

An energy balance method calculates only monthly heating and cooling needs. From these the perhaps best known method is the standard proposal ISO FDIS 13790, *Thermal Performance of Buildings – Calculation of Energy Use for Space Heating and Cooling (2005).* This is a modification and an addition to the standard EN 832 *Thermal Performance of Buildings – Calculation of Energy Use for Space Heating*. The latest version of ISO FDIS 13790 also includes a calculation method for monthly cooling energy and a simplified hourly calculation method for heating and cooling energy.

The role of buildings' energy analysis using calculations is coming more important also due to new regulations. *The directive on the energy performance of buildings* (EPBD, 2002) demands, that the energy efficiency (e.g. energy consumption/floor area) must be calculated for new buildings in the design phase. EPBD also demands the use of an energy certificate for buildings, when they are sold or rented. This certificate is based for new buildings on calculations. It is naturally important that these calculations are made in an accurate way.

The accuracy of buildings' energy calculations depends on three issues:

1. On the skills of the modeller to describe the reality into a calculation model

2. On the reliability of physical input data (e.g. dimensions of surfaces, values of materials' thermal properties, heat transfer coefficients) and
3. On the calculation method used.

The first two issues are not handled here. It is clear that the more skilled and experienced the modeller is and the more reliable input data is obtainable the more reliable results he/she can obtain. However, interesting is to find out if more complex analysis methods give more accurate results and if there are some faults in the simplifications used in the monthly calculation method. E.g. the correctness of the gain utilisation factor of ISO FDIS 13790 has been questioned sometimes, partly therefore that its origin and background is unclear.

The accuracy of buildings' energy analysis is a much studied issue in international co-operation (e.g. IEA work of Lomas (1994, 1997)). However, there is no much information on the reliability of the accuracy of energy calculation in Nordic climate and for Nordic buildings and what is the accuracy of the standard proposal ISO FDIS 13790.

The results of this study are based on the research Kalema & al (2006). This was a joint Nordic research, which was financed by the building material industry. There were involved researchers from Finland, Sweden and Norway from two universities (Tampere University of Technology and Kungliga Tekniska Högskolan), two research institutes (VTT and Sintef) and three companies (maxit energy Ab, Cementa Ab and Ax-Consulting Oy). Six thermal simulation programs CONSOLIS ENERGY (Jóhannesson, 2005), IDA Climate and Energy (2006), SciaQpro, VIP (2002), VTT House model (Tuomaala, 2002) and TASE (Kalema, 1992) and a monthly energy balance method (maxit energy (2006) based on EN 832) were used. From the six simulation programs CONSOLIS ENERGY and VIP are less complex than the four other.

2. Utilisation factor for heat gains and heat losses

The central idea in ISO FDIS 13790 is to take into account the useful part of internal and solar heat gains in the energy need for heating by using *the gain utilisation factor*. Correspondingly the useful heat loss can be taken into account in the energy need for cooling by using *the loss utilisation factor*. The utilisation factor is a correlation equation based on thermal simulations. It has been studied e.g. in the PASSYS project (1989). However, its exact background is ambiguous.

We have compared in this study two forms of gain utilisation factors; those of EN 832 and ISO FDIS 13790 (Eqs. 3 and 4) and those presented by van Dijk & Arkestejn (Eq. 9). Parameters $a_0 = 1.0$ and $\tau_0 = 15$ h of ISO FDIS 13790 are the same both in the calculation of monthly heating energy using the gain utilisation factor as well as in that of monthly cooling energy using the loss utilisation factor.

The gain utilisation factor for heating (subscript H) is defined by Eq. 1 and the loss utilisation factor for cooling (subscript C) by Eq. 2:

$$Q_{NH} = Q_{LH} - \eta_{GH} Q_{GH} \tag{1}$$

$$Q_{NC} = Q_{GC} - \eta_{LG} Q_{LC} \tag{2}$$

Q_N is monthly energy need (H heating, C cooling)
Q_L monthly heat loss
Q_G monthly heat gain (internal and solar gains)
η_G monthly gain utilisation factor for heating
η_L monthly loss utilisation factor for cooling

The standard proposal *ISO FDIS 13790* gives for the gain utilisation factor for heating (η_{GH}) Eq. 3 as a function of the gain/loss ratio (γ_{GH}). Correspondingly, for the loss utilisation factor for cooling (η_{LC}) Eq. 4 is given as a function of the loss/gain ratio λ_{LC}. In addition there are equations for the special case when the gain/loss ratio is exactly 1:

$$\eta_{GH} = \frac{1 - \gamma_{GH}^{\,a_H}}{1 - \gamma_{GH}^{\,a_H + 1}} \tag{3}$$

$$\eta_{LC} = \frac{1 - \lambda_{LC}^{\,a_C}}{1 - \lambda_{LC}^{\,a_C+1}} \quad (4)$$

$$\gamma_{GH} = \frac{Q_{GH}}{Q_{LH}} \quad (5)$$

$$\lambda_{LC} = \frac{Q_{LC}}{Q_{GC}} \quad (6)$$

The total heat loss Q_L is the sum of transmission (Q_T) and ventilation heat losses (Q_V) and the total amount of heat gains (Q_G) consists from the internal heat gains (such as lighting and heat from appliances and persons) (Q_i) and from the solar heat gains (Q_S), which mainly consists from the solar radiation transmitted trough windows.

The dimensionless parameters a_H and a_C in Eqs. 3 – 4 are calculated from Eq. 7, which is the same for heating and for cooling:

$$a = a_H = a_C = a_0 + \frac{\tau}{\tau_0} \quad (7)$$

a_0 is parameter, which is $a_0 = 1.0$ for continuously heated buildings and for monthly calculations

τ_0 reference time constant, which is τ_0 = 15 h for continuously heated buildings and monthly calculations

The time constant of a building or its zone is

$$\tau_H = \frac{C_m}{H_L} \quad (8)$$

C_m is internal heat capacity of the building or its zone
H_L heat loss coefficient of the building or its zone

van Dijk & Arkesteijn (1987) report as a result of the PASSYS project some gain utilisation factors. From the equations they have studied the best fit for the gain utilisation factor for the cases of our study seems to be obtainable with Eq. 9:

$$\eta_{GH} = 1 - e^{\frac{-K}{\gamma_H - D}} \quad (9)$$

with the values K = 1.35 and D = 0.27 for a massive building and K = 1.19 and D = 0.0 for a light building.

When evaluating the validity of the monthly utilisation factors of Eq. 3 and Eq. 9 reference utilisation factors of this study are calculated monthly from two simulations using Eq. 10. Simulation 1 is made using a fixed interior temperature (both the heating and the cooling set point temperatures are 21 °C), which gives a heat loss comparable with that of ISO FDIS 13790. Simulation 2 is made using real set-point temperatures (21 °C for heating and 25 °C for cooling in this study). The latter calculation gives a real heating energy need. With these two simulations twelve monthly values for the gain utilisation factor are obtained from Eq. 10:

$$\eta_{GH} = \frac{Q_{L1} - Q_{NH2}}{Q_{GH}} \quad (10)$$

Q_{L1} is monthly heat loss from simulation 1 calculated at a fixed interior temperature
Q_{NH2} monthly heating energy need from simulation 2 with real set point temperatures
Q_{GH} monthly total heat gain (same in both simulations)

In this study the utilisation factors were mainly analysed using TASE and CONSOLIS ENERGY programs.

3. Input data of calculations

Calculations were made for a 162 m^2 single-family house and for apartment flats having either a single-zone 57 m^2 flat or a double-zone 78 m^2 flat. The flats are located on the second or on the third floor of a four-storey building, so that the floor and the ceiling are interior surfaces. The basic model for both building types is a double-zone model, but also single-zone modelling is used. In addition the single-family house is also calculated as a 15 room model with the VTT House model.

The basic direction of the exterior facade of the single-family house is east – west. The main windows (45 % from the total window area) are facing towards south and the total window area/floor area is 12 %. The basic direction of the exterior facade of the double-zone model of the apartment flat is north – south. The main windows (84 % from the total window area) are facing towards west and the total window area/floor area is 25 %. For the single-zone flat the window is facing towards west and its size/floor area is 21 %.

The single-family house is a ridge roofed building having alternatively four structures; the extra light, the light, the semi-weight and the massive ones. Their thermal capacities per floor area are 45 - 560 kJ/K/m^2 and their time constants 15 – 190 h, when the building is modelled as a single-zone one (TABLE 1). The U-values of the corresponding components of the exterior envelope are exactly the same for all structures and fulfil the present Finnish building regulations (2003). For the sake of simplicity and unambiguity the floor is assumed to be a ventilated floor, below which exterior temperature prevails.

The apartment flat has two constructions; the extra-light and the massive one. Their thermal capacities and time constants for the double-zone case are 55 and 1330 kJ/K/m^2 and 17 and 410 h, respectively. In the extra-light flat all constructions (floor, ceiling, exterior wall and interior walls) are light and in the massive one they are heavy (concrete). Because we have studied only one light apartment flat structure, it is later called also the light one.

The set point temperature for heating is 21 °C and that for mechanical cooling 25 °C. Mechanical cooling was used to prevent the overheating of rooms in summer and to describe the natural ventilation used during summer time. The ventilation air change rate was for the single-family house 0.58 1/h and 0.75 1/h for the flat. Correspondingly the efficiency of the heat recovery system was for the single-family house 0.50 and 0.30 for the flat. The internal heat gains of both building types were 5 W/m^2 calculated per floor area on the average. They were 50 % convective and 50 % radiative. The weather data used was the synthetic weather of Meteonorm for Helsinki (Meteonorm, 2005).

Also in order to avoid unambiguity as far as possible due to different modelling principles in different simulation programs the long-wave radiation and the absorption of solar radiation on exterior walls and roofs was neglected as it also usually is neglected in calculations made by ISO FDIS 13790.

4. Accuracy of calculating of heating and cooling energy

The absolute inaccuracy in calculating the annual heating energy is approximately 5 kWh/m^2 for the single-family house as well as for the apartment flat, when the evaluation is made using the results of 4 or 3 programs (TABLES 2 and 3). For the annual cooling energy the corresponding inaccuracy for the single-family house is approximately 5 kWh/m^2, but for the flat clearly poorer, approximately 20 kWh/m^2. As relative inaccuracies these are 8 – 55 %. The relative inaccuracy in cooling energy is high due to the small absolute energy need.

If the calculation results for the annual energy need of the single-family house are compared by neglecting the effects of the zoning (single-zone, double-zone or a detailed 15- zone model) and those of the thermal mass (an extra-light or a massive building) the heating energy needs calculated are 58 – 76 kWh/m^2 and the cooling energy needs 4 – 20 kWh/m^2 (FIG. 1). The clearly highest energy needs are obtained with the 15 zone VTT House Model with closed interior doors. In this case, simultaneous heating and cooling increases both heating and cooling energy needs. Thus from the point of the accuracy of the results it is extremely important that the specification of the calculation is made detailed enough.

The calculation of the cooling energy of a flat is really a challenging task. Part of the great differences of TABLE 3 can be due to various ways to utilize outdoor air for cooling in the simulation programs. However, this does not change the fact, that the calculator obtains very different results.

The monthly calculation method of ISO FDIS 13790 gives for the cooling energy of the extra-light and the massive single-family houses approximately 7 and 1 kWh/m^2a, which are slightly lower than the values obtained

with IDA and TASE programs (TABLE 2). Thus, it can be stated that the results obtained with ISO FDIS 13790 for cooling energy are comparable with those of the simulation programs, when the total inaccuracy of all calculations is taken into account.

TABLE 1: Thermal capacities and time-constants of the single-family house studied.

Symbol	**Structure**	**Thermal capacity**	**Time constant**
		kJ/Km²	*h*
ExL	**Extra-light**, all structures light	45	15
Lig	**Light**, concrete floor, other structures light	190	64
SWe	**Semi weight**, block walls, concrete roof and floor	430	150
Mas	**Massive,** all structures concrete	560	190

TABLE 2: Maximum differences in the energy needs of the double-zone case of the single-family house. Results of IDA, CONSOLIS ENERGY, TASE and SciaQPro.

Thermal mass	**Energy**	**Energy need**		**Difference between max and min energy needs**		**Programs**	
		Max.	**Min.**	**Absolute**	**Relative***	**Max**	**Min**
		kWh/m²/a		*kWh/m²/a*	*%*		
Mas	Heating	63.8	58.8	5.0	8	SciaQPro	IDA
Mas	Cooling	7.8	3.5	4.3	55	SciaQPro	IDA
ExL	Heating	66.5	61.2	5.3	8	SciaQPro	IDA
ExL	Cooling	12.5	7.0	5.5	44	SciaQPro	TASE

* Calculated from the greater energy consumption

TABLE 3:. Maximum differences in the energy needs of the double-zone case of the apartment flat. Results of CONSOLIS ENERGY, TASE and SciaQPro.

Thermal mass	**Energy**	**Energy need**		**Difference between max and min energy needs**		**Programs**	
		Max.	**Min.**	**Absolute**	**Relative***	**Max**	**Min**
		kWh/m²/a		*kWh/m²/a*	*%*		
Mas	Heating	68.2	63.0	5.2	8	Consolis	TASE
Mas	Cooling	42.0	22.0	20.0	48	SciaQPro	TASE
ExL	Heating	71.8	66.0	5.8	8	SciaQPro	TASE
ExL	Cooling	49.5	28.0	21.5	44	SciaQPro	TASE

* Calculated from the greater energy consumption

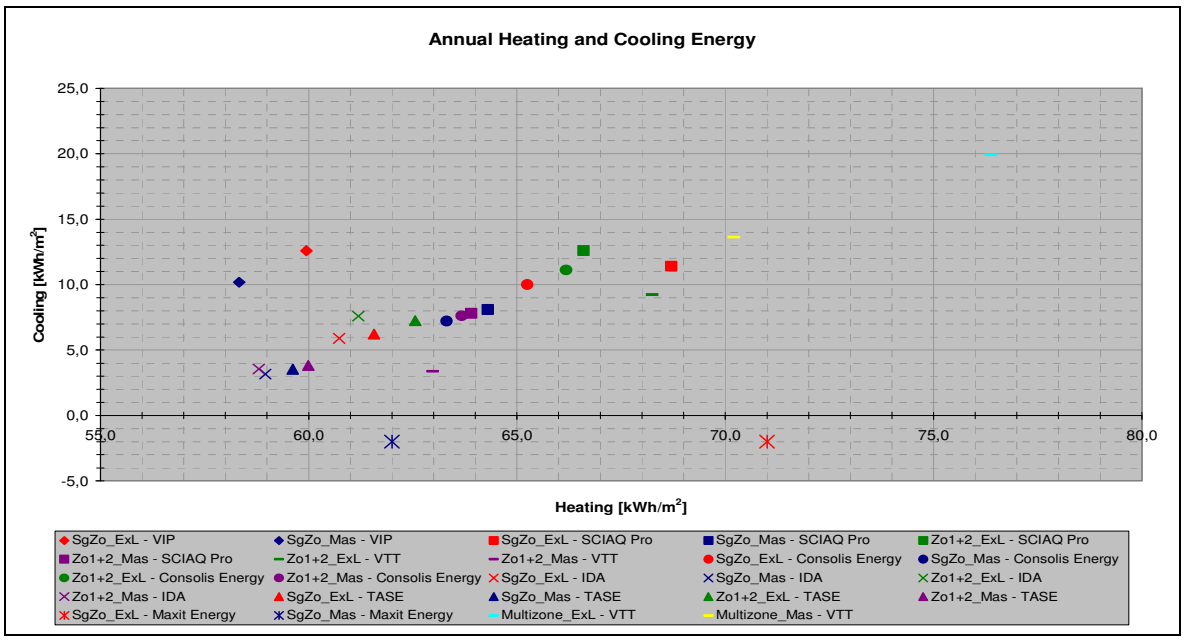

FIG. 1: Heating and cooling energy need for the basic case of the single-family house. Single-zone (SgZo), double-zone (Zo1+2) and 15-zone (MulZone) cases. For maxit energy cooling energy is a fictive value, because it is not calculated.

5. Gain utilisation factor

The accuracy of the gain utilisation factor of Eqs. 1and 3 is essential in the accuracy of the calculation of energy need according to ISO FDIS 13790. The background and the validity of Eq. 3 is somehow ambiguous. FIG.2 shows the gain utilisation factor for the extra-light single-family house calculated with TASE and CONSOLIS ENERGY programs and those calculated with Eqs. 3 and 9. Each point presents one monthly calculation result. The utilisation factors of ISO FDIS 13790 as well as that of van Dijk &Arkesteijn give clearly too low values for the extra-light building. This error can also be seen from FIG. 1 in which the heating energy of the extra-light building is approximately 15 % higher than that of the massive building, when the energy need is calculated using EN 832. The right value for this difference is approximately 3 % according to the simulation models of this study.

On the other hand FIG. 3 shows that the gain utilization factor of ISO FDIS 13790 gives a good fit for the massive house compared with the simulation results obtained with TASE and CONSOLIS ENERGY. This good fit is obtained also for the light and the semi weight houses. The practical validity area for the use of ISO FDIS 13790 is that the building must have at least one massive surface (usually floor) when its time constant and thermal capacity are at least 50 h and 150 kJ/Km^2. However, the exact validity area was not tried to find out in this study.

Same results as for the single-family house were obtained for also for the apartment flat. The utilization factor of ISO FDIS 13790 was valid for the massive apartment flat but gave too low values for the extra-light flat without any massive surfaces.

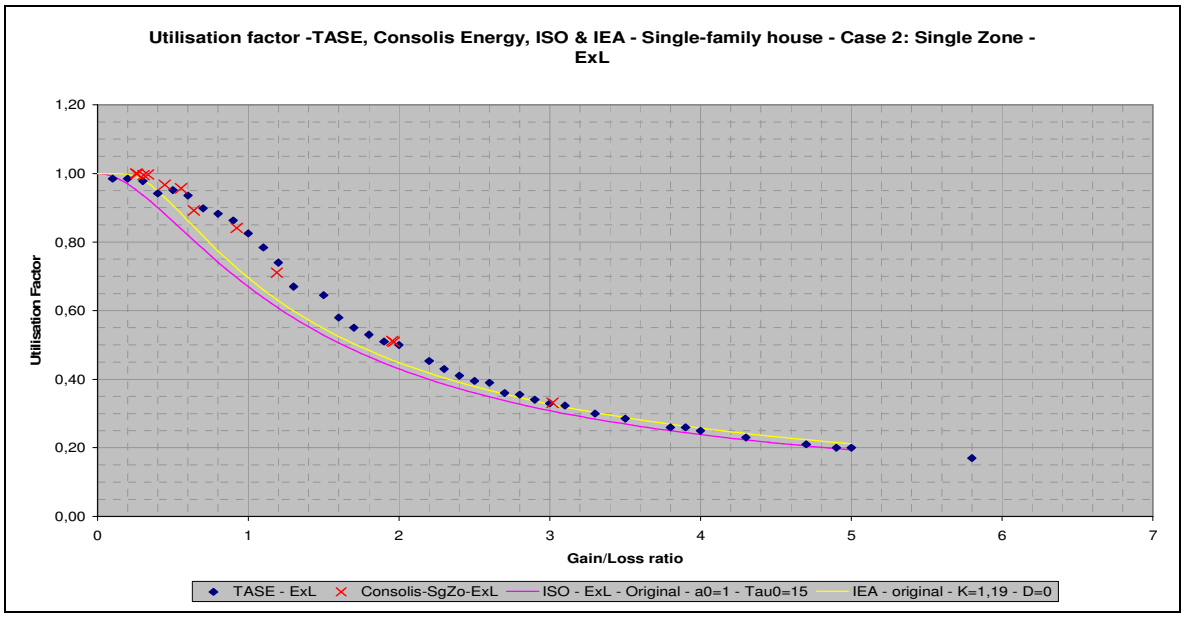

FIG. 2: Gain utilisation factor for the extra-light single-zone, single-family house according to TASE, CONSOLIS ENERGY, ISO FDIS 13790 and van Dijk & Arkesteijn (IEA).

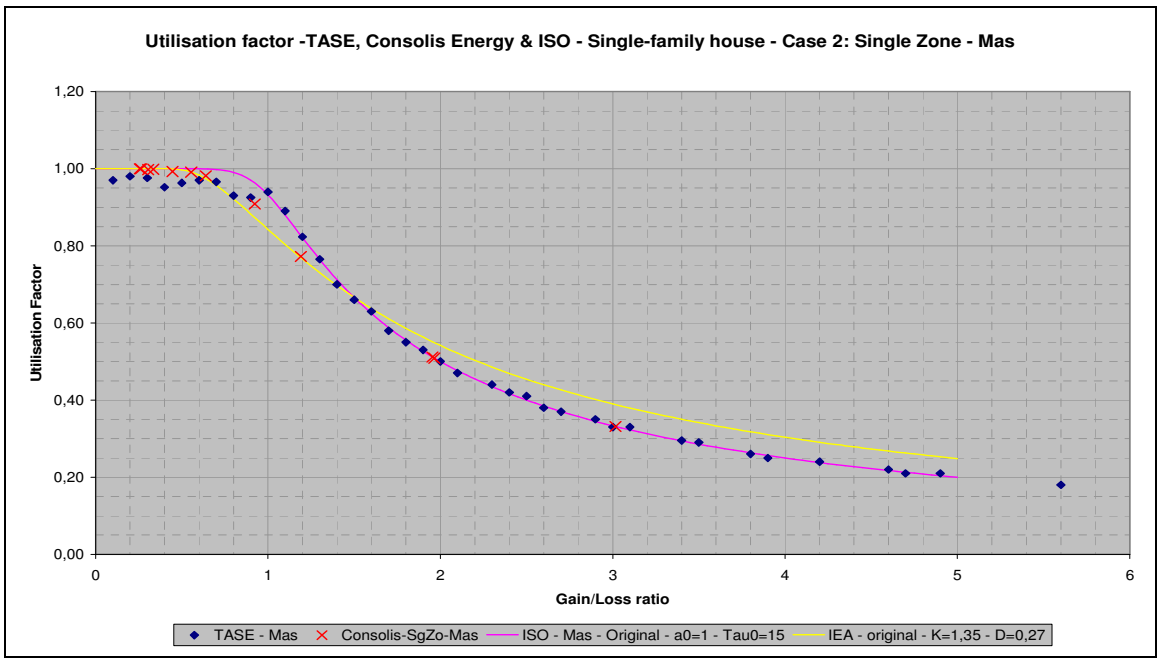

FIG. 3: Gain utilisation factor for the massive single-zone, single-family house according to TASE, CONSOLIS ENERGY, ISO FDIS 13790 and van Dijk & Arkesteijn (IEA).

6. References

van Dijk H.A.L. and Arkesteijn C.A.M. (1987). Windows and Space Heating Requirements; Parameter studies leading to a simplified calculation method. The Netherlands National Report on Activities within Step 5, TNO Institute of Applied Physics. *International Energy Agency, Energy conservation in buildings and community systems programme, Annex XII, Windows and fenestration.* 151 p.

Directive 2002/91/EC of the European parliament and of the Council of 16 December 2002 on the energy performance of buildings. Brussels 2002.

European standard EN 832 (1998). Thermal performance of buildings – Calculation of energy use for heating – Residential buildings. European Committee for Standardisation. Brussels. Belgium.

Finnish Building Regulations, Part C3, Thermal insulation of Buildings. Regulations (2003). Ministry of Environment. http://www.finlex.fi/data/normit/1919-C3s.pdf. Read 22.12.2006.

IDA Indoor Climate and Energy 3.0 (2006). http://www.equa.se/eng.ice.html. Read 22.12.2006.

ISO/FDIS 13790 (2005). Thermal Performance of Buildings – Calculation of Energy Use for Space Heating and Cooling, ISO TC 163/SC 2. International Organization for Standardisation. Geneva.

Jóhannesson G. (2005). Building energy – A practical design tool meeting the requirements of the EPBD. http://www.byv.kth.se/avd/byte/reykjavik/pdf/art_125.pdf. Read 22.12.2006.

Kalema T. (1992). Thermal Analysis of Buildings – Verification and Further Development of the TASE Program, Tampere University of Technology. Publication 87. 185 p.

Kalema T., Pylsy P., Hagengran P., Jóhannesson G., Airaksinen M., Dokka T. H., Öberg M., Pöysti M., Rapp K. and Keski-Opas J. (2006). Nordic Thermal Mass – Effect on Energy and Indoor Climate (2006), Tampere University of Technology, Report 184, 105 p.

Lomas K. J., Eppel H., Martin C. and Bloomfield D. (1994). Empirical Validation of Thermal Building Simulation Programs Using Test Room Data, Volume 1, Final Report. *International Energy Agency, Annex 21 and Task 12.* 34 p + Appendices.

Lomas K. J., Eppel H., Martin C. J. and Bloomfield D. (1997). Empirical Validation of Building Energy Simulation Programs. *Energy and Buildings 26 (1997), p. 253 – 275.*

maxit energy 2.0 (2006), Calculation of the net space heating energy. maxit Oy Ab. Helsinki.

Meteonorm (2005). Global meteorological database for engineers, planners and education. Version 5.0. Meteotest, Switzerland. www.meteotest.ch. Read 22.12.2006.

The PASSYS Project Phase 1 (1989). Subgroup Simplified Design Tools. Final Report. 1986 – 1989. EUR 12998 EN. 081 – 89 – PASSYS – SDT – FP- 020. Commissioning of the European Communities. Directorate-General XII for Science, Research and Development. 208 p.

Tuomaala P. (2002). Implementation and evaluation of air flow and heat transfer routines for building simulation tools, VTT Publications 471.

VIP+ (2002). Computer program for energy balance calculations. STRUSOFT, Malmö, Sweden.

An Analysis of Stochastic Properties of Room Air Temperature and Heating/Cooling Load

– Analytical Method of Non-Gaussian Noise –

Shuichi Hokoi, Professor,
Department of Architecture and Architectural Engineering,, Kyoto University;
hokoi@archi.kyoto-u.ac.jp

KEYWORDS: Heating/cooling load, External climates, Stochastic properties, Non-Gaussian noise, ARMA model, Characteristic function

SUMMARY:
External climatic conditions such as outdoor air temperature and solar radiation fluctuate randomly with time, and cause the random fluctuation of room air temperature, humidity and heating/cooling load. So far, the authors have presented a method which analyzed the stochastic properties of room air temperature, humidity and heating/cooling load assuming that the probability distribution of the external parameters is Gaussian (Normal). In this paper, a new method is proposed which gives the (probability) density function of room air temperature and heating/cooling load taking into account non-Gaussian external climates. This method is a simple extension to the second-order analysis already shown in previous papers. A thermal system composed of one mass (node) is used to examine the relationship between the eigenvalue of the system and the degree of non-Gaussianity. Next, the similar calculation using a simple room clarifies the influence of non-Gaussianity on room air temperature and heating/cooling load. The utility of the second-order calculation method, which gives only the mean and variance, is discussed through comparison with the present results.

1. Introduction

Exact estimation and prediction of heating/cooling load is required for an energy saving design and operation of both a building and its air-conditioning systems. For this purpose, an appropriate meteorological data and a method of thermal calculation are necessary.
Since the external conditions such as outdoor temperature and solar radiation change randomly, it has to be considered in the load calculation[1)2)]. In this regard, we have been investigating calculation methods of the room temperatures and loads mainly in case of intermittent heating/cooling[3)4)]. In these analyses, the means and variances of the room air temperature and load were calculated based on the assumption that the outdoor temperature and solar radiation are the sum of the deterministic and random components, and the random components can be expressed as linear models with white noises as inputs. When the system dealt with is linear and the input noise is white noise with Gaussian distribution (Normal distribution), the room temperature and load also become Gaussian, thus the (probability) density function ("pdf" hereafter) of them can be obtained by using the calculated means and variances (called "second-order method", hereafter). Based on the pdf, the maximum load and the cumulative distribution of the heating/cooling load can be determined easily.
The results of the past studies on the climatic data show that the outdoor temperature and humidity ratio have almost Gaussian distributions[5)6)]. Although the solar radiation is not distributed as Gaussian[5)6)7)], an approximation as Gaussian gives a reasonable result from a practical point of view.
However, there are several cases where the Gaussian approximation may not be appropriate. For example, since the incident solar radiation through the windows becomes the cooling load without affected by the thermal buffering of the walls, the pdf's of the cooling load reflects the non-Gaussianity of the solar radiation. In this case, the approximate Gaussian distribution may not be appropriate, and thus the exact pdf is required. This may be especially important when the nonlinear nature of the partial load of the equipment plays an important role. From this point of view, the present study proposes a thermal method of calculating pdf of the room temperature and heating/cooling load when the input variables are non-Gaussian, and investigates its influence.

2. Method of Analysis

2.1 State space expression of system, and mean and variance

A linear building thermal system building can be described by the following state space expression, when the outdoor temperature and solar radiation are expressed by ARMA (Auto-Regressive Moving Average) time series models[4].

$$\mathbf{X}^{j+1} = [\mathbf{A}]^j \mathbf{X}^j + [\mathbf{B}]^j \mathbf{G}^j + [\mathbf{C}]^j \mathbf{E}^j \quad (1)$$

where,
$\mathbf{X}^j$: state variable vector of order n representing room and wall temperatures and heating/cooling load etc.
$\mathbf{G}^j$: vector of order m representing deterministic components of outdoor temperature and solar radiation etc.
$\mathbf{E}^j$: vector of order k representing random components of outdoor temperature and solar radiation etc.
$[\mathbf{A}]^j$, $[\mathbf{B}]^j$, $[\mathbf{C}]^j$: matrices of order (n×n), (n×m) and (n×k), respectively. These are derived from thermal characteristics of room, walls and ARMA models of outdoor temperature and solar radiation.
superscript *j*: (discrete) time
By averaging Equation (1), the equations regarding the mean and variance of $\mathbf{X}^{j+1}$ can be obtained[4].

$$\mathbf{m}_{\mathbf{X}}{}^{j+1} = [\mathbf{A}]^j \mathbf{m}_{\mathbf{X}}{}^j + [\mathbf{B}]^j \mathbf{G}^j \quad (2)$$

$$[\mathbf{\Lambda}_{\mathbf{X}}]^{j+1} = [\mathbf{A}]^j [\mathbf{\Lambda}_{\mathbf{X}}]^j [\mathbf{A}]^{jT} + [\mathbf{C}]^j [\mathbf{\Lambda}_{\mathbf{E}}][\mathbf{C}]^{jT} \quad (3)$$

where, $\mathbf{m}_{\mathbf{X}}{}^j$ is the mean vector of $\mathbf{X}^j$, $[\mathbf{\Lambda}_{\mathbf{X}}]^j$ and $[\mathbf{\Lambda}_{\mathbf{E}}]^j$ are the variance matrices of $\mathbf{X}^j$ and $\mathbf{E}^j$, respectively. By solving these equations, the means and variances of the state variables are calculated. In this level of calculation, only the mean and variance of the random component $\mathbf{E}^j$ of the climatic variables are used, and there is no need for $\mathbf{E}^j$ to be Gaussian. Of course, the pdf's of the room temperature and heating/cooling load cannot be calculated without the pdf of $\mathbf{E}^j$. When $\mathbf{E}^j$ is Gaussian, the room temperature and the heating/cooling load also distribute as Gaussian, and thus the information only about the mean and variance is sufficient to calculate pdf.
In the following section, a method of calculating pdf's of the room temperature and heating/cooling load when the white noise $\mathbf{E}^j$ is not Gaussian.

2.2 Transformation of probability density function and characteristic function

In this section, the fundamentals is given about the pdf and the characteristic function of a random variable when it is linearly transformed, for the theoretical development in section 2.3.
(1) Density function of random variable after linear transformation
Consider the situation where a random variable vector of order n **X** is transformed to a new vector of order n **Z** by the following linear equation.

$$\mathbf{Z} = [\mathbf{A}]\mathbf{X} + [\mathbf{B}]\mathbf{G} \quad (4)$$

where, **G** is a deterministic vector of order m, and **[A]** and **[B]** are matrices of order $(n \times n)$ and $(n \times m)$, respectively. Then the pdf of **Z**, $f_Z(\mathbf{z})$, is expressed in terms of pdf of **X**, $f_X(\mathbf{x})$ as follows[8].

$$f_Z(\mathbf{z}) = |J| f_X(\mathbf{x} = h^{-1}(\mathbf{z})) = \left| \frac{\partial \mathbf{x}^T}{\partial \mathbf{z}} \right| f_X([\mathbf{A}]^{-1}(\mathbf{z} - [\mathbf{B}]\mathbf{g})) \quad (5)$$

where superscript *T* and -1 are transpose and inverse of function and matrix, respectively. *h* is an inverse function of Equation (4). The Jacobian *J* of Equation (4) is given as,

$$J = \left| \partial \mathbf{x}^T / \partial \mathbf{z} \right| = \left| [\mathbf{A}]^{-1T} \right| \quad (6)$$

Thus, it becomes a (time dependent) constant under this transformation.
(2) Transformation of characteristic function
Given the characteristic function of **X**, that is a Fourier Transform of **X**, as $\phi_X(\mathbf{u})$,

$$\phi_X(\mathbf{u}) = \int \ldots \int f_X(\mathbf{x}) e^{i\mathbf{x}^T\mathbf{u}} d\mathbf{x} \quad (7)$$

where, i means unit imaginary number. Then, the characteristic function of **Z**, $\phi_Z(\mathbf{u})$, is given as follows by using Equation (5).

$$\phi_Z(\mathbf{u}) = \int \dots \int f_Z(\mathbf{z}) e^{i\mathbf{z}^T\mathbf{u}} d\mathbf{z} = \int \dots \int \left|J\right| f_X([\mathbf{A}]^{-1}(\mathbf{z}-[\mathbf{B}]\mathbf{g})) e^{i\mathbf{z}^T\mathbf{u}} d\mathbf{z} \tag{8}$$

Then, the following transformation of variable

$$\mathbf{y} = [\mathbf{A}]^{-1}(\mathbf{z}-[\mathbf{B}]\mathbf{g}) \quad (\mathbf{z} = [\mathbf{A}]\mathbf{y} + [\mathbf{B}]\mathbf{g}) \tag{9}$$

is introduced to Equation (8).

$$\begin{aligned}\phi_Z(\mathbf{u}) &= \int \dots \int \left|\frac{\partial \mathbf{x}^T}{\partial \mathbf{z}}\right| f_X(\mathbf{y}) e^{i([\mathbf{A}]\mathbf{y}+[\mathbf{B}]\mathbf{g})^T\mathbf{u}} \left|\frac{\partial \mathbf{z}^T}{\partial \mathbf{y}}\right| d\mathbf{y} \\ &= \int \dots \int f_X(\mathbf{y}) e^{i\mathbf{y}^T[\mathbf{A}]^T\mathbf{u}} e^{i\mathbf{g}^T[\mathbf{B}]^T\mathbf{u}} d\mathbf{y} = e^{i\mathbf{g}^T[\mathbf{B}]^T\mathbf{u}} \int \dots \int f_X(\mathbf{y}) e^{i\mathbf{y}^T[\mathbf{A}]^T\mathbf{u}} d\mathbf{y} \\ &= e^{i\mathbf{g}^T[\mathbf{B}]^T\mathbf{u}} \phi_X([\mathbf{A}]^T\mathbf{u})\end{aligned} \tag{10}$$

(3) pdf of sum of two independent random variables

The pdf of random variable **Q**, the sum of independent two random variables **Z** and **W** of n-th order, is given as[8)]

$$f_Q(\mathbf{q}) = \int \dots \int f_Z(\mathbf{q}-\mathbf{s}) f_W(\mathbf{s}) d\mathbf{s} \tag{11}$$

The characteristic function of this pdf is,

$$\begin{aligned}\phi_Q(\mathbf{u}) &= \int \dots \int f_Q(\mathbf{q}) e^{i\mathbf{q}^T\mathbf{u}} d\mathbf{q} = \int \dots \int [\int \dots \int f_Z(\mathbf{q}-\mathbf{s}) f_W(\mathbf{s}) d\mathbf{s}] e^{i\mathbf{q}^T\mathbf{u}} d\mathbf{q} \\ &= \int \dots \int f_Z(\mathbf{q}-\mathbf{s}) e^{i(\mathbf{q}-\mathbf{s})^T\mathbf{u}} d\mathbf{q} \int \dots \int f_Z(\mathbf{s}) e^{i\mathbf{s}^T\mathbf{u}} d\mathbf{s} = \phi_Z(\mathbf{u})\phi_W(\mathbf{u})\end{aligned} \tag{12}$$

Thus, it can be expressed as the product of two characteristic functions.

(4) Different dimensions of random variables before and after transformation

In general, the dimensions of $\mathbf{X}^{j+1}$ and $\mathbf{E}^j$ in Equation (1) are different. That is,

$$\begin{matrix}\mathbf{W} = [\mathbf{C}]\mathbf{E} \\ n \quad n\times k\, k\end{matrix} \tag{13}$$

In this case, since the inverse of the matrix [**C**] does not exist, the manipulations in sections (2) and (3) cannot be applied. Thus, this equation is first extended to n-dimension by introducing a small number ε and white noises $E_{k+1}, \cdots, E_n$ independent of $\mathbf{E}_A$ (=**E**).

$$\begin{bmatrix} W_1 \\ \dots \\ W_k \\ W_{k+1} \\ \dots \\ W_n \end{bmatrix} = \begin{bmatrix} c_{11}, \dots\dots, c_{1k}, & 0, \dots\dots, 0 \\ \dots\dots\dots\dots & 0 \\ c_{k1}, \dots\dots, c_{kk}, & 0, \dots\dots, 0 \\ c_{k+11}, \dots, c_{k+1k}, & \varepsilon, \dots\dots, 0 \\ \dots\dots\dots\dots & \\ c_{n1}, \dots\dots, c_{nk}, & 0, \dots\dots, \varepsilon \end{bmatrix} \begin{bmatrix} E_1 \\ \dots \\ E_k \\ E_{k+1} \\ \dots \\ E_n \end{bmatrix} \tag{14}$$

$$\mathbf{W}' = [\mathbf{C}']\mathbf{E}' = [\mathbf{C}, \mathbf{D}] \begin{bmatrix} \mathbf{E} \\ \mathbf{E}_B \end{bmatrix} = [\mathbf{C}, \mathbf{D}] \begin{bmatrix} \mathbf{E}_A \\ \mathbf{E}_B \end{bmatrix} \tag{15}$$

By setting $\varepsilon \rightarrow 0$, the vector **W**'will be changed to **W** at the final stage. Since the inverse matrix of [**C**'] exists, Equation (10) can be applied. Since this corresponds to the case where [**A**]→[**C**'], [**B**]→[**0**] in Equation (4),

$$\phi_{W'}(\mathbf{u}) = \phi_{E'}([\mathbf{C}']^T \mathbf{u}) \tag{16}$$

can be obtained. At this stage, by setting $\varepsilon \to 0$, $\phi_{W'} \to \phi_W$ and $[\mathbf{C}'] \to [\mathbf{C}|\ \mathbf{0}]$ result. Thus, Equation (16) becomes as follows.

$$\phi_W(\mathbf{u}) = \phi_{E'}([\mathbf{C}|\ \mathbf{0}]^T \mathbf{u}) \tag{17}$$

Dividing **E**' into two independent components $\mathbf{E}_A$ (with order k) and $\mathbf{E}_B$ (with order n-k), whose pdf's are $f_{E_A}(\mathbf{e}_A)$ and $f_{E_B}(\mathbf{e}_B)$ respectively, then Equation (16) becomes,

$$\begin{aligned}
\phi_{E'}([\mathbf{C}']^T \mathbf{u}) &= \int \cdots \int f_{E'}(\mathbf{e}') e^{i\mathbf{e}'^T [\mathbf{C}']^T \mathbf{u}} d\mathbf{e}' = \int \cdots \int f_{E_A}(\mathbf{e}_A) f_{E_B}(\mathbf{e}_B) EXP(i \begin{bmatrix} \mathbf{e}_A \\ \mathbf{e}_B \end{bmatrix}^T [\mathbf{C}|\ \mathbf{0}]^T \mathbf{u}) d\mathbf{e}_A d\mathbf{e}_B \\
&= \int \cdots \int f_{E_A}(\mathbf{e}_A) f_{E_B}(\mathbf{e}_B) EXP(i[\mathbf{e}_A{}^T, \mathbf{e}_B{}^T] \begin{bmatrix} [\mathbf{C}]^T \mathbf{u} \\ [\mathbf{0}]^T \mathbf{u} \end{bmatrix}) d\mathbf{e}_A d\mathbf{e}_B \\
&= \int \cdots \int f_{E_A}(\mathbf{e}_A) EXP(i\mathbf{e}_A{}^T [\mathbf{C}]^T \mathbf{u}) f_{E_B}(\mathbf{e}_B) EXP(i\mathbf{e}_B{}^T [\mathbf{0}]^T \mathbf{u}) d\mathbf{e}_A d\mathbf{e}_B \\
&= \phi_{E_A}([\mathbf{C}]^T \mathbf{u}) \phi_{E_B}([\mathbf{0}]^T \mathbf{u}) = \phi_{E_A}([\mathbf{C}]^T \mathbf{u}) \phi_{E_B}(\mathbf{0}) = \phi_{E_A}([\mathbf{C}]^T \mathbf{u}) = \phi_E([\mathbf{C}]^T \mathbf{u})
\end{aligned} \tag{18}$$

where, $\mathbf{e}_A$ and $\mathbf{e}_B$ are two vectors with orders n and n-k, respectively. Also, the relationship $\phi(\mathbf{0})=1$ for any characteristic function was used. By inserting Equation (18) into Equation (17),

$$\phi_W(\mathbf{u}) = \phi_E([\mathbf{C}]^T \mathbf{u}) \tag{19}$$

is obtained. This means that Equation (10) is applicable even in this case.

2.3 Characteristic function of $\mathbf{X}^{j+1}$

By making use of the relationships obtained in section 2.2, pdf of $\mathbf{X}^{j+1}$ will be calculated, given the pdf of $\mathbf{X}^j$ in Equation (1). First, by making use of Equation (10), the characteristic function $\phi_Z(\mathbf{u})$ of **Z**,

$$\mathbf{Z} = [\mathbf{A}]^j \mathbf{X}^j + [\mathbf{B}]^j \mathbf{G}^j \tag{20}$$

can be expressed as follows.

$$\phi_Z(\mathbf{u}) = e^{i\mathbf{g}^{jT} [\mathbf{B}]^{jT} \mathbf{u}} \phi_{X^j}([\mathbf{A}]^{jT} \mathbf{u}) \tag{21}$$

Next, the characteristic function of $\mathbf{W}=[\mathbf{C}]^j\mathbf{E}^j$ can be given as,

$$\phi_W(\mathbf{u}) = \phi_{E^j}([\mathbf{C}]^{jT} \mathbf{u}) \tag{22}$$

by making use of Equation (19). Since **W** and **Z** are independent each other, the characteristic function of $\mathbf{X}^{j+1}$ can be obtained by inserting Equations (21) and (22) into Equation (12), as

$$\phi_{X^{j+1}}(\mathbf{u}) = e^{i\mathbf{g}^{jT} [\mathbf{B}]^{jT} \mathbf{u}} \phi_{X^j}([\mathbf{A}]^{jT} \mathbf{u}) \phi_{E^j}([\mathbf{C}]^{jT} \mathbf{u}) \tag{23}$$

2.4 In case of Gaussian distributions

By making use of the characteristic function of $\mathbf{X}^{j+1}$ obtained in section 2.3, the pdf of $\mathbf{X}^{j+1}$ is calculated in this section by giving a concrete form of the pdf of the random component $\mathbf{E}^j$. First of all, the case where the pdf's of all variables are Gaussian is examined. The characteristic function of a Gaussian distribution is given as[9],

$$\phi(\mathbf{u}) = e^{i\mathbf{m}^T \mathbf{u} - \mathbf{u}^T [\mathbf{\Lambda}] \mathbf{u}/2} \tag{24}$$

where, $\mathbf{m}$ is the mean vector and $[\boldsymbol{\Lambda}]$ is the variance matrix. This equation shows that the mean and variance of a random variable $\mathbf{u}$ can be obtained easily by expressing its characteristic function in a form of Equation (24), where the exponent part is a quadratic function of $\mathbf{u}$. Since the initial states $\mathbf{X}^0$ and the noise $\mathbf{E}^0$ are Gaussian distributed they are expressed as follows.

$$\phi_X(\mathbf{u}) = e^{i\mathbf{m}_{X0}{}^T\mathbf{u} - \mathbf{u}^T[\Lambda_{X0}]\mathbf{u}/2} \tag{25}$$

$$\phi_E(\mathbf{u}) = e^{i\mathbf{m}_e{}^T\mathbf{u} - \mathbf{u}^T[\Lambda_e]\mathbf{u}/2} \tag{26}$$

where, subscript 0 was omitted in $\mathbf{E}^0$ since the noise $\mathbf{E}^j$ is assumed not to change with time. Setting j=0 in Equation (23), and using Equations (25) and (26),

$$\begin{aligned}\phi_{X^1}(\mathbf{u}) &= e^{i\mathbf{g}^{0T}[\mathbf{B}]^{0T}\mathbf{u}}\phi_{X^0}([\mathbf{A}]^{0T}\mathbf{u})\phi_E([\mathbf{C}]^{0T}\mathbf{u}) \\ &= e^{i\mathbf{g}^{0T}[\mathbf{B}]^{0T}\mathbf{u}}\, e^{i\mathbf{m}_{X0}{}^T[\mathbf{A}]^{0T}\mathbf{u} - \mathbf{u}^T[\mathbf{A}]^0[\Lambda_{X0}][\mathbf{A}]^{0T}\mathbf{u}/2} e^{i\mathbf{m}_e{}^T[\mathbf{C}]^{0T}\mathbf{u} - \mathbf{u}^T[\mathbf{C}]^0[\Lambda_e][\mathbf{C}]^{0T}\mathbf{u}/2} \\ &= e^{i(\mathbf{g}^{0T}[\mathbf{B}]^{0T} + \mathbf{m}_{X0}{}^T[\mathbf{A}]^{0T} + i\mathbf{m}_e{}^T[\mathbf{C}]^{0T})\mathbf{u} - \mathbf{u}^T([\mathbf{A}]^0[\Lambda_{X0}][\mathbf{A}]^{0T} - \mathbf{u}^T[\mathbf{C}]^0[\Lambda_e][\mathbf{C}]^{0T})\mathbf{u}/2} = e^{i\mathbf{m}_{X1}{}^T\mathbf{u} - \mathbf{u}^T[\Lambda_{X1}]\mathbf{u}/2}\end{aligned} \tag{27}$$

Therefore, the mean and variance of $\mathbf{X}^1$ (at the next time step j=1) are given as follows.

$$\mathbf{m}_{X1} = (\mathbf{g}^{0T}[\mathbf{B}]^{0T} + \mathbf{m}_{X0}{}^T[\mathbf{A}]^{0T} + \mathbf{m}_e{}^T[\mathbf{C}]^{0T})^T \tag{28}$$

$$\boldsymbol{\Lambda}_{X1} = [\mathbf{A}]^0[\boldsymbol{\Lambda}_{X0}][\mathbf{A}]^{0T} + [\mathbf{C}]^0[\boldsymbol{\Lambda}_e][\mathbf{C}]^{0T} \tag{29}$$

2.5 Noise $\mathbf{E}^j$ composed of two Gaussian distributions

In this case, Equation (26) becomes as follows.

$$\phi_E(\mathbf{u}) = d_1\phi_{E_1}(\mathbf{u}) + d_2\phi_{E_2}(\mathbf{u}) = d_1 e^{i\mathbf{m}_{e1}{}^T\mathbf{u} - \mathbf{u}^T[\Lambda_{e1}]\mathbf{u}/2} + d_2 e^{i\mathbf{m}_{e2}{}^T\mathbf{u} - \mathbf{u}^T[\Lambda_{e2}]\mathbf{u}/2} \tag{30}$$

where, d_2=1-d_1. The same procedure as that in section 2.4 gives the following result.

$$\begin{aligned}\phi_{X^1}(\mathbf{u}) &= e^{i\mathbf{g}^{0T}[\mathbf{B}]^{0T}\mathbf{u}}\phi_{X^0}([\mathbf{A}]^{0T}\mathbf{u})d_1\phi_{E_1}([\mathbf{C}]^{0T}\mathbf{u}) + e^{i\mathbf{g}^{0T}[\mathbf{B}]^{0T}\mathbf{u}}\phi_{X^0}([\mathbf{A}]^{0T}\mathbf{u})d_2\phi_{E_2}([\mathbf{C}]^{0T}\mathbf{u}) \\ &= d_1 e^{i(\mathbf{g}^{0T}[\mathbf{B}]^{0T} + \mathbf{m}_{X0}{}^T[\mathbf{A}]^{0T} + i\mathbf{m}_{e1}{}^T[\mathbf{C}]^{0T})\mathbf{u} - \mathbf{u}^T([\mathbf{A}]^0[\Lambda_{X0}][\mathbf{A}]^{0T}\mathbf{u}/2 - \mathbf{u}^T[\mathbf{C}]^0[\Lambda_{e1}][\mathbf{C}]^{0T})\mathbf{u}/2} \\ &\quad + d_2 e^{i(\mathbf{g}^{0T}[\mathbf{B}]^{0T} + \mathbf{m}_{X0}{}^T[\mathbf{A}]^{0T} + i\mathbf{m}_{e2}{}^T[\mathbf{C}]^{0T})\mathbf{u} - \mathbf{u}^T([\mathbf{A}]^0[\Lambda_{X0}][\mathbf{A}]^{0T}\mathbf{u}/2 - \mathbf{u}^T[\mathbf{C}]^0[\Lambda_{e2}][\mathbf{C}]^{0T})\mathbf{u}/2} \\ &= d_1 e^{i\mathbf{m}_{X11}{}^T\mathbf{u} - \mathbf{u}^T[\Lambda_{X11}]\mathbf{u}/2} + d_2 e^{i\mathbf{m}_{X12}{}^T\mathbf{u} - \mathbf{u}^T[\Lambda_{X12}]\mathbf{u}/2}\end{aligned} \tag{31}$$

By Inverse Fourier Transform of Equation (31), the pdf of $\mathbf{X}^1$ can be calculated. Since ϕ_{X1} is expressed as the sum of two characteristic functions of Gaussian distributions, the pdf of $\mathbf{X}^1$ becomes the sum of two Gaussian distributions with the mean and variances, $\mathbf{m}_{X11}$, $[\boldsymbol{\Lambda}_{X11}]$ and $\mathbf{m}_{X12}$, $[\boldsymbol{\Lambda}_{X12}]$ (Thus, the pdf can be expressed explicitly.). In a similar manner, ϕ_{X2} can be obtained. Since the pdf of $\mathbf{X}^1$ is expressed as the sum of two Gaussian distributions, the pdf of $\mathbf{X}^2$ becomes the sum of four Gaussian distributions. In this method of calculation, thus, the number of the terms increases twice with one time step. It is quite simple to generalize the present method to the case where the pdf of the noise is expressed by a several number of Gaussian distributions.

3. Example Calculations

3.1 Case of one variable (node)

In this section, a system with one variable is dealt with in order to examine the validity of the proposed method and to clarify the influence of non-Gaussian nature. The basic Equation (1) in section 2 is simplified as follows.

$$X^{j+1} = aX^j + E^j \tag{32}$$

Regarding X^j in Equation (32), the room temperature is meant in this section. Consider a room enclosed by a thermally thin wall. The room temperature is assumed to be influenced by the outdoor temperature via the heat transmission through the walls and ventilation. Then, the room temperature θ_r is given as follows,

$$C\frac{d\theta_r}{dt} = (\sum K_i S_i + c\gamma Vn)(\theta_o - \theta_r) \tag{33}$$

where, θ_o is outdoor temperature, C is heat capacity of room, K_i and S_i are overall heat transfer coefficient and surface area of wall i, $c\ \gamma$ is heat capacity of air, V is room volume and n is air exchange rate.
Equation (33) is discretized with time increment Δt as follows.

$$C\frac{{\theta_r}^{j+1} - {\theta_r}^{j}}{\Delta t} = \overline{KS}({\theta_0}^{j} - {\theta_r}^{j}) \tag{34}$$

where, $\overline{KS} = \sum K_i S_i + c\gamma Vn$. By setting $a = 1 - \overline{KS}\Delta t / C$, Equation (36) can be rearranged as,

$${\theta_r}^{j+1} = a{\theta_r}^{j} + (1-a){\theta_0}^{j} \tag{35}$$

Thus, if ${\theta_o}^{j}$ fluctuates randomly, Equation (35) takes the form of Equation (32).
The parameter "a", determined by the heat capacity of the room and heat loss factor, determines the rate of the room temperature change. The closer to 1 the value of "a" is, the more the room temperature receives the past influence. The relationship between the value of "a" and the influence that the non-Gaussian nature of the input noise E^j has on the X^j is focused in the following.
It is assumed that the pdf of the input noise is given by the following equation.

$$f_{e^j}(e^j) = b\frac{1}{\sqrt{2\pi}\sigma_{e1}}\exp[-\frac{(e^j - m_{e1})^2}{2{\sigma_{e1}}^2}] + (1-b)\frac{1}{\sqrt{2\pi}\sigma_{e2}}\exp[-\frac{(e^j - m_{e2})^2}{2{\sigma_{e2}}^2}] \tag{36}$$

The noise E^j is assumed to have the pdf shown as the broken line (j=1) in **Figure 1**. This distribution with two peaks is quite different from any Gaussian distribution.
Figure 1 (a) shows the time profile of the pdf of X^j in case of a=0.99. Although the input noise has strong non-Gaussianity, the pdf of X^j becomes very close to a Gaussian distribution after time step 3 (j=3). This corresponds to Central Limit Theorem, that is, X^j is calculated as the sum of the non-Gaussian variable in the previous time step and that at the present step with nearly the same distribution since the influence in the previous time remains almost as it was because the value of "a" is close to 1 with no attenuation. The results in the case of a=0.99×0.5

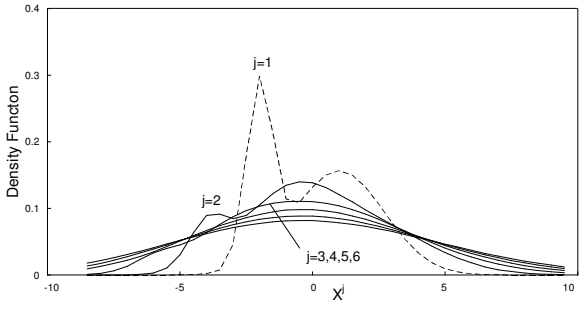

(a)a=0.99

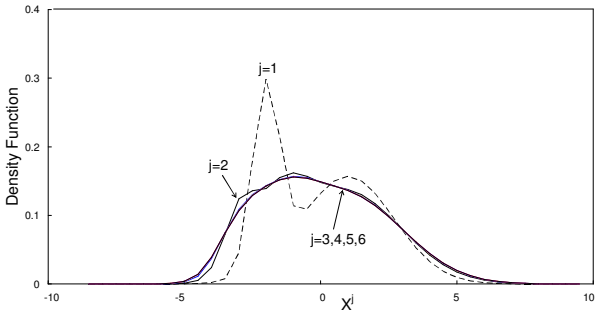

(b)a=0.99×0.5

FIG. 1: Time Profile of Density Function of X^j : (a)a=0.99, *(b)a*=0.99×0.5, *(c)a*=0.99×0.1.

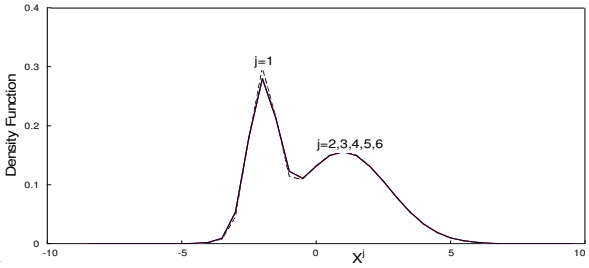

(c)a=0.99×0.1

are shown in **Figure 2 (b)**. The shape of the distribution curves after j=3 remains almost the same. Although the two peaks disappear, the deviation from a Gaussian distribution is larger than that in the case of a=0.99.
Figure 3 (c) shows the result when the value of "a" is 0.99×0.1. Contrary to the case of a=0.99, the influence from the previous time step almost disappears, and thus the non-Gaussian nature of the noise remains.
From these calculations, the non-Gaussian character remains in the rapidly decaying system, while the pdf of the state variable is close to Gaussian distribution in a slowly changing system.

3.2 Example calculation of simple building

(1) Building and input conditions

The calculated simple building is 8×5×2.5 m^3 with a 5 m^2 window on the south facing wall. The walls are made of concrete (12cm thick) and the floor is assumed to be adiabatic. The hourly mean values of the outdoor temperature and solar radiation in Tokyo[5)] are shown in **Figure 2** along with their standard deviations. The random components of them, z^j and y^j, are obtained based ARMA and ARMAX models[4)5)] as follows.

$$z^j + a_1 z^{j-1} + a_2 z^{j-2} + a_3 z^{j-3} = e^j + b_1 e^{j-1} + b_2 e^{j-2} + b_3 e^{j-3} \tag{37}$$

$$y^j + c_1 y^{j-1} + c_2 y^{j-2} + d_0 z'^j + d_1 z'^{j-1} + d_2 z'^{j-2} = e'^j + g_1 e'^{j-1} + g_2 e'^{j-2} \tag{38}$$

where, $z'^j = \sigma_j(j)\, z^j$ and $\sigma_j(j)$ is hourly standard deviation of solar radiation with a period of 24 hours. The pdf's of the input noises e^j and e'^j are approximated as a sum of two Gaussian distributions (**Figure 3**) and a Gaussian distribution, respectively.

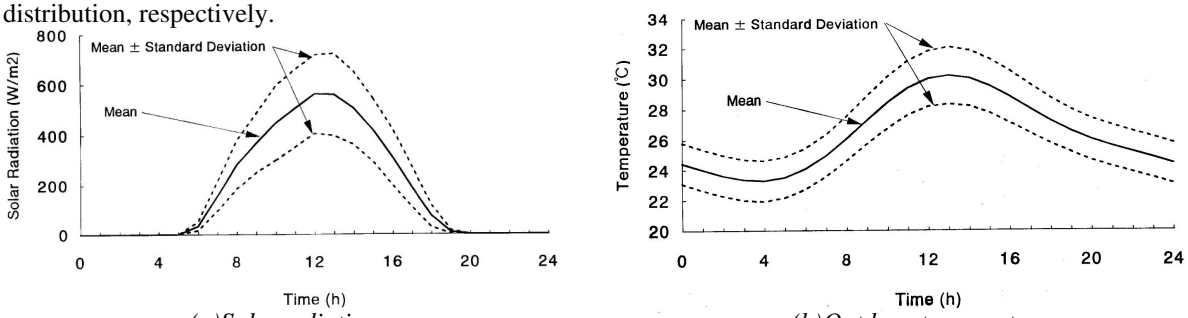

(a)Solarradiation *(b)Outdoor temperature*

FIG. 2: Hourly Mean and Standard Deviation of Solar Radiation and Outdoor Temperature in Tokyo

(2) Probability density functions of solar radiation and outdoor temperature

The pdf's of the random components z^j, y^j of the solar radiation and outdoor temperature were calculated based on the method in section 2, regarding Equations (37) and (38) as the basic equations with e^j, e'^j as inputs and z^j, y^j outputs. The results are shown in **Figure 4**. In the solar radiation, non-Gaussianity remains, although the degree of the non-Gaussianity is less than the noise e^j.

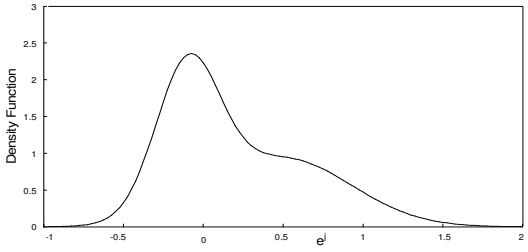

FIG. 3: Density Function of Random Component e^j of Solar Radiation Model

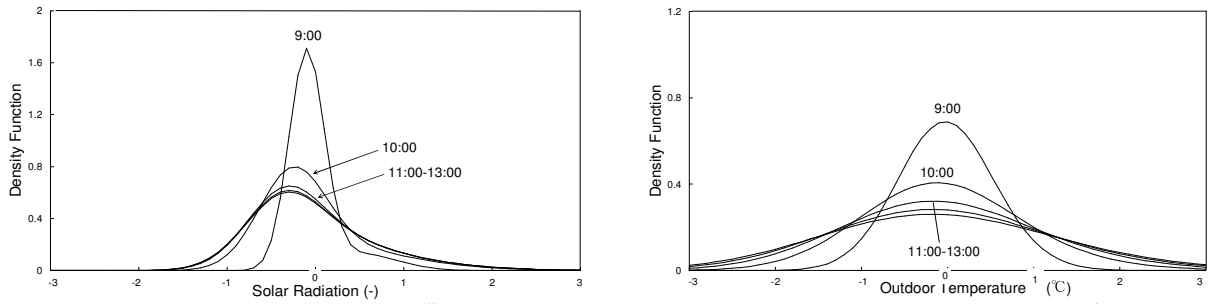

(a)Solar Radiation z^{jj} *(b)Outdoor Temperature y^j*

FIG. 4: Density Function of Solar Radiation and Outdoor Temperature

(3) Probability density functions of room temperature and cooling load

Figure 5 shows the calculated density functions of the room air temperature and the cooling load. Since the calculated time of the day is from 9:00 to 14:00 (air-conditioned times), the room temperature remains within a narrow range of 1 degree. Thus, an approximation as a Gaussian distribution is allowable from a practical point of view. On the other hand, the cooling load increases with time, because the outdoor temperature and the solar radiation increase with time. The pdf of the cooling load has assymetrical forms. This is because the system response during air-conditioning time is very quick and the pdf of the cooling load directly reflects the characteristics of the solar radiation in **Figure 4**. Since the deviation from a Gaussian distribution is not so large, however, the error may be small even if approximated as Gaussian with the mean and standard deviation calculated by second-order method. Furthermore, judging from the results in section 3.1, pdf in the non-air-conditioned time will be almost Gaussian since the time change is very slow.

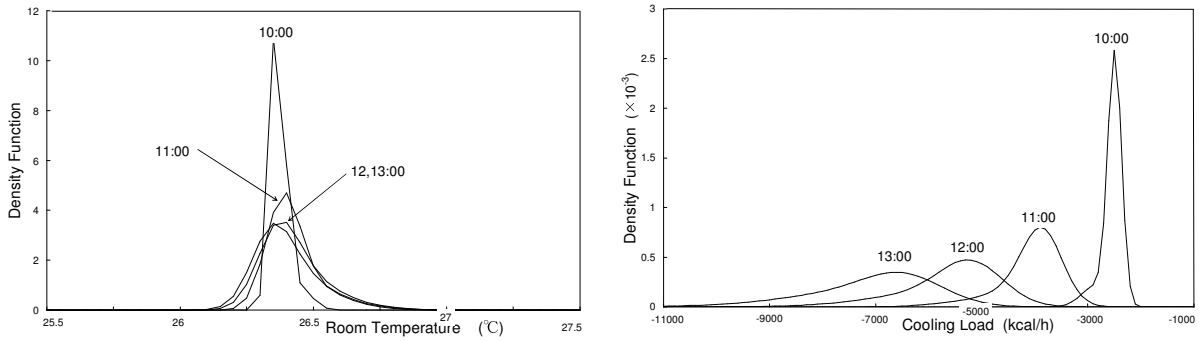

(a)Room temperature *(b)Cooling load*

FIG. 5: Density Function of Room Temperature and Cooling Load

4. Conclusion

A thermal method of calculating the density functions of the room temperature and the heating/cooling load was proposed, in case where the building thermal system, outdoor temperature and solar radiation are expressed as linear system and the random components of the outdoor temperature and the solar radiation are non-Gaussian. This method can deal with the random input expressed by the sum of several Gaussian distributions, and thus it is an extension of the second-order method calculating the mean and the standard deviation. By using one node case, the relationship between the thermal inertia of the system and the degree of the non-Gaussian nature was clarified. That is, the influence of the non-Gaussianity of the input noise is small when the response of the system is slow, and thus the second-order method giving the mean and standard deviation can be effective. Next, based on the analysis on a simple building structure, the influence of non-Gaussianity was examined. Non-Gaussian distribution of the cooling load was shown, although it was not so significant.

5. References

1) T. Terai, K. Nitta and H. Hiraoka. (1978). Statistical prediction of the room air temperature (in Japanese), Proc. of Kinki Branch, Architect. Inst. of Japan, No.18, pp.65-68.
2) Y. Nakazawa and Y. Okada. (1982). Stochastic estimation method of room temperature (in Japanese), Trans. Environ. Eng. Architect., Architect. Inst. of Japan, Vol. 2, pp.131-136, pp.137-140.
3) S. Hokoi and M. Matsumoto. (1988). An analysis of stochastic properties of the heating load in an intermittently air-conditioned building, Energy and Building, Vol.11, pp.259-266.
4) S. Hokoi, K. Niwa and M. Matsumoto (1990). An analysis of stochastic properties of the cooling load in an intermittently air-conditioned building : Analysis of discrete-time system, ASHRAE Transactions, Vol. 95, Part 2, 3322.
5) S. Hokoi, M. Matsumoto and M. Kagawa. (1990). Stochastic models of solar radiation and outdoor temperature, ASHRAE Transactions, Vol. 96, Part 2.
6) H. Yoshida and T. Terai. (1992). Modeling of weather data by time series analysis for air-conditioning load calculations, ASHRAE Transactions, Vol. 98, Part 1.
7) Y. Nitta, Y. Nakazawa and Y. Okada. (1982). Stochastic characteristics of meteological data and stochastic model (in Japanese), Trans. Environ. Eng. Architect., Architect. Inst. of Japan, Vol. 2, pp.125-130.
8) T.T. Soong (1973). Random Differential Equations in Science and Engineering, Academic Press.
9) G.E.P. Box and G.M. Jenkins. (1976). Time series analysis, Holden-day.

A Method for more specific Simulation of Operative Temperature in Thermal Analysis Programmes

Jørgen E. Christensen, Associate Professor,
Department of Civil Engineering, Technical University of Denmark;
jec@byg.dtu.dk

KEYWORDS: Angular factor between a person and a surface, inhomogeneous radiation, mean radiant temperature, operative temperature, projected area factor, thermal building simulation.

SUMMARY:
Simulation of energy consumption of buildings on hourly basis is closely connected to the thermal indoor climate. The operative temperature can be used as a simple measure for thermal environment. The operative temperature is a function of the air temperature, the mean radiant temperature and the relative air velocity. However, in many programs the model for calculating the mean radiant temperature has traditionally been based on the calculation of an area weighted mean value independently of the location in the room. In practice the location of the person in the room has a significant influence and inhomogeneous radiation plays an important role for the usability and functionality of the room. In order to calculate the mean radiant temperature as function of the person´s location in the room one needs to calculate the angular factor between the person and the surfaces. The angular factor between surfaces can easily be calculated; however the angular factor between a person and a surface cannot be found directly from a formula, but needs to be approximated in order to be used in computer simulations. The paper describes different kinds of validations that have been done to compare different models for calculating the angular factor and shows how a matrix solution for the angular factor can easily be implemented in programs for dynamic building thermal analysis.

1. Introduction

Nowadays many new and old buildings have large glass surfaces, which create a lot of consequences for the thermal indoor climate. Designing rooms with big glass areas has a great effect on the thermal comfort in the rooms. The outside air temperature is closely related to the temperatures on the surface of the walls and the windows. Since the insulation of walls in Scandinavia is 4 to 15 times better than the insulation of the glass, the inside surface temperature is much more affected on the inside of the glass than on the inside of the wall. On a cold day this will result in the surface temperature of the glass being quite lower than the rest of the surfaces and occupants being exposed to inhomogeneous radiation. Many other effects can result in inhomogeneous radiation, by way of example may be cited solar radiation transmitted through glass, hot radiators, hot floor/roof, etc, and the consequences of this can be that the functionality and productivity of the room can be reduced.

When calculating the consequences for the thermal indoor climate, the operative temperature can be used as a simple measure for the heat loss from a person. The operative temperature is a function of the air temperature, the mean radiant temperature and the relative air velocity.

In most of the programs for dynamic building thermal analysis, the model for the operative temperature has traditionally been based on a relatively simple model independently of the location of the person in the room. In reality this model will not be able to give a correct picture of the thermal condition for a person in a room since the person's location plays an important role. Another factor is the real consequences of shading devices. A person behind a window directly exposed to the direct sun light will have a completely different operative temperature than a person behind a shading device. The author has made many simulations with different programs and the indication is that this effect is not being taken into account in the right way, since the effect of a shading device only shows minor effect on the results of the air- and operative temperature.

The air temperature and the temperature on the surfaces can easily be calculated. When one wants to find the angular factor between two surfaces, one can find a specific equation for the angular factor to be used in the calculations. However, the real problem is calculating the mean value of the angular factor between a sedentary/standing person and a vertical/horizontal rectangle since there are no direct formula for calculation of the angular factor between the surface and a person.

This paper describes the background for the calculation of the angular factor between a sedentary/ standing person and a vertical/horizontal rectangle. From this study a model for calculation of the operative temperature dependent on the location of the person in the room will be set up, and from this make a proposal for an improvement of the computer

program package BSim used for analyzing indoor climate and energy consumption. Since the improvement has not yet been implemented in BSim it has not been possible to make any simulation showing the effect on operative temperatures and energy consumption.

2. Description of the computer program package BSim

As part of the author's Ph.D. study from 1982 to 1987 at the Thermal Insulation Laboratory, Danish Technical University, with the subject utilization of passive solar energy under Danish climate conditions, the author used the software BLAST (Hittle, 1979) and SUNCODE (Palmiter et al., 1985). One of the important differences between the two programs is the solution of the in stationary heat conduction through walls.

In BLAST the response factor method has been used to make the approximation to Fourier's equation. The method is fast, once the response factors have been calculated. The calculations of the factors are, however, complicated. In SUNCODE an explicit difference method was used for solving Fourier's equation which resulted in limits on the time step, especially for thin light materials.

One of the advantages of using a difference method rather than the response factor method is that the solution model is much simpler and gives the user much better possibility to follow the process inside the constructions, this being of importance for example in floor heating and combined hygrothermal simulation in buildings/walls. From an overall aspect it was decided to use the principles from SUNCODE for the heat balance model and combine it into a Danish program *tsbi2*. For the in stationary heat conduction through the wall a full implicit solution model was chosen and the program was developed into the *tsbi3* program released in 1990 (Johnsen et al., 1993; Johnsen et al., 1994). Later the program has been incorporated as *tsbi5* into the computer program software package (BSim, 2005).

BSim is being used for research and commercial calculations by consulting engineers in the field of heating and air-conditioning. The program provides means for detailed, combined hygrothermal simulations of buildings and constructions. BSim can be used for analyzing indoor climate, energy consumption, passive solar energy, automatic control functions, etc. in connection with the planning and design of buildings, energy-conservation measures, renovation of buildings, and heating and air-conditioning systems. The program is the most used program in this field in Denmark. The BSim package (BSim, 2005) consists of several modules:

- SimView – Graphic model editor and input generator
- *tsbi5* – Hygro-Thermal building simulation core
- Simligth – Tool for analysis of daylight conditions in simple rooms
- XSun – Graphical tool for analysis of direct sunlight and shadowing
- SimPV – a simple tool for calculation of the electrical yield from PV systems
- NatVent – Analysis of single zone natural ventilation
- SimDxf – a simple tool which makes it possible to import CAD drawings in DXF format

In the module *tsbi5* it is possible to make a combined transient thermal and transient indoor humidity and surface humidity simulation. This paper deals with a suggestion on how to improve the model in *tsbi5* for the operative temperature for a specific location in the room, since *tsbi5* only calculates the mean radiant temperature as an area mean parameter.

3. The operative- and mean radiant temperature

To find a simple measure for the heat loss from a person and a simple measure for the thermal indoor climate, the operative temperature can be calculated, (ISO 7730, 1994):

$$t_o = A \cdot t_a + (1 - A) \cdot t_r \qquad (1)$$

Where t_o is the operative temperature [ºC], t_a is the air temperature [ºC], t_r is the mean radiant temperature [ºC], A is a factor accordance to the relative air velocity (A=0.5 for v_{ar}=0.2 m/s, A=0.6 for v_{ar}= 0.2-0.6 m/s, A=0.7 for v_{ar}= 0.6-1.0 m/s).

The mean radiant temperature between a person and the surrounding surfaces:

$$\bar{t}_{r,P} = F_{P-1} \cdot t_1 + F_{P-2} \cdot t_2 + ... + F_{P-n} \cdot t_n \qquad (2)$$

Where $t_{r,P}$ is the mean radiant temperature for a person [ºC], t_i is the temperature of surface i [ºC], F_{P-i} is the angular factor between a person and surface i [–]

The surface temperature can easily be measured or calculated. However, the angular factor between a sedentary/standing person and a rectangle on the wall, floor or ceiling is far more complicated calculating. In most cases the angular factor is read from a figure since there is no exact formula for calculation of the angular factor between a person and a surface. In the following a proposal for solving this problem shall be discussed.

4. The projected area factor and the angle factor

In order to calculate the angle factor between a person and a surface $F_{P\text{-}A}$ it is necessary to use *the projected area factors* f_p (Fanger, 1970):

$$f_p = \frac{A_p}{A_{eff}} \quad \wedge \quad F_{P-A2} = function\left(f_p\right) \tag{3}$$

Where A_{eff} is the effective radiation area of the subject, $F_{P\text{-}A2}$ is the angle factor between the person and the sphere (A_2), A_p is projected area of a person on a plane perpendicular to the direction to d_{A2}

At the time when this theory (Fanger, 1970) was developed it was only possible to find a person´s projected area A_p from experiments. Later in this paper newer methods will be described in which the human body has been modelled by using a detailed 3D geometry and radiation model.

f_p as a function of (α, β) can be determined from experiment or from 3D geometry and radiation models. The angle factor $F_{P\text{-}A2}$ is a function of the dimensionless relationship *a/c* and *b/c*, figure 1. In this way a simple diagram can be used to find the angle factor for a rectangle of any size, placed as shown in figure 1 with the normal at the corner point passing through the centre of the person.

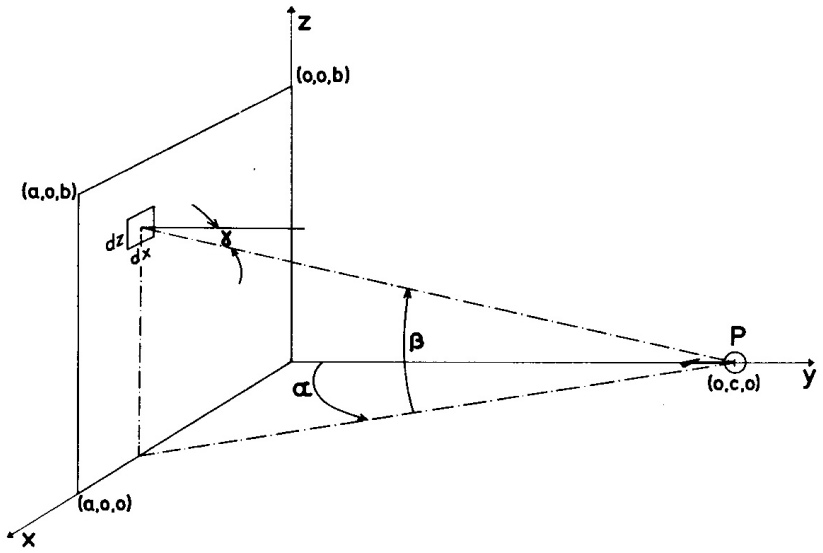

FIG. 1: The geometric principle for development of the evaluation of the angle factor between a person and a rectangle (Fanger, 1970).

To find an angle factor in a room in which a person is facing one of the walls, there will, according to the book (Fanger, 1970), be 6 cases, which means that 6 diagrams have to be drawn: 4 vertical surfaces and 2 horizontal surfaces. In most cases the location of the person in the room will be known, however the person's orientation will change from time to time. This means that it will be natural to find the mean value of the angle factor for a person rotating around himself $\bar{F}_{P-A}$ $(0< \alpha < 2\pi)$, meaning that for a vertical rectangle the angle factor can be found by using formulary (4) (Fanger, 1970):

$$\bar{F}_{P-A} = \frac{1}{2\cdot\pi^2} \int_{x/y=0}^{x/y=a/c} \int_{z/y=0}^{z/y=b/c} \int_{\alpha=0}^{\alpha=2\pi} \frac{f_p}{\left[1+\left(\frac{x}{y}\right)^2+\left(\frac{z}{y}\right)^2\right]^{\frac{3}{2}}} d\left(\frac{x}{y}\right) d\left(\frac{z}{y}\right) d\alpha \tag{4}$$

Since we now calculate the mean value of the angle factor between the person and the rectangle, where the person now is rotating around his own axis, we need to mark the angle factor as an average: $\bar{F}_{P-A}$. This simplification reduces the number of diagrams which need to be drawn from 6 to 2 – one for horizontal rectangles and one for vertical.

5. Experiments to predict projected area factor

Several researchers have used different kinds of photographic methods to find the projected area factors f_p. Fanger (Fanger, 1970) is the researcher who did the most extensive experiments to determine f_p. Fanger performed his experiments for measuring A_p using a photographic technique of the persons from many different directions. From a given viewing angle each photo provided the projected area of the body. By taking photos it was possible to find the projected area of the body for all these angles – and then the projected area factors f_p can be calculated. In the study ten males and ten females participated in standing and sedentary positions for azimuth (α) and altitude (β) angels between 0º to 180º and 0º to 90º, respectively. The persons were a fair sample of the adult population.

In the experiment Fanger wanted for solar radiation to determine the projected area factor f_p, which is why the radiation rays should be as close as possible to be parallel, meaning that the distance between the person and the camera has to be infinite. In Fanger´s case he positioned the camera in a distance of about seven meters and was then able to make his experiment with quite a good approximation to the simulation of parallel rays from the subject to the radiant source. Fanger presented his results as a form of graphs.

Fanger showed that the projected area factor f_p can be used in practice independently of the clothing, size and sex of the person, however one has to distinguish between a standing and a sedentary human body. The consequence of this is that all the mean values of the f_p-values can be plotted into one diagram, e.g. for a sedentary human body, see figure 2.

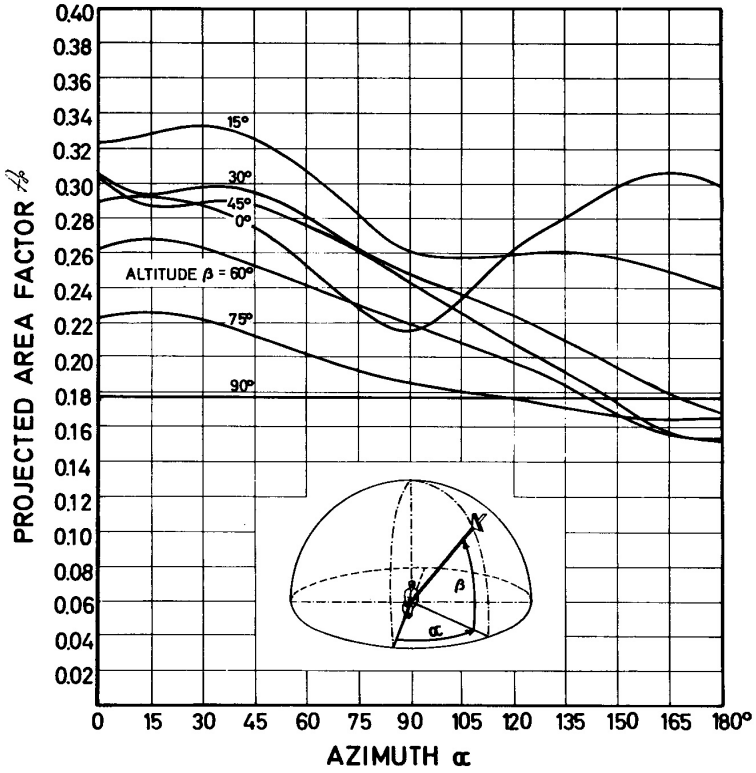

FIG. 2: Projected area factor for seated persons, nude and clothed to an infinitely small surface (Fanger, 1970).

The diagram in figure 2 for the projected area factor shows the factor as a function of the azimuth α and the altitude β to an infinitely small surface. Since equation (4) uses the *projected area factor* – f_p, it is impossible to solve the equation exact since f_p is a function of the azimuth α and the altitude β in an irregular way because it is based on experimental measurement from the human body. However it is possible from the actual measured data to make integration using equation (4) over all the angles for the azimuth α and the altitude β and draw a diagram for the angle factors between a human body and vertical or horizontal rectangles based on the mean values of f_p shown for a sedentary person in figure 2. If we look at the case with a fixed position for a person in a room but the facing of the person is unknown, the mean

value of the angle factor can be found when the person rotates around a vertical axis. An example of the mean value of the angle factor between a sedentary human body and a vertical rectangle is shown in figure 3. Since the figure shows the mean value for the person rotating around his own axis, only one diagram is necessary. If the orientation for the person has been fixed it will be necessary to use four diagrams.

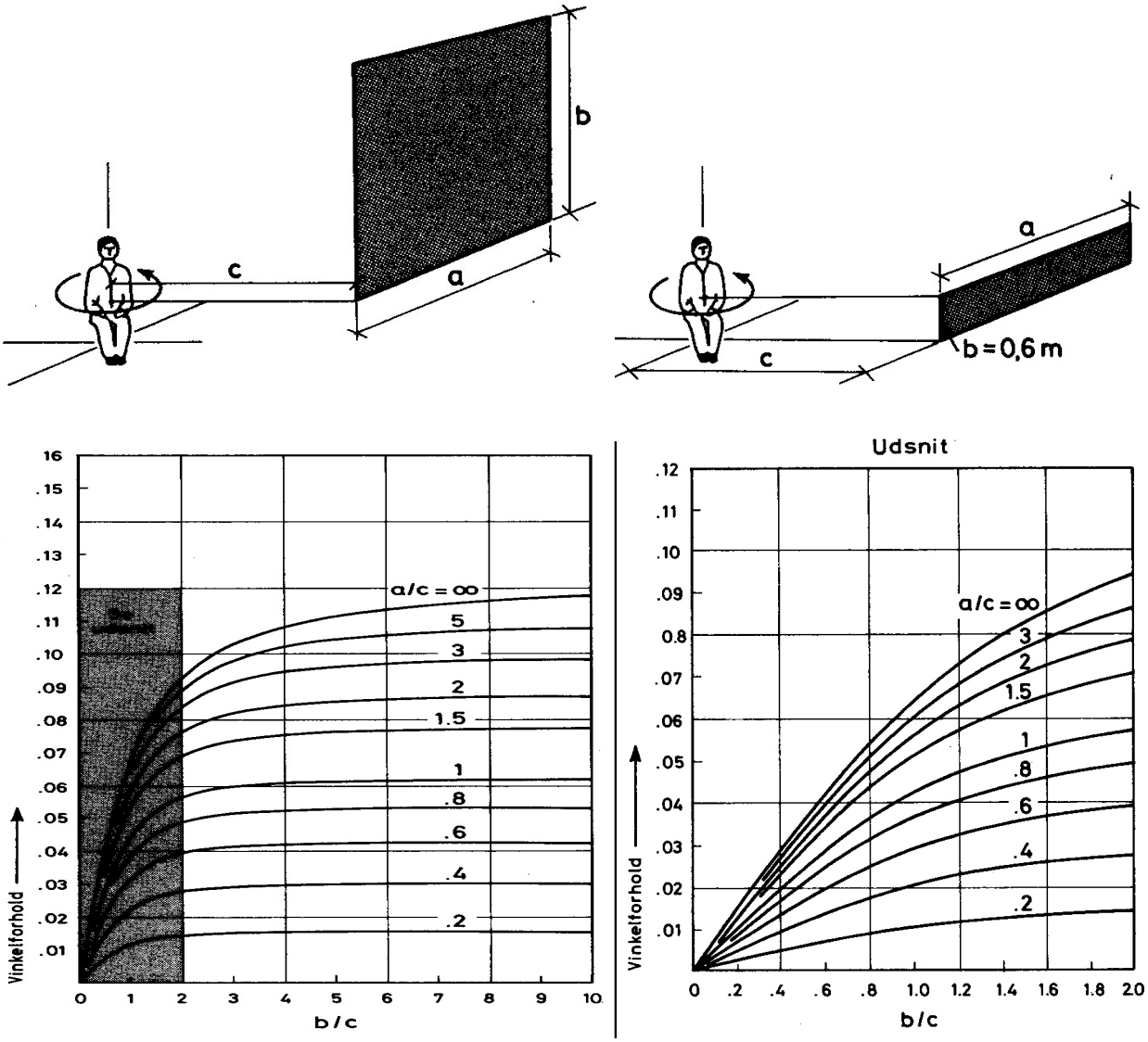

FIG. 3: Mean value of angular factor between a sedentary person and a vertical surface when the person is rotated around a vertical axis. (Fanger, 1970).

6. Geometry model and numerical simulation model used to predict projected area factor

In the last ten years computer animation programs have been developed for cinemas and computer games for which detailed 3D models have been developed for the human body geometry. This means that body posture can be generated in the general case from these software tools in order to make detailed modelling of the human radiation heat exchange with the surrounding surfaces. As a consequence of this experimental investigation of the thermal radiation from the human body will be used less since the computerized models are superior. This will create a new world of investigations in which the possibilities are nearly unlimited.

In the paper (Kubaha et al., 2004) they made a detailed study for human projected area factors for detailed direct and diffuse solar radiation analysis using commercial software (Curious Labs, 2000) in which they modelled persons in

standing or sedentary posture. The software was used to generate a detailed 3D model of the human body. The model of the human body was extremely detailed and consisted of 10,995 small surface elements, which made it possible to make a radiation simulation with sufficient details.

In order to compare the 3D geometry model with a simulation model – the human body was transformed to 3D humanoid geometries that were imported into a thermal analysis software package (ThermoAnalytics, 2001). The software uses ray tracing technique to predict the absorbed short-wave radiation energy for all the surface elements.

This method (Kubaha et al., 2004) gives the possibility for a detailed analysis of the human projected area factors. The authors made an impressive verification and validation process in which they first verified the new 3D geometry model against simulation results from the thermal analysis software package (ThermoAnalytics, 2001). The comparison showed that the predictions with the 3D geometry model agreed well with the results of the ray tracing simulations in the whole range of angles for the azimuth *(α)* and altitude *(β)*. This comparison will not be described further in this paper since the importance in this matter is a calculation of the angle factor between the whole human body in a standing/sedentary position and the surrounding surfaces.

Since experimental data are only available for the whole body it is necessary, in order to make a comparison with these measurements, to make integration over the whole body surface for the 3D geometric model. Since Fanger (1970) produced the most experimental data with the best details these have been the best materials for the comparison. The validation shows that for the most altitude and azimuth angels the relative error has only been approximately five percent. The agreement has been good for both standing and sedentary postures, however for the sedentary posture the projected area factors were higher than ten percent relative error for an altitude angle of $\beta = 15°$ and $\alpha < 60° / \alpha > 300°$.

One of the reasons for differences in results could be that the experiments were performed in a finite distance between the camera and the persons (7 m) – as opposed to the predicted results that was using an infinite distance between the radiant source and the human being, which resulted in parallel rays.

7. Selecting of model for calculation of the angle factor

Since the results have shown such fine agreement comparing the two models developed by (Kubaha et al., 2004) with Fanger´s data (Fanger, 1970) it has been decided to use Fanger´s data in this study.

However, since the projected area factor for a seated person in figure 2 cannot be used directly to solve equation (4), for the case illustrated in figure 3, it is necessary to go through an integration of the projected area factor to find the angular factor. Seeing that the data were only in an irregular form in figure 2 and the data behind were not available, it was not possible to find the value for f_p directly. To solve this problem it was decided to find f_p in a reverse process, in which the data from figure 3 were being used to find the solution for the angular factor F_{P-A} from the diagram for a specific case, depending on the position of the seated person, the size of the window, and the distance from the window.

These results were then entered into equation (4), and iterations have been used to find a solution for the projected area factor f_p. This value of f_p could only be used for this one special case. For other values, the error becomes increasingly larger. In order to solve this problem, a 20 by 26 matrix was created for the specific case in figure 3, and iterated solutions for all the projected area factors f_p. In this way, the error was reduced to less than one per cent.

Equation systems can then be created for the operative temperature for a general case. Real data for the specific case can be entered to calculate the thermal indoor climate, without having to spend time reading tables and making calculations. If the results show that the operative temperature under special winter conditions will be too low, the user can quickly make alternative calculations with other assumptions. For example, the glass in the window can be changed to a better quality with a lesser loss of heat. However the purpose for this paper is not to make a small program for analysing a stationary situation but to implement the final model including more features in (BSim, 2005). By looking at different stationary results under different climate and building conditions it will be possible to get a good idea about what kind of features will be wanted.

As a platform for setting up the equations the mathematical program software (Mathcad 14, 2007) and (Matlab version 7.5, 2007) have been used. It is the plan that – when the model has been created to the wanted form – the model can be rewritten to C++, which is being used in the BSim package. In this model other kinds of features have to be included in a more specific way in order to find the operative temperature depending on the location of the person in the room: direct solar radiation to a sedentary/standing human body, effect from shading devices, hot radiators, hot floor/roof, air velocity, etc.

8. Practical example – The operative temperature in an office

As a little demonstration of the principles an office has been simulated during winter conditions. The office is facing south and has the following dimensions (inside measurements): area 12 m^2, width 2.8 m, height 3.0 m and depth 4.4 m. The U-value of the exterior wall is 0.6 W/m^2 K and of the glass in the window changed to, respectively, single glass (6.0 W/m^2 K), double glass (3.0 W/m^2 K) and triple glass (1.6 W/m^2 K). The outside temperature is fixed to -12 ºC and the inside air temperature as well as the temperature on the inside surfaces set to 21 ºC. The simulations have been done for a person situated in the middle line of the room 0.4 m from the window and to the far side of the room. A picture and a plan of the room are shown in figure 4.

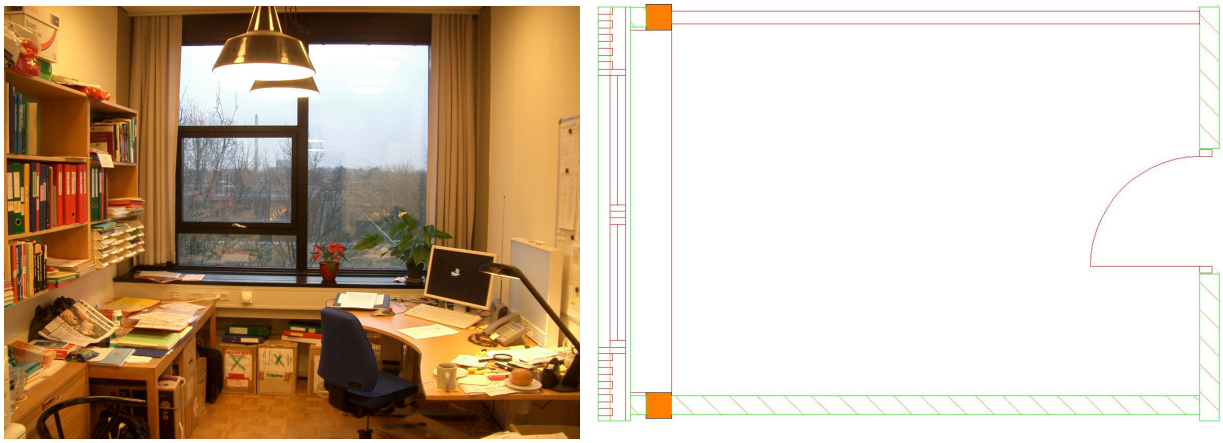

FIG.4: To the left a picture of the room and to the right a plan of the room.

The results of the calculations of the mean radiant temperature (left) and the operative temperature (right) have been shown in figure 5. The figure to the left shows 3 pairs of curves for the three different kinds of glass types: The mean radiant temperature respective as 1) a function of the distance from the window and 2) an area weighed mean value independently of the distance – fixed value. As expected the mean radiant temperature is lower near the window and increasing as the distance from the window is being increased. Better U-value of the glass reduces the inconvenience from the cold radiation of the window. These results will give a more correct picture of the thermal condition in the office in which the location of the person has been taken into account. This is as opposed to what has been done in many programs for dynamic building thermal analysis, in which the mean radiant temperature has been calculated as an area weighted mean value independently of the location in the room – see the three curves with fixed values (horizontal curves). If a person is seated 0.4 m from a double glassed window the difference between the mean radiant temperature as function of distance (18.6ºC) and independently of the distance (20.1ºC) will be 1.5ºC. For the operative temperature the similar numbers will be (19.8ºC), (20.6ºC) and 0.8ºC, respectively. Increasing glass area and lower U-value will increase the differences.

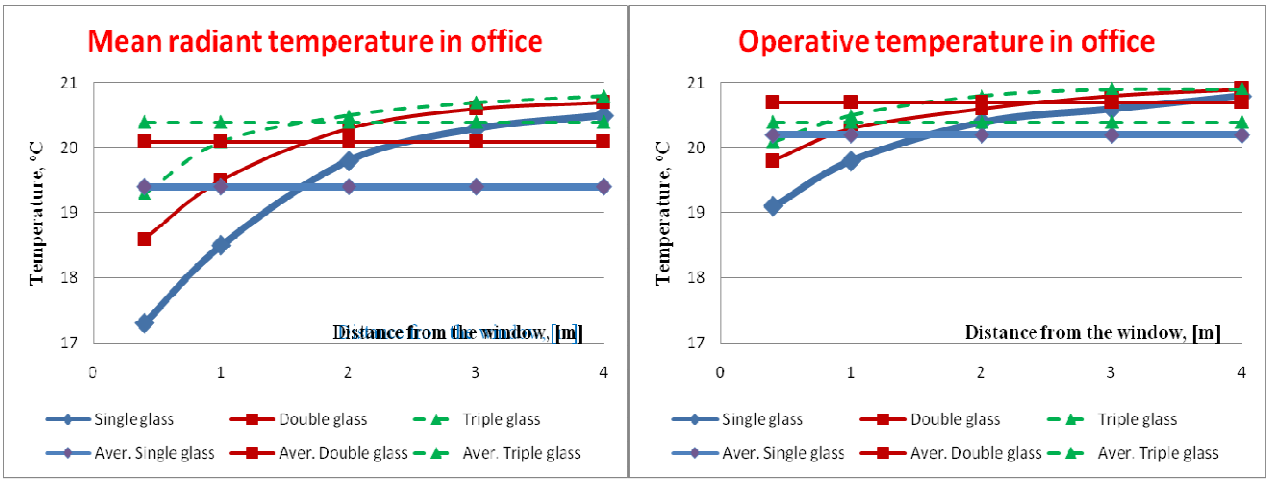

FIG.5: The mean radiant temperature and the operative temperature as a function of the distance from the window

In practice it will be natural for people to have a higher air temperature in the room if they are situated nearby a cold window in order to compensate for being exposed to the inhomogeneous radiation and the lower operative temperature. As a result of this the energy consumption for heating will be increased in order to keep satisfactory indoor thermal environment.

This problem could have been shown already in the design phase, if the simulation had taken into account the specific location of the person in the room. One can argue that this will complicate the calculations of the energy / thermal indoor climate too much, since the location will often be changed in the life time of the building. However it is natural for human beings to wish to sit nearby the window and have the view and daylight, and if it is too cold the person can easily solve part of the problem by turning up the heat and by this way increase the air temperature. The individuals in the building will normally only have very little or no idea about the total heating demand in the building and will more focus on their own personal comfort.

9. Conclusion

The possibility to simulate the operative temperature depending on the location of the person in the room has been a neglected topic in many simulation programs for thermal simulation. The result can be a deviation of the operative temperature with up to several degrees Celsius near for example a large window compared to a mean operative temperature based on the calculation of the mean radiant temperature as an area weighted mean value. The energy consumption in the winter situation can also be increased significantly if the persons in the room turn up the thermostat in order to increase the air temperature as compensation to cold radiation from a glass surface. The consequences energy wise of the inhomogeneous radiation could have been analysed in the design phase, if the necessary design tool had been available where the exact location of the person could have been used as input to the program.

The paper shows a possible way to calculate the angular formula using a matrix model. The matrix model is based on Fanger´s data (Fanger, 1970) since the validation done by (Kubaha et al., 2004) has shown such fine agreement comparing the two models developed by (Kubaha et al., 2004) with Fanger´s data (Fanger, 1970). The model has been set up in the software (Mathcad 14, 2007) and (Matlab version 7.5, 2007), which have shown to be a good platform for performing the necessary equations in the right order and built up knowledge on how the model is working. The model can later on be rewritten to for example to C++ and implemented to the BSim package. The model needs more development in order to take into account direct solar radiation through windows, airflow, PMV-values, etc. In addition the model will need more testing of other possible models for calculation of the angular factor.

10. References

Hittle D.C. (1979). BLAST – The Building Loads Analysis and System Thermodynamics Program, CERL – the US Army Construction Engineering Research Laboratory, Champaign, Illinois.

BSim. (2005). Danish Building Research Institute, Hørsholm, Denmark.

Curious Labs. (2000). POSER4: the premier 3D character animation and figure design tool. Curious Labs, Santa Cruz

Fanger P.O. (1970). Thermal comfort, McGraw-Hill, New York.

ISO 7730. (1994), Moderate thermal environment – Determination of the PMV and PPD indices and specification of conditions for thermal comfort, Reference number ISO 7730:1994(E), CH-1211 Genève 20, Switzerland

Johnsen K., Grau K. and Christensen J.E. (1993). *tsbi3*, Edb-program til beregning af bygninger og installationer, Brugervejledning. Danish Building Research Institute, Hørsholm, Denmark.

Johnsen K. and Grau K. (1994). *tsbi3*, comuter program for thermal simulation of buildings, user´s guide. Danish Building Research Institute, Hørsholm, Denmark.

Kubaha K., Fiala D., Toftum J. and Taki A. H. (2004). Human projected area factors for detailed direct and diffuse solar radiation analysis. *Int J Biometeorol,* No. 49, 113-129.

Mathcad 14. (2007). PTC Corporate Headquarters, Needham, USA

Matlab version 7.5 (2007), MathWorks Inc., Natick, MA, USA

Palmiter L., Wheeling T. and Ecotope Inc. (1985), SUNCODE-PC – A Program User´s Manual, Ecotope Group, Seattle, Washington, USA

Thermo Analytics. (2001). RadTherm technical documentation. Thermo Analytics, Calumet

Feasibility of mechanically driven night ventilation in a high profile office building

Jelle Laverge, Assistant,
Research group for Building Physics, Department of Architecture and Urban Planning, Ghent University;
jelle.laverge@ugent.be

Arnold Janssens, Associate Professor,
Research group for Building Physics, Department of Architecture and Urban Planning, Ghent University;
arnold.janssens@ugent.be

Els Vanlonderseele, Researcher ,
Research group for Building Physics, Department of Architecture and Urban Planning, Ghent University;
els.vanlonderseele@gmail.com

Stef Diels, Ir. Student,
Department of Civil Engineering, Ghent University;
stef.diels@ugent.be

KEYWORDS: *night ventilation, energy saving, efficiency, passive cooling, thermal mass.*

SUMMARY:
Since the Energy Performance for Buildings Directive (EPBD) was accepted and implemented over the course of the last years, buildings are audited energetically to receive the necessary construction licenses. This augmented the already high attention for research on innovative (passive) energy saving system concepts even further. Validation of the viability – energetical, economical, ecological, comfort wise … - of these innovative systems thus became an important issue.

In this paper, the energetic feasibility of mechanically driven night ventilation, combined with an earth-air heat exchanger (EAHX) and a heat wheel, as an active cooling replacement is assessed through a performance evaluation of the concept in a high profile office building in Nazareth (Belgium).

First results indicate that both the EAHX and the heat wheel deliver substantial energy savings, whereas the mechanically driven night ventilation seems incapable of doing the same. Supplementary ventilator energy at night is within the range of the avoided cooling energy in both measurements and simulations.

By means of more detailed modeling of variants, this problematic balance is investigated further in order to analyze the sensitivity of the system to more effective control parameters. This bares more nuanced insight into the value of the concept.

1. Description of the test case Building

As stated in the introduction, the reported research investigates the energy saving potential of (passive) systems introduced in a high profile office building in Nazareth, Belgium. It is home to the Omega Parma Belgian head quarters.

1.1 Geometric characteristics

The building consists of a ground floor with reception desk, three office floors on top and a basement containing technical installations. Figure 1 shows the front façade, which is oriented almost exactly to the east. Figure 2 depicts the typical plan of the office floors.

FIG. 1: Front façade of the building

Some characteristic numbers for this building are:

- Netto floor area: 2112 m²;
- Netto volume: 5803 m³;
- Budget: 3.300.000 € (VAT excl.).

It has been completed in December 2005. The measurements used for this research were conducted in the summer of 2006 and the winter of 2006-2007. They are based on data from the building management system combined with additional logger data and electric load measurements.

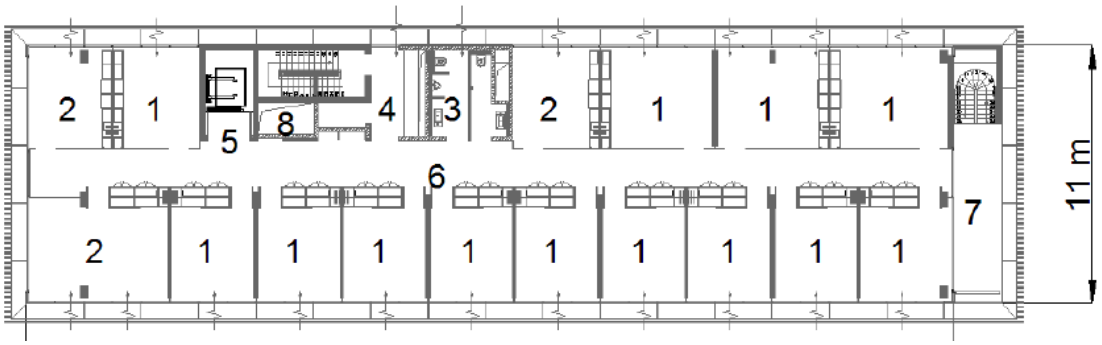

FIG. 2: Office floor plan

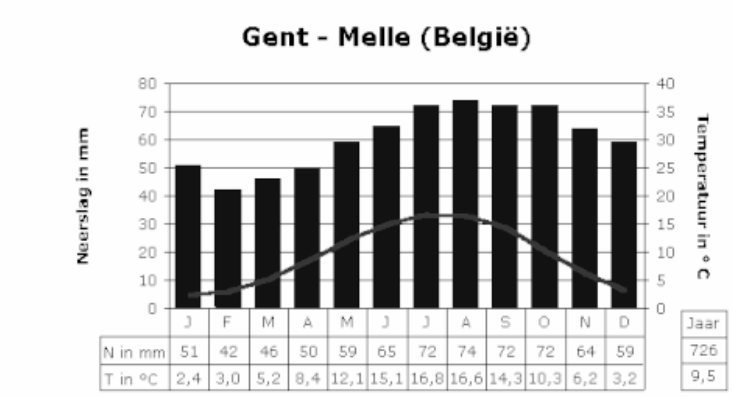

FIG. 3: Ghent climatogram

1.2 Climatisation approach

1.2.1 Included systems

The high percentage of glazing in the Eastern and Western façade subject the building to large sun gains, giving rise to superheating problems in summer. Several techniques are implemented to minimize this effect:

- Reflective glazing is used throughout, with a g-value of 0.26;
- Concrete 'balconies' act as fixed shading devices for the façade. (depth: 0.5 meter);
- An earth to air heat exchanger (EAHX) to precool (summer) and -heat (winter) all ventilation air;
- A 'heat wheel' heat recuperation system to further precool and -heat ventilation air;
- Mechanically driven intensive night ventilation.

Except for the heat wheel and the mechanically driven night ventilation, these techniques have are passive and do not need additional working energy. Figure 3 is a graphical representation of how the night ventilation flows circulate trough the building. Extraction fans pull fresh air in trough electronically controlled valves in the technical floors. The air then circulates trough the offices and corridors and is extracted in the kitchenette area.

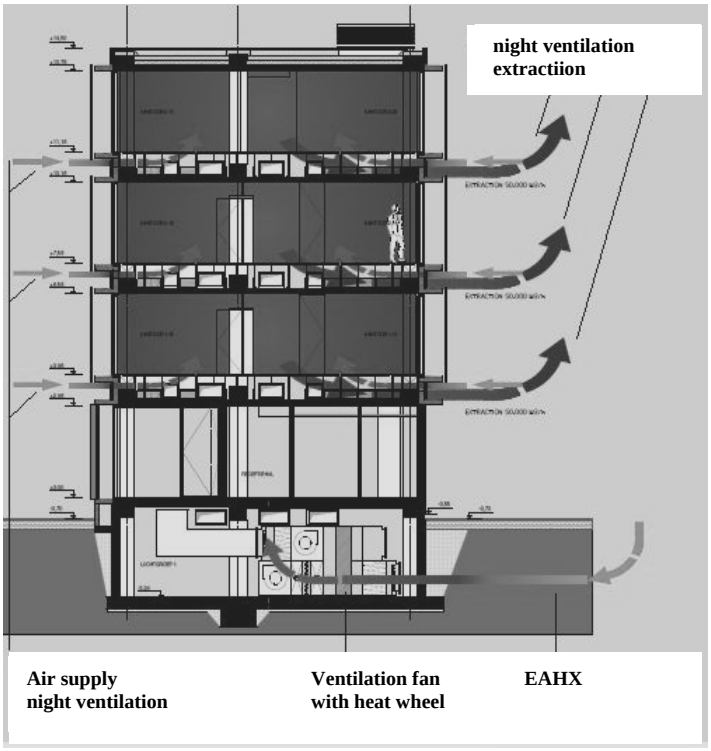

FIG. 4: Section trough the building showing night ventilation principle

1.2.2 Energy use

Taking all these measures into account, the building performs rather well in comparison to other low energy office buildings and office buildings in general, as can be seen in table 1.

TABLE. 1: This table shows energy/floor area ratio data for the building concerned compared to others.

[kWh/m² floor*year]	Omega Pharma	SD Worx (low energy)	Flemisch office building stock
Electricity	51.20	65	140
Natural Gas	242.11	57	40-350

The very large use of natural gas is due to bad commissioning of the systems during the winter period. Problems reported include malfunctioning of the heat wheel, constant ventilation at high volume of the kitchen area, activation of mechanical night ventilation during winter period. In addition to all of this, the high percentage of glass in the façades (over 90 %) induces large heat losses.

The mechanical night ventilation is activated when the following conditions are cumulatively met:

- Time control: between 22h and 6h, 7 days a week;
- Indoor temperature > 23 °C;
- Temperature difference inside-outside > 2 °C;
- Outdoor temperature > 15 °C;
- Max. outdoor temperature over the last day > 22°C
- Wind speed < 50 km/h
- Max. indoor temperature over the last day > 23°C

These parameters were based on the BSRIA Night Cooling Strategies final report. Soon after the completion, an eighth parameter was introduced, limiting activation to cases where the indoor relative humidity was below 70%. As stated before, some commissioning problems caused the system to malfunction during the winter period, activating the night ventilation and causing large heat losses.

1.3 Comfort assessment

First the realised comfort for the original constellation was assessed. To analyse measurement data, the ATG method was used because it provides a nuanced image of the comfort that is reached. Figure 5 clearly shows that both superheating and subcooling occur quite regularly, while Figure 3 demonstrates the typical climate for the region of Ghent, where the building is situated.

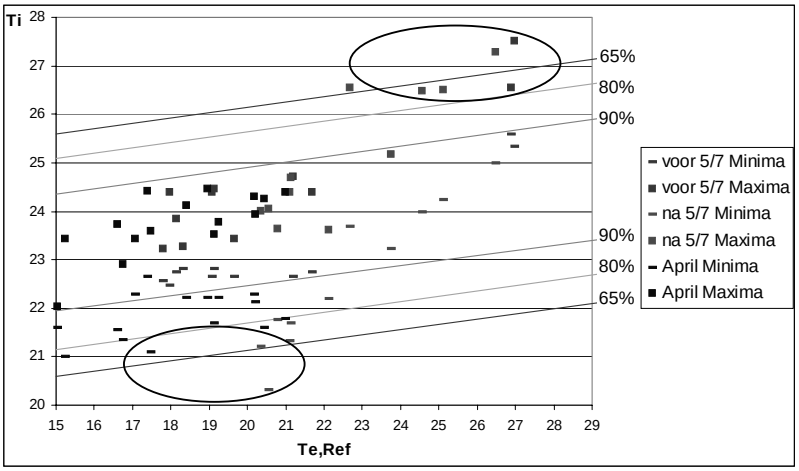

FIG. 5: ATG comfort assessment for different periods, showing minima and maxima

This discomfort is mainly caused by the night ventilation. To achieve acceptable temperatures during office hours, the night ventilation has to be activated for a long period at night, even with cold outdoor temperatures, causing the low minima in the morning. Even with this long activations, superheating at the end of workday can not be prevented.

2. Energy balance for mechanical night ventilation

The effectiveness of the EAHX and the heat wheel are well described in literature. As the measurements are coherent with it, the energy saving potential of these systems will not be discussed further, except for mentioning that to ensure maximal rendability of the EAHX a bypass is absolutely necessary. This is particularly the case in this building because of the high superheating risk especially in springtime.

To assess the energy saving potential of the mechanical night ventilation, the trade off between saved active cooling and consumed electrical energy needs to be evaluated. For this purpose a TRNsys model was constructed that represents one bay of the building. As can be seen on the plan, this model comprises three zones: a southside office, a corridor zone and a northside office.

2.1 Assumptions of the model

Walls separating the bay from neighbouring bays and both floor and ceiling were treated as adiabatic surfaces. This makes the model representative for the middle office floor of the building. Although this strategy neglects possible energy flows between the different floors and bays, it accurately models the physically present thermal mass in the bay and with it, the thermal capacitance available for night cooling.

A few of the geometrical and numerical constraints are listed below:

- Glass surface of the bay: 9.36 m², U-value: 1,1 W/m²K, g-value: 0,26;
- Gains: 280W per office, from 8 to 22h;
- Separations between offices and corridor: single glass pane: U-value: 6,75;
- HVAC set points: heating 20 °C, cooling 26 °C;
- HVAC operation hours: 8 to 22h.

The activation algorithm respects all criteria described above. The convective heat transfer coefficients towards the concrete ceiling are changed in relation to the activation of the night ventilation. Although in reality they depend on the temperature difference between air and concrete, implementation of this lead to divergence of the model. Because of the fact that one of the activation criteria dictates that outdoor air must be cooler then indoor temperature and the adiabatic conditions assumed, it is concluded that this strategy is acceptable.

To ensure that an acceptable comfort is reached in the simulation cases, active heating and cooling is introduced in the model. These installations have unlimited maximal power and are configured to the set points indicated above. Furthermore, it is assumed that the fans for mechanical night ventilation, once activated, always run at maximum capacity and consume 130 W of electrical energy per office. With the design air flow rate, these fans have a Specific Fan Power of 811 Ws/m3 or SPF category 3, which fairly good. These data are deducted from ons site electricity consumption measurements, as can be seen in figure 6. Two fans serve eleven bays.

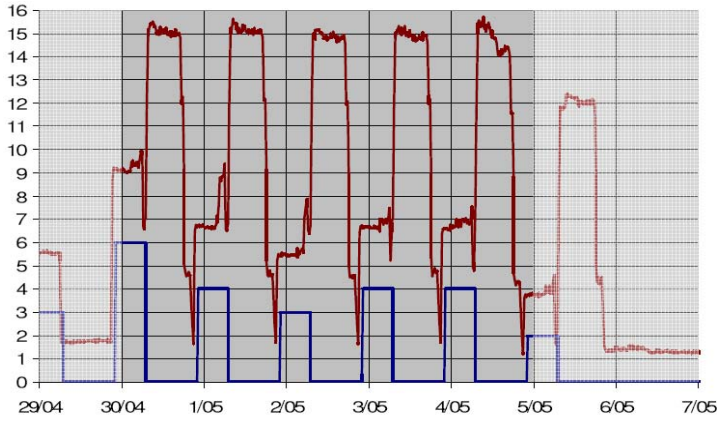

FIG. 6: Graph showing power consumption (kW) and number of activated ventilators (-)

2.2 Used criteria

To assess the energy saving potential of the mechanical night ventilation under different activation criteria, a year long simulation is ran for each variant, integrating sensible heat demand for cooling and heating. This data is then compared to a base case without mechanical night ventilation. The activation time of the extraction fans is then multiplied by their nominal electric load to assess additional power consumption of the system. The ratio of the saved cooling and heating demand to this additionally required energy should not exceed the COP of a modern cooling unit for this technique to be energetically interesting.

In the model, four parameters were varied over the following ranges:

- Time control: 7 days a week, starting at 20, 22 and 24h and stopping at 4, 6, 8, 10h;
- Indoor temperature > 25, 23, 20 °C;
- Outdoor temperature > 20, 15, 10 °C;
- Temperature difference indoor / outdoor > 0, 2, 4 °C

2.3 Analysis

Together, all possible combinations with these values represent 324 different configurations, ranging from very stringent to very tolerant. In the graph below, the resulting 'SPF' values for these strategies are plotted.

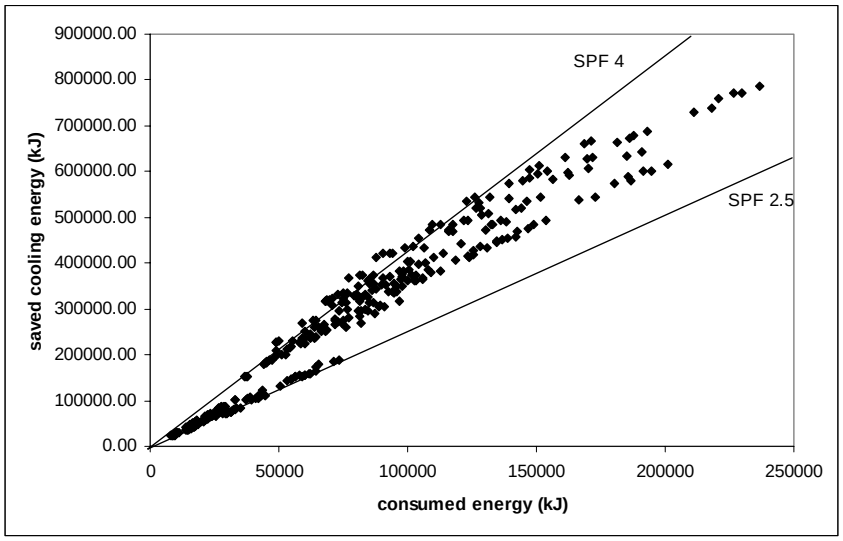

FIG. 7: Graph showing fan energy (x axis) vs. saved energy (y axis)

The realised SPF of the mechanical night ventilation for these different assumptions falls in three main categories, from 2.5 over 3.5 to 4. The major differentiating parameter is the actual outdoor temperature. Since lowering it allows for greater maximal temperature differences, the SPF can be significantly higher. All other parameters vary the activation time, but have a much smaller impact on the SPF.

Moreover, the next graph shows that in general, more stringent control strategies – and thus shorter activation time – result in a higher SPF. Of course, these control strategies also limit the cooling capacity of the night ventilation, so a trade off between cooling demand and performance needs to be made.

Given the height glazing factor of the façades, the cooling season starts very early. Simulations show that around the beginning of March, the first cooling demand occurs. Since the outside temperature limit states that there can be no night cooling unless the outside temperature of the previous day reached at least 20 °C, no night cooling will be applied in this season.

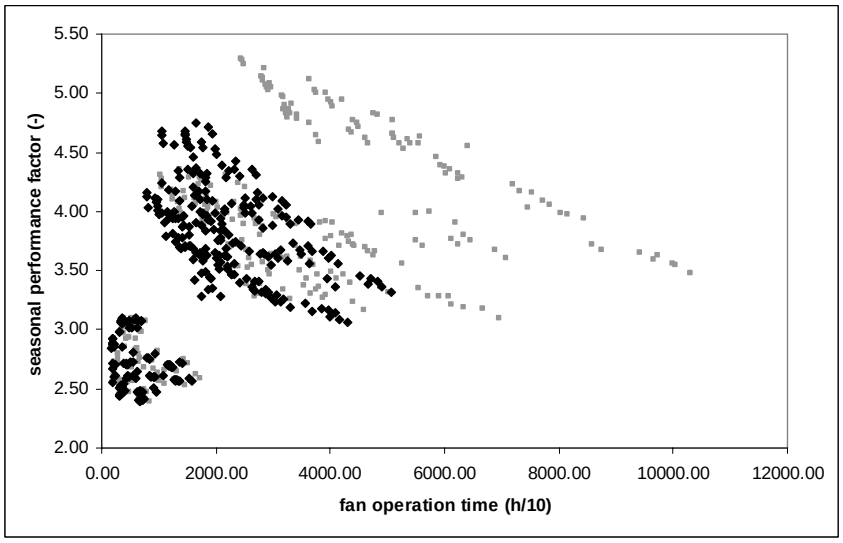

FIG. 8: Graph showing trade off activation time (x axis) vs. SPF (y axis)

Although the best strategy would undoubtedly be to reduce solar gains, this was unacceptable for aesthetic reasons. Therefore, this barrier was lowered to 15 degrees, producing the following results (grey dots):

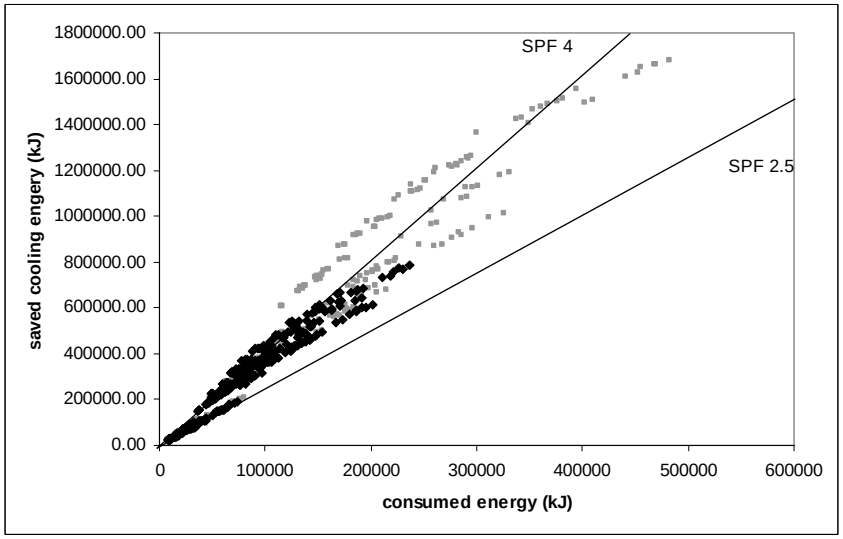

FIG. 9: Graph showing fan energy (x axis) vs. saved energy (y axis)

This strategy improves both SPF and saved active cooling demand.

3. Conclusions

The results of the different analysis show that mechanical night ventilation does not deliver significant energy savings in comparison to regular active cooling systems in this case where a high cooling demand is to be satisfied.

It further demonstrates that control strategies have a large impact on both seasonal performance factor and cooling capacity of the system. Ofcourse this is relative to system parameters like specific fan power, which are determinant for the performance of the base case.

The trade off between consumed energy and saved active cooling demand, is especially influenced by the allowed minimal outdoor temperature. Special care needs to be given to this factor – in combination with the minimal allowed indoor temperature – to avoid undercooling discomfort in the morning.

Because of the tight energetical trade off, the impact of other factors (for example investment costs) is all the more important to assess the feasibility of a mechanical night ventilation system in comparable circumstances. The implementation of this system is certainly not cheap – think of mechanical supply valves, transit openings, fans… - and are highly complex to commission.

Further research that is done on the subject could concentrate on the performance of mechanical night ventilation in combination with lowered ceilings and controllable openings.

4. References

Martin, A., Fletcher, J. (1996). Night Cooling Strategies, *BSRIA*, Final Report.

Breesch, H., Bossaer, A., Janssens, A., (2005) Passive cooling in a low-energy building, *Solar Energy* 79 (6), p. 682-696

Van der Linden, K., Boerstra, A.C., Raue, A.K., Kurvers, S.R. (2002). Thermal indoor climate building performance characterized by human comfort response, *Energy and Buildings* 34, p. 737-744.

Van der Linden, K., Boerstra, A.C., Raue, A.K., Kurvers, S.R., de Dear, R. J., (2006). Adaptive Temperature limits: A new guideline in The Netherlands. A new approach for the assessment of building performance with respect to thermal indoor climate, *Energy and Buildings* 38, p. 8-17.

Diels, S., Janssens, A. (2007) Evaluation regarding building physics of a high-tech office building: measurements & simulations, *Masters thesis*, Ghent.

Janssens, A., Van Londersele, E. (2004) Studie zonwering en passieve koeling Omega Pharma, *Report*, Ghent.

Energy-saving concepts for supermarkets

York Ostermeyer, Dipl.-Ing.,
Leibniz University Hannover
yorkostermeyer@iek.uni-hannover.de, www.iek.uni-hannover.de

Holger Wallbaum, Assoc. Professor,
ETH Zürich
holger.wallbaum@ibb.baug.ethz.ch, www.baug.ethz.ch

Christian Brand
REWE Deutscher Supermarkt KGaA
christian.brand@rewe-group.com

KEYWORDS: *supermarket, energy efficiency, concept, energy consumption,*

SUMMARY:
Supermarkets consume high amounts of energy, mainly electricity to power the freezers and lights. Strict laws for the conditions for selling food exist, demanding low temperatures to ensure the quality of the food. At the same time however the customer asks for comfortable conditions while shopping. This conflict of conditions has to be solved in one room, as a fragmentation into several more specialized rooms is contrary to the core supermarket concept. Often cooling and heating takes place in the same market at the same time, generated by two separated systems. As the surrounding conditions can not by changed, a flexible house technical system was developed, that is able to use the possible synergies by attaching the different components to one main system and therefore is able to transport heat energy within the market, causing cooling in one place and heating in another. Four markets have already been built using this system, two of them with the specific purpose of gathering data on the performance of the concept.

1. Introduction

Energy-efficient supermarkets offer a challenge mainly because of an ongoing conflict between marketing research of user behaviour and the demands of the German laws for selling food. The current limits by law for temperature and humidity are listed below.

aimed for conditions	customer	frozen food	fresh fruit and vegetable	cooled food
air temperature	19 °C – 21 °C	- 18 °C	15 °C	4 °C
relative humidity	40% - 70%	70%	90%	90%
absolute humidity	6,5g/m³ - 12,8g/m³	0,9g/m³	11,5g/m³	5,7g/m³
condensation point	5,1 °C -15,3 °C	-22,1 °C	13,4 °C	2,5 °C

Table 1: Guidelines for temperatures in supermarkets

These differences in aimed for conditions are already high and are further enlarged due to presentation measures. Food is, as an example, often presented by light spots generating heat directly on and inside the food. Simplified, every measure to save energy is directly opposing the situation deemed optimal by the marketing specialists:

- Slide doors on freezers are good in regard of keeping a temperature difference, but pose a hindrance for the customer to touch the food – lowering the chance of buying.
- Heating the space in front of the freezers by radiant heating raises comfort for the customer, but lowers the efficiency of the heat pump based freezer.

Problematic are situations where heating and cooling takes place at the same time or when there are intern heat sources inside the market during summer, requiring additional cooling.

Two cases have to be taken into account when designing a sound concept for markets – summer and winter. In winter the intern heat sources can be used to lower the need for heating, so a certain amount of intern gain is acceptable or even aimed for. During summer the intern gains to be countered by cooling measures. The development of more insulation and a growing number of freezers per market result in a growing number of yearly cooling days and a constantly shrinking number of heating days. Most modern markets do not need a separate heating system at all instead having a constant need for cooling.

2. Current standard of supermarkets

2.1 Internal heat sources

The following table lists average sources of internal heat in a market of average size.

				7°°-20°° (day)		20°°-7°° (night)	
light	**number**	**output (W)**	**total (W)**	**ED AKTIV**		**ED PASSIV**	
AEG Maxos TL 5 80 W EVG	183,0	80W	**14.640**	1,0	**14.640**	0,2	**2.928**
AEG Maxos TL 5 86 W EVG	25,0	56W	**1.400**	1,0	**1.400**	0,2	**280**
Phillips MRS 702 70	29,0	70W	**2.030**	1,0	**2.030**	0	**0**
Phillips MRS 702 100	40,0	100W	**4.000**	1,0	**4.000**	0	**0**
Phillips MRS 430 150	15,0	150W	**2.250**	1,0	**2.250**	0	**0**
AEG Maxos FR 50 W EVG	14,0	50W	**700**	1,0	**700**	0,2	**140**
Phillips MPK 630 70	37,0	70W	**2.590**	1,0	**2.590**	0	**0**
AEG Isolux PCF 58 W EVG	16,0	58W	**928**	1,0	**928**	0	**0**
light personal							
Phillips TBS 331 42	6,0	42W	**252**	1,0	**252**	0,1	**25,2**
Phillips Opal 60 W	6,0	60W	**360**	0,5	**180**	0,1	**36**
bakery							
Ofen Debak 18.9	1,0	18900W	**18.900**	0,25	**4.725**	0	**0**
GährSchrank 2,4	1,0	2400W	**2.400**	0,25	**600**	0,25	**600**
Phillips MRS 702 70	16,0	70	**1.120**	1,0	**1.120**	0,2	**224**
Phillips TBS 331 42	6,0	42	**252**	1,0	**252**	0	**0**
PRE Back DEBAK Mini R8	1,0	12800	**12.800**	0,25	**3.200**	0	**0**
electr. freezer							
Stolper Truhen	16,0	1500	**24.000**	0,73	**17.520**	0,73	**17.520**
AHT 210	26,0	495	**12.870**	0,8	**10.296**	0,8	**10.296**
AHT 175	4,0	495	**1.980**	0,75	**1.485**	0,75	**1.485**
Getränke KS	2,0	1000	**2.000**	0,5	**1.000**	0,4	**800**
house technik							
radiator	10,0	150	**1.500**	0,5	**750**	0,2	**300**
venting	2,0	3500	**7.000**	0,3	**2.100**	0,15	**1.050**
heating	1,0	1000	**1.000**	0,3	**300**	0,3	**300**

Cooling devices	30,0	-1400	**-42.000**	0,2	**-8.400**	0,1	**-4.200**
			72.972 W		**63.918 W**		**31.784,2 W**

Table 2: intern sources of heat in a medium sized supermarket

The building service system currently consists of four basic components:

- A heating system – most often based on natural gas or heat from a district heating network
- A venting system – most often without heat exchanger, either regulated manually or by CO_2-sensors
- A cooling system – in many markets
- Lights – consisting of a basic lighting by fluorescent tubes with spotlights in event areas (fresh fruit etc.)

The freezers form a system within the system. Two kinds have to be viewed separated:

- Plug – freezers, that are directly linked to wall sockets (because of the reliability of these systems they are preferred over the wall freezers when situation allows for both)
- Wall-Freezers that are linked to a fluid circulation and regulated by a central heat pump

These established systems are working less and less well because the intern gains (number of freezers, lights) are increasing as well as the opening hours. 15 years ago supermarkets where open 45- 50 hours per week, while currently most markets open for approximately 90 hours every week. The strategy of regulating the inside conditions especially during the hot summer months by venting in the night in combination with thermal mass ceases to work, as the time outside the opening hours is filled with the delivery of supplies and other logistical tasks.

Another reason is the growing strictness of the laws regarding the necessary conditions for the sale of food. This is the case for the temperature conditioning of the food as well as for the air quality inside the market. With CO_2 sensors regulating the air conditioning the situation has grown worse in many markets especially in summer when outside temperature rises above 25°C, the critical temperature inside the market for the heat pumps of the freezers. The constant warm air stream causes the foods temperature to rise above the allowed mark – a situation under which the market has to be closed, which means a great economical and marketing loss for the company.

The main point of a concept for saving energy in supermarkets is a need for intern gains during winter and a need for avoiding intern gains in summer. A flexible system is needed that can flexibly apply the heat energy inside the market when needed and outside the market when not needed.

3. Flexible system for conditioning in supermarkets

During the concept phase several proposals for a reduction of the consumption of supermarkets where made. The main proposals where:

- Reduction of intern heat gain by reducing the heat generated by lights and the number of freezers in combination with more insulation in the outer hull.
- Flexible transfer of heat by house technical measures
- Flexible transfer of heat by constructive measures (by placing the heat-pump in a separate room, open to the market in winter and to the outside in summer).
- General improvement of energy-efficiency by adding slide doors to wand-freezers, adding a space between the freezers in order to prevent heat accumulation near the heat pumps

The reduction of internal heat gain by reducing lights, number of freezers etc. was found to be unrealistic. The amount of profit to be made by more freezers could not economically be countered by saving energy and the marketing specialists insisted on the current lighting concept.

The general improvement of energy-efficiency was partially successful. While the lights are near the limit of current technology, the heat accumulation near the plug-freezers could be countered by placing them more apart.

For the flexible transfer of heat the house technical solution was chosen, mainly out of economical reasons. The current system uses one closed loop on which most of the components (plug-freezers remain) are docked on to. In places cooling and heating is required during the year the system can either densify the fluid or expand it, lowering or raising its temperature level and therefore generation the aimed for conditions by transporting energy within the market and to the outside.

Calculation under lab-conditions reductions the system will yield a reduction in CO2 Emissions by app. 20 tons per market in comparison to conventional systems. Under field-conditions 16 tons is deemed realistic.

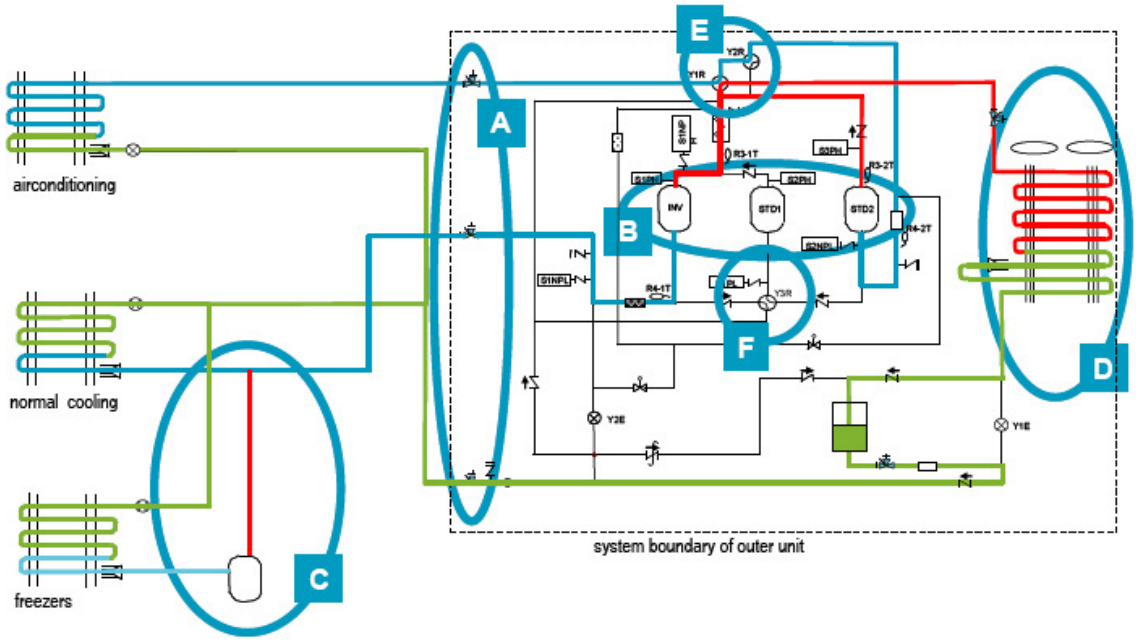

Picture 1: Schematic of the house technical system

A – The system uses a triple pipe system (-10°C for normal cooling, +7°C for airconditioning and upt to +55°C for heating).

B – The core of the system consists of three compressors, one inverter compressor (INV) and two standard compressors. The inverter compresser is assigned to the normal cooling; the standard 2 (STD2) compressor is assigned to the conditioning cycle. The system develops its flexibility out of the standard 1 compressor (STD1) that is mainly assigned to normal cooling but can be assigned to the conditioning cycle case by case.

C – Additional satellite compressor for the freezer units.

D – The heat exchanger of the outer unit is adjustable and can flexibly serve as compressor and evaporator.

E – Valves, taking care of the distribution inside the system

F – Valves responsible for the configuration of the compressors. As emergency solution the standard 2 compressor can be assigned to normal cooling as well, leaving the market without air conditioning but reducing the risk of loosing food due to insufficient normal cooling.

From the economical point of view the system currently costs about 10% more than a conventional system. In this calculation the omission of space for the central heating room is included. With the reduction of energy consumption taken into account the concept might pay off in about three years, depending mainly on the outer climate. A change towards the synergetic system is economically especially sound if a change in system asked for out of other reasons. An example for this is the current change in cooling fluids due to legislative changes in Germany.

4. Prototype markets and consumption data

Two supermarkets are equipped with the above described system. One of them (Oberweißbacher Strasse) is a new market, the other one (Ulzburger Strasse) is a renovated market whose complete house technical system was changed, while the outer hull remained the same. Both markets concrete frame constructions with lime sand bricks (Ullburger Strasse)/ gas concrete (Oberweißbacher Strasse), adding to the thermal mass of the building. Both markets are about 800m² in size. Data on the market in Ulzburger Strasse is shown below.

To the disappointment of all developers involved this year's winter was a rather warm one. As the concept relies on a heat-pump system the more extreme conditions are of special interest.

The other key point of interest was the amount of energy saving possible with the synergetic system. Comparison of similar days before and after the renovation in the market in Ulzburger Strasse shows a reduction in heat energy consumption of about 90%. Taking into account the change from a natural gas based system without cooling towards an electrical based system a reduction of prime energy consumption of about 50% to 60% is realistic, depending on climate conditions. However as the amount of data is rather small at the moment this comparison takes into account only the outer air temperature, not the number of customers and other relevant frame conditions.

Measured were the overall consumption of the market as well as the inner temperature and the consumption on several critical points of the system. The shown peakload is only available for the synergetic system in 2008. The daily consumption from 2007 is a calculated value as the traditional system is composed of electricity based heat pumps and a gas heating system. The main energy saved is the gas that is no longer needed for heating.

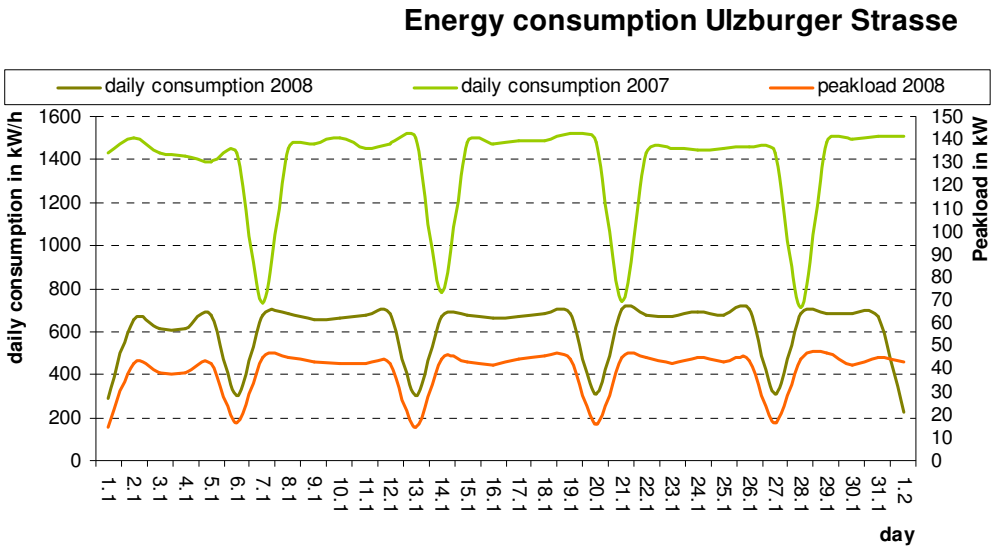

FIG. 1: Energy consumption / peak load of the supermarket Ulzburger Strasse

Longer term evaluations are available for other countries however. The following figure shows the monthly energy consumption of an average convenience store in central Japan. As these are average consumption values, the diviation of many actual markets is rather high (as high as 15%), mainly due to differences in the number of customers and mikro climate.

It can be clearly seen, that during the very hot Japanese summer, the synergetic system is consuming about 20% energy less than traditional concepts. The difference however is increases during the colder seasons where up to 75% less energy are consumed. This makes the synergetic system extremely attractive for supermarkets in Germany where the summer conditions are less extreme than in Japan.

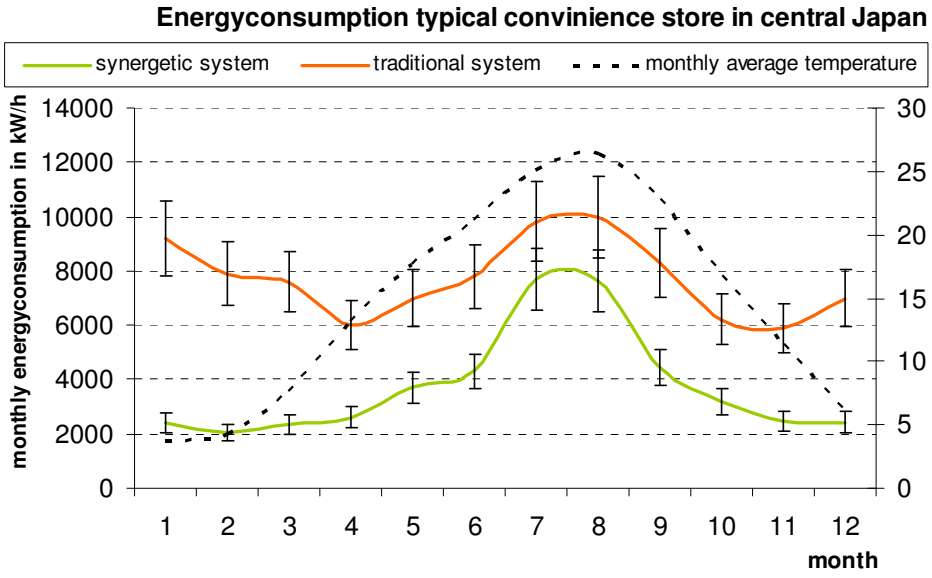

FIG. 2: Energy consumption over the year in a typical market in central Japan

5. Conclusion

As there is no long term data under German climate conditions available yet, evaluating the performance of supermarkets outfitted with the synergetic system is difficult. Long term data from several convenience shops in Japan show that the difference in performance between traditional and synergetic systems is dropping considerably when the outer temperature is rising above 12°C. At lower outer temperatures the synergetic system is clearly superior, as no additional energy is needed for heating – it is just moved within the market. The exact relation towards the outer hemperature is dependant on the design of the market however. German markets (mostly with areas above 800m²) will differ from the Japanese example (mainly 400m²).

First prototype markets in Germany show a consumption that matches the expectations based on the comparable winter conditions in central Japan and central Germany. The consumption of the market in Ulzburger Strasse (800m²,) that was equipped with the synergetic system in autumn 2007, was about 60% lower in January 2008 (average monthly temperature 5,3 °C) compared to January 2007 (average monthly temperature 5,9 °C). Additional long term evaluations are needed to more clearly describe the potential reduction in energyconsumprion under German climate conditions, as there are several other parameter to be taken into account that differ a lot from Japanese conditions (humidity, market size, number of customers/ m²month).

As last remark, the energy saved is mainly the gas as no separate heating system is needed. Dependant on the generation process of the applied electricity the primary energy balance will vary.

6. References

Data on the system components (Pic 1): DAIKIN Airconditioning Germany GmbH

Data on supermarket components (Tab 2): REWE Deutsche Supermarkt KGaA

Data on energy consumption of typical Japanese covinience store (Fig 2): DAIKIN Airconditioning Germany GmbH

Data on energy consumtion of supermarket (Fig 1): REWE Deutsche Supermarkt KGaA

Cost-efficient lowest-energy multifamily houses in Vienna

Part 1: Design strategies

Thomas Bednar Assoc.Prof. Dr.
University of Technology Vienna
thomas.bednar@tuwien.ac.at

Tanja Höfer
University of Technology Vienna

Jürgen Dreyer Em.Prof. DDr.
University of Technology Vienna

KEYWORDS:cost-efficient, lowest energy houses, energy performance, indoor comfort, heating load

SUMMARY:
During the last years research on the design of cost-efficient lowest energy houses had been finalized and in September 2006 the occupation of the first multifamily house started.The paper describes the general rules of the design strategies, the tools used to calculate energy performance and indoor comfort. Especially the question, if a flat can be heated only by heating the ventilated air, is discussed. Regarding the energy performance, different methods for calculating the energy demand for heating are discussed. Using a whole building simulation tool with 300 zones, the monthly energy balances for each of the 39 flats and the monthly energy balance for the whole house are compared. Finaly the results of the optimisation process is presented for the building Vienna-Utendorfgasse.

1. Multifamily houses in Vienna

The first certificated lowest energy multifamily houses in Vienna – Utendorfgasse are social tenements. There are 39 flats in the complex of three houses. The buildings are made of reinforced concrete. The balconies are in the south so the projecting slabs are shading the windows . There are little windows in the north. Occupation had started in September 2006.

In the following paper the focus will be on the freestanding house of Vienna-Utendorfgasse.

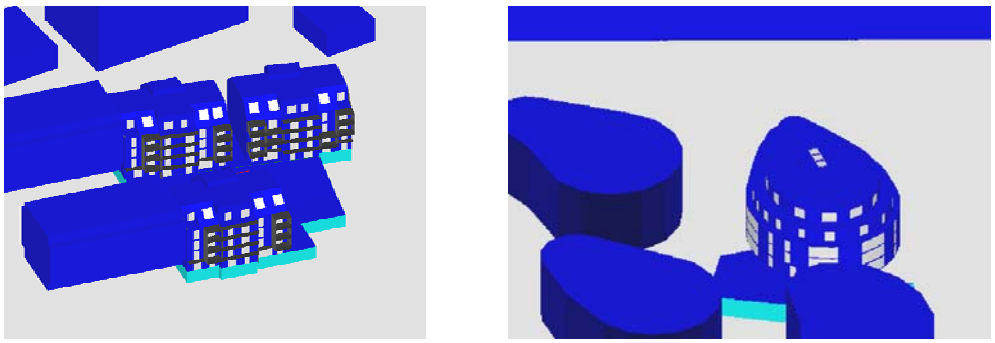

FIG. 1: Complex of the three lowest-energy- houses in Vienna – Utendorfgasse (left) and wire frame model of the second investigated complex Dresdnerstraße (right)

The second example is also a multifamily house in Vienna – Dreherstrasse with 27 flats. The longitudinal axis is orientated north-south. The building has a partial basement und the surrounding neighbours shade the building partly. Occupation had started in December 2007. Both buildings had been investigated regarding the possibility to use the ventilation system for heating and therefore avoiding radiators.

1.1 General rules of the design strategies

The general rules for the design result from the passiv house standards and from the building promoter.
The design objectives were :

- cost efficiency
  - limited extra costs for passive house standard
  - limited building costs to receive funding from the state for social housing(<1055€/m²)
- low energy consumption – lowest energy house
  - heating demand ≤ 15 kWh/m²a
  - heat load ≤ 10 W/m²
  - airtightness $n_{50} \leq 0.6\ h^{-1}$
  - primary energy demand ≤ 120 kWh/m²a
- high indoor comfort
  - controlled air change, high surface temperatures during winter
  - high acoustic and hygienic standards for ventilation system

1.2 Limits of the heating by ventilation system

The main points for indoor comfort are the temperature, the air humidity and the temperature assymetrie.

The heating load in lowest energy houses of this type is limited because of the possibility to supply the heating demand by warmed input air via the ventilation system. The limiting factors therefor are the maximum input air temperature with 50°C due to the smouldering and the air change rate focusing on low indoor air moisture contents. The higher the air change rate the lower is the air humidity in the flat. In FIG. 2 the absolute humidity against air change rate and the minmimal absolute humidity for indoor comfort is presented. In the Figure is also shown the range concerning the the air change rate when the utilisation and so the humidity production varies. The assumption of 300 g/h humidity production is from a family with three members and cooking, bathing, clothes drying and plants. The humidity can vary because of the utilization by the inhabitants. The intersection of the curve and the limit is at the air change rate of about 0.4 1/h.This air change rate is used to calculate the maximum of heat input.

The calculation of the curve was done with the following parameters:

TABLE 1: Parameters for the curve of absolute humidity

		outdoor air	limit für comfortable indoor climate
Temperature (monthly average january)	°C	-1	22
relative humidity	%	80	40
$u_{outdoor}$	g/m3	3.58	7.77
moisture production p	g/h	300	

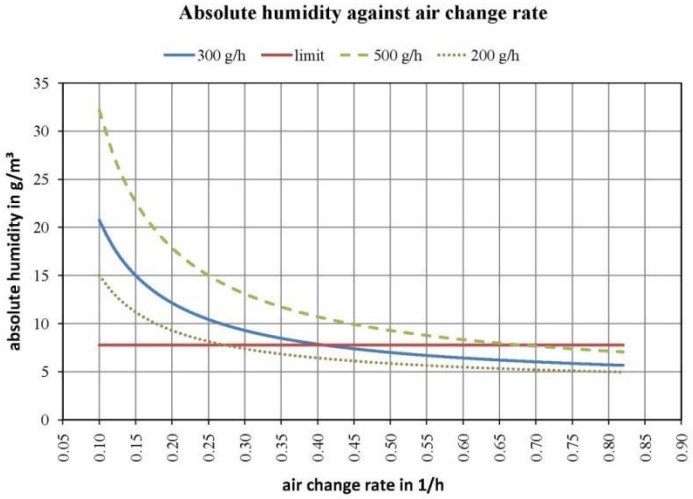

FIG. 2: Absolute humidity against air change rate and the minimum limit of the absolute humidity for indoor comfort at 20°C and 40% relative humidity

TABLE 2: Maximum heat input by warmed input air

flat area (A)	m²	70	70
ceiling height (h)	m	2.5	2.5
Volume (V)	m³	175	175
air change rate	1/h	**0.4**	**0.4**
$t_{input\ air}$	°C	50	50
t_i	°C	20	22
heat input	W	693.00	646.00
	W/m²	**9.90**	**9.24**

$$= 0.33 \cdot n \cdot V \cdot \left(t_{inputair} - t_i \right)$$

The maximum possible heat input by warmed air of 9.9 W/m² must supply the losses by transmission and infiltration. That is the base for the boundary conditions for the calculation of the heat load. This heat load must be verified flat by flat.

1.3 Heating load - Parameters for steady state calculations

The heat load is the decisive factor in the question if a heating only by warmed input air is possible. The passive house works because of the fact that heat losses and heat gains are taken into account.

The simulation of a building delivers the most exact results for the heat load but they need some time and resources to calculate. With a steady state calculation it is easier and faster to get results. The following formula is for the steady state calculation of the heat load on the relevant day at the location.

The steady state calculation includes the transmisson losses to the exterior and to unheated neighbours, ventilation losses because of infiltration and ventilation, solar gains and internal energy gains. The unknown parameters in the calculation for the maximum heat load are the outdoor temperature for transmission losses T_{eT}, air temperature of input air (infiltration, ventilation) $T_{eL,}$ temperature in neighbouring room $T_{in,}$ and the solar energy gains $P_{solar,k}$.

The calculations of the unknown parameters were made by separating the parts of the formula. By simulating the heat load for different shoe box shaped rooms with the Programm BSIM 2000 the heat load could be determined

and the equation could be used to determine the unknown parameters. The box models where light and heavy constructions and different windowsizes and orientations. Deatils can be found in Höfer 2006.

$$\begin{aligned} HeatingLoad = & \left[\sum_n A_n \cdot U_n + \sum_m l_m \cdot \psi_m \right] \cdot \left(T_i - T_{eT} \right) + \sum_{n'} A_{n'} \cdot U_{n'} \cdot \left(T_i - T_{i,n'} \right) \\ & + 0,34 \cdot \left(\dot{V}_{inf} + \dot{V}_{mech,inf} + n_{anlage} \cdot (1-\eta) \cdot V \right) \cdot \left(T_i - T_{eL} \right) \\ & - \sum_k A_{g,k} \cdot g_k \cdot versch_k \cdot P_{Solar,k} \cdot 0,9 \\ & - P_{intern} \end{aligned} \quad (1)$$

A_n ..... structural element area, internal dimension [m²]
U_n ..... thermal transmission coefficient [W/m²K]
l ..... internal length thermal bridge [m]
ψ..... thermal bridge losses coefficient [W/mK]
T_i ..... indoor temperature [°C]
T_{eT} ..... outdoor temperature for transmittance losses [°C]
$A_{n'}$ ..... joining area to neighbour [m²]
$U_{n'}$ ..... thermal transmission coefficient to neighbour [W/m²K]
$T_{in'}$ ..... temperature in neighbouring room [°C]
$\dot{V}_{inf}$ ..... volume flow by infiltration = n_{inf} .V [m³/h]
$\dot{V}_{mech,inf}$ ..... volume flow by underpressure caused by the ventilation system [m³/h]
n_{Anlage} ..... volume flow through the ventilation system [h^{-1}]
η ..... efficiency factor of the heat recovery
V..... volume, internal dimension [m³]
T_{eL} ..... air temperature of input air (infiltration, ventilation) [°C]
$A_{g,k}$ ..... window area [m²]
g_k ..... solar heat gain coefficient
$versch_k$..... shadowing effects by projecting elements, adjoining buildings
$P_{solar,k}$ ..... solar energy gains [W/m²]
P_{intern} ..... energy gains by internal heat sources [W]

TABLE 3: Temperatures and solar energy gains for the heat load relevant days for Vienna

	T_{eT}	T_{eL}	P south	P east/west	P north	
01.Feb	-14.5°C	-14.0°C	60 W/m²	23 W/m²	9 W/m²	very cold, sunny
21. Jan	-4.0°C	-4.0°C	6 W/m²	6 W/m²	6 W/m²	mild, cloudy

The validation of these parameters was made with the passive house Vienna-Dreherstrasse. The building hosts 27 flats and alltogether there are 244 rooms. The heat load of the building was simulated with the programm buildopt developed at the center of building physics and the steady state calculations were done with the same program so the input data of the constructions are the same.

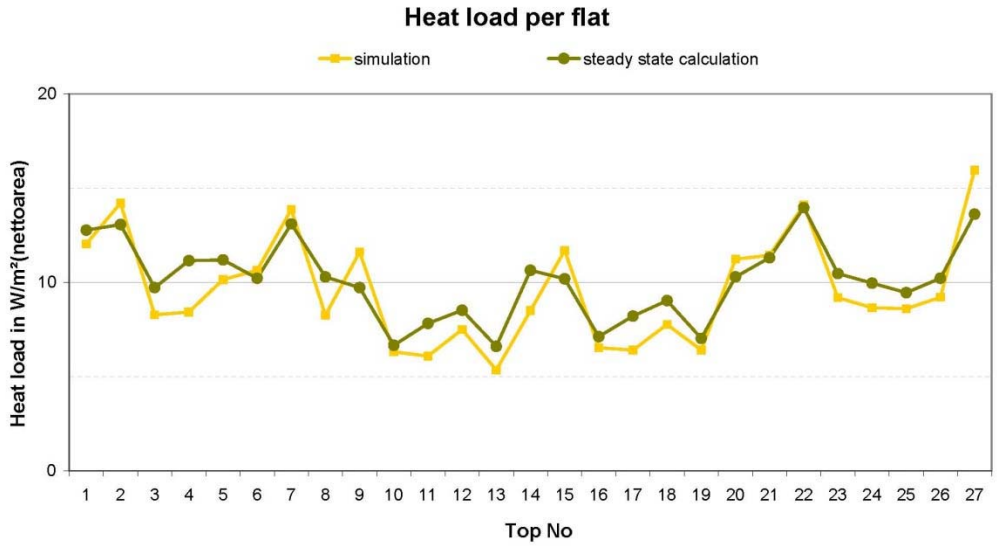

FIG. 3: Comparison of simulation and steady state calculation

Figure 3 shows the comparison of the results by simulation and steady state calculation. The difference between the steady state calculation and the simulation is less than 1 W/m² on average.

1.4 Calculation method – Heating load

The boundary conditions to calculate the heat load to check the possibility of heating only by ventilation system are:

TABLE 4: Boundary conditions for the steady state heat load calculation for evaluation of the indoor comfort

T_i	Neighbours	$q_{i\ nettoarea}$	n_{Anl}	η	n_{mech}	n_{50}	$n_{Inf,\ rooms}$	$n_{Inf,\ flats}$
°C		W/m²	h^{-1}	–	h^{-1}	h^{-1}	h^{-1}	h^{-1}
22	heated	1.6	0	0	0	0.4	n_{50} * e * 2	n_{50} * e

As the heating by input air must only cover the transmission and infiltration losses in flats the mechanical ventilation is zero. The infiltration at the room is calculated with the n_{50}-value and a factor which includes the wind protection and the numbers of openings in the room. The factor e is 0.01 according to ONORM EN 12831 for good windprotection (city) and one opening in the room. The factor 2 is for the worst case because the n_{50}-value is for the whole building.

The parameters for evaluating the indoor comfort in the flat and the dimensioning of the ventilation system with heated input air are different. For dimensioning the ventilation system inside the flat the neighbours are assumed to be not heated and there are also no internal thermal gains calculated.

1.5 Calculation method – Heating energy demand

As the heating energy demand is calculated for an average situation the parameters are different from those used for the heating load.

TABLE 5: Boundary conditions for the steady state heating demand calculation

T_i	Neighbours	$q_{i\ bruttoarea}$	n_{Anl}	η	n_{mech}	n_{50}	$n_{Inf,\ rooms}$	$n_{Inf,\ flats}$
°C		W/m²	h^{-1}	–	h^{-1}	h^{-1}	h^{-1}	h^{-1}
20	heated	2.1	0.4	0.8	$n_{Anl} * (1-\eta)$	0.4	$n_{50} * e$	$n_{50} * e$

There are different modes of calculation for the heating demand. Balances can be build for the whole building, flat by flat or room by room. As the heating energy demand is calculated from the heat losses minus the usable part of the heting gains the hidden assumption is that losses are locally compensated by the gains. In reality doors inside one flat are open and therefore the most realistic zoning should be the second one, where each flat is one zone. For comparision the next figure shows all three results.

building

$$HWB = HWB_{building}$$

flats

$$HWB = \sum HWB_{flat}$$

rooms

$$HWB = \sum HWB_{room}$$

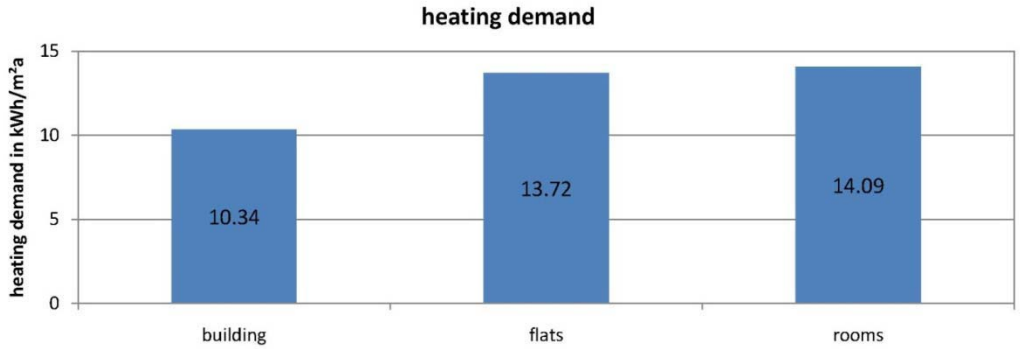

The results for the heating demand vary depending on the mode of calculation. When the calculation is made for the whole building the heat losses and gains are much more compensated compared to the calculation room by room.

1.6 Summertime Overheating

The room temperature during summertime are determined by solar and internal loads, ventilation losses especially during night and the possibility to store heat in the construction. The standardized method to asses the risk of summertime overheating in Austria is ÖNORM B 8110-3. For the design process a different method has been used. As in Rouvel et.al. 2000 described, the solar and internal gains not covering the transmission and ventilation losses can be used the asses the time the room temperatures will be higher than a certain limit. For the optimisation the limit for the room temperature was set to be 26°C.

2. Optimisation – Vienna Utendorfgasse

The main criteria for optimising the building structure were the costs, as a certain limit had to be kept to receive funding from the state. From building physics point of view the heating load should be less than 10 W/m² to be able to use heating by ventilation without radiators in the flats, the heating energy demand should be less than 15 kWh/m² and overheating during summertime has to be avoided. Using these four criteria, the thickness of the insulation, the type of window and the size of the windows had been determined. Details can be found in Jachan 2003. The following figure shows the ratings for different window sizes. The performance is rated with one point for each criterion. The summertime behaviour is always rated as fulfilled because the necessary solar protection is determined and the costs for the solar shading are part of the total costs. Total costs in this case are investment for windows, walls, solar protection and the costs for heating for 30 years.

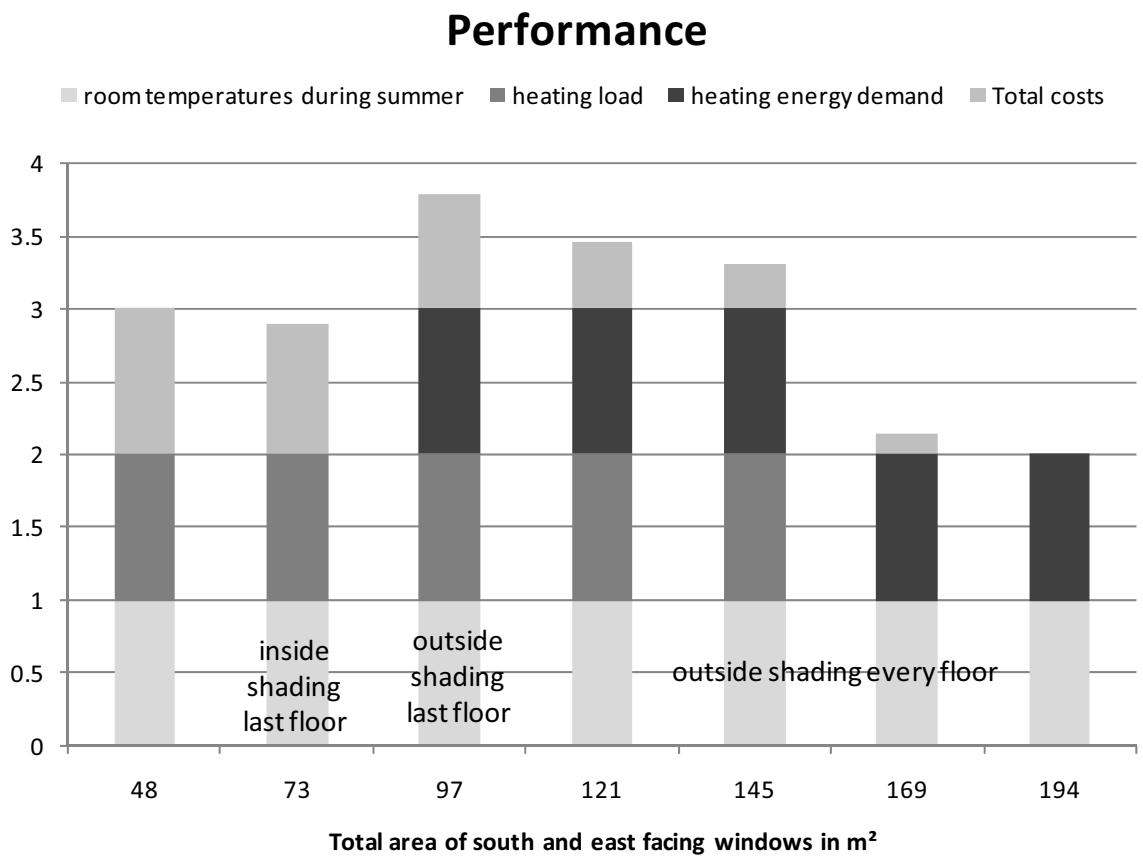

FIG. 4: Comparison of simulation and steady state calculation

As can be seen the optimum window size for the investigated scenario is around 100 m² for the building. If less windows are used the heating energy demand does not fulfil the criteria, if more windows are used the total costs increase and above 150 m² the heating load will be too high. Using the optimum window size an outer shading protection for the last floor has to be used to avoid the risk for summertime overheating.

In FIG. 5 are the necessary air change rates for heat supply in each flat of the house 2 – Utendorfgasse is shown. For a good indoor climate an air change rate less than 0.4 1/h is preferable. In the passive house Utendorfgasse only the last roof-top apartment needs more heat input. The air change rate for the dimensioning of the heating coil contains the eventuallity that none of the neighbours are heating and no internal gains are present. As one can see the heating coil and the ventilation system should be able to deliver a 0.7 1/h with 50°C for each flat to cover this maximum.

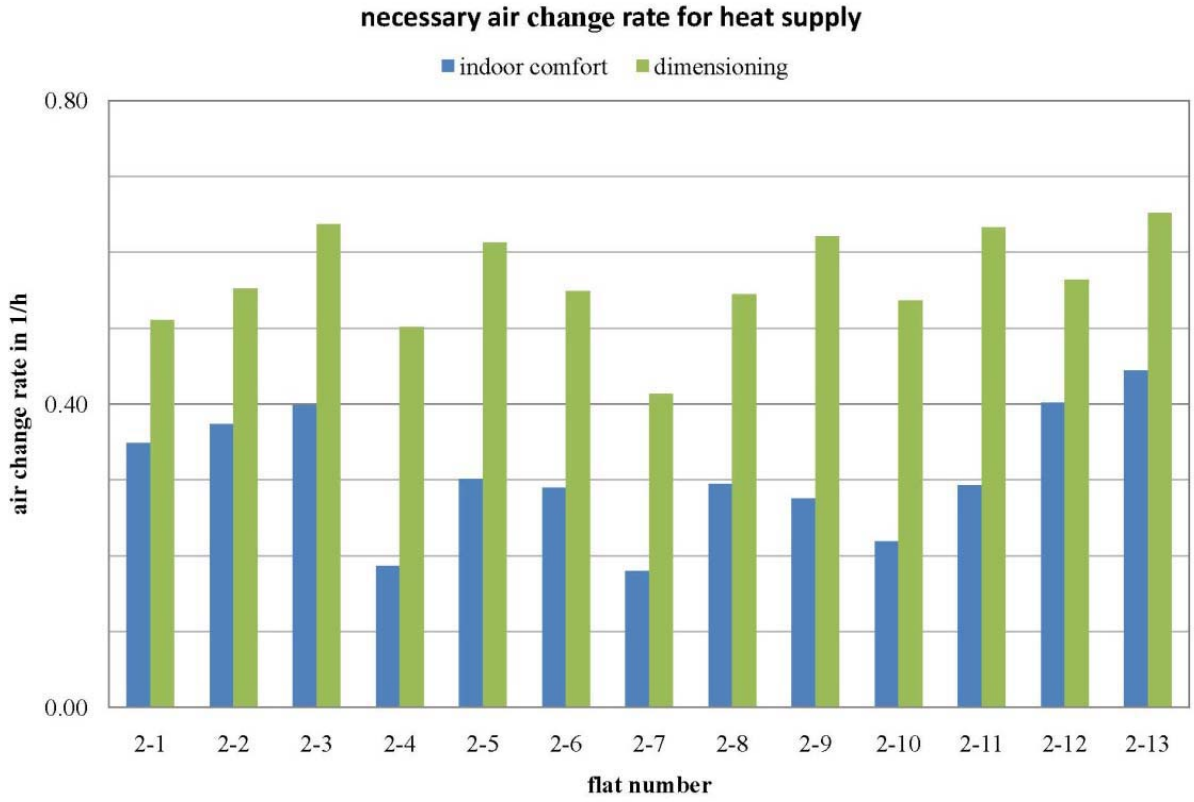

FIG. 5: Necessary air change rate with 50°C for the heat supply in the 22°C warm flats. If all flats are heated the air change "indoor comfort" has to be used. If all neighbours of a flat are not heated and no internal gains are present in the flat the scenario "dimensioning" has to be used.

Th normal use of the ventilation system should be that the inhabitants use a reduceded air change rate of around 0.2-0.3 1/h. During cold days the "normal" air change 0.4 1/h should be used. For other reasons the air change of the ventilation system can be increased up to 0.7 1/h.

3. References

Jachan Ch. (2003). Thesis, Hygienischer Tauglichkeitsnachweis und Optimierung der bauphysikalischen Performance von Gebäuden in Passivbauweise. University of Technology Vienna

Höfer (former Glöckl) T. (2006) Master thesis, Analyse der Heizlastberechnung für Niedrigstenergiehäuser am Beispiel einer Wiener Passivhausanlage. University of Technology Vienna

ÖNORM EN 12831 (2003). Heizungsanlagen in Gebäuden - Verfahren zur Berechnung der Norm-Heizlast; Austrian Standardization organisation

Rouvel, L., Deutscher, P., Elsberger, M. (2000). Sommerlicher Wärmeschutz, Eine einheitliche Methodik für die Anforderungen an den winterlichen und sommerlichen Wärmeschutz, Bauphysik 22, Verlag Ernst & Sohn

Strategic optimization of non-residential buildings

Sofic Mario, Dipl.Ing.,
Vienna University of Technology;
mario.sofic@tuwien.ac.at and http://www.bph.tuwien.ac.at/

Bednar Thomas, Ao.Univ.Prof. Dipl.-Ing. Dr.techn. ,
Vienna University of Technology;
thomas.bednar@tuwien.ac.at and http://www.bph.tuwien.ac.at/

KEYWORDS: *optimization, non-residential building, office buildings key, heating energy demand, cooling energy demand*

SUMMARY:
The paper compares the Monthly Balance Method (DRAFT ISO/DIS 13790) with whole building simulations and shows the effects of night ventilation and coupling of zones in office buildings.

A model of a typical office building is used (40x13x8 meters, with north and south orientated windows).
In the first part the energy demand for heating and cooling for different climates with whole building simulations and monthly zone methods is compared. To create a coupled and an uncoupled model the U-value of the intermediate wall is varied and the effects of coupling are presented.

In the second part a systematic variation of the model to get a strategy for an optimization of office buildings is performed. The location is in Vienna, the climate is a typical European continental climate. Three parameters Gamma, Tau and C (storage capacity) are important values for optimization of buildings. The reduction of the parameter K is the first step to minimize the energy demand of buildings. The next step is the intelligent choose of window part because if the window part of a building is high the parameter G is big. And the energy demand for cooling increases with the G-value. The next important point is the storage capacity of the building materials. Walls and Slabs storages energy and a good storage characteristic of a building reduce the energy demand for heating and cooling.

In diagrams the difference between whole building simulations and monthly zone methods for different Gamma and Tau values is shown. Furthermore the effects of coupling and night ventilation to reduce the energy demand for cooling and heating are presented.

1. Introduction

The DRAFT ISO/DIS 13790 (Thermal performance of buildings – Calculation of energy use for space heating and cooling, 2005) describes the so called Monthly Balance Method to calculate the heating and cooling demand [1] for the European energy certificate and will be used very often to optimize buildings.
Due to a lot of assumptions in the method the paper compares the Monthly Balance Method with whole building simulations.
The energy demand for heating and cooling will be calculated by a systematic variation of building properties (like gain/loss ratio and time constant) and outdoor climate.
Part of the variation is using of Night Ventilation Concept to decrease cooling energy demand. Especially for this strategy the coupling between different zones (staircase, offices etc,.) is very important.
Out of the large number of results recommendations for adaption and the limits for the Monthly Balance are presented.

2. Model

2.1 Geometry and Orientation

The model is a six zone model with four office zones and two corridors. The size of one office zones is: width = 40 meters, length = 5 meters and height = 4 meters. The size of one corridor is: width = 40 meters, length = 3 meters and height = 4 meters.

The model has two floors and the geometry of the model should be a typical office building.

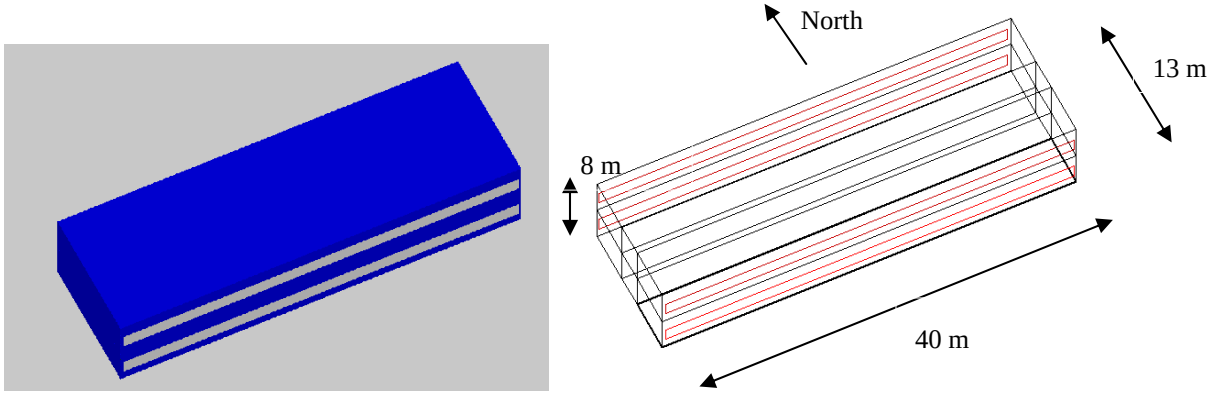

FIG.1 – Office and corridors model

The office zones have windows on the north and on the south facade, the corridor and the east and west facade are simulated without any windows. The orientation of the model is north/south.

The construction elements are simulated with following components and U-values:

Floor	
marking	thickness in cm
cementscreed	4
EPS	20
reinforced concrete	20
U = 0.19 W/m²K	

Intermediate Slab	
marking	thickness in cm
cementscreed	4
EPS	3
reinforced concrete	20
U = 0.94 W/m²K	

External Slab	
marking	thickness in cm
EPS	25
reinforced concrete	20
U = 0.15 W/m²K	

Intermediate wall	
marking	thickness in cm
Vertically perforated brick	5
ultra heat insulation	5
Vertically perforated brick	5
U = variable	

External wall	
marking	thickness in cm
EPS	20
vertically perforated brick	20
U = 0.16 W/m²K	

FIG.2 U-values of the construction elements

The different U-values of the intermediate walls are:

1. Coupled model:

   U = 4.96 W/m²K

   The coefficient of thermal conductivity of the vertically perforated brick and the ultra heat insulation is 100 W/mK

2. Not coupled model:

   U = 0.002 W/m²K

   The coefficient of thermal conductivity of the vertically perforated brick is 0.2 W/mK and coefficient for the ultra heat insulation is 0.0001 W/mK

Only the intermediate wall has different U-values, the intermediate slab has always an U-Value of 0.94 W/m²K. The difference between the ground floor and the first floor is not very big. The variation of the material parameters is only used for the intermediate wall.

2.2 Windows

U-value = 0.85 W/m²K, Solar heat gain coefficient: g-value = 0.50, shading reduction factor: $F_{sh,gl}$ = 0.80 [1], Orientation: North and South. The size of the windows is length = 39.50 meters and height = 1.50 meters. (typical light-band facade). The sunscreen is activated by radiation above 300 W/m²K or an operative room temperature above 23 ° C.

2.3 Use

The use of the building is simulated as a typical office. The use of the corridors is different to the use of the offices.

Temperature for heating = 20 °C

Temperature for cooling = 26 °C

The air change rate for each time step is defined with the following decision:

If $T_{op} > T_{decision}$ and $T_e < T_{air}$ the maximum of the air change rate is used. In every other case the minimum of the air change rate is used for each time step.

T_{op} operative temperature of the room

$T_{decision}$ aim temperature for the room for the air change rate

T_e temperature of the external environment

T_{air} air temperature in the room

2.3.1 Internal gains and air change rate for simulation

Internal heat gains from 9:00 a.m. to 7:00 p.m. 16 W/m² in the offices and 0 W/m² for the corridors. The air change rates are between a minimum and a maximum value

office air change rate in h^{-1}		
hours	minimum	maximum
0:00 - 1:00	0.1	2
1:00 - 2:00	0.1	2
2:00 - 3:00	0.1	2
3:00 - 4:00	0.1	2
4:00 - 5:00	0.1	2
5:00 - 6:00	0.1	2
6:00 - 7:00	0.1	2
7:00 - 8:00	0.1	2
8:00 - 9:00	0.4	0.4
9:00 - 10:00	0.4	0.4
10:00 - 11:00	0.4	0.4
11:00 - 12:00	0.4	0.4
12:00 - 13:00	0.4	0.4
13:00 - 14:00	0.4	0.4
14:00 - 15:00	0.4	0.4
15:00 - 16:00	0.4	0.4
16:00 - 17:00	0.4	0.4
17:00 - 18:00	0.4	0.4
18:00 - 19:00	0.4	0.1
19:00 - 20:00	0.1	0.1
20:00 - 21:00	0.1	0.1
21:00 - 22:00	0.1	2
22:00 - 23:00	0.1	2
23:00 - 24:00	0.1	2

corridor air change rate in h^{-1}		
hours	minimum	maximum
0:00 - 1:00	0.1	5
1:00 - 2:00	0.1	5
2:00 - 3:00	0.1	5
3:00 - 4:00	0.1	5
4:00 - 5:00	0.1	5
5:00 - 6:00	0.1	5
6:00 - 7:00	0.1	5
7:00 - 8:00	0.1	5
8:00 - 9:00	0.4	0.4
9:00 - 10:00	0.4	0.4
10:00 - 11:00	0.4	0.4
11:00 - 12:00	0.4	0.4
12:00 - 13:00	0.4	0.4
13:00 - 14:00	0.4	0.4
14:00 - 15:00	0.4	0.4
15:00 - 16:00	0.4	0.4
16:00 - 17:00	0.4	0.4
17:00 - 18:00	0.4	0.4
18:00 - 19:00	0.1	0.1
19:00 - 20:00	0.1	0.1
20:00 - 21:00	0.1	0.1
21:00 - 22:00	0.1	5
22:00 - 23:00	0.1	5
23:00 - 24:00	0.1	5

FIG.3 Maximum and Minimum of air change rate for the offices and the corridors

2.3.2 Internal gains and air change rate for monthly balance method

For the monthly method the values for the air change rate and the internal gains which used in the simulation must be the average value of 24 hours.

The average for the internal gains is for the offices: 6.66 W/m² and for the corridor it is 0 W/m².

The air change rate for the offices to calculate the heating energy demand is the average of the minimum it is 0.225 h^{-1}, to calculate the cooling energy demand the average of the maximum is 1.1 h^{-1}.

The air change rate for the corridors to calculate the heating energy demand is the average of the minimum it is 0.225 h^{-1}, the same value as for the offices, to calculate the cooling energy demand the average of the maximum is 2.47 h^{-1}.

3. Results for different climates

The simulation program (buildopt) was designed by the Center for Building Physics and Building Acoustics in Vienna, the program has been validated by using data from the ANNEX 41. [2]

To change the climate, different locations for the model were choosed. The following locations are used:

Vienna (European continental climate), Beijing (Asiatic continental climate), Palermo (mediterranean climate), Moscow (winter cold climate).

The aim temperature for the air change rate in the following results is 23 °C.

3.1 Heating and cooling demand

The results for heating and cooling demand:

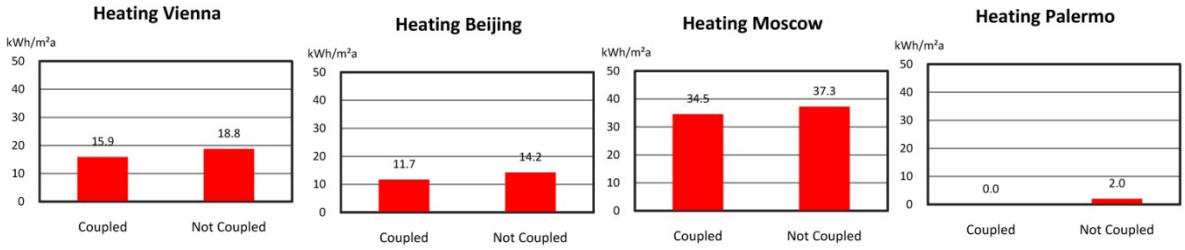

FIG.4 Heating demand for office and corridors model

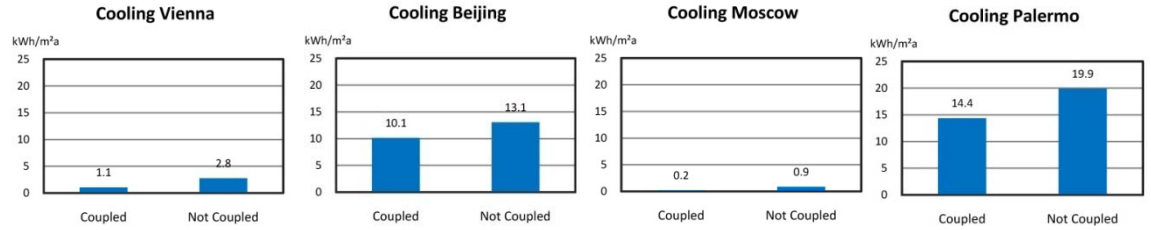

FIG.5 Cooling demand for office and corridors model

The effects of coupling reduce the energy demand for heating and cooling. Furthermore is a coupled model a realistic model, coupling effects (transmission) are very important for the cooling demand to reduce the maximum cooling loads. The U-value of an intermediate wall in real is between 0.2 and around 1.0 W/m²K.

3.2 Comparison of simulation with monthly method

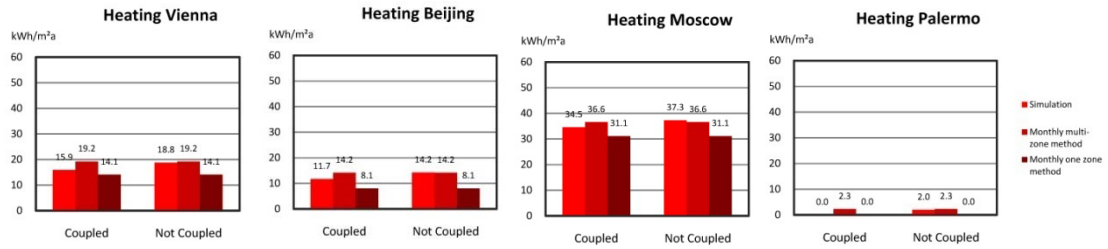

FI.6 Heating demand for office and corridors model – monthly method and simulation

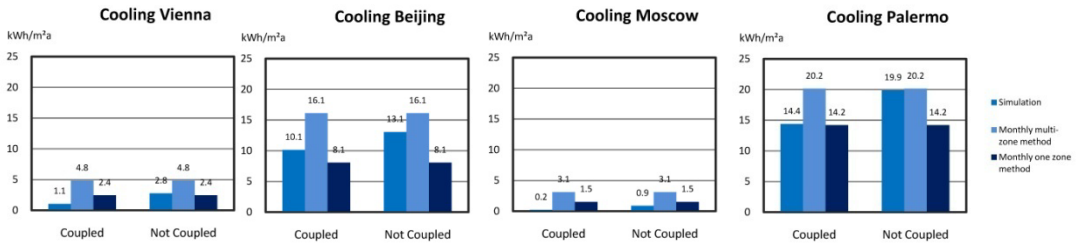

FIG.7 Cooling demand for office and corridors model – monthly method and simulation

For each location the results of the monthly one zone method is not so big as the results of the simulation. For the location Vienna the monthly one zone method is not correct for not coupled models.

4. Results of systematic variation

To get a systematic variation of the gain loss ratio and the time constant the parameters Gamma and Tau must be varied for the office and corridors model.

To get a variation of gain loss ratio the size of the windows for each orientation was varied (a model without any windows to a full glazing facade model). The variation of the time constant was realized by the variation of the storage capacity for each material.

The following results are calculated with a coupled model but not only with transmission between the offices and the corridors also with airflow of 800 m³/h airflow between the corridor and the offices for better coupling.

Three parameters Gamma, Tau and C (storage capacity) are important for the following diagrams:

$$G = \frac{1}{A_{ges}} \sum_i A_{g,i} \cdot g_i \quad (1)$$

$$K = \frac{1}{A_{ges}} \left(\sum_j A_{e,j} \cdot U_j + 0.33 \cdot \sum_k V_k \cdot n_k \right) \quad (2)$$

$$C = \frac{1}{A_{ges}} \sum_l A_l \cdot \sum_m c_m \cdot \rho_m \cdot d_m \quad (3)$$

$$\text{Gamma} = \frac{G}{K} \text{in} \frac{m^2K}{W} \quad (4)$$

$$\text{Tau} = \log \left(\frac{\frac{C}{K}}{\text{hours}} \right) \quad (5)$$

G	Total energy transmission value
K	Heat transition value in W/m²K
C	Storage capacity in J/m²K
A_{ges}	Outer surface of the building in m²
$A_{g,i}$	Area of transparent construction element in m²
g_i	Total energy transmission value for one construction element
$A_{e,j}$	Outer surface of one construction element in m²
U_j	U-value of one in construction element W/m²K
V_k	Volume of the building in m³
n_k	Necessary minimum effective air change rate in h^{-1}
A_l	Area of one construction element in m²
c_m	Specific storage capacity in J/kgK
ρ_m	Density in kg/m³
d_m	Thickness in m

4.1 Air change rate for simulation and monthly balance method

The aim temperature for the air change rate in the following results is 23 °C during the summer period (summer is the period between 01th May and 30th September) and 20 °C during the winter period (winter is the period between 01th October to 30th April) for the offices. The aim temperature for the air change rate in the following results is 23 °C during the summer period (summer is the period between 01th May and 30th September) and 15 °C during the winter period (winter is the period between 01th October to 30th April) for the corridors.

The location for the calculation is Vienna.

office air change rate in h^{-1}		
hours	minimum	maximum
0:00 - 1:00	0.1	2
1:00 - 2:00	0.1	2
2:00 - 3:00	0.1	2
3:00 - 4:00	0.1	2
4:00 - 5:00	0.1	2
5:00 - 6:00	0.1	2
6:00 - 7:00	0.1	2
7:00 - 8:00	0.1	2
8:00 - 9:00	0.1	2
9:00 - 10:00	0.4	2
10:00 - 11:00	0.4	2
11:00 - 12:00	0.4	2
12:00 - 13:00	0.4	2
13:00 - 14:00	0.4	2
14:00 - 15:00	0.4	2
15:00 - 16:00	0.4	2
16:00 - 17:00	0.4	2
17:00 - 18:00	0.4	2
18:00 - 19:00	0.4	2
19:00 - 20:00	0.1	2
20:00 - 21:00	0.1	2
21:00 - 22:00	0.1	2
22:00 - 23:00	0.1	2
23:00 - 24:00	0.1	2

corridor air change rate in h^{-1}		
hours	minimum	maximum
0:00 - 1:00	0.1	5
1:00 - 2:00	0.1	5
2:00 - 3:00	0.1	5
3:00 - 4:00	0.1	5
4:00 - 5:00	0.1	5
5:00 - 6:00	0.1	5
6:00 - 7:00	0.1	5
7:00 - 8:00	0.1	5
8:00 - 9:00	0.1	5
9:00 - 10:00	0.1	5
10:00 - 11:00	0.1	5
11:00 - 12:00	0.1	5
12:00 - 13:00	0.1	5
13:00 - 14:00	0.1	5
14:00 - 15:00	0.1	5
15:00 - 16:00	0.1	5
16:00 - 17:00	0.1	5
17:00 - 18:00	0.1	5
18:00 - 19:00	0.1	5
19:00 - 20:00	0.1	5
20:00 - 21:00	0.1	5
21:00 - 22:00	0.1	5
22:00 - 23:00	0.1	5
23:00 - 24:00	0.1	5

FIG.8 Maximum and Minimum of air change rate for the offices and the corridors

For the monthly one zone model the following air change rates are used:

The air change rate for the offices to calculate the heating energy demand is the average of the minimum it is 0.225 h^{-1}, to calculate the cooling energy demand the average of the maximum is 0.86 h^{-1}. The air change rate for the corridors to calculate the heating energy demand is the average of the minimum it is 0.10 h^{-1}. To calculate the cooling energy demand the average of the maximum is 0.73 h^{-1}.

4.2 Comparison of simulation and monthly one zone method

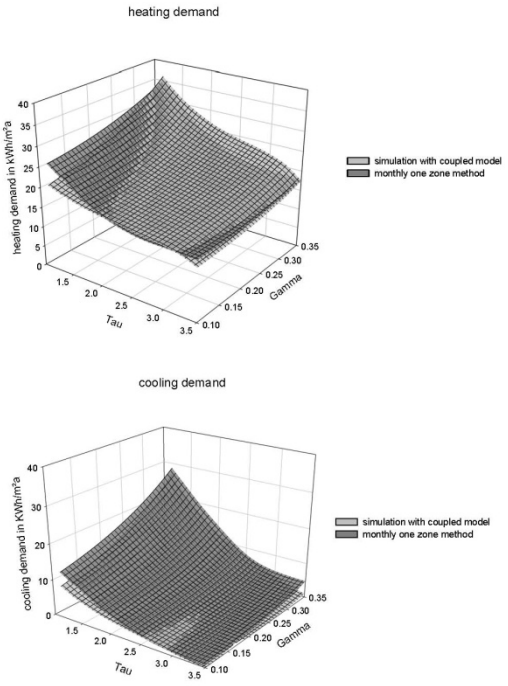

FIG.9 Heating and cooling demand for the office and corridors model with different Gamma and Tau/simulation and monthly one zone method

For Vienna the cooling demand with the monthly one zone method for real office buildings (Tau < 1.50, Gamma 0.20 – 0.35 m²K/W) is bigger than the simulated results. The heating demands calculated with the monthly one zone method for real office buildings under values the simulated results.

The next diagram is the comparison of coupled and not coupled models. The coupled model has an intermediate wall with an U-value of 4.96 W/m²K and 800 m³/h airflow between the corridor and the offices.

4.3 Effect of coupling

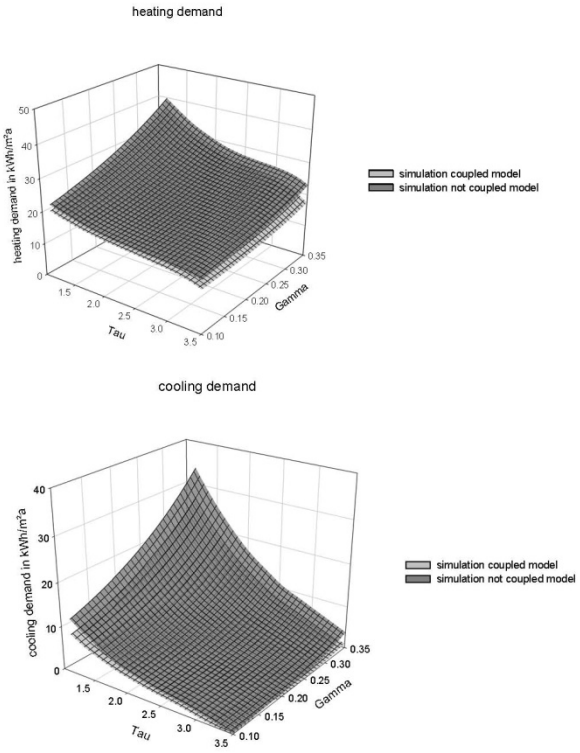

FIG.10 Heating and cooling demand for the office and corridors model with different Gamma and Tau/coupled and not coupled

The energy demand for a coupled model is smaller than the energy demand for not coupled model. The difference between an energy demand calculated by the monthly one zone method and a not coupled model simulation cannot be unconsidered.

4.4 Effect of night ventilation

For the results without night ventilation the air change rates are, for the corridors: 0.10 h^{-1} all the time and for the offices 0.40 h^{-1} from 8:00 a.m. to 7:00 p.m. otherwise 0.10 h^{-1}. The aim temperature for the results without night ventilation is for the offices the aim temperature without night ventilation is 23 °C the whole year, for the corridor it is 23 °C during the winter period and 20 °C during the summer period.

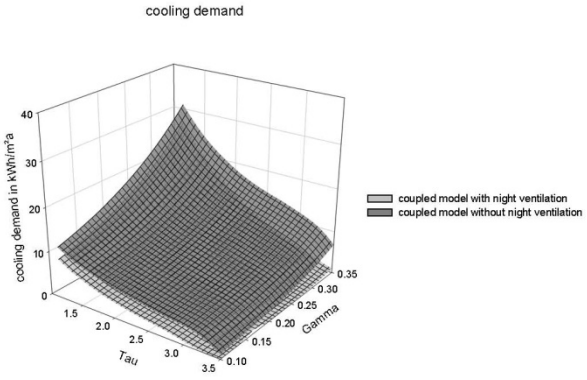

FIG.11 Cooling demand for the office and corridors model with different Gamma and Tau/coupled model with night ventilation and without night ventilation

5. Conclusions

The so called Monthly Balance Method calculates the heating and cooling demand for Vienna in a realistic way. The comparison of the simulation and the monthly method demonstrates that the monthly multi-zone method most of the time overvalues the real energy demand, not only for Vienna also for different climates. This method even overvalues the simulations of ventilation concepts and coupling effects. The one zone method undervalues coupling effects but for Vienna the difference between the results of the simulation and the monthly one zone method is not very big even for realistic buildings. For other locations the monthly one zone method is not adequate. For Beijing and Palermo the real energy demand is higher than the result of the monthly one zone method.

The comparison of simulation and monthly one zone method for different Tau and Gamma values leads to the conclusion that the monthly one zone method for Vienna calculates realistic values, if the building has coupling effects. The effect of coupling is shown and with coupling effects the energy demand for heating and cooling can be reduced. The influence of night ventilation for the cooling demand in Vienna is for buildings with many windows very high. The cooling demand can be reduced to halve if the storage capacity is very high. (τ higher than about 300 hours)

6. References

[1] DRAFT ISO/DIS 13790 (2007). Energy performance of buildings – Calculation of energy use for space heating and cooling, *International Standard ISO/FDIS 13790: 2007(E)*

[2] Final report of IEA ANNEX 41 (in preparation) 2008

Numerical methods for optimizing the performance of buildings

Frank Pedersen, Researcher,
Danish Building Research Institute, Dr. Neergaards Vej 15, DK-2970 Hørsholm, Denmark;
frp@sbi.dk, www.sbi.dk

KEYWORDS: building energy, building economy, indoor climate, numerical optimization, SQP filter algorithms.

SUMMARY:
The many different parties that influence design and control decisions for buildings, such as building owners, users, architects, consulting engineers, contractors, etc, may have different and to some extent contradicting requirements to buildings. Furthermore, national building regulations specify requirements to (among others) the energy performance and quality of the indoor climate, which also must be satisfied. This paper describes numerical methods intended for estimating design decisions that satisfy the given requirements, and that at the same time are optimal in some sense, for instance with respect to the economy, energy performance, or indoor climate. This is addressed by combining building simulation methods with numerical optimization methods. The paper describes a problem formulation that represents optimal design decisions, and the numerical simulation and optimization methods used for solving the problem. The paper furthermore provides a case study regarding a small office building.

1. Introduction

The parties who influence design and control decisions for buildings (referred to as *decision makers*), such as building owners, users, architects, consulting engineers, contractors, etc., often have different and to some extent conflicting requirements to buildings. For instance, the building owner may be more concerned about the budget for the building, rather than the indoor climate, which is more likely to be a concern of the building user.

Furthermore, it is a well-established fact that it is easier and less costly to make design changes in the early stages of the design process for buildings rather than later. See for instance Poel (2005) and Nielsen (2003) for a more detailed description and discussion of the design process for buildings. Decision-makers may therefore benefit from software-based building optimization methods, developed for the early stages of the design process.

Simulation and optimization methods have been combined in many different ways for supporting building-related decisions. For instance, the studies by Peippo et al. (1999), Bouchlaghem et al. (2000) and Wright et al. (2002) all use this approach for estimating efficient design decisions related to, among others, the shape and orientation of the building, the amount of insulation, and the shape and area of the windows. The problem formulations used in the studies are single- or multi-criteria optimization problems, involving either energy performance, construction or operational costs, or measures for thermal discomfort.

In general, there are many combinations of decision variables and performance calculations that are relevant to include in the problem formulation. This motivates the development of building optimization methods that give the end-user full control over the problem formulation.

Furthermore, the numerical optimization methods must address the following issues: (1) partial derivatives of the functions can not be expected to be available, and (2) the optimization method must provide valid input to the simulation methods; otherwise they may not provide valid output.

The purpose of this paper is to describe a combination of numerical simulation and optimization methods that can be used for estimating efficient design decisions at the early stages of the design process for buildings. The problem formulation and the involved numerical methods are described. The paper furthermore provides a case study involving a small office building.

This paper is based on the thesis by Pedersen (2006), where further details can be found.

2. General aspects of the method

Decision-making is supported by calculating optimal design decisions for a conceptual building model. The problem formulation, the model and the elements included in the problem formulation are described in the following.

2.1 Problem formulation

Figure 1 shows an illustration of the elements involved in decision-making. The figure illustrates the simple fact that decisions made under given circumstances result in a number of consequences. The figure furthermore illustrates the requirements made by decision-makers to the decisions as well as to the resulting consequences.

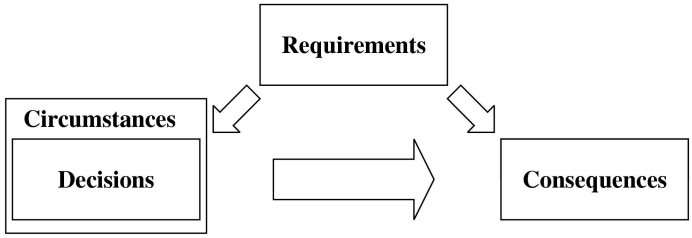

FIG. 1: Elements involved in decision-making.

The term *decision* refers to the aspects of the building that decision-maker has control over, and *circumstances* refers to the aspects that the decision-maker has no control over, or do not wish to control.

Decisions are represented by a set of *decision variables* $x \in \mathbb{R}^n$, and the circumstances are represented by a set constant parameters $y \in \mathbb{R}^{n_y}$. The consequences are represented by a set of *utility functions* $q : D \times \mathbb{R}^{n_y} \rightarrow \mathbb{R}^{n_q}$, that depend on x and y. The consequences of a set of decisions x made under the circumstances y can therefore be evaluated by calculating the function values $q(x, y)$.

The domain $D \subseteq \mathbb{R}^n$ for the utility functions is defined in the following way:

$$D = \left\{ x \in \mathbb{R}^n : d(x) \geq 0 \right\}, \tag{1}$$

where the functions $d : \mathbb{R}^n \rightarrow \mathbb{R}^{n_D}$ are referred to as *domain constraint functions*.

The following optimization problem is used for estimating efficient decisions:

$$\begin{aligned} &\min_{x \in D} && r_O^T q(x, y) \\ &\text{subject to} && A_I \begin{bmatrix} q(x, y) \\ x \end{bmatrix} \geq b_I \quad \text{and} \quad A_E \begin{bmatrix} q(x, y) \\ x \end{bmatrix} = b_E \end{aligned} \tag{2}$$

This formulation allow the user to specify which utility function to minimize or maximize, as well as linear inequality and equality relations, involving decision variables and utility functions. The user can thus choose between, for instance, energy optimal or economical optimal design decisions. The inequality constraints can be used for specifying upper and lower bounds on utility functions and decision variables. The equality constraints can be used for specifying required values for utility functions and decision variables.

2.2 A conceptual building model

The required utility functions are based on performance calculations for a building with a simple geometry, representing general features, such as volume, surface area, mass of constructions, window area, etc. This so-called *conceptual building model* is shown in Figure 2.

All floors are identical, and each floor has window “bands” on two of the four external walls. The staircase tower is omitted, and only a single internal wall is included, which divide the building into two thermal zones. The performance of each of the two thermal zones is calculated separately.

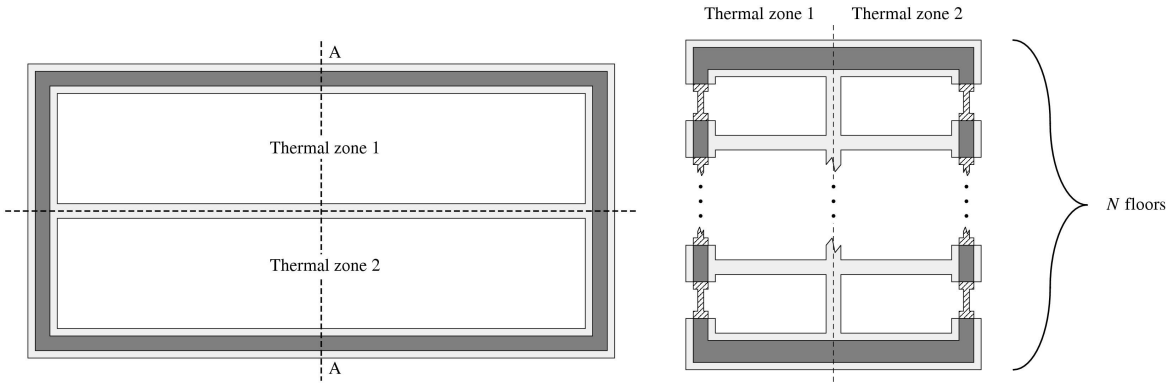

FIG. 2: Left: Layout of the conceptual building. Right: The cross-section A-A.

2.3 Decision elements

The following decision variables are included in the problem formulation:

- The shape of the building (represented by the width to length ration and the number of floors)
- The window fraction of the façade areas
- Discrete selections of windows from a product database
- Amount of insulation used in ground slab, roof construction and external walls

The following main groups of utility functions are included in the problem formulation:

- The energy performance (energy for heating, cooling, ventilating, producing DHW, U-values for constructions, among others)
- The indoor environment (overheating and daylight utilization)
- Economy (construction and operational costs)

3. Utility functions

The utility functions involved in the problem formulation are described in the following, as well as the domain constraint functions, that specify the domain of the utility functions.

3.1 Energy and indoor climate

The performance with respect to energy and indoor climate is calculated using the method described by Nielsen (2005). One simulation is conducted for each of the two thermal zones of the building. The method gives, among others, hourly values for the internal air temperature, and hourly values for energy required for heating, cooling and ventilating the building.

These results are used for calculating the utility functions related to the energy performance of the building. The internal air temperatures are furthermore used for calculating the annual number of hours, where overheating occurs, which is used as a measure for thermal discomfort. The ratio between the depth of the room and the window height is used as a (primitive) measure for the level of daylight utilization. The calculation of this measure is based on the geometry of the building. Notice that high values represent low daylight utilization, and low values represent high daylight utilization.

3.2 Economy

Two utility functions are used for representing economical consequences of design decisions: The cost of constructing the building, and the annual cost of operating the building. The cost of constructing the building is estimated by interpolating values found in price catalogues, such as the V&S price catalogue (2005), which concerns unit prices for construction jobs in Denmark.

Some of the prices only depend on the number of purchased units, where other prices also depend on secondary parameters. For instance, the unit price of pouring concrete depends on the amount of concrete, and the required strength of the concrete.

The prices are interpolated using the following three models:

$$p_1(u,\beta) = \beta_1 \exp(\beta_2 u) + \beta_3 \tag{3}$$

$$p_2(u,s,\beta) = \beta_1 s + \beta_2 \exp(\beta_3 u) + \beta_4 \tag{4}$$

$$p_3(u,s,\beta) = \beta_1 \exp(\beta_2 s) + \beta_3 \exp(\beta_4 u) + \beta_5, \tag{5}$$

where u is the number of purchased units, β is a vector of model parameters, and s is the secondary parameter. Note that the length of β depends on the model.

The model (3) is used for representing unit prices that do not involve a secondary parameter, and the models (4) and (5) are used for representing unit prices involving a secondary parameter.

The model parameters β are calculated as a least squares solution to the over-determined system of non-linear equations that can be formed using the unit prices from the price catalogue.

The cost of operating the building is calculated using the annual consumption of electrical energy and energy for heating the building, together with the energy prices for electricity and district heating.

3.3 Domain constraints

The purpose of the domain constraints is to ensure that the input to the simulation methods is valid. The domain constraints ensure (among others) that the input satisfies the following requirements:

- The width to length ratio of the building is positive
- The number of floors is larger than or equal to 1
- The window fraction of the façade area is between 0 and 1
- The amount of insulation used in the ground slab, roof construction and external walls is positive.

4. A gradient-free SQP filter algorithm

The method described in this section is based on the SLP filter method by Fletcher (1998), but with a number of modifications, in order to make it suitable for solving (2). First of all, the method must not require gradient information of the functions used for defining (2), secondly, it may only evaluate these functions for iterates x_k, that belong to the domain D.

The method is intended for finding solutions to constrained optimization problems on the following form:

$$\begin{aligned} &\min_{x \in D} && f(x) \\ &\text{subject to} && c_I(x) \geq 0 \quad \text{and} \quad c_E(x) = 0, \end{aligned} \tag{6}$$

which includes the problem (2). The method needs to distinguish between the following three situations:

- The current iterate x_k belongs to the domain D
- The current iterate has provided an unsolvable (or *incompatible*) subproblem
- The current iterate does not belong to the domain D.

In the first situation, the method calculates a step Δx_k towards a stable point for (6), by forming an approximated subproblem $\mathrm{QP}(x_k, \mu_k)$, using first order Taylor expansions of the functions involved in (6). The step length is restricted by adding a quadratic damping term μ_k to the objective function. This approach provides the following quadratic program:

$$\mathrm{QP}(x_k,\mu_k)=\begin{cases}\min\limits_{\Delta x\in\mathbb{R}^n} & B_{f,k}\Delta x+\frac{1}{2}\mu_k\Delta x^T\Delta x\\ \text{subject to} & c_I(x_k)+B_{c_I,k}\Delta x\geq 0\\ & d(x_k)+B_{d,k}\Delta x\geq 0\\ & c_E(x_k)+B_{c_E,k}\Delta x=0\end{cases}, \tag{7}$$

The following gradient approximations are used in the definition of (7):

$$B_{f,k}\approx\nabla f(x_k),\ B_{c_I,k}\approx J_{c_I}(x_k),\ B_{c_E,k}\approx J_{c_E}(x_k)\ \text{and}\ B_{d,k}\approx J_d(x_k). \tag{8}$$

These approximations are initialized using finite difference calculations, and subsequently updated using the rank one updating formula described by Broyden (1965).

In the second situation, where $\mathrm{QP}(x_k,\mu_k)$ is incompatible, the method calculates a step towards the feasible region of (6). This is done by calculating a so-called *regular restoration step*, which is a step in a direction that minimizes the maximum violation of the constraints in (6). The step length is restricted by adding a quadratic damping term to the objective function. This approach provides the following subproblem:

$$\mathrm{RRQP}(x_k,\mu_k)=\begin{cases}\min\limits_{z\in\mathbb{R},\Delta x\in\mathbb{R}^n} & z+\frac{1}{2}\mu_k\Delta x^T\Delta x\\ \text{subject to} & z\geq v(x_k)+B_{v,k}\Delta x\end{cases}, \tag{9}$$

where $v(x_k)$ is a vector of constraint violations:

$$v(x)=\begin{bmatrix}-c_I(x)\\ c_E(x)\\ -c_E(x)\\ -d(x)\end{bmatrix}, \tag{10}$$

and where $B_{v,k}\approx J_v(x_k)$ is an approximation of the gradient of v at x_k. In (9), the parameter z is introduced in order to rearrange the problem into a QP.

The last situation, where $x_k\notin D$, is handled by calculating a so-called *domain restoration step*, which is a step in a direction that minimizes the maximum violation of the domain constraints, and can be calculated by solving the following subproblem:

$$\mathrm{DRQP}(x_k,\mu_k)=\begin{cases}\min\limits_{z\in\mathbb{R},\Delta x\in\mathbb{R}^n} & z+\frac{1}{2}\mu_k\Delta x^T\Delta x\\ \text{subject to} & z\geq -d(x_k)-J_d(x_k)\Delta x\end{cases}, \tag{11}$$

Once a step Δx_k is calculated by solving either (7), (9) or (11), and the step is accepted, the next iterate becomes:

$$x_{k+1}=\Delta x_k+x_k, \tag{12}$$

The damping parameter μ_k is required for solving (7), (9) and (11), and is calculated by relating it to the so-called *trust region radius* ρ_k, which is an upper limit on the step length, such that $\|\Delta x_k\|\leq\rho_k$ for all iterations. The details of the relations between μ_k and ρ_k are quite lengthy, and are therefore omitted.

The filter concept, described by Fletcher (1998), is used as acceptance criteria. A filter is a set of pairs $\{(f(x_i),\ \ h(x_i))\}$, $i\in F$, that are non-dominating in the Pareto (1969) sense of the word. The function h is defined as:

$$h(x)=\max\{0,\max\{v(x)\}\}, \tag{13}$$

where $v(x)$ is given by (10). In order for a step Δx_k to be accepted, it must provide a pair $\{(f(x_{k+1}), \quad h(x_{k+1}))\}$, that is acceptable to the filter, i.e. the pair must not be dominated by any other pair in the filter. Furthermore, the iterate must be a so-called *h*-type iterate. See Fletcher (1998) for details regarding this concept.

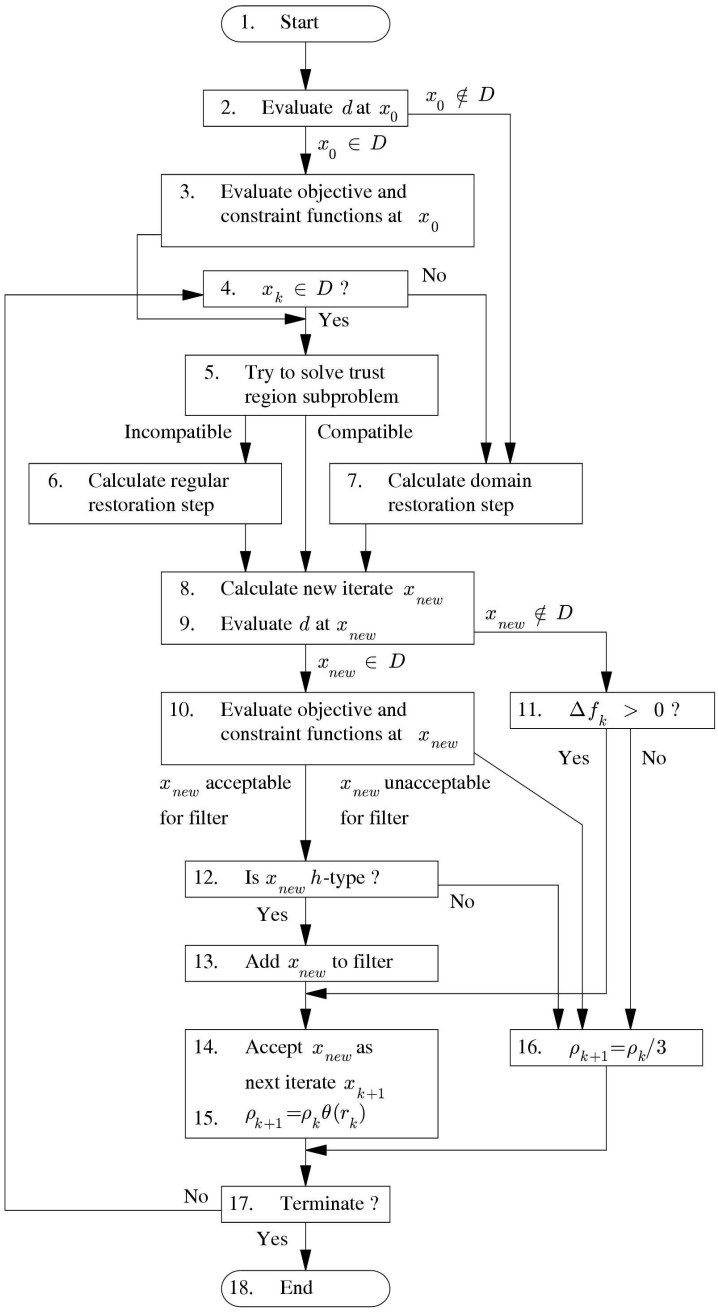

FIG. 3: Flowchart for the gradient-free SQP filter algorithm.

The trust region radius is increased if there is a good match between the expected and actual decrease in the objective function value, and decreased otherwise. This criterion is evaluated using the so-called *gain factor* r_k, given by:

$$r_k = \Delta f(x_k)/\Delta l(x_k)\,, \tag{14}$$

where $\Delta f(x_k)$ is the decrease in the relevant objective function, and where $\Delta l(x_k)$ is the decrease in the corresponding Taylor approximation. The parameter ρ_k is updated using the expression $\rho_{k+1} = \rho_k \theta(r_k)$, where

$$\theta(r_k) = \tfrac{2}{3}\tanh\left(10\left(r_k - \tfrac{1}{2}\right)\right) + 1 \quad (15)$$

The trust region is reduced with a factor of 3, if the iterate is unacceptable to the filter, if the iterate is not *h*-type, or if the domain constraint violation did not decrease for an iterate $x_k \notin D$.

Figure 3 shows a flowchart for the algorithm. Details regarding the stopping criteria are omitted.

5. Case study

The combination of simulation and optimization method are used for estimating efficient design decisions for a 3 storey, 2000 m^2 office building. The aim is to optimize the building with respect to the energy performance. The annual energy consumption is therefore required to be minimal. Table 1 shows the initial and optimal values for decision variables and utility functions, as well as the requirements to the solution. The list of decision variables and utility functions are only partial, full lists are provided by Pedersen (2006). The omitted utility functions do not influence the solution.

Notice that the optimal energy consumption is higher than the initial one. This is because the initial decisions are infeasible, since the requirements to daylight utilization are not satisfied. The building provided by the optimum decisions is the one with the lowest annual energy consumption, that at the same time satisfy all requirements. Notice also that the optimal construction cost is the one that fully exploits the allowed limits.

The solution is restricted by the upper limits on the amount of insulation used in the ground slab and roof construction, as well as the upper limits on the daylight utilization measure and the construction costs.

The requirements to the solution can be arranged as entries in the parameters r_O, A_I, b_I, A_E and b_E, in problem (2), which is solved using the gradient-free SQP filter algorithm, in order to calculate the optimum decision variables. If the decision-maker wishes to change the requirements, it can be done simply by changing these parameters. This feature enables the formulation (2) to be used for optimizing buildings in many different ways, for instance with respect to energy, economy or indoor climate.

TABLE. 1: Initial and optimum values for decision variables and utility functions.

Decision variable		Requirement	Initial value	Optimum value
Width to length ratio	[]		0.200	0.146
Number of floors	[]	= 3	3.000	3.000
Window percentage, front	[]		0.400	0.396
Window percentage, back	[]		0.400	0.396
Insulation, ground slab	[m]	≤ 0.5	0.200	0.500
Insulation, roof	[m]	≤ 0.5	0.200	0.143
Insulation, external walls	[m]	≤ 0.5	0.200	0.500
Utility function		**Requirement**	**Initial value**	**Optimum value**
Annual energy use	[kWh]	minimal	136392.96	138981.18
U-value for ground slab	[W/m^{2}K]	≤ 0.30	0.18	0.07
U-value for external walls	[W/m^{2}K]	≤ 0.40	0.17	0.22
U-value for roof	[W/m^{2}K]	≤ 0.25	0.13	0.06
Daylight utilization, front	[]	≤ 4	4.66	4.00
Daylight utilization, back	[]	≤ 4	4.66	4.00
Construction cost	[DKR]	≤ 10^7	9318393.71	10000000.00
Annual operational cost	[DKR]		67243.00	69577.85

The thermal resistance of the uninsulated parts of the ground slab, roof construction and external walls are 0.42 m^2K/W, 0.68 m^2K/W and 2.5 m^2K/W, respectively. The internal and external surface resistances are 0.13 m^2K/W and 0.04 m^2K/W, respectively. The external surface resistance is only used for the external walls. The thermal conductivity of the insulation material is 0.039 W/mK.

6. Conclusion

This paper concerns numerical methods for optimizing the performance of buildings, and describes how decision-making can be supported at early stages of the design process by combining numerical simulation and optimization methods.

A problem formulation is provided that enables decision-makers to formulate requirements to buildings in a highly flexible way. The problem formulation facilitates decision-makers to specify what aspect of the building performance to optimize, for instance energy performance, economy or indoor environment. Upper and lower bounds on decision variables and utility functions can furthermore be specified. It is believed that the proposed problem formulation is useful for developing highly flexible software systems for building-related decision support.

Efficient design decisions are estimated by optimizing decision variables for a conceptual building model. The purpose of this model is to represent general features of the building, such as volume, surface area, mass of constructions, window areas, etc.

The details of a gradient-free SQP filter algorithm are described. The method solves constrained optimization problems without requiring gradient information, and furthermore ensures that the input given to the simulation methods is valid.

A case study regarding an office building is conducted. The initial building has a low annual energy use, but is infeasible, where the optimized building has a higher annual energy use, but is feasible.

7. References

Bouchlaghem N. (2000). Optimising the design of building envelopes for thermal performance, Automation in Construction, vol. 10, pp. 101-112.

Broyden C.G. (1965). A class of methods for solving nonlinear simultaneous equations, Mathematics of Computation, vol. 19, pp. 577-593.

Fletcher R., Leyffer S. and Toint P.L. (1998). On the global convergence of an SLP-filter algorithm, Numerical Analysis Report NA/183, Department of Mathematics, University of Dundee, Scotland.

Nielsen T.R. (2003). Optimization of buildings with respect to energy and indoor environment, Ph.D. Thesis BYG-DTU R-036 (ISBN 87-7877-094-7), Department of Civil Engineering, Technical University of Denmark, DK-2800 Kgs. Lyngby, Denmark.

Nielsen T.R. (2005). Simple tool to evaluate energy demand and indoor environment in the early stages of building design, Solar Energy, vol. 78, no. 1, pp. 73-83.

Pareto V. (1969). Manual of political economy, Augustus M. Kelley Pubs, New York, USA.

Pedersen F. (2006), A method for optimizing the performance of buildings, Ph.D. Thesis R-148, Department of Civil Engineering, Technical University of Denmark.

Peippo K., Lund P.D. and Vartiainen E. (1999). Multivariate optimization of design tradeoffs for solar low energy buildings, Energy and Buildings, vol. 29, pp. 189-205.

Poel B. (2005). Integrated design with a focus on energy aspects, in: Proceedings of the ECEEE Summer Study 2005, pp. 505-512.

V&S price catalogue (2005). Gross prices for house construction (Danish title: V&S prisbogen 2005, husbygning brutto), Byggecentrum, Lautrupvang 1B, DK-2750 Ballerup, Denmark.

Wright J.A., Loosemore H.A. and Farmani R. (2002). Optimization of building thermal design and control by multi-criterion genetic algorithm, Energy and Buildings, vol. 34, pp. 959-972.

Method for integrated design of low energy buildings with high quality indoor environment

Steffen Petersen, PhD student,
Department of Civil Engineering, Technical University of Denmark and ALECTIA A/S;
stp@byg.dtu.dk

Svend Svendsen, Professor
Department of Civil Engineering, Technical University of Denmark;
ss@byg.dtu.dk

KEYWORDS: *Design methods, integrated design, performance evaluation, space of solutions*

SUMMARY:
Energy performance and indoor environment have due to new increased regulatory demands become decisive design parameters in the building design process. In order to comply with the increased regulatory demands, we present an integrated design method which argues that the design of buildings must start on room level rather than total building level. The proposed method starts with the establishment of design goals, including goals regarding energy performance and indoor environment, followed by a building physical analysis of performance-decisive parameters. This analysis is used to establish a space of solutions from which the designer can obtain an overview of the consequences of their design decisions in terms of energy performance and indoor environment. Based on the space of solutions the designer can set up possible room designs which fulfil the design goals prior to the total building form giving. The possible room designs can be combined in to a number of overall building designs from which the best performing proposal can be selected and optimised. In this way the final building design will have an energy performance and indoor environment inherited from the room designs, thus fulfilling design goals in terms of energy performance and indoor environment. The method has been tested and evaluated in courses in integrated design at the Technical University of Denmark. Based on the experiences gained through these tests, the proposed method has been adjusted and refined in order to become the preferred method for integrated design of low energy buildings with high quality indoor environment.

1. Introduction

A steadily growing awareness about the impact of human activity on the environment has increased the demand for sustainable development. This leads to an increasing pressure on building developers and designers to produce buildings with a high level of environmental performance. Chief amongst environmental loads from buildings is the consumption of energy from fossil fuels. More than 40% of the total energy consumption in the EU is related to buildings, which also mean that this is an area with significant potential for economic savings. The growing demand for sustainable development is reflected in regulatory performance requirements. In the EU, the Energy Performance of Buildings Directive (EPBD. 2002) is introduced as a regulatory initiative to improve the energy performance of buildings. The introduction of EPBD is a regulatory paradigm shift from standards based on specific requirements regarding the properties of individual constructions and systems to a performance-based requirement regarding the total energy performance of the building. Furthermore, a regulatory for performance-based requirements in terms of indoor environment (prEN 15251:2006. 2006) is to be implemented in the EU member countries ultimo 2007.

As a consequence of this development, energy performance and indoor environment have become decisive design goals in the building design process. Therefore it is important to understand that many design decisions in the building design process is affecting both energy performance and the indoor environment. In practice many building designers do not know the consequences of their initial design decisions in terms of energy performance and indoor environment leaving the task of complying with design goals to expensive sub-optimisations later on in the building design process. If buildings are to contribute to a sustainable development, new methods and tools which integrate energy performance and indoor environment at the earliest state of the building design process is needed. This paper presents such an integrated design method.

2. Method

The initial stage in the building design process contains a number of crucial design decisions which tends to commit the environmental performance throughout the remaining design process (Reed W. G. and Gordon E. B. 2000). Therefore the first step in current definitions of performance-based design methods and integrated design methods (Löhnert G. et. al. 2003) (Spekkink D. 2005) is to define design goals, which support sustainable development including performance-based demands in terms of energy performance and indoor environment. When these design goals are set, the next step is to generate a number of alternative designs which, when assessed, respect the design goals. This design approach is critical and is ultimately derailing the integrated design process. Functional issues, or design goals, are becoming less simple all the time thus increasing the complexity in the process of designing buildings (Alexander C. 1964). If designers do not understand the complex relations between the properties of physical design-defining parameters and the intended design goals, there is a distinct risk that designers are suggesting building designs which, when assessed, do not initially fulfil all design goals. The suggested building design which is not initially fulfilling all design goals can be either rejected or the designer can try to adjust the suggestion to fulfil all design goals. The ladder is a challenging task because the adjustment of the suggestion might favour a certain design goal but lead to the failure another design goal forcing the designer to perform time consuming design iterations. Designing sustainable buildings based on investigation of alternatives is thus inefficient because this evaluative approach to design is not prescribing what to do to remedy oversteppings of design goals which require the designer to operate by time consuming trial-and-error analysis. Furthermore this evaluative design approach is assigned to current popular simulation tools which is focusing on only one part of building performance (Chen Z. et. al. 2006) separating the individual design goal from the overall building design turning them into problems rather than parts of the solution (Radfort A.D. and Gero J.S. 1980).

Despite of the current motivation and interest in integrated design of buildings, the notion of a holistic building design approach has been a subject to building design researchers for decades. There have been many efforts to map out the activities and processes related to the complex task of designing a building to suggest reliable design methods which consistently would lead to high-quality results. In the following, we develop the argument for the suggested method for integrated design of low energy buildings with high quality indoor environment based upon these earlier endeavours in the research of design methods.

2.1 Development in design methods

The earliest efforts to define design as a method or process was focused on approaching design through the classic scientific methodology hence justifying design as an academic, scientific discipline. This effort has made the development of design methods broadly accepted as an academic discipline but there is an ongoing discussion whether design can or should be handled in a traditional scientific context or in its own designerly way (Rittel H. W. and Webber M. M. 1984) (Cross N. 2006).

According to Rittel (Rittel H. 1973), the earliest endeavours of formulating design methods in modern time can be categorised in to a ‘first generation’ and a ‘second generation’ of design methods. The so-called first generation of design methods was formulated in the 1960s by early pioneers like Archer (Archer B.L. 1965), Asimov (Asimov M. 1964), Broadbent and Ward (Broadbent G., Ward A. 1969) and others. These methods were characterised as methods constructed with focus on optimisation using the term ‘method’ in a classic scientific context where a ‘method’ is considered to be a systematic, rational and logical way of approaching a problem – in this case design problems. A leading mantra in the quest of such methods is the notion ‘Form Follows Function’ formulated by Sullivan (Sullivan L. H. 1934), which ultimately means that a form must facilitate a given set of functional needs. Design methods rooted in this mantra are therefore trying to find the causal relationship between form and function, typically trough one of the two fundamental paradigms *problem-solving* or *puzzle-making*, where problem-solving is the search for a form which facilitates a desired function and puzzle-making is the adaptation of a form until it reach a some desired functional qualities (Kalay Y. E. 1999). The so-called second generation of design methods emerged in the late 1960s/early 1970s where researchers, in some cases even researchers which established the first generation of design methods (Cross N. 2007), wanted to abandon the problem solving approach of the first generation of design methods which they criticised for being too narrow and functional contingent definition of rationality not fit for design problems. Instead supporters of the second generation of design methods argued that design problems, especially architectural design problems, are ‘wicked’ problems full of intuitive leaps, fundamentally irreconcilable with the techniques of science and engineering, which dealt with ‘tame’ problems (Rittel H. W. and Webber M. M. 1984) (Norman R. B. 1987).

Because design problems are perceived as wicked problems they are fundamental indefinable which means that it is impossible to determine when a design problem is solved: it can always be improved thus no ultimate, optimal solution exists (Rittel H. W. and Webber M. M. 1984) (Lang J. 1987) (Rowe P. G. 1987). The design process is argumentative and based on empirical knowledge, rather than rational knowledge as in the first generation design methods, beginning with an incubation, introspective phase, followed by iterative refinement of both form and function until some harmonious coexistence emerges (Akin O. 1978) – a so-called satisfactory solution (Rittel H. 1973).

As an offshoot of the empirical, second generation methods, a more recent notion is that there is a designerly way of knowing (Cross N. 2006) based on intuitive knowledge. The main problem about design as an intuitive process is that it is an unspoken process hence very difficult to explain and pass on as objective knowledge. This does not necessary means that unspoken methodical knowledge is irrational (Harfield S. 1999). But if this is the case for design processes the dilemma is obvious according to Shön (ibid): if knowledge is defined as that which can be expressed explicitly from person to person, then what does designers know? And if we acknowledge unspoken knowledge, how can we be sure that designers possess and have access this knowledge? The argumentation for design as an intuitive process is also seen as an intentional attempt to mystify a process which is impossible to justify objectively as a mean to gain power in the decision-making process. By ascribing their design some sort of brilliant divinity instead of the outcome of a certain explicit method, they avoid the argumentative discourse and make the design process a ‘game of virtuosity and mystique’ where mystique is a token of virtuosity (Ward A. 1990).

Whereas the first generation methods based on the application of systematic, rational approaches is mainly found in engineering and industrial design, the second generation approaches and the intuitive approach is mainly found in architecture and planning (Cross N. 2007). It is the conviction of the authors of this paper that this corresponds to the current practice. However, we believe that there is a need for some degree of rationality in the building design process mainly because of the complexity of today’s problems in building design and because rationality is the mean to reach design goals in terms of sustainable development. Many building designers seem to have an inhered suspicion regarding rationality. There is a misinterpretation of logic, or rationality, as a kind of force which is telling us what to do. On the contrary, rationality is a powerful way of identifying the real formal order of a design problem. If the designer ignores rationality and falls back on arbitrary chosen formal order, the design problem, due to its complexity, remains unsolved (Alexander C. 1964). Rationality has by nature no embedded power to decide or prescribe; only the designer has that ultimate power. What rationality can do is help the designer to gain prior knowledge regarding the correlations between the physical parameters which form the building and the certain context of the building with respect to predefined design goals. The context of a building is usually quite obvious: the building is to be situated in a well-defined environment, or context, with certain physical limitations for size and orientation. How the building fits this certain context is a question about whether it fulfils all predefined design goals. It might be hard to define design goals in terms of aesthetics, thus assessing aesthetics, but other design goals in terms of e.g. energy performance and indoor environment are measurable design goals which can be defined and assessed.

We suggest a rational method to establish a decision platform for design of sustainable buildings. The goal is to develop an integrated design method which is integrating sustainable development issues in to the building design process. This means that the current evaluative approach in integrated building design, where more or less arbitrary design decisions are defining design suggestions which is then assessed in terms of the predefined design goals (Löhnert G. et. al. 2003), is substituted with a design process where the development of design suggestions are based on consequence-conscious design decisions in terms of the design goals. If the generation of building design suggestions is based on such decisions, all suggested designs will automatically fulfil the predefined design goals because the design method it self is an integrated performance evaluation.

2.2 Suggested building design method

The proposed integrated design method is based on the identification of possible room designs which fulfil predefined performance demands in terms of energy performance and indoor environment (design goals) prior to the actual building form giving. The main reason that we suggest an integrated design method based on performance analysis on room level is that we believe it is easier to handle design goals regarding energy performance and indoor environment in an integrated way on room level rather than building level. Especially when it comes to indoor environment: it makes no sense to evaluate indoor environment on building level because the indoor environment differs from room to room in the building dependent on the specific orientation,

internal loads and many other performance-decisive parameters of the room. By designing rooms before buildings, the building designer is capable of ensuring the quality of indoor environment in each room of the building while the corresponding energy performance of the room is included in an integrated evaluation. If the room designs are fulfilling design goals regarding energy performance and indoor environment, then a final buildings design composed by these rooms is also most likely to fulfil the design goals.

The key to the integrated design of rooms, thus integrated design of buildings, is the space of solutions. Space of solutions constitutes a decision platform from which all design decisions can be evaluated with respect to the established design goals. The space of solutions is not controlling the design process; it is merely a statement of the boundary conditions in which all design decisions are possible. The space of solutions is used to generate several possible designs of room geometries and sections which, because of the space of solutions, will fulfil the predefined design goals. Now the actual form giving of the building can start: the designer selects from the predefined rooms/sections and merge them in to suggestions for overall building geometries. A final building design is then selected and optimised before detailed design starts. A simple description of the total integrated design process is shown in FIG. 1.

The suggested integrated design process is led by a design facilitator. The specific professional background of this design facilitator is not of importance; however the person must be a specialist in architectural and/or technical energy design solutions and possess outstanding skills in team management, communication and mediation. The design facilitator is managing a building design team which consists of architects, engineers and other relevant experts. The content four steps of the suggested integrated design method are developed further in the following sections.

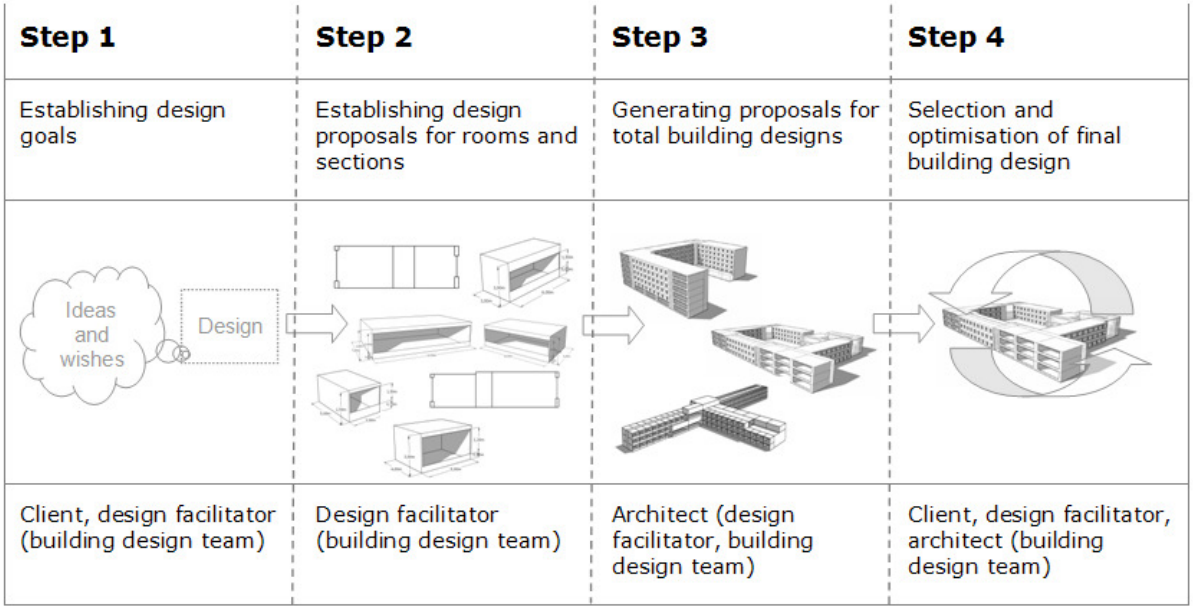

FIG. 1: A simple description of the total integrated design process: the pictures and the text above the pictures describe each step in the design process, and the text below the pictures describes the main responsible person(s).Those stated in brackets should be available for consultancy, if needed, during the current design step.

2.2.1 Step 1: Establishing design goals

The first step in the integrated design process is to set up design goals for the specific building. Design goals should be set up based on the building owner's ideas and wishes, which often contain some superior design goals/wishes such as type of building and the number of people using the building. It is the task of the design facilitator to explicitly outline the demands and wishes from the building owner in a way that the content and scope of the task is clear when presented to other participant of the building design team. The design facilitator may involve different experts to help establish the design goals. It is important to outline, that anyone who is involved in this phase of the integrated design process should be in 'possibility-mode' – not 'solution-mode'. Essentially, the process of setting up design goals should end up with a number of typical, repeated room

typologies, e.g. single offices or open space offices, and design goals regarding energy performance according to the Danish building code (Danish Building Code. 2006) and indoor environment according to prEN 15215 (prEN 15251:2006. 2006). The final building design has to fulfil these design goals in order to be successful in the eyes of the building owner. Therefore design goals are the decisive parameters in the design process and all design decisions should be evaluated with respect to these.

2.2.2 Step 2: Establishing design proposals for rooms and sections

The first task of step 2 is to create a space of solutions (Petersen S. et. al. 2008) for each room typology according to the design goals established in step 1. Based on these space of solutions the building designers identify constellations of performance-decisive parameters which define the physical layout of room and/or section which fulfils the design goals. The output of step 2 is sketches of a suitable amount of room geometries and building sections which can be used to compose suggestions of total building designs. All alternative room and section designs which fulfil the design goals are in principle possible solutions. However, based on the performance with respect to indoor environment and total energy for the different solutions it is possible to identify the best solutions for use in the next steps of the design process.

The space of solutions is found through parameter analysis of performance-decisive parameters. These parameter analyses constitute a decision platform, the space of solutions, in which all design decisions can be evaluated with respect to the established design goals. The procedure of establishing a space of solutions is as follows:

1. A reference of the room to be analysed is established based on the output from step 1. The reference is described in physical design-defining parameters; geometry, construction properties and building service properties.
2. The reference is implemented in the tool iDbuild together with the design goals for the indoor environment. iDbuild is a tool developed for parameter variations and is based on the tools BuildingCalc (Nielsen T. R. 2005) and LightCalc (Hviid C.A. et. al. 2008). iDbuild is capable of integrated evaluation of the energy performance, thermal indoor environment, air quality and daylight conditions in single sided offices, class rooms and alike meaning that there can be only one window in the simulation model at present time. Furthermore only buildings of simple shapes, like quadrangular shape, can be evaluated. A parameter variation is based on the reference value of a performance-decisive parameter and two variations of this: a lower value and a higher value. Designers may pick whatever performance-decisive parameter is found relevant to vary.

The purpose of the space of solutions is to show relations between performance-decisive parameters, and the energy performance and indoor environment. This is very important to building designers: it gives them a chance to create an overview of the consequences of changing a performance-decisive parameter and at the same time shows the relative influence of the single or combined performance-decisive parameter in terms of the design goals. Based on this overview the designers are now able to perform transparent, consequence-conscious design decisions which does not conflict with the design goals. The designers may now go in to ‘solution-mode’ and use the space of solutions as a flexible platform for design decisions to create numerous design proposals for all room typologies established in step 1. The setup of a design proposal starts with no design decision, meaning that the space of solutions is completely open. As design decisions are made, the design proposal takes more and more form with increasing constrains on other design decisions as a consequence. One design decision is almost certain to exclude a number of other design decisions which were there before the design decision was made. Realisations like this may occur during the use of the space of solutions. But instead of just rejecting design decisions which exceeds the design goals, the suggested integrated design process allows the designers to adjust either the design goals or to make other design decisions which compensates for the exceeding of the design goals. The designer may also go back to step 2 and add more parameter variations to the space of solutions which might compensate.

When a number of possible room designs are established it is recommended to produce a number of possible building sections in a sectional view. The possible building sectional views have two purposes, 1) they are a valuable help in the composition of the total building design and 2) sectional views might identify of possible compensations for oversteppings of design goals in terms of energy performance on room level through the total energy performances of sectional views. A single room design might not fulfil the design goal regarding energy performance. But by combining such a room with room designs, which have an energy performance lower than the design goal, the total combination may end up having an area-weighted total energy performance which fulfils the design goal.

All valid room design or building section should be graphically presented to the rest of the design team as the basis for the form giving of the entire building. Furthermore the single room and building section could be given an index number indicating its integrated energy and indoor environment performance relative to the performance of the other suggested rooms and building sections encouraging the choice of the best performing solutions.

2.2.3 Step 3: Generating proposals for total building designs

The third step in the integrated design process is to combine design proposals of rooms and sectional views in to total building design proposals. The key person in this part of the process is the architect who until now has been an integrated part of the building design team. The architect may, together with relevant experts from the building design team, freely combine the rooms and sections in to a number of total building designs. The total building design is automatically fulfilling the design goals regarding energy performance and indoor environment because the single room and section is initially fulfilling these design goals. The setting up of total building design also includes considerations regarding the principles for the constructional systems, HVAC routes, fire safety, adaptability and other issues which are relevant on total building level.

2.2.4 Step 4: Selection and optimisation of final building design

In step 4 a final building design has to be selected from the number of proposed building designs. Although all of the proposed building designs are initially fulfilling the design goals in terms of needed space, indoor environment and energy consumption, it is most likely that there are some relative differences between the proposed designs regarding these design goals. Furthermore there might be distinctions regarding initial cost and perceptions of architectural quality. In order to select a final building design, a complete overview of all these performance issues is needed. We suggest the use of an integrated total performance index based on economical considerations regarding the main performance issues related to the total building design: 1) initial costs, 2) cost of energy consumption over the life cycle of the building, 3) the quality of indoor environment and 4) the architectural quality. The first two performance issues are trivial to quantify in terms of economics. The economical link between the quality of indoor environment and economy is productivity (Fisk W. J. 2001) (Jensen K. L. 2008). Quantification of architectural quality in terms of economics might be possible based on recent research where architectural quality is given a theoretical body, functional structure and verbal expression which is contributing to the understanding, handling and communication of architectural quality (Christoffersen L. K. 2007).

The theory behind the total performance index should be formulated in a general way so that other relevant performance issues are easily integrated in the total performance evaluation.

3. Discussion

The suggested method described in this paper has been tested and evaluated in courses in integrated design at the Technical University of Denmark (TUD) in the fall 2006 and again in the fall 2007. Furthermore the method has been the main topic in an international Ph.D. course and a course for practitioners at TUD in the fall 2007.

The experience gained in these courses is that the overall idea of designing rooms before buildings is quite controversial especially to practicing architects. Furthermore the idea of introducing a platform for knowledge-based design decisions, the space of solutions, prior to the form giving of the building was very hard to accept even in the context of an experimental exercise. For some student groups there was a tendency to abandon the suggested method in favour of a trial-and-error approach of randomly generated design proposals based on some arbitrary notions regarding the design order. The result was that these groups failed to establish more than one design proposal on room level or even failed to create a design which fulfilled the predefined design goals. The student groups who was insisting on following the suggested method easily generated more than one alternative room design all fulfilling the predefined design goals. However the task in defining the space of solutions was sometimes quite time consuming and a source of frustration because it was perceived as a hindrance to the creative drive of the design process. This is mainly due to insufficient knowledge regarding the use of building simulation tools and some technical problems when using the suggested design tool iDbuild. This led to criticism of the method in general. Even though it is important to distinguish between ‘method’ and ‘tool’ this criticism shows a crucial correlation between these two. A well-functioning and easy-to-use tool to facilitate the design method, especially regarding the generation of the space of solutions, is important if the suggested method is to

become a practical preferred method for integrated design of low energy buildings with high quality indoor environment.

4. Conclusion

The proposed method for integrated design of low energy buildings is based on the overall idea of designing rooms before buildings. We believe that this approach will make it easier for building designers to design buildings with explicit predefined design goals regarding sustainability. The design of rooms should be based on a series of consequence-conscious design decisions in terms of the predefined design goals rather than time-consuming trial-and-error analysis of arbitrary design proposals. In order to establish such a knowledge-based decision platform, we suggest the concept of space of solutions. Using this space of solutions, the designer is able to develop numerous room design proposals which consistently are fulfilling the predefined design goals. The possible room designs can be combined in to a number of overall building designs from which the best performing proposal can be selected and optimised. In this way the final building design will have an energy performance and indoor environment inherited from the room designs, thus fulfilling the predefined design goals. Recent tests and evaluations of the method different design classes at the Technical University of Denmark has shown that the method, if followed, in practice is consistently leading to building design proposals which fulfils predefined design goals regarding energy performance and indoor environment. However, the self-same tests and evaluations also shows that further research and development is needed in order to utilise the full potential and intent of the method. The design tool iDbuild for facilitation step 2 in the suggested method needs to be developed for better usability and understanding, and so does the idea of a total performance index of step 4. Furthermore there is a need for a better educational program in which the proposed design method is communicated in an efficient and understandable way in order to avoid misinterpretations regarding the intentions of the design method. This research and development is currently being conducted in a Ph.D. project at the Department of Civil Engineering, Technical University of Denmark.

5. References

Aggerholm S. and Grau K. (2005). SBi-anvisning 213. Bygningers energibehov. PC-program og beregningsvejledning. Danish Building Research Institute, Hørsholm, Denmark.

Akin O. (1978). How do architects design? *Artificial Intelligence and Pattern Recognition in Computer-Aided Design* (Latombe Ed.), IFIP, North-Holland, New York, USA

Alexander C. (1964). Notes on the Synthesis of Form, Harvard University Press, Cambridge, MA, USA.

Archer B.L. (1965). Systematic methods for designers in: Developments in Design Methodology (Cross N. Ed.), Wiley, Chichester, 57-82.

Asimov M. (1964). Introduction to Design, Englewood Cliffs, New Jersey, USA

Broadbent G., Ward A. (1969). Design methods in architecture, London, England.

Chen Z., Clements-Croome D., Hong J., Li H. and Xu Q. (2006). A multicriteria lifespan energy efficiency approach to intelligent building assessment. *Energy & Buildings* Vol. 38, Issue 5, 393-409

Christoffersen L. K. (2007). Arkitektonisk kvalitet (Ph.D. dissertation). Aarhus School of Architecture, Aarhus, Denmark

Cross N. (2006). Designerly ways of knowing. Springer, London, England

Cross N. (2007). Forty years of design research. *Design Studies* Vol. 28, issue 1, editorial

Danish Building Code. (2006). Bygningsreglement for erhvervs- og etagebyggeri. National Agency for enterprise and construction, Copenhagen, Denmark

EPBD. (2002). Directive 2002/91/EC of the European parliament and of the council of 16 December 2002 on the energy consumption of buildings. Webpage: http://europa.eu.int/eur-lex/pri/en/oj/dat/2003/l_001 /l_00120030104en00650071.pdf

Fisk W. J. (2001). Estimates of potential nationwide productivity and health benefits from better indoor environments: an update. IAQ Handbook (Spengler J., Sammet J. and MacCarthy J.F. Ed.), McGraw Hill, Ney York, USA

Harfield S. (1999). The Lure of the Sirens' Song: Part 1, First Thoughts on Process. *Journal of Architectural Education* Vol. 52, issue 3, 174-188

Hviid C.A., Nielsen T.R. and Svendsen S. (2008). Simple tool to evaluate the impact of daylight on building energy consumption, *Proceeding of the 8th Nordic symposium on building physics,* submitted

Jensen K. L. (2008). A Bayesian network approach to the evaluation of building design and its consequence for employee performance and operation costs. *Building and Environment*, submitted

Kalay Y. E. (1999). Performance-based design. *Automation in Construction* Vol. 8, issue 4, 395-409

Lang J. (1987). Creating Architectural Theory: The Role of Behavioral Sciences in Environmental Design, Van Nostrand Reinhold, New York, USA

Löhnert G., Dalkowski A.. and Sutter W. (2003). Integrated Design Process. A guideline for sustainable and solar-optimised building design. International Energy Agency (IEA) Task 23 Optimization of Solar Energy Use in Large Buildings subtask B: Design process guideline,

Nielsen T. R. (2005). Simple tool to evaluate energy demand and indoor environment in the early stages of building design. *Solar Energy* Vol. 78, issue 1, 73-83

Norman R. B. (1987). Intuitive design and computation. *Computability of Design* (Y.E. Kalay Ed), Wiley-Interscience. New York, USA

Petersen S., Hviid C. A. and Svendsen S. (2008). Space of Solutions – design of buildings with respect to performance-based demands. *Building research & information*, submitted

prEN 15251:2006. (2006). Indoor environment input parameters for design and assessment of energy performance of building-addressing indoor air quality, thermal environment, lighting and acoustics. Date: 2006-07-31

Radfort A.D. and Gero J.S. (1980). Tradeoff diagrams for the integrated design of the physical environment in buildings. *Building and Environment* Vol.15, Issue1, 3-15

Reed W. G. and Gordon E. B. (2000). Integrated design and building process: what research and methodologies are needed. *Building Research & Information* Vol. 28, issue 5-6, 325-337

Rittel H. (1973). The state of the art in design methods Design Research and Methods. *Design Methods and Theories* Vol. 7, issue 2

Rittel H. W. and Webber M. M. (1984). Planning problems are wicked problems in: Developments in Design Methodology (Cross N. Ed.), Wiley, New York, USA, 135-144

Rowe P. G. (1987). Design Thinking, MIT Press, Cambridge, MA, USA

Spekkink D. (2005). Performance based design: Bringing Vitruvius up to Date. CIB (PeBBu) General Sectretariat, Rotterdam, the Netherlands

Sullivan L. H. (1934). Kindergarten chats on architecture in: Education and Democracy (C.F. Bragdon Ed.), Scarab Fraternity Press, Washington, D.C., USA

Ward A. (1990). Ideology, Culture and the Design Studio. *Design Studies*, vol. 11, issue 1, 10-16

Combining building thermal simulation methods and LCA methods

Frank Pedersen, Researcher,
Danish Building Research Institute, Dr. Neergaards Vej 15, DK-2970 Hørsholm, Denmark;
frp@sbi.dk

Klaus Hansen, Senior Researcher,
Danish Building Research Institute, Dr. Neergaards Vej 15, DK-2970 Hørsholm, Denmark;
klh@sbi.dk

Kim B. Wittchen, Senior Researcher,
Danish Building Research Institute, Dr. Neergaards Vej 15, DK-2970 Hørsholm, Denmark;
kbw@sbi.dk

Karl E. Grau, Senior Researcher,
Danish Building Research Institute, Dr. Neergaards Vej 15, DK-2970 Hørsholm, Denmark;
kg@sbi.dk

Kjeld Johnsen, Senior Researcher,
Danish Building Research Institute, Dr. Neergaards Vej 15, DK-2970 Hørsholm, Denmark;
kjj@sbi.dk

KEYWORDS: Thermal simulation, energy performance, life cycle assessment.

SUMMARY:
This paper describes recent efforts made by the Danish Building Research Institute regarding the integration of a life cycle assessment (LCA) method into a whole building hygro-thermal simulation tool. The motivation for the work is that the increased requirements to the energy performance of buildings (as expressed in EU Directive 2002/91/EC), may in the future be supplemented by requirements to the environmental impact of buildings. This can be seen by the fact that EU recently has given CEN mandate to prepare standards for environmental assessment of buildings (CEN/TC 350).

Combining LCA methods with hygro-thermal simulation tools enables designers to assess both sets of requirements in one operation, without the need to input redundant data in different tools. Another advantage of combining the two tools is that it makes it possible to compare the environmental impact of buildings during the construction and operational phases. This is of particular interest for low-energy buildings, where a relatively large amount of resources is used during construction, compared to the amount of resources used during operation. The result of this is that the environmental impact during the two phases can easily be of the same order of magnitude.

The paper describes how the LCA method is integrated into the thermal simulation tool, and the prerequisites for using them. A case study regarding a single-family house is used to illustrate how the combination of the two methods can be used for generating design alternatives with high performance regarding energy use as well as environmental impact.

1. Introduction

This paper describes recent efforts made by the Danish Building Research Institute regarding the integration of the life cycle assessment (LCA) method by Petersen (1999), into the whole building hygro-thermal simulation tool BSim, Wittchen et al. (1999-2008).

The motivation for the work is that the increased requirements to the energy performance of buildings, as expressed in the EPBD Directive (2002), may in the future be supplemented by requirements to the

environmental impact of buildings. This can be seen by the fact that EU recently has given CEN mandate to prepare standards for environmental assessment of buildings.

Furthermore, assessing energy performance and environmental impact simultaneously is particularly important when considering low-energy buildings. The reduced amount of energy used for operating the building, combined with an increased use of renewable energy, reduces the environmental impact of the building during operation. On the other hand, more resources are required during construction and rehabilitation of low-energy buildings, especially for production of building materials. The result of this is that the environmental impact during construction becomes comparable with the environmental impact during operation. Sartori and Hestness (2007) present data for passive houses, for which the consumption of primary energy for construction and rehabilitation of buildings is 40-50% of the energy needed for operation. Besides, the use of building materials contribute significantly to a number of other environmental effects, related to e.g. dangerous substances and waste.

Combining LCA methods with hygro-thermal simulation tools enables designers to assess both sets of requirements in one operation, without the need to input redundant data in different tools. Designers can thereby easier investigate the compromise between the potentially conflicting goals of minimizing the amount of resources used during construction, and minimizing the energy use during operation.

This paper describes the LCA calculation methods, and the results. A case study regarding a single-family house illustrates how the tool can be used for generating design alternatives that support decision-making during the design phase. Further improvements of the tool are also discussed.

2. The life cycle assessment method

The Building Environmental Assessment Tool (BEAT) by Petersen (1999) is an LCA method based on the Environmental Design of Industrial Products (EDIP) method, which is described by Hauschild and Wenzel (1998). BEAT is intended for assessing the environmental impact of buildings, by providing quantifiable measures for environmental effects, caused by the construction of buildings.

2.1 Life cycle inventory analysis

The LCA calculation is based on a life cycle inventory (LCI) analysis, which provides detailed information about the amount of resources extracted from the environment, and the amount of pollutants emitted to the air, water and soil, during the production of building elements and construction of the building.

In order to perform the LCI analysis, the EDIP method uses a set of unit processes, each of which represent the process of producing one unit of a given product. It is assumed that the process requires other products as input, as well as natural resources, and has the considered product as output, as well as emissions to air, water and soil. Figure 1 shows a unit process.

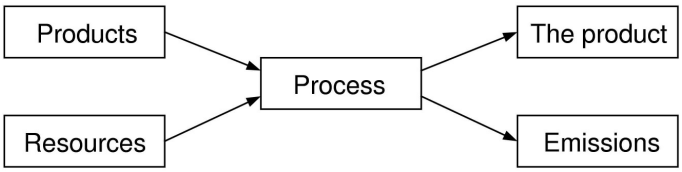

FIG. 1: A unit process.

All products and resources used for constructing a building form a product system, as shown in Figure 2. In order to perform a LCI analysis, the product system is traced backwards from the building over the manufacturing of the components to the processes where resources are extracted from the environment. During these calculations, the extracted resources and emitted pollutants are added up. Given the lifetime of the constructions used in the building, the average annual amount of extracted resources and emitted pollutants is calculated.

The building model in the BSim simulation tool contains (among others) information about the geometry and constructions used in the building. The BSim database contains information about the constructions and materials, such as lifetimes and the amount of materials used in the constructions. This information is used for performing an inventory analysis on the construction and material levels of the product system.

In order to trace the product system further back, each material in the BSim database must be related to a corresponding product in the BEAT database. When this relation is known, the product system can be traced from the building to the processes where natural resources are extracted from the environment.

The entries (material or product) in both databases are associated with a SfB index. The SfB classification system is described by Ray-Jones and Clegg (1991). For each material in the BSim database, a relation is established by locating the first product in the BEAT database with a corresponding SfB index.

This correspondence is, however, not unique, since there are usually many products in the BEAT database with the same SfB index. Future versions of the BEAT tool will provide more flexibility for the user to establish relations between the two databases.

The LCI analysis method described above requires an acyclic product system. A depth-first search (DFS) is performed in order to locate cycles in the product system. DFS is an algorithm for analysing a graph consisting of vertices and edges, such as a product system. The DFS algorithm provides a spanning tree of the graph, which can be used for classifying the edges belonging to graph as being either (1) tree edges, (2) back edges, (3) forward edges or (4) cross edges. The graph contains cycles if one or more back edges is found. In this case, the LCI analysis is aborted. see Cormen et al. (2001) for further details regarding the DFS algorithm.

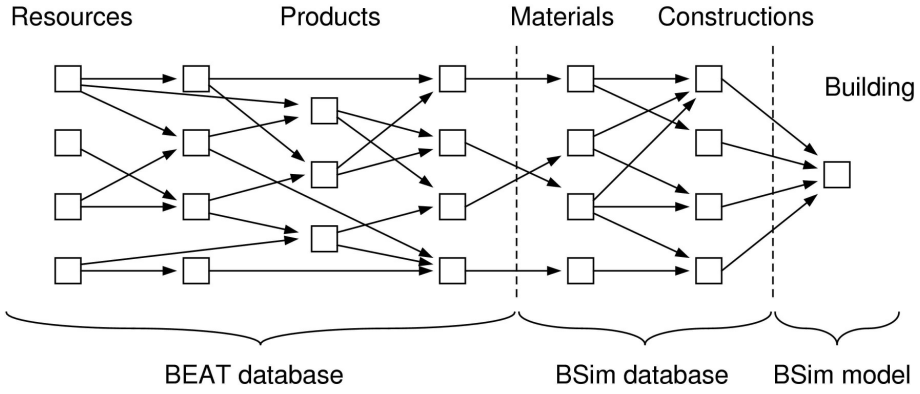

FIG. 2: A product system for constructing a building. The emissions resulting from the processes are omitted. The arrows indicate directions of the material flows.

2.2 Calculating the environmental effects

Each extracted resource and emitted pollutant contribute to one or more environmental effect, such as global warming, water pollution, depletion of rare resources, etc. The environmental effects are calculated with the EDIP method, described by Hauschild and Wenzel (1998), using the expression:

$$\text{environmental effect} = \frac{\sum \text{amount} \cdot \text{effect factor}}{\text{normalizing factor}} \cdot \text{weighting factor} . \qquad (1)$$

The effect factors are used for calculating an equivalent amount of reference resource or pollutant. For instance, for all pollutants that contribute to global warming, an equivalent amount of CO_2 is calculated, and the sum of these contributions is used for calculating the environmental effect.

The normalization factor is the average amount of extracted resource or emitted pollutant per person. Extracted resources are weighted with the inverse of the supply period. This means that highly demanded rare resources, which have short supply periods, have large weights. Weights for emitted pollutants are often politically decided.

3. Case study

The combination of BEAT and BSim is demonstrated by using a beta version of the combined tool in a case study regarding the single-family house shown in Figure 3. The aim of the study is to illustrate the impact of either increasing or reducing the amount of insulation in the building envelope. Intuitively, increasing the amount of insulation will decrease the energy use during operation, but increase the environmental impact during

construction, since a larger amount of natural resources is used for producing insulation material. Reducing the amount of insulation should have the opposite effect.

The study is conducted by parameter variations of the insulation thickness used in the external walls, slab on ground and ceiling. The contribution to global warming and the annual amount of energy required for heating the building are treated as dependent parameters. The contribution to global warming only includes the construction phase, and therefore only includes emissions related to the production of building materials. Emissions related to the use of natural resources during operation are disregarded.

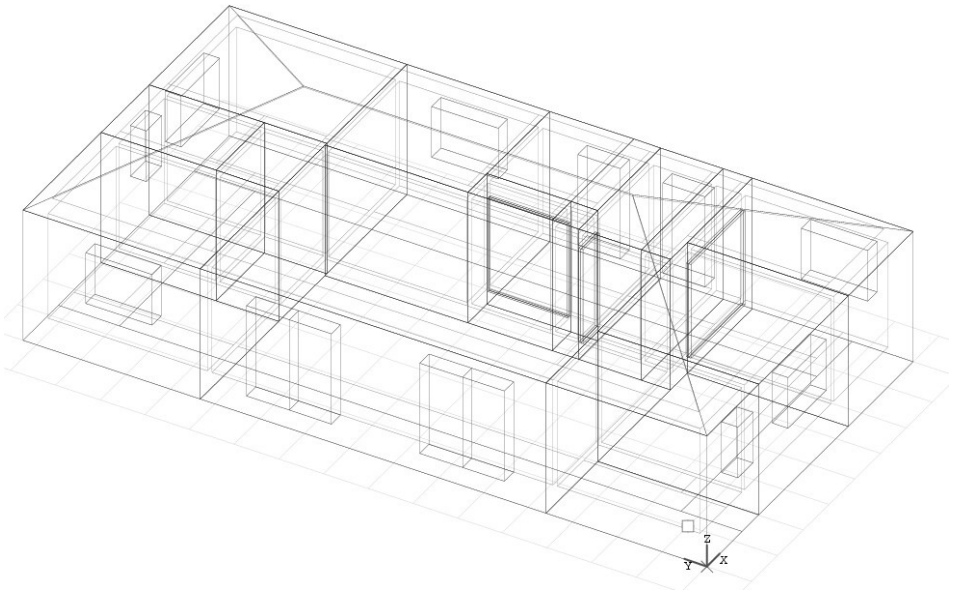

FIG. 3: BSim wire frame representation of the considered single-family house.

The LCA calculations are based on the lifetimes shown in Table 1, which are consistent with the values provided by Nielsen et al. (1985).

TABLE. 1: Lifetimes for the constructions used in the case study.

Construction	Lifetime
External walls	60 years
Internal walls	60 years
Floors, including ground slab	60 years
Ceiling	60 years
Roof construction	60 years
Windows and doors	40 years

Variations of the insulation thicknesses in the external walls, slab on ground and ceiling are calculated by scaling them relative to their original values. The scaling is performed in the range from 50 % to 150 %. Table 2 show the insulation thicknesses, the resulting annual energy use for heating the house, as well as the contribution to global warming due to the production of construction materials.

Figure 4 shows a plot of the environmental impact and energy use against the scaling factor for the insulation thicknesses. When the amount of insulation is increased, the environmental impact increases, and the annual energy use decreases, which is expected.

Figure 5 shows a plot of the environmental impact against the energy use, also known as a Pareto plot (see Pareto (1969) for details), since two objective functions are plotted against each other. This type of plot is particularly useful for investigating the compromise between objectives, and is therefore often used as a tool for supporting decisions.

Figure 5 thus shows the compromise between the objectives of minimizing the environmental impact and minimizing the energy use. It indicates that reducing the energy use during the operational phase of the building can only be done by increasing the environmental impact during the construction phase.

TABLE. 2: Impact of scaling the insulation thicknesses on the energy use and the environmental impact. The insulation thicknesses are rounded to the nearest mm.

Scaling [%]	50.0	62.5	75.0	87.5	100.0	112.5	125.0	137.5	150.0
Walls [mm]	75	94	113	132	150	169	188	206	225
Slab on ground [mm]	63	78	94	109	125	141	156	172	188
Ceiling [mm]	150	188	225	263	300	338	375	413	450
Energy use [kWh]	8682	7616	6848	6251	5780	5382	5054	4773	4531
Environmental impact [10^{-2} CO_2 equivalents]	5.30	5.51	5.71	5.91	6.10	6.28	6.46	6.63	6.79

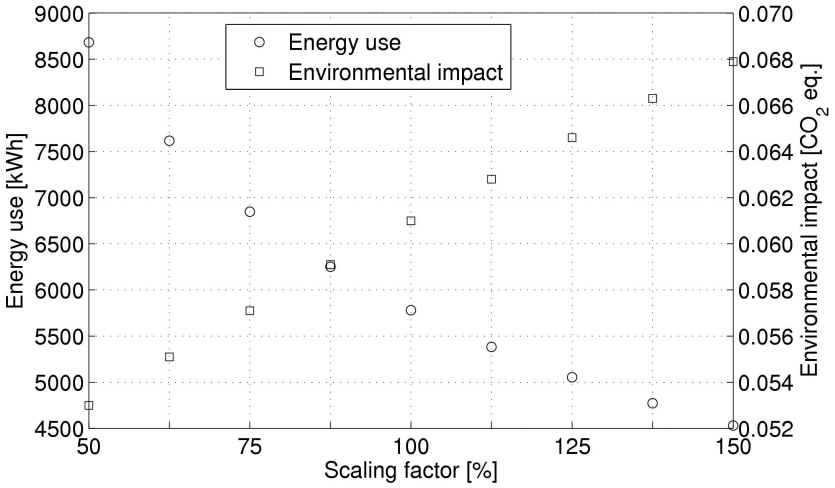

FIG. 4: Environmental impact and energy use plotted against the scaling factor.

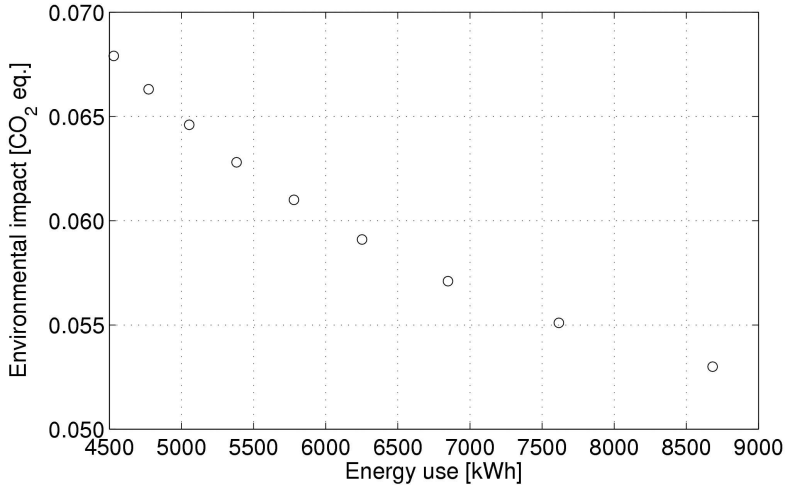

FIG. 5: Environmental impact plotted against energy use.

4. Discussion

Integration of the BSim and BEAT tools seems to be useful for supporting decisions during the design phase, e.g. investigating compromises between design objectives. There are, however, some details that must be addressed.

The current version does not include heating, ventilation and air-conditioning (HVAC) systems in the LCA calculations, since these systems do not have geometrical representations in the BSim model. It is therefore not possible to calculate the amount of materials attributed to these systems. Furthermore, the BEAT database needs an extension to include environmental data for these systems, which complicates the problem further in terms of collecting relevant data.

Assuming that environmental data for the HVAC systems can be found – which is a far from trivial task to undertake - the issue regarding the missing geometry can be resolved by using average material amounts for the different systems, related to the heated floor area and simulated energy demand. For instance, the average length of ventilation ducts in different building types per unit of heated floor area can be used for estimating the total amount of materials used for producing the ventilation ducts.

The current version of the BEAT tool only calculates the environmental impact of constructing the building, and omits the impact of operating and maintaining the building. The impact of operating the building can be handled by making the results from thermal simulations of the building available to the BEAT tool, and by requiring that the user specifies the method used for producing the required heat and electricity.

The impact of maintaining the building can be handled by relating each construction type in the BSim database with processes needed for its maintenance, representing for instance cleaning, reparation, or replacement processes. These relations need though to be defined in the BEAT database.

The LCI calculation method currently used is not able to handle product systems with cycles; however, there are methods that resolve this issue. For instance, the IO-based LCI calculation method described by Suh and Huppes (2005) is able to handle systems with cycles. This method furthermore performs LCI calculations using matrix operations, which most likely will speed up the calculations and reduce the requirements to the data provided by the user.

Using the current beta version of the tool requires that the user specifies lifetimes for the constructions in the BSim database, as well as relations between materials in the BSim database and products in the BEAT database. This process can be quite time-consuming, especially for buildings consisting of many different materials.

Providing default lifetimes in the BSim database, and default relations between the two databases may reduce the time needed for specifying these parameters. In case the user adds new materials to the BSim database, it may be necessary to add the same material in the BEAT database and create the required relation. This should be done in an integrated user interface, allowing access to both databases.

5. Conclusion

This paper describes a prototype integration of a LCA method into a whole building hygro-thermal simulation tool. The life cycle inventory calculations are described and a case study is performed in order to demonstrate the tool on a realistic example. A number of issues need to be addressed in future versions of the tool to make it usable outside the academic society.

The case study indicates that the results obtained with the tool are useful for supporting energy- or environmentally oriented building design. The tool can be used for highlighting the compromise between the environmental impact during the construction phases of the building, and the energy required during the operational phase. The tool is thus suitable for addressing the increased requirements to the energy performance of buildings, which in the future are likely to be supplemented with requirements to the environmental impact of buildings.

A number of issues need to be addressed in order to ensure that all contributions to the environmental impact during the construction and operational phases of the building are accounted for, and to make the tool easier to use:

- The HVAC systems must be included in the calculations. This requires environmental data for these systems, and an estimate of their use of materials, which for instance can be accomplished by

using statistical data for the average system size per unit of heat floor area in different building and system types.

- The processes needed for operating and maintaining the building must be included in the calculations, which can be done by relating the constructions in the BSim database to relevant processes in the BEAT database, and make sure that the BEAT tool includes these relations when performing the LCI calculations.
- Implementation of an IO-based LCI calculation method will enable the BEAT tool to handle product systems with cycles, which reduces the requirements to the data provided by the user.
- The graphical user interface needs further development in order to make it easier for the user to specify the required relations between the two databases and analyse the results.

6. References

Cormen T.H., Leiserson C.E., Rivest R.L. and Stein C. (2001). Introduction to Algorithms, The MIT Press, Cambridge, USA.

EPBD Directive (2002). Directive 2002/91/EC of the European Parliament and of the Council of 16 December 2002 on the energy performance of buildings.

Nielsen K., Hansen P. and Kjær B. (1985). Planning easily operated buildings (Original title: Planlægning af driftsvenligt byggeri), Byggeriets Udviklingsråd, Copenhagen, Denmark.

Pareto V. (1969). Manual of political economy, Augustus M. Kelley Pubs, New York, USA.

Petersen E.H. (1999). LCA Tool for Use in the Building Industry, International Journal of Low Energy and Sustainable Buildings, vol. 1.

Ray-Jones A. and Clegg D. (1991). CI/SfB Construction indexing manual - 1976 revision Abridged reprint 1991, RIBA Publications Limited, London, England. ISBN: 0 947877 04 5.

Sartori I. and Hestness A.G. (2007). Energy use in the life cycle of conventional and low-energy buildings: A review article, Energy and Buildings, vol. 39, no. 3, pp. 249-257.

Suh S. and Huppes G. (2005). Methods for life cycle inventory of a product, Journal of Cleaner Production, vol. 13, pp. 687-697.

Hauschild M. and Wenzel H (1998). Environmental assessment of products, Chapman & Hall, London, England.

Wittchen K.B., Johnsen K. and Grau K. (1999-2008). BSim - User Guide. Danish Building Research Institute, Dr. Neergaards Vej 15, DK-2970 Hørsholm, Denmark.

An Exergetic Analysis and Potential for Improving the Rational Energy Use in Dwellings

Marco Molinari, Ph.D. student.
Division of Building Technology, Department of Civil and Architectural Engineering
KTH - The Royal Institute of Technology
SE-10044 Stockholm, Sweden
Marco@byv.kth.se

Gudni A. Jóhannesson, Professor, Director General
The Icelandic National Energy Authority
Grensásvegur 9, IS 108 Reykjavík
KTH , Division of Building Technology
Brinellvägen 34 SE-10044 Stockholm, Sweden
gudni.a.johannesson@os.is

KEYWORDS: *Exergy, energy, efficiency, buildings, appliances.*

SUMMARY:

The quality of a certain amount of energy is defined as the relative exergy content of this energy. Most of our buildings with their heating and cooling systems today are built for conversion of high quality energy sources to low quality use with destruction of the available exergy as a result. Globally we have a huge potential for transforming our processes to more efficient use of the exergy and also for feeding our processes directly from renewable energy sources without the use of high quality energy sources. Exergy analysis is also important as an innovation driver in buildings and building systems. This work is carried out within the frame of IEA Annex 49 Low Exergy Systems for High-Performance Buildings and Communities. The scope of the annex is to improve, on a community and building level, the design of energy use strategies, taking into account the different qualities of energy sources, from generation and distribution to consumption within in the built environment. In particular, this is carried our by the method of exergy analyses to provide assessment of the thermodynamic features of any process and to achieve a clear, quantitative indication of both the irreversibilities and potential for matchmaking between the resources used and the end-use energy flows. The paper contains a systematic survey of the exergy consuming processes for building and building appliances, their role in exergy balance, the level of energy quality needed in primary process and the potential for developing processes towards improved exergy efficiency. The work presented here gives a listing of the important processes in buildings with a discussion of their nature from an exergy point of view. The methodology for analysis is exemplified for a limited number of processes, dealing with the energy use and exergy destruction in processes, the potential for exergy saving and the discussion on the technical and economical feasibility

1. Introduction

Traditionally, when we refer to the usual processes in household buildings the main parameter considered is the energy consumption (see, for instance, the energy labelling concept [1]). From a thermodynamic perspective this is only partially correct: considering the energetic efficiency in a boiler might lead to some pretty good results, but would these figures really describe the “actual” efficiency?

The idea of exergy may be useful to answer this question: exergy is a function that takes into account both the first and the second law of thermodynamics. The most general formulation of the exergy equation will be now written [1] for an open system as a room, considering the exergy associated to heat and mass transfer and neglecting other components of exergy transfer, such as kinetic and potential exergy; under steady state assumption, the first law of thermodynamics can be written as:

$$E_{in} = E_{out} \quad (1)$$

On the other hand, according to the second law of thermodynamics, the entropy production in the above mentioned system is:

$$S_{in} + S_{gen} = S_{out} \quad (2)$$

Where $S_{gen} = 0$ only in a reversible process.

By multiplying the equation *(2)* by the reference temperature T_0 and subtracting it to the equation *(1)* the result is:

$$(E_{in} - S_{in}T_0) - S_{gen}T_0 = (E_{out} - S_{out}T_0) \quad (3)$$

That is

(Energy input –Anergy input)-Anergy generated = (Energy output – Anergy output)

$$Ex_{in} - Ex_{consumed} = Ex_{out} \quad (4)$$

Anergy is the product of the entropy related to an energy flow and its environment temperature: it is the part of the energy flow that cannot be converted into work. By subtracting this amount to the energy flow, the exergy flow is obtained, i.e. the valuable quantity of the energy that can entirely converted into work.

The equation *(4)* is a general equation for the exergy balance: Ex_{out} is the maximum amount of exergy that can be obtained from a system whose supplying exergy is Ex_{in}: the smaller the exergy consumed, the smaller the exergy loss.

In buildings, since Ex_{out} is "fixed" by the overall needs to warm up the building and to feed its appliances, the aim is to reduce the Ex_{in} in order to lower the $Ex_{consumed}$. Most of the traditional systems, in fact, use energy sources with high exergy content. A boiler can easily reach efficiency values over 90% or even greater than 100% with condensing boilers, but its exergetic efficiency is much lower [1], [2], [8], [9]. The low values here are the "mathematic" translation of what the second law of thermodynamic states: in a boiler, different processes take place: first the conversion from a more valuable form of energy, the fuel chemical energy, to the lower exergy of the high temperature gases. Secondly, heat is exchanged to a lower temperature fluid and a second and bigger thermodynamic loss takes place. Even assuming that the conversion from chemical exergy to heat exergy is virtually free of energy losses (i.e. no heat given to exhaust gases and no heat dispersions toward the external environment) there is still an exergetic loss, due to the bad matching between an high exergy source and a low exergy output: the difference between input and the output in the system is irreversibly lost. It is therefore mandatory to review the different outputs, i.e. the energy levels, in the most common household energy processes, to quantify the exergy, i.e. the energy quality, in the processes considered And to understand how rationally the energy is used.

Common energy sources in dwellings are fossil fuels: it would be possible to redirect the high exergy sources where they are really needed (like for instance the production of electricity) and to supply the low exergy needs with low exergy sources, usually low-cost, renewable ones. In this way it would be virtually possible to shift most of the high exergy sources from buildings processes, usually with very low exergy needs, to other energy fields: if we assume that the whole household energy needs were covered by renewable sources (solar panels for instance), some 30% of the energy consumption could be saved. These are just theoretical values, because innovations like these have to face cultural inertias, because there would be technical problems and it would be necessary to create a markets; anyway this might be a relatively feasible way of saving energy and that would have positive implications on the development of further markets.

2. Analysis of household exergy needs

As a first step, an exergy needs analysis of the most common processes has been drawn by determining an exergy factor value for each process: this factor is the ratio between exergy in a household and energy flowing into the considered system. The aim here is to find out which is the exergetic level of every process, more than

the absolute exergy consumption, to obtain an order of magnitude of the energy quality involved in the processes: space heating at 40°C has a much lower exergy level than an oven running at 250°C, as Carnot factors -here considered as the exergy factor- will clearly show.

In many appliances there is both a consumption of hot water and mechanical energy - for instance, for the pumps: in these cases the exergy is referred to the main energy flow, neglecting the smaller energy uses. For instance, in an oven there are commonly electrical devices such as fans, lights and thermostats that consume an amount of energy much smaller than the one used to cook: therefore they have not been taken into account.

The following Table 1 has been drawn by means of Carnot factor F_Q:

$$F_Q = 1 - \frac{T_0}{T} \qquad (5)$$

T_0 is the reference temperature and T is the temperature in the considered process; as regards T_0, 15°C, the yearly average temperature on Earth, has been chosen for every process due to the general perspective of this paper. The exergetic heat amount in processes is therefore:

$$Ex_Q = Q * (1 - \frac{T_0}{T}) \qquad (6)$$

Table 1: Typical processes in dwellings and related exergy factor

Process	Typical Temperatures [°C]	Typical Temperatures [K]	Carnot Factor [ ]
Freezing	-20	253	0.138
Refrigerator	4	277	0.040
Air Cooling	10	283	0.018
Floor Cooling	12	285	0.011
Zero level	15	288	0
Air heating	26	299	0.037
Floor heating	35	308	0.065
Shower/bathing	40	313	0.080
Hair-drying	55	328	0.122
Dish washing	60	333	0.135
Laundry-drying	60	333	0.135
Radiator heating	70	343	0.160
Washing	70	343	0.160
Boiling	100	373	0.228
Frying	200	473	0.391
Ironing	210	483	0.404
Baking	250	523	0.449

The Table 1 and the Figure 1 show how rather small are the exergy needs in a dwelling house: this becomes of great importance considering that most of these processes are supplied with high exergy sources: fossil fuels, whose chemical exergy is close to the unity, are commonly used for space heating – in boilers - and electricity for most of the other processes.

An exergetic efficiency can be introduced as ratio between the desired output, i.e. the exergy in the process, and the supplied input to feed the considered process: since in both cases the supplied exergy has a quality factor equal (electricity) or nearly equal to 1 (chemical exergy), the Carnot factors shown in Figure 1 are also the exergetic efficiencies.

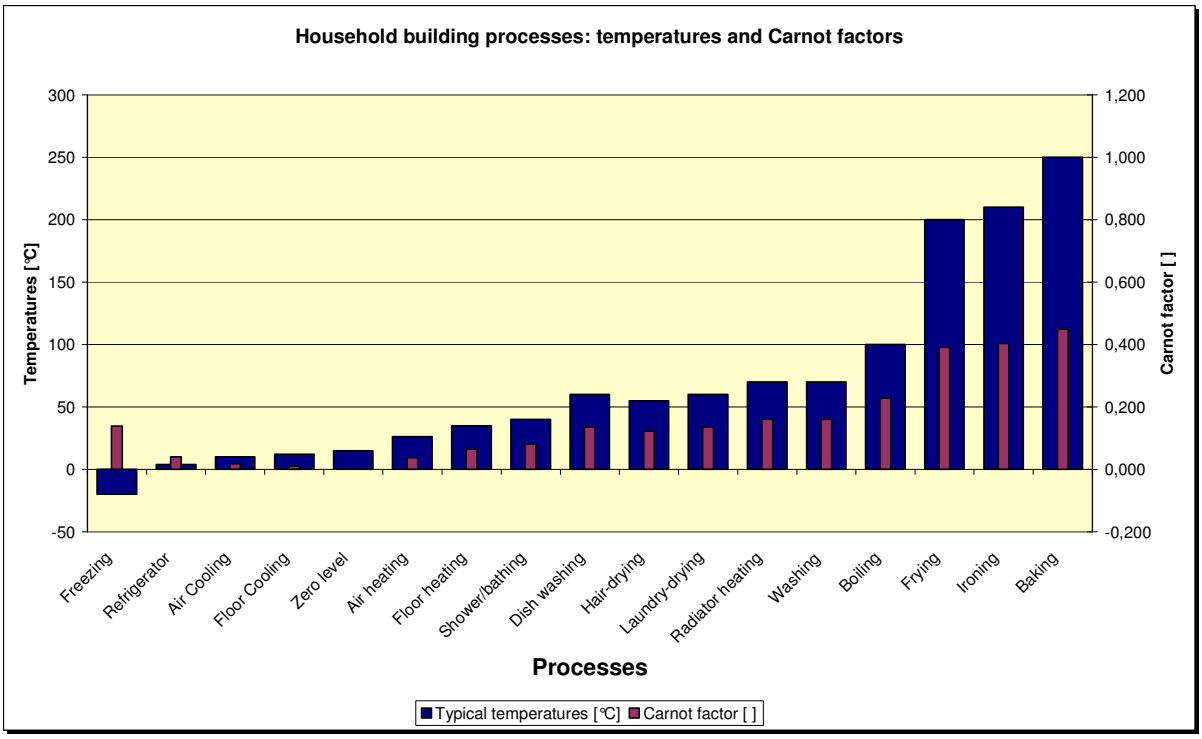

Figure 1: Dwelling processes: exergy level and temperatures

It is clear how thermodynamically inefficient, or, in another way irrational, is the energy usage in households, due to the use of high exergy supply like electricity, easy to transport and to use, flexible, and relatively cheap to produce. On the other hand, the potential for energy saving is impressive: this high quality energy could be shifted where it is really necessary, i.e. where work needs to be produced by the exploitation of pure exergy: a great amount of primary energy could be therefore be saved. The energy use in buildings, in fact, accounts for about one third of the total yearly energy consumption in the world, with rather small differences in the Western countries [10].

3. Three examples

Among the considered processes, three of them have been chosen for a deeper analysis:

1. Dishwashing, as example of relatively low temperature heat needs for appliances
2. Refrigerator, as representative of cooling needs
3. Space heating, as example of space conditioning

3.1. Dishwashing

The first example taken into account is the working of a dishwasher: according to the European Energy labelling the energy consumption for each cycle typically varies from about 1 kWh to 2 kWh, depending on the class. Most of the energetic consumption, roughly 80%, goes toward heating water, the rest being used in drying and water pumping. In this example the hot water temperature is set at 60°C; 0.8 kWh of the energy consumed by a class "A" equipment, supplied by electricity, contains an amount of exergy that can be calculated via the Carnot factor with a reference temperature of 15 °C and results in 0.1 kWh.

Which is the utility of this result? Indeed, it doesn't mean that the amount of energy that is actually needed is 100 Wh, but it gives really useful information on how rationally it is used. It is actually required to satisfy both of the needs, but what is mandatory to be stressed here is that this process allows us to use other kinds of energy that can be supplied otherwise. These energy sources wouldn't be profitable in a power plant producing electricity: the matter is how to use this "thermodynamic opportunity"?

In this case a possible alternative is to use freely available energy from the sun, by using a solar panel coupled with a storage system to let the energy available even in cloudy days: so, a supplying temperature of 70 degrees can be reached.

A measure of the improvement of the matching between the different forms of energy is once again calculated by dividing the Carnot factor of the two input and output energy flows and assuming that the energy losses are negligible, so that:

$$\eta_{EX} = \frac{EX_{out}}{EX_{in}} = \frac{1-\frac{T_{ref}}{T_{need}}}{1-\frac{T_{ref}}{T_{\sup ply}}} = \frac{1-\frac{15+273}{60+273}}{1-\frac{15+273}{70+273}} = 0.84 \qquad (7)$$

The exergy efficiency was before around 0.13, proof of the bad matching between source and actual exergy need: in this second solution, the efficiency is closer to the unity. Two effects have been obtained: a decrease of the exergy waste and the exploitation of freely available solar energy: this is not always possible, as the next example will show.

3.2. Refrigerator

A simple scheme of a refrigerator unit is made up of four elements: an evaporator, a compressor, a condensing unit and an expansion unit (usually a throttling process) and the system scheme is the one drawn in the figure below:

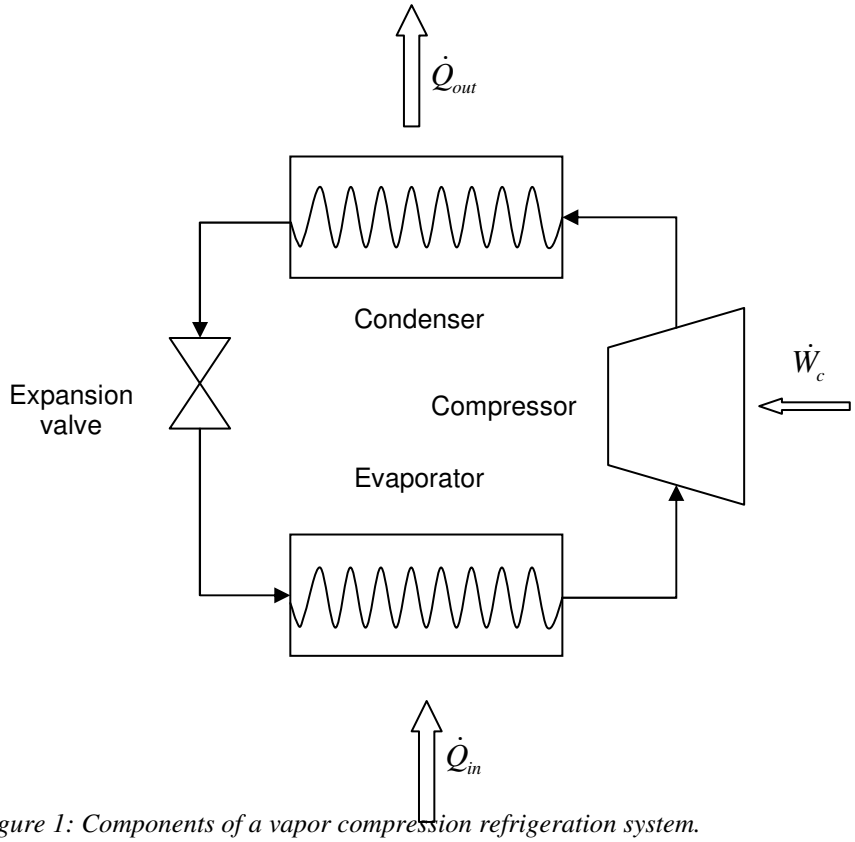

Figure 1: Components of a vapor compression refrigeration system.

Typically, the saturated vapour at the evaporator outlet is at a temperature of about 0°C to draw heat from the cold ambient at 4°C, while the temperature at the condenser can reach the value of 50°C, assuming an outside temperature of 20°C.

The exergy factor here results in 0.04 -the reference temperature being 15°C: the same value as the exergetic efficiency, assuming an electric supply wit an exergetic factor of 1. In this case as well there is a great potential for exergetic saving: more than 95% of the exergetic supply is destroyed: however, there is not a technical solution as easy as in the previous case. Cooling loads are less easy than heating loads to be rationally satisfied from an exergetic point of view: while it is possible to obtain "free" warm exergy from the sun, it is much more difficult to obtain low temperatures cooling flows for free: the use of heat pumps supplied with hi-quality energy is therefore needed.

Two alternatives can be here addressed: the use of a cold heat storage that could supply directly the evaporator: the cooling heat capacity can be charged during the night time, taking advantage of the lower temperatures. This system wouldn't possibly accumulate cooling energy with temperatures low enough to supply the system directly: therefore the second solution with the interposition of a reverse cycle would be necessary.

In this second way there would be no exergetic improvement with respect to the basic case, i.e. a fridge, because the exergy efficiency would stay the same. There would be instead an increase in the COP and a reduction of the energy use: this is an energetic saving, i.e. a limitation of the energy in use, but not a more rational use of the energy, because no alternatives are easily available.

3.3. Space heating

The case considered in this third example has been a low temperature (35°C) floor heating: similarly to the first case study, the exergy content, seen as ratio between exergy and energy, is rather low, 0.064. Energy is supplied

by the use of as boiler: the fuel (gas, diesel) energy content is converted into heat and conveyed to the floor heating:

Here too, the value of the supply exergy is much higher than the chemical exergy, assuming, as suggested for instance in [1], a quality factor of 0.9: as a result, the exergy efficiency would result in 0.071, quite low.

A possible solution to improve the exergy efficiency can be the use of solar panels. In this case another kind of problem has to be faced: the technical feasibility of this solution depends on the necessary energy amount required., The heat energy needs of a dwelling of 150 m^2, with an U-value for external walls of 0.2 W/(m^2 K), can reach the order of magnitude of hundreds of kWh for a week in a continental climate location [4], that need to be supplied by the energy storage system itself in case of lack of solar radiation.

4. Conclusions

A general analysis focused on exergy consumption of the processes that take place in a household has been drawn. Exergy and exergy efficiency has been used as parameter of the rational use of energy. Three study cases, to deeper analyze the different situations, have been taken in consideration: it has been shown that the exergetic efficiencies are low in processes using the common energy supplies are. Several examples of possible improvement have been proposed in a theoretical way. It has been stressed how alternative solutions have to be met studying every system in particular to obtain the best matching of what is available and what is to be satisfied from an energetic point of view.

5. References

[1] Mahlia T.M.I., Masjuki H.H., Choudhury I.A. (2002). *Theory of energy efficiency standards and labels, Energy Conversion and Management* (2002) 743-761
[2] Schmidt D. (2004). Methodology for the modelling of thermally activated building components in low exergy design, *Doctoral thesis*, KTH, Stockholm, Sweden.
[3] Molinari M. (2006). Exergy analysis in buildings, *Master thesis*, DFT, Padua University, Padua, Italy.
[4] Noguera Casselles J. (2007), Calidohogar: low energy house, *Master thesis*, KTH, Stockholm, Sweden.
[5] Asada H., Shukuya M. (1999). numerical analysis of annual exergy consumption for daylighting, electric lighting and space heating cooling system, *Sixth international IBPSA conference*, Kyoto, Japan.
[6] Shukuya M. (2004). Energy entropy exergy and environmental physics, *The ninth Asian Physics conference* (9th APPC), Hanoi, Vietnam.
[7] Shukuya M. (1994). Energy entropy and space heating systems, *Healthy buildings '94 Proceedings of the 3rd international conference*, Budapest, Hungary.
[8] www.lowex.net
[9] www.ecbcs.org
[10] www.enea.it

Benchmarking of Low "Exergy" Buildings

Dietrich Schmidt, Tekn. Dr.
Fraunhofer Institute for Building Physics
Project Group Kassel
Gottschalkstrasse 28a
D-34127 Kassel
email: dietrich.schmudt@ibp.fraunhofer.de
http: www.ibp.fraunhofer.de

KEYWORDS: *Energy conservation and efficiency in buildings, exergy analysis.*

SUMMARY:
There is an obvious and indisputable need for an increase in the efficiency of energy utilisation in buildings. Heating, cooling and lighting appliances in buildings account for more than one third of the world's primary energy demand. In turn, building stock is a major contributor to energy related environmental problems. There is great potential to be obtained through a more efficient use of energy in buildings.

An optimisation of the exergy flows in buildings and the related supply structures, similar to other thermodynamic systems such as power stations, can help in identifying the potential of increased efficiency in energy utilisation. It can be proven through analyses that calculations based on the energy conservation and primary energy concept alone are inadequate for gaining a full understanding of all important aspects of energy utilisation processes. The high potential for a further increase in the efficiency of; for example, boilers, can not be quantified by energy analysis - the energy efficiency is close to 100%; however, this potential can be shown by using exergy analysis, the exergy efficiency of a common gas boiler is about 8%.

The Low Exergy (LowEx) approach entails matching the quality levels of exergy supply and demand, in order to streamline the utilisation of high-value energy resources and minimise the irreversible dissipation of low-value energy into the environment. This approach is the key concept for the work of ECBCS Annex 49 on energy use and supply structures in the built environment.

The advantages of the analyses and the differences between energy and exergy analyses have been demonstrated using a typical case. In conclusion, based on an analysis of a real and existing building, suggestions are presented for a benchmarking system for so-called LowEx buildings. In order to achieve an exergy optimised building design, loads on the building service system must be reduced as much as possible. The suggested benchmarking method gives an engineering approach to archive those building system configurations.

The presented research work is related to the ongoing international cooperation work in the IEA ECBCS Annex 49 "Low Exergy Systems for High-Performance Buildings and Communities", the established Network for "Low Exergy Systems in Buildings - LowExNet" and ongoing German activities in the collaboration project in the exergy field from industry partners and research institutes.

1. Introduction

The growing concern of environmental problems, such as global warming, which have been linked to the extended use of energy, has increased both the importance of all kinds of so-called "energy saving measures", and the necessity for an increased efficiency in all forms of energy utilisation. A number of national programmes have been launched to advertise retrofit measures to increase energy efficiency of the building stock (DENA 2007). Despite the efforts made to improve energy efficiency in buildings, the issue of gaining an overall assessment, and comparing different energy sources still exists (Schmidt and Shukuya 2003). Today's analysis and optimisation methods do not distinguish between different qualities of energy flows during the analysis. An assessment of energy flows from different sources is first carried out at the end of the analysis by weighing them against the primary energy factors. In the building codes of a number of countries, these problems have been solved via the transformation of all energy flows to the primary energy demand. The primary energy factors

necessary for the calculation are based neither on analytical ground nor on thermodynamic process analyses, yet they have been derived from statistical material and political discussion.

In the theory of thermodynamics, the concept of exergy is stated to be the maximum work that can be obtained from an energy flow or a change of a system. The exergy content expresses the quality of an energy source or flow. This concept can be used to combine and compare all flows of energy according to their quantity and quality (Rant 1956, Rant 1964, Schmidt 2001, Schmidt, Müller and Henning 2006). Exergy analysis is commonly used in, for example, the optimisation processes of power stations. The feasibility of these methods is more closely examined here for the assessment of buildings. Buildings still account for more than one third of the world's primary energy demand (ECBCS 2008) and most of the energy is used to maintain room temperatures of around 20°C. In this sense, because of the low temperature level, the exergy demand for applications in room conditioning is naturally low. In most cases, however, this demand is satisfied with high quality sources, such as fossil fuels or with electricity (Schmidt 2004).

The presented research work is related to the international co-operation work in the IEA ECBCS Annex 49 "Low Exergy Systems for High-Performance Buildings and Communities"(Annex 49 2008).

2. The Exergy Concept

As described above, all our energy assessment of energy utilisation in buildings is based on quantitative considerations alone. By weighing different energy sources against primary energy factors, some aspects of a somewhat qualitative assessment are considered. Yet, in principle, the design of supply structures is founded on the satisfaction of the quantitative demand within buildings. With the so-called LowEx approach, a step further is to be taken. Not only are the quantitative aspects of demand and supply considered, but also, the qualitative aspects are included (Johannesson and Schmidt 2001, Ala-Juusela et al 2004, Keller 2007, Schmidt and Shukuya 2005).

To clarify these ideas, different uses of energy within buildings are concentrated on. If we heat indoor space up to 20°C, we have to supply heat at a slightly higher temperature than 20°C. An exergetic analysis shows that the required energy quality, the exergy fraction or quality factor q, for this application is very low ($q \approx 7\%$ only). At the same time, we need the largest amount of energy in a building to satisfy the heating demands. If the production of domestic hot water is considered as heating water up to temperatures of about 55°C, the needed energy quality is slightly higher ($q \approx 15\%$). For cooking or heating of, for example, a sauna, we need an even higher quality level ($q \approx 28\%$), and for the operation of different household appliances and lighting we need the highest possible quality ($q \approx 100\%$).

On the other hand, our energy supply in not structures or sophisticated in the same manner as the use. Energy is commonly supplied as electricity or as a fossil energy carrier. The energy quality of the supply for all different uses are the same and unnecessarily high ($q \approx 100\%$).

An adaptation of the quality levels of supply and demand could be managed by covering, for example, the heating demand with suitable energy sources, as there is available district heating with a quality level of about 30%. There is a large variety of technical solutions to supply buildings with the lowest possible supply temperatures ($q \approx 13\%$) on the market. Commonly known water borne floor heating systems are one of these solutions.

In Germany, the typical primary energy efficiency for heating of newly erected dwellings, equipped with good building service systems, is about 70%. If exergy is considered, the picture changes. The exergetic efficiency of the heating process is only about 10%. In the following, the question will be discussed as to whether an exergy analysis could help to increase energy use efficiency.

An exergy analysis has to start with the definition of the boundary conditions and with the estimation of the exergetic demand of the occupied zones. A typical outdoor ambient air temperature in winter is considered as 0°C in central/northern Europe, which is also the reference temperature for the exergy analysis. With an indoor air temperature of 21°C within the heated spaces, the exergy fraction of the heating energy turns out to be 7%. The quality factor is equal to the Carnot efficiency for this purpose. This factor is dependent on the temperature inside the room and on the ambient environment. In addition, in extreme conditions, it will not exceed 15%. Similar considerations can be made for summer and cooling conditions, but are not the subject of this paper and will be covered in future research activities.

3. A Case Study

For the following considerations, a building from the IWU study (IWU 2003) – a single-family dwelling, built between 1995 and 2000 – has been chosen as an example. For this home, an indoor air temperature of 21°C is assumed as the reference temperature, and the ambient air temperature during a typical winter day is 0°C. The mean heat transmission coefficient of the building envelope H'_T, a measure for the insulation standard of the building, is 0.44 W/m²K. The building is to be ventilated via windows and natural forces, and a mean air exchange rate of 0.6 ACH has been assumed. The preparation of the needed domestic hot water is done via direct electrical heating elements and assumed to be 45 l/(pers*d) with about 2.5 persons present as a mean value.

The calculation for this study have been conducted with the Annex 49 analysis tool (Annex 49 2008), an Excel based spreadsheet tool for steady state calculations. The method described in detail in and based on (Schmidt 2004). The calculated figures are actual loads for typical conditions.

For the building service equipment and the heating system of the building, six different variants have been studied intensively:

1. A condensing boiler as the primary heat generator and standard radiators with the temperature levels for supply and return of 55/45°C have been assumed as the emission system.
2. Again, a condensing boiler is the heat generator and a floor heating system with temperature levels for supply and return of 28/22°C has been assumed.
3. A biomass-fired boiler (e.g. wooden pellet burner) is the heat generator and a floor heating system with temperature levels for supply and return of 28/22°C is the chosen emission system.
4. A condensing boiler is assumed as the primary heat generator and the solar thermal system, covering 40% of the heating load, is the secondary heat source. Floor heating with temperature levels for supply and return of 28/22°C is again the chosen emission system.
5. A ground source heat pump with a ground heat exchanger is the primary heat source and a floor heating systems with temperature levels for supply and return of 28/22°C is the chosen emission system.
6. The heat supply is covered by a district heating connection, which is fired with fossil or renewable sources. Also, for this variant, a floor heating systems with temperature levels for supply and return of 28/22°C is the chosen emission system.

4. Results

A common energetic assessment of the building, here conducted under steady state conditions, is shown in the following figure. Because of the different primary energy factors of the used fuel sources, the fossil part of the energy supply varies between the analysed variants. Also taking the renewable amounts of used energy into consideration, the total energy consumption is about the same. This is self-evident, since the same building is presented in all cases. Only the efficiency of the chosen building service system may vary.

Just considering the primary energy helps to identify saving measures for fossil energy sources and the related CO_2 emissions, but can hardly give any real indication about efficient energy use.

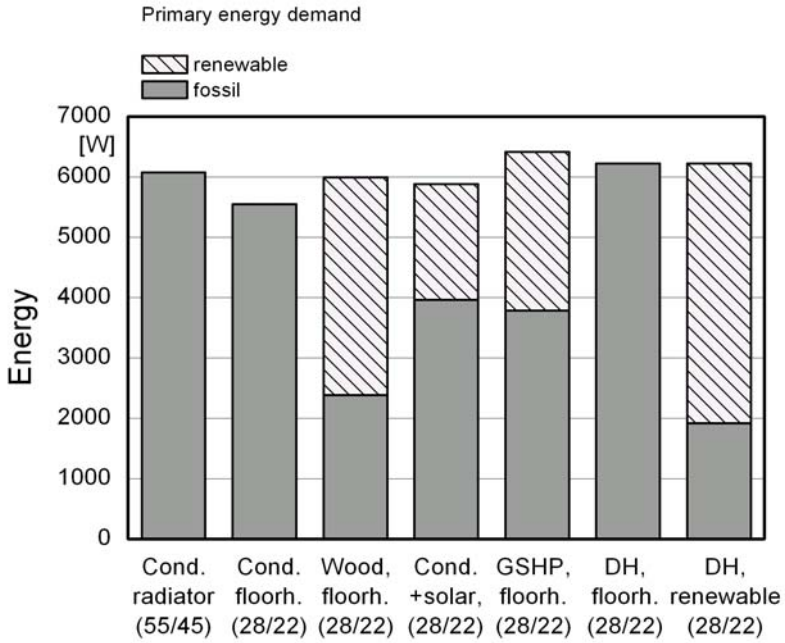

Figure 1: Calculated primary energy demand (fossil and renewable) for the chosen variants of the building service equipment (steady state calculation)

A comparison of an energetic and exergetic assessment of the primary energy demand from fossil and renewable sources in shown in the next figure. It can be clearly seen that the different building service system configurations could handle the same requirements to fulfil the heating task of the same building, with a largely varying amount of exergy. Especially the condensing boiler, where natural gas is used and burned, utilises about 100% exergy for that task. This is also true for the wooden pellet burner. Other systems are able to satisfy the requirements with less than half of the exergy. This is shown in the results from, for example, the systems operating with a district heating supply.

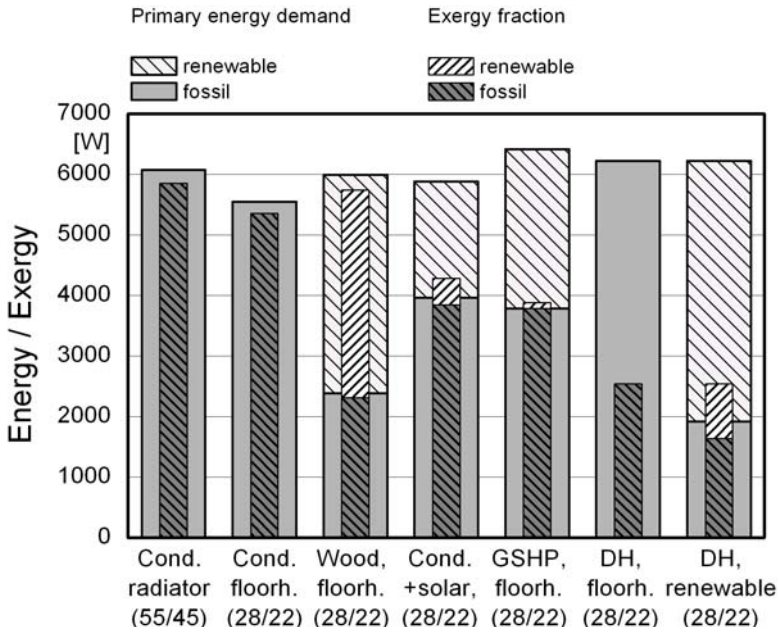

Figure 2: Calculated primary energy demand (fossil and renewable) and the related exergy fractions for the chosen variants of the building service equipment (steady state calculation)

The exergetic assessment of the regarded heating systems opens up for the possibility to compare the performance (and the efficient use of different the energy sources) in an equal and thermodynamic way. This basis is free from the influence of political discussions and national borders. The potential of renewable energy sources has also correctly been taken into consideration. It can be concluded that a rational use of energy has to be assessed with an additional exergy analysis and that exergy use should be limited, as it is done today with primary energy. This has to happen under the consideration of the entire building as one system (Schmidt and Ala-Juusela 2005, Schmidt 2007).

5. A LowEx Benchmark

To make the quantity exergy manageable for building designers and to allow for engineering-based orientation for the choice of building service solutions, a new parameter is presented here. This parameter, the exergy expenditure figure ε, is a quotient from the exergetic effort (produced by a component) and the energetic use of this component. It is defined as:

$$\varepsilon = \frac{\text{effort}}{\text{use}} = \frac{\dot{\text{Ex}}_{\text{in}} + \dot{\text{Ex}}_{\text{aux}}}{\dot{\text{En}}_{\text{out}}} \qquad (1)$$

A component, e.g. a radiator, is designed to supply a specified heating power. This implies it should heat the room with a certain amount of heat, which is to be delivered to the room space. Energy is transmitted and used within the space, and heat has been exchanged from the heat carrier water to the air within the room. A component should perform this task with the smallest possible amount of exergy. Furthermore, the use of high quality (auxiliary) energy, e.g. electrical power, should be low, as should unused losses to the environment.

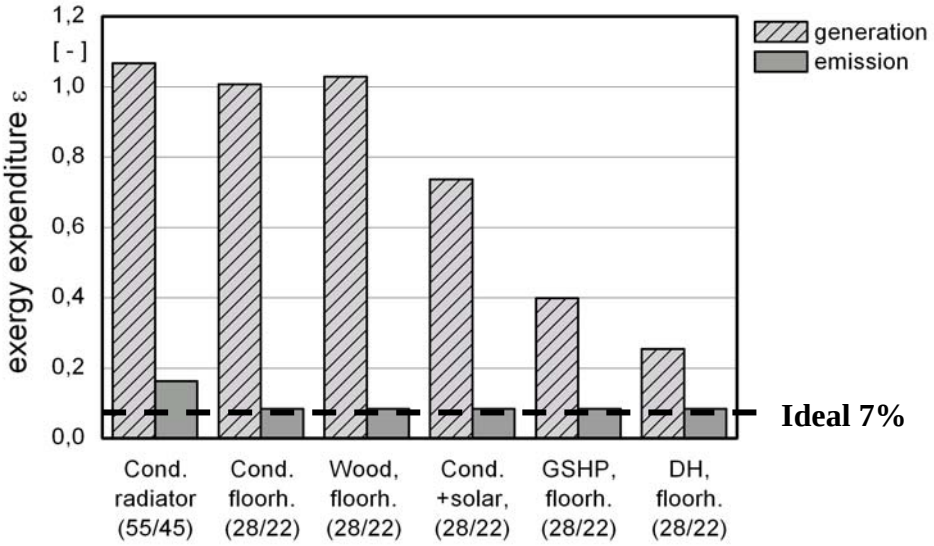

Figure 3: Assessment of the components "heat generation" and "emission system" with the exergy expenditure figure for the chosen variants of the building service system.

As described above, the exergy demand, the exergy fraction of the needed energy, of a zone is only 7%. This value can be directly compared to the exergy expenditure figures of the different components, as has been done in Figure 3. It is shown that different heat generators satisfy the demand with a more or less well-adapted supply. Heat generators, which utilise a combustion process, use much more exergy than required, and are thus less "LowEx". These differences can also be demonstrated for emission systems. The radiator system uses more exergy than the floor heating system to heat the same room. The floor heating system is close to ideal conditions.

6. Conclusions

Since the exergy approach enables a comparison of different energy utilisation systems in buildings on an equal basis, a limitation of the exergy fraction of the primary energy demand is suggested here.

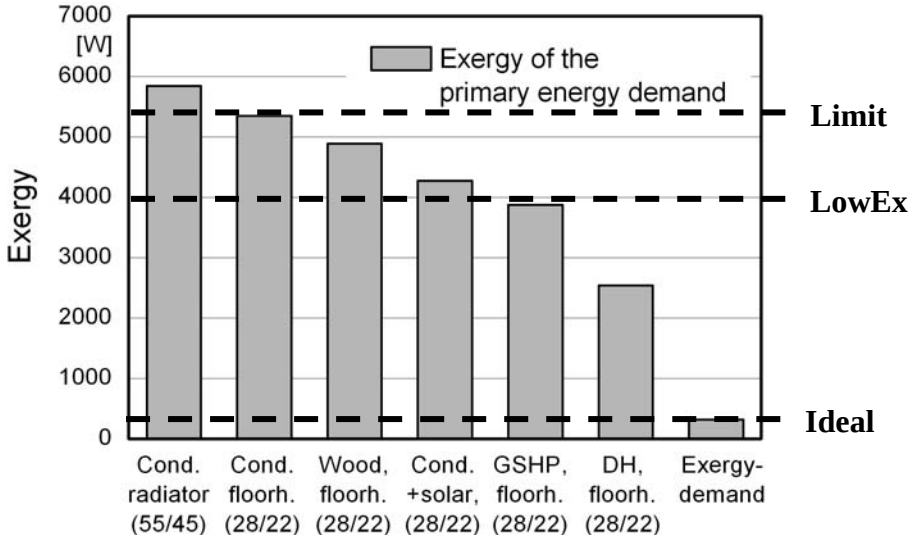

Figure 4: Calculated exergy fractions of total primary demand (fossil and renewable) for the chosen variants of the building service equipment (steady state) and a suggested possible classification.

An ideal line can be drawn based on the real exegetic demand of the regarded zone. Furthermore, the upper limit of the exergy demand should be limited according to the demand with the use of a good building service equipment solution, similar as done for the limitation of fossil primary energy demands. As the supply matches

the needed demand and the exergy destruction in the regarded building is kept to a limit, then this building can be regarded as a LowEx-building.

From these general statements, a number of conclusions can be drawn from the cases analysed. The following three main design principles can be extracted:

- The limitation of the primary energy demand is a useful tool to reduce energy consumption and the related CO_2-emissions from buildings. This is already mandatory in a number of European countries (e.g. Germany). Moreover, the expanded analysis of energy systems shown in this paper strengthens the need for this limitation of the primary energy demand. The German additional condition of the limitation of the maximal heat transmission losses by limiting the mean transmission heat loss coefficient is a good means of securing a good building envelope construction. The energy demand should be reduced.
- To assess and use the thermodynamic potential of the utilised energy, the exergy demand of fossil and renewable sources should be limited. This limitation could be done in a similar manner as already known from the procedure of limiting the primary energy demand.
- The covering of the exergetic demand of a zone should be satisfied with a suitable supply system, e.g. the exergy expenditure figure should be oriented to the actual exergetic demand of the zone.

7. Acknowledgements

The author gratefully acknowledges the support given by the German Federal Ministry for Economy and Labour for the related research work.

8. References

Ala-Juusela M. (Ed.), Schmidt D. et. al. (2004). Heating and Cooling with Focus on Increased Energy Efficiency and Improved Comfort. Guidebook to IEA ECBCS Annex 37. *VTT Research notes 2256*, VTT Building and Transport, Espoo, Finland.

Annex 49 (2008). Low Exergy Systems for High-Performance Buildings and Communities. *Energy Conservation in Buildings and Communities Service Programme*, web homepage: http://www.annex49.com.

Dena (2007). Zukunft Haus – Energie sparen, Wert gewinnen – Deutsche Energie Agentur. URL: http://www.zukunft-haus.info [10.10.2007]

ECBCS (2008). Energy Conservation in Buildings and Communities Service Programme. *International Energy Agency*, web homepage: http://www.ecbcs.org.

Institut Wohnen und Umwelt (IWU) (Publ.) (2003). Deutsche Gebäudetypologie – Systematik und Datensätze. Darmstadt, Germany, December 2003.

Jóhannesson G. and Schmidt D. (2001). Energi eller exergi – en kvalitetsfråga. *Miljöforskning*, Vol. 5, No. 6, pp. 20-21.

Keller B. (2007). Bauphysik - Wohin? Gedanken jenseits des Mainstreams. *Bauphysik*, Vol. 29, No. 3, pp. 260-264.

Rant Z. (1956). Exergie, ein neues Wort für „technische Arbeitsfähigkeit“. *Forschung auf dem Gebiet des Ing.-Wesens*, Vol. 22, No.1, pp. 36-37.

Rant Z. (1964). Thermodynamische Bewertung der Verluste bei technischen Energieumwandlungen. *Brennstoff-Wärme-Kraft*, Vol. 16, No. 9, pp. 453-457.

Schmidt D. (2001). What is this thing called Exergy? *IEA ECBCS Annex 37 LowEx News*, No. 2, pp. 1-2.

Schmidt D. (2004). Design of Low Exergy Buildings - Method and a Pre-Design Tool. *The International Journal of Low Energy and Sustainable Buildings*, Vol. 3, pp. 1-47.

Schmidt D. (2007). Low Exergy Systems for High Performance Buildings and Communities. In: *Proceedings Well Being Indoors CLIMA 2007 Conference*, June 10-14, 2007, Helsinki, Finland.

Schmidt D. and Shukuya M. (2005). Exergy: The Step Beyond the "Energy"- Conscious Design - a New Look at Sustainable Building. *Proceedings to the Sustainable Building Conference 2005*, September 27-29, 2005, Tokyo, Japan. Paper 01-068, 8 pages.

Schmidt D. and Ala-Juusela M. (2004). Low Exergy Systems for heating and Cooling of Buildings. *Proceedings to the 21st International Conference Passive and Low Energy Architecture*, September 19-22, 2004, Eindhoven, The Netherlands, pp. 151-156.

Schmidt D. and Shukuya M. (2003). New ways towards increased efficiency in the utilization of energy flows in buildings. *Proceedings to the Second International Building Physics Conference 2003*, September 14-18, 2003, Leuven, Belgium. pp. 671-681.

Schmidt D., Müller D. and Henning H.-M.(2006). Heating and Cooling with Advanced Low Exergy Systems. *Proceedings EPIC2006AIVC Conference*, November 20.-22., 2006, Lyon, France, pp. 307-312.

Concept for exergy balancing on community level for enhanced sustainable energy performance in a residential development in Kassel

Christina Sager, Dipl.-Ing.,
Fraunhofer Institute for Building Physics
Project Group Kassel
Gottschalkstrasse 28a
D-34127 Kassel
Christina.sager@ibp.fraunhofer.de www.ibp.fraunhofer.de

KEYWORDS: *energy performance, community planning, low exergy supply systems, energy efficiency in planning law.*

SUMMARY:
For the time being, energy efficiency is majorly focussed on the building physics and technical systems of single buildings. While the energy performance that can be achieved in the building is determined by aspects like technological feasibility, economical potential and individual know-how of planners, the realisation of efficiency potentials on a larger scale, such as at the community level, faces decisive additional obstacles mainly at the technological and judicial level. For most municipal planning authorities holistic energy planningon acommunity level is not a familiar task. Nevertheless, the potential for energy savings is significantly higher if several units and both supply and demand side are taken into account. Exergy balancing has the potential of making possible efficiency relationships between supply and demand sides visible and, thereby, calculable. In a pilot project in Kassel, this approach is being traced, using exergy analysis for the design of a low-energy, low-exergy housing estate in an existing community structure. The goal is to supply all buildings on the site with low-exergy energy sources by using the optimised energetic building design and optimised supply structure and the district heating return line. All planning aspects, from legal and economic to technological and communication aspects, are beeing covered in the pilot project. By this the project hopes to come to transferable results to support the municipal decision making process. The goal is to supply general guidelines for calculation procedures and design and communication strategies, and to clarify legal questions and boundary conditions for the development of similar projects. The project is currently at the very starting phase; nevertheless putting effort in the development of a holistic strategy is worthwhile.

1. Introduction

Due to the impending climate change and the growing scarcity of global resources, a growing effort must be made to conserve high quality, or primary, energy resources. One major sector of energy consumption is the existing building stock, where there is still huge potential to save energy. Nevertheless, the results of the recently finished ECBCS Annex 37 - Low Exergy Systems for Heating and Cooling of Buildings - show that there is equal or greater potential in exergy management. This implies working with the whole energy chain, taking into consideration the different quality levels of energy sources involved, from generation to final use, in order to significantly reduce the fraction of primary or high-grade energy used and thereby minimise exergy consumption. At the building level, new and advanced technology to reduce exergy consumption could be the focus of various research projects, both at the national and international level, as shown by Ala-Juusela et. al. (2004).

Leaving the scope of single buildings, a significant potential for higher energy efficiency can be found in the structure of settlements, communities and city districts. At this level, energy supply structures can be found at an extended level, such as in district and local heating systems, and within different profiles on the demand side. To extend the scope towards the energy and exergy flows at a community level, this issue has been addressed by ECBCS Annex 49 (2007) and the newly established ECBCS Annex 51 (2007), as well as by the newly established R&D programme of the German Federal Ministry of Economics and Technology BMWi (2007).

To transfer research results into the building practice, all of these programmes place strong emphasise on pilot projects and the monitoring of case studies. The following article focuses on the planning approach of a case

study part of the German R&D programme located in Kassel. The project is still at the very beginning of the building process. Typical obstacles to be encountered within urban planning processes as shaping of political commitment, difficult ownership structures of land and premises on noise protection and land use have struck the project to some extent. Therefore the paper will focus on the planning approach and the targeted goals of the R&D project.

2. Motivation for the project

The city of Kassel, situated in the centre of Germany, is aiming at carrying out an environmentally ambitious housing project within the coming years. The building site is situated on the estate of the former School for Horticulture of the University of Kassel in the city district of Oberzwehren. The buildings are to comply with high ecological standards to sensitise citizens for environmentally-friendly living in the city of Kassel.

The goal is to develop an ecological building estate with high urban and architectural quality and to make an innovative energy supply system possible. In the year 2005, the planning office of the city council held a kick-off workshop with eight architectural and two landscaping offices from Kassel. The workshop resulted in four alternative distinguished urban concepts that formed the basis for a structural concept.

The city of Kassel has devised the ecological goal of a CO_2-neutral energy supply as the overall concept for the project. The concept aims at:

- Optimising the CO_2-emissions caused by the heating and DHW energy demand by high energy efficiencies and the use of renewable energy sources to achieve a neutral CO_2-balance
- Reducing the overall material and energy flows over the life-cycle
- Realising the goals in an economic way and with reliable and commercially available technology

The project is meant to lead the way in adapting urban structures to changing climatic conditions.

3. The building site

3.1 Urban context

The building site is situated in the district of Oberzwehren in Kassel. It is bordered by access roads and private estates. To the north, a mixed-use area borders the site. To the north-west, there is a university campus, to the west, multi-family buildings, and to the south-west and east, single-family houses can be found. Floodplains from a small river can be found to the south. Bus and tram connections to the city centre exist.

On the agricultural sample area of the site, an ecological nursery was established in 2006. This is to remain. The new buildings will be developed in two separate areas, for which different urban and energetic solutions will be developed.

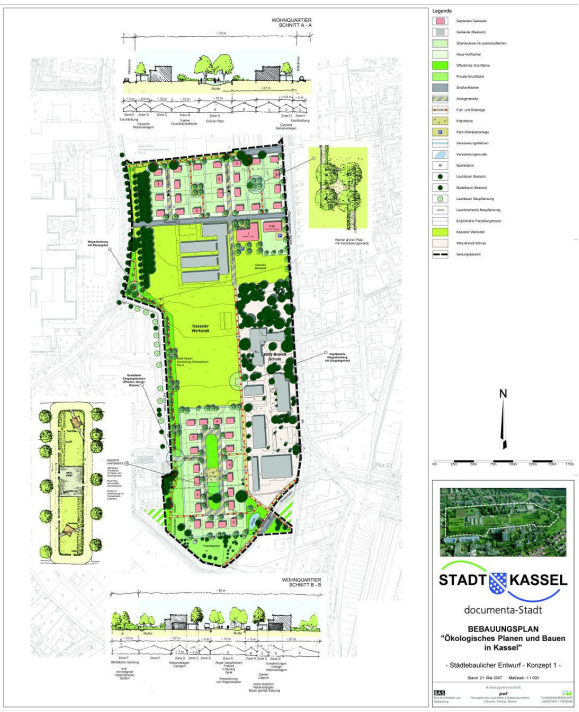

FIG. 1: Location of the building site [source: Google]. *FIG. 2: Basic concept for the estate development.*

3.2 Existing energy supply structure

In the northern area of the building site, the local utilities operate a district heating line that supplies the buildings of the existing eco-nursery and the Professional School for Horticulture. The southern area is at present not connected to the district heating net. Because of the long distances and the small connected loads to be expected with the buildings, the connection is not an economic option. For this area, alternative energy supply concepts have to be developed.

4. Energy concept

The overall goal of the building development is to achieve a neutral balance in CO_2-emissions caused by heating and domestic hot water production (DHW). This is to be realised by renewable energy sources and efficient building design. The heating demand and the use of renewable energy sources must be adjusted and optimised.

An efficient use of energy is the necessary premise for low CO_2-emissions. To use renewable energy sources for heating purposes, radiant heating systems are opportune because they use low supply temperatures. To reduce the heating demand, the insulation level of the buildings will be set to a level close to the passive house standard. This leads to a primary energy demand of about 40 kWh/(m^2a).

Currently, there are two different building concepts under discussion for the project. The basic concept contains single-family buildings and, as an alternative, a more condensed structure with row-houses. In order to reach an average energy demand for the further planning process, several standardised calculations based on the German Energy standards were made to come to the total heat demands and heat loads. With this data, the local utility suppliers were able to estimate the development costs for different energy supply structures.

FIG. 3: Building structure for the energy concept. In this case, both sites with single-family buildings.

The single-family buildings in the south amount to an approximate energy demand for heating of about 78 MWh per year, with an additional 42 MWh per year for DHW. For the more condensed structure of row-houses in the north, the heating demand sums up to about 87 MWh per year, the demand for DHW rises to about 79 MWh per year because of the larger number of units. The total energy demand adds up to approximately 165 MWh per year for heating and about 121 MWh for DHW.

TABLE. 1: Energy demand of the buildings in the two building sites, Otto (2007).

	Total area [m²] / units	Heat Demand [kWh]	Heat Load [kW]	Domestic Hot Water [kWh]
Building site - north	13,430 m²			
Row houses	37	87,045.5	40,984.1	78,591.7
Building site - south	11,414 m²			
Single-family buildings	20	78,400.0	45,120.0	42,482.0
Total (including public green areas and roads)	85,612 m²	165,445.5	86,104.1	121,073.7

The ideal orientation of the buildings for a small energy demand is always discussed during the first planning phases. Calculation results from thermal simulations show that the building orientation is of minor significance for the heating demand. This means that the useable solar contribution to the heating decreases with better building insulation. For an active solar energy use with photovoltaic and solar thermal collectors, the building orientation and lack of shading by trees and neighbouring buildings is an important factor. Since the city has set the zero CO_2 target the compensation of the remaining fossil demand by renewable electricity is an important issue. To achieve this goal the installation of PV will have to be a mandatory requirement for the future building owners. Since the planners regard the east-west orientation of a large number of buildings in the southern building site essential for the appearance of the urban space, the question of equal options for all future building owners has to be solved.

5. LowExergy approach

The topic of the research project associated with this building project is the development of a potential analysis for the building site in Oberzwehren in order to achieve an energy efficient and low exergy heat supply for the new buildings. The heat supply is to be achieved by low temperature heat and will be balanced on energy and exergy basis.

The use of energy will be connected to low temperature systems close to the room temperature, meaning that the supply will be very efficient, with minimal losses. Presently, usually high quality energy sources like oil and gas are used for the heating of buildings. Such sources produce high process temperatures and therefore contain a large exergy potential. This high potential is basically wasted by using these energy sources for heating purposes that generally only demand temperatures of up to 60°C. There are, however, renewable energy sources available in large quantities that supply energy at low or moderate temperatures, like solar energy and the heating and cooling potential of underground heat exchangers. These energy sources fit well to the demands of buildings and can be used cost-efficiently. To make use of these sources, the overall building system has to be adjusted to the low process temperatures. This leads to applying the LowExergy approach.

In the project, the heat supply for the new houses is based on the use and extension of the existing infrastructure. Since the targets were set at an early stage of the project, the possibilities of setting legal requirements in the development plan can be used on the buildings' side. The amendment of the German Building Code, BauGB (2004), the German building code, has brought some new options for setting targets for CO_2-reduction at the community level[i]. The question as to whether the general climate protection can be addressed by the development plan has not been legally clarified. The project in Oberzwehren shall provide some representative experience in this issue. The limited size, the "downtown" location of the building site (recycling of urban building sites and redensification) and the general questions addressed, make the project a good example of an initial case study.

Approach for Kassel-Oberzwehren

The requirements on the energetic standard of the buildings are to be set by definition in the development plan and by the contracts of sale of the premises. Further improvements concerning the energy efficiency shall be made during the building phase directly with the building owners, the authorities of the city of Kassel and the assigned planners and researchers. For the building site, an energetic standard is to be achieved that is significantly lower than the current legal requirements set by the energy conservation ordinance. The requirements include:

- Low energy demand for heating, good insulation and air-tightness
- Radiant heating systems like floor and wall heating, slab heating, capillary tube systems
- Solar energy systems for DHW
- Heat pumps
- Innovative approaches for Legionella-prevention in DHW storages by alternative techniques

In order to contribute to the discussion of upcoming climate change and possibilities of dealing with rising temperatures of extraordinary hot summer spells, the cooling of residential buildings is becoming a significant topic for the future. The cooling of residential buildings is not common in Germany today. Up until now, the use of air-conditioning systems for cooling has had to be avoided by recommendation of the Energy Conservation Ordinance. In order to prevent over-heating in summer, the reduction of window areas and the use of shading devices are the only means architects have been able to use. The new Energy Conservation Ordinance, EnEV (2007) allows the use of technical cooling devices under the precondition that the maximum primary energy demand is not exceeded. In the course of the project, the possibilities for exergetic efficient cooling strategies are being tested to gain a surplus quality factor for the new buildings. The use of underground heat exchangers in connection with the large area exchange systems is a promising approach.

The northern part of the building site offers the possibility of having a heat grid that is optimised according to the exergy demand by avoiding fossil fuel use. The existing district heating pipeline supplies several buildings with a large energy demand. The temperature level in the return line is high enough to supply heating energy for all the buildings planned in the northern area. The local utility providers have shown a large interest in the project, since the cooling of the overall return temperatures in the district heating grid rises the efficiency of the heating plants. Of course, the size of the building site in Oberzwehren is too small to produce a significant efficiency rise in the total system, but the utility suppliers expect important results from the monitoring of the project.

[i] The general climate protection was introduced into §1 para. 5 as a responsibility of town and country planning. In § 9 para. 1 No. 23, the definition of areas, where certain measures for the use of renewable energies, explicitly solar energy, may be defined mandatory, was added.

During the first steps, different supply strategies were defined to allow a comparison of the costs and the pros and cons of the alternatives. In the first approach, the entire building site was taken into consideration.

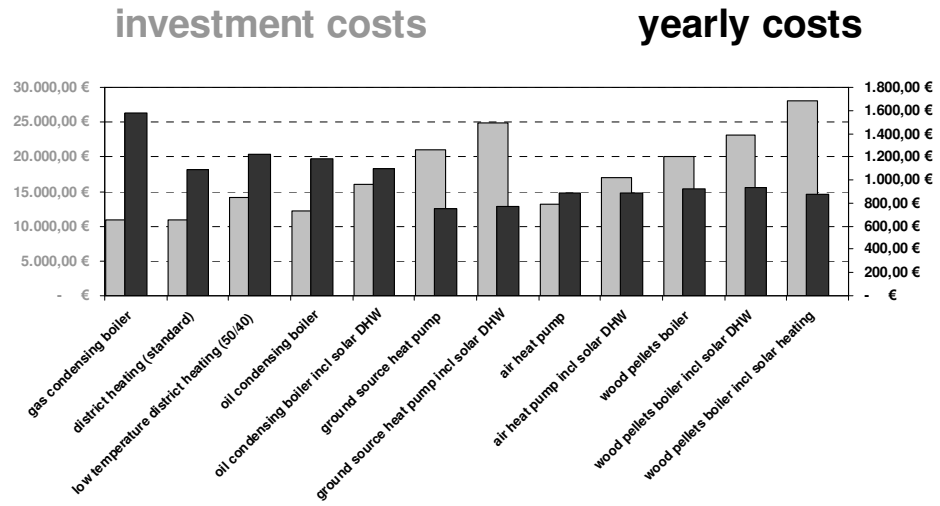

FIG. 4: Basic cost analysis for energy supply alternatives for the building site in Oberzwehren, Raatz (2007).

The calculations (Fig. 4) show that the low temperature district heating is still fairly expensive compared to standard solutions like gas or oil boilers and even a standard district heating grid. One reason for this is that the calculation is based on supplying both building sites in the north and in the south. In the southern part, there is no existing district heating grid, therefore the use of a low temperature return line would require a district heating pipe connection and the necessary infrastructure. Also, the yearly costs for the low temperature heating are based on the standard district heating prices. Currently, the local utility providers are discussing the possibilities of a reduced fare for the heat taken from the return line.

From the discussion of this first cost analysis, a more differentiated concept has been derived. The extension of the district heating grid to the southern area can not be realised on an economic basis. Nevertheless, the use of the return line of the district heating grid in the north ought to be traced in greater detail. The southern area will serve as a “renewable reference area”. The area shall be dedicated to single-family buildings with passive house standard. The energetic infrastructure may be limited to electricity only. Possible energy supply systems are heat pumps, thermal solar collectors and efficient ventilation systems with heat recovery. The different reference systems will be defined in the further course of the project. Because of the problems with respirable dust, the use of wood boilers shall be avoided, even though the CO_2-emissions (Fig. 5) appear to be very small using renewable fuels.

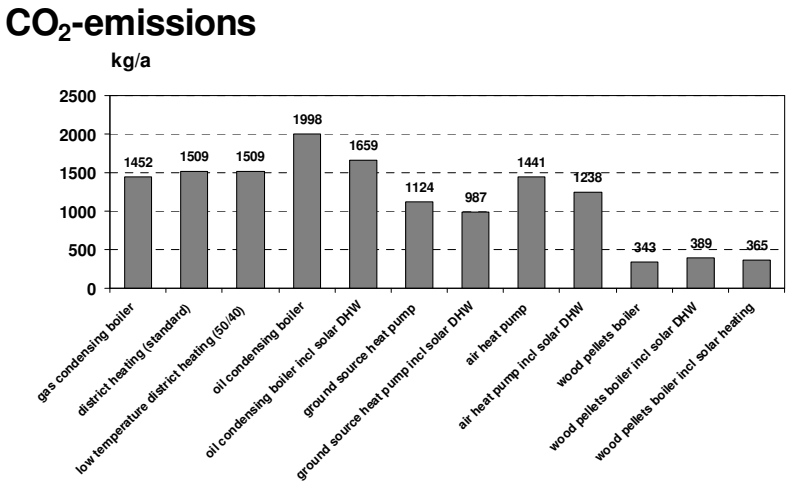

FIG. 5: CO_2-emissions of system alternatives based on GEMIS 4.4 data, GEMIS (2007).

In order to be able to balance the necessary energy for heating and DHW, a certain roof area must be dedicated to the installation of photovoltaic. The electricity produced by the photovoltaic panels will be fed into the network and substitute electricity from the conventional power plants. In this way, building owners will be able to balance the CO_2-emissions produced by their buildings. The calculations show that using the district heating concept the necessary PV-area can well be fitted on the available roof area (Fig. 6).

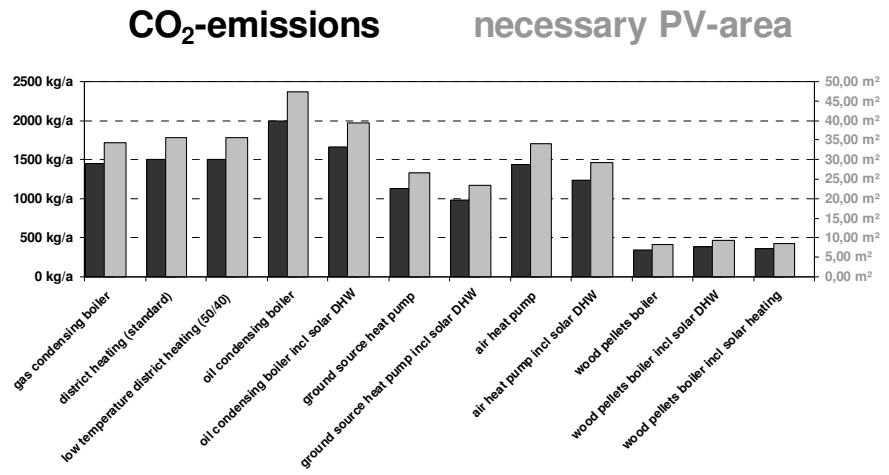

FIG. 6: Necessary PV-area to balance the CO_2-emissions of the system alternatives.

6. Conclusions

The project is still at the very beginning. The scenarios outlined within this article represent the current state of discussion. Within the next several weeks, the city council will have to decide on the further direction of the project and the project executing organisation will give the kick-off for the research project. Following this general decision, more detailed energy and exergy analysis and a more differentiated view on possible building types will clarify the full efficiency potential of the project. The assessment and rating of combined heat and power processes, with regard to the use of the district heating return line from an exergetic point of view, is ongoing. The aim is to come to a realistic view towards the efficiency potential of low temperature heating in a district heating grid, including the connected power plants. In the end, the realisation phase of the project will only succeed if the innovative approaches can be communicated to both decision makers in the council and future building owners. Among the technical obstacles to be overcome, this aspect will be of growing importance in the coming months.

7. References

Ala-Juusela M. (Ed.), Schmidt D. et. al. (2004). Heating and Cooling with Focus on Increased Energy Efficiency and Improved Comfort. Guidebook to IEA ECBCS Annex 37. *VTT Research notes 2256*, VTT Building and Transport, Espoo, Finland.

BauGB (2004). Baugesetzbuch (BauGB) vom 23.09.2004. *Deutscher Taschenbuch Verlag GmbH & Co. KG*, München 2007

BMWi (2007). Bundesministerium für Wirtschaft und Technologie (BMWi): „EnEff:Stadt"- Forschung für die energieffiziente Stadt; *Förderkonzept im Rahmen des 5. Energieforschungsprogramms der Bundesregierung; 28.09.2007*

ECBCS Annex 49 (2007). International Energy Agency - Low Exergy Systems for High-Performance Buildings and Communities – Annex 49. *Web Homepage, http://www.annex49.com/background.html*

ECBCS Annex 51 (2007). International Energy Agency - Energy Efficient Communities – Annex 51. *Web Homepage, http://www.ecbcs.org/annexes/annex51.htm*

EnEV (2007). Verordnung über energiesparenden Wärmeschutz und energiesparende Anlagentechnik bei Gebäuden (Energieeinsparverordnung – EnEV) vom 24.07.2007; *Bundegesetzblatt Jahrgang 2007 Teil I Nr. 34*

GEMIS (2007). Globales Emissions-Modell Integrierter Systeme (GEMIS); *Öko-Institut e.V.; Darmstadt,* May 2007

Otto F. (2007). Berechnungen Heizwärmebedarf Oberzwehren. Zentrum für Umweltbewusstes Bauen, *internal working document.*

Raatz A. (2008). Präsentation Umweltausschuss Stadt Kassel. deENet Kassel, *internal working document*.

Exergetic assessment and contribution of solar energy systems to the energy performance of buildings

Herena Torío, M.Sc.,
Fraunhofer Institute for Building Physics; Gottschalkstr. 28a, D-34127, Kassel (Germany)
herena.torio@ibp.fraunhofer.de; http:www.ibp.fraunhofer.de

Dietrich Schmidt, Dr.,
Fraunhofer Institute for Building Physics; Gottschalkstr. 28a, D-34127, Kassel (Germany)
dietrich.schmidt@ibp.fraunhofer.de; http:www.ibp.fraunhofer.de

KEYWORDS: *exergy analysis; built environment; solar energy; solar thermal systems; heating and cooling; energy and exergy efficiency.*

SUMMARY:
In the exergy assessment of direct solar systems, the conversion of solar radiation is typically included within the analysis. This approach leads to very high exergy losses in the solar conversion devices, which leads to an apparently wide optimisation potential in this part of the system. However, the conversion process from solar radiation into other energy sources is commonly not regarded for other energy sources (e.g. wood or geothermal heat). In consequence, physical inconsistencies arise between the analysis framework commonly used for direct solar system, and that used for the rest of energy sources, furthermore leading to misleading conclusions. In this paper futile conclusions obtained from the use of this commonly used framework for the optimization of direct solar systems will be shown. For this purpose, dynamic energy and exergy analyses have been performed on different configurations of a solar thermal system for the heating and cooling purposes of a hotel building.

Exergy analysis has been widely used for the optimisation and allocation of losses in energy systems. Similarly, it can be applied to the optimisation of energy processes in buildings. Exergy demands for the heating and cooling of buildings are low due to the low temperature levels required to supply these needs. Therefore, the use of low temperature environmental heat for supplying these demands allows an increase in the performance of the systems form an exergy perspective. The proposed framework allows for the recognition of the suitability of direct solar energy systems for covering exergy demands in buildings.

Furthermore, from the cases analysed, optimisation potential for the control and operation of solar thermal systems for the heating and cooling of buildings and thermally driven cooling machines could be recognised.

1. Introduction

Exergy is a thermodynamic magnitude defined as the maximum theoretical work obtainable from the interaction of a system with its environment as the equilibrium state is reached between both (Moran and Saphiro, 1998). Exergy analysis allows for the detection and quantification of the improving potential of complex energy systems (Ahern, 1980; Szargut, 2005) and has been widely used for the optimization of thermodynamic systems since the middle of the last century (Rant, 1964).

Most of the energy in the building sector is used for heating and cooling purposes, i.e. to maintain constant room temperatures within the range of 20°C to 26°C. Because of the low temperature level, the actual demand for exergy in space heating and cooling applications is low. In turn, solar radiation, just as fossil fuels or electricity, is undisputedly a high quality source, i.e. with high exergy content (Jeter, 1981; Petela 2003). Consequently, if the conversion of direct solar radiation into useful energy forms for the built environment (e.g. low-temperature heat) is taken into regard, high exergy losses arise. Apparently, it could then be concluded that direct solar energy based systems seem to be unsuitable, from an exergy perspective, for covering building energy demands.

To a great extent, thanks to the fact that solar radiation is a high quality energy source, many of the energy processes and energy interactions on earth are possible (Dincer and Rosen, 2007). For then, its degradation into low quality energy forms is allowed. Exergy losses resulting from the conversion of solar radiation into other so-called energy sources, e.g. fossil fuels or ground-source heat, also occur, similarly as those which occur in direct

solar systems, but they are usually disregarded in the analysis of the systems. For instance, if a building with a boiler is analysed, the wood or fossil fuel burned into the boiler is directly considered as the input into the energy system. Yet, the prior conversion from solar radiation into those energy carriers, wood or fossil fuel, is commonly not taken into consideration.

In consequence, if the conversion of solar radiation is only regarded for the analysis of direct solar systems, physical inconsistencies arise as compared to any other energy systems analysis. Furthermore, including the conversion of solar radiation only in the evaluation of direct solar systems may lead to misleading and irrelevant conclusions, as it will be shown in this paper.

1.1 Boundaries for analysis of direct solar energy systems

Several researchers have used the exergy method as a tool for optimising the performance of active solar systems for building applications. Most of the studies using this approach also include the conversion of solar radiation into low-temperature heat or electricity in the analysis (Bejan, 1982; Izquierdo et al., 1996; Luminosu and Fara, 2005; Gunerhan and Hepbasli, 2007; Xiaowu and Ben, 2005; Cervantes and Torres-Reyes, 2002). In consequence, the greatest exergy losses in the systems occur in the solar collector field, as it is there that the degradation of high quality solar radiation into other energy forms takes place. Following this approach, an optimisation of direct solar systems is necessarily aimed at increasing the exergy output from the direct solar systems, so as to reduce the exergy losses in this system component.

Furthermore, as mentioned in the previous section, including the conversion of solar radiation into other energy forms in the analysis of systems which make a direct use of it (i.e. direct solar systems) is physically inconsistent with the analysis used for the assessment of all other energy sources.

In order to be consistent with the analysis of other energy sources, the conversion of solar radiation in direct-solar systems must be left out of the energy and exergy analysis. The present paper shows results from energy and exergy analyses of several solar thermal systems for the heating and cooling of a building using this approach, i.e. without regarding the conversion of solar radiation into low-temperature heat. This approach was also used by Sandnes (2003). In consequence, the heat output from the collector field, and not solar radiation incident on the collector area, is considered as the very first energy and exergy input into the building heating and cooling system. In the following, this approach will be referred to as “physical-viewpoint boundary”. For completeness, the same system will also be analysed with the conventional assessment approach, i.e. regarding solar radiation as input into the energy system, which in the following will be referred to as “technical-viewpoint boundary”.

2. Description of the systems analysed

The building object chosen for analysis has been taken from the building models developed within IEA SHC Task 25 (Henning, 2003). It corresponds to the hotel building located in Freiburg (Germany). The building is defined as a free-standing six storey building, oriented along its west-east axis. Glazed surfaces amount to 25% of the north and south facades and 4% of the east and west facades. U-values for the external enclosing surfaces of the building are within the range of 0.35 W/m^2K for external walls and ground floor and 0.17 W/m^2K for the roof, thus representing a well-insulated building. Further details on the occupancy profiles and constructive details of the defined external building elements can be found in (Henning, 2003). Energy loads were calculated only for the fourth floor of the building, with a surface of 642.60 m^2 (including areas covered by internal walls). Infiltration rate was regarded as 0.5 h^{-1}. Minimum and maximum comfort temperatures, determining the heating and cooling demands were set to 22°C and 26°C respectively.

A solar thermal system with fossil-fuel based back up burner was considered to cover the heating and cooling demands of the building. A thermally driven absorption cooling machine, using the thermal energy output from the solar system as the driving input, supplies chilled water for covering the cooling loads.

In all cases studied, the solar collector field, consisting of 100 or 50 m^2 flat plate solar collectors, was oriented directly to the south, i.e. with an azimuth of 180°, and an inclination angle over horizontal surface of 45°. A hot water tank of 12 m^3 with 4 m height (6 m^3 in case 2) was regarded as storage for the solar system. The backup ratio from the fossil-fuelled burner was regarded as 100%. The main characteristics of the regarded systems are listed in Table 1.

In order to check the impact of the outlet temperature from the collector field as a control variable, and its influence on the exergy losses throughout all the components of the building system, two different setpoint outlet temperatures from the collector field were investigated: in cases I, II and IV constant outlet temperatures of 80°C was regarded; in turn, in case III an outlet temperature of 55°C was regarded for the heating mode and 75°C was regarded as collector outlet temperature and driving generation temperature for the cooling machine. These temperatures were set constant throughout the whole year, and therefore 80°C and 75°C were also used as the driving temperature for the absorption cooling machine in cases I, II, IV and III respectively. In case II the lower driving temperature regarded causes also a reduction in the nominal cooling power that can be delivered by the cooling machine.

TABLE. 1: Brief description of the building systems regarded in the cases analysed.

Cases	I	II	III	IV(*)
Components	Solar thermal syst. ($100m^2$)+fossil burner;	Solar thermal syst. ($50m^2$)+fossil burner;	Solar thermal syst. ($100m^2$)+fossil burner;	Solar thermal syst. ($100m^2$)+fossil burner;
	Stationary water-based heating 80/60°C;	Stationary water-based heating 80/60°C;	Stationary water-based heating 55/45°C;	Stationary air-based heating 80°C;
	Stationary water-based cooling unit 16/20°C;	Stationary water-based cooling unit 16/20°C;	Stationary water-based cooling unit 16/20°C;	Stationary air-based cooling unit 16°C;
	Absorption cooling machine Wegra15 (20kW)	Absorption cooling machine Wegra15 (20kW)	Absorption cooling machine Wegra15 (17kW)	Absorption cooling machine Wegra15 (18kW)
				VAV(**) Balanced ventilation unit with heat recovery (η=0.8)

(*)In the case of an air-based system for heating and cooling purposes (case IV), the temperatures shown correspond to inlet and outlet temperatures of the water to air heating and cooling coils; (**) VAV stands for variable air volume.

2.1 Method for energy analysis

Dynamic energy simulations of the building systems under analysis were carried out using the SolAC programme, which is the design tool developed within IEA SHC Task 25. In this simulation tool, the load of the building is regarded as a fixed input, and no backward calculation of the interaction from insufficient capacity of the building systems chosen is performed. In other words, the tool performs a dynamic analysis of the building systems, without taking into consideration any interaction with the indoor climate, defined as input by the building load.

Analysis of the exergy flows on the systems was performed following a quasi-steady state approach on an hourly basis, using the data for the energy flows and temperatures from the dynamic energy simulation of the system as input. The modular approach described in (Schmidt, 2004) was used. However, for simplicity, the building systems as a whole, i.e. solar thermal system and absorption cooling machine, were regarded as one single module called “generation”. Therefore, the exergy and energy losses in the individual components of the solar storage tank, the generator and evaporator of the cooling machine, and pumps for running the systems were not regarded individually but on a global basis, using an input-output approach. For this purpose, all exergy inputs into the building systems, i.e. solar energy from collector field, energy input into the cooling tower of the cooling machine, and auxiliary electrical energy required for the operation the systems, were calculated for each hourly time step. Similarly, the exergy outputs, i.e. exergy delivered to the heating or cooling units in the building, were calculated for each time step. The difference between both (input-output) represents subsequently the whole exergy losses in the so-called “generation” module. Figure 1 shows the hydraulic schema of the building systems considered and the components encompassed within the generation module.

Cooling tower for the operation of the thermally driven cooling cycle is modelled as an open cycle wet cooling tower, where ambient air is regarded as the cooling medium. Desired outlet temperature of the cooled water was set at 27°C.

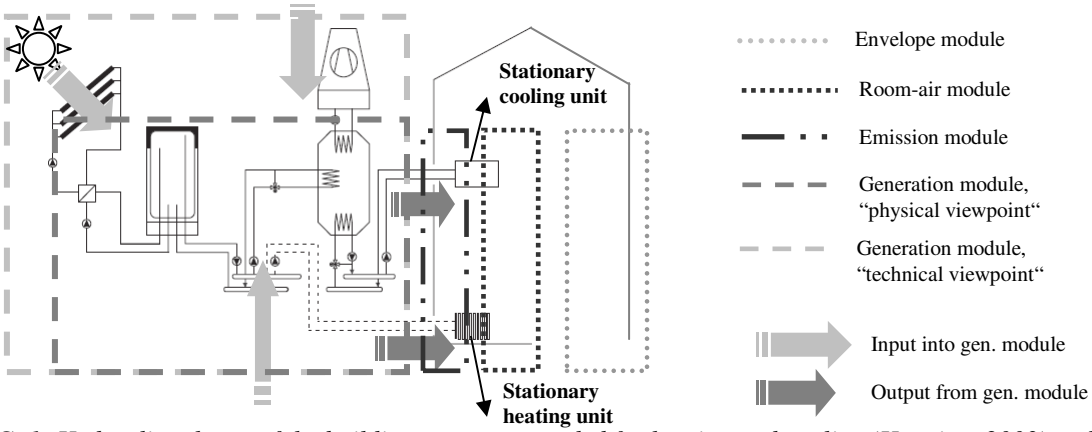

FIG. 1: Hydraulic schema of the building systems regarded for heating and cooling (Henning, 2003) and boundaries defining the modules for exergy analysis.

Simplified control strategies investigated here for the solar system consist on a constant outlet collector temperature, substantially limiting achievable solar output. Control strategies with variable outlet temperature need to be investigated in order to get a more realistic view of the influence of different space heating systems on the solar yield.

2.2 Method for exergy analysis

One of the main aims of this paper is to compare the "technical-viewpoint" and "physical-viewpoint" based approaches for the evaluation of direct solar energy systems. As shown in Figure 1, the main difference between the two methods is the consideration of the solar thermal energy from the collector field: in the "technical-viewpoint" approach solar radiation onto collector surface is regarded as energy and exergy input into the generation module. In turn, in the "physical-viewpoint" approach, the thermal energy output from the collector field is regarded as first energy and exergy input into the generation module. Obviously, the energy efficiency of the solar collectors is also implicitly taken into regard in this latter approach, for it ultimately determines the energy yield from the collector field.

For calculating the exergy of incident solar radiation onto the collector field, I_{sun}, the approach from Jeter (1981) is used (see equation 1). The sun temperature, T_{sun}, was assumed to be 6000 K (Sandnes, 2003). In turn, the exergy of thermal energy output from the collector field is evaluated according to equation 2. Since the inlet temperature into the collector field could not be obtained as output from the dynamic energy simulations with SolAC, a temperature difference of 10 K between the inlet and outlet of the collector field was assumed.

$$Ex_{solar,rad} = I_{sun} \cdot \left[1 - \frac{T_0}{T_{sun}}\right] \qquad (1)$$

$$Ex_{solar,th} = \frac{Q_{solar}}{(T_{inlet} - T_{outlet})}\left[(T_{inlet} - T_{outlet}) - T_0 \ln \frac{T_{inlet}}{T_{outlet}}\right] \qquad (2)$$

3. Results

In Table 2, the main figures for characterising the energy performance of all cases under analysis are shown. Typical solar fractions for cooling and heating are usually usually within the range of 60-80% and 10-20% for German climatic conditions, indicating that the configuration chosen here for analysis represents a rather small solar system. In the four cases analysed, the collector type, orientation and inclination of the solar collector field were the same. Following, for a given demand and setpoint outlet collector temperature (80°C in cases I, II and IV) the gross efficiency of the collector field, representing the ratio among the energy yield from the solar collectors and the solar radiation incident on them, is also the same. In turn, in case II the setpoint for the collector outlet is reduced (55/75°C for heating and cooling respectively) allowing a higher net energy output from collector field and rising also its gross efficiency significantly. In case III, the COP of the cooling machine is reduced due to the lower driving temperature for the generator of the cooling cycle.

TABLE. 2: Main figures for characterising the energy performance of the solar system configurations chosen.

	Symbol	I	II	III	IV
Annual gross coll. efficiency	η_{gross}	9.8%	9.6%	18.7%	10.0%
Solar fraction cooling	$SF_{cooling}$	49.1%	25.4%	62.5%	68.2%
Solar fraction heating	$SF_{heating}$	14.2%	7.7%	36.7%	13.0%
COP thermal cooling machine	$COP_{thermal}$	0.88	0.88	0.85	0.82

3.1 Approaches for exergy and energy analysis

Figure 2 shows the energy and exergy flows through the modules considered (generation, emission, room-air and envelope) for cases I and II using the "physical-viewpoint" boundary, i.e. the approach proposed in this paper. In turn, in Figure 3, results are shown for the same cases obtained using the "technical-viewpoint" boundary.

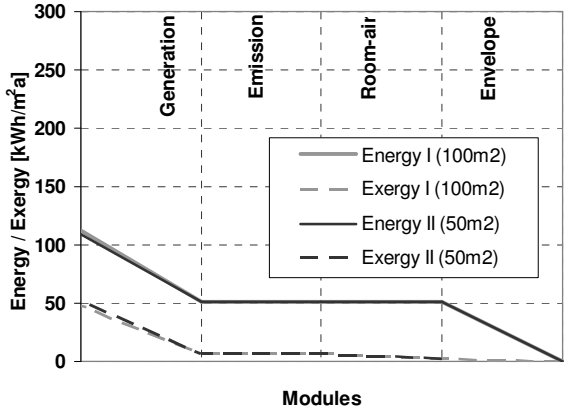

FIG. 2: Energy and exergy flows for cases I and II following the "physical-viewpoint" approach

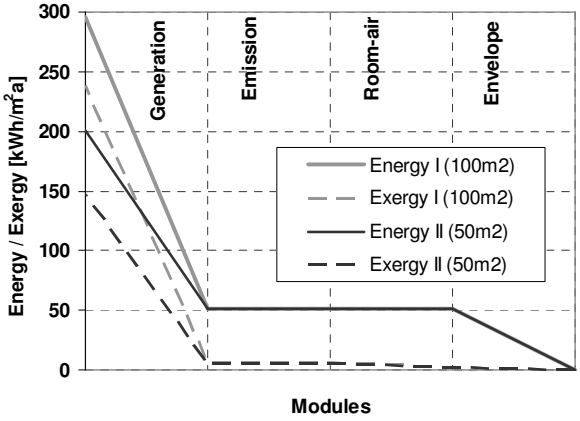

FIG. 3: Energy and exergy flows for cases I and II following the "technical-viewpoint" approach

Following the "technical-viewpoint"-based approach, a very high exergy input is required for the operation of the building systems chosen, namely solar radiation onto collector area, as it is a high quality energy source. Subsequently, very high exergy losses arise in the generation module.

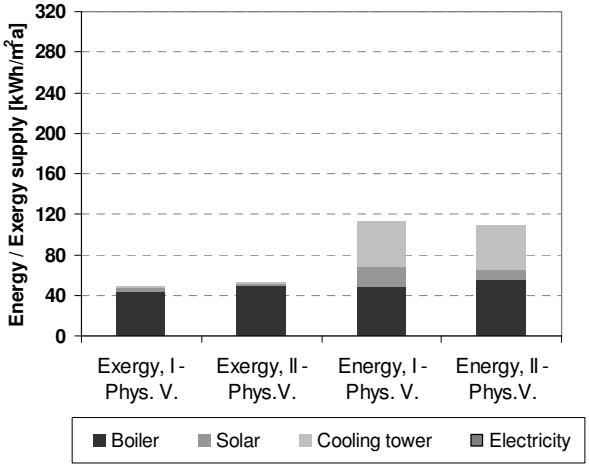

FIG. 4: Energy and exergy inputs to the generation module in cases I and II following the "physical-viewpoint" approach

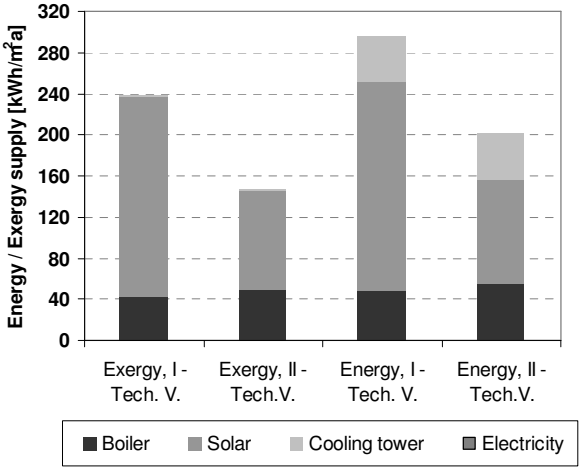

FIG. 5: Energy and exergy inputs to the generation module in cases I and II following the "technical-viewpoint" approach

As can be seen in Figure 5, if incident solar radiation is included in the analysis, the main input, both in energy and exergy terms, comes from the solar thermal system. In consequence, most of the energy and exergy losses are derived from the conversion of solar radiation into heat in the collector area. Thus, in order to optimise the system, the energy and exergy performance of the collector needs to be increased in the first place. However, for a given collector area, the exergy input following the "technical-viewpoint" approach is constant, since the area directly determines the amount of solar radiation incident onto the given surface. As a result, reducing the collector area by half, 50m^2 (case II), significantly reduces the energy and exergy losses in the generation module, as shown in Figure 3. In other words, according to this approach, reducing the solar fraction and increasing the percentage of demand covered by the boiler would optimise the performance of the system.

In turn, energy input from solar thermal system is insignificant in exergy terms if the "physical-viewpoint" approach is used (Fig. 4). Thus, with the "physical-viewpoint" based approach, reducing the collector surface does not reduce the total energy input, but increases the total exergy input and exergy losses by about 6% in the generation module. Thus, this approach allows for the conclussion that substituting high quality fossil fuels with low-temperature environmental solar heat represents an optimised strategy from an exergy perspective, enabling to show the better matching achieved between the quality levels of supply and demand.

3.2 Comparison of different systems

Both cases I and III have the same water-based building components for heating and cooling, and accordingly, energy demands (i.e. input) into the emission module are the same. However, due to the different temperature level required for the operation of the water heaters (80/60°C in case I, and 55/45°C in case III), exergy demands of this module are slightly lower for case III: exergy demands for the emission system amount to 6.80 kWh/m^{2}a in case I and 5.22 kWh/m^{2}a in case III.

The use of lower driving temperatures for the operation of the cooling machine (75°C) reduces the COP of the absorption machine. On the other hand, reducing the setpoint for the outlet temperature of the collector field allows increasing the solar yield. Thus, the decrease in the COP of the cooling machine can be compensated by the increased yield of solar low temperature heat. As a result, the total energy required as input in case III is 12% higher than in case I, but in exergy terms the total input required is 10% lower.

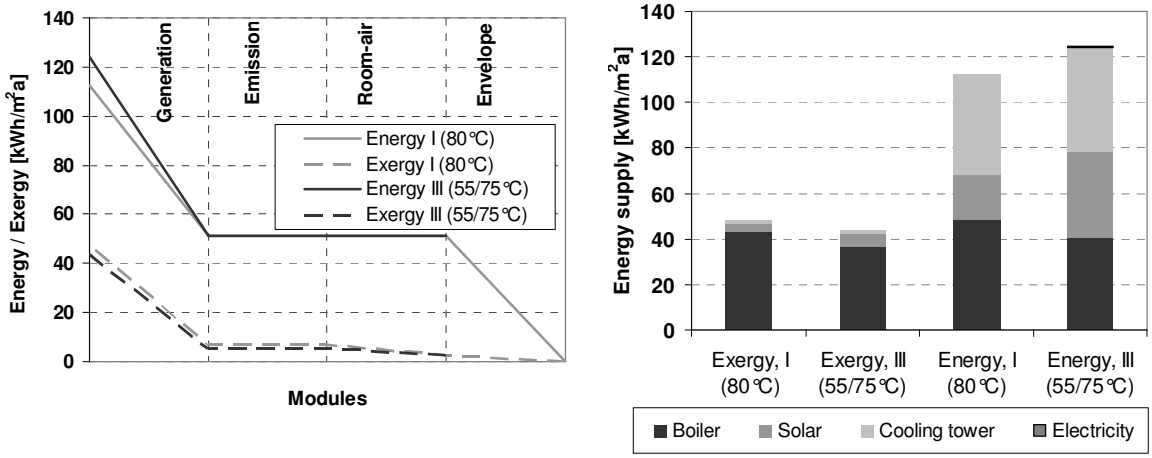

(a) (b)

FIG. 6: a) Energy and exergy flows for cases I and III; b) Energy and exergy inputs into the generation module for cases I and III. All results in the figure correspond to the "physical-viewpoint" approach.

In Figure 7, results from the energy and exergy flows throughout the modules for cases I and IV are shown. The use of an air-based system increases significantly the necessary air exchange, which for climatic conditions in Freiburg causes a reduction of almost 50% in the cooling loads. This causes, in turn, an increase of 30% in the heating loads, despite the heat recovery unit. Energy recovered by the heat exchanger in the balanced ventilation unit, mainly during heating conditions, can be seen in Figure 7b. It represents a significant energy input that otherwise had to be covered with the boiler and solar thermal system. Yet its exergy content is almost negligible.

Input into the room-air in case IV occurs in the form of heated (32°C) or cooled (18°C) air, which again reduces the exergy demands for these modules as compared to case I where the exergy input in the room-air occurs via heat transfer from the heater or chiller surfaces (at effective temperatures[i] of around 75°C and 19°C for heating and cooling respectively).

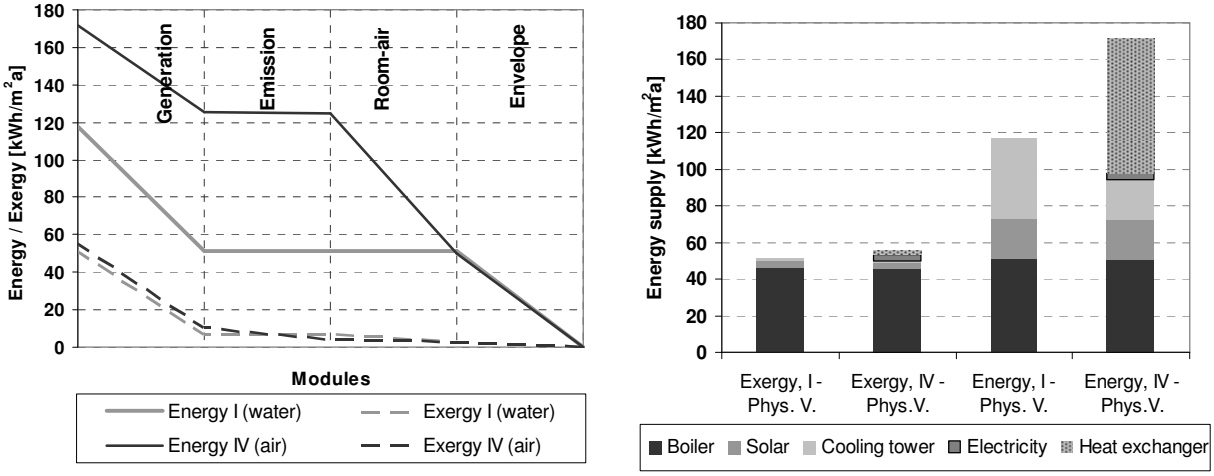

(a) (b)

FIG. 7: a) Energy and exergy flows for cases I and IV; b) Energy and exergy inputs into the generation module for cases I and IV. All results in the figure correspond to the "physical-viewpoint" approach.

To characterise the energy and exergy performance of the systems, energy and exergy efficiencies have been calculated for each case. These efficiencies are calculated as the ratio between the energy or exergy input into the generation module (i.e. in the building system) and the energy or exergy demanded by the envelope module (i.e. heating and cooling loads for each case, in energy and exergy terms respectively).

TABLE. 3: Main figures for characterising the energy performance of the solar system configurations chosen.

	Symbol	I	II	III	IV
Energy efficiency [%]	η_{system}	45.3	46.8	41.1	33.1
Exergy efficiency [%]	ψ_{system}	5.2	4.8	5.8	5.2

4. Conclusions

Including the conversion of solar radiation in the evaluation of direct-solar systems (i.e. "technical-viewpoint" boundary) leads to extremely high exergy losses in the direct solar systems. Subsequently, the optimisation of these systems should be oriented so as to reduce the magnitude of exergy losses in the conversion device. However, trying to optimise solar systems in this direction may lead to wrong or misleading conclusions, as shown in section 3.1, where the system seems to be optimised when the solar fraction and collector surfaces are reduced. These results arise from the physical inconsistencies behind the definition of this "technical-viewpoint" based boundary. In turn, the approach proposed in this paper, the "physical-viewpoint" boundary, regards the same physical processes for direct solar systems as any other energy system, thus avoiding such misleading conclusions and representing a common basis, anchored on physical considerations, for comparing direct and indirect-solar energy systems.

Increasing the solar fraction of the systems regarded, i.e. increasing the part of energy or exergy demands being covered by low-temperature solar thermal energy increases the exergy performance of the system. In turn, energy efficiencies (including all energy inputs) for the systems analysed do not show the same behaviour.

[i] Effective temperatures for the heat transfer are calculated for each timestep by adding the logarithmic mean temperature difference (LMTD) to the room air temperature.

Reducing the setpoint for temperature outlet of the solar thermal system (case III) and using heating systems with lower desing temperatures, increases the exergy efficiency of the building systems. Therefore space heating systems with the lowest possible temperature level and reducing the outlet temperature of the collector field to the minimum level required for covering the heating or cooling loads are of advantage. Yet control strategies investigated here represent a worst-case scenario. Control modes based on variable outlet temperatures should be investigated to obtain more realistic picture on the influence of this parameters. Driving temperatures further below 75°C might also allow a better solar energy yield for cooling operation, but will also reduce the performance of the cooling machine. Therefore, further research is required in order to reduce driving temperatures for these devices and similar analysis should be carried out to determine their optimal operation point.

5. Acknoledgement

The authors warmly thank the German Federal Fundation for Environment and the German Federal Ministry of Economy and Technology for their financial support.

6. References

Ahern J. (1980). The Exergy Method of Energy System Analysis. *Wiley Interscience Publication*, John Wiley and Sons, New York.

Bejan A. (1982). Extraction from exergy from solar collectors under time-varying conditions. International *Journal of Heat and Fluid Flow*, 3 (2), pp. 67-72.

Cervantes J.G. and Torres-Reyes E. (2002). Experiments on a solar-assisted heat pump and an exergy analysis of the system. *Applied Thermal Engineering*, 22, pp.1289-1297.

Dincer I. and Rosen M. (2007). Exergy: Energy, Environment and Sustainable Development. First Edition, *Elsevier Scientific Publications*, USA.

Gunerhan H. and Hepbasli A. (2007). Exergetic modelling and performance evaluation of solar water heating systems for building applications. *Energy and Buildings*, 39 (5), pp.509-516.

Henning H.M. (2003). Solar-Assisted Air-Conditioning in Buildings – A Handbook for Planners. Springer *Wien-New York Verlag*, Austria.

Izquierdo Millan M. et al. (1996). Available solar exergy in absorption cooling process. *Solar Energy*, 56 (6), pp. 505-511.

Jeter S.M. (1981). Maximum conversion efficiency for the utilization of direct solar radiation. *Solar Energy,* 26 (No. 3), pp. 231–236.

Luminosu I., Fara L. (2005). Determination of the optimal operation mode of a flat solar collector by exergetic analysis and numerical simulation. *Energy*, 30, pp. 731-747.

Moran M.J. and Shapiro H.N. (1998). Fundamentals of Engineering Thermodynamics. 3rd Edition, *John Wiley & Sons*, New York, USA.

Petela R. (2003). Exergy of undiluted thermal radiation. *Solar Energy,* Vol. 74, pp. 469-488.

Rant Z. (1964). Thermodynamische Bewertung der Verluste bei technischen Energieumwandlungen, *Brennstoff-Wrme-Kraft*, 16 Nr. 9, pp. 453-457.

Sandnes B. (2003). Energy efficient production, storage and distribution of solar energy. Doctoral Thesis, *University of Oslo,* Norway.

Schmidt, D. (2004). Design of Low Exergy Buildings – Method and Pre-design Tool. *The International Journal of Low Energy and Sustainable Buildings,* Vol. 3, pp. 1-47.

Szargut J. (2005). Exergy Method - Technical and ecological applications. *WIT Press*, Southampton, United Kingdom.

Xiaowu W., Ben H. (2005). Exergy analysis of domestic-scale solar water heaters. *Renewable and Sustainable Energy Reviews,* 9, pp. 638-645.

Exergy Consumption for Heating in Retrofitted Detached Houses

F. Kalmár, assoc. prof.,
University of Debrecen, Faculty of Engineering, Department of Building Services;
fkalmar@mfk.unideb.hu

T. Kalmár, assist. prof.,
University of Debrecen, Faculty of Engineering, Department of Building Services;
kalmar_tk@mfk.unideb.hu

KEYWORDS: energy, exergy, refurbishment, low temperature, surface heating.

SUMMARY:
In Hungary from the total energy consumption of the country the building sector, with its 32%, is the biggest energy consumer. In 2006 based on the EU Directive new energy requirements were established for residential, office and educational buildings. In Hungary there are 4 millions of households and more than 50% are placed in detached houses. In the last years different national programs were started in order to encourage the owners to refurbish their buildings. Reducing the heat demand of the building according to the new requirements the supplied heat amount might be reduced considerably. Having a central heating system with certain heat output of the boiler, certain dimensions of pipes and pumps, the adjustment might be done decreasing the supply temperature. But in this case the exergy consumption of these heating systems might be reduced too. This paper presents the analysis of the refurbishment effects on the heat demand and energy consumption of detached houses built in different periods of time from different materials. Taking into consideration the initial state of the building and heating system, the exergy savings are between 69-82.9% for SD brick and 78.7-88.1% for B30 building.

1. Introduction

Reduction of energy consumption is one of the main purposes in European countries taking into account that the main energy carriers, natural gas and oil, are imported in a proportion of ca. 60% and 80% respectively (Mantzos, 2003). Energy consumption in the building sector represents nearly 40% from the total energy consumption. In this context, according to Directive 2002/91/EC, new national standards/regulations are introduced in order to force people to build energy efficient buildings. The energy saving interventions has to be done improving the thermal comfort level of these buildings. In Hungary from the total number of households more than 50% are placed in houses. The structure of the external envelope of these houses is various. The mean U value of the envelope is higher than 1.3 W/m^{2}K at more than 78% of houses. In this context thermal rehabilitation of these buildings is sorely needed taking into account that the expected lifetime is more than 30 years at 72% of houses.

Improving the thermal resistance of the building envelope not only the heat losses in the winter, but also the heat gains in the summer are reduced (Kalmár and Csiha, 2006). So, the better indoor thermal comfort is obtained as a side-effect of the additional thermal insulation of the building envelope (Zöld, 2000). In houses the situation is critical both from energy and thermal comfort point of view. In the last years more and more houses were equipped with central heating systems using mainly natural gas as fuel. In this way at least the heating system may have acceptable efficiency. The new houses are built especially from brick with vertical cavities, but the spread of light-frame structures utilisation may be also observed. At light-frame construction the external building elements consist by 14…16 cm mineral wool between two wood panels. The heat transfer coefficient of these elements is lower than 0.45 W/m^{2}K. At light structures values around 0.22 W/m^{2}K are obtained. In this way at these buildings the energy consumption for heating is significantly lesser than at old houses.

Beside the energy quantity consumed in buildings it is important to see which the quality of the energy used is for heating and cooling (Schmidt,2004). This is given by the exergy content of energy. The exergy need depends on the energy demand and the mean operation temperature. The low is the mean operation temperature the low the exergy need will be. As a consequence, having an energy quantity, surface heating will give better results from exergy point of view (Olesen, 2007). The existing central heating systems were designed for a temperature drop 90/70 ^{o}C until 1990. In the last years having houses with better physical properties of the envelope the

supply return temperatures used are 75/55 °C. The floor and wall heating is used too, but having high heat demand of the rooms these can be used only in combination with radiator heating.

In the followings detached houses with similar geometrical properties but different structures of the envelope will be anylysed both from energy and exergy point of view before and after refurbishing taking into account the new energy requirements.

2. Energy consumption for heating

The heat demand of a building can be determined in function of heat loss coefficient *K* and the difference between indoor and outdoor design temperatures:

$$Q = K(t_{i0} - t_{e0}) \tag{1}$$

The energy need for heating can be calculated, taking into account the specific degree-day curve, based on the following equation:

$$E = K\int_0^N (t_i - \bar{t}_e)\,dx \tag{2}$$

where: $\bar{t}_e$ is the daily mean outdoor temperature; N – is the number of days in a heating season.

Describing the degree day curve, specific for Budapest, with a function:

$$\bar{t}_e = -15 + 3.55x^{0,3835} \tag{3}$$

the number of days in a heating period could be easily determined, if the balance point temperature of the building (t_b) is known:

$$N = \left(\frac{t_b - t_{e0}}{3.55}\right)^{2.6} \tag{4}$$

The balance point temperature represents that external temperature according to which the heat losses of the building are equal to the heat gains (the heat capacity and time constant of the building is taken into account):

$$t_b = t_i - \frac{Q_s + Q_i}{K} - 2 \tag{5}$$

where: Q_s are the solar gains, [W]; Q_i – internal gains, [W].

Solving the equation (2) taking into account the equation (3), (4) and (5), results the energy demand for a heating season in kWh:

$$E = 0.024K\left(\frac{t_i - t_{e0} - \frac{Q_s + Q_i}{K}}{3.55}\right)^{2.6}\left[(t_i - t_{e0}) - 2.566\left(\frac{t_i - t_{e0} - \frac{Q_s + Q_i}{K}}{3.55}\right)\right] \tag{6}$$

Assuming the indoor temperature equal to 20 °C, using the design values according to existing standard for external temperature, heat gains and ACH the following values were obtained for the analysed buildings:

TABLE. 1: Data related to energy consumption before refurbishment.

Building	t_b, [°C]	N	E, [kWh]	η_s, [%]	E_c, [kWh]	Gas consumption, [m^3]
SD brick	12,71	209	31262,1	80	39077,64	4142
B30	14,22	240	46641,3	80	58301,63	6170
Light	8,01	129	12521,1	90	13912,31	1474

If the old buildings envelope is refurbished according to the new requirements, the energy consumption will decrease significantly. The replaced or refurbished building elements have the heat transfer coefficient lower or equal to the requirement. The SD brick walls were provided with an additional insulation of 8 cm expanded polysteryne, the B30 structure needs an additional insulation layer of 10 cm polysteryne.

Having now almost the same thermal characteristics of the envelope the heating system output in the retrofitted buildings will be the same. Using the equations (4) – (6) the energy consumption data can be determined after refurbishment. These data are presented on Table 2.

TABLE. 5: Data related to energy consumption after refurbishment.

Building	t_b, [°C]	N	E, [kWh]	η_s, [%]	E_c, [kWh]	Gas consumption, [m^3]
SD brick	9.08	145	15398.34	94	16381.21	1846.81
B30	9.06	145	15373.48	94	16354.76	1843.83

As it can be seen the reduction of energy consumption is around 58% for SD brick and 72% for B30.

3. Exergy consumption for heating

Exergy is the quality of energy, the maximum work that can be obtained from an energy flow. Having a given quantity of energy the exergy content can be calculated with the following relation:

$$Ex = E\left(1-\frac{T_0}{T}\right) \tag{7}$$

where: T is the operation temperature, [K]; T_0 – is the reference temperature, [K]

The reference temperature in our case can be assumed to be the outdoor temperature, because the room or the heat carrier will cool down to this temperature if no energy/exergy source is taken into consideration (Halász and Kalmár, 2007). As a consequence the reference temperature values are given by the degree-day curve. At the same value of the external mean temperature the exergy need of the room, heating system and boiler are different because the operation temperature of these subsystems is different. For all these subsystems the exergy efficiency can be defined:

$$\nu^x = \frac{needed\ exergy}{consumed\ exergy} = 1-\frac{exergy\ losses}{consumed\ exergy} \tag{8}$$

In the room the temperature T can be assumed to be constant. The temperature T for radiators and distribution is given by the control curve. At the boiler the exergy content of the burned gas is given by:

$$Ex = \dot{m}_{gas} H_0 \tag{9}$$

where: H_0- represents the upper heating value of the fuel; $\dot{m}_{gas}$ - represents the mass flow of the fuel.

If the heat source is a heat pump then the exergy consumed will be equal to the electrical energy consumption.

The yearly exergy consumption for analysed buildings before refurbishment is shown in Figure1. The exergy efficieny for different subsystems is presented in Table 3.

TABLE. 3: Exergy efficiency before refurbishment.

Building	Heating system	Boiler
SD brick	0.384	0.119
B30	0.374	0.117
Light	0.477	0.109

The supply and return temperature values are 90/70 °C for SD brick and B30, and 70/50 °C for light structure building.

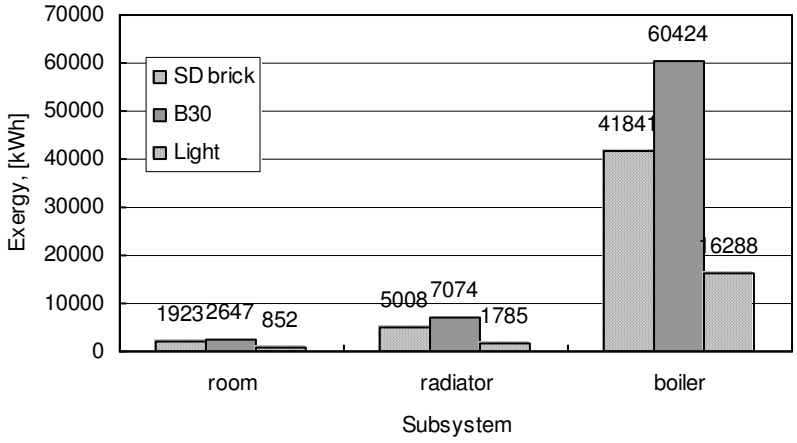

FIG. 1: Yearly exergy consumption in different subsystems before refurbishment.

After refurbishment, if the existing heating system is kept, the heating system output has to be adjusted to the new energy demand of the buildings. A possibility is to keep the same temperature drop and reduce the supply temperature. The new value of the supply temperature can be determined depending on the new heat demand ratio, taking into account that the radiator heat transfer coefficient will change. The variation of the heat transfer coefficient k_R, depending on the thermal agent temperature, is given by:

$$k_R = k_{R0}\left(\frac{T_R}{60}\right)^{n-1} \tag{10}$$

where: k_{R0} = value of the heat transfer coefficient at the nominal conditions (t_s =90 ^oC; t_r = 70 ^oC; t_i = 20 ^oC); n = exponent, for the usual radiators between: 1.24…1.36.

If the new heat demand of the room is $Q_h^{'}$, using the equation (12) results the new value of the average logarithmical temperature difference:

$$T_R^{'} = 60\left(\frac{Q_h^{'}}{Q_h}\right)^{\frac{1}{n}} \tag{11}$$

If the temperature drop in the system Δt_w is known, the values of the forward and return temperatures can be determined:

$$T_s = \frac{\Delta t_w \exp\left(\frac{\Delta t_w}{60}\left(\frac{Q_h}{Q_h^{'}}\right)^{\frac{1}{n}}\right)}{\exp\left(\frac{\Delta t_w}{60}\left(\frac{Q_h}{Q_h^{'}}\right)^{\frac{1}{n}}\right)-1} \tag{12}$$

$$T_r = \frac{\Delta t_w}{\exp\left(\frac{\Delta t_w}{60}\left(\frac{Q_h}{Q_h^{'}}\right)^{\frac{1}{n}}\right)-1} \tag{13}$$

Using the above presented equations and keeping the 20 ^oC temperature drop, for SD brick and B30 buildings results a supply/return temperature equal to 71/51 ^oC. In this case the exergy efficiency is presented in Table 4 and the exergy consumption in Figure 2.

TABLE. 4: Exergy efficiency after refurbishment.

Building	Heating system	Boiler	Condensing boiler
SD brick, B30	0.477	0.111	0.133

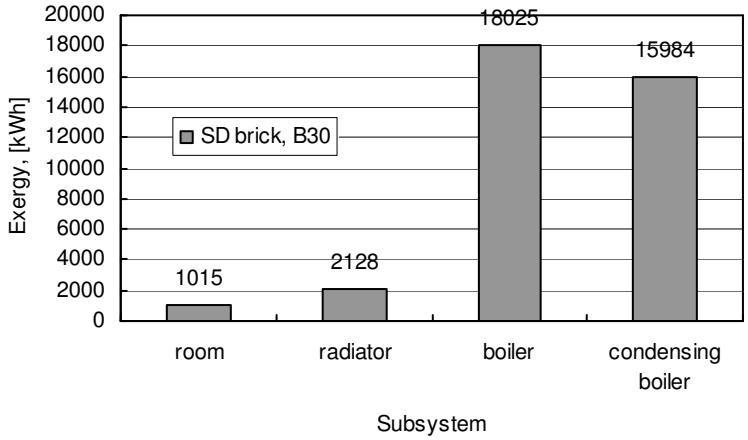

FIG. 2: Yearly exergy consumption in different subsystems after refurbishment.

Heat losses decrease considerably after refurbishment. Using surface heating placed on the external building elements (floor, wall, ceiling) this value decreases more (fig. 3)

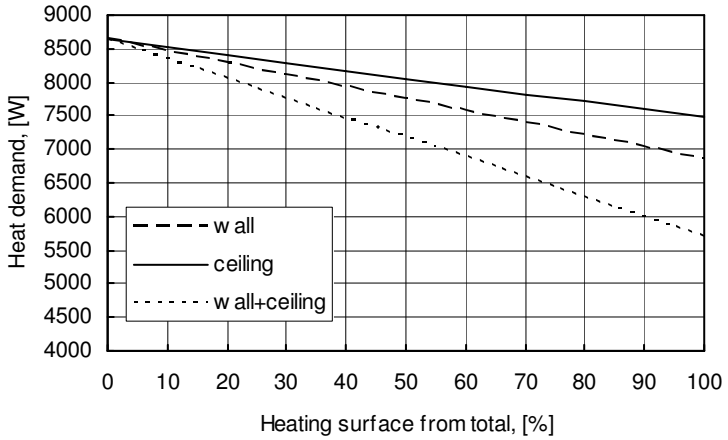

FIG. 3: Heat demand of the building using surface heating.

Having low heat losses and energy demand for heating the utilisation of low temperature surface heating has to be analysed. If wall heating or ceiling heating is used, in the calculus we have to take into account that the heat losses will decrease in function of the heated surface. This is not valid for floor heating if we have the floor placed directly on the soil. The supply and return temperatures taken into consideration are: 40/30 ^{o}C, 35/28 ^{o}C and 30/25 ^{o}C and 27/23 ^{o}C. The last values were used only for ceiling heating, because in this case the surface temperature is limited. Measurements have shown that the tolerated ceiling temperatures are around 27-28 ^{o}C if the occupancy zone is only 1.2 m (sitting person). The necessary heating surfaces are presented in Figures 4-6.

If the heating pipes are placed on the external walls, the higher is the heating surface, the lower the heat demand will be. Of course in practice the whole external wall surface cannot be used for wall heating, but 50% might be accepted. The situation is similar for floor heating where a useful heating surface ratio around 70% is the upper limit of the possibilities. In this case the maximal value of the surface temperature is other factor which influences the maximal output of floor heating. Ceiling heating usually is not used in detached houses, but based

on the measurements low surface temperature might be tolerated from thermal comfort point of view. In this case there is no limitation related to heating surface ratio.

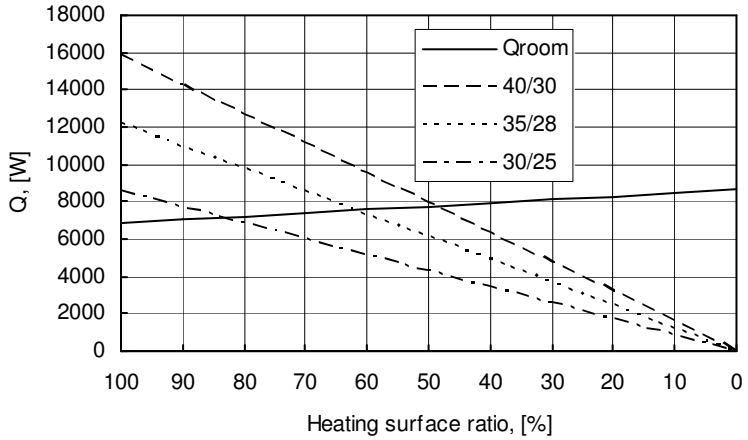

FIG. 4: Heat losses and delivered heat for wall heating.

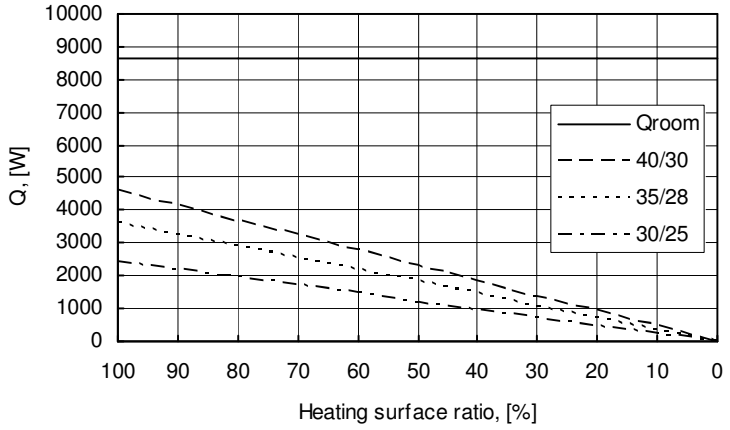

FIG. 5: Heat losses and delivered heat for floor heating.

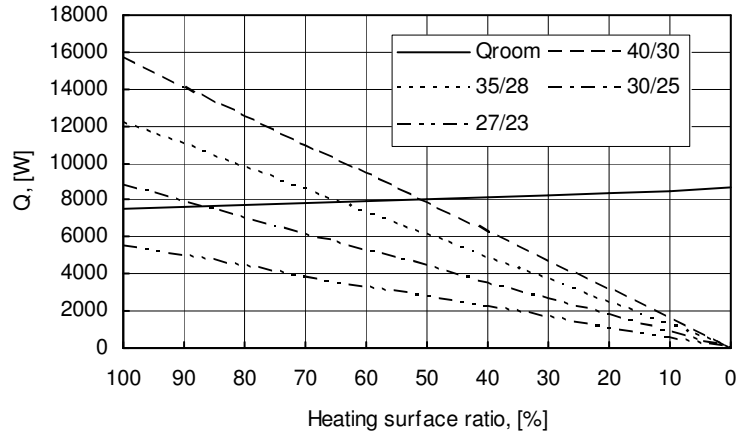

FIG. 6: Heat losses and delivered heat for ceiling heating.

For these heating systems heat pumps might be used as heat source. Taking into consideration heat pumps with different COP values the exergy consumption is presented in Figure 7 for different temperatures of the heat carrier.

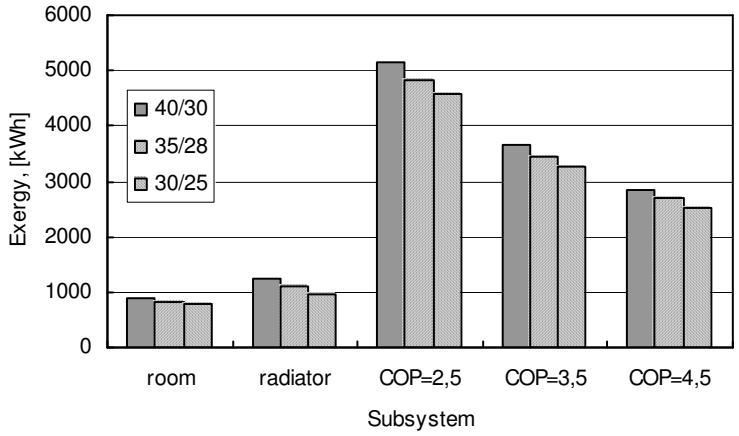

FIG. 7: Exergy consumption in different subsystems for wall heating.

As it could be seen using heat pumps the exergy consumption of the building for heating decreases with more then two thirds.

To find the exergy consumption in the primary phase, when the electricity is produced, the primary energy transformation factor has to be taken into account, which in Hungary is 2.5 (TNM rendelet, 2006). If the COP is higher than the primary energy transformation factor exergy savings will be obtained (on the market there are heat pumps with COP=5.5). The exergy efficiency for analysed cases is presented in Table 5.

TABLE. 5: Exergy efficiency after refurbishment using low temperature heating systems.

Temperatures, [^{o}C]	Heating system	Heat pump, (COP=2,5)	Heat pump, (COP=3,5)	Heat pump, (COP=4,5)
Wall, 40/30	0.71	0,225	0,315	0.405
Wall, 35/28	0.762	0.212	0.296	0.381
Wall, 30/25	0.83	0.195	0.273	0.352
Ceiling, 40/30	0.708	0.218	0.306	0.393
Ceiling, 35/28	0.761	0.204	0.285	0.367
Ceiling, 30/25	0.828	0.188	0.263	0.339
Ceiling, 27/23	0.88	0.177	0.248	0.319

The best solution from exergy consumption and thermal comfort point of view will be given by a combination of these surface heating systems. Assuming that for wall and floor heating the supply and return temperatures are the same (30/25 ^{o}C) and for ceiling heating the 27/23 ^{o}C heat carrier temperatures are used, and half of floor and ceiling respectively 40% of external walls are used as heating surfaces, the energy and exergy consumption data are:

heat demand of the building: 7347 W,

heat output of floor heating: 1210 W (t_{floor}=22,4 ^{o}C)

heat output of wall heating: 3416 W (t_{wall}=25,5 ^{o}C)

heat output of ceiling heating: 2750 W ($t_{ceiling}$=24 ^{o}C)

number of days in a heating period: 122 days,

energy demand: 11697 kWh,

exergy effieciency of the heating system:	0.83,
exergy consumption/efficiency:	4679 kWh/0.187 (COP=2.5),
exergy consumption/efficiency:	3342 kWh/0.274 (COP=3.5),
exergy consumption/efficiency:	2600 kWh/0.352 (COP=4.5).

4. Conclusions

Thermal refurbishment of a detached house built until 1990 will lead to important energy savings. If the existing heating system is not replaced, only adjusted to the new energy demand of the building the energy savings can reach 58-72%. If surface heating is installed after refurbishment the energy consumption will decrease much more, because the heat losses by transmission are lower (Fig. 8). Initially the exergy consumption is between 42000-60000 kWh. If the radiator heating system is kept the exergy consumption is reduced to 18000 kWh using a low temperature boiler, which means a reduction of 57-70%. If condensing boiler is used an additional exergy economy of 2000 kWh can be obtained. Installing surface heating and heat pumps the exergy consumption of the building decreases to 2855-5142 kWh, depending on the heat pump COP and supply/return temperatures of the heat carrier. Taking into account the primary energy transformation factor for electricity the real value of the exergy consumption will be 7137.5-12855 kWh, which is much lower than the exergy consumption having a boiler. Taking into consideration the initial state of the building and heating system, the exergy savings are between 69-82.9% for SD brick and 78.7-88.1% for B30 building. Even for light structure, if the radiator heating system is replaced with a surface heating with a supply/return temperature of 40/30 ^{o}C and heat pump is installed the exergy consumption (taking into account the primary energy transformation factor) decreased to 6990-12582 kWh (22.7-57%). As a consequence, when the envelope of a building is refurbished from thermal point a view, the surface heating installation have to be preferred in order to obtain the best solution from energy, exergy and thermal comfort point of view.

5. References

Halász E. – Kalmár T. Különböző hőtermelővel ellátott fűtési rendszerek exergetikai összehasonlítása, Magyar Épületgépészet, LVI évf., 12 sz.

Kalmár F.- Csiha A. (2006) Interrelation between galated surfaces, building structure and thermal comfort, 23rd Conference on Passive and Low energy architecture, 6-8 September 2006, Geneva.

Mantzos L. (2003). EC Directorate-General for Energy and Transport, European Energy and Transport Trends to 2030.

Olesen B. (2007) Heating and cooling systems for better energy efficiency, Magyar Épületgépészet, LVI évf., 12 sz.

Schmidt D. (2003) Design of low exergy buildings – Method and a pre-design tool, Int. Journal of low energy and sustainable buildings, vol 3.

Zöld A. (2000) A paneles lakóépületek utólagos hőszigetelésének közvetlen és közvetett hatásai, Energiagazdálkodás, 41 évf., 7 sz.

Influences of the Indoor Environment on Heat, Air and Moisture Conditions in the Component: Boundary conditions modeling.

Paul W.M.H. Steskens, Ph.D. Student,
Department of Civil Engineering, Technical University of Denmark;
pas@byg.dtu.dk

Carsten Rode, Assoc. Professor,
Department of Civil Engineering, Technical University of Denmark;
car@byg.dtu.dk

Hans Janssen, Assist. Professor,
Department of Civil Engineering, Technical University of Denmark;
haj@byg.dtu.dk

KEYWORDS: *HAM component modeling, boundary conditions.*

SUMMARY:
Current models to predict heat, air and moisture (HAM) conditions in building components assume uniform boundary conditions, both for the temperature and relative humidity of the air in an indoor space as well as for the heat and moisture surface transfer coefficients. The heat and moisture surface transfer coefficients strongly depend on the local air velocity, local temperature, water-material interactions, water content at the material surface, and the surface texture of the material. Moreover, due to local heat and moisture sources, imperfect mixing and microclimatic effects, temperature and relative humidity in the adjacent air are seldom uniform. In order to obtain a reliable prediction of the HAM conditions in a building component, an accurate description of the indoor (and outdoor) boundary conditions is required. The objective of the present paper is to analyze the influence of the variations of the surface transfer coefficients near the surface of a building component on the HAM conditions in the component. A parameter study has been used to investigate this influence. The research showed that the surface transfer coefficients have a relatively large influence on the predicted HAM conditions in a building component. Building researchers and designers should be aware that the appropriate indoor environmental conditions are applied, when performing a HAM component simulation and analysis.

1. Introduction

The durability of building components is strongly dependent of the heat, air and moisture (HAM) conditions in the component. Current models to predict heat, air and moisture conditions in building components commonly assume uniform indoor boundary conditions, both for the temperature and relative humidity of the neighboring interior air as well as for the interior surface heat and mass transfer coefficients. Due to local heat and moisture sources, imperfect mixing and microclimatic effects, temperature and relative humidity in the adjacent air are seldom uniform. Similarly, the convective surface heat and moisture transfer coefficients strongly depend on the local air velocity, local temperature, water-material interactions and water content at the material surface and surface texture of the material. The HAM conditions on or in building components resulting from such non-uniform boundary conditions cannot be accurately predicted by current HAM models. This paper investigates how the variability of the surface heat and mass transfer coefficients may affect the HAM performance of building components.

Common practice is to assume average, uniform and constant values for the convective surface heat and mass transfer coefficients when performing a HAM component analysis. The convective surface transfer coefficients are obtained from fundamental theory or experimental work, in (Hens 2007) for example, values of 3.5 W/m^2K and $3 \cdot 10^{-8}$ s/m for the interior convective heat and moisture transfer coefficients respectively are recommended.

Previous research (Novoselac 2005) has shown that different relationships for the surface heat transfer coefficient for mixed convection near a building component have been reported. Similar experimental investigations of the relationship between the surface mass transfer coefficient and the local airflow velocity have been described in (Bednar & Dreyer 2003), (Mortensen et al. 2006) and (Iskra & Simonson 2007). Other

researchers, for example (Steeman et al. 2007) (Neale et al. 2007) determined the surface heat and mass transfer coefficients by using Computational Fluid Dynamics (CFD).

The literature study showed that a considerable number of relationships between the local velocity of the airflow near a building component and the surface heat transfer coefficients have been developed, all having their specific limitations and applications. When performing a HAM building component analysis, often, researchers arbitrarily use these relationships for a HAM component simulation, without considering these limitations. The use of these correlations may introduce errors in the predicted HAM conditions. The objective of the present paper is to analyze the influence of the non-uniform distribution of the transfer coefficients caused by variations in the air velocity near the surface of a building component on the HAM conditions on and in the component.

2. Analysis and Methods

A parameter study is used to investigate the influence of non-uniform surface transfer coefficients - caused by variations in the air velocity near the surface of a building component - on the HAM conditions in the building component. Two calculation objects have been selected for analysis. Different values for the surface heat and moisture transfer coefficients have been applied. The Heat, Air and Moisture response of the building components has been simulated.

2.1 Calculation objects

The HAM performance of a lightweight concrete wall and a concrete floor penetrating the wall of a building has been investigated. The composition of the wall element is presented in Figure 1. It is the objective to analyze the influence of the convective heat and moisture transfer coefficients near the component using a relatively well-insulated wall.

Besides the relatively well-insulated wall, a floor penetrating the external wall of a building is analyzed. Two rooms (on top of each other) are connected by a concrete floor. Both rooms are connected to the outdoor climate by the lightweight concrete wall, which composition is presented in Figure 1. The building detail is presented in Figure 2. The reader should notice that the original geometry of the building has been extended. For this analysis, the building could be considered as two original buildings on top of each other. It is the objective to study the influence of the convective heat and moisture transfer coefficients near a thermal bridge, such as a balcony.

2.2 Simulation strategy

The simulation strategy which has been applied is as follows:

First, the geometry of the calculation object is defined in CHAMPS-BES (Nicolai, Grunewald 2006), which is an envelope model for the coupled simulation of heat, air, moisture and pollutant transport in a building component. The HAM performance of the calculation objects has been investigated using the geometry of a building which is defined along the lines of Common Exercise 1 of the IEA-ECBS Annex 41, (Rode, Woloszyn 2004) using the external boundary conditions: the Test Reference Year (TRY) for Danish (Copenhagen) outdoor climatic conditions.

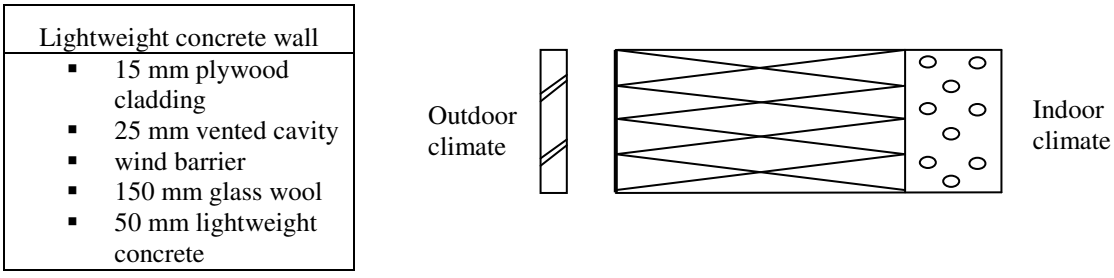

Figure 1. Composition of the lightweight concrete wall element.

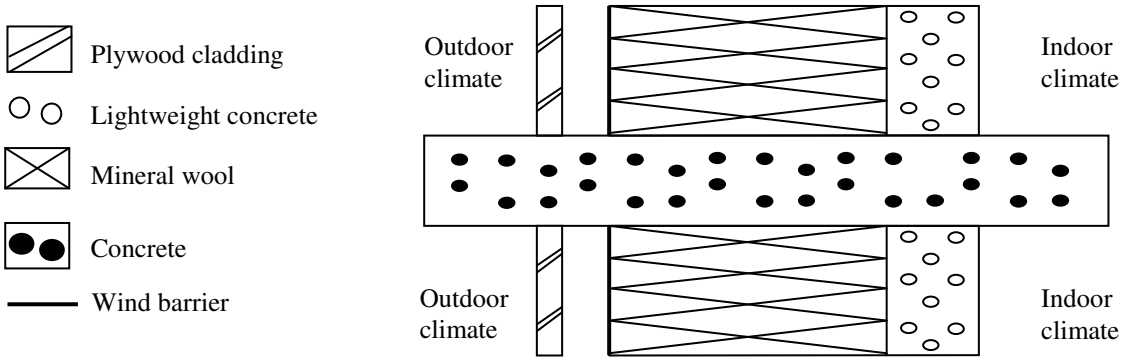

Figure 2. Building detail selected for analysis. Two rooms, connected to the outdoor climate by a lightweight concrete wall consisting of a plywood cladding, a wind barrier, mineral wool insulation and a lightweight concrete layer. The surface heat and moisture transfer coefficients near the corners are relatively low compared to the surface transfer coefficients in the centre of the components

Second, the indoor environmental conditions have been applied. According to the requirements of Common Exercise 1 the (Rode, Woloszyn 2004) temperature in the building is controlled to be between 20°C and 27°C during the entire year. To obtain comfortable indoor environmental conditions, which serve as the internal boundary conditions for the HAM component simulation, a prediction of the required heating and cooling load has been obtained using a whole building simulation in HAMBASE (Wit 2006)? A similar building geometry and external boundary conditions have been applied in HAMBASE. The resulting heating/cooling power is supplied to the building component in CHAMPS-BES. In this way, the indoor air temperature lies between 20°C and 27°C during the entire year. The building has been simulated in HAMBASE using set points of 20°C (during office hours) and 12°C (outside office hours) for heating and 27°C for cooling (during office hours). With respect to the moisture production in the building, an average vapor production of 500g/h between 9:00h and 17:00h has been applied. The indoor environmental conditions resulting from the simulation are applied as boundary conditions on the surfaces at the internal sides.

Third, different values for the surface heat and moisture transfer coefficients have been applied. Lower and higher limits for the surface transfer coefficients have been applied as well as a combination of a standard surface heat transfer coefficient with a lower and a higher limit for the moisture transfer coefficient. Additional information on the specific values for the surface transfer coefficients is presented in Section 2.3.

Then, an initial temperature and relative humidity of 20°C and 50 % RH respectively have been applied throughout the entire building component. The HAM performance of the building component has been simulated for one year. The investigations showed that a transition period may be neglected using these initial conditions of 20°C and 50 % RH, which are average conditions, representative for the entire year.

2.3 Parameter analysis

Several indoor environmental conditions, presented in Table 1, have been investigated. Typical values for the convective heat and moisture transfer coefficients have been applied for the different indoor environmental conditions. The objective of the investigations (1 and 2) is to determine minimum and maximum HAM conditions, which are likely to occur in the building component. The objective of studying the conditions using a standard value for the convective surface heat transfer coefficient (conditions 3 and 4) is to compare the influences of the convective surface heat transfer coefficient and the surface moisture transfer coefficient separately. The Heat, Air and Moisture response of the building component has been simulated using the presented values for the convective surface transfer coefficients.

Table 1. Convective heat and moisture transfer coefficients, which have been applied for the different indoor environmental conditions.

Conditions	α_c [W/m^{2}K]	β_c [10^{-7} s/m]
1 Lower limits	1	0.1
2 Upper limits	8	1
3 Lower limit β_c and standard α_c	3.5	0.1
4 Higher limit β_c and standard α_c	3.5	1

3. Results

This section presents the predicted HAM conditions on the internal surface of the components which have been presented in Figure 1 and 2. First of all, the surface temperature and relative humidity on the lightweight concrete wall during 3 days are presented. Second, the surface temperature and relative humidity in the corner of the thermal bridge are shown. Third, weekly averaged surface conditions on the presented components are analyzed using an isopleth representation.

3.1 Lightweight concrete wall

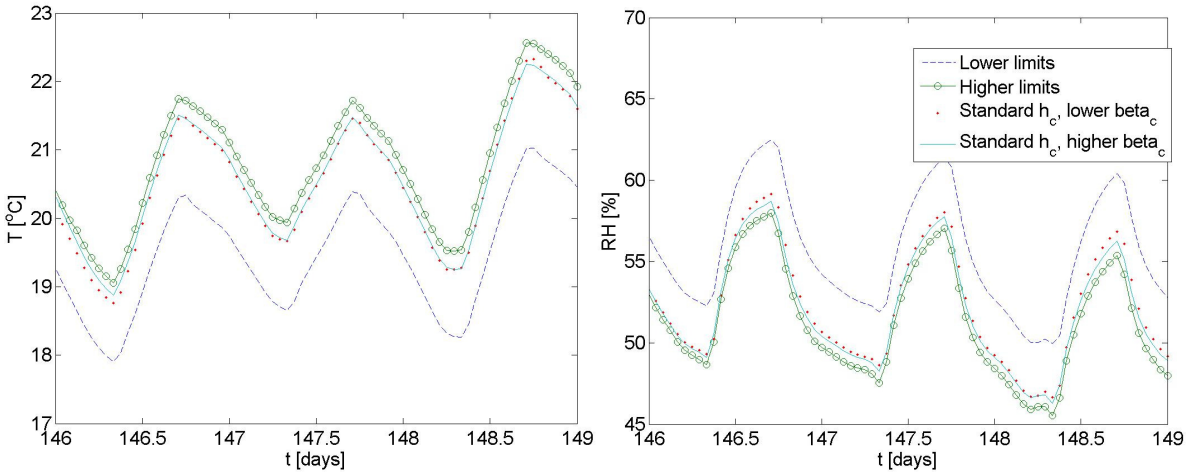

Figure 3: Surface temperature and relative humidity at the internal side of the light weight concrete wall.

Figure 3 presents the surface temperature and relative humidity at the internal side of the construction during 3 days (from May 26. till May 29.). The selected period is representative for the entire year. Figure 3 shows that a relatively large difference is present between the lower limit (1) and the higher limit (2). Comparing the surface conditions for the standard surface heat transfer coefficient and lower and higher limits for the surface moisture transfer coefficient (conditions (3) and (4)), Figure 3 presents a relatively small deviation.

Figure 4 presents the partial vapor pressure at the internal side of the lightweight concrete wall. The figure shows that a relatively small difference in partial vapor pressure between the investigated limits is observed. From this observation, it may be concluded that the influence of the convective surface heat transfer coefficient on the HAM performance is relatively large compared to the influence of the convective surface moisture transfer coefficient.

In Figure 5, the surface conditions on lightweight concrete wall predicted over the entire year have been analyzed using an isopleth representation. The isopleths are based on weekly averaged values for the surface temperature and relative humidity. The isopleth shows that the a considerable difference between the observed conditions when applying lower (1) and higher limits (2) for the surface transfer coefficients is observed. The histograms in (Figure 5) show that for both wall elements the time of the year at which a surface relative

humidity above 70% RH increases when applying lower limits (1) for the surface transfer coefficients compared to the application of higher limits (2).

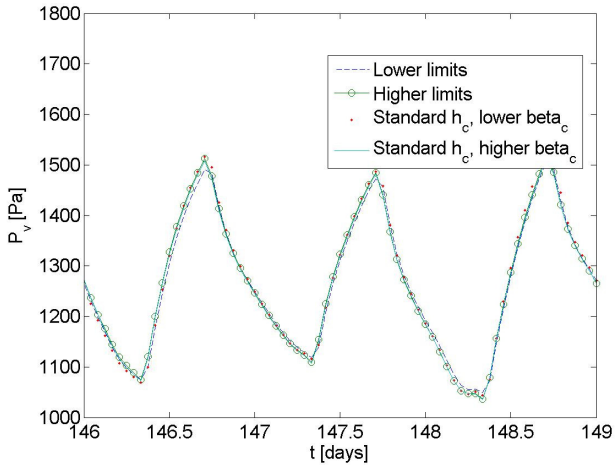

Figure 4: Partial vapor pressure at the internal side of the lightweight concrete wall

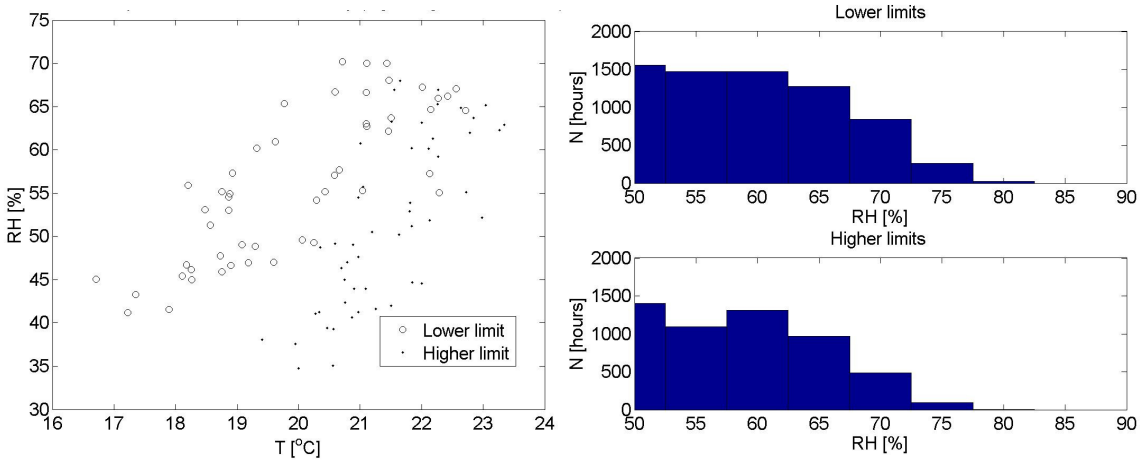

Figure 5. Predicted surface conditions for the lightweight concrete wall using lower (1) and higher limits (2) for the surface transfer coefficients. Isopleth representation of the surface conditions during one year (left). Histogram of the observed surface relative humidity as a function of the number of hours (right).

3.2 Thermal bridge

Figure 6 presents the temperature and relative humidity in the corner of the building component during 50 days (from February 19. till April 10.). The figure shows that a relatively large difference is present between the lower limit (1) and the higher limit (2). Moreover, considering the diverging HAM conditions obtained with the standard surface heat transfer coefficient and with the lower and higher limits for the surface moisture transfer coefficient (conditions (3) and (4)), the difference is significant.

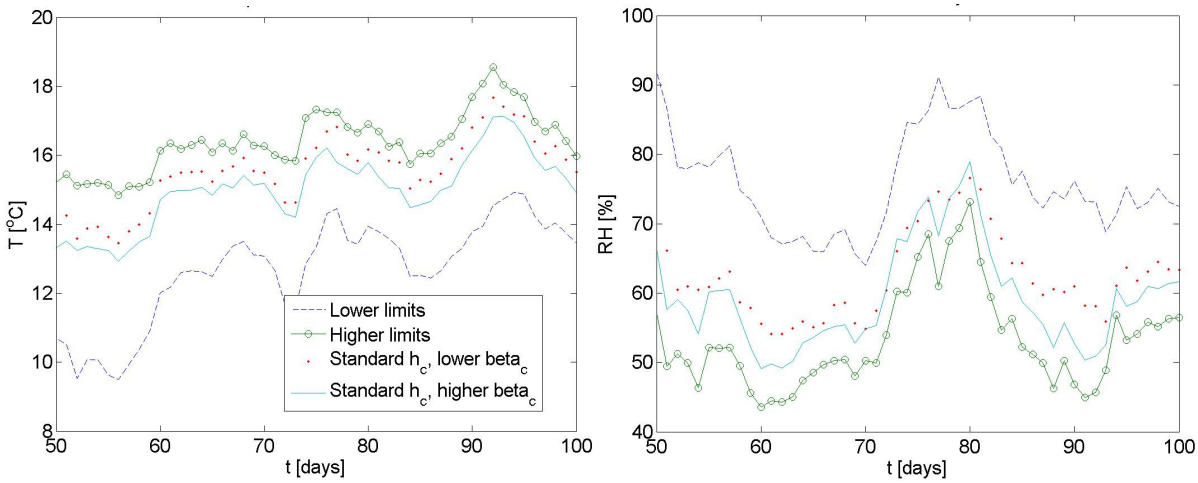

Figure 6. Surface temperature (left) and relative humidity (right) in the corner of the building component. The different conditions, i.e. lower limits, higher limits and standard values for the surface heat transfer coefficient.

Comparing the simulation results with a standard value for the surface heat transfer coefficients, the predicted HAM surface conditions are relatively comparable. The influence of the convective surface heat transfer coefficient on the HAM performance may be relatively large compared to the influence of the convective surface mass transfer coefficient.

Figure 7 shows the partial vapor pressure in the corner of the building component. Comparing the simulation results of the well-insulated lightweight concrete wall and the thermal bridge for the standard surface heat transfer coefficient and lower and higher limits for the surface moisture transfer coefficient (conditions (3) and (4)), the surface moisture transfer coefficient shows to be relatively important when considering the thermal bridge. The influence of the convective surface moisture transfer coefficient on the HAM performance of the thermal bridge is thus relatively large.

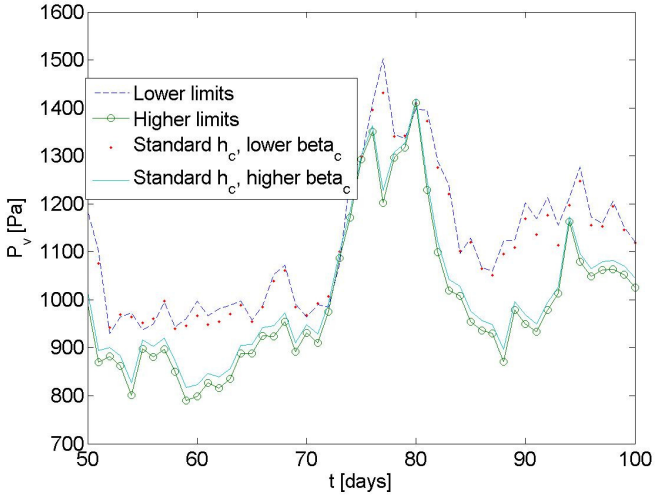

Figure 7: Partial vapor pressure in the corner of the thermal bridge.

Figure 8 presents the complete set temperatures and relative humidities in the corner of the building component. The predicted conditions when applying lower limits (1) and higher limits for the surface transfer coefficients have been compared. The daily averaged temperatures and relative humidities are presented in the isopleth. The difference in the predicted HAM conditions is relatively large. The analysis shows that whenever the building engineer or researcher is asked to provide a reliable prediction of the HAM performance of a building component, this prediction is strongly influenced by the applied values for the surface transfer coefficients.

Moreover, this influence may become even more important when considering building components where non-uniform conditions are more likely to occur, for example thermal bridges.

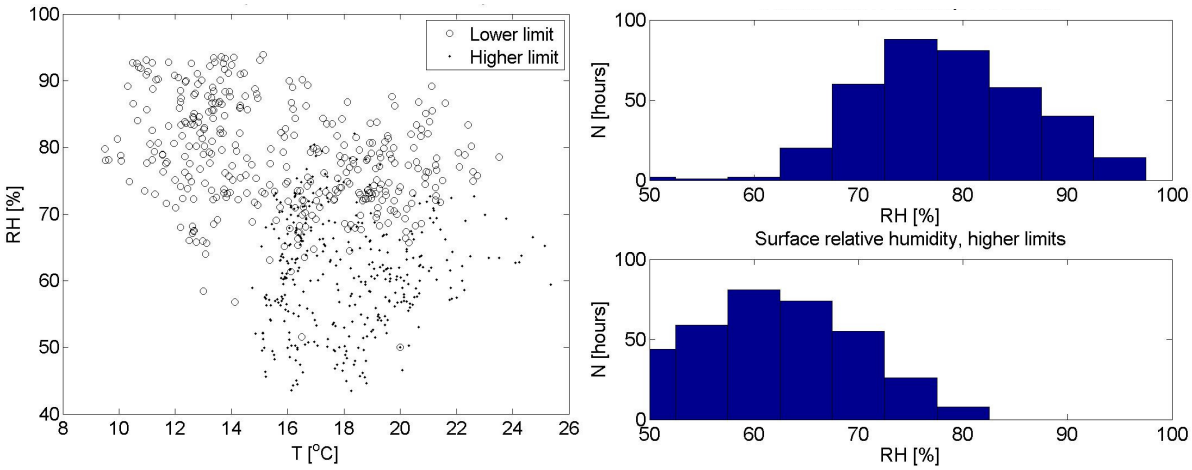

Figure 8: Temperature and relative humidity in the corner of the thermal bridge using lower (1) and higher limits (2) for the surface transfer coefficients. Isopleth representation of the surface conditions during one year (left). Histogram of the observed surface relative humidity as a function of the number of hours (right).

4. Conclusions and Discussion

This section presents the conclusions from the parameter study and the consequences of the investigations for HAM component performance analysis. The influence of the non-uniform surface heat and moisture transfer coefficients on the HAM conditions in the building component has been analyzed. Lower and upper limits for the convective surface transfer coefficients (α_c and β_c), assuming respectively 'still' air and 'moving' air conditions, have been assigned. A parameter study is used to investigate the influence of the non-uniform surface transfer coefficients - caused by variations in the air velocity near the surface of a building component - on the HAM conditions in the building component and the indoor environment. The simulated conditions resulted in minimum and maximum HAM conditions in the building component.

It is concluded that:

- The non-uniform distribution of the transfer coefficients caused by variations in the air velocity near the surface of a building component may have a relatively large influence on the predicted HAM conditions on a building component. Different surface temperatures, relative humidities and vapor pressures are predicted, when different convective surface transfer coefficients are applied. When performing a HAM performance analysis and simulation, it is important to take the local airflow velocity near the component into account.
- Focusing on the HAM performance of a well-insulated wall, the influence of the convective surface heat transfer coefficient on the HAM performance is relatively large compared to the influence of the convective surface moisture transfer coefficient. With respect to the analyzed wall, the investigations showed that assuming an average value for the surface moisture transfer coefficient is acceptable, while assuming an average value is not acceptable for the convective surface heat transfer coefficient. The study showed that the influence on the surface relative humidity is limited.
- Focusing on the HAM performance of a thermal bridge, the influence of both the convective surface heat and moisture transfer coefficient on the HAM performance is relatively large. The analysis showed that assuming an average value for these coefficients is not acceptable.

Building researchers and designers should be aware that the appropriate indoor environmental conditions are applied, when performing a HAM component simulation and analysis. The local airflow conditions near the component have a relatively large influence on the predicted HAM performance of the component. It is

recommended that, for example in a design stage, different local airflow conditions are investigated to predict the influence of these conditions on the HAM performance of the specific component.

Future research should focus on the analysis and determination of the relationship between the local air velocity near the component and the convective surface heat transfer coefficient. A more detailed description and prediction of the interaction between the indoor environment and the HAM conditions in the building component is desired. The quality of such an analysis could be improved by providing guidelines and relationships between the convective surface heat transfer coefficient and the local air velocity near the building component.

5. References

Bednar, T. & Dreyer, J. (2003), Determination of moisture surface transfer coefficients under transient conditions, *International Building Physics Conference II,* Leuven.

Hens, Hugo S. L. C. (2007), Building Physics - Heat, Air and Moisture - Fundamentals and Engineering Methods with Examples and Exercises, ISSN/ISBN 3-433-01841-3

Iskra, C.R. & Simonson, C.J. (2007), Convective mass transfer coefficient for a hydrodynamically developed airflow in a short rectangular duct, *International Journal of Heat and Mass Transfer*, **50**[11], 2376-2393.

Mortensen, L.H., Rode, C. & Peuhkuri, R. (2006), Effect of airflow velocity on moisture exchange at surfaces of building materials, *Proc. Int. Building Physics Conference III*, *Research in Building Physics and Building Engineering*, Montreal, Canada, 27-31 August 2006.

Neale, A., Derome, D., Blocken, B. & Carmeliet, J. (2007), Coupled Simulation of Vapor between Air and a Porous Material, *Buildings X Conference Proceedings,* American Society of Heating, Refrigerating and Air-Conditioning Engineers, Inc., Clearwater, US, 2-7 December 2007.

Nicolai, A. & Grunewald, J. (2006), CHAMPS-BES Program for Coupled Heat, Air, Moisture and Pollutant Simulations in Building Envelope Systems (User Manual), BEESL - Building Energy and Environmental Systems Laboratory, Department of Mechanical and Aerospace Engineering, Syracuse University, NY.

Novoselac, A. (2005), Combined airflow and energy simulation program for building mechanical system design, Ph.D. thesis, Pennsylvania State University; The Graduate School; College of Engineering.

Rode, C. & Woloszyn, M. (2006), Simulation tests in whole building heat and moisture transfer, *Proc. Int. Building Physics Conference III, Research in Building Physics and Building Engineering*, Montreal, Canada, 27 31 August 2006.

Steeman, H.J., Janssens, A. & De Paepe, M. (2007), About the use of the heat and mass analogy in building simulation, *Proc. 12th Symposium for Building Physics*, Dresden, Germany, 27 31 March 2007, pp. 455-461.

Wit, M.H. de (2006), HAMBASE - Heat Air and Moisture model for Buildings and Systems Evaluation, Eindhoven University Press, Eindhoven, the Netherlands.

Worch, A. (2004), The behavior of vapor transfer on building material surfaces: The vapor transfer resistance, *Journal of Thermal Envelope and Building Science*, **28**[2], pp. 187-200.

The influence of surface treatment on mass transfer between air and building material

Jerzy Kwiatkowski, Ph.D. Student,
CETHIL, Universite de Lyon, CNRS UMR5008, Universite Lyon 1, INSA de Lyon;
jerzy.kwiatkowski@insa-lyon.fr

Carsten Rode, Assoc. Professor,
Department of Civil Engineering, Technical University of Denmark;
car@byg.dtu.dk

Kurt Kielsgaard Hansen, Assoc. Professor,
Department of Civil Engineering, Technical University of Denmark;
kkh@byg.dtu.dk

Monika Woloszyn, Assoc. Professor,
CETHIL, Universite de Lyon, CNRS UMR5008, Universite Lyon 1, INSA de Lyon;
monika.woloszyn@insa-lyon.fr

Jean-Jacques Roux, Professor,
CETHIL, Universite de Lyon, CNRS UMR5008, Universite Lyon 1, INSA de Lyon;
jean-jacques.roux@insa-lyon.fr

KEYWORDS: *Mass transfer measurements, surface treatment, climatic chamber.*

SUMMARY:
The processes of mass transfer between air and building structure and in the material influence not only the conditions within the material but also inside the connected air spaces. The material which absorbs and desorbs water vapour can be used to moderate the amplitude of indoor relative humidity and therefore to participate in the improvement of the indoor air quality and energy saving. Many parameters influence water vapour exchange between indoor air and building material. The aim of this work is to present the change of mass transfer under different climatic and material conditions. The measurements were performed at the Technical University of Denmark (DTU), Department of Civil Engineering. Two climatic chambers were used for the tests, the first one for dynamic and the second for steady state conditions. Two commonly used building materials exposed to the indoor environment were chosen for the experiments: gypsum board and calcium silicate. The wallpaper and paint were used as finishing materials. Impact of the following parameters for changes of RH was studied: coating, temperature and air movement.
The measurements showed that acryl paint (diffusion open) can significantly decrease mass uptake. It was shown also that higher air velocity speeds up the process of mass exchange between indoor air and materials but apparently decreases the total amount of exchanged water after a longer period. The experiment allows not only to check the influence of surface treatment on mass transfer, but can be used also as validation for simulation programs. At the end of the article, a mass uptake calculation using the HUMIMUR model is presented.

1. Introduction

The water vapour exchange between indoor air and materials influences many aspects of indoor climate. The relative humidity is one of the most important parameters influencing perceived indoor air quality and the human comfort. Moisture is also needed to initiate microbiological growth at the surface of building envelope. Most of the building materials have ability to absorb and desorb water vapour; therefore it is important to study mass transfer between them and the surrounding air. In reality in dwellings we will not find any pure building material. In most of the cases they are covered with some finishing materials. Also the indoor conditions are not always the same but change every day, hour and even minute. In order to study water vapour exchange between indoor air and building materials at minimum the following parameters should be taking into account: material,

coating, temperature and air velocity, in addition to the hygric condition in the air and within the building material.

A lot of measurements of mass exchange between air and materials have been presented in the literature. In some experiments a few parameters influencing water vapour transfer were examined. May and Woloszyn (2006) performed test of mass absorption for two building materials: gypsum board and red brick, in order to study the link between sorption mechanism and microstructure. The influence of temperature for gypsum board was also checked in this work. Osanyintola and Simonson (2006) investigated moisture buffering capacity of plywood. Their studies were done for two cases: the first without air movement in a sealed jar and the second with fully developed, forced convection air flow in a small wind tunnel. The moisture buffer value and the influence of two kinds of paint have been investigated by Peuhkuri and Rode (2005).

In this paper the influence of the finishing material (diffusion open paint and wallpaper), temperature (20 and 24 °C) and air movement (tests with and without fan working in the chamber) on mass uptake is presented. Also the water vapour transfer under dynamic changes of relative humidity is shown. Finally an example of mass uptake calculation using HUMIMUR model (Kwiatkowski et al. 2008) is presented.

The experimental measurements were divided into two parts. In the first the part the change of mass transfer between indoor air and building material with step-change of the relative humidity has been examined. The second part of the measurements concerns water vapour uptake under dynamic changes of relative humidity. In the experiments two building materials exposed to the indoor environment were used. In the tests with step-change of relative humidity level also the influence of paint and wallpaper has been investigated.

2. Samples description

For the measurements two different commonly used building materials in contact with indoor air were chosen: gypsum board and calcium silicate. Three variants of gypsum board were used: naked gypsum board, gypsum board with paint layer and gypsum board with wallpaper. For calcium silicate only naked samples and samples with a paint layer were used. The size of the samples was 200x200 ±1 [mm]. The thickness of the specimens was 12.5 ±0.5 [mm] for gypsum and 10 ±0.5 [mm] for calcium silicate. Five sides of the samples were sealed with the aluminium tape and only one side was exposed to the outside conditions. As coating materials wallpaper and a diffusion open paint were chosen. Wallpaper paste was used to coat the samples with the wallpaper. The specimens with paint layer were primed and then painted with two layers of paint. The total permeability of the paint coating was equal to $1.6481*10^{-11}$ [kg/m.s.Pa]. Prepared specimens were used in tests few days after being coated in order to avoid influence of drying of the glue and paint on measurements.

3. Tests with step-change of relative humidity

In the experiment with step-change of the relative humidity it was sought to examine the influence on moisture exchange of each of the two finishing materials, of different temperatures and of air movement over the samples. The tests were carried in a climatic chamber with precise control of temperature and relative humidity. There was no possibility to cool the air in the chamber so the lower limit of temperature depended on the ambient temperature in the room. In order to get as high range of temperatures the room was cooled down to 18.5 ±0.5 °C. The upper limit of temperature was 25-26 °C. The relative humidity could be varied between 4-5% and 96-98%. A photo and schematic drawing of the climatic chamber is presented in FIG. 1.

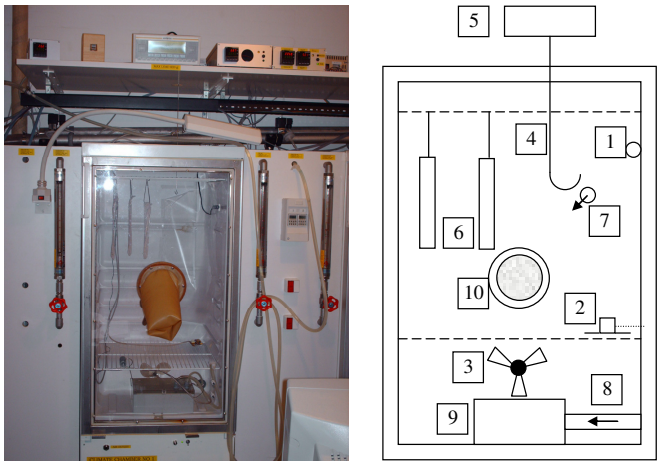

FIG. 1: Photo and scheme of the climatic chamber used in the measurements.

Relative humidity inside the chamber is controlled by a PID controller with humidity sensor (1) and regulated by mixing of dry and 100% saturated air in the chamber. The injection of dry air into chamber was by a small pipe (7). The saturated air was achieved by injection air by a pipe (8) into water tank (9). The temperature is also controlled by a PID controller but regulated by electric resistance heater (2) placed inside the chamber. A fan (3) is placed in the lower part of the chamber, to mix the air and thereby avoid temperature and humidity stratification inside the chamber. A wire (4) comes into the chamber through the upper part, connecting accurate balance (5) with the hook in the chamber. During weighing of the specimen (6), the air-conditioning system is stopped (in order to not to influence weighing) and the specimen is hung on the hook. The precision of the sensors is ±0.003 g for the balance, ±0.3 °C for the temperature sensor and ±1.0 % for relative humidity sensor.

The measurements of mass uptake in the chamber were divided into four parts. For each part, the samples of material were preconditioned at constant temperature of 20 or 24 °C (depending on the test) and in constant relative humidity of 35% for two days. At the beginning of each test the relative humidity was set to 75% and then after 24h again to 35%. The parameters describing each test are presented in TABLE 1.

TABLE 1. Parameters in the Tests 1-4.

	Test 1	Test 2	Test 3	Test 4
Temperature [°C]	20	20	24	24
Fan	On	Off	On	Off

In the Test 1 and 2 the temperature was fixed to 20 °C, and in Test 3 and 4 to 24 °C. In order to check the influence of air movement on mass uptake, the fan in the chamber has been switched off in the Test 2 and 4. Additional measurements have been made of the air velocity inside the chamber when fan was working. The velocity has been measured in six points between the hanging specimens (see FIG.2).

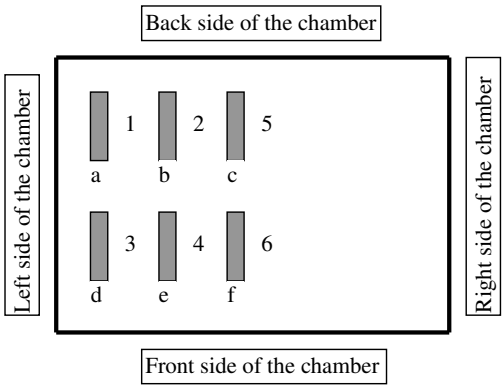

FIG. 2: Scheme of the velocity measurement points distribution in the climatic chamber, seen from above.

The velocity under condition from Test 1 was measured using Brüel & Kjær Indoor Climate Analyzer Type 1213 with the precision of 2 [cm/s] and the results of the measurements are presented in TABLE 2. For each

point the mean, maximal and minimal velocity was measured over five minute periods. Also the standard deviation for each point was calculated.

TABLE 2. Results of the velocity measurements inside the climatic chamber (Test 1).

Velocity	Position of the measuring point					
[cm/s]	1	2	3	4	5	6
Mean	1.5	1.0	2.0	3.0	5.0	4.0
Max	3.0	2.0	5.0	7.0	8.0	6.0
Min	0.0	0.0	0.0	1.0	3.0	1.0
Std. dev.	2.0	1.0	2.0	4.0	4.0	4.0

The measurements showed that even when the fan was working well, the velocities in the chamber were lower then 10 [cm/s]. It can be noticed that the velocity profile was not uniform, and the variation between the different measuring points was high. Also the temporal deviations for each point are high.

The water vapour exchange between air and materials was measured by weighing the samples and calculating the difference in weight. From the beginning of each experiment (step-change of the relative humidity in the chamber) the measurements were done according to the following scheme: for the first 2 hour every 15 minutes, for the next 2 hours every 30 minutes and later every one hour. The last measuring point was taken after 24h from the change of the relative humidity.

3.1 Influence of coatings on mass uptake

The influence of different coatings for gypsum board and for calcium silicate is presented in FIG. 3. For the gypsum, diffusion paint and wallpaper have been used as finishing. For the calcium silicate only paint has been used as coating.

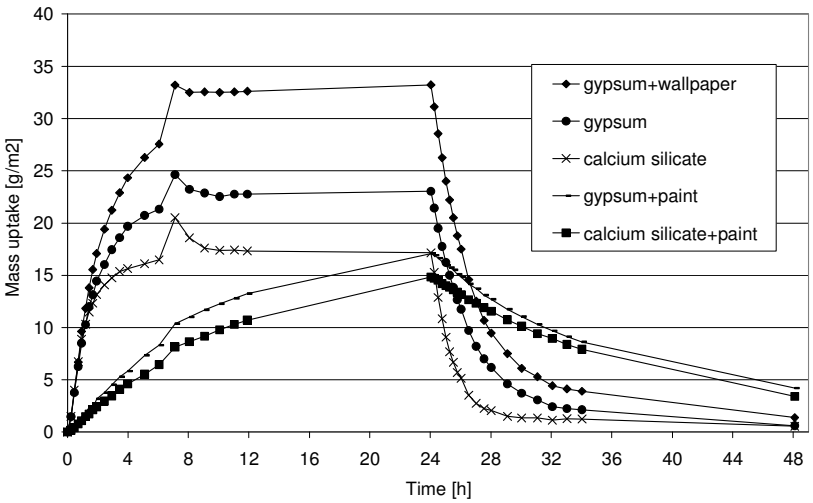

FIG. 3: The chart of the mass uptake for the all variation of samples for the TEST 1.

As it can be noticed, the mass uptake for various materials and coatings differs a lot. The gypsum board and calcium silicate are rather diffusion open materials, and the speed of absorbing/desorbing of mass in the first stage of the process is almost the same for both of them. The difference can be seen in the amount of water vapour absorbed by materials. The calcium silicate has less hygroscopic structure than gypsum board and therefore the amount of absorbed water is smaller.

It can be noticed that for both materials covered with paint the process of adsorption/desorption is slower. The dispersion in mass uptake between specimens without and with paint layer can be well seen on FIG. 3. Even after 24h the samples with paint layer could not get to equilibrium with the surrounding air.

There is no difference in the initial rate of adsorption/desorption between the gypsum board without and with wallpaper. The difference occurs in the amount of exchanged water, what is a result of the hygric properties of wallpaper. Wallpaper is very hygroscopic material so it can absorb an additional amount of water.

Between the seventh and eighth hour of test, there appears a peak in the mass uptake profile. This peak is the result of a short dysfunction of the air conditioning system in the climatic chamber.

3.2 Influence of temperature on mass uptake

In order to check the influence of temperatures on water vapour uptake similar tests but for different temperatures have been performed (see TABLE 1). The results of the measurements are presented in FIG. 4.

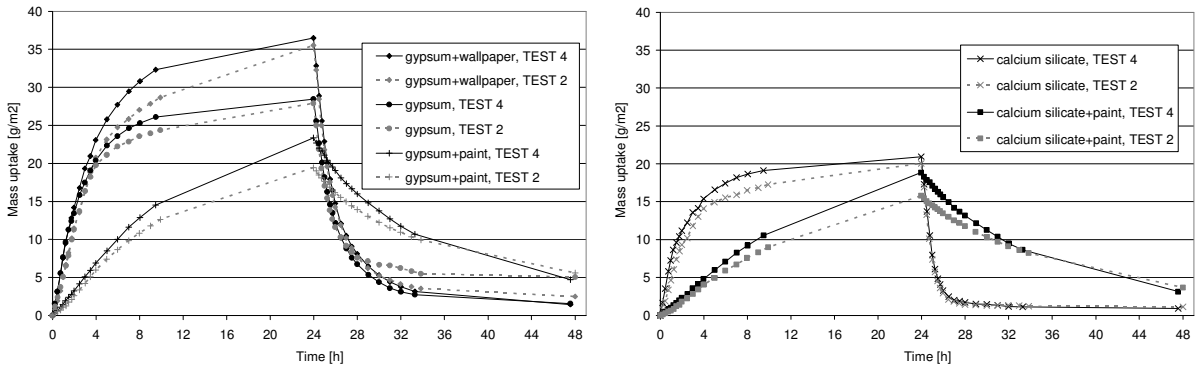

FIG. 4: Mass uptake comparison for TEST 2 (20 °C) and 4 (24°C).

TEST 2 was performed at the temperature 20 °C and TEST 4 at 24 °C. The slight differences between results from both tests can be noticed for all variants of the materials. It can be seen that the initial rate of the absorption/desorption process in the first part of measurements is slightly higher in the temperature of 24 °C than in 20 °C. Eight hours after the step-change of relative humidity the relationship between rate of the process and the temperature is inversed. The mass uptake is growing faster at 20 °C than at 24 °C. The reason is that the samples got closer to equilibrium already within the first 8 hours when the temperature was higher. Therefore it is obvious they could not absorb so much more in the next 16 hours. Similar results were presented by May and Woloszyn (2006) for 20 and 30 °C. The only exception are the samples with paint layer, when the process of absorption/desorption is faster at 24 °C for whole duration of the experiment (24 hours). The reason is that the diffusion paint has high resistance on water vapour transfer and slows down the mass exchange process.

3.3 Influence of air movement on mass uptake

The influence of air movement on water vapour exchange has been checked by performing similar tests but with and without the fan in operation in the climatic chamber. The measured velocities in the chamber with the running fan were presented in the TABLE 2. When the fan was off the velocity measurements showed that there was no air motion in the chamber. The differences in mass uptake for both situations are presented in FIG. 5.

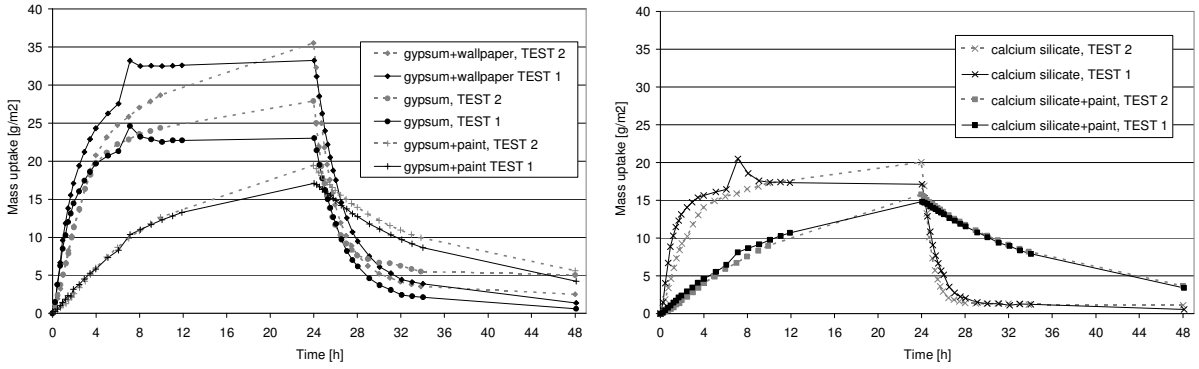

FIG. 5: Mass uptake comparison for TEST 1(fan on) and TEST 2 (fan off).

TEST 1 represents the measurements with the fan on, and TEST 2 with the fan off. It can be noticed that for all materials and finishing, except the samples with paint layer, the difference in the rate of adsorption process is

significant. The mass uptake during the first 7-8 hours is faster in the TEST 1 than in TEST 2. Then the situation is inversed: mass uptake rate is faster in the TEST 2 than in The TEST 1. In the desorption process this dependency is opposite, first the process of desorption is faster in the TEST 2 but after few hours it is slower than in the TEST1. The measurements show that the amount of absorbed water after 24 hours for the test with fan off is higher than for test with fan on. This behaviour can be connected with hygric properties of the materials, however some additional investigations are needed to explain the origin of this phenomena. The difference in the speed of the mass absorption/desorption for the samples with paint layer is not so significant, which is a result of paint high resistance on water vapour transfer.

4. Tests with sinusoidal oscillation of relative humidity

The climatic chamber called Mega-Cup (Padfield et al. 2002) was used for the experiment with sinusoidal changes of relative humidity. The climatic chamber is an open topped cylinder of stainless steel with a double-wall. The top can be sealed with a metal plate so that the cylinder encloses the specimen under test in an airtight space. The climatic chamber is well insulated and the inside temperature and relative humidity can be controlled between 8 and 30 °C and from 30 to 95% of relative humidity. The temperature is controlled by air circulating in the annular space of the double-wall. The air in the chamber is cooled by water circulating in a ribbed copper coil and is heated by an electric resistive element. The relative humidity in the chamber is controlled by condensating water into, or evaporating water from a small water tank placed inside the chamber. The temperature of the water is controlled by a thermostatic device fixed beneath the tank. The water vapour flux to and from the tank is measured by checking the weight of the tank.

The tests with dynamic, sinusoidal oscillations of relative humidity from 30 to 70% with a time cycle of 24h were performed for gypsum board without any coating. The measurements were done at two different temperatures: 20 and 24 °C. Before each test the specimens were preconditioned in the temperature of 20/24 °C and 50% relative humidity. The results of the experiment are presented in FIG. 6 and FIG. 7.

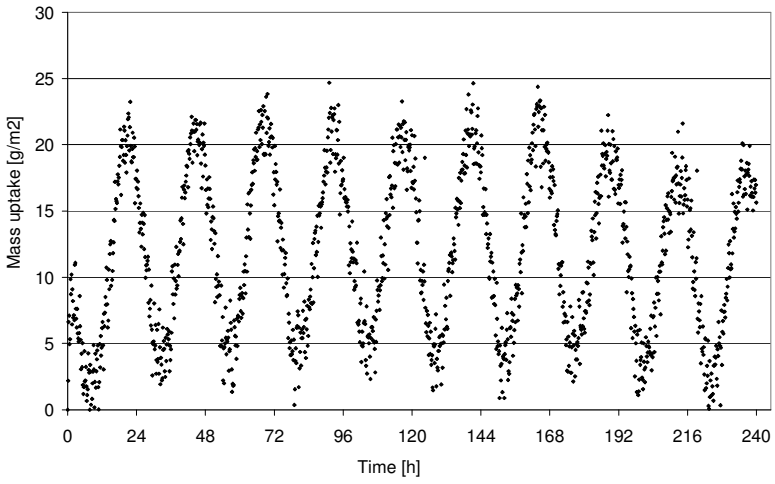

FIG.6: Mass uptake under dynamic changes of relative humidity for gypsum board in 20 °C.

The measurements of mass transfer between air and gypsum board under dynamic changes of relative humidity were done for a period of some days. The test in the temperature of 20 °C was performed over ten days and the results are presented on the FIG. 6. It can be noticed that the amplitude of water vapour exchange is almost the same as in the test with the step change of relative humidity (TEST 1) after 12 hours. It can also be seen that the mass uptake profile is slightly changing with the time. This phenomenon is better seen for the longer experiments. Therefore the measurements in 24 °C were done for 25 days and the results are presented in FIG. 7.

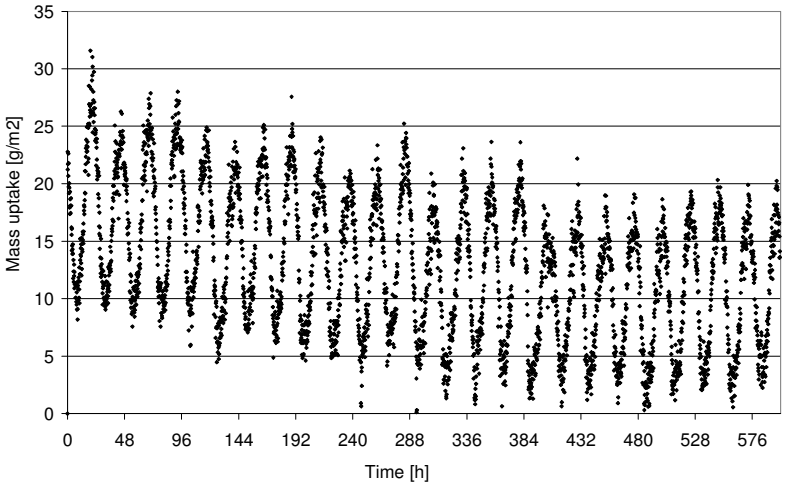

FIG.7: Mass uptake under dynamic changes of relative humidity for gypsum board in 24 °C.

As for the test at 20 °C also here the amplitude of mass uptake profile is approximately constant for the whole time of the experiment and equal to the mass uptake from measurements with the step-change of relative humidity (TEST 3) after 12 hours. It can be noticed that the change of the mass uptake profile is more significant here than for the test at 20 °C. It can also be seen that for the last few days of the experiment the mass uptake profile is not changing. This might indicate that the hygric condition in the material reached oscillatory equilibrium for this sorption/desorption process. The slight decline in mass might be due to too short preconditioning of the specimen.

5. HUMIMUR simulations

The experiments of water vapour exchange between air and building material can be used as validation for simulation programs. Some preliminary results of TEST 1 from HUMIMUR simulation are presented hereafter. The HUMIMUR program was elaborated in order to simulate isothermal water vapour transfer between air and material and the moisture flow inside the material (Kwiatkowski et al. 2008). The simulations are performed using Control Volume Method (CVM) with 1-D model and a first order explicit time scheme. For the calculation the measured water vapour permeability and the sorption curves of gypsum board were implemented into model. The results of calculation for TEST 1 are presented in the FIG. 8.

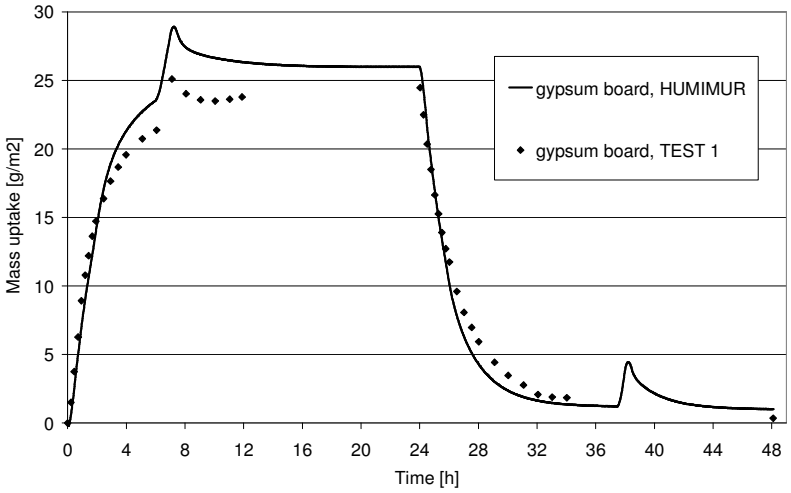

FIG.8: HUMIMUR calculation of the TEST 1.

Although some differences can be noticed the HUMIMUR model gave results close to the measurements. The shape of the calculated mass uptake profile is similar to the experimental data. The difference between

calculation and test can be due to experimental uncertainty on the material and climatic data implemented into model. The differences between simulation and measurements show how important precise material and climatic data are for mathematical models.

6. Conclusions

This paper presented the influence of different parameters on mass transfe. It was shown that even diffusion open paint significantly decreases the rate of the mass transfer. The wallpaper does not change the rate of the absorption/desorption but increases the amount of buffered water. It was pointed out that the change of the temperature from 20 to 24 °C is changing the rate of adsorption/desorption process for the specimens with wallpaper and without any coatings, making it faster in the first part and slower in the second part. For the specimens covered with paint, the change of the temperature causes a uniform change of water vapour transfer rate for the whole duration of the experiment. In the test with higher temperature (24 °C) the mass uptake rate is higher than in the test with lower temperature (20 °C). Also investigations of the mass transfer for different air movements have been presented. In the tests without any air movement, the rate of mass uptake for the first part of the absorption/desorption process was first lower, but after 7-8 hours from the step-change of the relative humidity, higher than in the test with air movement in the chamber. The measurements under dynamic changes of relative humidity showed that the oscillatory equilibrium for adsorption/desorption process are obtained after few days from the start of the experiment and might depend on initial condition in the material.

Finally the preliminary results from HUMIMUR simulation were presented. Despite differences, the calculations gave similar results to experimental data. Some more simulations for other test with step-change of relative humidity and tests with sinusoidal oscillations of relative humidity will be done in the near future.

7. References

Kwiatkowski J., Woloszyn M. and Roux J-J. (2008). Modelling of hysteresis influence on mass transfer in building materials, Submitted for publication.

May M. and Woloszyn M. (2006). A41-T2-F-06-3 Dynamic moisture behaviour of building materials links with microstructure, *Annex 41 Working meeting*, Kyoto 3-5 April.

Osanyintola O. F. and Simonson C. J. (2006). Moisture buffering capacity of hygroscopic building materials: Experimental facilities and energy impact, *Energy and Buildings*, 38. 1270-1282.

Padfield T., Peuhkuri R., Rode C. and Hansen K. K. (2002). Non-isothermal water vapour transmission through porous insulation. Part 1: the climatic chamber, *Proceedings of the 6th Symposium on Building Physics in the Nordic Countries*, Trondheim, Norway.

Peuhkuri R. and Rode C. (2005). A41-T2-Dk-05-1 Using dynamic moisture loading tests for determination of moisture buffer value, *Annex 41 Working meeting*, Montreal 16-18 May.

The dependable characterisation of the moisture buffer potential of interior elements

Hans Janssen, Assist. Professor,
Department of Civil Engineering, Technical University of Denmark;
haj@byg.dtu.dk

Staf Roels, Professor,
Department of Civil Engineering, Katholieke Universiteit Leuven;
staf.roels@bwk.kuleuven.be

KEYWORDS: *sustainability, durability, indoor air quality, interior moisture buffering, moisture buffer value*

SUMMARY:
The hygrothermal performances of building zones, building components and building occupants are strongly related to the interior humidity, and this is in turn related to the moisture buffering by the interior enclosure. This paper presents a methodology for the characterisation of the moisture buffer potential of a single interior element, by introduction of the production-adapted MBV. It is shown that this weighted-average of a long- and a short-term value allows dependably characterising the moisture buffer potential for a multitude of moisture production schemes. As such, the introduced MBV* yields a dependable characterisation of single-element moisture buffer potential, which allows direct qualitative comparison of different elements and which can be measured by simple and fast measurement techniques and equipment. It extension towards the room enclosure level, and its ensuing use for quantification, is the topic of the companion paper (Roels and Janssen, 2008).*

1. Introduction

1.1 Assessment of interior moisture buffering

The influences of interior humidity on the performance of building zones, building parts and building occupants are strongly multifaceted and highly interrelated. The levels of interior humidity substantially affect the energy performance of building zones, via latent cooling loads and transmission loads. The levels of interior humidity moreover considerably affect the appearance and stability of a building part, via the biological action of moulds and fungi. Finally, the levels of interior humidity clearly affect the health, comfort and productivity of building occupants. The correct management of these influences requires the assessment of interior humidity variations. Many authors do though emphasise the influences of moisture storage in the hygroscopic materials in the room, like finishes, furniture, carpets, books, etc. (Padfield, 1999; Rode and Grau, 2002; Simonson et al., 2004). The evaluation of such moisture exchange between the room air and enclosure is a fairly complex problem however, and a comprehensive simulation of the moisture buffering by interior elements remains currently unrealistic. A simplified methodology, most commonly via the *effective capacitance* or the *buffer storage* models, is thus usually preferred. The application of such models to realistic interior enclosures, with multimaterial and/or multidimensional features, is mostly hampered by the lacking scientific basis for the apt choice of parameters, the lacking applicability for multimaterial or multidimensional elements, and/or the lack of readily measurable input data (Roels and Janssen, 2008).

This paper and its companion paper (Roels and Janssen, 2008) introduce a complete methodology, going from a simple and fast characterisation of the moisture buffer potential (MBP) of interior enclosures to a simple and fast quantification of interior moisture buffering effects. This paper is restricted to the characterisation of only single elements, its extension to the enclosure level and its use for quantification are topic of the companion paper.

First, five criteria for the proper characterisation of enclosure MBP are formulated, yielding the evaluation basis for various recent proposals. Three similar procedures, based on cyclic step-change (de)sorption measurements, are retained. The second section demonstrates that the differences in protocols have a substantial influence, and that proper choices need to be made. It is though also demonstrated that fundamentally none of the protocols allows dependably characterising the MBP for a multitude of potential moisture production schemes. This defect is corrected by introducing a production-dependent single-element MBP characterisation.

2. Single-element MBP characterisation

The hygric interaction between room air and enclosure is governed by the contributions of the different elements of the enclosure: interior finishes as well as interior objects. To dependably characterise the MBP of enclosures, and to use it for quantification of interior moisture buffering, a characterisation of the MBP of single elements is thus required first. Foremost any single-element MBP characterisation has to dependably assess the potential of the element to absorb and release moisture, in response to variously timed humidity variations in the ambient atmosphere. The MBP characterisation thus has to target the finite surface mass transfer coefficient controlled response of realistic elements, with (multiple) finite thickness (layers) and/or multidimensional features. Moreover, the MBP characterisation should result in a limited set of values, allowing direct qualitative comparison of different elements. Finally the MBP characterisation should preferably only necessitate simple and fast measurement techniques and equipment. This yields three criteria for the single-element MBP characterisation:

1. dependable assessment of the element's MBP (dependability);
2. direct qualitative comparison of different elements (comparison);
3. characterisation with quick and simple methods (measurement);

Moreover, straightforward extension to the room enclosure level, for both qualitative and quantitative purposes, should be possible, defining two additional criteria:

4. extendable to the level of the whole room enclosure (extendibility);
5. quantification of the moisture buffer performance (quantification);

These five criteria form the basis for the selection and elaboration of a proper procedure for the characterisation of single-element and room-enclosure MBP. For conciseness, the paper here deals with homogeneous single-layer finishes only, but the methodology analogously applies to more complex interior finishes or objects.

Recently, numerous proposals for MBP characterisation of single finishes or finishing materials have been introduced, besides the materials' standard moisture capacity and permeability. The material's effusivity was proposed as "theoretical description" of the single-finish MBP by Rode et al. (2007). Delgado et al. (2006) suggested the use of sorption kinetics: the moisture accumulation in a sample due to a single step-change in ambient relative humidity (RH) is curve-fitted with a formula involving equivalent storage and transport parameters. Conclusively, the Japanese Industrial Standard A 1470-1 (2002), the Draft International Standard 24353 (2006) and the Nordtest Moisture Buffer Value protocol (Rode et al., 2007) advise using the amplitude of the moisture accumulation in a sample exposed to cyclic step changes in ambient RH. In (Janssen and Roels, 2008), it is argued that only the latter may realise the criteria of dependability, comparison and measurement, and these are retained for analysis here.

The Japanese Industrial Standard (JIS), the Draft International Standard (DIS) and the Nordtest protocol (NT) all formulate similar procedures making use of cyclic step-change (de)sorption measurements: the sample, conditioned to a specific RH and sealed at all but its normally exposed sides, is alternatingly exposed to a high and a low ambient RH for predefined intervals of time. The sample moisture mass evolution is recorded, and its amplitude defines the MBP. NT defines the 'Moisture Buffer Value' (MBV) [kg/m²·%RH] as:

$$MBV = \frac{m_{\max} - m_{\min}}{A \cdot \left(\varphi_{high} - \varphi_{low}\right)} \qquad (1)$$

where $m_{max/min}$ [kg/m²] are the sample's maximum/minimum moisture mass (obtained in the final stable cycle), A [m²] is the exposed surface of the element's sample, and $\varphi_{high/low}$ [%] are the high/low RH levels imposed during the measurement. In this paper all MBP's are expressed with Eq. (1), in [g/m²·%RH] for improved readability.

The procedures differ however concerning the sample thicknesses, surface mass transfer coefficients, relative humidity levels and time intervals involved, as shown in Table 1. While NT furthermore targets a stable final cycle with fairly equal amounts of sorbed and desorbed moisture, JIS and DIS use a limited number of cycles, and thus allow for differences between sorption and desorption. It is not clear how these need to be interpreted or applied, thus only steady-periodic MBP characterisations are studied here. Table 1 reveals another fundamental difference between NT and JIS & DIS: NT's choices for a sufficiently thick sample and a sufficiently large surface mass transfer coefficient reveal that NT in essence desires to determine a material property instead of the finite surface mass transfer coefficient controlled response of real claddings with (multiple) finite thickness (layers). The influence of sample thickness and surface mass transfer coefficients will be shown significant below.

TABLE. 1: Synthesis of the JIS, DIS and NT protocols for cyclic (de)sorption MBP measurements.

	RH levels high / low [%]	time intervals high / low [h]	surface transfer coefficient [s/m]	sample thickness
JIS A 1470-1	53 / 33, 75 / 53, 93 / 75	24 / 24	$2.1 \cdot 10^{-8}$	as applied in practice
DIS 24353	53 / 33, 75 / 53, 93 / 75	12 / 12	$2.1 \cdot 10^{-8}$	as applied in practice
Nordtest	75 / 33	8 / 16	sufficiently high	sufficiently thick

3. Materials and methods

3.1 Materials applied

Seven materials are analysed as homogeneous finishes: wood fibreboard (WFB), plywood (PW), gypsum plaster (GP), aerated cellular concrete (ACC), cellulose insulation (CI), flax insulation (FI), perlite insulation (PI). While some of the materials may in reality never be used as finishing materials for a room, they are selected for their differing sorption isotherms, water vapour permeabilities and penetration depths, in such a way that different dynamic responses can be expected. Table 2 presents a synthesis of the key material parameters for the seven materials considered (all values evaluated at 50 % RH).

TABLE. 2: Synthesis of materials parameters for the seven cladding materials investigated.

	WFB	PW	GP	AAC	CI	FI	PI
moisture capacity [$\cdot 10^{-3}$ kg/m³·Pa]	13.7	21.4	1.36	2.34	3.37	1.37	0.10
vapour permeability [$\cdot 10^{-11}$ kg/m·s·Pa]	1.97	0.11	4.56	1.97	10.9	14.9	10.2
1/e penetration depth [$\cdot 10^{-2}$ m]	0.63	0.12	3.04	1.52	2.99	5.47	16.4
moisture effusivity [$\cdot 10^{-7}$ kg/m²·s$^{0.5}$·Pa]	5.19	1.54	2.49	2.15	6.06	4.51	1.03

3.2 Methods applied

All results in this paper are obtained by simulation with a numerical model for moisture transfer in building parts (Janssen et al., 2007). All simulations are isothermal with temperatures constant at 20 °C. In the single-element MBP characterisation, the surface mass transfer coefficient governed response of the material to the rectangular-wave variation in ambient relative humidity is simulated with:

$$\frac{\partial w}{\partial t} = \nabla(\delta_p(p_v)\nabla p_v) \qquad g_s = \beta(p_{vi} - p_{vs}) \tag{3}$$

with w [kg/m³] the moisture content, t [s] the time, δ_p [s] the water vapour permeability, p_v [Pa] the vapour pressure, g_s [kg/m²s] the vapour exchange at the cladding surface, β [s/m] the surface mass transfer coefficient, and $p_{vi/vs}$ [Pa] the interior/surface partial vapour pressure. The results are expressed as MBV following Eq. (1).

In the interior moisture buffering assessment, the hygroscopic response of the room & finish combination to an imposed moisture production regime is simulated. The room moisture balance considered is:

$$\frac{V}{R_v T_i}\frac{\partial p_{vi}}{\partial t} = (p_{ve} - p_{vi})\frac{nV}{3600 R_v T_i} + G_{vp} - A g_s \tag{4}$$

with V/R_vT_i (m³kg/J) the moisture capacity of the zone air, $p_{vi/e}$ (Pa) the exterior/interior partial vapour pressure, n (1/h) the air change rate per hour, V (m³) the volume of the zone, R_v (J/kgK) the gas constant for water vapour, T_i (K) the indoor air temperature (K), G_{vp} (kg/s) the indoor vapour production, A (m²) the surface area of hygroscopic material and g_s (kg/m²s) the water vapour exchange with this surface, calculated via Eq. (3).

For this study a room with a total volume of 90 m³ is assumed, with 60 m² surface area of hygroscopic finishing material. The air change rate in the room is maintained at 0.5 /h, and the surface moisture transfer coefficient at $2.0 \cdot 10^{-8}$ m/s. Three moisture production regimes are considered: (1) a *long* regime with 300 g/h between 0 and 8 am, 0 g/h at all other times, (2) a *short* regime with 600 g/h between 0 and 1am, 6 and 7 am, 12 am and 1 pm and 6 and 7 pm, and 0 g/h at all other times, and (3) a *peak* regime with 325 g/h between 6 and 8 am and 5 and 9 pm, and 25 g/h at all other times. Two ventilation air cases have been investigated: (1) academic: the vapour content of the incoming air is taken constant at 6.11 g/m³ (10 °C & 65 % RH), and (2) realistic: real climatic data are applied for the vapour content of the incoming air. The academic case is simulated for a 10-day interval: a steady-periodic cycle is achieved after such interval, which is retained. The realistic case is simulated for one year plus a preceding adjustment interval of 3 months: only the full year results are retained.

The results are expressed as (average) interior RH amplitudes, which are obtained as:

- for the academic case: half the difference in interior RH levels at respectively the start and end of the moisture production interval implying that two amplitudes result for the peak regime: one for the 6 to 8 am, and one for the 5 to 9 pm production respectively;
- for the realistic case: running 24-h maxima and minima are used, resulting in 8760 hourly values of the 'running amplitude'. Their yearly average is used as representative amplitude. In this case, all regimes result in a single amplitude;

4. Results and discussion

4.1 Sensitivity of MBP characterisation

To illustrate the sensitivity of the MBP characterisation along the JIS/DIS/NT protocols, the MBV's of the seven materials considered are determined, for various sample thicknesses, transfer coefficients, time intervals, and RH levels. The standard case MBV is determined on a 10 cm thick sample, with a $2.0 \cdot 10^{-8}$ m/s surface mass transfer coefficient, under the 33/75 %RH and 8/16 hour NT protocol. Table 3 presents the findings. It is clear that all of the parameters have a significant influence on the resulting MBV value. The influence of the various parameters is though interdependent as well as dependent on the material. This implies that the differing prescriptions in the JIS/DIS/NT protocols will lead to differing qualitative and quantitative MBP characterisations.

For a dependable MBP characterisation thus, proper choices need to be made: samples with build-up and dimensions similar to practice, surface mass transfer coefficients as anticipated in practice, RH levels according to the expected ambient RH, and time intervals in agreement with the likely moisture production. More details on this can be found in (Roels and Janssen, 2006; Janssen and Roels, 2008). While a designer will be able to make proper choices for the first three criteria (build-up & dimensions, surface mass transfer coefficient, ambient relative humidity), the next section hints on a multitude of potential moisture production regimes. Since those cannot be dependably characterised with just a single MBV value, the production-adapted MBV* is introduced.

TABLE. 3: Synthesis of potential MBV values for the seven cladding materials investigated.

		WFB	PW	GP	AAC	CI	FI	PI
sample thickness	1 cm	1.92	0.69	0.43	0.61	0.98	0.46	0.03
	3 cm	1.85	0.69	0.91	0.82	2.00	1.20	0.10
	10 cm	1.86	0.69	0.94	0.81	2.01	1.64	0.31
transfer coefficient	$1.0 \cdot 10^{-8}$ m/s	1.55	0.64	0.86	0.75	1.67	1.41	0.30
	$2.0 \cdot 10^{-8}$ m/s	1.86	0.69	0.94	0.81	2.01	1.64	0.31
	$3.0 \cdot 10^{-5}$ m/s	2.27	0.75	1.03	0.87	2.43	1.95	0.32
time intervals	NT 8/16 h	1.86	0.69	0.94	0.81	2.01	1.64	0.31
	DIS 12/12 h	2.12	0.77	1.06	0.90	2.25	1.85	0.33
	JIS 24/24 h	3.09	1.08	1.55	1.29	3.39	2.82	0.34
RH levels	33/53 %RH	1.73	0.57	0.80	0.77	1.82	1.40	0.20
	53/75 %RH	2.28	0.85	1.13	0.94	2.29	1.94	0.42
	75/93 %RH	4.16	2.41	2.23	1.56	3.62	3.52	1.04

4.2 Dependability of MBP characterisation

4.2.1 Moisture production regimes in dwellings

Figure 1 shows the RH's measured in a detached single-family dwelling ('social' house with natural ventilation, Nieuwpoort, Belgium) for a three-day period in February 2004 (BBRI, 2004). Analysing the measured RH evolutions, it can be noted that the main bedroom agrees well with the NT 8/16 h loading/ unloading scheme. In the bathroom, living room and kitchen, on the other hand, the loading schemes are much more variable. The typical short-term moisture peaks are observed for the bathroom while the kitchen and living room exhibit moisture production intervals with lengths from one to five hours. Similarly variable moisture production schemes are found for non-residential buildings, like offices, museums or schools. For that reason, three different moisture production regimes – long, short, peak – were defined earlier for simulation of moisture buffering in building zones. In conclusion, Figure 1 also demonstrates that the influence of the exterior climate on the interior RH is limited: the key interior RH variations are caused by interior moisture production events.

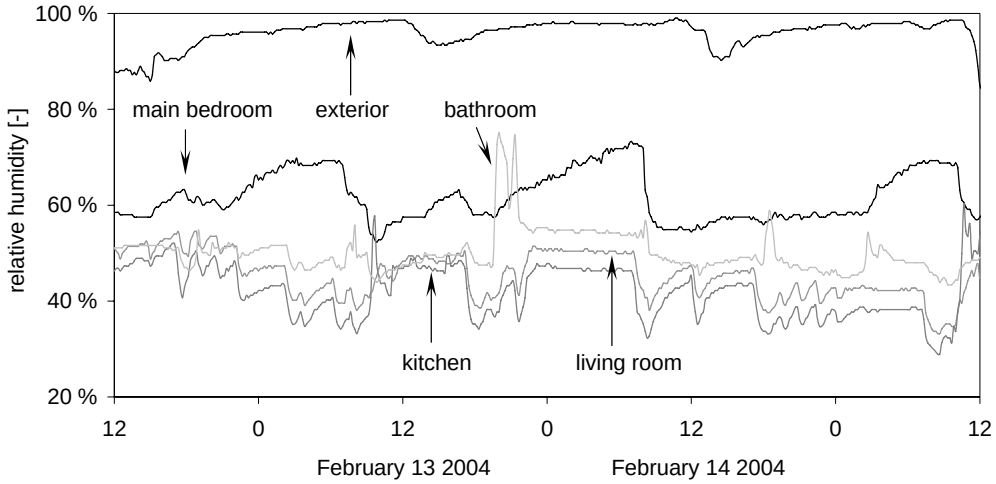

FIG. 1: Variation of exterior RH and interior RH in different rooms of a single-family dwelling.

4.2.2 Interior moisture buffering simulations

The preceding section has demonstrated that the MBP characterisation is significantly influenced by the imposed sample thickness, surface mass transfer coefficient, RH levels and time intervals. It has however not been shown yet that the suggested protocols for MBP characterisation indeed dependably characterise the moisture buffering by single elements. To this aim, an appreciably unique relation between the MBP and the dampening of interior RH variations should exist. Therefore, simulations of moisture buffering in a room with a hygroscopic finish are performed, for the academic and realistic ventilation air cases and with the long, short and peak moisture production regimes as defined above. In the simulations 15 different finishes are considered: one non-hygroscopic and the seven materials applied at thicknesses of 1 and 10 cm.

The relation between MBV – determined on a sample with the actual thickness, with a $2.0 \cdot 10^{-8}$ m/s surface mass transfer coefficient, under the 33/75 %RH and 8/16 hour NT protocol – and the interior RH amplitude is depicted in Figure 2. It is evident that an appreciably unique relation between the two exists for the long moisture production regime, but that the relations for the short and peak regimes are far less distinct. It should thus be concluded that the suggested MBV characterisation is currently only dependable if a clear accord between the actual production scheme and the measurement loading protocol exists. If this condition is not met, the MBV can not reliably be used for assessment of the single-cladding moisture buffer potential. Similar conclusions would have resulted if the MBV had been determined based on the 24/24 hour JIS or 12/12 hour DIS protocol, although for those, the agreement even with the long moisture production regime would have been less. As it is impractical to characterise claddings by various MBP values, one for each potential production scheme, the production-adapted value is introduced in the following section. It will be verified that the weighted average of a short term and a long term MBV, with the weight factor depending on the expected moisture production regime, gives excellent results.

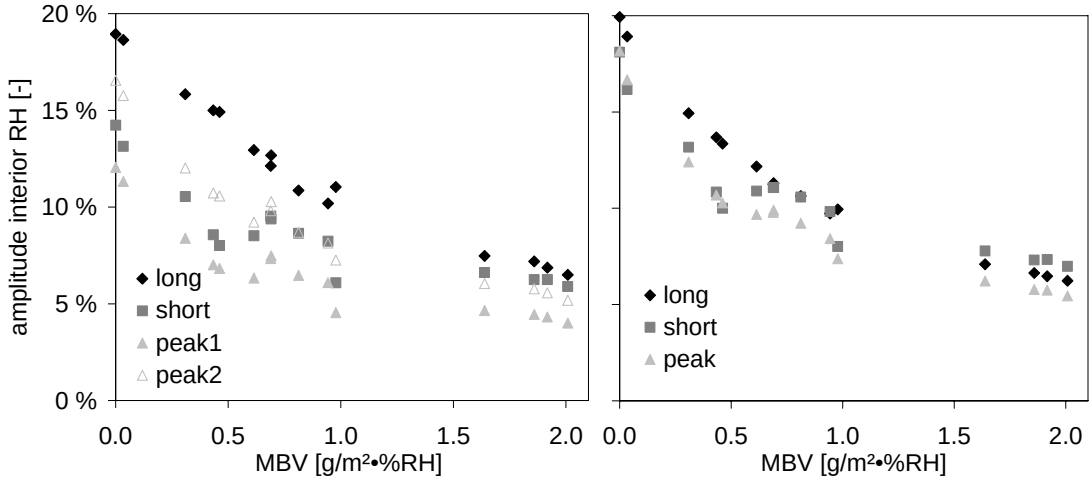

FIG. 2: Relation between MBV and interior RH amplitudes for academic (left) and realistic (right) conditions.

4.2.3 Production-adapted MBP characterisation

As it is impractical to characterise claddings by various MBP values, one for each potential production interval, a weighted-average value is proposed:

$$MBV^* = \alpha \cdot MBV_{8h} + (1-\alpha) \cdot MBV_{1h} \qquad (5)$$

with MBV* the production-adapted MBV, $MBV_{8h/1h}$ the measured MBV values (see below) and α is a weighting factor (see below). The MBV* is introduced here for the NT protocol, the methodology is however similarly applicable to the JIS or DIS protocol. The $MBV_{8h/1h}$ both result from the normal MBV measurement and the use of MBV* does hence not introduce any additional measurement effort. MBV_{8h} is calculated from the accumulated moisture after eight hour at high RH, MBV_{1h} is derived from the accumulated moisture after just one hour at the high RH level within the 8/16 h measurement. The determination of $MBV_{8h/1h}$ is graphically illustrated in Figure 3 for 1 cm and 10 cm GP. The following values are proposed for the weighting factor α:

- 0 hour < production interval ≤ 2 hour: α = 0.0;
- 2 hour < production interval ≤ 6 hour: α = 0.5;
- 6 hour < production interval ≤ 10 hours: α = 1.0;

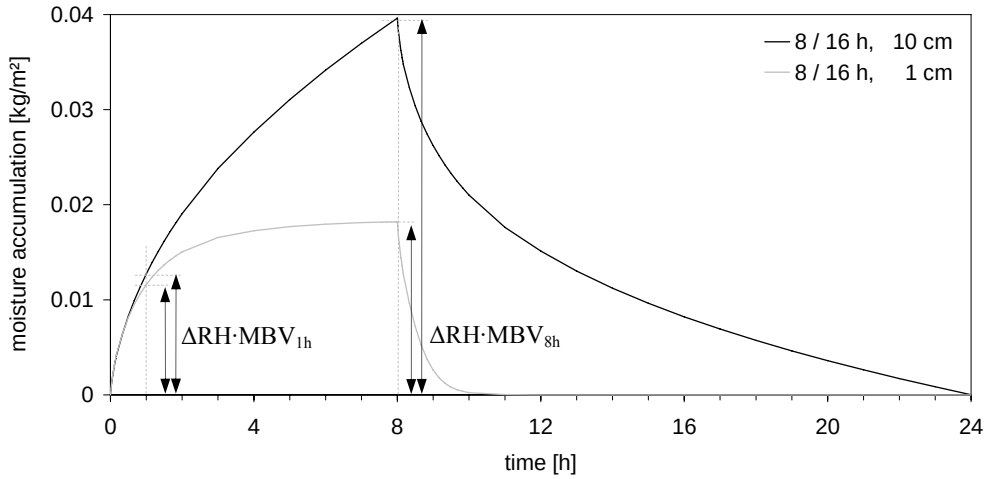

FIG. 3: Graphical illustration of the single-measurement determination of $MBV_{8h/1h}$.

When accurate information on the production regime is available, more detailed values for α may be applied. If longer moisture production intervals are anticipated, a similar weighted-average could be derived for the 24/24 h JIS protocol scheme. In that case, a determination of MBV_{1h}, MBV_{8h} and MBV_{24h}, with appropriate interpolation factors is recommended. For the long, short and peak production regimes considered in this paper, Eq. (5) is deemed appropriate, and α is assumed 1.0, 0.0 and 0.5 respectively.

The resulting relations between MBV* and the interior RH amplitudes are brought together in Figure 4. Comparison with Figure 2 indicates that applying MBV* results in far more consistent MBP - interior RH amplitude relations. The stronger uniqueness of all relations shown in Figure 4 points out that the production-adapted MBV* yields a dependable characterisation of single-element MBP. Observe that this is also true for the peak production regime, where the average of MBV_{8h} and MBV_{1h} is used for both the 2- and a 4-hour production.

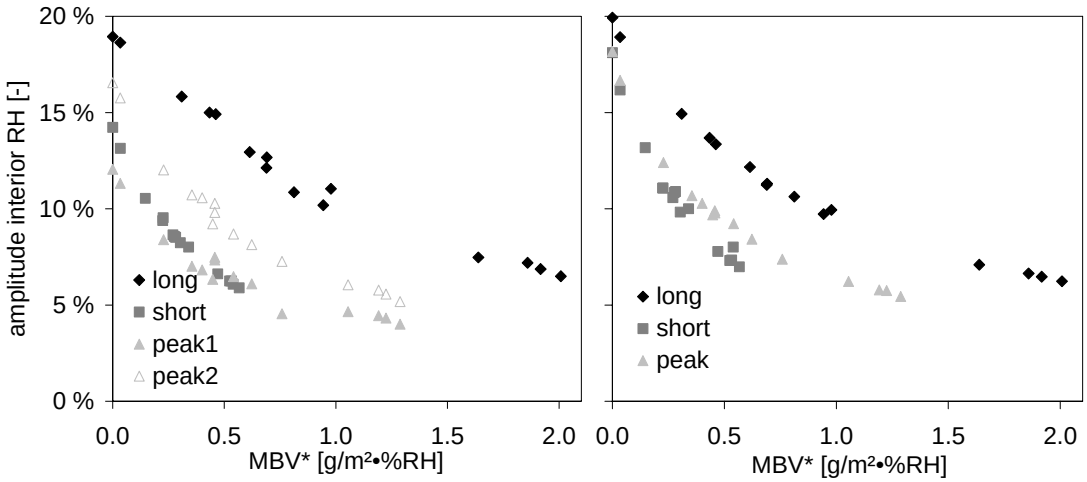

FIG. 4: Relation between MBV and interior RH amplitudes for academic (left) and realistic (right) conditions.*

5. Conclusion

The interior humidity levels influence the sustainability of building zones, the durability of building parts and the health, comfort and productivity of building occupants. The correct management of such influences requires the assessment of interior humidity variations, which are though strongly affected by the passive contributions of the interior enclosure's hygric inertia. Since the comprehensive simulation of interior moisture buffering is currently still unrealistic, simplified methods are usually preferred. Applications of the common *effective capacitance* and *buffer storage* models to realistic interior enclosures are however easily disturbed by a lacking scientific basis for the correct choice of parameters, a lacking applicability for multimaterial and/or multidimensional elements, and/or the lacking readily measurable input data (Roels and Janssen, 2008).

This paper and its companion paper (Roels and Janssen, 2008) put forward a complete methodology to attain the double goal of characterisation and quantification of the moisture buffering by interior enclosures. In this paper, the dependable characterisation of the moisture buffer potential of single elements has been introduced. The extension towards the enclosure level, and the application for quantification, are topic of the companion paper.

Recently, numerous proposals for MBP characterisation of single finishes or finishing materials have been introduced. From these, protocols based on the moisture accumulation amplitude from cyclic step-change (de)sorption experiments were shown to potentially fulfil the criteria of dependability, comparison and measurement. The different sample thicknesses, surface mass transfer coefficients, RH levels, and time intervals prescribed by JIS, DIS and NT triggered an investigation of their respective influence. The following conditions for the dependable single-element MPB characterisation were derived:

- samples with build-up and dimensions similar to practice;
- surface mass transfer coefficients as anticipated in practice;
- RH levels in accordance with the expected ambient RH;
- time intervals in agreement with the likely moisture production;

To account for the potential variability of moisture production schemes met in practice, the production-adapted MBV* was introduced, interpolating between the original long-term MBV_{8h} and the newly presented short-term MBV_{1h}. By means of interior moisture buffering simulations, it was shown that MBV* indeed yields a dependable single-element MBP characterisation, as it can be related to the interior RH amplitudes with appreciable uniqueness. While the development here has focused on homogeneous single-layer finishes only, it is analogously equally valid for more complex interior finishes or objects.

The companion article (Roels and Janssen, 2008) will show that the proposed single-element MBP characterisation by means of MBV* can easily be extended to the level of the room enclosure. It will moreover demonstrate that the resulting room-enclosure MBP characterisation can be used for the approximate quantification of the effects of interior moisture buffering on the interior humidity levels.

6. Acknowledgements

The results in this paper have been partially obtained within KUL OT/04/28 'Towards a reliable prediction of moisture stress on building enclosures', funded by the K.U.Leuven. This financial support is gratefully acknowledged.

7. References

BBRI - Belgian Building Research Institute (2004). Moisture problems in roofs – Impact of the actual boundary conditions and construction types in Belgium (in Dutch), *Final report CC CIF – 966*.

Delgado J.M.P.Q., Ramos N.M.M. and De Freitas V.M. (2006). Can moisture buffer performance be estimated from sorption kinetics ? *Journal of Building Physics*, Vol. 29, p. 281-299.

Janssen H., Blocken B. and Carmeliet C. (2007). Conservative modelling of the moisture and heat transfer in building components under atmospheric excitation. *International Journal of Heat and Mass Transfer*, Vol. 50, p. 1128-1140.

Janssen H. and Roels S. (2008). Interior moisture buffering by enclosures. Part I: characterisation of the moisture buffer potential of single claddings. *Submitted to Energy and Buildings*.

JIS A 1470-1 (2002). Test method of adsorption/desorption efficiency for building materials to regulate an indoor humidity - part 1: response method of humidity.

ISO/DIS 24353 (2006). Hygrothermal performance of building materials and products – determination of moisture adsorption/desorption properties in response to humidity variation.

Padfield T. (1999). Humidity buffering of the indoor climate by absorbing walls, *Proceedings of the 5th Symposium on Building Physics in the Nordic Countries*, Chalmers University of Technology, p. 637-644.

Rode C. and Grau K. (2002). Integrated calculation of hygrothermal conditions of buildings. *Proceedings of the 6th Symposium on Building Physics in the Nordic Countries*, The Icelandic Building Research Institute, p. 23-30.

Rode C., Peuhkuri R., Time B., Svennberg K. and Ojanen T. (2007). Moisture Buffer Value of building materials. *Journal of ASTM International*, Vol. 4, No. 5.

Roels S. and Janssen H. (2006). A comparison of the Nordtest and Japanese test methods for the moisture buffering performance of building materials. *Journal of Building Physics*, Vol. 30, p. 137-161.

Roels S. and Janssen H. (2008). Characterisation of the hygric inertia of a room for a reliable prediction of interior humidity variations, *Proceedings of 8th Symposium of Building Physics in the Nordic Countries*, Technical University of Denmark.

Simonson C.J., Salonvaara M. and Ojanen, T. (2004). Heat and mass transfer between indoor air and a permeable and hygroscopic building envelope : part I – Field measurements. *Journal of Thermal Envelope and Building Science*, Vol. 28, p. 63-101.

Characterisation of the hygric inertia of a room for a reliable prediction of interior humidity variations

Staf Roels, Professor,
Department of Civil Engineering, K.U.Leuven;
staf.roels@bwk.kuleuven.be

Hans Janssen, Assistant Professor,
Department of Civil Engineering, Technical University of Denmark;
haj@byg.dtu.dk

KEYWORDS: *moisture buffer value, building energy simulation, effective capacitance model, buffer storage model, moisture penetration depth.*

SUMMARY:
The hygric inertia of a building zone is characterised as a function of the moisture buffer potential of the finishing materials and furniture in the room. To account for the different time schedules of moisture loads, the production-interval adapted MBV as introduced in the companion paper (Janssen and Roels, 2008a) is used. Numerical simulations demonstrate that the hygric inertia of an entire zone can be determined from its different contributing components, independent of the boundary conditions considered. The second part of the paper shows that the determined hygric inertia of a building zone can be used as a quantitative design value, which can easily be implemented in building energy simulation tools by means of an effective capacitance model or a buffer storage model.*

1. Introduction

Indoor variations in relative humidity are governed by indoor moisture sources, water vapour transport by ventilation air and moisture exchange by temporal storage in available hygroscopic materials in the room as claddings, furniture, carpets, drapes, books and so on. Several authors stress the importance of the latter in the global indoor RH-course (Padfield, 1999; Rode et al., 2002; Simonson et al.,2004). The moisture exchange between indoor air and surrounding hygroscopic materials is however a very complicated problem and until now, a comprehensive simulation of moisture transport and storage in interior hygric buffering elements remains unrealistic. Therefore, most building energy simulation (BES) codes as TRNSYS, Energyplus, CONTAM,.. handle moisture storage in a simplified way. As starting point, the simplified models all assume the air in the room to be well mixed in a way that air temperature, humidity and pressure are equal all over the building zone. Solving the moisture balance of the building zone, two methods can typically be found to account for the moisture storage in the surrounding porous materials.

In the first method, often called *effective capacitance model*, the buffer effect of adsorptive materials is solved within the moisture balance of the room by correcting the moisture capacity of the indoor air. Doing so, the effective capacitance model is a very easy method, since no extra equations have to be solved. The underlying assumption is however, that the moisture buffered in the adsorptive materials is at any moment in equilibrium with the room humidity (Stehno, 1982). As a consequence the effective capacitance model gives only a reasonable estimate of the minima and maxima of indoor humidity, but is unable to predict the exact course of indoor humidity variations since the time dependent behaviour of moisture storage is not included. Furthermore, the reliability depends on the correction factor for the air capacity, where it is hard to find guidelines for.

The second model, mostly referred to as *buffer storage model*, treats the moisture storage in the sorptive material as an additional source/sink term in the moisture balance of the room. Determining the sink term requires at least one extra equation which has to be calculated separately. This is commonly done in a simplified way, as in the *effective moisture penetration depth model* (EMPD-model), where moisture storage and transport in the sorptive layer are described with a single-control-volume equation.

Though more precise than the effective capacitance model, the buffer storage model has the disadvantage that it relies on the moisture penetration depth which can only be calculated from the materials moisture capacity and

vapour permeability, measurements which are time and labour intensive. Furthermore, the calculation of the moisture penetration depth is not well-defined for claddings with multiple layers. To overcome this problem some recent studies applied building envelope models - developed for the analysis of coupled heat and moisture transport within the building walls - to calculate the storage term (e.g. Kunzel et al, 2003, Rode et al, 2003). These models are able to simulate the dynamic storage behaviour of surrounding elements in a more precise way, but yet again require precise material property data. And even these more sophisticated models – and this is probably the most important limitation for all buffer storage models – are mainly deduced for one-dimensional building walls and hardly applicable to carpets, drapes and furnishing or other more-dimensional objects, which are often the most important buffer capacity of a room.

The present study tries to overcome the drawbacks of the common models based on a dependable characterisation of the moisture buffer potential (MBP) of room enclosures, with enclosures defined as the combination of interior claddings and objects. Starting point is the generalisation of the single cladding MBP characterisation to the room enclosure level. In (Janssen and Roels, 2008a) five criteria were defined for single cladding characterisation: 1) a dependable assessment of the cladding's moisture buffer potential; 2) a direct qualitative comparison of different claddings; 3) a characterisation based on fast and simple methods, 4) extendable to the level of the room enclosure and 5) usable for a quantitative assessment of the moisture buffer performance. To account for criteria 1-3 the companion paper proposed single cladding characterisation as a weighted average between a short term and long term moisture buffer potential value (MBV) derived similar to the prescriptions in the Nordtest-protocol (Rode et al. 2007). This paper focuses on the fourth and fifth criterion. In the first part of this paper the hygric inertia of a room (HIR) is characterised as the superposition of the moisture buffer vaulue (MBV) of the finishing materials and furniture in the room. The validity of the proposed expression is studied numerically. It is shown that the hygric inertia of an entire room can be determined from its different contributing components, independent of the boundary conditions considered. An appreciably unique relationship between the dampening of the interior relative humidity (RH) variations and the HIR-value of the building zone is found. The second part of the paper focusses on the quantitative prediction of moisture buffering in building enclosures. Two methodologies are applied. In the first, the HIR-model is implemented into the moisture balance for a building zone by adding the hygric inertia of the room to the moisture capacity of the zone air. This corresponds to the simple moisture capacitance model, but now a reliable prediction of the effective moisture capacitance of the zone can be deduced. The second methodology uses the buffer storage model. By taking into account the short term and long term HIR-value, the hygric inertia of the whole room can be transformed into an equivalent moisture storage layer as implemented in common BES-codes. Beforehand, the next section recapitulates the general moisture balance equation of a building zone and the mathematical description of the common simplifications.

2. Moisture balance equations of building zones

Assuming ideal convective mixing, no surface condensation and considering only air exchange between the building zone and outside and neglecting the temperature dependency of the air density, the moisture balance of a building zone can be written as:

$$C \cdot \frac{\partial p_{vi}}{\partial t} = (p_{ve} - p_{vi}) \frac{nV}{3600 R_v T_i} + G_{vp} - G_{buf} \tag{1}$$

with $C=V/(R_vT_i)$ the moisture capacity of the zone air (m³.kg/J), $p_{vi/e}$ the partial vapour pressure of indoor/outdoor air (Pa), n the air change rate per hour (-), V the volume of the zone (m³), R_v the gas constant for water vapour (462 J/kg/K), T_i the indoor air temperature (K), G_{vp} the indoor vapour production (kg/s) and G_{buf} the moisture exchange between indoor air and all surrounding hygroscopic materials (kg/s). The latter is determined by the vapour diffusion in the thin stagnant air layer near the surfaces of the materials and can be written as:

$$G_{buf} = \sum_k \beta_k \cdot A_k \cdot \left(p_{vi} - p_{vs,k}\right) \tag{2}$$

with β_k the convective surface film coefficient for vapour transfer (s/m), A_k the surface area in m² and $p_{vs,k}$ the vapour pressure at the hygroscopic surface k. The moisture transfer in each hygroscopic material k is described by:

$$\frac{\partial w_k}{\partial t} = \frac{\xi_k}{p_{v,sat}} \cdot \frac{\partial p_{v,k}}{\partial t} = \nabla(\delta_k(p_{v,k})\nabla p_{v,k}) \tag{3}$$

with w_k the moisture content (kg/m³), ξ_k the moisture capacity of the hygroscopic material in terms of relative humidity (kg/m³) and δ_k the water vapour permeability of the absorbing material *k*. Hence, analysing the hygric behaviour of a building zone, taking into account hygric buffering, means simultaneously solving the moisture balance equation (1) and Eq.(2-3) for each hygroscopic material. Note furthermore that Eq.(3) is non-linear: both the vapour permeability δ_k and the moisture capacity ξ_k are highly RH-dependent. As a result, solving the system of equations can only be performed with a finite element or control volume method, unless simplifications are introduced.

The most common simplification is a lumped approach, best known as the effective moisture penetration depth model (Keresteciogl u et al., 1989). The primary assumption in it is that only a thin surface layer (d_b) of the solid material contributes to the storage process. Moisture storage and transport in the sorptive layer are described with a single-control-volume equation. For a single humidity buffer layer with available surface *A* (m²), Eq. (2-3) combine to:

$$G_{buf} = A \cdot \frac{p_{vi} - p_{vb}}{\frac{1}{\beta} + \frac{d_b}{2.\delta}} = \frac{A \cdot \xi \cdot d_b}{p_{v,sat}(\theta_b)} \frac{\partial p_{vb}}{\partial t} \tag{4}$$

Here p_{vb} (Pa) is the average vapour pressure in the active thickness d_b of the humidity buffer layer (m) and $p_{v,sat}(\theta)$ the water vapour saturation pressure at temperature θ. The thickness d_b of the sorption-active layer is – as the effective moisture penetration depth d_p – dependent on the period of the water vapour fluctuations at the wall surface:

$$d_b = a \cdot d_p = a \cdot \sqrt{\frac{t_p \cdot \delta \cdot p_{v,sat}(\theta_b)}{\pi \cdot \xi}} \qquad a=min(d/d_p,1) \tag{5}$$

where t_p is the cycling time (s) and *a* an adjustment factor (-) to account for the fact that the actual thickness *d* can be less than the effective moisture penetration depth d_p. Hence, simplifying the humidity buffer layer to a single active layer with thickness d_b gives only reliable results for cyclic moisture variations with a constant period. To overcome this problem, more precise models make use of surface and deep storage layers. In this way, both short-term and long-term exchanges can be modelled.

The EMPD-model is sometimes also used in the effective capacitance model to determine the multiplication factor of the air capacity. At that moment, the temperature and vapour pressure in the humidity buffer layer are assumed to be the same as in the room air and the whole problem slims down to one single differential equation:

$$\left(C + \frac{A.\rho.\xi.d_b}{p_{v,sat}(\theta_i)}\right) \cdot \frac{\partial p_{vi}}{\partial t} = M \cdot C \cdot \frac{\partial p_{vi}}{\partial t} = (p_{ve} - p_{vi}) \frac{nV}{3600 R_v T_i} + G_{vp} \tag{6}$$

with *C* the moisture capacity of the zone air (m³.kg/J) and *M* the multiplication factor (-).

3. Characterisation of the hygric inertia of building enclosures

As the moisture exchange between indoor air and enclosures is determined by the contribution of the different hygroscopic materials comprised in the enclosure, the companion paper (Janssen and Roels, 2008a) elaborated the characterisation of a single-cladding MBP. To fulfil the first three criteria mentioned in the introduction (dependable assessment, direct qualitative comparison and fast and easy characterisation), a production-interval adapted MBV* characterisation of a single cladding was presented as an interpolation between a long term MBV_{8h} and a short-term MBV_{1h}, both derived from the same material characterisation – cyclic step-change (de)sorption – experiment:

$$MBV^* = \alpha \cdot MBV_{8h} + (1-\alpha) \cdot MBV_{1h} \tag{7}$$

with α a weighting factor depending on the production scheme:

0 hour < production interval ≤ 2 hour: $\alpha = 0.0$;
2 hour < production interval ≤ 6 hour: $\alpha = 0.5$;
6 hour < production interval ≤ 10 hours: $\alpha = 1.0$;

Numerical simulations under both academic and realistic boundary conditions demonstrated that MBV* results in a reliable MBP characterisation of cladding materials. The experiment to determine the MBV* of a cladding is easy to perform and straight forward, but its application is currently restricted to single cladding materials. Real rooms on the other hand are generally cladded with different materials and may comprise other hygric buffers as furniture, decoration elements, carpets, drapes, books, etc.. Recently Ramos et al. (2005) proposed to characterise a room's hygric inertia as a function of the MBP of the finishing materials and furnishing in the room:

$$HIR = (\sum A_k \cdot MBP_k + \sum MBP_l^{'}) / V \tag{8}$$

with *HIR* the hygric inertia per cubic meter of room volume (g/m³/%RH), MBP_k (g/m²/%RH) and A_k (m²) respectively the moisture buffer potential and area of finishing material *k*, MBP'_l (g/%RH) the equivalent moisture buffer potential of element *l* and *V* the volume of the room (m³). Generalising Eq.(8) to a production-interval adapted *HIR** characterisation by use of MBV* we obtain:

$$HIR^{*} = (\sum A_k \cdot MBV_k^{*} + \sum MBV_l^{'*}) / V = \alpha \cdot HIR_{8h} + (1-\alpha) \cdot HIR_{1h} \tag{9}$$

where $HIR_{8h/1h}$ (g/m³/%RH) are the long/short term inertia and α the weighting factor depending on the moisture production scheme concerned. As for claddings the MBV'_l is determined from the moisture mass evolution during cyclic step-change (de)sorption, normalised per %RH change. As an example Figure 1 compares the *MBV*-characterisation of 1 m² of cork-board (4mm) with the *MBV*'-characterisation of a 1 meter long wooden bookshelf with books.

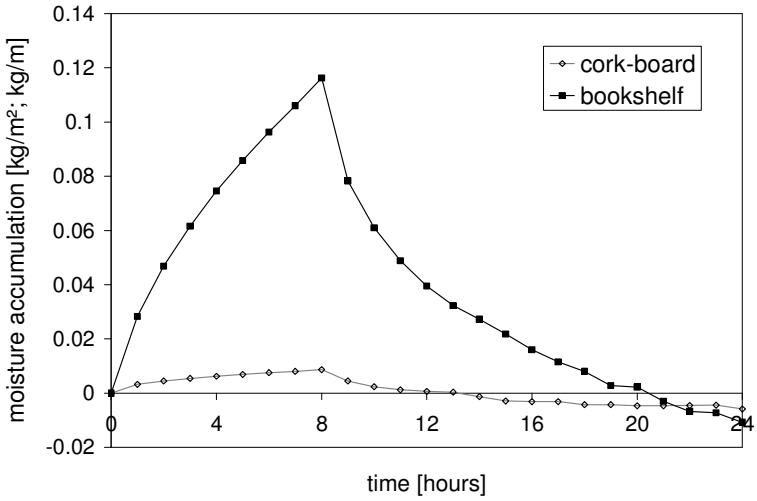

FIG. 1: MBV-characterisation of cork-board and of a one meter long wooden bookshelf with books.

While its thermal analogue is generally accepted and widely used, the validity of Eqs.(8-9) still requires confirmation. To that aim, the set of numerical simulations of moisture buffering in a building zone of 90 m³ under academic and realistic ventilation air conditions as performed in the companion paper to validate the MBV*-approach (Janssen and Roels, 2008a) are extended with simulations using different surface area's (40 m² and 100 m²) of single cladding materials and using combinations of different cladding materials (total surface area: 60 m²). As the former investigations of MBV* proved generalisation to all kind of production regimes and boundary conditions, the current numerical simulations are limited to the academic ventilation air condition (ventilation rate of 0.5 ACH with the vapour concentration of the incoming air constant at 6.11 g/m³) and to the long moisture production scheme (300 g/h produced between 0 and 8 am, and 0 g/h at all other times).

The resulting relations between HIR* and the interior RH amplitude are shown in Figure 2. As for MBV*, an appreciable unique relationship between the dampening of the interior RH-variations and the HIR*-value of the building enclosure is found. Based on the proved generalisation of the MBV*, it can be stated that the hygric

inertia of an entire room can be determined from its different contributing components, independent of the boundary conditions considered. This implies that the fourth criterion, which stated that the MBP-characterisation has to be extendable to the level of the room enclosure, is met and that the hygric inertia of a building enclosure can be qualitatively assessed based on its HIR*-value, which only requires simple and fast step-change sorption/desorption measurements and is applicable not only for homogeneous claddings, but also for multilayered and multidimensional interior elements and for furnishing or other interior objects. That the influence of the latter is important can easily be shown based on the *MBV'* obtained for the wooden book shelf. To have a similar buffer potential as a book shelf of one meter, one needs for instance ± 5 m² of uncoated (!) gypsum plaster or more than 12 m² of cork-board. Unfortunately, until now, making use of the EMPD-model, interior objects are difficult to incorporate and the building enclosures are mostly characterised based on the finishing claddings only. In the next section it will be shown that the characterisation of a building enclosure's hygric inertia with a HIR*-value can also be employed as a basis for quantification of the moisture buffering effects in BES-models (the fifth criterion), resolving some of the shortcomings of the commonly used methods.

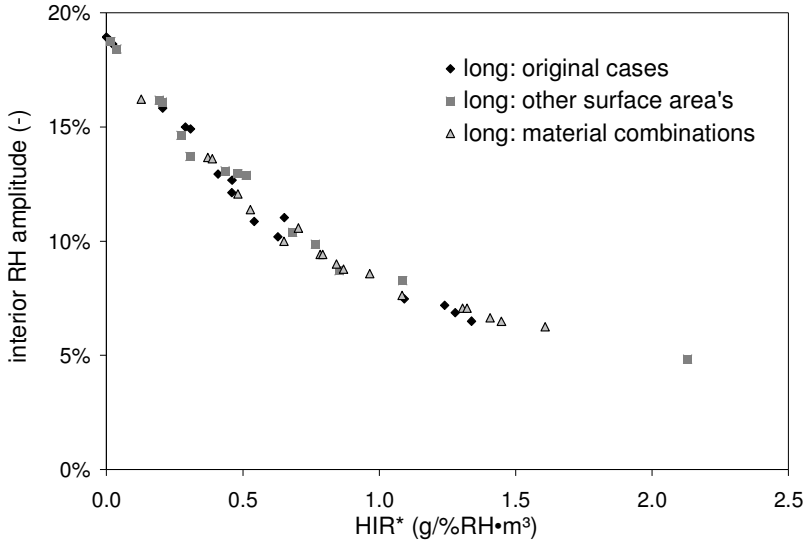

FIG. 2: Relation between HIR and interior RH-amplitude for the original cases, for cases with different surface areas of cladding and for cases with combinations of claddings.*

4. Quantification of building enclosure's buffer effects

The previous section demonstrated that – in analogy to the thermal inertia – the hygric inertia of a building enclosure can be determined through superposition. Making use of the weighted average MBV* of the different claddings and objects in the room, the proposed characterisation showed to be applicable to a multitude of different moisture production schemes. Ultimately though, one doesn't only want to characterise the enclosure's hygric inertia, but aims to quantitatively assess its effect on the indoor RH-variations. To that aim, the determined HIR*-value is implemented in two common BES-methodologies to calculate the effect of moisture storage on indoor RH-variations: the effective capacitance model and the effective moisture penetration depth model.

4.1 Effective capacitance model

Assuming the mass of moisture buffered in the hygric inertia of the building zone M_{buf} (kg) in equilibrium with the room humidity and proportional to the HIR*-value of the building enclosure, the water vapour exchange G_{buf} of Eq.(1) can be written as:

$$G_{buf} = \frac{\partial M_{buf}}{\partial t} = \frac{HIR^* \cdot V}{10 \cdot p_{v,sat}} \frac{\partial p_{vi}}{\partial t} \tag{10}$$

The factor 10 appears in the equation to convert the g/%RH/m³ unit of the HIR*-value back to kg/m³. Eq.(10) transform Eq.(6) into:

$$\left(C + \frac{HIR^* \cdot V}{10 \cdot p_{v,sat}}\right)\frac{\partial p_{vi}}{\partial t} = (p_{ve} - p_{vi})\frac{nV}{3600 R_v T_i} + G_{vp} \tag{11}$$

and the multiplicationfactor *M* of Eq.(6) for a given building enclosure is now defined as:

$$M = \left(1 + \frac{HIR^*}{10 \cdot \rho_{v,sat}}\right) \tag{12}$$

with $\rho_{v,sat}$ the saturation value of the interior vapour density (kg/m³). Compared to the rough estimates for the multiplication factor *M* mentioned in some BES-code manuals or the value determined with the EMPD-model, the proposed value of Eq.(12) corresponds to a reliable total enlarged moisture capacity of the building enclosure.

4.2 Effective moisture penetration depth model

The EMPD model is originally developed for moisture storage in building walls, assuming that only a thin layer near the interior surface interacts with the indoor air: the buffer storage layer. Some models solve Eq.(4) for all available humidity buffering surfaces separately (e.g. EnergyPlus). In most BES-codes, however, all surrounding surfaces are transformed into one equivalent humidity buffering layer. The moisture properties of this equivalent surface have to be chosen in such a way that they result in similar storage behaviour as all available surfaces together. This latter approach can also be applied to transform furniture or other multidimensional objects into an equivalent humidity buffer layer or even the whole hygric inertia of the building enclosure, if the equivalent moisture properties can be derived.

For a single homogeneous cladding, by describing the active layer thickness d_b as *a*-times the moisture penetration depth d_p making use of Eq.(5), Eq. (4) can be written as:

$$A \cdot \frac{p_{vi} - p_{vb}}{\frac{1}{\beta_i} + a \cdot \sqrt{t_p/\pi}/(2.b)} = A \cdot a \cdot \sqrt{t_p/\pi} \cdot b \frac{\partial p_{vb}}{\partial t} \qquad a=min(d/d_p,1) \tag{13}$$

with *b* is the cladding's effusivity ($s^{3/2}$/m). Eq.(13) implies that the effective moisture penetration depth model is essentially governed by the cladding's effusivity *b* and the thickness adjustment factor *a*. The analytic solution for moisture accumulation in a finite homogeneous slab due to a step-change in environment vapour pressure (Carslaw and Jaeger, 1990) – as in the MBP-characterisation procedure – is equally governed by *b* and *a*, implying that the measured $MBV_{8h/1h}$ can hence be used for their determination through a fitting procedure. Conclusively $MBV_{8h/1h}$ can be employed via Eq. (13) as basis for quantifying the moisture buffer effects not only of homogeneous claddings, but also to transform multidimensional objects into an equivalent single buffer layer. Similarly, the $HIR_{8h/1h}$-values, characterising the hygric inertia of a complete building enclosure, can be used to obtain an enclosure equivalent *b* and *a*.

Note in Eq.(13) that when the effect of the surface film transfer coefficient on the moisture transport is not negligible, a reliable fit of *a* and *b* can only be obtained with a good assumption of the exchange surface *A*. For cladding materials the real surface area can be taken. To transform the hygric inertia of a whole building zone into an equivalent single buffer layer, the exchange surface area should be taken close to the sum of all surface areas of claddings and other sorptive active interior elements in the zone. Determination of it could possibly be based on a 3D-room model as presented in [Nielsen, 1999]. If the effect of the surface film coefficient is negligible, fitting can be performed on *a* and *A.b* instead of *a* and *b*.

4.3 Comparison of the results

To illustrate the HIR*-application in the effective capacitance and effective moisture penetration depth model, simulations of interior humidity variations in the 90 m³ room are shown here for the same boundary conditions as described in §3. Examples of similar results obtained for other boundary conditions and other production

regimes can be found in (Janssen and Roels, 2008b). We limit the hygric inertia in the room to different types of single cladding materials, so the two simplified methodologies can be compared with a full numerical simulation of the enclosure's moisture storage and transport. Two different cladding materials – each applied at 60 m² - were considered: 10 cm of wood fibre board (WFB) and 10 cm of plywood (PW). While these claddings might be considered academic, it is assumed that they are equally illustrative. The cladding properties are given in (Janssen and Roels, 2008).

To transform the HIR*-values into an equivalent single humidity buffer layer in the effective moisture penetration depth model, a cycling time t_p has to be chosen (Eq.13). As the weighing factor α in the HIR*-approach, the cycling time is function of the moisture regime period. In the current case it is set as t_p=24 hours, 12 hours and 6 hours for respectively the long regime (α=1.0), the peak regime (α=0.5) and the short regime (α=0.0).

In all simulations, the interior and cladding temperature was maintained at 20°C and the surface mass transfer coefficient was set at $2.0 \cdot 10^{-8}$ s/m. Simulations were run for 10 days and the RH variation of the final day is shown as measure for the interior moisture buffering in Figure 3. A close agreement is found between the fully numerical and the effective moisture penetration depth solution, supporting the applicability of the HIR*-approach for the dependable quantification of an equivalent single buffer capacity and permeability in agreement with the hygric inertia of a building zone. As could be expected the effective capacitance model predicts fairly well the RH minima and maxima but is not able to predict exact course of the indoor RH-variations. This is an inherent shortcoming of the effective capacitance model.

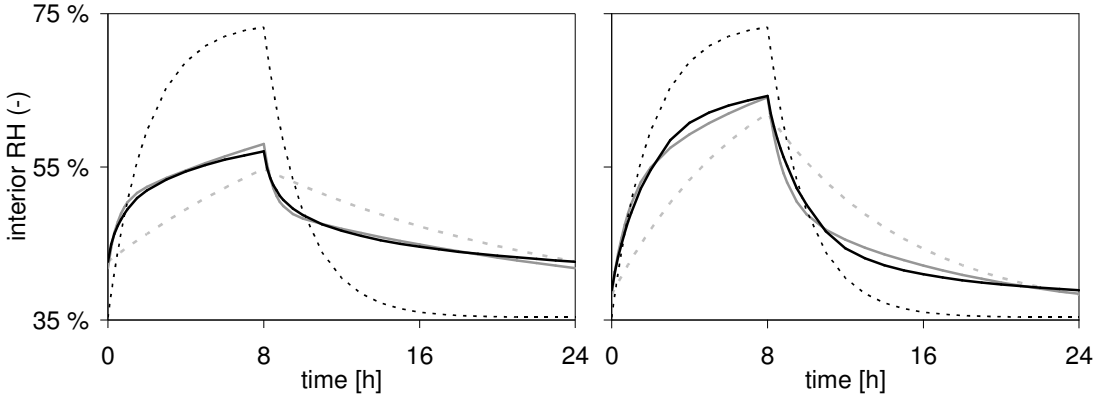

FIG. 3: Comparison of full numerical (full black line), effective moisture penetration depth (full gray line), effective capacitance (dashed grey line) for the WFB (right) and PW (left) claddings, under the long regime. The dashed black curve is the non-hygroscopic reference.

5. Conclusions

In the companion paper (Janssen and Roels, 2008a) a production-interval adapted MBV* characterisation of a single cladding was presented as an interpolation between a long term MBV_{8h} and a short-term MBV_{1h}, both derived from the same material characterisation experiment. As building zones commonly are cladded with more than one building material, the present paper generalised the approach to the level of the room enclosure by introduction of the specific hygric inertia of a room HIR*. With simulations using different surface areas and different combinations of cladding materials it was shown that the hygric inertia of a building enclosure can be determined through superposition. Making use of the production interval adapted MBV* of the different claddings and objects in the room, the proposed characterisation showed to be applicable to a multitude of different production intervals as met in practice. In this way it was verified that HIR*-values of a building zone qualitatively assesses the hygric inertia of the building enclosure.

In the final part of the paper, it was demonstrated that the HIR*-characterisation does not solely allow qualitative assessment of the moisture buffering in a building enclosure, but can also be used in a quantitative analysis. It was shown how the HIR*-characterisation of the hygric inertia of a building enclosure can easily be implemented in two commonly applied BES-techniques to account for moisture storage in building enclosures: the effective capacitance model and the effect moisture penetration depth model. As such, the HIR*-approach gives a reliable and well defined prediction of the multiplication factor to correct the moisture capacity of the

indoor air in the effective capacitance model or can easily be used to transform the global hygric inertia of the building enclosure into an equivalent single buffer layer in the effective moisture penetration depth model. Numerical simulations comparing the two simplified methodologies with a full numerical analysis of the moisture transport and storage in cladding elements proved the validity of the approach.

In this way the MBV*-characterisation of which the companion paper (Janssen and Roels, 2008a) proved to fulfil the required conditions of dependability, comparison and easy measurement, was shown in this paper to be expandable towards the characterisation and quantification of room enclosures by means of a HIR*-value. Main advantage is that the HIR*-approach – compared to the standard methodologies – makes a comprehensive characterisation of the hygric inertia of a building enclosure possible, since also multilayered and multidimensional objects as furniture, carpets, drapes, books, etc. can easily be taken into account and this based on a simple straight forward cyclic step-change (de)sorption experiment without having to measure any other material property.

6. Acknowledgements

The results in this paper have been partially obtained within KUL OT/04/28 'Towards a reliable prediction of moisture stress on building enclosures', funded by the K.U.Leuven and IWT SBO 050154, 'Heat, air and moisture performance engineering: a whole building approach', funded by the Flemish Government. These financial supports are gratefully acknowledged.

7. References

Carslaw H. and Jaeger J. (1990). Conduction of heat in solids (2nd edition). At the Claredon Press, Oxford, U.K.

Janssen H. and Roels S. (2008a). The dependable characterisation of the moisture buffer potential of interior claddings, *Proceedings of 8th Symposium of Building Physics in the Nordic Countries*, Technical University of Denmark.

Janssen H. and Roels S. (2008b). Interior moisture buffering by enclosures. Part II: qualitative and quantitative assessment of room enclosures. Submitted to *Energy and Buildings*.

Keresteciogl u A. Swami M. and Kamel A. (1989). Theoretical and computational investigation of simultaneous heat and moisture transfer in buildings: effective penetration depth theory. *ASHREA Winter meeting,* Atlanta GA.

Künzel H. Zirkelbach D. and Sedlbauer K. (2003). Predicting indoor temperature and humidity conditions including hygrothermal interactions with the building envelope. *Proceedings of 1stIinternational Conference on Sustainable Energy and Green Architecture*, Bangkok.

Nielsen A. (1999). 3D room models for moisture balance calculations. *Proceedings of the 5th Symposium on Building Physics in the Nordic Countries*, Chalmers University of Technology, 645-652.

Padfield T. (1999). Humidity buffering of the indoor climate by absorbing walls, *Proceedings of the 5th Symposium on Building Physics in the Nordic Countries*, Chalmers University of Technology, 637-644.

Ramos N. de Freitas, V. and Delgado J. (2005) Hygroscopic inertia of a room. Evaluation of finishing materials contribution. Paper presented at IEA-Annex 41 working meeting in Montreal, A41-T2-P-05-2.

Rode C. and Grau K. (2002). Integrated calculation of hygrothermal conditions of buildings. *Proceedings of the 6th Symposium on Building Physics in the Nordic Countries*, The Icelandic Building Research Ins., 23-30.

Rode C. Salonvaara M. Ojanen T. Simonson C. and Grau K. (2003). Integrated hygrothermal analysis of ecological building. *Proceedings of 2nd International Building Physics Conference*, K.U.Leuven.

Rode C. Peuhkuri R. Time B. Svennberg K. and Ojanen T. (2007). Moisture Buffer Value of building materials. *Journal of ASTM International*, Vol. 4, No. 5.

Simonson C.J. Salonvaara M. and Ojanen, T. (2004). Heat and mass transfer between indoor air and a permeable and hygroscopic building envelope : part I – Field measurements. *Journal of Thermal Envelope and Building Science*. Vol. 28, No. 1, 63-101.

Stehno V. (1982). Praktische Berechnung der instationären Luftzustandsänderungen in Aufenthaltsräumen zur Beurteilung der Feuchtigkeitsbelastung der raumbegrenzenden Bauteile. *Bauphysik*, Vol.4, 128-134.

Simulation of dynamic moisture response of autoclaved aerated concrete

Olga Koronthalyova, PhD.,
Institute of Construction and Architecture, SAS, Dubravska c 9, 845 03 Bratislava, Slovakia;
usarkoro@savba.sk

Peter Matiasovsky, PhD.,
Institute of Construction and Architecture, SAS, Dubravska c 9, 845 03 Bratislava, Slovakia;
usarmat@savba.sk

Juraj Veselsky, Assoc. Professor,
Slovak Technical University, Faculty of Civil Engineering, Radlinskeho 11, 813 68 Bratislava, Slovakia

Daniel Szabo, MSc.,
Slovak Technical University, Faculty of Civil Engineering, Radlinskeho 11, 813 68 Bratislava, Slovakia

Anton Puskar, Professor
Slovak Technical University, Faculty of Civil Engineering, Radlinskeho 11, 813 68 Bratislava, Slovakia

KEY WORDS: sorption curve, hysteresis, moisture buffer value, AAC, measurements, modelling.

SUMMARY:
The dynamic moisture response of a hysteretic material – autoclaved aerated concrete was tested under three different regimes of relative humidity time step changes. Results of the tests were analysed and compared with a numerical simulation of the dynamic hygric response. On the basis of the analysis the effects of hysteresis on resultant moisture buffer effect at different dynamic regimes were evaluated.

1. Introduction

The indoor air relative humidity is an important parameter influencing the hygro-thermal performance of building structures and the indoor climate as well. An interaction between the indoor air and the hygroscopic material can be used for moderating the indoor humidity variations. For a correct simulation of the moisture buffer effect of building materials it is necessary to know not only the basic hygric parameters determined from steady state measurements but to determine also the possible differences between the steady and dynamic behaviour.

The aim of the work was to simulate the dynamic moisture response of a hysteretic material and to evaluate the influence of hysteretic behavior on a moisture buffer effect under different dynamic boundary conditions regimes – when different parts of material were involved in the moisture uptake/release process.

Tests were done for the autoclaved aerated concrete (AAC) plate. The pore structure of the AAC is characteristic by two distinctly separated pore subsystems consisting of about 30% volume of micropores and about 50% volume of macropores (Matiasovsky and Koronthalyova 2002). For this kind of material the hysteretic behaviour is typical.

2. Experiments

Main adsorption isotherm for AAC was been determined by conditioning the samples in desiccators under a constant relative humidity and temperature (23 °C) until the static equilibrium had been achieved. The following saturated salt solutions were used: LiCl for 12%, $MgCl_2$ for 33%, $Mg(NO_3)_2$ for 53%, NaCl for 75%, NH_4Cl for

79.5%, KCl for 85% and KNO_3 for 94% RH. The samples were oven dried beforehand at 105 °C. The primary scanning desorption curves were determined starting from the equilibrium moisture contents corresponding to 94% RH, 75%, and 53%. The water vapour permeability was measured by standard dry-cup (0 – 53% RH – silica-gel and climatic chamber) and wet-cup (100 – 53% RH - water and climatic chamber) methods.

Dynamic tests were performed in a climatic chamber. The tests were performed uder three different regimes of the cyclic RH step changes: 8/16, 24/48 and 48/96 hours between 49/79, 45/80, 56/79% RH respectively. The temperature during the tests was kept at a constant value of 23.0 ± 0.5 °C. The relative humidity changes in the chamber were controlled by dry and wet air streams. The relative humidity near the sample was monitored by the capacitative RH sensor with ± 1.5% RH precision. The temperature was measured by the resistance sensor Pt 100. The specimens were sealed on all but two surfaces by the epoxy resin in order to guarantee 1D water vapour flow. Simultaneously two specimens with the dimensions of 200 x 108.5 x 39.5 mm were tested (the area of active surface was 0.0868 m^2). The mass of the samples was weighed by the Sartorius balance with the accuracy 0.1g. The mass of samples, the temperature and RH in the chamber were registered every hour. The air flow velocity near the samples varied between 0.05 and 0.15 m/s that corresponded to common interior conditions.

3. Simulation of dynamic response

The moisture content during a scanning between the main adsorption and desorption curves was expressed by the relation:

$$u_m = u_{m,0} + \xi_{hys} \cdot \Delta\varphi \qquad (1)$$

where $u_{m,0}$ is the initial moisture content, $\Delta\varphi$ is the small RH step and ξ_{hys} is the moisture capacity in the hysteresis region. It was expressed by following empirical relations (Pedersen 1990):

$$\xi_{hys} = \frac{\gamma_a \cdot (u - u_a)^2 \cdot \xi_d + (u - u_d)^2 \cdot \xi_a}{(u - u_a)^2} \quad \text{during adsorption} \qquad (2)$$

$$\xi_{hys} = \frac{(u - u_a)^2 \cdot \xi_d + \gamma_d \cdot (u - u_d)^2 \cdot \xi_a}{(u - u_a)^2} \quad \text{during desorption} \qquad (3)$$

where ξ_a is the adsorption moisture capacity at actual RH, ξ_d is the desorption moisture capacity at actual RH, u is the actual moisture content, u_a is the adsorption moisture content corresponding to actual RH, u_d is the desorption moisture content corresponding to actual RH, γ_a, γ_d are empirical parameters, which can be determined by fitting the measured primary scanning adsorption and desorption curves.

The 1D simulation tool WUFI (version 2.2) was used for calculations of the moisture content in samples. The standard value of the interior surface film coefficient for diffusion $\beta_v = 2.5 \cdot 10^{-8}$ s · m^{-1} was used. The 0.5 hour time step was used in calculations in case of 8/16 hours RH change test and the 1 hour time step in case of 24/48 and 48/96 hours RH change tests. The computational mesh size of 0.5 mm was used.

4. Results and discussion

4.1 Steady-state measurements

The basic material properties of the tested AAC are in Table. 1. In the simulations of moisture uptake and release the vapour permeability moisture dependence was approximated by the relation:

$$\mu(\varphi) = \frac{1}{(a + b \cdot exp(c \cdot \varphi))} \qquad (4)$$

Where φ is the relative humidity [-], a, b, c are parameters, $a = 0.13$, $b = 0.003$, $c = 5.0$.

The results of steady – state sorption and desorption measurements and their approximations are shown in Figure 1.

TABLE. 1: Basic material properties of tested AAC material.

Open porosity [-]	Bulk density [kg/m^3]	μ (0 – 53%) [-]	μ (53 - 100%) [-]	∂w/∂φ sorp [1][kg/m^3]
0.8	500	7.6	3.9	17

[1)] in the RH range 50 – 80%

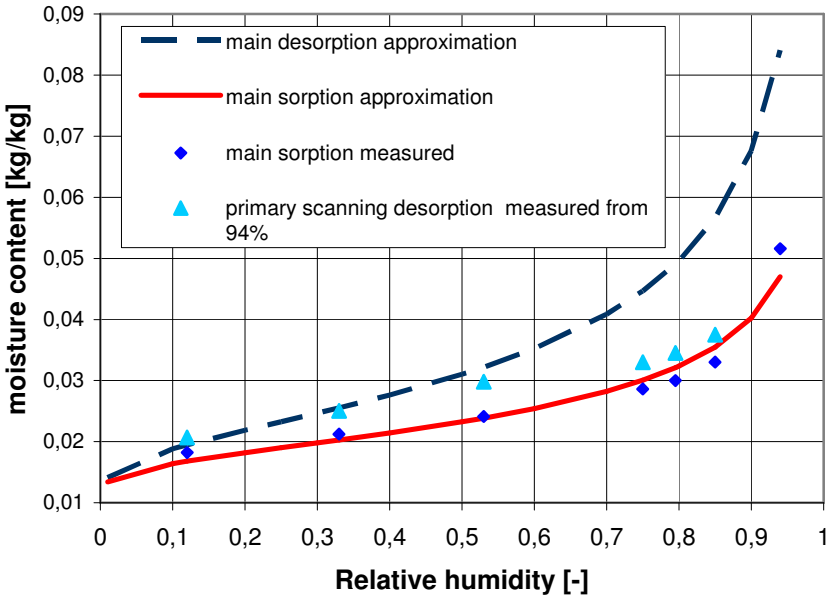

FIG. 1: Main adsorption and desorption curve: measured and approximated values, primary scanning desorption curve measured from 94% RH.

The main adsorption and desorption curve were described by the following equation (Hansen 1986):

$$u_m = A \cdot \left(1 - \frac{\ln \varphi}{B} \right)^{-\frac{1}{n}} \qquad (5)$$

Where u_m is the moisture content [kg/kg], φ is the relative humidity, A, B, n are parameters.

Fitting relation (5) to the main adsorption curve gave the values of parameters: $A = 0.4$, $B_a = 0.00004$, $n_a = 3.43$ (Figure 1).

The measurements of adsorption were done in the 12 – 94% RH interval. Therefore the main desorption curve was not determined directly from the measurements. The estimation of the main desorption curve was done on base of analysis of the previous measurements of AAC samples (Hansen 1986) combined with fitting relation (5) to measured values of the primary scanning desorption curve (from 94%) in the region of low relative humidities (below 50%). The received values of parameters were: $A = 0.4$, $B_d = 0.0015$, $n_d = 2.4$ (Figure 1).

The empirical parameter γ_d was determined by the fitting the relations (1) and (3) to the measured primary scanning desorption curves. The resultant value was $\gamma_d = 0.95$.

The measured primary scanning desorption curves were also compared with an approximation based on the phenomenological hysteresis model (Carmeliet et al 2005). According to the model the moisture content during the primary scanning desorption, starting from relative humidity φ_1, is expressed by the relation:

$$u_m(\varphi) = u_a(\varphi) + (u_a(\varphi_1) - u_a(\varphi)) \cdot A(\varphi) \qquad (6)$$

Where $A(\varphi)$ is the accessibility function, determined from the main adsorption and desorption curves and the maximum achieved moisture content u_{max} (Carmeliet et al 2005):

$$A(\varphi) = \frac{u_d(\varphi) - u_a(\varphi)}{u_{max} - u_a(\varphi)} \qquad (7)$$

In Figure 2 a comparison of the measured and approximated primary scanning desorption curves is shown. The approximation by relation (3) was closer to measured values for desorption starting from higher relative humidities. In the region of lower relative humidities the relation (6) seemed to be a better approximation. On the other hand the noticed differences could be caused by uncertainties contained in the estimation of the main desorption curve.

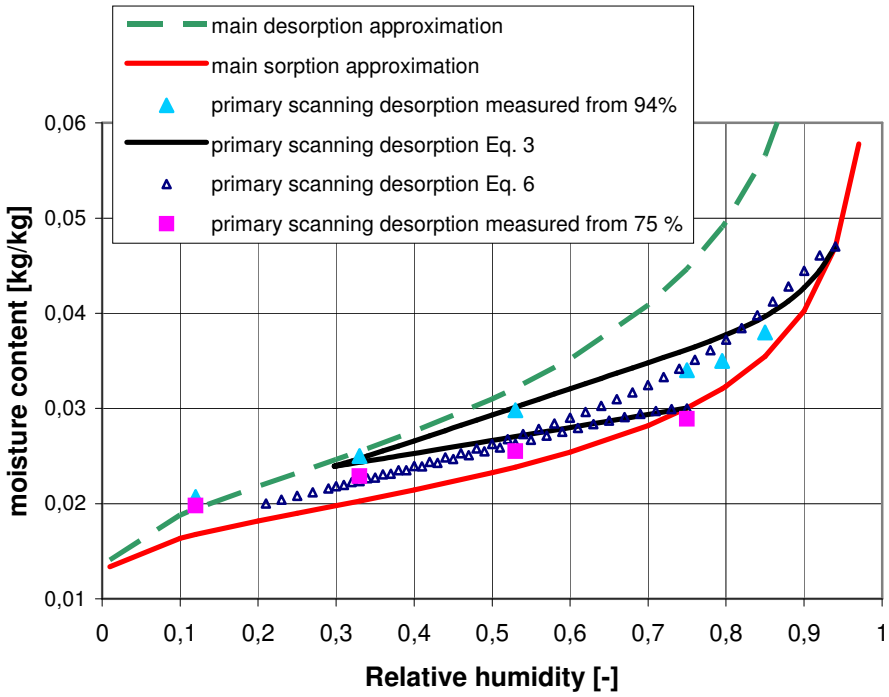

FIG.2 : Primary scanning desorption curves from 94 and 75% RH: measured and approximated curves

4.2 Dynamic moisture response

The measured values of mass changes during step changes of relative humidity and their simulations are shown in Figures 3 – 5. In case of 8/16 hours RH change after the 3rd cycle the quasi-steady state stage was reached. In case of 24/48 and 48/96 cycles the process of sample moisture uptake continued during the whole test.

The hysteretic behaviour had significant effect on the resultant samples mass changes in case of all three regimes.

In the simulations three different moisture capacities were considered: The "main adsorption" line was the result of simulation using the main adsorption curve described by equation (5). It coincided quite well with the 1st uptake in all three tested regimes but it did not involve hysteretic effects present during subsequent releases and uptakes. The "1st scanning desorption" line was the result of simulation with primary scanning desorption curve described by equations (1) and (3). The used empirical parameter γ_d value was 0.95. As it can be seen from the Figures the coincidence of the line with measured 1st release courses was good in 24/48 and 48/96 cycles. In case of 8/16 cycle the simulated release was slightly slower than the measured one. The "1st scanning adsorption" line is the result of simulation with primary scanning sorption curve described by equations (1) and (2). The used

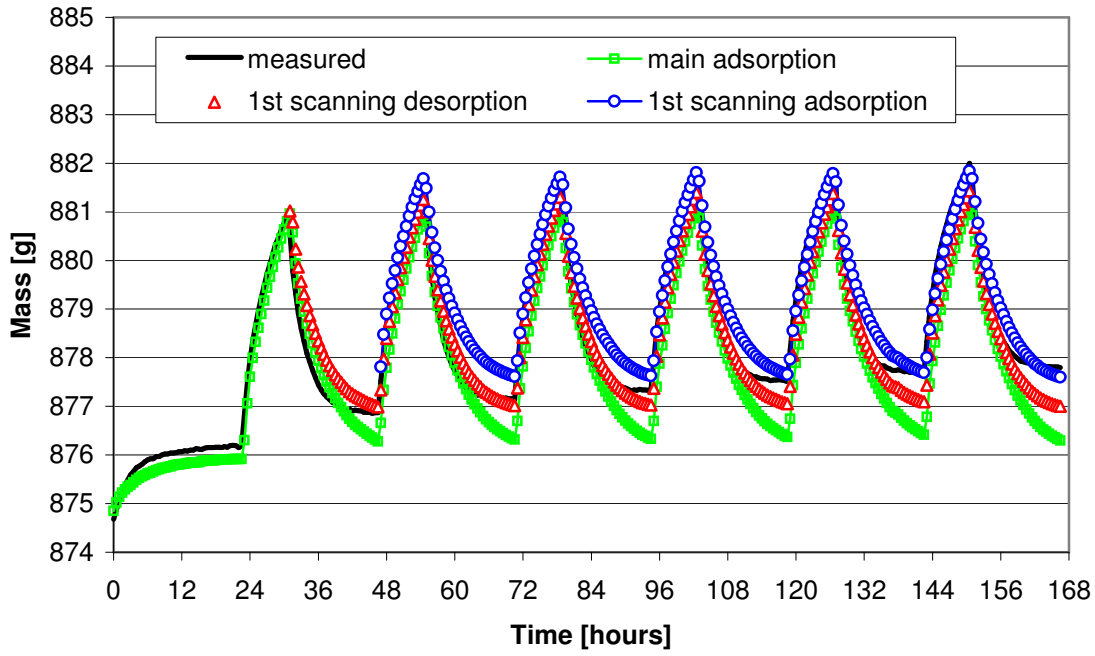

FIG. 3: Measured and simulated mass change during the 8/16 hour RH change test

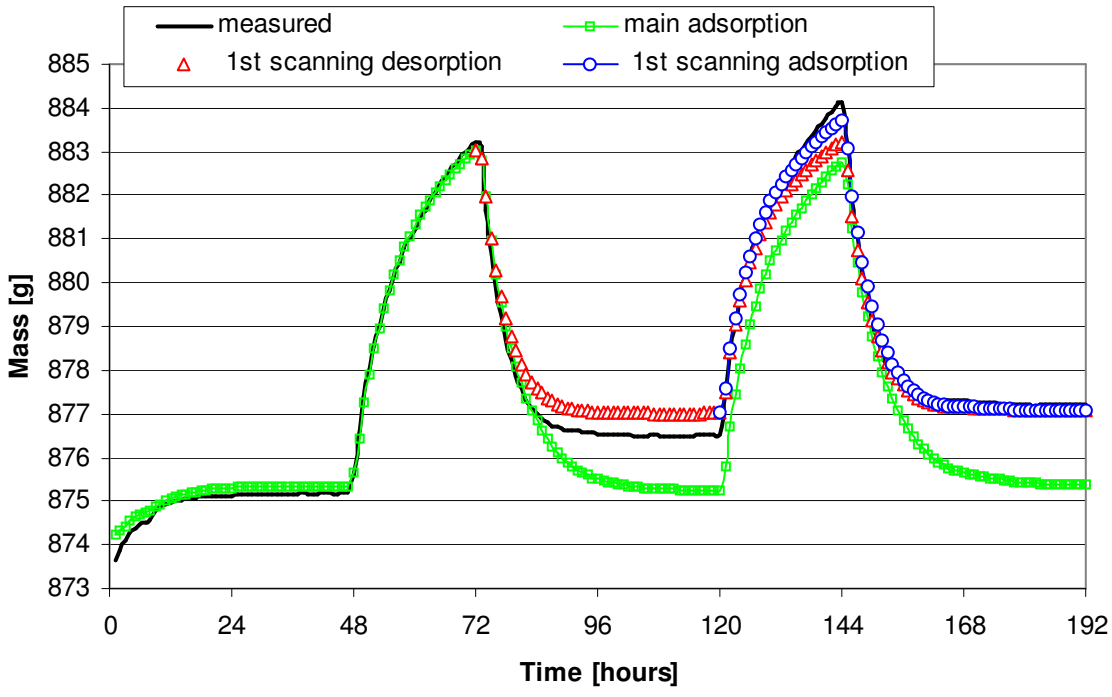

FIG. 4: Measured and simulated mass change during the 24/48 hour RH change test

empirical parameter γ_s value was the same as in case of desorption $\gamma_s = 0.95$. The agreement between the measured and simulated 2nd uptake was satisfactory.

The simulated values were very sensitive to the used approximation of the scanning curves. A relatively good agreement between the measured and simulated mass changes can be explained by the fact that in the measured RH changes region the coincidence between the modelled and experimental scanning curves was also good.

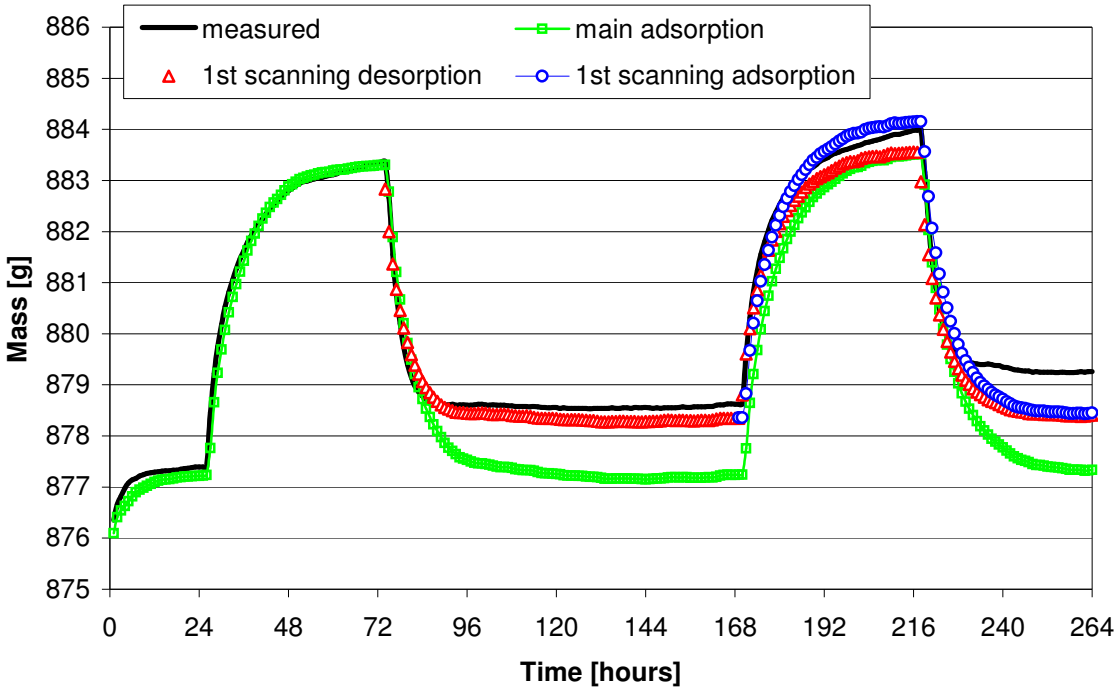

FIG.5: Measured and simulated mass change during the 48/96 hour RH change test

4.3 Moisture buffer value

The moisture buffer capacity of a material can be evaluated by moisture buffer value (*MBV*). The *MBV* is defined as the accumulated moisture uptake/release that happens during the considered period by the material area of 1 m^2 at the 1% RH step change. It can be estimated theoretically from standard material properties using the ideal moisture buffer value MBV_{ideal}. In case of the periodical step RH change, where the high level humidity is present within 1/3 of the period t_p, the MBV_{ideal} [kg / %RH·m^2] is given as follows (Rode C. et al. 2005):

$$MBV_{ideal} = 0 \cdot 00568 \cdot \sqrt{p_s \cdot \delta_p \cdot \frac{dw}{d\varphi} \cdot t_p} \qquad (8)$$

Where p_s is the saturation water vapour pressure [Pa], δ_p is the water vapour permeability [s], $dw/d\varphi$ is the slope of sorption curve in the corresponding relative humidity interval [kg/m^3], φ is the relative humidity [-], t_p is the period [s].

The theoretical moisture buffer ability of the tested AAC was calculated according to relation (8) using the main adsorption moisture capacity and the mean μ value $\mu_{mean} = 4.8$. The comparison with the dynamic test results is in Table 2. The theoretical moisture buffer ability was in a good agreement with the MBV determined from the 8/16 cycle in spite of the fact that hysteretic behaviour was not considered in the calculation. It can be explained by the relatively small difference between the main adsorption moisture capacity and scanning curves moisture capacities in the considered RH interval (Figure 2).

In case of 24/48 and 48/96 cycles the quasi-steady state was not reached.

TABLE. 2: Comparison of the calculated values MBV_{ideal} and the measured MBV values of AAC material for three different RH change regimes (MBV_{ideal} is calculated at 23°C), using main adsorption moisture capacity and mean value of)

RH change regime	MBV_{ideal}	1st moisture uptake / release	2nd moisture uptake / release	3rd - 6th moisture uptake / release
	[g/m² %RH]	[g/m² %RH]	[g/m² %RH]	[g/m² %RH]
48 / 96	3.1	3 / 2.4	2.7 / 2.4	-
24 / 48	2.2	2.6 / 2.2	2.5 / 2.3	-
8 / 16	1.4	1.8 / 1.5	1.7 / 1.6	1.6 / 1.6

5. Conclusions

Dynamic hygric behaviour of the autoclaved aerated concrete was tested by the measurements in a climatic chamber under three different step-change cyclic regimes. In case of 8/16 hours RH change regime after the 3rd cycle the quasi-steady state stage was reached. In case of 24/48 and 48/96 cycles regimes the process of sample moisture increase continued during the whole test.

It was found that hysteretic properties had significant effect on resultant moisture content of the AAC samples. Therefore in cases when the actual material moisture content is of importance the simulation model involving hysteretic behaviour is needed.

The process of moisture uptake and release was numerically simulated using the steady-state hygric properties. In the simulation of hysteretic behaviour of the AAC the empirical approach, based on the application of the experimentally determined scanning curves was used. The accuracy of simulation results was strongly dependent on the scanning curves approximation. The agreement achieved between measured and simulated mass changes was satisfactory due to the coincidence between the model and experimental scanning curves in the considered RH region.

Acknowledgements: The financial support of Slovak Science and Technology Assistance Agency under number APVT-51-030704 and of Slovak Grant Agency VEGA (Grant No 2/7113/27) was gratefully acknowledged.

6. References

Carmeliet J., deWit M. H. D. and Janssen H. (2005). Hysteresis and moisture buffering of wood. *Proceedings of the 7th Symposium on Building Physics in the Nordic Countries,* Icelandic Building Research Institute. Reykjavik.

Hansen K. K. (1986). Sorption isotherms. A catalogue. Department of Civil Engineering, Technical University of Denmark.

Matiasovsky P., Koronthalyova O. (2002). Modelling of the AAC intrisinic and moisture permeabilities from MIP data. *Proceedings of the 6th Symposium on Building Physics in the Nordic Countries,* Norvegian University of Science and Technology, Trondheim.

Pedersen C. R. (1990). Combined Heat and Moisture Transfer in Building Constructions. PhD Thesis. Thermal Insulation Laboratory, Technical University of Denmark.

Rode C. et al. (2005). Moisture Buffering of Building Materials. *Report BYG DTU R-126.* Department of Civil Engineering, Technical University of Denmark.

Moisture accumulation within porous bodies – simplified calculation method for indoor air humidity balance

Maciej Mijakowski, Ph.D.
Faculty of Environmental Engineering, Warsaw University of Technology;
maciej.mijakowski@is.pw.edu.pl

KEYWORDS: indoor air humidity, moisture accumulation

SUMMARY:
The paper describes a simplified method of calculating moisture flows between indoor air and porous materials. The simplified method is based on dynamic heat transfer through the building partition – Thermal Response Factors (TRF). The paper presents examples of humidity step and impulse responses for different porous materials. Formula based on impulse responses was developed and simplified for practical calculation. Presented solution based on TRF methods is close to equation developed by A. TenWolde (1994).
Proposed simplified method was implemented for calculating the whole year moisture flows between different building materials and indoor air. The paper presents comparison between proposed method and more accurate calculations. In the comparison the simulating software like MOIST 3.0 was used. It was showed that proposed simplified method is accurate enough for indoor air moisture balance (the difference for whole year sum of absorbed and desorbed water vapour is about 10%).
Presented method may be useful for indoor moisture balance calculation. The method showed that moisture accumulation may have significant impact on indoor humidity balance and indoor relative humidity.

1. Introduction

Indoor relative humidity is one of the most important feature of indoor climate. It has great influence on the thermal comfort, perceived air quality and building components durability as well. The most important for formation of indoor relative humidity are water vapour emission and movement of water vapour with air flows. These processes are essential for predicting short time averages of indoor moisture content. For long time period also the process of moisture accumulation within porous bodies may have significant impact on indoor relative humidity, (Emmerich, et al. 2002, Haupl, et al. 2001, Patfield 1998, Plathner, et al. 1999, Straube, et al. 2001). Fig. 1 a) presents potential of moister buffering by porous materials. For example for 30 m^3 of air you need 210 g of moisture to change the indoor RH from 50% to 90%RH, but if there is 10 kg of wood within the box (room) in steady – state conditions amount of moisture increase to 1400 g.

a) b)

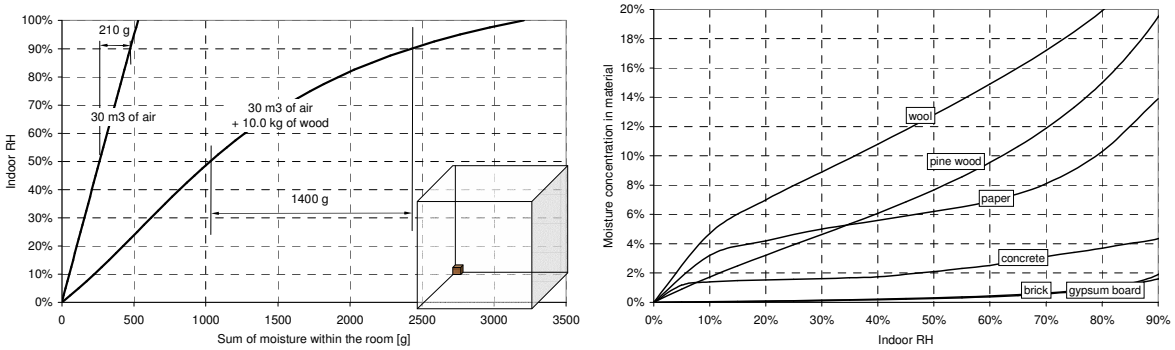

FIG. 1. Potential of moisture buffering by porous materials (a), and sorption isotherms for some building materials (b) (ASHRAE, Burch, et al. (1997), Künzel (1996))

2. Influence between porous bodies and indoor air

Moisture accumulation appears within building partitions, furniture and other inner materials. In most cases these materials may be treated as porous bodies. At equilibrium state the moisture flows from the surrounded air to porous materials is the same to the flow from material to air. In case of changing the parameters of surrounded air the flow of moisture is going to reach the new equilibrium state.

Moisture content of porous bodies in steady state conditions depends on humidity, temperature and pressure of surrounded air (Axley 1991). For typical materials and air parameters typical for indoor conditions the relation is mainly depending only on indoor humidity. This relation is called as a sorption isotherm. Building materials, furniture and inner materials are characterised by II and III type of BET (*Brunauer*, *Emmett*, *Teller)* sorption isotherms. Some examples of sorption isotherms for concrete, gypsum, bricks, wood and paper are presented on Fig. 1. b) (ASHRAE 2001, Burch, et al. (1997), Künzel (1996)):

During dynamic changing of indoor air humidity there is always moisture flow between indoor air and porous materials. Moisture flow may be described within the time ∂t as a sum of water vapour and capillary water flow at the distance ∂y according the formula, Burch, et al. (1997):

$$\rho_m \cdot \frac{\partial w}{\partial t} = \frac{\partial}{\partial y}\left(\delta_m \cdot \frac{\partial P_v}{\partial y}\right) - \frac{\partial}{\partial y}\left(D_l \cdot \frac{\partial P_l}{\partial y}\right) \tag{1}$$

where:

ρ_m - density of dry material, kg/m^3,
w - moisture concentration in material, kg/kg,
δ_m - water vapor permeability, kg/(s·m·Pa),
P_v - water vapor partial pressure, Pa,
D_l - capillary water conductivity, kg/(s·m·Pa),
P_l - capillary pressure, Pa.

Equation (1) should be completed by initial and boundary condition. Moisture transport intensity strongly depends on heat distribution, for example according the Burch, et al. (1997):

$$\rho_m \cdot (c_m + w \cdot c_l) \cdot \frac{\partial T}{\partial t} = \frac{\partial}{\partial y}\left(\lambda_m \cdot \frac{\partial T}{\partial y}\right) + h_{l-v} \cdot \frac{\partial}{\partial y}\left(\delta_m \cdot \frac{\partial P_v}{\partial y}\right) \tag{2}$$

where:

c_m - dry specific heat of material, J/(kg·K),
c_l - specific heat of water, J/(kg·K),
T - temperature, K
λ_m - thermal conductivity of material, W/(m·K)
$h_{l\text{-}v}$ - latent heat of vaporization, J/kg.

3. Simplified method of moisture accumulation flow

Description of accumulation flow may be analogous to dynamic heat transport through building partitions. Presented simplified method of moisture accumulation flow is based on *Thermal Response Factors* (TRF) method. This method describes the heat flow (ϕ) at the surface of the material as a function of impulse responses (g) and air temperature (T) in the past, Mitalas, et al. (1967):

$$\phi_1 = \sum_{k=0}^{n}\left(g_{1-1_k} \cdot T_{1_{t-k\cdot\delta t}}\right) - \sum_{k=0}^{n}\left(g_{1-2_k} \cdot T_{2_{t-k\cdot\delta t}}\right) \tag{3}$$

Dimension of coefficients $g_{1\text{-}1k}$, $g_{1\text{-}2k}$ is the same as the U – value, and the sum of coefficients should fulfil relation:

$$\sum_{k=0}^{n} g_{1-1_k} = \sum_{k=0}^{n} g_{1-2_k} = U \tag{4}$$

Describing an accumulation of water vapor according the TRF method the temperature should be replaced by relative humidity. The assumption of constant conditions of moisture transport in the whole range of relative humidity is essential in that case. For range of relative humidity typical for indoor condition the error of that assumption not exceed 3.5%, Mijakowski (2002). According above, equation (3) changes form to:

$$wm_1 = \sum_{k=0}^{n}\left(gw_{1-1_k} \cdot \varphi_{1_{t-k\cdot\delta\tau}}\right) - \sum_{k=0}^{n}\left(gw_{1-2_k} \cdot \varphi_{2_{t-k\cdot\delta\tau}}\right) \tag{5}$$

where wm is specific moisture flow (kg/s·m^2)

In case of describing the accumulation of water vapor, the time series of relative humidity for "both" sides of material are the same and the formula (5) may be written as:

$$wm = \sum_{k=0}^{nw}\left(\varphi_{t-k\cdot\delta\tau} \cdot \left(gw_{1-1k} - gw_{1-2k}\right)\right) \tag{6}$$

After replacing $gw_k = gw_{1-1k} - gw_{1-2k}$ the equation (6) change to:

$$wm = gw_0 \cdot \left(\varphi - \sum_{k=1}^{n}\left(\frac{gw_k}{-gw_0} \cdot \varphi_{t-k\cdot\delta\tau}\right)\right) \tag{7}$$

and because of formula (4) the sum $\sum_{k=1}^{n}\frac{gw_k}{-gw_0} = 1$. The ratio of coefficients gw_k/gw_0 may be set as w_k and gw_0 may be replaced by κ. After changing the time step of discretisation and follow the above replacements the moisture flow (A in kg/s) may be written as:

$$A = \kappa \cdot F \cdot \left(\varphi - \sum_{k=1}^{n}\left(w_k \cdot \varphi_{t-k\cdot\frac{\tau}{n}}\right)\right) \tag{8}$$

Formula (8) is close to model developed by A. TenWolde (1994). The moisture flow is a function of moisture storage coefficient (κ) and difference between current and previous indoor relative humidity. The previous humidifies are weighted by coefficients (w_k) which are the function of impulse response coefficients (gw_k).

4. Application of simplified method

Simplified method is useful for prediction of moisture accumulation flow which can reduce or increase indoor relative humidity. For example the moisture accumulation flows for two extremely different materials were calculated (1 cm layer of wool and 10 cm of concrete). Calculations were made by proposed simplified method and as comparison by MOIST Release 3.0 (Burch, et al. (1997) software based on equations (1) and (2). The moisture flows after step change of indoor relative humidity were analyzed. Next the required coefficients of simplified method were calculated. It was the base for comparison of results for simplified and accurate methods. Comparison was made for whole year indoor relative variation.

4.1 Results for step change of indoor relative humidity

Moisture flows after step change of indoor relative humidity form 20%RH to 70%RH for 1 cm layer of wool (Fig. 2. a) and 10 cm of concrete (Fig. 2. b) are presented on Fig. 2.

Presented step responses after assumption discussed before equation (5) are the base for calculating impulse responses (gw_k) and next coefficients (w_k) occurred in formula (8). Coefficients w_k are illustrated on Fig. 3.

It is essential that the sum of w_k should be equal 1. For some materials it is the reason to take into account a lot of coefficients, for example for 10 cm layer of concrete at least 10000 hours – Fig. 4. a).

The solution may be using w_k as a values of normalised function $f(k)$ ($w_k = f(k) / \sum f(k)$). It was shown (Mijakowski 2002) that the best results are given using function $f(k) = 1/k^2$, (fig. 4. b). If 10 values of $f(k)$ are used than κ and τ for analysed materials are as below:

- for 1 cm layer of wool: κ= 1.4 g/(h·m^2·%RH), τ= 2.0 h;
- for 10 cm layer of concrete: κ= 0.3 g/(h·m^2·%RH), τ= 66 h;

It is worth to see that after changing the function $f(k) = 1/k^2$ to $f(k) = \exp(-k)$, equation (8) became the same as developed by A. TenWolde (1994).

Obtained results were the base for calculation of whole year moisture transfer between indoor air and porous materials.

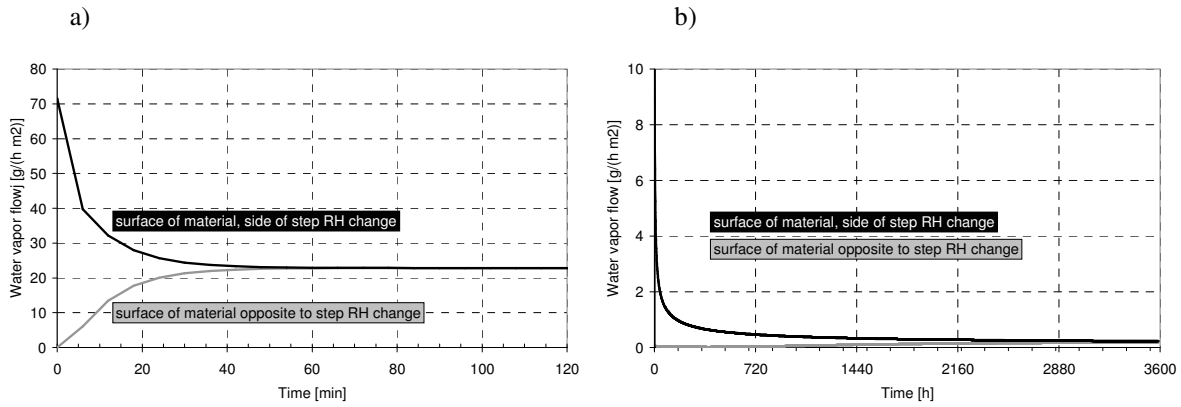

FIG. 2. Moisture flow after step change of indoor relative humidity; a) 1 cm layer of wool; b) 10 cm of concrete

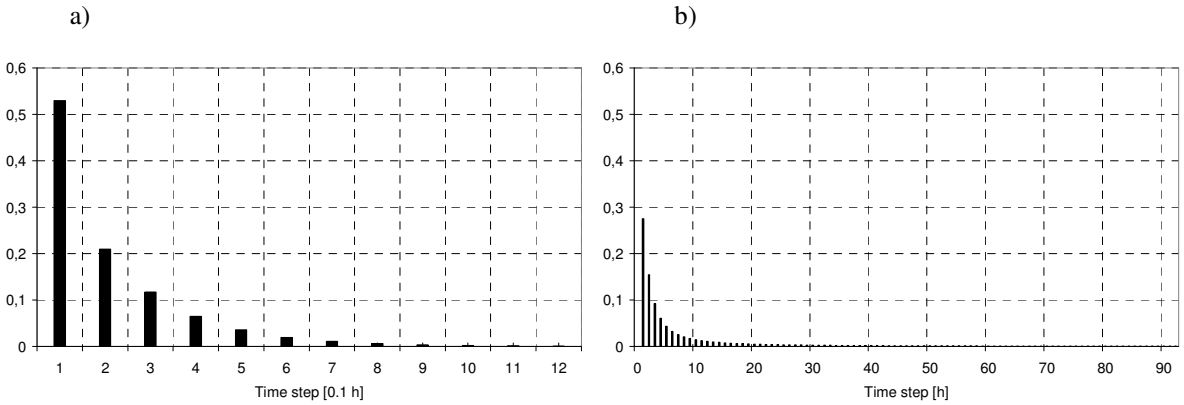

FIG. 3. Coefficients w_k equation (8); a) 1 cm layer of wool; b) 10 cm of concrete

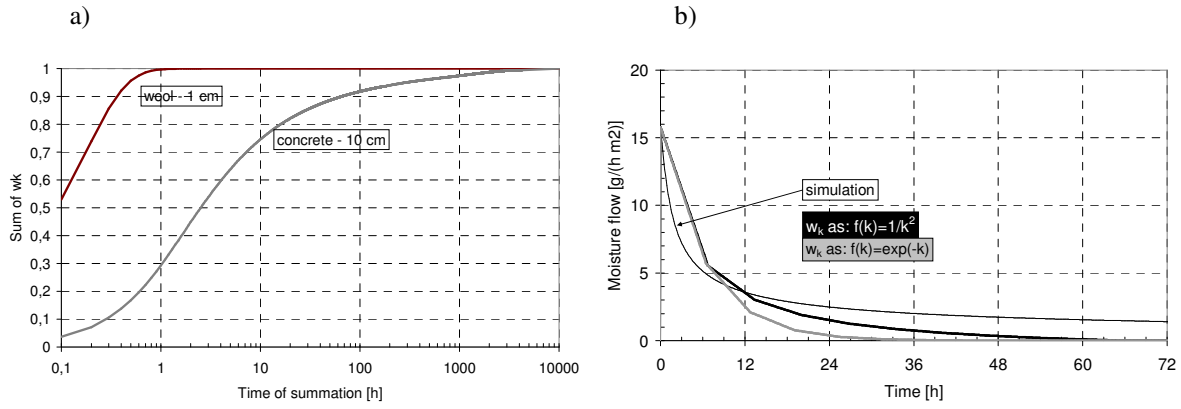

FIG. 4. Sum of w_k as a function of summation period of time (a), and comparison of different form of w_k function (b)

4.2 Results for whole year moisture flow between indoor air and porous materials

Indoor relative humidity time series typical for naturally ventilated dwellings (Mijakowski 2002) was used for calculation of moisture flow. The whole year moisture flow was calculated by simplified and accurate methods. Results of calculation are presented on Fig. 5. (for better view only one winter week is presented).

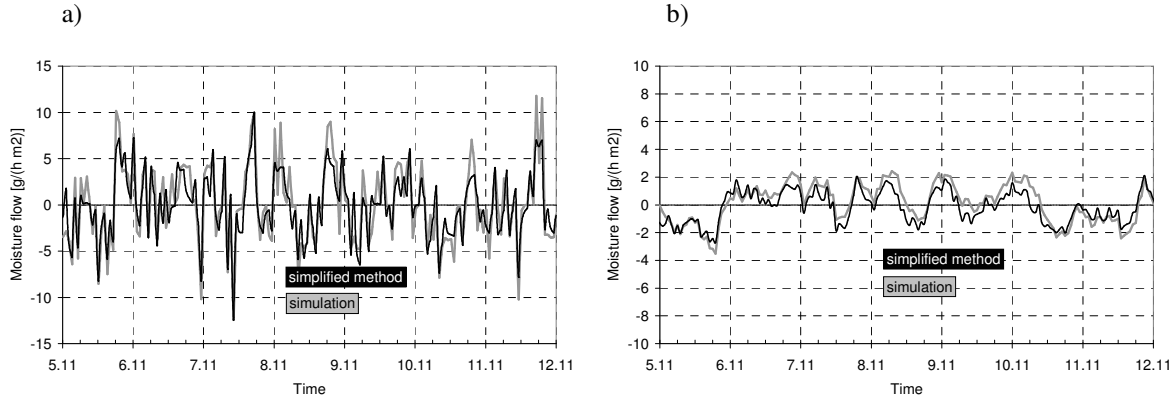

FIG. 5. Moisture flow between indoor air and porous material; a) 1 cm layer of wool; b) 10 cm of concrete

Moisture flow between indoor air and porous materials for typical indoor RH and temperature time series is up to ±20 g/(h·m^2) for 1 cm layer of wool and ±4 g/(h·m^2) for 10 cm layer of concrete. Average error for simplified method is less than 0.9 g/(h·m^2) for 1 cm layer of wool and 0.3 g/(h·m^2) for 10 cm layer of concrete. Total yearly moisture transfer is presented in Table 1.

TABLE. 1: Total moisture flow between indoor air and porous materials.

Porous material	Water vapour adsorption			Water vapour desorption		
	accurate method	simplified method	error	accurate method	simplified method	error
	g/(m^2·year)		-	g/(m^2·year)		-
Wool - 1 cm layer	10045	9115	9.26%	9748	9109	6.55%
Concrete - 10 cm layer	3612	3214	10.99%	3535	3208	9.23%

5. Conclusion

Proposed simplified method is accurate enough for indoor air moisture balance (the difference for whole year sum of absorbed and desorbed water vapour is about 10%). Fig. 6. presents correlation between results of simulation and simplified method for whole year calculation of moisture flow between indoor air and wool and concrete.

The example calculation showed that moisture accumulation may have significant impact on indoor humidity balance and indoor relative humidity. For example moisture accumulated by wool may be up to ±20 g/(h·m^2) when moisture generated by one person is about 80 g/h. During the whole year total absorbed/desorbed moisture is about 10 kg per 1 m^2 of porous material (1 cm layer of wool).

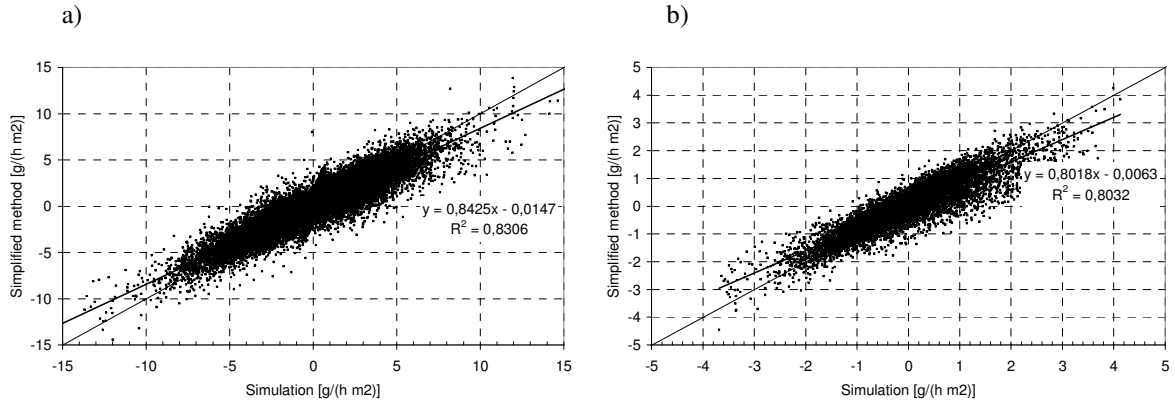

FIG. 6. Whole year moisture flows simulation versus simplified method; a) 1 cm of wool; b) 10 cm of concrete

6. Acknowledgments

Support for research on moisture transfer between the indoor air and porous bodies was provided by the EEA/Norway Grants under the project STEP (PL0077) “Sustainable thermo modernization of public buildings”.

7. References

ASHRAE Handbook, Fundamentals, SI Editions, American Society of Heating, Refrigerating and Air-Conditioning Engineers, Inc., Atlanta, 2001.

ASHRAE Handbook, HVAC Applications, SI Editions, American Society of Heating, Refrigerating and Air-Conditioning Engineers, Inc., Atlanta, 1999.

Axley J. (1991), Reversible sorption modelling for multi-zone contaminant dispersal analysis, Proceedings of Building Simulation '91, p. 20-28, Nice, France; August 20-22, 1991

Burch D.M., Chi J. (1997). MOIST a PC program for predicting heat and moisture transfer in building envelops. Release 3.0, NIST, Washington, 1997

Emmerich S.J., Persily A.K., Nabinger S.J. (2002). Modelling moisture in residential buildings with a multizone IAQ program, Indoor Air 2002, Proceedings: 9th Inter-national Conference on IAQ and Climate, Monterey, California, June 30 - July 5, 2002

Haupl P., Fechner H., Grunewald J., Petzold H. (2001). The thermal improvement of a wooden framework house by means of a capillary active inside insulation, Materiały Konferencyjne VIII Polskiej Konferencji Naukowo - Technicznej Fizyka Budowli w Teorii i Praktyce, Łódź, 2001

Künzel H.M. (1996). WUFI: Simultaneous heat and moisture transport in building components, Fraunhofer Institut Bauphysik, Stuttgart, 1996

Mijakowski M. (2002). Indoor air humidity in naturally ventilated single family buildings - analytical model and its verification (in polish), Ph.D. thesis, Warsaw University of Technology, Warsaw, 2002

Mitalas G.P., Stephenson D.G. (1967). Room Thermal Response Factors, ASHVE Transactions 73 (1), 1967

Patfield T. (1998). The role of absorbent building materials in moderating changes of relative humidity, Ph.D. thesis, The Technical University of Denmark, Lyngby, Denmark, 1998

Plathner P., Littler J., Stephen R. (1999). Dynamic water vapour sorption: Measurement and modelling, The 8th International Conference on Indoor Air Quality and Climate, Indoor Air 99 1, Edinburgh, 1999

Straube J.F., deGraauw J.P. (2001). Indoor air quality and hygroscopically active materials, ASHRAE Transactions, Vol. 107, Pt 1, 2001

TenWolde A. (1994). Ventilation, humidity, and condensation in manufactured houses during winter, ASHRAE Transactions 100 (1), 103-115, 1994

Moisture accumulation within porous bodies – simplified calculation method for indoor air humidity balance

Maciej Mijakowski, Ph.D.
Faculty of Environmental Engineering, Warsaw University of Technology;
maciej.mijakowski@is.pw.edu.pl

KEYWORDS: indoor air humidity, moisture accumulation

SUMMARY:
The paper describes a simplified method of calculating moisture flows between indoor air and porous materials. The simplified method is based on dynamic heat transfer through the building partition – Thermal Response Factors (TRF). The paper presents examples of humidity step and impulse responses for different porous materials. Formula based on impulse responses was developed and simplified for practical calculation. Presented solution based on TRF methods is close to equation developed by A. TenWolde (1994).
Proposed simplified method was implemented for calculating the whole year moisture flows between different building materials and indoor air. The paper presents comparison between proposed method and more accurate calculations. In the comparison the simulating software like MOIST 3.0 was used. It was showed that proposed simplified method is accurate enough for indoor air moisture balance (the difference for whole year sum of absorbed and desorbed water vapour is about 10%).
Presented method may be useful for indoor moisture balance calculation. The method showed that moisture accumulation may have significant impact on indoor humidity balance and indoor relative humidity.

1. Introduction

Indoor relative humidity is one of the most important feature of indoor climate. It has great influence on the thermal comfort, perceived air quality and building components durability as well. The most important for formation of indoor relative humidity are water vapour emission and movement of water vapour with air flows. These processes are essential for predicting short time averages of indoor moisture content. For long time period also the process of moisture accumulation within porous bodies may have significant impact on indoor relative humidity, (Emmerich, et al. 2002, Haupl, et al. 2001, Patfield 1998, Plathner, et al. 1999, Straube, et al. 2001). Fig. 1 a) presents potential of moister buffering by porous materials. For example for 30 m^3 of air you need 210 g of moisture to change the indoor RH from 50% to 90%RH, but if there is 10 kg of wood within the box (room) in steady – state conditions amount of moisture increase to 1400 g.

a) b)

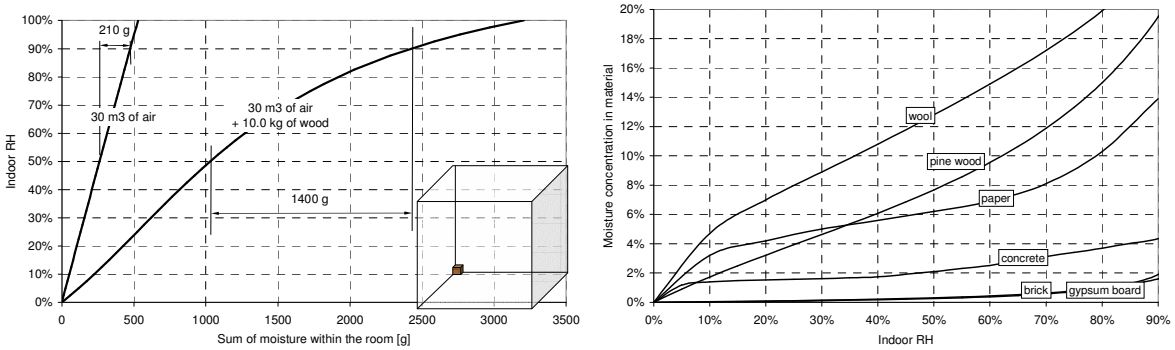

FIG. 1. Potential of moisture buffering by porous materials (a), and sorption isotherms for some building materials (b) (ASHRAE, Burch, et al. (1997), Künzel (1996))

2. Influence between porous bodies and indoor air

Moisture accumulation appears within building partitions, furniture and other inner materials. In most cases these materials may be treated as porous bodies. At equilibrium state the moisture flows from the surrounded air to porous materials is the same to the flow from material to air. In case of changing the parameters of surrounded air the flow of moisture is going to reach the new equilibrium state.

Moisture content of porous bodies in steady state conditions depends on humidity, temperature and pressure of surrounded air (Axley 1991). For typical materials and air parameters typical for indoor conditions the relation is mainly depending only on indoor humidity. This relation is called as a sorption isotherm. Building materials, furniture and inner materials are characterised by II and III type of BET (*Brunauer*, *Emmett*, *Teller)* sorption isotherms. Some examples of sorption isotherms for concrete, gypsum, bricks, wood and paper are presented on Fig. 1. b) (ASHRAE 2001, Burch, et al. (1997), Künzel (1996)):

During dynamic changing of indoor air humidity there is always moisture flow between indoor air and porous materials. Moisture flow may be described within the time ∂t as a sum of water vapour and capillary water flow at the distance ∂y according the formula, Burch, et al. (1997):

$$\rho_m \cdot \frac{\partial w}{\partial t} = \frac{\partial}{\partial y}\left(\delta_m \cdot \frac{\partial P_v}{\partial y}\right) - \frac{\partial}{\partial y}\left(D_l \cdot \frac{\partial P_l}{\partial y}\right) \tag{1}$$

where:

ρ_m - density of dry material, kg/m^3,
w - moisture concentration in material, kg/kg,
δ_m - water vapor permeability, kg/(s·m·Pa),
P_v - water vapor partial pressure, Pa,
D_l - capillary water conductivity, kg/(s·m·Pa),
P_l - capillary pressure, Pa.

Equation (1) should be completed by initial and boundary condition. Moisture transport intensity strongly depends on heat distribution, for example according the Burch, et al. (1997):

$$\rho_m \cdot (c_m + w \cdot c_l) \cdot \frac{\partial T}{\partial t} = \frac{\partial}{\partial y}\left(\lambda_m \cdot \frac{\partial T}{\partial y}\right) + h_{l-v} \cdot \frac{\partial}{\partial y}\left(\delta_m \cdot \frac{\partial P_v}{\partial y}\right) \tag{2}$$

where:

c_m - dry specific heat of material, J/(kg·K),
c_l - specific heat of water, J/(kg·K),
T - temperature, K
λ_m - thermal conductivity of material, W/(m·K)
$h_{l\text{-}v}$ - latent heat of vaporization, J/kg.

3. Simplified method of moisture accumulation flow

Description of accumulation flow may be analogous to dynamic heat transport through building partitions. Presented simplified method of moisture accumulation flow is based on *Thermal Response Factors* (TRF) method. This method describes the heat flow (ϕ) at the surface of the material as a function of impulse responses (g) and air temperature (T) in the past, Mitalas, et al. (1967):

$$\phi_1 = \sum_{k=0}^{n}\left(g_{1-1_k} \cdot T_{1_{t-k\cdot\delta t}}\right) - \sum_{k=0}^{n}\left(g_{1-2_k} \cdot T_{2_{t-k\cdot\delta t}}\right) \tag{3}$$

Dimension of coefficients $g_{1\text{-}1k}$, $g_{1\text{-}2k}$ is the same as the U – value, and the sum of coefficients should fulfil relation:

$$\sum_{k=0}^{n} g_{1-1_k} = \sum_{k=0}^{n} g_{1-2_k} = U \tag{4}$$

Describing an accumulation of water vapor according the TRF method the temperature should be replaced by relative humidity. The assumption of constant conditions of moisture transport in the whole range of relative humidity is essential in that case. For range of relative humidity typical for indoor condition the error of that assumption not exceed 3.5%, Mijakowski (2002). According above, equation (3) changes form to:

$$wm_1 = \sum_{k=0}^{n}\left(gw_{1-1_k} \cdot \varphi_{1_{t-k\cdot\delta\tau}}\right) - \sum_{k=0}^{n}\left(gw_{1-2_k} \cdot \varphi_{2_{t-k\cdot\delta\tau}}\right) \tag{5}$$

where wm is specific moisture flow (kg/s·m^2)

In case of describing the accumulation of water vapor, the time series of relative humidity for "both" sides of material are the same and the formula (5) may be written as:

$$wm = \sum_{k=0}^{nw}\left(\varphi_{t-k\cdot\delta\tau} \cdot \left(gw_{1-1k} - gw_{1-2k}\right)\right) \tag{6}$$

After replacing $gw_k = gw_{1-1k} - gw_{1-2k}$ the equation (6) change to:

$$wm = gw_0 \cdot \left(\varphi - \sum_{k=1}^{n}\left(\frac{gw_k}{-gw_0} \cdot \varphi_{t-k\cdot\delta\tau}\right)\right) \tag{7}$$

and because of formula (4) the sum $\sum_{k=1}^{n}\frac{gw_k}{-gw_0} = 1$. The ratio of coefficients gw_k/gw_0 may be set as w_k and gw_0 may be replaced by κ. After changing the time step of discretisation and follow the above replacements the moisture flow (A in kg/s) may be written as:

$$A = \kappa \cdot F \cdot \left(\varphi - \sum_{k=1}^{n}\left(w_k \cdot \varphi_{t-k\cdot\frac{\tau}{n}}\right)\right) \tag{8}$$

Formula (8) is close to model developed by A. TenWolde (1994). The moisture flow is a function of moisture storage coefficient (κ) and difference between current and previous indoor relative humidity. The previous humidifies are weighted by coefficients (w_k) which are the function of impulse response coefficients (gw_k).

4. Application of simplified method

Simplified method is useful for prediction of moisture accumulation flow which can reduce or increase indoor relative humidity. For example the moisture accumulation flows for two extremely different materials were calculated (1 cm layer of wool and 10 cm of concrete). Calculations were made by proposed simplified method and as comparison by MOIST Release 3.0 (Burch, et al. (1997) software based on equations (1) and (2). The moisture flows after step change of indoor relative humidity were analyzed. Next the required coefficients of simplified method were calculated. It was the base for comparison of results for simplified and accurate methods. Comparison was made for whole year indoor relative variation.

4.1 Results for step change of indoor relative humidity

Moisture flows after step change of indoor relative humidity form 20%RH to 70%RH for 1 cm layer of wool (Fig. 2. a) and 10 cm of concrete (Fig. 2. b) are presented on Fig. 2.

Presented step responses after assumption discussed before equation (5) are the base for calculating impulse responses (gw_k) and next coefficients (w_k) occurred in formula (8). Coefficients w_k are illustrated on Fig. 3.

It is essential that the sum of w_k should be equal 1. For some materials it is the reason to take into account a lot of coefficients, for example for 10 cm layer of concrete at least 10000 hours – Fig. 4. a).

The solution may be using w_k as a values of normalised function $f(k)$ ($w_k = f(k) / \sum f(k)$). It was shown (Mijakowski 2002) that the best results are given using function $f(k) = 1/k^2$, (fig. 4. b). If 10 values of $f(k)$ are used than κ and τ for analysed materials are as below:

- for 1 cm layer of wool: κ= 1.4 g/(h·m^2·%RH), τ= 2.0 h;
- for 10 cm layer of concrete: κ= 0.3 g/(h·m^2·%RH), τ= 66 h;

It is worth to see that after changing the function $f(k) = 1/k^2$ to $f(k) = \exp(-k)$, equation (8) became the same as developed by A. TenWolde (1994).

Obtained results were the base for calculation of whole year moisture transfer between indoor air and porous materials.

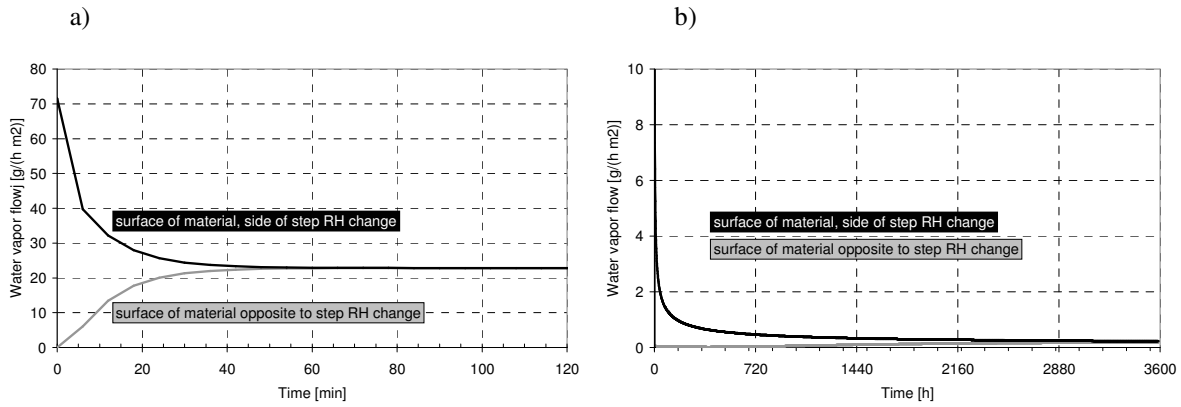

FIG. 2. Moisture flow after step change of indoor relative humidity; a) 1 cm layer of wool; b) 10 cm of concrete

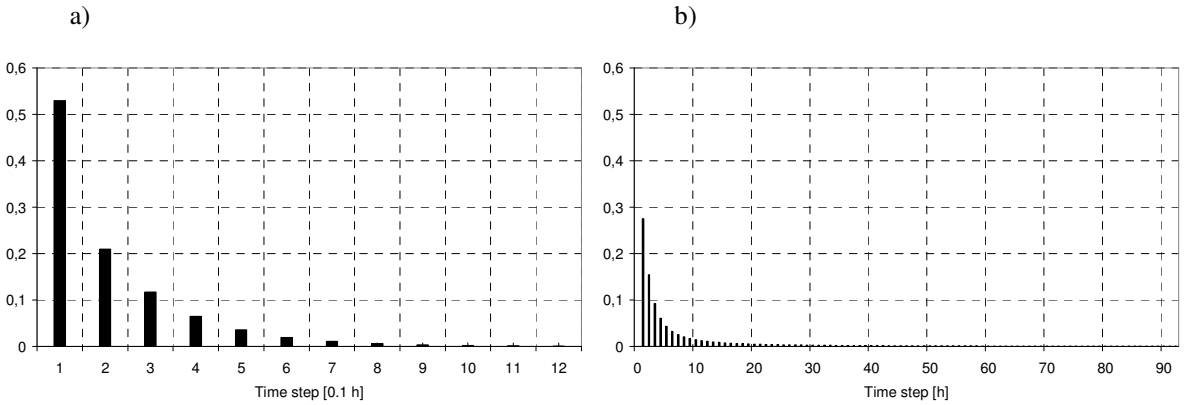

FIG. 3. Coefficients w_k equation (8); a) 1 cm layer of wool; b) 10 cm of concrete

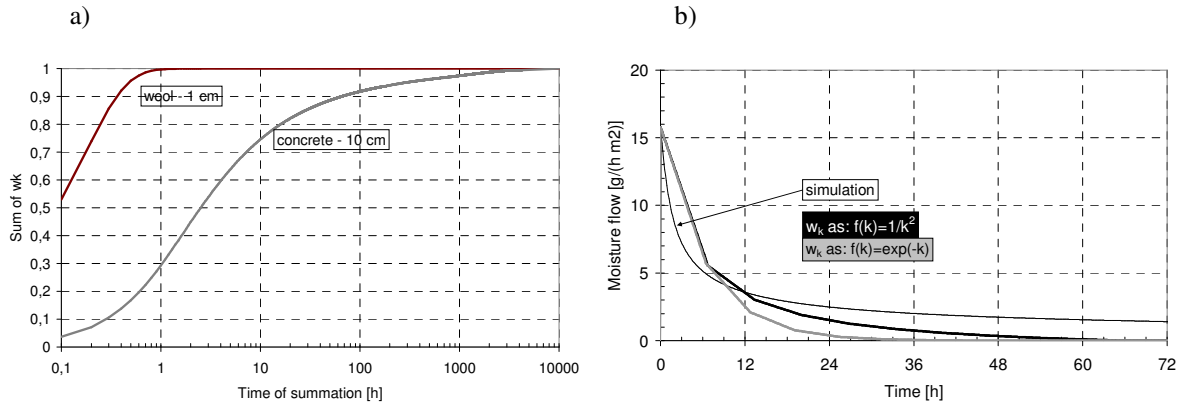

FIG. 4. Sum of w_k as a function of summation period of time (a), and comparison of different form of w_k function (b)

4.2 Results for whole year moisture flow between indoor air and porous materials

Indoor relative humidity time series typical for naturally ventilated dwellings (Mijakowski 2002) was used for calculation of moisture flow. The whole year moisture flow was calculated by simplified and accurate methods. Results of calculation are presented on Fig. 5. (for better view only one winter week is presented).

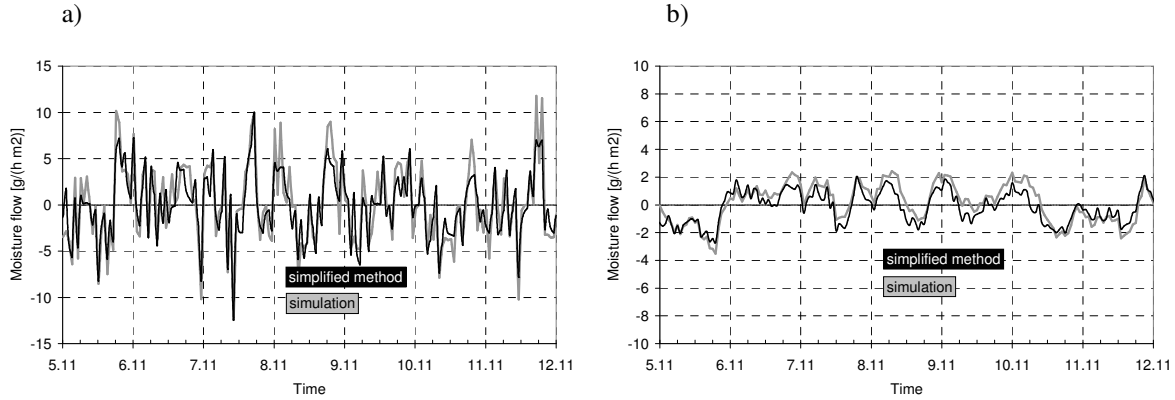

FIG. 5. Moisture flow between indoor air and porous material; a) 1 cm layer of wool; b) 10 cm of concrete

Moisture flow between indoor air and porous materials for typical indoor RH and temperature time series is up to ±20 g/(h·m^2) for 1 cm layer of wool and ±4 g/(h·m^2) for 10 cm layer of concrete. Average error for simplified method is less than 0.9 g/(h·m^2) for 1 cm layer of wool and 0.3 g/(h·m^2) for 10 cm layer of concrete. Total yearly moisture transfer is presented in Table 1.

TABLE. 1: Total moisture flow between indoor air and porous materials.

Porous material	Water vapour adsorption			Water vapour desorption		
	accurate method	simplified method	error	accurate method	simplified method	error
	g/(m^2·year)		-	g/(m^2·year)		-
Wool - 1 cm layer	10045	9115	9.26%	9748	9109	6.55%
Concrete - 10 cm layer	3612	3214	10.99%	3535	3208	9.23%

5. Conclusion

Proposed simplified method is accurate enough for indoor air moisture balance (the difference for whole year sum of absorbed and desorbed water vapour is about 10%). Fig. 6. presents correlation between results of simulation and simplified method for whole year calculation of moisture flow between indoor air and wool and concrete.

The example calculation showed that moisture accumulation may have significant impact on indoor humidity balance and indoor relative humidity. For example moisture accumulated by wool may be up to ±20 g/(h·m^2) when moisture generated by one person is about 80 g/h. During the whole year total absorbed/desorbed moisture is about 10 kg per 1 m^2 of porous material (1 cm layer of wool).

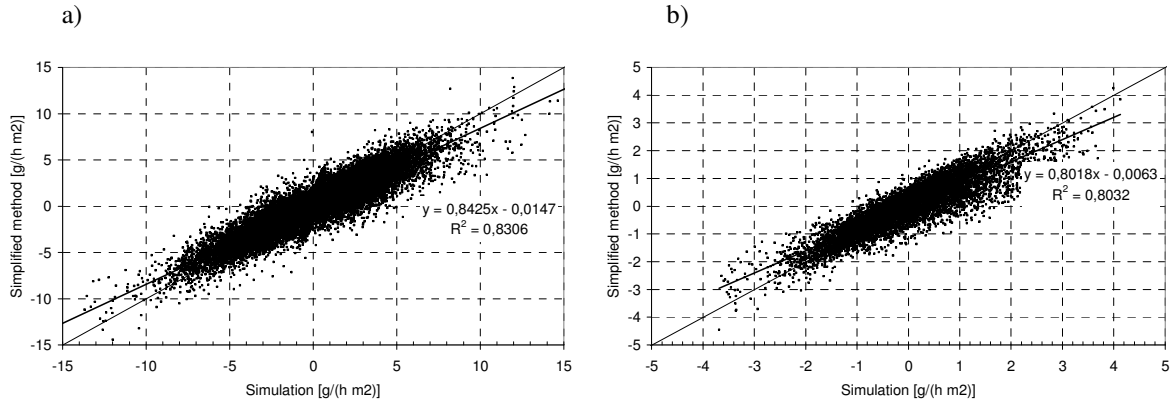

FIG. 6. Whole year moisture flows simulation versus simplified method; a) 1 cm of wool; b) 10 cm of concrete

6. Acknowledgments

Support for research on moisture transfer between the indoor air and porous bodies was provided by the EEA/Norway Grants under the project STEP (PL0077) “Sustainable thermo modernization of public buildings”.

7. References

ASHRAE Handbook, Fundamentals, SI Editions, American Society of Heating, Refrigerating and Air-Conditioning Engineers, Inc., Atlanta, 2001.

ASHRAE Handbook, HVAC Applications, SI Editions, American Society of Heating, Refrigerating and Air-Conditioning Engineers, Inc., Atlanta, 1999.

Axley J. (1991), Reversible sorption modelling for multi-zone contaminant dispersal analysis, Proceedings of Building Simulation '91, p. 20-28, Nice, France; August 20-22, 1991

Burch D.M., Chi J. (1997). MOIST a PC program for predicting heat and moisture transfer in building envelops. Release 3.0, NIST, Washington, 1997

Emmerich S.J., Persily A.K., Nabinger S.J. (2002). Modelling moisture in residential buildings with a multizone IAQ program, Indoor Air 2002, Proceedings: 9th Inter-national Conference on IAQ and Climate, Monterey, California, June 30 - July 5, 2002

Haupl P., Fechner H., Grunewald J., Petzold H. (2001). The thermal improvement of a wooden framework house by means of a capillary active inside insulation, Materiały Konferencyjne VIII Polskiej Konferencji Naukowo - Technicznej Fizyka Budowli w Teorii i Praktyce, Łódź, 2001

Künzel H.M. (1996). WUFI: Simultaneous heat and moisture transport in building components, Fraunhofer Institut Bauphysik, Stuttgart, 1996

Mijakowski M. (2002). Indoor air humidity in naturally ventilated single family buildings - analytical model and its verification (in polish), Ph.D. thesis, Warsaw University of Technology, Warsaw, 2002

Mitalas G.P., Stephenson D.G. (1967). Room Thermal Response Factors, ASHVE Transactions 73 (1), 1967

Patfield T. (1998). The role of absorbent building materials in moderating changes of relative humidity, Ph.D. thesis, The Technical University of Denmark, Lyngby, Denmark, 1998

Plathner P., Littler J., Stephen R. (1999). Dynamic water vapour sorption: Measurement and modelling, The 8th International Conference on Indoor Air Quality and Climate, Indoor Air 99 1, Edinburgh, 1999

Straube J.F., deGraauw J.P. (2001). Indoor air quality and hygroscopically active materials, ASHRAE Transactions, Vol. 107, Pt 1, 2001

TenWolde A. (1994). Ventilation, humidity, and condensation in manufactured houses during winter, ASHRAE Transactions 100 (1), 103-115, 1994

Design of a test chamber for the investigation of moisture transport in air flows and porous materials

Marnix Van Belleghem, Ph.D. Student,
Department of Flow, Heat and Combustion Mechanics, Ghent University;
marnix.vanbelleghem@ugent.be

Hendrik-Jan Steeman, Ph.D. Student,
Department of Flow, Heat and Combustion Mechanics, Ghent University;
hendrikjan.steeman@ugent.be

Michel De Paepe, Professor,
Department of Flow, Heat and Combustion Mechanics, Ghent University;
michel.depaepe@ugent.be

Marijke Steeman, Ph.D. Student,
Department of Architecture and Urban Planning, Ghent University;
marijke.steeman@ugent.be

Arnold Janssens, Professor,
Department of Architecture and Urban Planning, Ghent University;
arnold.janssens@ugent.be

KEYWORDS*: experiment, humid air, hygroscopic material, CFD, climate chamber.*

SUMMARY*:*
This paper describes the design of a test chamber for the investigation of the interaction of humid air and porous materials. Currently computational fluid dynamics (CFD) is gaining in importance as a tool to model the indoor climate in buildings. Meanwhile coupled CFD-material models are being developed which are capable of modelling moisture exchange between air and materials. The newly developed climate chamber can be used to validate these models.

The test chamber, in which different materials can be placed, represents a small room (height: 1.8m, width: 1.8m, depth: 2.1m). This allows full scale experiments for different flow regimes: natural as well as mixed and forced convection can be induced.

Two operating modes are distinguished. In the first mode hygroscopic materials are placed in front of an air jet entering the room. Temperature, air speed and relative humidity of the jet are closely controlled. Temperature and relative humidity in and around the material are measured. The velocity field is measured by a 2D hotwire anemometer. These measurements can then be used to validate CFD codes.

In the second mode hygroscopic buffering of materials is evaluated. Different hygroscopic materials are placed inside the test chamber. Air at a predetermined temperature and relative humidity enters the room at a controlled flow rate. The response of the test chamber with hygroscopic materials to different moisture loads is then measured.

1. Introduction

Growing environmental concern has resulted in an increasing awareness for energy use, comfort and durability of the built environment. Therefore a sustainable development policy is applied. This involves lowering the energy use in buildings.

On the other hand indoor air quality demands are rising. Not only in offices but also at home people want to live in a comfortable climate. Temperature and relative humidity play an important role in the perceived air quality

(PAQ) and occupant comfort as shown in previous studies (Fang et al., 1998). Relative humidity and temperature also influence moult growth and strong fluctuation in relative humidity can damage building materials or artefact such as paintings.

Simonson (Simonson et al., 2002) showed that there was a possibility to improve comfort and perceived air quality by using hygroscopic materials. Fluctuation in temperature and relative humidity can be tempered by these materials. These materials absorb water from humid air and release this water to the air when relative humidity drops. By using these materials in a smart way, the needed heating and cooling rates can be reduced and thus a smaller HVAC system can be installed (Osanyintola and Simonson, 2006).

Computational fluid dynamics (CFD) can be used as a tool to study the interaction of materials and humid air. Classic lumped models only calculate average values for the whole room and don't take local effect into account. In these models well mixed air conditions are assumed. CFD gives the possibility to study flow patterns and moisture distributions in detail and to study local effect (Steeman et al., 2006, Steeman et al., 2008). Results are promising but many of the newly developed models have not yet been validated due to a lack of experimental data.

For validation experiments it is very important that the boundary conditions are well known. Influences from the surroundings should be reduced to a minimum. This is often not the case with field measurements where many external influences are unknown or hard to measure like weather conditions, building occupation… etc. Hence a new test chamber is designed and built where the boundary conditions are meticulously measured and controlled.

2. Test facility

2.1 Purpose of test chamber

The test setup is designed to operate in two modes. This corresponds to the two types of experiments that can be conducted inside the test chamber.

The first type of experiments are the validation experiments for new developed CFD models. Here a conditioned jet is created that enters the room at a predetermined air speed. The relative humidity and temperature of the jet are closely controlled. The velocity field inside the room is measured with a 2D hotwire anemometer. Hygroscopic materials can than be placed in front of the jet. Relative humidity inside the material is measured with small capacitance type humidity sensors. Such measurements on materials have already been conducted for airflow in a short rectangular duct (Talukdar et al., 2007). The newly developed test setup ,described in this paper, however allows other flow conditions: by altering the air inlet velocity forced as well as mixed and natural convection can be induced.

In a second type of experiments hygroscopic materials are placed inside the test chamber. The objective of these experiments is to study the response of the room when a moisture source is present. Air speeds are much lower in this configuration.

2.2 Test setup: general description

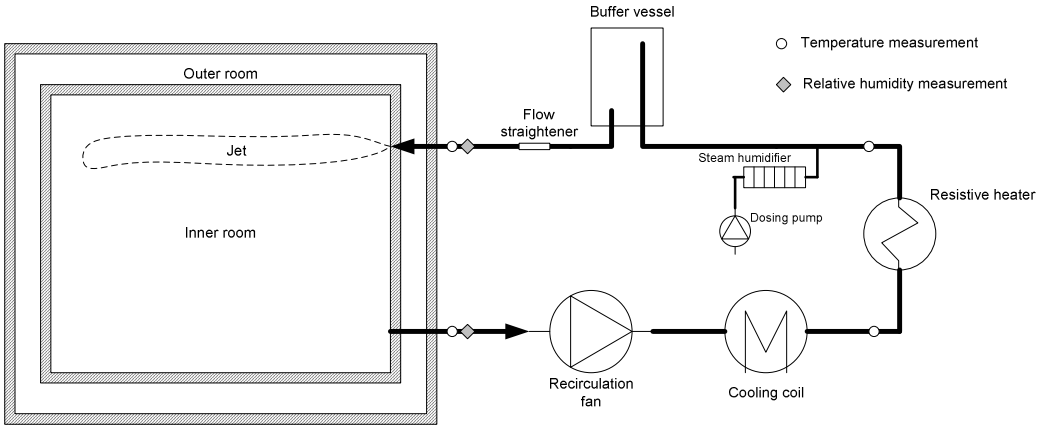

FIG. 1: Schematic representation of the test facility

The test facility consists of two main parts. The climate chamber with inner and outer room is shown on the left hand side of FIG. 1. On the right hand side the climate control group is shown.

The inner room is 1.8m wide, 1.8m high and 2.1m deep. Here the conditioned air enters at the top. Air is drawn from the room at the bottom and passes though the climate control unit. The position and shape of the air in- and outlet of the room can easily be altered by connecting them to ducts which lead to other positions in the room. The outer room is placed around the inner room to reduce influences from the outside environment such as temperature fluctuations.

The wall panels of the inner and outer room consist of 6 cm rigid high density polyurethane foam sprayed in between two skins of white polyester lacquered, galvanized steel plate, 0.63 mm in total thickness. The floor panels consist of multiplex panels with phenol anti-slip surface reinforced with glass fibre. The permissible charge is 500 kg on 4 rubberized wheels or 3000 kg/m² distributed load. The λ-value is 0.366 W/m²K.

Inside the room a hotwire anemometer is placed. The anemometer is connected to a robot arm which is controlled by a computer. The robot arm can move in two directions, allowing measurements in a plane. The velocity profile of the jet as well as velocity fields near walls can by measured.

A recirculation fan draws air from the inner chamber. The air change rate (ACR) is adjustable between 0 and 10 ACH (air changes per hour). The volume of the inner room is approximately 6.8m³ resulting in a needed air flow rate of 0.0189 m³/s.

The conditioning of the air is done in tree steps: first dehumidification, followed by heating and humidification. The air drawn from the climate chamber passes through a cooling coil. Ethanol at low temperature (±0°C) flows through the tubes of the heat exchanger and cools the air (1-2-3 on FIG. 2). When the air reaches its dewpoint, condensation starts and the humidity ratio (grams of moisture per kilogram of dry air) of the air drops (2-3 on FIG. 2). The air at lowered temperature passes through a second heat exchanger where a resistive heater heats up the air to a desired temperature (3-4 on FIG. 2). By heating the air, the relative humidity drops. Steam is then added to the dry air and the humidity ratio rises. At the same time the high temperature of the steam heats the air explaining the slope of line 4-5.

By altering the power to the resistive heater and the amount of steam added, other end temperatures and relative humidity can be attained (FIG. 2 dotted line). The cooling load at a certain air mass flow is kept constant by supplying the compact heat exchanger with ethanol at a constant temperature.

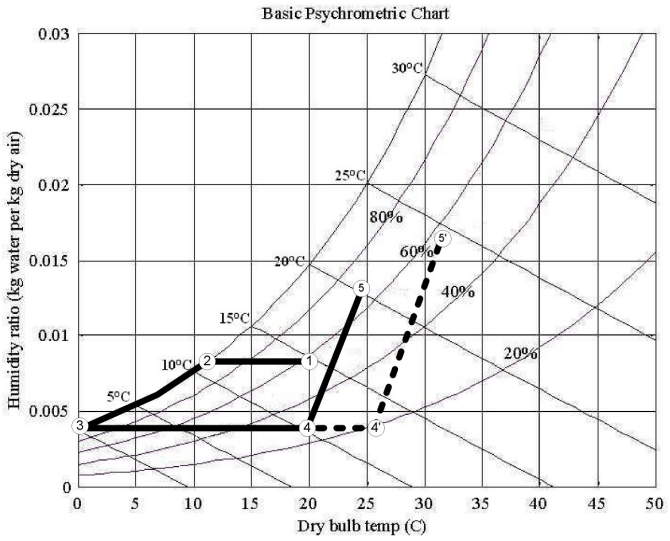

FIG. 2 Conditioning of the air represented on a psychrometric chart (two possible paths shown: 1-2-3-4-5 and 1-2-3-4'-5')

FIG. 3 shows the schematics of the steam humidifier. A dosing pump supplies a heated cylinder with demineralised water. The cylinder is kept at a high temperature (300°C) by a resistance wire that is wrapped around it. The water that enters the cylinder immediately evaporates when it comes in contact with the hot

cylinder wall. This way the time delay between the moment the liquid water enters the cylinder and the moment this water leaves the cylinder as steam is minimal. The dosing pump has a manually adjustable stroke length and the rotation speed is controllable. With a maximum of 180 rpm (revolutions per minute) and a stroke volume of up to 0.13ml this results in a maximum flow rate of 1.4 litres per hour.

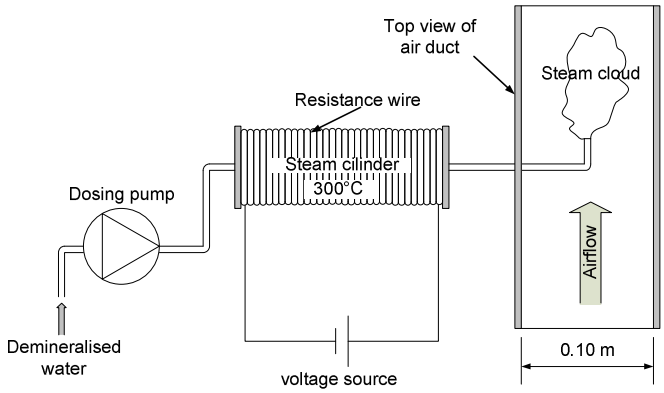

FIG. 3 Schematics of the steam humidifier

The produced steam is then injected into the air duct. Contact of the steam with the colder duct walls must be kept to a minimum to avoid condensation. A buffer vessel with a volume of 25 litres is placed not far from the steam injection point. This ensures a good mixture of the water vapour. This buffer vessel has two functionalities. First the vessel levels out the relative humidity fluctuations caused by the humidification system. At low steam demands, the pump works at a low rotation speed and the pulsations of the pump become visible in the steam flow rate. The buffer vessel also levels out temperature fluctuations. This buffering of temperature and relative humidity is necessary to enable a smooth control.

2.3 Control algorithm

Two parameters need to be controlled during operation: temperature and relative humidity at the inlet of the chamber. Temperatures are measured with thermocouples type K, the relative humidity at the inlet of the chamber is measured by a capacitive humidity sensor TRANSMICOR T232 from GEFRAN. This sensor has an accuracy of ±2% between 5% and 95% RH. The sensor signals are read by a Keithley voltage scanner. The measured values are then sent to a computer where they are stored.

The applied control strategy is shown in FIG. 4. Temperature and relative humidity at the inlet of the chamber are measured. The computer compares these measured values to the setpoint values. A PID-controller then generates the necessary voltage signals. In case of the temperature control this voltage is sent to the resistive heater, in case of the relative humidity control the voltage signal is used to steer the pump and adjust its rotation speed. G11, G12 and G22 represent the transfer functions of the system. In reality we are dealing with a multiple-input-multiple-output system (MIMO). This means that the temperature and relative humidity loop can not be entirely separated. Changes in temperature change the relative humidity and the hot steam added to the air flow influences the temperature. The temperature loop has a smaller time constant then the relative humidity loop. Therefore the influence of the relative humidity on the temperature is small and can be neglected. The influence of the temperature on the relative humidity on the other hand (represented by G12) can not be neglected as also concluded by (Huang et al., 2007).

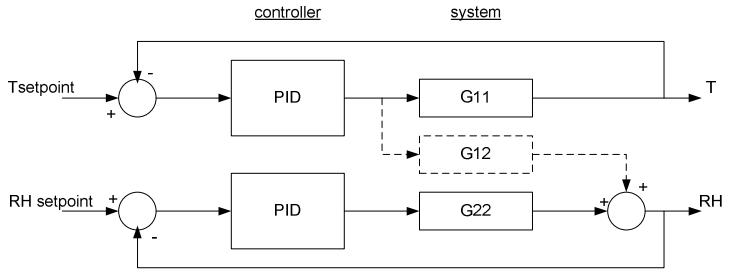

FIG. 4 Configuration of the feedback control system

In order to find the appropriate PID-controller parameters in an easy and fast manner, controller tuning procedures based on the work of Ziegler and Nichols are used (Corripio, 2000).

The first procedure used for the tuning of the temperature loop is the *closed-loop (ultimate gain) tuning procedure*. For this procedure the following steps are followed:

1. Both derivative and integral time on the PID controller are set to 0.
2. With the controller in automatic mode, the proportional gain (K_c) is carefully increased in small increments. A small change in the setpoint is made after each increment to disturb the loop. As K_c is increased, the value of the process variable begins to oscillate. K_c is changed until the oscillation is sustained, neither growing nor decaying over time.
3. The proportional band (PB_u) is recorded as a percent, where $PB_u=100/K_c$.
4. The period of the oscillation (T_u) is recorded in minutes.
5. The new PID parameters are calculated by using TABLE. 1

The second procedure used here for tuning the relative humidity control parameters is the *open-loop (step test) tuning procedure*. The open-loop tuning procedure assumes that you can model any process as a first-order lag and pure dead time. The following steps are followed:

1. The controller is put to manual mode, the output is set to a nominal operating value and the process variable is allowed to settle completely.
2. A step change is made in the output and the new output value is recorded.
3. From the recorded output the deadtime (T_d), time constant (T) and process gain (K) = change in process variable/change in output are determined.

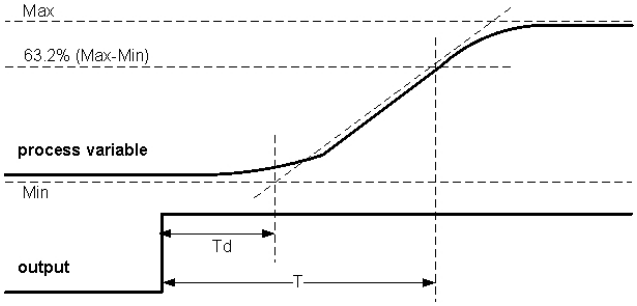

FIG. 5 Output and process variable strip chart

TABLE. 1 Factors for determining tuning parameters

Controller	PB(percent)	Reset (Minutes)	Rate (Minutes)
PID (closed loop)	1.67 PB_u	0.50 T_u	0.125 T_u
PID (open loop)	80 (KT_d/T)	2.00 T_d	0.50 T_d

To evaluate the performance of the controllers, the step response for temperature and relative humidity are measured. FIG. 6 shows the response of the temperature at the inlet of the chamber when the setpoint is altered from 20°C to 25°C and then back to 20°C. An overshoot is recorded when the setpoint is changed from 20°C to 25°C indicating that the system is under-damped. The overshoot recorded here is due to the humidification system. A sudden elevation of the temperature will result in a drop of the humidity as can be seen on FIG. 6. This causes the steam humidifier to respond and hot steam is injected into the air, augmenting the air temperature, which results in an increased overshoot. The opposite effect can be seen when the temperature is lowered from 25°C to 20°C. When the temperature drops the relative humidity rises. The controller lowers the amount of steam added the air flow, which causes an undershoot.

FIG. 7 shows the response of the relative humidity on a step change from 50% to 70% RH. Fluctuations of the relative humidity are kept between ±1%, well within the accuracy of the humidity sensor. Again a small overshoot is recorded, indicating that still some improvements in the control design are possible.

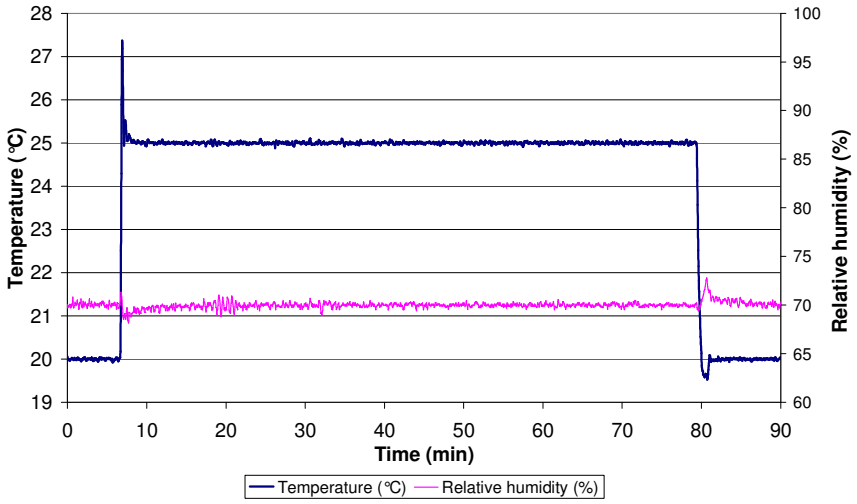

FIG. 6 Temperature step 20°C-25°C-20°C and effect on relative humidity

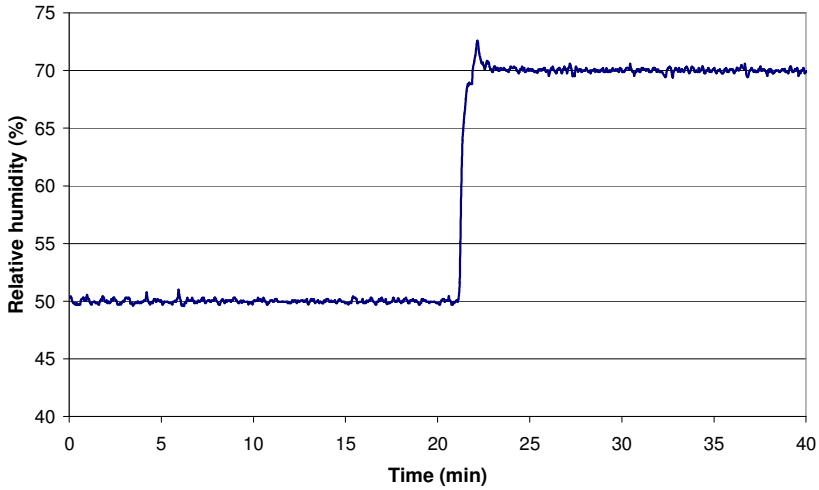

FIG. 7 Step in relative humidity 50%-70%

2.4 Preliminary measurements of velocity field in the room

To measure the velocity field in the room a 2D hotwire anemometer is used. The hotwire is attached to a robotic arm which can move in two directions. Here a part of the middle plane of the room is measured for the recirculation fan working at full capacity. The jet reaches across the entire room and has a maximum diameter of approximately 0.2m. A small upward movement of the jet is recorded, probably caused by a small slope of the inlet tube. A uniform inlet profile is assured by a flow straightener in the inlet tube.

The velocity profile of the air inlet measured in two perpendicular planes (FIG. 9). Notice that the velocity profile in the XZ plane is measured at a distance of 68mm from the inlet. The velocity profile in the YZ plane is measured at a distance of 25mm. This explains why there is a deviation in the velocity at the centre of the tube.

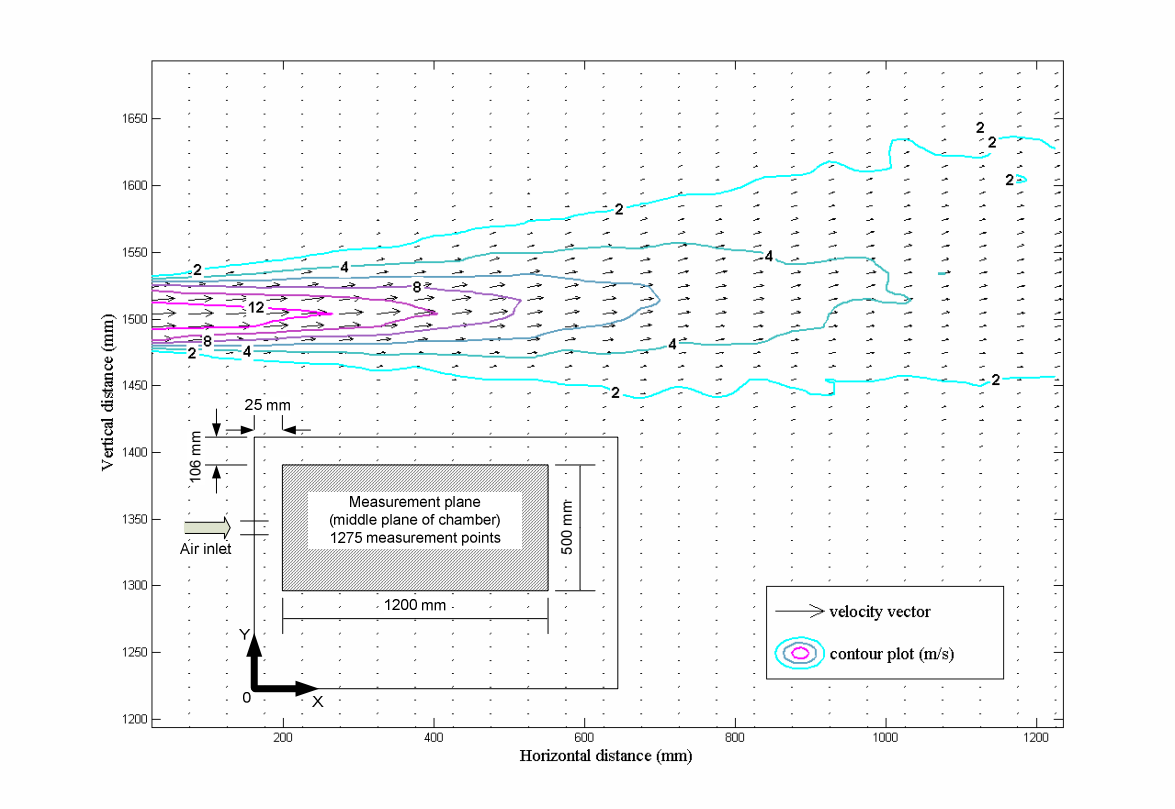

FIG. 8 Velocity field in the middle plane of the chamber, the location of the measurement plane is shown on the schematics at the bottom left

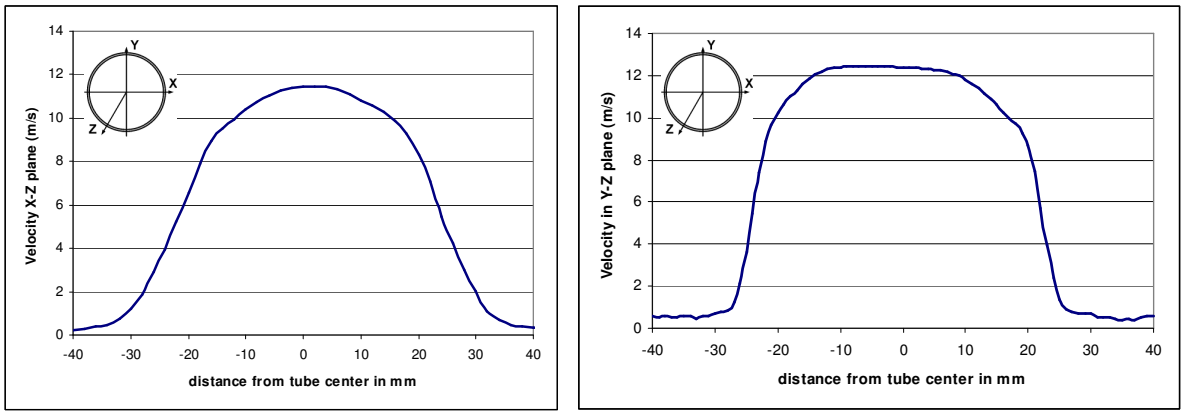

FIG. 9 Velocity profile at the air inlet measured in the XZ- and YZ-plane

3. Conclusions and future work

In this paper the design of an environmental chamber is discussed. The control strategy for temperature and relative humidity implemented here gives good results but improvements are still possible.

In the next face of this research a test setup will be built. Hygroscopic materials will be placed in front of the jet. The response of the room and the air near the hygroscopic wall can than be measured. These results can than be used to validate CFD code.

A second series of experiments will study the moisture buffering of materials and the response of the room to the presence of a moisture source.

4. Acknowledgement

The results presented in this paper have been obtained within the frame of the FWO project B/05836/02 funded by the FWO-Flanders (Research Fund Flanders) and the IWT SBO-050451 project *heat, air and moisture performance engineering a whole building approach* funded by the IWT (institute for science and technology in Flanders). There financial support is gratefully acknowledged.

5. References

Corripio A. B. (2000). Tuning of Industrial Control Systems, ISA, Research Triangle Park, New York, USA.

Fang L., Clausen G. and Fanger P. O. (1998). Impact of temperature and humidity on the perception of indoor air quality. *Indoor Air-International Journal of Indoor Air Quality and Climate,* 8**,** 80-90.

Huang B. J., Liao Y. C. and Kuo, T. C. (2007). Study of a new environmental chamber design. *Applied Thermal Engineering,* 27**,** 1967-1977.

Osanyintola O. F. and Simonson C. J. (2006). Moisture buffering capacity of hygroscopic building materials: Experimental facilities and energy impact. *Energy and Buildings,* 38**,** 1270-1282.

Simonson C. J. Salonvaara M. and Ojanen T. (2002). The effect of structures on indoor humidity - possibility to improve comfort and perceived air quality. *Indoor Air,* 12**,** 243-251.

Steeman H.-J., Janssens A., Carmeliet J. and De Paepe M. Modelling indoor air and hydrothermal wall interaction: comparison between CFD and a well mixed zonal model, submitted to: *Building and Environment.*

Steeman H., T'Joen C., Willockx A., De Paepe M. and Janssens A. (2006). CFD Modelling of HAM Transport in Buildings : Boundary Conditions. *3rd International Building Physics Conference.* Montréal, Canada.

Talukdar P., Olutmayin S. O., Osanyintola O. F. and Simonson C. J. (2007). An experimental data set for benchmarking 1-D, transient heat and moisture transfer models of hygroscopic building materials. Part I: Experimental facility and material property data. *International Journal of Heat and Mass Transfer,* 50**,** 4527-4539.

Experimental and numerical determination of convective vapour transfer coefficients

Adam Neale, M.A.Sc.,
Department of Building, Civil and Environmental Engineering, Concordia University, Canada;
aj_neale@encs.concordia.ca

Dominique Derome, Ph.D.,
Empa, Swiss Federal Laboratories for Materials Testing and Research,
Wood Laboratory, Dübendorf

Bert Blocken, Ph.D.,
Building Physics and Systems, Technische Universiteit Eindhoven, The Netherlands;
b.j.e.blocken@tue.nl

Jan Carmeliet, Ph.D.,
Chair of Building Physics, Swiss Federal Institute of Technology ETHZ, Zürich
Empa, Swiss Federal Laboratories for Materials Testing and Research, Laboratory for Building Technologies, Dübendorf

KEYWORDS: CFD, vapour transfer, laminar flow, forced convection.

SUMMARY:
An experimental setup was designed for the purpose of validating a coupled CFD-diffusion model. In the CFD-diffusion model, heat and mass transport in the air domain is solved using CFD, while, in the material domain, vapour transport is modelled using a control-volume vapour diffusion model. This CFD-diffusion model allows the prediction of the convective vapour transfer coefficient for developing momentum and moisture boundary layers. In the traditional vapour diffusion model, a convective vapour transfer coefficient is used. This model allows the indirect determination of the vapour transfer coefficient from experiments. The experiment consisted of a wind tunnel placed in an environmental chamber with climate control capability. The air flow in the wind tunnel was driven by a variable-control fan that allows for a range of speeds in the laminar regime. Convective vapour transfer coefficients were indirectly determined based on the experimenta measured moisture content changes in the material for a number of air speeds. The results were compared with CFD-diffusion model for the purpose of validation and sensitivity analysis.

1. Introduction

Convective heat and vapour transfer coefficients, also called surface transfer coefficients, are generally applied as boundary conditions for hygrothermal calculations in building applications. Surface coefficients are theoretically dependent on velocity and type of the air flow, surface temperature, reference temperature of the air, surface relative humidity, reference relative humidity of the air and porosity at the surface of the material. Since the boundary layers for heat and moisture content are similar for specific conditions, it is often assumed that there exists an equivalence relationship between the heat and vapour transfer coefficients, such as the one proposed by Chilton and Colburn (1934). However, studies have shown discrepancies between equivalence equations and measurements, which suggest the need for further study on the determination of convective vapour transfer coefficients. Authors such as Masmoudi and Prat (1990), Wadsö (1993), Derome (1999), Hukka and Oksanen (1999), and Salin (2003) have reported errors as high as 300% between experimentally determined vapour transfer coefficients and values obtained using analogy equations.

In this paper, an investigation on numerical and indirect experimental determination of convective vapour transfer coefficients is presented. Convective vapour transfer for laminar air flow over gypsum samples is studied for a number of air speeds. The corresponding convective vapour transfer coefficients are compared for experimental and numerical cases. The models are presented in Section 2. The material property data used in the numerical simulations are then presented in Section 3. Next, Section 4 presents the experimental setup, the methodology used to determine indirectly the convective vapour transfer coefficients, and the comparison

between the indirect results and CFD-diffusion simulations. Finally, some general conclusions are presented in Section 5.

2. Numerical models and preliminary model validation

The convective vapour transfer between air and a porous material can be defined by the following relationship:

$$g = -\delta \left.\frac{\partial p_v}{\partial y}\right|_{y=0} = h_m \left(p_{vs} - p_{vf}\right) \tag{1}$$

where g is the mass flux per unit area (kg/m^{2}s), δ is the vapour permeability of the material (s), $(\partial p_v/\partial y)$ is the vapour pressure gradient in the direction normal to the surface (Pa/m), p_{vs} and p_{vf} are, respectively, the partial vapour pressure at the surface and the fluid reference vapour pressure (Pa), and h_m is the convective vapour transfer coefficient, which in this case is derived with vapour pressure as the driving potential (s/m). Note that the convective vapour transfer coefficient, sometimes referred to as β, will henceforth be referred to as h_m.

In order to model the vapour transfer between a moving air layer and a porous material, a number of numerical methods exist. Two models are proposed to simulate the moisture uptake of gypsum samples: a vapour diffusion model with an imposed convective vapour transfer coefficient as a boundary condition, and a coupled CFD-vapour diffusion model that resolves the moisture transfer in the boundary layer.

2.1 Vapour diffusion model

The diffusive vapour flux within a solid material was expressed in part earlier in equation 1. When considering diffusion in a porous material, the storage of moisture must be considered. If one considers vapour transport in one direction (x), the resulting equation can be expressed as:

$$A\frac{\partial w}{\partial t} = \frac{\partial}{\partial x}\left[-\delta A\frac{\partial p_v}{\partial x}\right] \tag{2}$$

where w is the moisture content (kg$_{moisture}$/m^3), δ is the vapour permeability of the material (s), A is the area perpendicular to the vapour flow, p_v is the partial vapour pressure (Pa), and x is the direction of the vapour flow (m). The gradient $\partial w/\partial t$ represents the vapour storage within the material. Material properties are often expressed in terms of relative humidity, and therefore equation 2 can be transformed as:

$$A\frac{\partial w}{\partial \phi}\frac{\partial \phi}{\partial t} = \frac{\partial}{\partial x}\left[\delta A\, p_{vsat}\frac{\partial \phi}{\partial x} + \delta A\phi\frac{\partial p_{vsat}}{\partial T}\frac{\partial T}{\partial x}\right] \tag{3}$$

where ϕ is the relative humidity, p_{vsat} is the saturation vapour pressure (Pa), and the gradient $\partial w/\partial \phi$ represents the slope of the sorption isotherm for the material. Equation 3 together with the heat balance equation was subsequently implemented in Matlab using a control volume discretization scheme.

The primary purpose of the vapour diffusion model is to determine the change in mass of the material due to moisture adsorption or desorption in order to indirectly determine the vapour surface coefficient from experimental findings.

2.2 Coupled model

Since the convective vapour transfer at the surface of a material is dependent on the boundary layer development, it is interesting to obtain a highly accurate resolution of the air flow field in order to study the effects of varying air speeds on the convective vapour transfer. In commercial CFD codes such as Fluent 6.3.26, a highly accurate solution of the momentum boundary layer can be obtained. In addition, an equally accurate vapour boundary layer can be calculated. However, in Fluent, it is difficult to solve for vapour transport in hygroscopic porous materials without significantly altering the program functionality through the use of user-defined functions. Therefore, in order to accurately solve the air flow domain and the material domain, CFD is coupled with the vapour diffusion model mentioned previously. Details on the coupling methodology can be found in Neale et al (2007). In brief, the commercial software Matlab is used as a controller to iterate between the vapour diffusion model and the CFD solution. It is important to note that the coupled model does not make

use of any surface coefficients to obtain a solution, though the surface coefficients may be calculated from the solution data. In addition, while the cases presented in this paper are all isothermal, the coupled model can be used to solve non-isothermal problems.

3. Material property data

The average moisture content for the gypsum panels used in this study was measured at 30% and 80% relative humidity for 8 samples. The resulting sorption curve was interpolated using the function that resulted from a round-robin sorption curve determination for gypsum board (IEA 2008). It was assumed that the behaviour of the gypsum board used in the tests would be the same as reported in IEA (2008). However, additional testing showed that the gypsum board attains higher moisture. The difference is likely due to the different fabrication process and materials found in North American gypsum board panels. The different sorption curves are presented in Figure 1 (left), which show how the moisture content varies in the range of relative humidity of interest. Based on the two measured points the actual hygroscopic curve was corrected using a same functional description as in IEA (2008). Note that the gypsum board was assumed to be a homogeneous material for the purpose of this study, but in reality it is a composite material of paper and gypsum, with some coatings on the paper for fabrication purposes.

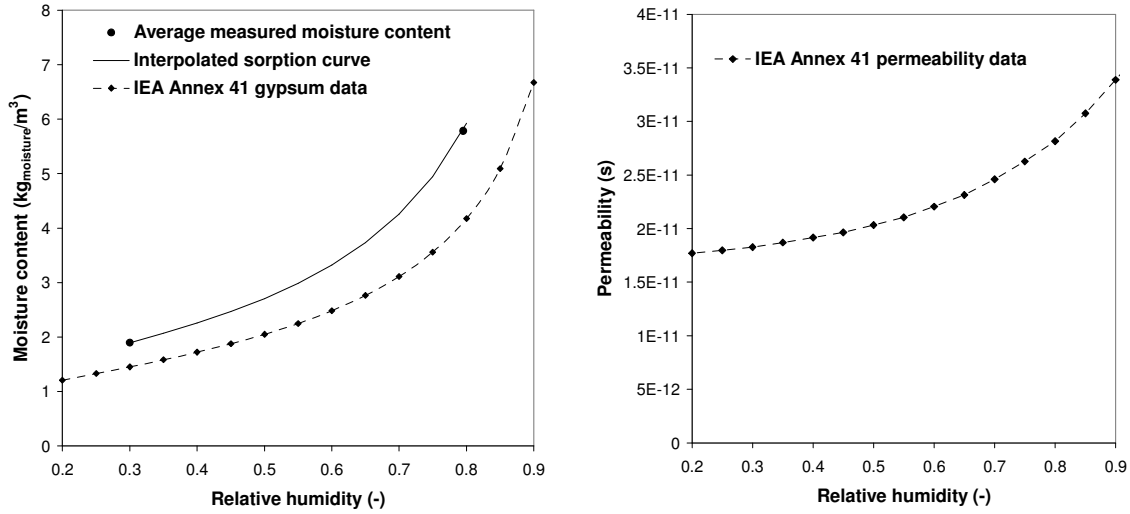

Figure 1. a) Sorption isotherm and b) permeability data for gypsum board.

The permeability of the gypsum board as a function of relative humidity was obtained from the Annex 41 measurements, which are shown in Figure 1 (right).

The properties of air were calculated for a mean ambient temperature of 20°C and implemented accordingly.

4. Experimental measurements

In order to describe the methodology used to determine the convective vapour transfer coefficients, the experimental setup is presented first. The diffusion model results are subsequently presented, which illustrate how the experimental measurements are used to indirectly determine h_m values. Finally, the experimental data is compared with the coupled model data and the results are discussed.

4.1 Experimental setup

The experimental setup was designed to measure the convective vapour transfer coefficients for laminar air flow over a given porous material. The material selected for the present study was gypsum boards cut in to 20 cm x 20 cm specimens. The experimental setup consisted of five main components shown in Figure 2: 1) a variable control humidifier, 2) a variable speed fan with a working range of 0.05 to 1 m/s, 3) the gypsum sample bed, 4) a PMMA open circuit wind tunnel with a relative humidity probe upstream and manual anemometer downstream, and 5) an adiabatic/impermeable sealed environmental chamber. The air tunnel was 0.025 m high

by 0.4 m by 2.8 m long. Due to sufficient length of the windtunnel before the test section, the small height of the windtunnel, the low air speeds varying between and the 0.1 and 0.35 m/s, the air flow is fully developed and laminar. Note that the set-up components and the specimens were all at the same temperature as the air at the start of the test.

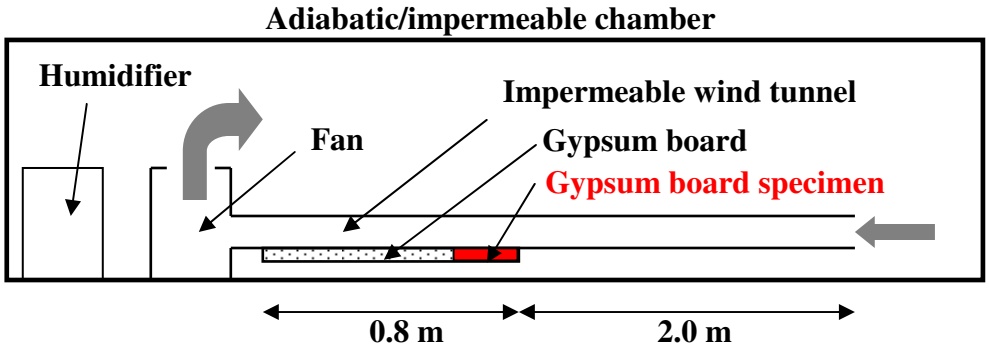

Figure 2. Schematic of the experimental setup (not to scale).

The gypsum board samples were pre-conditioned at a relative humidity of 30%. The edges of the samples were sealed with wax to ensure one-dimensional moisture transport. While there was 0.8 m of gypsum panel in the experimental setup, only the first sample (0.2 m) was used for measurement purposes. The air inside the environmental chamber was maintained at 77.5% RH, with an accuracy of ±2.5%. Once the air inside the chamber reached the desired setpoint, the humidifier was shut off and the samples were placed in the test bed. The velocity of the air passing over the samples was maintained at the desired setpoint (0.1 to 0.35 m/s) with an accuracy of ±0.01 m/s. The samples remained in the tunnel for a period of 10 minutes, after which the change in mass of the gypsum board was recorded. Note that over the course of 10 minutes, the relative humidity in the chamber would only decrease between 3% and 5% from the starting value, which allows the assumption that the boundary conditions were constant during the test..

The convective vapour transfer process described in equation 1 can be rearranged to isolate the h_m value:

$$h_m = \frac{g}{(p_{vs} - p_{vf})} \tag{4}$$

The mass flux g is expressed in terms of the change in mass per unit time (kg/s per unit area), but the relationship between the uptake in moisture versus time is not linear. Consequently, the flux cannot be calculated by simply dividing the measured change in mass by the time period. In addition, the surface vapour pressure p_{vs} cannot be directly measured, particularly for a material such as gypsum board. Therefore, the value of h_m was determined indirectly based on the experimental results using the vapour diffusion model.

4.2 Diffusion model numerical simulations

In this section, we explain the procedure to indirectly determine the vapour transfer coefficients from measurements. The diffusion model allows the determination of the accumulation of moisture in a porous material for different boundary conditions. At the surface of the gypsum board, a convective vapour transfer boundary condition was implemented in the diffusion model for a number of different convective surface coefficients (h_m). The reference relative humidity was set to be equal to 77.5% RH, which is the average of the relative humidity in the chamber for the different experiments. The gypsum samples were initialized to 30% relative humidity, which is equal to the laboratory RH. The material properties of the gypsum panels were implemented as described in Section 2. The values of h_m were varied from 0.5×10^{-8} s/m to 10×10^{-8} s/m and the resulting accumulation of moisture in the gypsum was determined for each case by numerical simulation. The results are shown in Figure 3, which are ten curves showing the change in mass of the gypsum board samples over time.

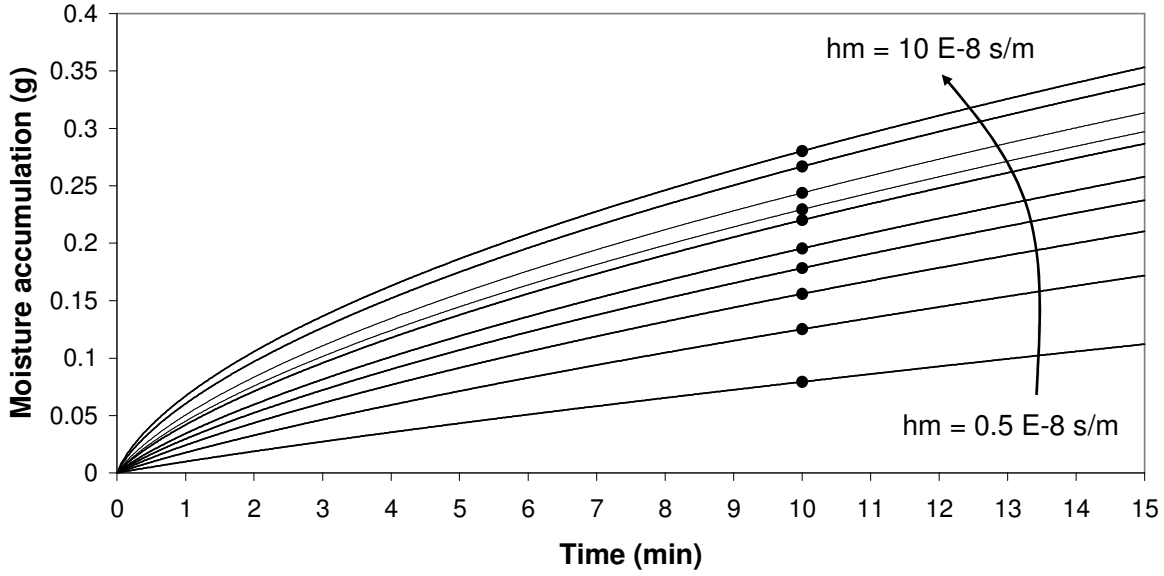

Figure 3. Diffusion model results – moisture accumulation for varying values of h_m over time.

The data points (●) in Figure 3 indicate the change in mass of the gypsum panel for various values of h_m after 10 minutes. When the change in mass is graphed versus h_m, the result is a curve that allows the prediction of the h_m value for a given change in mass of a sample loaded under specific conditions, which is shown in Figure 4.

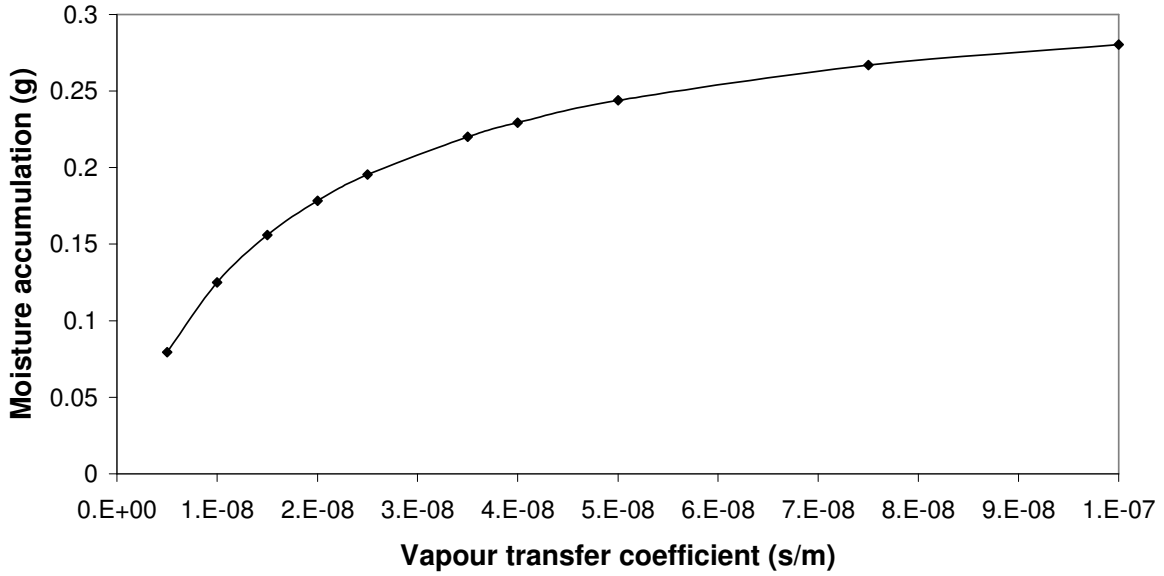

Figure 4. Diffusion model results - moisture accumulation vs vapour transfer coefficient after 10 minutes.

Using the relationship shown in Figure 4, the experimentally measured change in mass of the samples can then be associated with a convective vapour transfer coefficient.

4.3 Results

Eight different gypsum samples were used in the experimental setup described previously. The samples were all obtained from the same gypsum panel and cut to be approximately the same dimension. The surface

area for each sample was measured and taken into consideration. Experiments were performed for three different air speeds: 0.1 m/s, 0.2 m/s and 0.35 m/s. The change in mass of the gypsum specimens was measured after 10 minutes, which was converted into an h_m value using the relationship shown in Figure 4. The estimated error for the velocity and mass measurements was ±0.01 m/s and ±0.01 g, respectively.

The coupled model was used to simulate the experimental setup for a range of air speeds from 0.05 m/s to 0.5 m/s. The computational domain of the coupled simulation matched the experimental conditions in most aspects, except that the length of the gypsum board simulated was longer: 0.5 m instead of 0.2 m. The extra length did not affect the simulation results in any way, but provided extra information as will be shown below. The material properties for gypsum and air were as described in Section 2. A fully developed laminar air velocity profile was imposed at the inlet of the computational domain. The water vapour concentration profile was expected to evolve to a fully developed boundary layer along the length of the gypsum board. For each case of velocity, the average values of h_m were calculated above each grid cell in the computational domain.

The values of h_m as obtained indirectly from the diffusion model (dots) are compared to the coupled model simulations in Figure 5. The error bars for the x- and y-directions were calculated based on the estimated error for the air speed and mass measurements, respectively. Note that for an error of ± 5-7% in the mass measurement there was a corresponding error of ±12-15% in the value of h_m, which illustrates the sensitivity of the results on the mass measurements. The results from the coupled model simulation were analyzed at two locations along the length of the panel: h_m value was averaged for the first 0.2 m of the simulation domain (denoted as developing) and also averaged from 0.3 m to 0.5 m (denoted as developed region). Note that the notations developing and developed are adopted as a naming convention, and further analysis has to confirm these notations.

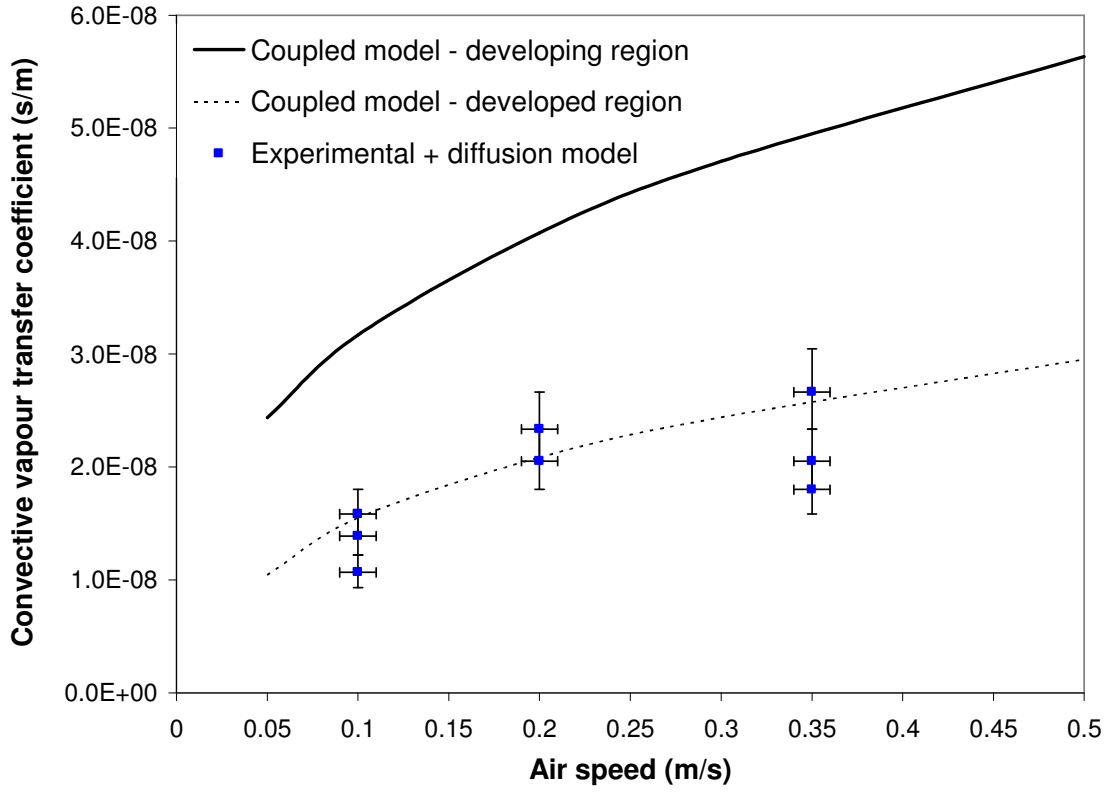

Figure 5. Convective vapour transfer coefficient results for various air speeds resulting from the two calculation approaches.

The coupled model results for the region where the mass concentration profile was expected to be developing tend to overestimate the convective vapour transfer coefficient when compared with the experimentally-based results. The 'developed' results show a closer agreement with the experimentally-based results, which indicates that the mass concentration profile is becoming developed faster than expected. One

explanation of the faster response could be due to the fact that the layered composition of the gypsum board consists at the surface of a very hygroscopic paper layer with limited thickness, while on the other hand gypsum is less hygroscopic but very vapour permeable. This means that in reality, the paper will quickly stabilize the boundary layer, which would have the effect of creating a more uniform surface condition. For this reason, after a certain amount of time elapses, the case of moisture uptake for gypsum panels behaves closer to a developed moisture boundary layer, which is illustrated by the 'developed region' results shown in Figure 5. Further work is on-going to analyse the influence of the composite structure of gypsum board and to further validate the model for other materials.

5. Conclusions

An experimental setup was designed and the determination of convective vapour transfer coefficients (h_m) was performed for laminar air flow at around 80%RH over gypsum panel samples that had been in equilibrium with 30%RH. The moisture content of the gypsum samples was determined experimentally for two relative humidities, which were used to adapt the Annex 41 round-robin gypsum panel sorption curve data for the samples used in this study. The gypsum properties were assumed to be homogeneous across the panel thickness.

A vapour diffusion model was used to determine the predicted change in mass for gypsum panels exposed to convective vapour transfer for a period of 10 minutes. The values of h_m were varied from 0.5 x10^{-8} to 10 x10^{-8} s/m and imposed as a surface boundary condition. The change in mass of the samples was calculated for each case and a function describing the relationship between the change in mass vs h_m was then established for then indirectly determining the vapour transfer coefficient from experimental data.

Experimental measurements were performed for eight gypsum panel samples exposed to laminar air flow for forced convection vapour transport. The change in mass of the gypsum samples was recorded after 10 minutes for three different air speeds. The corresponding h_m values were indirectly determined based on the change in mass of the samples using the vapour diffusion model. The estimated error for the h_m values was between 12 and 15% for the different samples. The experimentally determined h_m results were compared with values calculated using a coupled CFD. The coupled model tends to over-predict the convective vapour transfer coefficient if the moisture boundary layer is assumed to be developing. If the moisture boundary layer is assumed to be developed after 10 minutes, the coupled model predicts the h_m values within the experimental uncertainty. It is suspected that the influence of the paper layer in the experiment causes the surface relative humidity to be more uniform, which explains the good agreement between the developed case and the measurements. In future work it is planned to test the effect of modeling the gypsum panels as a composite material with paper and gypsum layers, instead of modeling gypsum panels as a homogeneous material.

6. References

Chilton T.H., Colburn A.P. (1934). Mass transfer (absorption) coefficients. Industrial and engineering chemistry 26, 1183-1187.

Derome D. (1999). Moisture occurrence in roof assemblies containing moisture storing insulation and its impact on the durability of the building envelope. Ph.D. Thesis, Montreal: Concordia University.

Hukka A., Oksanen O. (1999). Convective mass transfer coefficient at wooden surface in jet drying of veneer. Holzforschung 53, 204-208.

Masmoudi W., Prat M. (1991). Heat and mass transfer between a porous medium and a parallel external flow. Application to drying of capillary porous materials. Int. J. Heat Mass Transfer 34, 1975-1989.

Neale A., Derome D., Blocken B., Carmeliet J. (2007). Coupled simulation of vapour flow between air and a porous material. *Proceedings of Performance of Exterior Envelopes of Whole Buildings X Conference*, ASHRAE, Atlanta, 11 pages.

Roels S. (2008) Subtask 2 Report, IEA Annex 41: Whole building heat, air and moisture response, *to be published*.

Salin J-G. (2003). External heat and mass transfer – some remarks. 8th Int. IUFRO Wood Drying Conference, 343-348.

Wadsö L. (1993). Surface mass transfer coefficients for wood. Drying Technology 11, 1227-1249.

Coupling moisture transport in air flows and porous materials using CFD

Hendrik-Jan Steeman,
Department of Flow, Heat and Combustion Mechanics, Ghent University-UGent, Sint-Pietersnieuwstraat 41 9000 Gent, Belgium;
Hendrikjan.Steeman@ugent.be, www.floheacom.ugent.be

Arnold Janssens, PhD,
Department of Architecture and Urban Planning, Ghent University-UGent, Jozef Plateaustraat 22, 9000 Gent, Belgium;
Arnold.Janssens@ugent.be, www.architectuur.ugent.be

Michel De Paepe, PhD,
Department of Flow, Heat and Combustion Mechanics, Ghent University-UGent, Sint-Pietersnieuwstraat 41 9000 Gent, Belgium;
Michel.Depaepe@ugent.be, www.floheacom.ugent.be

KEYWORDS: *HAM, CFD, model, porous material.*

SUMMARY:
Modelling local moisture content in objects and walls inside buildings requires the knowledge of the interaction of the material with the local indoor climate. Computational Fluid Dynamics (CFD) can be used to model the local climate and is currently already used to model heat exchange at the interface of air and porous materials. In this paper a coupled CFD-material model is presented which is capable of modelling non-isothermal transient moisture exchange between air and porous materials. The coupled model integrates a 2 or 3D heat and moisture transport model for porous materials in a commercial CFD solver. A verification and validation study of the new model results in an excellent agreement between simulations on the one hand and analytical reference solutions and experiments on the other hand.

1. Introduction

The use of numerical models for heat and moisture transfer in building components is becoming increasingly popular. Numerical simulation allows for an accurate analysis of the hygric and thermal performance of building components. Yet to obtain realistic results it is eminent that realistic boundary conditions are provided to the model. In a recent paper Janssen *et al.* describe the integration of atmospheric boundary conditions in a numerical heat and moisture model (Janssen, 2007). As boundary conditions such as wind driven rain are highly variable in space and time Computational Fluid Dynamics (CFD) is used in the latter paper to simulate the outdoor environment and generate (part of) the boundary conditions.

If the interest of a study lies in simulating the local hygrothermal response of building components or objects facing the indoor air, a strong coupling between the air and the porous materials can occur. Unlike the outdoor environment, which is independent of the situation in the building component, the temperature and relative humidity of the indoor air are influenced by the interaction with the building components. Hence in this situation it is no longer sufficient to pass information from the CFD model to the hygrothermal model, but a two-way coupling between both models is necessary.

Recently several models which feature a two way coupling between CFD and a hygrothermal material model have been developed. These models can be divided in two categories: the directly coupled models and the indirectly coupled models. Directly coupled models are those models which solve both the fluid domain as the porous material domain with one solver. Models which use an indirect coupling solve the fluid and the porous domain with a different solver and exchange information between both solvers. Examples of indirectly coupled models can be found in (Amissah, 2005) and (Erriguible, 2006). In (Amissah, 2005) a 3D CFD model is coupled to a 1D hygrothermal material model, while in (Erriguible, 2006) a 2D CFD and a 2D hygrothermal material model are coupled. Both these indirectly coupled models use explicit time stepping to link the CFD solver and

the hygrothermal solver as information between the solvers is exchanged once each time step. An example of a direct coupled model can be found in (Mortensen, 2007). In this model a 3D steady state CFD solver was adapted to include the governing equations for heat and moisture transfer in porous materials. The transport equations in the air and the porous material were separated and an algorithm was developed that predicts the moisture flux at the air-material interface and reconciles the water vapour content at both sides of this interface.

In this paper a coupled 3D CFD hygrothermal material model is developed that is capable of performing transient simulations. The governing equations in the porous material and the fluid are written in function of the same variables and are solved with the CFD solver. This implies that the continuity at the fluid-material interface will be automatically fulfilled. As the new model is directly coupled and continuous at the material interface no time consuming iteration between two codes is needed. Also the coupling between the fluid and the material is no longer explicit, which allows for larger time steps in the simulation. A detailed verification and validation study of the newly developed model is performed in the second part of the paper.

2. Coupled CFD-material model

The strategy followed here to develop a directly coupled CFD-material model is integrating the governing equations for heat and moisture transport in hygroscopic porous media into the commercial CFD solver Fluent® (Fluent Inc., 2006). The advantage of using a commercial CFD solver is that new advances in fluid modelling are integrated in the CFD solver with every new release. In the CFD solver transport equations for heat and moisture transfer in fluids are available. By writing the governing equations for heat and moisture transport in porous media as function of the same transported variables as those used in the CFD solver, source terms, diffusion terms and unsteady terms are obtained to convert the standard CFD heat and moisture transport equations. The CFD solver is used to solve the transport equations in the entire domain (fluid and porous zones) taking into account the changed source terms in the porous zone.

2.1 Heat and moisture transfer in air

In Fluent®, the CFD solver used in this paper, heat and moisture transfer in the air can be simulated using the energy and the species transport equations. The air can be modelled as an incompressible fluid in which case the energy and species transport equations can be simplified to:

$$\rho C_p \left(\frac{\partial}{\partial t}(T) + \vec{v}.\nabla(T) \right) = \nabla.\left(k\nabla(T) - \left(c_{vap} T + L_{vap} \right) \vec{g} \right) \quad (1)$$

$$\rho \left(\frac{\partial}{\partial t}(\omega) + \vec{v}.\nabla(\omega) \right) = \nabla.\left(\rho D \nabla(\omega) \right) \quad (2)$$

where ρ is the air density, C_p the air thermal capacity, k the thermal conductivity, c_{vap} the thermal capacity of the water vapour, L_{vap} the latent heat of vaporization, g the water vapour diffusion flux and D the diffusion coefficient of water vapour in air. The transported variables are the temperature T and the mass fraction of water vapour in the air, ω.

2.2 Heat and moisture transfer in porous materials

2.2.1 Governing equations

In the porous material only moisture transport due to water vapour diffusion is considered. The modelled materials are capillary active and are characterized by a sorption curve giving the moisture content w (kg/m³) as function of the relative humidity. Heat and moisture transfer is modelled under the assumptions that:

- No air transfer, no liquid transfer and no radiation heat transfer occurs
- Moisture storage is independent of temperature
- The temperature remains below the boiling point

Under these assumptions the moisture transport equation and the heat transport equation can be written in function of ω and T (Eq. 3-4).

$$\frac{dw}{dt} = -\nabla.\vec{g} \Leftrightarrow \frac{\partial w}{\partial RH}\frac{\partial RH}{\partial \omega}\frac{\partial \omega}{\partial t} + \frac{\partial w}{\partial RH}\frac{\partial RH}{\partial T}\frac{\partial T}{\partial t} = \nabla.\left(\rho\frac{D}{\mu}\nabla(\omega)\right) \tag{3}$$

$$\begin{aligned}&\frac{dh}{dt} = \nabla.\left(k_{mat}\nabla(T) - \left(c_{vap}T + L_{vap}\right)\vec{g}\right) \Leftrightarrow \\ &\rho_{mat}c\frac{\partial T}{\partial t} + c_{liq}T\frac{\partial w_{liq}}{\partial t} + \left(c_{vap}T + L_{vap}\right)\frac{\partial w_{vap}}{\partial t} = \nabla.\left(k_{mat}\nabla(T)\right) - \left(c_{vap}T + L_{vap}\right)\nabla.\vec{g}\end{aligned} \tag{4}$$

with

$$h = \rho_{mat}c_{mat}T + c_{liq}w_{liq}T + \left(c_{vap}T + L_{vap}\right)w_{vap} \tag{5}$$

$$c = c_{mat} + \frac{c_{liq}w_{liq}}{\rho_{mat}} + \frac{c_{vap}w_{vap}}{\rho_{mat}} \tag{6}$$

$$w_{liq} = \frac{\phi - \dfrac{w}{\rho_{vap}}}{\dfrac{1}{\rho_{liq}} - \dfrac{1}{\rho_{vap}}} \tag{7}$$

$$w_{vap} = \frac{\dfrac{w}{\rho_{liq}} - \phi}{\dfrac{1}{\rho_{liq}} - \dfrac{1}{\rho_{vap}}} \tag{8}$$

where μ is the vapour resistance factor, the subscript *mat* refers to dry material conditions and ϕ is the porosity of the material. In the right hand side of Eq. (4) the assumption is made that the energy associated with the water vapour flux is quite constant and can be brought outside the divergence operator.

2.2.2 Conservative implementation

Because of the non-linear nature of the transport equations (3) and (4) mass and energy conservation is not guaranteed: e.g. the storage term $\partial w/\partial RH\,.\partial RH/\omega$ varies with ω and is not constant during a time step. To solve this problem Janssen proposed an iterative solution procedure in which the property that has to be conserved is estimated by a truncated Taylor series (Janssen, 2007; Janssen, 2002) This approach proved to be very effective and is implemented here. This approach, together with the segregated solution procedure of the CFD solver, leads to the following discretization of equations (3) and (4):

$$\frac{\partial w}{\partial RH}\frac{\partial RH}{\partial \omega}\frac{\omega^{t+\Delta t,m+1} - \omega^{t+\Delta t,m}}{\Delta t} + \frac{w^{t+\Delta t,m} - w^{t}}{\Delta t} = \nabla.\left(\rho\frac{D}{\mu}\nabla(\omega)\right) \tag{9}$$

$$\rho_{mat}c\frac{T^{t+\Delta t,m+1} - T^{t+\Delta t,m}}{\Delta t} + \frac{h^{t+\Delta t,m} - h^{t}}{\Delta t} = \nabla.\left(k_{mat}\nabla(T)\right) + \left(c_{vap}T + L_{vap}\right)\left(\nabla.\left(\rho\frac{D}{\mu}\nabla(\omega)\right)\right) \tag{10}$$

Note that the equations (9) and (10) are written in function of T and ω.

2.3 Practical implementation in Fluent®

In the previous section the differences between the transport equations in the fluid and the porous zone are discussed. In Fluent® it is not possible to transform the standard energy and species transport equations into equations (9) and (10). It is however possible to use 'empty' transport equations, so called UDS transport, which can be altered at will. For this reason the standard energy and species transport equations are not used, instead equations (1-2) and (9-10) are implemented in the UDS transport equations.

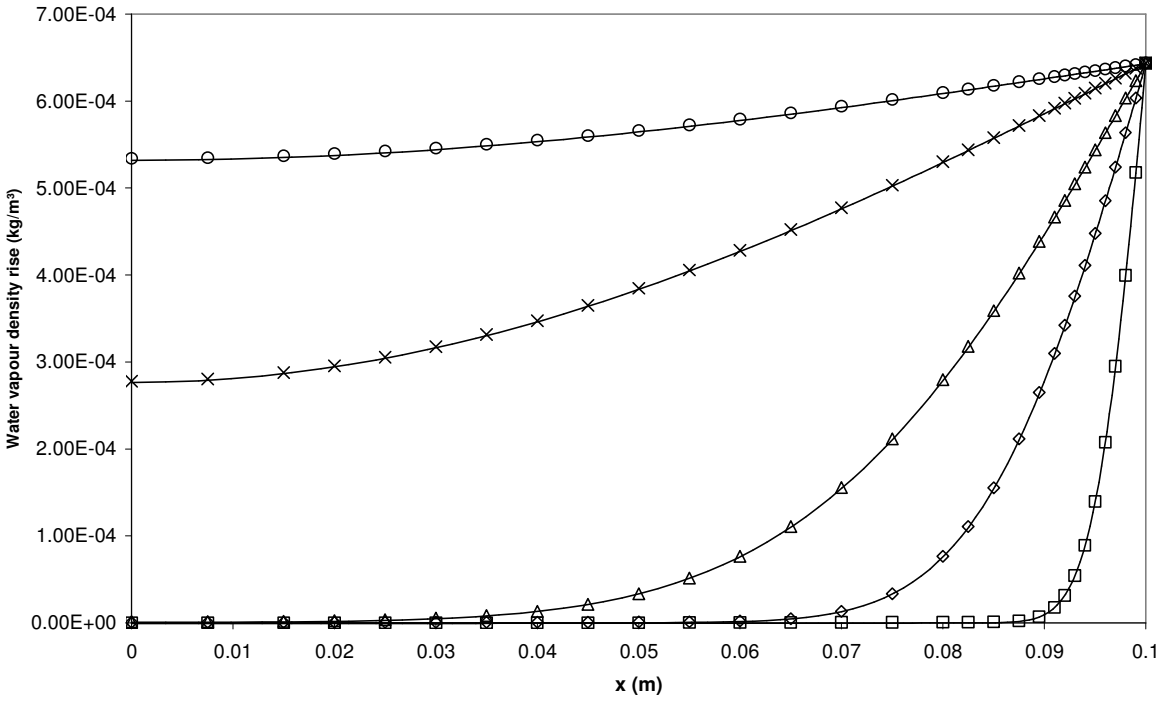

FIG. 1: Comparison between the increase in water vapour density predicted by the numerical model (__) and the analytical model (500s ( ), 5000s (◊), 20000s (Δ), 200000s (×) and 500000s (O))

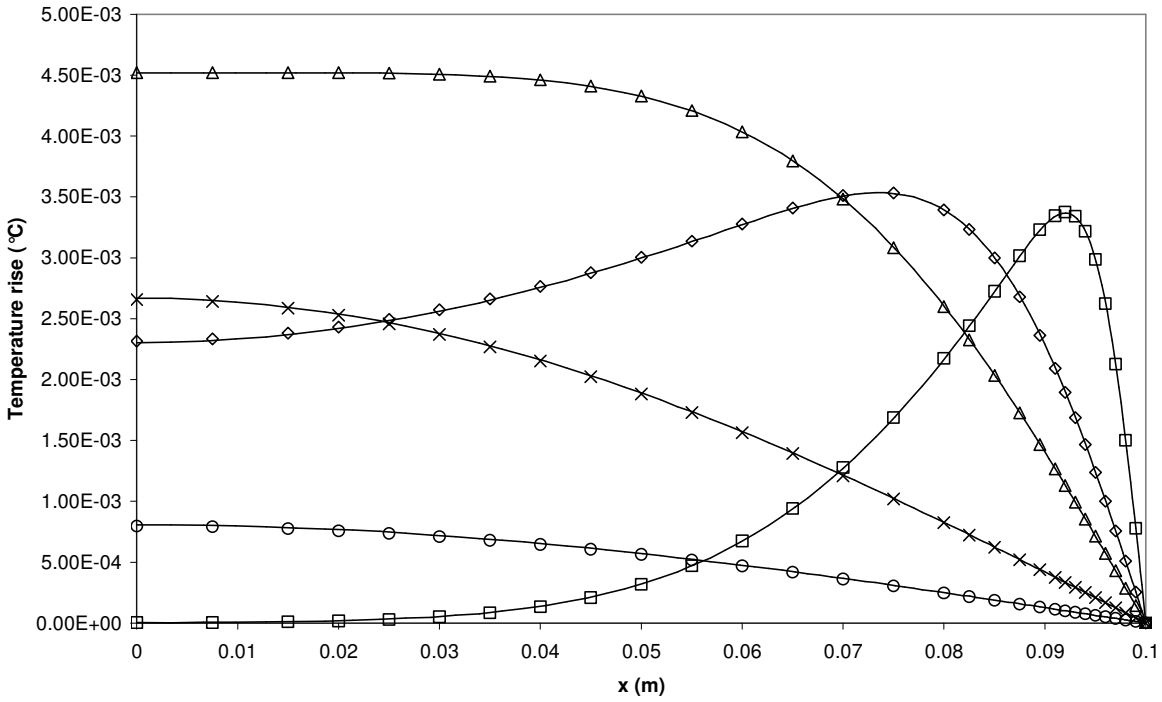

FIG. 2: Comparison between the increase in temperature predicted by the numerical model (__) and the analytical model (500s ( ), 5000s (◊), 20000s (Δ), 200000s (×) and 500000s (O))

3. Verification and validation study

3.1 Verification

The aim of the verification study is to check the correct implementation of the equations given in the previous chapter. A test case for which the analytical solution is available, is simulated using the numerical model. Comparison of the analytical and numerical results allow for the assessment of the accuracy of the numerical model.

3.1.1 Test case

The considered test case was designed by (Milly, 1982) and represents the one dimensional, coupled diffusion of heat and water vapour in a 10 cm high porous material. Initially the temperature in the material is 20°C and the relative humidity is 23.45%. A step change is imposed at the top of the material: the relative humidity changes to 27.11% while the temperature at the top is maintained at 20°C. This causes water vapour to diffuse into the porous material and leads to a varying temperature inside the material (due to latent heat release). The bottom of the material is considered to be vapour tight and adiabatic.

To obtain an analytical solution for this test case the following assumptions have to be made: (1) the transfer of sensible heat by vapour diffusion and the storage of sensible heat in the liquid water and the water vapour are negligible, (2) the perturbations in temperature and vapour density are so small that the relation between the moisture content w and the relative humidity can be considered linear around the initial state with all other material properties considered constant. If these assumptions are valid the analytical solution developed by (Crank, 1989) can be used to describe the coupled heat and water vapour diffusion. The following material properties are used: $w = 4.615RH + 74.261$ kg/m³; D/μ = 4.37E-6 m²/s ; c = 2E6 J/kgK ; k_{mat} = 1.5 W/mK. Note that an extremely high heat capacity c is chosen to guarantee small changes in temperature and hence assure the linear nature of the transport equations.

3.1.2 Results

Figure 1 and Figure 2 respectively give the increase of the vapour density and the temperature inside the porous material, as predicted by the analytical and numerical model. Figure 2 shows how the water vapour diffusion into the material triggers a temperature increase which levels out in time under influence of the heat conduction to the surface. The excellent agreement between both models shows that the equations in the numerical model have been correctly implemented and that the interaction between heat and water vapour transport is accurately represented.

3.2 Validation

In the validation study it is checked whether the hygric interaction between the air flow and the porous material simulated with the newly developed model agrees with reality. To this end an experiment for the benchmarking of 1D transient heat and moisture models of hygroscopic materials (Talukdar, 2007; Talukdar, 2008) is simulated. This particular benchmark experiment is well suited for the validation of the new model as the temperature, humidity and velocity of the airflow above the material are accurately controlled. This makes it possible to model the heat and moisture transport in both the air flow and the porous material.

3.2.1 Experiment

The experimental set up is elaborately described in (Talukdar, 2007). The test case simulated in this paper is not the case discussed in (Talukdar, 2008), but is a test case developed within the frame of IEA Annex 41(IEA Annex 41, 2008). The most important characteristics of the set up and test case are briefly discussed here. During the experiment conditioned air is sucked through a duct which passes over a porous specimen. This test specimen is placed in an impermeable container with adiabatic walls. A step change in the humidity of the conditioned air is imposed and the resulting temperature and relative humidity change in the porous specimen are measured. The cross section of the duct has a height of 20.5mm. The porous specimen has a height of 37.5mm and a length of 498mm. Temperature and relative humidity sensors are placed inside the porous specimen at a depth of 12.5mm and 25mm.

The porous material used in the validation experiment is gypsum board. Three different experiments were carried out: the response of uncoated gypsum board (Test1), gypsum board coated with 0.1mm acrylic paint (Test2) and gypsum board coated with 0.1mm latex paint (Test3) were measured in the test set up. The material properties (sorption isotherm and vapour resistance factor) of the gypsum board, acrylic paint and latex paint were measured in (IEA Annex 41, 2008) and were used as input for the numerical model. The average velocity of the airflow in the duct is 0.82m/s which corresponds with a Re number of 2000. The test conditions for the three different validation cases are given in Table 1. In all three tests the relative humidity of the air flow is high during the first 24 hours. Next a step change is imposed to the air relative humidity resulting in a low relative humidity.

TABLE. 1: Test conditions for the three validation cases

Test	Used material	Initial conditions		Airflow conditions	
		T (°C)	RH (%)	T(°C)	RH(%)
1	uncoated gypsum	23.3	30	23.8	71.9
				22.5	29.6
2	acrylic coated gypsum	24	34.6	23.2	72.2
				23.2	30.8
3	latex coated gypsum	24.1	31.4	23.4	70.9
				23.4	31.2

3.2.2 Model settings

The simulations are performed under the assumption of isothermal water vapour transfer: a constant temperature is imposed to the air and the porous material. To model the material properties as accurately as possible 5th order polynomial functions are used for the sorption isotherm and the vapour resistance factor of the gypsum board, acrylic paint and latex paint. The air flow in the duct is assumed to be laminar and to have a hydrodynamically fully developed profile. This is in agreement with measurements performed by (Iskra, 2007). The time step used in the transient simulation is 60s.

3.2.3 Results

Figure 3 shows the distribution of the relative humidity in the porous material and the air. In this figure the developing boundary layer for moisture transfer and its effect on the distribution of the relative humidity in the material is clearly visible.

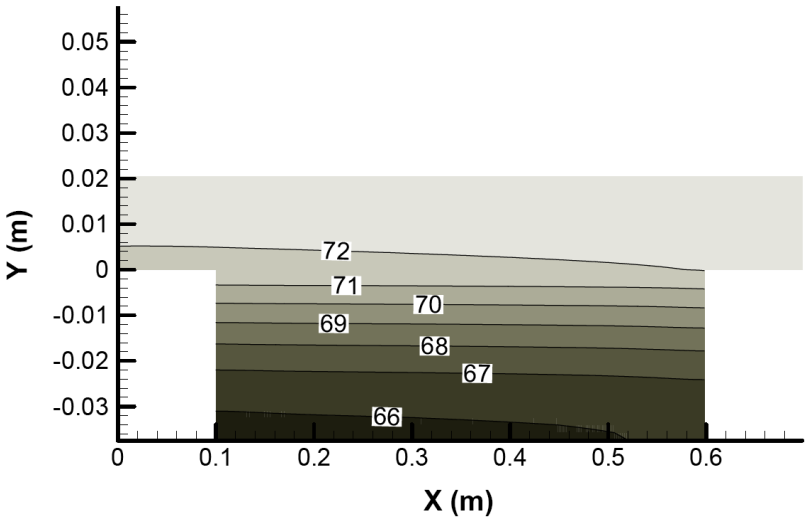

FIG. 3:Relative humidity in the porous material (Y<0) and air (Y>0) after 24 hours for Test case1

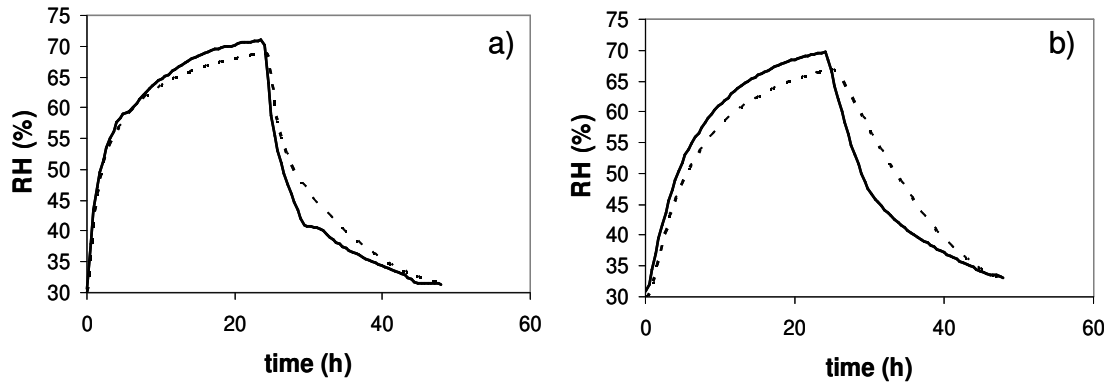

FIG. 4: Comparison of the measured (__) and simulated (_ _) evolution of the average relative humidity for Test1 at a depth of a) 12.5mm b) 25mm

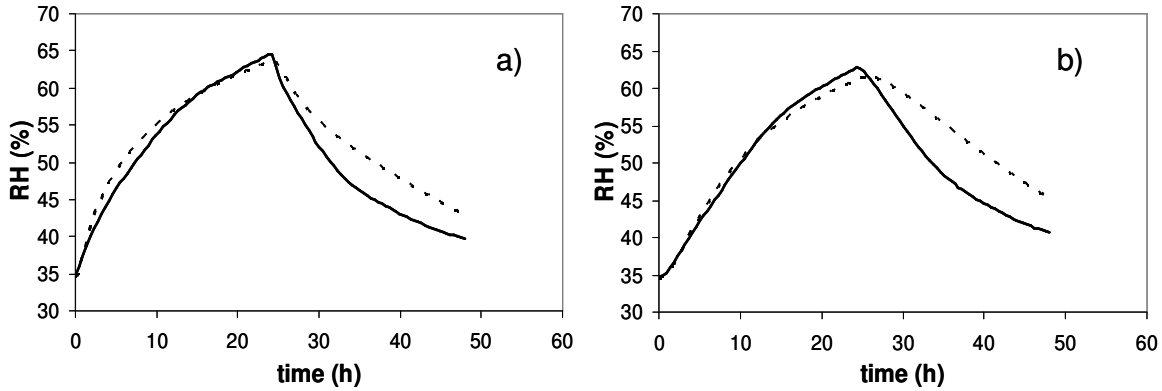

FIG. 5: Comparison of the measured (__) and simulated (_ _) evolution of the average relative humidity for Test2 at a depth of a) 12.5mm b) 25mm

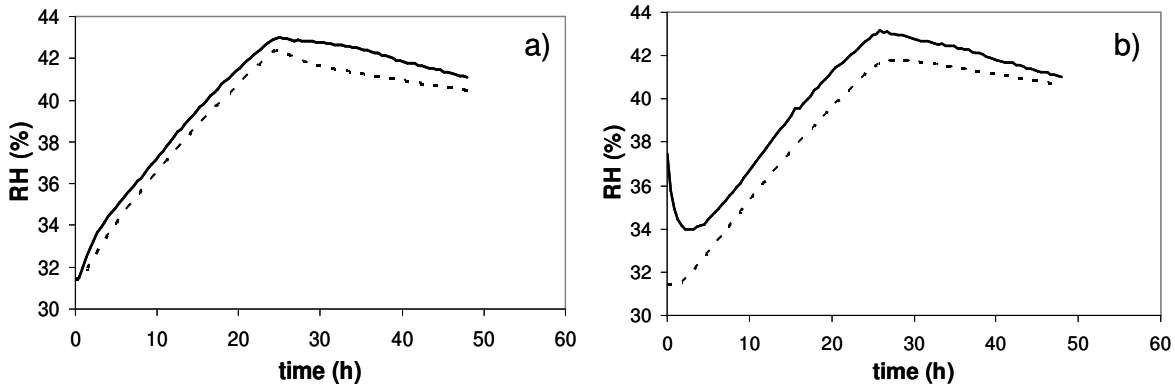

FIG. 6: Comparison of the measured (__) and simulated (_ _) evolution of the average relative humidity for Test3 at a depth of a) 12.5mm b) 25mm

In Figure 4, Figure 5 and Figure 6 the evolution of the average relative humidity at a given depth inside the porous material is compared for the numerical model and the experiments. A good agreement is found, especially during the absorption phase. The larger deviations during desorption might be caused by hysteresis in the material. By comparing the latter figures it can be seen that the humidity increase in the gypsum board decreases as the coating becomes more vapour tight (uncoated → acrylic paint → latex paint). This phenomenon was accurately predicted by the numerical model. The validation cases show that the new model is capable of simulating the hygric response of a porous material to a change in the properties of the air flowing over it.

4. Conclusion

In this paper a coupled CFD - hygrothermal material model is presented. A mass and energy conservative formulation of the heat and moisture transport equations in porous materials is implemented in the commercial CFD solver Fluent®, hence assuring a direct coupling between the fluid and the porous zone. A verification of the newly developed model was performed by comparing the model with the analytical solution for a simplified test case. Next experiments for the benchmarking of one dimensional heat and moisture transfer model were simulated. The good agreement between the simulation and the experiment proves the capability of the new model to accurately predict the hygrothermal interaction at the air-material interface.

5. References

Amissah P. K. (2005). Indoor Air Quality - Combining air humidity with construction moisture. Department of Mechanical Engineering. University of Strathclyde, Glasgow.

Crank J. (1989). The mathematics of diffusion. Oxford Science Publications, Oxford.

Erriguible A., Bernada F., Couture F. and Roques M. (2006). Simulation of Convective Drying of a Porous Medium with Boundary Conditions provided by CFD, *Chemical Engineering research and design,* Vol 85(A2), p.113-123.

Fluent Inc. (2006). Fluent users's guide. Version 6.3. Lebanon, NH, USA

I.E.A. Annex 41 (2008), Whole building heat, air and moisture response

Iskra C. R. and Simonson C.J. (2007). Convective mass transfer coefficient for a hydrodynamically developed airflow in a short rectangular duct, *International Journal of Heat and Mass Transfer*, Vol 50 (11-12), p. 2376-2393.

Janssen H. (2002). The influence of soil moisture transfer on building heat loss via the ground. Department of Civil Engineering. Katholieke Universiteit Leuven, Leuven.

Janssen H., Blocken B. and Carmeliet J. (2007). Conservative modelling of the moisture and heat transfer in building components under atmospheric excitation. *International Journal of Heat and Mass Transfer*, Vol 50(5-6), p. 1128-1140.

Milly P. C. D. (1982). Moisture and heat transport in hysteretic, inhomogeneous porous media: a matric head-based formulation and a numerical model. *Water Resources Research* **,** Vol 18, p. 498-498.

Mortensen L. H., Woloszyn M., Rode C. and Peuhkuri R. (2007). Investigation of microclimate by CFD modeling of moisture interactions between air and constructions. *Journal of Building Physics* , Vol 30(4), p. 279-315.

Talukdar P., Olutmayin S. O., Osanyintola A. F., Simonson C. J. (2007). An experimental data set for benchmarking 1-D, transient heat and moisture transfer models of hygroscopic building materials. Part I: Experimental facility and material property data. *International Journal of Heat and Mass Transfer* , Vol 50(23-24), p.4527-4539.

Talukdar P., Olutmayin S. O., Osanyintola A. F., Simonson C. J. (2008) . An experimental data set for benchmarking 1-D, transient heat and moisture transfer models of hygroscopic building materials. Part II: Experimental, numerical and analytical data. to be published in: *International Journal of Heat and Mass Transfer*

Measurements of the Convective Mass Transfer Coefficient between the Water Surfaces and Still Air

Goce Talev, PhD candidate
Department of Civil and Transport Engineering,
Norwegian University of Science and Technology (NTNU)
Goce.Talev@ntnu.no

Jan Vincent Thue, Professor
Department of Civil and Transport Engineering,
Norwegian University of Science and Technology (NTNU)
Jan.Thue@ntnu.no

Arild Gustavsen, Professor
Department of Architectural Design, History and Technology
Norwegian University of Science and Technology (NTNU)
Arild.Gustavsen@ntnu.no

KEYWORDS: *Convective mass transfer coefficient, natural convection, heat balance, water surface,*

SUMMARY:
The study of moisture migration from the surface of building materials and construction elements is of great importance for the characterization of their hygrothermal performance. In particular, transient calculation of moisture migration from the surface requires knowledge of the convective mass transfer coefficient, CMTC and the moisture buffering properties of the building materials. In this paper the influence of the evaporation, radiation, and convection (of heat) on the convective mass transfer coefficient between the warmer air and a horizontal upward facing colder water surface is explored under atmospheric pressure. The air temperature and the water surface temperature in water-filled square cups are obtained by measurements with T type thermocouples connected to a data-logger. The results from this measurements and observations are analyzed and discussed. Increased temperature difference between the water surface and surrounding air leads to higher value of the convective mass transfer coefficient. In addition slightly decreasing value of the mass transfer coefficient is detected during the experiments. At relative humidity of 35 % and air temperature at 30°C and 24°C, the measured water surface temperature is 24.8°C and 20.4°C respectively; and the mass transfer coefficient were 0.002032 to 0.002116 m/s 0.001566 to 0.001974 m/s respectively.

1 Introduction

It is of great scientific interest to determine the parameters of heat and vapor exchange in the boundary layer in order to study the effects of the convective moisture migration mechanism between building materials and the surrounding air. Over the past decade, a lot of research has been carried out on the effect of moisture transfer and storage in building materials as it affects indoor climate.

Many parts of the world experience large changes in temperature and relative humidity from season to season. The indoor relative humidity, is an important parameter to determine the occupants' perception of indoor air quality, and is also an important parameter as a cause of harmful processes that may occur on surfaces of materials, such as microbial growth (O'Reilly et al. 1998). Several studies have shown that high moisture contents in indoor air and building materials increase the risk of "sick building syndrome" (Sundel, 1996). Thus, it is known that humidity has an impact on both the working efficiency and health of occupants. Due to the varying loads, the indoor humidity exhibits significant daily or seasonal variation. Materials that absorb and release moisture can be used positively to reduce the extreme values of humidity levels in indoor climates.

The use of hygroscopic building materials to moderate the hygrothermal indoor environment has been a topic of research in hygrothermal conditions for buildings since at least the beginning of the 1980's, and the results have been used in building design and analyses since then (Plathner and Woloszyn, 2002). (Simonson et al. 2004) discovered that moisture transfer between indoor air and hygroscopic structures significantly reduced the peak indoor humidity, which lead to an improvement in the quality of the indoor air as perceived by occupants. There is now an interest in including in the analyses the moisture buffering properties of absorbent, porous building materials.

The microclimate of an area is largely determined by nature of the surface which governs the rate of the energy and moisture exchange between the boundary layer. The indoor thermal environment is strongly affected by the boundary condition at the room surfaces, due to the radiation and convection heat, evaporation or condensation flux, indoor temperature, airflow ventilation, envelope material properties, etc.

Many moisture transfer processes involve the vaporization of a liquid to the surrounding air. In this presented work, the constant value of vaporization enthalpy of 2 453 040 (J/kg) (in the first set of experiments) and 2 442 480 (J/kg) (in the second group of experiments) were used. Moisture transfer problem involving phase change such as water evaporation and solution of such problem needs to be analyzed by considering simultaneous heat and mass transfer. A simple free-water interface is analyzed during the evaporation of water. This condition over a water surface for estimation of the convective mass transfer coefficient is analogous to the saturated building material surface.

CMTC encountered in forced convection is typically proportional to the fluid velocities associated with forced evaporation. As a result, we tend to ignore natural convection effect in moisture transfer analyses that involve forced evaporation, although that natural convection may contribute even in forced convection situation. The error involved in ignoring natural convection is negligible at high velocities but may be considerable at low velocities. In addition many applications in building science and environmental engineering have zero air speed over building surfaces and therefore require CMTC at still air condition.

Thermodynamic and fluid mechanic assume variation in temperature as well as a sharp discontinuity in the density across water – air boundary layer. Therefore, it is important to investigate and understand the physical mechanism and direction of the interfacial discontinuity during the evaporation, in order to determine the convective mass transfer coefficient during the evaporation process.

There are many related work on the determination of heat and mass transfer coefficients considering the effect of free and forced convection such as (Iskra and Simonson, 2007, Yan, 1996). Sparrow et al. (1983) discovered that downward airflow dominated in the evaporation of water from circular pans when the water temperature was less than ambient air temperature. The importance of natural convection heat transfer for thermal developing flow in rectangular duct has been subject of other researchers. Heated water evaporation from a circular pan in a low speed wind tunnel has been investigated by Pauken (1999). Evaporation boundary layer was result of turbulent forced and turbulent natural convection boundary layer, where the forced convection was dominated by the air velocity and free convection was a function of the density difference between the air at the surface of the water and the surrounding air.

The heat balance is one of the basic quantitative indicators that define evaporation migration from the pure water due to the radiation and convection heat, evaporation or condensation flux, and indoor temperature.

The experimental work in this paper is focused on measuring the evaporation flux from water surface, relative humidity in the air, temperature at the water surface, surrounding surfaces as well as in the air in cases without airflow over the water surface. The aim of this present work is to study the process of the mass evaporation of pure water not only to determine the CMTC but also to show the importance of the water evaporation itself without any contribution of the ventilation. These measured results are used to validate calculated convective mass transfer coefficient from the surface energy balance.

2 Description of the experiment and the calculation model

The primary goal of presented work is to measure the convective mass transfer coefficient between the still air and water surface at atmospheric pressure.

A climatic laboratory room of a volume of 17.56m^3 (2. 4 x 3. 05 x 2.4m) is constructed at Norwegian University of Science and Technology, NTNU. The temperature and relative humidity of the room can be controlled individually in the range 4 - 30° C (± 1° C) and 30 – 90 % RH (± 2 %RH). The air velocity is measured to be in the range 0. 1 – 0. 3 m/s.

Two equal water sample holders, named cup 1 and 2 are placed into a plywood box (with dimension 0. 7m x 0. 7m x 0. 5m) not only to avoid the air circulation inside the climatic room but also to provide a stable condition for natural evaporation. Water cup 1 was put on a scale while the other, cup 2, was a control sample for surface temperature, in order to examine the effects of the heat flux from the electrical scale on the water cups. (It was discovered that the scale released heat into the sample (cup 1) in the early stage of the experiment). For this purpose an isolation material is fixed between the balance surface and water cup 1 in order to avoid the transient heat from the electrical balance. A plastic curtain is situated along the front side of the plywood box for visual inspection of the specimens during the test. A water container was kept inside the climatic room. The system was adiabatic i.e. no external heat source/sink was used, and the latent heat for evaporation was extracted from the surrounding air. The system was allowed to stabilize at constant (but different) air and water temperature upon the saturation experiment. Each sample holder has a square shape with opening area of 100 mm x 100 mm and is filled with water from the container just before they are placed inside the plywood box. The cups are manufactured from polyester and are easily removable and adjustable from the box. Polyester has a low thermal conductivity, hence the heat leakage through the polyester walls were negligible. Water cup 1 is placed on an electrical analytical balance – Sartorius LA 1200S. The weighting capacity of the balance is 1200g with readability of 0.001g. The calibration of the electrical balance is done according to the manual of the producer (Sartorius 2004). The output electronic signal of the electrical balance is transferred to a PC through a LABVIEW program (NI 2007). The interval of reading the changes of the weigh is set to be two minutes. A schematic diagram of the experimental setup for the analysis of the evaporation processes are shown in (Fig.1)

Very sensitive and inexpensive T type of thermocouples has been used to measure the air temperature of the air inside the plywood box as well as the temperature on the water surface. The wall temperature of the plywood box were very close to air temperature so that we have assumed that internal surfaces of the box has temperature equal to the air temperature. The thermocouples calibration employed an ice point bath, which consists of crushed ice and water held in an insulated thermos. The ice-point provides a convenient way to check the calibration of the thermocouples whose range includes 0°C. The output signal was stored into the Hydra Data Logger (HYDRA 1990). It was continuously scanning at each two minute intervals.

Evaporation moisture flux in the present study is defined as the evaporation expected from a continuously saturated surface. The evaporative mass flux G (kg/s) from water cup 1 can be estimated as a function of temperature and density of the water surface as well as the air then compared with measured water loss by the electrical balance. Then the convective mass transfer coefficient β was determined as a ratio between the measured mass flux G and the driving force (difference between the density of the moist air at the surface of the water $\rho_{w,sat}$ and the free stream vapor density $\rho_{w,air}$) for the given surface area A:

$$\beta = \frac{G}{A \cdot (\rho_{sat} - \rho_{air})} \tag{1}$$

The value of the surface mass transfer coefficient β (m/s) is determined as a function of the measured evaporation flux from the water surface due to the evaporation, radiation, and convection (of heat).

The theoretical model is taken from (Cengel, 2006) based on the redistribution of the energy across the water surface is accomplished primarily through three processes: sensible heat flux (convection), latent heat flux (evaporation) and heat transfer by radiation.

Sensible heat flux is the process where excess of the heat energy is extracted from the water surface to the surrounding air by convection. The amount of the sensible heat depends mainly on the temperature difference between water surface and overlying air. Horizontally heat energy migration (advection) is neglected. Latent heat flux moves energy globally when liquid water is converted into the vapor (evaporation). Due to the higher temperature of the surrounding surfaces long wave radiative exists between the surrounding surfaces and water surface. The sum of the three above mention components is the total rate of energy exchange between the atmosphere air and the water surface.
So, the theoretical model that we consider is:

$$Q_{tot} = h \cdot A \cdot (T_{air} - T_w) - \beta \cdot A \cdot (\rho_{sat} - \rho_{air}) \cdot h_{fg} + \varepsilon \cdot \sigma \cdot A \cdot (T_{air}^4 - T_w^4) \quad (2)$$

where h is the convective heat transfer coefficient (W/m^{2}K), h_{fg} is the enthalpy of vaporization of water which depends on water surface temperature (J/kg), Stefan – Boltzmann constant $\sigma = 5.67 \times 10^{-8}$ (W/m^{2}K^4), and ε emissivity of the water surface 0.96 (-) (Cengel, 2006).

The value of the convective heat transfer coefficient was obtained from (Hiramatsu et al. 1998) by Eq. (3).

$$h = 3.5 + 4.7 \cdot 10^{-2} \cdot (T_{air} - T_w) + 3.5 \cdot 10^{-4} \cdot (T_{air} - T_w)^2 \quad (3)$$

The value of the convective heat transfer coefficient for horizontal water surface in still air has been suggested by (Abdel and Elmroth 2007) between 8 and 10 (W/m^2 K) for air speed lower than 0.3 m/s, and by (Cengel 2006) 3. 1 (W/ m^{2}K) for velocity 0 < V < 0. 2.

Various theoretical models of the heat transfer coefficient for estimation of the convective mass transfer coefficient were considered. But a theoretical model based on (Hiramatsu et al. 1998 shows best agreement between the measured and predicted results.

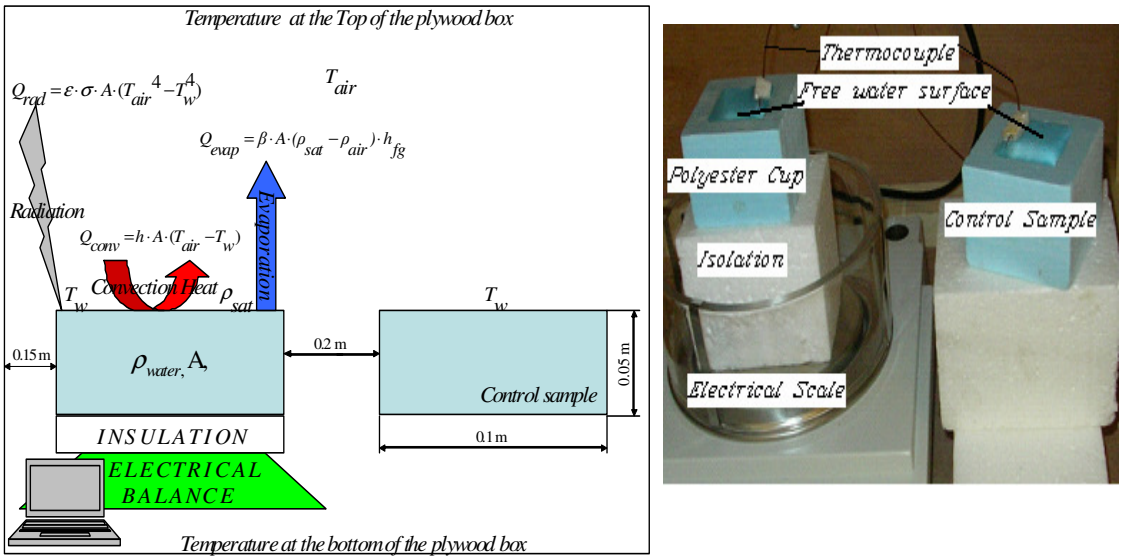

FIG. 1: Description of the experimental setup (not in scale)

3 Results and Discussion

For obtaining the physical properties (density, and specific heat capacity) of the water surface as well as the humid air, the temperature at the water surface and temperature in the air just above the water surface were used. The experimental work has been based on a couple of sets of water evaporation carried out under different test condition according to the experimental procedure explained in the previous section. In the first set of experiments, the average air temperature was 24°C and the average temperature of the water surface was measured to be 20.4°C. For the second group of experiments the average temperature of the air was 30°C and the temperature of the water surface was measured to be 24.8°C. The relative humidity of the air was 35% ± 3% for both experimental groups. Slightly increased value of the relative humidity is detected within the both group of experiments due to the water evaporation inside the plywood box.

The atmospheric pressure was measured once per hour inside the room by a manometer that was connected to the computer.

In this presented work, the density of the moist air at the surface of the water is always larger than that of the bulk airflow, since the water temperature is always less than the bulk airflow temperature, which causes a buoyancy-driven down flow of air towards the surface of the water.

The value of the mass transfer coefficient β for the both groups measurements are given in the tables. Table 1 presented the values of the mass transfer coefficient at air temperature 24°C, and water surface temperature of 20.4°C while table 2 shows the measured results at air temperature 30°C, and water surface temperature of 24.8°C. From the both tables we see that the value of the mass transfer coefficient β in table 1 is between 0.001566 (m/s) and 0.001974 (m/s) for the first group or 0.002032 (m/s) and 0.002116 (m/s) in the second table.

TABLE1 . Measured and calculated values for mass transfer coefficient at air temperature 24°C. water surface temperature 20.4°C

Experiment	A [m/s]	B [m/s]	C [m/s]	D [m/s]
Average Measurements	**0.001566**	**0.001974**	**0.001820**	**0.001784**
Max. Measurements	0.001954	0.002185	0.002073	0.002050
Min Measurements	0.001226	0.001595	0.001558	0.001458
Sample standard deviation	0.000133	0.000108	0.000098	0.000106
Median	0.001564	0.001977	0.001813	0.001791
Average Calculation	**0.001607**	**0.002022**	**0.001794**	**0.001869**
Max Calculation	0.001676	0.002095	0.001854	0.001920
Min Calculation	0.001226	0.001943	0.001746	0.001809

TABLE. 2: Measured and calculated values for mass transfer coefficient at air temperature 30°C, water surface temperature 24.8°C

Experiment	1 [m/s]	2 [m/s]	3 [m/s]	4 [m/s]
Average Measurements	**0.002054**	**0.002032**	**0.002116**	**0.002052**
Max. Measurements	0.002355	0.002265	0.002350	0.002144
Min Measurements	0.001817	0.001756	0.001842	0.001767
Sample standard deviation	0.000093	0.000087	0.000075	0.000086
Median	0.002057	0.002027	0.002010	0.002045
Average Calculation	**0.002089**	**0.002051**	**0.002189**	**0.002063**
Max Calculation	0.002240	0.002208	0.002287	0.002303
Min Calculation	0.002004	0.001957	0.002099	0.001986

The sample standard deviation is defined as

$$S = \sqrt{\sum_{i=1}^{n} \frac{(x_i - \bar{x})^2}{(n-1)}} \tag{4}$$

where the x_i is the values of the sample data and n is the number of the measurements.

In the second group of the experiments, slightly increased value of the averaged surface mass transfer coefficient is noted due to the higher temperature difference between the still air and the water surface.

In Table 1 we are presenting the measured and calculated value for the mass transfer coefficient at average temperature of the air 24°C and the temperature of the water surface of 20.4°C. The average measured value of the mass transfer coefficient in this case varies between 0.001566 (m/s) and 0.001974 (m/s) while the sample standard deviation varies between 0.000098 and 0.000133.

Table 2 list the measured and calculated values for the mass transfer coefficient (CMTC) at average air temperature of 30°C and the temperature of the water surface was measured 24.8°C. The average measured value of the mass transfer coefficient in this case varies between 0.002032 (m/s) and 0.002116 (m/s) while the sample standard deviation relative deviation between 0.000075 and 0.000095.

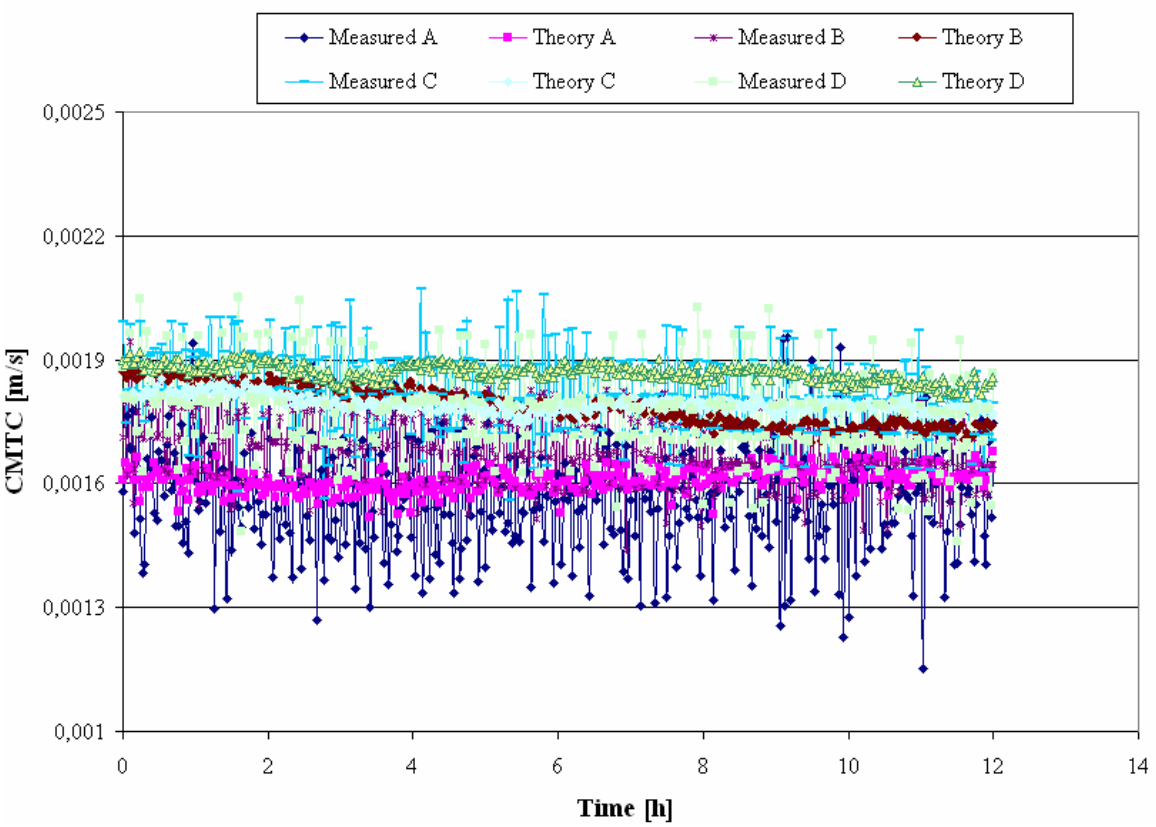

FIG. 2: Comparison between the measured and calculated values for mass transfer coefficient at air temperature 24°C. water surface temperature 20.4°C from Table 1

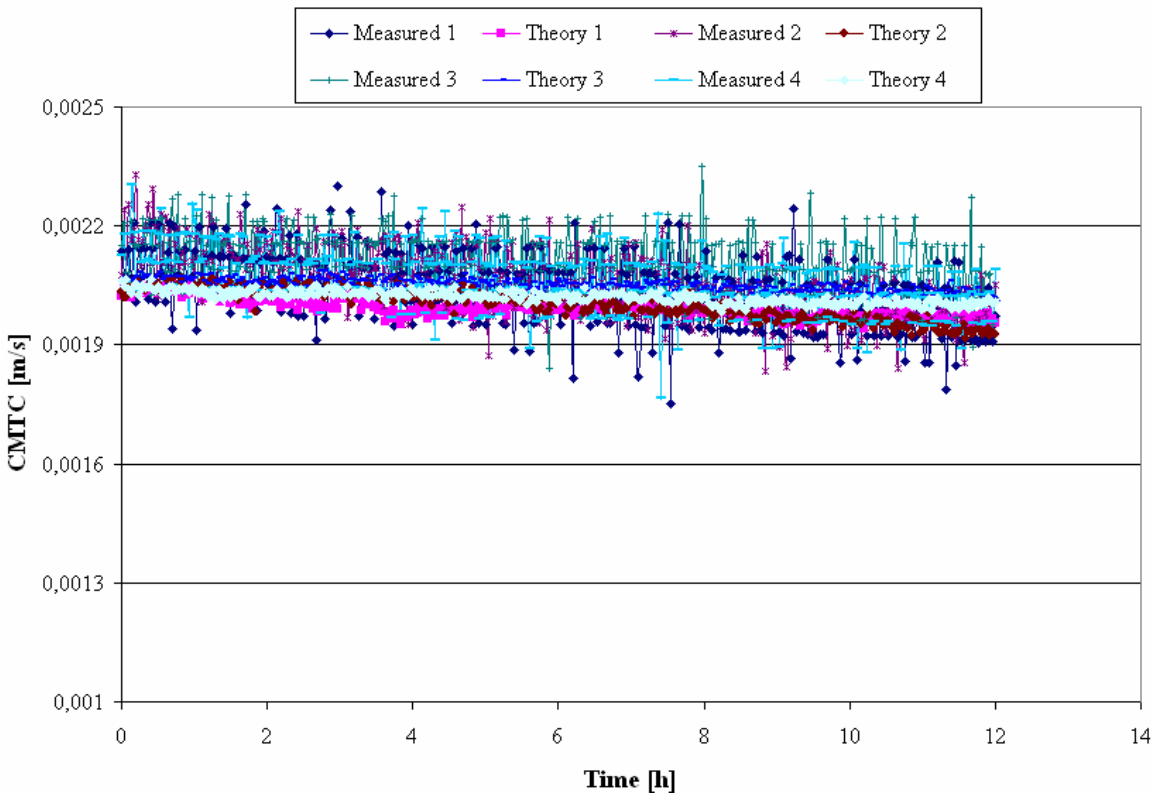

FIG. 3: Comparison between measured and calculated values for mass transfer coefficient at air temperature 30°C. water surface temperature 24.8°C from Table 2

4 Conclusion

The practical application of this work is related to building physics in cases where the air temperature is higher than surface temperature of the wet material surfaces during the evaporation at extremity low air speed.

The basic idea of this experimental work is to study the influence of temperature differences between the still air water surface and hence to determine the mass transfer coefficient during the evaporation process.

From the both groups of measurements can be concluded that the mass transfer coefficient increases with increasing temperature differences between the water surface and surrounding air.
Slightly decreasing value of the mass transfer coefficient is noted within the time of experiments. The explanation for this can be given with the fact that the higher relative humidity leads to lower mass transfer coefficients.

At relative humidity of 35 % and air temperature at 30°C and 24°C, the measured water surface temperature is 24.8°C and 20.4 0°C respectively; and the mass transfer coefficient were 0.002032 to 0.002116 m/s 0.001566 to 0.001974 m/s respectively.

Slightly higher effect on the total evaporative mass flux is also noted for the second group of experiments. In contrary, the experimental results of the mass transfer coefficient in this paper can be related mainly to the combined natural convection and forced convection, (but when the forced convection is dominant over the natural convection this effect will be neglected) from a horizontal surface.

An additional research goal is rising from this experimental work. Detailed investigation of the responsibility of the measured parameters such as temperature, relative humidity, evaporation on the CMTC as well as the experimental uncertainty of measured value of the CMTC will part of the further

research. Design new mathematical model that can describe the dimensionless convective moisture transfer coefficient when neither forced nor natural evaporation is negligible.

5 References

Abel E. and Elmroth A. (2007). Buildings and energy – a systematic approach. Formas. Stockholm, Sweeden p 253-256.

ASHRAE (2005). *Handbook of fundamentals*. American society of heating. Refrigerating and air conditioning engineers. Atlanta, USA.

Cengel Y.A. (2006). *Heat and mass transfer.* A practical approach third edition. McGraw-Hill. Singapore p 773-840.

Hiramatsu T., Harada T., Kato S., Murakami S., and Yoshino H. (1998). Analysis of indoor thermal environment with cooling condition and natural ventilation. - Study of thermal environment in real-scale atrium part 3*, J. Archit. plann. environ. Eng.. AIJ.* No. 523. p.23-30.

HYDRA (1990). Applications software. Fluke. Litho USA.

NI 2007. LABVIEW 8.2. National Instruments.

Iskra, C.R. and Simonson, C.J. (2007) Convective mass transfer coefficient for a hydrodynamically developed airflow in a short rectangular duct, *Int. J. heat mass transfer* 50 p. 2376–2393.

O'Reilly J., Hagan P., Gots. R., and Hedge. A, (1998). Keeping buildings healthy. How to monitor and prevent indoor environmental problems. John Wiley Sons. INC., New York. USA

Padfield T. (1999). The role of absorbent building materials in moderating changes of relative humidity. PhD. thesis. Dept. of structural engineering and materials*. Technical University of Denmark*. Series R No 54.

Pauken M.T. (1999). An experimental investigation of combined turbulent forced convection evaporation, Exp. therm. fluid Sci. 18 p. 334- 340.

Plathner P., Woloszyn M. (2002). International air and moisture transport in a test house: experiment and modeling. *Building environment 37 (2)* p.189-199.

Sartorius (2004). Operating instructions. Sartorius master series. LA models. Electronic analytical and precision balances. Goettingen. Germany.

Simonson C. J., Salonvaara M., Ojanen T. (2004). Heat and mass transfer between indoor air and a permeable and hygroscopic building envelope. Part I: Field Measurements. *J. thermal envelope building science*, 28 (1) p.63-101.

E.M. Sparrow, G.K. Kratz and M.J. Schuerger, (1983) Evaporation of water from a horizontal surface by natural convection, *J. heat transfer, Trans. ASME* 105 (3), p. 469–475.

Sundel S. (1996). What we know and what we don't know about sick building syndrome. J. *Ashrae . 38* p.51-57.

Yan, W.M. (1996). Combined buoyancy effects of thermal and mass diffusion on laminar forced convection in horizontal rectangular ducts, *Int. J. heat mass transfer* 39 p. 1479–1488.

Numerical Simulation Aided Design of an experimental protocol

Amandine Piot, PhD. Student,
Centre Scientifique et Technique du Bâtiment, F38400 Saint Martin d'Hères;
CETHIL, Universite de Lyon, CNRS UMR 5008, Universite Lyon 1, INSA Lyon, France;
amandine.piot@cstb.fr

Charlotte Abelé, engineer,
Centre Scientifique et Technique du Bâtiment, F38400 Saint Martin d'Hères;
charlotte.abele@cstb.fr

Monika Woloszyn, Associate Professor
CETHIL, Universite de Lyon, CNRS UMR 5008, Universite Lyon 1, INSA Lyon, France;
monika.woloszyn@insa-lyon.fr

Jean Brau, Professor
CETHIL, Universite de Lyon, CNRS UMR 5008, Universite Lyon 1, INSA Lyon, France;
jean.brau@insa-lyon.fr

KEYWORDS: *light-weight envelope, heat, air, moisture, simulation.*

SUMMARY:
A study was planned in order to improve the knowledge on heat, air and moisture transfers within light-weight building envelopes. In this aim, an experimental cell exposed to real climate, consisting of a small wooden frame structure and panel walls is being built. The aim of this large scale experiment is to evaluate the influence of different elements, such as the thickness of insulation, the thermal inertia and the vapour-barrier on the indoor environment and the building structure. The experiments will be followed by a numerical parametric study. The first phase, design of the experiment using numerical simulation, is discussed here. Two ways are exposed, the first one consisting in simulating several possible configurations, and evaluating the best sequence from the results, the second one consisting in giving information for the location of sensors. Concerning experimental sequences, the results of numerical simulations showed that it is more relevant to install additional insulation, prior to extra thermal inertia. Concerning sensor locations, 2D simulations showed that the effect of thermal bridges was visible on a length of about 15 cm. This information allowed choosing relevant locations for thermocouples in order to measure the effect of multidimensional transfers.

1. Introduction

The need for sustainable buildings led to the development of high performance envelopes. Building sciences have now to get to a better understanding of the conditions within the wall, and their consequences on the indoor environment. Depending on indoor conditions, insulation and hygroscopic properties of materials, condensation can occur and insulation level can thereby seriously decrease. Such phenomena are particularly important for light-weight envelopes, where mass transfers may seriously affect heat transfers.

To get information on the behaviour of such a structure, an experimental cell exposed to real climate, consisting of a wooden frame structure and panel walls is being built. The aim of this full scale experiment is to evaluate the influence of different parameters: the thickness of the insulation, the thermal inertia, the vapour-barrier, etc. on the behaviour of indoor environment and building structure.

The whole study consists of 3 phases:

- Design of the experiment using numerical simulation
- Large scale experimentation and model validation/improvements
- Parametric study using numerical model

The first phase, design of the experiment using numerical simulation, is discussed here. Numerical simulation was used to answer the following questions:

- What experimental protocol should be adopted in terms of evolutions of the experimental cell?
- Where the sensors should be located in order to perform relevant measurements?

The first question is a key point to optimise experimental investigations. Indeed, switching between steps requires serious modifications of the experimental cell, such as adding or removing additional insulation layer and/or vapour or air barrier, etc. Also the duration of each step is rather long, several weeks will be needed. It is then necessary to make sure that each step, and the sequence of steps, will be relevant, and no experimental time and effort will be wasted. Here, the required simulation tool has to be able to represent whole building approach, including outdoor climate, internal loads and coupled heat and mass transfers within the envelope.

The second question is very important in places such as corners, structural elements etc, where multi-dimensional transfers occur. Therefore numerical simulations should be performed using detailed tools, able to represent multi-dimensional effects.

2. Overall experimental protocol

2.1 Experimental set-up

The experimental measurements will be performed in a full scale test cell exposed to real outdoor climate. The test house, presented in figure 1, is built based on the European Technical Approval concerning wooden frame constructions [1], and is located at CSTB Grenoble, France. It consists of one room (≈ 5×5×2.5m^3) plus a naturally ventilated attic, not studied here. It will be ventilated and an occupation will be simulated using a humidifier and a heating system.

The structure is based on a wooden frame, consisting of spruce posts (70×16 mm²) positioned every 60 cm.

The ceiling and the floor are highly insulated (thermal resistance of 12.5 m²K/W, permeability of the vapour barrier of $2.08.10^{-12}$ kg/m²sPa), in order to have heat and moisture transfer mainly across vertical walls.

Initially, the lateral panels were to be built as shown on fig. 1b. The aim of the air gap between the gypsum board and the insulation was to leave us the possibility to increase the thickness of the insulation material without changing, in particular, the quantity of wood and the presence of thermal bridges. This composition for the wall panels is the one used in the simulations discussed in this paper; however, after discussion with other members of the project, some changes were made.

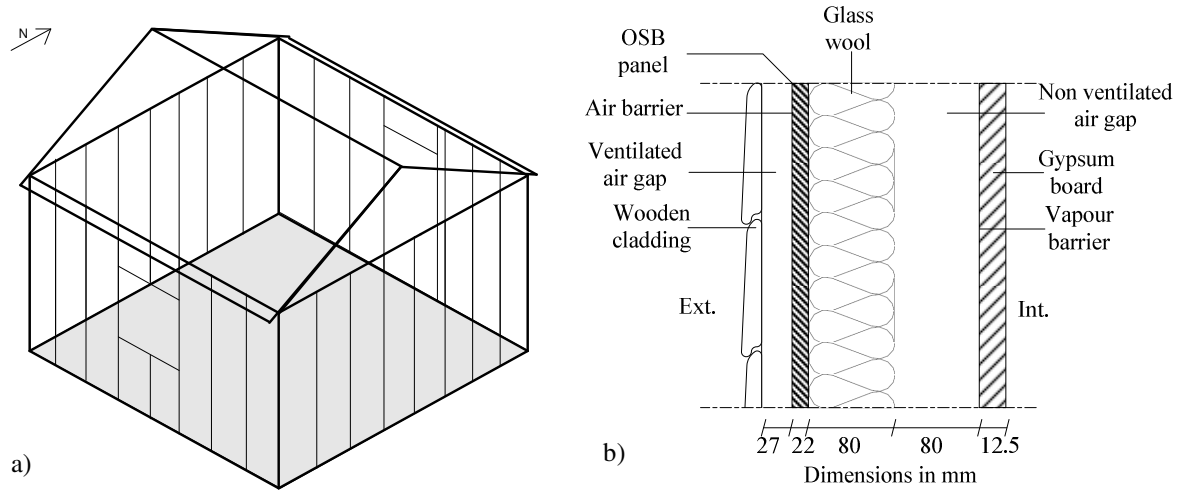

FIG. 1: Schematic drawing of the test cell (frame and wall section)

The objective is to study the influence of some construction parameters (*e.g.* the thickness of insulation, the quality of air- and vapour-barriers), and the potential leak points (around the window, in the corners, close to the posts), etc.

The instrumentation comprises the measurements of temperature and relative humidity in the room, within the walls and at their surfaces, heat flux through walls, as well as energy consumption and outdoor conditions.

As a first step, the test cell is built in a basic configuration, referred to as “base case” (C0) in the following. From this base case, we have the possibility to test several construction configurations, in order to evaluate the influence of some elements. We show in this paper the interest of using numerical simulations to help designing the subsequent steps of the experiment.

2.2 Methodology for the use of numerical simulation

Apart from the window, the following 4 parameters were chosen as primary parameters to vary: the thickness of insulation, the vapour-barrier, the air-barrier, the thermal inertia (concrete plates can be added on the floor).

The base case (C0) has no window, in order to diminish the influence of solar radiation, and to have homogeneous wall compositions. The basic characteristics are: single layer of insulation (80 mm), presence of vapour- and air-barrier, and no extra thermal inertia.

Then, a window will be added, in order to have a more realistic building. This will be called the "reference case", or C1.

From here, with the variation of 4 parameters, 16 different configurations are possible, see figure 2.

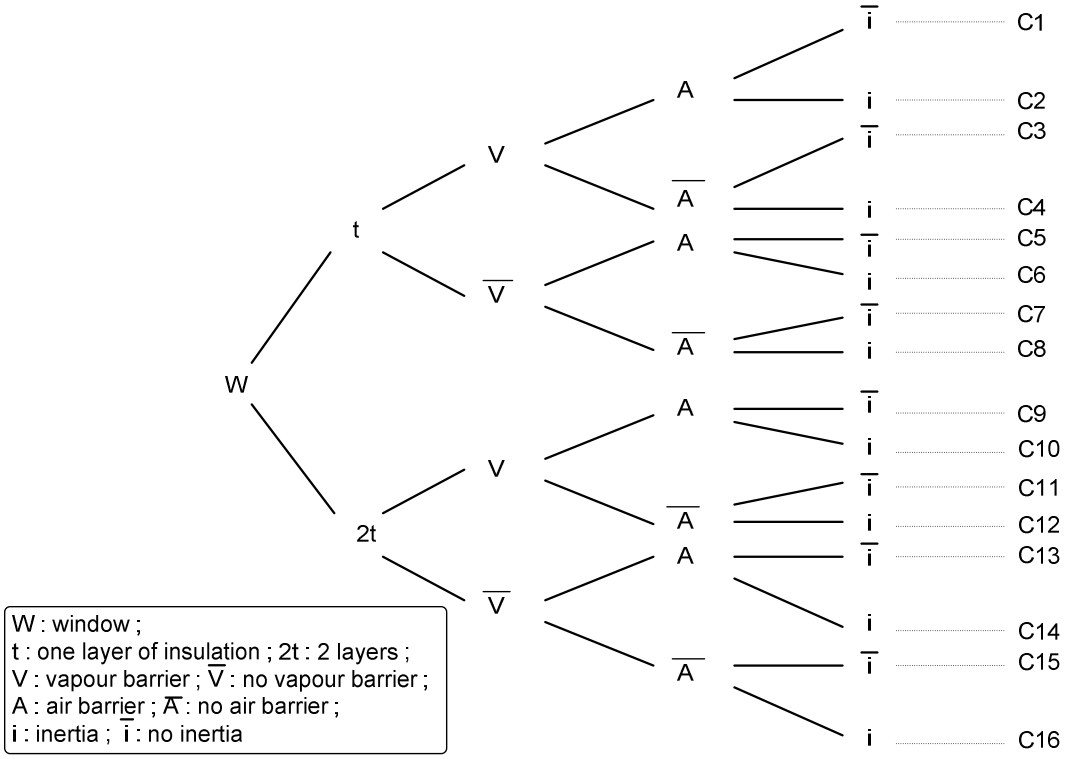

FIG. 2: Chart of the possible configurations

Two types of evolutions are possible:

- Impacting mainly mass transfer (adding/removing air- and vapour- barrier)
- Impacting mainly heat transfer (adding/removing insulation and thermal mass).

We had to define one sequence of experiments, that is, choosing among those 16 possible cases the configurations to carry out practically; the rules are that we have to change one parameter between two successive cases, and we want to have as visible effects as possible. The numerical simulations are used here to answer the question: which evolutions are the most relevant for experimental measurements (*i.e.* showing the most visible differences between steps *n* and *n+1*)?

To better observe the impact of mass transfers, it was decided that the tests on vapour- and air-barrier should follow each other, helping us to see their respective behaviour/role.

From here, 3 "main directions" could be identified:

- 1st modification of mass transfer / 2nd modification of mass transfer / 1st modification of heat transfer / 2nd modification of heat transfer
- 1st modification of heat transfer / 2nd modification of heat transfer / 1st modification of mass transfer / 2nd modification of mass transfer
- 1st modification of heat transfer / 1st modification of mass transfer / 2nd modification of mass transfer / 2nd modification of heat transfer

As there are always two possibilities for mass and heat transfer modifications, a total of 12 possible sequences is obtained. To choose the most interesting sequence, the impact of heat transfer modifications was studied first, considering that we have both vapour- and air-barrier. Therefore the following configurations were simulated: C1 (one layer of insulation and no additional thermal mass), C2 (one layer of insulation and additional thermal mass), C9 (two layers of insulation and no additional thermal mass), C10 (two layers of insulation and additional thermal mass). The differences between the 2 possible “paths” between C1, initial case, and C10, final case (*via* C2 or *via* C9) are presented in the section “results”.

3. Numerical models

3.1 Whole building modelling

3.1.1 The HAM-tools

The software used here, HAM-Tools (Heat, Air and Moisture simulation Toolbox), is a simulation toolbox developed by the Chalmers University of technology (Sweden), and by the Technical University of Denmark. It is described in details in [2] and [3]. It is open source, free for research and available on www.ibpt.org.

The toolbox is a component library, running with Matlab-Simulink, which allows simulating the thermal, hygric and airflow behaviour of a building in its entirety (walls in detail and volume). The walls are modelled using a 1D finite differences scheme, and the air zones are considered homogeneous (1 node per zone). At each time step, the temperature and relative humidity are computed for each node, as well as the air pressure of the zone and the moisture content of the materials. The material properties are functions of the temperature and/or moisture content. The HAM-Tools can also read a climate file, and provides a simplified heating/cooling system, ventilation, and gains due to occupants (heat/vapour). The software computes the energy loads of the building.

The main interest of HAM-Tools in this study is that it simulates both the room air and the construction elements, giving detailed temperature and moisture fields inside the walls. This is a key point in our work, as focus is put on the behaviour of the construction elements. For this reason also we will install sensors inside the walls and at the thermal bridges locations.

To achieve this study, 2D modules for the HAM-tools will be developed in order to be able to simulate also the thermal bridges, and to have an overall model for the building. The models will be validated against the experimental results.

3.1.2 Non-ventilated cavity

In the first version of the test-cell, 80 mm of insulation have been installed, but, in order to easily add a second layer of insulation, the posts are 160 mm wide. This means we have a non-ventilated cavity inside the walls, between the insulation and the gypsum board.

To model the walls of our test house, we used the default block “exterior wall” in HAM-Tools. This block describes a wall made of 3 layers: one exterior material, one insulation material, and one interior material. Between the two latter, a possibility is given to add a heat, vapour and/or liquid resistance, generally used to insert a vapour barrier. We used this possibility to model both the vapour barrier and the non-ventilated cavity.

As no liquid transfer at all can occur through the air gap, the resistance for liquid transport was set to a very high value. Also a large value for the resistance to vapour transfer was used, to represent the vapour-barrier.

We modelled the heat exchanges within the cavity with a constant resistance, because the convection correlations (based on Nusselt number calculations) required a loop that the model couldn’t solve. To estimate the value of this resistance, we used the calculation method from EN ISO 6946 standard [4], considering both radiation and convection. The convection heat transfer is given as a function of the thickness of the cavity. By using the calculation method in [5], based on dimensionless numbers and empirical correlations, we obtained the same value for a temperature gradient of 5 K (which seems reasonable), that is, h_c=1.25 W/m²K. The radiation heat transfer coefficient is a function of the emissivity of both sides of the cavity, giving h_r=5.7 W/m²K, resulting in a total resistance for the cavity of 0.17 m²K/W.

3.1.3 Simulation parameters

The exterior temperature and relative humidity were defined as sinusoidal curves (both of daily and yearly period), based on the climate in Grenoble.

The cladding itself is not modelled, but is supposed here to protect the wall from wind-driven rain and partly from radiation. Therefore and to simplify, no rain and no radiation (both short and long wave) are taken into account.

The chosen period corresponds to the coldest part of the winter, the ambient relative humidity being at its maximum. The simulation ran for 30 days, until dynamic pseudo-equilibrium is reached; only the last days are shown in this paper. For this period, the temperature and relative humidity had an average daily evolution between -8°C (resp. 98%) and +2°C (resp. 88%).

In the simulations, the room was heated, using a variable temperature set point, in order to observe the effect of some inner additional thermal inertia. Set points were 20°C during “office hours” (9h-17h), 17°C otherwise. The heater is the default one in HAM-tools, with a proportional regulation. A constant humidification of 40g/h was added, in order to take into account latent loads, while not having parasitical effects due to a varying amount of humidification. This rate corresponds to 1 occupant sitting at a desk. The ventilation rate is constant and set to 0.5 ach.

The materials used are taken from the material library in HAM-Tools, the properties of which are based on [6]

3.2 Thermal bridges modelling

We used in parallel the software COMSOL and WUFI 2D, in order to have a better confidence in the results.

COMSOL allows the user to input his own equations, domain and boundary conditions, and solve the system by a finite elements method. WUFI 2D is dedicated to heat and moisture transfers, containing a large library of materials.

We modelled the heat transfer by conduction inside 2D blocks, representing the main thermal bridges that we will face in our test-cell. These are the junction between the floor or ceiling and the vertical walls, the vertical corners and the junction between the panels and the wooden frame elements.

Only thermal simulation was carried out, in order to determine the temperature field. From this, we will assume one or a few locations where condensation or high relative humidity could occur. This can either be due to high absolute humidity (no vapour-barrier, or on its inside face), or cold temperature (mostly close to the exterior surface). Hygroscopic materials, such as wood, can also release moisture while the local temperature is falling (time delay), resulting also in such risks.

The other point of those simulations was to evaluate the extent (length) of the influence of the thermal bridge on the regular part of the wall, in order to place the thermocouples so as to get a “profile” of this influence.

The boundary conditions were chosen constant, 5°C on the outside, 20°C on the inside. The material thermal conductivity and heat capacity are defined identically to HAM-Tools materials.

4. Results

4.1 Configurations and sequences to study

We ran the 4 simulations corresponding to the evolution of the test-cell from single insulation layer, no inertia, to double insulation layer, with additional thermal inertia (C1, C2, C9 and C10). The interesting parameters to observe were the indoor temperature, and, mostly, the heating power. Very few effects, if any, could be seen in the other parameters evolution (such as room absolute or relative humidity, or walls temperature or humidity).

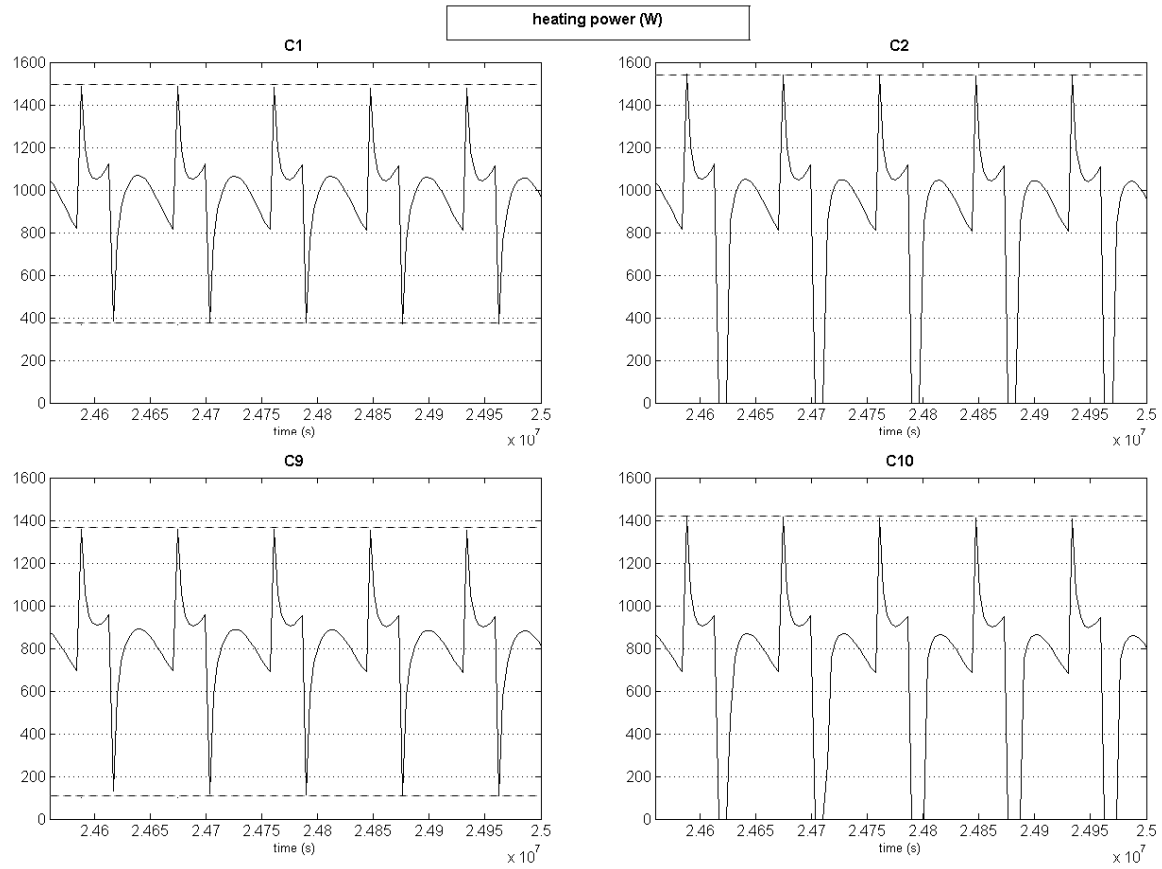

FIG. 3: heating power demand

In figure 3 we can see the evolution of the heating needs as a function of time, for the last 5 days of the simulation period. The shape of curves, with very strong variations is due to the intermittent temperature set point and the proportional control of the heating device.

We can see, both from C1 to C2, and C9 to C10, the effect of adding thermal inertia. The amplitude of variations, when the set point changes, is much stronger with the additional thermal inertia. In cases C2 and C10 the heater can even be stopped for a while.

We can also observe, both from C1 to C9, and C2 to C10, the effect of adding supplementary insulation. The insulation makes the whole plot lower, C1/C2 needing globally more power than C9/C10; if we calculate the energy consumption for the last day of simulation, using a trapezoidal method to integrate the power needs, we get 72.13 kJ in C1, 65.10 kJ in C2, 67.19 kJ in C9 and 58.84 kJ in C10.

The effect of adding inertia is slightly more significant with a standard insulation (C1 to C2) than with a thicker insulation (C9 to C10), regarding the evolution of the power. The main reason is that with a better insulation, the power need already falls down to a low value, making the inertia less probing in this case.

The interesting fact to denote here is that the difference between C1 and C9 is clearly visible (in average 200 W lower for the maximum and minimum value), whereas when we have more inertia, adding insulation (C2 to C10) produces less effect (approximately 100 W for the maximum value, hardly any difference at all for the period of stop).

After analysing the results of numerical simulations, we have chosen to install first some more insulation, and then to add extra thermal inertia, corresponding to the sequence C1 (one layer of insulation and no additional thermal mass) - C9 (two layers of insulation and no additional thermal mass) - C10 (two layers of insulation and additional thermal mass).

4.2 Sensors positioning

For each case, the results from both WUFI 2D and COMSOL simulations agreed very well (difference less than 0.5°C); only the latter is presented in figure 4 (wooden frame within wall, figure 4a, floor junction, figure 4b, and vertical corner, figure 4c). The case modelled corresponds to a complete filling of the cavity by insulation.

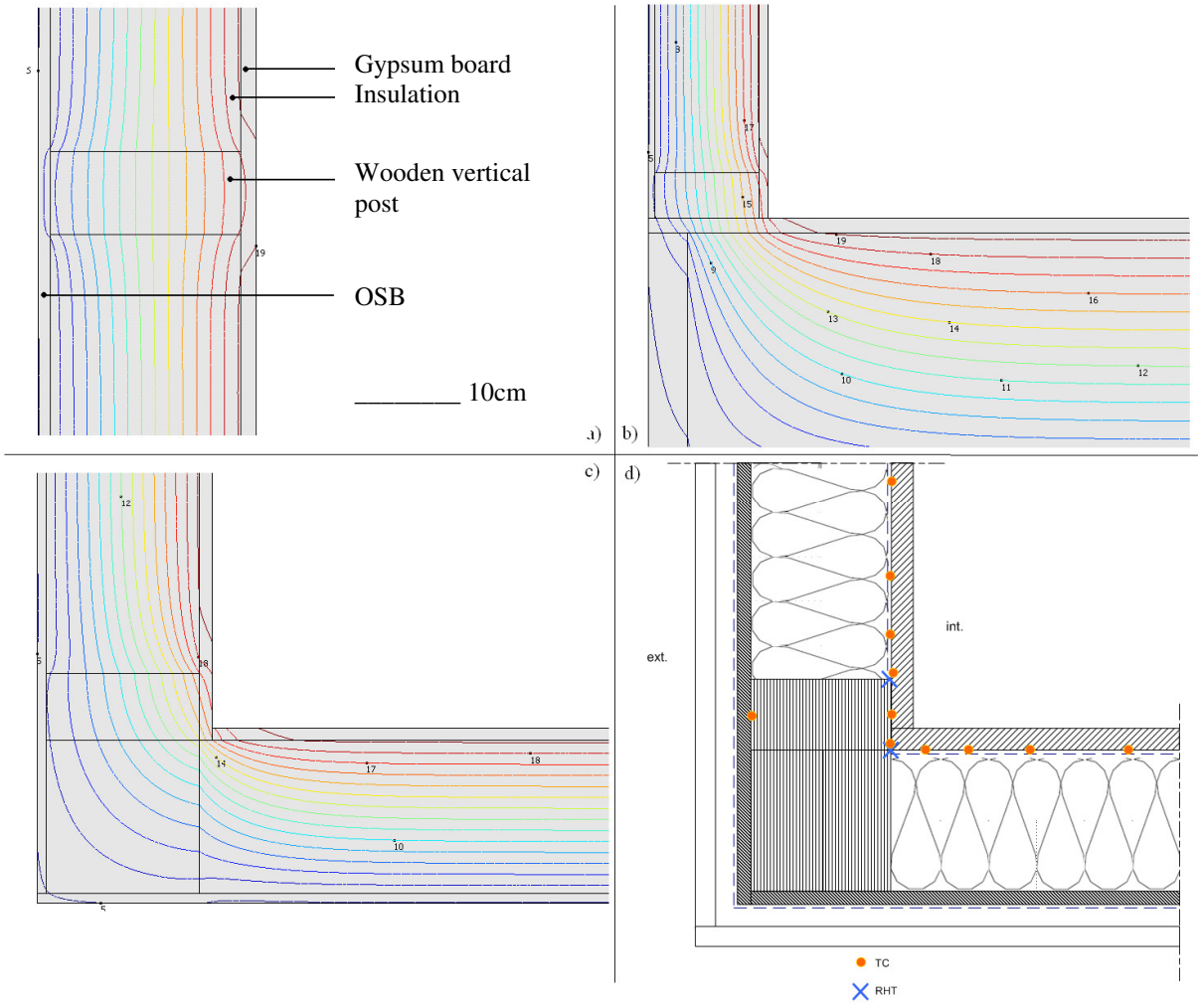

FIG. 4: the 3 thermal bridges and the location of sensors on the vertical corner

On figure 4a, b and c, the lines represent isothermal values, every 1°C, from 5°C to 19°C. On figure 4d, TC stands for thermocouple, RHT for relative humidity and temperature sensor.

The interesting information was to learn that 15 cm away from the coldest point, no more effect of the thermal bridge could be seen. We therefore decided (see figure 4d for the example of the vertical corner) to place thermocouples at distances regularly increasing from the coldest point to 20 cm away. We also placed a thermocouple on the exterior side of the wooden element.

5. Conclusions and Perspectives

This paper presented the methodology of using numerical simulations as an aid for designing an experimental protocol.

Two ways were exposed here, the first one consisting in simulating several possible configurations, and evaluating the best sequence from the results, the second one consisting in giving information for the location of sensors. Concerning experimental sequences, the results of numerical simulations showed that it is more relevant to install first additional insulation, and then to add extra thermal inertia. Concerning sensor locations, 2D simulations showed that the effect of thermal bridges was visible on the length of about 15 cm. This information allowed choosing relevant locations for thermocouples in order to measure the effect of multidimensional transfers.

The practical aspects of the modifications, and the period of the year, will be key points for the choice of the sequence, but we show here that interesting information can be obtained using numerical simulation. For some of the parameters to study, it can even be decisive. Another point in using numerical simulations before making the experiment is to help us determining which data will be the most interesting to observe in the different configurations, and most relevant to compare between 2 cases.

The next phase in our work is to perform the chosen sequence of experiments; the climate measured data will be used as an input for the numerical model, then the simulation results will be compared to the measures, and the model will be adjusted.

Then, we will use the numerical model to perform the parametric study itself, in the same conditions for the different configurations. The conclusions should help in understanding coupled heat and mass transfers in lightweight envelopes and to give indications on the ways to improve the performance of wooden frame constructions.

6. References

[1] European technical approval ETA-05/0022 (valid from 12/05/2005 to 12/05/2010). Timber frame building kits. *European Organisation for Technical Approvals.*

[2] Kalagasidis A. S., P. Weitzmann, T. R. Nielsen, Ruut Peuhkuri, Carl-Eric Hagentoft and Carsten Rode (2007). The International Building Physics Toolbox in Simulink. *Energy and Buildings*, Vol. 39, No. 6, 665-674

[3] Kalagasidis, A.S. (2004). HAM-Tools, An Integrated Simulation Tool for Heat, Air and Moisture Transfer Analyses in Building Physics. PhD thesis, Chalmers University of Technology, Gothenburg, Sweden.

[4] NF EN ISO 6946 (2005). Building components and building elements -Thermal resistance and thermal transmittance - Calculation method.

[5] Hens H. (2007). Building physics - Heat, air and moisture. Ernst & Sohn, Berlin, Germany.

[6] Kumaran K (1996). Heat, air and moisture transfer in insulated envelope parts. IEA annex 24 - Final report - Task 3: Material Properties.

Laboratory Testing Protocols for Exterior Walls in Canadian Arctic Homes

Steve Cornick, Research Officer,
Institute for Research in Construction National Research Council Canada;
Steve.Cornick@nrc-cnrc.gc.ca

Madeleine Rousseau, Research Council Officer,
Madeleine.Rousseau@nrc-cnrc.gc.ca

Marianne Manning, Technical Officer,
Marianne.Manning@nrc-cnrc.gc.ca

KEYWORDS: *Arctic, wood-frame housing, wall testing, protocols, climate, moisture, hygrothermal simulation*

SUMMARY:
Two wall-testing protocols used for evaluating wall assemblies in the Canadian arctic were developed. The protocols were developed as part of a project to develop building envelope assemblies that are energy efficient and durable under extreme cold outdoor climates and indoor conditions typically found in these climes. The objective of the testing phase was to evaluate the hygrothermal performance of wall assemblies as well as providing input for hygrothermal simulations. The exterior test protocol was based on a representative arctic location selected on the basis of a climate characterization study carried out using Canadian locations. The exterior protocol comprises four parameters: temperature, wind, atmospheric moisture, and solar irradiance. An accelerated test lasting six weeks was defined. Three seasons are represented; winter, spring, and summer. The interior protocol was based on data obtained from a survey of interior conditions of Canadian houses located in cold regions as part of the project. The interior protocol comprises two parameters: temperature and interior moisture, and is intended to be used in conjunction with the exterior protocol.

1. Introduction

Most Canadian Arctic communities are accessible only by air, sea, or ice road and consequently the cost of utilities in these northern communities is significantly higher as compared with communities having road or rail access. The cost of infrastructure and transportation is also quite high. Extreme northern climates greatly affect the durability of building envelopes, which in turn affects the quality of the built environment and its energy budget as well as the global environment. These factors emphasize the need for the development of energy efficient, durable, healthy, and sustainable housing. Although there is readily available information on the design of building envelopes and technologies for northern Canadian communities little attention has been given to the performance of innovative building envelopes exposed to such extreme conditions (Saïd 2006). Many demonstration projects have been built in the North stretching back to the 1980's however in general there has been little review of the performance and service life of these projects or indeed typical houses (Cornick and Rousseau 2007). Data on acceptable typical indoor conditions in these communities are scant and limited (Kovesi et al. 2006a and b, Rousseau et al. 2007). To address some of these issues, a four-year project was undertaken to assess the performance of innovative wall systems for the Canadian North, (Saïd 2005).

The scope of this project includes a review of published literature on high energy efficiency building envelopes, outdoor climate characterization, a field survey of indoor temperature and relative humidity in selected homes and a community consultation on typical current practices for construction methods of the building envelope. Data collected in these field surveys has supported the development of experimental and modelling studies to predict the hygrothermal performance and the energy and environmental impact of several wall assemblies for the Canadian Arctic. The experimental study will be conducted in an environmental chamber, which can simulate climate on one side and indoor conditions on the other (Maref et al. 2007). Six wall systems, five considered innovative and a reference wall will be tested. The overall energy and hygrothermal performance of the walls will be assessed and will ultimately lead to recommended Arctic wall types based on wall performance and cost. In preparation for this work it was necessary to define the limiting conditions to which these walls would be exposed on the exterior and interior sides. Computational studies were coordinated with the laboratory testing studies in order to obtain data to benchmark computation as well as provide data for the design of the laboratory testing. Since it is not practical to test all combinations the test results will also form the basis of a parametric study to assess the hygrothermal performance of the selected building envelope assemblies. Two

studies supported this effort, a survey of interior conditions, and a climate study. The protocols for testing of wall assemblies described in this paper were developed for this project as no standardized existing test protocols were deemed adequate for reproducing the extreme environmental loads that the building envelope of housing can be subjected to in the Arctic. The development of the protocols is described by Cornick (2008a and b).

2. Accelerated test protocol

Accelerated tests are designed to induce, in a short period of time, changes in properties representative of those caused by natural aging so that long-term performance can be predicted from the test results (Masters and Wolfe 1974). There is an enormous amount of published work on accelerated test-protocols focusing on the corrosion or deterioration of individual components or materials. Mehlhorn and Herlyn (1998) describe a double climate chamber system facility at the Fraunhofer-Institut für Holzforschung where full-scale specimens can be tested. The facility is designed to be used for accelerated aging or short–term testing and has been used to test interior insulation materials used in wood-frame construction.

For the exterior protocol expected in-service conditions were intensified so as to provoke high rates of moisture transfer in a short period time by subjecting the specimens to typical and extreme conditions. Moisture management is assessed through the application sustained high temperature and pressure gradients combined with high indoor moisture conditions and with rapid changes in the exterior conditions. The main reason for proposing accelerated tests was time. Rather than testing for an entire year the accelerated exterior climate test protocol was designed to represent three seasons: winter season, spring, and summer, as the sequencing of these were deemed to present the critical conditions for moisture accumulation and moisture drying potential. The advantage of an accelerated test is the collection of data in a shorter time frame than full year cycle studies. The difficulty lies in the ability to predict performance to actual constructions in the field. This stresses the importance of complementary studies involving field monitoring, as well as review of documentation maintenance, repairs, energy consumption of buildings built with the walls characterized in the laboratory.

Since the main objective of the laboratory testing is to examine the cold weather performance, a long period of cold weather testing was selected. Specimens are first acclimatized, then subjected to mean conditions, followed by mean minimum conditions, followed by a brief period of extreme cold conditions, and returned to mean conditions, approximately 4 weeks providing enough time to fully characterize the performance of the wall during cold weather. The spring season and summer seasons are included to assess ability of the wall specimens during a rapid transition season. The summer and spring phase each last approximately one week. The interior protocol is linked to the exterior protocol in that the temperatures and relative humidity (RH) values are linked to the exterior parameters. There was sufficient data to develop an interior daily profile for the winter phase (Rousseau et al. 2007). The spring and summer interior profiles were developed by using interior temperature and RH models (ASHRAE 2006). The total test duration is 6 weeks. Although a six-week protocol can hardly be called accelerated, the protocols will be evaluated after the testing of the first set specimens is complete.

3. Exterior extreme cold climate test protocol

The proposed exterior test protocol for the extreme cold regions is described in this section. The protocol comprises four climate parameters: ambient temperature, wind speed, atmospheric moisture and solar irradiance. Not all the parameters need to be used in the testing program; they can be used singly or in combination as required.

3.1 Representative Cold Location

The cold climate protocol was developed using weather data extracted from one cold location. The selection of this representative location was made from a pool of locations for which long-term data sets of hourly weather conditions were available. Many of the locations had up to 48 years of data, starting as early as 1953, and ending in 2001. To winnow the list of potential locations, only locations that met the cold climate criteria outlined by Cornick (2005) were considered. The criteria were: 1) 100 or more days where daily min. is less than –20^{o}C, and/or 2) 8000 or more heating degree-days below 18^{o}C. Fig. 1 shows the mean min. daily temperatures for locations with long-term data meeting the criteria. The three coldest populated locations considered were Cambridge Bay (*Iqaluktuuttiaq*), Hall Beach (*Sanirajak*), and Resolute (*Qausuittuq*), all in Nunavut. Of the three possible locations with long-term data, Cambridge Bay was selected as the representative location. Cambridge Bay shows the greatest seasonal temperature range.

3.2 Temperature

Winter. Temperature was the most important testing parameter for the extreme protocol. Three seasons were considered; winter (Dec. to Feb.), spring (Mar. to May), and summer (Jun. to Aug.). In determining the thresholds for the winter season, min. daily temperatures were considered. The average min. temperature for the three winter months is –35°C, the suggested baseline for the winter temperature cycle. There are significant periods where the temperatures are –40°C and below. A threshold temperature of –42°C is proposed to mimic typical cold spells lasting about a week. There are significant periods when the temperatures drop below the winter design temperature, –46°C (NBCC 2005). During these periods, the heating systems in buildings may not be able to maintain the design temperature. To simulate extreme cold spells, a threshold temperature of –50°C held for 36-hours is proposed. The rates of temperature change in winter fall between 0 and 2°C/h (Cornick 2008b). It was clear from the data that there is no regular pattern of diurnal temperature cycling during the winter season therefore no diurnal temperature cycling for the winter portion of the test protocol is provided. The suggested winter temperature profile for the cold regions protocol is given in Table 1.

Spring. There is a rapid warming during the spring season. Large diurnal cycles may result in melting and refreezing of moisture accumulated in the wall stud cavity. Daily max. temperatures are proposed as the basis of the spring season profile to increase the possibility of freeze/thaws in the cavity. Temperatures for the typical spring months vary significantly around the mean value. A steady warming trend was observed. Suggested steps are at –25°C for March, –15°C for April, and –5°C for May. The rates of temperature change in spring fall between 0 and 4°C/h, however most of the values fall between 0 and 2°C/h. Data obtained for the spring months show a clear pattern of diurnal cycling due to insolation. To maximize the effect of springtime variation it is recommended that a 10°C 24-hour diurnal swing around the base line temperatures be incorporated into spring season profile. The solar model assumes a simple symmetric cosine variation around the daily mean temperature shifted to accommodate the peak, at 16:00 hours (Cornick 2008b). The spring solar profile is given in Table 1.

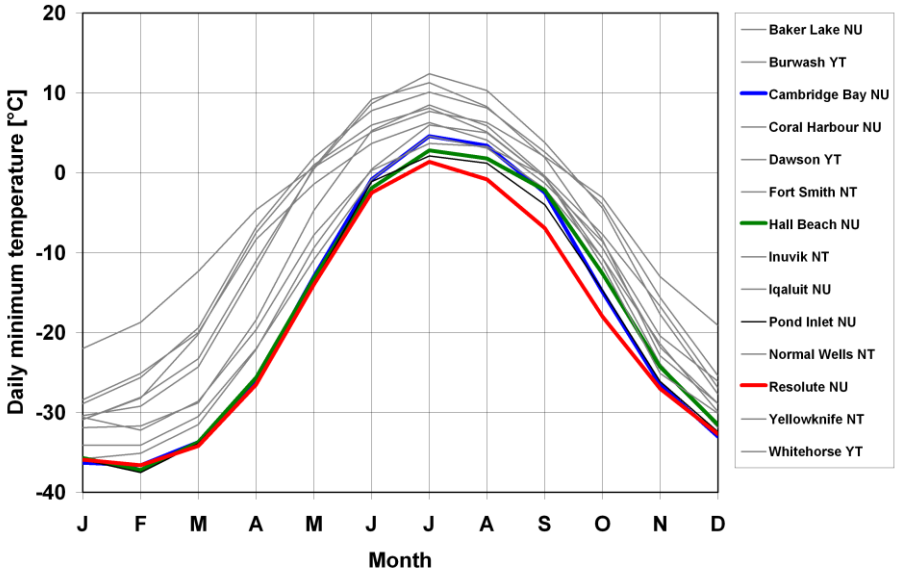

FIG. 1: Mean daily minimum temperatures for various Northern locations.

Summer. The summer months show a progressive warming due to increased amounts of insolation. Regular diurnal cycles can raise the temperature of exterior envelope elements much above ambient temperature leading to possible heat damage or premature aging. To maximize the potential for such effects to occur in the test the daily max. temperatures were selected as the basis of the summer season profile. The mean max. temperatures for the typical summer months are 5°C, 15°C, and 10°C in steps. To simplify the protocol a single condition of temperature, 15C was selected. There was less variation in heating and cooling rates than in the spring. This is expected due to the prolonged daylight periods. Most of the rates of temperature change in summer fall between 0 and 2°C/h although there were excursions of up to 8°C/h. The summer months also show a strong pattern of diurnal cycling due to solar irradiance. The spring diurnal temperature profile is recommended (see Table 1).

3.3 Wind

Wind is an important climate parameter in the performance of exterior envelopes in extreme cold climates. The Canadian arctic can be divided roughly into two regions, the east and west, the Eastern Arctic being the windier of the two. Comparing various Northern communities, Cambridge Bay can again be used as a representative location for windy locations. The mean monthly mean wind speeds tend not to vary by season while the direction is consistent from the North. For the protocol a constant wind condition, 22 Km/h or 6.1 m/s, close to the annual mean, was suggested. To simulate wind in a test chamber a fan can be used or a pressure difference maintained across the sample to simulate the effect of wind. When using a pressure difference a heat transfer coefficient must be maintained on the exterior surface to simulate the effect of heat removal. In determining the appropriate pressure difference, ΔP, across the sample, the following assumptions were made: 1) the building height was 6m, 2) the location of the neutral pressure plane was at grade, 3) the station pressure was 101.3 kPa, 4) the indoor temperature was 25ºC, 5) the wind pressure coefficient on the leeward side was 1.0, and 6) the stack and wind pressures were added.

Wind velocity pressures at the wind speed recommended for the protocol vary from 23 to 30Pa, depending on temperature. The absolute stack pressure was calculated for various temperature differences. For the spring and summer time conditions the stack pressure is much reduced, approximately 5Pa. The wind velocity pressure and stack pressures were added to give the worst case. For the winter profile, assuming an ambient temperature of –35ºC, the long-term mean, and the wind velocity pressure is approximately 27Pa. The stack pressure at this temperature is approximately 17Pa. The combined pressure is 44Pa. Rounding up the recommended pressure difference across the envelope was 50Pa. The recommended spring and summer period pressure differences across the envelope were 35Pa and 25Pa respectively. The variation of Heat Transfer Coefficient (HTC) using the ASHRAE Handbook of Fundamentals, Chapter 3 formula (ASHRAE 2005, McAdams 1954) shows that the heat transfer coefficient should be in the range of 30 $W/m^2 \cdot K$ for the wind speed recommended. The suggested pressure difference and heat transfer coefficient profile is given in Table 1.

TABLE 1: Parameters that comprise the exterior protocol, the complete protocol is given by Cornick (2008b).

Stage No.	Season	Description	Ext. T [°C]	Time [h]	ΔP Pa/HTC [$W/m^2 \cdot K$]	RH [%]
1	Winter	Initial conditioning	–35ºC	168	50/30	70
2	Winter	Average conditions	–35ºC	168	50/30	70
3	Winter	Typical conditions	–42ºC	168	50/30	70
4	Winter	Extreme conditions	–50ºC	36	50/30	70
5	Winter	Average conditions	–35ºC	168	50/30	70
6	Spring	Spring (Mar.)	–25ºC	72	35/30	80
7	Spring	Spring (Apr.)	–15ºC	72	35/30	80
8	Spring	Spring (May)	–5ºC	72	35/30	80
9	Summer	Summer season	15ºC	120	25/30	85

3.4 Atmospheric Moisture

Atmospheric moisture in the extreme cold regions does not directly play a large role in the performance of the envelope. Temperatures are too cold throughout most of the year for the atmosphere to hold significant amounts of moisture. The importance of this parameter depends largely on the interior environment. During the winter months the average humidity ratio is about 0.6 g water g/kg dry air. For the temperatures specified for the winter portion of the protocol the saturation humidity ratios are less than 0.14 g/kg. Compare these values with typical values for indoor moisture content, which vary between 2 and 4 g/kg during the winter. Control of humidity on the cold side of the test chamber is not crucial during the winter portion of the test protocol. If humidity control is desired and possible, a suggested target RH is 70% for the winter portion of the test. In spring, like the winter months, the amount of water vapour in the atmosphere is still low. The average humidity ratio is about 1.0 g/kg. If humidity control is desired and possible, it is suggested that the target RH be held at 80% for the spring part of the test. In the summer months the average humidity ratio is 5.0 g/kg. This is more significant than the other periods. The suggested target RH is 85% for the summer part of the test. The RH profile is given in Table 1.

3.5 Insolation

The decision to include solar radiation in the cold regions test protocol was based on anecdotal evidence provided by building specialists in Northwest Territories during community consultation, to the effect that solar driven moisture was a major consideration with respect to performance and premature aging of materials on

certain building facades (Cornick and Rousseau 2007). Global horizontal radiation in Cambridge Bay NU shows a sharp rise in the spring months and a sharp fall off in the autumn with a slight double peak. The direct irradiance pattern follows a similar pattern but shows a more pronounced double peak. Diffuse radiation reaches a peak on the longest day of the year. The pattern on a vertical surface is different. In Cambridge Bay the south orientation receives the most radiation. The peaks occur at the end of March or beginning of April. The peak solar radiation received on a southern exposure occurs during the spring swing season around Day 93 (April 3rd). The peak mean total irradiance corresponds with the peak mean hourly irradiance as well. Day 93 is suggested for the solar profile for the spring portion of the exterior test protocol. Direct solar irradiance on a vertical surface is less in the summer months than in spring. Diffuse radiation is high due to the longer daylight hours. The peak values occur towards the beginning of June. Since there is almost constant daylight for the summer months, the direct and diffuse profiles are all similar. The suggested daily profile occurs on the summer solstice (June 21st or Day 172). The hourly irradiance values, direct normal plus diffuse, rounded to the nearest 20 W/m^2 for practical purposes are given in Table 2. The values given are direct normal radiation on a south facing vertical surface plus the diffuse radiation. The recommended irradiance for the winter is 0 W/m^2.

Table 2: Mean total irradiance W/m2 for selected days on a south face vertical surface in Cambridge Bay NU.

Season/Hour	**Day**	**1**	**2**	**3**	**4**	**5**	**6**	**7**	**8**	**9**	**10**	**11**	**12**
Spring	3 April	0	0	0	0	0	20	40	180	380	580	720	820
Summer	21 June	20	20	40	40	80	100	120	180	280	360	440	500
Season/Hour	**Day**	**13**	**14**	**15**	**16**	**17**	**18**	**19**	**20**	**21**	**22**	**23**	**24**
Spring	3 April	860	820	700	540	360	160	20	0	0	0	0	0
Summer	21 June	520	520	460	360	260	160	100	80	60	40	20	20

4. Interior extreme cold climate test protocol

The interior test protocol for the cold regions was based on measurements undertaken in 16 homes in Inuvik Northwest Territories and Carmarks Yukon Territory (Rousseau et al. 2007, Cornick and Kumaran 2008).

4.1 Temperature

From the measurement data, the following observations were made, 1) temperatures were kept high, 2) the ranges are different; 5°C to over 35°C for Carmacks, 16°C to 35°C for Inuvik, 3) the mean temperatures in the Carmacks and Inuvik data sets were similar, and 4) there was considerably more variability in the Carmacks data. There were two distinct patterns in the data. The difference in the data sets was that the majority of the Yukon houses surveyed were heated using wood burning stoves without heat distribution systems. Since the majority of houses in the Arctic are not heated by wood, a heating profile was developed using the Inuvik data, i.e. houses with forced-air or baseboard heating systems. In houses with working heat distribution systems temperatures were kept high, temperature control was good, and the range was narrow (see Fig. 2). Setbacks were not used. Several Nordic residents where occupants tend to use high set points and open windows for temperature control confirmed this anecdotally. The recommended profile is 21°C, the 10% temperature. In houses that use wood stoves, temperature control was more variable and setbacks were observed when the occupants were away or sleeping. Seven of the eight houses surveyed in the Yukon used wood burning stoves as the primary heat source. There were no central heat distribution systems or thermostats. A separate temperature profile was developed for houses with wood burning stoves, details of which are given by Cornick (2008a). Spring and summer temperatures for the cold locations were not measured as part of the project. Predictions of the interior temperatures were based on the procedure outlined in ASHRAE 160P (2006). Springtime temperatures for Cambridge Bay NU are still cold. Interior temperatures in the spring were set to 21°C. The month chosen for summer was July 1983 a typical warm summer month. The 24-hour running average temperature never rises above 18.3°C consequently the summer profile is set at a constant 21°C.

4.2 Relative humidity

Three strategies for setting the boundary relative humidity conditions on the room side were examined: 1) constant conditions, 2) an offset from the exterior conditions, and 3) an interior daily moisture profile.

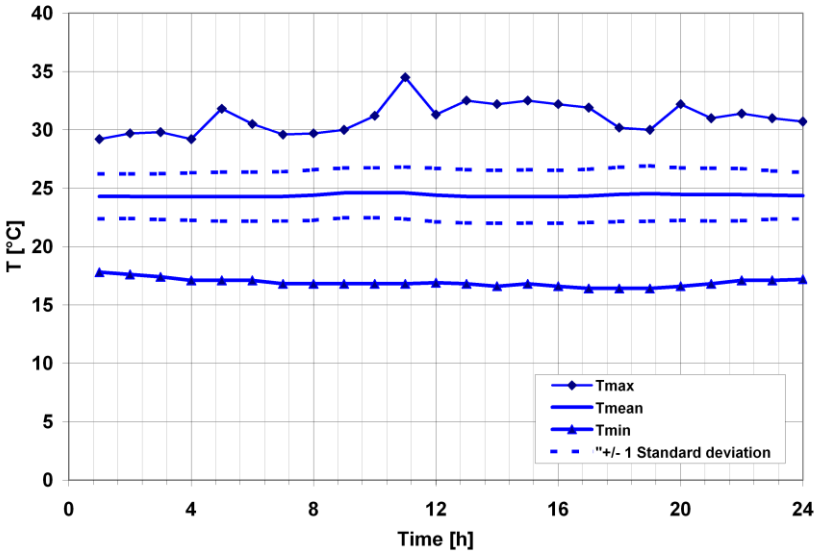

FIG. 2: Hourly temperatures for the houses surveyed, Inuvik NT. Minimum, maximum and mean temperatures of the houses surveyed for each hour of the day, plus or minus one standard deviation are shown.

4.2.1 Constant conditions

The sample period for the surveys was in winter. The 90th percentile value of the combined dataset was chosen for the RH level threshold. The RH at this level was 41%, rounded down to 40%. This threshold is in line with the recommended value in ASHRAE 160P (2006). Spring and summer data for Inuvik and Carmacks were not measured as part of the project. Predictions of the interior RH were based on the procedure outlined in ASHRAE 160P. For the representative location the month chosen was May 1991. The mean daily temperature for May was –5.3°C, which using the procedure yielded a relative humidity of 44.7% rounded up to 50%. Similarly for summer RH conditions the month chosen was July 1983. The mean daily temperature for July was 12.3°C, which using the procedure yielded a relative humidity of 62.3%, rounded up to 65%.

4.2.2 Dynamic/Offset

Another method proposed was to use an offset from the exterior conditions, applied to the interior chamber of the test facility. The offset expressed in terms of difference between indoor and ambient humidity ratio was determined from the survey data in a manner similar to that used in determining the constant RH conditions. A lognormal distribution was assumed. In selecting the moisture load threshold for the test protocol the 90% value of the combined dataset was chosen. The moisture load at this level is 5.0 g/kg. It was suggested that this moisture loading, be used for all seasons, since there was no data to suggest that the loading was seasonal.

4.2.3 Interior moisture profile

A daily moisture profile based on the survey results was produced. The profile accounts for moisture added to the interior during the day. The advantages of this method are that a typical 24-hour profile can simulate typical occupant behaviour and other profiles exist for comparison. The disadvantage of the approach is that it may be difficult to achieve in the lab. Examples of daily moisture profiles already exist (Ellinger 2004). Tariku (2008) developed a moisture profile by estimating the daily moisture generation based on occupancy (Christian 1994), determining a schedule for the occupants, then distributing the moisture according to the schedule. In the case of the survey data it was difficult to generate a moisture generation schedule lacking information on occupancy, house characteristics, and the use of ventilation equipment. A moisture profile based on the measured data that imposes humidity conditions rather than imposing a load added to ambient conditions was developed. The humidity ratio was derived from the recommended RH and temperature profiles.

Different rooms type were monitored, bathrooms, kitchens, bedrooms, common areas, and storage spaces. Certain rooms have a specific use and distinct moisture profiles. A generalized profile is shown in Fig. 3. There was much data on bathrooms and kitchens. Three profiles were generated: 1) a bathroom profile, 2) a kitchen profile, and 3) a whole house profile. The normalized mean RH for each hour in each room was plotted in order

to identify patterns. The thresholds were based on statistical analysis. The hourly profiles are given in Table 3. Profiles for the other time steps were also developed (Cornick 2008a).

5. Discussion

Testing protocols developed for the assessment of the hygrothermal performance of building envelope for extremely cold regions, such as the Arctic are scarce. The protocols here may be furthered refined as actual testing experience is acquired. The key to developing the exterior protocol was the selection of a representative location. Other locations may be selected, however, the methodology for determining the thresholds values remains valid (Cornick 2008b). No account was made for increasing temperatures in the Arctic. Recently the Canadian meteorological service has made the modelling data on the Intergovernmental Panel on Climate Change 4th Assessment Report (IPCC 2007) scenarios available. A reassessment of the exterior protocol is perhaps in order to reflect future trends. With respect to the interior protocol more survey data is required, particularly for spring and summer seasons. Although there was sufficient data for developing the winter portion of the interior protocol, the survey pointed to areas where more information would be useful. Specifically, more information on specific rooms, a better assessment of air-change rates, air pressure difference and occupant behaviour are required. As well, a longer monitoring program needs to be established to provide hourly data on the interior conditions throughout all seasons.

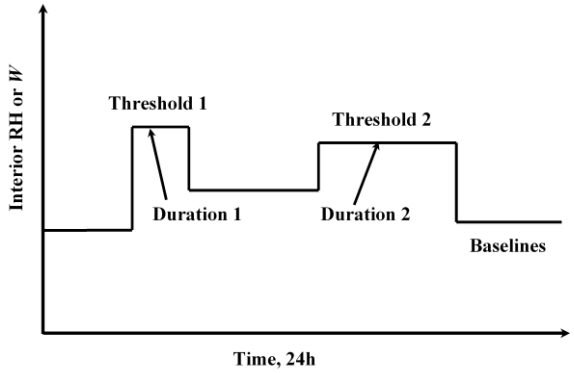

Fig. 3: A generalized moisture profile.

TABLE 3: Hourly whole house profile

Time [h]	RH [%]	T [°C]	*W* [g/kg]	Notes	Time [h]	RH [%]	T [°C]	*W* [g/kg]	Notes
Whole house average									
0	10	21	1.5	10th percentile	16	40	21	6	90th percentile
7	40	21	6	90th percentile	20	20	21	3	Mean
8	20	21	3	Mean	23	10	21	1.5	Mean
Bathroom Profile									
0	10	21	1.5	10th percentile	18	50	21	8	99th percentile
7	50	21	8	99th percentile	20	20	21	3	Mean
8	20	21	3	Mean	23	10	21	1.5	Mean
Kitchen Profile									
0	10	21	1.5	10th percentile	16	40	21	6	90th percentile
7	40	21	6	90th percentile	20	20	21	3	Mean
8	20	21	3	Mean	23	20	21	3	Mean

6. Summary

This paper gives an overview of the development of two test protocols for testing building envelopes exposed to extreme cold conditions as found in the Canadian Arctic. The exterior protocol comprises four parameters:

temperature, wind, atmospheric moisture and solar irradiance. An accelerated test was defined; the length of the test is 6 weeks or 42 days. Three seasons comprise the test, a winter season, a spring or swing season and a summer season. Not all the parameters need to be used in the test. The most important parameter is temperature. Other parameters can be added as required. A corresponding interior test protocol was also developed. The protocol comprises two parameters: temperature and moisture. The protocol was based on the results of monitoring the indoor environment of 16 residential units for one winter month.

7. References

ASHRAE. (2005). Fundamentals, Atlanta, Ga.: Am Soc of Heating, Refrigerating and Air-Conditioning Eng.

ASHRAE. (2006). SPC 160P, Public Review Draft Sept 2006. Atlanta, Ga.

Christian J. E. (1994) Moisture Sources, "Moisture control in buildings" Heinz R. Trechsel, ed. ASTM, Philadelphia, Pa. Chapter 8.

Cornick, S. M., M. Manning, M. Z. Rousseau, M. C. and Swinton. (2008a). Task 5 Proposed Test Protocol for Walls of Houses in Extreme Cold Regions Part 2: Defining Interior Conditions, NRC-IRC Client Report B1239.6 2008.

Cornick S. M. (2008b). Task 5 Proposed Test Protocol for Walls of Houses in Extreme Cold Regions Part 1: Defining Exterior Conditions, NRC-IRC Client Report B1239.5 March 2008. http://irc.nrc-cnrc.gc.ca/pubs/fulltext/b-1239.5/

Cornick S. M. and Kumaran M. K. (2008). A Comparison of Empirical Indoor Relative Humidity Models with Measured Data, Journal of Building Physics Vol. 32. No. 1. pp. 243-268.

Cornick, S.M.; Rousseau, M.Z. (2007). Community Consultation on Wall Construction Methods, Institute for Research in Construction, National Research Council Canada, IRC-RR-233 pp. 25 June 2007. http://irc.nrc-cnrc.gc.ca/pubs/rr/rr233/

Cornick, S.M. (2005). Task 3: Report on Task 3: Extreme Canadian Climates - Northern and Coastal, pp. 60, July, 2005 http://irc.nrc-cnrc.gc.ca/pubs/fulltext/b-1239.3

Ellinger, M. (2004). Feuchtepufferwirkung von Holzinnenraumverkleidungen. University of applied science Rosenheim. Thesis.

IPCC (2007). Climate Change 2007: Fourth Assessment Report, http://www.ipcc-data.org/ddc_ar4pubs.html

Kovesi T, Creery D, Gilbert N.L., et al. (2006a). Indoor air quality risk factors for severe lower respiratory tract infections in Inuit infants in Baffin Region, Nunavut: a pilot study. Indoor Air 2006; 16:266-75.

Kovesi T, Stocco C, Dales R,E,, et al. (2006b). A multi-community survey of indoor air quality risk factors for severe lower respiratory tract infections (LRTI) in Inuit infants in Baffin region, Nunavut, Canada [abstract]. Proc Am Thorac Soc 2006;3:A397.

Maref, W, Manning, M.M., Lacasse, M.A. et al. (2007) "Laboratory demonstration of solar driven inward vapour diffusion in a wall assembly," 11th Canadian Building Science and Technology Conference Banff, Alberta, March 22, 2007, pp. 1-8, (NRCC-49203) http://irc.nrc-cnrc.gc.ca/pubs/fulltext/nrcc49203/

Masters, L. W. and W. C. Wolfe. (1974). The Use of Weather and Climatological Data in Evaluating the Durability of Building Components and Materials, NBS Technical Note 838, Institute for Applied Technology, National Bureau of Standards, Washington D.C. 20234.

McAdams, W. H. (1954). Heat Transmission, 3rd edition, McGraw Hill, New York

Mehlhorn L. and J. W. Herlyn. (1998). Bauteilentwicklung durch simulierte Bauteilprüfung in der Doppeklimakammer, Bauen mit Holz und Holzwerkstoffen: Stand der Technik und Entwicklungstendenzen Braunschweig (Deutschland, Bundesrepublik):Selbstverlag 1998, S.1-14, Abb.,Lit. Serie: WKI-Bericht; 33, (Development of Building Components through simulated testing of Building Components in a 'Double Climate Chamber' *TT*).

NBCC (2005). National Building Code of Canada, Canadian Commission on Building and Fire Codes, National Research Council of Canada, Ottawa, Volume 1: Division B, Appendix C, Table 9.25.1.2, p. 9-141

Rousseau, M., M. Manning, M.N. Said, et al. (2007). "Characterization of Indoor Hygrothermal Conditions in Houses in Different Northern Climates", Thermal Performance of the Exterior Envelopes of Whole Buildings X International Conference, Clearwater Beach, FL, pp. 14, Dec. 2-7.

Saïd, M. N. (2005). Building envelope researchers to develop wall assemblies suited to construction north of 60°. Construction Innovation. Institute for Research in Construction National Research Council Canada. **10**: 9.

Saïd, M. N. (2006). Task 2: Literature Review: Building Envelope, Heating, and Ventilating Practices and Technologies for Extreme Climates, pp. 120. http://irc.nrc-cnrc.gc.ca/pubs/fulltext/b-1239.2/

Tariku F. (2008). Whole Building Heat, Air, and Moisture Analysis, PhD Thesis, Concordia University, April 2008.

Durability of Crawl Space Based on Damage due to Wood Rot

Atsushi IWAMAE, Dr.Eng.,
Department of Architecture, School of Science and Engineering, KINKI University;
ai@arch.kindai.ac.jp http://www.arch.kindai.ac.jp/~ai

Hirotaka Suzuki, Dr.Eng.,
Hokkaido Northern Regional Building Research Institute;
Suzuki@hri.pref.hokkaido.jp http://www.hri.pref.hokkaido.jp/

KEYWORDS: *wood rot, damage function, humidity, condensation, laboratory test, numerical simulation*

SUMMARY: *This study consisted of three parts. The first comprised development of a model of the wood rotting process, and is based on observations in the laboratory. We set a huge number of wood pieces with various water contents and waited for rotting to start. We then measured the weight and water content of the pieces every few weeks. The second part of our study comprised development of a numerical model to represent the rotting process under various conditions. The model is based on the growth of fungi hypha in the wood. The third part comprised calculation of the humidity variation in the crawl space of dwellings in Japan. The results of the above were then used to estimate the durability of the crawl space.*

1. Introduction

It is said that the wood rotting process is divided into two phases (Nofal 2000). In the first phase, called the "Initial stage", fungi in the air stick to the wood surface and their hypha grow into the pores in the wood. The hypha absorb water and nutritients such as nitrogen from the wood cells along the pore walls, and the fungi grow bigger.

When the fungi have grown to a certain size, they start to "eat wood". This is the beginning of the second phase, called the "Growth stage". In Japan, Dr. Saito has been studying the growth stage of wood fungi (Saito et al. 2007). He has calculated the weight loss caused by fungi growth together with heat and moisture variation.

Our object is to clarify the initial stage, which past studies have regarded as a simple linear relation with time.

Our study was composed of three parts. The first part comprised observation of the wood rotting process in the laboratory. We set a huge number of wood pieces with various water contents and waited for rotting to start. We then measured the weight and water content of the pieces every 2 weeks. The second part comprised development of a numerical model to represent the rotting process under various conditions. This model was based on the growth of fungi hypha in the wood. The last part comprised development and application of a numerical model.

2. Observation of wood rotting

The test conditions for all samples were as follows.

a) No specific fungi were pre-planted on the sample surfaces.

b) The samples were placed in small plastic bags after the water contents were adjusted to the planned range. (See Figure-2 and 3)

These were the major points of difference with past studies, and were the main reason why our focus was on the initial stage. In previous studies, specific fungi were placed on test pieces, and the growth processes of those specific fungi were obtained, as intended. In our study, we could not obtain the growth processes of specific fungi. However, we determined the growth processes of several fungi common in real houses.

Table 1 shows the test conditions, which are divided into 2 groups: constant and daily variation.

"Constant" means that the temperature and humidity were constant. The water content, which was set by adding water to the test pieces at the beginning of the observation, decreased with time. We measured the weight of the pieces every 2 weeks and calculated the water contents. If a piece was too dry, we added water.

Daily variation conditions of daily condensation in an insulated wall of a house were simulated by controlling the temperature and humidity of the laboratory room and adding water once a day. The amount of added water was determined from calculations of annual T & RH variations of a wall using the HAM-tool before the tests. However, during the actual test period, we occasionally failed to add the correct amount of water.

We chose Japanese hemlock as the standard wood since this is known as being the most easily rotted.

Table-2 shows the test schemes for A1 and A2.

Table 1: Test conditions

Code	Place		Environment condition			Type of wood	Number of pieces	Test period
			Temperature & Humid.	Water content	Added water			
A1	Nara	C	30C RH-uncontrolled	20~30%wt 40~70%wt 80~120%wt	None	Hemlock	111	2000.6-2001.7
A2	Nara		30C 95%RH	20~70%wt	None	Hemlock	60	2003.1-2004.1
A3	Mie U		30C 95%RH	30~50%wt	None	Hemlock, Pine, Cypress, Spruce	270	2005.8-
B2	HNR BRI	D	27C 95%RH ~ 26C 70%RH	15~45%wt	0, 0.4, 0.8, 1.6 g/day	Hemlock	42	2001.10-2004.3
B4	HNR BRI		27C 95%RH ~ 26C 70%RH	30~70%wt	1.6, 2.4 g/day	Hemlock	40	2003.1-2007.9
B5	HNR BRI		27C 95%RH ~ 26C70%RH	30~50%wt	1.2, 2.0g/day	Hemlock	90	2005.7-2007.9
F	KIU	C	30C 95%RH	45~55%wt - 30%wt	None	Hemlock	108	2007.8-

C: Constant, D: Daily variation, T: Transient

Table 2: Test scheme of A1 and A2

Step 0	Preparation of the test pieces		Cut and make 60×50×20mm piece
Step 1	Measure dry weight of test pieces		Measure weight after 48 hours at 60 degree C.
Step 2	Set water content	20~30%wt	Set pieces in glass box with pure water in bottom. No direct contact between piece and water. (Photo-1)
		40~70%wt	Soak piece in pure water.
		Over 80%	Soak piece in the pure water in glass box and evacuate air.
Step 3	Set pieces in incubator		Set piece in plastic bag or box (Photo-2) Then set piece in T&RH controlled room (Photo-3)
Step 4	Weigh every 2 weeks, and observe rotting Adjust water content based on measured weight		
Step 5	Measure dry weight as in Step 1 after rotting is detected.		

Figure 1: Set water content

Figure 2: Wood piece in plastic case

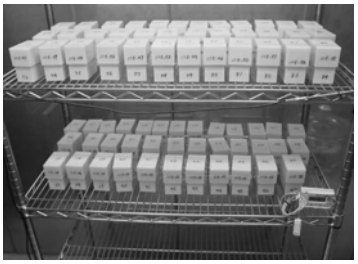

Figure 3: Set in T&RH controlled room

3. Observation results

Table-3 shows the rotting process of each piece after Test A1. All rotted pieces, which were found after 16 weeks, had water contents of 40 ~ 70%wt.

This suggests that the wood rot needs 100 days and a water of 40 ~ 60%wt under constant conditions. This is very significant.

Table 3: Number of rotted pieces

Time Elapsed (Weeks)		0	10	14	16	18	20	24	28	38	40	54
Number of rotted pieces	WC 20 ~ 30 %wt	0	0	0	0	0	0	0	0	0	0	0
	40 ~ 70 %wt	0	0	0	0	1	2	5	8	11	11	14
	80 ~ 120 %wt	0	0	0	0	0	0	0	0	0	0	0

In test-B, 3 pieces had rotted after 120 weeks. The water contents in this test varied through the day. This result is reasonable because the rotting period would be expected to be longer than that under constant conditions.

In this test, we did not record the weight variations. We only recorded of the volume of added water and the times it was added. We calculated the change of water content by the following method.

The water content depends on the volume balance between evaporation and volume of added water. The evaporation rate is estimated as shown in Table-4.

Table 4: Estimated evaporation rate

Temperature Deg.C.	RH %	Vapor pressure [mmHg] Pieces	Ambient air	Difference	Vapor transfer coefficient kg/m^{2}sPa	Evaporation rate per unit area g/m^{2}h	Surface area m^2	Evaporation rate g/h
T	RH	$P_v s(T)$	$P_v s(T)$ x RH	ΔP_v	α_l'	$J = \alpha_l' \Delta P_v$	A	$J*A$
26	70	3,360	2,360	1,000	2.1e-8	77.2	0.002*	0.154
27	95	3,573	3,386	187		13.6		0.027

*Test pieces were sealed on 4 sides with a vapor barrier, leaving 2 free surfaces of 2cm x 5cm. Thus, the evaporative area is 0.02 x 0.05 x 2 = 0.002 m^2.

Table-5: Evaporation rate of water adding day and non-water adding day

	T & RH	Evaporation rate	
Water adding day	9:00~18:00 26C70%RH 18:00~ 27C95%RH	0.154 x 9 + 0.027 x 15	1.8 g/day
Non-water adding day	27C95%RH	0.027 x 24	0.66 g/day

The amount of water in the wood piece is determined from the following formula.

$$X^{n+1} = X^n + \Delta X \qquad (1)$$

The term ΔX is given by,

At water adding day ΔX = 2.4 - 1.8 = 0.6 g/day

Other days ΔX = -0.66 g/day

Figure-4 shows the calculated water content variations of the 3 rotted pieces. Measured results of water content are also plotted in the figure as square symbols. It can be said that the calculated result corresponds with the changing trend of the measured result.

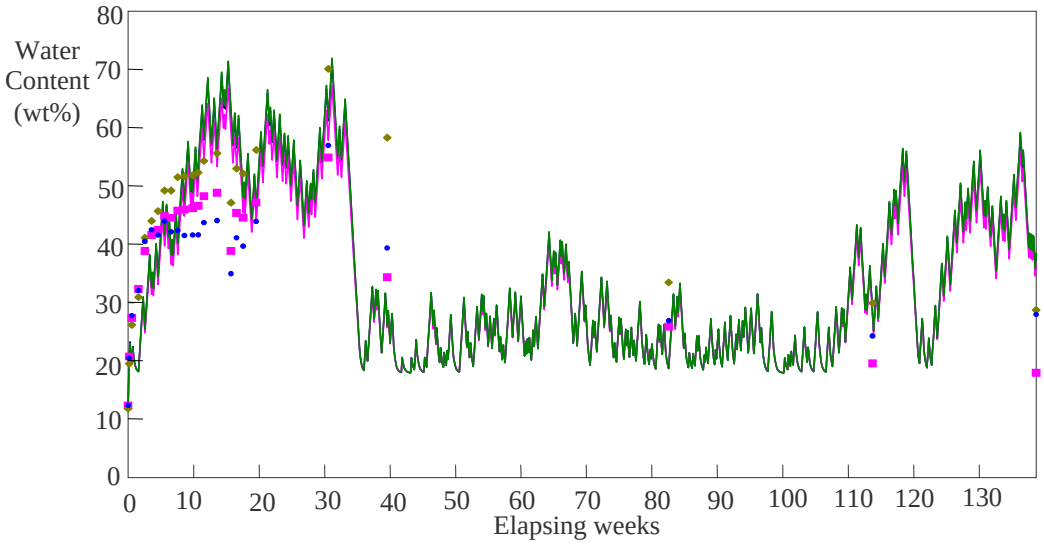

Figure 4: Water content variation of three rotted pieces

In the beginning to 35 weeks, the water contents were about 40 ~ 60%wt, which is fitted to the rotting required condition obtained in the constant tests. However, from 35 weeks to 110 weeks, the water content was 20 ~ 30%wt. This was caused by the decrease in water adding frequency. After that, the water adding frequency increased, thus increasing the water content.

Figure-5 shows the variation of number of days when the water content was in the range of 45 ~ 55%wt. According to this result, it can be said that the rotting conditions under variable condition is same as in the constant tests. It needs a water content of 45 ~ 55%wt and a period of more than 100 days.

These tests also suggest that during the period where the water content was 20 ~ 30%wt there was no rotting. The rotting process seems to have stopped during this period. This is also very important in clarifying the initial stage of wood rotting.

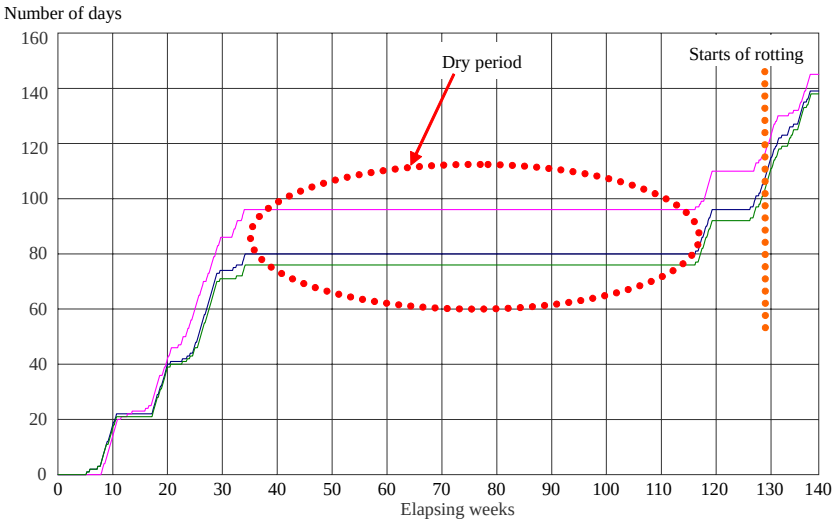

Figure-5: Number of days when the water content was 45-55%wt

In order to clarify the initial stage, we tested the effect of a drier state on the number of days needed for rotting to start. The former result shows that 20~30%wt did not have any influence on rotting, so we tried a drier state, such as below 20%wt.

Test-F was the same test as Test-A in the beginning. However,after 8 weeks, we move the test pieces to a room at 20 Deg. C. and 50%RH to dry the pieces and set their water contents to 10 ~ 20 %wt. After 4 weeks in the dry condition, we added water to the test pieces and adjusted the water content to 40~60%wt again. Then we continued to observe the pieces.

Figure-6 shows the water content variations of test pieces in Test-F. The water content, which was set to 40~60%wt at the beginning, dried after 8 weeks to 13~15%wt.

After the number of days at 40~60%wt exceeded 120 days, which was the rotting condition we had already established, no rotting was found.

It can be considered that the drying period below 20%wt decreases the number of days needed for rotting.

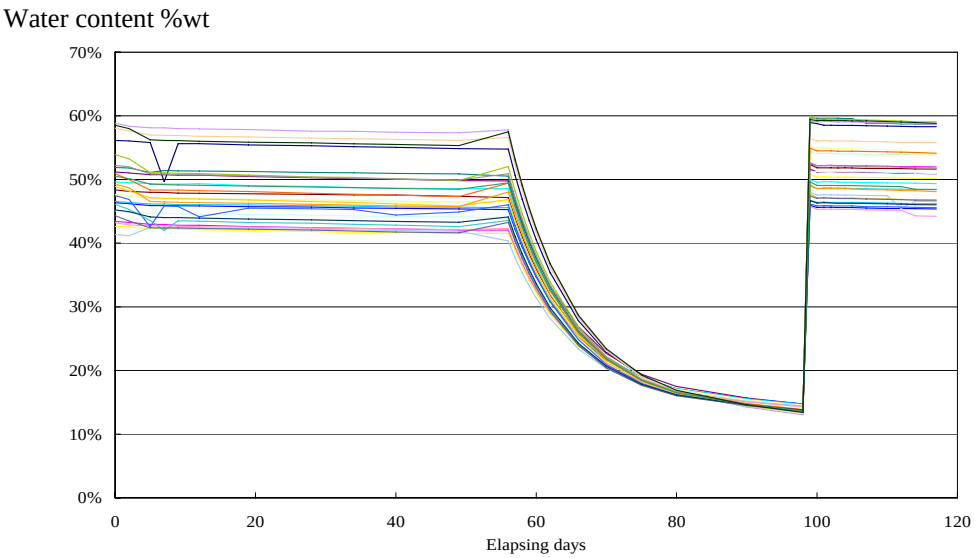

Figure-6: Measured results of water content of Test-F

4. Numerical modeling of initial stage of rotting

We considered the fungi growth process that explain the results of our measurements and a literature survey, and we constructed a numerical model based on the following assumptions.

a) The hypha of fungi needed for its growth hastens fungi growth after it has some length.

b) The hypha, with vacuum water and nutrition around it, can not absorb water rapidly while the water content is below the fibrous saturated point (30%wt) since the pore water is balanced by pore retention power.

c) If the water content is up to 40~60%wt, the water in the pores is free of pore retention and can be sucked by the hypha. If it exceeds 80%wt, hypha does not get the air (oxygen) to be needed for growth.

d) The hypha's ability of to vacuum water is maintained while the surroundings are dry, until they can not sustain their organization. Once the organization of the hypha is broken by drying, the ability is lost.

We call the 40~60%wt period "Growth period", the 20~30%wt period after the growth period "Stopping period" and the below 20%wt period "Cancelling period". Figure-4 shows the basic concept of our model.

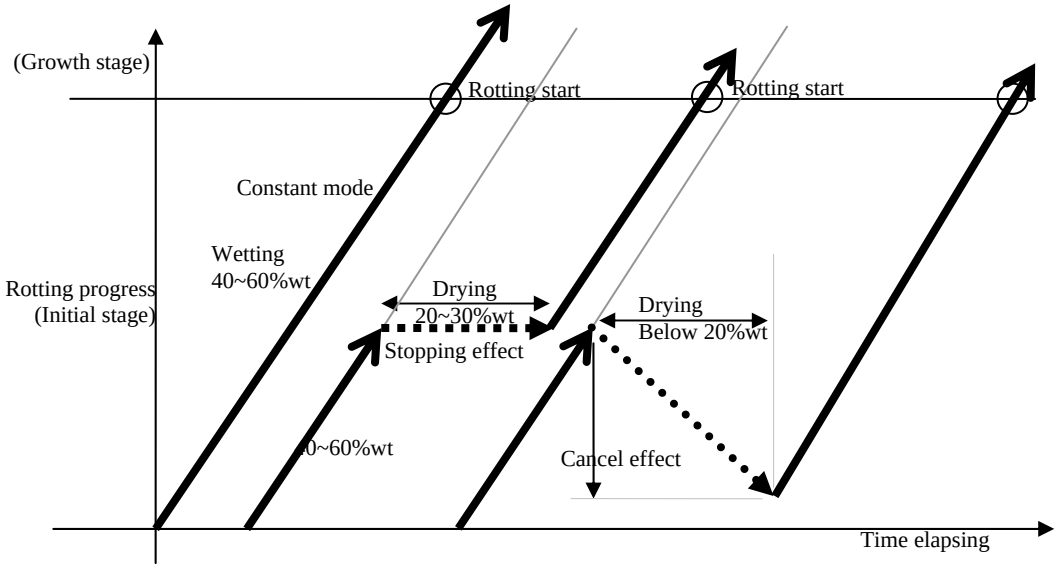

Figure 7: Basic concept of initial stage of wood rotting

The numerical model based on the assumptions is formulated as follows.

When $T_d <= T_f$ Structural strength $L = f(W)$

*This is the relation between water content and strength, which is shown by many measurements.

When $T_d > T_f$ Structural strength $L = L_d$ (*This is the strength of rotted wood.)

Here,

W : Water content %wt, T_f: Allowance term, T_d : Equivalent hypha growth term

T_d = MAX($T(WU1 <= W <= WU2) - p \times T(W <= WD)$, 0)

T ($WU1 <= W <= WU2$) : The term when the water content is in the range of $WU1$and $WU2$ (Hypha growing term)

T ($W <= WD$) : The term when the water content is below WD (Hypha decreasing term)

p : Hypha decreasing parameter

The term *WD* <= *W* <= *WU1* is the "Stopping term". According to our tests and observations, T_f =100 days (Elapsed time needed for rotting at a constant state), *WU1* 40%wt, *WU2* 60%wt, *WD* 20%wt, respectively. We have to investigate parameter P more.

5. Application to crawl space durability

We show an application example of the damage function of wood rotting to durability estimation of buildings. In the Japanese summer, crawl space humidity rises because of the humid outdoor air and the coolness of ground heat capacity. (Iwamae et al. 2003) We calculate the annual variation of humidity of crawl space by simultaneous heat and moisture transient processes. The floor consists of plywood 30mm thick. The ventilation rate of the crawl space with the outdoors is 10 times per hour. This is normally used in Japan.

According to the water content of the floor wood, we calculate the wood rotting progress.

Figure 8 shows the annual variation of crawl space humidity with the outdoor air of Osaka. It is shown that summer does not have high humidity in the outdoors, but crawl space humidity is very high.

Figure 9 is the calculation results of the water content at the floor wood surface facing the crawl space. This is called "the standard case".

Figure 10 show the wood rotting progress at the point. We calculate three cases from the damage function of wood rotting mentioned above. "Case x1.5" and "Case x 2.5" are the water content with the standard case multiplied by 1.5 and 2.5, respectively. In the standard case, there is a lot of condensations. However, according to our durability estimation, these condensations cause no damage to the wood. If the water content is higher than 1.5 times, the rotting proceeds to about half of the initial stage. But with the end of summer, the rotting progress starts to go back and no damage remains in the autumn. For the case of x2.5, the rotting progress goes headlong into the growth stage. At the beginning of September, the fungi will be visually detected in this case.

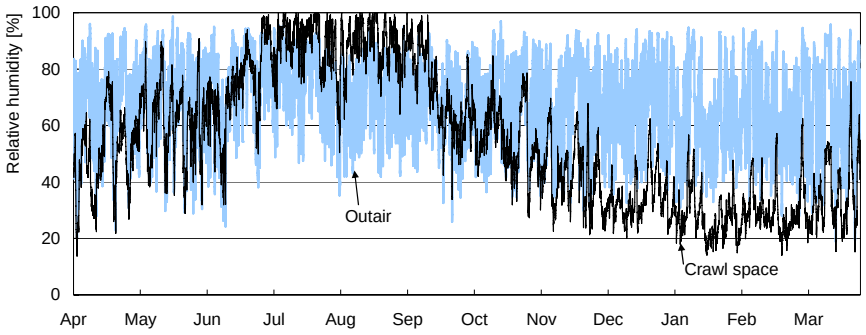

Figure 8: Crwal space temperature and relative humidity

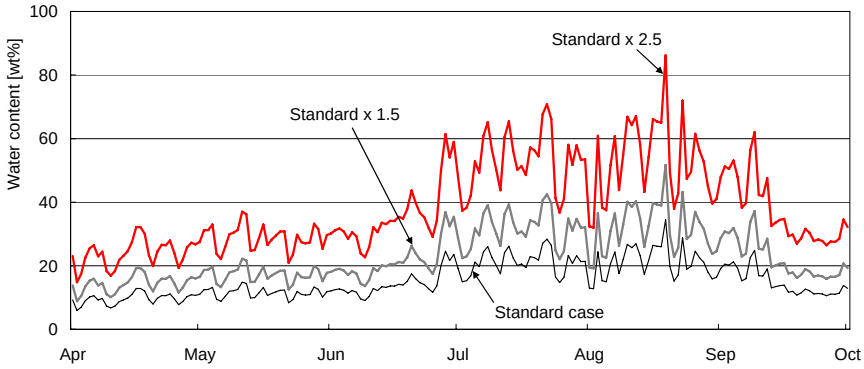

Figure 9: Calculated water content at wood floor surface facing crawl space

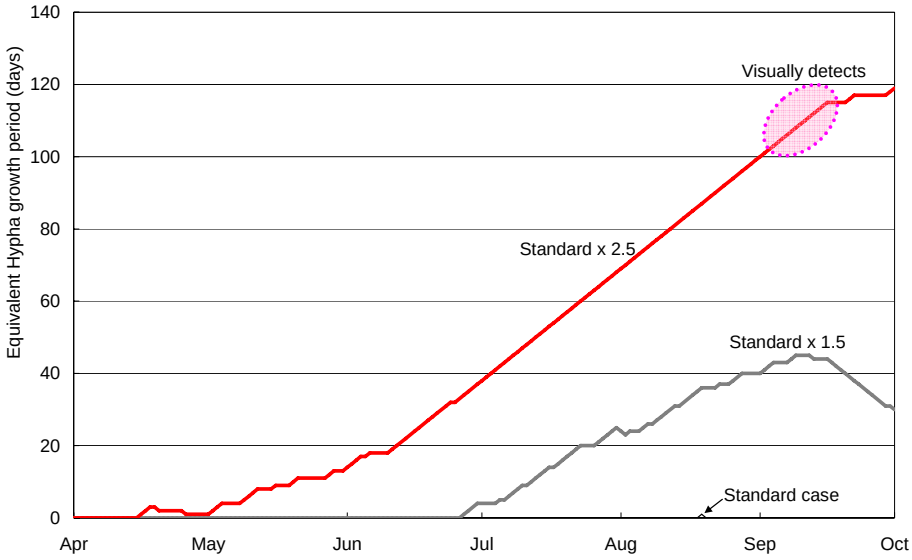

Figure 10: Rotting progress of floor wood surface in crawl space

6. Conclusion

We constructed a numerical model for wood rotting, especially in the initial stage, based on laboratory tests. This numerical model represents the results of our tests well. However, we don't think this model can represent all rotting phenomena around the world. We have to investigate and validate more, and the problem remains as follows.

1) Identify parameters in model, including variations for different wood

   As stated above, hemlock is known to rot easily,. In our tests on other woods, we did not find any fungi growth. Thus, we think the parameters based on Hemlock tests are safer. But too much safety is expensive and restricts design. It should be better to identify the parameters for the each kind of woods.

2) Influence of mold growth on rotting progress

   Mold itself does not have any influence on structural strength. However, it affects human health. On the other hand, it interferes with fungi growth. Health problems should be handled by an air flow path in houses. We should try to study mold at any rate.

7. References

Mostafa Nofal, Kumar Kumaran: On Implementing Experimental Biological Damage-Functions Models in Durability Assessment System, Proceedings of Japan-Canada Housing R&D Experts Working Group Meeting Building Envelope, pp111-124, 2000

Saito, H. et al.: Prediction Model for Wood Rot Decay Based on Moisture Balance in Durability Assessment of Building Envelopes- Outline of Prediction Model and Determination of Parameters -, Proceedings of annual meeting AIJ, Vol. D2, 2007, pp.339-340

Iwamae A. and M. Matsumoto: The Humidity Variation in Crawl spaces of Japanese houses, J. of Thermal Envelope & Building Science Vol. 27 No.2, October 2003, pp. 123-134

Moisture Content in Insulated Basement Walls

Peter Blom,PhD,
SINTEF Building and Infrastructure;
peter.blom@sintef.no, www.sintef.no/byggforsk

Sverre B. Holøs M.Sc.
SINTEF Building and Infrastructure;
sverre.holos@sintef.no, www.sintef.no/byggforsk

KEYWORDS: *moisture, basement, field measurement, simulations*

SUMMARY:
The paper investigates moisture content in bottom and top sills in an internally insulated basement wall. Moisture and temperatures in the wall are measured from May 2007 until January 2008. The moisture content in the sills are also simulated in the program WUFI 2D. During the measurement period, the sills take up very little moisture. Long term simulations with high initial moisture content in the construction indicate that the sills in the wall dry out. However, this is not confirmed by the measurements, partly because of low initial moisture content in the sills and a short measurement period. Further, the bottom sill does not dry during the winter season as predicted by the calculations. The results from the project can not be used to confirm the validity of Norwegian guidelines concerning insulated basement walls.

1. Introduction

In Norway, areas in basements are often used as normal, heated living spaces. Basements walls therefore need good heat insulation and protection against moisture damages. Given the often limited drying possibilities of built-in moisture in basement walls, one would prefer wall constructions without organic constituents. However, basement walls with an inner, insulated wooden framework are nevertheless popular, partly of economical reasons. Such walls may experience moisture problems of different causes:

- Built-in moisture due to exposure to rain or snow during the building process
- Ground water or storm water infiltrate through cracks in walls
- Condensation on concrete surface due to entrance of moist room air
- Condensation on concrete surface due to moist air entering in cracks between floor and wall

In this paper, problems with built-in moisture from the building process are focused. There are numerous examples of rot in bottom sills in basements walls due to built-in moisture, especially in several kinds of prefabricated building elements combining in-situ concrete and an internal, wooden framework. In order to reduce the risk on moisture damages, the following guidelines are now recommended in Norway:

- At least 1/3 of the total thermal resistance should be located outside the concrete wall
- The wooden framework should be separated from the concrete wall with insulation, as shown in figure 1.
- No vapour barrier should be used on the inside of the wall, unless more than 50 % of the wall is above grade.

The aim of the study is to examine whether these guidelines are sufficient to avoid moisture damages due to built-in moisture from the building process. The study is based on measurements in a basement wall (figure 1) in a new house outside Oslo and on calculations with the program WUFI 3.2 (www.wufi-pro.com).

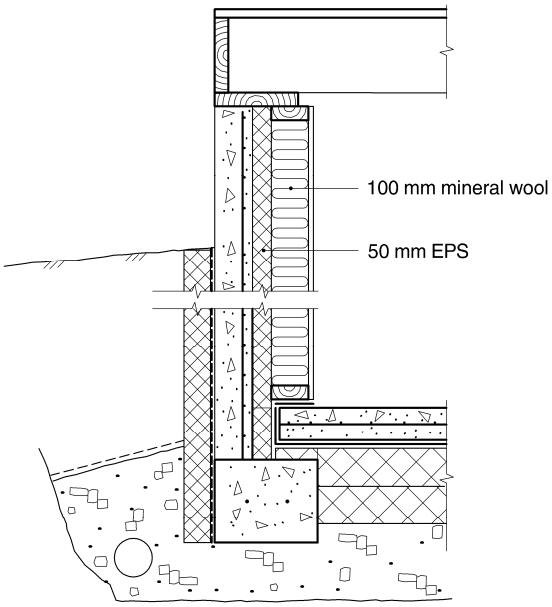

FIG. 1: Basement wall used for thermal and moisture measurements. The house is situated in Lommedalen, south of Oslo.

2. Measurements

Description of the materials in the basement wall is shown in Table 1. Water vapour diffusion resistance factor and the initial water content are used in the WUFI calculations. The wall is instrumented with thermocouples, sensors for relative humidity and conductivity moisture meter for wood moisture content. Hourly data are stored on a logger inside the house. Measurement data from the period 23.6.2007 until 10.01.2008 are used in the paper.

TABLE 1: Materials in basement wall. The materials are listed as shown in figure 1, ranged from inside and out.

Material	Width [mm]	Water vapour diffusion resistance factor (-)	Initial water content
Gypsum board	9	8	1.8
Mineral wool	100	1	1.8
Sills and studs	100	100	44
Expanded polystyrene	50	50	1.8
Concrete, w/c ratio 0,4	100	180	85
Water membrane [i)]	100	10^6	-
Expanded polystyrene	50	50	1.8

[i)] Membrane under bottom sill and outside concrete wall

Figure 2 shows measured relative humidity inside the wall and average moisture content in bottom and top sills. The relative humidity is measured between the mineral wool and the EPS-insulation. The moisture content in the sills is corrected according to actual air temperature.

The moisture content in the bottom sill is higher and more constant than the moisture in the top sill. The moisture in the top sill reacts faster to changes in the surrounding climate. The sharp drop in the moisture content in the top sill towards the end of the measuring period is caused by a cold spell in the outside temperature, which in turn lead to low indoor relative humidity.

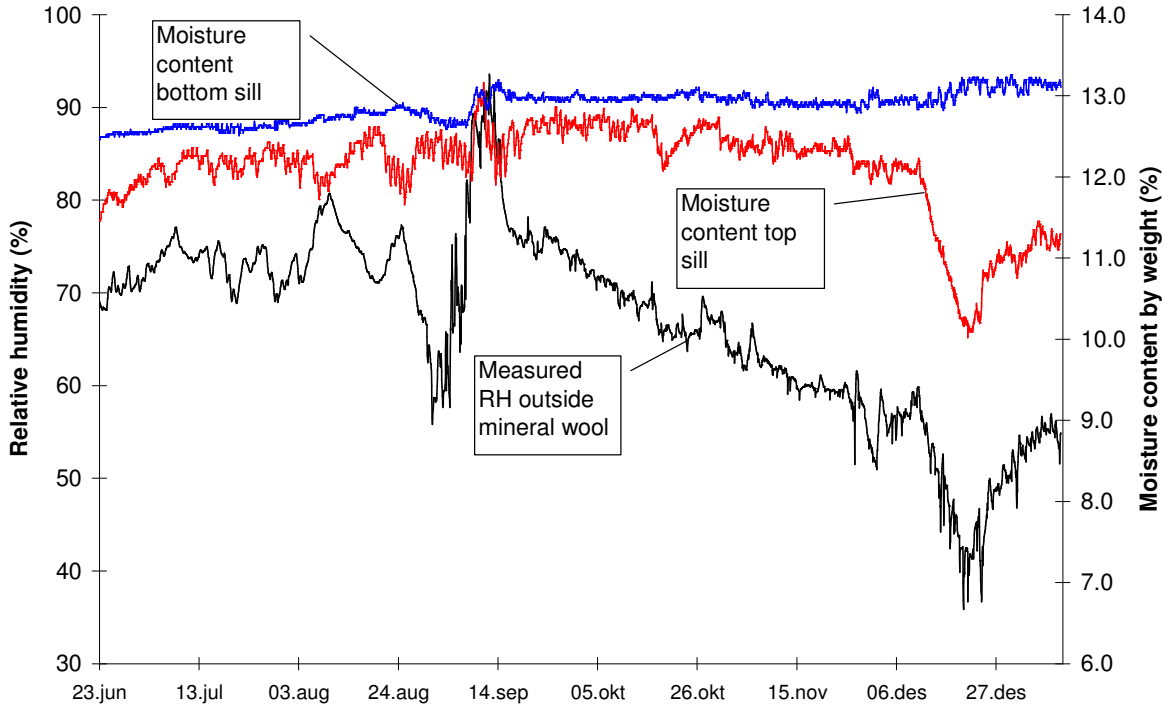

FIG. 2: Measured moisture content by weight (%) in bottom and top sill and measured relative humidity between mineral wool and EPS. The relative humidityis measured 0,2 m above the bottom sill.

3. Simulations of heat and moisture transport

3.1 Calculation model

WUFI 2D 3.2 (www.wufi-pro.com) is a program for calculation of coupled heat and moisture transfer in building components. WUFI 2D 3.2 calculate transient heat and mass transfer in two dimensions. The mathematical model in the program is described by differential equations for heat and moisture transfer. The differential equations are discretised by means of an implicit finite volume method and are iteratively solved (Künzel 1995). For heat transfer, the program takes in to account thermal conduction, short wave solar radiation, long wave radiation cooling and enthalpy flows through moisture movement with phase change. For moisture transfer, the program takes into account vapour diffusion, solution diffusion, surface diffusion and capillary suction. Convective heat and moisture transport is disregarded.

3.2 Simulation results

The main input data for the calculations are shown in Table 1. The climate files used in the calculations are sinus-curves fitted to the measured climate data, see Table 2. Figure 3 shows the grid used in the calculation. Figure 4 shows measured and calculated moisture content in top and bottom sill throughout the measurement period. Figure 5 shows calculated moisture content in top and bottom sill assuming an initial high moisture content in sills and studs (18 % by weight) and concrete (90 % RH).

The calculated moisture content fits reasonably well to the measured moisture content in the top sill. The calculations for the bottom sill, however, do not concur very well with the rather constant moisture content in the bottom sill.

The long term calculations in Figure 5 indicate that the sills dry out.

Table 2: Description of sinus climate files used in the calculations

Climate	Temperature/ amplitude	Day of maximum	Relative humidity (%)	Day of maximum
Indoor air	20/0	-	60/30	18. aug
Soil, 1-1.8 m	11.5/3	3. aug	100	-
Soil, 0-1 m	10/10	3. aug	100	-
Outside air	10/20	3. jul	70/10	18. aug

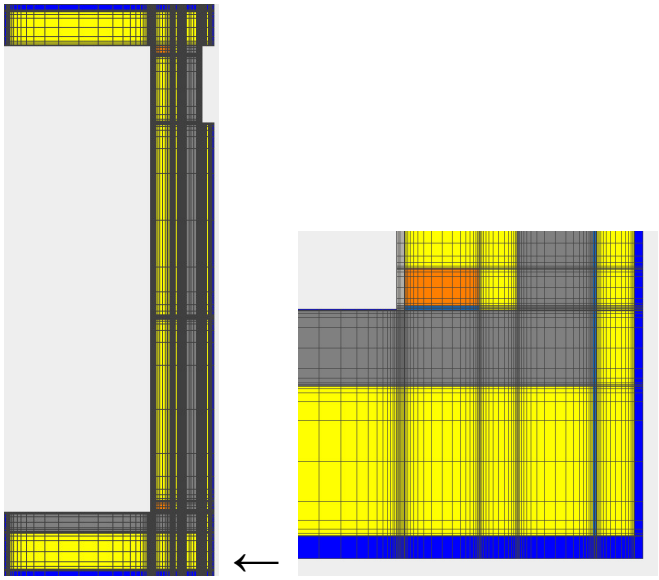

FIG. 3: Grid used in the WUFI2D 3.2 simulations. The right figure is an enlargement of the corner of the wall.

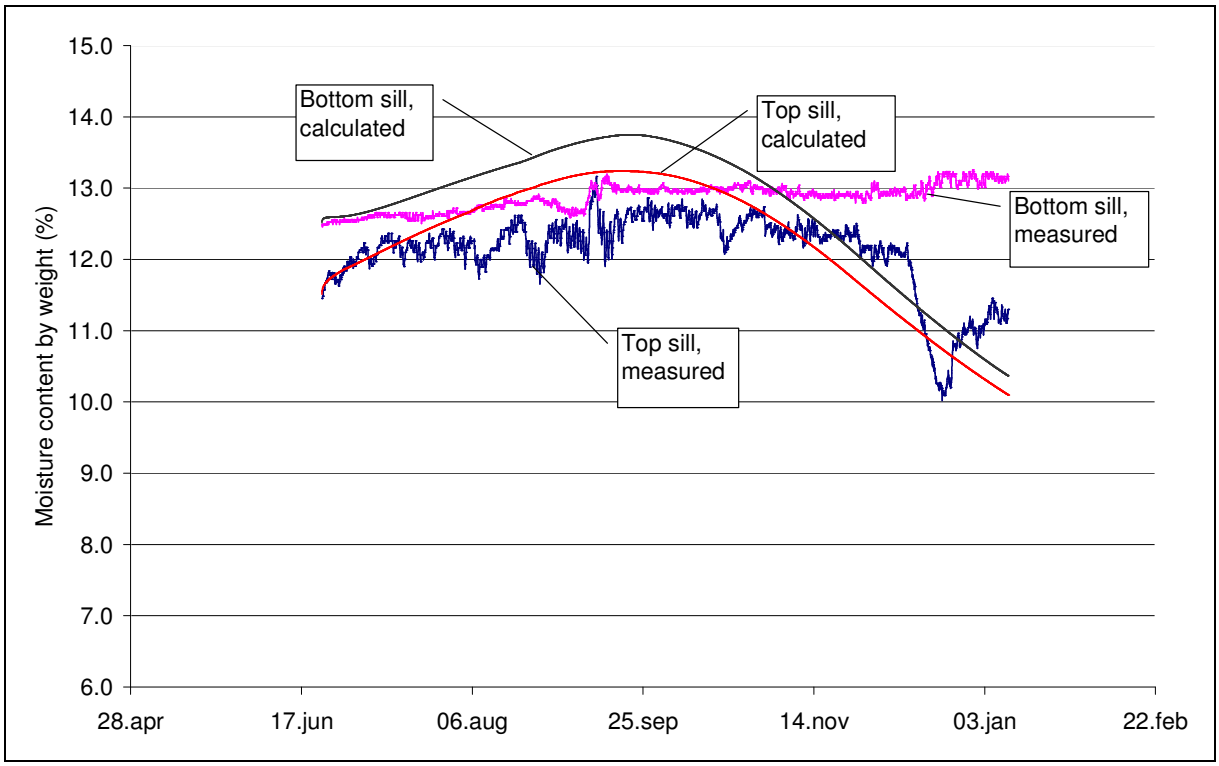

FIG. 4: Measured and calculated moisture content by weight in top and bottom sill

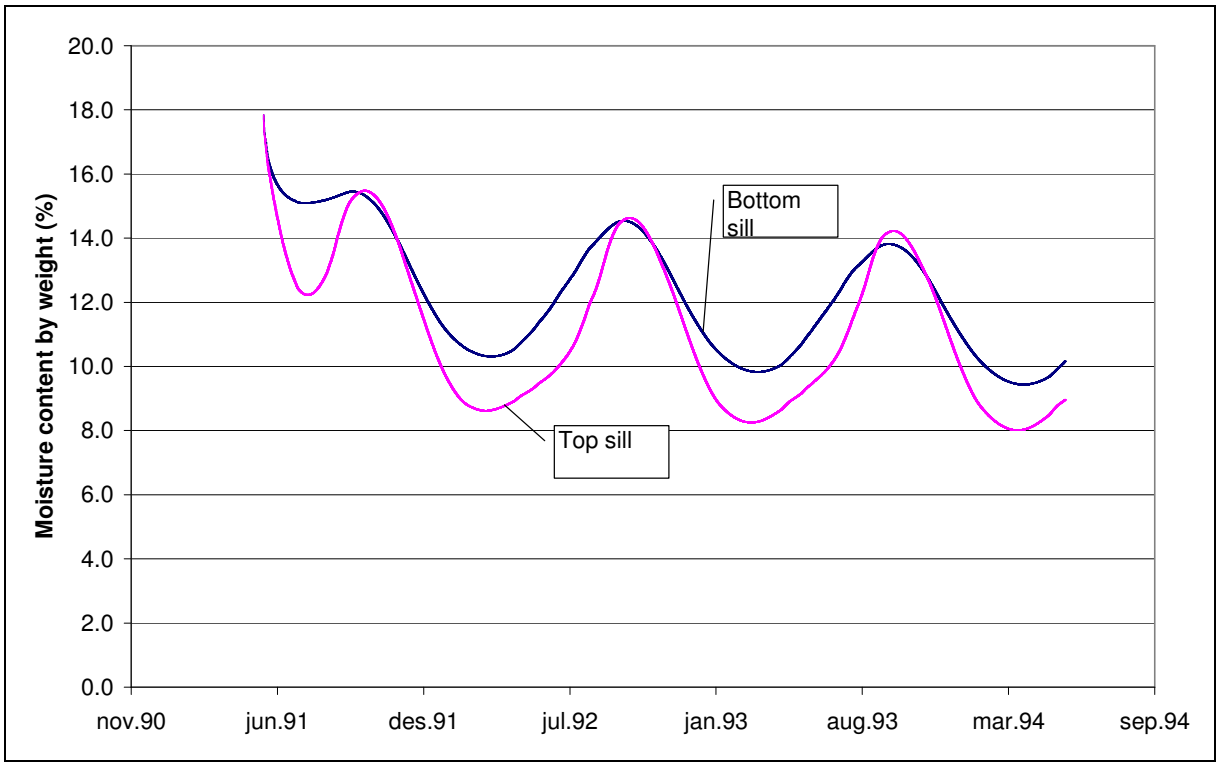

FIG. 5: Calculated development moisture content in sills, assuming a high initial moisture content in sills, studs and concrete

4. Discussion

The sills in the wall were quite dry when the building process was completed and the measurements started. During the measurement period, the sills take up very little moisture. The moisture content in the top sill seems to follow the changes in the surrounding atmosphere, while the moisture content in the bottom sill show small variations.

The calculated moisture content fits reasonably well to the measured moisture content in the top sill (figure 4). The fit between measured and calculated values are poorer for the bottom sill. One possible explanation for this could be air leakages to the ground. Moist air from the ground may prevent the seasonal drying of the bottom sill during wintertime.

Long term simulations with high initial moisture content in the construction indicate that the sills in the wall dry out. This is not confirmed by the measurements, partly because of low initial moisture content and a short measurement period.

The wall construction does not fully comply with the guidelines for insulation of basement walls in Norway. Only about ¼ of the thermal resistance in the wall is located outside the concrete, it should have been ⅓. Secondly, the external insulation should have covered the concrete wall also above grade. Without the external insulation in this area, there is a condensation risk on the inner surface of the concrete. This type of condensation is not confirmed in this project, but both simple condensate calculations and general experience from practice indicate that no external insulation in this area is a problem. In general, it is a challenge for the building industry in Norway to prioritise external insulation of basement walls.

5. Conclusion

Field measurements in an internally insulated basement wall show that the sills take up very little moisture during the first year after the building period. The calculated moisture content fits reasonably well to the measured moisture content in the top sill. The fit between measured and calculated values are poorer for the bottom sill, possibly because of air leakages to the ground.

Long term simulations with high initial moisture content in the construction indicate that the sills in the wall dry out, with seasonal variations. However, this is not confirmed by the measurements, partly because of low initial moisture content in the sills and a short measurement period. Further, the bottom sill does not dry during the winter season as predicted by the calculations. Consequently, the results from the project can not be used to confirm the validity of the Norwegian guidelines concerning insulated basement walls.

6. Acknowledgements

This paper has been written within the ongoing SINTEF strategic institute projects “Climate 2000 – Weather Protection in the Construction Process”. The authors gratefully acknowledge the Research Council of Norway.

7. References

Künzel, H.M. Simultaneous Heat and Moisture Transport in Building Components: One and two-dimensional calculations using simple parameters. Fraunhofer-Informationszentrum Raum und Bau. IRB Verlag, Stuttgart, 1994.

Oustad, M., Gustavsen, A. Uvsløkk, S. Calculation of Moisture and Heat Transfer in Compact Roofs and Comparison with Experimental data. Proceedings of the 7th Symposium on Building Physics in the Nordic Countries. Reykjavik, 2005.

Swinton, M.C., Maref, W., Bomberg, M.T., Kumaran, M.K., Normandin, N..In situ performance evaluation of spray polyurethane foam in the exterior insulation basement system (EIBS)Building and Environment, Volume 41, Issue 12, December 2006, Pages 1872-1880.

Tightening against rain and wind for facades – experience from practice

Trond Bøhlerengen, Senior Scientist,
SINTEF Building and Infrastructure;
Trond.Bohlerengen@sintef.no and www.sintef.no

Anna Næss Rolstad, Research Scientist,
SINTEF Building and Infrastructure;
Anna.Rolstad@sintef.no and www.sintef.no

Arild Gustavsen, Professor,
NTNU/SINTEF Building and Infrastructure;
Arild.Gustavsen@ntnu.no and www.ntnu.no

Håkon Einstabland, Adviser,
SINTEF Building and Infrastructure;
Hakon.Einstabland@sintef.no and www.sintef.no

Vivian Meløysund, Research Scientist,
SINTEF Building and Infrastructure;
Vivian.Meloysund@sintef.no and www.sintef.no

KEYWORDS: *Facades, wind-driven rain, rain penetration, two-stage tightening, building defects.*

SUMMARY:
This paper presents results from field investigations on facades. Examples of typical weak points and alternative solutions which have proved to be more reliable are presented. Due to higher insulation thicknesses and more wind-driven rain solutions with one-stage tightening are more vulnerable and more often results in building defects. In the future only two-stage tightening systems should be used.

1. Introduction

SINTEF Building and Infrastructure's archive of building defect assignments represents one of Norway's most important sources of knowledge on types of process induced building defects and related causes. This knowledge has been thoroughly analysed during the last years (Lisø et al. 2006). At least 75 % of these defects are related to moisture, and most of the defects are related to moisture from outside the building (for instance wind-driven rain). Earlier, most building defects were related to roofs. However, an analysis of building defects from 1993 to 2002 reveals that the majority of the defects in this period are related to walls. More than 35 % of the defects are related to walls, while about 22 % of the building defects are related to roofs, see Figure 1.

In 1997 the thermal insulation requirements were restricted. The U-value requirement for walls was set to 0.22 W/m^2K. In 2007 new requirement levels were introduced. 0.18 W/m^2K was the new requirement for walls. For roofs the U-value was restricted from 0.15 to 0.13 W/m^2K, from 1997 to 2007. The thermal performance requirement was also restricted for most of the other building sections. The result is a building envelope with more thermal insulation and less transmission heat losses. As a result, the outer part of walls on the average has a lower temperature. This may lead to reduced drying of built-in moisture and moisture penetrated into the construction from outside. New constructions are therefore more dependent on correct workmanship and solutions built according to sound building physical principals.

Buildings to be developed in the future demand new solutions due to increased focus on cost efficient building, energy efficiency, environmental material use, indoor environment, life cycle costs etc. This focus is a result of higher performance demands from users and more stringent governmental requirements. In addition climate change may result in increased precipitation, higher temperatures and increased frequency of extreme weather. The climate changes may in Norway also lead to temperatures more often passing the freezing point, resulting in

freeze-thaw cycles and accelerated material decay.

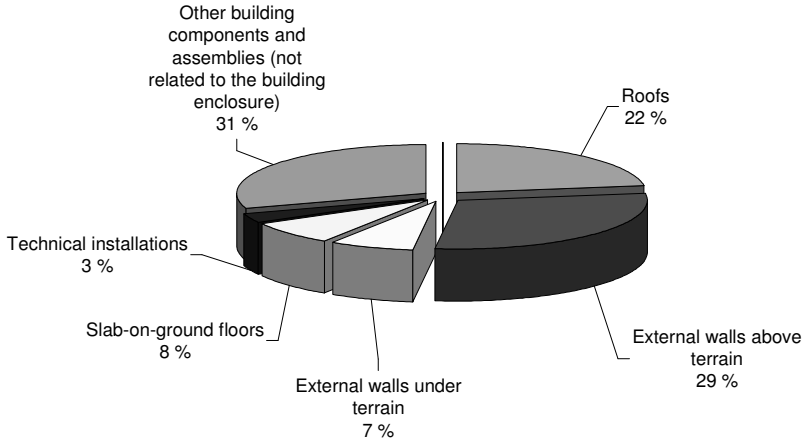

FIG. 1: Process induced building defect cases for the 10-year period 1993-2002 (a total of 2,423 building defect cases), distributed by localization of defects (Lisø et al. 2006).

SINTEF Building and Infrastructure has carried out several field investigations on facades. In this paper some results from this work is presented. Examples of typical weak points like detailing around openings and the in boundary between materials or construction parts will be shown. Alternative solutions which have proved to be more reliable are also presented. The majority of the defects have been found in systems with one-stage tightening, but building defects may also occur in systems with two-stage tightening.

1.1 Tightening techniques

Using a two-stage tightening to prevent rain water from entering the construction has been an important principle in Norway for more than 50 years. This principle is based on a separate rain and wind barrier like shown to the left in Figure 2 and in Figure 3.

The purpose of the *rain barrier* is to avoid moisture to penetrate into the construction, in addition to being a mechanical protection for the construction behind. The *ventilation gap* separates the rain and wind barriers. It provides ventilation and drainage of both moisture passing through the rain barrier, and moisture from the inner constructions. It also contributes to pressure balancing, which again will reduce the probability of penetration of moisture from the ventilation gap through the wind barrier. If moisture penetrates the first barrier it may be transported out of the construction in the ventilation gap, without entering the main part of the construction.

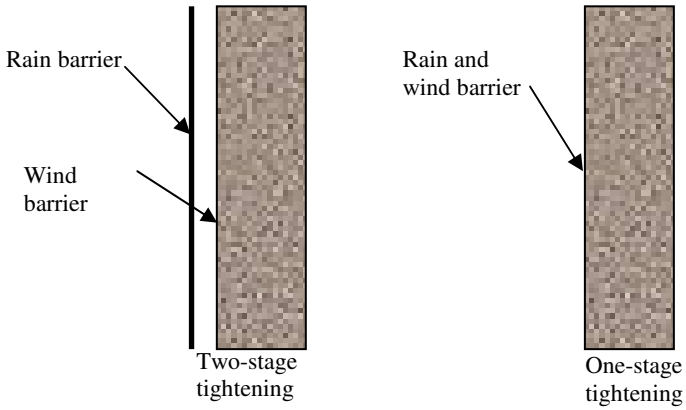

FIG. 2: Schematics of common tightening techniques.

The properties of the outer cladding and ventilation openings may however vary a lot from building to building

and the actual solution may not be as robust as desired (i.e. having a high resistance against failure, e.g. moisture problems). One-stage tightening wall systems are often also used, see the right construction in Figure 2. Here, the rain and wind barrier is within the same material layer. This construction is usually considered more vulnerable considering external moisture than the two-stage tightening construction, often due to insufficient workmanship.

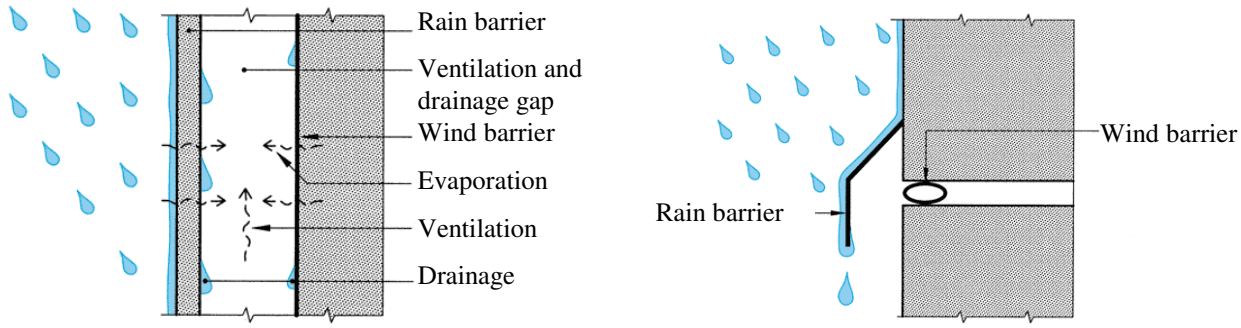

FIG. 3: Detailed explanation of two-stage tightening. The left figure shows a ventilated cladding. A typical joint is shown to the right. Vertical cross-sections. (SINTEF Building Research Design Guides 542.003)

2. Examples of building defects in one-stage tightening systems

Several examples can be found on one-stage tightening wall constructions. But instead of showing typical examples of these, an example of a not so obvious one-stage tightening construction detail is shown. The construction shown in Figure 4 resulted in leakage. The figure shows a horizontal cross section of the detail where the window is inserted into a wall. The wall itself is a ventilated façade (two-stage tightening) while a one-stage tightening construction is chosen where the window connects to the wall. The construction resulted in lots of water entering the interior space due to wind driven rain on the façade. Rain water penetrated the gap between the outer barrier of the wall and the window frame and entered the interior space through small openings in the intersection between the window frame and the wall.

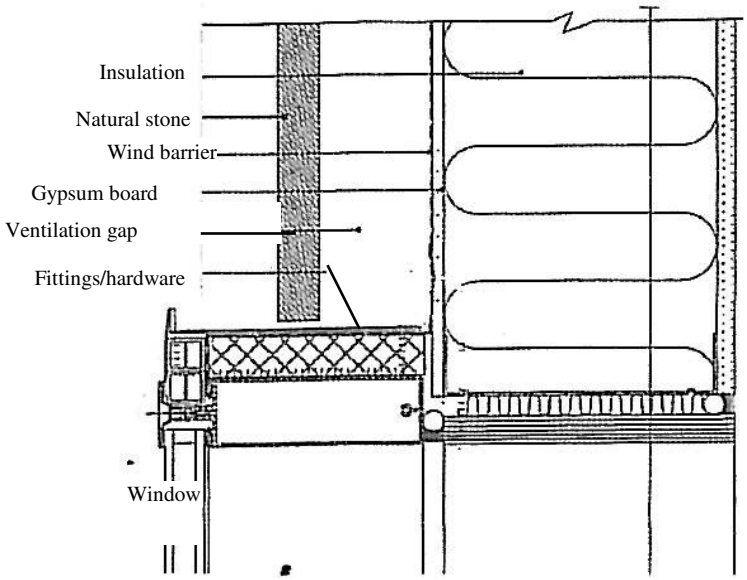

FIG. 4: Example of combination of one- and two-stage tightening. Horizontal cross-section of the connection between a wall and a window.

Figure 5 shows an example of insufficient tightening around windows in a one-stage tightening wall construction. The wall consists of aerated concrete blocks. The plastering is directly in connection with the architrave lining of the windows and doors. The plastering is therefore the only rain- and wind barrier around the openings. After some time, there will be small gaps between the plastering and the window- and door lining, where water may penetrate. The detail shown in Figure 5 leads to substantial water leakage and build-up of moisture in the walls.

FIG. 5: Example of insufficient tightening around windows in a one-stage tightening wall construction of aerated concrete blocks. The plastering is the only rain- and wind barrier around the openings.

In the boundary between the construction parts in Figure 5 there should have been an elastic sealant, and a separate capping with a cavity behind it, for drainage of penetrated water, see Figure 6.

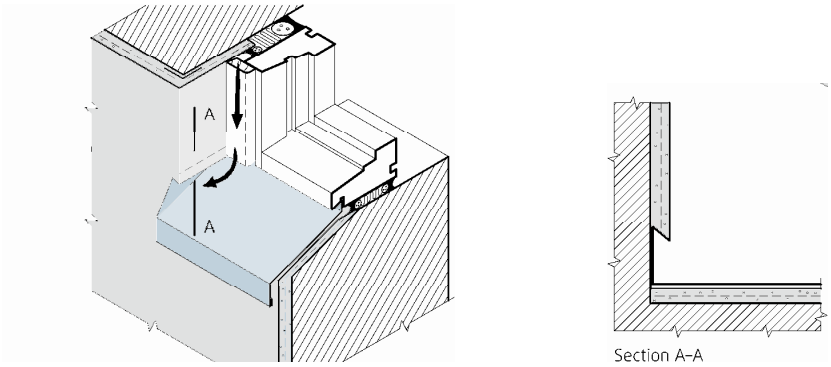

FIG. 6: Example of sufficient tightening around windows in a one-stage tightening wall construction, with an elastic sealant and a separate capping with a cavity for drainage and ventilation, from Lisø and Kvande (2007).

3. Examples of building defects in two-stage tightening systems

3.1 Brick walls

A tiled wall is considered to follow the two-stage tightening technique because the rain and wind barriers are considered as separate layers. But the wall is not really ventilated because there seldom are ventilation openings at the top, and only a few drainage openings at the bottom of the wall. Also, according to ISO 6946 (ISO 2007) the gap is considered unventilated because of the limited opening to the exterior. In most cases the drainage

effect is also limited because of mortar partially filling the gap, see Figure 7.

Up to recently, this has not been a large source of building defects in Norway (providing the use of frost-safe stones). Now, this construction type seems to get some attention due to more defects, probably because the heat loss through the construction is reduced as a result of better insulated walls. This leads to less effective drying-out of moisture in the construction. Wet facades are observed more often. Mortar filling parts of the gap, and also closing the few drainage openings usually found at the bottom of such walls does not help. Larger gaps and more/larger drainage openings at the bottom of the walls may be the solution. In addition openings should also be located at the top of the brick-wall, making the cavity truly ventilated, see Figure 8. This will reduce the insulation effect of the gap and the bricks themselves, but the insulation effect of this part of the wall is small compared to the rest of the wall anyway (having to comply with U-value requirements of 0.18 W/m^{2}K or better).

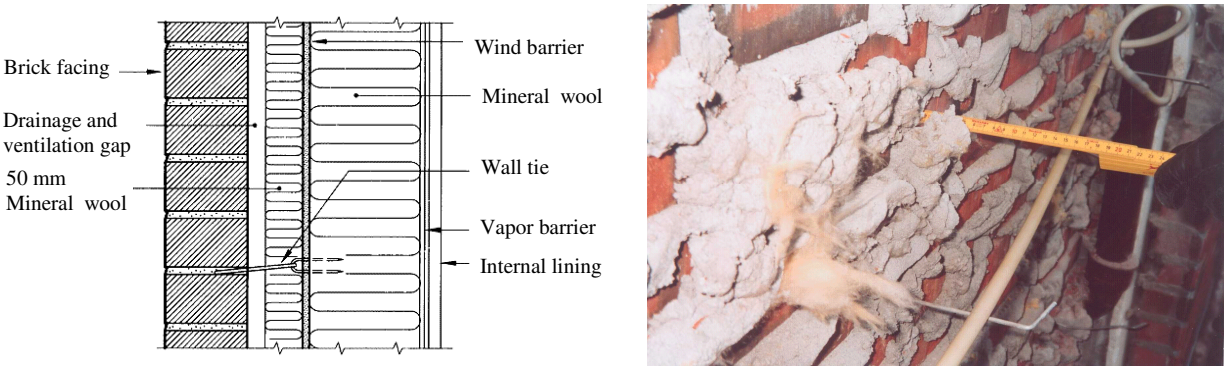

FIG. 7: Figure of the construction principal of a brick wall to the left. The figure to the right shows an example of constructed brick wall where mortar partially fills the ventilation gap and thus substantially reduces the effect of the gap.

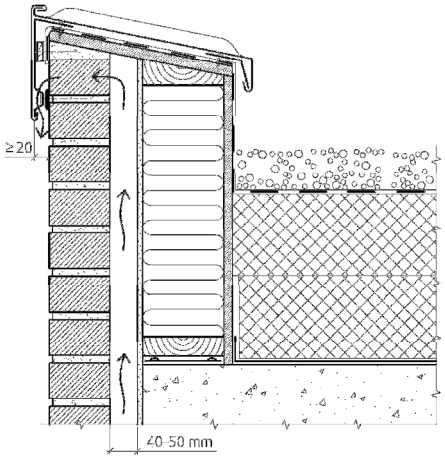

FIG. 8: Construction principal of a brick wall with a larger ventilated opening behind the bricks and with openings on the top. The gap behind the bricks should be large enough to prevent it from being closed by mortar.

3.2 Ventilated claddings

Walls with ventilated claddings are considered to follow the two-stage tightening technique. However, insufficient understanding of the principles may lead to defects. This may be because the cladding in not ventilated, because drainage openings close to the bottom of the cladding are not installed, or because there might be openings in the cladding itself. Figure 9 shows an example of a ventilated cladding of wood. The cladding has openings between each panel and a ventilation gap of 30 mm between the panel and the wind barrier. Even with several ventilation openings to the exterior environment, this wall experienced problems after only 2 years, in a moderate climate. The wind barrier and the gypsum board were observed to be wet, and the wooden studs of the inner wall had started to rot.

The moisture that penetrated the outer cladding (rain barrier) did not dry out. Also, the construction did not have sufficient drainage openings at the bottom of the wall. The openings in the façade allowed wind driven rain to penetrate the outer layer and reach the wind barrier, which was not robust enough to withstand moisture.

Thus, in constructions with openings between cladding elements, the function of the ventilation and drainage gap is of extended importance. A wind barrier that can withstand larger rain loads is also necessary. In this example, the whole cladding had to be removed, and damaged materials in the construction behind had to be replaced. A new, tighter cladding which also provided sufficient ventilation and drainage was then supplied.

FIG. ~~999~~: Example of a construction with openings in the façade and limited drainage openings.

Figure 10 shows an example of a construction with a cladding of cement based sheets. The sheets were fastened to 23 mm thick furring strips. However, the ventilation and drainage gaps are closed at the upper and lower edges of all windows and doors, and at the bottom of the wall. This leads to an accumulation of moisture in the construction, and the sheets were damaged by frost.

FIG. 10: Example of construction with cement based sheets. Due to insufficient ventilation and drainage of moisture the sheets were damaged by frost.

In ventilated claddings, the panels must be fastened to vertical furring strips of at least 23 mm. Larger openings may be necessary in some climates. It is of great importance that the gap is provided with sufficient ventilation/drainage openings at the top and bottom of the wall, to ensure sufficient ventilation and drainage of the construction.

Vertical furring strips are the most common practice of achieving a ventilated cavity behind the outer cladding; see the two figures to the left below (Figure 11). If horizontal furring strips are used these must be fastened to vertical furring strips to ensure ventilation and drainage of the gap, as shown in the two right figures of Figure 11.

It is important to ensure that the ventilation and drainage gap is not blocked by windows, other openings etc. The inner part of the wall construction (behind the cladding) must have a wind tight and water resistant surface. To prevent access of mice etc. behind the cladding, the ventilation openings should be covered by a metal net (mouse barrier etc.).

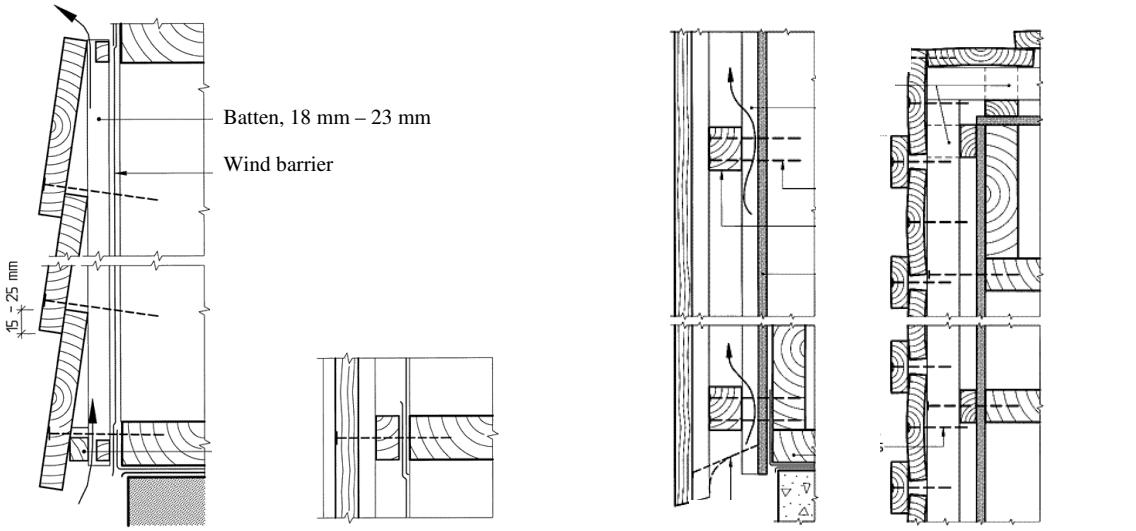

FIG. 11: Example of ventilated claddings of horizontally (two left figures) and vertically mounted wooden panel, from SINTEF Building Research Design Guides 542.101 and 542.102.

4. Conclusions

Building defects in facades have been studied in field investigations. The number of building defects for solutions with one-stage tightening has increased. The reason is probably higher insulation thicknesses and more wind-driven rain. These solutions are vulnerable to moisture problems and should be avoided in the future. Two-stage tightening systems also experience problems in a higher degree, often due to no or reduced ventilation.

As a consequence of restricted thermal insulation requirements and a more severe climate, it is more than ever important to understand the principles of two-stage and one-stage tightening, and come up with alternative designs when traditional constructions have to be improved.

5. References

Lisø, K.R., Kvande, T. and Thue, J.V. 2006. Learning from experience - an analysis of process induced building defects in Norway, *Proceedings of the 3rd International Building Physics/Science Conference*, Montreal, Canada, August 27-31, 2006.

ISO. 2007. ISO 6946:2007. Building components and building elements -- Thermal resistance and thermal transmittance -- Calculation method. International Organization for Standardization.

Kvande, T., Lisø, K.R. and Time, B. 2007. Ventilated Claddings (in Norwegian), SINTEF Report 2, SINTEF Building and Infrastructure. ISBN: 978-82-536-0974-4.

Lisø, K.R. and Kvande, T. 2007. Climate adapted buildings (in Norwegian), SINTEF Building and Infrastructure. ISBN: 978-82-536-0960-7.

Pressure equalisation as design strategy for watertight windows

Nathan Van Den Bossche, Doctoral Researcher
Department of Architecture and Urban Planning, University of Ghent
nathan.vandenbossche@ugent.be

Arnold Janssens, Senior Lecturer, Professor
Department of Architecture and Urban Planning, University of Ghent
arnold.janssens@ugent.be

Jan Moens, VisitingProfessor
Department of Architecture and Urban Planning, University of Ghent
jan.moens@ugent.be

KEYWORDS: *windows, pressure equalisation, test method, experiments, gust effects*

SUMMARY:
In order to shield the indoor environment from the exterior most building components are assembled out of several layers of materials to meet different performance requirements (watertightness, airtightness, thermal resistance, stability etc). In that regard windows and doors are usually the weak spot of the building because it is a transition from the building component to the glass where all the different materials and functions are literally forced together. On top we want them to open and close, so that interface becomes even more crucial and we need to use somewhat exotic fabrics to rise up to the challenge (the bill will rise accordingly). This research area is much too often left to the industry.

Pressure equalisation is the basic principle where windows and doors derive their performance from, but how can this be realised, and what are the main parameters that influence it? As in walls and roofs we can distinguish different elements in the window casement that will fulfil those needs and influence the performance: the section, joggles, gaskets and fittings (handle, gearbox, locking bar, corner pivot, stay, hinges…). Using high frequency measuring equipment the influence of the different elements is examined in both dry as well as rainy conditions during static and dynamic pressure differences. The pressure equalisation in the chamber is depending on the collaboration of the profile and the gaskets, the design of the vents and drainage holes, and the fine-tuning of the fittings.

Analysing the performance of windows and doors one comes to the conclusion that the European Standard EN 1027:2000 may not properly benchmark the watertightness: certain damage initiation phenomena are underestimated in the current procedure.

1. Pressure equalisation in windows

The most common design strategy for watertight windows is pressure equalisation, although pressure moderation might be a more appropriate name (Straube J.F. 1998). The performance of different types of cladding that use pressure equalisation has well been studied over the last 40 years: an extensive literature review can be found in (Suresh Kumar K. 2000). The Pressure Equalised Percentage (PEP) is a specific value between 0 and 100% which measures the rapidity and degree to which the internal air pressure within the cavity can equalise with the external air pressure (Burgess J.C., 2000). A PEP value of 100% implies a perfect pressure equalisation of the cavity with the same amplitude and in phase with the external air pressure. As window frames only have a small cavity volume, we expect the phase shift of the pressure to be relatively small because the major determinant of response speed is the compressibility of the air (Straube J.C., 2001). The PEP can be calculated with following formula (1):

$$PEP = 100\left(1 - \frac{1}{2PT}\int_0^T \left|P_e(t) - P_c(t)\right|\right) \quad (1)$$

PEP: Pressure Equalisation Percentage [%]

P: Amplitude of external air gauge pressure [Pa]

T: Period [s]

$P_e(t)$: Gauge air pressure outside at time t [Pa]

$P_c(t)$: Gauge air pressure in cavity [Pa]

Due to the complex geometry of windows (caused by thermal and mechanical characteristics) and the fact that they have to open and close, it is practically impossible to create a face-sealed watertight window that is impervious to water and air through time under all circumstances. As a result we take for granted that failure will occur: the window should be designed as a drained construction with a water barrier, an air barrier, and drainage paths as separated functions. The water barrier is in fact just a shedding device to prevent water from entering in the cavity of the window frame, like the exterior facing of a masonry brick wall. The air barrier is utterly important for the performance of the window because it must withstand high pressure loads to enable pressure equalisation at all times. Any penetration of the airtight barrier by hinges, joggles or fittings may be crucial to the overall performance. Any water that penetrates into the cavity should be drained to the exterior by weep holes at the bottom, and in order to prevent negative pressures effects in the cavity by static watercolums in the weep holes vents are located at the top of the window.

The pressure equalisation is just one principle of water management. If we also take the buffering effect into account and realistic weather data, it becomes clear that some windows may perform quite well under high pressure loads, without obtaining real good pressure equalisation (See also: Rousseau J., 1999). The effect of external pressure gradients is strongest along the vertical edges of buildings for wind angles between 30 and 60 degrees, but usually this does not coincide with the greatest wetting intensities (those occur during perpendicular winds). In this paper only windows of relatively small dimensions are discussed, so external pressure gradients are not taken into account. The biggest mean pressure difference as well as the biggest peak pressure differences do in fact coincide with the greatest wetting intensities (Suresh Kumar K., 2003) The outer 5 to 10% of the building width and the top 5 to 10% of the building height experience the largest gradients and normal compartmentalization should be adjusted to that (Inculet D., 1997).

There are reservations concerning all of the current watertightness tests available, and research is needed on the principles and requirements of dynamic testing (Kerr D., 1997) In order to design a new standard test, there should be a good agreement between the performance under real conditions, and the performance according to the lab test. The different damage initiation phenomena need to be closely examined to develop the test conditions for dynamic testing. On one hand there is a difficult balance between the conditions and performance of a window during its total service time, and the conditions and performance in the test facility (Cornick S.M., 2004) On the other hand there is also a balance between creating a test method that comes close to reality and a test method that is economically realistic and viable.

2. Watertightness test method

In order to test the watertightness of windows the test method described in (EN 1027:2000) is used: the window is framed into a box and put against the test wall that can simulate rain and apply pressure differences. The first 15 minutes of the test water is sprayed on the window (2 L/min/m²) without any pressure difference. After 15 minutes a pressure difference of 50Pa is imposed while the spray rates remain the same. Every 5 minutes the pressure difference is changed according to the following sequence: 0-50-100-150-200-250-300-450-600-750-900-1050-1200 Pa (figure 1). The level of watertightness of the window tallies with the highest pressure difference that is achieved without any water infiltration during that stage. The moment water is visible on the inside surface of the window, or water can be found on the backside of the gasket (for windows with central gaskets) this is considered as failure. The type of water infiltration can be classified according to the place, cause and level of failure. We can distinguish 6 different places of failure when it comes to water penetration in and around windows in buildings, but the test procedure only allows evaluating 3 of them (figure 2):

- L1: Leakage path along the glazing stop to the interior
- L2: Leakage path around the operable unit to the interior
- L3: Leakage path through the joint of frame members

The other leakage paths interact with the construction surrounding the window (L4: leakage path through the window to wall interface to the interior, L5: through the window assembly into the adjacent wall assembly, L6: through the window to wall interface into the adjacent wall assembly). More information on water penetration in and around windows can be found in (RDH Building Engineering Limited, 2002). In order to test these failures a complete mock-up of a construction should be necessary, or the testing should take place in-situ.

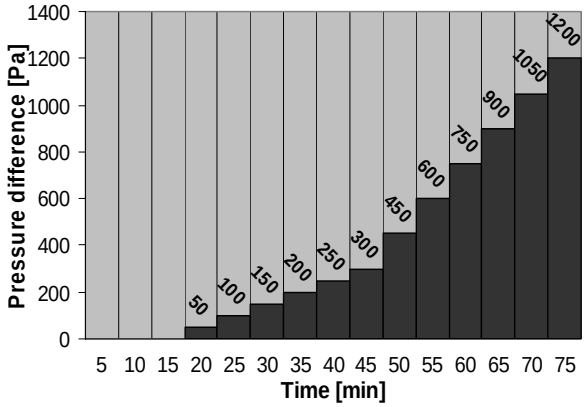

Figure 1: watertightness test according to EN 1027:2000

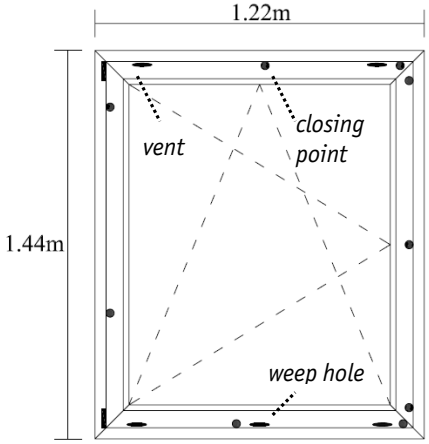

Figure 2: dimensions of test window

Next to the place we can also make distinction in the cause. The first and most prevalent cause of water infiltration has to do with the accumulation of water in the cavity between the frame and the sash. When the level of water rises too high two things are possible: the hydrostatic pressure on little cracks can cause water to flow into the interior, or the water just runs over the edge of the profile and past the gasket. The second cause of water infiltration is the velocity of the air flow when it enters the cavity: if the airtightness is too small the wind will flow into the interior of the building with too much speed and the kinetic energy of the raindrops will enable water to reach the airtightness barrier. We can distinguish three levels of failure:

- Construction error (bad mitre joint, bad coupling between frame members and mating extrusions, discontinuous gaskets, penetrations...)
- Poor adjustment (poor installation of operating hardware, poor installation of the glass, lack of weep holes or vents...)
- System failure (limits of water buffering, limits of pressure equalisation...)

The sequence of these levels of failure reflects the achievable level of watertightness of the window. If there is a weld failure at the mitre or butt joint of a vinyl window, there can even be infiltration without any pressure difference, and a better adjustment of the hardware of the gaskets will not help. If there is no construction error the quality of adjustment will limit the watertightness. Eventually the overall design and collaboration of the hardware, the gaskets and the section of the window will determine at which level the window reaches the end of its abilities to prevent water from infiltrating into the interior. Each type of failure will define a level of watertightness that can be achieved, so only if there are no construction errors and the window is well adjusted, the system can reach its full potential. It is beyond any doubt that manufacturers should focus on robust and feasible designs of window frames to achieve better performance on site.

3. Survey of 207 certified watertightness tests

Between 1994 and 2008 the façade test facility of the University of Ghent has tested a lot of windows including their performance regarding watertightness, airtightness and resistance to wind loads. We were able to retrieve 207 test reports, containing tests of 136 aluminium windows (66%), 52 vinyl windows (25%) and 19 wooden windows (9%). While the aluminium windows achieve high levels of watertightness more frequently than the other materials, wooden windows are better represented on the other end of the spectrum. Airtightness does not give the same result: aluminium windows have better airtightness, followed by wooden and vinyl windows. The

airtightness of the windows is specified by a level according to EN 12207 ranging from 1 to 4, level 4 being the most airtight windows.

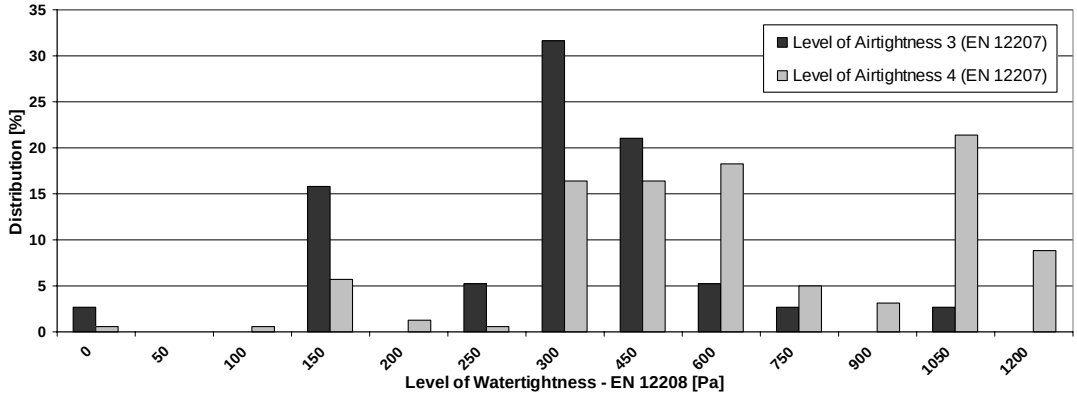

Figure 3: Watertightness vs. Airtightness – analysis of 197 test samples according to current EN standards

Figure 3 shows the correlation between airtightness and watertightness of windows: it may be clear that the level of airtightness is a stipulation for good watertightness because only 6% of the windows of level 3 achieve a watertightness level above 600 Pa (for the airtightness level 4 windows that percentage is 38). A close examination of those results shows that at least airtightness level 3 is required for watertightness levels above 150 Pa, level 4 is required for airtightness above 450 Pa, and the air leakage needs to be half of level 4 to reach 1200 Pa.

The correlation between mechanical resistance to wind (the deformation when submitted to a certain pressure difference) and watertightness is slightly less explicit, but more rigid frames do achieve a better watertightness performance, and slack windows (relative sag under a 1000 Pa load is bigger than 1/350) do not reach watertightness above 600 Pa. Good pressure equalisation and watertightness depend on the collaboration between the frame, hardware and gaskets. Apparently the gaskets in the less rigid frames are not able to follow the bigger deformation: either this is a physical limitation, or none of those windows had gaskets adjusted to the type of frame. The mechanical resistance is a combination of the stiffness of the frame and sash, the fine tuning of operating hardware and the number of hinges, stays and other elements that connect the sash to the frame.

4. Experiments with high frequency measuring equipment

In order to analyse the effect of different parameters on pressure equalisation in windows experiments are conducted at our certified test facility on a vinyl window (1.44m high by 1.22m wide, see figure 2). The window has 3 drainage openings (a slot of 5mm wide and 30mm long) at the bottom and 2 vents of the same size at the top. It is a turn and tilt window and it uses an inner- and outer gasket for respective water- and airtightness. Including the hinges there is a total of 11 closing points for a contour of 5.04m. The sash is well dimensioned in accordance to the frame, the hardware is adjusted correctly, and the glass is also placed as it should be.

Three pressure taps are used: one to measure the pressure on the exterior of the frame, and two to measure the pressure in the cavity of the window. These are placed in the left and right jamb of the frame to see if there is a difference caused by the place of the tilting hardware that is situated in the upper left corner. The pressure taps are calibrated very low range differential pressure transmitters with a full scale error of less than 1.0 % (GEMS 5266 transmitter). The output of the taps is transmitted to a data acquisition module with a full scale error of 0.1% (Dataq DI-158) into the computer for direct processing with the software WinDaq.

Between every test there was a period of at least 20 hours to let the window dry. Doing two tests on one day is not possible because the results of the second test do not match those of the first in identical circumstances (the achieved pressure difference at the moment water infiltration occurs can be half the pressure difference during the first test). A possible explanation would be that the surface friction of the gaskets could be slightly altered for a period of time when it has been wet. Lower surface friction might lower the airtightness of the gasket and hence the watertightness. Further research needs to be done to confirm these theses.

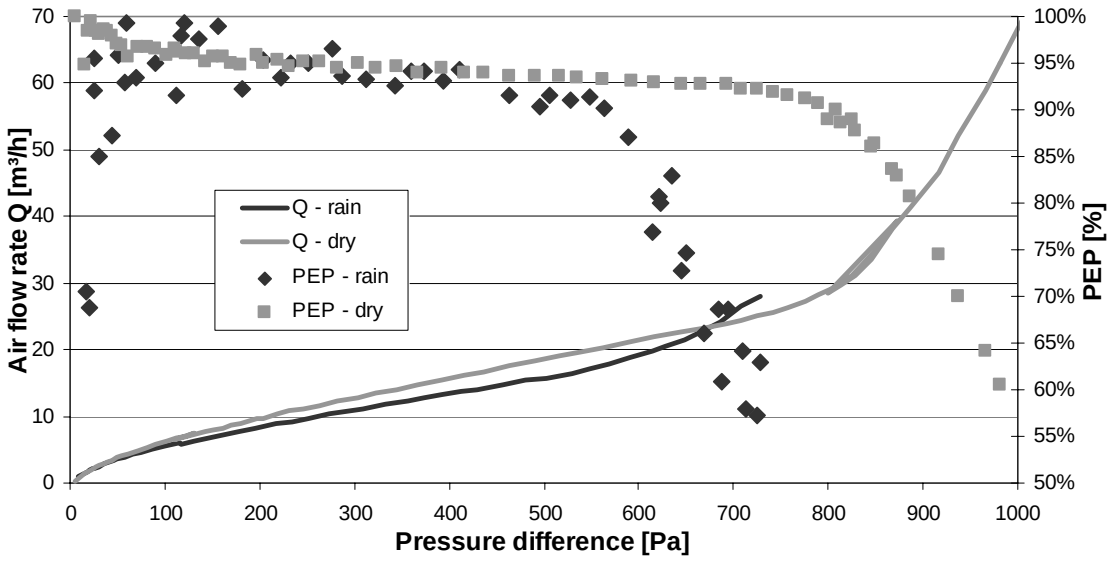

Figure 4: Air flow rate and PEP plotted against the total pressure difference over the window

Figure 4 shows the air flow rate of the window as a function of the pressure difference across it, both in dry as well as in rainy conditions. On the second Y-axis the PEP is plotted for the two situations. The measurement for the rainy conditions does not go beyond 730 Pa because water infiltration occurred at that stage (raising the pressure difference beyond that point would distort the measurements). During a rain event the film of water will partially close the vents and weep holes, thus reducing the airflow but also reducing the pressure equalisation of the cavity. The amount of water that is entering the cavity depends mainly on the pressure difference and the geometry and deformation of the window frame and sash. When the pressure rises all of a sudden the water cannot be drained quickly enough by the weep holes any more and static water columns in the weep holes block the pressure equalisation (for this particular window that phenomenon started at 620 Pa). This causes the pressure in the cavity to fluctuate with an amplitude of 20 up to 50 Pa and a period of 0.1 to 0.2. second (figure 5). From that moment on the average pressure in the cavity drops when the total pressure difference across the window is raised. The amplitude of the fluctuation on the other hand rises up to 100 Pa at the point of failure (730 Pa). If the total pressure difference is decreased, the fluctuating of the pressure in the cavity will not cease until all the water has drained. The amplitude of the fluctuation seems to be a measure to predict the failure of the window in different circumstances, however more research is needed to confirm these preliminary conclusions. One could think that the deformation of the window is the most critical factor for the balance between the airtightness of the outer and inner plane, but apparently the water film and imbalance of the water drainage system causes the pressure equalisation to fail preliminary and water will infiltrate into the interior.

The difference between the two pressure taps built into the frame is smaller than 10 Pa for 71% of the measured points, in some cases the difference rises up to 30 Pa (over 90% of the time the difference between the taps is within 10% of the pressure in the cavity). Over 70% of the time the left jamb (where the stay arm of the turn and tilt hardware penetrates the airtightness seal) is at a higher pressure than the right one. The penetration enables a higher air flow rate at that spot, so the pressure equalisation will be slightly modified in the left upper corner of the window.

As stated before the normal test procedure according to EN1027:2000 contains a wetting period of 15 minutes followed by a number of pressure steps of 5 minutes each (figure 1). Every window in Europe is tested that way to measure its performance regarding watertightness. It is up to member states to define which level of performance is required and obliged in a certain situation, based on a correlation between the test conditions and the conditions of the window in situ. In order to define that correlation a parametric analysis on the testing protocol has been started. Experiments point out that the level of watertightness drops when the time step becomes smaller. According to the certified test procedure the window fails at 900 Pa (after 1 minute), while it fails at 750 Pa (after 2.5 minutes) if every time step is 4 minutes in stead of 5. The total testing time is 8 minutes shorter, because 8 time steps are 1 minute shorter. This excludes the water buffering system to be the

predominant factor in the watertightness. The longer every time step takes, the more time the water has to rise in the cavity and eventually run over the edge past the sealant. Apparently there must be another factor that influences the overall performance of the system. That factor must enable a parametric change between the 4th and the 5th minute of the test or during the total time of the sequence of pressure steps. The hardware is too rigid to change any characteristic with such a time delay, so it comes down to the torsion of the vinyl sash or the compression of the gasket. It could be possible that every pressure step the total pressure difference moves the sash a little bit away from the frame while the gaskets can not follow that movement and need more than 4 minutes to expand from their compressed situation.

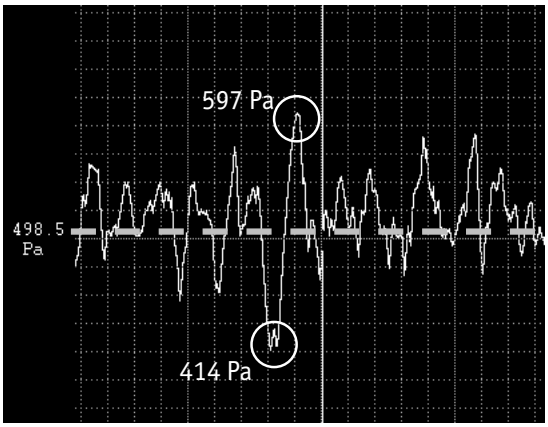

Figure 5: fluctuation of pressure in cavity during rain

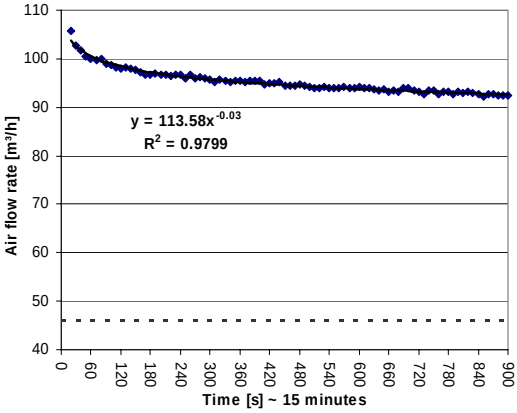

Figure 6: air flow rate at 900 Pa during 15 minutes

Figure 6 shows the air flow rate plotted against the time when a pressure difference of 900 Pa is directly applied. The results have been corrected to take the temperature, barometric pressure and relative humidity into account. The fan of the test stand is frequency controlled, so as the window gets more airtight because the gaskets slowly expand, the pressure difference over the window will rise (fan frequency remains the same). The computation also takes this into account and figure 6 shows the results for a constant pressure difference of 900 Pa. The dotted line on the figure is the air flow rate of the window at 900 Pa during a normal test procedure (46 Pa). These results show it is worthwhile investigating the correlation between the test method and reality. As wind does not blow continuously the test should take the same damage initiation phenomena into account: the effect of time is totally different in reality and in the test.

5. Gust effects

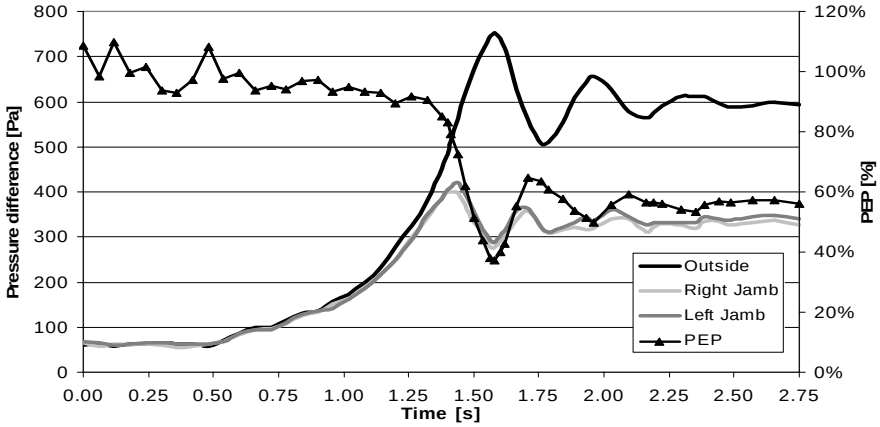

Figure 7: Pressure difference and PEP during a gust effect

Figure 7 shows the pressures outside and in the cavity during a gust effect, on the second Y-axis the PEP is plotted against the time. It clearly shows the pressure equalisation in general is very poor during the gust effect: as different lengths of gusts were tested (up to 10 seconds), the PEP never did rise above 60%. This is in shear contrast with the pressure equalisation during static testing which is above 90%. The fluctuation of the outside pressure is caused by the interaction of the shifting of the glass panel and the shifting of the working point of the fan. The quick change of pressure on the glass panel will cause a volume change in the outside volume of the test setup of about 5470cm³ (temporary shift of 4mm), while the airflow per second at that moment is about 11100 cm³/s. This slightly postpones the build op of pressure in that volume. Once the fan reaches its working point the glass panel shifts back a little due to the torsion in the sash, and this will again interact with the working point of the fan, causing the fluctuation of the outdoor pressure. Although the PEP may be below 40% at a certain point in time, the ability to press water into the cavity during that short period of time needs investigation but seems unlikely.

As the window fails at 900 Pa (after 1 minute) in normal test conditions according to the European standard, it is interesting to see when it would fail when subjected to gust effects. For this experiment gusts of 5 seconds were used, alternated with 5 seconds at about 10% of the gust pressure difference (for example: 900 Pa – 90Pa). When a gust pressure difference of 900 Pa is applied water infiltration starts during the second gust. The window fails after 5 gusts when a gust pressure difference of 750 Pa is applied, and with 600 Pa it does not fail during a test with 50 gusts. So even if there is no water buffering in the cavity, the inability of the gasket to close quick enough will cause water infiltration to occur at a lower pressure difference than under static conditions.

The PEP (Pressure Equalisation Percentage) is expected to rise when the period of the gust gets longer: slow external pressure changes will be followed well by the pressure in the cavity (when there is no influence of the gasket). If the external pressure is changed much faster, there will be a more pronounced phase shift in the equalisation and the amplitude in the cavity will be slightly tempered (Straube J.F., 1998). However, in general 3 Hz has been selected as threshold for pressure equalised rainscreen joints, where a PEP of 95% is an appropriate benchmark (Burgess J.C., 1995). But does this apply for windows? Preliminary research points out that there is a clear difference in the way the pressure equalisation reacts in cladding and in window frames.

Although there might be a little change in volume of the cavity due to the movement of the insulated glass unit during pressure changes, we do not consider these changes to be that big to have a major influence on the phase shift and amplitude of the pressures. According to (Choi C.C.E., 1998) a vent factor (venting area to cavity volume A_{rs}/V_c) should be more than $0.035m^{-1}$ to achieve a good pressure equalisation for a frequency of 1 Hz or less in building envelopes. The volume of the cavity of the window is 5095cm³ and the venting area is 7.5cm², resulting in a vent factor of $0.0015m^{-1}$, over 20 times too small (this does confirm the low PEP during the dynamic testing). Further research is needed to test whether this rule of thumb does apply for windows, and whether windows need the same level of pressure equalisation for those frequencies to be weathertight.

6. Conclusions

A survey on 207 tests according to current EN standards shows there is a clear connection between airtightness and watertightness: apparently a certain level of airtightness is required to realize a corresponding level of watertightness. On top the window needs to be rigid enough to enable the gaskets to follow any movement of the sash to avoid premature failure. At least 13.7% of all windows (incomplete dataset, probably higher) does not pass the watertightness test for the pressure level stated by the manufacturer of the window. Without passing a judgement on that number, it should be clear that this is only true for those windows, especially prepared with kid gloves to be put to the test. In order to get any idea on the performance of windows in real buildings, one should test them in situ, or arbitrarily choose windows that are produced in the factory.

The proportion of the airtightness of the outer plane to the airtightness of the inner plane is crucial to the pressure equalisation in the cavity of the window. Once the Pressure Equalisation Percentage drops below 90% the window will fail shortly after. During rain events a water management imbalance originates at a certain pressure difference causing pressure fluctuations in the cavity. Speeding up the current EN test standard advances the infiltration of water at lower pressure differences. The importance of the mass-balance of water in the cavity is outstripped by the time-dependant functioning of the gasket. The Pressure Equalisation Percentage does not rise above 60% during gust effects up to 10 seconds in duration, and the air flow rate at that time is twice as high compared to the normal test procedure. Windows can not withstand the same pressure difference for dynamic testing as during static testing procedure.

More research is required to verify these results on other windows with different materials and different configurations. A computer model based on the helmholz resonator theory or mass continuity equations needs to be developed and validated in order to predict the performance of pressure equalised window systems.

7. Acknowledgements

The authors would like to express their sincere appreciation to the Test Centre for façade elements of the University of Ghent, especially to Mr. Huwel and Mr. De Poortere. Without their extensive experience, counselling and guidance this work would not have been possible.

8. References

Burgess J.C. (1995). Air Pressure equalisation in rainscreened joints by geometric alteration, *Building and Environment*, Vol. 30, pp.13-18

Burgess J.C. and McCradle G. (2000). Building cladding air pressure equalisation investigations- comparison between field results and a numerical model, *Building and Environment*, Vol. 35, pp.251-256

Cornick S.M. and Lacasse M.A. (2004). A review of Climate Loads Relevant to Assessing the watertightness Performance of Walls, Windows and Wall-Window Interfaces, Performance and Durability of the Wall-Window Interface, *ATSM STP*, B.G. Hardman, C.R. Wagus and T.A. Weston, Eds., ASTM International, West Conshohocken, Pennsylvania, US

Choi C.C.E. and Wang Z. (1998). Study on pressure-equalization of curtain wall systems, *Journal of Wind Engineering and Industrial Aerodynamics*, Vol. 73, pp. 251-266

EN 1027:2000 (2000). Windows and Doors. Watertightness. Test Method

Inculet D. and Surry D. and Davenport A.G. (1997). Unsteady pressure gradients and their implications for pressure-equalised rainscreens, *Proceedings of ICBEST '97*, Bath, U.K., pp.457-463

Kerr D. and Matthews R. and Kirmayr T. (1997). To Develop a European Standard Watertightness Dynamic Test for Curtain Walling, *Proceedings of the 2nd European and African Conference on Wind Engineering*, Genova, Italy, 22-26 June 1997, Volume 2, pp. 1051-1058

RDH Building Engineering Limited (2002). Water penetration resistance of windows, study of manufacturing, building design, installation and maintenance factors, CMHC, Vancouver, Canada

Rousseau J. (1999). Laboratory investigation and field monitoring of pressure-equalised rainscreen walls, *research highlight*, Technical series 96-236, CMHC-SCHL, Canada

Straube J.F. (1998). Moisture Control and Enclosure Wall Systems, *Ph.D. Thesis*, Civil Engineering Department, University of Waterloo, Canada

Straube J.F. (2001), Pressure Moderation and Rain Penetration Control, *OBEC PER Seminar 2001*, University of Waterloo, Canada

Suresh Kumar K. (2000). Pressure equalization of rainscreen walls: a critical review, *Building and Environment*, Vol. 35, pp.161-179

Suresh Kumar K. and Stathopoulos T. and Wisse J.A. (2003). Field measurement data of wind loads on rainscreen walls, *Journal of Wind Engineering and Industrial Aerodynamics*, Vol. 91, pp.1401-1417

Moisture convection performance of wall and attic floor joint

Targo Kalamees, PhD,
HVAC-Laboratory, Helsinki University of Technology, Finland;
targo.kalamees@ttu.ee

Jarek Kurnitski, DrTech,
HVAC-Laboratory, Helsinki University of Technology, Finland;
jarek.kurnitski@tkk.fi

KEYWORDS: *moisture convection, air leakages, hygrothermal performance of building envelope*

SUMMARY:
Full-scale laboratory measurements were taken to determine the moisture convection performance of the joint of an external wall and attic floor. This joint is one of the most typical air leakage paths, where the highest air pressure difference forms in winter. Two commonly used external walls (timber-frame and autoclaved aerated concrete walls) and two different sheathing materials (wood fibreboard and mineral wool) were studied. The attic floor was in both cases a timber-frame structure. A two-dimensional heat, air, and moisture transport computer model was used to study the hygrothermal behaviour of the joint studied. Results from the laboratory measurement series and computer simulation showed that, in leaky joints of this kind, the moisture convection due to positive air pressure remarkably raised the moisture accumulation rate on the inner surface of sheathing. At same time, the sheathing material played an important role in the hygrothermal behaviour of the joint. Moisture convection at constant pressure difference and humidity load conditions was possible to control with airtightness (exfiltration rate) and sheathing material. The results of this study are used to determine the airtightness requirements of structures for several positive pressure and airtightness levels.

1. Introduction

Accurate assessment of hygrothermal performance of building envelopes is important to prevent moisture damages and to guarantee longer service life, as well better indoor air quality for buildings.

Water leakage has the most critical influence on the hygrothermal performance of building envelopes. Neither air convection nor vapour diffusion is comparable (Karagiozis 2002). If the ventilated facade claddings are used, they should protect the wall from driving rain. Vapour diffusion is controllable by a vapour barrier (Vinha, 2007). If the building envelope has a vapour barrier that controls the vapour diffusion, the major humidity load is usually carried by the outgoing airflows due to air leakage. Hygrothermal loads caused by air leakage may be much more important those caused by vapour diffusion. The role of air exfiltration for the hygrothermal performance of the building envelope is analysed in many studies (Burch and TenWolde 1992, Hagentoft and Harderup 1996, Ojanen and Kumaran 1996, Janssens (1998), Kilpelainen et al. 2000, Janssens and Hens 2003). The uncontrolled air movement through a building envelope leads also to problems relating to health, energy consumption, performance of the ventilation systems, thermal comfort, noise, and fire resistance.

Air leakage through a building envelope depends on the result of air-pressure differences over the envelope and the airtightness of the building envelope. The positive air pressure difference over the building envelope can be utilised in the control of radon, particulate matter, fungal spore or other contaminants transported to the indoor air. At the same time, high indoor humidity load and positive air pressure conditions may cause intensive moisture accumulation in the building envelope and it is not recommended in most of cases in cold climate. As an air pressure difference over the building envelope cannot be avoided even in typical residences (Kalamees et al. 2007) and as buildings are not totally airtight (Granum and Haugen 1986, Kronvall 1980, Brunsell and Uvslokk 1980, Nilsson et al. 1982, Polvinen et al. 1983, Hamlin 1997, Stephen 1998, Sherman and Dickerhoff 1998, Kauppinen 2001, Korpi et al. 2004, Kalamees 2007), convection should be taken into account in the process of hygrothermal design.

To assess and predict the long-term heat and moisture performance of building envelope systems, we can use simulation tools or experimental investigations. As laboratory and field experiments are expensive and time consuming, the use of calculation methods to assess the moisture behaviour of building components is

increasing. As air leakages are concentrated in the joints of different envelope parts (wall, roof, floor, window), the air leakage is multidimensional and two-dimensional measurements and simulation should be carried out. To know how closely computer models can simulate real life, we must also compare calculated results with those of laboratory experiments. Users of models have to know the exact input data (material properties, climate data) and the limitations of the model to use them to assess the moisture behaviour of building components effectively.

In this study, typical air leakages and their locations were determined from the field measurement data reported in Kalamees et al. (2008). Full-scale laboratory measurements were carried out to determine the moisture convection performance of the joint between the external wall and attic floor. The studied two-dimensional heat, air, and moisture transport simulation model was validated for future simulations.

2. Methods

2.1 Laboratory measurements

Two commonly used external wall (timber-frame wall (Figure 1) and autoclaved aerated concrete (AAC) wall (Figure 2)) joints with a timber-frame attic floor are measured in laboratory conditions between climatic chambers. The studied two-dimensional joint details consist of a 1.2 by 0.7 m (width by height) external wall part and a 1.2 by 0.9 m attic floor part.

The warm climatic chamber is equipped with heating and humidification units and simulates the indoor climate. The cold climatic chamber is equipped with refrigeration, heating and humidification units simulating the outdoor climate. The climatic chambers are automatically controlled and continually maintain an equilibrium of various climatic parameters, such as air temperature, relative humidity (RH) and air pressure difference, over the examined structure.

The influence of the sheathings on the hygrothermal performance of the joint was studied by using two commonly used sheathings material. First, a test series was conducted with 12 mm wood fibreboard. Later the joint was modified and a 20 mm mineral wool board covered with spun bounded polyolefin (SBPO (Tyvec)) film was used. The attic floor was insulated with 220 mm thick mineral wool.

There were two test samples in sheathings that were weighted during the test to control the moisture accumulation. When test samples were removed, the possible condensation on the inner surface of the sheathings was also determined.

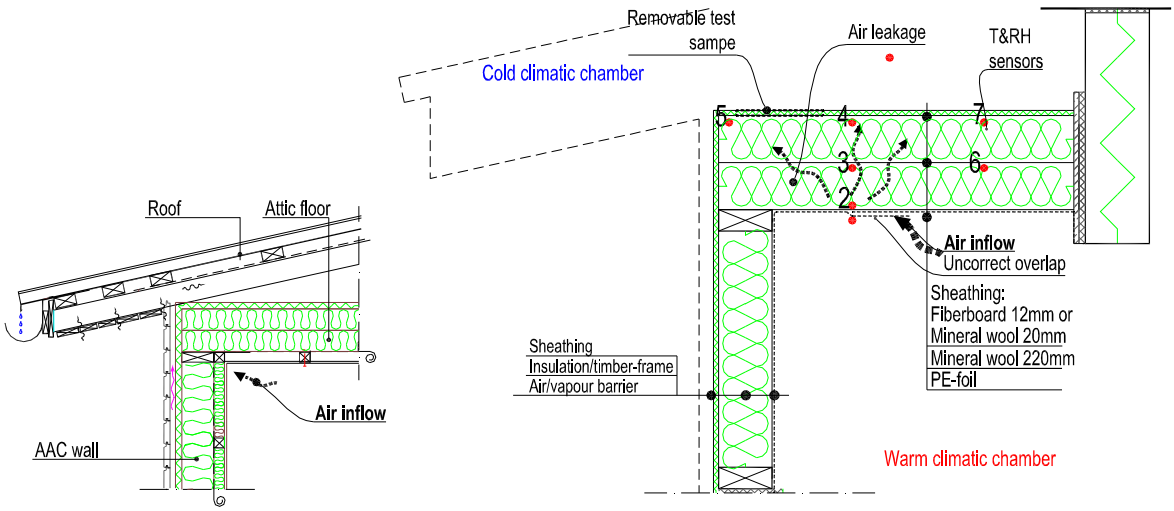

Figure 1 *Studied timber-frame wall joints with timber-frame attic floor (left) and the studied joint in laboratory conditions between climatic chambers (right). Temperature and RH measurement points are shown by red dots.*

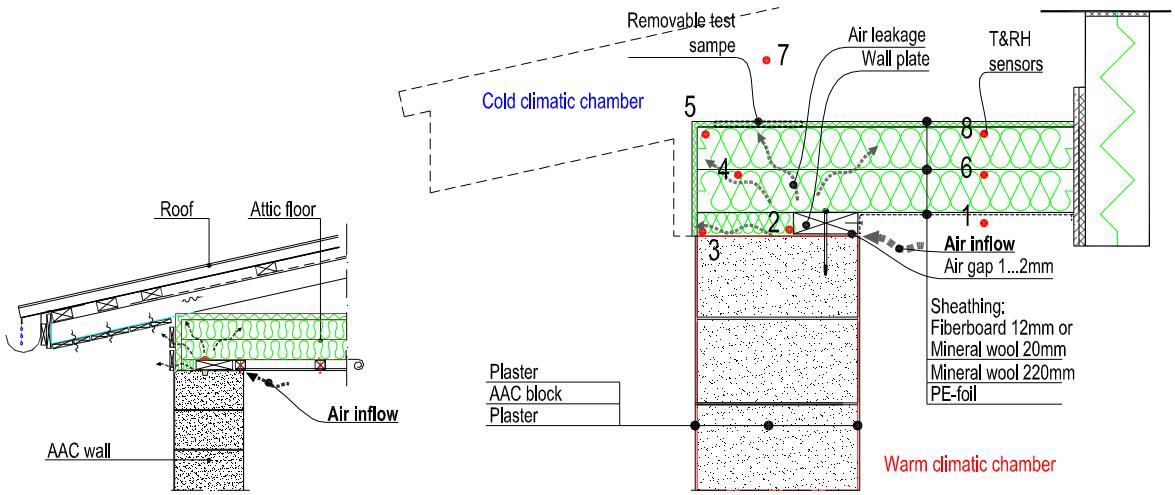

Figure 2 *Studied autoclaved aerated concrete wall connection with attic floor (left) and the structure in laboratory conditions between climatic chambers (right).Temperature and RH measurement points are shown by red dots.*

In the timber-frame wall/attic floor joint, air leakage was allowed between two air/vapour barrier foils. In the AAC wall/attic floor joint, a 1…2 mm thick air gap was left between wall plate and AAC block. The wall/attic floor joint was tested with different airflow conditions. First, three test series were carried out with opened air leakage joints After that, a test series was conducted with narrower, i.e. 10 cm wide, air gaps. The real air inflow through the air leakage part was measured with an electronic soap film calibrator (bubble flow meter). Figure 3 shows the real air inflow through the 10 cm wide air leakage part. The trend lines of these data were used to determine the exfiltration airflow for simulations. The overall airtightness of the joint with the closed air leakage part was measured with wood-fibreboard sheathing. Even the studied setup was built to be as airtight as possible as there was only 15% leakage compared to the airflow though the target air gap.

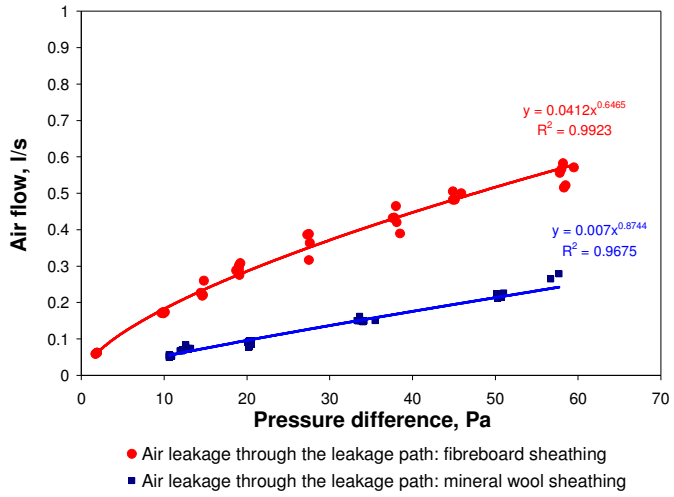

Figure 3 *Measured air leakage through the airgap between two air/vapour barrier foils (timber-frame wall/attic floor).*

The laboratory measurements were taken between ±0 °C and -11 °C outdoor temperature conditions. The moisture excess (Δν, the difference between the humidity by volume of indoor and outdoor air) was 4 g/m^3 in both tests. According to measurements in detached houses, this is the design value of moisture excess for dwellings with low occupancy (Kalamees et al. 2006, Kalamees 2006). The air pressure difference (ΔP) over the test setup was +10…+11 Pa. According to measurements and simulations in detached houses, the design value of air pressure difference over the building envelope should be at least ±10Pa (Kalamees et al. 2007).

2.2 Simulation mode

Based on laboratory measurements, the simulation model built with the CHAMPS-BES program (Coupled Heat, Air, Moisture and Pollutant Simulation in Building Envelope Systems) was validated for future analysis. This program is an outcome of a joint effort between the Building Energy and Environmental Systems Laboratory at Syracuse University, U.S.A. and the Institute for Building Climatology at the University of Technology, Dresden, Germany.

CHAMPS-BES modelling comprises the description of fluxes in the calculation domain or in the field (between volume elements including material interfaces) and at the boundary (between volume elements and exterior or interior rooms) by physical models. Also included are models for storage processes like adsorption, desorption and release. The numerical solution is performed by semi-discretization in space (using a finite/control volume method) and subsequent integration in time (Grunewald and Nicolai 2006).

In the simulation of the material properties such as density, thermal conductivity, moisture permeability, and moisture storage function, the measured material properties from Tampere University of Technology (Vinha et al. 2005) were used.

3. RESULTS

3.1 Laboratory measurements

Full-scale laboratory measurements were performed to analyse the moisture convection performance of the joint of an external wall and attic floor and to obtain reference data to compare simulation results. Boundary conditions for the measurement series are shown in Table 1. Laboratory tests were carried out in two cycles: first, to stabilise the joint of the external wall and attic floor, the test was conducted with a closed (taped) air leakage path. This cycle continued 1…3 weeks. After that, the air leakage gap was opened between the air/vapour barrier foils (timber-frame wall/attic floor joint) and between the wall plate and AAC block (AAC wall/attic floor joint) and measurement continued in positive pressure conditions.

The first seven tests were conducted with 12 mm wood fibreboard sheathings and the last three tests were conducted with 20 mm mineral wool-board sheathings. After the first three test series, the air inflow gap was reduced to decrease the air inflow. The air flow was smaller also during three last test series, because mineral wool-board sheathing was covered with SBPO film and it was possible to tape all joints better so that the test structure became more airtight.

Table 1 Boundary conditions and determined condensation on the inner surface of the sheathings for the measurement series

Test	Tout, °C	Tin, °C	Δv, g/m3	ΔP, Pa	q, l/s@10Pa	Determined condensation on the inner surface of the sheathings		Sheathings material
						Timber-frame wall	AAC wall	
1	0	+22	+4	+20	0.31	No	Yes	12 mm wood fibreboard sheathings
2	-10	+22	+4	+20	0.31	Yes	Yes	
3	-10	+22	+4	+10	0.31	Yes	Yes	
4	0	+22	+4	+10	0.18	No	No	12 mm wood fibreboard sheathings
5	0	+22	+4	+20	0.18	No	No	
6	-5	+22	+5	+10	0.18	No	No	
7	-10	+22	+4	+10	0.18	Yes	Yes	
8	-5	+22	+4	+10	0.05	No	No	20 mm mineral wool-board sheathings
9	-10	+22	+5	+10	0.05	No	No	
10	-5	+22	+2.5	+10	0.05	No	No	
11	-5	+22	+2.5	+20	0.05	No	No	

There was condensation and frost formation on the inner surface of the sheathing of the attic floor at the end of some tests, see Figure 4 and Table 1. During the 30-day measurement period of Test 1, the increase in the mass-related moisture content of the wood fibreboard sheathing of the attic floor in Test 1 was 10 % and the final moisture content was 22 %.

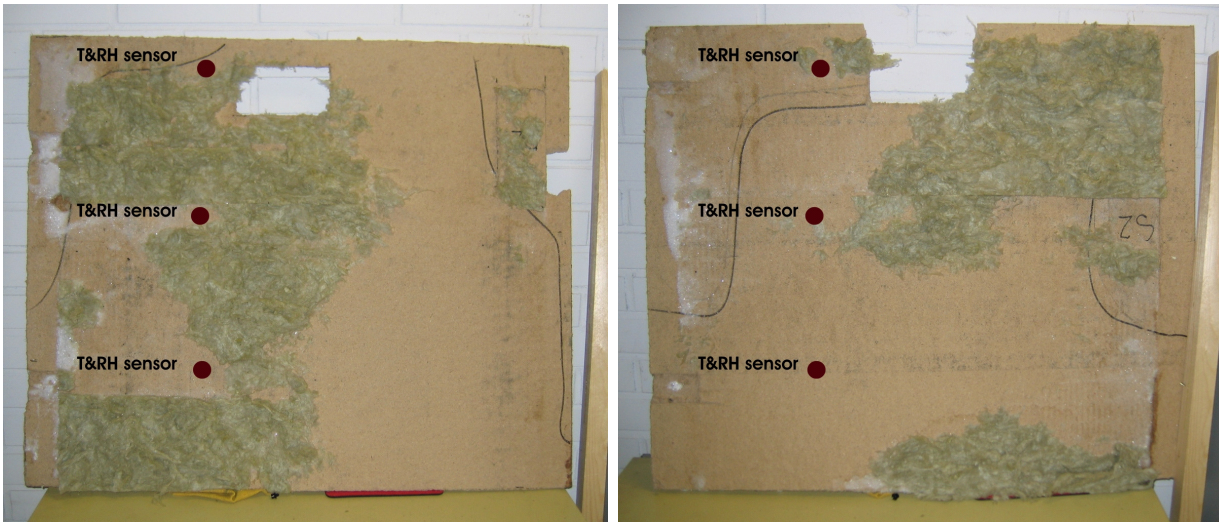

Figure 4 *Condensation and frost with mineral wool pieces on the inner surface of the sheathing of the attic floor and on the timber-frame wall (left) and the AAC wall (right).*

3.2 Comparison of laboratory tests and results of simulations

To develop the model for future analysis, the study was started with simulation program CHAMPS-BES to validated the simulation model based on the full-scale laboratory measurements. The first two cases were Test 2 (12 mm wood fibreboard sheathings) and Test 11 (20 mm mineral wool-board sheathings).

Comparison of measured (Test 2, Table 1) and simulated temperature, RH, and the humidity by volume between the outer surface of insulation and the sheathing of the attic floor (T&RH sensors 4, 5, 7 in Figure 1) are shown in Figures 5-7.

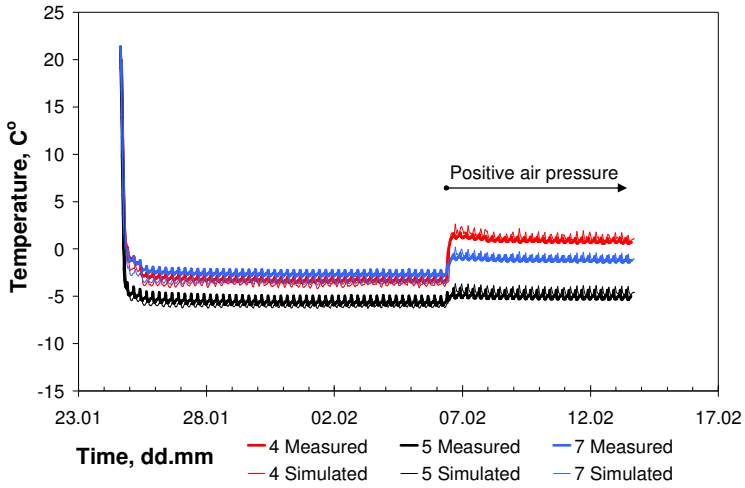

Figure 5 *Simulated and measured temperatures behind the sheathing of the attic floor in the case of timber-frame wall connection with attic floor.*

The calculated temperatures are rather accurate. RH and humidity by volume show larger difference between measured and calculated results. Measured and simulated results did not show condensation (Figure 6), but condensation and frost formation occurred of the sheathing of the attic floor (Figure 4). Reasons for that could be

the geometrical change of fiberboard sheathing whereby sheathing retreated from the surface of the insulation and lower surface temperature caused interstitial on the surface of the sheathing. The locations of the T&RH sensors were not exactly on the places, where the frost formatted. In addition, condensation of moisture may impairs the accuracy of the measurement results so that RH sensors show slightly lower values, Vinha (2007).

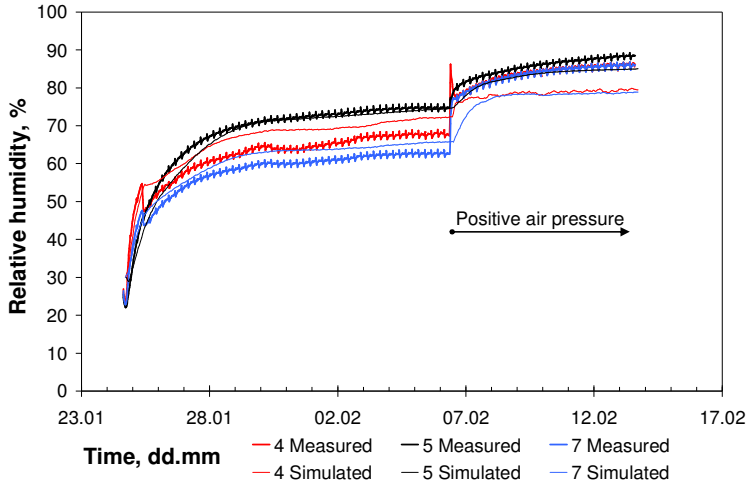

Figure 6 *Simulated and measured RH behind the sheathing of the attic floor in the case of timber-frame wall connection with attic floor.*

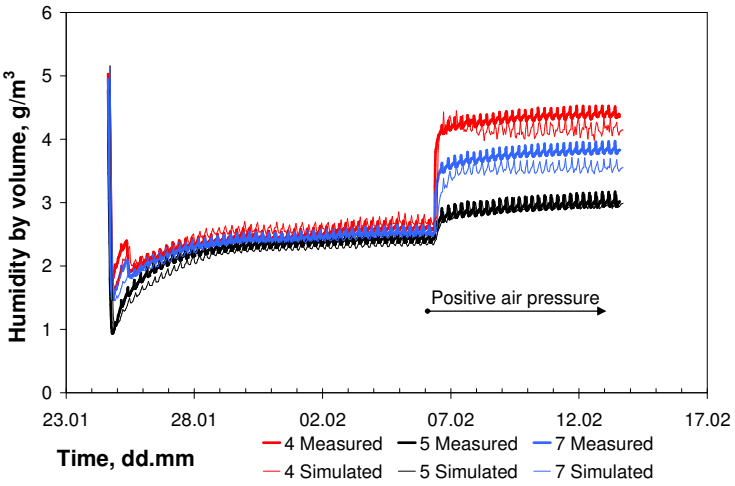

Figure 7 *Simulated and measured humidity by volume behind the sheathing of the attic floor in the case of timber-frame wall connection with attic floor.*

The simulations are continued with other indoor humidity loads, air pressure differences, air leakage conditions, and other sheathing materials to determine the influence of moisture convection to the building envelope.

3.3 DISCUSSION

There was condensate and frost formation on the inner surface of the sheathing of the attic floor in the case of positive air pressure difference +10…11 Pa and moisture excess +4 g/m^3 in the structure with 12 mm wood fibreboard sheathings. Exfiltration remarkably raised the moisture accumulation rate: during Test 1 (T_{out} -11°C), the increase in the moisture content of the wood fibreboard sheathing of the attic floor after a 30-day period was 10 % and the final moisture content was 22 %. During Test 2 (T_{out} -6°C), the frost formation took longer. Higher temperature and lower airflow rate remarkably improved the hygrothermal performance of the tested joint of the wall and attic floor.

Field measurements in Finnish detached houses (Kalamees et al. 2008) showed that one typical air leakage place was in the joint of the attic floor with the external wall. Measurements in Estonian detached houses (Kalamees 2007) showed that a more typical air leakage place was in the joint of the interstitial floor with the external wall. The RH at the connection of the intermediate floor and external wall can be rather high, causing the risk of mould growth and rot fungi when there is positive air pressure inside the building (Kalamees 2007). As the air pressure difference over the building envelope of the joint of the attic floor with the external wall is higher than in the joint of the intermediate floor with the external wall, this joint was analysed in the current study.

It is not possible to take into account the geometrical change of materials in simulation programs. Nevertheless, during measurements, the fibreboard sheathing swelled due to moisture accumulation. The joints of timber-frame and AAC walls with the timber-frame attic floor were simulated as two-dimensional joints. In reality, the convection in the joint was surely three-dimensional (see condensation areas in Figure 4). These two facts, as well as the fact that the studied joints contain small imperfections that cannot be modelled, may be the main reasons for the difference in the comparison of simulation and measurement results. There was a tendency, that the moisture accumulation continued in measurements, while, in the simulations, the moisture content remained at a fixed level (especially measurement point 4, Figure 7).

Tests with mineral wool-board sheathing showed better hygrothemal performance compared to fiberboard sheathing. Larger vapour permeability and thermal resistance caused better drying potential of the mineral wool-board sheathing. At the same time the test with mineral wool-board were conducted with smaller air flow rate, Table 1. The leakage path of on the air/vapour barrier was same in all tests, but in the case of mineral wool-board sheathing covered with SBPO film, it was possible to tape all joints better so that the test structure became more airtight. This shows that the selection of the sheathing material may play an important role for improving the airtightness of the building.

4. CONCLUSIONS

The moisture convection performance of the joint of external wall and attic floor was studied by full-scale laboratory measurements. A two-dimensional heat, air and moisture transport computer model was validated for future analysis.

Results from the laboratory measurement series showed that, in the leaky joint, the exfiltration remarkably raised the moisture accumulation rate on the inner surface of sheathing. Sheathing material with higher thermal resistance and water vapour permeability, as well higher outdoor temperature and lower airflow rate, remarkably improved the hygrothermal performance of the tested joint of the wall and attic floor.

Despite some discrepancies between the results of laboratory measurements and computer simulations, the simulation program CHAMPS-BES showed good performance and is a useful tool in assessing the moisture behaviour of building components, including moisture convection.

The results will be utilized in further analyses where relevant properties for moisture control are specified.

4.1 ACKNOWLEDGEMENT

This study was supported with a grant from the Finnish Academy (grant 210683). The authors are grateful to Professor John Grünewald and to Andreas Nicolai from Dresden University of Technology, one of the authors of the CHAMPS-BES program, for permission to use the program in this study.

4.2 REFERENCES

Brunsell, J.T., Uvslokk, S. (1980). Boligers lufttetthet: resultater fra lufttetthetsmaalinger av nyere norske boliger [Airtightness of buildings: results from airtightness measurements in new Norwegian houses]. Norges Byggforskningsinstitutt report no. 31, 1980 (in Norwegian).

Burch, D.M and TenWolde, A. (1993). Computer analysis of moisture accumulation in the walls of Manufactured housing. ASHRAE Transactions;99(2):977-990.

Granum H, Haugen T. (1986). Ventilation and indoor air quality in new Norwegian dwellings. Proceedings of AIC seventh conference “Occupant interaction with ventilation systems”, 29 September–02 October, Stratford-upon-Avon, UK, 1986. p. 10.1–10.10.

Grunewald, J., Nicolai, A. (2006). CHAMPS-BES Program for Coupled Heat, Air Moisture and Pollutant Simulation in Building Envelope Systems, version 1, 2006. User manual. 107p.

Hagentoft, C.-E., Harderup, E. (1996). Moisture Conditions in a North Facing Wall with Cellulose Loose Fill Insulation: Constructions with and without Vapor Retarder and Air Leakage. Journal of Thermal Envelope and Building Science;19(3):228-243.

Hamlin, T. (1997). Airtightness and energy efficiency of new conventional and R-2000 housing in Canada, Canada Centre for Mineral and Energy Technology, Natural Resources Canada, Ottawa (1997).

Janssens, A. (1998). Reliable control of interstitial condensation in lightweight roof systems. Calculation and assessment methods [dissertation]. Leuven: K.U.Leuven; 1998.

Janssens, A., Hens, H. (2003). Interstitial condensation due to air leakage: a sensitivity analysis. Journal of Thermal Envelope and Building Science;27(1):15–29.

Kalamees, T. (2006). Indoor hyrgothermal loads in Estonain dwellings. The 4th. European Conference on Energy Performance & Indoor Climate in Buildings. 20-22 November 2006, Lyon, France.

Kalamees, T., Vinha, J., Kurnitski, J. (2006). Indoor Humidity Loads and Moisture Production in Lightweight Timber-frame Detached Houses. Journal of Building Physics, 29(3):219 - 246.

Kalamees, T. (2007). Airtightness and air leakages of new lightweight single-family detached houses in Estonia. Building and Environment;42(6):2369-2377.

Kalamees, T., Kurnitski, J., Jokisalo, J., Eskola, L., Jokiranta, K., Vinha, J. (2007). Air pressure conditions in Finnish residences. In: Proceedings of Clima 2007 WellBeing Indoors : Proceedings CD: REHVA World Congress: Clima 2007 WellBeing Indoors; 10–14 June 2007 Helsinki, Finland. (Edit.) Seppänen, O; Säteri, J.. Helsinki: FINVAC, 2007, (CD).

Kalamees, T., Korpi, M., Eskola, L., Kurnitski, J., Vinha, J. (2008). The distribution of the air leakage places and thermal bridges in Finnish detached houses and apartment buildings. In: Proceedings of the 8th Symposium on Building Physics in the Nordic Countries: Copenhagen, Denmark, 16-18 June 2008.

Karagiozis, A. (2002). Building enclosure hygrothermal performance study phase I, ORNL/TM-2002/89, Oak Ridge National Laboratory.

Kauppinen, T. (2001). Airtightness of buildings in Finland. Proceedings of SPIE Thermosense XXIII, 16–19 April 2001, pp. 4360–36.

Kilpelainen, M., Luukkonen, I., Vinha, J., Käkelä, P. (2000). Heat and moisture distribution at the connection of floor and external wall in multi-storey timber-frame houses. World Conference on Timber Engineering Whistler Resort, British Columbia, Canada July 31 - August 3, 2000.

Korpi, M., Vinha, J., Kurnitski, J. (2004). Airtightness of timber-frame houses with different structural solutions. Proceedings of IX international conference on performance of exterior envelopes of whole buildings, 5–10 December, Session XIB, (CD), Florida, USA, 6p.

Kronvall J. (1980). Airtightness measurements and measurement methods. Stockholm: Swedish Council for Building Research, D8, 1980.

Nilsson I, Rosell L, Thorstensen E. (1982). Luftkvalitet och ventilation i täta småhus—en uppföljning av 44 Hjältevadshus byggda under åren 1982-89. [Air quality and ventilation in airtight houses—follow up of 44 houses during 1982–89]. Borås: SP Swedish National Testing and Research Institute (SP REPORT/RAPPORT), 1993. p. 18.

Ojanen ,T. and Kumaran, K. (1996). Effect of Exfiltration on the Hygrothermal Behaviour of a Residential Wall Assembly. Journal of Thermal Insulation and Building Environments; 19(3):215-227

Polvinen M, Kauppi A, Saarimaa J, Haalahti P, Laurikainen M. (1983). Rakennusten ulkovaipan ilmanpitävyys [Airtightness of the building envelope]. Technical Research Centre of Finland, VTT. Research Reports 215. Helsinki, (in Finnish).

Sherman, M.H. and Dickerhoff, D.J. (1998). Airtightness of US dwellings, ASHRAE Transaction; 104(2): 1359-1367.

Stephen, RK. (1998). Airtightness in UK dwellings: BRE's test results and their significance. Report 359, Building Research Establishment, United Kingdom, 1998.

Vinha, J. (2007) Hygrothermal Performance of Timber-Framed External Walls in Finnish Clima-tic Conditions: A Method for Determining the Sufficient Water Vapour Resistance of the Interior Lining of a Wall Assembly, Doctoral thesis, Tampere University of Technology.

Vinha, J., Valovirta, I., Korpi, M., Mikkilä, A., Käkelä, P. (2005). Rakennusmateriaalien rakennusfysikaaliset ominaisuudet lämpötilan ja suhteellisen kosteuden funktiona (Building physic material properties as a function of temperature and relative humidity). Tampere University of Technology, Department of Civil Engineering, Structural Engineering Laboratory. Research report 129. Tampere 2005 (in Finnish).

Measurement of Moisture Transport through Perforated Vapour Barriers

Petr Slanina, Ing., PhD-student,
Faculty of Civil Engineering, Czech Technical University in Prague;
petr.slanina@fsv.cvut.cz

Sarka Silarova, Assoc. Professor,
Faculty of Civil Engineering, Czech Technical University in Prague;
silarova@fsv.cvut.cz

KEYWORDS: envelope, roof, moisture transport, diffusion bridge, water vapour permeability measurement, vapour barrier, perforation.

SUMMARY:
In the European Standards EN 15026 and EN ISO 13788, moisture transport in building envelopes is assumed one dimensional. In fact, three-dimensional moisture transport occurs due to layer perforation or building assembly details. The article is focused on cases of flat roofs where the vapour barrier is perforated. Water vapour permeability measurement of different vapour barriers with different degrees of perforation is done by the wet-cup method. Results are presented. A significant increase of moisture transport is found through vapour barriers which are perforated. A note on setting the apparatus to measure materials with very high water vapour resistance factor is presented. Finally, based on the results we discussed new recommendations to design more efficient flat roofs and avoid future failures.

1. Introduction

Flat roof sandwich assemblies with classical order of layers (roof membrane, insulation, vapour barrier) are regularly designed and build in central and north Europe (Silarova, 2005) and also in cold regions of North America (Mehta et al., 2008). A vapour barrier is included in these assemblies to avoid excessive interstitial condensation of water vapour usually below the roofing membrane during cold seasons. Vapour barriers are designed based on calculations described in International and European Standards EN 15026 (2007) and EN ISO 13788 (2001). In these standards, moisture transport in building envelopes is assumed to be one-dimensional. This is correct when each roof layer is homogeneous, without any perforation, and when the roof assembly is truly planar. However, under certain circumstances, three-dimensional transport of moisture may occur in the roof assembly and then the calculations – according to the standard method – are not realistic, then failure comes, the service life is shortened and the roof assembly loses its integrity.

Three-dimensional moisture transport occurs in roof (envelope) assemblies due to several reasons:

- imperfect joining of material strips;
- bad connection of vapour barrier to openings;
- mechanically fastenings puncturing the roof layers;
- bad workmanship during construction;
- structure and assembly details;
- aging of sealing materials.

The main problem is with materials which have high sd-value and which are usually used for vapour barrier layers. We name a place of imperfection or perforation of an envelope layer a “diffusion bridge” because moisture transport noticeably increases in this place and because of similarity with the term “thermal bridge”. A diffusion bridge in the case of a perforation of the vapour barrier in the roof assembly is shown in *FIG.1.* Slanina S. and Silarova S. (2006).

It is very difficult to simulate 3D moisture transport in envelope (roof) assembly Karagiozis A.N. (2001) therefore we have decided to use measurement to show how much moisture can be transported through perforated vapour barriers. Perforations can result for example from a mechanical fixing which penetrates the vapour barrier or perforation of vapour barrier due to work negligence. We focused more on flat roof assemblies where moisture transport due to convection does not occur because roofing membranes are air impermeable.

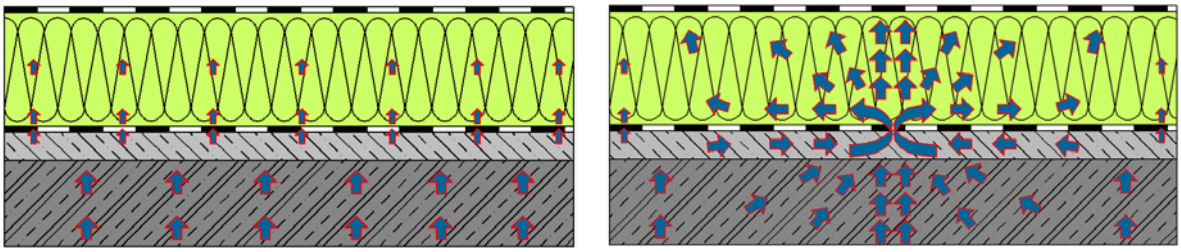

FIG. 1: 1D and 2D(3D) moisture transport in roof assembly. A diffusion bridge is demonstrated on the right.

2. Previous Work

In the past, water vapour permeability of perforated materials with high sd-value was measured by Seiffert (1960), Bauer (1965) and Mrlik F. (1985). K. Seiffert measured sd-value of 1,5 mm thick aluminium sheet with percentage of perforation from 0,01% to 0,22%. His measurements showed a significant decrease in the sd-value. W. Bauer did similar measurements. He measured sd-values of three different materials (aluminium sheet d=1mm, PVC foil, fiberglas board). The percentage of perforation for these materials was between 0,03% to 10%. His measurements show that the decrease in sd-values is greater in the case of materials with higher water vapour resistance factor (i.e. aluminium sheet). Above 1% of perforation, the sd-value does not dependent on material because all measured materials have the same sd-value with similar perforation.

The strange result of Bauer's measurement is the sd-value of aluminium sheet without any perforation because he had measured s_d = 54 m and according to standards it should be at least 1500 m. Also Bauer's and Seifert's measurements vary in sd-values of aluminium sheet for percentage 0,03% and 0,0275%. The sd-value should be higher for Seifert (greater thickness of Al-sheet and smaller percentage of perforation) but the result is twice higher for Bauer's aluminium sheet s_d = 5m than Seiffert's aluminium sheet s_d=2,02m. These two discrepancies make all the results uncertain.

Other similar measurements were done by F. Mrlik. He measured the sd-value of PE foil that was perforated by staples. First he measured sd-value of PE foil with staples then he pulled out the staples and measured the sd-value of PE foil again only with pinholes. A factor of 2 to 3 was found between these two measurements.

3. Measurements

3.1 Method

As we were not able to find other results and the results shown above are unclear, we had decided to perform our measurement in the laboratory of Faculty of Civil Engineering, CTU in Prague.

We use the wet-cup method as basis mechanism for our measurements. Advantages of this mechanism are: simplicity, low cost, accuracy, wet-cup method is described in several international standards (ASTM E 96/E 96M (2005), EN ISO 12572 (2001), EN 1931 (2000)), and also the conditions of the method are similar to real condition in roof assemblies. One disadvantage for the measurement is the long time period needed to get results.

The principle of the wet-cup method is to create two environments with different relative humidity (RH). RH inside a cup is 50% and RH outside the cup is 95%. Temperature is the same for both environments. Vapour flux then goes from the cup with higher RH through a sample to the environment with lower RH according to simple equation (1).

$$g_v = -\frac{\delta_a}{\mu(\varphi)} \nabla p_v \qquad (1)$$

where:

g_v water vapour flux [kgm^{-2}s^{-1}],

p_v water vapour partial pressure [Pa],

δ_a water vapour diffusion coefficient of dry air [kg Pa^{-1} s^{-1} m^{-1}],

μ water vapour resistance factor of measured material [-],which depends on moisture content.

The cup with the sample is weighed at regular time interval. When the vapour flux reaches steady state (decrease of mass is constant per time period), a minimum of four additional weightings are done. The sd-value of the sample is calculated using following equations.

$$\mu = \frac{\Delta t \; A \; \Delta p_v \; \delta_a}{\Delta m \; d} \tag{2}$$

Where:

Δt time difference between weighing with constant decrease of weight [s],

Δm weight difference between weighing with constant decrease of weight [kg],

A measured area of the sample [m^2],

d thickness of the sample [m],

δ_a water vapour diffusion coefficient in air [kg Pa^{-1} s^{-1} m^{-1}], calculated from simplified Schirmer's equation, see in WTA 6-2-0, (2004).

$$\delta_a = \frac{1{,}97 \,.\, 10^{-7} \,.\, T^{0{,}81}}{P} \tag{3}$$

where:

T absolute temperature [K],

P barometric pressure [Pa], we used constant value; P = 101325 Pa,

and

Δp_v water vapour partial pressure difference between the sides of the sample [Pa], EN ISO 13788 (2001),

$$\Delta p_v = \frac{\Delta rh}{100} \,.\, 610{,}5 \,.\, e^{\frac{17{,}269 \,.\, \theta}{237{,}3 + \theta}} \tag{4}$$

where:

Δrh different relative humidity between the sides of the sample [%],

θ constant temperature during the measurement [°C].

The equation (4) is for temperatures equal to or higher than zero degree Celsius ($\theta \geq 0$ °C). The sd-value of the sample is calculated using equation (5):

$$s_d = d \,.\, \mu \tag{5}$$

where:

s_d water vapour diffusion-equivalent air layer thickness (sd-value) [m].

As we measured materials with high sd-value, we assume that water vapour transfer coefficients on the both sides of the samples are insignificant and thus these coefficients are not taken into account.

Furthermore, in our calculation we did not use corrections for the sd-value calculation as are mentioned in ASTM E 96/E 96M (2005) or Mukhopadhyaya et al. (2007). These corrections are: water vapour resistance due to still air between saturated solution and specimen surface, edge mask effect and buoyancy correction. The first two corrections – water vapour resistance due to still air and edge mask effect – are insignificant in our case because the resistance due to still air is too small to compare with water vapour resistance of the samples and edge mask effect is used only for thick samples. To eliminate buoyancy effect we employed a "blind test".

3.2 Experimental set-up

The principle of wet-cup method is simple but special care is required to measure materials with very high μ-factor. The apparatus needed improvement. After three years of measurement we can recommend the following:

1. Cup – Aluminium cups of thickness 1mm were used. The cups were painted to avoid chemical reaction with saturated solution. The surface in contact with the sample and sealing material must not be painted. Glass cups are also good but quite heavy.
2. Scale – Scale resolution 0,001g is necessary (resolution 0,0001g would be even better). A scale with resolution 0,001g was used for the results presented here.
3. Area of the sample – The area of samples should be as large as possible. Samples with measured area 0,03m^2 were used here.
4. Sealing material – The sealing material is the most important technical issue to obtain accurate measurement results as shown is several round-robin tests, e.g. Toas M. (1989) or Time B. and Uvsløkk S. (2003). Four sealing materials (silicon, bee wax, bitumen mastic and butyl mastic) were tested for half a year with help of the "blind tests". The blind test is a measurement where the sample is replaced by the material from which the cup is made. In this case aluminium sheets (1mm) were used instead of samples. Butyl mastic was finally chosen from the following reasons: almost impermeable for water vapour, almost no moisture adsorbed, good adhesion, easy to fit and no chemical reactions with sample or aluminium cup.
5. Monitoring – Relative humidity and temperature outside of the cups were monitored every half an hour. RH inside of the cups was monitored only once and atmospheric pressure was monitored every time when the samples were weighed.
6. Set-up – Three or four cups with samples and one cup as the blind test were used in the same time period. The blind test was used to compensate for leakage and varying atmospheric pressure. A suggestion of similar principle can be found in ASTM E 96/E 96M (2005). The final sd-value should be calculated by equation (6),

$$s_{df} = \frac{\sum s_{dn}}{n} - \frac{\sum s_{d\,i}}{i} \qquad (6)$$

where:

s_{df} final sd-value of the material [m],
s_{dn} the sd-value of each sample [m],
sd_i the sd-value of each blind test [m],
n number of samples [-],
i number of blind cups [-].

The schema of final experimental apparatus is outlined on *FIG.2* and real experimental apparatus is shown on *FIG.3*.

3.3 Procedure of Measurement

First we measured materials without any perforation. We perforated vapour barrier materials with a sharp pin after four or five weightings which had showed constant decrease of mass. Then we weighed cups with perforated samples and after four or five constant decreases of the mass per time period we perforated samples again with higher percentage of perforation and etc.

The area of the perforation was calculated from the diameter of the pin. The sample with 1, 3, 6, 12 and 24 holes were measured and sd-value was calculated. The holes evenly positioned over the surface of samples.

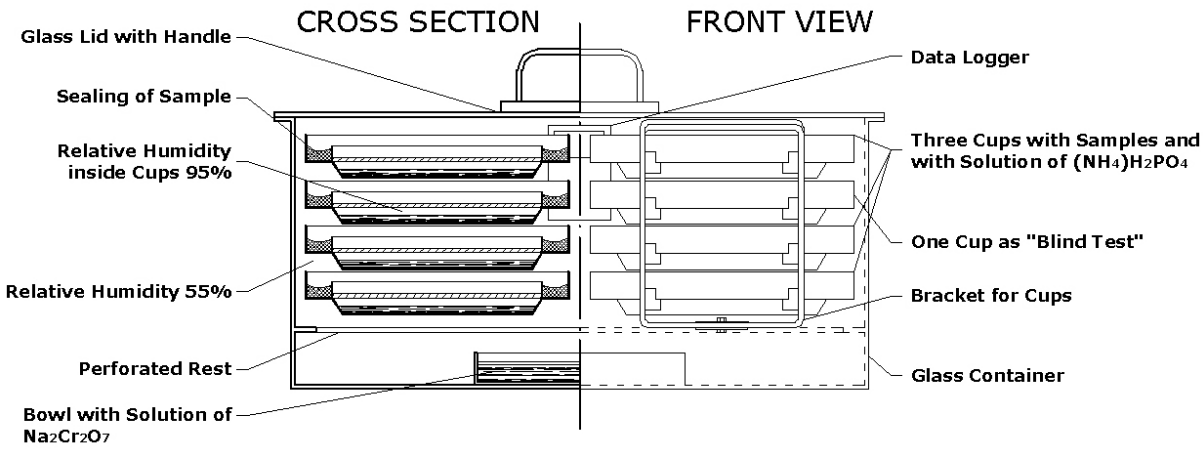

FIG. 2: Schema of experimental apparatus for water vapour permeability measurement

FIG. 3: Final experimental apparatus for water vapour permeability measurement with only one tray of cups.

4. Results of Measurement

Measurements of sd-value were made in the laboratory of Faculty of Civil Engineering, CTU in Prague on five different materials; three foil membranes and two bitumen membranes. The results of the measurement are shown in tables 1-4 and were calculated with help of equations (2)-(5).

TABLE 1: Results of the measurements, the sd-value of perforated vapour barrier – Material A

Material A: Polyethylene	Number of samples: $n = 4$	Thickness: $d = 0{,}15$ mm	Manufacturer's sd-value: $s_{dp} = 21$m
Percentage of perforation [%]	Average sd-value [m]	Standard deviation [m]	
0,0000	86,0	14,8	
0,0024	47,4	2,0	
0,0071	30,5	1,5	
0,0143	20,3	0,8	
0,0285	12,5	0,3	
0,0570	6,7	0,1	

TABLE 2: Results of the measurements, the sd-value of perforated vapour barrier – Material B

Material B: LD Polyethylene	Number of samples: $n = 3$	Thickness: $d = 0{,}22$ mm	Manufacturer's sd-value: $s_{dp} = 198$m
Percentage of perforation [%]	Average sd-value [m]	Standard deviation [m]	
0,0000	187,6	19,0	
0,0024[a]	109,2	0,9	
0,0071	49,1	4,1	
0,0143	30,2	1,6	
0,0285	16,1	0,5	
0,0570	8,5	0,2	

[a]Only two samples of Material B were calculated in this percentage of perforation

TABLE 3: Results of the measurements, the sd-value of perforated vapour barrier – Material C

Material C: LD/HD Polyethylene	Number of samples: $n = 3$	Thickness: $d = 0{,}30$ mm	Manufacturer's sd-value: $s_{dp} = 360$ m
Percentage of perforation [%]	Average sd-value [m]	Standard deviation [m]	
0,0000[a]	661,9	107,7	
0,0024	192,4	13,6	
0,0071	57,5	2,7	
0,0143	30,4	0,5	
0,0285	13,9	0,4	
0,0570	7,8	0,1	

[a]Due to lack of time only three weightings with constant decrease of mass where used to calculate the average sd-value of non-perforated Material C.

TABLE 4: Results of the measurements, sd-value of perforated roof membrane – Material D

Material D: Bitumen membrane	Number of samples: $n = 4$	Thickness: $d = 2{,}7$ mm	Manufacturer's sd-value: $s_{dp} = 130$ m
Percentage of perforation [%]	Average sd-value [m]	Standard deviation [m]	
0,0000	137,1	21,8	
0,0024[a]	181,9	26,9	
0,0056[b]	144,0	4,3	
0,0113[b]	84,4	6,9	
0,0169[b]	89,8	5,9	
0,0338[b]	64,4	7,7	
0,0675[b]	41,4	1,3	

[a]A hot pin(ø =0,975 mm) was used to perforate samples.
[b]A hot pin(ø =1,26 mm) was used to perforate samples.

Another bitumen membrane with thin Aluminium sheet was also measured. To determine the steady state of water vapour flux through the membrane was impossible during period of two months and thus the measurement was stopped.

5. Discussion of Results

The results of the measurement show a significant decrease in sd-values of materials which have high water vapour resistance factor and which are perforated. The decrease in the sd-value is greater for materials with

higher value of water vapour resistance factor. This result is in accordance with the measurements in Bauer (1965).

We found very interesting that sd-values for foils (Material A,B and C) does not depend on the material for percentage of perforation higher than 0,03%; all three vapour barriers have almost the same sd-value, see in *FIG.4.*

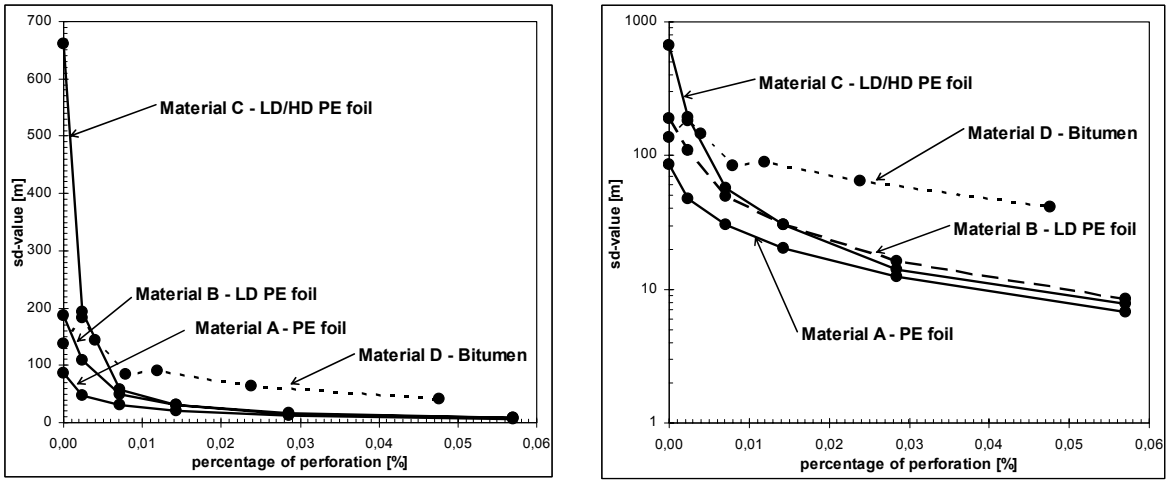

FIG. 4: Dependence of sd-value on percentage of penetration – regular, logarithmic scale

On the right side of *FIG.4* can be seen a crossing of curves (Material B and Material C). The crossing is probably due to difference in an area of pinholes. The area of pinholes has not been checked for example by a microscope.

The decrease in the sd-value is greater for foil membranes than for bitumen membrane. We assume that this is due to a contraction of the pinholes after perforation, but other measurements are needed. Great adsorption of moisture was observed in the bitumen membranes unlike foil vapour barriers. The adsorption and the fact that to perforate bitumen membranes is more difficult – we had to use a hot sharp pin – probably caused that the curve of bitumen membrane (Material D) is not so smooth.

The results show exact measurement up to 200m of sd-value. The results above this level are varied more than 10%. Blind tests that were employed during the measurements confirmed the good sealing quality of butyl mastic. We used three blind tests with samples of Material B, C and with bitumen membrane with aluminium sheet. These blind tests ran in the same time in two glass containers showed different changes in weight. During a period of 105 days two blind tests showed increase in weight 0,07g and 0,20g and the third blind test decreased in weight 0,11g. This difference was mainly caused at the beginning of the measurement. If we look at period between 40^{th} and 105^{th} day we will find the difference in weight 0,001g, 0,037g and minus 0,077g. We assumed that the difference was caused by dirt on the surface of aluminium sheets because the sheets had been used before for testing of different sealing materials. Due to this difference we did not employ the equation (6) for final sd-values.

6. Conclusion

We described in the first part of the paper some problems with simulation of moisture transport in building envelopes and what diffusion bridges are. Some recommendations on how to measure water vapour permeability of materials with high sd-value were provided. The most important points are to use the setup of cups with samples and cups as a blind test and as the sealing to use butyl mastic.

The results of our measurement show significant increases of vapour transport through vapour barriers due to a small percentage of perforations and that is the reason why a perforation of a vapour barrier and multidimensional moisture transport must be taken in an account when a simulation of moisture transport is done in building envelope assemblies especially when it is known in advance that the multidimensional moisture transport will occur (e.g. mechanical fixing, building details).

7. Acknowledgement

This research has been supported by the Ministry of Education, Youth and Sports under Contract No. MSM6840770001. Thank you.

8. References

ASTM E 96/E 96M (2005). *Standard Test Methods for Water Vapor Transmission of Materials*. ASTM International. West Conshohocken. USA. 11p.

Bauer W. (1965). Influence of holes on water-vapor permeability of vapor-checking surface layers, *Symposium Moisture Problems in Buildings,* RILEM-CIB, Helsinki, Finland.

EN 15026 (2007*). Hygrothermal performance of building components and building elements – Assessment of moisture transfer by numerical simulation.* CEN; 2007.

EN 1931 (2000). *Flexible sheets for waterproofing. Bitumen, plastic and rubber sheets for roof waterproofing. Determination of water vapour transmission properties*, CEN, 14 p.

EN ISO 12572 (2001). *Hygrothermal Performance of Building Materials and Products – Determination of Water Vapour Transmission Properties*, CEN, 27p.

EN ISO 13788 (2001). *Hygrothermal performance of building components and building elements - Internal surface temperature to avoid critical surface humidity and interstitial condensation - Calculation methods.* CEN; 2001.

Karagiozis A.N. (2001). Advanced Numerical Models for Hygrothermal Research, *Moisture Analysis and Condensation Control in Building Envelopes*. (Trechsel H.P., editor), ASTM, Philadelphia, USA, 90-106.

Mehta M., Scarborough W. and Armpriest D. (2008). *Building construction: principles, materials, and systems,* Upper Saddle River, New Jersey, USA, 992 p.

Mukhopadhyaya, P., Kumuran, M.K., Lackey, J. and van Reenen, D. (2007). Water vapor transmission measurement and significance of corrections. *Journal of ASTM International,* Vol. 4, No. 8, p.1-12

Mrlik F. (1985). *Vlhkostne problemy stavebnych materialov a konstrukcii (Moisture problems of building materials and structures),* Alfa, Bratislava, Slovakia, 269p.[in Slovak]

Seiffert K. (1960). Messungen von Diffusionswiderstandsfaktoren (Measurements of Diffusion Resistance Factors). *Kaltetechnik,* Vol.12, No. 7, p.187-190 [in German]

Silarova S. (2005*).* Jednoplášťové střechy (Compact roofs), *Ploche strechy (Flat roofs),*(Hanzalova L. and Silarova S., editors) Informacni centrum CKAIT, Prague, Czech Republic, 325 p. [in Czech]

Slanina P. and Silarova S. (2006). Difuzni mosty (Diffusion bridges). *Strechy, fasady, izolace,* Vol. 13, No. 4 p.66-67 [in Czech]

Time B. and Uvsløkk S. (2003). *Intercomparison on measurement of water vapour permeance*, Norges byggforskningsinstitutt, Oslo, Norway, 29p.

Toas M. (1989) Results of the (1985) Round/Robin Test Series using ASTM E96-80, *Mechanisms and Measurement*, ASTM STP 1039, (Trechsel H.R and Bomberg M., editors) American Society for Testing and Materials. Philadelphia. USA. p.73-90

WTA 6-2-0 (2004). *Simulation of heat and moisture transfer*, WTA Publicatons, Munchen, Germany, 16p.

Simulating the Energy Benefits and Reduction in Condensation Formation that is obtained from Houses with Cold Pitched Roofs

Emmanuel Adu Essah, PhD Student,
RICH Centre, School of BNE, Glasgow Caledonian University, Glasgow;
ees1@gcal.ac.uk

Chris H. Sanders Mr,
RICH Centre, School of BNE, Glasgow Caledonian University, Glasgow;
C.H.Sanders@gcal.ac.uk

Paul Baker, Dr,
RICH Centre, School of BNE, Glasgow Caledonian University, Glasgow;
Paul.Baker@gcal.ac.uk

Graham H. Galbraith, Professor,
Glasgow Caledonian University, Glasgow;
G.H.Galbraith@gcal.ac.uk

Angela Sasic Kalagasidis, Dr,
Department of Building Technology, Chalmers University of Technology, Sweden;
Angela.Sasic@chalmers.se

KEYWORDS: *Vapour permeable underlay, airtightness, condensation, cold pitched roofs, HAM Tools*

SUMMARY:
Ventilation often accounts for a significant portion of the heating or cooling load and also affects the moisture levels of buildings. Arguably in the UK, houses with cold pitched roofs, with insulation on a horizontal ceiling, are the most vulnerable to the formation of condensation in the roof. This study is a numerical investigation that compares the occurrence and the risk of condensation formation in a cold pitched roof fitted with two underlay (a vapour permeable underlay (VPU) and an impermeable bituminous felt). The energy benefits that would be obtained from reducing the ventilation gaps in the eaves and improving the airtightness of the ceiling are investigated. In order to visualize these effects, several cases and scenarios have been modelled with a HAM software package. The results showed that, the VPU with a very low vapour resistance, Sd< 0.02 is most effective in reducing condensation formation when the roof is sealed. It was observed that reducing the thickness of insulation on the ceiling would increase the energy losses but would reduce condensation formation risks. To a large extent, the proposed characteristic performance of the VPU as predicted by manufacturers and some researchers may only be realistic if gaps in the ceiling are sealed off completely when houses are being built, which may be practically difficult given current construction practice. Substantial energy gains were predicted when the roof was completely sealed off. Ideally, reducing the overall tightness of the building envelope to smaller air change rates (<5 ach at 50 Pa), would reduce the airflow through the ceiling, and would help in controlling condensation formation in the roof as well as reduce the energy loss through the roof and hence of the building as a whole.

1. Introduction

Building designs of the past were simple and took into account the environmental conditions. However, at the end of the 19th century, new building construction technology with increasing complexity and size was introduced (Essah et al 2006a). As a result, thermal insulation levels were increased and buildings were better sealed. This eventually led to colder loft spaces, higher internal vapour pressure and complaints of condensation problems within the loft space (Sanders and Haig 2004; Essah et al 2006b). This contributed to the persistent problems associated with *cold pitched roofs* in the United Kingdom (UK) (i.e. those with insulation on a horizontal ceiling, which make up 75- 80% of domestic roofs in UK) (Essah at al 2006a).

One key factor that has contributed to these effects is air movement. Air movement in and around buildings has a major influence on the efficiency and effectiveness of space heating and cooling load of a building as well as the moisture levels in buildings (Riffat and Eid 1988; Jones and Whittle 1992).

In recent years, several methods of resolving these problems, the risk of condensation formation coupled with maintaining an energy efficient house, have been suggested. One such proposed remedy has been the manufacture and introduction of vapour permeable underlay (VPU) (Essah et al 2006b) as a replacement for the traditional bituminous felt (1F felt) in cold pitched roofs, as characterised in BS EN 13707 (NHBC 2006).

The inception of this technology in roofs has been talked about continuously with regard to issues raised by manufacturers and some researchers. They have argued that there is no need for eaves and/or ridge ventilators because the roof 'breathe' through the VPU (i.e. with a breathing roof, moisture vapour from the building can easily diffuse through the VPU) (NHBC 2006; Essah et al 2006b). However, for the VPU to work properly, it implies that any moisture vapour entering the roof from rooms below (kitchen, bathroom etc) needs to pass through to the outside. If the amount of moisture vapour exceeds what can pass through the underlay at any given time, there is a high risk of condensation forming on the underside of the underlay (NHBC 2006).

Considering the second issue, studies by Sanders and Haig (2004) suggest that reducing the air flow through the eaves into the loft will significantly improve the energy efficiency of the roof and consequently reduce the energy consumption of the house (Sanders and Haig 2004). However, the fact still remains that occupancy behaviour (relative to household numbers) such as opening or closing windows and doors has a substantial impact on the total energy consumption of a building (Santamouris et al. 1998).

In order to visualize these effects, three cases have been modelled with a HAM software package. Ideally, to understand the effects of these influencing factors: all the necessary parameters affecting building structures, including; wind speed, temperature variations, positions of leakage paths and ventilation systems must be monitored for all surfaces. However, as in most experimental research work, this is not usually the case because of limited resources, resulting in limited data or information. The use of modelling softwares has therefore evolved over the past years to help resolve some of these limitations (Blocken et al. 2005; Chen and Kooi 1988).

This paper discusses the results obtained from a numerical investigation of the occurrence and risk of condensation formation in a cold pitched roof fitted with two different underlay (a VPU and a bituminous felt) as well as the energy benefits that would be obtained from reducing the ventilation gap in the eaves and improving the airtightness of the ceiling. In another instance the possible variation of energy consumption by varying the insulation levels of the ceiling is investigated. These analyses are achieved by a HAM (Heat, Air and Moisture) modelling tool, using a Matlab modelling platform with a Simulink simulation tool.

2. The Numerical Model

The numerical HAM model is designed and developed using Simulink, a graphical programming environment. It is developed as a library of block diagrams, where each block represents a particular building structure. These models are basically one dimensional (1D), and governed by mathematical equations. Since it was first developed, it has been improved and validated with experimental results (Sasic 2004 and 2007).

In this study, the modelled structure is based on dimensions obtained from a standard duo-pitched house with a typical cold pitched roof construction. Though the model considers the entire dimensions of the house (developed in the workspace), the graphical interface, shows only that of the roof. The building is a two storey house of height measuring approximately 7.1m (i.e. 5.1m from the ground to the ceiling and 1.96m from the ceiling). The dimensions of the roof are 9.7m span and 6.8m wide and pitched at a 30° angle. The ceiling floor covers an area of 66.0m^2 and the volume of the roof is approximately 64.7m^3.

Mineral wool of thickness, approximately 250mm was laid on the ceiling in conformity with requirements of the UK Building Regulations. The distribution of air leakage paths is considered to be concentrated around the windows, doors and less concentrated around non-visible penetration paths (such as gaps and cracks). For the purpose of this study, it is assumed that the walls are of equal leakage paths and the floor of the house is completely airtight. The ceiling was modelled based on practical situations with the air leakage (permeability) factor identified by a parameter *"b"*. Within the model, it is assumed that the ceiling is very air permeable if b = 1 and completely sealed if b = 0. In this study these two extremes (b= 0 and b=1) are modelled for the cases under investigation. However, depending on the permeability of the ceiling, "b" can be set to values between 0 and 1.

The internal conditions for condensation modelling and calculations in a house are dependent on the moisture content or vapour pressure distribution of the air in the building. This is primarily determined by sources of moisture production (cooking, washing and drying of clothes and other forms of washing are identified as producing most water vapour), which are influenced by the household occupancy levels and ventilation rates (CIBSE 2006).

2.1 Visualising the problems

Modelling the formation of condensation in a roof and its materials is currently the ideal option to visualise its effects. This is because measuring condensation is practically difficult if not impossible. Integrated within the model are algorithms to estimate the amount of condensate that forms in the roof space when fitted with different underlays of known resistance.

When the surface temperature of the underlay is less than the dew point temperature of the air in the loft, vapour will condense at the surface of the underlay. From Figure 1, if the $P_{loft} > P_{sat}(T_s)$ then condensation is formed on the underside of the underlay. However, if $P_{loft} < P_{sat}(T_s)$ then it shows the moisture transfer ($M_{Transfer}$) through the underlay and hence no condensation formation (Figure 1).

$$g_{cond} = \beta_p * \left[p_{loft} - p_{sat}(T_s) \right] A \qquad (1)$$

Where g_{cond} is the amount of condensate, kg/s; A is the surface area, m^2; β_p is the moisture transfer coefficient in the loft space, kg/s·m^2·Pa; P_{loft} is the vapour pressure in the loft space, Pa, P_{sat} is the saturated vapour pressure, Pa and T_s is the surface temperature of the underlay, °C.

It must be noted that, the amount of condensate (g_{cond}) appears as a moisture sink, implying relative humidity (RH) in the loft will drop when condensation occurs. g_{cond} is integrated over time to obtain the total amount of condensate during the year, G_{cond} in kg.

$$G_{cond} = \int_0^t g_{cond}\, dt$$

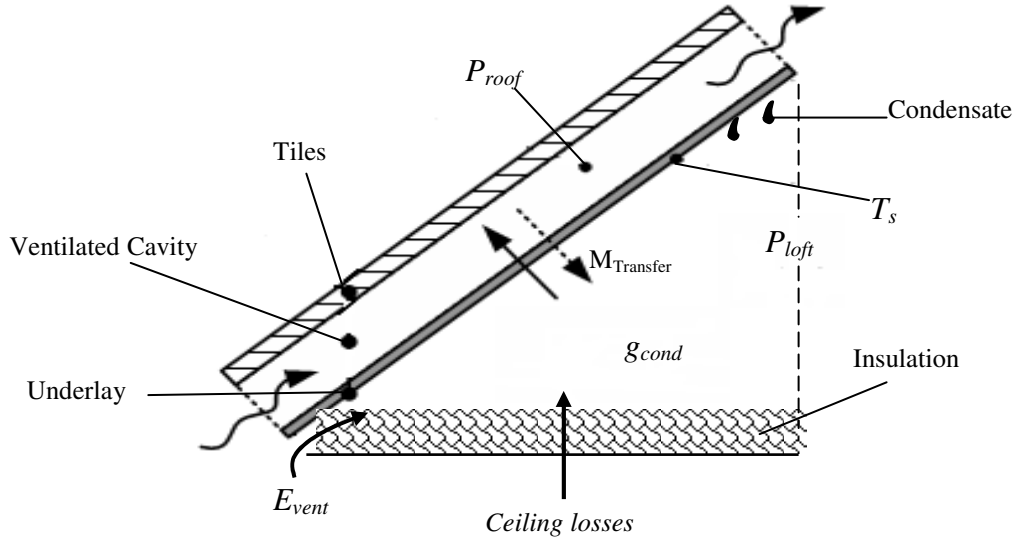

FIG 1: Cross-sectional diagram illustrating the likelihood of condensation formation on the underside of the underlay

The energy losses across the ceiling are also monitored within the model. This is necessary in order to understand the effects of air movement into the roof through the eaves (E_{vent}) and through the ceiling into the loft

on the energy efficiency of the roof. These are in two separate forms; one is due to the ventilation (leakage) losses through the ceiling in the loft and the other due to the transmission losses (i.e. by conduction).

2.1.1 Case Study

To understand how the underlay responds, the building envelop was considered for a typical tightness (n_{50}) value of 5 ach, as would be typical for UK houses. Since airflows are the major contributing factor for moisture transport, it was considered in all aspects of the study. The two underlays were compared; one of which is the normal bituminous felt with resistance of 200 MNs/g (i.e. Sd = 40m) while the second is a VPU with resistance of 0.1 MNs/g (i.e. Sd = 0.02m). The following cases were categorised to give further insight into the problems at hand. In all these cases, both energy benefits and condensation formation risks effects are analysed.

- **Case 1:** the initial study considers a house with n_{50}= 5 ach and of high occupancy. In this, the vapour transfer through the ceiling is by diffusion and air convection and with varying eaves gap sizes and ceiling permeability factors.
- **Case 2:** in this, a similar situation to that of case 1 is considered but with a tighter leakage factor of n_{50}= 2 ach for only one eaves gap scenario.
- **Case 3:** this case compares the energy benefits that would be obtained by enhancing the insulation levels on the ceiling and the effects that it would have on condensation formation risk.

These cases were chosen to reflect arguments related to problems that are associated with cold pitched roof in the UK.

2.2 Results

Considering the cases in this study, when the model has n_{50} reduced from 5 to 2 ach, the whole building envelope is tightened which reduces the air flows from outside to the house. However, as illustrated throughout this study, the ceiling can also be tightened by reducing the leakage factor "b" from 1 through to zero (as discussed above). All cases were modelled for households with high occupancy (a 5 person household). The results obtained from these cases are discussed in this section.

2.2.1 Case 1

Table 1 illustrates the results obtained when case 1 was modeled. From the results it is noticed that, sealing the ceiling off completely (i.e. b = 0), as well as the eaves, from any infiltrations and ventilation would be an ideal option to reduce the risk of condensation formation. Setting b = 0, may be practically difficult to achieve, for instance in the UK (i.e. due to pipe works and recessed lights and other services that are fed through the ceiling into the roof), but not impossible.

Comparing the two underlays (bituminous felt and the VPU), the VPU is most effective in reducing the formation of condensation when there is no eaves gap. In addition, it is equally more effective than the bituminous underlay as eaves gap size increases, though substantial amounts of condensate are formed in roofs with both materials. From this model, though ventilation helps to reduce the amount of condensate formed, sealing the roof off completely would be the most appropriate option.

With regard to energy benefits, irrespective of the roof underlay used, the losses due to leakage through the ceiling are the same for a particular eaves gap size. To reduce the losses and hence improve the energy efficiency of the roof and the house, the ceiling gaps should be reduced considerably. The results obtained show that, ventilation (leakage) losses increase with increasing eaves gap while the transmission losses which are due to the temperature variation across the ceiling are relative the same between 13-15 kWh/m^2.

The results also shows that significant energy benefits would only be obtained if the eaves gap could be reduced to less than 3mm, beyond this (i.e. between 3mm and 20mm) energy losses are high and relatively the same (Table 1). This confirms the results obtained in a study performed by Sanders and Haig (2004). Figure 2 shows the trend of leakage losses into the loft space due to the ceiling leakage. It shows that during the summer months, there is some energy gain.

TABLE. 1: Illustrates the effects that are obtained when the eaves gap and ceiling leakage factors of the roof are varied for a building tightness of 5 ach.

Eaves Gap [mm]	Leakage factor *"b"*	Condensation [kg/yr]		Annual Losses (due to leakages)
		Bituminous Felt	VPU	[kWh/m^2]
0	0	87	2	0
	1	94	5	0
3	0	0	0	0
	1	625	596	52
5	1	546	516	54
20	1	416	382	58

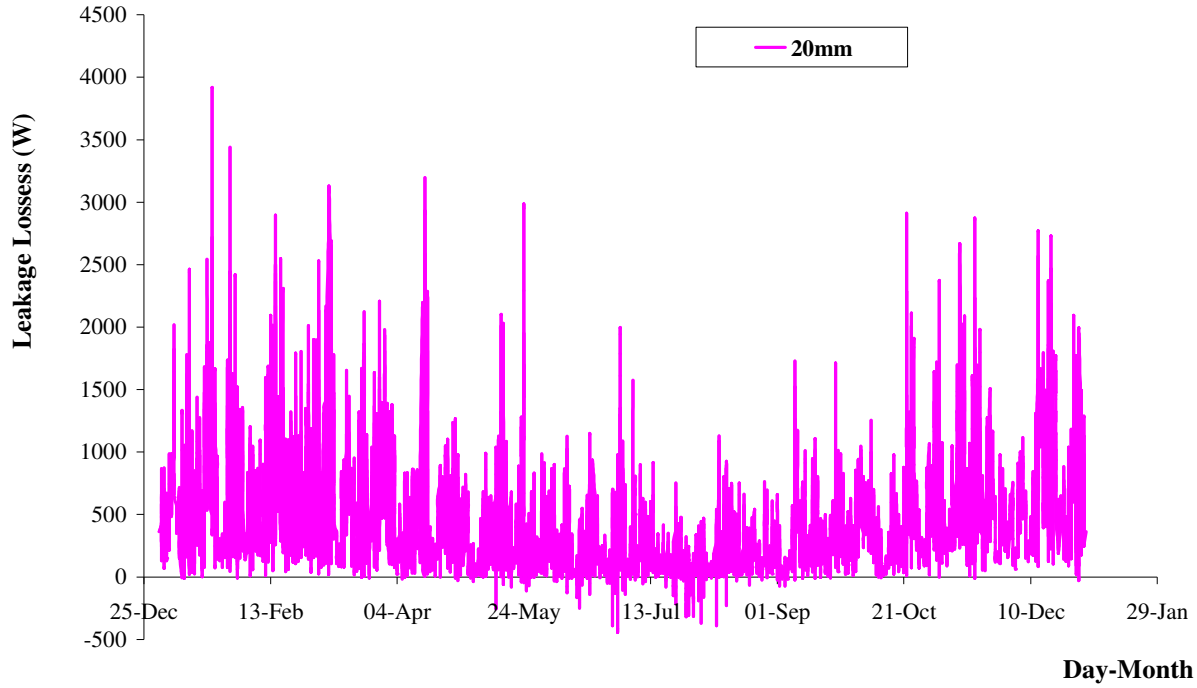

FIG 2: Illustrates the leakage losses through the ceiling for a 20mm eaves gap size

2.2.2 Case 2

Considering the roof with bituminous felt , 20mm eaves gap and a leakage factor of b =1, Table 2 illustrates the fact that reducing the overall tightness of the house from n_{50} = 5 to n_{50} = 2 would reduce the overall risk of condensation formation by about 50% and energy losses through the roof by approximately 42%. From previous studies, Sanders and Haig (2004) identified that for a UK house, 10% of the annual energy losses from the house is through the ceiling. Considering this basis, tightening the building envelope to 2 ach (as in this case) would reduce the losses by at least 4% which is a significant energy gain.

Research shows that this possibility is achievable but can only be attained by putting parameters in place from the onset of building a house (AIVC, 2006). In this example, the vapour pressure inside the dwelling is the same as that of n_{50}=5. In modelling this case (n_{50}=2), the house is modelled as a house with mechanical ventilation

(exhaust-supply ventilation), where the vapour pressure can be kept at the desired level (high or normal for simulations).

This comparison is made in relation to building constructions in Norway and Sweden, where the building envelope is made tighter and the internal vapour pressure is kept at the desired (AIVC, 2006) levels by the introduction of mechanical ventilation systems. If this system was not considered, then like most houses in UK, making the building tighter, would increase the internal vapour pressure, which would increase the flow through the ceiling and hence increase in the risk of condensation formation in the roof.

TABLE. 2: Illustrates the benefits that would be obtained from a tighter building envelope.

n_{50}	Condensation [kg/yr]	Annual Losses (due to leakages) [kWh/m^2]	Transmission Losses [kWh/m^2]	Total Annual Energy Losses [kWh/m^2]
2 ACH	211	27	14	41
5 ACH	416	58	13	71

2.2.3 Case 3

This case compares the energy benefits that would be obtained by enhancing the insulation of the ceiling with possible variation of energy consumption. To access the effect of the insulation, the ventilation gap was kept constant at 20mm for the same underlay (bituminous felt) and for a constant ceiling leakage factor of b=1.

Comparing the effects less insulation (i.e. 50mm thick) on the ceiling would reduce the condensation formation risk significantly. However, it would increase the total annual energy losses across the ceiling into the roof. This is because though leakage losses increases with insulation thickness, the transmission losses decrease significantly with insulation thickness, as illustrated in Table 3. Considering the design and construction of UK houses (at 5 ach),the model shows that increasing the insulation on the ceiling would go to increase the condensation formation risks but would decrease the losses through the ceiling to the roof.

TABLE. 3: Illustrates the effects of varying insulation thickness on the ceiling of the roof

Insulation Thickness [mm]	Condensation [kg/yr]	Annual Losses (due to leakages) [kWh/m^2]	Transmission Losses [kWh/m^2]	Total Annual Energy Losses [kWh/m^2]
50	299	53	48	101
100	376	56	29	85
250	416	58	13	71
500	423	59	7	66

3. Conclusions

The analysis in this paper, has demonstrated that both energy benefits and condensation formation risks in a *cold pitched roof* are significantly dominated by air movements into the loft through the ceiling and from the outside through ventilation vents. This study was performed using a simulation tool for a whole building HAM design with a Matlab software package. Within the contest of this study, the following deductions and conclusions are made about houses in UK with cold pitched roofs:

- Comparing the two underlay, the VPU responds better to reducing the risk of condensation formation in the roof in all scenarios (case 1). However, it is most effective when the roof is completely sealed.
- Ventilating the loft space does improve the risk of condensation formation slightly though not significantly because ventilation does to some extent increase the moisture loads. However, the overall energy losses through the ceiling are increased with increase ventilation.

- As demonstrated, to improve the energy efficiency of the house and reduce the risk of condensation formation, the quality of ceilings should be improved by sealing the gaps around pipes, recess lights amongst others to prevent air infiltration into the roof from occupied spaces. This is of importance because air movement in houses are coupled with the transfer of moisture.
- An alternative strategy to improve these two parameters is to improve the airtightness of the building (including the ceiling) by reducing its n_{50} value from 5 ach to 2 ach. This approach improves the energy efficiency and the condensation risks by at least 42%.
- In another development, increasing the insulation thickness on the ceiling does improve the overall energy efficiency of the roof but does increase the condensation formation risks considerably.

The results presented in this paper provides insight into the effects of airflows into cold pitched roofs to control condensation formation risks and improve the energy benefits of the roof as well as the house. In all aspect of this study, the analysis would not support these energy benefits and condensation formation reductions, unless the loft can be thoroughly sealed, which within limits of human error are practically difficult to achieve.

4. References

AIVC, (2006) Air Information Review. A quarterly newsletter from the IEA Air Infiltration and ventilation Centre (AIVC). Vol 27, No.4, pp 3-4.

Blocken B., Roels S. and Carmeliet J. (2005). A combined CFD-HAM approach for wind-driven rain on building facades. *Journal of Wind Engineering and Industrial Aerodynamics,* p. 1-23.

British Standards, BS EN 13707 (2004). Flexible sheets for waterproofing-Reinforced bitumen sheets for roof waterproofing-Definitions and characteristics

Chartered Institute of Building Services Engineers (CIBSE) (2006) Environmental Design: Guide A. **Section 7**, pp. 7.1-7.4

Chen Q. and Van Der Kooi J (1988). Accuracy- A program for combined problems of energy analysis, indoor air flow and air quality. *ASHRAE Transactions,* No. 3158, p. 196-214.

Essah E.A., Sanders C.H., Baker P., Galbraith G.H. and McLean, R.C. (2006a) Comparing experimental measurements and modelling of airflow patterns in a house and its loft space. *Proceedings of the Healthy Buildings (HB 2006) conference,* Lisbon, Vol 4, p. 415-420.

Essah E.A., Sanders C.H., Galbraith G.H. and McLean R.C. (2006b). Airflow between houses and their roofs. *Proceedings of the Third international Building Physics Conference*, *Research in Building Physics and Building Engineering*, Concordia University, Montreal,Canada., p. 737-744.

Jones P.J. and Whittle G.E. (1992). Computational Fluid Dynamics for building air flow prediction-current status and capabilities. *Journal of Building and Environment,* Vol 27, No.3, p 321-338.

National Housing Building Council (NHBC) (2006) *NHBC's technical news letter*- Standards Extra, Vol 36**.** Available at: http://www.nhbcbuilder.co.uk/NHBCpublications/LiteratureLibrary/Technical/StandardsExtra/filedownload,27506,en.pdf), (accessed 8 February 2007).

Riffat S.B. and Eid M. (1988). Measurement of Air flow between the floors of a house using a portable SF_6 system, *Journal of Energy and Buildings,* Vol 12, p 67-75.

Sanders C.H. and Haig J. (2004). Heat, air and moisture transport through cold pitched roofs: *CIB W40*, Glasgow meeting, p 1-13

Santamouris M. et al. (1998). *Natural ventilation in buildings*: *a design handbook*. London-UK, James and James (Science Publisher) Ltd. p. 1-4.

Sasic Kalagasidis A. (2004) HAM-Tools: An Integrated Simulation Tool for Heat, Air and Moisture Transfer Analyses in Building Physics. PhD Thesis, p. 1-5.

Sasic Kalagasidis A. (2007). Simulations as the way of bridging the gaps between desired and actual hygrothermal performance of buildings. *Building Simulation Conference 2007*, Beijing, China

Indoor air humidity in Norwegian houses

Stig Geving, Dr.Ing.
SINTEF Building and Infrastructure, Norway;
stig.geving@sintef.no and www.sintef.no/byggforsk

Jonas Holme, Cand Scient, PhD-fellow,
SINTEF Building and Infrastructure, Norway;
jonas.holme@sintef.no and www.sintef.no/byggforsk

Jon A. Jenssen, MSc,
Trondheim Municipality, Norway
jon-andreas.jenssen@trondheim.kommune.no

KEYWORDS: *moisture supply, indoor air humidity, hygrothermal calculations, indoor climate, indoor relative humidity*

SUMMARY:
In this study indoor air humidity levels have been measured in 117 houses in Trondheim, Norway. The houses were randomly selected for each of the following types; detached one family houses, semidetached two family houses, undetached (chained) houses and apartment buildings. The temperature and relative humidity were measured at 15 minutes interval over a period of one week during the heating season. The measurements were made in bedrooms, living rooms, bathrooms, cellars/basements and outdoors. The moisture supply, which is the difference between indoor and outdoor air water vapour content, were determined. The dependence on outdoor temperature were analyzed. The effect of other influencing factors such as occypancy (area per person), type of house, type of room, age of house and ventilation type were also investigated.

1. Introduction

Large scale measurements of indoor air humidity levels in buildings are required for many purposes. One of the most important input parameters when doing a hygrothermal analysis of the building envelope using simulation models is knowledge about typical levels of indoor air humidity. Knowing the typical variations of indoor air humidity in a specific type of buildings, it is also possible to compare with measurements in one specific building, for instance to assess the risk for moisture problems.

A common way of expressing the indoor air humidity load is by the *moisture supply*. The moisture supply (Δv), is defined as the difference between indoor (v_i) and outdoor (v_e) air water vapour content (in g/m^3). The moisture supply is used when the relative humidity is not controlled but allowed to undergo wide variations due to several factors such as weather conditions, building characteristics, moisture generation and ventilation. It is generally considered that the moisture supply tend to be relatively constant in a house during the colder part of the heating season (outdoor temperature < 0 - +5 ^{o}C), while it decreases when the outdoor temperature increases. In the standard EN ISO 13788 (EN ISO 13788, 2001) this is expressed as the moisture supply being contant for outdoor temperatures below 0 ^{o}C, while the moisture supply decreases linearily to 0 g/m^3 at outdoor temperatures of 20 ^{o}C, se example in Figure 1. Above 20 ^{o}C the moisture supply is 0 ^{o}C. EN ISO 13788 defines five standard humidity classes to be used as design values in hygrothermal calculations. For houses two classes applies; Δv = 4 g/m^3 for dwellings with low occupancy and Δv = 6 g/m^3 for dwellings with high occupancy (constant value when outdoor temperature is below 0 ^{o}C). According to Kalamees, Juha and Kurnitski (2006) a more correct representation of the design curves would be a contant moisture supply below approximately +5 ^{o}C and a linear decrease down to a constant value at approximately +15 ^{o}C and higher temperatures.

The indoor moisture supply in houses have been investigated in many earlier field studies. Tolstoy (1993) measured the moisture supply during winter in about 1500 houses in Sweden. The moisture supply for single-

family houses was between 2 – 5 g/m^3, with an average of 3,6 g/m^3. For multi-family dwellings the moisture supply was between 1,5 – 4 g/m^3, with an average of 2,9 g/m^3. Several other field studies have been performed, a summary is given in (Kalamees, 2006). According to Kalamees (2006) most of the studies yields average moisture supply during winter between about 2 – 3 g/m^3 for living rooms. The variation between different houses are on the other hand quite large, meaning that design values for hygrothermal calculations should be selected somewhat higher than the average values. The International Energy Agency Annex 24 (Sanders, 1996) has recommended the use of the 10% critical level for climate loads when doing a hygrothermal simulation of the external envelope. This means a moisture supply higher than the critical level should not appear in more than 10% of the cases. Kalamees, Juha and Kurnitski (2006) did full year measurements in houses with low/medium occupancy (average 42 m^2/person) and calculated that the 10 % critical level was close to 4 g/m^3 during the cold period ($T_{out} \leq +5$ ^{o}C) and close to 1,5 g/m^3 during the warm period ($T_{out} \geq +15$ ^{o}C). The average values were 1,8 g/m^3 and 0,5 g/m^3 for the cold and warm period respectively.

The measurements presented in this paper has been part of the study "Prevention of atopy among children in Trondheim" (Jenssen et.al., 2001). This analysis work of the measurements have been part of the ongoing SINTEF strategic institute project "Climate 2000 - Weather Protection in the Construction Process".

Indoor air humidity levels have been measured for a week during the heating season in 117 houses in Trondheim, Norway. The houses were randomly selected for each of the four following building types; 44 detached one family houses, 32 semidetached two- or four family houses,18 undetached (chained) houses and 21 apartment buildings. Most of the houses in Norway (except for apartment buildings) are lightweight timber-frame houses, and so was the case also in this study. In each house measurements were made in a children bedroom, the main living room, the most used bathroom and the basement/cellar. The basement/cellar are a mix of (partly) heated basements and non-heated storage cellars. Most of the studied rooms had the possibility of opening the windows for airing purposes. The houses had all types of basic ventilation; no ventilation (i.e. not planned with airing inlets/outlets), natural ventilation, exhaust ventilation and balanced ventilation.

2. Method

In 32 of the 117 houses the indoor air humidity levels were measured during the heating season November 2000 – March 2001 as a part of a preproject for the "Prevention of atopy" – study. These measurements are previosly presented in (Jenssen, Geving and Johnsen, 2002), but are also included in this work. The rest of the houses (85 houses) were measured during the period May - July 2003, September 2003 – June 2004, September – December 2004.

The first 32 houses were selected through this procedure: A total of 300 buildings in Trondheim were randomly selected for each of the four building types mentioned above. For each building, one family was selected to receive a questionnaire. The response rate was 35 %. 8 or 9 buildings of each type were randomly selected for home inspections and measurements.

The last 85 houses were selected through this procedure: Parents of the children that were included in the "Prevention of atopy"-study were asked for permission to perform inspection of their houses until enough participants had accepted. There were 200 participants in this home inspection study, but RH and temperature were measured in only 85 of these 200 houses. This means the houses were "randomly" selected among a population (with small children in the house) that had accepted to participate in the "Prevention of atopy"-study.

The temperature and relative humidity (RH) were measured at 15 minutes interval over a period of seven days. Small logging units were used (Tiny tag, TGU 1500, Intab). The loggers were positioned away from windows, heating units, direct sunlight or outer door. The loggers were placed between 1,5 – 2,0 m above floor level. The accuracy of the loggers were $\pm$ 5 % RH and $\pm$ 0,5 ^{o}C. Hourly data for outdoor RH were retreived from an automatic weather station located in Trondheim operated by the Norwegian Meteorological Institute, with an accuracy of $\pm$ 2 % RH and $\pm$ 0,5 ^{o}C. The moisture supply (Δv) was calculated on an hourly basis. Mean weekly values for the moisture supply were calculated from these hourly values.

3. Results

The results are given in tables 1-4, and figures 1 and 2. All analysis are made on the basis of weekly means of the moisture supply and outdoor temperature. The 90% percentile (i.e. 10% critical level) has been calculated

together with the mean values (when enough valid N). Design curves from EN ISO 13788 for houses (low and high occupancy) are given for comparison in the figures.

A significantly higher ($p < 0,03$, Paired samples t-test) mean weekly moisture supply for outdoor temperatures below + 5°C compared to moisture supply for outdoor temperatures above + 5°C was found. This applies for all room types, except for bedrooms ($p = 0,08$).

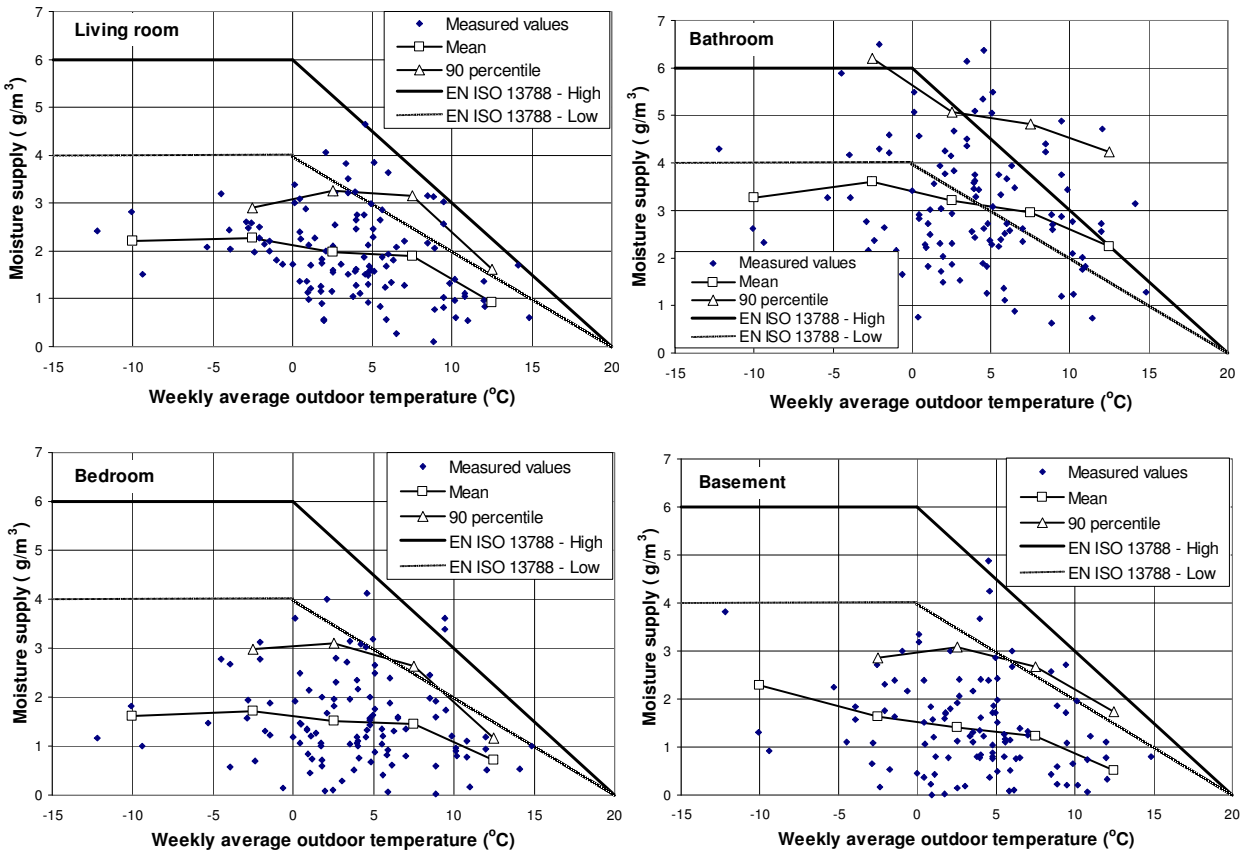

FIG. 1: Moisture supply for varius outdoor temperature in living rooms, bathrooms, bedrooms and basements.

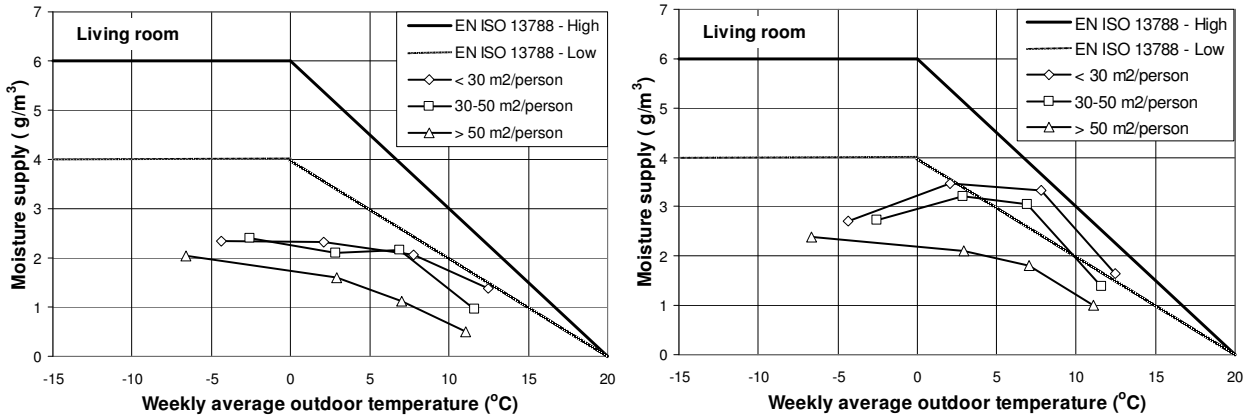

a. Mean moisture supply b. 90 % percentile of moisture supply

FIG. 2: Moisture supply for varius outdoor temperature and level of occupancy for living rooms.

The analysis showed that the mean weekly moisture supply in bathrooms were significantly higher ($p < 0,05$, Anova-test) than all other rom types for all outdoor temperatures (below and above +5°C). The moisture supply in living rooms were significantly higher than in the bedrooms and basements for outdoor temperatures below +5°C. For temperatures above + 5°C the moisture supply were significantly higher in living rooms compared to the basements. There were no significant difference between bedrooms and basements. Due to the strong dependance of room type, the rest of the analysis is made for each room type separately.

An effect of level of occupancy was found for living roms. The mean weekly moisture supply was significantly lower ($p < 0,05$, Anova-test) for high occupancy (> 50m^2/person) compared to lower occupancy (< 50 m^2/person). It was however no significant difference between a low level of occupancy (< 30 m^2/person) and a medium level of occupancy (30 – 50 m^2/person). This effect is illustrated in figure 2. There was no significant effect of occupancy for the other room types, except that for bathrooms the moisture supply was significantly lower ($p < 0,05$, Anova-test) for high occupancy (> 50m^2/person) compared to medium occupancy (30 - 50 m^2/person). There was found no significant difference ($p >> 0,05$, Anova-test) in mean weekly moisture supply between the various building types. There were also no significant difference ($p >> 0,05$, Anova-test) in moisture supply when comparing the year of construction (three periods; before 1961, 1961 – 83, after 1983). Furthermore there was found no significant difference between the various types of basic ventilation systems of the houses (no ventilation, natural ventilation, exhaust ventilation and balanced ventilation). The effect of a single exhaust fan in the bathroom was not investigated.

TABLE. 1: Moisture supply for various outdoor temperature intervals.

			Moisture supply (g/m^3)		
Room type	T outdoor	Valid N	Mean	Std dev	90%
Bathroom	< -5°C	N=5	3,26	0,81	.
	-5°C - 0°C	N=14	3,60	1,44	6,20
	0°C - +5°C	N=50	3,21	1,28	5,08
	+5°C - +10°C	N=30	2,95	1,21	4,82
	+10°C - +15°C	N=12	2,24	1,06	4,24
Basement	< -5°C	N=5	2,28	1,21	.
	-5°C - 0°C	N=14	1,64	0,85	2,85
	0°C - +5°C	N=55	1,41	1,14	3,08
	+5°C - +10°C	N=29	1,23	0,84	2,67
	+10°C - +15°C	N=12	0,51	0,73	1,74
Bedroom	< -5°C	N=5	1,62	0,66	.
	-5°C - 0°C	N=13	1,72	0,93	2,98
	0°C - +5°C	N=57	1,51	1,04	3,10
	+5°C - +10°C	N=30	1,44	0,94	2,64
	+10°C - +15°C	N=12	0,72	0,40	1,16
Living room	< -5°C	N=5	2,20	0,48	.
	-5°C - 0°C	N=14	2,28	0,39	2,90
	0°C - +5°C	N=57	1,98	0,95	3,26
	+5°C - +10°C	N=30	1,89	0,97	3,15
	+10°C - +15°C	N=12	0,92	0,48	1,61

TABLE. 2: Moisture supply for various degree of occupancy (heated area per person) and outdoor temperature.

		Moisture supply (g/m^3)							
	Occupancy	T outdoor ≤ 5 °C				T outdoor ≥ 5 °C			
Room type	(m^2/person)	Valid N	Mean	Std dev	90 %	Valid N	Mean	Std dev	90 %
Bathroom	≤ 30	N=12	3,20	1,16	4,92	N=8	2,63	1,28	.
	30 - 50	N=37	3,54	1,41	5,95	N=21	3,12	1,03	4,66
	≥ 50	N=17	2,88	1,01	4,31	N=12	1,95	0,89	3,26
Basement	≤ 30	N=14	1,40	0,94	3,02	N=8	1,17	1,24	.
	30 - 50	N=39	1,58	1,24	3,35	N=20	1,08	0,77	2,52
	≥ 50	N=18	1,25	0,83	3,02	N=12	0,76	0,73	2,07
Bedroom	≤ 30	N=16	1,74	1,00	3,31	N=8	1,17	1,26	.
	30 - 50	N=38	1,57	1,01	2,81	N=21	1,48	,81	2,63
	≥ 50	N=18	1,43	1,02	3,18	N=12	0,80	0,58	1,69
Living room	≤ 30	N=16	2,27	0,89	3,60	N=8	1,89	1,08	.
	30 - 50	N=39	2,17	0,81	3,21	N=21	1,77	0,82	3,08
	≥ 50	N=18	1,60	0,84	2,64	N=12	0,97	0,69	2,11

TABLE. 3: Moisture supply for various periods of building year and outdoor temperature.

		Moisture supply (g/m^3)							
		T outdoor ≤ 5 °C				T outdoor ≥ 5 °C			
Room type	Building year	Valid N	Mean	Std dev	90 %	Valid N	Mean	Std dev	90 %
Bathroom	← 1960	N=26	3,38	1,35	5,51	N=16	2,75	1,16	4,42
	1961 - 83	N=29	3,01	1,23	4,56	N=12	2,93	1,15	4,96
	1983 →	N=11	3,39	1,01	4,97	N=12	2,48	1,44	5,17
Basement	← 1960	N=29	1,69	1,14	3,18	N=15	0,85	0,99	2,83
	1961 - 83	N=31	1,31	0,87	2,36	N=12	1,14	0,78	2,46
	1983 →	N=11	1,67	1,53	4,66	N=12	1,22	0,79	2,54
Bedroom	← 1960	N=28	1,75	1,13	3,65	N=16	1,54	0,87	2,88
	1961 - 83	N=33	1,51	0,93	2,96	N=12	1,04	0,79	2,31
	1983 →	N=11	1,14	0,67	2,05	N=12	1,14	0,96	3,13
Living room	← 1960	N=29	2,19	0,94	3,39	N=16	1,78	1,17	3,30
	1961 - 83	N=33	1,99	0,87	3,05	N=12	1,36	0,59	2,34
	1983 →	N=11	1,80	0,41	2,45	N=12	1,60	1,06	3,46

TABLE. 4: Moisture supply for various types of ventilation and outdoor temperature.

		Moisture supply (g/m^3)							
	Type of	T outdoor ≤ 5 °C				T outdoor ≥ 5 °C			
Room type	ventilation	Valid N	Mean	Std dev	90 %	Valid N	Mean	Std dev	90 %
Bathroom	No vent	N=6	3,30	1,31	.	N=1	3,49	.	3,49
	Natural	N=45	3,32	1,38	5,66	N=22	2,87	1,15	4,63
	Exhaust	N=15	3,13	1,02	4,62	N=14	2,67	1,40	5,18
	Balanced	N=2	4,36	1,03	.	N=4	1,99	0,93	.
Basement	No vent	N=6	1,91	1,10	.	N=1	1,40	.	1,40
	Natural	N=48	1,42	1,03	3,02	N=21	0,90	1,00	2,65
	Exhaust	N=17	1,58	1,39	4,02	N=14	1,21	0,81	2,58
	Balanced	N=2	2,01	0,56	.	N=4	0,87	0,32	.
Bedroom	No vent	N=6	1,67	1,63	.	N=1	1,57	.	1,57
	Natural	N=49	1,54	1,02	3,03	N=22	1,23	0,87	2,48
	Exhaust	N=17	1,50	0,73	2,87	N=14	1,36	1,01	3,50
	Balanced	N=2	1,64	0,74	.	N=4	0,90	0,61	.
Living room	No vent	N=6	2,27	0,66	.	N=1	2,08	.	2,08
	Natural	N=50	2,11	0,96	3,23	N=22	1,64	0,99	3,15
	Exhaust	N=17	1,82	0,57	2,63	N=14	1,72	1,03	3,44
	Balanced	N=2	1,87	0,83	.	N=4	0,90	0,58	.

4. Discussion and conclusions

The results showed that the moisture supply is not a constant value over a year, but dependant of the outdoor temperature. This effect is probably due to more ventilation (more open windows) and less moisture production (less indoor activity) during the warm period of the year. This confirms previous investigations, such as Kalamees, Juha and Kurnitski (2006) and the design curves given in the standard EN ISO 13788. The deflection point of the moisture supply curve (i.e. when it goes from a constant value to a linear decrease as temperature increases) is not 0 ^{o}C as given in EN ISO 13788, but seems according to figure 1 to be closer to + 5-7 ^{o}C. This confirms the findings of Kalamees, Juha and Kurnitski (2006) who claims that the deflection point should be approximately + 5 ^{o}C.

According to EN ISO 13788 the moisture supply is 0 g/m^3 when the outdoor temperature reaches 20 ^{o}C or higher temperatures. We did not perform measurements when the outdoor temperatures were higher than +15 ^{o}C, so we can not conclude on that aspect. However when looking on the moisture supply curve for bathrooms, figure 1, it seems improbable that the moisture supply should reach 0 g/m^3. Since windows can not be open all the time even at high outdoor temperatures it is probable that the moisture supply is higher than 0 g/m^3 during the warm period, as was measured by Kalamees, Juha and Kurnitski (2006). Assuming that the moisture supply will reach a constant value > 0 g/m^3 during the warm period, it seems from figures 1 and 2 that this deflection point is closer to + 15 ^{o}C than + 20 ^{o}C as given for the design curves in EN ISO 13788. The same observation were made by Kalamees, Juha and Kurnitski (2006).

According to our measurements it seems that the design curves given in EN ISO 13788 need to be modified to be used in hygrothermal analysis, both in regard to the shape and deflection points, and in regard to the level for various occupancy and room type. The highest levels of moisture supply have been measured in the bathrooms,

but it is probably unnecessary conservative to design the whole house according to these high levels. It is probably better to use the measurements for the living rooms as basis for the design of the whole building, and do a special analysis for the bathrooms (and other similar rooms such as laundry room) if necessary. In our measurements the bedroom values are significantly lower than the living room values. It should however be noted that the bedrooms are children bedrooms, and that the parent bedrooms might have higher values. Kalamees, Juha and Kurnitski (2006) report slightly higher values for bedroms than for living rooms (0,2 g/m^3 higher in average, $T_{out} < + 5^oC$) and this might be due to this beeing parents (two persons) bedrooms. It should however be noted that in Norway it is rather common to sleep with open windows in the bedroom also during winter, giving a better ventilation and a lower temperature. In (Jenssen, Geving and Johnsen, 2002) the weekly mean temperature in 31 childrens bedrooms in Trondheim were measured to +13,5 ± 4,3 ^{o}C.

While there were no significant effect of the ventilation system, there was found a significant effect of the level of occupancy for living rooms as shown in figure 2. From our findings and the findings of Kalamees, Juha and Kurnitski (2006) we propose the following moisture design curves based on the 10% critical level as given in figure 3. "Low" could be used for living rooms in houses with low occupancy (>50 m^2/person) and areas where the moisture production is low (e.g. cellars), "Medium" for living rooms with medium/high occupancy (<50 m^2/person) and bedrooms, and "High" for bathrooms and laundry rooms. Whether it applies for other countries than Norway must however be further investigated.

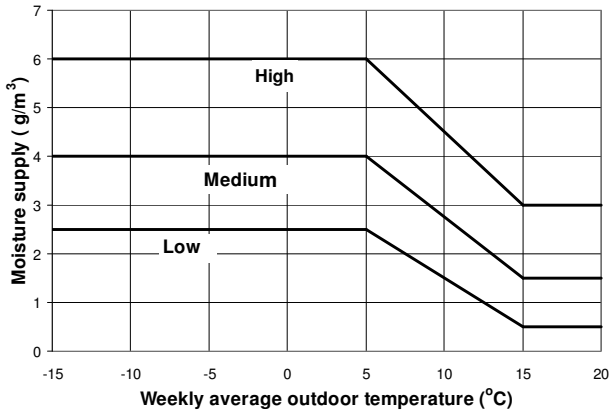

FIG. 3: Proposed moisture supply design curves for Norwegian houses (based on 10% critical level).

5. References

EN ISO 13788. (2001). *Hygrothermal perfomance of building components and building elements. Internal surface temperature to avoid critical surface humidity and interstitial condensation. Calculation methods.* International Organization for Standardisation.

Jenssen J.A. et.al. (2001). Children allergy study in Trondheim. (In Norwegian: Barneallergistudien i Trondheim). *Allergi i praksis*, nr. 4, 34-38.

Jenssen, J.A, Geving, S. and R. Johnsen, 2002. *Assessment of indoor air humidity in four different types of dwellings randomly selected in Trondheim, Norway.* Proceedings of 6th Symposium of Building Physics in the Nordic Countries, Trondheim, Norway, June 17-19th, pp 729-735.

Kalamees T. (2006). *Hygrothermal criteria for design and simulation of buildings.* Doctoral thesis, Chair of Building Physics and Architecture, Tallinn University of Technology.

Kalamees T., Vinha J. and Kurnitski J. (2006). Indoor humidity loads and moisture production in lightweight timber-frame detached houses. *Journal of Building Physics*, Vol. 29, No. 3, Jan 2006.

Sanders, C. 1996. *IEA-Annex 24 HAMTIE, Final Report, Volume 2, Task 2: Environmental conditions.* Laboratorium Bouwfysica, K.U.-Leuven, Belgium.

Tolstoy N. (1993). Humidity levels in the Swedish housing stock. *Proceedings of Indoor Air '93 conference*, Helsinki, Finland, Vol. 6: 91-96.

Laboratory Testing for Daily Hygroscopic Inertia Assessment

Nuno Ramos, Assist. Professor,
Department of Civil Engineering, Faculty of Engineering – University of Porto;
nuno.ramos@fe.up.pt

Vasco Peixoto de Freitas, Full Professor,
Department of Civil Engineering, Faculty of Engineering – University of Porto;
vpfreita@fe.up.pt

KEYWORDS*: Moisture, Hygroscopic Inertia, Experiments, MBV.*

SUMMARY*:*
This article describes an extensive experimental campaign aiming at the characterization of the moisture buffering capacity of interior finishing system and the assessment of the hygroscopic inertia of a room. The MBV – Moisture Buffer Value is evaluated for gypsum based products finished with different coatings. The assessment of hygroscopic inertia at room level is implemented using a flux chamber designed specifically for this experiment. A daily hygroscopic inertia index, $I_{h,d}$, is defined using MBV as a basis for the assessment of materials contribution to the buffering capacity of a room. The correlation between that index and peak dampening is proved using the presented experimental results.

1. Introduction

The variation of inside Relative Humidity (RH) is influenced by the moisture exchange between air and building elements. The relevance of that exchange is linked to the active moisture buffer capacity present in a room, which can be identified with its hygroscopic inertia. The laboratory evaluation of that capacity can be approached in three different levels.

At material level, international standards already support the determination of the basic properties that constitute moisture storage performance, such as sorption isotherms and vapour permeability. Recently, a new property defined as MBV, Moisture Buffer Value, was proposed by (Rode et al, 2005), allowing for a direct experimental measure of the moisture accumulation capacity of a material under transient conditions.

At element level, where several materials can be combined by their application in different thicknesses, MBV can also be applied as an experimental measure of each specific element moisture accumulation capacity.

At room level, the authors believe that a laboratory measurement of the active moisture buffer capacity should be directly linked to the RH peak dampening promoted by the room's interior configuration, compared to the peaks in the same room without any active hygroscopic surfaces.

2. Building element MBV

2.1 Experimental procedure

The MBV experiments, as described in (Rode et al, 2005), propose a cyclic climatic exposure which consists of 8h of high relative humidity, followed by 16h of low relative humidity. This test tries to replicate the cycle seen in bedrooms. For the specific tests described in this article, low value was fixed at 33% RH and the high value at 75% RH, for a constant temperature of 23ºC, which is the basic test configuration proposed in the protocol. The cycles were repeated until the specimen weight over the cycle varied less than 5% from day to day.

The tests were conducted in a climate chamber ensuring a good control level of the test conditions. All the samples tested were put into the chamber at the same time. Three similar samples were tested for each configuration. Each sample was put on a balance when it was likely to have reached a stable mass variation over the cycle. With this procedure it was possible to test a large number of samples. The balance was connected to a computer allowing for a continuous record of the sample mass variation.

The samples were placed horizontally on the balance. The back of the samples was previously treated with epoxy paint and the four edges were covered with aluminium tape, allowing vapour transfer only in the main face.

Additionally, office paper commonly used in printers was also tested for MBV. Although it's not a building material, important amounts of paper are usually in contact with the room air, contributing to the room moisture buffer capacity. The paper sheets were tested grouped in stacks of different amounts of sheets.

2.2 Results

The MBV test, as described in the previous section, was performed on the samples described in Table 1 and Table 2. Base materials GC (gypsum board) were coated with different combinations of primer and finish coatings, commonly used inside Portuguese dwellings.

TABLE. 1: Building materials configurations used in MBV experiments.

Conf.	Base	Primer	Finishing coating
GC	12,5 mm GC	—	—
GC2	12,5 mm GC	—	Vinyl – 50 µm
GC2A	12,5 mm GC	25 µm	Vinyl – 50 µm
GC3	12,5 mm GC	—	Acrylic 1 – 50 µm
GC3A	12,5 mm GC	25 µm	Acrylic 1 – 50 µm

TABLE. 2: Paper configurations used in MBV experiments.

Conf.	Description
500 Sheets	Stack of 500 sheets of white office paper size A4
250 Sheets	Stack of 250 sheets of white office paper size A4
125 Sheets	Stack of 125 sheets of white office paper size A4

The stable cycle for each configuration is presented in Figures 1 and 2. This type of experiment is interesting in the way it provides an easy assessment of the transient behaviour of a building element. Just by watching the curves, the effect of painting is easily highlighted. The configurations GC2A and GC3A, painted with primer and finishing coating had a much lower MBV then the GC samples. On the other hand, it can also be observed that the primer was particularly relevant, as revealed by the comparison GC2-GC2A and GC3-GC3A.

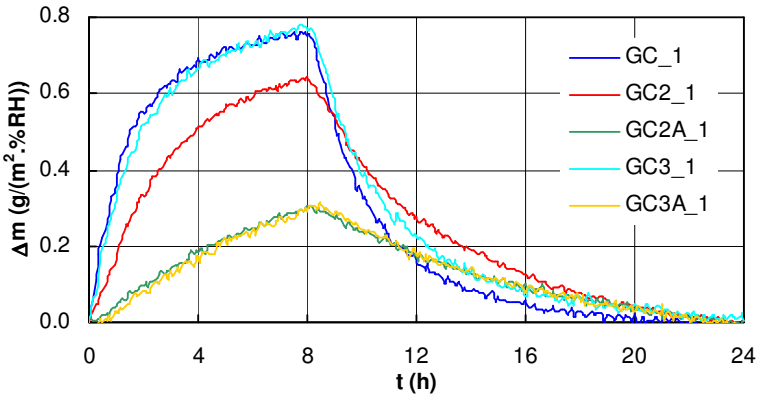

FIG. 1: Mass variation stable cycle in MBV experiments with GC based materials.

The tests on sheets of paper supplied an indication of its moisture buffer capacity. It can be seen that the amount of moisture stored in a small stack of paper is in the order of magnitude of the amount stored in a square meter of finished wall.

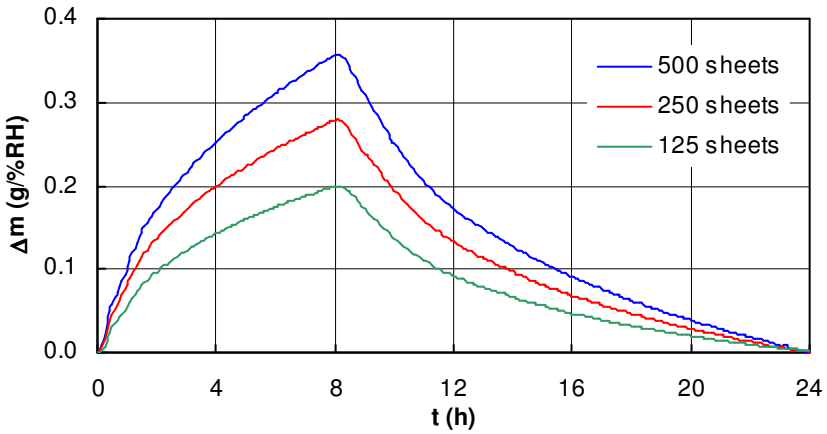

FIG. 2: Mass variation stable cycle in MBV experiments with stacks of office paper sheets.

Figure 3 presents the MBV retrieved from each stable cycle obtained for building elements samples. Each value resulted from the average of three samples. The variation between samples was not very relevant, having in mind that painted elements were under test. This graphic shows how easy element buffer capacity is compared by means of MBV experiments.

Note that for an MBV of 0.7 g/(m^2.%RH), in a common bedroom with a surface of 50 m^2, for a 10%RH difference during a daily cycle, 350 g of moisture will be buffered in the walls and returned to the room air during the period without occupation.

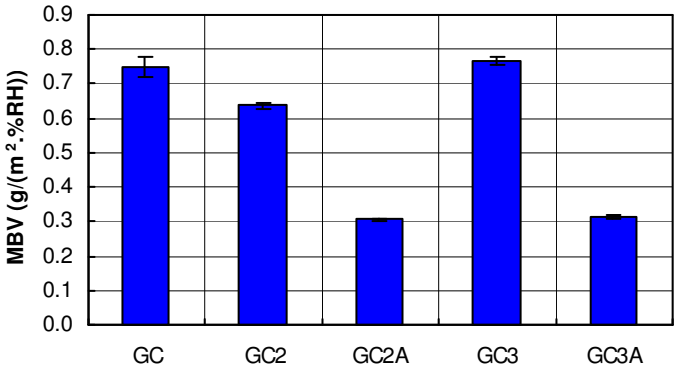

FIG. 3: MBV for GC based elements.

3. Hygroscopic Inertia experiments

3.1 Flux chamber

A way of evaluating the impact of renderings and furnishings on the moderation of inside relative humidity variation is to actually determine the peak reduction of that variation caused by those materials. Ideally, that evaluation would be conducted in full size rooms where each combination of hygroscopic materials could be tested, facing real climate situations. As it would be impossible for LFC-FEUP to build such rooms, due to the costs involved, a decision was made to try to replicate those conditions in a small scale flux chamber. The

facility, inspired by Padfield's flux chamber (Padfield, 1998), is presented in Figures 4 and 5. Other experimental setups have been recently used for hygroscopic inertia effect assessment (Rode et al, 2002, Yoshino et al, 2005).

The flux chamber was built inside an existing climatic chamber, allowing for the control of temperature (15ºC – 35ºC) and relative humidity (30% - 90%) of the whole system. The flux chamber consists of a Plexiglas box, placed over two steel tables, with three openings that can be used to gain access to the interior of the box. Its inside dimensions correspond to 1500x524x584 mm^3.

The ventilation system uses a pump that extracts air in two points inside the box. An inlet on top allows for the air to get in and, at the same time, prevents pressure differences. The air that enters the box comes directly from the climatic chamber, and therefore its characteristics are known. The air flux value is controlled by two flow meters allowing for a range of 2-130 l/min, corresponding to a range of air changes of 0.26-17 h^{-1}.

The data acquisition system uses a set of Rotronic® sensors for measuring temperature and relative humidity. These sensors are connected to a data logger, which transmits to a personal computer. The results can be stored in EXCEL format files.

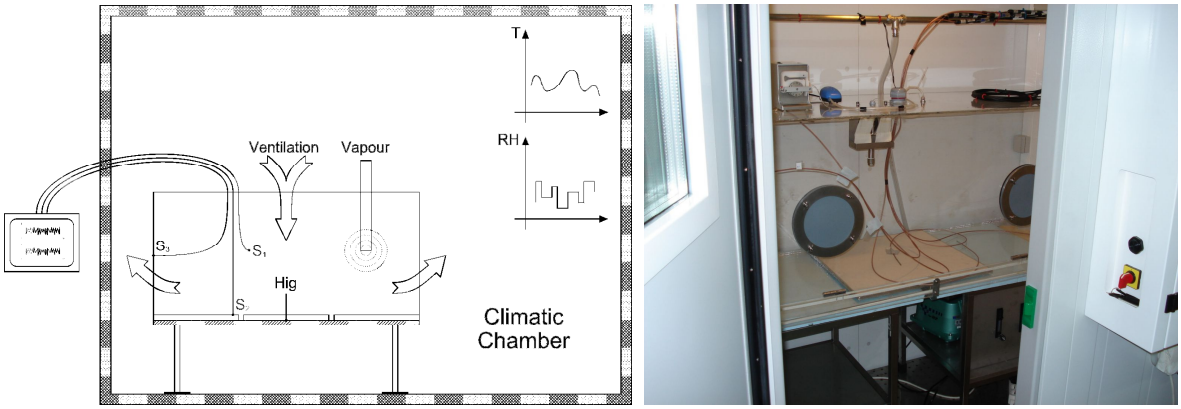

FIG. 4: Test facility principle and picture of the actual flux chamber inside a climatic chamber.

Although the flux chamber has an independent vapour production device, for the specific tests presented in this text, the combined effect of ventilation and climatic chamber RH variations was used to emulate vapour production effect on the mass balance.

The authors believe that this facility, although providing a small scale experiment, can be an interesting contribution to the experimental measurement of the hygroscopic inertia effect. The simplicity in changing the test configuration or swap samples inside the flux chamber allows for the development of test scenarios in a relatively short time. At the same time, there's a high level of control of hygrothermal parameters, allowing for a rigorous analysis of the results.

3.2 Results

One of the tests performed in the flux chamber consisted of the definition of the stable daily RH cycle for a hygrothermal scenario. The selected scenario was defined assuming a ventilation rate, ach, of 0.5 h^{-1} and a vapour production of 2 g/h, during 8 hours in the daily cycle. As the temperature of the system was fixed at 23º C, the vapour production was obtained with the RH variation of the climatic chamber between 40% and 80% RH. Using that scenario, different combinations of samples were placed inside the flux chamber, resulting in different RH cycles. The samples used in these tests had the same configuration as the ones in MBV tests. For each configuration, the daily hygrothermal cycle is repeated until the flux chamber RH falls in a stable cycle.

The results of the tests are referred in Table 3 and Figure 5 displays the RH variation inside the flux chamber for the tested combinations. For quantification of the test results, the difference between the average RH and the RH 90^{th} percentile, RH_{90} - RH_m, is used. The average RH value obtained for each stable cycle showed a small variation, demonstrating the high control level of the experiments.

These results clearly illustrate the application of the flux chamber in measuring the actual RH dampening caused by the presence of different levels of moisture buffering in contact with inside air.

TABLE. 3: Configurations and results in Flux Chamber tests.

Test	Samples	RH_m (%)	RH_{90} (%)	RH_{90} - RH_m (%)
HI1	-	54.6	73.2	18.6
HI2	0.75 m^2 GC2A	54.6	68.3	13.7
HI3	0.75 m^2 GC	54.5	64.6	10.1
HI4	0.75 m^2 GC + 0.75 m^2 GC3	55.1	61.2	6.1
HI5	500 Sheets	54.4	67.8	13.4
HI6	4 x 125 Sheets	54.7	64.2	9.5
HI7	8 x 125 Sheets	53.9	61.2	7.3
HI8	0.75 m^2 GC + 8 x 125 Sheets	54.3	60.2	5.9

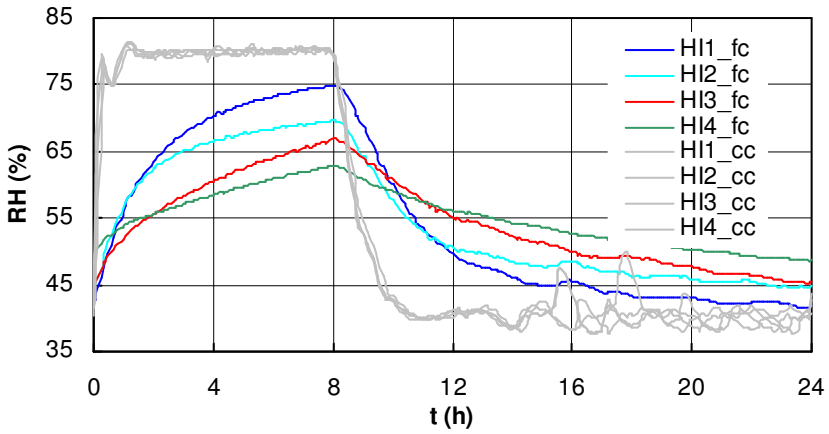

FIG. 5: Flux chamber tests HI1-HI4 stable cycles (fc – flux chamber, cc – climatic chamber).

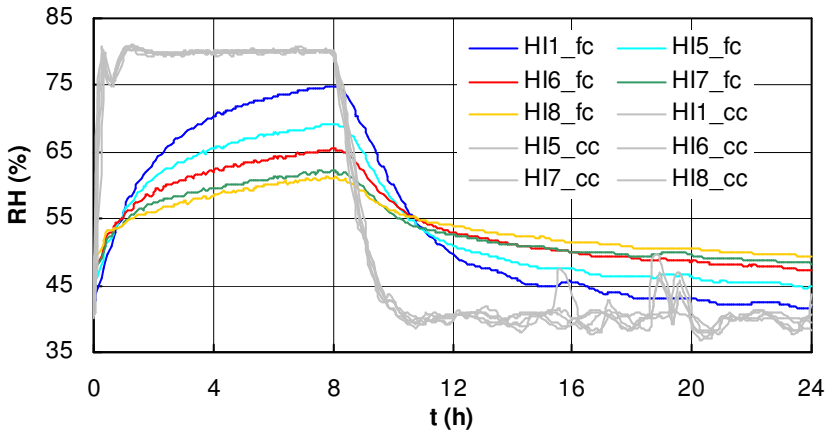

FIG. 6: Flux chamber testsHI1 and HI5-HI8 stable cycles (fc – flux chamber, cc – climatic chamber).

4. Daily Hygroscopic Inertia Index, $I_{h,d}$

4.1 Concept

There is a need for a single parameter that can characterize the daily hygroscopic inertia of a room and correlate to the expected dampening of the RH variation of that room.

The proposed daily hygroscopic inertia index, $I_{h,d}$, is defined by Ramos (2007) as a function of MBV, according to expression (1), where MBV_i = Moisture buffer value of element i (g/(m^2.%RH)); S_i = surface of element i; MBV_{obj} = Moisture buffer value of complex element j (g/%RH); C_r = Imperfect mixing reduction coefficient (-); ach = air exchange rate (h^{-1}); V = room volume (m^3); TG = Vapour production period (h). The $I_{h,d}$ can be understood as the room MBV, homogenized to air renovation conditions and vapour production period variations.

$$I_{h,d} = \frac{\sum_{i}^{n} C_{r,i} \cdot MBV_i \cdot S_i + \sum_{j}^{m} C_{r,j} \cdot MBV_{obj,j}}{ach \cdot V \cdot TG} \quad \left[\frac{g}{m^3 \cdot \%RH}\right] \tag{1}$$

The AMDR parameter was defined according to expression (2), where HR_m is the average relative humidity variation and $\overline{HR_{90}}$ stands for the daily average of the 90th percentile of the relative humidity variation. The index *ref* refers to the base scenario of a room without hygroscopicity and *sim* identifies a scenario under study for that same room. The AMDR parameter can therefore be interpreted as relative daily average amplitude of a RH variation of a room hygroscopic configuration. This parameter is interesting since the average RH variation in long term analysis will not be affected by daily hygroscopic inertia.

$$AMDR = \frac{\left(\overline{HR_{90}} - HR_m\right)_{sim}}{\left(\overline{HR_{90}} - HR_m\right)_{ref}} \tag{2}$$

4.2 Application

The application of the concept referred above resulted in the curve displayed in Figure 7. This curve was supported by numerical and experimental studies. In this paper, the application of the presented concept to the experimental results is presented in Table 4 and also plotted in Figure 7.

Two important considerations must also be stated:

- The $I_{h,d}$ and AMDR values for the empty chamber, corresponding to test HI1, were determined numerically. They are explained by the effect of the materials that being part of the flux chamber aren't absolutely inert.
- The C_r (Imperfect mixing reduction coefficient) was taken as 0.5 for all the tests (Ramos, 2007).

It's possible to conclude on the validity of the method by comparing the experimental results on the flux chamber with the theoretical curve that supports the daily hygroscopic inertia classes. The theoretical curve development had already been approached in (Ramos and Freitas, 2006). Note that the black dots in Figure 7 have full experimental determination.

TABLE. 4: Configurations and results in Flux Chamber tests.

Test	Samples	$I_{h,d}$ (g/(m^3.%RH)	AMDR (%)
HI1	-	0.035	80.1
HI2	0.75 m^2 GC2A	0.094	58.7
HI3	0.75 m^2 GC	0.182	43.3
HI4	0.75 m^2 GC + 0.75 m^2 GC3	0.328	26.5
HI5	500 Sheets	0.128	57.6
HI6	4 x 125 Sheets	0.243	40.9
HI7	8 x 125 Sheets	0.452	31.4
HI8	0.75 m^2 GC + 8 x 125 Sheets	0.598	25.4

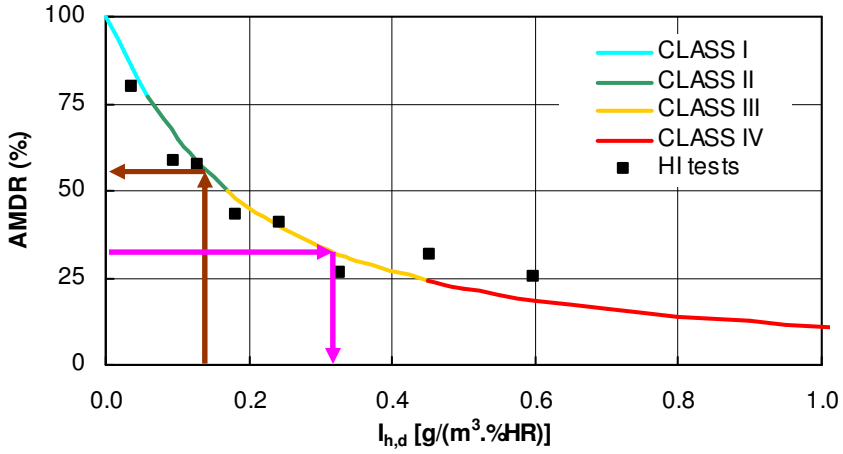

FIG. 7: Flux chamber results and hygroscopic inertia classes.

The application of the hygroscopic inertia classes concept in design is illustrated by the pink and brown arrows drawn on Figure 7. Suppose a designer has enough data to analyse a given room, and obtains an $I_{h,d}$ value below 0.2. He'll conclude on a low hygroscopic inertia, base on the path set by the brown arrows. He then can set an AMDR he considers adequate and follow the pink arrow type of path, to conclude on the ideal room configuration that will lead to the $I_{h,d}$ value indicated by his analysis.

5. Conclusions

This study allows for the following conclusions:

— The finishing coatings have a relevant influence on moisture buffering of building elements.

— The primer usually used on coating systems can introduce an important reduction of the MBV of an element.

— A small stack of A4 size paper can have a moisture buffering capacity comparable to a square meter of a building element.

— MBV is a relevant property for means of comparing different elements that are present in a room.

— Hygroscopic inertia tests were conducted in a flux chamber that represents a small scale room. The influence of different elements on RH variation was obtained and the experimental evidence of daily hygroscopic inertia was demonstrated.

— The application of a daily hygroscopic inertia index allowed was verified with full experimental data, proving its validity.

— Plotting the hygroscopic inertia index against a parameter indicating the RH amplitude reduction (AMDR in this paper) proved that hygroscopic inertia will reduce RH daily peaks according to a logarithmic type variation. This implies that there may be an interest in ensuring some amount of moisture buffering inside a room, but the limits to the benefits of inertia to RH variation will be met, more or less easily depending on ventilation rate.

— The introduction of moisture buffering materials in a room must always ensure that the durability of those materials is not affected by their moisture content variation.

6. Acknowledgement

This study was financially supported by Fundação para a Ciência e Tecnologia (FCT) and project POCI/ECM/57722/2004 co-financed by FEDER.

7. References

Padfield, T. (1998). The role of absorbent building materials in moderating changes of relative humidity. Department of structural engineering and materials. Lyngby, The technical university of Denmark.

Ramos, N. (2007). The importance of hygroscopic inertia in the hygrothermal behaviour of buildings (in Portuguese). PhD Thesis. Department of Civil Engineering, Faculty of Engineering – University of Porto.

Ramos, N., Freitas, V. (2006). Evaluation Strategy of finishing materials contribution to the hygroscopic inertia of a room. Research in Building Physics and Building engineering – Proceedings of the Third International Building Physics Conference, pp. 543-548. Concordia University, Montreal, Canada, 27-31 August.

Rode, C., Peuhkuri, R., Mortensen, L., Hansen, K., Time, B., Gustavsen, A., Svennberg, K., Arfvidsson, J., Harderup, L., Ojanen, T. and Ahonnen, J. (2005) Moisture Buffering of Building Materials. Report BYG-DTU R-126. Department of Civil Engineering. Technical University of Denmark.

Rode, C., Mitamura, T., Schultz, J., Padfield, T. (2002) Test cell measurements of moisture buffer effects. 6th symposium on building physics in the Nordic countries. Trondheim, Norway.

Yoshino, H., Mitamura, T., Hasegawa, K., Matsumoto, S., Adachi, M. (2005) Experiment for synthetic evaluation of moisture buffering effect in a room. IEA Annex 41 meeting. Trondheim, Norway.

Accuracy of simplified indoor humidity simulation

Olga Koronthalyova, PhD.,
Institute of Construction and Architecture, SAS, Dubravska c 9, 845 03 Bratislava, Slovakia;
usarkoro@savba.sk

Peter Mihalka , Ing.,
Institute of Construction and Architecture, SAS, Dubravska c 9, 845 03 Bratislava, Slovakia;
usarmipe@savba.sk

KEYWORDS: indoor humidity, simulation, EMPD.

SUMMARY:
Accuracy of simplified indoor humidity simulation, based on EMPD concept, was evaluated by a comparison with complex model. The evaluation of the EMPD model was done for different moisture production/ventilation regimes, outdoor weather changes and temperature gradients in hygroscopic layer. The analysis was limited to the cases of 1-zone space, constant material properties of hygroscopic layers and negligible vapour transmission through the exterior structures. The accuracy of simplified EMPD approach was found satisfactory in cases with limited thickness of hygroscopic layer and on condition that the moisture production and ventilation could be described as regular cyclic process or in cases where the hygroscopic surfaces were mostly placed on inner structures.

1. Introduction

Indoor air relative humidity is an important parameter influencing the hygro-thermal performance of building structures and the indoor climate as well. In order to predict the resultant indoor humidity in the zone with the designed inner surfaces and moisture production/ventilation regime and to suggest possible improvements, a sufficiently accurate dynamic model is necessary.

The computational codes simulating the interaction between indoor air and interior hygroscopic materials can be divided roughly into two groups: codes using simple lumped models and complex codes using a detailed description of the heat and mass transfer through the building structures. The complex models provide reliable information about resultant indoor humidity as well as the description of the hygro-thermal field in the structures but generally they are relatively time-consuming. Therefore in some cases a simplified approach could be more convenient way of indoor humidity evaluation.

The scope of the presented paper was limited to cases when assumption of well-mixed air in interior is acceptable. The analysis was focused on evaluation of accuracy of one of the simplified approaches – the approach based on effective moisture penetration depth (EMPD) concept.

Theoretical background of the EMPD concept was explained for example in (Cunningham 1992, Cunningham 2003, Rode et al. 2005). A method for determination of EMPD in cases when material properties are non-linear was described in (Arfvidsson 1999). Comparison of the simplified and more complex approach to indoor humidity simulation for the case of relatively vapour transmission open exterior walls was presented in (Janssens, De Paepe 2005).

In this paper a capability of simplified approach was evaluated for the case when water vapour transmission through the building envelope was negligible in comparison to the convective transfer by ventilation. The analysis was also limited to the case of common indoor relative humidities, excluding the cases with extreme high humidities of indoor air. Therefore constant material properties could be used in the simulations.

2. Description of complex and EMPD approach

In the both considered approaches the model of indoor humidity simulation is based on the solution of the water vapour mass balance equation in case of well-mixed air in the single zone space (IEA-Annex XIV 1991):

$$\frac{\partial p_i}{\partial \tau} = \frac{462 \cdot T_i \cdot \left\{ G_p + \sum G_{sk} - \sum \left[\beta_j \cdot A_j \cdot (p_i - p_{sat,sj}) \right] \right\}}{V} + n \cdot (p_e - p_i) \qquad (1)$$

Where p_i is the indoor air partial vapour pressure [Pa], p_e is the outdoor air partial vapour pressure [Pa], τ is the time [s], T_i is the indoor air temperature [K], G_p is the indoor vapour production [kg.s^{-1}], ΣG_{sk} is the sum of the moisture flows from or into the room construction surfaces, V is the volume of the room [m^3], β_j is the surface film coefficient for water vapour transfer [s.m^{-1}], A_j is the area of the surface where condensation or drying takes place [m^2], $p_{sat,sj}$ is the saturation vapour pressure on that surface [Pa], n is the ventilation rate [s^{-1}].

The difference between the approaches is in the way of simulation of the interaction between indoor air and hygroscopic surfaces:

The complex model consists in the solution of the equation (1) coupled with 1D numerical simulation of the coupled heat and moisture transport through the room structures. It enables to take into account material parameters moisture dependency.

The EMPD approach is based on assumption of cyclic variation of vapour pressure at the hygroscopic surface. Then only a thin layer of defined thickness interacts with interior air (Cunningham (2003)). In EMPD approach it is moreover assumed that the temperature in this layer can be considered as uniform and material parameters can be considered constant. This approach doesn't simulate in detail the water vapour transmission through the exterior structures. The moisture transfer to/from the hygroscopic surface is then described by the following equation:

$$\frac{dp_{EMPD}}{d\tau} = \frac{p_{sat,EMPD}(t) \cdot (p_i - p_{EMPD})}{d_{EMPD} \cdot \xi_{w,EMPD} \cdot Z_{EMPD}} \qquad (2)$$

Where d_{EMPD} [m] is thickness of humidity buffering layer, $\xi_{w,EMPD}$ is the slope of sorption curve expressed by water content in relation to relative humidity [kg/m^3], t is temperature [K] and Z_{EMPD} is vapour resistance [m/s], calculated from the relation:

$$Z_{EMPD} = \frac{1}{\beta_i} + \frac{a \cdot d_{EMPD}}{\delta} \qquad (3)$$

Where δ is water vapour permeability [s], a is coefficient; in the simulations a = 0.5 was used.

The thickness of humidity buffering layer is given by the following relation:

$$d_{EMPD} = \sqrt{\frac{\delta \cdot p_{sat,EMPD}(t) \cdot T}{\xi_{w,EMPD} \cdot \pi}} \qquad (4)$$

Where T is the period of cyclic variations [s].

The d_{EMPD} calculated according to the relation (4) represents the thickness of buffering layer, where the relative humidity variation is reduced to ca 27% of the surface variation (Arfvidsson 1999).

In reality the assumption of cyclic variation of vapour pressure at the hygroscopic surface is not fulfilled. The deviations from the cyclic variation are caused by variations exterior water vapour partial pressure and by irregularities in moisture production/ventilation. On the other hand in cases when the thickness of the hygroscopic layer interacting with the indoor air is limited – as it is in case of vapour barrier application, in case of hygroscopic plasters placed on concrete structures or in case when the prevailing part of indoor air - hygroscopic surface interaction takes place at room equipment surfaces – the assumption of constant thickness of interacting hygroscopic material could be considered as an acceptable simplification.

The assumption of constant material properties is acceptable for great deal of hygroscopic materials on condition of common indoor climate conditions where the indoor air relative humidity values don't exceed ca 70 %. In case of extreme conditions with high indoor humidities the usability of EMPD concept depends on concrete humidity variation interval as well as the hygroscopic layer material properties.

3. Comparison of EMPD and complex simulation results

3.1 Presentation of simulated case

With the aim to compare and analyse the results of indoor humidity simulation by complex and EMPD approach the simulation of the resultant indoor air relative humidity were done for the chosen simply object. The code PenDepth (Mihalka, Matiasovsky and Drzik 2007) was used for the EMPD calculations and NPI code (Koronthalyova 2006) was used for complex model calculations.

The calculations were done for the case when water vapour transmission through the structure could be neglected. The indoor humidity values corresponded to common indoor climate conditions and therefore constant material properties were used also in NPI calculations. The aim of the simulations was to quantify the effect of limited thickness of hygroscopic layer, moisture production/ventilation regimes irregularities and presence of temperature gradient in hygroscopic layer on the ability of EMPD approach.

The calculations were done for the simply 1-zone space with the hygroscopic surfaces area S = 64.49 m^2 (walls and ceiling) and the volume V = 49 m^3. For the simplicity it was assumed that the room walls and ceiling have the same composition. The considered structure composition was (from interior): 12.5 mm thick layer of gypsum board, plaster (0.02 m), brick (0.24 m), PPS insulation (0.07 m) and plaster (0.02 m). In case of the limited thickness of hygroscopic layer the gypsum board was separated from the outer part of structure by water vapour barrier. The total thermal resistance of the structure was R = 2.4 $m^2 \cdot K/ W$. The used material properties of gypsum board are presented in Table 1. The thickness of humidity buffering layer used in PenDepth code for considered period T = 12 h was d_{EMPD} = 9 mm.

The effect of moisture production/ventilation irregularities was tested by simulation of two different cases of moisture production/ventilation regimes:

- Regular moisture production and ventilation regimes. The moisture production and ventilation schedule was the same during the whole simulated period and corresponded to the working day regime (Table 2).

- Irregular moisture production and ventilation. The irregularities were caused by different moisture production and ventilation regime during the working days and weekends, representing the case that the room was not occupied during weekends (Table 2).

Table 1. Material properties of gypsum board.

Thermal conductivity [W/(m.K)]	Density [kg/m^3]	Specific heat capacity [J/(kg.K)]	Moisture content at 80% RH [kg/m^3]	Vapour resistance factor [-]
0.3	710	850	9.5	8

Table 2. Moisture production and air change rate schedule used in simulations.

	Working days						Weekends
Hour	0 - 6	6 - 8	8 - 16	16 - 21	21 - 24	22 - 24	0 - 24
Air change rate [1/h]	0.45	1.2	0.45	1.0	1.0	0.45	0.1
Moisture production [kg/h]	0.025	0.4	0.025	0.2	0.2	0.025	0.025

With the aim to evaluate the effect of temperature gradient on the resultant indoor humidity the NPI calculations were done for two cases: In the first case it was assumed that all structures were inner structures and therefore their temperature was the same as the temperature of interior. In the second case all structures were considered as envelope ones, changing their temperature profile in concordance with the outdoor conditions.

The comparison of the calculation results was done for the period from 14th February to 22nd April. The outdoor clima parameters were taken from the Holzkirchen data for the year 2005 (Lenz, Holm 2005). Indoor air temperature was considered constant $t_i = 20°C$.

3.2 Results and discussion

In Table 3 the average and the maximum differences between indoor air relative humidities calculated by NPI and PenDepth are presented for all considered cases. The comparison of the simulation results for two chosen week periods are presented in Figures 1 – 5. The period from 16th to 23rd March was characterised by significant changes of exterior partial vapour pressure (between 450 and 1100 Pa) (Figures 1 – 4). The period from 21st to 28th February was characterised by extreme low temperatures of outdoor air (between –3 and -24 °C), but due to the temperature decrease also exterior vapour pressure decrease took place (Figure 5).

In the Figures 1 – 4 the effect of sudden increase of external vapour pressure during 1802nd - 1866th and 1924th – 1944th hours can be observed. The sudden significant change of exterior water vapour pressure was the main reason of differences between the calculated humidities in case of hygroscopic layers placed on inner structures and regular moisture production/ventilation regime.

In case of external structures the effect of temperature gradient in the structures on resultant indoor humidity was noticeable in spite of their relatively good thermal insulation. Therefore in Figures 1 – 5 also the NPI results corresponding to case when half of hygroscopic surfaces were placed on inner structures and half on exterior ones - which is closer to common sitting of hygroscopic surfaces in interior – are shown (NPI inner + envelope). The effect of temperature gradient in external walls can be seen in Figure 5. It resulted in relatively high difference between the NPI results for case of inner structures and case of half inner/half exterior structures. The differences between NPI and PenDepth results were not so high during the period because the effect of temperature gradient was partly compensated by coupled phenomenon of exterior water vapour pressure decrease.

As can be seen from results in Table 3 the results of the complex and EMPD approach were in satisfactory agreement in case of limited thickness of hygroscopic layer (presence of vapour barrier) and regular moisture production/ventilation regime or in case that hygroscopic layers belonged to internal structures.

In case without water vapour barrier the differences between the NPI and PenDepth results were significant. The highest differences between the EMPD and NPI simulation results were achieved in case of unlimited thickness of the hygroscopic layer and coupled effect of moisture production irregularity and temperature gradient in the structure.

TABLE. 3: Differences between he the results of complex (NPI) and EMPD (Pen Depth) model during the considered period

Hygroscopic layer	Moisture production regime	Structure	RH difference between EMPD and complex model [%RH]	
			Average	Maximum
Limited	Regular	Inner	1	3
		Envelope	2.3	4.6
	Irregular	Inner	1	3
		Envelope	3.8	10.1
Unlimited	Regular	Inner	2.5	10.1
		Envelope	3.7	10.3
	Irregular	Inner	2.6	11.6
		Envelope	6.1	17.8

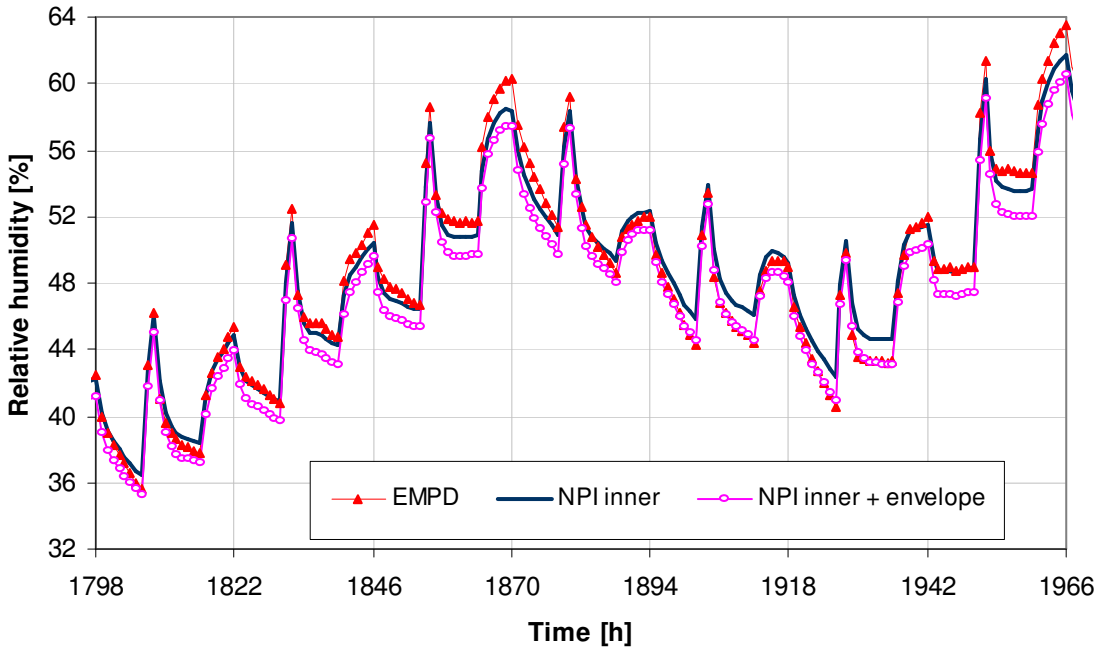

FIG. 1: Comparison of the calculated indoor air relative humidity courses for 1-week period from 16th to 23rd March: Vapour barrier and regular moisture production/ventilation regimes.

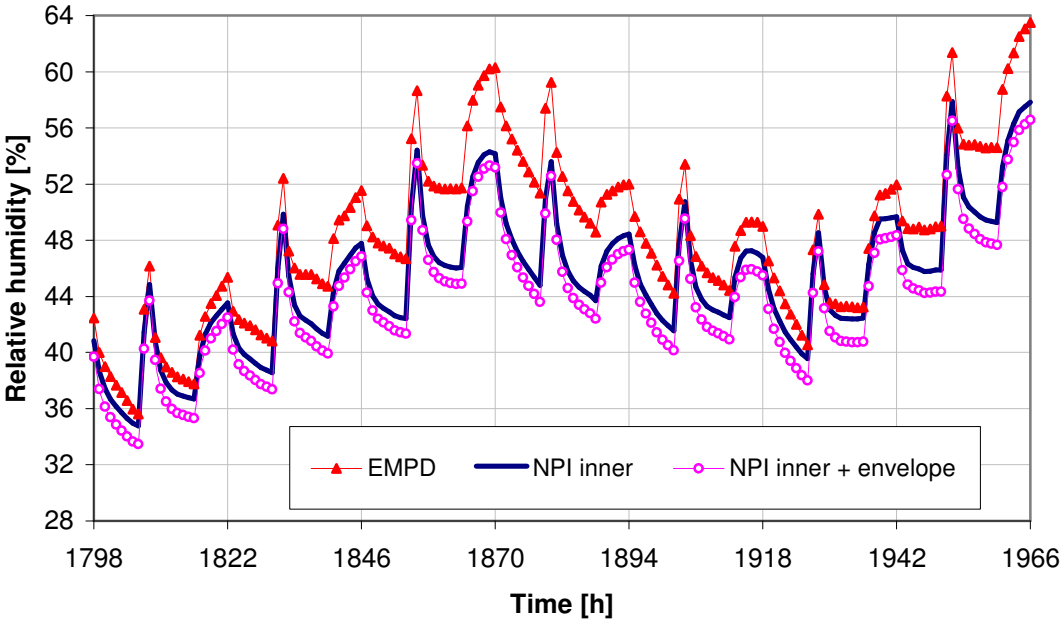

FIG. 2: Comparison of the calculated indoor air relative humidity courses for 1-week period from 16th to 23rd March: Regular moisture production/ventilation regimes without vapour barrier.

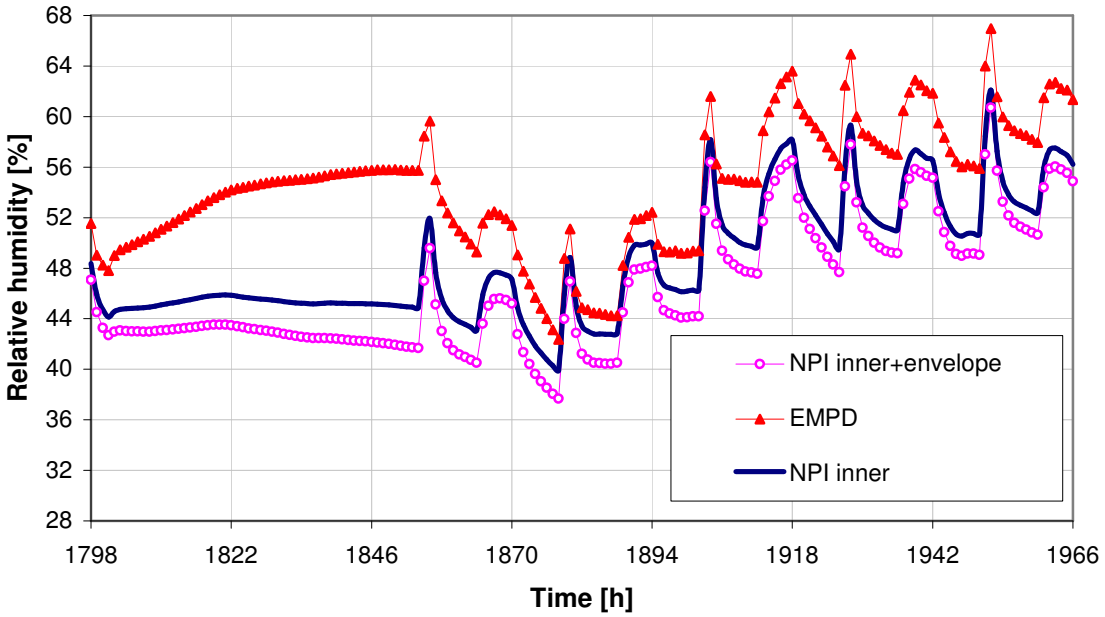

FIG. 3: Comparison of the calculated indoor air relative humidity courses for 1-week period from 16th to 23rd March: Irregular moisture production/ventilation regimes without vapour barrier.

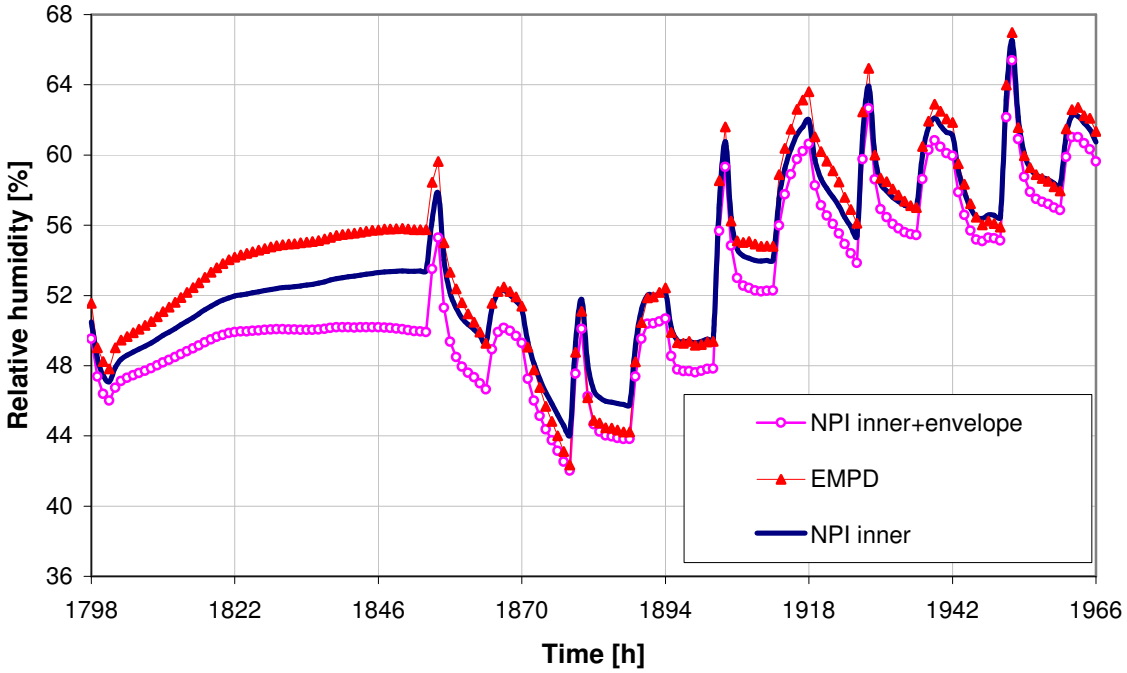

FIG. 4: Comparison of the calculated indoor air relative humidity courses for 1-week period from 16th to 23rd March: Vapour barrier and irregular moisture production/ventilation regimes.

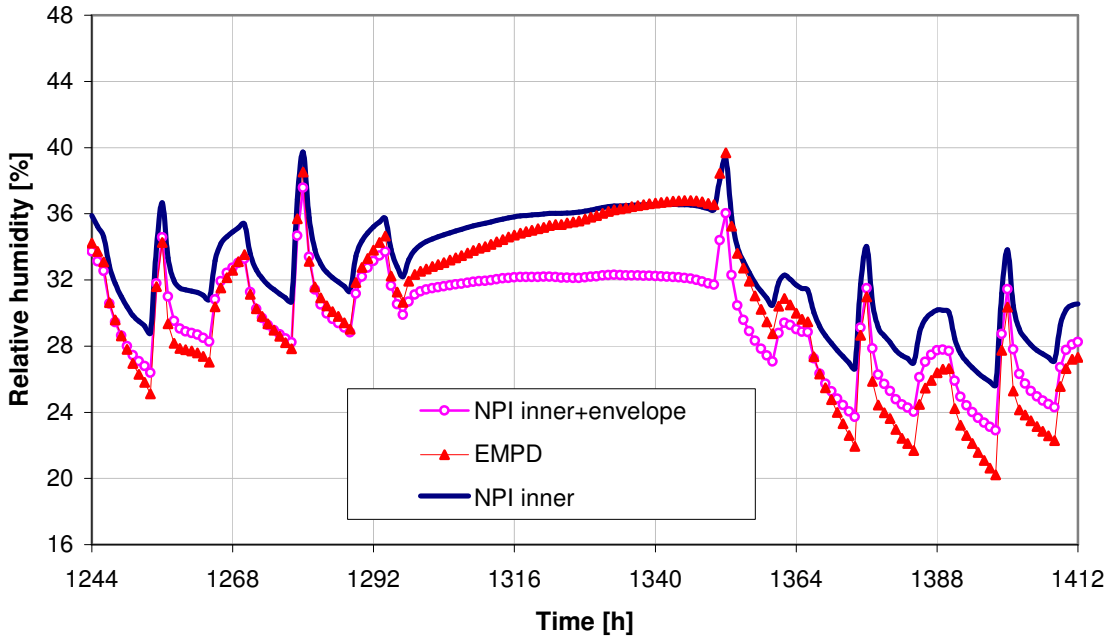

FIG. 5: Comparison of the calculated indoor air relative humidity courses for 1-week period from 21st to 28th February: Irregular moisture production/ventilation regimes without vapour barrier.

4. Conclusions

The conditions for reliable using simplified EPMD concept were analysed for the case of 1-zone space by the comparison with the complex model. The analysis dealt with cases when the assumption of well-mixed air was acceptable and water vapour transmission through the building envelope was negligible in comparison to the convective transfer by ventilation. The analysis was also limited to the case of common indoor relative humidities, excluding the cases with extreme high humidities of indoor air.

In spite of relatively good thermal insulation of the considered structures the influence of temperature gradient in the envelope structures on resultant indoor humidity was noticeable.

In case of limited thickness of the hygroscopic layer the results of PenDepth code were in good agreement with the complex model results on condition that the moisture production and ventilation could be described as regular cyclic process or in case that the most of the hygroscopic surfaces was placed on inner structures and therefore the influence of temperature gradient in the structures was negligible.

The most significant differences between the EMPD and NPI simulation results were achieved in the case of unlimited thickness of the hygroscopic layer and coupled effect of moisture production irregularity and temperature gradient in the structure.

Acknowledgements: The financial support of Slovak Science and Technology Assistance Agency under number APVT-51-030704 and of Slovak Grant Agency VEGA (Grant No 2/7113/27) was gratefully acknowledged.

5. References

Arfvidsson J. (1999) A New algorithm to Calculate the Isothermal Moisture Penetration for Periodically Varying Relative Humidity at the Boundary. *Nordic Journal of Building Physics.* Vol. 2

Cunningham M. J. (1992). Effective Penetration Depth and Effective Resistance in Moisture Transfer. *Building and Environment*. Vol. 27, p. 379-386.

Cunningham M. J. (2003). The building volume with hygroscopic materials: an analytical study of a classical building physics problem. *Building and Environment*. Vol. 38, p. 329-337.

IEA-Annex XIV (1991), *Condensation and Energy, Source Book,* 1991.

Janssens A., De Paepe M. (2005) Effect of moisture inertia models on the predicted indoor humidity in a room. In *Proceedings of 26th AIVC Conference.*

Koronthalyova O. (2006) Determination of moisture buffer ability of 1-zone space. *Building Research Journal.* Vol. 54, Number 3-4, p. 221-232.

Lenz K., Holm A. (2005) Annex 41 subtask1. Common Exercise 3: Whole building heat and moisture analysis. Fraunhofer Institute for Building Physics, Holzkirchen Branch.

Mihalka P., Matiasovsky P. and Drzik, M. (2007). Numerical modelling of local convective internal surface heat transfer coefficient. IEA ANNEX 41 Paper A41-T3-Sl-07-2.

Rode C. et al. (2005). Moisture Buffering of Building Materials. *Report BYG DTU R-126.* Department of Civil Engineering, Technical University of Denmark

Object-oriented hygrothermal building physics library as a tool to predict and to ensure a thermal and hygric indoor comfort in building construction by using a Predicted-Mean-Vote (PMV) control ventilation system

Thierry Nouidui, Dipl.-Ing.,
Fraunhofer Institute for Building Physics;
nouidui@ibp.fraunhofer.de

Christoph Nytsch-Geusen, Prof. Dr.-Ing.,
Berlin University of the Arts;
Fraunhofer Institute for Computer Architecture and Software Technology;
nytsch@udk-berlin.de

Andreas Holm, Dr.-Ing.,
Fraunhofer Institute for Building Physics;
holm@ibp.fraunhofer.de

Klaus Sedlbauer, Prof. Dr.-Ing.,
Fraunhofer Institute for Building Physics;
sedlbauer@ibp.fraunhofer.de

KEYWORDS: bulding physics library, Predicted-Mean-Vote, ventilation system, comfort.

SUMMARY:
The indoor temperature and humidity conditions of the building envelope are important parameters for the evaluation of the thermal and hygric indoor comfort. In the research project GENSIM a new hygrothermal building library, based on the object- and equation-oriented model description language Modelica® has been developed by the Fraunhofer Institutes IBP and FIRST. This library includes many models as for instance a hygrothermal wall model, an air volume model, a zone model, a window model and an environment model. Due to the object-oriented modelling approach, some models of this library can be configured to a complex hygrothermal room model, which can predict the time dependent indoor temperature and humidity conditions in a building construction.

In this paper we will introduce in a first step the object-oriented hygrothermal room model of this library. In a second step, the validation of the room model with some field experiments will be shown. In a third step we will present some simulation results, we obtained by coupling the room model with an implemented Predicted-Mean-Vote (PMV) control ventilation system to predict and to ensure a thermal and hygric indoor comfort in one case study.

In the conclusion, the possible range of future applications of this new hygrothermal building physics library and demands for further research are indicated.

1. Introduction

The heat and moisture behaviour of the building envelope are important parameters for the evaluation of the thermal and hygric indoor comfort. In the research project GENSIM (Nytsch et. al., 2005) a new hygrothermal building library, based on the object- and equation-oriented model description language Modelica® (Modelica, 1997) has been developed by the Fraunhofer Institutes IBP and FIRST. This library includes many models as for instance a hygrothermal wall model, an air volume model, a zone model, a window model and an environment model. Due to the object-oriented modelling approach, some models of this library can be configured to a

complex hygrothermal room model, which can predict the time dependent indoor temperature and humidity conditions in a building construction. In this paper the hygrothermal whole building simulation model and its experimental validation will be presented. Furthermore, we will show some simulation results we obtained by coupling the validated building simulation model with a PMV control ventilation system to ensure a thermal and hygric comfort in the building envelope.

1.1 Hygrothermal room Model

The hygrothermal room model of the building library is built by coupling following models of the developed building physics library:

- a wall model, which takes in account vapour diffusion, liquid flow and thermal transport. This model is based on the physical model for the dynamic coupled heat and moisture transport in building components. A detailed model description is given in (Nouidui et. al., 2006).
- an air model, which takes in account the coupled energy and mass balance of the air volume in the building envelope according to following equations:

Energy Balance

$$\rho \cdot V \cdot c \frac{dT}{dt} + c_{vap} \left(\frac{dT}{dt} m_{vap} + T_a \frac{dm_{vap}}{dt} \right) + r_{H2O} \frac{dm_{vap}}{dt} = \dot{Q}_{cv,surfaces} + \dot{Q}_{cv,\,sources} + \dot{H}_{airchange}\ ; \quad (1)$$

ρ: density of the air, [kg/m³]

T: temperature of the air volume, [K]

t: time, [s]

c: heat capacity of the air [J/kgK]

c_{vap}: heat capacity of the vapour [J/kgK]

r_{H20}: enthalpy of vaporization for water [J/kg]

m_{vap}: mass of the vapour [kg]

$\dot{Q}_{cv,surfaces}$: convective heat fluxes through the building envelope, [W]

$\dot{Q}_{cv,\,sources}$: internal convective gains such as people, lights and equipment, [W]

$\dot{H}_{airchange}$: heat fluxes gained or lost due to natural infiltration, [W]

V: volume, [m³]

Mass Balance

$$\frac{dm_{vap}}{dt} = \dot{m}_{vap,sources} + \dot{m}_{vap,airchange} + \dot{m}_{vap,airmassflows} + \dot{m}_{vap,surfaces}; \quad (2)$$

m_{vap}: mass of the vapour [kg]

$m_{vap,surfaces}$: moisture fluxes through the building envelope, [kg/s]

$m_{vap,\,sources}$: internal moisture gains such as people, and equipment, [kg/s]

$m_{vap,airchange}$: moisture fluxes gained or lost due to natural infiltration, [kg/s]

- a zone model, which calculates the geometry of a zone, the sum of all heat and moisture loads of the zone, the sum of the solar gain through transparent components, the specific long wave and shortwave heat flow of each wall surface of the zone.

- a window model, which calculates the solar gains and the heat losses through the glasses of the window.
- an environment model, which calculates the necessary climate parameters for the simulation of the room model.

1.2 Validation of the hygrothermal room Model

The hygrothermal wall model has already been validated by comparison with some well-established HAM-simulation tools (Nouidui et. al., 2006). HAM means **H**eat, **A**ir and **M**oisture. For the validation of the hygrothermal room model some fields experiments were carried out in the first two months of the year 2007 at the outdoor testing site of the Fraunhofer-Institute of building physics in Holzkirchen. The aim of these experiments was to compare the measurements with the developed model.

1.2.1 Experimental setup

The experiments were carried out in a building, erected on the IBP test site in the 80s. One of the five rooms of this building is suitable for our purpose, because of the well defined boundary conditions. The ground plan of the testroom is shown in FIG. 1. The rooms have a ground area of 20 m² and a volume of 50 m³. They are well insulated (200 mm of polystyrene) towards the ground. The floor has a vinyl covering to avoid moisture flow through it. The external walls consist of 240 mm thick brick masonry with 100 mm exterior insulation (ETICS). Walls and ceiling of the rooms are coated with 12 mm standard interior plaster. The double-glazed windows are facing south (U-value: 1.1 W/m²K, total solar energy transmittance: 0.57, frame ratio: 30 %). The walls and ceiling are rendered moisture inert by sealing them with aluminium foil. During the tests a wool blanket was situated in front of the window on the outside in order to exclude any solar radiation into the room.

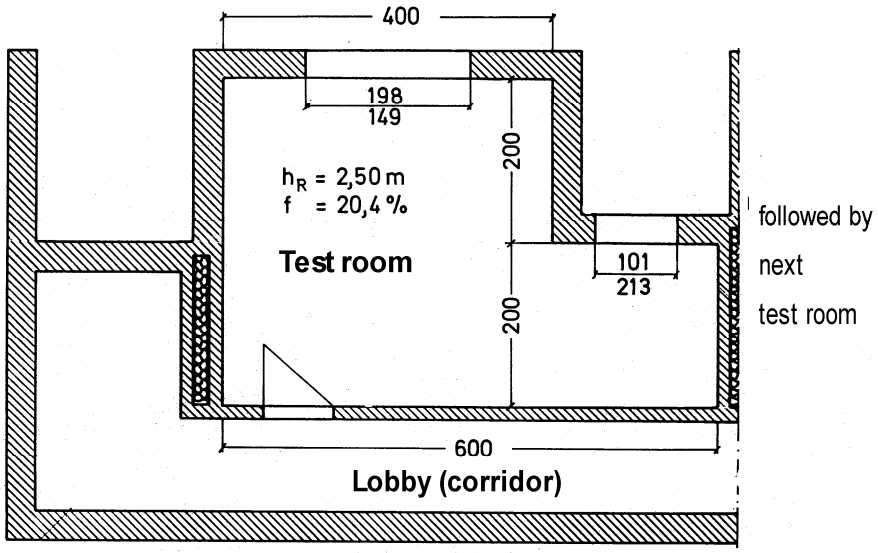

FIG. 1: Ground Plan of the testroom

The temperature in the room is controlled to 20±2°C. A moisture production of 2.4 kg per day has been set in the room. This represents the production of a three persons household (Hartmann et. al., 2001). FIG. 2 shows the diurnal moisture pattern in the testroom. The permanently present basic humidity production of 0.025 kg/h is due to e.g. plants or pets. In the early morning hours between 6 am and 8 am, this value is increased to a peak level of 0.4 kg/h in order to simulate human activities, like having a shower and washing. Subsequently, the moisture production will drop back to the basic rate of production 0.025 kg/h. In the late afternoon the moisture production will increase again to a moderate level (0.2 kg/h) until the evening hours (4 pm until 10 pm), which represents certain activities like cooking, cleaning or doing the laundry.
The air-tightness of the rooms was measured with blower-door method. After conversion to the air change by infiltration under normal pressure conditions, a value of $n = 0.07\ h^{-1}$ was obtained for the testroom. The

additional air change rate of the ventilation system is n = 0.5 h^{-1} , which means a constant air flow of about 25 m³/h.

1.2.2 Simulation setup

For the simulation of the hygrothermal room model, we used material parameters taken from the WUFI® database (Künzel, 1994). The moisture production and ventilation rate are the same as in the experiment. The outdoor climate data, which are continuously recorded at the meteorological station of the IBP are introduced as hourly averages.

1.2.3 Results

The measured and calculated evolutions of the absolute humidity in the test room during two days in January 2007 are plotted in FIG. 3. The figure shows a very good agreement between experiment and simulation.

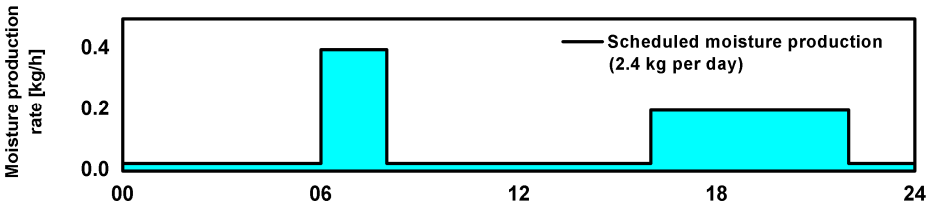

FIG. 2: Diurnal moisture production pattern in the experimental room

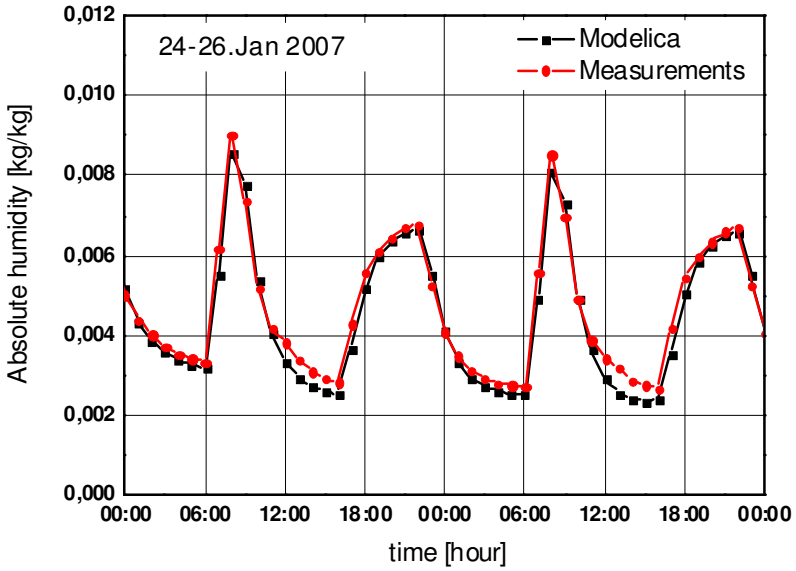

FIG. 3: Calculated (black) and measured (red) absolute humidity of the test room

1.3 Coupling of the hygrothermal room Model and a PMV control ventilation system to ensure a thermal and hygric comfort.

A PMV control ventilation system has been implemented. PMV represents the '**p**redicted **m**ean **v**ote' (on the thermal sensation scale) of a large population of people exposed to a certain environment (DIN, 2005). The inputs of the ventilation system are the time dependent calculated PMV (see equation (3)) and PPD. The PPD is

the **p**redicted **p**ercent of **d**issatisfied people at each PMV. It can be derived from the PMV according to the equation (4):

$$PMV = [0.303 \cdot \exp(-0.036M) + 0.028] \left\{ \begin{array}{l} (M - W) - 3.05 \cdot 10^{-3}[5733 - 6.99(M - W) - P_a] - 0.42(M - W) - 58.15 \\ -1.7 \cdot 10^{-5} M(5867 - P_a) - 0.0014M(34 - t_a) \\ -3.96 \cdot 10^{-8} f_{cl}[(t_{cl} + 273)^4 - (\overline{t_r} + 273)^4] - f_{cl} h_c (t_{cl} - t_a) \end{array} \right\} \quad (3)$$

$$PPD = 100 - 95 \cdot \exp(-0.03353 \cdot PMV^4 - 0.2179 \cdot PMV^2) \quad (4)$$

M : metabolic rate, [W/m^2]

W : external work [W/m^2]

t_{cl}: surface temperatur of the cloth [°C]

$\overline{t_r}$: mean radian temperatur [°C]

t_a: air temperatur [°C]

f_{cl}: clothing area factor [-]

h_c: convective surface coefficient [W/m^{2}K]

P_a: water vapour pressure [Pa]

The maximum possible air change rate of the system, the relative humidity and the temperature of the air volume, where the PMV control system will be integrated, are necessary inputs for the ventilation system. The air change rate of the system is regulated in a way that a critical PPD-value set by the user could not be reached. For testing the implemented ventilation system, we integrated it in a model room. The boundary conditions of the room, used for the simulation are described in the next paragraph. We compared for our purpose three ventilation systems: a traditional shock ventilation, a constant ventilation system and a PMV-control ventilation system. As the worst case, we consider the model room without ventilation system.

1.3.1 Model room and Simulation parameters for the ventilation systems

The geometry and the material parameters of the model room are identical to the testroom used in paragraph 1.2. The temperature in the room is controlled to 20°C. A new moisture profile for a typical living room of a four persons household has been assumed (see FIG. 4 (left)). This production is derived from the activities of the occupants (Kainz, 2004). The metabolic equivalent of task profile used for the simulations is plotted in FIG. 4 (right). We assumed a constant clo-value of 1.0. For the shock ventilation, we assumed that the occupants open the windows for 10 minutes anytime they entry in the room. We assumed for the constant ventilation system an air change rate of 0.6 h^{-1}. For the PMV-ventilation system, we assumed a maximal air change rate of 0.6 h^{-1}. A critical PPD of 10% has been set for the simulation. This corresponds to the interval, which will be felt as acceptable for the most of people (DIN, 2005). We make the simulation over the last three months of the year 2006 with the weather data recording at the Fraunhofer Institute IBP in Holzkirchen.

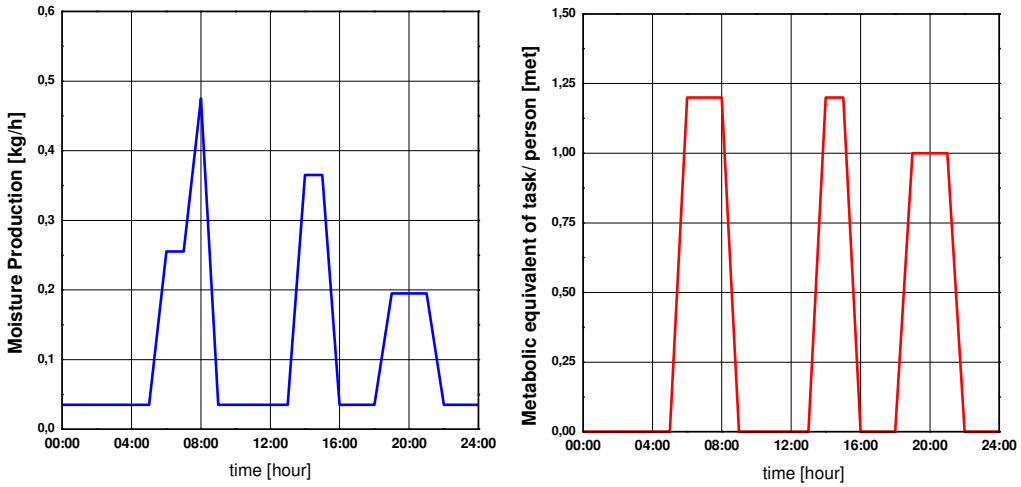

FIG. 4: Daily moisture production and metabolic equivalent of task used for the simulation

1.3.2 Results

FIG. 5 shows the air change rates of the three ventilation systems used in the simulation. The first four figures in FIG. 6 show the simulated relative humidity of the air volume without and with the use of the three ventilation systems for the last two months in the year 2006. The maximum (blue) and minimum (red) values of the comfort interval are plotted in the four figures. The violation frequency ratio of the comfort criterion has been calculated for all the cases and is plotted in the same figure. The simulation results for the case without ventilation system show that it is not possible to be at anytime in the month in the comfort interval. The use of the constant ventilation system allows being about 90 percent of the time in the comfort interval. With the shock ventilation, it is only possible to be about 40 percent of the time in the comfort interval. The use of the PMV-ventilation system gives the best results. With this system and a maximal air change of 0.6 h^{-1}, it is possible to be in the comfort interval for more than 99 percent of the time in the two months interval.

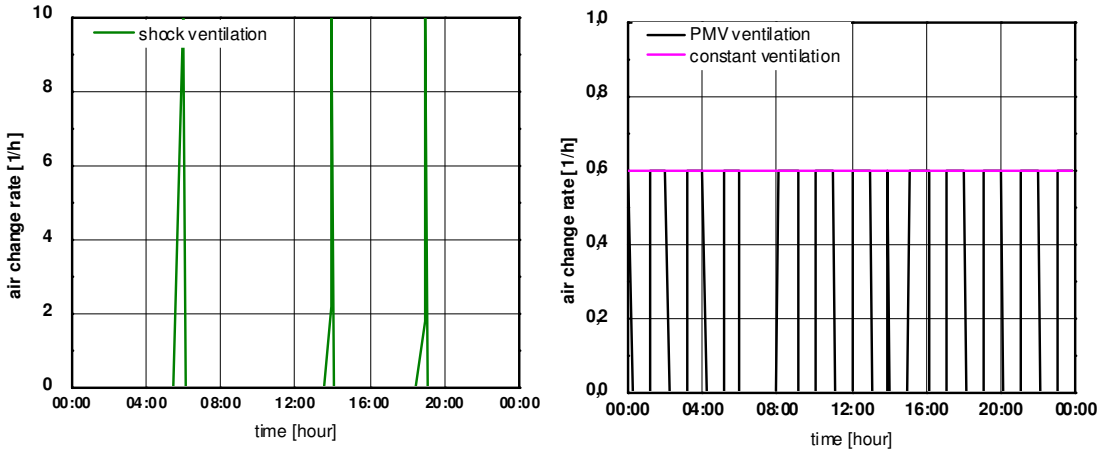

FIG. 5: Air change rate (one day) of the three ventilation systems (schock-, constant-, PMV-ventilation)

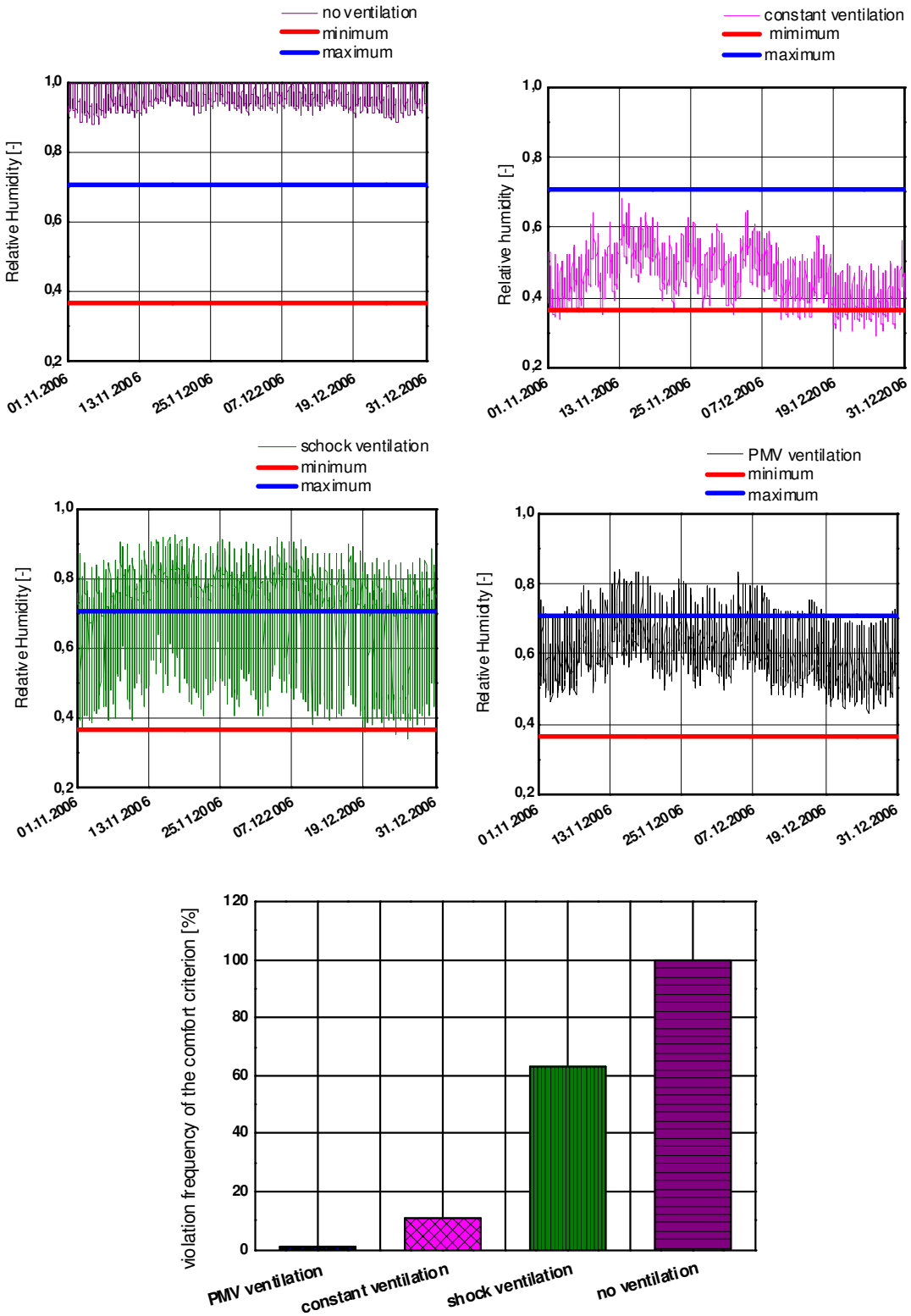

FIG. 6: Relative humidity in the room without (no ventilation) and with ventilation systems (constant-, schock-, PMV ventilation), violation frequency of the comfort criterion with and without ventilation systems

2. Conclusion

In this paper we present the object-oriented hygrothermal room model of the new building physics library developed in the research project GENSIM. We show the first validation results of the room model we obtained by comparing the room model with measurements of field experiments. The results are promising, but many more validation examples are necessary in order to gain confidence in the new model. In a last step we introduce the PMV control ventilation system. We implemented it to ensure a thermal and hygric comfort in building constructions. This system has been integrated in the room model. The simulation results show that the coupling of the room model with the PMV control ventilation system can ensure a thermal and hygric comfort over a long time compared to a shock or constant ventilation.

The developed models open the possibility in the future to improve the energy efficiency of buildings. At the same time it will be possible to design and to test new ventilation systems, which could be used for instance to minimize the risk of mould growth or to guarantee a thermal, hygric and hygienic comfort in building constructions.

3. References

DIN (2005). DIN EN ISO 7730: Ergonomie der thermischen Umgebung Analytische Bestimmung und Interpretation der thermischen Behaglichkeit durch Berechnung des PMV- und des PPD-Indexes und Kriterien der lokalen thermischen Behaglichkeit (ISO 7730:2005); Deutsche Fassung EN ISO 7730:2005, Germany.

Hartmann et. al. (2001). „Feuchteabgabe in Wohnungen alles gesagt?" Gesundheitsingenieur. 122. Jahrgang. Heft 4. S. 189-195, Germany.

Kainz E. (2004). Lüftungskonzepte zur Erhaltung der Raumluftqualität und gleichzeitiger Vermeidung von Schimmelpilzen. Diplomarbeit, Rosenheim, Germany.

H. M. Künzel (1994). Verfahren zur ein- und zweidimensionalen Berechnung des gekoppelten Wärme -und Feuchtetransports in Bauteilen mit einfachen Kennwerten. Dissertation, Stuttgart, Germany.

Modelica (1997). http://www.modelica.org.

Nouidui T. et al.(2006). Validierung der eindimensionalen hygrothermischen Wandmodelle der Modelica-Bibliothek *BuildingPhysicsLibrary*. Proceedings BAUSIM 2006, München, Germany.

Nytsch-Geusen C. et. al (2005). MOSILAB: Development of a Modelica based generic simulation tool supporting model structural dynamics, Proceedings of the 4th International Modelica Conference, Hamburg-Harburg, Germany.

Stochastic analysis of moisture buffering in rooms

Jan Carmeliet, Ph.D.,
Chair of Building Physics, Swiss Federal Institute of Technology ETHZ, Zürich
ETH-Hönggerberg, CH-8093 Zürich
Empa, Swiss Federal Laboratories for Materials Testing and Research, Laboratory for Building Technologies, Überlandstrasse 129, CH-8600 Dübendorf

Dominique Derome, Ph.D.,
Empa, Swiss Federal Laboratories for Materials Testing and Research,
Wood Laboratory, Überlandstrasse 129, CH-8600 Dübendorf

Robert Guyer, Ph.D.,
University of Massachusetts, USA, Los Alamos National Laboratory, USA

KEYWORDS: *moisture design, moisture buffering, moisture damage, stochastic and risk analysis.*

SUMMARY:
This paper presents a stochastic method to obtain design values for the necessary moisture buffering of wall materials in order to prevent moisture damage. The difference in maximal and minimal relative humidity in the room during a day is chosen as an indicator for the moisture damage risk. Choosing an acceptable probability of occurrence of moisture damage allows then to determine the necessary moisture buffering capacity. The moisture buffering capacity is defined as the average reduction in moisture damage risk in comparing a room with and without moisture buffering. Using a penetration depth model, an average equivalent surface mass coefficient for the walls of the room is defined, taking into account the vapour transport from air to the surface, through paint layer and finally to the active surface material layer. The existence of a unique relation between the moisture buffering capacity and the average equivalent surface mass coefficient, called the moisture buffering design curve, allows to determine the necessary moisture buffering of the wall materials.

1. Introduction

During the last decade, a number of 'whole building' moisture simulation models were developed with different levels of complexity (IEA, 2008). These models can be used for moisture design analysis of buildings. Standarized methods have been proposed in the literature to determine the indoor humidity load in residential building without mechanical humidity control (Jones 1995, TenWolde and Walker, 2001). The methods were compared in Roppel et al. (2007) and the impact of ventilation, moisture production and moisture storage was analysed. Ideally, a moisture design analysis involves the determination of the probability of moisture damage, treating all design parameters and loads as stochastic variables (Geving 2000). For the outdoor boundary conditions, climatic data can be used as stochastic input. However, sufficient data regarding ventilation and occupancy moisture production are often not available to make a full stochastic approach practical (TenWolde and Walker, 2001). Therefore, most moisture design models are deterministic, treating only average moisture production and average ventilation rates on weekly or monthly basis. In reality, most of these factors may vary randomly in time and place.

This paper presents a stochastic analysis of moisture buffering in a room, where the ventilation rate, the outside vapour pressure and temperature and the moisture production rate are considered to be stochastic variables. First, a moisture balance model including moisture buffering is presented. The resulting inside relative humidity is considered as a stochastic process and a reliability approach is presented. Based on the reliability analysis, a new method for moisture design analysis is presented.

2. Moisture balance of a room: deterministic model

The relative humidity (RH_i) in a room depends on the ventilation rate G_v (or supply of air with a different RH and temperature), the moisture production rate G_p and the moisture uptake/release rate by finishing materials, also called moisture buffering. The $RH_i(t)$ process in a room can be modelled by the moisture balance of the

room including the moisture uptake/release rate by the different moisture buffering materials. The moisture balance for a room is given by

$$\frac{d\rho_i(t)V}{dt} = -G_v(t)V\left(\rho_i(t)-\rho_e(t)\right) - \sum_{j=1}^{k} A_j g_j + G_p(t)V \quad (1)$$

The LHS of (1) describes the change in the vapour density ρ_i in the room as a function of the time t, with V the volume of the room. The first term at the RHS describes the exchange of inside and outside air at a ventilation rate G_v. The second term of the RHS describes the uptake/release of moisture by the k different moisture buffering materials, which have a surface A_j. The moisture buffering by air and furniture is not considered, but can be easily introduced. The last term of the RHS is the water vapour production rate. Dividing LHS and RHS of equation 1 by the volume, we can define the surface to volume ratio of a wall as $\alpha_j=A_j/V$.

The water vapour uptake/release by the surface materials is modelled using an effective penetration depth (EPD) model, where an equivalent surface coefficient $\beta_{eq,j}$ for the wall j is introduced to model the vapour transport from the room to the (painted) wall

$$g_j = -\frac{\left(p_{wj}-p_i\right)}{\frac{1}{\beta_j}+\frac{\mu d_{\text{paint,j}}}{\delta_a}+\frac{d_{p,j}}{2\delta_j}} = -\beta_{eq,j}\left(p_{wj}-p_i\right) \quad (2)$$

with β_j the water vapour surface coefficient, p the vapour pressure (subscript w = wall), $\mu d_{paint,j}$ the equivalent water vapour resistance thickness for the paint layer, δ_a the vapour permeability of dry air, $d_{p,j}$ the penetration depth and δ_j the water vapour permeability of the material. The penetration depth is defined as the thickness of the surface layer where hygric interaction with the indoor air occurs, or

$$d_{p,j} = \sqrt{\frac{\delta_j\, p_{sat} t_p}{\xi_j\, \pi}} \quad (3)$$

with p_{sat} the water vapour saturation pressure and t_p the period of time (one day). In the EPD model, it is assumed that the hygroscopic moisture capacity ξ and water vapour permeability δ of the material are constants. The differential equation for the j^{th} moisture buffering of the wall then reads

$$\frac{\mathrm{d}p_{wj}(t)}{\mathrm{d}t} = -\gamma_{wj}\beta_{eqj}\left(p_{wj}(t)-p_i(t)\right) \quad \text{with } \gamma_{wj}=\frac{p_{sat}}{d_{pj}\xi_j} \quad (4)$$

Equations 1 and 4 define a set of (k+1) ordinary differential equations, which are solved numerically.

3. Stochastic approach and reliability problem

3.1 Stochastic model

The independent stochastic variables $X_i(t)$ in this model are the ventilation rate $G_v(t)$, the outside vapour pressure $p_e(t)$ and temperature $T_e(t)$, the moisture production rate $G_p(t)$. The mass surface coefficient β and the material properties are considered to be deterministic. The inside temperature is considered to be constant equal to 20°C.

The outside conditions - vapour pressure $p_e(t)$ and temperature $T_e(t)$- are climatic variables, showing a daily and yearly periodicity and randomness with trends. In this paper, we model the outside conditions in two ways: (1) as measured climatic data showing a daily and yearly periodicity (see e.g. the outside vapour pressure in Figure 1a); (2) as random variables showing a periodic daily variation (see Figure 1b).

The ventilation rate G_v depends on the airtightness of the building and the pressure difference outside/inside due to wind and thermal stack effects. Due to the random variation of wind effects, the ventilation rate is considered as a stochastic process characterised by a random variation around daily and hourly values. The daily variation accounts for windy versus non-windy days, while the hourly variation accounts for the short time stochastics of wind pressure. The minimum ventilation rate is limited to G_{vbas}=0.2 1/h. The average ventilation rate is 0.6 1/h. A typical variation of G_v(t) is given in Figures 1c-d, respectively for 1 and 10 days.

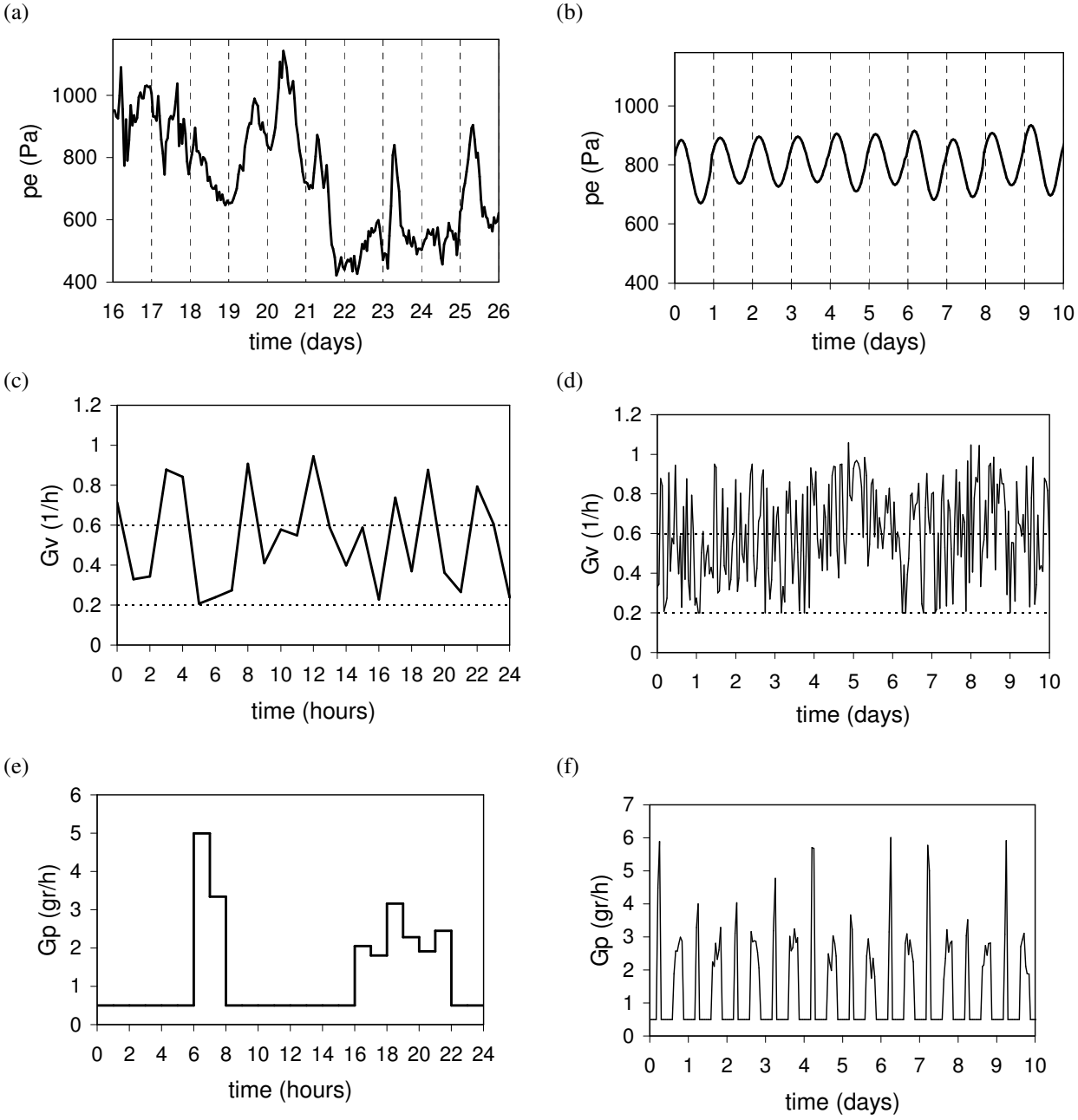

Figure 1. (a) 'climatic': outside vapour pressure variation during 10 days in April for Belgium; (b) 'random' variation of outside vapour pressure during 10 days; (c) random variation of ventilation rate during 1 day; (d) random variation of ventilation rate during 10 days; ; (e) random variation of water vapour production rate during 1 day; (f) random variation of water vapour production rate during 10 days

We consider the vapour production rate to consist of two components: a basic production rate accounting for permanent vapour production due to the presence of e.g. presence of people and plants and two peak production rates during the morning and late afternoon. The morning period, between 6 and 8 am, accounts for human activities, such as showers and washing. The late afternoon period from 4 pm until 10 pm simulates certain activities like cooking, cleaning, laundry. Since the peak water vapour production rates depend on human activity, they are considered to be stochastic. Figure 1e-f gives a typical variation of the vapour production rate during 1 and 10 days.

3.2 Definition of the reliability problem

Due to the stochastic characteristics of $X_i(t)$, the fluctuation of the relative humidity in a room $RH_i(t)$ can be seen as a stochastic process $Y(t)$. An example of time train for $Y(t)$ is given in Figure 2a. A possible measure to evaluate the moisture damage risk is the difference in maximal and minimal relative humidity during a day

$$\Delta Y(n) = \max(Y_n(t)) - \min(Y_n(t)) \tag{5}$$

where n is the index for the day (see Figure 2b).

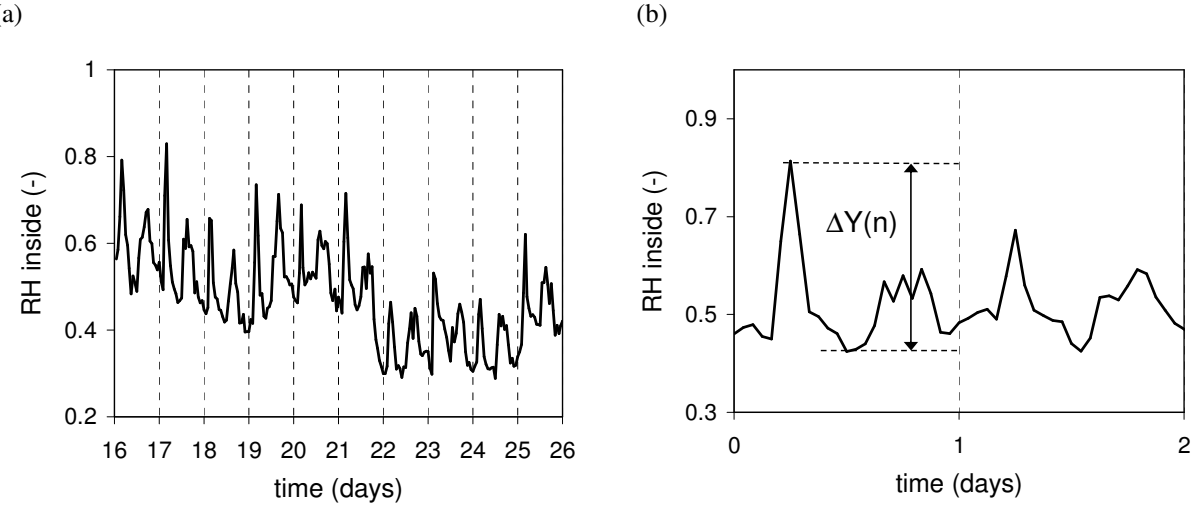

Figure 2. (a) Typical variation of the inside relative humidity for a period in April for Belgium; (b) Definition of the daily maximal variation of the inside relative humidity as damage risk indicator.

Since $Y(t)$ is a stochastic process, the damage indicator $\Delta Y(n)$ is random and can be described by a cumulative distribution function F_Y. Figure 3a gives the cdf for a room with and without buffering. The stochastic process $Y_A(t)$ for a room without any moisture buffering is obtained by putting for all walls α_j=0. As damage criterion (or limit state), we choose a maximal change in RH_i during a day equal to $\Delta Y_{\lim}$. The probability of moisture damage is then defined as

$$P_f = P\left[\Delta Y_{\lim} \le \Delta Y(n)\right] = 1 - F_Y(\Delta Y_{\lim}) \tag{7}$$

As performance criterion we may define a maximum probability of occurrence of moisture damage P_{max} given the damage limit $\Delta Y_{\lim}$. The reliability problem can then be defined as: find the distribution function F_Y, for which

$$F_Y(\Delta Y_{\lim}) = 1 - P_{\max} \tag{8}$$

The distribution function F_Y depends on the moisture buffering properties and α-values of the material surfaces given certain parameters for the stochastic processes G_v, G_p, T_e and p_e.

3.3 Moisture Buffering Capacity (MBC)

In order to properly identify the moisture buffering effect of surface materials in a room, we plot the results of the maximum daily variation of the inside relative humidity RH_i of the room with moisture buffering $\Delta Y(n)$ versus the results for the room without buffering $\Delta Y_A(n)$ (Figure 3b). $\Delta Y_A(n)$ is the maximum daily variation for the room without moisture buffering capacity. It is found that, despite some scatter, the results can

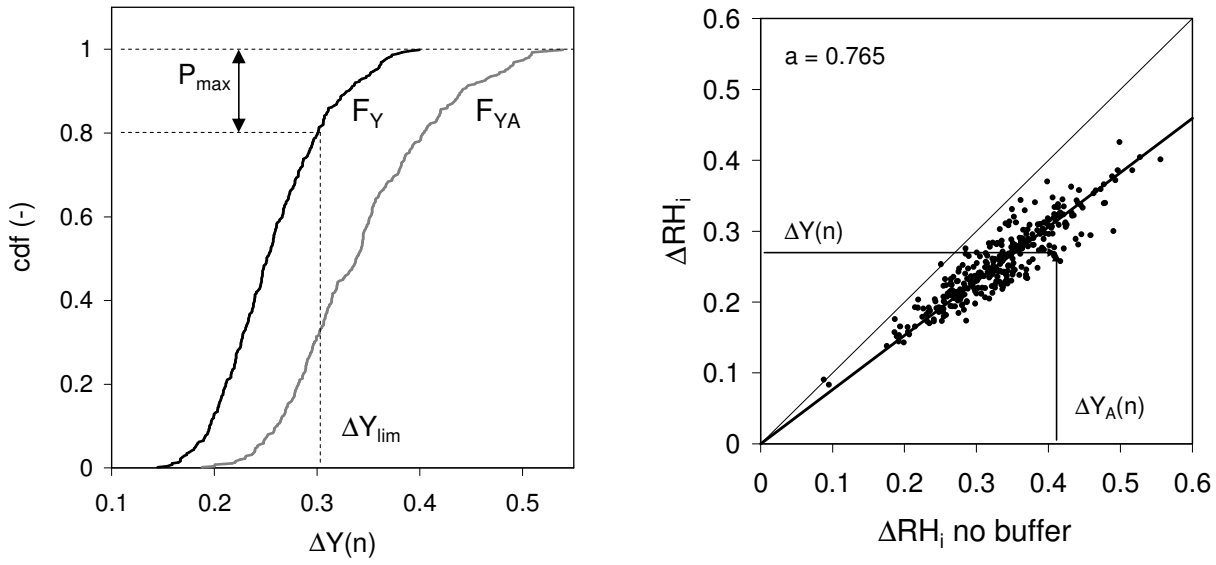

Figure 3. (a) Cumulative distribution function (cdf) of the maximum daily variation of inside relative humidity for the room with (F_Y) *and without* (F_{YA}) *moisture buffering. Definition of the maximum failure risk* P_{max} *at the limiting value of the maximum daily variation of inside relative humidity* $\Delta Y_{\lim}$ *; (b) Maximum daily variation of inside relative humidity for room with buffering versus maximum daily variation of inside relative humidity for room without buffering. The slope of the linear approximation is defined as 'a'.*

be approximated by a linear relation, or

$$\Delta Y_m = a\,\Delta Y_A \tag{9}$$

where ΔY_m is the estimated value of ΔY. For the room without buffering, a_A = 1. We define the moisture buffering capacity *MBC* of a room as the reduction of the slope *a* with respect to a_A, or

$$MBC = \frac{a_A - a}{a_A} = 1 - a \tag{10}$$

or using equation (9)

$$MBC = 1 - \frac{\Delta Y_m}{\Delta Y_A} \tag{11}$$

We now analyse if the *MBC* value can be seen as a characteristic for the moisture buffering in a room independent on the random variation of the variables X_i. In Figure 4a, we compare the slope of the linear relation (a-value) for the case with climatic outside conditions and the case with random outside conditions. Only a small difference in the slope *a* (or *MBC* value) can be observed. In Figure 4b, we consider the vapour production rate deterministic, i.e. a constant basic production rate with constant peaks during morning and evening. (Note that the constant values are equal to the expected values of the stochastic description during that particular period). In Figure 4c, the ventilation rate is taken constant and equal to the expected value of the stochastic description. We observe that the a-value remains accurately predicted, even when one of the basic variables is considered deterministic. We may conclude that the *MBC* value is rather independent on the particular stochastic variation, as long as the expected values of the stochastic processes are preserved. From the other side, the stochastic description allows to determine the a-value and *MBC* value rather exactly, which is found to be less evident for deterministic processes.

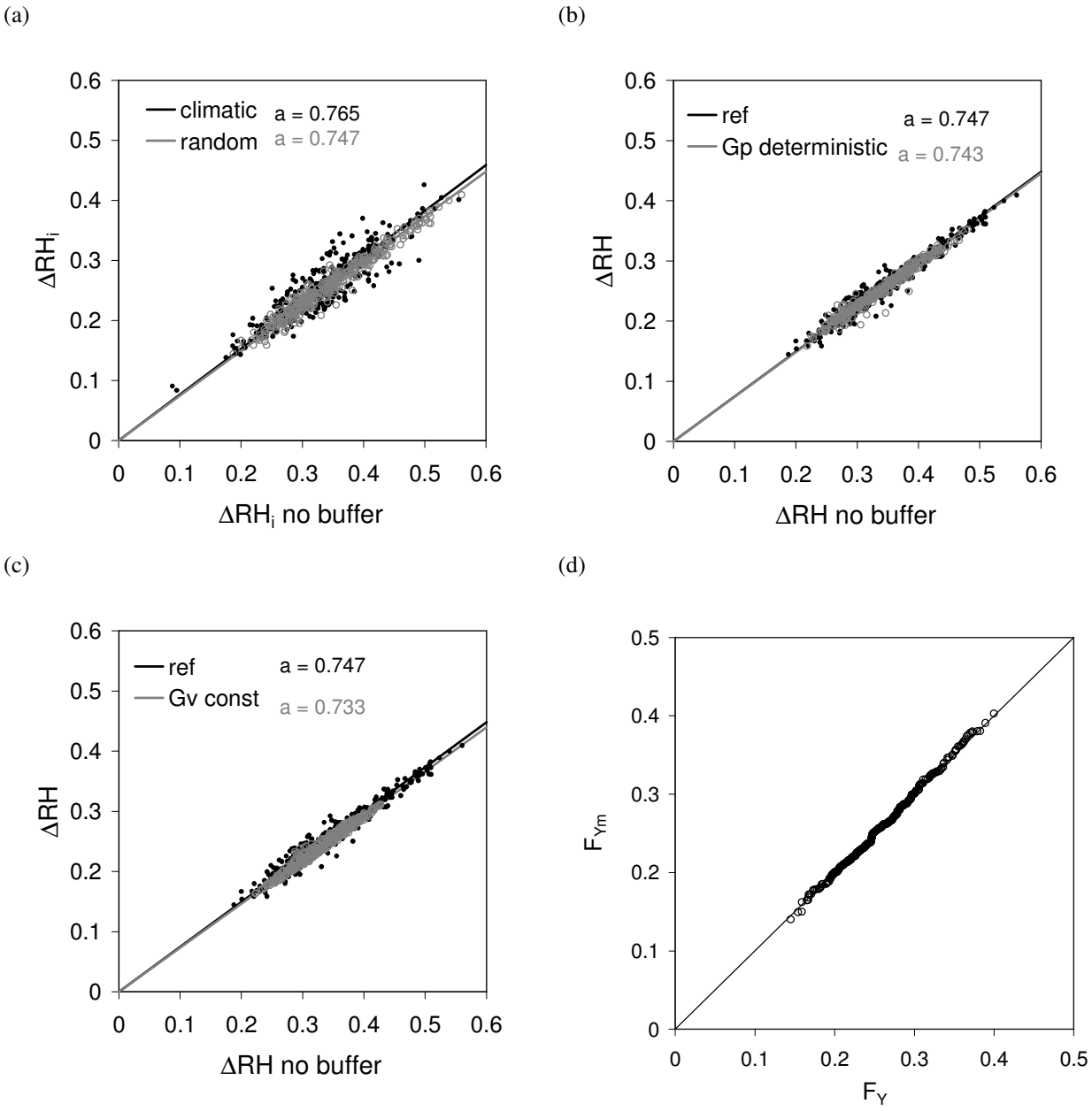

Figure 4. Maximum daily variation of inside relative humidity for a room with moisture buffering versus a room without moisture buffering: comparison between (a) climatic and random outside conditions, (b) random (ref) and deterministic variation of the moisture production rate, (c)) random (ref) and deterministic variation of the ventilation rate; (d) the one-to-one relation for the cumulative distribution function of the maximum variation of the inside relative humidity versus the reference cdf.

3.4 The reliability problem reformulated

Using equations (9) and (11), we can determine a 'modeled' cumulative distribution function F_{Y_m}, which is obtained from the cdf of the room without buffering F_{Y_A}, or

$$F_{Y_m}(\Delta Y) = F_{Y_A}\left(\frac{\Delta Y}{1-MBC}\right) \quad . \tag{12}$$

Figure 4d gives the one-to-one relation between the modelled cfd F_{Y_m} and the reference cfd F_Y. We observe a very good agreement.

Based on equation 12, the reliability problem can be redefined as finding the distribution function F_Y for which equation 8 holds, or

$$1-P_{\max} = F_Y(\Delta Y_{\lim}) = F_{Y_A}\left(\frac{\Delta Y_{\lim}}{1-MBC}\right). \tag{13}$$

Inverting equation 13, we find the required *MBC* value

$$MBC_D = 1-\frac{\Delta Y_{\lim}}{F_{Y_A}^{-1}(1-P_{\max})} \tag{14}$$

also called the design (subscript *D*) moisture buffering capacity.

3.5 Design of the moisture buffering in a room

In 3.4, we presented a method to determine the design moisture buffering capacity, when values for the damage limit and the acceptable probability of occurrence of damage are chosen. The question that now remains is how to choose the particular surface materials in order to achieve a sufficient moisture buffering capacity. A surface material is characterized by an equivalent surface mass coefficient $\beta_{eq,j}$ (equation 2) and a surface to volume ratio α_j. We found that a unique relation exists between the average equivalent surface mass coefficient $\overline{\beta}_{eq}$ and the moisture buffering capacity *MBC* value for a given room. This relation is called the *moisture buffering design* (*MBD*) curve. A room is further characterised by the total surface to volume ratio α_T. $\overline{\beta}_{eq}$ and α_T are defined as

$$\overline{\beta}_{eq} = \frac{\sum_{j=1}^{n}\alpha_j\beta_{eq,j}}{\alpha_T} \quad , \quad \alpha_T = \sum_{j=1}^{n}\alpha_j \tag{14}$$

For rectangular rooms (*L*=length, *W*=width and *H*=height), we find for α_T

$$\alpha_T = \frac{2}{L}+\frac{2}{W}+\frac{2}{H}$$

For example α_T = 60 for a cube of 0.1 m, α_T = 6 for a cube of 1 m and α_T = 0.6 for a cube of 10 m. Figure 5a gives the *MBD*-curve for a rectangular room with α_T = 1.5, where all the six walls are composed by one and the same material. Eight different wall materials are considered. The solid line gives the obtained relation. In a second step, the six walls are considered to be composed of all different materials. Fifty simulations are performed for at random combinations of wall materials chosen out of a set of eight materials with different equivalent surface mass coefficient $\beta_{eq,j}$. We observe that all simulations result in a single curve, the *MBD*-curve. In figure 5b, the *MBD*-curve is determined for different values of α_T. Small rooms with high α_T value only need low moisture buffering by the walls or a low equivalent surface mass coefficient. Large rooms with low α_T value need high moisture buffering by the walls or a high equivalent surface mass coefficient

Finally, the design methodology can be summarised by the following steps: (1) select the proper stochastic characteristics of the ventilation and moisture production rate; (2) determine the cumulative distribution function for the maximum daily variation in inside relative humidity for the room without buffering; (3) choose the damage limit and an acceptable probability of occurrence of damage: (4) determine the design *MBC* value using eq. 13; (5) determine the necessary moisture buffering by the surface materials using the *moisture buffering design* curve, as shown in Figure 5b.

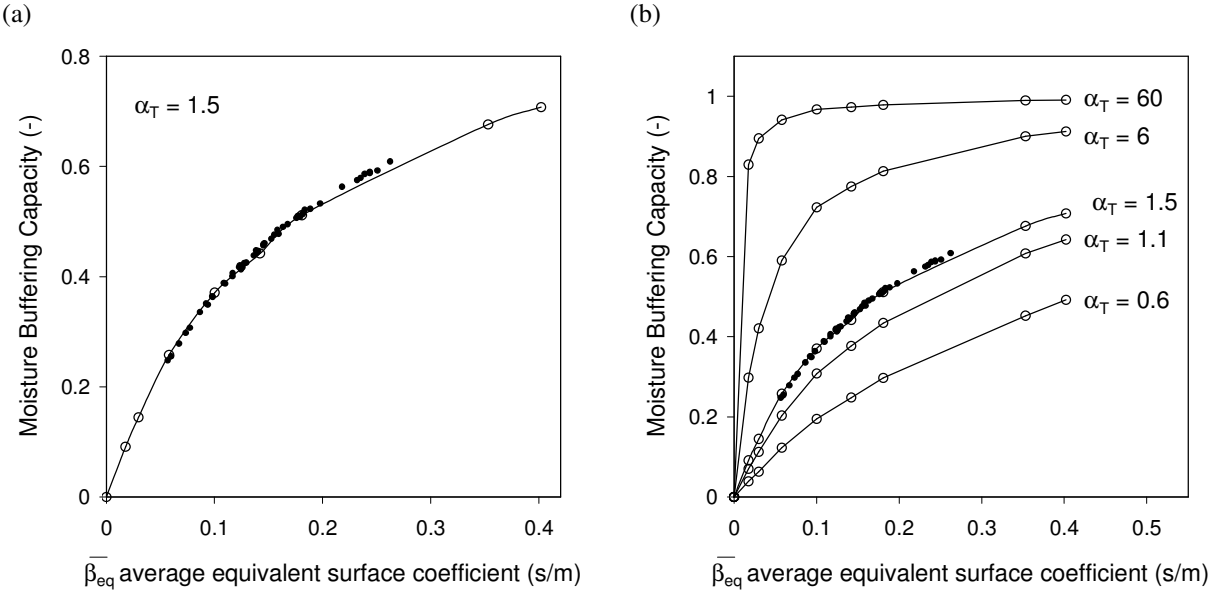

Figure 5. Moisture buffering design (MBD) curves representing the moisture buffering capacity versus the average equivalent surface mass coefficient. (a) comparison of MBD curves for a room with one and the same wall material (solid line) and with random wall materials (solid dots); (b) Moisture buffering design curves for rooms with different total surface to volume ratio's.

4. Conclusions

This paper presents a stochastic method to obtain design values for the necessary moisture buffering of wall materials in order to prevent moisture damage due to high fluctuations in relative humidity. The existence of a unique relation between the moisture buffering capacity and the average equivalent surface mass coefficient, called the *moisture buffering design* curve, allows to determine the necessary moisture buffering of the wall materials. The method has however some limitations: (1) the moisture balance model and wall model assume isothermal and well mixed air conditions with constant properties for the wall materials; (2) the moisture production rate and ventilation rate were assumed to be uncorrelated stochastic processes characterised by simple stochastic distributions. In reality, these variables may be correlated, since they both depend on the occupancy and human behaviour. Ventilation may also depend on outside climatic conditions, like wind pressure and thermal stack effects.

5. References

Geving, S. 2000. Hygrothermal analysis of building structures using computer models. Journal of Thermal Envelope & Building Science 23(3): 224-243.

IEA. 2008. Annex 41, IEA Annex 41 MOIST-ENG, Subtask 1 report – Modelling Principles and Common Exercises.

Jones, R. 1993. Modelling Water Vapour Conditions in Buildings. Building Services Engineering Research and Technology, Vol 14, No 3, pp.99–106.

Roppel, P. Brown,W.C. Lawton, M. 2007. Modeling of Uncontrolled Indoor Humidity for HAM Simulations of Residential Buildings. Proceedings of the Thermal Performance of the Exterior Envelopes of Whole Buildings X, Clearwater Beach, Fl.ASHRAE.

TenWolde, A., and I. S. Walker. 2001. Interior Moisture Design Loads for Residences. Proceedings of the VII International Conference on the Performance of Whole Buildings, Clearwater Beach Fl. ASHRAE.

The King's House on the Schachen – Indoor Climate Analysis of a Cultural Heritage Building

Ralf Kilian
Fraunhofer IBP
ralf.kilian@ibp.fraunhofer.de

Andreas Holm, Dr.-Ing.
Fraunhofer IBP
holm@ibp.fraunhofer.de

Jan Radon, Dr.-Ing. Habil
Agr. University of Cracow
jradon@kki.pl

KEYWORDS: indoor environment, hygrothermal building simulation, statistical analysis, preventive conservation

SUMMARY:
The King's House on the Schachen is a royal mountain chalet situated in the Bavarian Alps that has got a very finely preserved interieur. The statistical analysis of the indoor microclimate confirms that the range of temperature and humidity is in a region that is in generally considered save in regard to conservation. Of special interest in respect to the state of preservation is the climatic stability that is examined with the use of whole building simulation with the software tool WUFI Plus. It is shown that the interior furniture and the materials of the building envelope reduce the range of humidity changes inside very effectively by buffering and releasing moisture. Also the infiltration rate plays a significant role in the reduction of fluctuations. A low infiltration rate can aid to conservation of cultural heritage objects.

1. Introduction

The King's House on the Schachen is an impressive example of late 19th century royal interior design from the times of King Ludwig II of Bavaria. The building was finished in 1872 by the architect Georg Dollmann. The wooden post-and-infill structure in the form of a Swiss chalet has five living rooms downstairs with cembra wood panelling and a mixture of stylistic elements. Very much in contrast to the plain and simple exterieur is the luxurious "Moorish Hall" which takes up the entire upper floor of the hunting lodge (Fig. 1). The Turkish Saloon is decorated with painted and gilded wooden walls with carved ornaments, elaborate cushions, curtains and carpets in oriental fashion, carved, wooden lamps and a fountain in the middle of the room that is of course not used anymore today. In the King's times it could be heated by two ornate tiled stoves. The windows of the room are made of colourful stained glass in order to keep out the Bavarian mountain scenery and to aid to the perfect illusion of an oriental court.

Situated in the Bavarian Alps on the Schachen Mountain opposite the Zugspitze (Germany highest mountain) at around 1800 m the King's house faces a very rough mountain climate with cold winters, hot summers and extreme and fast weather changes all over the year. Nevertheless the state of preservation of the interior and the works of arts inside the Chalet is extraordinary good. Since the lodge can only be reached by foot and it is only open to the public from June to October the numbers of visitors is limited. During the winter months the whole building is completely closed.

2. Description of the building construction

A typical problem with historic buildings is how to obtain knowledge about the construction details. Unfortunately the available floor plans from last restoration works in the 1990ies do not show the whole construction for Schachen Chalet. Therefore the following estimations were made in the knowledge of traditional wooden constructions. The wooden outside walls are set on a stone foundation and have a width of approximately 0.5 metres. From the attic it is possible to see that the construction has got an inner and an outer shell made of wooden beams

with an air layer in between. The interior surfaces are made of wooden panels that are painted and gilded on the upper floor. The exterior is made of painted wooden shingles and boards. For the inside beams a width of 12-16 cm was assumed, for the outer shell of 8 cm with 2 cm of panelling on both sides. The overall volume of the building is 2035 m³. The windows have single glazing, only the upper floors have protective double glazing for the coloured stained glass windows. This was taken account for by using a shadowing function with a solar radiation reducing factor (b-value) of 0.2.

FIG. 1: Photographic view of the King's House on the Schachen from the outside (left, www.schloesser.bayern .de) and its oriental palace room on the first floor (right).

3. Analysing the hygrothermal conditions

During the period from October 2006 to September 2007 the hygrothermal conditions inside and outside the King's house on the Schachen were measured continuously in one hour time steps using stand-alone data-loggers. The outdoor climate data serves as one input for hygrothermal simulations. The weather data for the Schachen are not yet completely available. Instead, weather stations of the German National Weather Service (Deutsche Wetter Dienst) in the vicinity are used for solar radiation (Hohenpeißenberg), wind speed, rain and air pressure (Zugspitze). For relative humidity and temperature the values from the measuring devices at the north façade balcony of the Schachen House were used. In Fig. 2 the measured data for exterior and interior relative humidity as well as temperature are shown. The outdoor data-logger unfortunately had a measuring inaccuracy and does not show values above 96% RH. It must be stated, that the winter 2006/2007 was extraordinary mild. Therefore further measurements are currently going on with new measuring devices.

In order to get additional information like influence of moisture buffering materials, hygrothermal whole building simulations were carried out. For the simulation of the hygrothermal behaviour the software tool WUFI Plus that is described in (Holm; Künzel; Sedlbauer, 2003) is used. The whole building is simplified as a single zone with a perfect air exchange between the floors. For the model each outside wall and roof is described separately in its construction. The simulation runs one year from October 1st 2006 to September 30th 2007. For the first approximations the visitors during the summer months from June to October are neglected. Since there is no heating equipment in the Schachen House, its indoor environment is only influenced by the ambient weather conditions.

In Fig. 3 the course of measured and simulated indoor relative humidity and temperature from October, 1st 2006 to September, 30th 2007 is plotted. Several variations are used to approximate the behaviour of the King's House indoor environment. The variations with different infiltration rates show the best possible overall fitting for n=0.25 h^{-1}. An assumed infiltration rate of n=0.5 h^{-1} already leads to much larger fluctuations in relative humidity (Fig. 3). Infiltration rate measurements of the St. Renatus Chapel, a 17th century church near Munich, under different weather and wind conditions showed that infiltration rates of historic buildings can easily differ within in this range (Kilian, 2004). At the moment this is not taken account for in the simulation, only a fixed rate was used.

The interior surfaces and their ability to buffer humidity and temperature fluctuations is the second important variable for the climatic stability of the indoor microclimate. Simulations were at first carried out without any moisture buffering (MB) capacity and afterwards with moisture buffering materials (Fig. 3). As reasonable description of the interior surfaces the S_d-values were set to 0.1 for the walls and 0.5 for the floors because a general S_d-value of 0.5 led to much too high fluctuations, which are not shown here. To account for the indoor materials 200 m^2 additional inner wooden walls with a width of 10 cm were added, also with an S_d-value of 0.1.

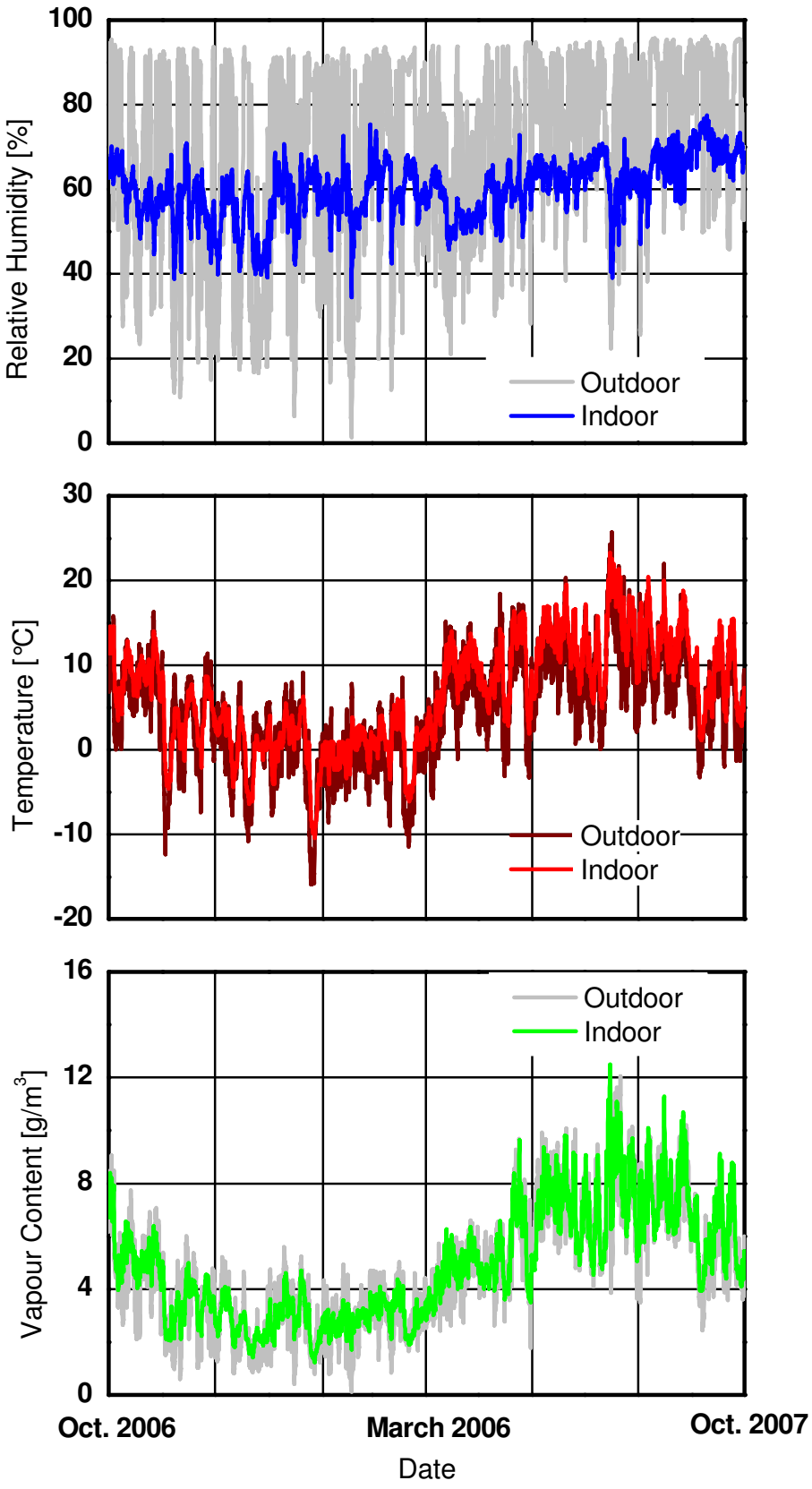

FIG. 2: Course of measured relative, humidity temperature and vapour content, indoors and outdoors from October, 1st 2006 to September, 31st 2007. Due to an inaccuracy of the measurement equipment the outdoor relative humidity does not reach 100% RH. The indoor temperature and vapour content clearly follow the outdoor values.

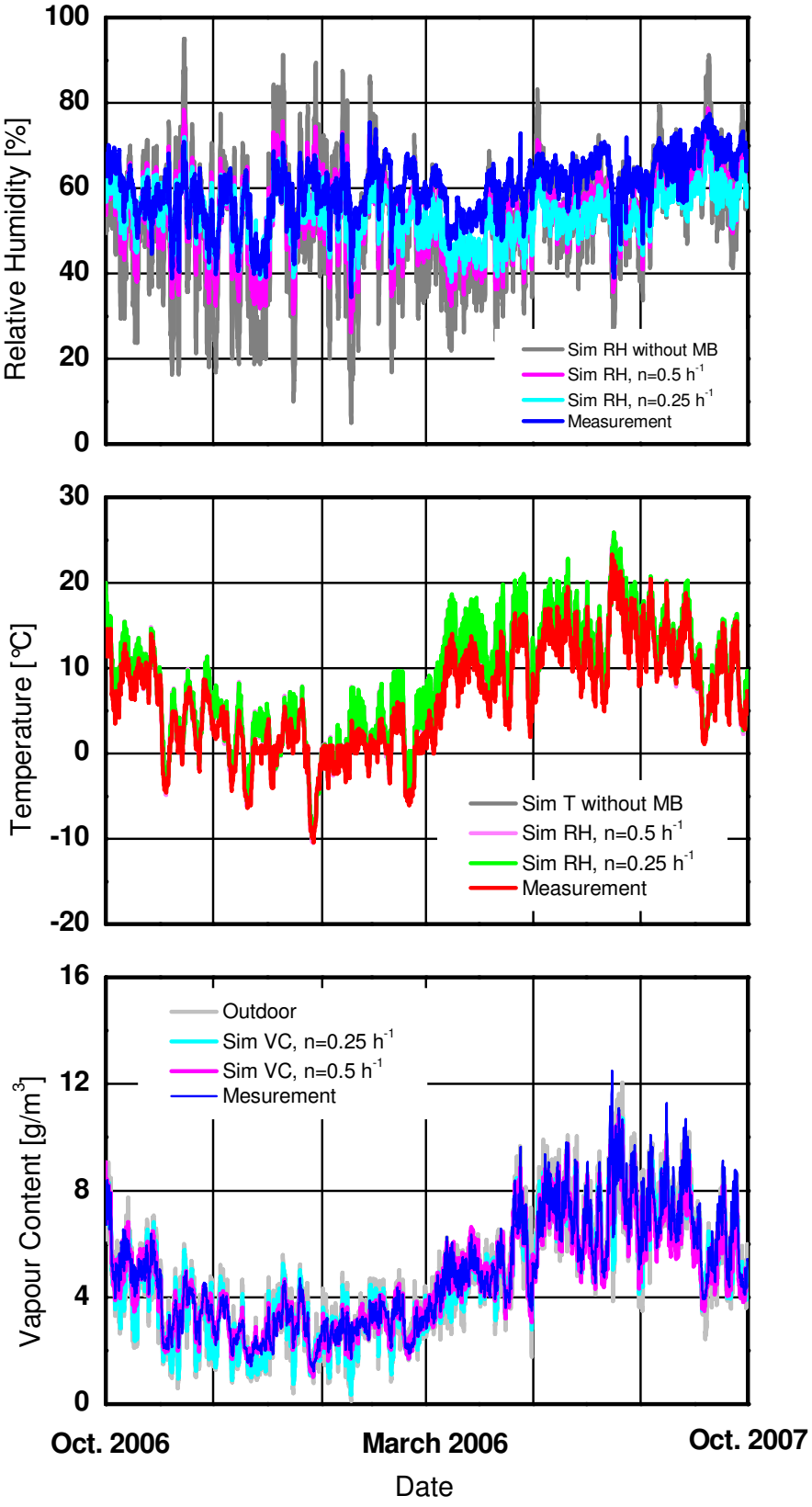

FIG. 3: Course of measured and simulated indoor relative humidity, temperature and vapour content from October, 1st 2006 to September, 31st 2007. Simulation results without moisture buffering (MB) and with moisture buffering at different infiltration rates (n=0.25 and n=0.5 h^{-1}).

The comparison of the simulations results with the measured data shows quite good fitting for the winter months. For the second part of the simulation the temperature is too high in comparison with the measured data due to necessary simplifications in regard to the building construction and uncertainties in regard to the available weather data in the approximation of the model, especially solar radiation and shading from the mountains during winter months. As the simulation of the vapour content of the air fits sufficiently well, the relative humidity is in consequence too low during summer (Fig. 3).

From June to October the Schachen House is open to visitors. Since the exact number of visitors is not known but the daily number is very strictly limited, it is assumed for the simulations, that no additional heat and moisture sources are present. This is of course another extreme simplification and might be one reason why especially in summer the difference between measured and simulated relative humidity is more than 5% RH.

4. Statistical Analysis of the indoor environment

The existing dataset is used for statistical analysis of the range, the rate of change of the hygrothermal conditions and possible effects on the buildings content (Fig. 4). The measured indoor relative humidity shows a median value of 60.8% RH for the examined one year period (Tab. 1). The relative humidity varies around this value within a range of ± 5% RH in 80% of the time.

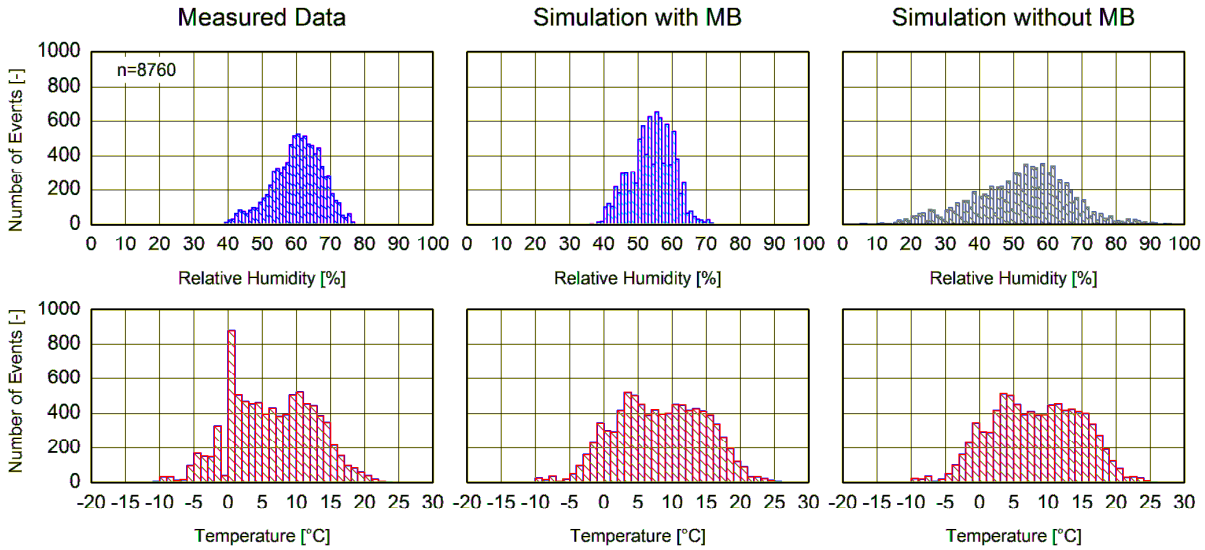

FIG. 4: Histograms of the hourly indoor relative humidity and temperature of the Kings House from October, 1st 2006 to September, 31st 2007. Measured data versus simulation, with and without moisture buffering (MB). The spike in the measured temperature at 0° C can be traced to a measurement inaccuracy.

In 95 % of the time the indoor relative humidity lies in between 40 and 70% RH (Fig. 4, left). Values below 40% RH take place in only 0.2 % of the time, values above 70% RH in approximately 5 % of the time. But even at higher relative humidity values lie still within a region with very little risk of mould growth due to low temperatures (Fig. 5).

Table 1: Statistical Analysis (percentiles, mean and standard deviation) of the one year hourly indoor and outdoor relative humidity and temperature measurements of the Kings House from October, 1st 2006 to September, 31st 2007

	Max	P95	P75	Median	P25	P5	Min	Range	Mean	sd
RH_in	77.5	70.9	65.4	**60.8**	55.7	46.9	34.5	43	60.2	7.1
T_in	23.3	16.2	11.2	**6.4**	1.5	-3.6	-10.4	33.7	6.4	6.2
RH_out	96.3*	93.3	87.4	**72.5**	54.2	26.9	1.3	94.8	68.5	21.2
T_out	25.7	14.2	8.9	**4.6**	0.5	-6.4	-15.9	41.6	4.5	6.2

** Due to an inaccuracy of the measurement equipment the relative humidity outdoors does not reach 100% RH*

The hourly variation of the relative humidity is below 1% RH in 84.5 % of all cases, in 96.5 % of all cases below 2% RH and in 99.7 % of the cases below 5% RH. That means that faster variations than 5% per hour happen only in less than 0.3 % of the examined cases. The median of the daily variations lies at 4.85% RH. Daily variations larger than 15% RH take place only in about 1.5 % of the cases.

5. Risk Assessment for Cultural Heritage

Although the King's House on the Schachen is situated in a region of rough mountain climate, the indoor environment seems to be well suited for the preservation of cultural heritage from a conservation point of view. Garry Thompson defines an indoor environment between 40 and 70% RH and temperatures that are sufficiently constant to maintain a stable relative humidity as suitable for a so called 'Class 2' museum (Thompson, 1986). The interior climate of the King's House stays within these limits in 95 % of the time during the examined one year period in 2006/2007. The region somewhere below 40% RH is considered to be dangerous for works of art because of shrinkage and the embrittlement of some materials (Erhard and Mecklenburg, 1994). The danger of mould growth decreases with lower temperature as the required relative humidity becomes higher (Krus; Kilian; Sedlbauer, 2007). For the measured period there is therefore basically no risk of mould growth for the works of art in the King's House (Fig. 5). A closer examination of the surface microclimate conditions of the building envelope will follow in a later period of the project.

(Holmberg, 2001) stated that the variations of relative humidity for interior decorations smaller than 15% RH during 24 hours do not cause damage to wooden objects. Statistical analysis of the daily variations in the King's House shows that during the one year monitoring this threshold was exceeded only on 5 days. A one day variation lager than 20% RH happened only once with a value of 21.2% RH. Low temperatures are in general not dangerous for most materials, at least if the amount of moisture is low enough to prevent frost damages (Holmberg, 2001). Low temperatures reduce the chemical decay rate and are sometimes used especially for cold storage solutions for archive materials. At the Schachen House the indoor environment is cold and reasonable dry. According to the measured data (Fig. 5, left) the overall climatic risk for the cultural heritage objects inside the Mountain Chalet can therefore be regarded as low. The climatic stability of the building derives from the ability of the indoor materials to buffer moisture. This can be seen from the direct comparison of the measured data with simulated hygrothermal balance calculated from the inside temperature and the outside absolute humidity (Fig. 5). Without moisture buffering materials the fluctuations would be much higher and the relative humidity would be much more often in regions that are considered unsafe for the cultural heritage materials inside the King's house.

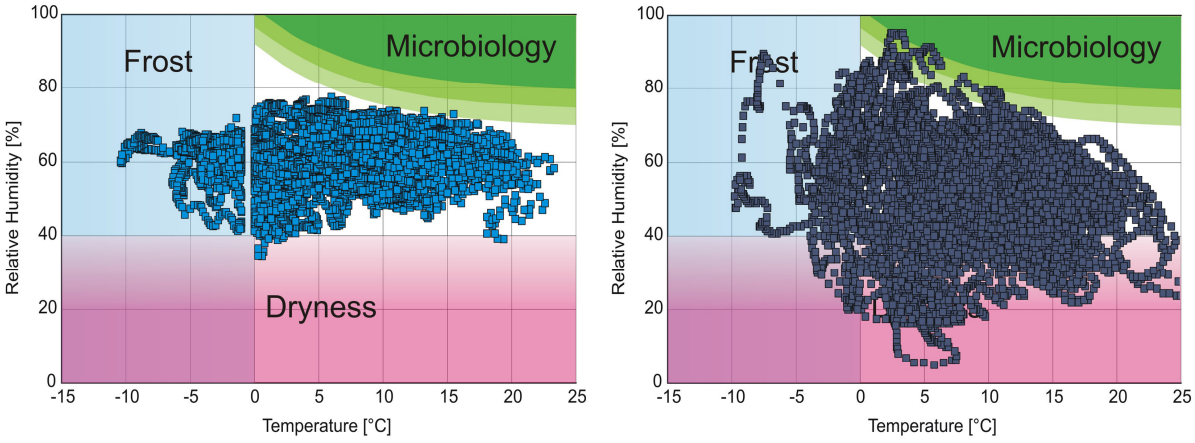

FIG. 5: Risk assessment of the measured indoor climate (left) shows that most of the data is in a safe region for the one year monitoring period from October, 1st 2006 to September, 31st 2007 . Frost is considered less dangerous when little humidity is present. The thermal building simulation without moisture buffering (right) shows a far wider range of relative humidity and temperature and the importance of buffering materials for the climatic stability.

6. Conclusions

For the preservation of works of art inside historic buildings from climate induced damages two factors are of importance. The first is the effect of the moisture buffering. From the comparison of the results of the hygrothermal simulation with and without moisture buffering it can clearly be seen how high amplitudes of the relative humidity due to rapid changes in the exterior conditions can be damped by the moisture buffering materials of the building envelope and the furniture. The simulation of the thermal performance without moisture buffering shows that the indoor relative humidity would be in a far wider range and that short term fluctuations would be much harder without the moderating buffer effect. The second important aspect is the infiltration rate. A low infiltration rate will aid significantly to climatic stability.

Future research work on the King's House will clarify some of the uncertainties and approximations that had to be made for these first simulations in order to improve results. Weather data will be collected on site for this purpose and information on the interior materials and their sorption properties will be collected.

The indoor environment of the measurement period from October 2006 to October 2007 lies within a rather stable and good range for the preservation of works of art especially in regard to relative humidity. The low temperatures during winter do not seem to have much negative effects on the interior decoration. It is also likely that only very stable art techniques were used for the purpose of furbishing the mountain hut. The craftsmen in King Ludwig II time had plenty of experience from centuries of decorating castles and churches in Bavaria to fall back upon. In further research these artistic techniques will be studied as well as their state of preservation from a close range.

7. References

Erhard D. and Mecklenburg M. (1994). Relative Humidity Re-Examined. In Roy, A. und Smith, P. (ed.): Preventive Conservation Practice, Theory and Research. Preprints of the Contributions to the Ottawa Congress, 12-16 September 1994. London, pp. 32–38.

Holm A.; Künzel H.; Sedlbauer K. (2003). The hygrothermal behaviour of rooms: combining thermal building simulation and hygrothermal envelope calculation; Eight International IBPSA Conference, Eindhoven, The Netherlands, 11-14 August 2003, pp. 499-505.

Holmberg J. G. (2001). Environment Control in historical buildings. Royal Institute of technology Building services engineering, Bulletin No. 53, Stockholm.

Kilian R. (2004). Die Wandtemperierung in der Renatuskapelle in Lustheim – Auswirkungen auf das Raumklima, Siegl, Munich.

Krus M.; Kilian R.; Sedlbauer K. (2007). Mould Growth Prediction by Computational Simulation. In: Museum Microclimates Conference Proceedings, Copenhagen.

Thompson G. (1986). The Museum Environment, 2nd edition, Butterworth-Heinemann, London.

Surface Condensation at the Roof of Ice Sports Arenas

Helmut Marquardt, Prof. Dr.-Ing,
Hochschule 21 University of Applied Sciences, Buxtehude, Germany;
marquardt@hs21.de and http://www.fh-buxtehude.de/marquardt

Georg-Wilhelm Mainka, Univ.-Prof. em. Dr.-Ing.,
Building Construction and Building Physics, Rostock University, Germany;
georg-wilhelm.mainka@uni-rostock.de and http://www.bau.uni-rostock.de/lehrko/bauko/fachgebiet.html

KEYWORDS: *condensation, corrosion, dew point, ice sports arena, mould, relative humidity, temperature.*

SUMMARY:
Because of damage to the wooden structure or mould on the suspended ceiling, examinations were made in three ice sports arenas in Northern Germany. Measurements of temperature and relative humidity inside and outside these arenas gave interesting results: During relatively warm winter periods the measured surface temperature at the bottom of the roof above the ice rink was lower than the air temperature in the arena, resulting in a significantly higher relative humidity at the roof than outside the building. Thus, condensed water was dripping from the roof construction to the ice. Depending on the construction, at the end of the winter the moisture content of the wooden structure was very high, partially resulting in wood destroying fungi, or the steel parts were corroding, respectively.

In this paper the climatic conditions in ice sports arenas are simulated including conductivity, convection and radiation in a simplified model. The results were discussed for different parameters. Finally two different solutions are shown to lower the moisture content in the timber construction or the steel corrosion, respectively:

- *An insulated suspended ceiling below the roof construction may protect timber or steel from the low ice temperature with the resulting high humidity.*
- *If the arena is closed to the outside air, an air-conditioning system may dry the air in the arena. By that means the relative humidity can descend as low as necessary for a durable construction.*

1. Introduction

After the collapse of the ice sports arena in Bad Reichenhall 2006, a lot of similar arenas in Germany were examined for construction damages. But, also in the years before, moisture problems in the roof construction of ice sports arenas were found. This paper describes the studies made of three ice sports arenas in Northern Germany, mentions simulation models for the climate inside of these arenas and comes to interesting conclusions.

a) *b)* *c)*

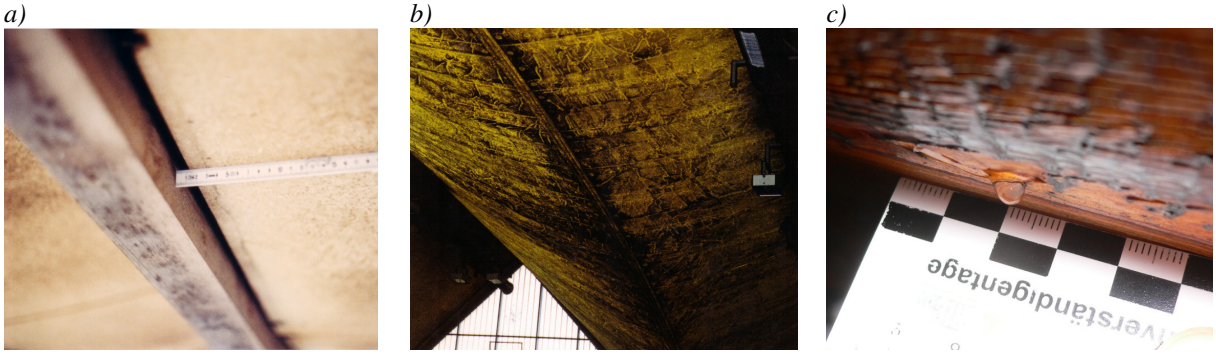

FIG. 1: Problems of ice sports arenas
a) Mould on the particle boards and the wooden beams of the suspended ceiling in the Hanover ice sports arena
b) Mould on the inside membrane of the Wolfsburg ice palace
c) Water dripping down from a glue-laminated timber beam of the Harsefeld ice sports arena.

2. Examined Ice Sports Arenas

All the examined ice sports arenas had problems with dripping water, mould or corroding steel parts (fig. 1). But, these problems are not depending on the size or the ventilation type of the arena (fig. 2).

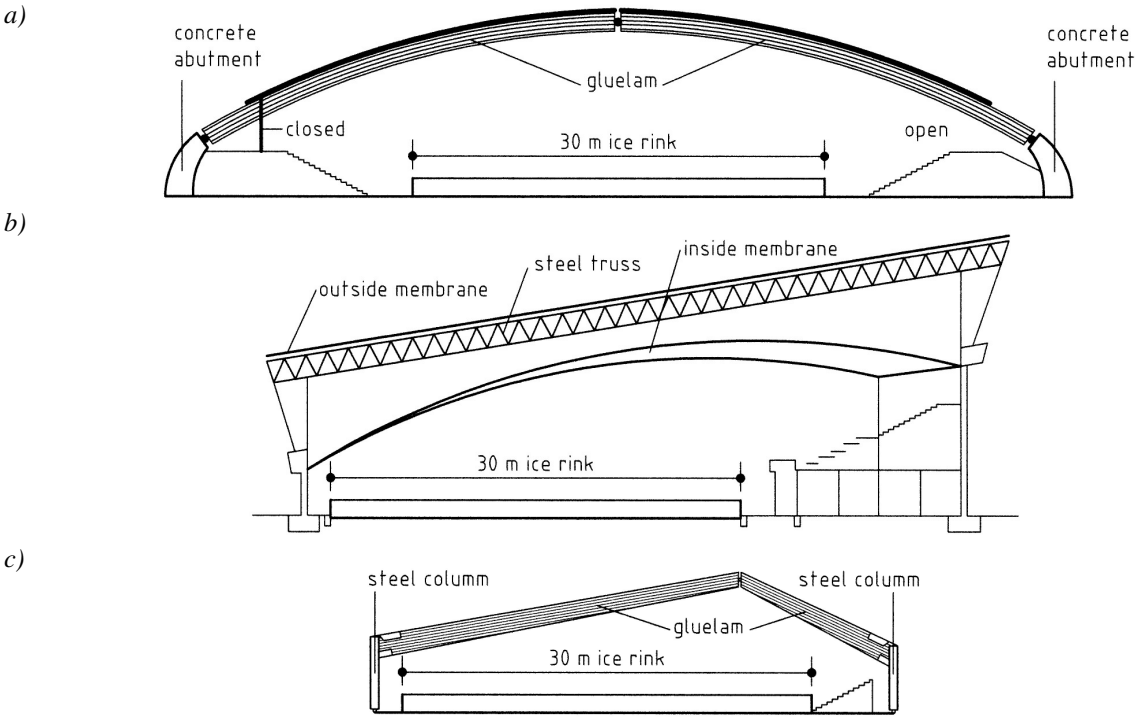

FIG. 2: Cross- sections of the examined ice sports arenas in Northern Germany
a) Hanover ice sports arena (open to the air outside)
b) Wolfsburg ice palace (closed to the air outside)
c) Harsefeld ice sports arena (open to the air outside).

3. Hypothesis

Mould, dripping water and corroding steel lead to the hypothesis that the roofs above the ice rink cool down by radiation exchange to temperatures lower than the dew point. Consequently condensation occurs there causing wood deterioration or steel corrosion.

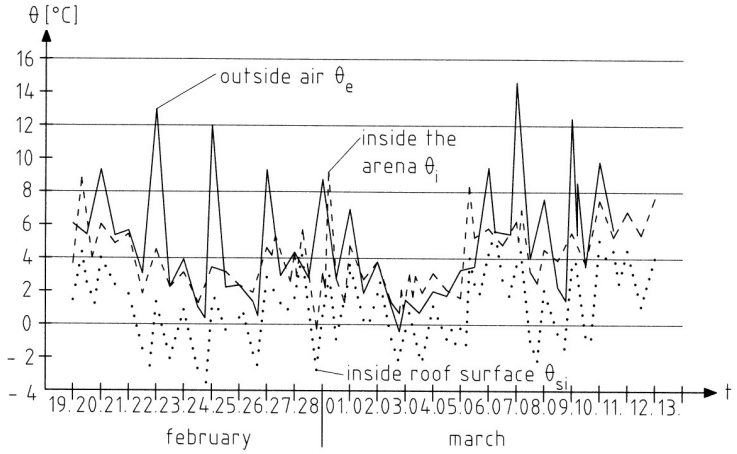

FIG. 3: Measured air temperature θ outside the Wolfsburg ice palace and at two measuring points inside.

4. Measurements of Temperature and Relative Humidity

At all three ice sports arenas, mentioned in fig. 2, measurements of temperature and relative humidity were made inside and outside the arenas. Examples from Wolfsburg are shown in fig.3 (Marquardt and Mainka, 2008) and from Harsefeld in fig. 4 and fig. 5 (Marquardt and Hofmann, 2008). During relatively warm winter periods the measured temperature near to the roof above the ice rink was significantly *lower*, the relative humidity near to the roof above the ice rink was significantly *higher* than outside the building.

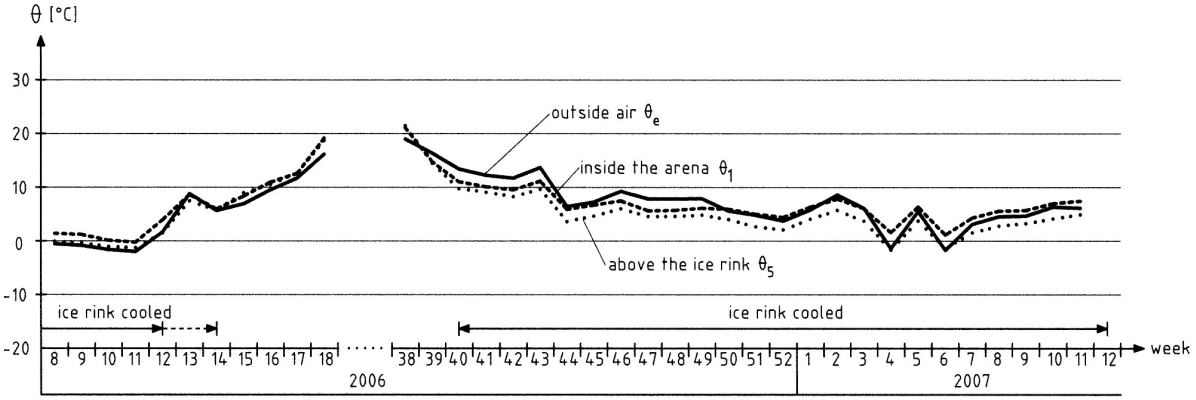

FIG. 4: Long-term measurements of the air temperature θ (mean values of the mentioned week) outside the Harsefeld ice sports arena and at two measuring points inside

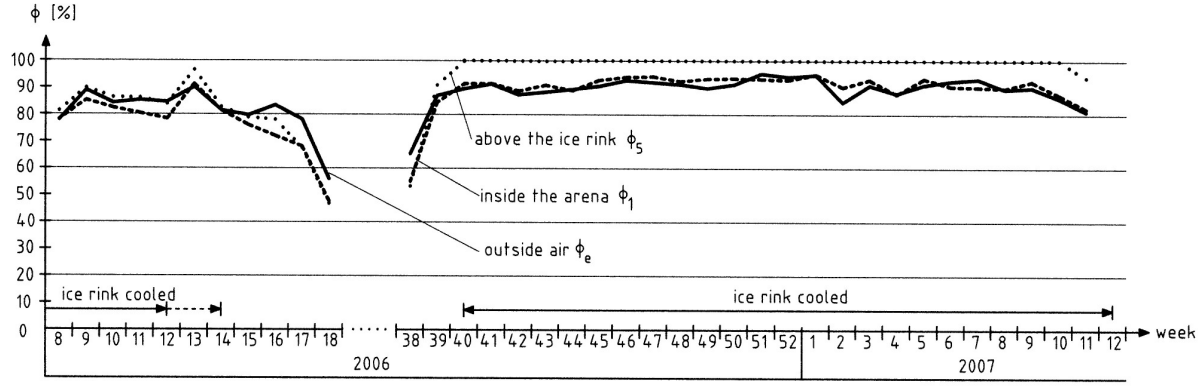

FIG. 5: Long-term measurements of the relative humidity ϕ (mean values of the mentioned week) outside the Harsefeld ice sports arena and at two measuring points inside

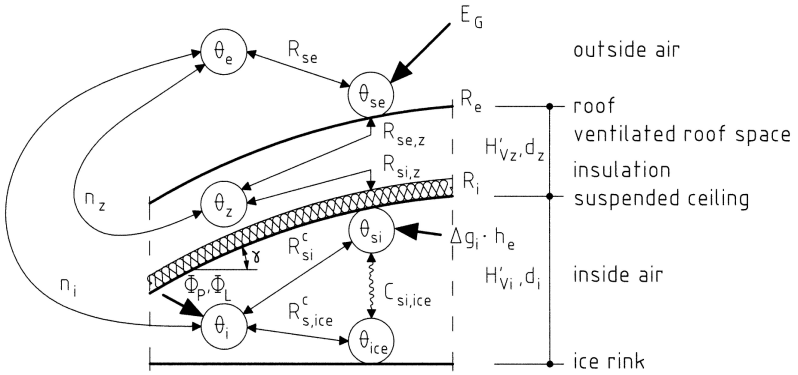

FIG. 6: Modelling of the temperatures in an ice sports arena with a suspended ceiling.

5. Simulation of the Temperatures in Ice Sports Arenas

5.1 Modelling

The modelling of the tempearatures in an ice sports arena with a suspended ceiling is shown in fig. 6. Knowing the temperature of the outside air θ_e and the ice temperature θ_{ice} the one-dimensional steady-state heat flow can be calculated at every node between outside air and ice surface

- node “se”

$$0 = \frac{1/\cos\gamma}{R_{se}} \cdot (\theta_e - \theta_{se}) + \frac{1/\cos\gamma}{R_e + R_{se,z}} \cdot (\theta_z - \theta_{se}) + E_G \quad \left[\frac{W}{m^2}\right] \quad (1a)$$

- node “z”

$$0 = \frac{1/\cos\gamma}{R_e + R_{se,z}} \cdot (\theta_{se} - \theta_z) + \frac{1/\cos\gamma}{R_i + R_{si,z}} \cdot (\theta_{si} - \theta_z) + H'_{Vz} \cdot (\theta_e - \theta_z) \quad \left[\frac{W}{m^2}\right] \quad (1b)$$

- node “si”

$$0 = \frac{1/\cos\gamma}{R_i + R_{si,z}} \cdot (\theta_z - \theta_{si}) + \frac{1/\cos\gamma}{R^c_{si}} \cdot (\theta_i - \theta_{si}) + C_{si,ice} \cdot \sigma \cdot \left[T_{ice}^{\ 4} - T_{si}^{\ 4}\right] + \Delta g_i \cdot h_e \quad \left[\frac{W}{m^2}\right] \quad (1c)$$

- node “i”

$$0 = \frac{1/\cos\gamma}{R^c_{si}} \cdot (\theta_{si} - \theta_i) + \frac{1}{R^c_{s,ice}} \cdot (\theta_{ice} - \theta_i) + H'_{Vi} \cdot (\theta_e - \theta_i) + \frac{\Phi_L + \Phi_P}{A} \quad \left[\frac{W}{m^2}\right] \quad (1d)$$

where

θ = temperature [$°C$]

T = temperature [K] ($T = \theta + 273{,}16\ K$)

R^c_s = convective surface resistance [$m^2 \cdot K/W$]

R_s = total (convective and radiant) surface resistance [$m^2 \cdot K/W$]

R = thermal resistance by a component [$m^2 \cdot K/W$]

E_G = global (direct and diffuse) radiation energy flow [W/m^2]

$C_{si,ice} \approx \varepsilon_{si} \cdot \varepsilon_{ice}$ = emissivity correction factor between suspended ceiling and ice surface [–], simplified for an emissivity $\varepsilon \geq 0{,}90$ (Hering et al., 2005)

σ = $5.67 \cdot 10^{-8}\ W/(m^2 \cdot K^4)$ = *Stefan-Boltzmann* constant

Δg_i = difference of the diffusive flux entering and leaving the suspended ceiling [$kg/(m^2 \cdot s)$] which condenses there

h_e = 2257 kJ/kg = 2 257 000 Ws/kg = specific enthalpy (latent heat) of evaporation

Φ_P = $m_P \cdot 100\ W$ = heat flow by m_P persons (sportsmen or spectators in the arena) [W]

Φ_L = heat flow by lighting [W]

A = area of the arena [m^2]

γ = inclination of the roof [°]

H'_V = specific heat loss by ventilation, applied to the area A:

$$= \rho_a \cdot c_{pa} \cdot n \cdot d \qquad \left[\frac{W}{m^2 \cdot K}\right] \quad (2)$$

where

ρ_a = 1,23 kg/m^3 = air density (EN 12524, 2000)

c_{pa} = 1008 $J/(kg \cdot K)$ = 1008 $Ws/(kg \cdot K)$ = specific heat capacitiy of dry air (EN 12524, 2000)

n = air changes per hour [h^{-1}]

d = height [m]

This system of equations (1) is solved by Marquardt and Mainka (2008).

5.2 Simplifying the Model

Usually in practice ice sports arenas are without suspended ceiling and open to the air outside (cp. fig. 2c). In this case the system of equations (1) can be simplified (cp. fig. 6) to

- node "se"

$$0 = \frac{1}{R_{se}} \cdot (\theta_e - \theta_{se}) + \frac{1}{R_e} \cdot (\theta_{si} - \theta_{se}) + E_G \qquad \left[\frac{W}{m^2}\right] \quad (3a)$$

- node "si"

$$0 = \frac{1}{R_e} \cdot (\theta_{se} - \theta_{si}) + \frac{1}{R^c{}_{si}} \cdot (\theta_i - \theta_{si}) + C_{si,ice} \cdot \sigma \cdot \left[T_{ice}{}^4 - T_{si}{}^4\right] + \Delta g_i \cdot h_e \qquad \left[\frac{W}{m^2}\right] \quad (3b)$$

- node "i"

$$0 = \frac{1}{R^c{}_{si}} \cdot (\theta_{si} - \theta_i) + \frac{1}{R^c{}_{s,ice}} \cdot (\theta_{ice} - \theta_i) + H'_{Vi} \cdot (\theta_e - \theta_i) + \frac{\Phi_L + \Phi_P}{A} \qquad \left[\frac{W}{m^2}\right] \quad (3c)$$

The solution of the square brackets in equation (3b) is

$$T_{ice}{}^4 - T_{si}{}^4 = \left(T_{ice}{}^2 - T_{si}{}^2\right) \cdot \left(T_{ice}{}^2 + T_{si}{}^2\right) = (T_{ice} - T_{si}) \cdot (T_{ice} + T_{si}) \cdot \left(T_{ice}{}^2 + T_{si}{}^2\right) \qquad [K] \quad (4)$$

The last brackets in equation (4) can be simplified solved (cp Hagentoft, 2001) to

$$\left(T_{ice}{}^2 + T_{si}{}^2\right) \approx \frac{(T_{ice} + T_{si})^2}{2} = 2 \cdot \left(\frac{T_{ice} + T_{si}}{2}\right)^2 = 2 \cdot T_m{}^2 \qquad [K] \quad (5)$$

Thus, with $(T_{ice} + T_{si}) = 2 \cdot T_m$ the summand with the square brackets in equation (3b) is

$$C_{si,ice} \cdot \sigma \cdot \left[T_{ice}{}^4 - T_{si}{}^4\right] \approx C_{si,ice} \cdot 4 \cdot \sigma \cdot T_m{}^3 \cdot (T_{ice} - T_{si}) \qquad \left[\frac{W}{m^2}\right] \quad (6)$$

where

T_m = $(T_{ice} + T_{si})/2$ = average temperature of the radiant surfaces [K]

T_{ice} = surface temperature of the ice [K]

T_{si} = inside surface temperature of the roof [K]

Using a reasonable estimated average temperature T_m and neglecting

- the global radiation energy flow E_G,
- the latent heat $\Delta g_i \cdot h_e$,
- the temperature difference between the air outside and inside the arena (i.e. $H'_{Vi} \cdot (\theta_e - \theta_i) \equiv 0$) and
- the heat flow by persons Φ_L and lighting Φ_P

the system of equations (3) becomes a linear system of equations with the unknowns θ_{se}, θ_{si} und θ_i.

- node "se"

$$\frac{\theta_{se}}{R_{se}} + \frac{\theta_{se}}{R_e} = \frac{\theta_e}{R_{se}} + \frac{\theta_{si}}{R_e} \Rightarrow \theta_{se} = \frac{1}{1/R_{se} + 1/R_e} \cdot \left(\frac{\theta_e}{R_{se}} + \frac{\theta_{si}}{R_e} \right) \quad \left[\frac{W}{m^2} \right] \quad (7a)$$

- node "si"

$$\frac{\theta_i}{R^c{}_{si}} + \frac{\theta_i}{R^c{}_{s,ice}} = \frac{\theta_{si}}{R^c{}_{si}} + \frac{\theta_{ice}}{R^c{}_{s,ice}} \Rightarrow \theta_i = \frac{1}{1/R^c{}_{si} + 1/R^c{}_{s,ice}} \cdot \left(\frac{\theta_{si}}{R^c{}_{si}} + \frac{\theta_{ice}}{R^c{}_{s,ice}} \right) \quad \left[\frac{W}{m^2} \right] \quad (7c)$$

- node "i"

$$0 = \frac{1}{R_e} \cdot \left(\frac{1}{1/R_{se} + 1/R_e} \right) \cdot \left(\frac{\theta_e}{R_{se}} + \frac{\theta_{si}}{R_e} \right) - \frac{\theta_{si}}{R_e} \quad \left[\frac{W}{m^2} \right] \quad (7b)$$

$$+ \frac{1}{R^c{}_{si}} \cdot \left(\frac{1}{1/R^c{}_{si} + 1/R^c{}_{s,ice}} \right) \cdot \left(\frac{\theta_{si}}{R^c{}_{si}} + \frac{\theta_{ice}}{R^c{}_{s,ice}} \right) - \frac{\theta_{si}}{R^c{}_{si}} + C_{si,ice} \cdot 4 \cdot \sigma \cdot T_m{}^3 \cdot (\theta_{ice} - \theta_{si})$$

$$\Rightarrow \left(\frac{1}{R_e{}^2/R_{se} + R_e} - \frac{1}{R_e} + \frac{1}{\left(R^c{}_{si}\right)^2/R^c{}_{s,ice} + R^c{}_{si}} - \frac{1}{R^c{}_{si}} - C_{si,ice} \cdot 4 \cdot \sigma \cdot T_m{}^3 \right) \cdot \theta_{si}$$

$$= -\frac{1}{R_e + R_{se}} \cdot \theta_e - \frac{1}{R^c{}_{si} + R^c{}_{s,ice}} \cdot \theta_{ice} - C_{si,ice} \cdot 4 \cdot \sigma \cdot T_m{}^3 \cdot \theta_{ice} \quad \left[\frac{W}{m^2} \right] \quad (8)$$

$$\Rightarrow \theta_{si} = \frac{U^* \cdot \theta_e + 1/R^c \cdot \theta_e + 1/R^r \cdot \theta_{ice}}{U^* + 1/R^c + 1/R^r} \quad [°C] \quad (9)$$

where

$$U^* = \frac{1}{R_e} - \frac{1}{R_e{}^2/R_{se} + R_e} = \frac{1}{R_e + R_{se}} \quad \left[\frac{W}{m^2 \cdot K} \right] \quad (10)$$

= U-value of the roof without inside surface resistance

$$\frac{1}{R^c} = \frac{1}{R_{si}} - \frac{1}{\left(R^c{}_{si}\right)^2/R^c{}_{s,ice} + R^c{}_{si}} = \frac{1}{R^c{}_{si} + R^c{}_{s,ice}} \quad \left[\frac{W}{m^2 \cdot K} \right] \quad (11)$$

= convective surface resistance; as estimated the arena is totally streamed by the outside air, thus, the inside roof surface is simplified to an outside surface according to EN ISO 6946 + A1 (2003), annex A

$$\frac{1}{R^c} = (4 + 4 \cdot v) \quad \left[\frac{W}{m^2 \cdot K} \right] \quad (12)$$

referencing to $\theta_i \equiv \theta_e$ instead of the ice temperature θ_{ice} and including v = air speed along the inside surface of the roof [*m/s*]

$$\frac{1}{R^r} = C_{si,ice} \cdot 4 \cdot \sigma \cdot T_m{}^3 \approx 0{,}8 \cdot 4 \cdot 5{,}67 \cdot 10^{-8} \frac{W}{m^2 \cdot K^4} \cdot T_m{}^3 \quad \left[\frac{W}{m^2 \cdot K} \right] \quad (13)$$

= simplified radiant surface resistance using the estimated average temperature T_m

θ_e = outside air temperature [°*C*]

θ_{ice} = ice temperature [°*C*], estimated to – 5 °*C*

5.3 Comparing the Simplified Model with the Measured Temperatures and Humidites

Looking at the Harsefeld ice sports arena with

- the thermal resistance of the roofing made of asbestos cement $R_e \approx 0{,}01\ m$ / $0{,}35\ W/(m \cdot K)$ $= 0{,}03\ m^2 \cdot K/W$ and $R_{se} = 0{,}10\ m^2 \cdot K/W$ (EN ISO 6946, 2003) $\Rightarrow\ U^* = 7{,}7\ W/(m^2 \cdot K)$,
- the air speed along the inside surface of the roof $v \approx 1\ m/s$, i.e. according to equation (12) $1/R^c = (4 + 4 \cdot 1) = 8\ W/(m^2 \cdot K)$ (cp. Jenisch and Stohrer, 2002: $1/R^c = 3$ to $10\ W/(m^2 \cdot K)$),
- the average temperature $\theta_m = (\theta_{ice} + \theta_e)/2$ where $\theta_{ice} = -5\ °C$ is the ice surface temperature and θ_e the outside air temperature (cp. eq. (6)),
- the outside air temperature θ_e as variable

the surface temperature of the roof θ_{si} is calculated in table 1 according to equations (13) and (9).

TABLE 1: Calculated surface temperatures of the Harsefeld ice sports arena roof θ_{si} depending on the outside air temperature θ_e.

θ_e [°C]	θ_m [°C]	$T_m = \theta_m + 273{,}2$ [K]	$1/R^r$ [W/(m²·K)]	θ_{si} [°C]
– 5,0	– 5,0	268,2	3,5	– 5,0
0,0	– 2,5	270,7	3,6	– 0,9
5,0	0,0	273,2	3,7	3,1
10,0	2,5	275,7	3,8	7,1
15,0	5,0	278,2	3,9	11,0

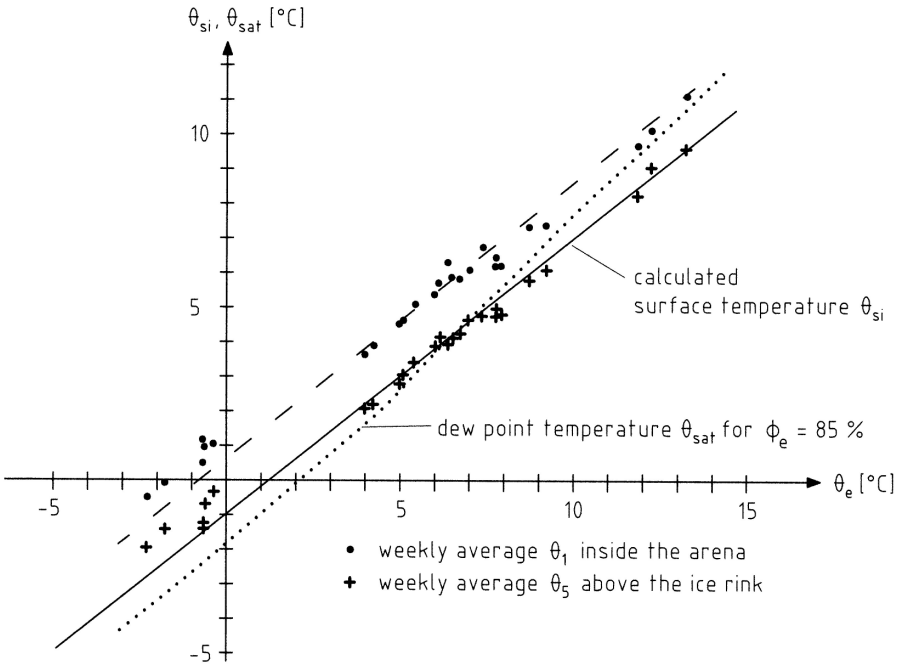

FIG. 7: Comparison of the measured surface temperatures θ_1, θ_5 (cp. Fig. 4) and the calculated surface temperature θ_{si} at the roof to the dew point temperature θ_{sat} of the outside air with $\phi_e = 85$ % r.h. depending on the outside air temperature θ_e.

A graphic comparison of the measured surface temperatures above the ice rink *mittl* θ_5 (dots) with the calculated temperatures there θ_{si} (solid line) can be found in fig. 7 as well as a comparison of the measured surface tempe-

ratures not above the ice rink *mittl* θ_l (crosses) with the calculated temperatures there θ_{si} (dashed line). Obviously the measured and the calculated temperatures correlate quite well.

In winter the average relative humidity in Northern Germany is about ϕ_e = 85 %. For this relative humidity the dew point temperature θ_{sat} can be calculated dependent of the outside air temperature θ_e which is shown in fig. 7 additionally (dotted line). It can be seen that outside air temperatures $\theta_e > 7$ °C results in condensation. By that it is confirmed that during mild winter weather, condensation at the roof occurs (cp. fig. 1c).

6. Conclusions

The conclusions of the mentioned measurements as well as the calculations of the climate in three ice sports arenas, paritally open to the air outside and partially closed, are:

- It can be confirmed that roofs above ice rinks cool down by radiation exchange to temperatures lower than the dew point. Consequently condensation occurs there causing wood deterioration or steel corrosion.
- Additionally, there is a temporarily high humidity inside the ice sports arena
  - on the one hand because of the preparation of the ice rink (usually clouds behind the ice preparation machine) and
  - on the other hand because of many persons inside the arena (during ice hockey matches 50 *g* vapour per person and hour) possibly condensing at the roof.
- It is often assumed that ice sports arenas which are open to the air outside, have a similar inside climate as other open buildings like stables, garages etc. But, that is wrong. Although these arenas are open buildings with roofs, the air at the timber structures does not exceed ϕ = 85 % *r. h.* only for a few weeks per year.

Finally two different solutions are possible to lower the moisture content in the timber construction or the steel corrosion, respectively:

- In both types of ice sports arenas (i.e. open or closed to the air outside) an insulated suspended ceiling below the roof construction may protect timber or steel from the low ice temperature with the resulting high humidity. Such a suspended ceiling must be moisture resistant and has to be joined air tight to all flanking building elements.
- If the ice sports arena is closed to the outside air, an air-conditioning system may dry the air in the arena. By that means the relative humidity can descend as low as necessary for a durable construction.

7. References

EN 12524 (2000). *Building materials and products – Hygrothermal properties – Tabulated design values*, European Committee for Standardization (CEN), Brussels, Belgium.

EN ISO 6946 + A1 (2003). *Building components – Thermal resistance and thermal transmittance – Calculation method*, European Committee for Standardization (CEN), Brussels, Belgium.

Hagentoft C.-E. (2001). *Introduction to building physics,* Studentlitteratur, Lund, Sweden.

Hering E., Martin R. and Stohrer M. (2005). *Taschenbuch der Mathematik und Physik,* 4th ed., Springer, Berlin, Germany.

Jenisch R. and Stohrer M. (2002). Wärme. *Lehrbuch der Bauphysik* (Lutz et al., ed.). 5th ed., B. G. Teubner, Stuttgart, Germany.

Marquardt H. and Hofmann M. (2008). Hohe Holzfeuchten in der Dachkonstruktion einer Eissporthalle. *Europäischer Sanierungskalender*, Vol. 3 (Venzmer H., ed.), Beuth, Berlin, Germany, 301-311.

Marquardt H. and Mainka G.-W. (2008). Tauwasserausfall in Eissporthallen. *Bauphysik*, Vol. 30, No. 2, Berlin, Germany, 91-101.

Water absorption in two-layer masonry systems
Moisture fixation measured over the complete moisture range

Peter S. Johansson, Dr,
Division of Building Materials, Lund Institute of Technology;
peter.johansson@byggtek.lth.se

Lars-Olof Nilsson, Professor,
Division of Building Materials, Lund Institute of Technology;
lars-olof.nilsson@byggtek.lth.se

KEYWORDS: *moisture fixation, sorption isotherms, suction, capillary range, retention curve, lime-silica brick, lime-cement mortar*

SUMMARY:
To be able to perform simulations of transient moisture profiles in the capillary range for a two-layer masonry system, both the diffusivity and the sorption isotherms are required for the considered materials. However, this paper will focus on the methods, how to obtain the required sorption isotherms both for the hygroscopic and the capillary moisture range. For testing, we chose materials with moisture properties corresponding to those of common inorganic façade materials. The sorption isotherms were experimentally determined over the complete moisture range, two separate methods had to be used for the hygroscopic and the capillary parts of the moisture range. In the hygroscopic moisture range, both absorption and desorption isotherms could be determined, but in the capillary moisture range only desorption isotherms could be determined. To allow measurement of absorption isotherms in the capillary moisture range, the measuring equipment had to be modified; however, despite the modifications, reliable absorption measurements were still not possible. The desorption isotherms determined by the two different methods generally agreed well for the tested material.

1. Introduction

Sorption isotherms covering the hygroscopic range are usually determined using the well-tried climate box method. During the tests, specimens are put into equilibrium with different levels of relative humidity created using saturated salt solutions. To verify the exact time when the equilibrium state is achieved, the specimens are weighed at certain intervals; moreover, the specimens must be of a certain minimum size depending on the accuracy of the balance used. With a normal laboratory balance with an accuracy of thousandths of a gram, the specimens normally have to be of such a size that a relatively long time is needed to achieve equilibrium. The measuring time can of course be shortened if different specimens are used for the different relative humidity steps. However, when this is done, variation in pore size distribution and in other material-related properties that vary spatially in the material will of course affect the results. By using the same specimen throughout the measurement process these sources of error can be avoided.

The sorption balance method can be used as an alternative to the climate box method. This method is based on the continuous weighing of a single sample: the surrounding climate is changed in terms of relative humidity and temperature while the mass of the sample is registered continuously. Since one objective is to determine a complete sorption isotherm in a relatively short time, the specimen should be quite small. Even if the specimens of the different materials tested are of the same weight, the time needed to reach the equilibrium state will still be utterly dependent on the pore size distribution in a given specimen. In this paper, sorption isotherms representing desorption were determined for two different materials using the sorption balance technique (see Section 3). For testing purposes, materials were chosen with properties representative of those of normally used inorganic façade materials.

Since a major share of the moisture storage capacity of common inorganic building materials lies above the hygroscopic range, another measurement method, other than the sorption balance or climate box method, was needed to enable measurement of the entire sorption isotherm from complete dryness to vacuum saturation. Instead of refining the previously mentioned methods, the pressure plate technique was used to complement the sorption balance technique above the hygroscopic range. This method was first developed in the field of soil

mechanics for studying the negative water pressure in different soil layers. One of the first reports in the literature concerning the pressure plate method was that of Richards (1948). The pressure plate technique was originally designed for making desorption measurements. Its principle of operation is based on the equilibrium existing between the excess pressure in the pressure plate extractor and the suction under the meniscus in the water-filled pores. Since the excess pressure can be regulated with considerable accuracy, high precision in terms of relative humidity can be attained. Sorption isotherms above the hygroscopic range were determined using the pressure plate method, which is further described in Section 4.

2. Materials

The materials used in this paper are commercial lime-silica brick with a density of 1911 kg/m^3 and lime-cement mortar with a density of 1673 kg/m^3, mixed and cured according to standards. The lime-cement mortar was fully carbonized before the tests took place. Further details are to be found in Johansson (2005).

3. Sorption balance

3.1 General

The basic principle of the sorption balance technique is essentially the same as that of the climate box technique, except that the specimen is weighed continuously while the complete sorption isotherm is being determined. During the measurement process a small sample was weighed continuously while the surrounding relative humidity was changed in a stepwise manner.

3.2 Method

The current study used the dynamic vapour sorption (DVS) method. DVS is a relatively new technique for water vapour sorption analysis, based on the principle of an air flow passing two sample holders connected to a microbalance. When the sample holders are symmetrically hung and balanced, distortions arising from differing buoyancy effects caused by the gas flow can be avoided (such differences can occur if the relative humidity or temperature of the gas flow passing one of the two sample holders differs from that passing the other). For this type of DVS apparatus, the type of gas, relative humidity, and temperature surrounding the two sample holders are equivalent, since the gas is mixed before entering the microbalance.

Because great temperature stability is required when sorption measurements are being performed, the DVS apparatus was placed in an incubator, permitting the temperature to be kept constant with a precision of ± 0.1ºC. The required relative humidity was created by mixing two gas flows of known relative humidity: one was a completely dry gas supplied directly from a gas cylinder; the other was the same type of gas, but moisture saturated by having passed through a water jar. Each flow was controlled by thermal conductivity mass flow controllers. The relative humidity of the mixed gas flow could be varied between 0 and 98%. Combined relative humidity and temperature probes were mounted in the gas flows beneath the sample holders to allow monitoring of the conditions of the sample and sample holder.

The main component of the DVS system is a Cahn D-200 microbalance, Cahn Instruments, U.S.A, which continuously registers the weight as a function of time. For a sample weight of 1.5 mg, the precision of the balance is 0.1 µg, according to Levoguer and Williams (1997). Using as small a sample as possible allows the time to achieve the equilibrium state to be minimized. The microbalance was protected against high relative humidity by a continuous flow of purge gas. The purge gas used during the measurement process was dry nitrogen.

Before the measurement process started, specimens of lime-cement mortar and lime-silica brick with measurements 50 × 50 × 4 mm, were vacuum saturated with deionized water. After saturation, the specimens were ground in a mortar to produce an approximately 1-mm fraction. From the ground sample, 50–60 µg was randomly chosen and put in the sample holder, which had been thoroughly cleaned with deionized water and alcohol before the tests were performed.

A full cycle of measurements was performed, starting with desorption at 93% relative humidity and continuing stepwise in seven steps to a completely dry gas flow of 0% relative humidity. After equilibrium with the completely dry gas flow, an inverted cycle was performed, consisting of seven steps reaching a final relative humidity of 93%. A maximum relative humidity of approximately 97% could have been used; however, 93%

relative humidity was chosen, since the time needed to reach equilibrium at a higher relative humidity was estimated to be too long. Nitrogen gas of high purity was used in all the experiments, but since the specimens were well cured and carbonized before testing (see Section 2), dry air could also have been used. Nitrogen gas is normally used to prevent carbonization during testing, when tests are performed on non-carbonized cement-based materials. All measurements were performed at 20 ± 0.1ºC.

Several different combinations of relative humidity steps of various durations were tested for lime–silica brick until satisfactory equilibrium could be reached for all relative humidity steps in the cycle. The highest and the lowest relative humidity steps needed the longest durations to achieve a sufficiently low rate of weight change. Even if the duration of a specific step was increased considerably, weight change was still detectible. To estimate the final weight at equilibrium, extrapolation was performed for the weight change at each relative humidity step. A general expression was used to extrapolate the equilibrium state without needing an infinite measuring duration (see Anderberg and Wadsö, 2004). The first 10% of the measurement data was excluded when the extrapolation was performed, since the rate of weight change in this first part of the phase was not representative.

4. Pressure plate

4.1 General

The sorption isotherm above the hygroscopic range is called the "suction curve" or "water retention curve", and it shows the relationship between moisture content and pore water pressure. The pore water pressure, ΔP, or "suction", can be transformed into a corresponding relative humidity, ϕ, using the Kelvin equation.

$$\ln \Phi = -\frac{v_s}{R \cdot T} \cdot \Delta P \qquad (1)$$

where

Φ is the relative humidity above a curved meniscus,

v_s is the molar volume of water [0.018 m^3/kmol],

R is the gas constant [8314 J/kmol·K],

T is the temperature [K], and

ΔP is the capillary suction [Pa].

The simplest way to determine a suction curve is to expose a specimen to a negative water pressure (cf. Fagerlund, 1973) on a suction plate. However, such a technique can only be used for a pressure range of –0.098·MPa< ΔP <0 MPa, which corresponds to a relative humidity of between 99.92% and 100%. To measure moisture fixation properties at lower humidity levels, corresponding to pore water pressures lower than –0.098 MPa, a pressure plate may be used. In such an apparatus, a positive gas pressure is applied to a wet specimen placed on a fine porous plate. When the water menisci in a material are exposed to a certain pressure difference, an equilibrium state is eventually reached. According to Equation 2, a specific pore radius corresponds to a certain suction level.

$$\Delta P = \frac{2 \cdot \sigma}{r} \qquad (2)$$

where

ΔP is the capillary suction [Pa],

σ is the surface tension of water at 293ºK [0.074 N/m], and

r is the radius of a meniscus [m].

For pores of larger radius, the suction forces will be unable to resist the pressure difference and the pores will be drained, while pores of smaller radius retain greater suction and will remain water filled. The pressure plate technique can also be used for determining pore size distribution, according to Fagerlund (1973) and Krus and Kieβl (1998).

4.2 Method

Retention curves have been measured for lime–cement mortar B. Since the results of the pressure plate and sorption balance tests were to be combined, it was of greatest importance that all materials be thoroughly cured and carbonized before testing. The curing and carbonizing of the different materials was described by Johansson (2005).

The specimens as prepared for pressure plate testing were 50 × 50 × 4 mm, and represented by eleven specimens. The length of the side of the specimen was chosen so that the area of the pressure plate membrane would be optimally used. The thickness of the specimen was chosen so that the smallest representative unit in the tested materials would be properly represented. For the mortar using the Baskarp aggregate in the 0–3-mm fraction, the smallest representative unit was 3 mm. Therefore, the smallest possible thickness was determined to be 4 mm. Of course, a greater thickness could have been used, but that would have prolonged the testing. Initial testing showed that the test duration for the cement-based mortar was approximately four weeks at each pressure step. Before the tests took place, all specimens were vacuum saturated using a procedure described by Fagerlund (1977).

For the test, three different pressure plate extractors were used with maximum pressures of 0.5, 1.5, and 10 MPa, respectively. Before the test was performed, all specimens were vacuum saturated. When the test started, certain pressures (see Table 1) were chosen for the study; the corresponding relative humidity levels are also shown in the table. The pressure steps were set so that a relatively even distribution was reached in terms of change of moisture content, i.e. a relatively even resolution over the complete moisture range in terms of moisture content by mass. Since the estimated sorption isotherm displayed an increasing slope from the hygroscopic range up to complete saturation for the studied materials, the pressure steps were chosen so as to be smaller as saturation was being approached.

TABLE. 1: Target pressure levels for retention measurements performed, the corresponding relative humidity levels given by Equation 1, and the radii of menisci according to Equation 2.

Pressure [MPa]	Relative humidity [%]	Radii of menisci [µm]
0.004	99.997	37
0.008	99.994	18.5
0.02	99.985	7.4
0.1	99.926	1.48
0.3	99.779	0.493
1	99.264	0.148
3	97.807	0.049
6.5	95.310	0.023
10	92.876	0.015

The schematic design of the two pressure plate extractors for pressures up to 0.5 and 1.5 MPa, respectively, is depicted in Figure 1. A room equipped with a climate control unit was used for the tests, and the room temperature was logged for the complete duration of the testing. Measurements showed that the temperature in the testing room was 20ºC ± 1ºC.

To ensure hydraulic contact between the ceramic plate and the specimen, a thin layer of kaolin clay was applied to the ceramic plate, as specified in the Nordtest standard (1997). Before the kaolin clay was applied, it was diluted with water to give a low enough viscosity that the kaolin could easily be applied to the ceramic plate. After an approximately 2-mm-thick layer of kaolin was applied, a nylon cloth was applied above the kaolin to prevent the specimen from being contaminated by direct contact with the clay. Keeping the specimens clean was of the greatest importance, since the specimens were to be weighed when equilibrium was achieved at each pressure step.

The need for a layer of kaolin clay to serve as an intermediary between the specimen and the ceramic plate was investigated by Janz (1997). In tests of brick, the bed of kaolin was replaced with a micro-fibre cloth comprising 85% polyester and 15% polyamide, or the specimen was placed directly on the ceramic plate with no

intermediate layer. Results of the three different setups showed that, regardless as to whether no bed, a kaolin clay bed, or a micro-fibre cloth was used, the water retention curve was not changed. However, the time required to reach equilibrium with the different bedding materials was not considered by Janz (1997), as the test started with the vacuum-saturated specimen being placed on the porous ceramic plate. To ensure that the equilibrium state was reached within a reasonable amount of time, kaolin clay was used as an intermediate layer.

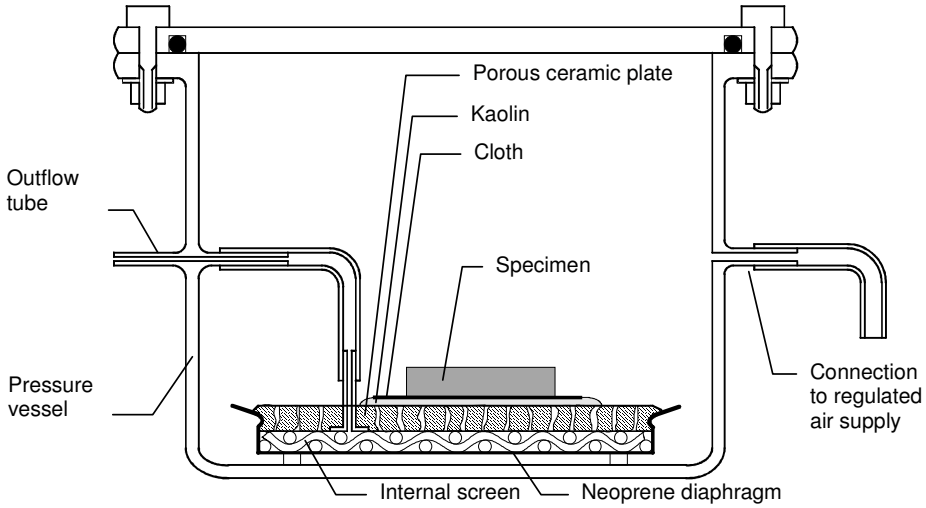

FIG. 1: Schematic sketch of the pressure plate extractors for pressures up to 0.5 and 1.5 MPa (Janz, 1997).

The inlet tube depicted on the right in Figure 1 was then connected to a cylinder of nitrogen gas. To enable fine adjustment of the pressure in the extractor, a pressure regulator was connected between the gas cylinder and the extractor, providing a control precision of $1 \cdot 10^{-4}$ MPa for the 0.5- and 1.5-MPa extractors. Nitrogen was used instead of air to prevent further carbonization during the test. This was probably an unnecessary precaution, since each material had been completely carbonized before testing began.

To determine the moisture content after equilibrium at a specific pressure level, the pressure plate extractor was opened and the specimen was brought out for weighing. A high-precision balance with a precision of thousandths of a gram was used; the balance was calibrated before and after the weighing of each series. To minimize evaporation from the specimens when opening the extractor, the specimens were immediately removed from the extractor after the lid was lifted off and put in plastic containers. Two containers were used for the eleven specimens. Since the different steps were relatively close together in pressure, there was a significant risk that evaporation during careless handling could result in considerable loss of moisture. A great enough loss in moisture could result in the occurrence of absorption instead of desorption in the next pressure step. Therefore, a piece of wet cloth was placed inside both of the plastic containers used for storing the specimens, to keep the humidity close to the saturation point.

During the measurements, the 0.5-MPa extractor was used for pressure steps from 0.004 MPa to 0.3 MPa, while the 1.5 MPa extractor was used for the 1-MPa pressure step. The various pressure steps are shown in Table 1. For pressure steps from 3 MPa to 10 MPa, a pressure plate extractor allowing pressures up to 10 MPa was used. The 10-MPa pressure plate extractor operated on the same principle as did the extractors with maximum pressures of 0.5 and 1.5 MPa and are further described by Johansson (2005).

By the pressure plate technique we also attempted to determine absorption isotherms, despite the fact that the equipment was designed for desorption tests. The absorption tests didn't show reliable results and are therefore not presented in this paper. The absorption tests are described by Johansson (2005).

5. Results

5.1 Sorption balance

Tests were performed until two complete desorption and absorption isotherms had been determined for the tested material. The variation between the results of the two tests was negligible, so a mean value was used without stating the standard deviation.

The desorption isotherms for lime-cement mortar and lime-silica brick are shown in Figure 3. The moisture content by mass is shown as a function of different relative humidities. When the moisture content by mass was determined, the dry weight of the specimen at 0% relative humidity was used to calculate the mass-time relationship.

5.2 Pressure plate

The results of the pressure plate tests are presented as water retention curves for lime-cement mortar and lime–silica brick in Figure 2. The figure also present the results of the sorption balance tests described in Section 3, which show moisture content by mass at specific relative humidity steps above 50%. Relative humidity levels below 50% were excluded, since the tested material showed insignificant moisture capacity in this range. Before the results of the sorption balance tests were included in the figures, the relative humidity levels were transformed into suction using Equation 1.

To illustrate the high resolution provided by the pressure plate technique above the hygroscopic range, the retention curves were also transformed into conventional sorption isotherms. The transformed retention curves are shown in Figure 3 the two materials.

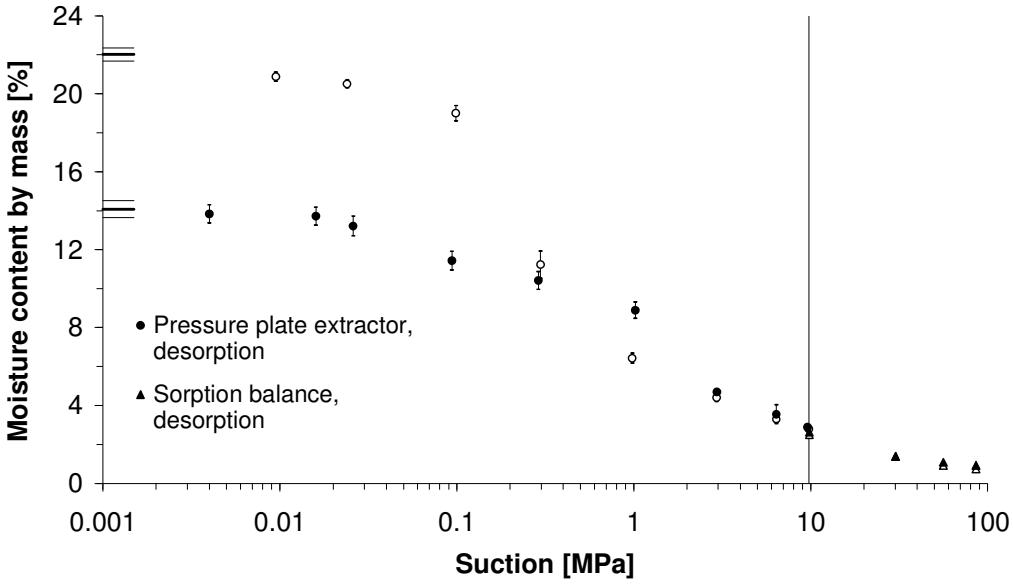

FIG. 2: Retention measurements performed using the pressure plate extractor on individual specimens of lime–silica brick (filled dots) and lime-cement mortar (unfilled dots). The moisture content by mass is presented as mean values, with the scatter expressed as one standard deviation. The horizontal lines represent vacuum saturation. Results of desorption measurements made using the sorption balance method are shown as mean values without scatter, to the right of the vertical line.

6. Discussion and conclusions

Moisture fixation properties are determined for lime-cement mortar and lime-silica brick using the sorption balance and pressure plate methods and are compared in Figure 3. The results obtained using the different methods are in significant agreement, despite the fact that different specimens were used for the two methods. There was also a considerable difference in the time required for the two measurement methods: the sorption balance method required approximately one week per material, while the pressure plate method required approximately six months per material. The agreement between the results of the different measuring methods most likely stemmed from the fact that the specimens were well cured and thoroughly carbonated before testing took place. In cases in which cement-based materials are allowed to carbonize during testing and when different measurement methods with different time requirements are used, it can be hard to obtain agreement in the results. Good agreement between the results of the two measuring methods used here was also found by Janz (2000) and Johannesson and Janz (2002), while good agreement between the results of the pressure plate technique and pore size measurements using mercury was found by Krus and Kieβl (1991).

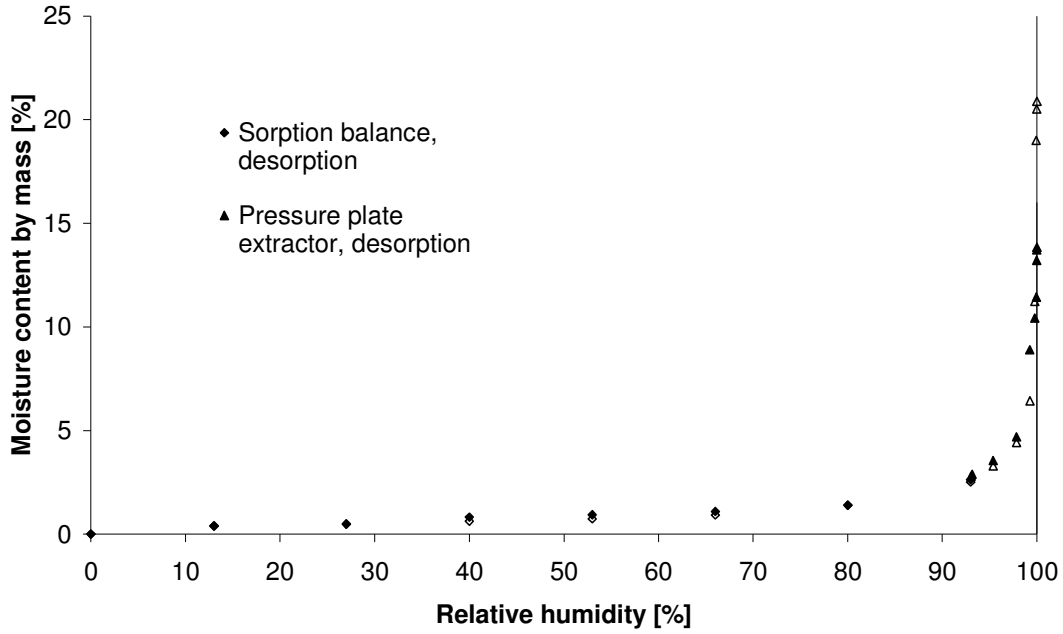

FIG. 3: Desorption isotherms for lime–silica brick (filled dots) and lime-cement mortar (unfilled dots) measured using the sorption balance and pressure plate extractor methods. Moisture content by mass is presented as mean values.

A sorption isotherm representing the complete moisture range according to Figure 3 can for example be used as input data for transient moisture profile simulations in the superhygroscopic range. Such simulations have been performed by Johansson (2005) for lime-cement mortar attached to lime–silica brick (as combined materials), see Figure 4. Each dot in the figure represents the mean value of the degree of vacuum saturation for the corresponding vertical row of cells. The unfilled circles and squares represent the moisture levels of the mortar. To make the results more obvious, the dots are connected by lines. The simulations were performed for water absorption phase lasting 2 days. As can be seen in the figures, the type of mortar used as an outer layer was lime–cement mortar in thicknesses of 7 and 14 mm.

It can clearly be seen in Figure 4 that the thickness of the mortar was of minor importance for the penetration depth of the moisture profile front. The effect of differences between the sorption isotherms of the two combined materials are however clearly shown in Figure 4, where the underlaying lime-silica brick attempt considerable higher moisture levels than the outer layer of lime-cement mortar despite that the water was supplied to the outer layer of mortar.

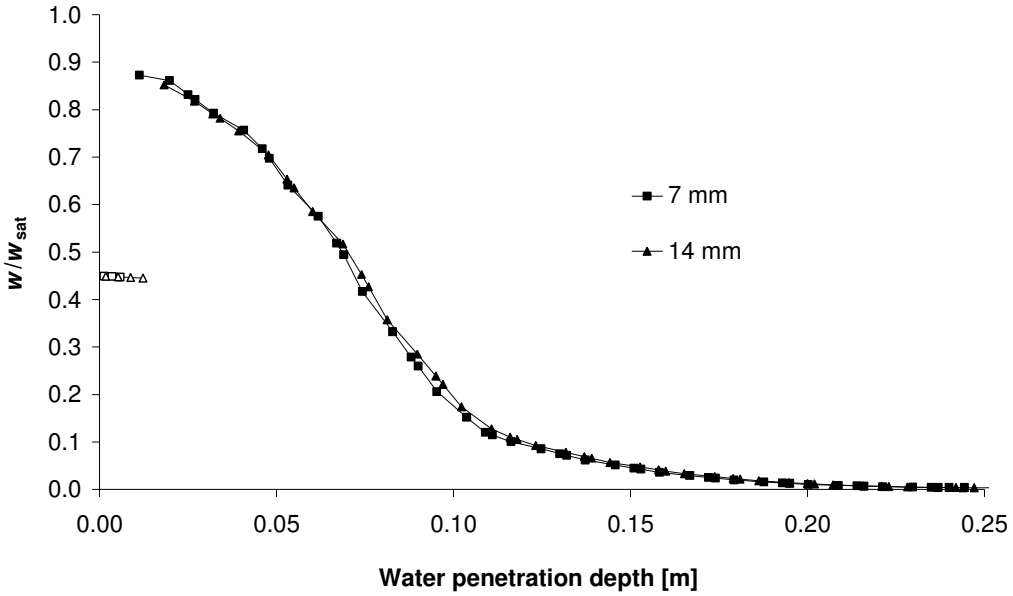

FIG. 4: Moisture profile simulations for specimens of lime–silica brick with a layer of lime–cement mortar attached. The surface of the mortar was exposed to a free surface of water for two days (Johansson, 2005).

7. References

Anderberg, A. and Wadsö, L. (2004), 'Moisture in self-levelling flooring compounds. Part II. Sorption isotherms', Nordic Concrete Research, Publication No. 32, 2/2004.

Fagerlund, G. (1973), 'Determination of pore size distribution by suction porosimetry', Materials and Structures, Vol. 6, No. 33, pp. 191-201.

Fagerlund, G. (1977), 'The critical degree of saturation method of assessing the freeze/thaw resistance of concrete', Materials and Structures, Vol. 10, No. 58.

Janz, M. (1997), 'Methods of measuring the moisture diffusivity at high moisture levels', Report TVBM 3076, Division of Building Materials, Lund Institute of Technology.

Janz, M. (2000), 'Moisture transport and fixation in porous materials at high moisture levels', Doctoral thesis, Report TVBM 1018, Division of Building Materials, Lund Institute of Technology.

Johannesson, B. and Janz, M. (2002), 'Test of four different experimental methods to determine sorption isotherms', Materials and Structures, Vol. 14, No. 6, pp. 471-477.

Johansson, P. (2005), 'Water absorption in two-layer masonry systems - Properties, profiles and predictions', Doctoral thesis, Report TVBM 1024, Division of Building Materials, Lund Institute of Technology.

Kieβl, K. and Krus, M. (1991), 'NMR-measurements of capillary penetration behavior of water and hydrophobing agent in porous stone and derivation of new capillary transport values', Report FtB-12e, Fraunhofer-Institut für Bauphysik, Holzkirchen.

Krus, M. and Kieβl, K. (1998), 'Determination of the moisture storage characteristics of porous capillary active materials', Materials and Structures, Vol. 31, pp. 522-529.

Levoguer, C. L. and Williams, D. R. (1997), 'The determination of permeability and diffusion rates in polymer films and packaging materials', Pharm. Technol. Europe, April 25-30.

Nordtest standard (1997), 'Retention curve and pore size distribution', NT BUILD 481.

Richards, L. A. (1948), 'Porous plate apparatus for measuring moisture retention and transmission by soil', Soil Science, Vol. 66, pp. 105-109.

Moisture transfer across the interface between brick and mortar joint

Hannelore Derluyn, M.Sc.,
Laboratory of Building Physics, Catholic University of Leuven;
hannelore.derluyn@bwk.kuleuven.be

Hans Janssen, Assis.Prof.,
Department of Civil Engineering, Technical University of Denmark;
haj@byg.dtu.dk

Peter Moonen, M.Sc.,
Faculty of Civil Engineering and Geosciences, Delft University of Technology;
peter.moonen@bwk.kuleuven.be

Jan Carmeliet, Prof.,
Chair of Building Physics, Swiss Federal Institute of Technology ETHZ Zürich, ETH-Hönggerberg, CH-8093 Zürich, Empa, Swiss Federal Labaratories for Materials Testing and Research, Laboratory for Building Technologies, Überlandstrasse 129,CH-8600, Dübendorf

KEYWORDS: Moisture transfer; mortar joints; interface resistance; hygric property; water extraction.

SUMMARY:
This paper reports on experimental and modelling work on moisture transport in masonry, with special attention to the liquid transport across the interface between brick and mortar joint. Experiments and simulations reveal that two aspects need to be taken into account: (1) the dependence of moisture transport properties on the curing of the mortar; (2) the presence of a hydraulic interface resistance between brick and mortar. The resistance is due to imperfect contact between brick and mortar, causing a reduction in flow through the interface compared to the assumption of perfect hydraulic contact.

1. Introduction

Moisture transport in masonry is an important research subject in building physics related to durability issues, such as algae and moss growth, staining due to salt efflorescences, cracking due to freeze-thaw cycles or crystallization of salts.

Moisture transfer in masonry, being a multi-layered material, is not as straightforward as in homogeneous porous material. A first aspect is the dependence of moisture transport properties of mortars on the curing conditions. The hygric properties of mould mortar, and mortars cured between wet or dry bricks differ. A second aspect is the contact between brick and mortar joint. Perfect hydraulic contact, meaning a continuity of the capillary pressure at the interface can only be assured artificially by applying a kaolin layer between brick and mortar. Real contact between brick and joint mortar seems to be an imperfect contact, resulting in a resistance for moisture transport.

From literature, we can conclude that some authors attribute the deviation in moisture transport in masonry solely to an interface resistance (Qui et al. 2002; Holm et al. 1996; de Freitas et al. 1996), while others attribute this behaviour to hygric property changes of the entire mortar joint (Brocken 1998). As water extraction by brick during the curing process is commonly reported as the underlaying cause of both phenomena (Brocken 1998; Holm et al. 1996), this study investigates the hygric behaviour of joint mortars cured between capillary-saturated and oven-dry bricks, in comparison with mould mortars.

In a first part of this paper, a detailed study of the hygric material properties of brick and mortars is given. Justification for this detailed analysis is that accurate modelling of moisture transport in masonry needs reliable moisture transport properties, which are however often lacking for mortars. The extraction of moisture from the

mortar layer to the brick during curing is studied to clarify the difference in hygric behaviour of the different mortars. The interface is further analysed by microscopic analysis.

In a second part, X-ray measurement of water uptake experiments on brick/mortar specimens are reported, together with their numerical simulation. The non-ideal contact condition is modelled using two different approaches: (1) as a resistance for flow, (2) as an imperfect interface contact, where a reduction parameter is introduced determining the continuity of flow. The results show that the non-ideal contact and the change of hygric properties both play an important role in moisture transport in masonry.

2. Material properties of brick, mortar and its interface

2.1 Hygric properties of brick and mortar

The preparation of the mortar samples is described in Janssen et al. (2007b). A detailed study of the hygric material properties of brick and mortar was performed, comprising vacuum absorption tests, free water uptake tests, sorption measurements, mercury intrusion porosimetry, X-ray profile measurements and dry and wet cup tests.

An overview of the basic moisture transport properties is given in Table 1. It was observed that brick is a vapor open material with high sorptivity, whereas mortar is vapor tight with lower sorptivity. The transport properties of dry cured, wet cured and mould mortar differ considerably. Going from mould, to wet cured and dry cured mortar, it was observed that the porosity and capillary moisture content decreases, while the density increases. Since the vapor resistance factor depends on porosity, mortars with lower porosity are more vapor tight. The sorptivity of the mortars also decreases with the porosity. This means there is a clear indication that the curing, and especially the possible loss of water of the mortar during curing, determines the pore structure and the relative moisture transport properties.

For numerical simulation, we need the knowledge of moisture permeability and capillary pressure curve. By combining sorption measurements and mercury intrusion porosimetry, the drying capillary pressure curve is obtained, having a maximum value equal to the saturated moisture content. This curve describes the equilibrium moisture content during drying of a fully saturated material. To obtain the needed wetting capillary pressure curve, describing the moisture content during wetting of an initially dry material, it is assumed that this curve has the same course as the drying curve; only the maximum value is lowered to the value of the capillary moisture content w_{cap}. This moisture retention curve can be analytically described by a bimodal function of the van Genuchten type (Carmeliet and Roels 2002):

$$w = w_{cap} \cdot \sum l_i \cdot \left[1 + (a_i \cdot p_c)^{n_i}\right]^{-m_i} \quad \text{with} \quad m_i = 1 - 1/n_i \tag{1}$$

with p_c the capillary pressure, and a and n shape parameters, l a weight parameter.

TABLE 1. Overview of hygric properties (minimum and maximum between brackets).

	brick	mould mortar	wet cured mortar	dry cured mortar
open porosity (-)	0.209 (0.198-0.216)	0.193 (0.184-0.198)	0.158 (0.156-0.161)	0.138 (0.133-0.143)
bulk density (kg/m³)	2087 (2070-2111)	2092 (2082-2118)	2166 (2155-2170)	2232 (2215-2249)
capillary absorption coefficient (kg/m²s$^{0.5}$)	0.1032 (0.0826-0.1288)	0.0193 (0.0175-0.0213)	0.0154 (0.0135-0.0174)	0.0098 (0.0071-0.0133)
capillary moisture content (kg/m³)	130 (118-150)	147 (138-158)	134 (130-137)	97 (92-103)
saturated moisture content (kg/m³)	209 (198-216)	193 (184-198)	158 (156-161)	138 (133-143)
vapor resistance factor of dry material(-)	25 (18-32)	133 (117-155)	379 (303-496)	407 (325-619)

In Figure 1, the drying and wetting capillary pressure curve is shown for mould mortar. The wetting curves for the different mortars are given in Figure 2. The parameters of equation (1) are given in Table 2. The corresponding pore volume distributions of the mortars are given in Figure 3. We observe that average pore size

for all mortars remains in the same pore size range, only the total porosity of the mortars decreases for the wet cured and especially for the dry cured mortar.

TABLE 2. Parameters of equation (1) for brick and mortars.

	brick		mould mortar		wet cured mortar		dry cured mortar	
l_1,l_2	0.846	0.154	0.322	0.678	0.505	0.495	0.657	0.343
a_1,a_2	$-1.4\ 10^{-5}$	$-9.0\ 10^{-6}$	$-2.2\ 10^{-8}$	$-2.9\ 10^{-7}$	$-2.7\ 10^{-8}$	$-2.8\ 10^{-7}$	$-3\ 10^{-8}$	$-2.9\ 10^{-7}$
n_1,n_2	4	1.69	2.41	2.15	2.28	2.86	2.14	3.24

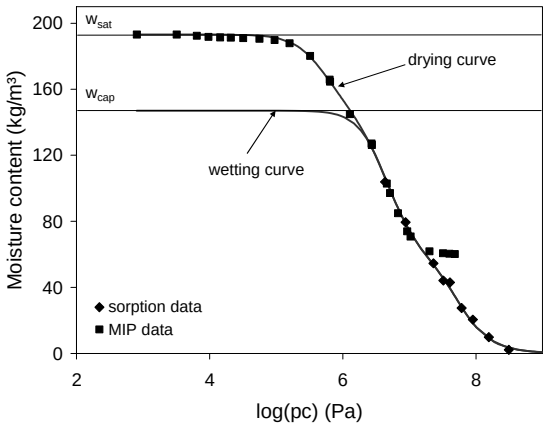

FIG. 1. Drying and wetting capillary pressure curve for mould mortar.

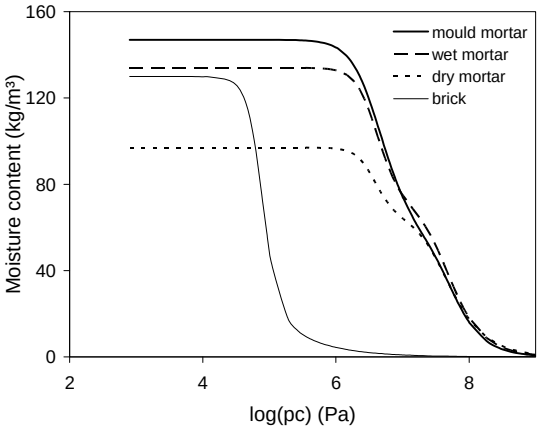

FIG. 2. Wetting capillary pressure curves for brick, mould, wet cured and dry cured mortar.

The moisture permeability is determined from X-ray moisture content profile measurements during capillary uptake and dry and wet cup tests determining the vapor permeability. Based on these measurements the moisture diffusivity is first determined (see Figure 4) and then recalculated into a moisture permeability according to the methodology described by Carmeliet et al. (2007). The obtained moisture permeability of the different mortars is shown in Figure 5.

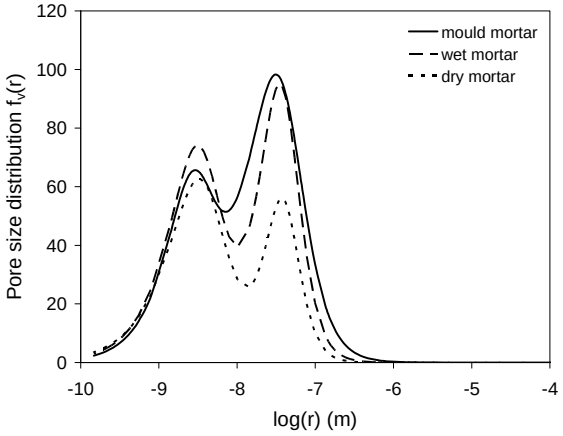

FIG. 3. Pore volume distribution of mortars.

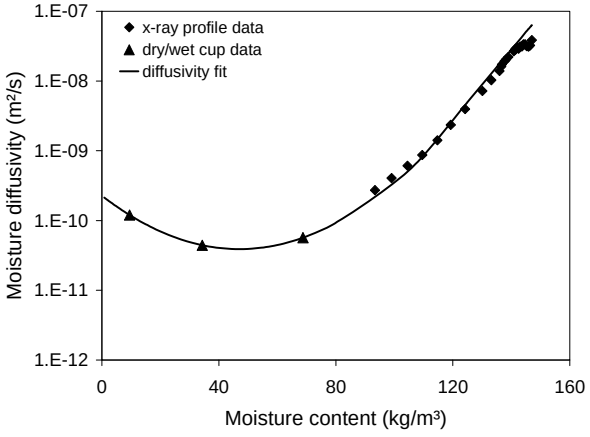

FIG. 4. Moisture diffusivity of mould mortar.

Figure 6 shows the moisture permeability curve for brick, together with the measurement data. At low moisture content (high capillary pressure), the permeability curve describes the dominant vapor flow, while at high moisture content (low capillary pressure) the permeability curve represents the dominant liquid water transport. Figure 5 shows that the vapor permeability of the mortar decreases due to curing of the mortar on wet and dry brick. The liquid water permeability at low capillary pressure however does not change so much.

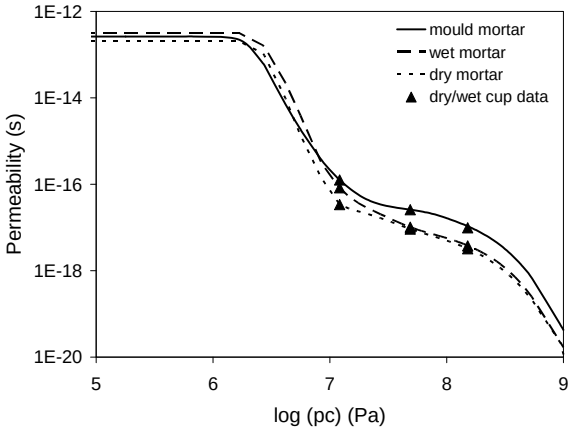

FIG. 5. Permeability of mortars.

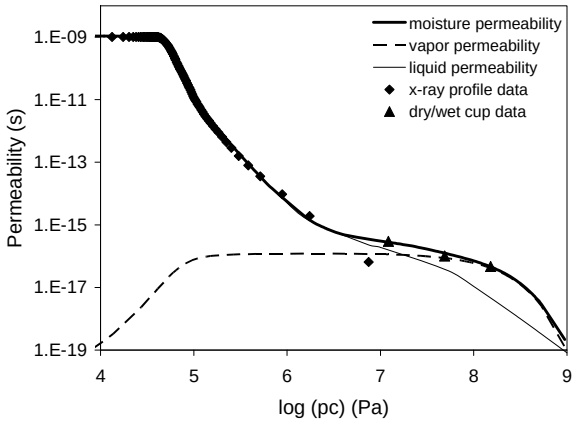

FIG. 6. Permeability of brick.

2.2 Water extraction from mortar by brick during curing

It was found that the mould mortar shows a higher porosity than wet cured mortar and especially compared to dry mortar. The hypothesis is that water extraction during curing may explain the observed differences. Four test series of eight brick samples of 7 x 7 x 3 cm³ were first dried at 50°C and 3% RH. Two series of bricks were then capillary saturated. The bricks were placed in a vapor tight cup, made of plexiglass. Mortar was applied on the bricks and the cups were closed to prevent evaporation. The mortar was removed from the bricks after respectively 2, 4, 8, 15, 30, 45, 60 and 90 minutes of contact time. In order to determine the amount of water taken up by the brick, the weight of the brick before applying the mortar and after removal of the mortar was determined. The amount of water taken up by the brick is expressed relative to the initial amount of water in the mortar. We found that the uptake of water amounts to 30% for mortar cured on dry bricks and to 6% for mortar cured on capillary saturated bricks. The initial W/C factor is 0.5. Due to the extraction of water by the brick, the W/C ratio of the mortar decreases to 0.35 for dry cured mortar, and 0.47 for wet cured mortar. The decrease in W/C ratio may explain the observed decrease of porosity for dry cured and wet cured mortar. Nyame and Illston (1981) and Goto and Roy (1981) show that porosity decreases with decreasing W/C ratio for hardened cement paste. Sanjuán and Muñoz-Marialay (1996) found for concrete a linear increase of the air permeability coefficient D_{air} (m²) with the W/C ratio. Nyame and Illston (1981) and Goto and Roy (1981) both show a decrease in permeability with decreasing W/C ratio, but point out that permeability depends both on the porosity and the pore size distribution. As shown in Figure 3, the pore size distribution of the three mortars shows almost no shift in the pore size range. This can explain why the difference in liquid water permeability at high moisture content between the different mortars is less pronounced.

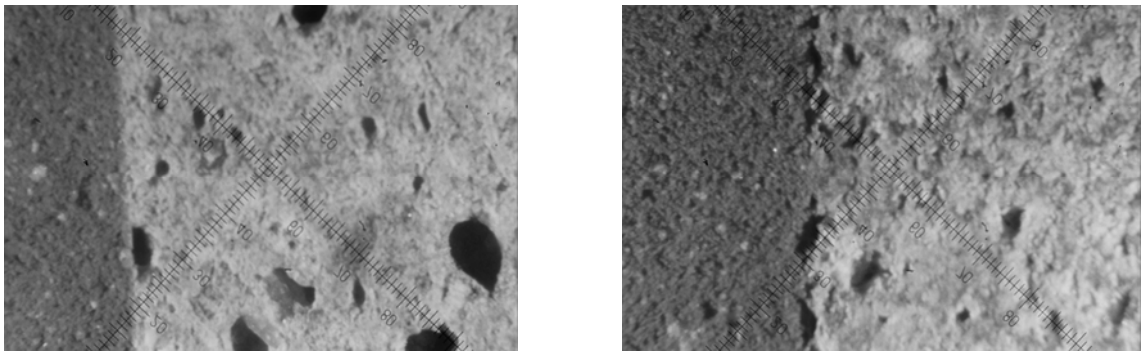

FIG. 7. Images (magnification x 15) of interface between brick and wet cured mortar (left) and brick and dry cured mortar (right).

The interface between mortar and brick was analyzed by microscopic analysis. Representative microscopic images of the interface between capillary saturated brick and joint mortar and between dry brick and joint mortar

are given in Figure 7. At the interface of the dry cured mortar, air voids (also called compaction pores) are clearly visible, whereas the interface of the wet cured mortar shows almost no voids. The measured water extraction can explain these observations, as the strong reduction of W/C ratio in dry cured mortar implies a fast compaction of mortar, leading to an insufficient contact. A similar observation is described in Brocken et al. (1998). He found that only 20-30% of the surface area of the cured mortar is in good contact with the brick.

3. Capillary uptake experiments in masonry and numerical simulation

Capillary uptake experiments were performed on three different masonry specimens:

1. brick – kaolin layer – mould mortar – kaolin layer – brick
2. brick – joint mortar (wet mortar) –brick
3. brick – joint mortar (dry mortar) –brick

The average dimensions of the specimens are given in Figure 8. Liquid water was applied at the bottom side of the specimen. The liquid water uptake is perpendicular to the mortar layer and is measured using X-ray radiography (Roels and Carmeliet 2006). The X-ray picture after one hour of water uptake (Figure 8) clearly shows the moisture front in the mortar, indicating a one-dimensional flow. From the X-ray pictures at different time steps, moisture profiles and the time evolution of the position of the moisture front are determined. The position of the moisture front is defined as the height at which the moisture content equals half of the capillary moisture content.

Isothermal moisture transfer is described as:

$$\frac{\partial w}{\partial t} = \nabla^T \left(K \nabla p_c \right) \tag{2}$$

with w the moisture content and K the moisture permeability. The experiments are simulated for a one-dimensional geometry using the Hamfem code (Janssen et al. 2007a). The initial capillary pressure in the dry specimen is equal to -10^9 Pa. At the bottom side of the model, a constant capillary pressure of -10 Pa, according to capillary moisture content, is imposed.

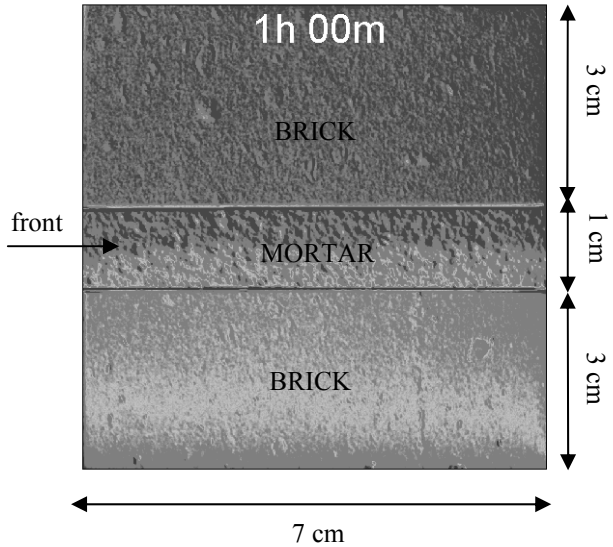

FIG. 8. Capillary uptake experiment in specimen 1 (mould mortar).

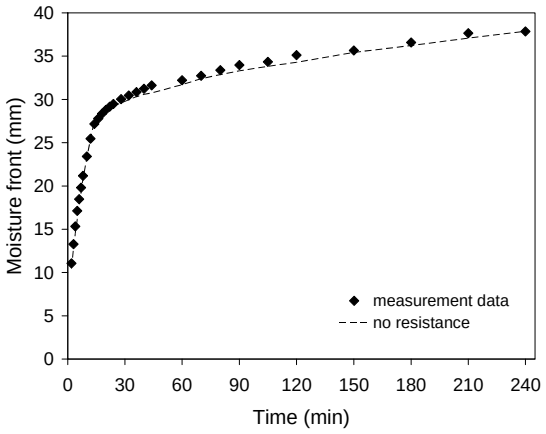

FIG. 9. Evolution of moisture front in specimen 1, experimental and numerical result.

For the mould mortar with the kaolin layer, an ideal hydraulic contact is assumed. Figure 9 compares the measured curve with the simulation. The figure shows that the ideal contact assumption is correct for the mould mortar with kaolin layer.

For masonry specimens 2 and 3 (wet cured and dry cured mortar) a first simulation is done, assuming perfect contact, but taking into account the proper hygric properties of the different mortars, as determined in the first section. As can be seen in Figures 10 and 11, the rate of propagation of the moisture front in the mortar is clearly overestimated. This indicates that a resistance is present at the interface.

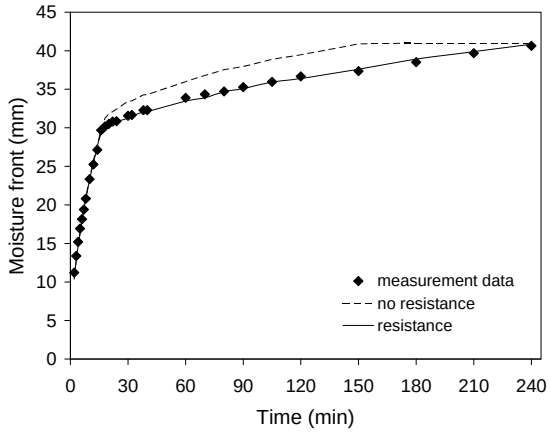

FIG. 10. Evolution of moisture front in specimen 2 (wet mortar), experimental and numerical result by imposing an interface resistance.

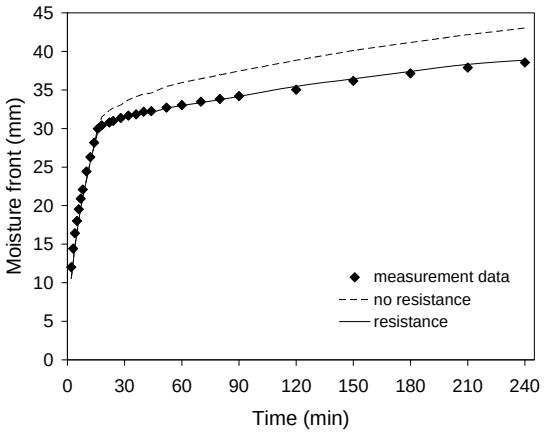

FIG. 11. Evolution of moisture front in specimen 3 (dry mortar), experimental and numerical result by imposing an interface resistance.

The existence of an interface resistance for joint mortars can be explained by: (1) a reduction of the contact surface due to the presence of compaction pores; (2) a mismatch in the pore systems of brick and mortar in the contact area (pore radius of bricks is a factor 100 larger than of mortars); (3) a change in pore structure of the interface layer due to e.g. blocking of pores by formation of mortar particles in the brick pores close to the interface, which reduce the permeability.

In a first modelling approach, these effects can be taken into account by defining a resistance at the interface. The flow across the interface with zero thickness (no capacity) is described by:

$$q = \frac{1}{R_{IF}} \cdot \Delta p_c \tag{3}$$

with Δpc the jump in capillary pressure at the interface. A constant interface resistance is assumed: 1.25 10^{10} m/s for the wet cured mortar and 2.5 10^{10} m/s for the dry cured mortar. The interface resistance is determined by inverse indentification and as such lacks some physical interpretation.

Figures 10 and 11 show a good agreement between measurement and simulation for the case with interface resistance. The calculated flow across the interface is compared with the measured flow in Figures 12 and 13. The measured interface flow is obtained from the moisture front velocity in the mortar, which is determined from moisture profiles at different time steps. A good agreement between measurement and simulation is obtained for the interface resistance. Comparison with the case of ideal contact shows that the interface resistance causes an important reduction of the flow across the interface in a short period just after the moisture front passed the interface.

In a second modelling approach, the interface zone is lumped onto a single plane. Due to the imperfect contact a jump in capillary pressure on this surface may occur. The capillary pressure in the domain Ω is described as:

$$p_c = \hat{p}_c + H.\tilde{p}_c \tag{4}$$

where $\hat{p}_c$ and $\tilde{p}_c$ are continuous functions on the domain and H is the Heaviside step function equal to zero at one side of the interface and one at the other side. The one-dimensional moisture flux through the interface under isothermal conditions can be expressed by:

$$q_\Gamma = \varphi \cdot \left(q_\Omega + k \cdot \left[\left| \tilde{p}_c \right| \right] \right) \text{ with } k = \left(\frac{1-\alpha}{K_{mat1}} + \frac{\alpha}{K_{mat2}} \right)^{-1} \tag{5}$$

where q_Ω is the flux in the continuum material described by $K\nabla p_c$. k is an effective moisture permeability; the term 'effective' means that the quantities are derived from the corresponding bulk properties of the two materials sharing the interface (K_{mat1} and K_{mat2}) . The factor α is a weighting parameter for the two materials. Because the permeability of the interface layer is mainly determined by the pore system of the mortar, a value of α equal to 1 is adopted in the simulation. $\left[\left|\tilde{p}_c\right|\right]$ represents the jump in capillary pressure over the interface. The factor φ is the reduction factor, describing the imperfect contact. This factor amounts 0.9965 for specimen 2 and 0.995 for specimen 3. The lower value of φ for specimen 3 is in agreement with the more pronounced imperfect contact between brick and dry cured mortar than between brick and wet cured mortar, as can be seen in the microscopic images (Figure 7). The modelling result for masonry specimen 2 and 3 is given in Figures 14 and 15 respectively.

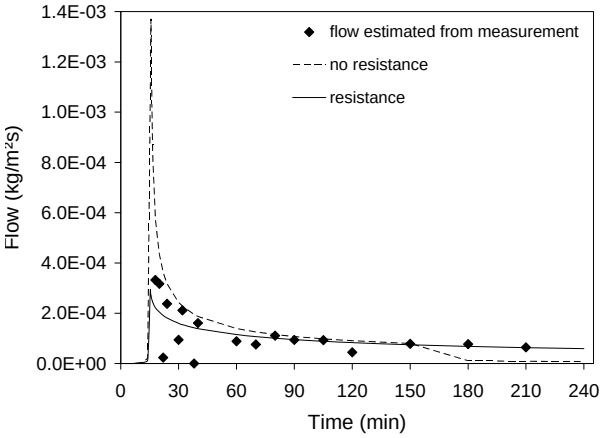

FIG. 12. Flow through the interface of specimen 2 (wet mortar).

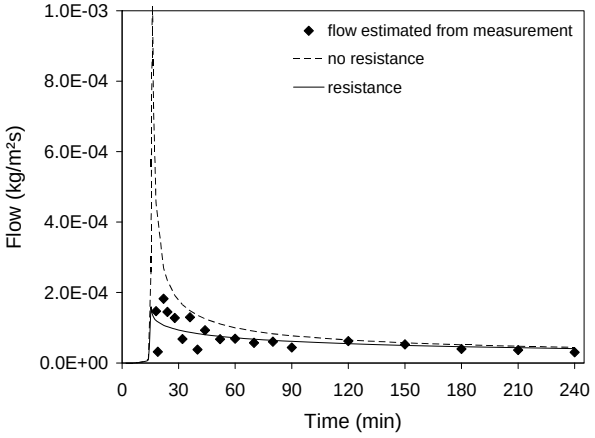

FIG. 13. Flow through the interface of specimen 3 (dry mortar).

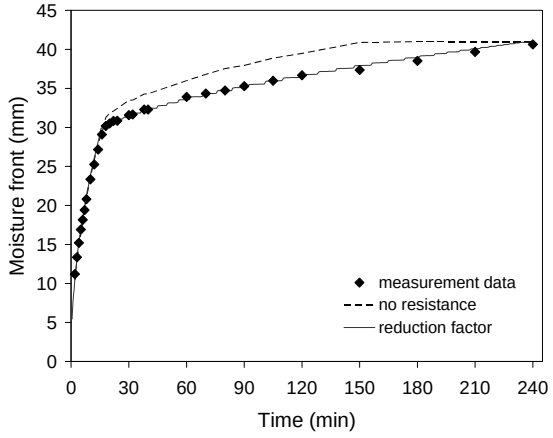

FIG. 14. Evolution of moisture front in specimen 2 (wet mortar), experimental and numerical result by using a reduction factor.

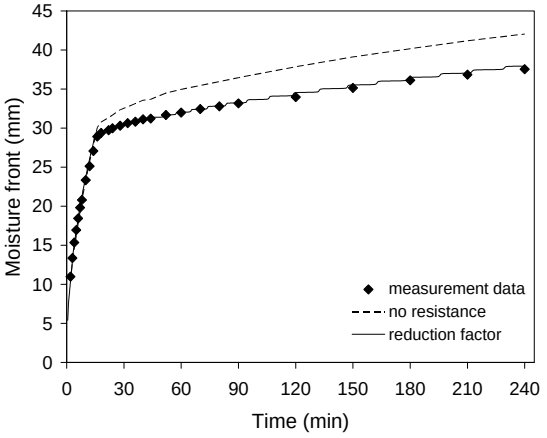

FIG. 15. Evolution of moisture front in specimen 3 (dry mortar), experimental and numerical result by using a reduction factor.

4. Conclusion

In this paper, it is shown that a detailed study of the moisture transport properties of joint mortars is needed to accurately simulate moisture flow in masonry. The experiments show that the hygric properties of the joint mortar change due to the curing conditions – i.e. a decrease of W/C factor due to water uptake by the brick resulting in a decrease of porosity and permeability - and that secondly an interface resistance between brick and mortar is present. For dry cured mortar, the formation of air voids plays an important role. These observations are supported by the results of numerical simulations.

Acknowledgements

The experimental work done by M.Sc. student Elke Deridder is highly appreciated. This research is sponsored by the Flemish Institute for Science and Technology, SBO project IWT03175 (Structural damage due to dynamic excitations: a multi-disciplinary approach).

References

Brocken, H.J.P. (1998). Moisture transfer in brick masonry: the grey area between bricks, Ph.D.Thesis, Eindhoven University of Technology, The Netherlands.

Brocken, H.J.P., M.E. Spiekman, L. Pel, K. Kopinga and J.A. Larbi. (1998). Water extraction out of mortar during brick laying: a NMR study, *Materials and structures*, Vol.31, January-February 1998, pp. 49-57.

Carmeliet, J. and S. Roels. (2002). Determination of the moisture capacity of porous building materials, *Journal of Thermal Envelope and Building Science*, Vol.25, January 2002.

Carmeliet, J., H. Janssen and H. Derluyn. (2007). An improved moisture diffusivity model for porous building materials, Proceedings of the 12th Symposium for Building Physics, Vol.1, pp.228-235, Dresden, Germany, March 29-31 2007.

de Freitas, V.P., V. Abrantes and P. Crausse. (1996). Moisture migration in building walls - Analysis of the interface phenomena, *Building and Environment*, 31(2): 99-108.

Goto, S. and D.M. Roy. (1981). The effect of W/C ratio and curing temperature on the permeability of hardened cement paste, Cement and concrete research, Vol.11: 575-579.

Janssen H., B. Blocken and J.Carmeliet. (2007a). Conservative modelling of the moisture and heat transfer in building components under atmospheric excitation. International Journal of Heat and Mass Transfer, 50: 1128-1140. DOI: 10.1016/j.ijheatmasstransfer.2006.06.048

Janssen, H., H. Derluyn and J. Carmeliet. (2007b). Moisture transfer through mortar joints: interface resistances or hygric property changes?, Proceedings of the 12th Symposium for Building Physics, Vol.2, pp.808-815, Dresden, Germany, March 29-31 2007.

Holm, A., M. Krus and H.M. Künzel. (1996). Feuchtetransport über Materialgrenzen im Mauerwerk, *Int. Zeitschrift für Bauinstandsetzen*, 2(5): 375-396.

Nyame, B.K. and J.M. Illston. (1981). Relationships between permeability and pore structure of hardened cement paste, *Magazine of Concrete Research*, Vol.33, No.116: September 1981.

Roels, S. and J.Carmeliet. (2006). Analysis of moisture flow in porous materials using microfocus X-ray radiography, *International Journal of Heat and Mass Transfer*, 49: 4762-4772.

Sanjuán, M.A. and R. Muñoz-Martialay. (1996). Influence of the water/cement ratio on the air permeability of concrete, *Journal of material science*, 31: 2829-2832.

Qui, X., F. Haghighat and K. Kumaran. (2002). Modeling moisture accumulation in multi-layered building materials, Proceedings of the Canadian conference on building energy simulation eSIM 2002, Montréal, Canada, September 11-13 2002.

A quantitative model of moisture redistribution in dual layer concrete slabs with regards to hysteresis

Magnus Åhs, Licentiate in Engineering,
Div. of Building Materials, Lund university, Lund, Sweden;
magnus.ahs@byggtek.lth.se
http://www.byggnadsmaterial.lth.se

KEYWORDS: *model, moisture redistribution, hysteresis, concrete.*

SUMMARY:
Moisture in a drying concrete slab redistributes subsequent to applying semi-permeable flooring, hence increasing the humidity beneath the flooring. Such a humidity increase may be substantial in terms of relative humidity, RH, even though the redistributed moisture content appears insignificant. This comparably large increase originates from the hysteresis, moisture history dependence, exhibited by sorption isotherms for cement based materials. In contrast to retracing the desorption isotherm pursued when drying, the material's moisture content traces a scanning curve, when the humidity increases. Scanning curves give a lower change of moisture content in relation to RH, moisture capacity, compared with the desorption isotherm.

A qualitative and quantitative model of moisture redistribution in a dual layer concrete slab with regards to initial RH distribution and scanning curves is presented. The model is validated by determining the RH distribution in a number of screeded concrete slabs, before flooring and after a certain time of redistribution. Sorption isotherms and scanning curves for three cement based materials are shown.

1. Introduction

Redistribution of moisture occurs in building materials, *e.g.* concrete, because of internal and external moisture potentials. This process is self-sustaining and continues until reaching equilibrium with environmental or internal conditions. The relative humidity, RH, is here used as a moisture potential governing redistribution. Because of its hygroscopicity concrete absorbs and releases moisture depending on the surrounding RH and temperature. Moisture content in concrete is therefore commonly expressed in relation to the surrounding RH, the sorption isotherm, see FIG. 1. In FIG. 1 desorption, absorption and scanning curve branches are represented by the solid, dashed and dash dotted lines, respectively, in the 10 - 95 % RH range. The x-axis represents relative humidity in % RH and the y-axis represents the mass ratio of evaporable moisture relative to cement. The shaded area in FIG. 1 illustrates all attainable mass ratio RH relationships.

Sorption isotherms for cement based materials exhibit hysteresis (Baroghel-Bouny and Chaussadent 1996; Baroghel-Bouny et al. 1999; Espinosa and Franke 2006; Baroghel-Bouny 2007). This means that the moisture content fails to retrace its values back when reversing the prior sorption process. Instead, a new path is pursued and the conceived pathway, a scanning curve, is dependent on the preceding desorption/absorption sequence. The hysteresis feature has to be accounted for in estimations of moisture redistribution in screeded slabs, as moisture is both released and gained during construction.

Building materials, *e.g.* floor coverings, adjacent to screeded concrete slabs may be negatively affected from moisture redistribution. Besides dimensional instability, wood floors may experience fungal growth (Pasanen et al. 2000) on surfaces adjacent to concrete if not properly protected. Adhesives beneath low permeable floorings may deteriorate and release volatile organic compounds, VOC, to the indoor air (Sjöberg 2001; Sjöberg and Engström 2002; Björk et al. 2003). In addition, mould may grow on the organic fibres in linoleum floorings. Such moisture related damages, may occur if the humidity level exceeds a certain critical humidity. Preventive measures should therefore be considered to avoid ending up above such levels. Allowing the screeded concrete slab sufficient drying before applying moisture sensitive material is one such method. This decreases the amount of physically bound moisture, thus limiting effects from redistribution.

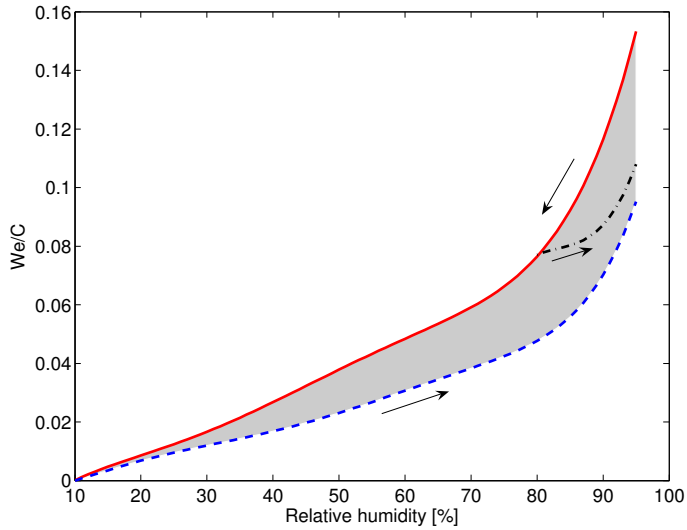

FIG. 1 Illustration of a sorption isotherm for concrete determined in the range between 10-95 % RH

At present there are a few models to estimate moisture distribution and drying of porous materials (Nilsson 1980; Holm and Kuenzel 2002; West and Holmes 2005). However, these models lack considering the hysteresis phenomenon and the reversal of sorption occurring when redistributing moisture. Therefore these models are not suitable to use for such applications. At screeding, moisture penetrates the slab's top surface, hence increasing the water content in the former dry concrete. As moisture is added the corresponding RH increase is not obtained by reversing the desorption process. Moisture from the screed will affect the relationship between moisture content and RH.

The main objective in this article is to describe a quantitative moisture redistribution model including the hysteresis phenomenon. The model is verified with RH measurements performed before flooring and after a certain time of moisture redistribution on a number of screeded concrete slabs. Material properties essential to the model were determined by using a sorption balance (Åhs 2005), including sorption isotherms and scanning curves (Åhs 2007) for w/c 0.65 concrete, C, w/c 0.55 mortar, M, and Floor 4310 Fibre flow, SFC, a self levelling flooring compound.

2. Qualitative model

Moisture redistribution in a screeded concrete slab is described in a qualitative manner for three distinct phases in order to display each horizontal section's moisture history, FIG. 2. Each phase represents important construction stages and the diagram shows current (solid line) and prior (dashed) moisture distribution. This model may work as a guide for determining each section's moisture capacity from a sorption isotherm based on previous moisture history. A sorption isotherm is located below phase 2 and 3, showing the complex interaction between redistributing moisture and concrete.

The first phase shows a homogenous concrete slab, experiencing single sided drying. Moisture distribution is characterised with a low surface humidity and a high slab base humidity. In the second phase a screed (shaded area) has been applied and started to dry. Moisture from the screed penetrates the slab surface hence increasing its humidity and screed surface humidity decreases because of drying. The final phase displays moisture distribution (vertical solid line) after flooring (thick solid horizontal line).

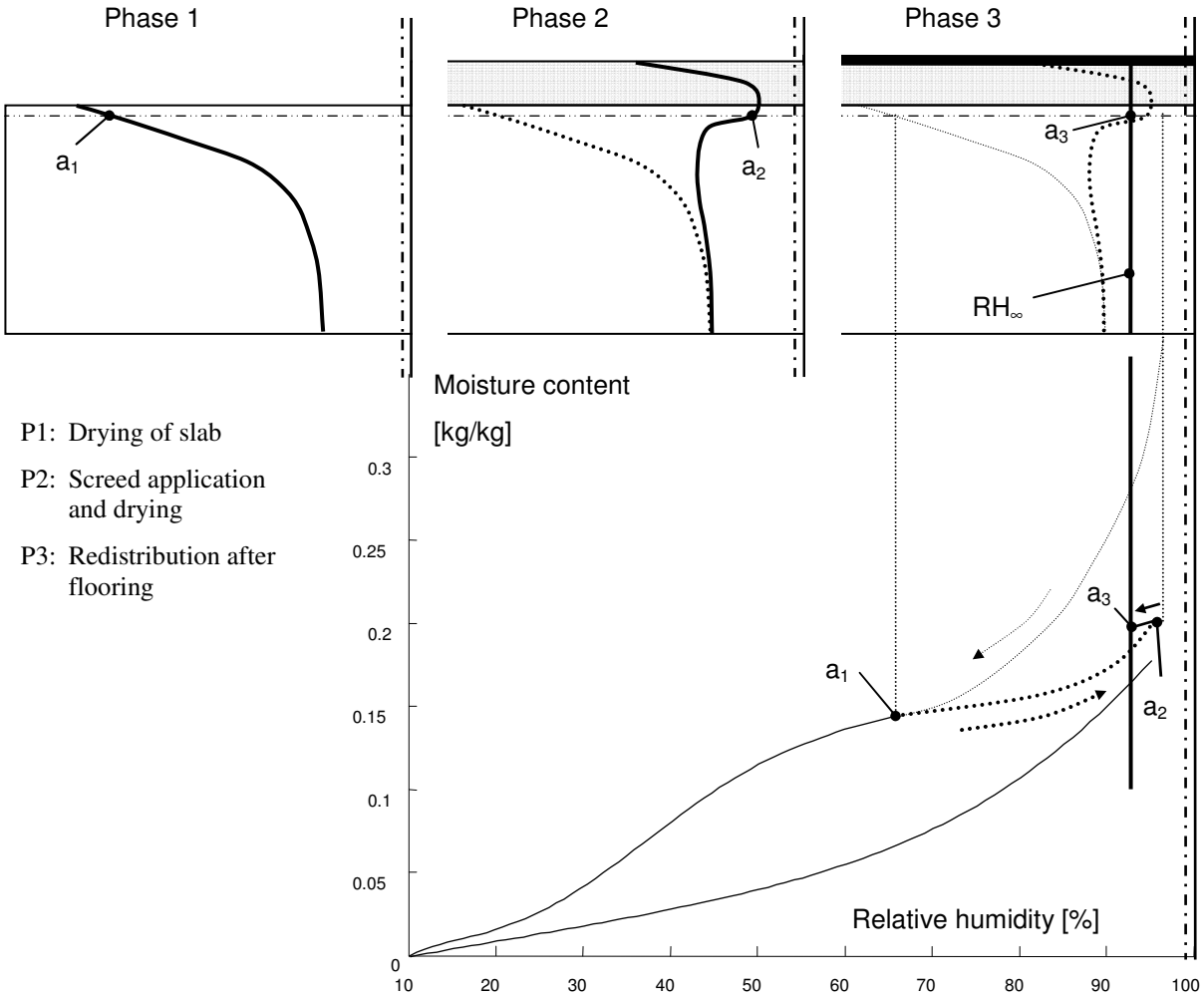

FIG. 2 Moisture redistribution in a concrete slab including a sorption isotherm with scanning curves

One particularly interesting horizontally oriented level, marked **a**, is indicated in the screeded slab, FIG. 2. This section's moisture content change is tracked with respect to RH variations in the sorption isotherm. The moisture content decreases in the concrete at drying, hence following the desorption curve (thin dashed line), until reaching $\mathbf{a_1}$, FIG. 2. In phase 2, the moisture content increases as a consequence of moisture being supplied from the screed application. Because of hysteresis the moisture content increase traces an ascending scanning curve to $\mathbf{a_2}$. As the humidity level is reduced in phase 3 during redistribution, a descending scanning curve is followed until settling at $\mathbf{a_3}$.

3. Quantitative model

Future moisture distribution in a screeded concrete slab is estimated by proposing a theoretical model, suggesting how to redistribute residual moisture after flooring. Four assumptions are made:

A) no further drying of the slab occurs after flooring
B) isothermal conditions
C) moisture transport is not considered
D) no additional chemical moisture binding during redistribution

Moisture redistributes in a sealed screeded slab until ultimately attaining a uniform vertical RH distribution, RH_∞, see FIG. 2. Provided each section's moisture history, RH change and moisture capacity are known their moisture content change is given. The preceding moisture history may be determined from the qualitative model. Moisture capacity is defined as the ratio of moisture content change relative to RH change. As no moisture is lost

through drying it is possible to determine RH_∞. Therefore the total moisture content change from flooring to a complete redistribution is 0 (zero). Moisture from wet sections redistributes to dryer conditions, and vice versa, until a uniform RH distribution is attained throughout the screeded slab. RH_∞ is achieved by iteration, as the moisture capacity is dependent on it.

RH_∞ will reach a level in between the extremes of the distribution as a consequence of assumption A. Therefore the midpoint of the two extremes may serve as a reasonable initial guess. Subsequently it is necessary to determine each section's moisture history in order to assign a realistic moisture capacity.

Based on the qualitative model, the slab base and screed solely undergo drying until flooring. Therefore such regions are assumed to have attained their moisture content and corresponding RH level through tracing the desorption isotherm. In contrast, other sections experienced drying and wetting cycles thus pursuing scanning curves. Such a qualitative analysis is fundamental when determining the proper moisture capacity for each section.

This theoretical analysis could be interpreted into an arithmetic expression, equation 1,

$$\sum_{\Delta x_i}(\overline{RH_i} - RH_\infty) \cdot d_i \cdot \left(\overline{\frac{\partial w}{\partial RH}}\right)_i = 0 \qquad (1)$$

where $\overline{RH_i}$ represents average RH level in [% RH], and RH_∞ represents the future uniform humidity level in [% RH], d_i represents the vertical thickness of each material section in [m], $\left(\overline{\frac{\partial w}{\partial RH}}\right)_i$ represents the average moisture capacity in [kg/(m^3 % RH)] evaluated from sorption (scanning) isotherms between current and future RH.

Equation 1 is based on the assumption that the total moisture content change within the screeded slab with respect to change from $\overline{RH_i}$ to RH_∞ is (zero). By a number of rearranging steps equation 1 gives equation 2, thoroughly explained in Åhs (2007)

$$RH_\infty = \frac{\sum_{\Delta x_i} \overline{RH_i} \cdot d_i \cdot \left(\overline{\frac{\partial w}{\partial RH}}\right)_i}{\sum_{\Delta x_i} d_i \cdot \left(\overline{\frac{\partial w}{\partial RH}}\right)_i} \qquad (2)$$

The obtained RH_∞ is compared with the initial guess. A new iteration is executed by substituting the initial guess with the achieved RH_∞, until obtaining an acceptable deviation.

4. Results

This section presents results from using the quantitative moisture redistribution model on four screeded concrete slabs, FIG. 3. Four floor structures were manufactured by using 220 mm of concrete C for the supporting slab, and 40 mm of mortar M as screed in slab 5 and 7, and 40 mm of self-levelling flooring compound SFC as screed in slab 6 and 8. The x-axis represents RH and the y-axis represents the distance from the top surface. The thin dashed line, solid line and thick dashed line represents moisture distribution before flooring, after a certain time of redistribution and calculated RH_∞ respectively. Moisture distribution measurements were performed relative to the flooring day, day 0 (zero), noted in each graph legend FIG. 3.

Sorption isotherms including several scanning curves were determined, in the range 10-95 % RH, for three cement based materials C, M, and SFC, FIG. 4-FIG. 6, (Åhs 2007). In FIG. 4 and FIG. 5 the x-axis represents RH in % RH. The y-axis, in FIG. 4, represents the mass ratio of evaporable moisture relative to cement content. In FIG. 5, the y-axis represents the mass fraction of evaporable moisture relative to mass at 10 % RH. FIG. 6 shows a detailed diagram of several ascending and descending scanning curves determined from three material C

samples. In FIG. 6 the x-axis represents change in RH and the y-axis represents the change in moisture content (We/C).

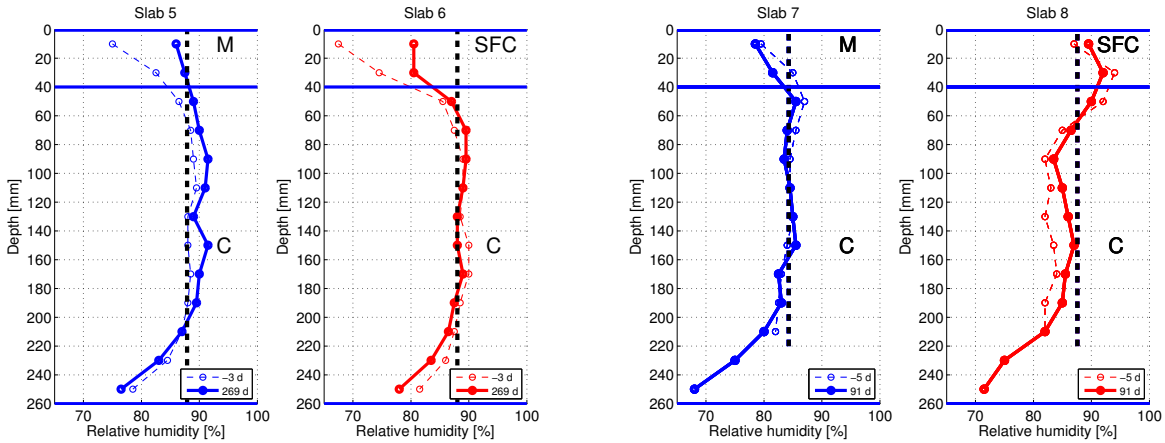

FIG. 3 A comparison of calculated RH_{∞} moisture distribution before and after flooring in four screeded slabs.

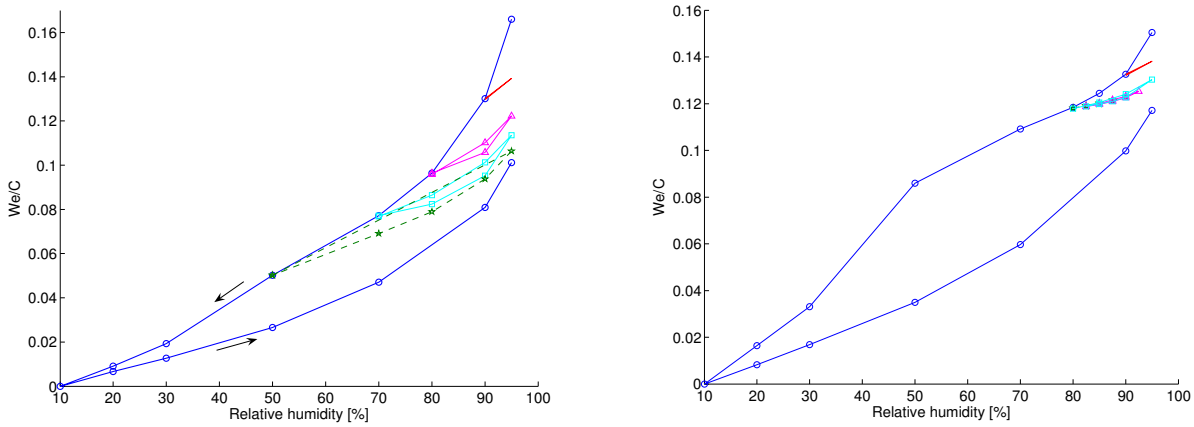

FIG. 4 Sorption isotherms of concrete C (left) and mortar M (right) including several scanning curves.

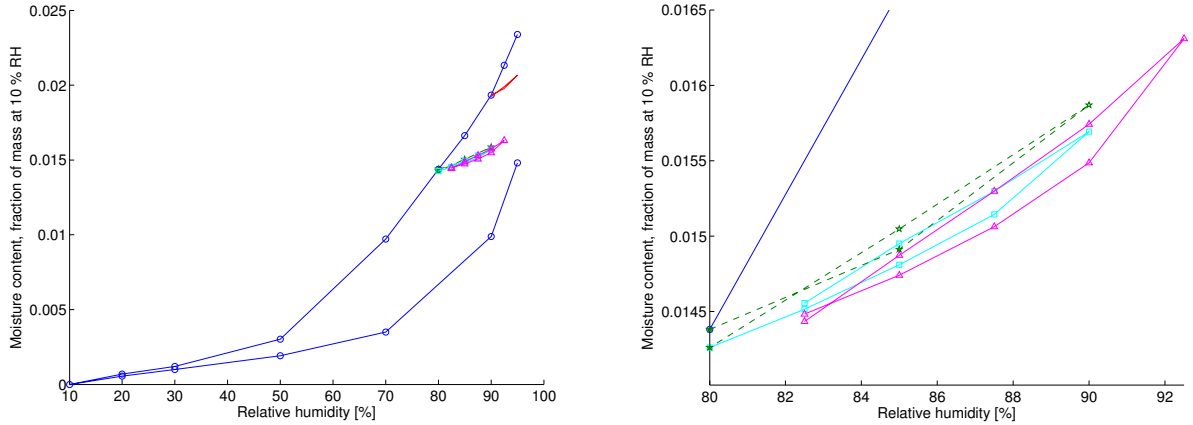

FIG. 5 Sorption isotherm of SFC, including scanning curves (left) and detail of SFC scanning curves (right)

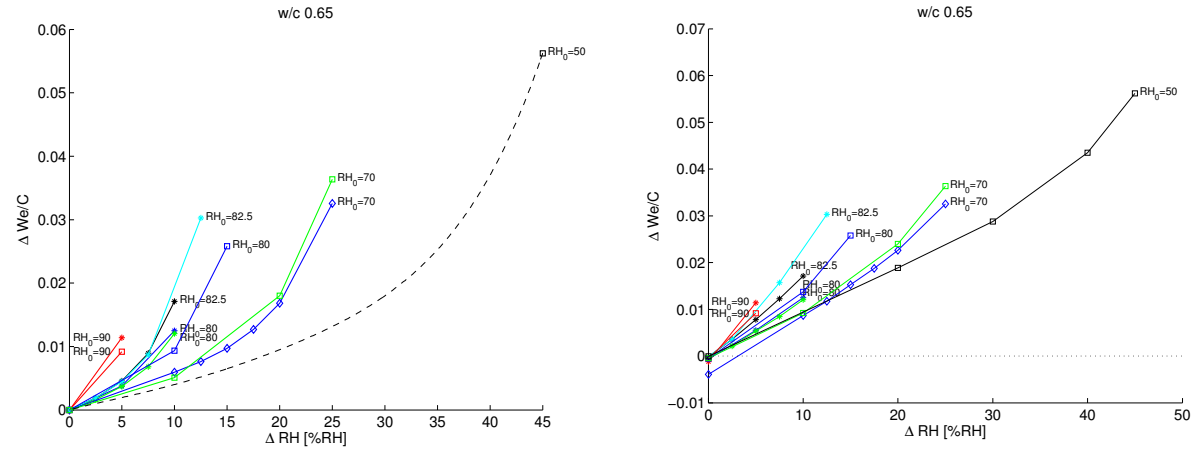

FIG. 6 Detail of ascending (left) and descending (right) scanning curves of concrete C.

5. Discussion

The vertical moisture distribution was determined before flooring and after a certain time of redistribution on four screeded concrete slabs, FIG. 3. The verifying experiments fit the qualitative moisture redistribution model fairly well. In addition, sorption isotherms, FIG. 4 and FIG. 5 including several scanning curves, FIG. 6, were determined on the applied materials. Results of the investigated parameters were applied in the quantitative moisture redistribution model, hence achieving a RH_∞ shown in FIG. 3 (vertical dashed lines).

Slab 5 and 6, FIG. 3 (right), were dried in 60 % RH and 20 °C for a long time (Åhs 2007) before flooring installation which explains the comparatively dry screed. However, the humidity increase after flooring is substantial exceeding 10 % RH in the surface layer (10 mm below the surface). Slab 7 and 8, FIG. 3 (left), were dried a short time (Åhs 2007) before flooring installation, hence explaining the comparatively humid screed. These two slabs, especially slab 8, bear the greatest resemblance to the qualitative model, showing a high humidity level in the screed. Further redistribution is to be expected in all slabs, since a uniform RH distribution is not yet attained, FIG. 3.

The determined moisture distribution after a certain time of redistribution corresponds to results achieved from the quantitative model, especially in slab 5-6. These two slabs represent a case when flooring is installed after a long time of drying. However, a humidity increase is expected in the screed surface, since redistribution is not yet completed. Given additional redistribution time the calculated RH_∞ may be achieved ultimately. Slab 7 and 8 represent a case where flooring is installed early after screeding, hence allowing limited drying of the screed.

Sorption isotherms for materials C, M, and SFC all demonstrate substantial hysteresis beginning from 10 % RH up to 95 % RH, FIG. 4 and FIG. 5. However, the hystesis for SFC is less significant below 50 % RH compared with material C and M. The ascending scanning curves retrieve the starting moisture content when returning to the desorption isotherm, indicating reversible characteristics. This feature is further demonstrated in FIG. 6 where the ascending (left) scanning curves' starting point is met by the descending (right) scanning curves.

Time aspects and possible chemical moisture fixation is not considered. The quantitative model is limited to determining the uniform moisture distribution, hence intermediate time steps is not achievable. Cement based materials are possibly still hydrating when flooring is applied and this may affect the redistribution process. Therefore, redistributed moisture may bind with unhydrated cement grains hence reducing the RH_{∞}.

The proposed quantitative moisture redistribution model requires input from the screeded slab's moisture distribution before flooring. Consequently its accuracy is dependent on the uncertainty of each input. It is therefore important to use material properties used and increase the precision of the determined moisture distribution. This may be achieved by a number of actions, i.e., determine humidity sensor uncertainty (Su and Wu 2004), evaluating measurement method, multiple moisture distribution determination and increasing the number of levels.

The current moisture distribution may be achieved from samples extracted from the floor slab or in-situ measurements. The uncertainty of such a measurement decreases with an increased sampling resolution and number of determined distributions. A higher resolution may demonstrate an unanticipated moisture distribution, hence improving data of each level's moisture history. Increasing the number of determined moisture distributions also exposes possible internal spread.

There are a few examples of sorption isotherms in literature (Powers and Brownyard 1947; Baroghel-Bouny and Chaussadent 1996; Johannesson and Janz 2002; Nilsson 2002; Anderberg and Wadsö 2004; Tada and Watanabe 2005; Espinosa and Franke 2006; Espinosa and Franke 2006; Baroghel-Bouny 2007; Åhs 2007). However, scanning curves for cement based materials are scarcely published (Ahlgren 1972; Baroghel-Bouny and Chaussadent 1994; Espinosa and Franke 2006; Espinosa and Franke 2006; Baroghel-Bouny 2007; Åhs 2007). Published cement based material properties are usually valid for old materials, in excess of 1 year old. Such data may be inappropriate to use on newly poured structures.

Besides material properties, temperature is decisive for moisture redistribution, as it affects the sorption isotherm in cement based materials and alters saturation vapour pressure. Ambient temperature conditions stabilise as the building envelope is finalized, hence diminishing the influence on moisture redistribution. However, a permanent temperature gradient is likely to occur since warm air is lighter than cold, thus heating the floor slab base. Such a temperature gradient may support a moisture transport towards the slab's upper surface hence increasing the humidity beneath flooring. In such a case, equation [2] must be rewritten in terms of vapour content v_{∞}, being constant after redistribution.

6. References

Ahlgren L. (1972). Fuktfixering i porösa byggnadsmaterial (in Swedish). Division of building technology. Lund, Lund University **Ph. D.:** 197.

Anderberg A. and L. Wadsö (2004). "Moisture in self-levelling flooring compounds. Part II. Sorption isotherms." *Nordic concrete research* 32(2): 16-30.

Baroghel-Bouny V. (2007). "Water vapour sorption experiments on hardened cementitious materials." *Cement and Concrete Research* 37(3): 414-437.

Baroghel-Bouny V. and T. Chaussadent (1994). Pore structure and moisture properties of cement-based systems from water sorption isotherms. Microstructure of Cement-based systems, Boston, Materials research society.

Baroghel-Bouny V. and T. Chaussadent (1996). Texture and moisture characterization of hardened cement pastes and concretes from water vapour sorption measurements. The modelling of microstructure and its potential for studying transport properties and durability, Kluwer Academic Publishers.

Baroghel-Bouny V.,M. Mainguy,T. Lassabatere and O. Coussy (1999). "Characterization and identification of equilibrium and transfer moisture properties for ordinary and high-performance cementitious materials." *Cement and concrete research* 29: 1225-1238.

Björk F.,C. A. Eriksson,S. Karlsson and F. Khabbaz (2003). "Degradation of components in flooring systems in humid and alkaline environments." *Construction and Building Materials* 17(3): 213-221.

Espinosa R. M. and L. Franke (2006). "Influence of the age and drying process on pore structure and sorption isotherms of hardened cement paste." *Cement and Concrete Research* 36(10): 1969-1984.

Espinosa R. M. and L. Franke (2006). "Inkbottle Pore-Method: Prediction of hygroscopic water content in hardened cement paste at variable climatic conditions." *Cement and Concrete Research* 36(10): 1954-1968.

Holm A. H. and H. M. Kuenzel (2002). "Practical application of an uncertainty approach for hygrothermal building simulations-drying of an AAC flat roof." *Building and Environment* 37(8-9): 883-889.

Johannesson B. and M. Janz (2002). "Test of four different experimental methods to determine sorption isotherms." *Journal of Materials in Civil Engineering* 14(6): 471-477.

Nilsson L.-O. (1980). Hygroscopic moisture in concrete - Drying, measurements & related material properties. Division of building materials. Lund, Lund University, Lund Institute of Technology. **Doctoral Dissertation:** 170.

Nilsson L.-O. (2002). "Long-term moisture transport in high performance concrete." *Materials and stuctures* 35: 641-649.

Pasanen A. L.,J. P. Kasanen,S. Rautiala,M. Ikaheimo,J. Rantamaki,H. Kaariainen and P. Kalliokoski (2000). "Fungal growth and survival in building materials under fluctuating moisture and temperature conditions." *International Biodeterioration and Biodegradation* 46(2): 117-127.

Powers T. C. and T. L. Brownyard (1947). "Studies of the physical properties of hardened portland cement paste, Bulletin 22." Res. Lab. of Portland Cement Association, Skokie, IL, U.S.A., reprinted from *Journal of the American Concerete Institute* (Proc.), vol. 43: 101-132, 249-336, 469-504, 549-602, 669-712, 845-880, 933-992.

Sjöberg A. (2001). Secondary emissons from concrete floors with bonded flooring materials - effects of alkaline hydrolysis and stored decomposition products. Department of building materials. Gothenburg, Chalmers University of Technology. **Ph. D-thesis**.

Sjöberg A. and C. Engström (2002). Measurements of stored decomposition products from flooring adhesives in a concrete floor, as a basis for choosing a new floor surface construction. Building Physics 2002 - 6th Nordic Symposium.

Su P. G. and R. J. Wu (2004). "Uncertainty of humidity sensors testing by means of divided-flow generator." *Measurement* 36(1): 21-27.

Tada S. and K. Watanabe (2005). "Dynamic determination of sorption isotherm of cement based materials." *Cement and concrete research* 35: 2271-2277.

West R. P. and N. Holmes (2005). "Predicting moisture movement during the drying of concrete floors using finite elements." *Construction and building materials* 19: 674-681.

Åhs M. (2005). Remote monitoring and logging of relative humidity in concrete. *Proceedings of the 7th symposium on building physics in the Nordic countries Reykjavik*, Iceland, The Icelandic building research institute.

Åhs M. (2007). Moisture Redistribution in Screeded Concrete Slabs. Div. of Building Materials Lund, Lund University, Lund Institute of Technology. **Licentiate in Engineering:** 54.

Åhs M. (2007). "Sorption scanning curves for hardened cementitious materials." *Construction and building materials* doi:10.1016/j.conbuildmat.2007.08.009.

Evidence on dynamic effects in the water content – water potential relation of building materials

Gregor A. Scheffler, Dr, post-doc
Danish Technical University
grs@byg.dtu.dk

Rudolf Plagge, Dr, Head of Laboratory.
Dresden University of Technolog
rudolf.plagge@tu-dresden.de

KEYWORDS: *heat and moisture transport, material modelling, hysteresis, moisture dynamics*

SUMMARY

Hygrothermal simulation has become a widely applied tool for the design and assessment of building structures under possible indoor and outdoor climatic conditions. One of the most important prerequisites of such simulations is reliable material data. Different approaches exist here to derive the required material functions, i.e. the moisture storage characteristic and the liquid water conductivity, from measured basic properties. The current state of the art in material modelling as well as the corresponding transport theory implies that the moisture transport function is unique and that the moisture storage characteristic is process dependent with varying significance for the numerical simulation.

On the basis of different building materials, a comprehensive instantaneous profile measurement study has been accomplished. Profiles of water content and relative humidity were obtained during a series of adsorption and desorption processes. The data provides clear evidence that the water content – water potential relationship is not only dependent on the process history, but also on the process dynamics. The higher moisture potential gradients were induced, the larger was the deviation between static and dynamic moisture storage data and the more pronounced was the corresponding dynamic hysteresis.

The paper thus provides clear experimental evidence on dynamic effects in the water content – water potential relation of building materials. By that, data published by previous authors as Topp et al. (1967), Smiles et al. (1971) and Plagge et al. (1999) is confirmed. Moreover, it is shown that moisture transport processes are well susceptible to dynamic effects already within the hygroscopic moisture content range.

1. Introduction

Hygrothermal material data often plays a key role in numerical simulation. Numerous attempts have been undertaken in the past to characterize and verify material properties, usually by determining the storage and transport properties individually and using different methods. Since it is very difficult, time-consuming and tedious to measure these properties, great effort has been made to develop appropriate laboratory methods. Reviews have been presented by Hillel (1980) and Klute & Dirksen (1986), while a more recent discussion of the respective advantages and setbacks of the various laboratory methods available has been worked out by Plagge (1991) and Scheffler (2008).

The research reported in this paper is based on dynamic adsorption and desorption experiments, measuring moisture content and moisture potential simultaneously at different sampling positions versus time. Evaluation of the measured data alone and in combination with numerical modelling of the experiments comparing measured and calculated results delivers information about the influence of different effects such as hysteresis of moisture storage or the process dynamics. This can be used to verify limits of employed simplified material models, which are commonly based on measured data from steady-state experiments. Moreover, the applied method supports a physical understanding of transport processes and opens possibilities to develop new physical models and evaluate numerical transport models in describing the moisture behaviour of capillary porous materials. Within this paper, this is to be shown on the basis of multiple experimental runs with two building materials.

2. Material and method

For the investigation reported here, the instantaneous profile measurement technique (IPM) was applied. First, the method is introduced for the hygroscopic and the overhygroscopic moisture range whereas an overview about the examined materials is given subsequently.

2.1 Measurement method

The basic idea of the IPM method is the use of the same material specimen in a series of experiments, where different flow regimes can be achieved by controlling the initial and boundary conditions. The development of the time domain reflectometry (TDR) as an accurate non-destructive laboratory method opens the possibility to determine the water content in a high temporal resolution. Therefore, a major effort has been undertaken to incorporate the TDR technique with miniaturized probes having 0.8 mm diameter rods, (Malicki et al. 1992) as a basic tool of the IPM method. Miniaturized relative humidity sensors of 5 mm sensor diameter are used for the determination of the water potential in the hygroscopic moisture range.

The experimental set-up consists of a material specimen with dimensions of 100x100x50 mm³. The vertical measuring sampler is provided with five pairs of holes, into which guide nuts are screwed prior to drill holes and to insert the specially designed sensors. The material sample is sealed at all but one sides and equipped by TDR-probes and relative humidity sensors, aligned at equal distances of 20 mm along the 100 mm long vertical container. For the hygroscopic measurements, the specimen is connected with its unsealed side to the open top of a desiccator in which the relative humidity is controlled. For the overhygroscopic experiments the sample container is placed into water for water uptake, sealed for equilibration or exposed to a constant air flow for drying. Figure 1 illustrates these setups.

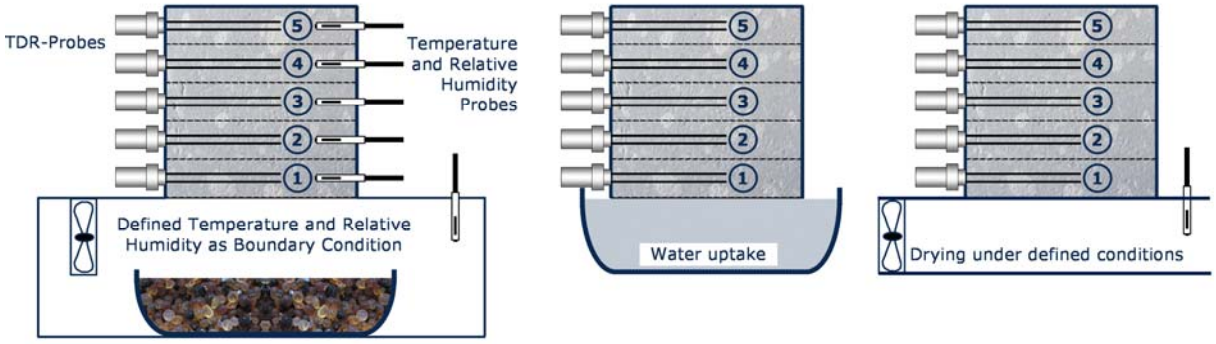

FIG. 1: Setup of the instantaneous profile method for the hygroscopic moisture region (left) and the overhygroscopic moisture region (middle and right).

To monitor, control and register material moisture content and water potential, a computer-aided automatic data acquisition system is used. Further information concerning the sensors in use, their calibration and additional experimental details are given by Plagge et al. 1990, Plagge 1991, Plagge et al. 1999, and Scheffler (2008).

2.2 Experimental set-up and investigated materials

The material is sampled, sealed and prepared for sensor installation. The material sample is equipped with 5 miniaturized TDR probes. For the first experimental run, 5 relative humidity sensors are also installed into the sample container. The sampling container is fixed upon the miniaturized climatic chamber box, where a small ventilator is used to mix the air volume below the specimen. The relative humidity is controlled by a vessel of silica gel as a drying agent or by aqueous salt solutions adjusting defined relative humidities. The whole setup is placed into a climatic chamber ensuring accurate temperature control. During the experimental run, the vessel can be removed to measure the increase or decrease of water in time. Water content and relative humidity within the sample and relative humidity and temperature in the chamber are continuously monitored and registered by the computer-controlled data acquisition system. Different measurement steps have been carried out to cover the whole hygroscopic moisture range. A list of the steps evaluated and discussed here can be found in Table 1.

TAB. 1: Measurement steps in the hygroscopic (left) and the overhygroscopic moisture range (right).

Step Name	*Relative Humidity*	*Duration*
… previous hygroscopic ad- and desorption runs		
large step adsorption	*32.9% to 97.4 %*	*35 days*
large step desorption	*97.4% to 32.9 %*	*35 days*
further experimental runs …		

For the overhygroscopic experiments, the relative humidity sensors are removed and the holes are sealed. Different experiments with changing boundary conditions are performed where phases of water contact, equilibration and drying are combined. A list of the experimental run treated here is given in Table 2.

TAB. 2: Measurement steps in the overhygroscopic moisture range.

Step Name	*Boundary Condition*	*Duration*
… previous overhygroscopic ad- and desorption runs		
Phase 4	*Water contact*	*20 min*
	No boundary condition	*14 days*
Phase 5	*Drying*	*35 days*

The investigation was done for two different materials, a brick and an insulation material. The brick is a typical burnt brick from Northern Germany. The insulation material is calcium silicate which is highly capillary active and typically applied as inside insulation material. The hydro-physical properties of both materials were investigated at the laboratory of the Institute of Building Climatology at Dresden University of Technology. A list of typical basic material properties is given in Table 3 and the adsorption and desorption moisture storage functions in Figure 2 for both materials.

TAB. 3: Basic material properties of calcium silicate and brick

Material property	*Calcium silicate*	*Brick*
Bulk density in [kg/m³]	270	1790
Porosity in [m³/m³]	0.91	0.35
Thermal conductivity in [W/mK]	0.069	0.87
Vapour diffusion resistance in [---]	4	14
Water uptake coefficient in [kg/m²√s]	1.11	0.23

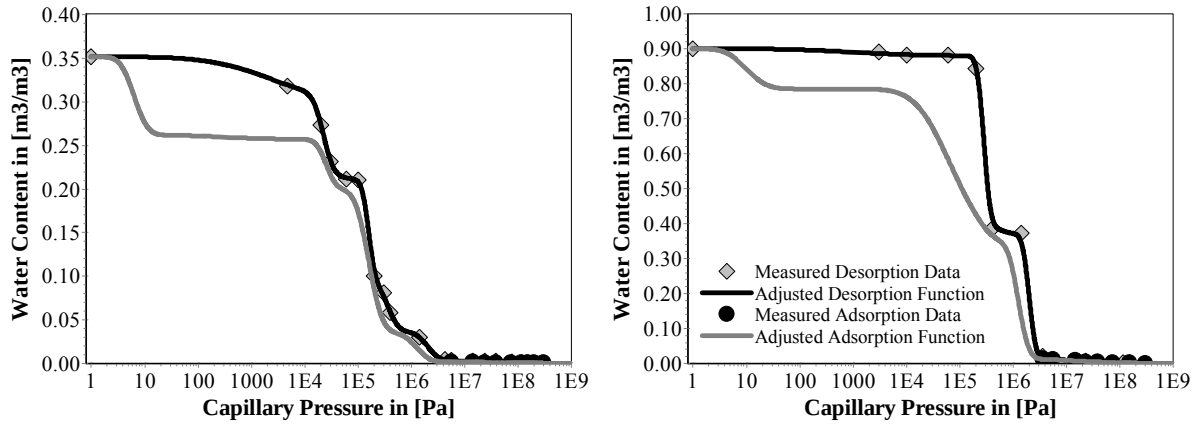

FIG. 2: Adsorption and desorption moisture storage characteristic for the building brick (left) and for the calcium silicate (right).

3. Experimental results

Out of the number of experiments which has been carried out, for each moisture range two significant experimental runs were selected to be shown and discussed here. For the hygroscopic moisture range, the calcium silicate material with large step adsorption and large step desorption (Table 1) has been chosen. For the overhygroscopic moisture range, the brick with phase 4 and phase 5 (Table 2) has been selected.

3.1 Hygroscopic moisture range

The boundary condition at the bottom of the calcium silicate material specimen is changed from 32.9% to 97.4% relative humidity using a saturated K_2SO_4 solution. During the experiment, temperature and relative humidity are measured by thermocouple sensors at 5 positions inside the material specimen (Figure 1). At the same positions, the water content is measured by TDR sensors delivering a set of moisture-content and moisture-potential profiles versus time. These profiles are evaluated as a dynamic sorption isotherm shown in Figure 3.

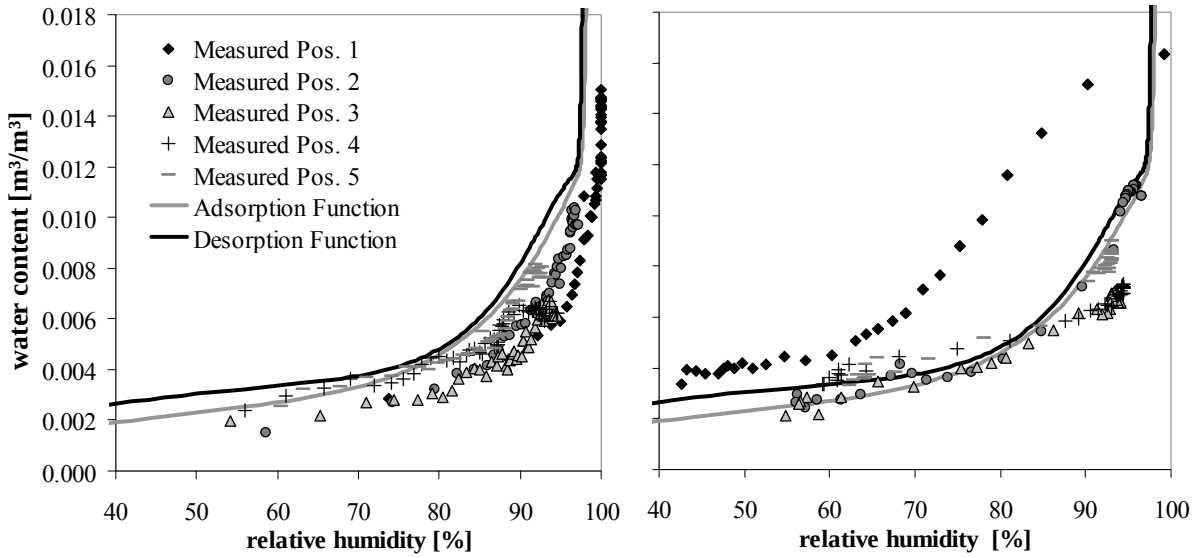

FIG. 3: Comparison of static and dynamic ad- and desorption isotherms for calcium silicate: large step adsorption at the left and large step desorption at the right.

Due to the general chronology of boundary conditions, the experiment did not start with equalized conditions but with the hygrothermal stage reached before. The two continuous lines in Figure 3 represent the functions of the adsorption and the desorption isotherm (as already shown in Figure 2). The data points mark the dynamic sorption isotherms for each position during the adsorption. Position 1 is at the bottom of the specimen which was exposed to the boundary conditions, position 5 is at the top of the specimen which was sealed. During the adsorption process, the dynamic sorption isotherm moves in direction of higher relative humidities (i.e., lower capillary pressures). At position 1, where the largest gradient in moisture potential occurs, this is most pronounced. However, all positions of the calcium silicate specimen show this behaviour (Figure 3 left).

Subsequent to the large step adsorption, the large step desorption is run. The boundary condition is changed from 97.4% to 32.9% relative humidity using a saturated $MgCl_2$ solution. The other conditions are the same as before. In Figure 3 at the left, the results of this experiment are displayed as a dynamic sorption isotherm for each measurement position. This dynamic sorption isotherm does again not follow the course of the static curve. The relation of moisture content and relative humidity becomes somehow shifted as higher values of moisture content correspond to lower values of relative humidity. The influence is most pronounced for position 1 although for the other positions, the same behaviour can be noticed.

3.2 Overhygroscopic moisture range

For the overhygroscopic moisture range, the experiments of phase 4 and phase 5 for the brick have been selected. Due to unavailability of an appropriate measurement method, the moisture potential could not be monitored in this moisture range. However, meaningful results could still be achieved which is shown in Figures 4 and 5. There, a comparison of measured and calculated moisture content profiles is shown. For numerical simulation, the program DELPHIN was used according to Grunewald (1997) and Nicolai (2006). The applied material functions were determined according to Scheffler (2008) distinguishing between ad- and desorption.

Figure 4 shows the water content profile versus time of phase 4 (Table 2). This is the second water uptake after a first one and an equilibration time of 14 days which is followed by another time of equilibration with a duration of 14 days. Due to the fast equilibration, only the first two days are displayed here.

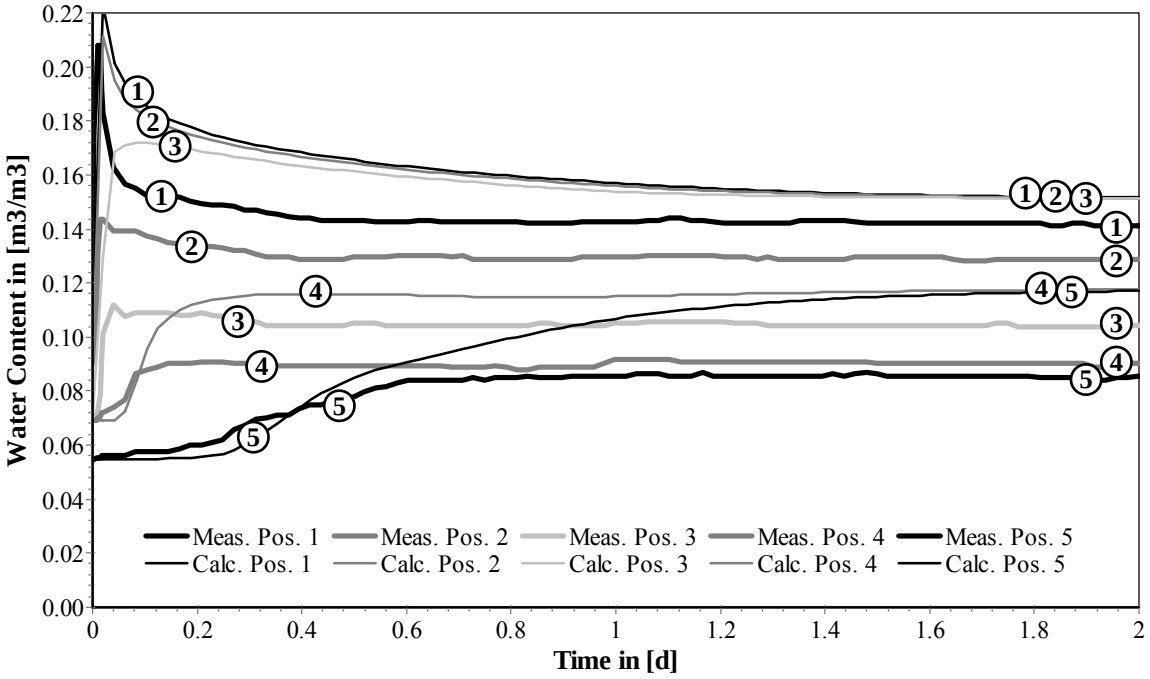

FIG. 4: Comparison of measured and calculated moisture content profiles versus time during water uptake and equilibration of the brick (phase 4 according to Table 2).

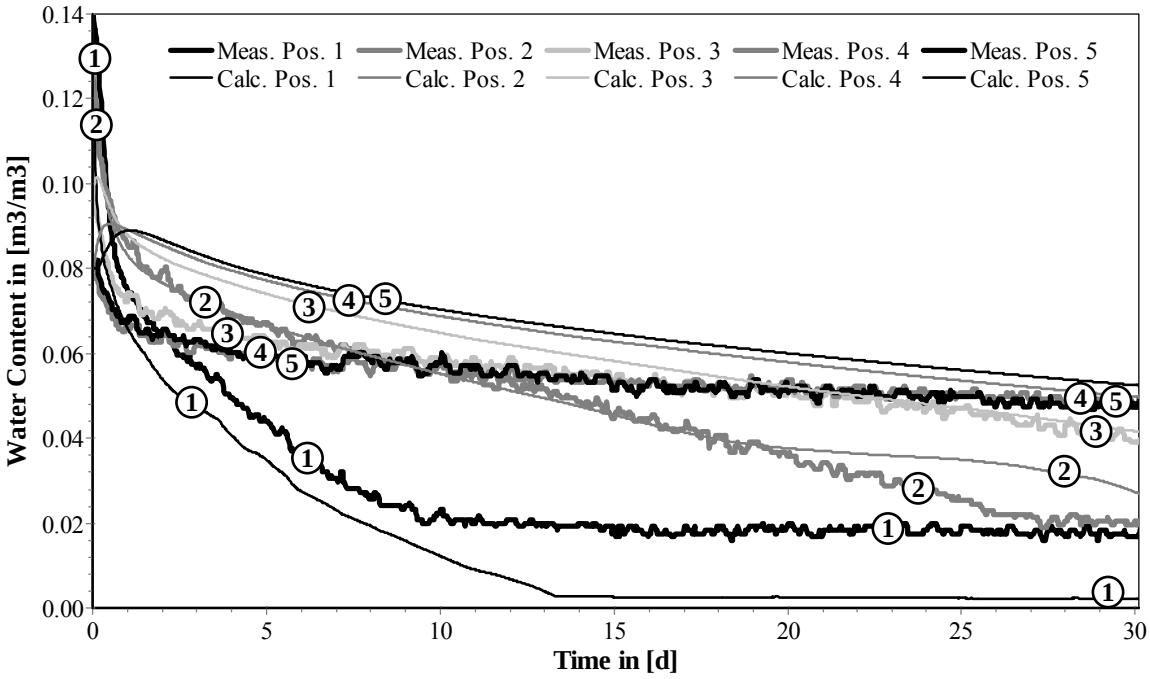

FIG. 5: Comparison of measured and calculated moisture content profiles versus time during drying of the brick (phase 5 according to Table 2)

The calculated data exhibits a quick water uptake leading to higher moisture contents than the measured data. Here, the simulation is done with the adsorption moisture storage function for the whole specimen. For the following equilibration, positions 1, 2 and 3 are calculated applying the desorption moisture storage function

while positions 4 and 5 still use the adsorption function. The results show that the distinct moisture profile, which was measured, could not be reproduced by simulation. Instead, two levels of moisture content emerge belonging to the corresponding moisture potential values of the different moisture storage functions. The simulation leads to a higher moisture level than the measured data reaches. This observation will be discussed in the context of the applied material functions under paragraph 4 Discussion.

Figure 5 shows a comparison of measured and calculated moisture content profiles versus time for the brick drying according to phase 5 (Table 2). The drying is performed in the laboratory with boundary conditions of 20°C and around 60% relative humidity, that are measured and applied during simulation. For calculation, the desorption moisture storage function is used in all positions. The calculated course differs significantly from the measured one. In position 1, the calculated drying is much faster than measured. In contrast to that, the water content of positions 3 to 5 increases at the beginning of the drying experiment. Only position 2 shows a rather good agreement between measured and calculated data.

Another interesting fact to be pointed out is that the measured water content decreases until a certain level (position 1 in Figure 6) which is higher than the equilibrium moisture content according to the boundary conditions. In contrast to that, the calculation dries until the equilibrium moisture content with the boundary conditions is reached. The same kind of behaviour could already be observed during the measurements in the hygroscopic moisture range, see e.g. Figure 2.

4. Discussion

4.1 Results of measurement and simulation

It could be shown, besides others, by Topp et al. (1967), Smiles et al. (1971), Stauffer (1977), Hassanizadeh et al (2002) and Scheffler (2008), that there exists an influence of the dynamics on the relationship between moisture content and moisture potential. However, this influence could mostly be proved for desorption processes only. As shown for the calcium silicate – and although not pictured here, the brick shows the same behaviour – this influence does also exist for the adsorption process. While for desorption processes under large gradients, the moisture content belongs to higher capillary pressures (i.e., lower relative humidities) than the static equilibrium, for an adsorption process, depending again on the moisture potential gradient, the same moisture content belongs to lower capillary pressures (i.e., higher relative humidities), see again Figure 3.

Unfortunately, the measurements within the overhygroscopic moisture range lack data of the moisture potential. Therefore, a dynamic moisture storage function could not be displayed. However, as the purpose of the whole investigation was to receive data for material model validation, numerical simulation could be applied. The employed material model, given in Scheffler (2008), is based on the bundle of tubes model using the moisture storage function to derive the capillary conductivity. This function is further adjusted to data from water uptake and drying experiments according to Plagge et al. (2005) and Scheffler & Plagge (2005). As proven e.g. by Tzimas (1979), the liquid water conductivity in dependence to the moisture content is not hysteretic. Thus, only for the moisture storage function the hysteresis has to be taken into account which was done for the adjustment of the conductivity function.

Figure 6 shows the final result of this calibration procedure. Both experiments are calculated with the same conductivity function, applying the adsorption moisture storage function for the water uptake experiment and the desorption moisture storage function for the drying experiment. Both storage functions are given in Figure 2. The agreement between measured and calculated integral moisture is almost perfect.

However, the comparison of measured and calculated moisture content profiles (Figures 4 and 5) shows significant deviations. One reason for that is the hysteresis of moisture storage. Up to now only the main drying and the main wetting curve can be applied, which does not allow us to follow one of the scanning curves. This becomes clear when looking at the measured moisture profile given in Figure 4 which could not be reproduced by simulation. We use the adsorption moisture storage function in all positions as long as water contact is applied (i.e., during the first 20 minutes). Then the desorption moisture storage function is assigned for the simulation of positions 1 to 3 whereas the adsorption function is used for positions 4 and 5. As a consequence, only two and not – as measured – five moisture levels are reached according to the equilibrium moisture content of either the adsorption or the desorption characteristic. Thus, the hysteresis in the moisture storage function is responsible for the developing steady-state moisture profiles.

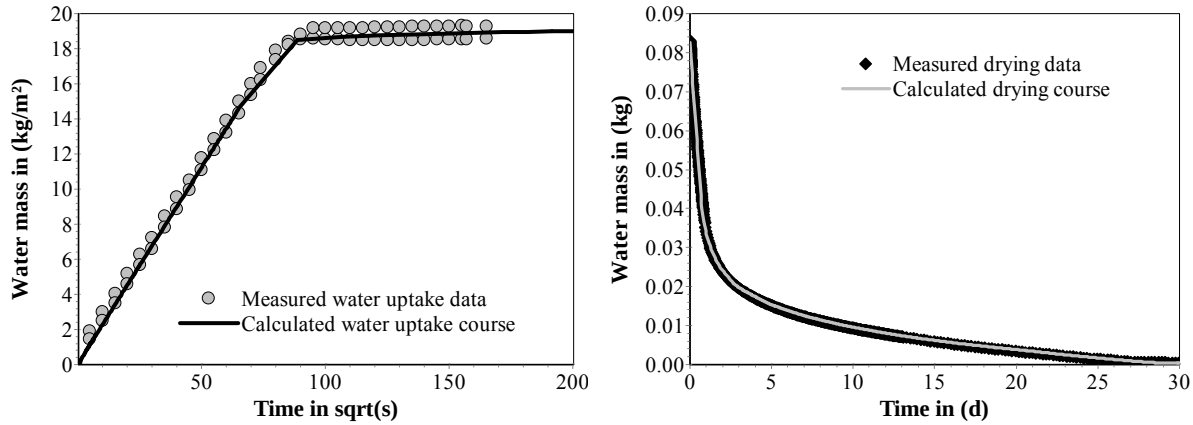

FIG. 6: Calibration of the liquid water conductivity for the brick – comparison of measured and calculated material behaviour, water uptake at the left and drying at the right

This, however, does not explain the generally higher moisture level of the simulation results. From the authors' point of view, this can only be explained with the influence of the process dynamics on the relation of moisture content and moisture potential, which is also not included within simulation. During adsorption processes under large gradients, the moisture potential quickly moves to lower capillary pressures (i.e., higher relative humidities) for the same moisture content compared with the static case. The simulations are carried out with a static adsorption moisture storage function which does not necessarily represent the states developing under the transient conditions of the experiment.

The liquid water flow is dependent on the liquid water conductivity and on the moisture potential gradient. As the moisture-content – moisture-potential relation is influenced by the process dynamics, this also influences the moisture potential gradient. In the case of an adsorption process, the corresponding capillary pressures will be lower than those of the static case. Since the capillary pressure is a logarithmic variable, this leads to moisture potential gradients which can differ by an order of magnitude for the static and the dynamic case. The higher moisture contents occurring in the simulation are thus attributed to the higher transport rates resulting from higher moisture potential gradients during the water uptake. Due to the dynamic effects, the corresponding potential gradients are lower during the actual measurements than during the simulation. In the simulation, the dynamic effects are not taken into account leading to an overestimation of the moisture transport rates.

4.2 Investigation of moisture transport phenomena in porous media

It was the original purpose of the reported investigations, to use the acquired data to quantify options and limits of hygrothermal material models. A number of simplifying assumptions are made during the modelling of hygrothermal processes. To identify the consequences of these assumptions the data obtained by the IPM technology is very suitable. Thus, a hygrothermal material model validation is proposed on the basis of this data (Scheffler, 2008). Associated with that, both, the measurement data and the comparison with numerical simulation results may lead to a further understanding of the observed phenomena. The hysteresis of moisture storage has been subject to research and modelling for more than 50 years but still most Building Physical simulation models do not include it. The obtained data is very suitable to further understand these phenomena and help to verify hysteresis models for building materials. Moreover, new models regarding the influence of both, hysteresis of moisture storage and the process dynamics, as proposed by Beliaev & Hassanizadeh (2001), gain an experimental basis. A model verification could be done with the aid of this data.

5. Summary and conclusions

A new application of the instantaneous profile measurement technique is shown for two materials, a brick and a calcium silicate insulation. With these measurements, a great deal of information concerning hygric material behaviour under dynamic conditions could be obtained, especially when the moisture potential was also measured, as done in the hygroscopic moisture range. In the hygroscopic moisture range, dynamic moisture storage functions have been derived from the measured data showing a clear change in the moisture-content – moisture-potential relation compared to static data. For the wet moisture region, the influence of hysteresis as well as the process dynamics has been shown using numerical simulation to reproduce the measured data.

The data can be further used for material model validation to quantify potential errors the implied model assumptions might cause. Furthermore, new approaches trying to include the hysteresis of moisture storage or the influence of the process dynamics can be verified. Only few data is currently available to show these influences, making the instantaneous profile measurement technology a very promising and innovative measurement method for further applications.

6. References

Beliaev A.Y. and Hassanizadeh S.M. (2001). A theoretical model of hysteresis and dynamic effects in the capillary relation for two-phase flow in porous media. *Transport in Porous Media* 43: 487-510.

Grunewald J. (1997). Diffusiver und konvektiver Stoff- und Energietransport in kapillarporösen Baustoffen. *PhD thesis at Dresden University of Technology, Institute of Building Climatology.*

Hassanizadeh S.M., Celia M.A. and Dahle H.K. (2002). Dynamic effect in the capillary pressure-saturation relationship and its impacts on unsaturated flow. *Vadose Zone Journal* 1: 38-57.

Hillel D. (1980). Fundamentals of soil physics. *Academic Press. New York*, p. 212-214.

Klute A. and Dirksen C. (1986). Hydraulic conductivity and diffusivity laboratory methods. In: Klute, A. (ed.). *Methods of soil analysis. Part I. Physical and mineralogical methods.* 2nd edition, No.9, Agronomy Series, Am. Soc. Agron., Soil Sci. Soc. Am. Madison. p. 687-734.

Malicki M.A., Plagge R., Renger M. and Walczak R.T. (1992). Application of time-domain reflectometry (TDR) soil moisture miniprobe for the determination of unsaturated soil water characteristics from undisturbed soil cores. *Irrigation Sci.* 1992, 13, 65-72.

Nicolai A. (2006). Delphin 5 - Coupled heat, air, moisture, pollutant and salt simulation software, http://www.bauklimatik-dresden.de/delphin5

Plagge R., Renger M. and Roth C.H. (1990). A new laboratory method to quickly determine the hydraulic conductivity of unsaturated soil within a wide range of textures. *Z. Pflanzenernähr. Bodenk.*, 153, 39-45.

Plagge R. (1991). Bestimmung der ungesättigten hydraulischen Leitfähigkeit im Boden. *PhD thesis at Technical University Berlin. Bodenökologie und Bodengenese*, Heft 3, pp 151.

Plagge R., Häupl P. and Renger M. (1999). Transient effects on the hydraulic properties of porous media. *Proceedings of the International Workshop on Characterization and Measurement of the Hydraulic Properties of Unsaturated Porous Media*, Riverside, California, 1999, edited by M. Th. van Genuchten et al., p. 905–912.

Plagge R., Scheffler G. and Grunewald J. (2005). Automatic measurement of water uptake coefficient of building materials. *Proceedings of the 7th Symposium on Building Physics in the Nordic Countries*, Reykjavik June 2005.

Scheffler G. and Plagge R. (2005). Defined drying behaviour measurement for building materials. *Proceedings of the 7th Symposium on Building Physics in the Nordic Countries*, Reykjavik June 2005.

Scheffler G.A. (2008). Validation of hygrothermal material modelling under consideration of the hysteresis of moisture storage. *PhD thesis at Dresden University of Technology, Institute of Building Climatology.*

Smiles D.E., Vauchaud G. and Vauclin M. (1971). A test of the uniqueness of soil moisture characteristic during transient, nonhysteretic flow of water in a rigid soil. *Soil Sci. Soc. Amer. Proc.*, Vol. 35: 534-539.

Stauffer F. (1977). Einfluss der kapillaren Zone auf instationäre Drainagevorgange. *Ph.D. thesis at ETH Zurich, Diss. ETH Nr. 5931.*

Topp G.C., Klute A. and Peters D.B. (1967). Comparison of water content-pressure head data obtained by equilibrium, steady-state, and unsteady-state methods. *Soil Sci. Soc. Amer. Proc.*, Vol. 31: 312-314.

Tzimas E. (1979). The measurement of soil-water hysteretic relationships on a soil monolith. *Journal of Soil Science*, 30, 529-534.

Acknowledgments: The work reported here was carried out at the Institute of Building Climatology at Dresden University of Technology as part of a PhD project which was funded by the German national foundation CUSANUSWERK (www.cusanuswerk.de). In addition, the authors wish to thank Frank Meissner for his assistance in the lab.

Humidity Migration and Condensation Risk in Autoclaved Aerated Concrete Walls

Anatolijs Borodiņecs, Dr.sc.ing;
Riga Technical university, Institute of Heat, Gas and Water Technology;
anatolijs.borodinecs@rtu.lv;

Andris Krelsins, Dr.hab. sc. ing. Prof.;
Riga Technical university, Institute of Heat, Gas and Water Technology;
kreslins@bf.rtu.lv;

Martins Vilnitis, M.sc.ing;
Riga Technical university, The Institute of Building Production;
martins.vilnitis@inbox.lv;

Juris Noviks, Dr.hab. sc. ing. Prof.;
Riga Technical university, The Institute of Building Production.

KEYWORDS: humidity migration, autoclaved aerated concrete

SUMMARY:
The paper is devoted to the analysis of problems of humidity migration in autoclaved aerated concrete walls. It presents the methods for monitoring of humidity migration processes. Especial attention is paid to the analysis of condensation risk on the surface between the autoclaved aerated concrete block and outdoor finishing. The paper gives theoretical calculation of condensation risk in autoclaved aerated concrete wall as well as presents the results of practical measurements. For the purpose of practical measurements, two experimental walls, on the northern and southern part of the building, were built in Tallinn imitating real living space. The analyzed walls had been constructed using autoclaved aerated concrete blocks 375 mm in thickness, volume weight ≤ 400 kg/m^3, glued together with a 2 mm thick layer of glue mortar. Starting from year 2005 the thermal measurements were carried out on the regular basis. The preliminary results of this experiment have shown that monitoring of humidity migration processes in autoclaved aerated concrete walls could be accurately done by cutting out test pieces and putting them on the scales. The influence of thermal qualities of autoclaved aerated concrete wall on the drying process of wall was also studied in the scope of this paper. As the result the dependences between heat conductivity coefficient and moisture content were developed.

1. Humidity evaporation process in autoclaved aerated concrete blocks

The main problem using autoclaved aerated concrete blocks in building construction is high initial moisture content of blocks. The average initial humidity of autoclaved aerated concrete blocks is up to 40% by weight. The optimal humidity of autoclaved aerated concrete blocks level is 4-6%. The evaporation process in newly constructed buildings in Latvian climatic conditions could be problematic due to the high outside air relative humidity. It is estimated that evaporation process could take up to 3 years long time period in order to reach optimal humidity level. The main parameters that could impact drying process are:

- surface finishing;
- outdoor and indoor air parameters;
- properties of additional heat insulation.

In the scope of this study 30 samples of autoclaved aerated concrete blocks were chosen in order to evaluate evaporation process. Analyzed samples were stored in non-heated warehouse. Two samples were artificially dried till optimal humidity level. The average weight of dry sample is 2.4 kg. The evaporation process in autoclaved aerated concrete samples is shown in Figure 1.

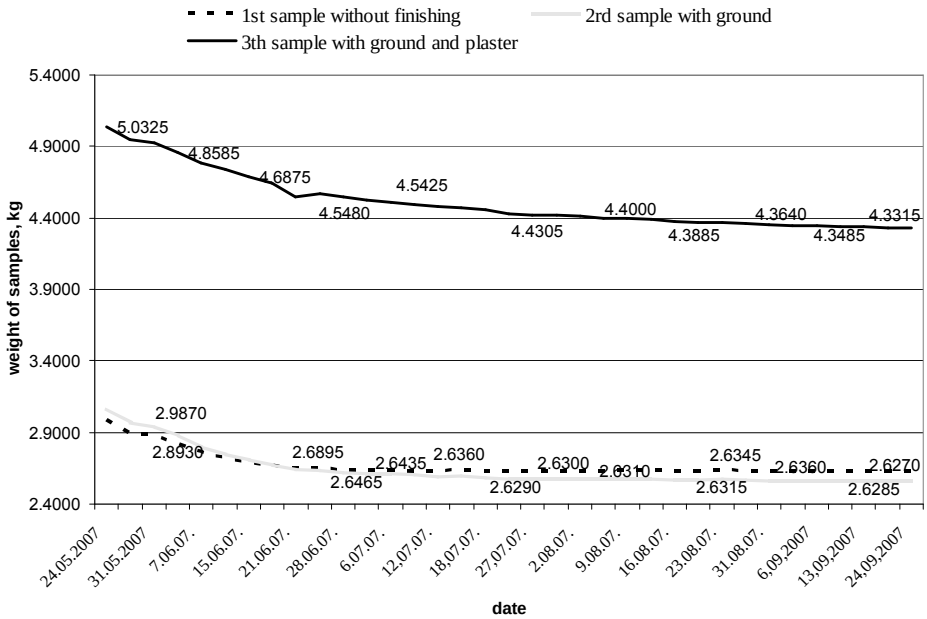

Fig.1. The3-dimensional evaporation process in autoclaved aerated concrete samples

As it could be seen from Figure 1, the most intensive evaporation process was taking place during the time period from May till July, when the average temperature was +14^{O}C. The initial weight of 1st sample was 2.987kg, of 2nd – 3.0605kg and 3rd – 5.0325kg. The average initial moisture content of analyzed samples was 29%. After three month evaporation process the humidity level of analyzed samples had reached for the 1 st sample – 2.610kg (the moisture content – 8%) 2nd – 2.581kg (the moisture content – 7%) and 3rd – 4.252 kg. It could be concluded that the most intensive evaporation process in autoclaved aerated concrete samples takes place during firs two months after their production.

2. The moisture impact on thermal properties of autoclaved aerated concrete blocks

In order to find out the dependences between wall thermal conductivity coefficient and humidity level, the heat flow through two walls was measured. The analyzed walls were constructed in Tallin using the autoclaved aerated concrete blocks with depth 375mm and capacity mass ≤400 kg/m^3. The monitoring of surface temperature and outdoor and indoor air parameters was done as well. Regular measurements were done during the time period from 20.01.2005 till 14.05.2007. The measurements of humidity level in blocs were done by two different methods:

- practically measured moisture content, using special measuring equipment (special meters were placed inside the wall);
- practically measured moisture content done by cutting out small samples from the wall (EN 1353 method [2]).

The practical implementation of both methods has shown that special measuring equipment could be effectively used for the materials with humidity ration up to 10%, but for material with humidity ration higher than 10% it is recommended to use EN 1353 method.
The results of wall surface temperature measurements are shown in Figure.2. Since the temperature fluctuations of inner surface within a year are not observable, only southern and northern wall surface temperature difference is plotted.

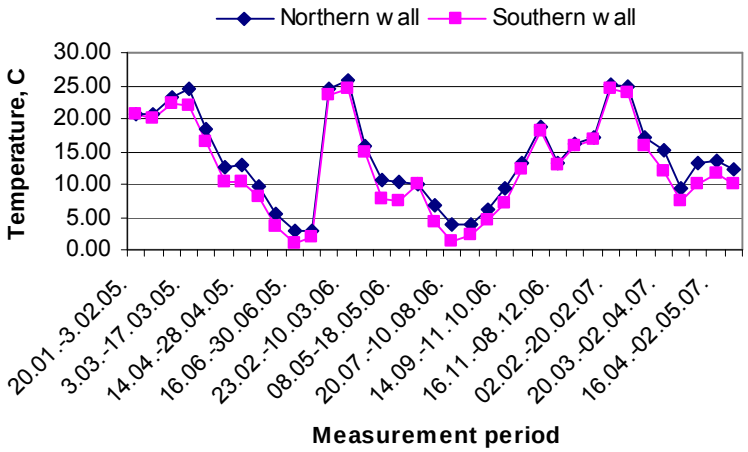

Fig.2. Temperature of external surface of wall

The value of heat transfer coefficient is determined by applying the data, acquired in the experiment, to the Equation 1.

$$U_k = \frac{Q}{t_i - t_e} \text{ W/(m}^2\text{K)} \quad (1)$$

where:
Q – heat flow (W/m^2); τi – surface temperature of inner wall (^{0}C); τe – surface temperature of exterior wall (^{0}C).

Performed heat flow measurements are gathered and displayed in Figure 3. While analyzing the acquired experimental data, it could be calculated that heat flow through wall is directly related to the temperature of external surface of the wall. Temperature fluctuations during the experiment were insignificant, therefore we can deduce that sun activity notably affects the heat flow. As it was mentioned before, the temperature fluctuation of inner surface of the wall is not significant; therefore the wall's external surface temperature difference is largely affected by the solar radiation. It is due to the solar radiation that surface temperature of the external wall depends on and in its turn affects both the process of wall drying and total heat flow through aerocrete wall.

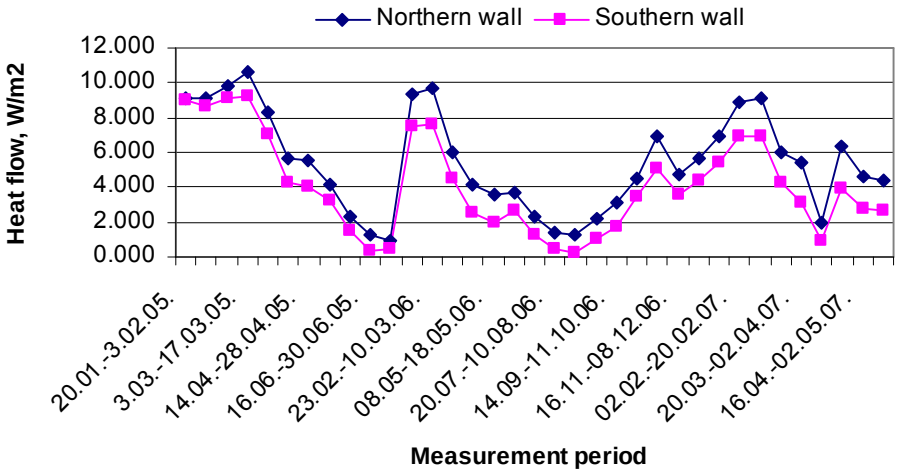

Fig.3. Heat flow through the wall

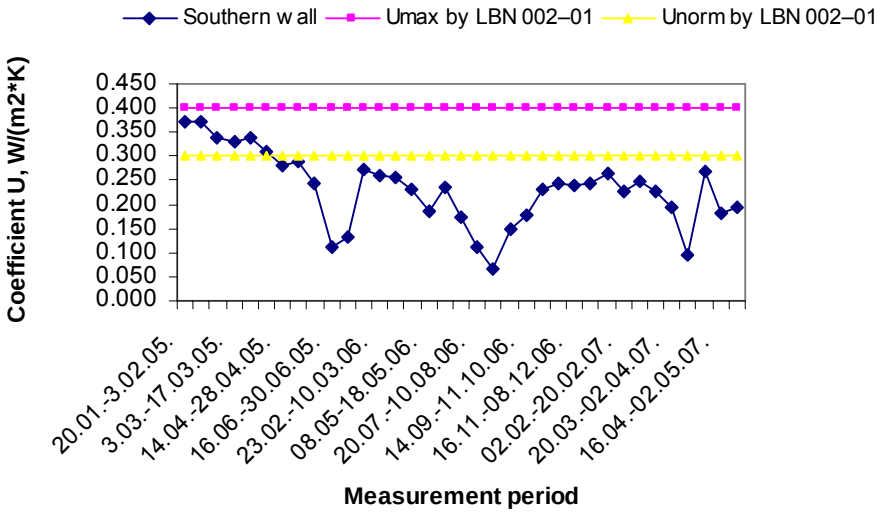

Fig.4 Apparent heat transfer coefficient of the wall

It could be seen from the Figure 4 that in the wintertime conditions the wall's, which is not yet dried and whose moisture is 24-14%, apparent heat transfer coefficient is equal to the Latvian building standard LBN 002 – 01 (1) requirements. According to Latvian building standard normative value of heat transfer coefficients for dwelling buildings is 0.25 W/(m^{2}K) and maximal value is 0.4 W/(m^{2}K). Calculation of the theoretical U value using Equation 2 has shown that heat transfer coefficient of aerated concrete wall with depth 375mm was 0.27 W/(m^{2}K).

$$U = \frac{1}{R_{si} + \frac{d}{l} + R_{Se}} \text{ W/(m}^2\text{K)} \qquad (2)$$

where: Rse – heat resistance of external surface, (m^{2}K) /W, Rse - heat resistance of internal surface,(m^{2}K) /W.

The difference between measured and calculated values can be explained with aerocrete's capacity to accumulate heat and material thermal inertia.

3. Analysis of condensation risk in autoclaved aerated concrete blocks

It is a well known fact that condensation of water vapour occurs when water vapour pressure exceeds saturated water vapour pressure. Usually the water vapour and saturated water vapour distribution is shown graphically. The saturated water vapour pressure depends only on the temperature distribution in the construction. In the wall's construction built from autoclaved aerated concrete blocks glued together without heat insulation these vapour pressure curves do not cross each other. But it should be taken into account that high condensation risk occurs on the surface between the autoclaved aerated concrete block and outdoor finishing in cases, when water vapour resistance factor of finishing is too high.

The theoretical evaluation of condensation risk was done on the example of the wall construction shown in Figure 5. In method traditionally used in Latvia water vapour pressure distribution is shown in the cross section of element drawn proportionally real element thickness d, m.

Water vapour distribution in element is found by Equation 3:

$$p_x = p_i - \frac{R_{tv}}{\sum R_{tv}}(p_i - p_e), \text{ Pa} \qquad (3)$$

where - p_i is water vapour pressure of the inside air, Pa; p_e is water vapour pressure of the outside air, Pa; R_{tv} is the sum of water vapour resistance of all previous layers, $m^2 \cdot h \cdot Pa/m$; ΣR_{tv} is total water vapour resistance of the element, $m^2 \cdot h \cdot Pa/m$.

Water vapour resistance of individual layer (4):

$$R_{tv} = \frac{d}{d}, \text{ m}^2 \cdot \text{h} \cdot \text{Pa/m} \quad (4)$$

where - d is thickness of the layer, m; δ is vapour transfer coefficient (vapour permeability of the material), mg/m·h·Pa.

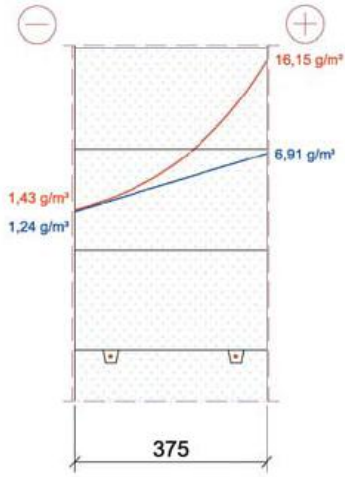

Fig.5. Cross section of element

The thermal conductivity coefficient of aerated concrete blocs with volume weight ≤400 kg/m^3 is 0.1W/(m*K) and vapour transfer coefficient 0.26 mg/m·h·Pa. The heat transfer coefficient of aerated concrete wall is equal to 0.27 W/(m^{2}K). The analysis of condensation risk in autoclaved aerated wall without extra insulation is shown in Table 1.

TABLE. 1: Vapour pressure distribution in aerated concrete wall without insulation

Nr	Layer	d, m	R_{tv}, $m^2 \cdot h \cdot Pa/m$	Inside temperature +20, outside (-20)			Inside temperature +20, outside (-10)		
				t ^OC	P_{sat}, Pa	p_x, Pa	t ^OC	P_{sat}, Pa	p_x, Pa
1	Indoor air			20	2336	1402	20	2336	1402
2	Indoor surface			18.7	2152	1402	19	2197	1402
3	Finishing	0.01	0.10	18.6	2137	1321	18.9	2186	1327
4	Aerated concrete	0.375	1.44	-19.5	108	153	-9.6	268	255
5	Finishing	0.01	0.10	-19.6	106	71	-9.70	266	181
6	Outdoor air			-20	102	71	-10	259	181

As it could be seen from the above mentioned table, vapour condensation occurs, when outside air temperature is -20^{O}C. Although the outside temperature below (-20) ^{O}C vapour condensation occurs for relatively short periods, in time the condensation will lead to the damage of external finishing. The additional calculations have shown that vapour condensation between the aerated concrete blocks and external finishing occurs, when outside air temperature is below -12^{O}C.

In order to find out the influence of additional outside insulation on vapour condensation risk in autoclaved aerated concrete walls, the calculations were done for the stone wool and expanded polystyrene materials (Table 2).

TABLE. 2: Vapour pressure distribution in aerated concrete wall with insulation (inside temperature +20 ^{O}C, outside temperature -20 ^{O}C)

Nr	Layer	d, m	Insulation: stone wool			Insulation: expanded polystyrene		
			R_{tv}, $m^2 \cdot h \cdot Pa/m$	P_{sat}, Pa	p_x, Pa	R_{tv}, $m^2 \cdot h \cdot Pa/m$	P_{sat}, Pa	p_x, Pa
1	Indoor air			2336	1402		2336	1402
2	Indoor surface			2196	1402		2196	1402
3	Finishing	0.01	0.10	2185	1324	0.10	2185	1348
4	Aerated concrete	0.375	1.44	264	204	1.44	264	572
5	Insulation	0.05	0.07	106	149	0.83	106	125
6	Finishing	0.01	0.10	105	71	0.10	105	71
7	Outdoor air			102	71		102	71

It could be seen from Table 2 that high condensation risk occurs between aerated concrete and expanded polystyrene heat insulation. Though use of stone wool prevents condensation on the surface between aerated concrete and insulation layer. In both cases the condensation risk occurs on the surface before external insulation.

4. Conclusions

1. The practical analysis has shown that the most intensive evaporation process in autoclaved aerated concrete samples takes place during first two months after their production. During this time moisture content reduces from 20% till 8%.
2. The practical measurements of moisture content in autoclaved aerated concrete blocks by two different methods have shown that special measuring equipment could be effectively used for the materials with humidity ration up to 10%, while for materials with humidity ration higher than 10% it is recommended to use EN 1353 method.
3. The results of measurement of heat flow through the autoclaved aerated concrete wall have shown that there are interdependence between the thermal conductivity coefficient, wall's external surface temperature and heat flow through aerocrete wall. In the wintertime conditions the aerocrete wall's, which is not yet dried and whose moisture decreased from 24% to 14%, coefficient U value corresponds to the standard LBN 002 – 01 requirements. Difference in the results of theoretical calculation of U value and experimental results could be explained by aerocrete's capacity to accumulate heat and material's thermal inertia.
4. Analysis of condensation risk in autoclaved aerated concrete blocks has shown that vapour condensation occurs, when outside air temperature is -20^{O}C. Although the outside temperature below (-20) ^{O}C occurs for relatively short periods, in time the condensation will lead to the damage of external finishing. The additional calculations have shown that vapour condensation between the aerated concrete blocks and external finishing occurs, when outside air temperature is below -12^{O}C.
5. In case when autoclaved aerated concrete blocks have additional external insulation, vapour condensation occurs between aerated concrete and expanded polystyrene heat insulation. Though use of stone wool heat insulation prevents condensation on the surface between aerated concrete and insulation layer. In both cases the condensation risk occurs on the surface before external insulation.

„This work has been partly supported by the European Social Fund within the National Programme „Support for the carrying out doctoral study programm's and post-doctoral researches" project „Support for the development of doctoral studies at Riga Technical University".

5. References

1. Latvian Building Code LBN 002-01 "Thermal Performance of Building Envelope", Riga, 2001.
2. BS EN 1353:1997. Determination of moisture content of autoclaved aerated concrete.1997.-10p.
3. Fokin K. F., Tabunsikov J.A., Gagarin V.G. Heat transfer of building envelope. 5th edition. – Moscow: ABOK-PRESS, 2006.- 256p. (ФокинК.Ф., Табунщиков Ю.А., Гагарин В.Г. Строительная теплотехника ограждающих частей зданий. Изд. 5-е. - Москва: Авок-Пресс, 2006. – 256 с.)

Mechanical, hygric and thermal properties of gypsum produced from different raw materials

Pavel Tesárek, Ph. D.,
Department of Materials Engineering and Chemistry, Faculty of Civil Engineering, Czech Technical University in Prague
tesarek@fsv.cvut.cz

Robert Černý, Professor,
Department of Materials Engineering and Chemistry, Faculty of Civil Engineering, Czech Technical University in Prague
cernyr@fsv.cvut.cz

KEYWORDS: gypsum, mechanical properties, hygric properties, thermal properties.

SUMMARY: Measurements of basic physical, mechanical, hygric and thermal parameters of calcined gypsum produced using three different raw materials are presented in the paper. Bulk density, matrix density, open porosity, water absorption coefficient, apparent moisture diffusivity, water vapor diffusion resistance factor, thermal diffusivity, thermal conductivity, volumetric heat capacity, bending and compressive strength are determined and compared for the three studied materials. The best results are achieved using the flue gas desulphurization gypsum as raw material which is probably due to its very high content of calcium sulphate and its better workability.

1. Introduction

Gypsum is a historical binder that was used already several thousands years ago. Nowadays, gypsum is produced from various raw materials. The natural gypsum as a source for calcined gypsum production is not prevailing any more and new sources appear mostly as secondary raw materials. Flue gas desulphurization (FGD) gypsum as waste material from thermal power plants and chemo-gypsum as waste material from production of phosphoric acid, hydrofluoric acid, citric acid and boric acid are the most typical representatives of these sources.

Calcined gypsum ($CaSO_4 \cdot 1/2H_2O$) can be produced from raw gypsum ($CaSO_4 \cdot 2H_2O$) by its dehydration at the temperatures of 110 to 150°C. The solid structure of calcined gypsum is created by reverse hydration when gypsum $CaSO_4 \cdot 2H_2O$ is formed again (Wirsching, 1984). However, the utilization of waste gypsum as raw material is still insufficient considering the amount of its production. This is particularly true for FGD gypsum. Calcined gypsum is produced from FGD gypsum only in one power station in Czech Republic (Počerady), the remaining production ends with gypsum that is used only partially as additive retarding the setting of cement or for the production of gypsum plasterboards. That part of produced gypsum, which is not utilized, is deposited as waste.

Due to the very low price and large availability of FGD gypsum, the material has a good potential for applications in building structures, possibly also as a material of load-bearing structures. Solubility of gypsum is 0.256 g in 100 g of water at 20°C. Therefore, in the raw state it cannot be utilized in exterior applications as the rain water could dissolve just the product that should safeguard the mechanical properties of the material. Modifications of gypsum aimed at the protection against water are then necessary. Possibilities of such modifications are basically two. The first one is using a hydrophobization admixture in the course of sample production. The second one is impregnation of specimen surfaces.

Very few information about material properties of gypsum products was published until now. Basic mechanical properties of calcined gypsum (compressive strength, tensile and flexural strength, Young's modulus, Poisson constant) are relatively well known, see, e.g. Klein and Ruffer (1997), Singh and Garg (1997), Tazawa (1998). Thermal properties of calcined gypsum (thermal conductivity, specific heat, thermal diffusivity) were

determined for instance in Danten et al. (1984), Mehaffey (1994) and Hanush (1974). Among the hydric properties of calcined gypsum, Hanusch (1997) introduced the water vapor diffusion resistance factor, Dahl et al. (1996) measured sorption and desorption isotherms, Lucas (1997) the sorptivity. However, the data sets presented by various investigators for different types of calcined gypsum are always incomplete so that their applicability is limited. Complete sets of thermal, hygric and mechanical parameters of practically any type of non-modified and modified gypsum are not available and without their knowledge it is impossible to perform any serious mechanical or hygrothermal analysis of building elements based on these materials. So, determination of a complete set of these parameters is still a very actual problem.

In this paper, measurements of basic physical, mechanical, hygric and thermal parameters of calcined gypsum produced using three different raw materials are presented.

2. Experimental methods

2.1 Bending and compressive strength

The measurement of bending strength was performed according to the Czech standard ČSN 72 2301 (1979) on the 40 x 40 x 160 mm prisms. The specimens were demolded 15 minutes after the final setting time and stored in the testing room. Every specimen was positioned in such a way that the sides that were horizontal during the preparation were in the vertical position during the test. The experiment was performed as a common three-point bending test using the WPM 50 kN device. The distance of the supporting cylinders was 100 mm. The strength was calculated according to the standard evaluation procedure. The measurements were done for the standard time of 2 hours after mixing and then also for the following other times: 1 day, 3 days, 7 days, 14 days and 28 days.

Compressive strength was determined in accordance with the Czech standard ČSN 72 2301 on the halves of the specimens left over after the bending tests. The specimens were placed between the two plates of the WPM 100 kN device in such a way that their lateral sides adjoining during the preparation to the vertical sides of the molds were in contact with the plates. In this way, the imprecision of the geometry on the upper cut off side was not affecting negatively the experiment. The compressive strength was calculated as the ratio of the ultimate force and the load area.

2.2 Moisture diffusivity

For determination of the apparent moisture diffusivity a common water sorption experiment was carried out. The specimen was water and vapor-proof insulated on four lateral sides and the face side was immersed 2-3 mm in the water. Constant water level in the tank was achieved using a bottle placed upside down. The known water flux into the specimen during the suction process was then employed to the determination of the water absorption coefficient. The samples were tested in constant temperature conditions.

For the calculation of the apparent moisture diffusivity D_w [m^2s^{-1}], the following approximate relation was employed:

$$D_w \approx \left(\frac{A}{w_c} \right)^2 \qquad (1)$$

where A is the water absorption coefficient [$kgm^{-2}s^{1/2}$], and w_c is the saturated moisture content [kgm^{-3}] (Kumaran,1994).

2.3 Water vapor diffusion coefficient

Water vapor diffusion coefficient was measured using standard cup methods (dry and wet). The water vapor diffusion coefficient *D* was calculated from the measured data according to the equation

$$D = \frac{\Delta m \cdot d \cdot R \cdot T}{S \cdot \tau \cdot M \cdot \Delta p_p} \quad (2)$$

where D is the water vapor diffusion coefficient [m^2s^{-1}], Δm the amount of water vapor diffused through the sample [kg], d the sample thickness [m], S the specimen surface being in contact with the water vapor [m^2], τ the period of time corresponding to the transport of mass of water vapor Δm [s], Δp_p the difference between partial water vapor pressure in the air under and above the specimen [Pa], R the universal gas constant [J mol^{-1} K^{-1}], M the molar mass of water [kg mol^{-1}], T the absolute temperature [K].

On the basis of the diffusion coefficient D, the water vapor diffusion resistance factor μ was determined:

$$\mu = \frac{D_a}{D} \quad (3)$$

where D_a is the diffusion coefficient of water vapor in the air [m^2s^{-1}].

In the dry cup method the sealed cup containing silica gel was placed in a controlled climate chamber with 50% relative humidity and weighed periodically. For wet cup method sealed cup containing water was placed in an environment with the temperature about 25°C and relative humidity 50%. The measurements were done at 25°C in a period of two weeks. The steady state values of mass gain or mass loss determined by linear regression for the last five readings were used for the determination of water vapor transfer properties (Roels et al., 2004).

2.4 Thermal conductivity, volumetric heat capacity and thermal diffusivity

Thermal properties were measured using the device ISOMET 2104 (Applied Precision, Ltd., SK). It is a multifunctional instrument for measuring thermal conductivity λ [W $m^{-1}K^{-1}$], volumetric heat capacity $c\rho$ [J m^{-3} K^{-1}] and temperature [°C] of a wide range of materials. The thermal diffusivity a [m^2s^{-1}] is calculated by the device from the formula

$$a = \frac{\lambda}{c \cdot \rho} \quad (3)$$

The measurement is based on the analysis of the temperature response of the analyzed material to heat flow impulses. The heat flow is induced by electrical heating using a resistor heater having a direct thermal contact with the surface of the sample. The measurements were done using surface probes with samples, which were placed at laboratory conditions of 25°C and 50% relative humidity.

3. Materials and samples

Three different gypsum-based materials produced using three different raw materials were investigated. The first one was β-form of calcined gypsum with purity higher than 98% of FGD gypsum, which was produced in the electric power station Pocerady, CZ. This gypsum material we will denote as “Pocerady” in what follows. Other two materials were commercial products of Gypstrend Inc. – Koberice. One of these materials was β-form of calcined gypsum with purity 80-95% and consisted of a blend of natural gypsum and chemo-gypsum. The commercial identification of this material was “Grey gypsum plaster.” It will be further denoted as “Koberice - grey.” The last material was gypsum plaster with commercial identification “White gypsum plaster” which is produced from chemo-gypsum with purity 95 %. We will denote it as “Koberice – white”.

The water/gypsum ratio of different types of studied gypsum materials was chosen as corresponding to the normal consistence according to the Czech standard ČSN 72 2301. The normal consistence was determined using the standard spillage test. Water and gypsum blend was filled up to the brim of a metal cylinder with the diameter 50 mm and length 100 mm. Then the cylinder was elevated up and the spillage was measured (in two

perpendicular directions and averaged out). The standard spillage was considered as 180 mm ± 5 mm in accordance with ČSN 72 2301. The standard-spillage criterion resulted in the following water/gypsum ratios: Pocerady 0.627, Koberice-grey 0.81, Koberice-white 1.0.

For a basic characterization, the classification of the three studied gypsum materials was done using the ČSN 72 2301 standard again. It consisted of three criteria. The first criterion was compressive strength for the time of two hours after mixing. The lowest compressive strength had to correspond to the requirements for the particular classes G-2 to G-25 (12 groups altogether). The second criterion was initial and final setting times using the Vicat device where the classes A to C meant fast, moderate and slow setting. The last criterion was grinding fineness using the 0.2 mm sieve residue where the binder was classified into coarsely, medium and finely milled (classes I to III). The results of the classification are summarized in *TABLE 1*.

TABLE 1: Classification of studied gypsum materials.

	Compressive strength [MPa]	Initial setting time [min]	Final setting time [min]	0.2 mm sieve residue [%]
Pocerady				
Measured values	13.3	9	13	1.79
Limiting values	Minimum 13.0	Earliest time 6	Latest time 30	Maximum 2
Classification	G-13	B		III
Koberice - white				
Measured values	2.1	6.5		1.22
Limiting values	Minimum 2	Earliest time 6	Latest time 30	Maximum 2
Classification	G-2	B		III
Koberice - grey				
Measured values	2.0	7	10	1.93
Limiting values	Minimum 2	Earliest time 6	Latest time 30	Maximum 2
Classification	G-2	B		III

4. Experimental results

Basic properties of the three studied gypsum materials, namely the bulk density, matrix density and open porosity, which were determined by water vacuum saturation method (Roels et al., 2004), are shown in *TABLE 2*. Maximum bulk density and minimum open porosity was observed for the material Pocerady with the lowest water/gypsum ratio.

TABLE 2: Comparison of basic properties of studied materials.

Material	Bulk density [kg m^{-3}]	Matrix density [kg m^{-3}]	Open porosity [m^3 m^{-3}]
Pocerady	1170	1900	0.38
Koberice - white	902	1960	0.54
Koberice - grey	982	2090	0.54

TABLE 3 shows the results of measurements of the water vapor diffusion resistance factor using the dry cup and wet cup methods. The results were similar for all studied materials. Slightly lower values were achieved for the material Pocerady; this corresponded with its lower value of open porosity.

TABLE 3: Water vapor diffusion resistance factor of studied materials.

Material	Water vapor diffusion resistance factor [-]	
	5/50 % RH	95/50 % RH
Pocerady	14	13
Koberice - white	18	16
Koberice - grey	17	18

TABLE 4 shows results of water absorption experiment. For the material Pocerady the water absorption coefficient and apparent moisture diffusivity were significantly lower than for Koberice - white and Koberice - grey. This corresponded once again with the values of basic properties in *TABLE 1* because the lowest water transport parameters were achieved for the material with the lowest value of open porosity. It should be noted in this respect that the two times lower value of apparent moisture diffusivity of the material Pocerady compared to others two materials is very positive from the point of view of the protection of the material against water penetration.

TABLE 4: Water transport properties of studied materials.

Material	Water absorption coefficient [$kgm^{-2}s^{1/2}$]	Apparent moisture diffusivity [m^2s^{-1}]
Pocerady	0.33	6.11 E-7
Koberice - white	0.70	1.63 E-6
Koberice - grey	0.55	1.13 E-6

TABLE 5 shows the basic thermal properties of the studied materials. The thermal conductivity was almost the same for the materials Koberice- white and Koberice – grey. For the material Pocerady it was about 33% higher. Differences in volumetric heat capacity of all materials were low, up to 10%, which was within the error range of the measuring method.

TABLE 5: Thermal properties of studied materials.

The material	Thermal conductivity [$Wm^{-1}K^{-1}$]	Volumetric heat capacity [$Jm^{-3}K^{-1}$]	Thermal diffusivity [m^2s^{-1}]
Pocerady	0.41	1.58 E+6	0.29 E-6
Koberice - white	0.31	1.38 E+6	0.22 E-6
Koberice - grey	0.31	1.53 E+6	0.20 E-6

The dependence of compressive strength and bending strength on time for the first 28 days after mixing is given in *FIG. 1* and *FIG. 2*. We can see that both strengths slightly decreased to approximately 3 days but then they began to increase (for the material Pocerady fast, for the other two slower). The maximum strengths were

achieved after 14 days for Pocerady, for the remaining two materials after 28 days. These changes were apparently related to the change of moisture content in the specimens. So, both compressive strength and bending strength were significantly improved by drying out of the specimens. The results also give evidence that the far best mechanical properties achieved the material Pocerady. Its compressive strength after 28 days was five times higher than for Koberice - grey and seven times higher than for Koberice - white. The bending strength after 28 days was three times higher than for Koberice - white and two times higher than for Koberice – grey.

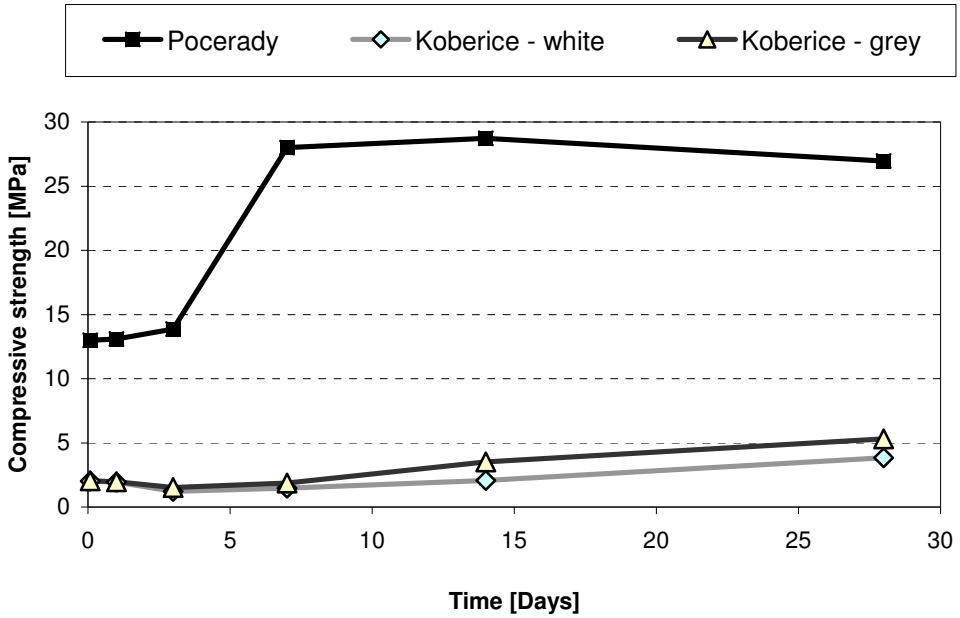

FIG. 1: Compressive strength of studied materials.

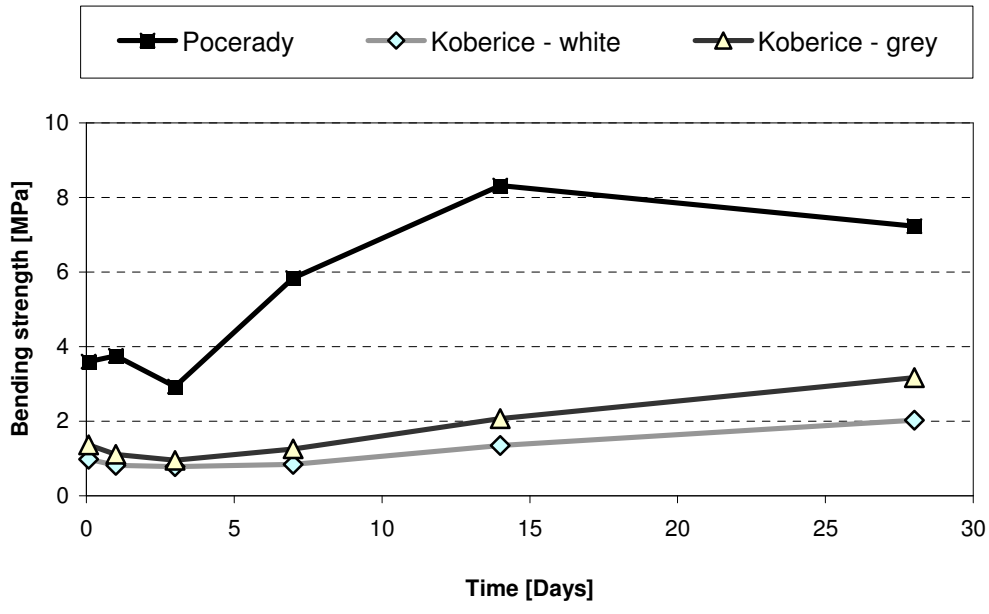

FIG. 2: Bending strength of studied materials.

5. Conclusions

The experimental investigations presented in this paper showed that among the three studied gypsum materials the far best properties were observed for the hardened gypsum produced using FGD gypsum as raw material (denoted as Pocerady throughout the paper). Several times higher strengths and significantly lower water transport parameters in comparison with the two other studied materials produced using chemo-gypsum (Koberice-white) and blend of chemo-gypsum and natural gypsum (Koberice-grey) are sound arguments to prefer this material to the other two.

The most important reason for the better properties of the material Pocerady was probably its very high purity. The worse workability of both Koberice-white and Koberice-grey gypsums leading to higher necessary water/gypsum ratios was the second important parameter in this respect. However, both these factors cannot explain the remarkable improvement of material properties completely. Therefore, complementary investigations are necessary to be done, microstructural studies including exact phase analyses in particular. This will be done in the near future.

6. Acknowledgement

This research has been supported by the Ministry of Industry and Trade of Czech Republic, under grant No FT-TA3/005.

7. References

ČSN 72 2301 (1979). Gypsum binding materials, Czech standard (in Czech), Bureau for Normalization and Measurement, Praha 1979.

Dahl, S.D., Kuehn, T.H., Ramsey, J.W., Yang, C.H. (1996). Moisture Storage and Non-Isothermal Transport Properties of Common Building Materials. HVAC&R Research, Vol. 2, p. 42-58.

Danten, A., Hostache, G., Murat, M., Dicard, L. (1984). Influence of Water Content on the Thermal Diffusivity of Gypsum Plaster. Materials and Structures, Vol. 17, p. 303-306.

Hanusch, H. (1974). Übersicht über Eigenschaften und Anwendung von Gipskartonplatten. Zement-Kalk-Gips, No. 5, p. 245-251.

Klein, D., von Ruffer, C. (1997). Grundlagen zur Herstellung von Formengips. Keramische Zeitschrift, Vol. 49, p. 275-281.

Kumaran M.K. (1994). Moisture Diffusivity of Building Materials from Water Absorption Measurements. IEA Annex 24 Report T3-CA-94/01, Ottawa, p. 230-235.

Lucas, G. (1997). Capillary Conductivity and Body Formation in Moulds of Special Plaster - Results from Laboratory and Practice. Interceram Vol. 46. p. 419-424.

Mehaffey, J.R., Cuerrier, P., Carisse, G.. A Model for Predicting Heat Transfer through Gypsum Board/Wood-Stud Walls Exposed to Fire. Fire and Materials, Vol. 18, p. 297-305.

Roels S., Carmeliet J., Hens H., Adan O., Brocken H., Černý R., Pavlík Z., Hall C., Kumaran K., Pel L., Plagge R. (2004). Interlaboratory Comparison of Hygric Properties of Porous Building Materials. Journal of Thermal Envelope and Building Science, Vol. 27, p. 307-325.

Singh, M., Garg, M. (1997). Retarding Action of Various Chemicals on Setting and Hardening Characteristics of Gypsum Plaster at Different pH. Cement and Concrete Research, Vol. 27, 1997, 947-950.

Sultan, M.A. (1996). Model for Predicting Heat Transfer through Noninsulated Unloaded Steel-Stud Gypsum Board Wall Assemblies Exposed to Fire. Fire Technology, Vol. 32, p. 239-259.

Šatava, V. (1996): Strength and microstructure of cast gypsum. Ceramics - Silikáty, 40, no. 2, p. 72-76.

Tazawa, E. (1998). Effect of Self-Stress on Flexural Strength of Gypsum-Polymer Composites. Advanced Cement Based Materials, Vol. 7, p. 1-7.

Wirsching, F.(1984): Drying and Agglomeration of Flue Gas Gypsum. In The Chemistry and Technology of Gypsum, Philadelphia: American Society for Testing and Materials, p. 161-174.

Hygric and thermal properties of materials used in historical masonry

Milena Pavlíková, Ing., Ph.D.
Department of Materials Engineering and Chemistry, Faculty of Civil Engineering,
Czech Technical University in Prague, Thákurova 7, 166 29 Prague 6, Czech Republic
milena.pavlikova@fsv.cvut.cz, https://tpm.fsv.cvut.cz/

Zbyšek Pavlík. Ing., Ph.D.
Department of Materials Engineering and Chemistry, Faculty of Civil Engineering,
Czech Technical University in Prague, Thákurova 7, 166 29 Prague 6, Czech Republic
pavlikz@fsv.cvut.cz, https://tpm.fsv.cvut.cz/

Robert Černý, Prof., Ing., DrSc.
Department of Materials Engineering and Chemistry, Faculty of Civil Engineering,
Czech Technical University in Prague, Thákurova 7, 166 29 Prague 6, Czech Republic
cernyr@fsv.cvut.cz, https://tpm.fsv.cvut.cz/

KEYWORDS: historical buildings, hygric properties, thermal properties, ceramic brick, sandstone, lime plaster, lime-metakaolin plaster.

SUMMARY:
In the reconstruction works on historical buildings, considerable financial means are spent. Therefore, it is desirable to assess the durability of applied materials in the particular conditions of a specific building. This cannot be done effectively without the knowledge of their hygric and thermal properties which can be used as input parameters of computational models. In this paper, hygric and thermal properties of several types of materials which are used in reconstructions of historical buildings on Czech territory, among them ceramic brick, sandstone, lime plaster, lime-metakaolin plaster, and hydrophobized lime-metakaolin plaster are investigated in the paper. Orientation values of moisture diffusivity are determined by methods utilizing the results of water sorptivity measurements, water vapor diffusion permeability is measured by the cup method. Sorption isotherms are determined by the desiccator method in the range of relative humidity of 11% – 96%. Thermal conductivity is measured in the moisture range from the dry state to full water saturation.

1. Introduction

Understanding the hygrothermal behavior of exposed components and structures of historical buildings represents a first step in avoiding damage or the undue heat loss from constructions. It also creates a basis for constitutive models for porous materials whose time-dependent properties, such as shrinkage, creep, strength etc., are strongly affected by the moisture and temperature fields. Their prediction is a very important task when preserving historical bridges and buildings or insulating existing buildings and components. Charles Bridge in Prague, which is currently subjected to reconstruction works, is a typical example of extensive damage mostly brought about by temperature and moisture impacts.

The damage assessment of historical masonry due to the negative effects of moisture and temperature can be done most effectively by means of mathematical and computational modelling. In this way, the time development of water concentration fields and temperature fields can be obtained which is a crucial for a proper assessment of possible future damage. The water-concentration and temperature values can be then assigned to the mechanical properties and to the risk of consequent damage.

Models for the description of water and water vapor transport can broadly be classified into three main categories, namely convection models, diffusion models and hybrid models [Černý R. and Rovnaníková P. (2002)]. Most of them draw on the assumption of incompressibility of the porous matrix, which is usually sufficient for constructions supposed to normal summer/winter based cycling. On the other hand, it should be noted that this assumption may no longer be valid if common transport processes are accompanied by water-ice

phase change processes, salt crystallization and if the transport phenomena take place at high temperatures. These more complex situations are captured by hygro-thermo-mechanical models.

An extensive historical review on modeling of transport phenomena can be found in [Boer R. (1996)]. A concise introduction to the development of porous media theories is given in [Černý R. and Rovnaníková P. (2002), and Lewis R. W. and Schrefler B. A. (1998)]. In spite of many models based on different principles were proposed, the accuracy and reliability of the obtained data is critically dependent on the availability of all input parameters.

In the modelling of coupled moisture, heat and momentum transport in historical masonry, there are two types of input parameters which have to be known in advance. The first are initial and boundary conditions. Initial conditions can be determined using on site (or subsequent exact laboratory) analysis of water and temperature fields in the historical masonry walls. Boundary conditions are of two types. The first of them are meteorological data for temperatures, relative humidities, rainfall and solar radiation, possibly also concentration of acid-forming gases in the atmosphere. This type of data can be obtained from meteorologists in the form of so-called TRY (Test Reference Year) data which present certain average values over a sufficiently long time period. The second type of boundary conditions involves water content (possibly also salt concentration) in the underground soil close to the studied building. These data can be obtained again by on site analysis.

The second type of input parameters represent water, temperature and mechanical properties which appear in the complex hygro-thermo-mechanical models. These parameters can be determined by common laboratory methods. Samples for the determination of material parameters can be obtained most easily from the walls of the analyzed historical building. If this is not possible, masonry stone samples can be taken from the original quarries which are usually known for a particular building. In case of brick masonry, similar bricks can be found.

In this paper we have focused on the experimental assessment of hygric and thermal properties of several types of materials which are used in reconstructions of historical buildings on Czech territory, among them ceramic brick, sandstone, lime plaster, lime-metakaolin plaster, and hydrophobized lime-metakolin plaster are investigated. In future work the obtained data will be completed with mechanical parameters. The main aim of the presented work is to obtain sufficiently wide set of input data for the computational damage assessment of historical masonry.

2. Experimental Methods

Basic material properties of all tested lime plasters, ceramic brick and sandstone were determined at first. Bulk density and matrix density were measured using gravimetric method and helium pycnometry, and then total open porosity was calculated. The samples for the basic material parameters determination were cut from cubic specimens with the size of 40 x 40 x 40 mm and their dimensions were 40 x 40 x 20 mm.

The thermal conductivity as the main parameter of heat transport was determined using the commercial device ISOMET 2104 (Applied Precision, Ltd.). ISOMET 2104 is a multifunctional instrument for measuring thermo-physical parameters which is based on the application of an impulse technique and is equipped with various types of optional probes. Thermal conductivity was measured in the moisture range from the dry state to full water saturation on the 100 x 100 x 100 mm cubes or on standard-size ceramic bricks.

The cup method was used for determination of water vapour transmission properties. The measurement performed in this work was based on the Czech standard [ČSN 72 7031]. The measurement is carried out in steady state under isothermal conditions. It is based on one-dimensional water vapour diffusion and measuring the water vapour flux through the specimen and partial water vapour pressure in the air under and above specific specimen surface. Water vapour transmission properties of a material are obtained by placing a specimen of the material on the top of a cup and sealing it. We used two versions of the common cup method in the measurements of the water vapour diffusion coefficient. In the first one, the sealed cup containing burnt $CaCl_2$ (0% relative humidity) was placed in a controlled climatic chamber at 25±0.5°C and 45% relative humidity and it was weighed periodically. In the second one, the cup containing saturated K_2SO_4 solution (97% relative humidity) was placed at 25±0.5°C and 45% relative humidity environment. The sample sizes of 95 mm in diameter x 20 mm were cut from the 100 x 100 x 100 mm cubes or from standard-size ceramic bricks and water vapour-proof insulated with epoxy resin. Then, the sealed cups with samples were weighed periodically. The steady state values of mass gain or mass loss were utilized for the determination of the water vapour transfer properties. The diffusion coefficient of water vapour and water vapour diffusion resistance factor were calculated from the measured data.

The liquid water transport parameters measurement was realized using a one-dimensional free imbibition experiment [Roels *et al.* (2004)]. The specimens, sizes of 40 x 40 x 20 mm, were cut from the original cubes and then water and vapour-proof insulated with epoxy resin on four lateral sides. Set up for measuring the water absorption coefficient consisted of tank filled with water, and the specimens were fixed on automatic scales and immersed 1-2 mm in the water. The scales allowed recording the increase of specimen´s mass. The constant water level in tank was achieved by so-called "Marriott's bottle". It was water-filled bottle with two capillary tubes. One of them, inside diameter 2 mm, was ducked under the water level, the second one, inside diameter 5 mm, above water level. If the water level was turned down air bubble went inside the tube and the second tube ejected water amount needed to alignment of water level in tank. The sample mass was measured continuously. The water absorption coefficient of each specimen was calculated from the linear part of the dependence of the increase of tested sample's mass on the square root of time. Then, the apparent moisture diffusivity was calculated using the saturated moisture content and water absorption coefficient [Černý R. et al. (2002)].

In the sorption isotherm measurement, the samples were placed into the desiccators with different salt solutions to simulate different values of relative humidity. The experiment was performed parallel in all desiccators in thermostatic chamber at 25 °C. The mass of samples was measured in specified periods of time until steady state value of mass was achieved. Then, the volumetric moisture content was calculated and sorption isotherm of each tested material was plotted.

3. Studied Materials

The reference lime plaster consisted of hydrated lime – 480 g, natural quartz sand with continuous granulometry 0 to 2 mm – 1 440 g and water – 480 g (we will denote it VO in what follows). The composition of the lime-metakaolin plasters was as follows: hydrated lime – 400 g, metakaolin - 80 g, natural quartz sand with continuous granulometry 0 to 2 mm – 1 440 g and water – 480 g (the plaster denoted as VOM), and hydrated lime – 400 g, metakaolin - 80 g, natural quartz sand with continuous granulometry 0 to 2 mm – 1 440 g , water – 480 g and zinc stearate – 2 g which was used as the hydrophobization admixture (the plaster denoed as VOMH). The lime CL 90 was produced by limekiln Morká, Czech Republic. Sand 0/2 mm fraction was delivered by Heidelberg Cement Group, Brněnské písky Inc., affiliate Bratčice. Metakaolin MEFISTO K05 was a product of České lupkové závody Inc., Nové Strašecí. Average particle size of metakaolin was in the interval of 3 to 5 μm. Plaster mixtures were prepared using laboratory mixing machine with forced rotation for 3 minutes and then compacted using vibrating machine. Each mixture was cast into a standard form, after two days all specimens were taken out of forms and then cured for 28 days in high relative humidity environment. As for the materials of load-bearing structures, two materials typical for historical buildings on Czech teritory were chosen. Siliceous raw-grained sandstone from the Mšené-lázně quarry (denoted as SS) was the first, ceramic brick produced in Žopa manufacture (denoted as CB) was the second one.

4. Experimental Results and Discussion

Basic properties of all tested materials are summarized in Table 1. Each result represents the average of five measured values. The open porosity of lime-containing plasters decreased due to the metakaolin and zinc stearate addition by 10 % in maximum. The other basic parameters were changed in a less significant way. All studied materials have proved high porosity, what is very positive factor from the point of view of their presumed application on historical buildings. The high porosity guarantees fast water and water vapour transport, and so their fast removal from the load bearing structures of reconstructed historical buildings.

TABLE 1: Basic parameters of tested materials.

Material	Bulk Density [kg m^{-3}]	Matrix Density [kg m^{-3}]	Open porosity [%]
VO	1 650	2 600	37.7
VOM	1 690	2 620	35.3
VOMH	1 740	2 620	33.4
CB	1 670	2 670	37.5

SS	1 810	2 670	32.2

Thermal conductivity of the studied materials in dry state is presented in Table 2. The lime-pozzolana plasters exhibited approximately 30% higher thermal conductivity than the reference lime plaster. This is in accordance with their higher bulk density and lower porosity (see Table 1). Ceramic brick and sandstone had lower thermal conductivity in dry state than the studied plasters although the differences in total open porosity were not very high. This was due to the different composition of the porous matrix and different pore size distribution of the particular materials.

TABLE 2: Thermal conductivity of tested materials.

Material	Thermal Conductivity [W m^{-1} K^{-1}]
VO	0.67
VOM	0.88
VOMH	0.85
CB	0.50
SS	0.40

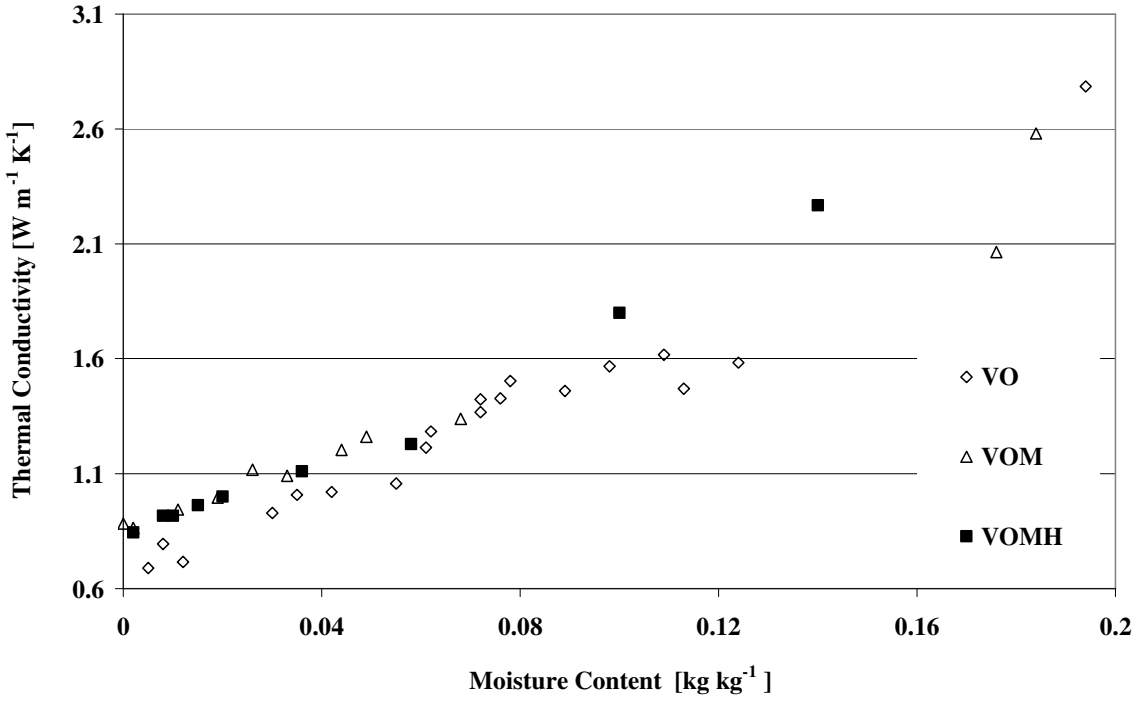

FIG. 1: Thermal conductivity of plasters as a function of moisture content.

Figs. 1-2 present thermal conductivities of tested materials in the dependence on moisture content. Clearly, the shapes of all λ(u) functions were very similar, very close to linear. The effect of moisture was for both the

plasters and the materials of load bearing structure very significant; the values of thermal conductivity of water saturated specimens were two to four times higher than of dry specimens.

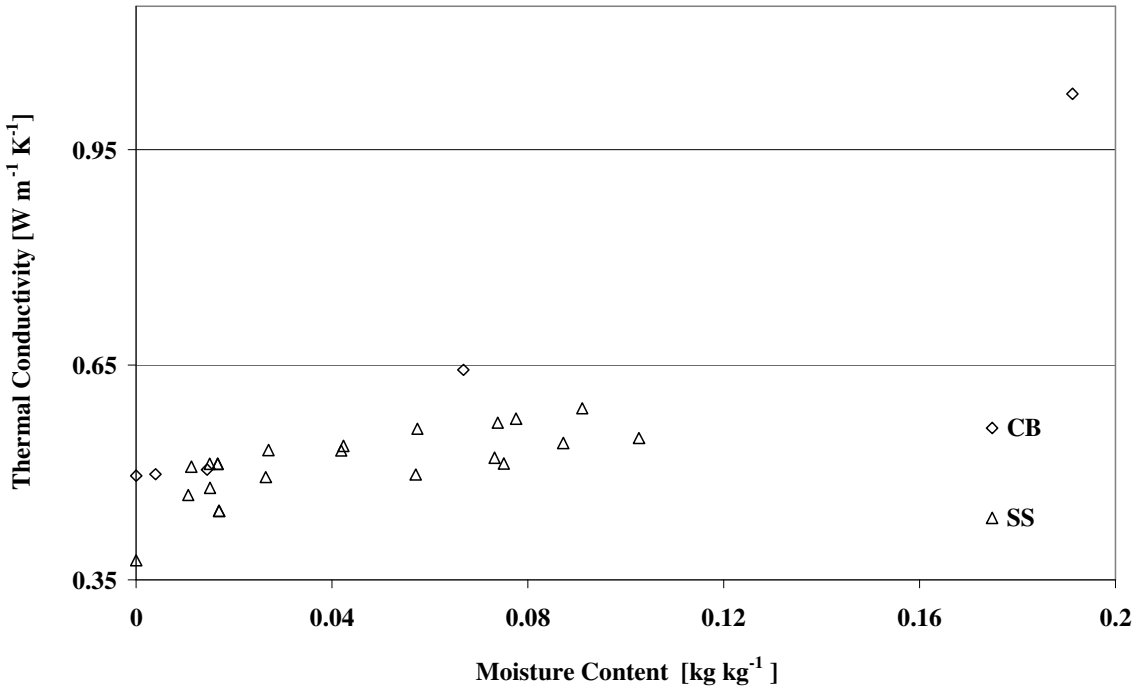

FIG. 2: Thermal conductivity of load bearing structure materials as a function of moisture content.

TABLE 3: Water vapour transport parameters of tested materials.

Tested Materials	Water Vapour Diffusion Coefficient [m^2 s^{-1}]		Water Vapour Diffusion Resistance Factor [-]	
	97-45% RH	0-45% RH	97-45% RH	0-45% RH
VO	5.4 E-6	2.9 E-6	4.3	8.9
VOM	6.2 E-6	2.5 E-6	3.7	10.1
VOMH	4.4 E-6	1.6 E-6	5.3	15.0
CB	1.5 E-6	1.2 E-6	14.7	19.5
SS	3.4 E-6	1.2 E-6	6.7	19.0

The results of water vapour and liquid water transport parameters measurement are presented in Tables 3 and 4; each result represents the average value from five measurements. In the dry-cup measurements the lime-metakaolin plasters had higher water vapor diffusion resistance factor μ than the reference lime plaster, the differences were more significant in the case of hydrofobized plaster, which was caused by the lower open porosity. The tested ceramic brick had similar water vapour transport parameters as sandstone; these values were nearly two times higher than the respective values of tested plasters. For the wet-cup arrangement the differences in water vapour diffusion resistance factors of plasters were lower; the hydrophobized plaster still achieved the

highest μ value. Sandstone had the water vapour diffusion resistance factor only about 25% higher than the hydrophobized lime-metakaolin plaster but ceramic brick exhibited two times higher μ than sandstone.

The values of liquid water transport parameters were for lime-metakaolin plaster similar to the pure lime plaster. However, the effect of zinc stearate in the hydrophobized plaster was quite important; the water absorption coefficient decreased more than three times in comparison with lime plaster, the apparent moisture diffusivity by about one order of magnitude, which is a very positive feature for a render of a historical building. Ceramic brick had only about 15% lower water absorption coefficient than lime and lime-metakaolin plasters which confirmed the good compatibility of these materials in building structures. The sandstone exhibited quite exceptional water transport capability; its apparent moisture diffusivity was two orders of magnitude higher than for ceramic brick. This was clearly a consequence of the preferential paths for liquid water transport in sandstone presented by a very substantial amount of large capillary pores.

TABLE 4: Liquid water transport parameters of tested materials.

Tested Materials	Water Absorption Coefficient [kg m^{-2} $s^{-1/2}$]	Saturated Moisture Content [kg m^{-3}]	Apparent Moisture Diffusivity [m^2 s^{-1}]
VO	2.20 E-1	359	4.40 E-7
VOM	2.20 E-1	342	4.30 E-7
VOMH	6.50 E-2	332	3.90 E-8
CB	1.90 E-1	370	2.65 E-7
SS	1.25	311	1.70 E-5

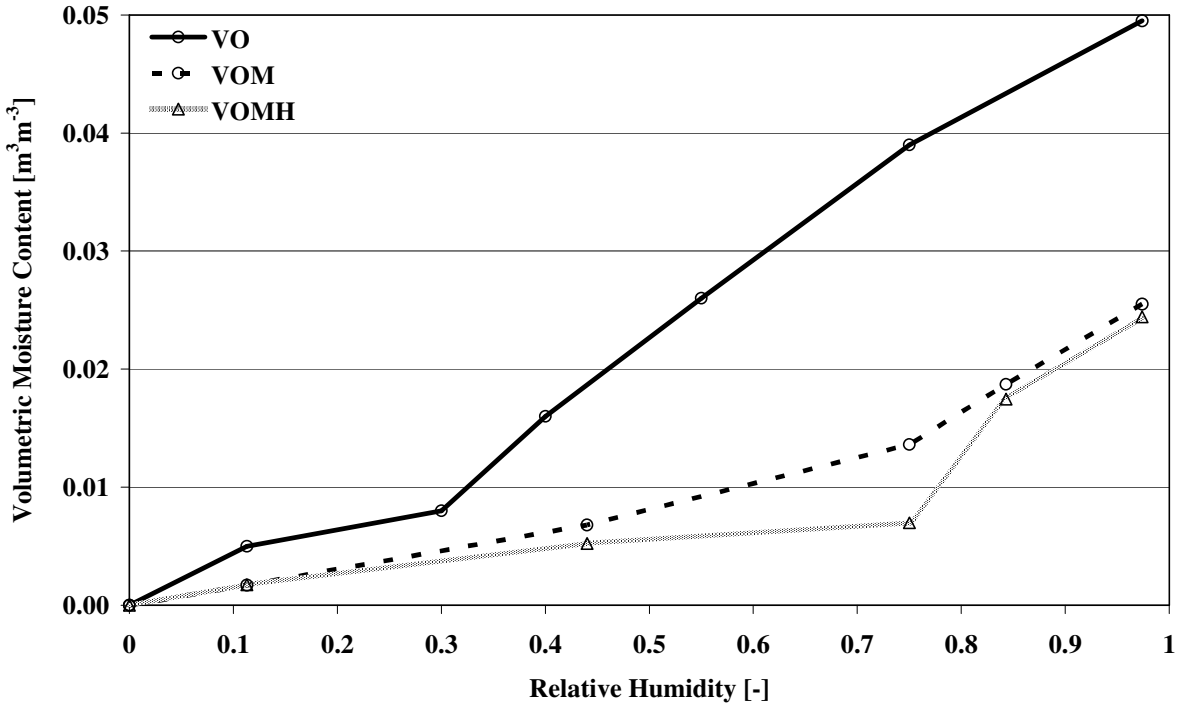

FIG. 3: Sorption isotherms of plasters as a function of moisture content.

Figs. 3 and 4 show the sorption isotherms of the tested plasters, ceramic brick and sandstone. Clearly, the highest values of adsorbed water achieved in all the range of relative humidity the lime plaster VO. The maximum hygroscopic moisture content of both lime-metakaolin plasters was about two times lower than for the pure lime plaster. The sorption isotherms of the plasters VOM and VOMH were similar each other. Thus, the effect of hydrophobization on water adsorption was relatively low.

The water vapor adsorption capacity of sandstone (Fig. 4) was very low, several times lower than for the studied plasters. This is a consequence of the relatively high amount of large pores in the material. In a combination with high water transport parameters it may mean a very good resistance of the material to the weathering. The water vapour adsorption capability of ceramic brick was only slightly lower than for lime plaster. Once again, this confirms the good compatibility of both these materials in a historical structure. It should be noted in this respect that the ceramic brick used for the investigations in this paper was not a high-quality well-burnt brick currently used in most new buildings. Quite intentionally, an imperfectly burnt brick similar to those which were used on the Czech territory in 17th and 18th century was chosen to get closer to a real historical material. This can explain the observed high hygroscopicity which is in contradiction with most results reported for ceramic bricks by other investigators and also with the own results of the authors obtained for other types of ceramic brick before [Roels *et al.* (2004)].

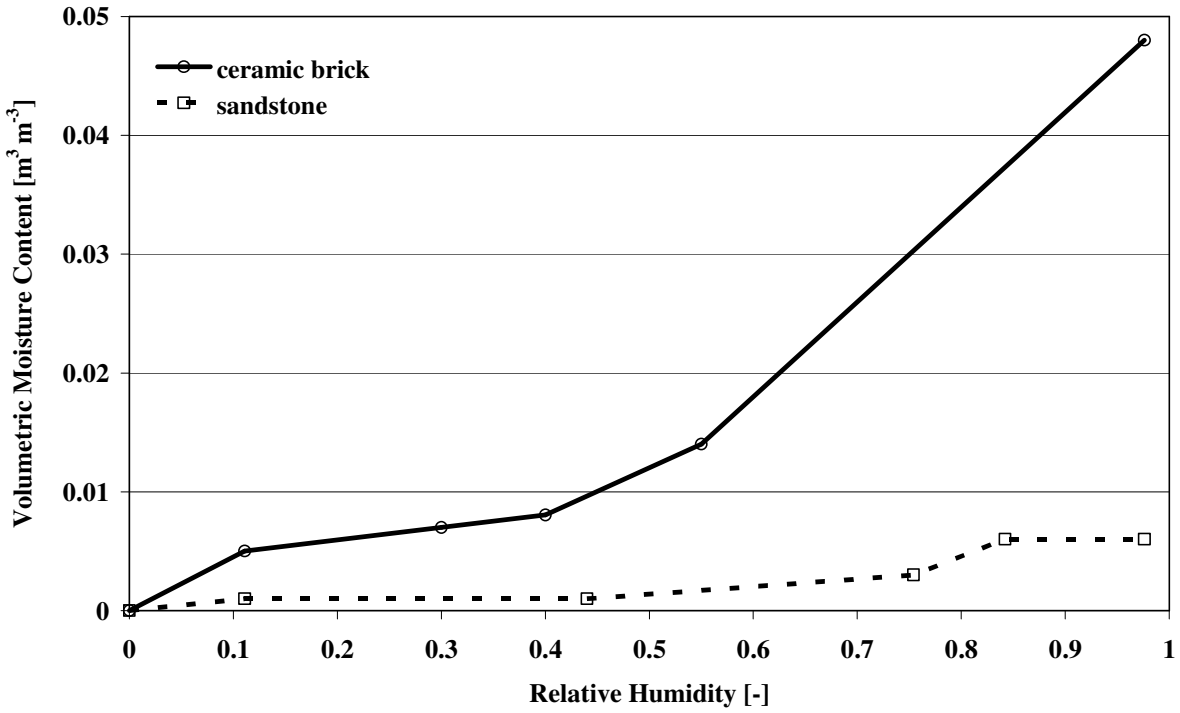

FIG. 4: Sorption isotherms of load bearing structure materials as a function of moisture content.

5. Conclusions

In this paper, principal parameters necessary at the description of moisture and heat transport in envelope parts of historical buildings were measured for several materials characteristic on the Czech territory. The obtained data - as input parameters of computational models - can facilitate the hygric and thermal performance assessment of old buildings. Also, they represent a part of input data necessary for computational damage assessment models of historical buildings.

In future work we will focus on the measurement of mechanical properties of the studied materials. In this way, the entire information on input material properties indispensable for application of fully coupled hygro-thermo-mechanical modelling of damage in historical masonry will be obtained.

Acknowledgements

This research has been supported by the Czech Science Foundation, under project No. 103/08/1531.

6. References

Černý R., Poděbradská J., Drchalová J. (2002) Water and Water Vapor Penetration through Coatings. Journal of Thermal Envelope and Building Science, Vol. 26, p. 165-177.

Černý R. and Rovnaníková P. (2002) Transport Processes in Concrete. Spon Press, London.

ČSN 72 7031. Měření součinitele difúze vodní páry stavebních materiálů metodou bez teplotního spádu.

de Boer R. (1996) Highlights in the historical development of the porous media theory: toward a consistent macroscopic theory. Appl. Mech. Rev. 49, p. 201 – 262.

Lewis R. W. and Schrefler B. A. (1998) The finite element method in static and dynamic deformation and consolidation of porous media. John Willey & Sons, Chichester – Toronto, p. 492.

Roels S., Carmeliet J., Hens H., Adan O., Brocken H., Černý R., Pavlík Z., Hall C., Kumaran K., Pel L. and Plagge R. (2004) Interlaboratory Comparison of Hygric Properties of Porous Building Materials. Journal of Thermal Envelope and Building Science, Vol. 27, p. 307-325.

Characterization of a hygro-regulated Wall Base Ventilation System for Treatment of Rising Damp in Historical Buildings

Vasco Peixoto de Freitas, Full Professor
Building Physics Laboratory
Faculty of Engineering – Porto University, Portugal
vpfreita@fe.up.pt, www.fe.up.pt

Ana Sofia Guimarães
Building Physics Laboratory
Faculty of Engineering – Porto University, Portugal
anasofia@fe.up.pt, www.fe.up.pt

KEYWORDS: *Rising Damp; Treatment; Wall Base Ventilation System; Historical Buildings; Condensation.*

SUMMARY:
The treatment of rising damp in the walls of historic buildings is very complex, due to the thickness and heterogeneity of the walls. The techniques traditionally used for dealing with this problem (such as watertight barriers, injection of hydrofuge products, etc.) have sometimes proved ineffective, and that is why it is necessary to find a new approach.

In recent years, the Building Physics Laboratory at the Faculty of Engineering, University of Porto has been conducting experimental research on the effectiveness of the wall base ventilation system, using natural or mechanical higro-regulate systems to reduce the level of the damp area. This experimental research and the simulations that were performed, clearly show that wall base ventilation is a system with potential.

This paper presents the characterization of the hygro-regulated systems' operation based on experimental studies developed in laboratory, which allowed the influence of the velocity of the air, condensation risk and the possibility of salt crystallization. This will also present the results of measurements conducted in churches in the North of Portugal in which these systems were implemented, with the purpose of validating its operation and establishing criteria for programming the ventilator.

1. Introduction

For the last few years, the Building Physics Laboratory (LFC) of the Faculty of Engineering, University of Porto (FEUP) has been conducting experimental research to validate a technique for treating rising damp in the walls of older buildings [1, 2 and 3]. The technique consists of ventilating the base of the walls using a natural ventilation process or by installing a hygro-regulated mechanical ventilation device. The experiments were designed to show how these walls are affected by rising damp in view of different boundary conditions. The configurations used are shown in Fig. 1.

To assess moisture transfer inside the walls, probes were inserted at different heights and depths to measure relative humidity and temperature. These probes were then connected to a data acquisition and recording system [1].

In Configuration 1, we measured the behaviour of a wall with both sides underground by placing sand on both sides of the wall up to a height of 45 cm above its base. In Configuration 2, in order to assess the effect of a ventilation system at the base of the wall, a ventilation box was placed on both sides of the wall. Two openings were left, to which flexible tubes were attached to ventilate the box. A mechanical extractor was placed at one opening, while the other was left free to allow air to enter freely. This extraction system was left running during the experiment to ensure that the temperature and relative humidity inside the box were identical to the conditions in the laboratory.

Figure 2 illustrates the change in relative humidity in the cross-sections located 61.5 cm (level 9) above the wall base.

Configuration 1 – Without ventilation.

Configuration 2 – With mechanical ventilation.

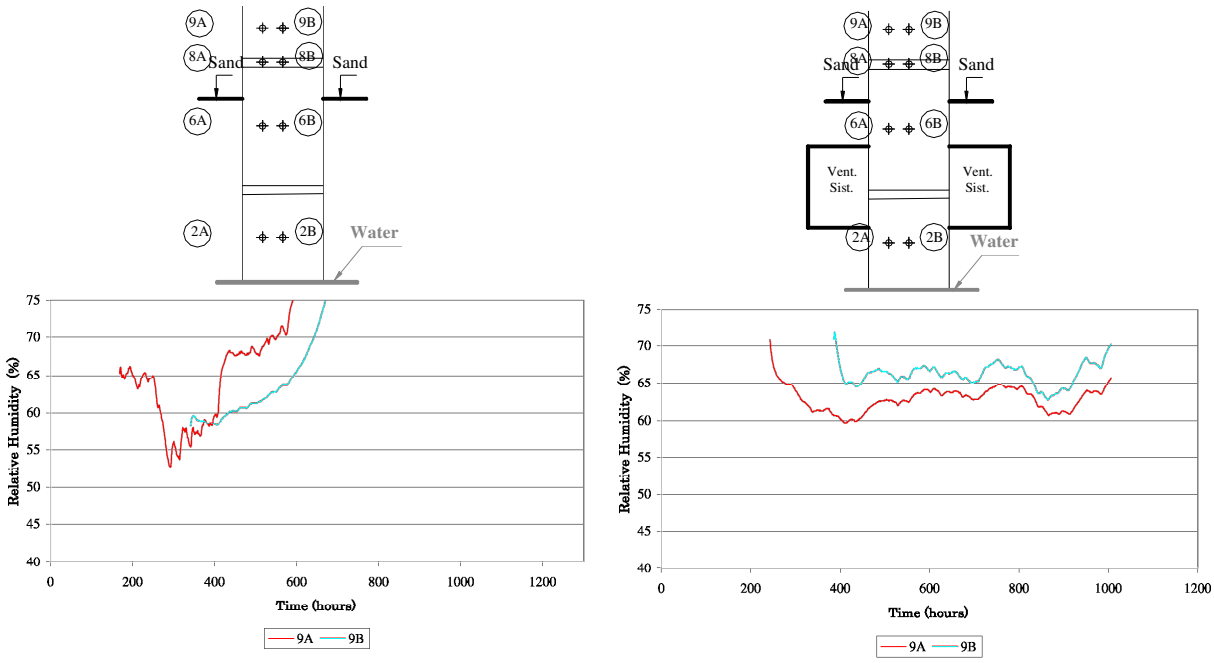

FIG. 1: Variations in relative humidity at level 9 in configurations 1 and 2 [2, 3].

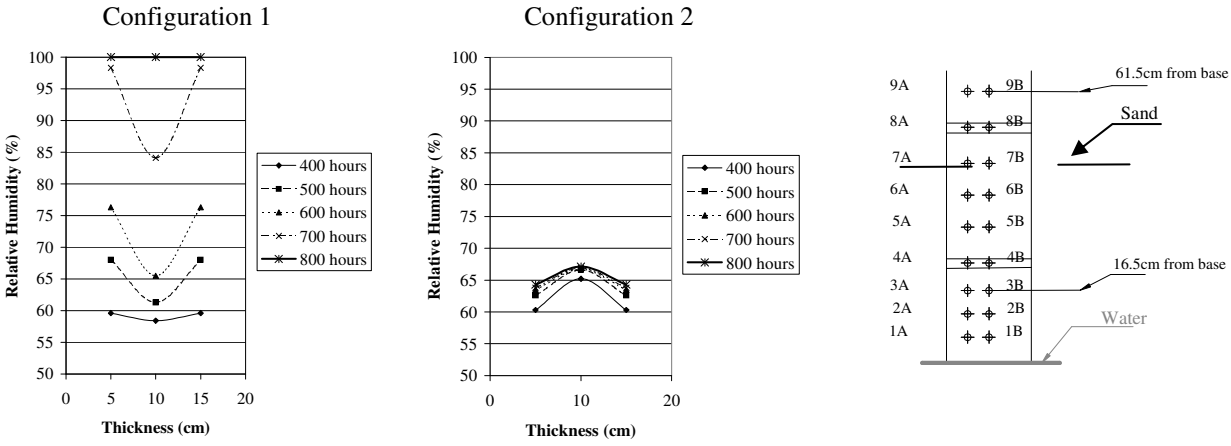

FIG. 2: Variation in relative humidity at level 9 [3].

We can conclude from the experimental research that a ventilation system placed at the base of the wall reduces the level of the rising damp (see Fig. 2).

The object of this paper is to present the results of experimental characterisation of a hygro-regulated ventilation system:

Laboratory measurements;

In field measurements.

2. Experimental characterization of the Wall Base Ventilation System

2.1 Model adopted and description of the experiment

We study three cells corresponding to specific boundary conditions (Configurations 2A, 2B and 2C) (Fig. 3) that were associated to a mechanical ventilation system with controlled velocity. Probes were placed in such a way as to obtain readings of the temperature and relative humidity inside the ventilation system all the time (Fig. 3).

Probes were installed in each cell: Probe S1 – Temperature (T) and Relative Humidity (RH) of the air at the entrance of the system; Probe S2 – T and RH of the air in the middle of the system; Probe S3 – T and RH of the air in the middle of the system and in the surface of the wall and Probe S4 – T and RH of the air at the exit of the system.

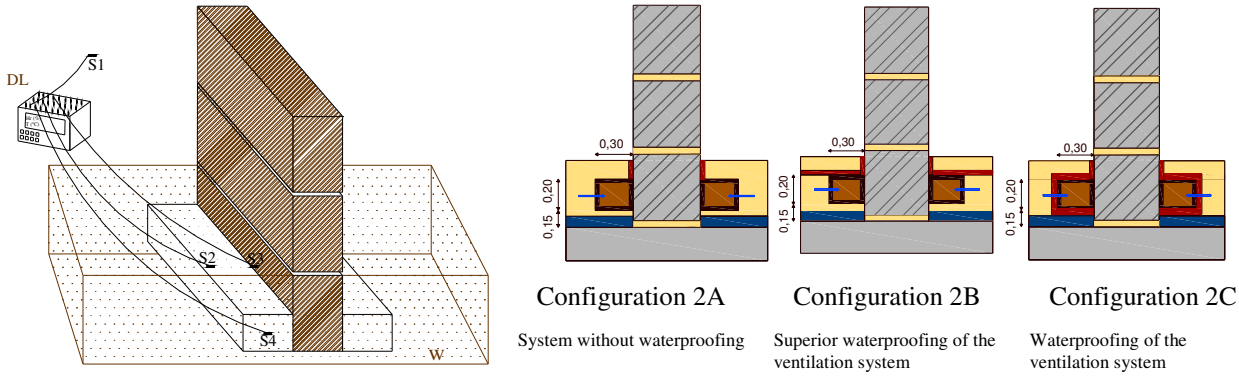

FIG. 3: Physical Model –Probes positions.

Table 1 shows the speeds throughout the time. The velocity was regulated and measured with a high precision anemometer.

TABLE. 1: Variation in velocity over time.

	Saturation of the wall	Test duration – 5 months									
Days		15	15	15	15	15	15	15	15	15	15
Velocity (m/s)		0.29	0.26	0.20	0.13	0.08	0.47	0.54	0.60	0.61	0.63

During the drying process, the interior of the ventilation system was monitored in accordance to the principle defined in Fig. 3.

2.2 Results

The analysis of the graphs of vapour pressure variation at the entrance and the exit, for the three configurations, clearly shows the occurrence of periods with negative differences of flow for the configurations 2A (Fig. 4) and 2B, which means the occurrence of condensations. It was possible to visualize that, in these periods of time, the system generates condensation moisture, had being seen the occurrence of drops of water. On the other hand, it was verified that the inversion of the gradient of pressures occurs near the exit. The length of the system presents a basic role in the functioning of the system.

Using the temperature and relative humidity values at the entrance and exit of the systems, we calculated the quantity of water vapour transported. Table 2 shows the model used to calculate the amount of water transported by the ventilation system.

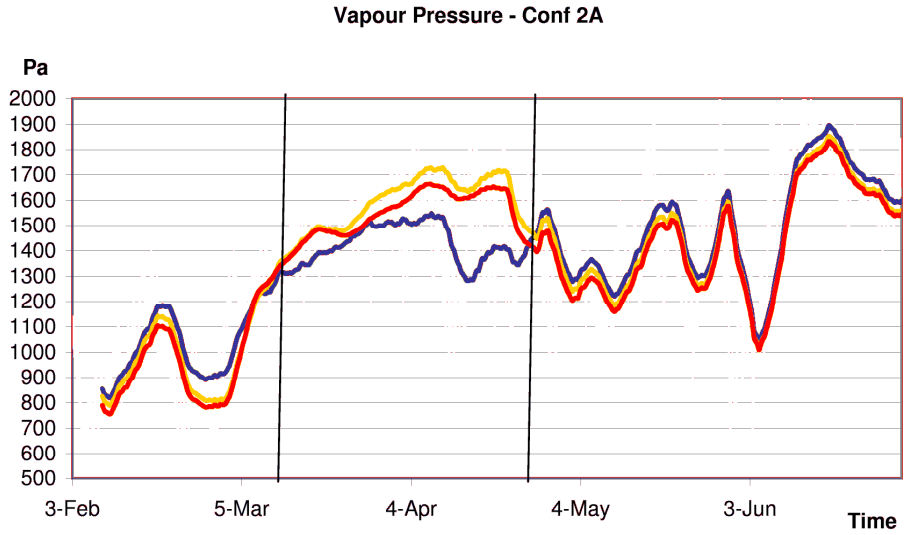

FIG. 4: Condensation occurrence in configuration 2A (red – entrance, yellow – middle and blue – exit).

TABLE. 2: Method of quantifying transported mass flows [4].

(I)	(II)	(III)
$P = e^{\frac{17.08*\theta}{234.18+\theta}} * RH$	w = 0.002167*P/ θ	W = (w_{exit}-$w_{entrance}$)*Q*Δt
P – Vapour pressure (Pa); θ – Temperature (ºC); RH – Relative Humidity (%).	w – Absolute air humidity (kg/m^3); P – Vapour pressure (Pa); θ – Air temperature (K).	W – Quantity of water removed (kg); w_{exit} – Absolute air humidity at exit of system (kg/m^3); $w_{entrance}$ – Absolute air humidity at entrance of system (kg/m^3); Q – Ventilation flow (m^3/s); Δt – Time interval (s).
Note: As the measurements were taken every half hour, the temperature and relative humidity are considered to be constant for this time interval.		

Figure 5 shows the quantity of accumulated water vapour transported during the testing period, for various air circulation speeds. The functioning of the system is greatly influenced by outside conditions. In Configuration 2A and 2B we can see that, in some periods of time, the quantity of accumulated water vapour transported decreases which mean that we have condensations inside the system.

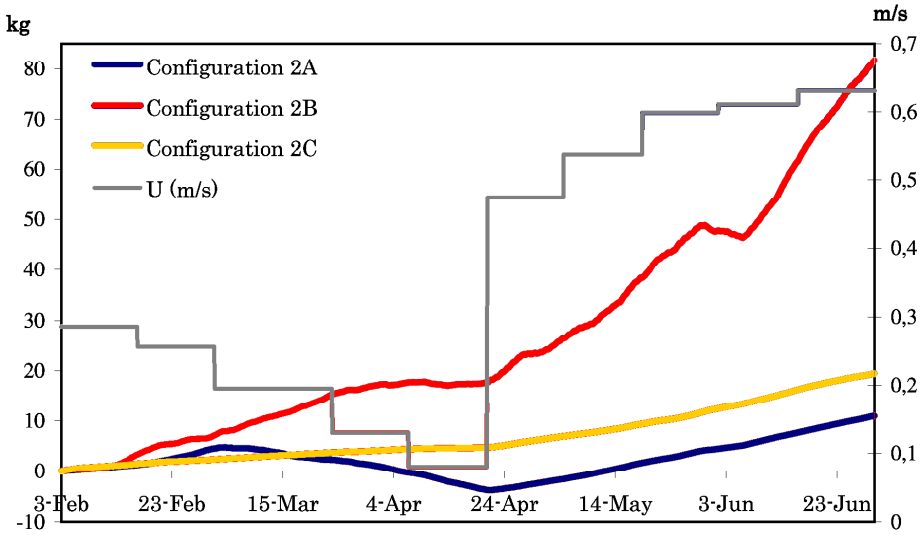

FIG. 5: Quantity of accumulated water vapour (kg) taken from the ventilation system.

2.3 Main conclusions obtained

The following conclusions were drawn from the results obtained:

The Configuration 2B had transported more water vapour;

In configurations 2A and 2B we had problems of condensations inside the systems;

The best behaviour is achieved by the configuration 2C;

The outside conditions of the air at the entrance influence the system functioning;

The velocity or flow extracted by the ventilation system, though necessary, contributes little to the efficiency of this system.

A hygro-regulated system is essential to control possible condensation inside the system. A hygro-regulated system is the one in which the vapour pressure is controlled by sensors placed at the entrance and exit, which instruct the system to switch off whenever the exit flow is less than the entrance flow.

3. In Field Characterization of the Wall Base Ventilation System

3.1 Description

To validate the system in field, a wall base ventilation system was installed in a church in the North of Portugal.

On the outer face of the church walls, a natural ventilation channel was created, consisting of prefabricated concrete parts. This channel could be opened to the outside air by means of a ventilation device (Fig. 6).

Inside the building, there were two distinct subsystems, both with hygro-regulated mechanical ventilation. Air was admitted into one subsystem through an opening in the façade. The other subsystem involved two admission grids located inside the building, with extraction to the exterior of the church. Extractions were controlled by an hygro-regulated variable speed engine, which would stop operating whenever the difference between the entrance and exit relative humidity was lower than 5%.

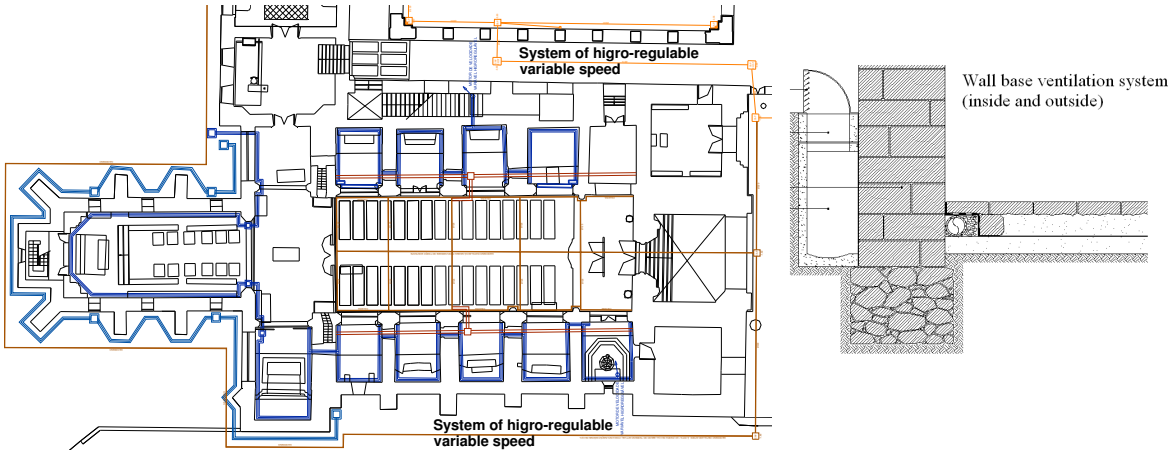

FIG. 6: Plan of the wall base ventilation system (inside and outside) – system of higro-regulated variable speed.

Each ventilation subsystem had two probes and two temperature and relative humidity transmitters, a control module and a data acquisition system for recording and operating the air extraction device.

3.2 Results

In Fig. 7 it is presented the differences of vapor pressure and the periods of functioning of the system. We can see that we have some periods of time where the system is operating but where we have condensation problems.

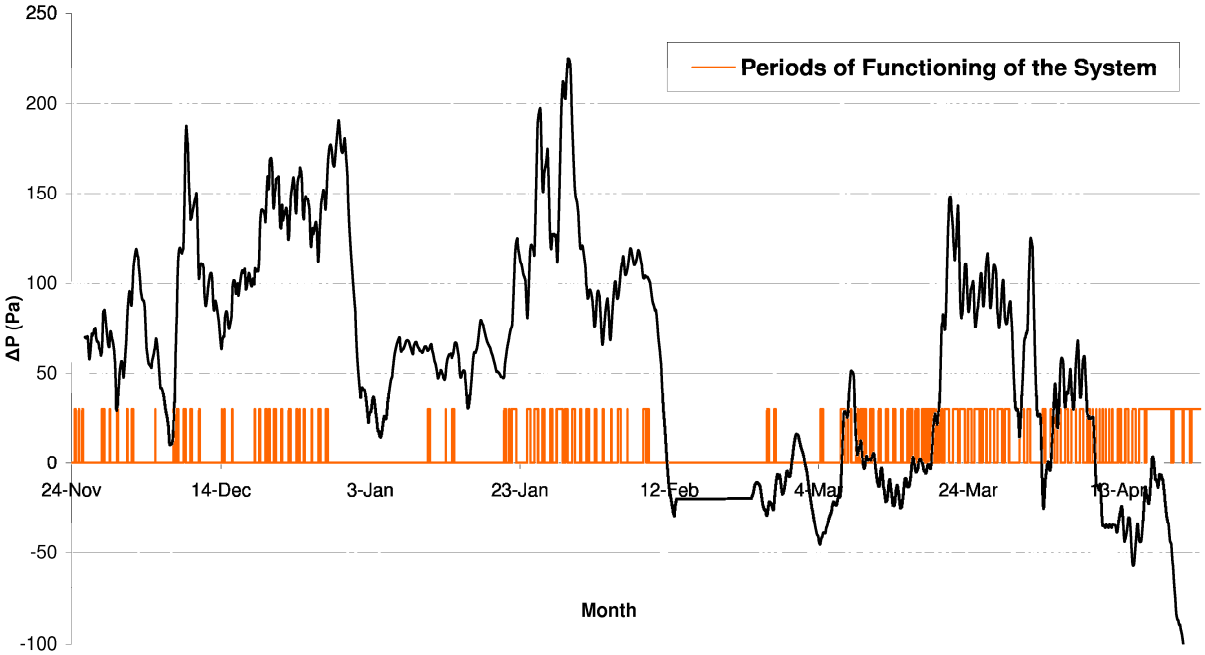

FIG. 7: Differences of vapor pressure and periods of functioning of the system.

With the goal of analysing the occurrences of condensations inside the system we focus on the differences of pressure between the exit and the entrance of the system that sometimes were negative, what means that exist periods of time where we have condensation problems. To solve this problem or, at least, minimizing the possibility of occurrence of condensations we place the cited hygro-regulated system.

Whenever the air that enters presents a relative humidity near the existing moistness in the interior of the system, it doesn't work having only natural drying. If we analyse Fig. 7 we can cross information between the periods where the system is working, mechanically and the periods where the condensations occur.

We can see that the criterion of 5% of difference between the exit and the entrance humidity isn't effective. The system doesn't work in the periods of drying, sometimes functioning in periods where we have condensations, being able to contribute for its intensification.

We propose a criterion based on vapour pressure where the system works when the difference between the vapour pressures at the exit an entrance is positive, which should be more efficient as we can see on Fig. 8. On the other hand, the occurrence of internal condensations can contribute to the crystallization/dissolution of salts present in the water warping the surface pores of the wall, putting in cause the effectiveness of this system.

The criterion we used to stop the system should be function of vapour pressure instead of relative humidity. It is suggested to stop the system, whenever the vapour pressure at the entrance is superior to the pressure at the exit, minimizing the occurrence of condensations.

It is considered that the recorded values of relative humidity, between 60% and 95%, do not cause serious risks of crystallization/dissolution of salts in the interior of the system.

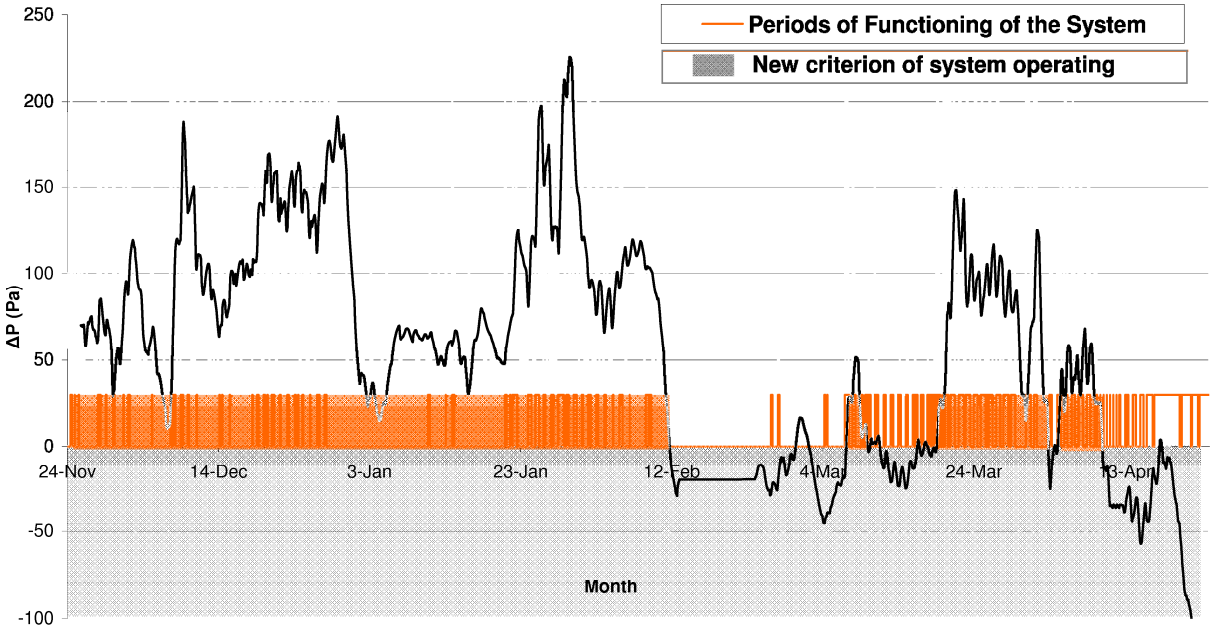

FIG. 8: New criterion of system operating and periods of functioning of the system.

4. Conclusions

Our assessment of the results led us to the following conclusions:

The wall base ventilation system is effective in historical buildings with thick and heterogeneous walls;

A mechanical hygro-regulated system is essential to control possible condensations inside the system;

Although it will be interesting in future to assess the possibility of the occurrence of crystallization / salt dissolution, we believe that this problem will be prevented by the hygro-regulated system;

The in field measurements, which are in course since October 2006, allow the results of the experiments to be validated in the laboratory.

5. Acknowledgement

The authors would like to thank the FCT – Fundação para a Ciência e Tecnologia, for supporting this research in the frame of "POCI/ENR/61524/2004".

6. References

[1] – Torres, M.I.M. (2004). Humidade Ascensional em Paredes de Construções Históricas. Ph.D. Thesis, Coimbra, FCTUC, 229 pgs *(in Portuguese)*.

[2] – Freitas, V.P., Guimarães, A., Torres, M.I.(2007). The Experimental Characterization of a Wall Base Ventilation System for the Treatment of Rising Damp in Historical Buildings. 12th Symposium for Building Physics. Dresden, 29-31 de Março de 2007.

[3] – Torres, M.I., Freitas, V.P. (2005). Treatment of rising damp in historical buildings: wall base ventilation. Building and Environment, 42 (2007), 424–435, January, 2005.

[4] – Kunzel, H.M. Connection between liquid water and vapour transport in porous media and its consequences for heat and moisture transfer models. Contribution to the Science. London. 12 pgs., December, 1992.

Why do we often get biological growth on thin rendering on thermal insulation constructions?

Sanne Johansson, M.Sc.
Division of Building Materials, LundUniversity
sane.johansson@byggtek.lth.se

Lars Wadsö, Ph.D
Division of Building Materials, Lund University
lars.wadso@byggtek.lth.se

Kenneth Sandin, Ph.D
Division of Building Materials, Lund University
kenneth.sandin@byggtek.lth.se

KEYWORDS: *rendered façades, temperature, relative humidity, biological organisms.*

SUMMARY: If one takes a closer look at almost any building facade one will find biological growth. Although this can be seen as an integral part of an antique building, for modern buildings it is in most cases seen as an aesthetical problem. All building facades will most likely be discolored by biological growth by time, but in Sweden we have had many cases of newly built rendered facades that have been discolored much more rapidly than usual. The problem is believed to occur mainly on thin rendering applied on thermal insulation -which is a common building facade construction in Sweden -but apart from this, it is difficult to find clear indications of which facades that will be affected. As it is well known that different biological organisms has different requirements in physical factors (especially temperature and relative humidity) for germination and growth on any substrate, it is important to define which conditions the organisms needs to grow on a building fasade. We have studied the temperature and relative humidity conditions on the surfaces of different rendered facade constructions. We find that the surface temperature on a facade of thin rendering on thermal insulation drops quickly during nights, as these constructions have low heat capacity in the rendering layer. This leads to high relative humidity and even condensation, during clear nights. Other abiotic factors that seem also to influence the risk for growth are surface color and rendering structure. From the temperature and relative humidity measurements in this study, we aim at giving insight of the surface climate on a building façade in order to fully understand the rendered façade as a biological habitat.

1. Introduction

Along with physical and chemical weathering, it is well known that some biological organisms can degrade natural stone and similar substrates (Warscheid and Braams 2000). There has therefore been a lot of attention on biodeterioration of buildings (see for example Caneva et al.(2005); Koestler and Vedral (1991); Papida et al. (2000) and review in Wainwright et al. (1993)). The organisms living on external building façades, algae, fungi, bacteria (incl. cyanobacteria and actinomycetes), myxomycetes and protozoa (Gaylarde and Gaylarde 2000; Hofbauer et al. 2003) form a biofilm, an interface between the substrate and the atmosphere consisting of these microorganisms and their metabolites. Some of them act as glues, which makes the surface harder to clean (Ortega-Morales et al. 2000). Although many papers deal with the identification of organisms living on the façades (de Miguel et al. 1995; Gaylarde and Gaylarde 2000; Kiel and Gaylarde 2006; Ortega-Calvo et al. 1991; Saiz-Jimenez et al. 1990; Tomaselli et al. 2000), sometimes by using several techniques (Crispim et al. 2006; Gaylarde et al. 2004; Welton et al. 2005), only a few investigate how to avoid the growth (Shirakawa et al. 2002). Avoiding such growth is highly important in the conservation of historical buildings, but can also have important implications for modern buildings. Biological growth on external building façades is the result of a complex interaction of the substrate and different physical and climatic factors controlling the growth. It is surprising that only few papers include investigations of climatic factors when studying the biological growth on façades (Carter and Viles 2003; Crispim et al. 2003; Danin and Caneva 1990; Häubner et al. 2006). It is well known that microorganisms need a high relative humidity to grow (Sedlbauer et al. 2002). Previous research has also shown that the organisms found on buildings, especially fungi, algae, lichens and cyanobacteria are

especially adapted to survive the repeated drying and rehydration cycles existing on a external building façade (Ortega-Calvoet al. 1991). Although all buildings will most likely be discolored by biological growth over time, current building tradition and the demand for energy savings has led to changes in our way of building residential houses, which, in some cases, have increased occurrence of biological growth on façades. In Sweden many new houses have for the last decades been built with a construction of thin rendering on thermal insulation. Anomalous biological growth often occurs on the façade only a few years after the building have been constructed. Even though this problem might only be of aestetic character, it can lead to various economical and social consequences, since a discolored façade, being perhaps the building's most salient element, will give an impression of a poorly mantainted building, even though the rest of the building is good condition. Sweden is not the only country which has experienced this phenomenon; some papers from Germany deal with the same problem (Karsten et al. 2005; Künzel and Sedlbauer 2001; Sedlbauer and Krus 2001; Sedlbauer et al. 2006). But the study of biological growth on modern buildings is otherwise scarce (Cockell and Knowland 1999; Hofbauer et al. 2003). This present study investigates the complex interacting factors related to both abiotic and biotic conditions of rendered façade systems, with the primary focus on relative humidity and temperature. The aim is to provide insight into when biological growth might occur on rendered façades. This will allow us to have a deeper understanding of the building façade as a biological habitat and to consider how to reduce the growth by non-chemical means.

2. Materials and Methods

A test house was built outside to measure temperature and relative humidity conditions constantly all year around on rendered façade surfaces (Fig.1). The framework and all interior parts of the house consist of wood. Its longest façades face north and south and each have six replaceable wall elements (1050 mm x 2100 mm). The house is located in Lund, Sweden on the Lund University campus. Lund is situated in the southernmost part of Sweden (55° 42′ N, 13° 12′ E) having a temperate climate with cold, cloudy winters and cool, partly cloudy summers. The average temperature is -2-0°C in January and 15-17°C in July and the annual precipitation is 500-1000 mm.

FIG. 1: Picture of the north side of the test house in Lund, Sweden.

On each side of the test house two facade constructions was built; one "heavy" and one "light" façade (fig. 2). Both construction types have the same type of rendering system (Stolit K, STO AB, Sweden) with a thickness of 3-5 mm and the only difference between them was that the heavy façade had a layer of bricks between the rendering and the inner thermal insulation. The inner part of both façade elements were built up from a wooden construction of wood studs 45 mm c/c 600 mm with thermal insulation of mineral wool (Rockwool A/S) in between the studs and a gypsum board on each side. On the external gypsum board a 45 mm polystyrene thermal insulation was placed. On the outside of the polystyrene thermal insulation plate a layer of bricks was applied on the heavy facade. A layer of thin rendering was applied directly on the brick wall afterwards. On the light façade the layer of thin rendering was applied directly on the polystyrene thermal insulation. To investigate the influence of façade colour, half of each façade element has a final rendering layer with red pigments whereas the other half has a white pigmented final rendering. It should be noted that the biocidal contents of the renderings

are unknown. The biological growth will therefore not be assessed on this test house, but on separate samples with known rendering compositions (another study).

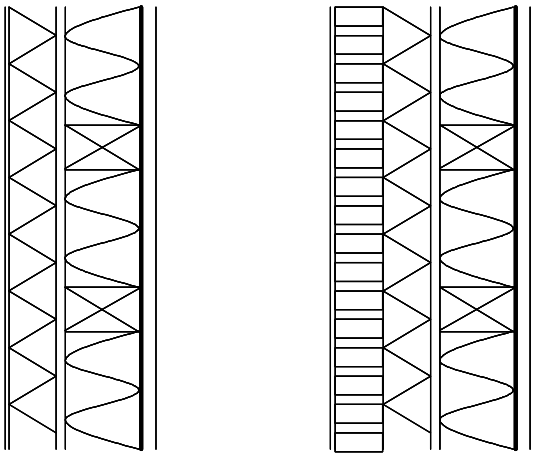

FIG. 2: Schematic of the constructions of the light (left) and heavy (right) façades. The structure of the light façade from left (outside) to right (inside): 3-5 mm rendering, 50 mm polystyrene, 9 mm gypsum, 145 x 45 mm wood studs c/c 600 and 145 mm mineral wool, 0.2 mm vapour barrier. The only difference between the light and heavy constructions is the layer of bricks between the rendering and the polystyrene thermal insulation in the heavy façade.

The relative humidity and temperature of the four walls were monitored continuously every hour from April 2005 to April 2007 (still on-going). Relative humidity and temperature were measured using monolithic IC sensors (Honeywell IH-3602C) mounted under the rendering, as close to the surface as possible and placed in the middle of the upper half of each façade alternative. The ambient temperature was monitored with sensors placed above each façade element under the roof.

3. Results

In this investigation we focus on how abiotic factors like temperature and relative humidity (RH) help us understand how biological organisms can establish and grow on a façade. In this paper we shortly give some interesting results from the investigation.

In this study of temperature and relative humidity conditions of rendered façades, we investigate the influence of following factors:

- heat capacity of construction (**L**ight / **H**eavy façade construction)
- color of façade (**R**ed / **W**hite)
- direction (north /south –facing façades)

3.1 Measurements on the south-facing side

The temperature on the different façade elements on the south-facing side followed the same pattern throughout the year. Figure 3 shows an example of the temperature conditions of the surface of the south-facing façade during 11 days of September 2006. The red façades reached the highest temperatures during daytimes; the light facade (LR) always higher than the heavy façade (HR). During night the temperature was always lower (difference up to 4 K) on the light façades than on the heavy façades. During summer, and especially when the sun was shining, the temperature difference between the different façade constructions became more pronounced. Generally the temperature varied more on the façades with thin rendering on thermal insulation than on the brick wall façade. In winter months all façade temperatures were almost the same day and night (data not shown). This pattern can also be seen when the sun is not shining for the rest of the year as illustrated of the 18th and 19th of September 2006 on Figure 3.

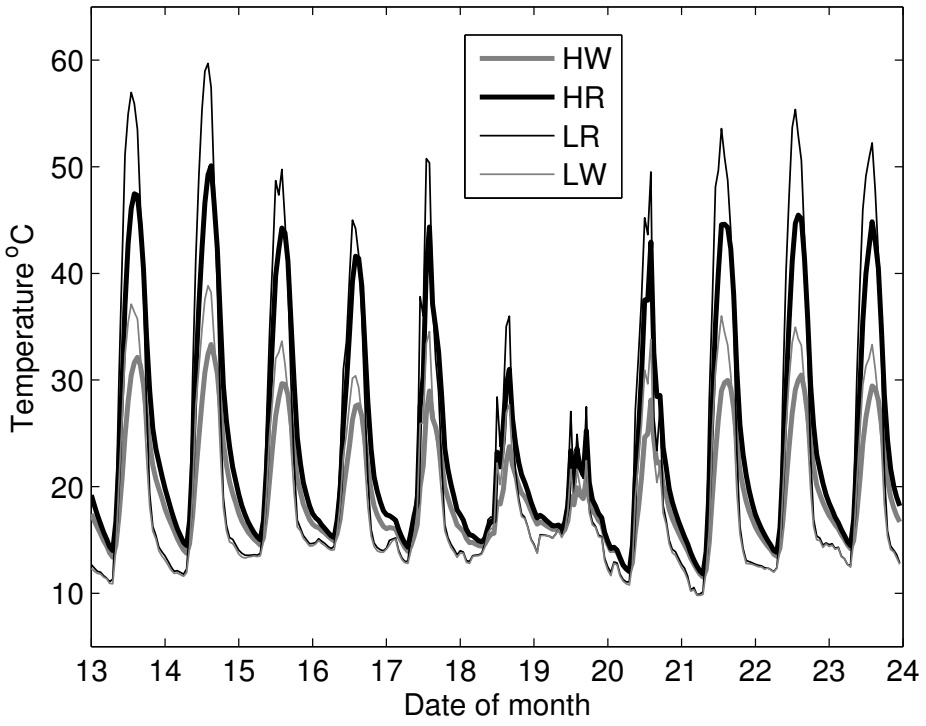

FIG. 3: The temperature distribution for all south-facing façades during 11 days in September 2006.

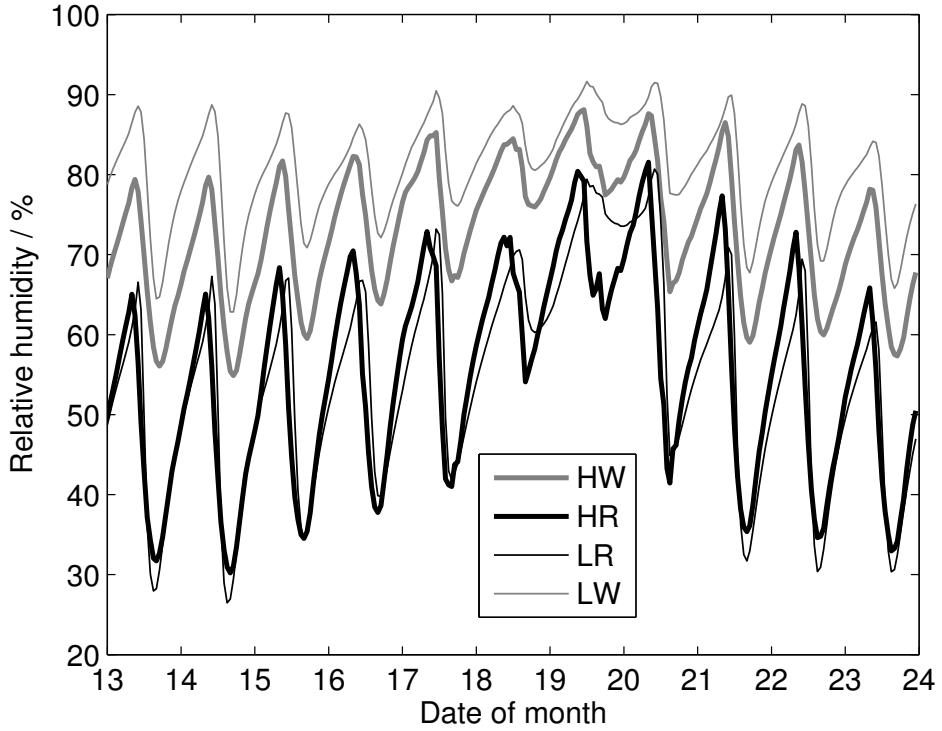

FIG 4: The relative humidity distribution for all south-facing façades during 11 days in September 2006.

The RH measurements showed similar patterns almost every day throughout the year. The RH was lower on the red- than the on white colored façades during daytime when the sun was shining, since the surface temperature was higher. Typically, the red-colored façades reaches lower maximum RH values compared with the white-colored façades, both during day and night. Interestingly, when the temperature was low during daytime (compared with other days within the same month), the RH for all façades varied much less over the day therefore the daytime RH remained higher. An example of this is shown in Fig. 4 (18th and 19th of September). On cloudy winter days, the RH on all façades was close to 100%, but when the sun was shining the RH decreased significantly. During winter the RH of LW were close to 100% day and night. On warm days during summer the relative humidity on the red-colored façades was under 70% day and night (data not shown). During daytime there was often a large difference in relative humidity between the white- and red-colored façades.

3.2 Measurements on the north-facing side

On the north-facing façade the same temperature pattern during night was seen as for the south-facing façade: the light façades had lower temperature than the heavy façades. The differences in temperatures between the HR and the LW were not as pronounced as on the south-facing façade. An example is given in Fig. 5. In addition, the difference between night and day temperatures on each façade was not as high as on the south-facing façade. Typically, the night temperature was higher the higher the temperature during daytime had been. During winter when the temperature difference was small between day and night, the temperature differences on the north-facing façades were also small.

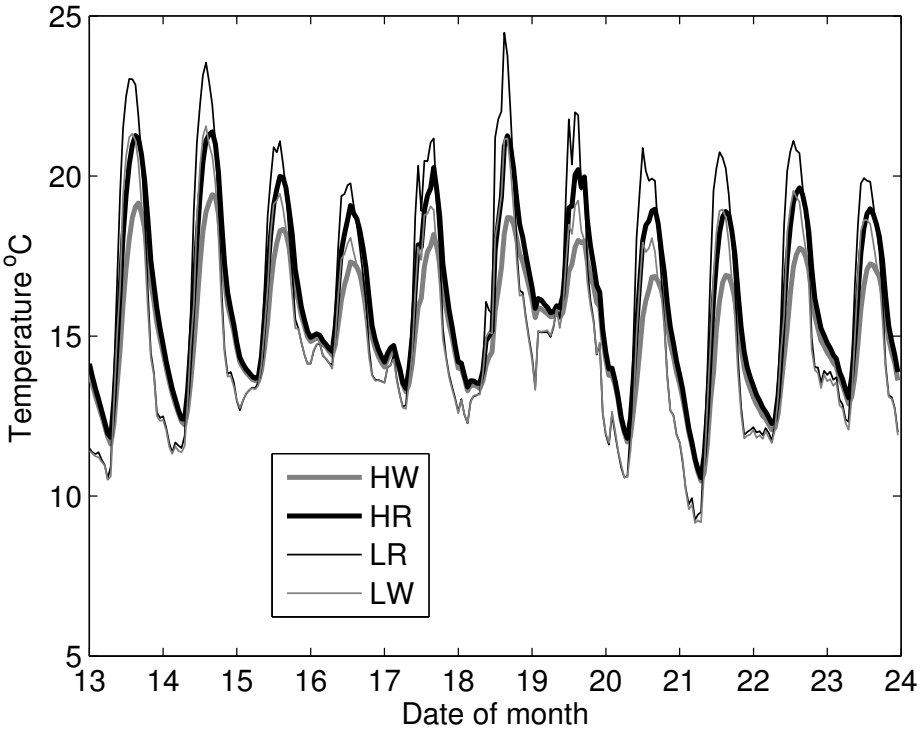

FIG. 5: The temperature distribution for all north-facing façades during 11 days in September 2006. During daytime the red façades have higer temperature than the heavy façades, during night time the light façades get colder than the heavy façades.

An example of RH on the north-facing façade is shown in Fig. 6. Generally, the RH are lower for the red-coloured than for white-coloured façades during daytime, but the RH during nights varies a lot between the façades. All façades reached RH values close to 100% almost every month, except for the summer months when the sun had been shining.

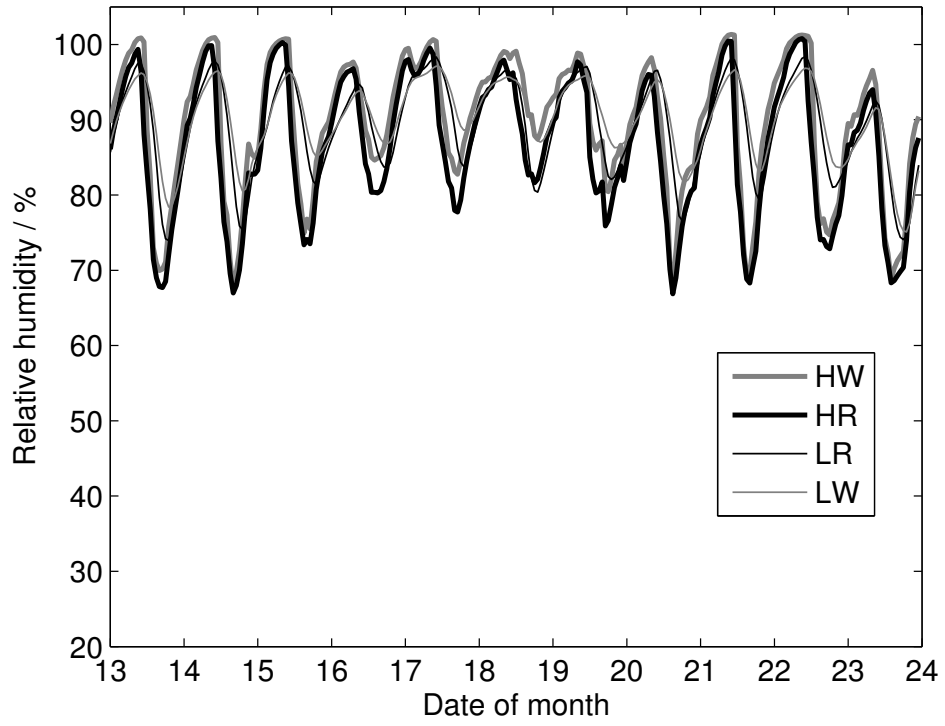

FIG 6: The relative humidity distribution for all north-facing façades during 11 days in September 2006.

4. Discussion

The temperature and RH show that light façades are more directly influenced by the weather conditions than the heavy façades. The temperature varied much more on the light façades than the on the heavy façades, especially on the south-facing façades, where the sun heats the surface by short-waved radiation. The color of the façades is also influencing the temperature conditions on the façade surfaces, especially during daytime. The LR gets much warmer during daytime than the HW. This is not surprising, as radiation from the sun causes high surface temperatures. However, which is maybe not so well known, the light façades gets colder in the night than the heavy façades due to their lower heat capacity: the heavy façades with a higher heat capacity can store the heat from day to night. Even if the HW reached the lowest maximum surface temperatures of all façades during daytime, it still has a higher night temperature than the light façades. During night the heavy façades had higher minimum temperatures than the light façades, but if we look at the RH during night on the south-facing façades we see that the HW had a higher maximum RH during night than the LR. The HW had the lowest maximum temperature during daytime, whereas the LR had the highest maximum temperatures, so even if the HW had a higher minimum temperature during night than the LR the maximum relative humidity values exceeds the maximum relative humidity values for the LR during night.

4.1 Study of length of time of high relative humidity on south-facing façade surfaces

As written earlier, the organisms living on a façade need a high relative humidity (within a certain temperature range) to establish and grow. Therefore, it is interesting to investigate how often a façade surface is within a given relative humidity range. As an example we give the duration of time the surfaces of the white coloured façades has a relative humidity above 90% from October 2005 to March 2006 (Table 1). The 90% RH is arbitrarily chosen as a measure of “high relative humidity”. It is not known at which RHs different organisms need to establish and grow on façades. It is well known that organisms living on façades (and other stone materials) are specialized in surviving repeated drying and rehydration cycles, but it is not known, how long these periods of time should be for optimial conditions.

TABLE 1: Percentage of time for each month inwhich the surface of the white coloured light façade (LW) and the white coloured heavy façade (HW) had a relative humidity above 90%.

	October 2005	November 2005	December 2005	January 2006	February 2006	March 2006
LW (south)	83%	100%	100%	100%	96%	78%
HW (south)	29%	84%	98%	96%	82%	34%
LW (north)	93%	98%	91%	58%	60%	82%
HW (north)	81%	92%	98%	96%	83%	61%

In Table 1 we see that the RH on LW was above 90% for a longer time than for the HW. Both for a few months on the north-facing side the opposite was the case. Even though the HW had a RH above 90% for a longer time as a percentage, the surface actually gets a significantly lower relative humidity each day, but for a short time. LW had a RH around 90% day and night. Therefore, the conditions for an organism to growth might still be better on LW even if the relative humidity gets under 90% for a longer period of time some months.

The above example is the first step to provide insight to when and how often the conditions for growth are suitable on a façade. Temperature and relative humidity are of course not the only abiotic factors of interest and in further studies we may also have to take other factors into account. With this study we have shown that constructions with thin rendering on thermal insulation get a high enough RH on the surface most of the year for growth of biological organisms.

5. References

Caneva G. Salvadori O. Ricci S. and Ceschin S. (2005). Ecological analysis and biodeterioration processes over time at the hieroglyphic stairway in the Copán (Honduras) archaeological site, *Plant biosystems*, Vol. 139, No. 3, 295-310.

Carter N.E.A. and Viles H.A. (2003). Experimental investigations into interactions between moisture, rock surface temperatures and an epilithic lichen cover in the bioprotection of limestone, *Building and environment*, Vol. 38, No. 9-10, 1225-1234.

Cockell C.S. and Knowland J. (1999). Ultraviolet radiation screening compounds, *Biological review*, Vol. 74, No. 3, 311-345.

Crispim C.A. Gaylarde P.M. and Gaylarde C.C. (2003). Algal and cyanobacterial biofilms on calcerous historic buildings, *Current microbiology*, Vol. 46, No. 2, 79-82.

Crispim C.A. Gaylarde P.M. Gaylarde C.C. and Neilan B.A. (2006). Deteriogenic cyanobacteria on historic buildings in Brazil detected by culture and molecular techniques, *International biodeterioration and biodegradation*, Vol. 57, No. 4, 239-243.

Danin A. and Caneva G. (1990). Deterioration of limestone walls in Jerusalem and marble monuments in Rome caused by cyanobacteria and cyanophilous lichens, *International biodeterioration*, Vol. 26, No. 6, 397-417.

de Miguel J.M.G. Sanchez-Castillo L. Ortega-Calvo J.J. Gil J.A. and Saiz-Jimenez C. (1995). Deterioration of building materials from the great jaguar pyramid at Tikal, Guatemala, *Building and environment*, Vol. 30, No. 4, 591-598.

Gaylarde C.C. Gaylarde P.M. Copp J. and Neilan B. (2004). Polyphatic detection of cyanobacteria in terrestrial biofilms, *Biofouling*, Vol. 20, No. 2, 71-79.

Gaylarde P.M. and Gaylarde C.C. (2000). Algae and cyanobacteria on painted buildings in Latin America, *International biodeterioration and biodegradation*, Vol. 46, No. 2, 93-97.

Hofbauer W.K. Breuer K. and Sedlbauer K. (2003). Algen, Flechten, Moose und Farne auf Fassaden, *Bauphysik*, Vol. 25, No. 6, 3-16.

Häubner N. Schumann R. and Karsten U. (2006). Aeroterrestrial microalgae growing in biofilms on facades - response to temperature and water stress, *Microbial ecology*, Vol. 51, No. 3, 285-293.

Karsten U. Schumann R. Häubner N. and Friedl T. (2005). Aeroterrestrische Mikroalgen. Lebensraum Fassade, *Biologie Unserer Zeit*, Vol. 35, No. 1, 20-30.

Kiel G. and Gaylarde C.C. (2006). Bacterial diversity in biofilms on external surfaces of historic buildings in Porto Alegre, *World journal of microbiology and biotechnology*, Vol. 22, No. 3, 293-297.

Koestler R.J. and Vedral J. (1991). Biodeterioration of cultural property: a bibliography, *International biodeterioration*, Vol. 28, No. 1-4, 229-340.

Künzel H.M. and Sedlbauer K. (2001). Algen und Wärmedämm-Verbundsystemen, *IBP-Mitteilung*, Vol. 28.

Ortega-Calvo J.J. Hernandez-Marine M. and Saiz-Jimenez C. (1991). Biodeterioration of building materials by cyanobacteria and algae, *International biodeterioration*, Vol. 28, No. 1-4, 165-185.

Ortega-Morales O. Guezennec J. Hernández-Duque G. Gaylarde C.C. and Gaylarde P.M. (2000). Phototrophic biofilms on ancient mayan buildings in Yucatan, Mexico, *Current microbiology*, Vol. 40, No., 81-85.

Papida S. Murphy W. and May E. (2000). Enhancement of physical weathering of building stones by microbial populations, *International biodeterioration and biodegradation*, Vol. 46, No. 4, 305-317.

Saiz-Jimenez C. Garcia-Rowe J. Garcia Del Cura M.A. Ortega-Calvo J.J. Roekens E. and Van Grieken R. (1990). Endolithic cyanobacteria in maarstricht limestone, *The science of the total environment*, Vol. 94, No., 209-220.

Sedlbauer K. and Krus M. (2001). Schimmelpilzbildung auf WDVS infolge "Baufehlern"?, *IBP-Mitteilung*, Vol. 28, 43-45.

Sedlbauer K. Krus M. and Zillig W. (2002). A new model for prediction and its application on dwellings with mould on the outer facades, *Building physics 2002 -6th nordic symposium*, Trondheim, Norway, 659-666.

Sedlbauer K. Krus M. Hofbauer W.K. Breuer K. and Fitz C. (2006). Neue erkentnisse zum mikrobiellen Bewuchs auf Aussenoberflächen, *Wärme, Kälte, Schall- und Brandschutz*, Vol. 56, No., 10-18.

Shirakawa M.A. Gaylarde C.C. Gaylarde P.M. John V. and Gambale W. (2002). Fungal colonization and succession on newly painted buildings and the effect of biocide, *FEMS micobiology letters*, Vol. 39, No., 165-173.

Tomaselli L. Lamenti G. Bosco M. and Tiano P. (2000). Biodiversity of photosynthetic micro-organisms dwelling on stone monuments, *International biodeterioration and biodegradation*, Vol. 46, No. 3, 251-258.

Wainwright M. Ali T.A. and Barakah F. (1993). A review of the role of oligotrophic micro-organisms in biodeterioration, *International biodeterioration and biodegradation*, Vol. 31, No. 1, 1-13.

Warscheid T. and Braams J. (2000). Biodeterioration of stone: a review, *International biodeterioration and biodegradation*, Vol. 46, No. 4, 343-368.

Welton R.G. Silva M.R. Gaylarde C. Herrera L.K. Anleo X. De Belie N. and Modrý S. (2005). Techniques applied to the study of microbial impact on building materials, *Materials and structures*, Vol. 38, No. 284, 883-893.

Development of an improved model for mould growth: Modelling

Hannu Viitanen, Ph.D., 1)
hannu.viitanen@vtt.fi

Juha Vinha, Dr. Tech.,2)
juha.vinha@tut.fi

Ruut Peuhkuri, Ph.D.,1)
ruut.peuhkuri@vtt.fi

Tuomo Ojanen, M.Sc., 1)
tuomo.ojanen@vtt.fi

Kimmo Lähdesmäki, M.Sc. Student,2)
kimmo.lahdesmaki@tut.fi

Kati Salminen, M.Sc., 2)
kati.salminen@tut.fi

1) Technical Research Centre of Finland, Finland;
2) Department of Civil Engineering, Tampere University of Technology, Finland;

KEYWORDS: *mould, modelling, experiments, sensitivity analysis.*

SUMMARY:

A large experimental study on 8 different building materials is going on in collaboration with the Technical Research Centre (VTT) and Tampere University of Technology (TUT), Finland. These materials are tested as pure materials and as a part of the building envelope constructions both in laboratory and outdoors. The laboratory tests are made partly under constant, but different conditions, and partly under varying conditions to simulate the effect of fluctuated wet, dry and frost periods. In the field exposures outdoors, the materials and constructions are tested under real conditions.

The main aim of this experimental programme is to use the measured results in the development of an improved model to predict mould growth. This improved model is based on an existing mathematical model developed on wood at VTT during 1990's. The focus in this new model is to extend the use for other materials and also for a greater variety of conditions.

This paper presents how the existing model is improved and also discusses the whole problem of modelling such a phenomenon. A sensitivity analysis of modelled mould growth and comparison with measured mould growth are also presented. The experimental set-ups and the results since 2005 from these extensive measurements on many different materials are presented more detailed in another paper to this conference.

1. Introduction

The requirements for durability of the buildings and indoor air quality are growing. Therefore the focus in hygrothermal modelling of whole buildings is moving towards a kind of risk analysis. One of the main risks in this sense is the mould growth and subsequent indoor air quality problems. More severe moisture problems can cause decay of the constructions. However, this paper concentrates on the mould modelling issue and predicting of mould growth. But what is more important, this paper also discusses the whole problem of modelling such a phenomenon. A sensitivity analysis of modelled mould growth and comparison with measured mould growth are also presented.

To understand the biological, chemical and physical phenomenon of the mould in building structures and modelling of it is challenging. However, approaches to model this kind of complex problem have been done and are still going on. The essential basis for a good model is a great amount of good measurements. A large experimental study on 8 different building materials is going on in collaboration with TUT and VTT, Finland. The studies and discussion in this paper are a part of developing of an improved mould growth model based on these experiments that are described in another paper to this conference (Lähdesmäki et al. 2008).

2. The nature of mould growth and modelling of it

The important starting point for the whole mould issue is to understand that mould spores are all over in our surroundings. Therefore we will never get totally rid of mould: The mould growth outdoors will always happen in our temperate climate, unless the building exterior surface is treated with fungicides and/or cleaned regularly. However, to provide durable and healthy buildings, we need to manage the conditions – especially the microclimate and the envelope constructions – in order to reduce the risk for mould growth. In this section, necessary conditions for mould growth are discussed shortly.

A certain **duration** of suitable exposure conditions is required before microbial growth will start. Particular emphasis is focused on this time period, the so-called response time or response duration in different humidity and temperature conditions for mould growth (Viitanen 1996, Hukka and Viitanen 1999). The lowest humidity level for mould growth is around RH 75 – 80 %. The response times have been proved to be short (from a few days to a few weeks) in pine sapwood in conditions favourable to the growth of micro-organisms and long (from a few months to a year) in conditions close to the minimum and maximum moisture or temperature levels. Critical humidity levels at different temperatures for mould growth as a function of duration time of exposure, are shown in Figure 1a.

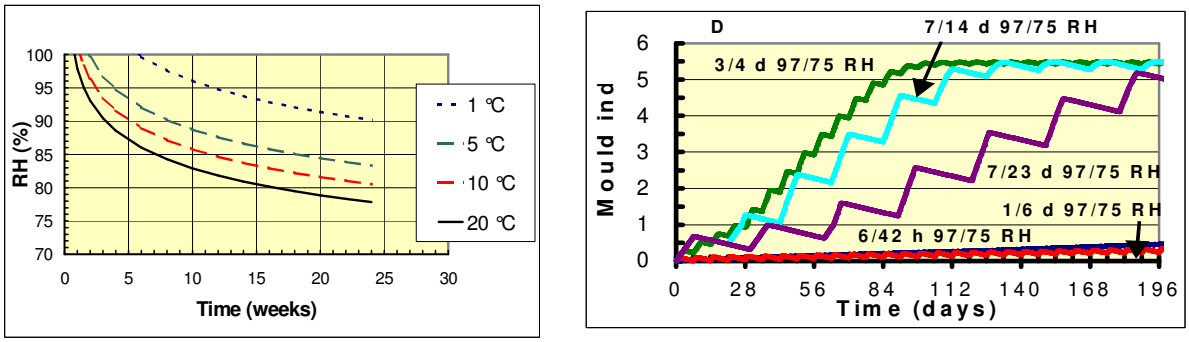

FIG. 1: a) Critical humidity (RH %), time (weeks) and temperature needed for the start of mould growth on pine sapwood (Viitanen et al, 2000). b) Impact of cyclically varying moist and dry periods on mould growth. Both figures are modelled, not measured.

Within fluctuating humidity conditions, the total exposure time for response of growth of mould fungi is affecting by the time periods of high and low humidity conditions as well as the humidity and temperature level. Short periods at high humidity conditions will not cause a fungal growth if the time periods at low humidity preventing mould growth are long enough (Viitanen and Bjurman 1995). When the period at high RH is longer than 24 hours, the effect of cumulative time at high humidity is more linear, but if the dry periods are very long, very low or neglected growth response can be expected. An exposure period at low RH prevents the growth and has a direct effect on the total response time required for mould growth. This is illustrated in Figure 1b.

In the simulation of mould growth it is crucial to know the lowest (threshold) conditions where fungal growth is possible in different material. Also the duration of these conditions is significant. There are certain minimum and maximum levels for moisture content of material (or water activity) or temperature between which fungi can grow in wood. Under these favourable conditions mould growth may start and proceed at different rates depending upon the interrelationship between humidity and temperature and upon other factors such as the organisms and the properties of the materials. There may exist different mould species but the mould index used is based on the growth activity of different mixed mould species. Different mould species depending on the conditions were found in the studies which were used as a data source for the modelling.

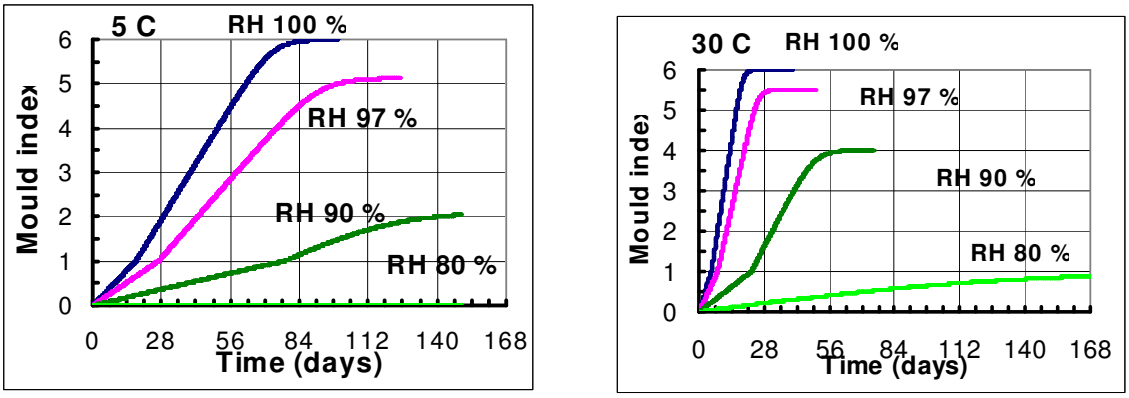

FIG. 2: The critical humidity, temperature and exposure time periods at varied constant conditions for initiation of mould growth on pine sapwood based on VTT mathematical mould growth model (Viitanen et al, 2000).

Time period needed for the initiation of mould growth and growth intensity are mainly regulated by water activity, temperature, exposure time and surface quality of the substrate. The experiments on pine sapwood material supported this theory and based on the results, a mathematical model was developed. The favourable temperature range for mould growth is 0-50 °C, and the critical relative humidity required for initiation and development of mould growth (mould index) is a function of temperature and exposure time (Figure 2).

3. Existing models for predicting mould growth

Two existing models predicting mould growth are presented below. The emphasis is on the models that are propably most comprehensive. Referring other modelling work is omitted here due to limited space.

3.1 VTT model

Mathematical modeling of mould growth has been a research topic at the VTT Technical Research Centre of Finland for many years. The research has included several experimental studies on conditions for mould growth primarily on wood, but also on other building materials. The experimental data has been used to create a mathematical model for mould growth. The present VTT model consists of a mathematical model that also takes into account the delay in mould growth rate due to the unfavourable conditions. There are different mechanisms for situations with delay:

a) the early stages (germination of spores),

b) too dry and too cold conditions and

c) the late stages of mould growth.

The model solves also the growth influenced by fluctuating humidity conditions. Equation (1) solves the mould growth index M as a function of time (weeks) t, temperature T, relative humidity RH, the wood species W (0 = pine and 1 = spruce) and the surface quality SQ from the drying process. k_1 and k_2 are coefficients expressing the delay in early and late stages of growth, respectively. These parameters and the model itself is described more detailed in (Hukka and Viitanen 1999) and (Viitanen et al. 2000).

$$\frac{dM}{dt} = \frac{1}{7 \cdot \exp(-0.68 \ln T - 13.9 \ln RH + 0.14W - 0.33SQ + 66.02)} k_1 k_2 \qquad (1)$$

The first version of this model was created as a part of a dissertation work, (Viitanen 1996), and it is based on a great number of measurements on pine and spruce. The mathematical model was generated with regression analysis of the measured data by Hukka and Viitanen for calculating the development of mould growth, which is expressed as mould index (Hukka and Viitanen 1999). The index is defined as in TABLE 1 and depends on if the growth can be detected using microscopy or visually. There may exist different mould species on a material, therefore this mould index is based on the growth activity of different **mixed** mould species.

TABLE 1: Mould growth index for the experiments and modelling (Viitanen and Ritschkoff 1991).

Index	Growth rate	Description
0	No growth	Spores not activated
1	Small amounts of mould on surface (microscope)	Initial stages of growth
2	<10% coverage of mould on surface (microscope)	
3	10-30% coverage mould on surface (visual)	New spores produced
4	30-70% coverage mould on surface (visual)	Moderate growth
5	> 70% coverage mould on surface (visual)	Plenty of growth
6	Very heavy and tight growth	Coverage around 100%

In the original model presented by Hukka and Viitanen (1999), the delay of mould growth occured only when the relative humidity was below 80% RH. Later the effect of low temperature has been also taken into account assuming that a simple delay process takes place also when temperature is below 0°C. However, the experimental research results from that phenomenon have been earlier limited.

In order to be able to analyse the critical humidity and temperature conditions in building constructions, this VTT model has been implemented in a hygrothermal simulation model TCCC2D (Ojanen et al. 1994, Ojanen 1996). This 2D model solves the transient heat, air and moisture transport fields of a structure that can consist of several material layers. The boundary conditions for the analysed structure can be, for example, hourly changing climate conditions and indoor conditions that have a set increase in humidity compared to outdoor conditions. Measured data can also be used as boundary conditions. The model solves the temperature and moisture content/ relative humidity value for every time step of the solution and for each node of the mesh representing the structure section. The mould growth index values can be solved for each node and the risk for mould growth in wood based or other organic (or soiled) material surface can be predicted.

Also, in a practical oriented moisture performance analysis of timber-framed exterior wall assemblies by Vinha (2007), this VTT mould growth model has been used to determine mould indices from hygrothermal calculation results carried out with WUFI-2D program (Künzel 1995).

At the moment, the model predicts only the mould growth for wood. However, wooden materials are among the most sensitive materials for mould growth and therefore the model can be used as a worst-case-scenario. Nevertheless, a research project to improve the model is going on as collaboration between VTT and TUT. The aim is to formulate a more diversified and improved application of the existing VTT model for mould growth. Some of the improvement aspects are:

- to develop reliability and range of use of the existing mathematical model in fluctuating temperature and humidity conditions
- to increase the number of material choices for the model
- to test usage of the model by doing experiments for structures and materials in laboratory and in field conditions, including the effects of adjacent material layers in a construction

3.2 Biohygrothermal model (WUFI Bio)

Sedlbauer (2001) has studied different models to evaluate spore germination and growth of different mould species on different type of materials. He found, that the isopleths based on artificial medium can be used to evaluate the growth rate of different fungi. He used a biohygrothermal model based on the relative humidity, temperature and exposure time needed for the spore germination of mould fungi based on the osmotic potential of spores. He analysed the effect of different climatic conditions on the spore moisture content and germination. He also evaluated the spore moisture content and germination time based calculated time courses of temperature and relative humidity in various positions of the exterior plaster of an external wall by implementing a model for mould growth in WUFI program (Sedlbauer & Krus 2003). The relationship between the different parameters in the biohygrothermal model is shown in Figure 3, i.e. a mould spore is given hygrothermal material parameters. This enables dynamic calculations, which again give the length and intensity of the conditions for mould growth based on critical limits for different type of materials (e.g. LIM I for bioutilizable substrates, such as wall paper, plaster board, building products made of biologically degradable materials, and LIM II for less bioutilizable substrates such as plasters and mineral building materials).

The time periods in the biohygrothermal model for spore germination are shorter than that of start of the growth (mould index 1) used in the VTT model. Also different type of material affect on the time periods needed for the spore germination.

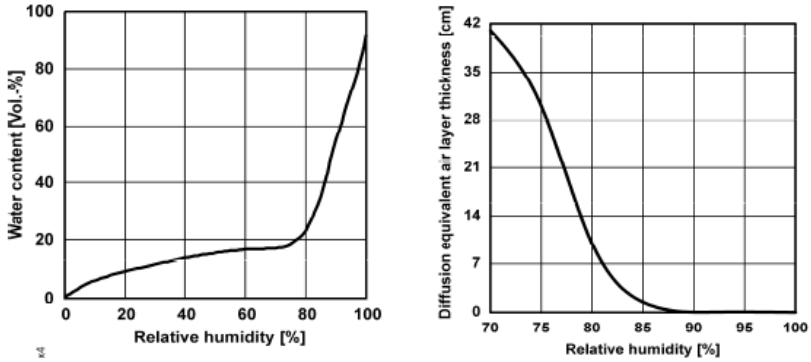

FIG. 3: Hygrothermal "properties" of a mould spore: The relationship between humidity and water content and diffusion resistance of the mould spore. (Sedlbauer & Krus 2003).

4. Sensitivity analysis - VTT Model

The following case study shows an example of how to use a mathematical model for predicting mould growth. The emphasis is on studying the effect of different assumptions on the resulting calculation result – the sensitivity analysis. The above described hygrothermal simulation tool TCCC2D, with the mould index calculation according to VTT-model is used together with field measurements. Also the biohygrothermal model implemented in WufiBio is used for some of the analysis for comparison.

The monitored temperature and humidity conditions from a field test of different building materials were used as boundary conditions for simulations when solving the mould growth for pine. These tests are part of the TUTand VTT collaboration project, still on-going and are presented in another paper (Lähdesmäki et al. 2008). The 48-hour-average values are shown in Figure 4. The detected mould growth level of pine samples were compared to those solved using different approaches for the mould index calculations. The period in focus is almost a year, starting in the summertime.

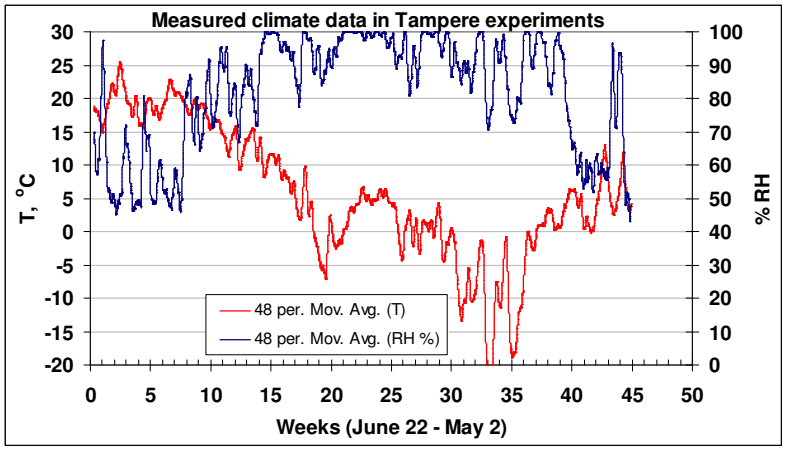

FIG. 4: Measured climate data presented using 48 hour moving average values. The simulations use the original hourly measured data.

4.1 Effect of modelling or not modelling heat and moisture capacity of materials

The first approach was to solve mould growth index for pine assuming that there is no delay between the outdoor and material surface conditions. The surface conditions of the material were assumed to be the same as those measured for the outdoor climate and there were no moisture or thermal capacity of the material that could have

effect on the moisture balance. The possible error caused by this non-capacity simplification was compared with dynamic simulations with TCCC2D, where the solution for mould growth according to VTT model is integrated in the heat, air and moisture field solution.

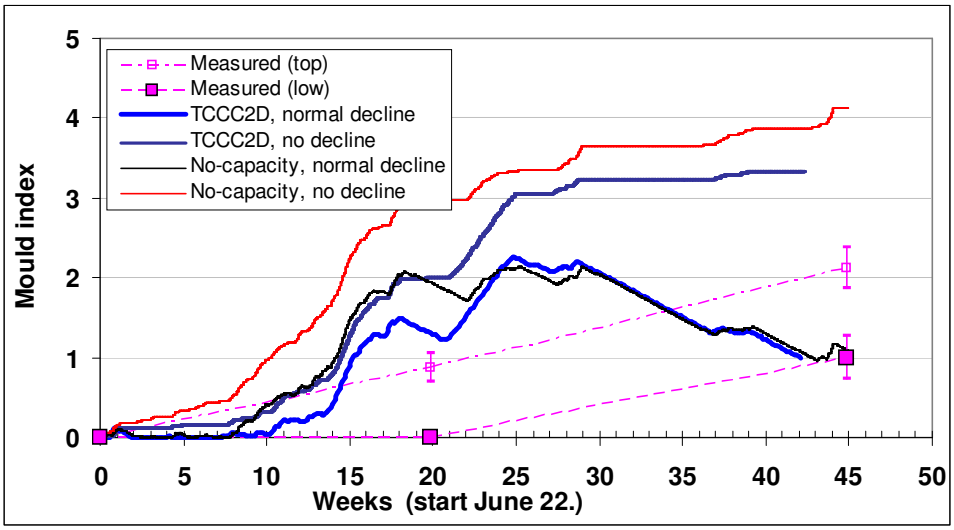

FIG. 5: Prediction of mould growth index of the wooden test board using measured climate data.Mould index was calculated using non-capacity and dynamic simulations (TCCC2D) with two different assumptions for decline of the mould growth. Measured (top) and (low) mould indexes stand for detected growth on the upper side and lower side of the sample. The upper side is exposed for soiling.

The results are seen in Figure 5 together with 2 different assumptions for decline of the mould growth within the model: No decline of mould index or normal decline: If the conditions are not favourable for mould growth – they are too dry or too cold – the mould index will decline according to a certain rate. The model used for decline is based on the measurements under relatively short period (days rather than weeks) dynamic condition cycles and it is meant to represent the delay in the starting of mould growth after a period of unfavourable conditions for the growth. It is obvious that this assumption cannot be totally correct for varying cases, especially for seasonal changes. This is one item that will be solved in the pending project.

The difference between the no capacity -model and dynamic simulations was significant during the first 20 – 22 weeks of simulation. The no capacity -approach predicted mould growth index 1 about two weeks and the level 2 in about 5 weeks before the dynamic solution. Only when the material had reached high enough moisture content, the two solutions had about the same mould growth level. The studied assumptions for decline – no decline vs. decline – gave results where the detected mould index corresponds best with a result which is between the no-decline and normal decline approaches.

4.2 Effect of initial moisture content and convection

The effect of initial moisture content of the material (80 % RH or 65 % RH) was also studied. It did not have any effect on the mould growth. If the conditions had been suitable for mould growth, already in the beginning of the simulation the initial moisture content level could have had some effect on the mould growth.

The moisture transport coefficient of the surface has an effect on the surface conditions and thus also to the mould growth. The case was studied using two different mass transfer coefficient levels: normal convection (with convective heat transfer coefficient 4.0 W/Km^2) and low convection (1.5 W/Km^2). The mass transfer coefficient is solved from the convective heat transfer coefficient.

The results showed a clear effect of surface moisture transfer coefficient on the mould growth of the material surface. With low convection the moisture transport into the material is lower and thus the surface conditions are more stabile under dynamic conditions than with high convection. This leads to lower mould index, in this case. The situation is opposite in a drying situation: If the convection is low, the conditions for mould growth will stay favourable for a longer period and the mould growth index will be higher.

5. Discussion

Prediction of mould growth, however, is always only predicting the risk and not the exact growth. The influence of the uncertainties, whether it is the model itself or e.g. the weather data, is significant. Figure 6 presents partly a comparison of two totally different models – WufiBio (Sedlbauer & Krus 2003) and VTT Model – and partly influence of weather data. In Figure 6 all cases but *"VTT model, normal decline, Espoo climate"*, are determined for measured storage room data, where samples of pine sap wood were exposed to outdoor conditions plus some humidification. *Espoo climate* is normal weather data measured for same period for some 150 km away. As a material class for prediction of mould growth was used pine sapwood (VTT model) and LIM I (Wufi Bio).

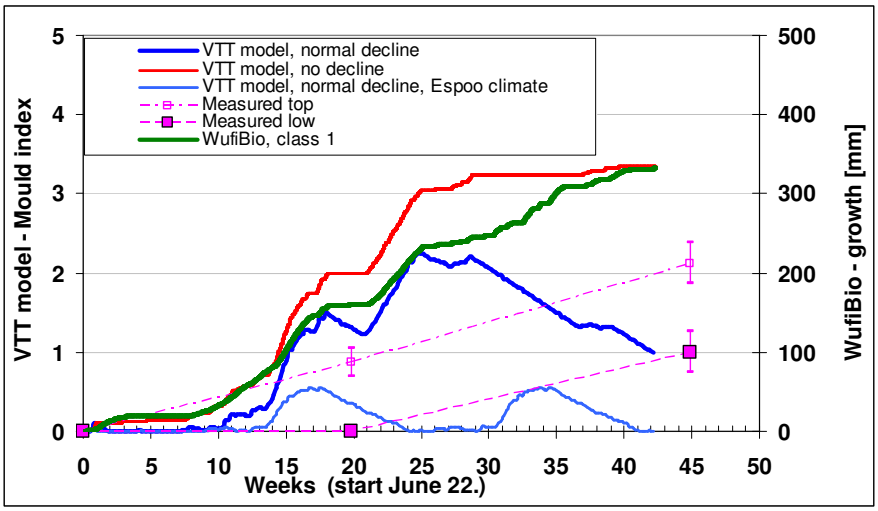

FIG. 6: Comparison of VTT Model and WufiBio – and measured mould index – on pine sap wood. Results with VTT Model have been calculated under several assumptions. "VTT model, no decline" is assumed to most comparable with the biohygrothermal model behind WufiBio.

The comparison of the results shows how sensitive the calculations are. VTT model without decline corresponds relatively well with the biohygrothermal model (Figure 6). This is logical, as the assumption also in the biohygrothermal model is that there is no decline, when the conditions are unfavourable for mould growth. However, there is a difference in the growth rate, especially during longer periods of very high RH: The VTT model predicts here higher growth rate than the biohygrothermal model. The temperature in these periods varies roughly from +10ºC to 0ºC. In contrary, when the temperature stays below zero, the mould growth rate according to biohygrothermal model is still active, while it is practically stopped according to VTT model. Nevertheless, this is a very simplified approach for an explanation as the models include several parameters that have effects in various directions. Yet another source for uncertainty and deviation for the results when predicting mould growth with any model is the choice of the critical level of e.g. temperature and humidity conditions. These conditions vary a lot depending on the material itself. In addition, any soiling during the time will change the sensibility of the surface for mould growth. Therefore, prediction of mould growth with calculations must always be assessed with expert knowledge on the nature of mould growth.

There are several aspects that have to be taken into account in the interpretation of the experiments and analysis of the mould growth levels: Under **dynamic tests** the conditions at the interface of the air and test sample are typically different than the air conditions adjacent to the test sample. Therefore it may cause errors if the measured dynamic climate conditions are used as the critical surface conditions. Even in constant conditions the **initial moisture content** of the test material should be known and reduced from the measured data. Under dynamic conditions the thermal and moisture **capacity** of material and the heat and mass **transfer coefficients** on the surface may cause a severe delay in the change of surface conditions, differences in the humidity level and in the mould growth when compared to the adjacent conditions. Dynamic simulation that solves the surface conditions should be used both in the analysis of dynamic mould experiments and when predicting the mould growth in structures under real climate conditions. The use of full simulation enables to separate the delay in the actual mould growth from the delay in the surface conditions. The existing VTT-model has **declination of**

mould index when the conditions are not suitable for growth. The origin was to model the delay of mould growth during the short period dynamic conditions (some days). This declination seems to be artificial and probably not proper to adopt in seasonal conditions. New seasonal experiments should provide information about the mould growth during and after too dry or cold conditions, which enables the improved modelling of the phenomena.

6. Conclusion

This paper has taken up the issue of modelling mould growth in building envelopes. There exist some model developments in different research institutions. Among them, there exists some kind of consensus about the overall criteria for mould growth as a function of temperature, relative humidity and time. Nevertheless, there is very little knowledge on mould growth on different kind of materials and effects of the aging of materials, coatings and dust accumulation on the mould growth.

The mould growth model can be used to study the risks for mould growth on (wooden) material surface when the surface conditions (temperature and relative humidity) are known. Typically the conditions vary dynamically and their hourly values should be known to be able to study the mould growth. Long period (daily, weekly. etc.) time averaged values may not show the risks of the actual conditions, i.e. the peak humidity levels etc. on the mould growth. The same kind of error may be caused when the adjacent climate conditions are used as critical conditions instead of the actual surface conditions. Therefore the effect of the structure and material should always be taken into account when solving the critical conditions for the mould growth.

7. References

Hukka A. & Viitanen H. (1999). A mathematical model of mould growth on wooden material. Wood Science and Technology 33(6): 475-485.

Künzel, H.M. 1995. Simultaneous Heat and Moistur Transport in Building Components – One- and Two-dimensional calculations using simple parameters. IRP Verlag, Stuttgart

Lähdesmäki K., Vinha J., Viitanen H., Salminen K., Peuhkuri R., Ojanen T., Paajanen L., Iitti H. & Strander T. (2008). Development of an improved model for mould growth: Laboratory and field experiments. Proceedings of 8th Nordic Symposium on Building Physics, Copenhagen.

Ojanen T., Kohonen R. & Kumaran M. (1994). Modeling HAM transport through building materials and components. Moisture Control in Buildings. Ed. H.R. Trechsel. ASTM. Philadelphia , pp. 18-34.

Ojanen T. (1996). Evaluation of simulation model TCCC2D using simplified weather data and material properties. IEA/Annex 24 Closing Seminar. Espoo 1996. Katholieke Universiteit Leuven. 22 p.

Sedlbauer K. (2001). Prediction of mould fungus formation on the surface of/and inside building components. University of Stuttgart, Fraunhofer Institute for building Physics, Doctoral thesis. Stuttgart. Germany.

Sedlbauer K. & Krus, M. (2003). A new model for mould prediction and its application in practice. In Research in Building Physics. Ed. by Carmelit et al. Proc. of 2nd International conference on Building Physics.

Viitanen H. (1996). Factors affecting the development of mould and brown rot decay in wooden material and wooden structures. Effect of humidity, temperature and exposure time. Doctoral thesis. Uppsala. The Swedish University of Agricultural Sciences, Department of Forest Products. 58 p.

Viitanen H., Hanhijärvi A., Hukka A. & Koskela K. (2000). Modelling mould growth and decay damages Healthy Buildings. Espoo, 6 - 10 August 2000. Vol. 3. FISIAQ, 2000, p. 341–346.

Viitanen H. & Bjurman J. (1995). Mould growth on wood under fluctuating humidity conditions. Mat. und Org. 29(1): 27-46.

Viitanen H. & Ritschkoff A. (1991). Mould growth in pine and spruce sapwood in relation to air humidity and temperature. Uppsala. The Swedish University of Agricultural Scienses, Department of Forest Products. Report no 221. 40 p + app 9 p.

Vinha J. (2007). Hygrothermal performance of timber-framed external wall in finnish climatic conditions: A method for determinig the sufficient water vapour resistance of the interior lining of a wall assembly. Doctoral thesis. Tampere. Tampere University of Technology. Publication 658. 338 p. + app. 10 p.

Development of an improved model for mould growth: Laboratory and field experiments

Kimmo Lähdesmäki, M.Sc. Student,1)
kimmo.lahdesmaki@tut.fi

Juha Vinha, Dr.Tech.,1)
juha.vinha@tut.fi

Hannu Viitanen, Ph.D., 2)
hannu.viitanen@vtt.fi

Kati Salminen, M.Sc., 1)
kati.salminen@tut.fi

Ruut Peuhkuri, Ph.D.,2)
ruut.peuhkuri@vtt.fi

Tuomo Ojanen, M.Sc., 2)
tuomo.ojanen@vtt.fi

Leena Paajanen, M.Sc., 2)
leena.paajanen@vtt.fi

Hanna Iitti, M.Sc., 2)
hanna.iitti@vtt.fi

Tomi Strander, M.Sc., 1)
tomi.strander@tut.fi

1) Department of Civil Engineering, Tampere University of Technology, Finland;
2) Technical Research Centre of Finland, Finland;

KEYWORDS: *mould growth, experiments, materials, laboratory test, field test*

SUMMARY:

This paper deals with the present results of some on-going mould growth experiments from a project "A Mathematical Modelling of Moisture Behaviour and Mould Growth in Building Envelopes". The work has been done in collaboration with Tampere University of Technology, Finland (TUT) and Technical Research Centre of Finland (VTT). The material experiments and experiments for exterior wall assemblies are performed both in laboratory and in field conditions. Mould growth on the surface of a material is detected using either microscope or visually with a naked eye. Determination of mould index depends on area of mould growth and type of mould growth. Experiments started in 2005 and will be going on at least until end of 2008.

The experimental results are used for further development of a present mould growth predicting model developed at VTT. The original model is based on numerous laboratory experiments on pine and spruce. The present model is improved in respect to expanded climatic conditions and for a greater variety of materials. Also the impact of naturally sedimented dirt and contact of other materials are studied.

The results until now show generally less mould growth than espected according to the original model based on pine and spruce sapwood.

1. Introduction

Mould growth in building materials has been an important research topic at the Tampere University of Technology (TUT) and Technical Research Centre of Finland (VTT) for many years. At TUT mould growth of envelope assemblies has been analysed in several field test projects during past decade. Moreover, numerous condition analyses have been done in old buildings and, therefore, a lot of experience has been got from muold growth in practice. At VTT a mathematical model of mould growth on pine and spruce sapwood was created in 1990's by Ph.D. Hannu Viitanen (Viitanen 1996). This model includes a mathematical basic model on humidity, temperature and exposure time, and it also takes into account the delay and influence of fluctuating humidity conditions (Hukka and Viitanen 1999 and Viitanen et al. 2000).

In this new collaboration project with TUT and VTT eight other construction materials have been tested in the laboratory and field set-ups. The test materials are edge-glued spruce board, polyurethane (paper-coated and grounded), glass wool, expanded polystyrene, polyester wool, concrete, autoclaved aerated concrete and expanded light aggregate concrete. The reference material is pine sapwood. The experiments have been performed partly under constant conditions and partly also under fluctuating moisture and temperature conditions both in the laboratory and in the field. One of the objectives of this research is to extend the range and reliability of the existing mathematical model. This is achieved by extending the measurement data necessary for the model development by applying several materials and different kind of fluctuating temperature and humidity conditions. New experimental results from the mould growth on different material surfaces and in exterior wall assemblies are presented in this paper. More detailed information from existing model is presented in another paper to this conference (Viitanen et al. 2008).

2. Determination of mould growth

Mould fungus needs favourable conditions to grow. Simplified these conditions can be expressed as that the temperature has to be between 0 and 50°C and relative humidity has to be at least 80% RH (when temperature is below 20°C even more). The exposing time under fluctuated conditions and the nutrient base have also influence on mould growth (Viitanen and Bjurman 1995). In Figure 1 are shown the favourable temperature and moisture conditions for mould growth.

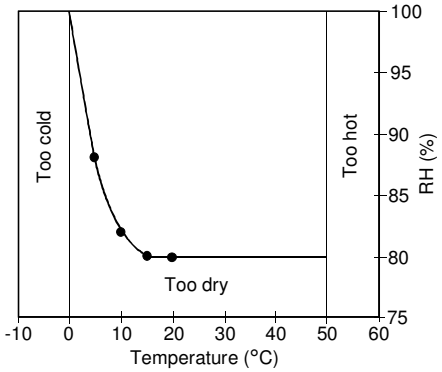

The mould growth on the surface of a material can be detected using microscope or visually with a naked eye. Determination of mould index depends on area of mould growth and the type of mould growth (detected under microscopy or without). In Table 1 are shown indexes for mould growth characterization. The index is based on the growth of mixed different fungus species (Viitanen and Ritschkoff 1991).

FIG. 1: Favourable temperature and relative humidity conditions for mould growth (Viitanen and Bjurman 1995).

TABLE 1: Mould growth index for the experiments and modelling.

Index	Growth rate	Description
0	No growth	Spores not activated
1	Small amounts of mould on surface (microscope)	Initial stages of growth
2	<10% coverage of mould on surface (microscope)	
3	10 – 30% coverage mould on surface (visual)	New spores produced
4	30 – 70% coverage mould on surface (visual)	Moderate growth
5	> 70% coverage mould on surface (visual)	Plenty of growth
6	Very heavy and tight growth	Coverage around 100%

3. Experimental arrangement of mould experiments

In the following, the experimental laboratory and field set-ups are described. There have been tested plain materials and the materials as a part of a thermal envelope construction.

3.1 Material experiments

Material experiments are performed for all test materials. Most of the specimens are sized 50mm x 50mm x 20mm. Test series consists of nine specimens. Each test series contain material from three different production runs. Reference material is pine sapwood. Material experiments are performed in different laboratory conditions and also in outdoor conditions in the shelter.

3.1.1 Material experiments in laboratory

Laboratory experiments for materials include seven different conditions. Most of the experiments are performed in constant conditions but some experiments are performed in fluctuating conditions in a way that two different conditions vary cyclically. In Table 2 are shown the target test conditions for material experiments in laboratory.

TABLE. 2: Target test conditions of the material experiments in laboratory.

Constant/cyclical conditions	Test condition 1	Test condition 2
Constant	97% RH / 22°C	
Cycle 4 – 8 weeks	97% RH / 22°C	97% RH / -5°C
Cycle 4 – 8 weeks	97% RH / 22°C	97% RH / -20°C
Cycle 4 – 8 weeks	97% RH / 22°C	50% RH / 22°C
Constant	97% RH / 5°C	
Constant	97% RH / -5°C	
Constant	90% RH / 22°C	
Constant	90% RH / 5°C	

One or two surfaces of the specimens were sprayed with mould suspension before the experiments started. The specimens are stored in closed plastic boxes with saturated salt solutions during the experiments to achieve the wanted humidity conditions.

3.1.2 Material experiments in field conditions

The material experiments in field conditions take place in the shelter. The wall structure of the shelter is designed so that temperature and relative humidity are same as in open-air conditions but specimens are sheltered against sun, rain and snow. Three data-loggers measure temperature and relative humidity in the shelter. This experiment is performed for all test materials. There are two different sized specimens: small specimens are approximately sized 50 mm × 50 mm × 20 mm and large specimens are approximately sized 300 mm × 300 mm × 50 mm. Some of them are seen in Figure 2. The specimens were not treated with mould suspension before the experiments started.

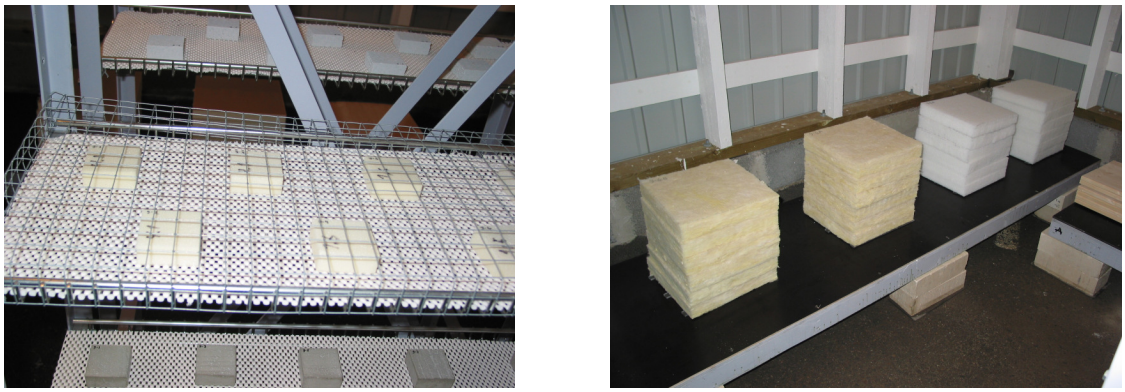

FIG. 2: The small specimens are placed on the steel shelves (on the left) and the piled specimens are palced on the platforms (on the right).

The small specimens are placed on the steel shelves (Figure 2). One test series consists of nine specimens. There are three extra stone based materials and wood specimens. These specimens were soaked in water for seven days before the experiments started.

The 300 mm × 300 mm × 50 mm sized specimens are piled up like in a storage. One pile consists of six specimens. There are two piles of all materials. The other pile of stone material and wood specimen were soaked in water for nine days before the experiments started. The specimens are placed on the platforms (Figure 2).

3.2 Experiments for exterior wall assemblies

The experiments for exterior wall assemblies are done both in laboratory and in field conditions. Purpose of these experiments is to study mould growth inside the assembly in the interface of two materials. Temperature and relative humidity of the interface is measured with temperature and relative humidity sensors. Experiments are done with studied materials so that each insulating material (glass wool, paper-coated polyurethane (PUR), expanded polystyrene (EPS) and polyester wool) form a structural combination with other studied materials (edge-glued spruce board, concrete, autoclaved aerated concrete and expanded clay aggregate concrete). The ground polyurethane is not tested in these wall assembly experiments.

3.2.1 Laboratory experiments for exterior wall assemblies

Laboratory experiments for assemblies are performed in two separate test series. Each series covers eight different exterior walls; thus a total of 16 different combinations are studied in the experiments. Size of one wall is 600 × 800 mm^2. The assemblies covered in the test series are listed in the Table 3. The experiments are performed in three different test phases. In the first phase, the assemblies are kept in a climate chamber under constant conditions (approx. 20 – 22°C / 95 – 97% RH). This arrangement is portrayed in Figure 3.

TABLE 3: The tested assemblies in the laboratory experiments.

First test series	Second test series
autoclaved aerated concrete + glass wool	autoclaved aerated concrete + polyurethane
autoclaved aerated concrete + polyester wool	autoclaved aerated concrete + expanded polystyrene
edge-glued spruce board + glass wool	edge-glued spruce board + polyurethane
edge-glued spruce board + polyester wool	edge-glued spruce board + expanded polystyrene
expanded clay aggregate concrete + glass wool	expanded clay aggregate concrete + polyurethane
expanded clay aggregate concrete + polyester wool	expanded clay aggregate concrete + expanded polystyrene
concrete + glass wool	concrete + polyurethane
concrete + polyester wool	concrete + expanded polystyrene

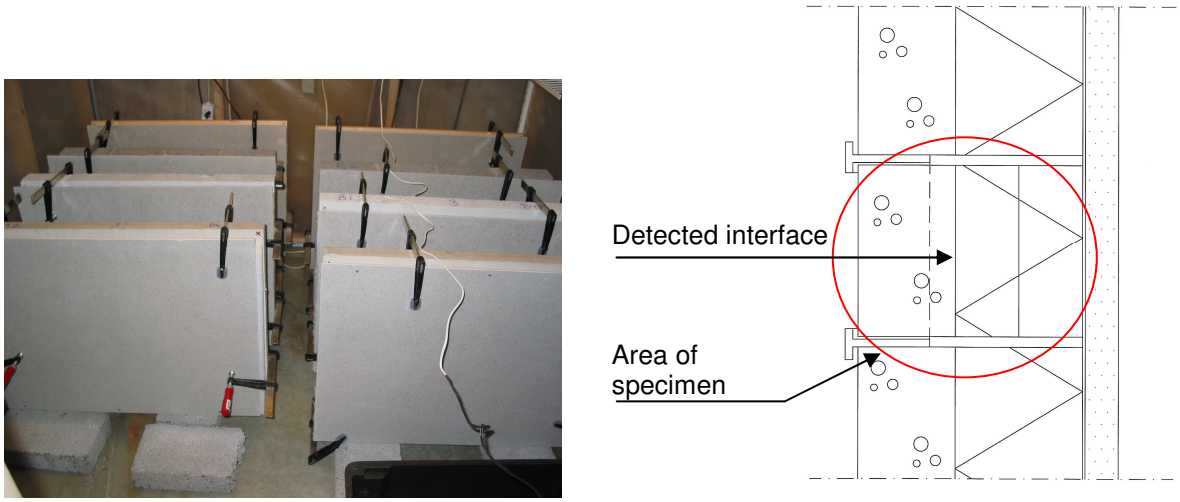

FIG. 3: The tested exterior wall assemblies in the climate chamber (on the left). The principle of the test specimen (on the right).

The second phase (winter) and the third phase (spring) of the experiments are performed in the weatherisation equipment. The tested assemblies are placed into the steel frame between the climate chambers. In the interface of façade and insulation material temperature is approximately -8 to -2°C and relative humidity 95 to 100% RH during the winter phase. During the spring phase temperature in the interface is from a few degrees below zero to 10 to 15°C. There is not relative humidity control in during the spring phase but a fast fluctuating temperature.

The mould growth in the interface is checked regularly. Diameter of the test specimen cylinder is approximately 70 mm. The specimen is settled into the plastic pipe so that it is easy to pull out from assembly and also diffusion is possible through the specimen. The principle of the test specimen is shown in figure 3.

3.2.2 Field experiments for exterior wall assemblies

The field experiments of wall assemblies are performed in the test building on the test field. There are installed two wall modules facing north and south. The module is divided into 4 separate exterior wall assemblies (Figure 4). The assemblies are same in both wall modules. The tested material combinations are edge-glued spruce board-glass wool, edge-glued spruce board – paper-coated polyurethane, edge-glued spruce board-expanded polystyrene and edge-glued spruce board-polyester wool. There are four specimens in every test assembly. Wood material of two specimens is edge-glued spruce board and of the other two is pine sapwood. There is also one specimen with a little piece of wood inside of it. This piece of wood is weighted regularly to determine the moisture content of wood and to check the relative humidity inside the assembly. There is also temperature and relative humidity sensors inside every assembly. The test walls are sheltered from driving rain with plywood boards.

The indoor temperature of the test house is approximately 20°C and moisture supply has been varied between 3 and 7g/m^3. Outdoor air conditions are measured by temperature and relative humidity sensors.

FIG. 4: The test building (on the left) and the wall module which is divided into four different exterior wall assemblies (on the right).

4. Results of mould experiments

4.1 Material experiments

4.1.1 Material experiments in laboratory

Growth of mould fungi was detected in all tested materials after different exposure time periods in high humidity exposure conditions (97% RH and 22°C). The mould growth on specimens has been detected with naked eye and using light microscope. In the pine sapwood, the first stage of growth (index 1) was found after one week exposure and index 3 (first visual symptoms) was detected after 4 – 8 weeks from the beginning of the test, depending on the test series (Figure 5). When the exposure progressed the highest mould index was detected in

pine sapwood. The mould fungi were mostly *Penicillium*- and *Aspergillus*-types. These same mould fungi were detected also in edge-glued spruce board (Spruce Gluelam), but less and much later than in pine sapwood. Also in the paper layer of polyurethane, the mould index 1 was detected after 4 – 8 weeks, only in surfaces where spore suspension were sprayed. On the upper side of glass wool where spore suspension was sprayed, first sign of mould growth was detected after 4 – 8 weeks. On the under side, the development of mould index was significant retarded. The same type of growth response was found for other insulation material.

When the exposing time continued, mould growth was detected in all studied materials. Plenty of thin mould hyphae were detected in autoclaved aerated concrete and in expanded clay aggregate concrete. These mould fungi were detected only using microscope. It was not possible to see it with the naked eye altought there were lots of greenish pores. Most of the mould fungi were *Paecilomyces*-typed, but also *Aspergillus*-typed were common. Thin hyphae were also detected in the concrete specimens especially in "open surface pores". In concrete were also in places detected dark *Cladosporium*-mould hyphae for index 3. In light coloured materials mould hyphae could be easily found which may affect the mould index level.

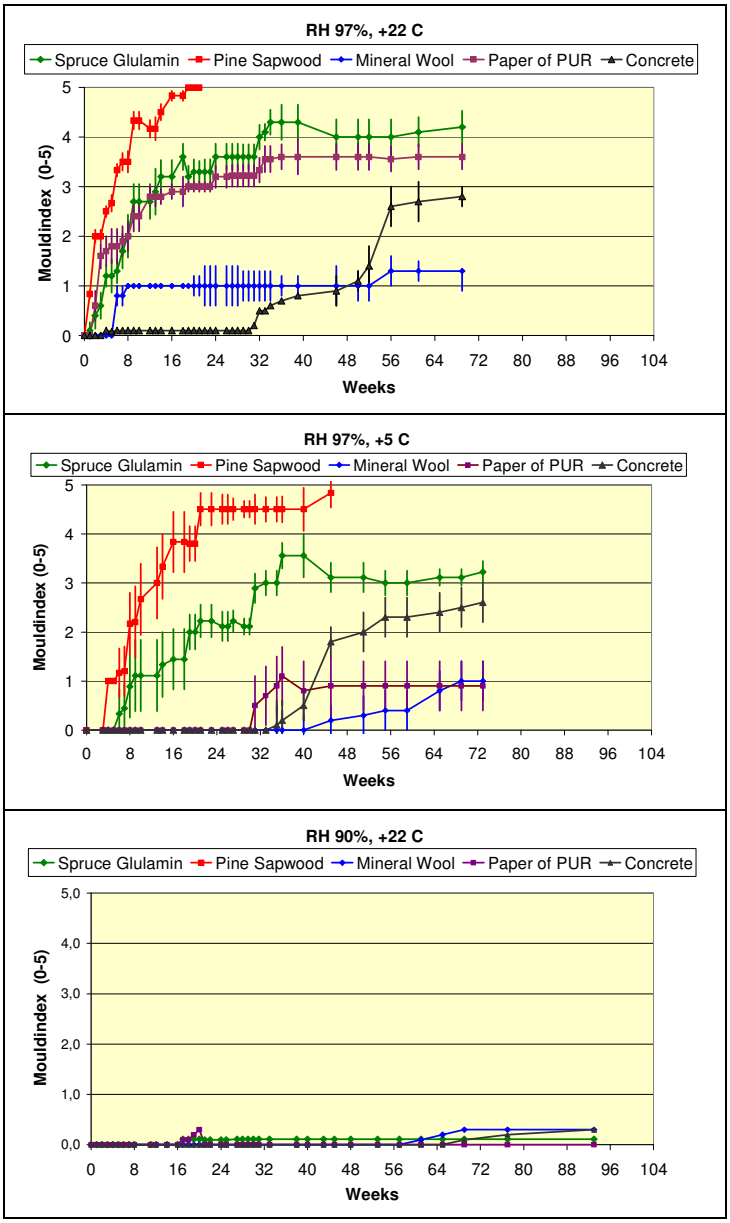

FIG. 5: Results on mould index development under constant high humidity conditions of 97% RH at 22°C and 5°C and humidity conditions of 90% RH and 22°C.

The mould growth type and intensity was different depending on the material. On paper coating of polyurethane mould fungi was also very dark and different from other moulds that were found. Only a slight growth response was found on the glass wool (like also other insulation materials). The solidity of glass wool seemed to weaken in the course of time what can affect the mould resistance. In glass wool there was mostly dark mould but also in some places light, soft mould with green spores.

Under lower humidity conditions (90% RH), no growth of mould fungi was detected in stone based materials and growth on wood-based and paper-coated products was retarded and slight. The growth at low temperatures (5°C) was also retarded.

4.1.2 Material experiments in field conditions

Mould growth in the field test materials is checked about every half a year, in spring and in autumn. The small specimens (50mm × 50mm × 20mm) are checked under microscope and the piled specimens (300 mm × 300mm × 50mm) are checked using loupe.

After five months from the beginning of the experiments the mould growth of the specimens was checked first time. On the upper surfaces of the specimens was a layer of organic dirt (for example pollen). Mould growth was detected under microscope (index 1 – 2) only on the surfaces of the small wood specimens. In the following checks mould growth was detected in the organic dirt. On the surface of the material there was more dirt if there were different open pores or microscopic holes. On the upper surfaces of the specimens is detected more mould growth than on the under side surfaces. The unexpected result is that in stone based materials there was detected more or the same degree of mould growth as in wood materials.

After 16 months from the beginning of the experiments there was mould growth on the upper surfaces of every material. The highest mould indexes were detected in paper coating of polyurethane (index 2.2) and in pine sap wood (index 2.1). The indexes are averages of nine specimens. In these materials was also visually detected mould growth (index 3). There was mould growth also on the under surfaces of edge-glued spruce board specimens which had been soaked in water. The lowest mould indexes were detected in polyester wool (mean value index 0.3) and in ground polyurethane (mean value index 0.3).

4.2 Experiments for exterior wall assemblies

4.2.1 Laboratory experiments for exterior wall assemblies

The exterior wall assemblies of the first series were approximately 7 months in the conditions of the first phase (autumn), approximately 4 months in the conditions of the second phase (winter) and approximately 6 months in the conditions of the third phase (spring). After the third phase the exterior wall assemblies are in the autumn phase again. The tested structures were treated with mould suspension before the experiments started.

After about three months from the beginning of the experiments mould growth was detected on the surfaces of edge-glued spruce board. In edge-glued spruce board – glass wool –combination was detected index 1 and in edge-glued spruce board – polyester wool –combination index 3. Mould growth was not detected on the surfaces of glass wool and polyester wool. After six months from the beginning of the test the mould indexes on the surfaces of the edge-glued spruce board specimens varied between 1 and 3. The mould indexes in the other materials varied between 0 and 1.

In the end of the first phase there were still highest mould index values on the surfaces of edge-glued spruce board. In edge-glued spruce board – glass wool –combination the indexes varied between 2 and 3 and in edge-glued spruce board – polyester wool –combination between 1 and 3. The mould indexes on the surfaces of the glass wool specimen were between 1 and 2 depended on the assembly. On the surfaces on polyester wool the index was 1, on the surfaces of autoclaved aerated concrete indexes were between 0 and 1 and on the surfaces on concrete the index was 1.

After three months from the beginning of the second phase there was not increase in mould growth in any material. On the surfaces of some materials like autoclaved aerated concrete the mould indexes were decreased one figure. The mould indexes on the surfaces on the wood specimen were same as in the end of the first phase.

After third phase the mould indexes were at same level as in the end of the second phase. Another autumn phase is still going on.

The exterior wall assemblies of the second series were in the conditions of the first phase about 7 months. The highest mould indexes were detected on the surfaces of concrete with both insulation materials. The indexes varied between 2 and 3. The mould index on the paper surfaces of polyurethane was 2 in autoclaved aerated concrete – polyurethane, concrete – polyurethane and wood – polyurethane combinations. The mould index on the paper surface of polyurethane was between 1 and 2 in expanded clay aggregate concrete – polyurethane combination. The mould index of expanded polystyrene was 2 with expanded clay aggregate concrete and autoclaved aerated concrete and the mould index of expanded polystyrene was 1 in another combinations. On the surfaces of the edge-glued spruce board specimens the mould indexes were 2. The exterior wall assemblies of the second series are in second phase at the moment.

4.2.2 Field experiments for exterior wall assemblies

The field experiments for exterior wall assemblies started approximately 13 months ago. The mould growth was checked after 5 and 11 months from the beginning of the experiment. The mould growth was not detected in any material. The temperature inside the tested assemblies was between -10 and 20°C. The relative humidity of the interfaces of expanded polystyrene and also of edge-glued spruce board and paper-coated polyurethane and edge-glued spruce board was between 50 and 70% RH. Inside the glass wool and polyester wool assemblies the relative humidity was between 70 and 90% RH.

5. Conclusion

Laboratory and field tests have been performed on eight different building materials and wall assemblies as combinations of these. The aim was to provocate mould growth and to follow the development of it. The motivation is to gain knowledge and experimental data for further mould modelling development work. The results will give valuable information on mould growth on some very different but common building materials and also whether a condition is critical or not.

There was detected mould growth in every material for the conditions where the target relative humidity was 97% RH. The highest mould indexes were found on pine wood, spruce (glue board) and papercoating of polyurethane. The present results of the experiments in the cyclical conditions are variable. It is possible that temperature -20°C has less influence on mould growth than temperature -5°C. In the conditions where target relative humidity is 90% RH, the detected mould indexes were very small, even for 22°C. It is important to notify that the detected mould growth has been insignificant (mould index ≤ 3) until now. In common usage of the tested construction materials, there may be a dirt layer on the surface that can cause some mould growth (index 1 – 2). However, the mould index will not likely increase further, if the dirt layer is the only reason for mould growth.

6. References

Viitanen H. (1996). Factors affecting the development of mould and brown rot decay in wooden material and wooden structures. Effect of humidity, temperature and exposure time. Doctoral Thesis. Uppsala. The Swedish University of Agricultural Sciences, Department of Forest Products. 58 p

Hukka A. & Viitanen H. (1999). A mathematical model of mould growth on wooden material. Wood Science and Technology 33(6): 475-485

Viitanen H., Hanhijärvi A., Hukka A. & Koskela K. (2000). Modelling mould growth and decay damages Healthy Buildings. Espoo, 6 - 10 August 2000. Vol. 3. FISIAQ, 2000, p. 341–346.

Viitanen H. & Bjurman J. (1995). Mould growth on wood under fluctuating humidity conditions. Mat. und Org. 29(1): 27-46.

Viitanen H. & Ritschkoff A. (1991). Mould growth in pine and spruce sapwood in relation to air humidity and temperature. Uppsala. The Swedish University of Agricultural Scienses, Department of Forest Products. Report no 221. 40 p + app 9 p.

Viitanen H., Vinha J., Peuhkuri R., Ojanen T., Lähdesmäki K. & Salminen K. (2008). Development of an improved model for mould growth: Modelling. Proceedings of 8th Nordic Symposium on Building Physics, Copenhagen.

Investigation of Microbial Volatile Organic Compounds and their Transport through the Building Envelope

Caroline. Hachem, Master's student,
Building Envelope Performance Laboratory (BEPL), CBS, Department of
Building Civil and Environmental Engineering (BCEE), Concordia University;
c_hachem@encs.concordia.ca

Paul Fazio, Professor,
BEPL, Centre for Building Studies (CBS), BCEE, Concordia University;
fazio@alcor.concordia.ca, http://www.bcee.concordia.ca/index.php/Dr._P._Fazio

Jiwu Rao, PhD,
BEPL, CBS, BCEE, Concordia University; raojw@alcor.concordia.ca

Karen Bartlett, Professor,
Associate Professor, School of Environmental Health, University of British Columbia;
kbartlet@interchange.ubc.ca

Yogendra P. Chaubey, Professor and Chair,
Dept. of Mathematics & Statistics, Concordia University;
chaubey@alcor.concordia.ca

KEYWORDS*: microbial volatile organic compound (MVOC), mold, stud wall, SPME VOC sampling, gas chromatography, mass spectrometry, multiple regression analysis.*

SUMMARY:

Full-scale wall specimens were constructed and tested to investigate the capacity of wall cavities to restrain mold products, emanating from studs with 10% of their surfaces covered with mold, from penetrating into the indoor space. The project was designed primarily to study the movement of spores. Tests were subsequently extended to investigate the identification of microbial volatile organic compounds (MVOCs) and their transport through the building envelope. This paper presents the approaches and results in the identification of the mold related VOCs, analyses of the MVOC transport from the cavity to the indoor space, and estimation of the influence of experimental parameters on this transport. The parameters investigated were: air leakage path; mold presence; wall construction configurations (insulation, vapor barrier and sheathing material) and ambient conditions (dry and wet conditions). The analysis of VOCs (volatile organic compounds) was performed using gas chromatography/ mass spectrometry (GC/MS) and the results were analyzed using multiple regression analysis to identify the mold related VOCs, and to determine the transport through the building envelope. Five VOCs were confirmed to be related to the mold presence in the cavity and the transport of these MVOCs was supported by these data. However no significant effect of the construction parameters was detected.

1. Introduction

Complex mixtures of volatile organic compounds (VOCs) are produced as metabolic by-products of fungal growth, and are detectable, in building environment, before visible indication of such growth. The emission of MVOCs is affected by different factors including, but not restricted to, the substrate, moisture content of the material and temperature (Sunesson et al., 1995). MVOCs can be used as a tracer of suspected or hidden microbial contamination, as well as in detection of moisture problems, risk of fungal development and sources of odours in buildings (e.g. Schleibinger et al., 2008; Fischer et al., 1999; Wessen and Schoeps, 1996). However, emission of volatile compounds in the indoor space is not restricted to mold growth. A large range of similar VOCs are generated by biogenic and nonbiogenic sources. Products used in buildings such as solvents, paints, and adhesives, as well as new furniture, release analogous VOCs, thus complicating the identification of MVOCs generated by mold contamination sources.

The experiment presented in this paper was originally designed to investigate the movement of spores, and was subsequently extended to include MVOCs sampling. The initial concept, design and results from trial runs of this project were published in Fazio et al. (2005). Subsequent to these initial trials, improvements were made to the test setup, material selection, and sampling methods. While the test program as a whole explores both spore and MVOC productions, the present paper is concerned only with the analysis of MVOC products. The objectives of this paper are to: a) identify mold-specific MVOCs; and b) assess the influence of wall construction parameters and air leakage on the transport of VOCs from the cavity to the indoor space.

2. Experimental design

Full size specimens of residential wood frame walls were designed and constructed in accordance with standard practice. The mold source was incorporated on the vertical studs on which molds had been grown to a relatively consistent coverage of 10%. Three different types of molds (*Aspergillus niger*, *Aureobasidium pullulans* and *Penicillium citrinum*) contributed to the levels of MVOCs within the specimen.

2.1 Test parameters

The parameters investigated in this research were related to air leakage characteristics, contamination, wall construction characteristics and moisture conditions, as listed in Table 1.

Parameters related to air leakage characteristics consisted of two designs of air leakage path: direct and long (Desmarrais et al., 1998). Parameters related to wall construction design were insulation, vapor barrier and sheathing material. Two different environmental conditions were tested, the first set under dry conditions and the second set after exposure of the specimens to simulated wet conditions. In all, six parameters are included under four categories. Most of the parameters were tested at two levels, as detailed in Table 1.

TABLE 1: Parameters selected for testing

Category	Design Parameter	Level	Symbol
Ambient conditions	Relative humidity	wet, dry	X_1
Contamination	Mold on studs	moldy, clear	X_2
Wall construction	Insulation	yes, no	X_3
	Vapor barrier	yes, no	X_4
	Sheathing	OSB, plywood, fiberboard	X_5
Air leakage	Air leakage path	direct, long	X_6

2.2 Specimen design

Each specimen consisted of: an outer plywood enclosure of dimensions of 889 mm wide by 2,404 mm high (Fig. 1(a)); a full stud cavity comprising two vertical studs and top and bottom plates; "guarded" zones of half stud cavities on both sides; the different layers of the envelope, namely (from inside to outside): drywall, vapor barrier, insulation, and sheathing (Fig. 1(b)). The outer layers of the envelope, i.e. the weather membrane and siding/cladding, were not included with the specimens.

In preparation of each specimen, all joints along the perimeter of the outer sheathing board were sealed with silicone caulking to eliminate air leakage from the edges of the sheathing and to restrict air leakage to the predetermined paths. Additional details about the specimen construction are presented in Rao et al. (2006).

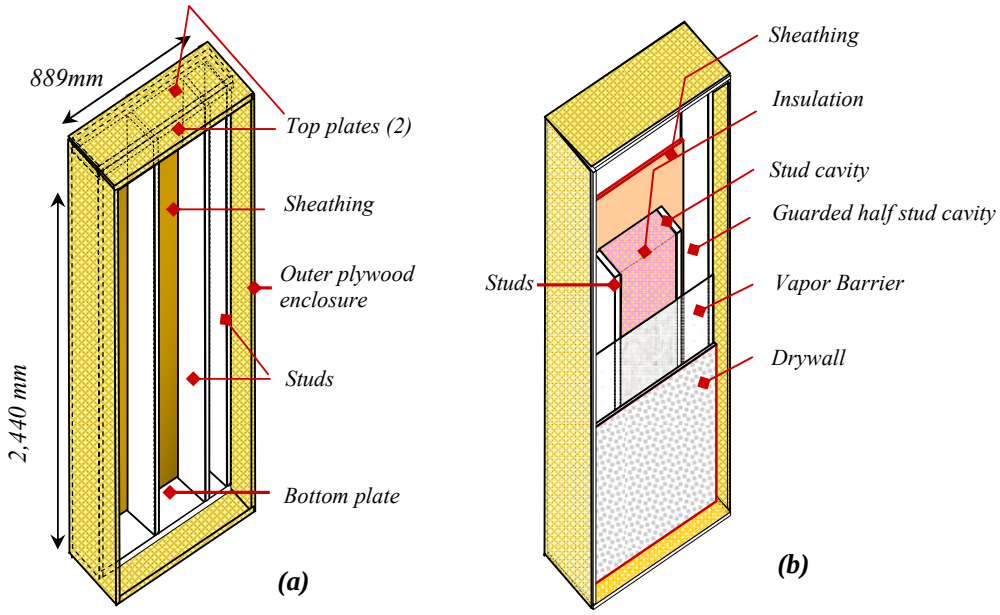

FIG 1: Isometric view of a specimen (a) specimen frame, (b) components of a specimen

2.3 Depressurization system

A stainless steel sampling chamber was designed to cover the drywall surface over the central stud cavity of a specimen, to simulate the indoor air space, and to provide depressurization force for the air infiltration (Fig. 2).

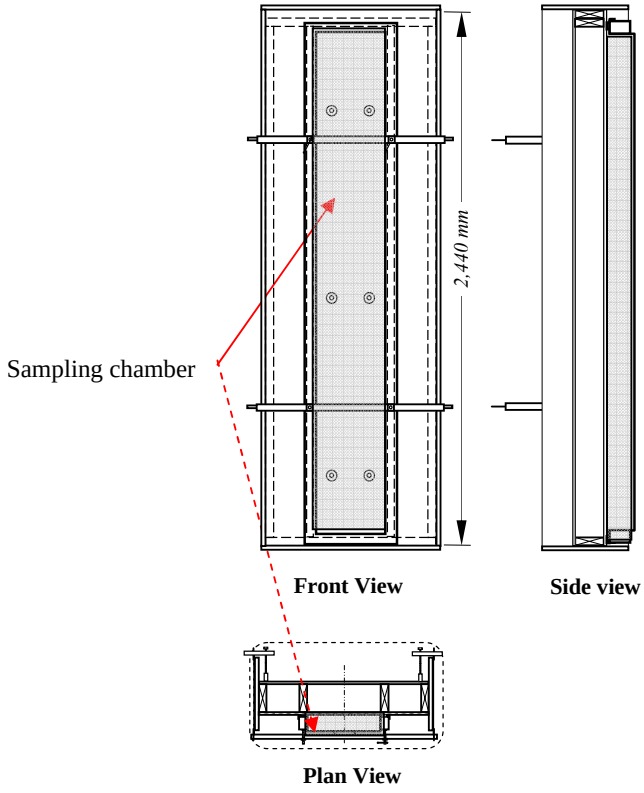

FIG. 2: Specimen design and the sampling chamber

The sampling chamber was tightened to the drywall surface of the specimens and depressurized, employing a centrifugal pump. Low rate air leakage represented the typical air leakage load that a wall may be exposed to. The shallow depth (76 mm or 3") of the sampling chamber reduced the enclosed air volume so as to reduce dilution of mold products once the air was forced into the room side through the specimen.

2.4 VOC sampling

Solid phase micro-extraction (SPME) probes (SPME Portable field samplers, 75 μm PDMS/Carboxen fiber, by Supelco) were used to collect MVOC samples. For each specimen, four VOC samples were taken simultaneously: two from the sampling chamber and two directly from the stud cavity through the external sheathing (Fig. 3). Each probe was placed in an air stream drawn at a constant rate (0.5 liter/min) using a portable pump (44XR Universal sample pump, SKC inc.). In addition to these four pumps, a depressurization setup was employed to induce air infiltration through the specimen at defined rates. During the sampling, the microfiber was pushed out of the needle of the SPME sampler and exposed to the air stream. After adsorption for 20 minutes, the fiber was retracted into the needle and removed from the specimen.

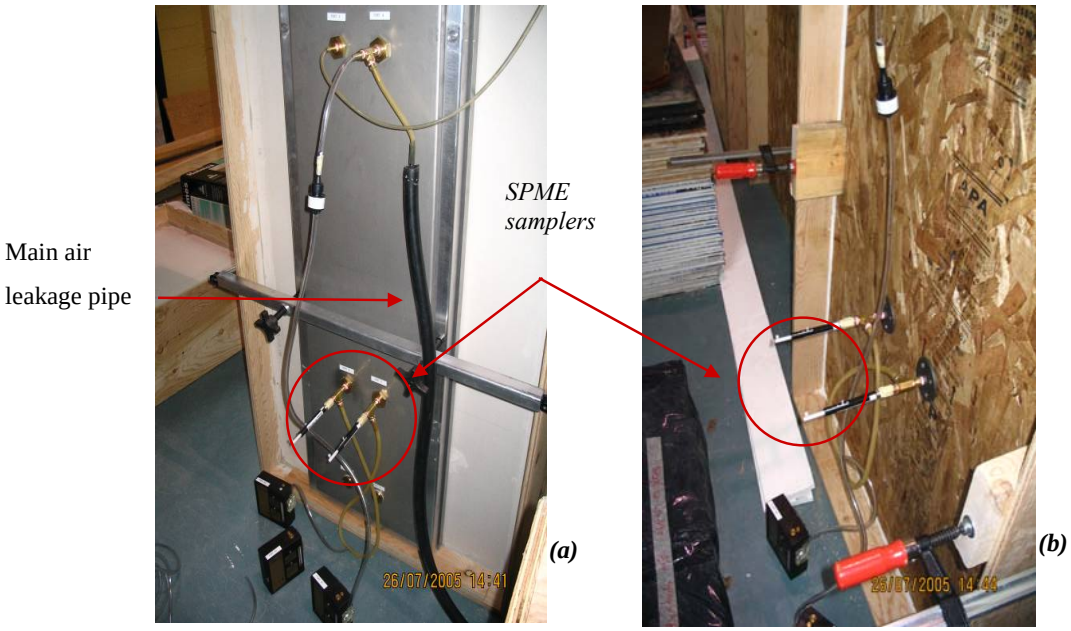

FIG. 3: Test setup for MVOC sampling with SPME probes, (a) from the sampling chamber, (b) sampling from the stud cavity

For each test run, a sample was taken from the background lab air to assess the influence this background may have on the measurements. Air sampling from the background was performed passively, without the employment of sampling pumps.

2.5 Test procedure

The test runs of the experimental program included two stages, dry runs and wet runs. In the dry test runs, each specimen was tested immediately following construction, in the ambient lab environment. In the wet runs, sampling was performed after the assemblies were subjected to wet condition (RH ≈ 90%) for six weeks. During the wetting period, specimens were covered with plastic sheet on the sheathing side. Humid air was pumped into the plastic sheet and pressurized from the sheathing side to the drywall side through the purposely opened holes/slots. The relative humidity of the infiltrating air was maintained at about 90%. After the wetting period, the same test procedure was applied, as for dry specimens.

A list of all test specimens, detailing their characteristics in terms of combination of parameters in each specimen, is presented in Table 2. Specimens 1 to 6 were tested only under dry conditions, while the remaining 14 specimens were tested initially under dry conditions, and subsequently after wet conditions.

TABLE 2: Parameters selected for testing

Specimen #	Ambient Condition		Mold presence		Vapor Barrier		Cavity Insulation		Sheathing			Air Leakage Path	
	Dry	Wet	Moldy	Clear	Yes	No	Yes	No	OSB	Ply-wood	Fiber-board	Direct	Long
1	■		■			■	■		■			■	
2	■		■			■		■	■			■	
3	■		■			■	■		■				■
4	■		■			■		■	■				■
5	■			■	■		■		■			■	
6	■			■		■		■	■			■	
7	■	■	■		■		■		■			■	
8	■	■	■		■			■	■			■	
9	■	■	■		■		■		■				■
10	■	■	■		■			■	■				■
11	■	■		■	■		■		■			■	
12	■	■		■	■			■	■			■	
13	■	■		■	■		■		■				■
14	■	■		■	■			■	■				■
15	■	■	■		■		■			■		■	
16	■	■	■		■			■		■		■	
17	■	■		■	■		■			■		■	
18	■	■	■		■		■				■	■	
19	■	■	■		■			■			■	■	
20	■	■		■	■		■				■	■	
Sub Total	20	14	12	8	15	5	11	9	14	3	3	14	6
Total	34		20		20		20		20			20	

3. Results and analysis

The analysis of MVOC samples was performed using gas chromatography/mass spectrometry (GC/MS). The following compounds were identified from the chromatograms: isopropyl alcohol; 1-propanol; 2-butanol; 1-butanol, 3-methyl; 1-butanol, 2-methyl; 1-propanol, 2-methyl; silanol trimethyl; 2-butanone; cyclohexanone; butyrolactone; hexanal; propanal, 2-methyl; benzene; toluene; ethylbenzene; m+p-xylenes; o-xylene; styrene; furan, 2-methyl; furan 3-methyl; alpha-pinene; benzothiazole; butylated hydroxytoluene; and pentadecane.

3.1 Identification of MVOCs

The identification of mold generated MVOCs was best achieved in the cavity, where the source of mold resides. A multiple regression model was used to verify the VOCs emitted by mold (MVOCs). The linear regression model establishes the relation between the level of VOCs in the cavity and the factors that may affect this level, namely, the six parameters listed in Table 1: ambient condition, mold growth, vapor barrier, insulation, sheathing material and air path, as well as the background level of VOCs. The regression model applied in the cavity is expressed as follows:

$$E(Y^{\lambda}) = \beta_o + \beta_1 X_1 + \beta_2 X_2 + \beta_3 X_3 + \beta_4 X_4 + \beta_5 X_5 + \beta_6 X_6 + \beta_7 X_7 \qquad (1)$$

where $E(Y^{\lambda})$ is the mean response expectation on a transformed scale; β_0 is the constant representing the value of the dependent variable $E(Y^{\lambda})$ when all the predictors (X) are 0; $\beta_1 \ldots \beta_7$ are the coefficients of each corresponding predictor, designating the average change of the dependent variable related to the independent variables. A positive coefficient indicates an increase of the independent variable, while a negative value indicates a decrease. $X_1 \ldots X_6$ are the values of the parameters listed in Table 1 and the background level is X_7.

The identification of mold related MVOCs, which was one of the objectives of the experiment, was achieved by finding those compounds for which the mold factor (X_2) was significant.

Prior to applying the regression analysis, Box-Cox transformation was used to approximately normalize the data, using the statistical analysis software (MINITAB). A natural log transformation was adopted for the data of most of the compounds; whereas the data of the others required power transformations with 1/3-th power. This data transformation is indicated by the power expression, Y^{λ}, of the VOC concentration levels.

3.1.1 Presentation and interpretation of results

To detect mold related VOCs, only a positive effect of mold presence (X_2) was of interest, whereas to find the effect of the other factors, both negative and positive values of the coefficients were considered. Therefore, a single-tailed test of significance was required for the analysis of mold effect while a two tailed test was employed in the analysis of the effect of the factors. The *p*-values of a single tailed test associated with the coefficient of X_2 is presented in Table 3. The *p*-values of the other factors correspond to two-tailed test. A positive sign (+), associated with a positive value of the coefficient indicates that the corresponding factor increases the level of VOCs, and a negative sign (-) indicates the opposite.

The mold presence was found to have significant positive effect, at the 0.1 level, on 1-Propanol, Cyclohexanone, Furan 3-Methyl, Alpha Pinene and Pentadecane (p = 0.0015, p = 0.01, p = 0.04, p = 0.04 and p = 0.015, respectively). Thus, these compounds may be considered as potential mold indicators.

The analysis of the factors, indicates that besides the mold effect, no significant effect was detected on the level of cyclohexanone in the cavity, while the concentration of furan 3-methyl and alpha pinene, was affected by factors other than mold presence. The regression analysis results (Table 3) showed that the vapor barrier (X_3) and OSB sheathing material (X_5) had a positive significant effect on the furan 3-methyl level (p = 0.03 and p =0.06, respectively). The effect of wet condition (X_1) was negatively significant (p = 0.04). The background level (X_7) of furan 3-methyl was very highly significant (p = 0.004), indicating that the level of this compound in the cavity was highly related to its level in the background. The background level (X_7) of alpha pinene, has a positive significant effect (p = 0.05), while the vapor barrier (X_3) and insulation (X_4) had negative significant effect on alpha pinene level (p = 0.08). Therefore, the significant impact of different factors on furan 3-methyl and alpha pinene levels suggests that these two compounds can not be used as absolute indicators of mold growth in this research, although they are frequently reported in literature as related to mold growth.

1-propanol is not particularly highlighted in literature as a mold specific MVOC or indicator of mold growth, and pentadecane is found to be emitted by copiers and printers, computers and other office and indoor sources. However, their high significance in the moldy specimens (p = 0.0015, and p = 0.015 respectively, Table 3), suggests considering the emission of these compounds as associated with mold growth, especially since the analysis was not affected by other parameters.

With all other factors held constant, the ambient condition (X_1) negatively affected most of the MVOCs (except alpha pinene), showing a moderate significant effect on 1-propanol (p = 0.06) and high significant effect on furan 3-methyl (p = 0.04), thus demonstrating that the level of these MVOCs decreased when sampled after the wet condition process. This does not necessarily indicate that wetting reduced VOC concentrations. It might be because that the time taken for the wetting allowed the VOCs to be removed or deeply absorbed.

TABLE. 3: Analysis of the factors affecting MOVC concentrations in stud cavities

MVOCs	**Value of β_0**	**Significance of the factors (*p*-values)**							
		β_0 (two-tailed)	β_1 (two-tailed)	β_2 (single tailed)	β_3 (two-tailed)	β_4 (two-tailed)	β_5 (two-tailed)	β_6 (two-tailed)	β_7 (two-tailed)
1-Propanol	0.48		(-) 0.06	(+) 0.0015	(+)	(+)	(+)	(+)	(+)
Cyclohexanone	- 2.69		(-)	(+) 0.01	(-)	(+)	(+)	(+)	(-)
Furan 3-Methyl	3.21	0.037	(-) 0.04	(+) 0.04	(+) 0.03	(+)	(+) 0.06	(+)	(+) 0.004
Alpha Pinene	110	0.013	(+)	(+) 0.04	(-) 0.08	(-) 0.08	(+)	(+)	(+) 0.05
Pentadecane	4.2		(-)	(+) 0.015	(+)	(+)	(+)	(+)	(+)

3.2 Analysis of MVOC transport

The analysis of the MVOC transport, from the stud cavity to the indoor space consisted of two objectives: first to confirm the transport of MVOCs from the cavity to the sampling chamber, and secondly to test whether the construction factors affected the transport.

The verification of the MVOC transport was approached by analyzing the MVOC presence in the sampling chamber. Similarly to the analysis conducted in the stud cavities, a regression analysis was performed on the transformed concentration levels of the mold related VOCs in the sampling chamber. The predictors employed in this analysis were the same as those for the cavity with the added levels of the compounds in the cavity as a factor affecting the levels in the sampling chamber. This last factor is, in fact, the main indicator of transport from the cavity to the sampling chamber. Significant positive effects of the cavity concentrations of MVOCs (X_7) on the concentrations in the sampling chamber imply that the chamber concentrations were highly dependent on the cavity concentrations, and thus indicate transport of those MVOCs from the cavity to the chamber. The multiple regression equation for MVOC concentrations in the sampling chamber is expressed as:

$$E(Y^{\lambda}) = \beta_o + \beta_1 X_1 + \beta_2 X_2 + \beta_3 X_3 + \beta_4 X_4 + \beta_5 X_5 + \beta_6 X_6 + \beta_7 X_7 + \beta_8 X_8 \qquad (2)$$

where $X_1 \ldots X_6$ are the values of the construction factors and X_7 is the cavity level and X_8 is the background level of MVOCs. The transport of MVOCs was confirmed by checking whether the coefficient of the cavity (β_7) had a positively significant impact on the level of MVOCs in the sampling chamber. Therefore a single-tailed test was required to analyse the effect of X_7. A two-tailed test was appropriate to evaluate the coefficients of the construction and testing parameters and their significance. Table 4 displays the *p*-values corresponding to a single test for β_7 and the *p*-values associated with a two tailed test for the other coefficients. Similarly to Table 3, the positive and negative signs indicate the sign of the coefficients.

3.2.1 Results and interpretation

The regression analysis shows that the cavity level effect (X_7) was significant for 1-propanol and cyclohexanone level, (p = 0.01and p = 0.007 respectively) and highly significant for the level of furan 3-methyl and alpha pinene (p = 0.000) in the sampling chamber. The application of the one-tailed test confirmed that the coefficient of the cavity was significantly positive, which confirmed the transport from the cavity to the sampling chamber. The reason for the high significance of the constant β_0 on the level of pentadecane (p = 0.004) and cyclohexanone (p = 0.003) is not clear.

Except for pentadecane which was negatively affected by the ambient condition (X_1) (p = 0.009, significant), none of the construction design parameters ($X_1 \ldots X_6$) had a significant effect on the level of MVOCs in the sampling chamber. The level of furan 3-methyl in the background (X_8) had a negatively significant effect (p = 0.01) on that in the sampling chamber. By contrast, the background level of alpha Pinene had a positively significant effect on the level of this compound in the sampling chamber. The level of alpha pinene in the sampling chamber appeared to be significantly affected by both cavity and background levels; however, the cavity effect had considerably higher significance level than the background. The apparent negative effect of the background level of furan 3-methyl on the level in the sampling chamber is difficult to interpret, however, in this case also, the positive effect of the cavity level was of considerably higher level of significance.

TABLE 4: Analysis of the factors affecting MVOCs levels in sampling chamber

MVOCs	**Value of β_0**	**Significance of the factors (p-values)**								
		β_0 (two-tailed)	β_1 (two-tailed)	β_2 (two tailed)	β_3 (two-tailed)	β_4 (two-tailed)	β_5 (two-tailed)	β_6 (two-tailed)	β_7 (single tailed)	β_8 (two-tailed)
1-Propanol	-1.70		(-)	(-)	(+)	(-)	(+)	(+)	(+) 0.01	(+)
Cyclohexanone	16.9	0.003	(-)	(-)	(-)	(-)	(-)	(-)	(+) 0.007	(+)
Furan 3-Methyl	- 0.831		(+)	(+)	(+)	(-)	(+)	(-)	(+) 0.000	(–) 0.01
Alpha Pinene	430323		(-)	(-)	(-)	(+)	(-)	(+)	(+) 0.000	(+) 0.02
Pentadecane	35.2	0.004	(-) 0.009	(+)	(-)	(-)	(-)	(-)	(+)	(+)

4. Concluding remarks

This study had three objectives: a) identifying the mold related VOCs, and b) analyzing the transport of these MVOCs through the specimens, and c) finding the effect of six experimental parameters on this transport. Five VOCs (1-propanol, cyclohexanone, furan 3-methyl, alpha pinene and pentadecane) were found to be related to mold growth. Three of these compounds, cyclohexanone, furan 3 methyl and alpha pinene, are reported in the literature as mold related VOCs, while the remaining two (1-propanol and pentadecane) were regarded as MVOCs in this research, due to the high significant effect that the mold presence exerts on their concentration in the cavity.

The ambient condition had a negative effect on the majority of the MVOCs in the cavity, demonstrating that their level decreased significantly after the wetting process. This did not necessarily indicate that wetting reduced MVOCs concentrations. The time taken for the wetting (6 weeks) may have allowed the VOCs to be diluted or deeply absorbed.

The construction parameters did not show consistent effects on the levels of MVOCs, where some factors affect the concentration of a particular compound and do not affect the others. The effect of the material (vapor barrier, insulation, or sheathing) on the cavity concentration level of a particular MVOC implied that this MVOC was emitted by the wall material, which would exclude it as a potential mold indicator.

The analysis of the MVOCs transport was conducted on the concentration data collected in the sampling chamber. The regression analysis showed that for all MVOCs (except for pentadecane), the cavity levels significantly affected the levels in the sampling chamber, thus confirming the transport of MVOCs from the cavity to the sampling chamber.

The construction factors (vapor barrier, insulation, and sheathing) and air path design did not show a significant effect on the MVOCs level in the sampling chamber, implying they do not significantly affect the transport process.

Acknowledgements

Drs. Alpha Barry and Dian Qing Yang of Forintek, now FPInnovations, conducted the work on the detection, characterization, and quantification of MVOCs and mold related compounds identification. They also contributed to the preparation and fabrication of moldy studs and specimen frames. This work was funded by the Natural Science and Engineering Research Council of Canada (NSERC) and by the wood industry.

5. References

Fazio, P., Bartlett, K., Yang, D.Q., Rao, J. and Miao, G., (2005). Development of experimental procedure to evaluate potential movement of mold spores from wall cavity to indoor environment, *10th International Conference on Building Science*, Ottawa, May 11-13.

Fischer, G., Schwalbe, R., Moller, M., Ostrowski, R. and Dott, W., (1999). Species-specific production of microbial volatile organic compounds (MVOC) by airborne fungi from a compost facility, *Chemosphere*, 39(5): 795-810.

Desmarais, G., D. Derome, P. Fazio, (1998), "Experimental Setup for the Study of Air Leakage Patterns", *Thermal Performance of the Exterior Envelopes of Building VII,* ASHRAE, Clearwater, Florida, Dec., p. 99-108.

Rao J., Miao G., Yang D. Q., Bartlett K., Morris P. , Fazio P., (2006). Experimental evaluation of potential mold spores movement from building envelope cavities to the indoor environment using full size wall specimens, *Proceeding of the Third International Building Physics Conference*, Concordia University, Montreal, Canada, Aug. 27 – 31, p. 845-852.

Sunesson, A.L., Vaes, W.H.J., Nilsson, C.A., Blomquist, G., Andersson, B. and Carlson, R. (1995). Identification of volatile metabolites from five fungal species cultivated on two media, *Appl. Environ. Microbiol.*, 61: 2911–2918.

Schleibinger, H., Laussmann, D., Bornehag, C., Eis, D. and Rueden, H., (2008), Microbial volatile organic compounds in the air of moldy and mold-free indoor environments, *Indoor Air*, 18(2): 113-124.

Wessen, B., and Schoeps, K-O., (1996), Microbial volatile organic compounds-what substances can be found in sick buildings? *The Analyst*, 121: 1203-1205.

Accelerated Climate Ageing of Building Materials and Application of the Attenuated Total Reflectance (ATR) Fourier Transform Infrared (FTIR) Radiation Experimental Method

Bjørn Petter Jelle[ab*], Tom-Nils Nilsen[c], Per Jostein Hovde[b] and Arild Gustavsen[d]

[a] Department of Building Materials and Structures,
[b] Department of Civil and Transport Engineering,
[c] Department of Chemical Engineering,
[d] Department of Architectural Design, History and Technology,

[a] SINTEF Building and Infrastructure, NO-7465 Trondheim, Norway.
[b,c,d] Norwegian University of Science and Technology (NTNU), NO-7491 Trondheim, Norway.

*Corresponding author: bjorn.petter.jelle@sintef.no (e-mail), 47-73-593377 (phone), 47-73-593380 (fax).

KEYWORDS: *Accelerated Climate Ageing, Durability, Lifetime, Building Materials, ATR, FTIR.*

SUMMARY:

Accelerated climate ageing investigations are carried out in order to study the durability of various building materials in a substantial shorter time span than natural weather ageing would have allowed. Climate parameters like temperature (including freezing/thawing cycles), relative air humidity, water spray amount, solar and/or ultraviolet radiation and exposure duration are controlled in different climate ageing apparatuses. Various ageing processes in the building materials, ageing both by natural and accelerated climate exposure, may be studied in an attenuated total reflectance (ATR) fourier transform infrared (FTIR) radiation analysis following the decomposition and/or formation of chemical bonds in materials or products.

The ATR-FTIR experimental method represents a powerful measurement tool on various materials. This method may be applied on both solid state materials, liquids and gases with none or only minor sample preparations, also including materials which are non-transparent to IR radiation. Such a facilitation is made possible by pressing the sample directly onto various crystals with high refractive indices, e.g. diamond, in a special reflectance setup. Thus ATR saves time and enables the study of materials in a pristine condition, i.e. the comprehensive sample preparation by pressing thin KBr pellets as in traditional FTIR transmittance spectroscopy is avoided.

However, the ATR-FTIR analysis of different building material samples exhibit various levels of experimental difficulties. In this investigation we have studied the FTIR spectra of climate weathered wood, wood rot, mould fungus on wood, mould fungus on plaster board and plastic degradation by ultraviolet radiation.

Both qualitative and quantitative results may be obtained by an ATR-FTIR analysis using regular recordings of FTIR spectra. In order to determine the ageing progress and assess the effective lifetime of materials, components or products, FTIR spectra should be recorded both before, during and after the climate ageing. Hence, FTIR may be developed as an important tool to track the condition of various materials, components and products during the lifetime of a building, and thereby be applied as a tool for condition assessment, selection of maintenance intervals and service life prediction of buildings.

1. Introduction

The climate ageing of various building materials represents a substantial strain to the buildings, both on a material, component and structural basis. The climate factors may be divided into the following:

- Solar radiation including ultraviolet (UV), visible (VIS) and near infrared (NIR) radiation.
- Ambient infrared (IR) heat radiation (the resulting elevated temperature increases the rate of chemical degradation reactions, and also the rate of growth of rot and fungus up to limiting temperatures).
- Temperature changes/cycles (relative temperature movements between different materials, number of freezing point passes during freezing/thawing).
- Water, e.g. moisture, relative air humidity, rain (precipitation), wind-driven rain.
- Wind.
- Erosion (also from above factors).
- Pollutions (e.g. gases and particles in air).
- Microorganisms (in general).
- Time (determining the effect for all the factors above to work).

Note that wood rot and mould fungus specifically, may not be listed as climate factors, i.e. the wood rot and mould fungus are in this context viewed as (unwanted) results of the specific climate factors moisture and temperature for a certain exposure time with a sufficient supply of nourishment (e.g. wood). In fact, although commonly not regarded as so, the availability of fungal spores may be seen as a special climate exposure factor. Fungal spores are almost always present, except under sterile conditions.

The various building materials have different resistance and durability towards the different climate exposure factors. It is important to protect the assorted materials versus the climate influence as a single material failure due to climate ageing may lead to failure of the whole building component and in the worst case even jeopardize the whole building structure. A material's resistance towards climate strains has therefore a direct impact on both economical and safety issues during the whole lifetime of a building. Various strategies exist to protect the materials versus deterioration, e.g. paints, varnishes and impregnation for wooden claddings and UV stabilizers for polymers like polyethylene, polypropylene, etc.

Natural climate ageing processes take long time to proceed, and often the buildings in question are supposed to be erected in the close future, i.e. it is impossible to wait for results from a long-term outdoor natural exposure test. To provide results fast enough, and within economical limits, accelerated climate ageing tests may be conducted. It is important *not* to induce any changes or chemical reactions in the materials that would not occur during an outdoor natural ageing process. That is, in an accelerated ageing test, only processes which would also occur in an outdoor natural ageing should be initiated and accelerated. For example, UV radiation with lower wavelengths than what exists in natural solar radiation should definitely not be applied in an accelerated climate ageing apparatus, as the short-wave UV radiation may bring about a degradation and chemical reactions that would never take place in nature. Earlier accelerated ageing apparatuses were in fact too often employing larger amounts of UVB radiation with too low wavelengths.

In this work we are trying to utilize the attenuated total reflectance (ATR) fourier transform infrared (FTIR) radiation experimental technique in order to study degradation of various building materials exposed to (accelerated) climate ageing. The ATR-FTIR technique makes it possible to study materials which are non-transparent to IR radiation in a pristine condition. That is, the extensive, time-consuming and often cumbersome sample preparation by pressing thin KBr pellets as in traditional FTIR transmittance spectroscopy is avoided. The traditional technique might even change the sample material in question. The ATR technique is based on a special reflectance setup where the sample is pressed directly onto various crystals with high refractive indices, e.g. diamond. One goal is to be able to quantitatively determine the wood decay by performing ATR-FTIR analysis. Fortunately, for life time predictions, it is not necessary to identify what species are formed/degraded, as it is sufficient to determine quantitative relative changes.

Experimentally the task is challenging. Firstly, for some materials it may be difficult to differentiate the degradation products on the attacked sample from the substrate material itself. Secondly, it may be complicated to be able to distinguish between various degradation products. Thirdly, some building materials are not homogenous, which may complicate the measurements. Finally, with the ATR technique it is important to achieve and ensure a good contact with no air pockets between the sample and the ATR crystal in order to obtain correct quantitative results. Several building materials have so relatively hard and rough surfaces that such a good contact might be difficult to achieve, and especially to ensure that the actual contact is the best one attainable.

Five different building material degradation categories are chosen in the work presented here, namely:

- Climate weathered wood.
- Wood rot.
- Mould fungus on wood.
- Mould fungus on plaster boards.
- Plastic degradation by ultraviolet radiation.

As we will see in the following, these five degradation categories exhibit various experimental difficulties.

Various works are carried out applying IR spectroscopy in studies of wood weathering and wood photodegradation, e.g. by Anderson (1991), Colom (2003), Humar (2006), Mohebby (2005), Pandey (2003, 2005), Sudiyani (2003) and Yamauchi (2004) and co-workers. Anderson et al. (1991) studied the effects of artificial weathering of softwoods and hardwoods with water alone, sunlight (xenon lamp) alone and both water and sunlight applied in conjunction. ATR analyses were performed by Humar et al. (2006) and Mohebby et al. (2005). Miscellaneous works are performed by applying IR spectroscopy in various studies of microorganisms, e.g. by Fischer (2006), Irudayaraj (2002), Kos (2002), Mohebby (2005), Naumann (2005), Ngo-Thi (2003), Orsini (2000), Pandey (2003, 2004) and Wenning (2002) and co-workers. Kos et al. (2002), Mohebby (2005) and Orsini et al. (2000) performed their works by employing the ATR-FTIR spectroscopical technique, which they describe as promising and with many advantages in these types of investigations. Several works are also carried out using IR spectroscopy in various studies of weather ageing and photodegradation of different polymer materials, e.g. by Commereuc (1997), Croll (2003), Gerlock (1998) and Muasher (2006) and co-workers. More general literature concerning photodegradation of polymers may be found in Pospíšil et al. (2006), Rånby and Rabek (1975) and Rabek (1995, 1996). The common practice and most widely applied experimental method is the traditional KBr pellet sample technique in infrared transmittance modus. Although there exists many experimental challenges using the ATR-FTIR method on various solid state materials (e.g. wood and fungus), this method is nevertheless very promising and with many advantages and is therefore the subject of our investigations in this work.

2. Experimental

2.1. Sample Materials

The results presented here is part of a larger study where several different building material samples are being subjected to both natural weather ageing and various accelerated climate ageing apparatuses. However, due to length limitations for this article, only one selected sample from each category is shown in the following:

Wood	Pine heartwood, Pinus silvestris L., measured dry mass density of 0.48 kg/dm^3. Raw, non-impregnated sample.
Wood Rot	Wood rot on wood, area on wood piece heavily infected with wood rot.
Wood Fungus	Mould fungus on wood. Mould fungus scraped off from wood, i.e. measured on a small mould fungus powder pellet.
Plaster Fungus	Mould fungus on plaster board. Mould fungus scraped off from GU plaster board, i.e. measured on a small mould fungus powder pellet.
Plastic	High density polyethylene (HDPE), intended for application as water barriers/repellants around building foundation walls.

The small sample materials for the FTIR measurements have been collected from the larger samples depicted in Figure 1. For the Plastic sample the FTIR measurements have been performed directly on the sample shown in Figure 1.

FIG. 1. Photos of the Wood, Wood Rot, Wood Fungus, Plaster Fungus and Plastic samples. Small pieces are cut from the samples for use in the FTIR investigations, except the Plastic sample which is used directly.

2.2. Accelerated Ageing in QUV Apparatus

The accelerated ageing of the Plastic sample shown here was performed in a QUV apparatus, Weathering Tester Horizontal Option with Ponding and Water Spray (The Q-Panel Company, Cleveland, Ohio, USA), which subjected the sample to UV radiation at a constant air temperature of 50ºC. The UVA and UVB intensities are averaged to 28 W/m^2 and 2.8 W/m^2, respectively. No water spray was applied. The shortened form QUV is applied throughout the text as an abbreviation for this specific exposure.

2.3. Accelerated Ageing in Atlas Solar Simulator

The accelerated ageing of the Wood sample shown here was carried out in an Atlas SC600 MHG Solar Simulator climate chamber with a 2500 W MHG lamp. The wood sample was tilted a bit from the horizontal (8 ± 2º) in order to let the water run off the surface. The sample was placed in the climate chamber with a distance of approximately 55 cm from the climate chamber glass ceiling to the samples, where the solar radiation intensity is reported to be 1200 W/m^2 at 100 % lamp power intensity. During the ageing period the UVA and UVB radiation intensity was measured at various times to be lying within the interval 60-80 W/m^2 and 3-6 W/m^2, respectively. The UV measurements were performed with a radiometer/photometer Model IL 1400A (International Light) with an UVA sensor and an UVB sensor. Note that a 6 % UVA fraction (like in sunlight) of the total solar intensity (1200 W/m^2) yields 72 W/m^2 UVA radiation. The exposure duration consisted of 115 whole cycles of 24 hours, each cycle divided into 20 hours with a solar radiation intensity of 1200 W/m^2 and 4 hours with water spray and no solar radiation exposure. The two water spray nozzles gave each 0.5 dm^3/min, i.e. 1 dm^3/min in total, which gives approximately 1.7 dm^3/(m^{2}min) assuming an even horizontal water distribution at the sample location in the whole climate chamber. Integrated up, the solar radiation (MHG lamp) energy is 24 kWh/m^2 per day and 2760 kWh/m^2 during 115 days. Likewise, assuming 70 W/m^2 as an average, the UVA radiation energy is 1.4 kWh/m^2 per day and 161 kWh/m^2 during 115 days. The temperature and relative air humidity were held constant at 63ºC and 50 % RH during the solar radiation exposure and at 10ºC and close to 100 % RH during the water spray application. The shortened form Atlas is applied throughout the text as an abbreviation for this specific exposure.

2.4. FTIR Measurements

The FTIR material characterization was carried out with a Thermo Nicolet 8700 FTIR spectrometer with a Smart Orbit accessory, i.e. a horizontal attenuated total reflectance (HATR) accessory (single reflection) with a diamond crystal, in the wavelength range 4000 cm^{-1} (2.5 μm) to 400 cm^{-1} (25 μm) in an atmosphere with minimalized CO2 and H2O content through purging by a Parker Balston 74-5041 FTIR Purge Gas Generator. Each FTIR spectrum presented is based on a recording of 32 scans at a resolution of 4 cm^{-1}. In order to ensure satisfactory contact between the ATR diamond crystal and the sample, a minimum of three or more FTIR spectra were recorded at various locations on the sample. The FTIR spectra given in this work have not been ATR corrected, neither with respect to penetration depths nor absorbance band shifts, which both are dependent on the refractive indices of the sample and the ATR crystal (diamond in this case) and the angle of incident radiation. The penetration depth is in addition also dependent on the radiation wavelength. Note that it should always be stated if an ATR-FTIR spectrum has been ATR corrected or not, e.g. important during computerized database spectra comparison searches.

3. Results and Discussion

FTIR transmittance spectra versus wave number between 4000-400 cm^{-1} for the different building material samples at various ageing levels are presented in Figs. 2-4 (left). Further close-ups of these spectra are shown as FTIR absorbance versus wave number are also shown in Figs. 2-4 (right). Furthermore, an unexposed wood sample and an unexposed GU plaster board sample are depicted in Figure 3. In addition in Figure 3, as a reference to avoid any misinterpretations, the distilled water, non-dried gypsum and dried gypsum spectra are also plotted. Note that the irregularities in the FTIR spectra between 2200-1900 cm^{-1} (Figs. 2-4) are due to the very large absorption in the ATR diamond crystal between these wave numbers, which represents the weak point in an otherwise excellent material choice for ATR applications.

As the absorption of electromagnetic radiation, e.g. IR radiation, follows the Beer-Lambert law, i.e. the radiation is decreasing exponentially with the penetration depth in the actual material, it is often helpful to plot the spectra on a logarithmic absorbance scale vs. wavelength. Hence, a representative spectrum is chosen from each of the samples and plotted on a logarithmic absorbance scale for quantitative studies. Mathematically and physically it follows that a doubling of the logarithmic absorbance, also called optical density, is interpreted as a doubling of material thickness or a doubling of concentration of absorption active agents.

The building material decay makes the sample material undergo chemical changes and may then as a result of the chemical reactions change the actual thickness of the sample. In this work the experiments are conducted by applying the ATR equipment with the FTIR spectrometer. Hence, the IR radiation is only penetrating into a thin surface layer of the actual sample. With respect to the experiments carried out in this work, the material thickness will then be regarded as approximately constant, i.e. the change in the IR absorbance is explained by an increase or decrease of absorption active species within the sample material undergoing the chemical transformation. Also note that different adjacent neighbour atoms in a compound, e.g. in a polymer chain, will shift the wave number somewhat for the absorbance peak corresponding to the chemical bond in question.

By inspecting the FTIR spectra in Figure 2 (and other spectra not shown here) more closely it is found that several absorbance peaks in the fresh, non-aged wood samples are diminished and finally vanished during the accelerated ageing in the Atlas Solar Simulator. These absorbance peaks are located around 1730-1710 cm^{-1} (varying with different wood specimens), 1510 cm^{-1}, 1260 cm^{-1} and 810 cm^{-1}. The peak around 1730-1710 cm^{-1} are attributed to carbonyl (C=O) stretching in hemicellulose, whereas the peak around 1510 cm^{-1} arises from the C=C stretching of the aromatic ring in lignin. These two peaks located around 1730-1710 cm^{-1} and 1510 cm^{-1} represent good candidates for studying wood decay by climate ageing through FTIR analysis. For the Wood sample (Figure 2) there are some other changes (i.e. increase and/or decrease) in the absorbance peaks during the ageing period also, but generally no completely disappearance of peaks and neither appearance of new peaks. Note that the water absorbance peaks are located at 3265 cm^{-1} (broader peak, -OH) and 1637 cm^{-1} (narrower

peak, -O-), and changes in the FTIR spectra around these wave numbers might also be due to various moisture levels in the samples.

In Figure 3 the narrow, large ellipse encircles FTIR absorbance peaks which may be related to mould fungus and/or wood rot, but this is more uncertain due to the water peak at this location. Note that any microbiological growth may increase the water content. Furthermore, in order to quantify any potential pollution (error) from any astray gypsum powder, the gypsum peaks are also depicted, as these falls in the same wave number range. The thick, small ellipse in Figure 3 encircles FTIR absorbance peaks which are found to be characteristic for the mould fungus and wood rot. These peaks, also including the other samples not shown here, lie between 1558 cm^{-1} and 1535 cm^{-1}. That is, the chemical bonds which is the source for the absorbance peaks at these wave numbers, are found to be present and characteristic for the various mould fungus and wood rot products studied in this work.

An inspection of Figure 4 reveals that due to the ageing processes large absorbance peaks are growing up at wave numbers around 1732 cm^{-1} and 1713 cm^{-1} and also around 1200 cm^{-1}. The peaks around 1732 cm^{-1} and 1710 cm^{-1} are attributed to carbonyl (C=O) stretching, i.e. an oxidation of the polymer occurs during UV exposure in the QUV apparatus.

Experimentally, all these solid state samples had so hard and rough surfaces that it could be difficult to obtain a good contact with no air pockets between the sample and the ATR crystal, and especially to ensure that this contact in fact was the best one attainable. The Plastic sample had the smoothest surface, and was therefore the easiest sample in this respect. In addition, the Plastic sample was homogenous, i.e. you are assured to be measuring on the same material over the whole sample surface. For the Wood, Wood Rot, Wood Fungus and Plaster Fungus samples it could be rather difficult and time-consuming to differentiate the degradation products on the attacked samples from the substrate materials themselves and to be able to distinguish between various degradation products.

Hence, in this preliminary study it has been demonstrated that the ATR-FTIR spectroscopical technique may be applied in order to detect different levels of climate induced building material decay or ageing. Further studies and experimental investigations are needed in order to elaborate the suitability, the reliability, the limitations and the future potential possibilities of this method. Note that miscellaneous building material samples exhibit various levels of experimental difficulties in the ATR-FTIR analysis. In future applications of this experimental method as a detection tool capable of differentiating between various building material decay or ageing levels, there is a need to build up large reference databases containing FTIR spectra of the different species.

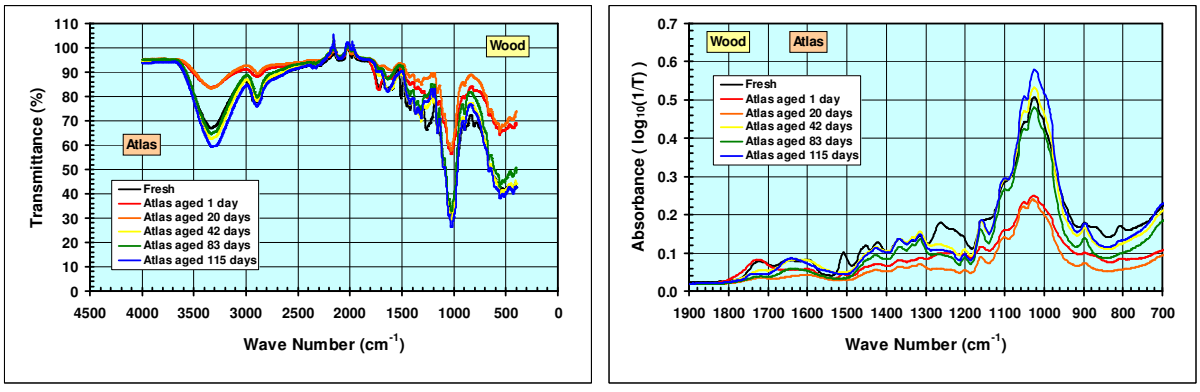

FIG. 2. Transmittance vs. wave number between 4000-400 cm^{-1} (left) and absorbance (logarithmic) vs. wave number between 1900-700 cm^{-1} (right) for the Wood sample during accelerated ageing in an Atlas Solar Simulator.

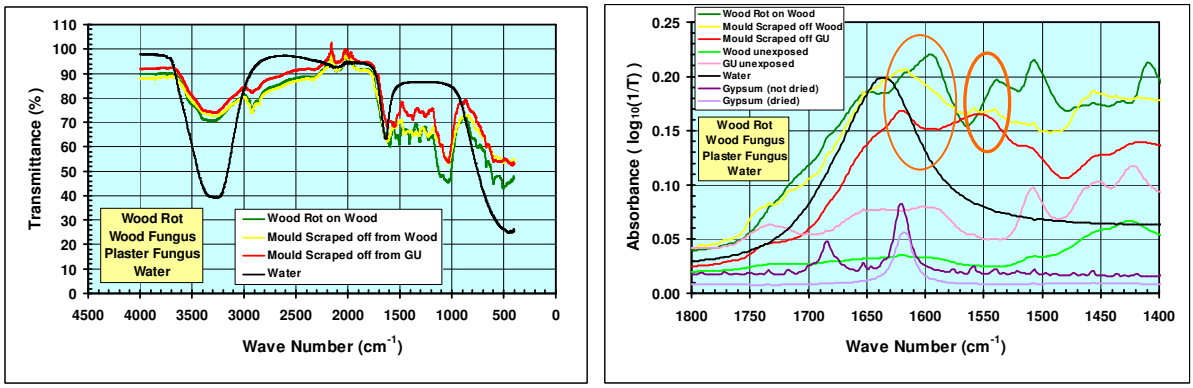

FIG. 3. Transmittance vs. wave number between 4000-400 cm^{-1} (left) and absorbance (logarithmic) vs. wave number between 1800-1400 cm^{-1} (right) for the Wood Rot, Wood Fungus and Plaster Fungus samples. In addition, the water spectrum is included as a reference. In the close-up spectra (right), unexposed wood, unexposed GU plaster board, water, non-dried gypsum and dried gypsum spectra are also plotted as a comparison. See discussion in text about the FTIR absorbance peaks within the narrow, large (left) and thick, small (right) ellipse encircling the absorbance peaks.

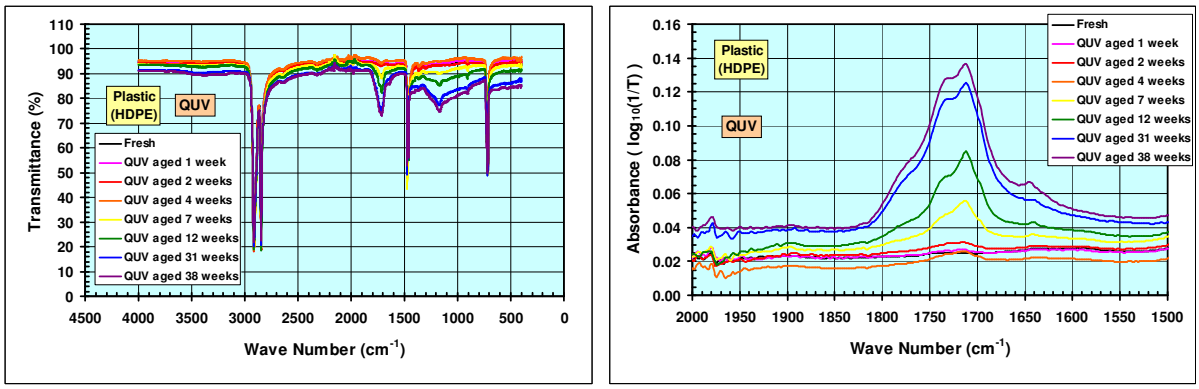

FIG. 4. Transmittance vs. wave number between 4000-400 cm^{-1} (left) and absorbance (logarithmic) vs. wave number between 2000-1500 cm^{-1} (right) for the Plastic sample during accelerated ageing in a QUV apparatus.

4. Conclusions

Miscellaneous building material samples exhibit various levels of experimental difficulties in a attenuated total reflectance (ATR) fourier transform infrared (FTIR) spectroscopical analysis. Nevertheless, this preliminary study has demonstrated that the ATR-FTIR technique may be applied in order to detect different levels of climate induced building material decay or ageing. However, further studies and experimental investigations are needed in order to elaborate the suitability, the reliability, the limitations and the future potential possibilities of this method.

References

E. L. Anderson, Z. Pawlak, N. L. Owen and W. C. Feist, "Infrared studies of wood weathering. Part I: Softwoods", *Applied Spectroscopy*, **45**, 641-647 (1991).

E. L. Anderson, Z. Pawlak, N. L. Owen and W. C. Feist, "Infrared studies of wood weathering. Part II: Hardwoods", *Applied Spectroscopy*, **45**, 648-652 (1991).

X. Colom, F. Carrillo, F. Nogués and P. Garriga, ”Structural analysis of photodegraded wood by means of FTIR spectroscopy”, *Polymer Degradation and Stability*, **80**, 543-549 (2003).

S. Commereuc, D. Vaillant, J. L. Philippart, J. Lacoste, J. Lemaire and D. J. Carlsson, ”Photo and thermal decomposition of iPP hydroperoxides”, *Polymer Degradation and Stability*, **57**, 175-182 (1997).

S. G. Croll and A. D. Skaja, ”Quantitative spectroscopy to determine the effects of photodegradation on a model polyester-urethane coating”, *Journal of Coatings Technology*, **75**, 85-94 (2003).

G. Fischer, S. Braun, R. Thissen and W. Dott, ”FT-IR spectroscopy as a tool for rapid identification and intra-species characterization of airborne filamentous fungi”, Journal of Microbiological Methods, 64, 63-77 (2006).

J. L. Gerlock, C. A. Smith, V. A. Cooper, T. G. Dusbiber and W. H. Weber, ”One the use of Fourier transform infrared spectroscopy and ultraviolet spectroscopy to assess the weathering performance of isolated clearcoats from different chemical families”, *Polymer Degradation and Stability*, **62**, 225-234 (1998).

M. Humar, B. Bučar and F. Pohleven, ”Brown-rot decay of copper-impregnated wood”, *International Biodeterioration & Biodegradation*, **58**, 9-14 (2006).

J. Irudayaraj, H. Yang and S. Sakhamuri, ”Differentiation and detection of microorganisms using Fourier transform infrared photoacoustic spectroscopy”, Journal of Molecular Structure, 606, 181-188 (2002).

G. Kos, H. Lohninger and R. Krska, ”Fourier transform mid-infrared spectroscopy with attenuated total reflection (FT-IR/ATR) as a tool for the detection of Fusarium fungi on maize”, Vibrational Spectroscopy, 29, 115-119 (2002).

B. Mohebby, ”Attenuated total reflection infrared spectroscopy of white-rot decayed beech wood”, *International Biodeterioration & Biodegradation*, **55**, 247-251 (2005).

M. Muasher and M. Sain, ”The efficacy of photostabilizers on the color change of wood filled plastic composites”, *Polymer Degradation and Stability*, **91**, 1156-1165 (2006).

A. Naumann, M. Navorro-González, S. Peddireddi, U. Kües and A. Polle, ”Fourier transform infrared microscopy and imaging: Detection of fungi in wood”, Fungal Genetics and Biology, 42, 829-835 (2005).

N. A. Ngo-Thi, C. Kirschner and D. Naumann, “Characterization and identification of microorganisms by FT-IR microspectrometry”, Journal of Molecular Structure, 661-662, 371-380 (2003).

F. Orsini, D. Ami, A.M. Villa, G. Sala, M.G. Bellotti and S.M. Doglia, ”FT-IR microspectroscopy for microbiological studies”, Journal of Microbiological Methods, 42, 17-27 (2000).

K. K. Pandey and A. J. Pitman, ”FTIR studies of the changes in wood chemistry following decay by brown-rot and white-rot fungi”, *International Biodeterioration & Biodegradation*, **52**, 151-160 (2003).

K. K. Pandey and A. J. Pitman, ”Examination of the lignin content in a softwood and a hardwood decayed by a brown-rot fungus with the acetyl bromide method and fourier transform infrared spectroscopy”, Journal of Polymer Science: Part A: Polymer Chemistry, 42, 2340-2346 (2004).

K. K. Pandey, ”Study of the effect of photo-irradiation on the surface chemistry of wood”, *Polymer Degradation and Stability*, **90**, 9-20 (2005).

J. Pospíšil, J. Pilař, N. C. Billingham, A. Marek, Z. Horák and S. Nešpůrek, ”Factors affecting accelerated testing of polymer photostability”, *Polymer Degradation and Stability*, **91**, 417-422 (2006).

J.F. Rabek, ”Polymer photodegradation. Mechanisms and experimental methods”, Chapman & Hall, 1995.

J.F. Rabek, ”Photodegradation of polymers. Physical characteristics and applications”, Springer-Verlag, 1996.

B. Rånby and J. F. Rabek, ”Photodegradation, photo-oxidation and photostabilization of polymers. Principles and applications”, John Wiley & Sons, 1975.

Y. Sudiyani, Y. Imamura, S. Doi and S. Yamauchi, ”Infrared spectroscopic investigations of weathering effects on the surface of tropical wood”, *Journal of Wood Science*, **49**, 86-92 (2003).

M. Wenning, H. Seiler and S. Scherer, ”Fourier-transform Infrared Microspectroscopy, a novel and rapid tool for identification of yeasts”, Applied and Environmental Microbiology, October 2002, 4717-4721 (2002).

S. Yamauchi, Y. Sudiyani, Y. Imamura and S. Doi, ”Depth profiling of weathered tropical wood using Fourier transform infrared photoacoustic spectroscopy”, *Journal of Wood Science*, **50**, 433-438 (2004).

Model for hysteretic moisture behaviour of wood

Dominique Derome, Ph.D.,
Empa, Swiss Federal Laboratories for Materials Testing and Research, Wood Laboratory, Überlandstrasse 129, CH-8600 Dübendorf

Hannelore Derluyn, Ph.D. student
Katholieke Universiteit Leuven, Laboratorium Bouwfysica, Kasteelpark Van Arenberg 41, B-3001 Heverlee, Hannelore.Derluyn@bwk.kuleuven.be

Wolfgang Zillig, Ph.D. student
Katholieke Universiteit Leuven, Laboratorium Bouwfysica, Kasteelpark Van Arenberg 41, B-3001 Heverlee, Wolfgang.Zillig@bwk.kuleuven.be

Jan Carmeliet, Ph.D.,
Chair of Building Physics, Swiss Federal Institute of Technology ETHZ, Zürich, ETH-Hönggerberg, CH-8093 Zürich, Empa, Swiss Federal Laboratories for Materials Testing and Research, Laboratory for Building Technologies, Überlandstrasse 129, CH-8600 Dübendorf

KEYWORDS*: hysteresis, sorption isotherm, wood.*

SUMMARY*:*
Sorption hysteresis of wood is modelled using a modification of the independent domain approach by taking into account capillary condensation as a hysteretic process and film adsorption as a non-hysteretic process. A change in moisture content in the porous material is the result of the behaviour of an assemblage of different sorption domains, described by a distribution function. A new description of the integrated distribution function is introduced, which can be identified from measured main adsorption and primary desorption curves. The model is validated by simulating the sorption moisture behaviour of wood in dynamic sorption tests for the three orthotropic directions.

1. Introduction

Sorption hysteresis of wood is known already for more than 100 years. Kollmann (1968) refers to van Bemmelen (1896), who published work in 1896. A simple elegant framework for modelling hysteresis is the Preisach model (Preisach, 1935). The Preisach model has been extensively used by Everett (1967) to model scanning curves and subloops in capillary condensation hysteresis. In the independent domain theory by Everett, each pore domain behaves as an independent isolated system that is in direct contact with the external environment. Mualem (1974) presented an independent domain model for hysteresis based on the similarity hypothesis, that requires only the boundary isotherms to predict the scanning curves. These models were explored by Peralta (1995, 1998a, 1998b) for describing sorption hysteresis of wood. Coasne et al (2005) proposed a modification to the original domain theory by taking into account the presence of a film of absorbed water on the non-wetted pores. More sophisticated models have been developed to describe the interaction of individually non-hysteretic units, where rules for the evolution of fluid configurations in pore networks are included (Guyer and McCall 1996, Carmeliet et al. 1999).

Recent work on sorption hysteresis was performed by Derome et al. (2003) and Time (2002) using scanning curves for sorption in wood. Carmeliet et al. (2005) formulated a hysteresis model based on the work of Mualem for oak and compared the results to the phenomenological model of Pedersen (1990) and Rode and Clorius (2004). In Zillig et al. (2007) and in Derluyn et al. (2007), the hysteresis model was applied respectively to spruce and paper, a wood-derived material. It was shown that water vapour permeability in a hysteretic model is dependent on the moisture content and not on relative humidity.

In this paper, we first present a hysteresis model, based on the work of Coasne et al (2005), taking into account the presence of a film forming process in not-filled sorption sites. Then, the hysteresis model is validated by comparing experimental results obtained in a dynamic sorption test.

2. Hysteresis model

2.1 Independent domain theory and PM model

Following the independent domain approach, the porous material contains a number of domains or sorption sites, which behave independently. Figure 1 describes the typical behaviour of a sorption site. With increasing relative humidity, first monolayer adsorption occurs, followed by multilayer adsorption forming a liquid film of increasing thickness. The film forming process is described by the function $m_f(\phi)$. At a critical relative humidity ϕ_a, the sorption site becomes totally filled by capillary condensation, resulting in a jump $m_c(\phi_a, \phi_d)$ in moisture content from $m_f(\phi_a)$ to a moisture content $m_T(\phi_a, \phi_d)$. When the relative humidity decreases again, the site evaporates at a relative humidity ϕ_d, resulting in a jump back to a moisture content $m_f(\phi_d)$. Since $\phi_d \leq \phi_a$ hysteresis occurs between adsorption and desorption. Remark that the jump m_c in adsorption does not equal the jump in desorption, which leads to a hysteresis effect due to the difference in film thickness in adsorption and desorption.

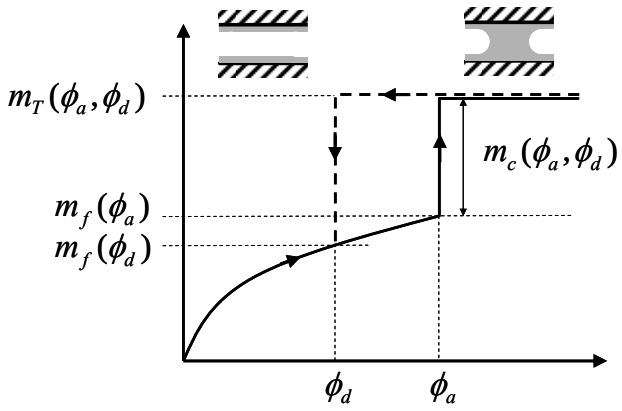

Figure 1 Characteristic behaviour of a hysteretic sorption site.

A porous material consists of a number of sorption sites. Changes in moisture content in a porous material are the outcome of the behaviour of an assemblage of independent sorption sites. An efficient way to represent sorption sites is to map a site characterized by (ϕ_a, ϕ_d), on the half ϕ_a-ϕ_d space, also called the PM space (referring to Preisach 1935 and Mayergoyz 1985). The PM space is represented in Figure 2b. On the PM space, a frequency density distribution $\rho(\phi_a, \phi_d)$ is generated, called the PM distribution, representing the number of sorption sites in (ϕ_a+dϕ_a,ϕ_d+dϕ_d). The PM space is triangular, since $\phi_d \leq \phi_a$. A typical snapshot of the PM space after a RH loading history is given in Figure 2a. The region of sites filled by capillary condensation is denoted Ω. The region of sites, where only film forming occurred is denoted Γ. Performing integration over the respective domains gives the moisture content due to respectively film forming and capillary condensation:

$$M_f(\phi) = \iint_{\Gamma} \rho(\phi_a, \phi_d)\, m_f(\phi)\, \mathrm{d}\phi_a\, \mathrm{d}\phi_d \quad , \quad M_c(\phi) = \iint_{\Omega} \rho(\phi_a, \phi_d)\, m_T(\phi)\, \mathrm{d}\phi_a\, \mathrm{d}\phi_d \tag{1}$$

with the total moisture content M given by

$$M(\phi) = M_f(\phi) + M_c(\phi) \tag{2}$$

For determining the integrals, the PM density $\rho(\phi_a, \phi_d)$, and the functions $m_f(\phi)$ and $m_T(\phi_a, \phi_d)$ have to be known. However, a direct determination of these functions is impossible. To simplify the identification process, we do not determine these specific functions directly, but only determine their integrals M_c and M_f.

(a)

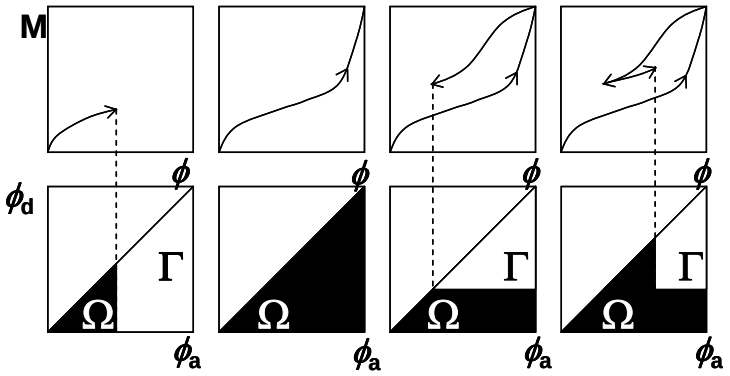

(b)

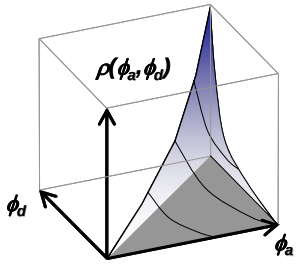

(c)

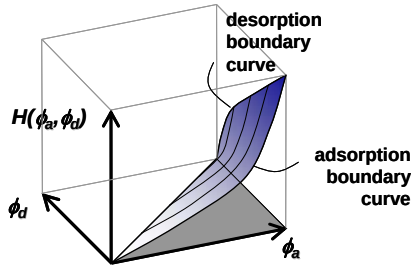

Figure 2 (a) A sequence of typical snapshot of the PM space after a RH loading history, where ϕ_a is the relative humidity in adsorption, ϕ_d the relative humidity in desorption, Ω is the region of domains completely filled by capillary condensation, Γ is the region containing the domains where only film forming occurred. (b) Example of a PM distribution function $\rho(\phi_a, \phi_d)$, commonly attaining maximal values on the diagonal and decaying away from the diagonal. (c) Representation of integral function $H(\phi_a, \phi_d)$ in the IPM space. The IPM function is zero on the diagonal and attains maximal values at the boundaries.

Capillary condensation is considered to be hysteretic and described by the PM model. Capillary condensation leads to the total filling of a sorption site accompanied by the disappearance of the adsorbed film. This means that when capillary condensation takes place in more and more sites, the moisture content due to film forming M_f will decrease. At RH = 100%, no water film will be present, or $M_f(1)=0$. The moisture content due to capillary condensation M_c attains the maximum moisture content, or $M_c(1)= M_{max}$. The influence of capillary condensation on the moisture content due to film forming can be described as

$$M_f(\phi) = G(\phi)\left(1-\frac{M_c(\phi)}{M_{\max}}\right) \tag{3}$$

where $G(\phi)$ is a function which describes the film forming process, when no capillary condensation would occur. Equation 3 shows that, although we assume that the film forming process in the pore scale is non hysteretic, the resulting moisture content M_f becomes hysteretic, since the moisture content M_c in equation 3 is hysteretic.

To determine the moisture content due to capillary condensation by the PM approach, we use the integrated PM (IPM) approach. The function H in the IPM space is defined as

$$H(\phi_a,\phi_d) = \int_{\phi_d}^{\phi_a}\int_{\phi_d}^{x_a} \rho(x_a,x_d)\, m_T(x)\,\mathrm{d}\,x_a\,\mathrm{d}\,x_d \tag{4}$$

where H equals the integral over the triangle (ϕ_{d1}, ϕ_{d1}), (ϕ_{a1}, ϕ_{d1}) (ϕ_{a1}, ϕ_{a1}). By the introduction of the IPM function H, the integral M_c in equation 1 can be calculated as

$$M_c(\phi) = H(\phi_{a1},\phi_{d1}) - H(\phi_{a1},\phi_{d2}) + H(\phi_{a2},\phi_{d2}) - H(\phi_{a2},\phi_{d3}) + ... \\ = \sum_{i=1}^{n} H(\phi_{ai},\phi_{di}) - H(\phi_{ai},\phi_{di+1}) \quad (5)$$

with n the number of vertical boundary segments. Keeping track of the boundary between the regions Ω and Γ, the moisture content M_c can be determined summing and subtracting values of H. The IPM function H covers the complete PM space, attains its maximum at the boundary axes, decreases towards the diagonal and becomes zero on the diagonal (Figure 2c). Therefore, we describe the IPM function as

$$H(\phi_a,\phi_d) = H(1,\phi_d) * F(y) \quad \text{with} \quad y = \frac{\phi_a - \phi_d}{1-\phi_d} \quad (6)$$

where $H(1,\phi_d)$ is the boundary curve on the desorption axis. The function $F(y)$ describes the decay from this boundary curve towards the diagonal. The functions $H(1,\phi_d)$, $F(y)$ and $G(\phi)$ are described by exponential functions introducing five parameters. These parameters including M_{max} are determined from measurement data.

2.2 Adsorption and desorption scanning isotherms

The wood studied is spruce *(Picea abies)* from Bavaria, where all specimens were cut from the same log. The average dry density is 402 kg/m³. The sorption isotherm was measured by conditioning samples in a dessicator over saturated salt solutions at a controlled temperature of 23°C. The samples were initially dried at 50°C and 10 % RH. Intermediate desorption curves were obtained by a stepwise reduction of the relative humidity from the adsorption isotherm. The measurement data are given in Figure 3. The solid curves give the fitted adsorption and scanning desorption curves obtained from the hysteretic model.

2.3 Film forming and capillary condensation

Figure 4b gives the moisture content curves due to film forming and capillary condensation for the main adsorption, main and intermediate desorption curves. The moisture content variation due to capillary condensation shows a typical hysteresis behaviour as described by the PM model. As foreseeable from equation 3, we observe that, although the film forming process itself is considered to be physically non hysteretic at the pore scale, the moisture content variations due to film forming become hysteretic.

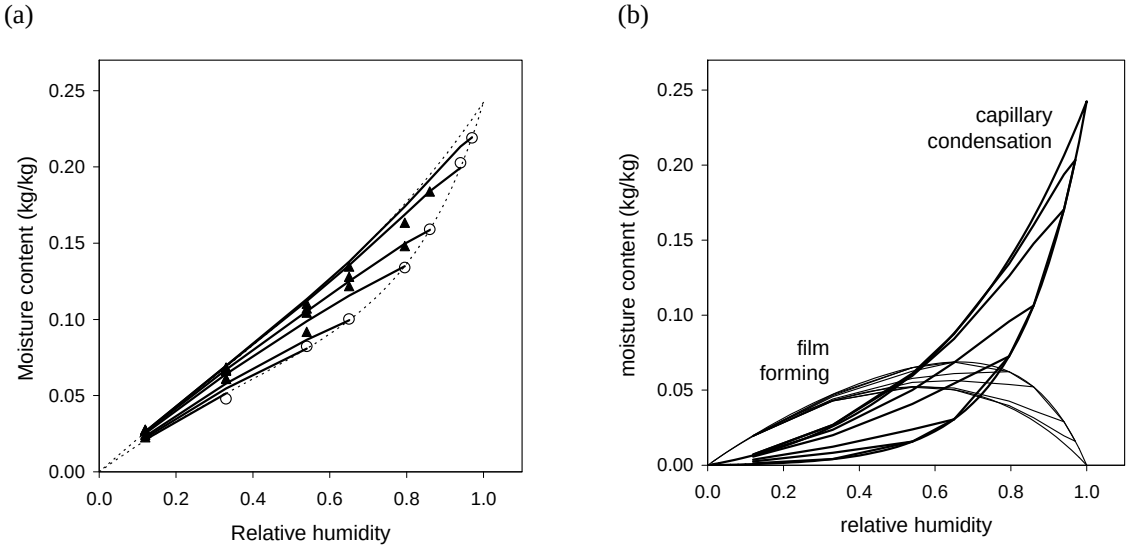

Figure 3. (a) Measured adsorption isotherm (○), scanning desorption isotherms (▲) and hysteresis model predictions (solid lines).(b)Hysteretic isotherms due to capillary condensation and film forming

3. Experimental validation

3.1 Experimental procedures

The samples were initially conditioned at 23°C and 54 % RH. Then the specimens were exposed to a step change in RH to 79.5 % during 14 days. Afterwards, the RH was again stepwise reduced to 54 % for another 14 days. Finally the RH was varied following a sinusoidal daily variation between 54 and 79 % RH. The test was performed for the three directions of wood (longitudinal, radial and tangential). The measurements are given in Figures 4. We observe that the response of wood in longitudinal direction is very fast compared to wood in tangential and radial directions. The different behaviour can be explained by the differences of the water vapour permeability for longitudinal, radial and tangential directions. The difference between tangential and radial directions is small. All specimens show hysteretic behaviour. Small differences in moisture content were observed between the two samples for each direction.

3.2 Water vapour transport model

Water vapour transport is described by combining Fick's law and the conservation of mass equation

$$\rho_d \frac{\partial u}{\partial t} = \nabla \delta \nabla p_v \quad , \quad u = M(\phi) \tag{7}$$

with ρ_d the dry density of the material, u the moisture content, p_v the water vapour pressure and δ the water vapour transport coefficient, depending on the vapour pressure. The boundary condition for vapour transport is given by $q = \beta(p_{ve} - p_{vs})$ with β the water vapour surface coefficient, p_{ve} the water vapour pressure of the environment, p_{vs} the water vapour pressure at the surface of the material.

The water vapour transport coefficient is measured in adsorption for different RH ranges using the dry/wet cup method. The nonlinear adsorption vapour transport coefficient is described by

$$\delta_{ad}(\phi) = \frac{\delta_a}{a + b\exp(c\,\phi)} \tag{8}$$

The increase of the water vapour permeability with relative humidity is commonly attributed to the enhanced microscopic liquid water transport in water filled pores due to capillary condensation. The water vapour transport coefficient for hysteretic materials thus depends on the moisture content. Using the main adsorption isotherm M_{ad}

$$\delta(u) = \delta\left(M_{ad}^{-1}(u)\right) \tag{9}$$

The material properties for the different directions are taken from Zillig et al. (2007). The surface transfer coefficient is fitted to the measurement data and assumed to be a constant.

3.3 Results

Figures 4 compare the simulated and measured response for the longitudinal, radial and tangential directions. A good agreement between simulations and measurements is obtained. Only the amplitude of the cyclic behaviour of spruce in longitudinal direction is underpredicted. In figure 4d, two additional variants for the tangential direction are examined. In a first case, the hysteretic effect is disregarded by using only the adsorption characteristics. In the second case, the water vapour permeability is assumed to depend on the relative humidity (as per eq. 8) and not on the moisture content. The results show clearly that in the first case (no hysteresis), the simulation overpredicts the moisture loss of the specimen in desorption. For the second case, the moisture loss in desorption is too slow when the water vapour permeability factor is assumed to be dependent on relative humidity. This can be explained by the fact that the vapour permeability dependent on RH is lower than the vapour permeability dependent on the moisture content.

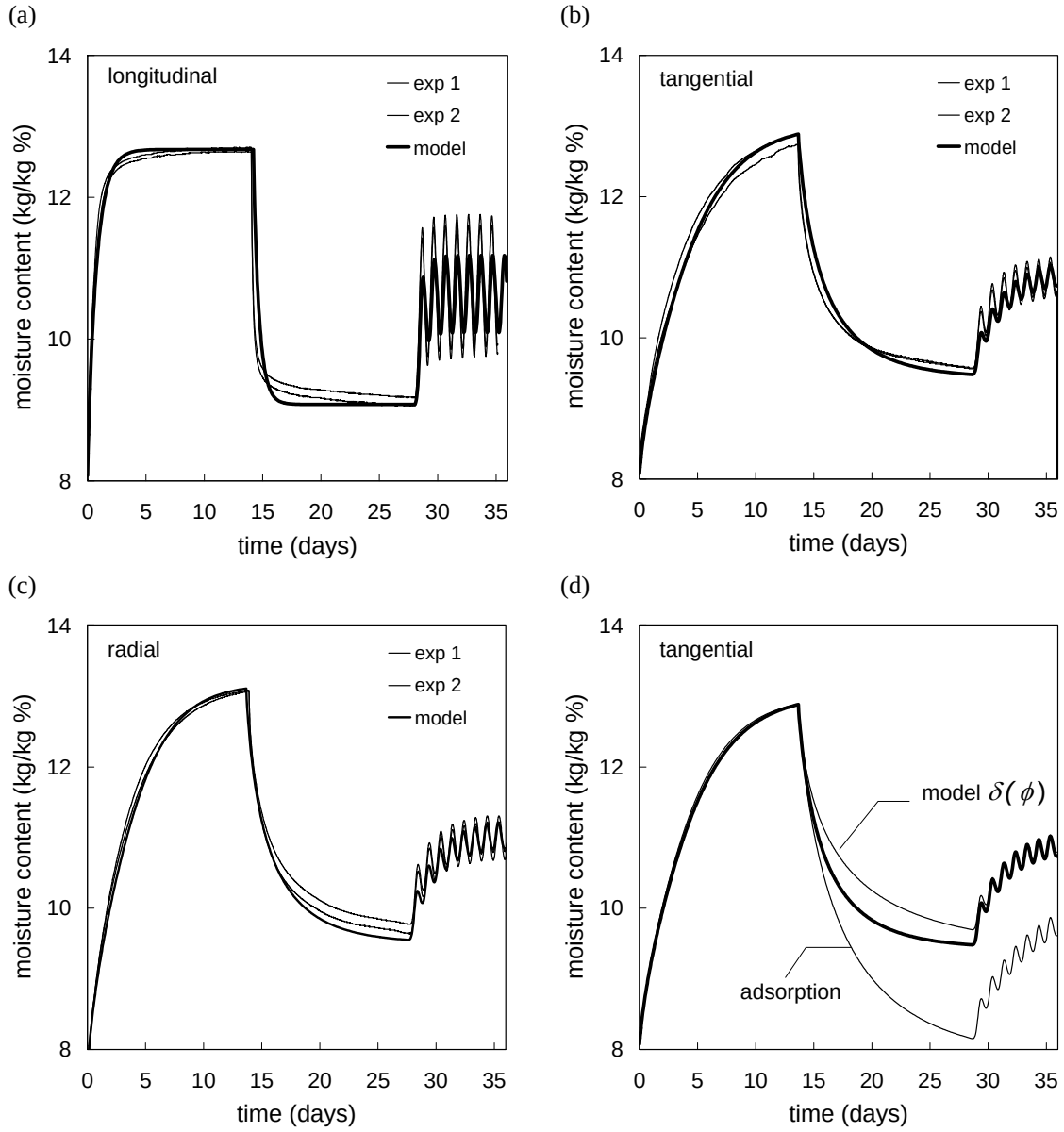

Figure 4

4. Conclusions

Sorption hysteresis of wood (spruce) is modelled using a modified Preisach-Mayergoyz (PM) approach taking into account independently water film adsorption and capillary condensation. A change in moisture content in the porous material is the result of the behaviour of an assemblage of different sorption sites, which show a non-hysteretic film forming and a hysteretic capillary condensation process. It is found that, although film adsorption on the pore scale is non hysteretic, the moisture content due to film forming becomes hysteretic due to the hysteretic behaviour of the capillary condensation process. The model is validated by analysing the moisture content variations of specimens of wood exposed to different relative humidity conditions in a dynamic test. It is shown that the water vapour permeability in a hysteretic material is dependent on the moisture content and not on the relative humidity. The model demonstrates a good agreement with experimental data for the longitudinal, radial and tangential directions.

5. References

Carmeliet, J., Descamps, F., Houvenaghel, G., (1999) Multiscale network model for simulating liquid water and water vapour transfer properties of porous materials, Transport in Porous Media, 35, 67-88.

Carmeliet, J., de Wit, M., Janssen, H. (2005). Hysteresis and moisture buffering of wood, Symposium of Building Physics in the Nordic Countries, June 13-15 2005, Reykjavik, Iceland, 55-62.

Coasne, B., K.E. Gubbins, R.J.-M. Pellenq (2005) Domain theory for capillary condensation hysteresis, Phys.Rev. B, Vol. 72, 024304 (9).

Derluyn, H., Janssen, H. Diepens, J., Derome, D., Carmeliet, J. (2007). Hygroscopic behavior of paper and books, Journal of Building Physics, 31 (9): 9-34.

Derome, D., Fortin, Y., Fazio, P. (2003) "Modeling of the moisture behavior of wood planks in non-vented flat roofs", ASCE Journal of Architectural Engineering, American Society of Civil Engineers, New York, March, pp. 26-40.

Guyer R.A., McCall, K.R. (1996) Capillary condensation, invasion percolation, hysteresis, and discrete memory, Physical Review B, Volume 54, number 1, pp. 18-21.

Kollmann, F., Côté, W. A. (1968). Principles of wood science and technology. Part 1: Solid wood. Springer-Verlag.

Mayergoyz, J.D. (1985) , Hysteresis models from the mathematical and control theory points of view, J. Appl. Phys., 57, 3803-3805

Mualem,Y. (1974). A conceptual model of hystersis, Water Resources research, Vol. 10 No. 3.

Pedersen, C. Rode. (1990). Transient Calculations of Moisture Migration Using a Simplified Description of Hysteresis in the Sorption Isotherm. Proceedings of the 2nd symposion on Building Physics in the Nordic Countries. Technical University of Norway, Trondheim, Norway.

Peralta, P. N. and A. Bangi (1998) Modeling wood moisture sorption hysteresis based on similarity hypothesis. Part 1. Direct approach. Wood and Fiber Science, Vol. 30, No. 1, pp. 48-55.

Peralta, P. N. and A. Bangi (1998) Modeling wood moisture sorption hysteresis based on similarity hypothesis. Part II. Capillary-radii approach. Wood and Fiber Science, Vol. 30, No. 2, pp. 148-154.

Peralta, P. N. (1995) Modeling wood moisture sorption hysteresis using the independent-domain theory. Wood and Fiber Science, Vol. 27, No. 3, pp. 250-257.

Preisach, F. (1935) Über die magnetische Nachwirkung. Z. Phys. 94, 277.

Rode C and Clorius C.O. (2004). Modelling of Moisture Transport in Wood with Hysteresis and Temperature Dependence Sorption Characteristics, Proceedings of the Conference Performance of Exterior Envelopes of Whole Buildings IX, Sheraton Sand Key Resort, Clearwater Beach, Florida, December 5-10, 2004.

Time, B. (2002). Studies on hygroscopic moisture transport in Norway spruce (Picea abies). Part 2: Modelling of transient moisture transport and hysteresis in wood Holz als Roh- und Werkstoff, 60, 405-410.

Van Bemmelen, J. M. (1896). Z. Anorg. Allgem. Chem. 23: 233.

Zillig, W., Derome, D., Diepens, J., Carmeliet, J. (2007) "Modelling hysteresis of wood", Proceedings of 12th Symposium for Building Physics, Technische Universität Dresden, Dresden, March 29-31, Vol. 1, pp. 406-413.

Sampling and Analysis of Natural Isotopes in Moisture Transport from Porous Materials. Applications to Capillary Suction.

Marcin Koniorczyk, PhD,
Division of Building Technology, KTH, Stockholm; Technical University of Lodz;
markon@p.lodz.pl

Kjartan Gudmundsson, PhD,
Division of Building Technology, KTH, Stockholm;
kjartan.gudmundsson@byv.kth.se

Gudni Johannesson, Professor,
Division of Building Technology, KTH, Stockholm;
gudni.johannesson@byv.kth.se

KEYWORDS: natural isotopes, moisture transport, oxygen, hydrogen, fractionation.

SUMMARY:
Water contains various isotopes of oxygen and hydrogen. In the environment, apart from ^{1}H and ^{16}O, there are also their most common sister isotopes: deuterium D and ^{18}O. Isotope fractionation (change in its concentration) occurs in any thermodynamic reaction. It is a consequence of the differences of thermodynamic properties for molecules with different isotopes. Therefore the knowledge of isotope fractionations will be useful during the analysis of moisture transport and processes involved.

To carry out the isotope analysis of pore water, which may be used to reveal the source of excessive water in building elements (Gudmundsson K. 2001), firstly one has to extrude water from voids. For this we tested three different methods of retrieving water from the porous material. Two of them, squeezing and evaporation, are direct methods. The third method is a dilution method, in which we take advantage of diffusion of isotopes from pores into surrounding water with known properties.

The influence of capillary suction on the hydrogen and oxygen isotopes abundance ratio was analyzed. In the last century water diffusion through the column of porous domain was used to separate isotopes. Material whose substantial part of voids are gel pores (cementitious materials) acts as a membrane during isotope transport separating lighter from heavier isotopes. In all these studies we tested transport processes taking place in samples built of light concrete $\rho = 960$ kg/m^3, which was made of expanded clay aggregates and cement CEM I 32.5 The isotope analysis was performed at the University of Iceland in Reykjavik using mass spectrometer Finnigan DELTA XP. The results of carried out experiments indicate that moisture transport (capillary suction) has an influence on the isotopic composition of water. Therefore the isotope analysis can be useful in the investigation of moisture behaviour of porous building materials.

1. Introduction

Moisture is one of major concern when the durability of the structure is considered. To counteract properly against it, firstly one has to reveal its origin. The sources of moisture in buildings are numerous. The indoor air contains water vapor, which might condensates and accumulates in roofs and walls during normal diffusion transfer through the constructions. Rainwater constitutes other external water load, seeking directly through roofs and walls. In case of luck of sufficient horizontal water barrier (in old, historical buildings) water might be sucked from the surrounding soil.

The isotopic composition of water can reveal its origin and provide information about the physical processes, which the water has passed. It has recently been used in the fields of hydrogeology (Clark I.D. et al. 1989, Mazor E. 2004), geology (Javoy M. et al. 1986), and environmental science (Wagner R. et al. 2006). The preliminary research devoted to utilization of isotopes in building physics was performed by Gudmundsson (Gudmundsson K. 2001). The isotopic fingerprints of a water sample were used to determine the source of leakage.

Water contains various isotopes of oxygen and hydrogen. Besides ^{1}H and ^{16}O there appear also their most commonly sister isotope as deuterium D and ^{18}O, which are naturally occurring isotopes. These isotopes are stable, which means that they do not spontaneously disintegrate by any known mode of decay, hence they might serve as a distinct signature to every water sample. Isotope fractionation (change in its concentration) occurs in any thermodynamic reaction. It is a consequence of a difference in the rate of reaction for molecules with different isotopes due to the differences of their thermodynamic properties. Therefore knowing the isotope fractionation of a particular water transport phenomenon and isotope ratio of water sample before and after some complex process one could estimate the contribution of particular phenomenon by inverse analysis.

In this study we tested three different methods of retrieving water from the porous material. Two of them are direct methods: squeezing the water from the sample and evaporation. The obtained water samples were directly tested. The last one is a dilution method, in which we take advantage of diffusion between the pore water and surrounding water with a known isotopic composition. Because we do not test directly the water from the porous material but surrounding water, it is called an indirect method. As it was mentioned above the isotopes may be used to determine the transport processes of water. Therefore in the second part of our study we tested how capillary suction influences the hydrogen and oxygen isotopes abundance ratio.

2. Terminology

As wildly known water is built of hydrogen and oxygen elements. There appear various isotopes (different number of neutrons and the same number of protons) of these elements in the environment: ^{1}H – common hydrogen, ^{2}H – deuterium (D), ^{3}H – tritium (T), ^{16}O – common oxygen, ^{17}O – heavy oxygen (very rare), ^{18}O – heavy oxygen. While tritium is radioactive, there appear only two stable isotopes of oxygen and hydrogen in nature commonly (D, ^{18}O). The isotope ratio of stable environmental isotopes describes the ratio of the two most ordinary isotopes of the element. A generally used term is the abundance ratio, R, which expresses the ratio of heavy to the light isotope. To avoid the systematic error of the particular mass spectrometer the relative isotopic concentration is introduced:

$$\delta = \left(\frac{R_{sample}}{R_{reference}} - 1 \right) \cdot 10^{3} \; [‰] \tag{1}$$

The reference for the abundance ratio ^{18}O and D in water is the Vienna Standard Mean Ocean Water (VSMOW). Isotope fractionation appears in any thermodynamic reaction because of differences in reaction rates for particles with different molecular composition. As a consequence the change of abundance isotope ratio on one side of the reaction occurs. It is expressed by the fractionation factor α which is the ratio of the isotopes ratios for the reactant and product:

$$\alpha = \frac{R_{reactant}}{R_{product}} \tag{2}$$

As an example it may serve the fractionation of ^{18}O during the water evaporation:

$$\alpha^{18}O_{water-vapor} = \frac{\left({}^{18}O / {}^{16}O \right)_{water}}{\left({}^{18}O / {}^{16}O \right)_{vapor}} \tag{3}$$

Because of ^{18}O-H bond between molecules is stronger than ^{16}O-H, the $H_2{}^{18}O$ has a lower vapor pressure than $H_2{}^{16}O$. Therefore this reaction favors the lighter isotope, so the fractionation factor is grater than 1.

Together with the fractionation factor α, there are some other useful parameters introduced. The isotopic separation, Δ, defines the change of δ between two compounds:

$$\Delta_{X-Y} = \delta_X - \delta_Y \tag{4}$$

The enrichment factor, ε, expresses the isotopic difference:

$$\varepsilon_{reactant\text{-}product} = \left(\frac{R_{reactant}}{R_{product}} - 1 \right) \cdot 10^3 = (\alpha - 1) \cdot 10^3 \text{ [‰]} \quad (5)$$

All these factors are associated and the appropriate relationships can be easily derived.

As it was mentioned before the physical or chemical reactions of water are always accompanied by isotope fractionation. The main processes, which undergo water in building elements and materials, are listed below. The relations describing associated fractionation factors are also given (Clark I.D. et al. 1989).

Diffusion fractionation factor is defined by Graham's Law, which links the ratio of diffusive velocity to the square root of mass ratio, as:

$$\alpha_{diffusion} = \sqrt{\frac{m_X (m_Y + m_{dom})}{m_Y (m_X + m_{dom})}} \quad (6)$$

Where m_{dom} is the molar mass of the domain where diffusion takes place, m_X, m_Y are the molar masses of the heavy and ordinary isotopes appropriately.

Effusion fractionation factor is described by analogous relation:

$$\alpha_{effusion} = \sqrt{\frac{m_X}{m_Y}} \quad (7)$$

The fractionation factor of the evaporation process depends on the temperature according to the formulas:

$$10^3 \ln\alpha^{18}O_{w\text{-}v} = 1.137\,(10^6/T^2) - 0.4156\,(10^3/T) - 2.0667 \quad (8)$$

$$10^3 \ln\alpha^{2}H_{w\text{-}v} = 24.844\,(10^6/T^2) - 76.248\,(10^3/T) - 52.612 \quad (9)$$

In diminishing reservoir the isotope ratio changes according to Rayleigh distillation equation. Isotope ratio (R) is a function of its initial isotopic ratio, the remaining fraction of that reservoir (f) and the equilibrium fractionation factor for the reaction ($\alpha_{product\text{-}reactant}$), as:

$$R = R_o f^{(\alpha-1)} \quad (10)$$

3. Isotopes study of porous water

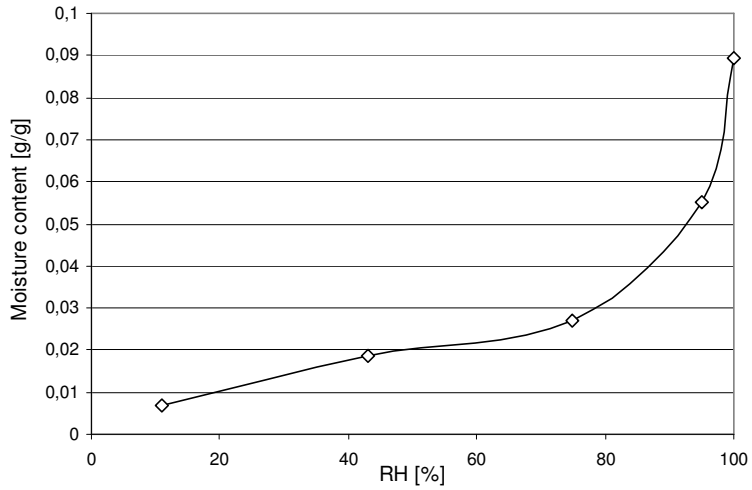

FIG. 1: Adsorption isotherm of analysed concrete.

In the presented research, transport of two most common isotopes of oxygen and hydrogen in light concrete were studied. Concrete, ρ = 960 kg/m^3, was made of CEM I 32.5 and expanded clay aggregates. The samples were

formed six years ago, hence we assumed that hydration of cement is almost completed. Therefore no additional fractionation due to hydration is taken account during isotopic analysis. The diffusion coefficient for concrete was determined using wet cup method, D = 1,47 10^{-6} [m/s^2] (Gudmundsson K. 2003). The adsorption isotherm was measured by means of saturated salt solutions for five different relative humidities: 11%, 43%, 76%, 95% and 100% at 20^{0}C is presented in Figure 1.

In order to determine the isotope abundance ratio of a water sample three different methods were proposed and tested. Two of them are direct methods: squeezing water from the sample using hydraulic press and evaporation of water in a rotary evaporator, Figure 2. The last one is a dilution method, in which we take advantage of diffusion of pore water in surrounding water with distinct isotopes ratio.

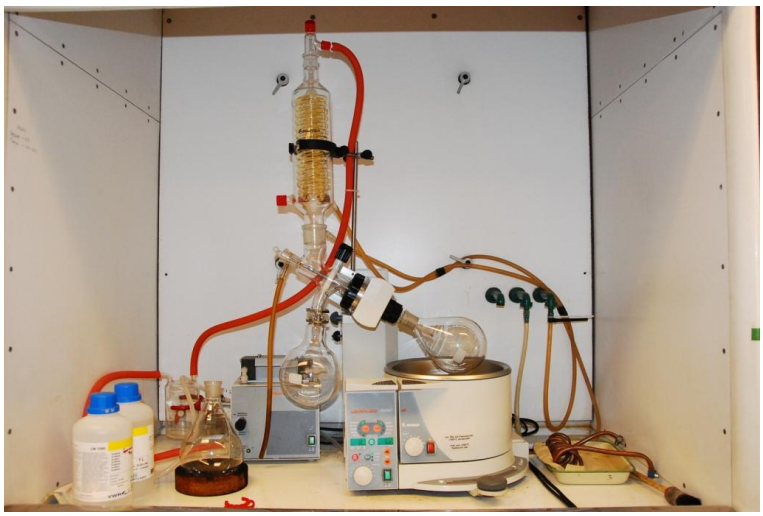

FIG. 2: Rotary Evaporator LABOROTA 4002-digital and vacuum pump.

The isotope abundance ratio of water samples was determined in the Institute of Earth Science in University of Iceland using a mass spectrometer Finningan Delta^{plus}XP. In both experiments the porous material was initially fully saturated with water .

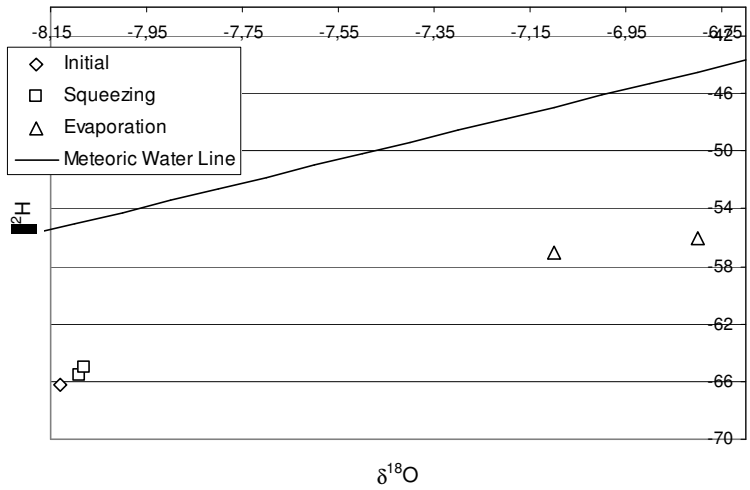

FIG. 3: Isotope abundance ratio of water retrieved by squeezing and evaporation.

The evaporation took place in the rotary evaporator LABOROTA 4002-digital, Figure 2. Crashed sample of about 300-500 cm^3 was put into the spherical glass vessel, which then was immersed into the hot oil. It caused evaporation of pore water. Then water vapor condensed onto a spiral pipe, which was kept cold by ordinary tap water flowing through it. The set of connected vessels and pipes was airtight with controlled air pressure inside

by vacuum pump. Condensed water drops were collected in the container. This method allowed us to retrieve about 50% of pore water.

For squeezing the sample of about 10 cm^3 was used. Samples were prepared in the same way as for the evaporation experiment. Squeezing allows water to escape through grooves, carved in the base plate of the equipment. Water, which was used to fill the porous sample, was collected for comparison. The squeezing lasted about 10 minutes; load applied was 50 kN and the diameter of cylinder about 3 cm. We were able to retrieve about 30% of the water from the pores.

Figure 3 shows the isotope composition of water retrieved by squeezing and by evaporation compared with original water. There is a small isotope fractionation induced by squeezing and quite substantial caused by evaporation. The fractionation in both of the analyzed processes is parallel to the Meteoric Water Line hence it is caused by both evaporation and condensation processes.

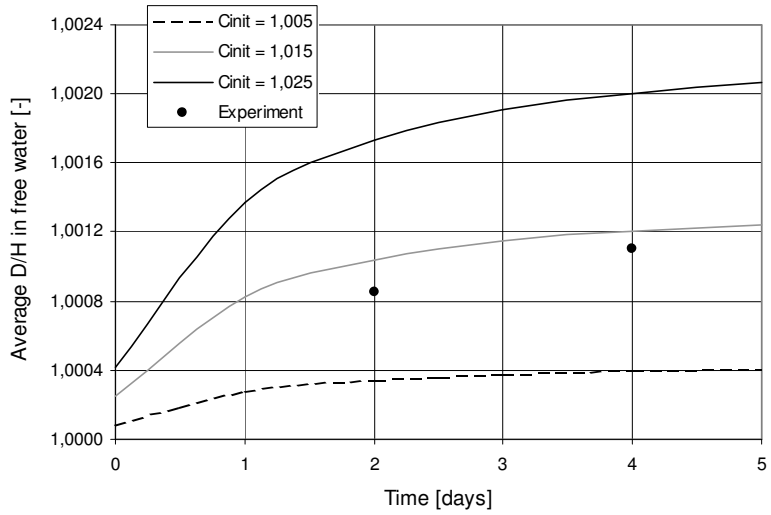

FIG. 4: Change of hydrogen isotope ratio of surrounded water as a function of time and different initial isotopes ratio of pore water.

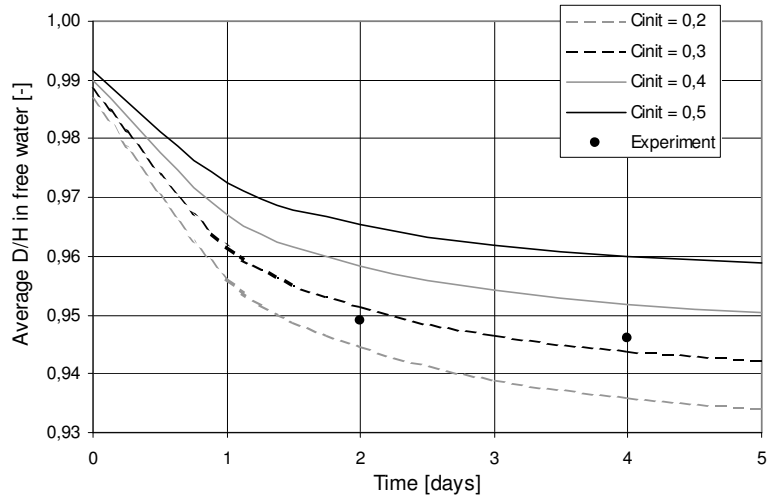

FIG. 5: Change of hydrogen isotope ratio of surrounded water as a function of time and different initial isotopes ratio of pore water.

The dilution method is based on diffusion of isotopes from porous material to surrounded water with distinct isotope ratio. The diffusion in this experiment can be modelled as 1D problem using II Fick's Law, as expressed:

$$n\frac{\partial c}{\partial t} = \nabla \cdot \left(D \nabla c\right) \tag{11}$$

where n – porosity, c – isotope concentration, D – diffusion coefficient. Because ^{2}H and ^{18}O concentration is very low their influence on the water density in equation (11) is neglected. It is also assumed that porosity does not change during the diffusion process. The equation is solved numerically; FEM and FDM are used for discretization of space and time respectively. Diffusion causes the isotope transport and therefore changes the isotope ratio in the surrounded and porous water simultaneously. At the end of the experiment the concrete sample was removed. The mixed water with homogeneous isotope concentration was collected for isotope measurement. By solving the inverse problem one is able to calculate the initial isotope ratio of the pore water. The thickness of the concrete samples equal 3 cm and the length of container equals 16 cm. The changes of isotope ratio D/H of surrounded water versus time are graphically presented in Figure 4, 5. Due to symmetrical boundary conditions, isotope transport was simulated for a half of the container, assuming zero mass flux on the plane of symmetry. Figure 4 represents the experiment (a) where, the isotope ratio in water occupying the porous material was higher than the surrounded water at the beginning, while the Figure 5 shows the results for the experiment (b) in which the initial isotope concentration was opposite. High concentration of deuterium in surrounding water was obtained by dissolving heavy water into ordinary tap water. By this way we are able to create any gradient of isotope concentration.

Based on the above curves and measured average isotope ratio of surrounded water at the beginning and at the end of the experiment (dots on the graphs) one is able to estimate the initial isotope ratio of the pore water. For comparison we measured isotope ratio of the pore water at the beginning of the experiment (a) and (b): 1,007 and 0,301 respectively. For both experiments, but especially for (b) with high isotope concentration gradient, we obtained quite good agreement between experimental data and the numerical simulation. For the convenience of reader all results are presented in their relative values, $c = 1$ for isotope concentration of the surrounding water in the container at the beginning of the experiment.

4. Changes of isotope ratio during capillary suction

The capillary suction occurs in building materials when there is no sufficient horizontal moisture barrier on the foundations or by heavy rains. Capillary transport also appears when water islands in the smallest pores are formed. In this case one can observe the following moisture transport mechanism; diffusion, condensation, capillary transport, evaporation, diffusion.

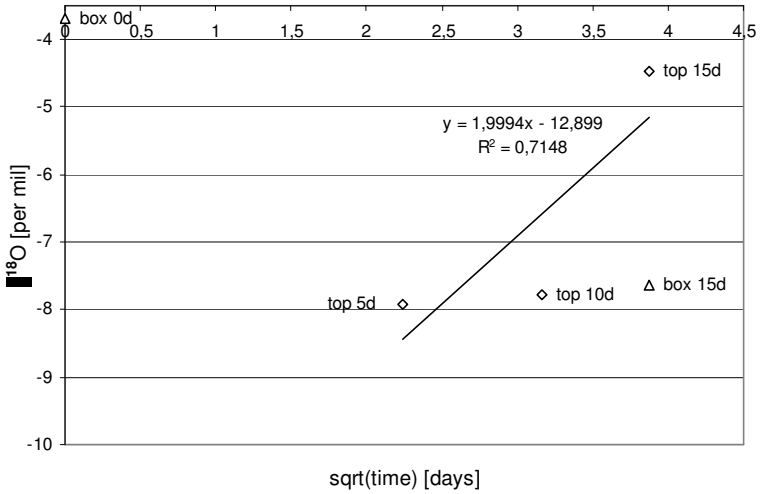

FIG. 6: Abundance ratio of isotope ^{18}O as a function of time.

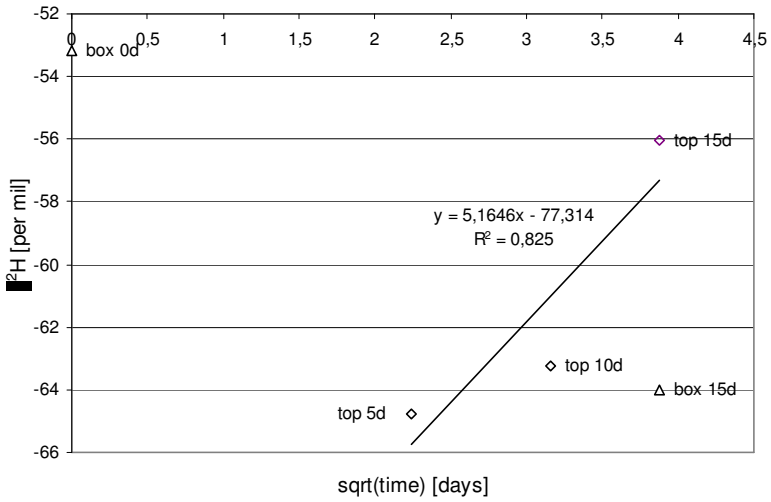

FIG. 7: Abundance ratio of isotope ^2H as a function of time.

During the suction experiment we also determined the capillary suction coefficient, $B = 0{,}32$ [kg/m^{2}s$^{0.5}$]. Blocks of concrete were cut into quadratic prism and were dried to constant mass. Lateral surface were coated with impermeable painting AquaStop to prevent any additional evaporation. Then, samples were put into water (1 cm of its high) to allow water to be absorbed.

The bottom and top area of the samples was 40 cm^2 while the height was 10 cm. Water samples were collected from the box at the beginning and at the end (15 days) of the experiment. Additionally we gathered water from the top of the concrete sample after 5, 10 and 15 days using a wettex sheet, which does not disturb the isotopic composition. The top of the sample and wettex sheet lying on it were covered by an impermeable material to prevent evaporation and additional isotope fractionation. Results are presented in Figures 6,7 and 8.

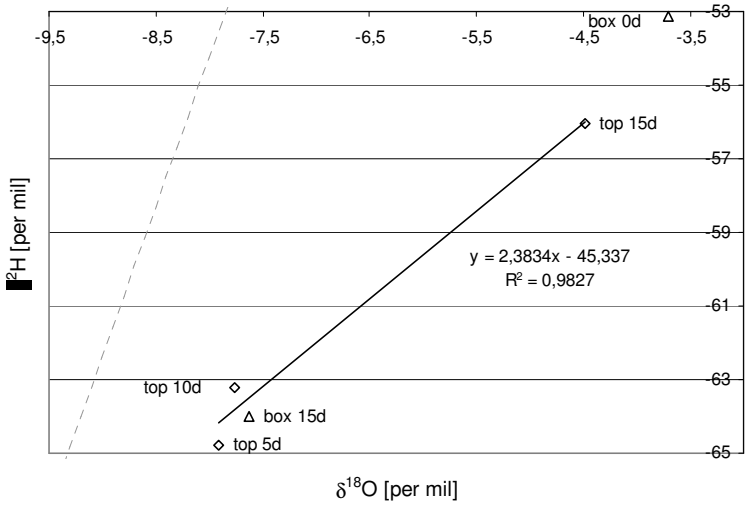

FIG. 8: The change of isotopes abundance ratio during capillary suction compared with Global Meteoric Line (dashed line).

One can notice depletion of heavier isotopes in water remaining in the box. It is caused by enrichment of heavier isotopes in water absorbed due to capillary forces. Increase of both $\delta^{18}O$ and δ^2H of water collected at the top of the concrete sample is observed, see Figure 6,7 and 8. At the first period of suction 5-10 days the change of isotope abundance ratio is parallel to the Global Meteoric Line.

5. Discussion and further research

Many physical and chemical processes influence the isotopic composition of water. Regarding transport of moisture in building materials their effects are well recognized and described by the fractionation factor. Therefore it might be helpful in providing the information about transport mechanisms of water and water vapor and their contribution in the total moisture flux through and within building envelopes.

The process of retrieving water from porous material is crucial and might determine failure or success of the whole research. Therefore three different methods of extruding water from material were carefully tested. Two of them are direct: evaporation, squeezing while the other is indirect: dilution, where the solution of porous water is tested in mass spectrometer. As one can notice the best results were obtained for squeezing water from the samples. Although the evaporation resulted in greater fractionation this method might also be used when the equipment for squeezing test is not applicable. All results got by direct methods are parallel to the Global Meteoric Line. It may indicate that the only processes, which took place during these tests, were condensation and evaporation of water. Squeezing water from the sample did change the isotopes ratio only slightly while the change was substantial for the evaporation procedure. The results of dilution are also quite satisfactory but this experiment is more time consuming and more expensive as one has to measure at least two water samples per one experiment.

Isotope fractionation (change in its concentration) occurs in any thermodynamic reaction. It is a consequence of the differences of thermodynamic properties of molecules with different isotopes. Therefore the knowledge of isotope fractionation has potential to enhance the knowledge of moisture transport and processes involved. We analyzed the influence of capillary suction on the hydrogen and oxygen isotopes abundance ratio.

In further studies we would like to test how diffusion effects the isotopic composition of porous water. The isotope based method might also be very useful in studying sorption of porous materials. By low relative humidity (RH) mono and then poly-layers of water molecules are created on the solid skeleton. When the RH increases the meniscuses form in the smallest pores and capillary condensation starts. As they are two different physical processes they should trigger different isotopes fractionation.

Acknowledgement

We greatly acknowledge the financial support of the Kami Research Foundation for the post doc year for Dr. Marcin Koniorczyk at KTH which made possible the research advances, reported in the presented paper. We also want to thank Dr. Arny Sveinbjornsdottir and her staff at the Institute of Earth Science in University of Iceland who provided the isotopic analysis for the water samples.

6. References

Arnikar H.J. (1989), Isotopes in the atomic age, Wiley, New Yor.

Clark I.D. and Fritz P.(1989), Environmental isotopes in hydrogeology, Lewis Publisher, New York.

Javoy M., Stillman C.J., Pineau F.(1986), Oxygen and hydrogen isotope studies on the basal complex of Canary Islands: implications on the conditions of their genesis, *Contributions to Minearology and Petrology*, No. 92, 225-235.

Gudmundsson K. (2001), Isotope tracing of moisture in buildings, *Nordic Journal of Building Physics*, Vol 2, .

Gudmundsson K. (2003), Alternative methods for analysing moisture transport inbuildings. Utilisation of tracer gas and natural stable isotopes, PhD thesis, KTH, Stockholm.

Mazor E. (2004), Chemical and Isotopic Groundwater Hydrology, 3th edition, Marcel Dekker Inc., New York.

Wagner R. and Wagner E. (2006), Influence of air pollution and site conditions on trends of carbon isotope ratio in tree rings cellulose, *Isotopes in Environmental and Health Studies*, No. 42, 351-365.

A New Method of Determining Moisture Flow Coefficients for both Isothermal and Non-isothermal Conditions

Stephen Burke, Tekn Lic.,
Building Physics, Lund University
Stephen.Burke@byggtek.lth.se

Johan Claesson, Professor,
Building Physics, Lund University
Johan.Claesson @byggtek.lth.se

Jesper Arfvidsson, Professor,
Building Physics, Lund University
Jesper.Arfvidsson@byggtek.lth.se

KEYWORDS: *isothermal, non-isothermal, moisture transport, experimental, phenomenological.*

SUMMARY:
The calculation of isothermal moisture transport requires a moisture flow coefficient, $D_\varphi(\varphi,T)$, for isothermal flow with φ as the moisture state variable. In the non-isothermal case, a second flow coefficient, $D_{T\varphi}(\varphi,T)$, is required to account for the temperature gradient. This means that a number of isothermal measurements are required for a few different temperature levels. It also means that a corresponding second set of measurements with temperature gradients are required.

This paper presents a new method of determining these flow coefficients for a set of moisture states and temperature levels. This is accomplished by measuring the change in mass over time as the sample absorbs or desorbs moisture. The sample is sealed and thermally insulated on all but one side with a heating pad at the top of the sample (within the insulation). This assembly is hung from a balance in a climate box that has a controlled temperature and relative humidity. The sample is exposed to a step-wise change in relative humidity and the change in mass over time is recorded. Care is taken to ensure that the sample is either absorbing or desorbing moisture in order to avoid complications with hysteresis. In the isothermal case, the sample is kept at a constant temperature during the measurements. In the non-isothermal case the sample has a known temperature gradient set by the temperature of the heating pad and the temperature of the climate box. The moisture flow coefficients are obtained from an analysis of the transient changes in mass.

The method and the ideas upon which it is based are presented. A few preliminary results, and technical difficulties encountered during the experimental development, are reported.

1. Introduction

1.1 Background

As buildings become more energy efficient, moisture management plays a more significant role in determining the performance of the building envelope. Without a proper understanding of moisture transport theory and the associated data, simulating different situations will be very difficult and could lead to unexpected moisture problems within a building envelope due to the lack of information. These problems can have a negative impact on both the structural integrity of the building and/or the health of the occupants (Bornehag et al., 2002, Fisk, 2000, Hägerhed et al., 2002, Nevalainen et al., 1998).

Moisture transport in materials is a complex phenomenon that has been studied quite a lot since the 1950s. Today's modern theory of moisture transport began with Philip and DeVries (1957) when they developed a theory of moisture transport which divided the total flow into liquid and water vapour flow and described this flow by equations involving gradients of moisture state and temperature. The difficulty with non-isothermal moisture transport is that it is impossible to directly measure the separate flows; only the sum is measurable.

Other experiments have been designed to try and quantify each effect independently through a combination of monitoring moisture transport through a material with salt solutions using a combination of isothermal and non-isothermal experiments (Arfvidsson and Cunningham, 2000, Avramidis and Siau, 1987, Bogoslovskii, 1965, Hedenblad, 1996, Li et al., 2006, Siau, 1985, Galbraith et al., 2000, Galbraith et al., 2004, Galbraith et al., 1998, Glass, 2007, Carmeliet and Roels, 2001, Segerholm, 2007).

The proposed method and experimental procedure is based on Arfvidsson (1990), Arfvisson and Cunningham (2000) and Segerholm (2007). Here, the method is presented. A few results and problems encountered in the ongoing experimental development are also reported.

1.2 Calculation of moisture flow – a phenomenological approach

The calculation of moisture flow processes in porous materials requires knowledge of equilibrium relations and equations for the moisture flux. Examples of equilibrium relations are Kelvin's equation and the relations between moisture content and relative humidity (sorption isotherm) or pore water pressure (water retention curve). These must be determined from measurements. The relation for moisture flux must also be determined experimentally. This is the key challenge, in particular for non-isothermal cases, when both moisture state and temperature vary in space and time.

First, consider the isothermal case. The generally accepted approach is to use a Fickian relation (1) between the moisture flux g and the gradient of the moisture state variable φ, which could be for example relative humidity or moisture content. The moisture flux is proportional to the gradient with a moisture flow coefficient D_φ as coefficient of proportionality. The basis for this kind of relation is the following. Consider a (thin) slab of a material with the moisture states φ_1 and φ_2 on the two sides. The flux is zero for equal moisture states, and it is reasonable to assume that the flux is proportional to the difference φ_1-φ_2 and inversely proportional to the slab thickness. This gives a Fickian moisture flow equation. It is clear that the coefficient, in general, varies with the level of the moisture state and with the temperature: $D_\varphi = D_\varphi(\varphi,T)$. This coefficient must be measured for different φ and for different temperatures. Fick's law is a *phenomenological* relation that is based on direct measurements:

$$g = -D_\varphi(\varphi,T)\cdot\frac{\partial\varphi}{\partial x} \tag{1}$$

Now consider the non-isothermal case. The moisture state *and the temperature* may now be different on the two sides of the slab. The direct generalization of Fick's law is to assume that the flux has an additional term that is proportional to the temperature difference and inversely proportional to the slab thickness. The generalization of Fick's law is then:

$$g = -D_\varphi(\varphi,T)\cdot\frac{\partial\varphi}{\partial x} - D_{T\varphi}(\varphi,T)\cdot\frac{\partial T}{\partial x} \tag{2}$$

This is again a phenomenological relation that should be based on direct measurements. There are now two flow coefficients which are functions of the moisture state φ and the temperature T. It is important to realize that these two functions must be determined experimentally. There are, to our best knowledge, no general theories or relations that make it possible to avoid direct measurements. The above discussion is presented in more detail in Segerholm (2007, Ch. 7).

The required measurements are quite extensive. The isothermal flow coefficient $D_\varphi(\varphi,T)$ must be determined as a function of φ for different temperature levels. This requires isothermal measurements for a number of temperature levels. The determination of the second flow coefficient $D_{T\varphi}(\varphi,T)$ requires a corresponding second set of measurements for which there is also a temperature gradient over the slab. In the second set of measurements, the first right-hand ("isothermal") part in (2) must be known in order to determine $D_{T\varphi}(\varphi,T)$ for any particular φ and T. This means, for example, that an attempt to measure non-isothermal coefficients without knowing the temperature dependence for $D_\varphi(\varphi,T)$ may be questioned. These problems are discussed in further in Segerholm (2007, Ch. 7).

2. Description of the measurement method

The measurements for the isothermal and non-isothermal coefficients are done in different experimental set-ups. The isothermal moisture transport coefficient, $D_{\varphi}(\varphi,T)$, is determined in the following way. The sample is exposed to a sequence of relative humidity steps as shown in Figure 1. The change in mass over time of a small sample is recorded using a DVS 1000 sorption balance using the methods presented in Arfvidsson (1990) and Anderberg & Wadsö (2005). The figure shows the result for Norway Spruce at 30°C. Thus information is obtained regarding the moisture transport when the sample's relative humidity changes from one level to another, e.g. from 50% to 75%. Using this data, moisture transport coefficients can be calculated for each level of relative humidity at the current temperature. One phenomenon not investigated here is hysteresis, which is avoided by ensuring pure absorption or desorption.

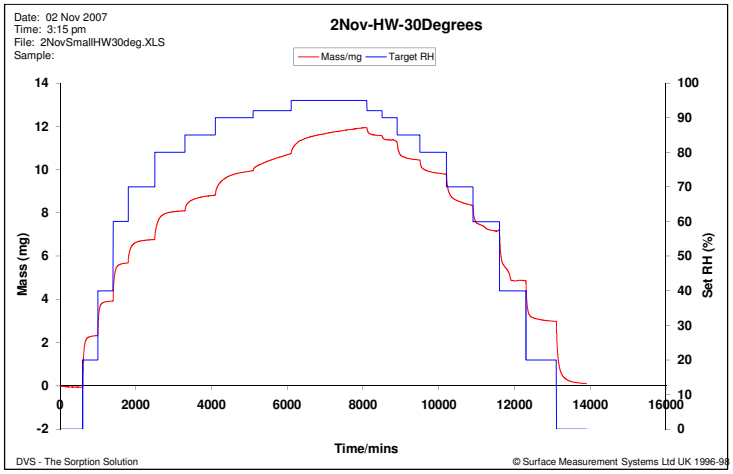

Figure 1: Data obtained from the DVS 1000 sorption balance for a 0.0529 g dry mass sample of heartwood from a Norway Spruce tree from Växjö, Sweden.

The non-isothermal moisture transport coefficient, $D_{T\varphi}$ (φ,T), is calculated by a modified weighing method. The sample is conditioned to a predetermined moisture level and sealed so that drying occurs in one direction. A temperature gradient is applied to the sample and the total moisture flow (g) over time is recorded for this temperature gradient and relative humidity in the climate box. After the sample is at steady state, the humidity is changed by changing the salt solution, and the total flow is measured again. This step is repeated for a third relative humidity, etc. The entire procedure is repeated for different temperatures. It is now possible to calculate $D_{T\varphi}(\varphi,T)$ for the specific sample being tested at the specific temperature and humidity range. Here, the isothermal coefficient and the measured temperature gradient are used. The precise evaluation procedure will be reported elsewhere.

This new method of measuring the non-isothermal moisture flow coefficient is based upon the idea of drying or wetting a material by applying a temperature gradient over the sample. The experimental set-up involves two parts. The first part, shown in Figure 2, is an insulated sample holder with a heating pad. The sample holder is made of Styrofoam insulation, aluminium and the System Platon sealing tape, which does not absorb any significant amounts of moisture. The sealing tape was tested in the sorption balance and absorbed approximately 0.4 mg/5000 mg sample of sealant from 0 to 95% RH. The sample holder is connected to a regulator with a sensor that ensures that the temperature at the top of the sample remains relatively constant, within ±0.1°C of the set temperature. This sample holder system is hung from a balance down into the climate box, Figure 3. A sample, which is sealed on all but one side, is inserted into the sample holder.

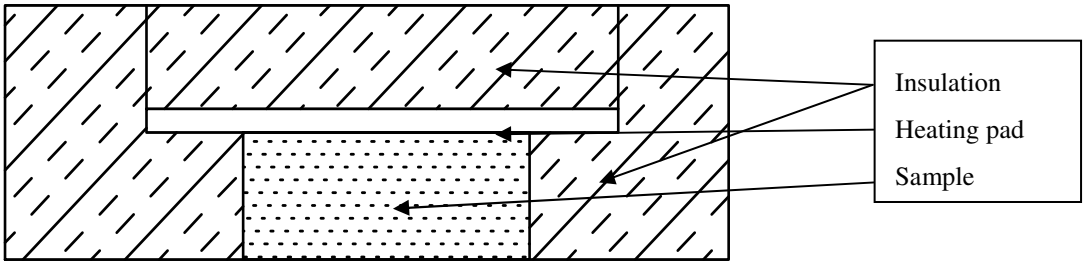

Figure 2: Cross section of sample holder.

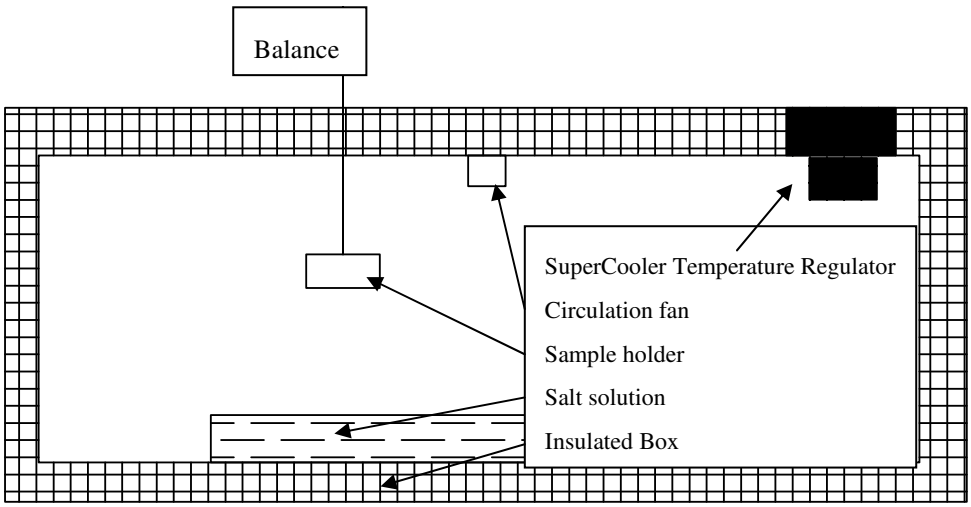

Figure 3: Section of the experimental apparatus with the sample holder hanging freely from a balance within the climate box.

The second part is an insulated climate box (Figure 3), which has a saturated salt solution at the bottom of the box, a circulation fan at the top of the box and a Supercool AA-024 thermoelectric air to air system with a PR-59 temperature controller. The AA-024 has both cooling and heating capacity with an accuracy of ±0.01°C. When the system is running, the temperature varies ±0.02°C from the set point. Figures 4 and 5 show photos of the two parts of the setup.

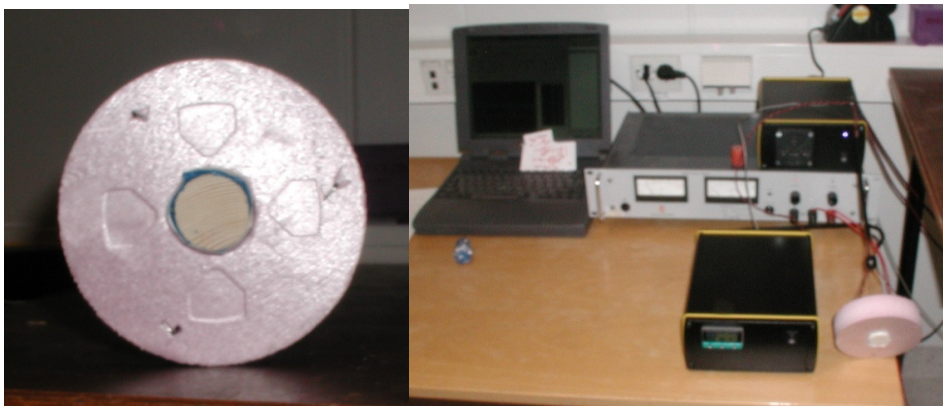

Figure 4: The left image shows the sample holder with a sample in the center. The right image shows the control units with the sample holder to the right.

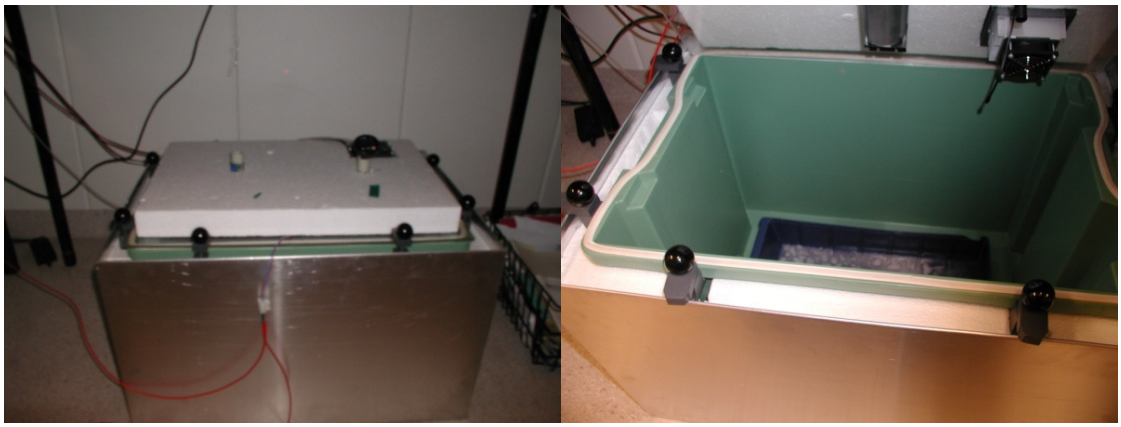

Figure 5: The insulated climate box with circulation fan, thermal regulator and salt solution.

3. Preliminary results and discussion

3.1 Isothermal moisture transport

The preliminary results for the isothermal component at the time of writing are incomplete due to the poor performance of the DVS1000 sorption balance. Only two of the minimum three complete runs were obtained between August 2007 and December 2007 for 20°C and 30°C. Each run took approximately 10 days. At 40°C condensation occurred in the sample chamber at 92% RH. The specifications of the DVS 1000 state that samples can be tested up to 95% RH at 60°C. It has been determined that the machine cannot properly condition the temperature of the sample's supply gas flow due to poor insulation in the climate chamber. The DVS is currently being modified and measurements will be re-done.

3.2 Non-isothermal moisture transport

3.2.1 Thermal analyses

When doing non-isothermal measurements, it is important that there is a one-dimensional temperature profile through the sample (with essentially straight horizontal isotherms as shown in Figure 6). Segerholm (2007) measured the surface temperature of his cup method samples and had problems with decreased temperatures around the outer edges. He minimized this effect by mounting the samples high on a plastic cup, which decreased the difference between the max and min top surface temperatures to about 0.5°C. However there are no temperatures recorded for the bottom surface where the isotherms would be cutting through the sample the most, hence having the greatest temperature variation. This temperature decrease around the outer perimeter of the samples using a cup method has also been confirmed through simulations.

Using HEAT2 (Blomberg, 1996), three-dimensional cylindrical thermal simulations were done in order to determine the optimal sample size and position compared to the heating pad and insulation thickness. In particular, the diameter of the sample was varied. The optimal case is shown in Figure 6.

An Infra Red (IR) camera was used to compare the actual thermal performance of the sample holder to the thermal simulation (Figure 7). The heating pad was set to 30°C and the indoor air temperature was 22°C. Both showed the sample to have a surface temperature of 26°C confirming the accuracy of the simulation.

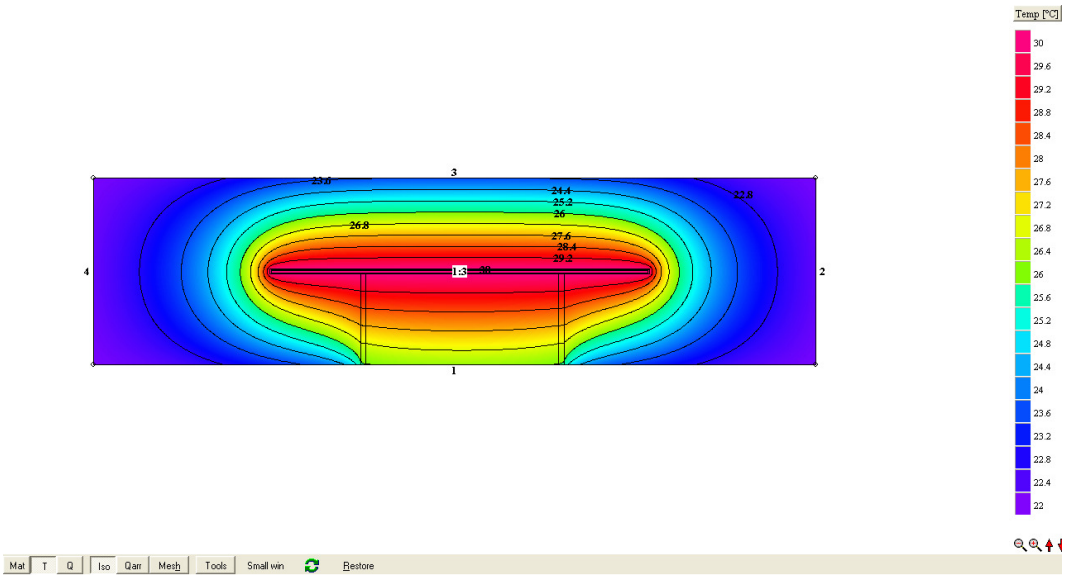

Figure 6: Optimal sample diameter to minimize the curvature of isotherms in the sample.

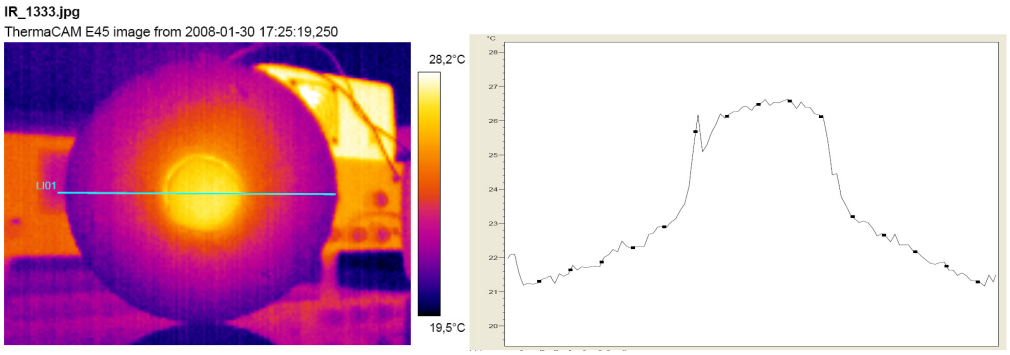

Figure 7: Left: IR image of the sample's surface. Right: The temperature profile along the width of the sample holder.

The thermal environment of the climate box is also an important factor. Any deviations in temperature can change the RH. Temperatures within the climate box have proved to be very stable (±0.2°C from the set point) so far. The temperature control system is able to compensate for any heat from the sample holder, fans, and climate outside of the climate box, to ensure a constant temperature. This also helps to ensure that RH from the salt solution remains fairly constant. The box is not affected by a slightly different environment outside of the box, so it is not necessary to place the climate box within a climate room. However there is a point where the heat losses/gains from an extreme exterior climate will be too great for the small system to handle. One test showed that the AA-024 can cool the interior of the climate box 10°C below the external temperature of the box while maintaining a stable internal temperature. If a greater temperature difference is desired, then a larger regulator should be used.

3.2.2 Problems with moisture control

Saturated salt solutions have been used as a means of controlling humidity for a long time and there are many salts to choose from (O'Brien, 1948). However, it can be difficult to control the humidity of a closed space as a number of factors can change the humidity level. Temperature is one of the primary factors determining humidity. Thermal layering in, for example, jars can cause differences in relative humidity. This can be minimised by the use of a circulation fan. A quick test was done to see if a noticeable effect could be seen on the RH in the empty climate box with and without a fan using an old, unknown salt solution. The RH decreased by around 5% with a fan on compared to no fan. This same effect was observed by Martin (1962), while running experiments with NH_4NO_3 and a sample. He did not investigate this further and concluded that the absorption of moisture by the sample lowered the equilibrium humidity level in the jar by about 4% RH when the fan was on.

A new supersaturated salt solution of $MgCl_2*6H_20$ was prepared at 100°C and the experiment was repeated. No change in RH was observed. This check will be done for each salt type used since it is not known if this effect is a result of the type of salt used, the quality of the salt solution, the method in which it was prepared or leaks in the climate box.

Leaks in the system are a source of error. They have no direct effect on the mass of the sample however they can cause instability with temperature and especially RH. In this case, the thermal regulator can compensate for leaks. However, salt solutions cannot compensate for leaks. In the preliminary runs, the salt $MgCl_2*6H_20$ was stable in an empty climate box at around 33.7% RH, which was expected. Unfortunately the preliminary run using K_2SO_4 only had an RH of 90%, which should be 97%. During both tests, the room temperature was 21°C and the RH was 30%. It is unknown if the problem is due to the salt solution or leaks in the climate box.

3.2.3 The sample holder

During a weighing, all fans in the climate box are shut down for about 20 seconds since the fans create a wind current within the climate box which is strong enough to affect the mass of the sample and sample holder. All data are recorded just before the fans start up again so that there is no interference from air flows within the box.

The wiring connecting the heating pad and temperature sensor to the regulator from the sample holder has proven to be problematic. During preliminary measurements, it was observed that the mass showed by the balance changed if the climate box was moved. In this case, the wires were connected to a clamp on the box, and then went to the regulator that was monthed on the cover of the climate box. A second run without the clamp, allowing the wires to hang freely from the sample holder to the regulator, showed a significant improvement. The mass did not change after adjusting the climate box. However, to reduce the error as much as possible, the whole system cannot be disturbed once the measurements have started as any movement of the wire position can potentially change the mass reading.

3.2.4 Planned experimental work

It is important to remember that the work presented here is not complete. Modifications are needed to improve this method and reduce errors. Errors were even discovered with the well proven sorption balance, errors that may not have been discovered running traditional analyses at one temperature.

It is also important to note that the method will have to be repeated for the other moisture flow directions. In the case above, the moisture transport is in the fibre direction. The entire method must be repeated for both the tangential and radial directions for the same sample in order to be able to calculate the total moisture flow in all directions.

More modifications to the method must be done in order to reduce leakage and to ensure a more stable humidity level inside the climate box before full-scale experiments can be run.

4. Conclusions

The method presented here is not complete but it shows potential. It should provide the isothermal and non-isothermal coefficients, $D_\varphi(\varphi,T)$ and $D_{T\varphi}(\varphi,T)$, with reasonable resolution in φ and T. This would allow for moisture transport simulations based on data where the flow coefficients are directly measured.

Preliminary results thus far show the non-isothermal apparatus is very stable in regards to thermal performance and functions according to simulations run during the design of the method. The temperature control system in combination with the insulation around the climate box is able to maintain a very stable temperature. The moisture control also functions well at a low RH. Unfortunately the moisture state is not yet stable at a high RH level. At the time of writing, it is unknown if this is due to leaks in the climate box, poor quality salt solutions or other effects.

Isothermal measurements with the DVS 1000 are very precise and relatively quick. It has a closed system that reduces external errors. Once it is repaired, it should be a fast, automated method of determining the isothermal moisture transport coeffecients for a large number of humidity steps at different temperatures.

5. References

Anderberg, A. & Wadsö, L. (2005) Method for simultaneous determination of sorption isotherms and diffusivity of cement based materials. *Proceedings of the 7th Symposium on Building Physics in the Nordic Countries.* Reykjavik, Iceland, The Icelandic Building Research Institute.

Arfvidsson, J. (1990) PC-MODELS FOR COMBINED HEAT AND MOISTURE FLOW IN BUILDING MATERIALS - Basic flow equations and required measurements. IN THUE, J. V. (Ed. *Building Physics in the Nordic Countries.* Trondheim, Tapir Publishers.

Arfvidsson, J. & Cunningham, M. (2000) A transient technique for determining diffusion coefficients in hygroscopic materials. *Building and Environment,* 35**,** 239-249.

Avramidis, S. & Siau, J. F. (1987) Experiments in nonisothermal diffusion of moisture in wood. *Wood Science and Technology,* 21**,** 329-334.

Blomberg, T. (1996) Heat conduction in two and three dimensions - computer modelling of building physics applications. *Department of Building Technology, Building Physics.* Lund, Lund University.

Bogoslovskii, V. N. (1965) The Moisture Potential. *Inzhenerno-Fizicheskii Zhurnal,* 8**,** 216-222.

Bornehag, C. G., Sundell, J., Hägerhed, L. & Janson, S. (2002) Dampness in buildings and health. Dampness at home as a risk factor for symptoms among 10 851 Swedish children (DBH-step 1). Monterey, USA.

Carmeliet, J. & Roels, S. (2001) Determination of the Isothermal Moisture Transport Properties of Porous Building Materials. *Journal of Thermal Envelops and Building Science,* 24**,** 183-209.

Fisk, W. J. (2000) Review of health and productivity gains from better IEQ (Indoor Environmental Quality). Helsinki.

Galbraith, G. H., Guo, J. S. & Mclean, R. C. (2000) The effect of temperature on the moisture permeability of building materials. *Building Research and Information,* 28**,** 245-259.

Galbraith, G. H., Kelly, D. J. & Mclean, R. C. (2004) Moisture permeability measurements under reduced barometric pressures *Materials and Structures,* 37**,** 311-317.

Galbraith, G. H., Mclean, R. C., Gillespie, I., Guo, J. & Kelly, D. (1998) Nonisothermal moisture diffusion in porous building materials. *Building Research and Information,* 26**,** 330-339.

Glass, S. V. (2007) Measurements of Moisture Transport in Wood-Based Materials under Isothermal and Nonisothermal Conditions. *Buildings X.* Florida, USA, ASHRAE.

Hedenblad, G. (1996) Moisture permeability of some porous building materials. *Building Physics in the Nordic Countries.* Espoo, Finland.

Hägerhed, L., Bornehag, C. G. & Sundell, J. (2002) Dampness in buildings and health. Building characteristics as predictors for dampness in 8681 Swedish dwellings. Monterey, USA.

Li, X., Zhang, B., Li, W. & Li, Y. (2006) Nonisothermal moisture movement in wood. *Front. For. China***,** 348-352.

Martin, S. (1962) The control of conditioning atmospheres by saturated salt solutions. *J. Sci. Instrum.,* 39**,** 370-372.

Nevalainen, A., Vahteristo, M., Koivisto, J., Meklin, T., Hyvärinen, A., Keskikarhu, J. & Husman, T. (1998) Moisture, mold and health in apartment homes. Gävle, Sweden.

O'brien, F. E. M. (1948) The Control of Humidity by Saturated Salt Solutions. *J. Sci. Instrum.,* 25**,** 73-76.

Philip, J. R. & De Vries, D. A. (1957) Moisture Movement in Porous Material under Temperature Gradients. *Transactions, American Geophysical Union,* 38.

Segerholm, I. (2007) Moisture Transport Processes in Scots Pine - Anomalous Capillary Suction. Nonisothermal diffusion. *Division of Building Technology - Building Materials.* Göteborg, Sweden, Chalmers.

Siau, J. F. (1985) Nonisothermal moisture diffusion experiments analyzed by four alternative equations. *Wood Science and Technology,* 19**,** 151-157.

Influence of the microstructure on the vapour transport in wood

Wolfgang Zillig, Ph.D. student
Laboratory of Building Physics, Department of Civil Engineering, Katholieke Universiteit Leuven, Belgium.; wolfgang.zillig@bwk.kuleuven.be http://www.kuleuven.be/bwf/eng/index.htm

Jan Carmeliet, Ph.D.,
Chair of Building Physics, Swiss Federal Institute of Technology ETHZ, Zürich, ETH-Hönggerberg, CH-8093 Zürich, Empa, Swiss Federal Laboratories for Materials Testing and Research, Laboratory for Building Technologies, Überlandstraße 129, CH-8600 Dübendorf

Dominique Derome, Ph.D.,
Empa, Swiss Federal Laboratories for Materials Testing and Research, Wood Laboratory, Überlandstraße 129, CH-8600 Dübendorf

KEYWORDS: *wood, microstructure, vapour transport, multiscale.*

SUMMARY:
Moisture transport in wood is complex due to its anisotropic material structure, resulting from the cells anatomy, growth rings, where early- and latewood alternate, and the presence of vessels, rays and pits. As a result, the water vapour transport properties of wood are highly dependent on the direction (longitudinal, radial or tangential). Moreover, due to variations in cell geometry, and growth ring structure, the transport properties, such as density and vapour diffusion coefficient, depend on location. The purpose of this paper is to develop a methodology to determine location dependent water vapour transport properties and to study their influence on the global hygroscopic behaviour of wood.

1. Introduction

Due to the anisotropic structure of wood with growth rings of early wood and late wood, wood properties depend on orientation (radial, tangential and longitudinal). Wood is therefore considered to be orthotropic. Examples of orthotropic moisture transport models can be found in Kowalski (2003), Zillig et al. (2006, 2007a, 2007b). The determination of material properties of wood can be done experimentally. However, due to variation of the geometry and thickness of the early wood and late wood layers, the presence of rays and variations in the underneath cellular structure, the macroscopic properties may show high variance with place. To understand better the relation between the macroscopic properties and the underlying wood cellular structure, multiscale methods using upscaling techniques have been proposed. Persson (2000) used a hexagon cell structure, with gradual reduction in cell size from early wood to late wood, to model the mechanical behaviour of a growth ring. Gu (2001) used a unit cell and a gradient approach with rectangular cell shapes to model the thermal heat conduction in wood.

A three-scale water vapour transport model to determine the homogenized transport properties was already formulated by Siau in 1995. At the cellular scale, a unit cell is used to determine the vapour transport properties of early- and latewood at the meso-scale. The unit cell approach assumes a cube shaped unit cell with fixed dimensions and wall thicknesses. The vapour permeability of the wall for early and latewood, in radial and tangential direction, is assumed to be equal, since the cell walls are all composed of the same materials (cellulose and hemicellulose). Differences in water vapour permeability in radial and tangential direction thus arise only from differences in cell geometry and wall thickness. This assumption may be not completely true since the wall is known to be composed of different layers with different composition. The vapour permeability in the three directions of the unit cell is determined using a simple parallel-serial resistance model. The properties of late and early wood at the meso-scale are further upscaled to the macro-level using a representative elementary volume (REV). The REV consists of two parallel plane layers, one of early- and one of late wood, and a ray layer normal to the other layers. This REV is also solved using a simple parallel-serial resistance model. The model has however some limitations: (1) the regular unit cell shape does not reflect the irregular cell geometry varying with place, (2) the gradual transition of cell geometry from early wood to late wood is neglected, (3) the curved shape of the early wood and late wood layers is neglected.

In Zillig et al. (2007b), a mesoscopic approach for vapour transport in wood is presented to overcome some limitations of the Siau model. In the mesoscopic model the curved geometry of the early wood and late wood layers as obtained from SEM images is modelled using 2D finite elements (the presence of rays was not taken into account). The vapour transport properties for the different layers were determined using the unit cell approach of Siau, where the average dimensions of the cell and the layer thickness were determined from SEM images. A good agreement was obtained between the mesoscopic and measured vapour permeability. However, in this model, two main problems remain unsolved: (1) average cell dimensions were used not taking into account the non-regular shape of the cells and (2) the gradually reduction in lumen size from earlywood to latewood is not considered.

In this paper, we present a model to overcome the limitations of the Siau model. The model is based on the determination of the water vapour transport properties directly from the cellular microstructure. First, we present the theory of orthotropic water vapour transport. Then, the upscaling method is presented and extended to determine location dependent water vapour transport properties of wood. Finally, we draw some conclusions.

2. Theory of water vapour transport

Isothermal water vapour transport in orthotropic materials is described by

$$\rho_d \frac{\partial u}{\partial t} = \nabla \boldsymbol{\delta} \nabla p_v \tag{1}$$

with ρ_d the dry density of wood [kg/m³], u the moisture content [kg/kg], t time [s], $\boldsymbol{\delta}$ the water vapor permeability tensor [s] and p_v the water vapor pressure [Pa]. The vapor permeability tensor is given by

$$\boldsymbol{\delta} = \begin{bmatrix} \delta_L & 0 & 0 \\ 0 & \delta_R & 0 \\ 0 & 0 & \delta_T \end{bmatrix} = \delta_a \begin{bmatrix} 1/\mu_L & 0 & 0 \\ 0 & 1/\mu_R & 0 \\ 0 & 0 & 1/\mu_T \end{bmatrix} \tag{2}$$

where the subscript L, R, T refer to respectively longitudinal, radial and tangential direction, δ_a is the water vapor permeability of air [s] and μ is the water vapor resistance factor [-].
Further derivation gives

$$\rho_d \frac{\partial u}{\partial \phi} \cdot \frac{\partial \phi}{\partial t} = \rho_d \xi \cdot \frac{\partial \phi}{\partial t} = \nabla \boldsymbol{\delta} \cdot p_{vsat} \nabla \phi \tag{3}$$

where ξ is the moisture capacity [kg/kg], ϕ the relative humidity (RH) [-] and p_{vsat} the saturation water vapor pressure [Pa]. The function describing $u(\phi)$ is called the sorption isotherm. Neglecting the density of dry air, the dry density of wood is given by:

$$\rho_d = \rho_w (1 - \phi) \tag{4}$$

with ϕ the porosity.

3. Multiscale model

3.1 Determination of the cellular structure

Analysis of the cell wall from early wood as well as from latewood cells reveals that the chemical composition is almost constant only differences in some sugars in the hemicellulose are found (Bertaud, 2004). Kärenlampi (2005) actually performed sorption measurements on early- as well as latewood separately and found no significant difference. It is therefore logical to assume that density and sorption characteristics of the cell wall are constant and do not vary with place. Based on this assumption, the water vapour transport properties (dry density, sorption isotherm, vapour permeability) only depend on the underlying cellular geometry. The cellular microstructure is determined using a Scanning Electron Micrograph (SEM) of a spruce specimen. Figure 1a shows an example of the cross section of one growth ring. We clearly distinguish the cellular structure of early and late wood. The grey contrast between wall and lumen is too limited in order to derive a binary image of the cellular structure by thresholding. Therefore, the lumens of the cells are first manually coloured white using a

graphical program (Photoshop). The rest of the image is considered to be the cell wall and is coloured in black. Figure 1b gives the obtained binary image of part of the cellular structure

3.2 Prediction of the upscaled water vapour permeability

The water vapour permeability of a growth ring can be determined solving a stationary directional water vapour flow problem. A directional flow problem can be simulated prescribing as boundary conditions on the domain, a water vapour pressure gradient between two opposite sides and no flow on the perpendicular sides. The solution yields the stationary flow rate Q over the domain. The upscaled water vapour resistance factor can then be determined as

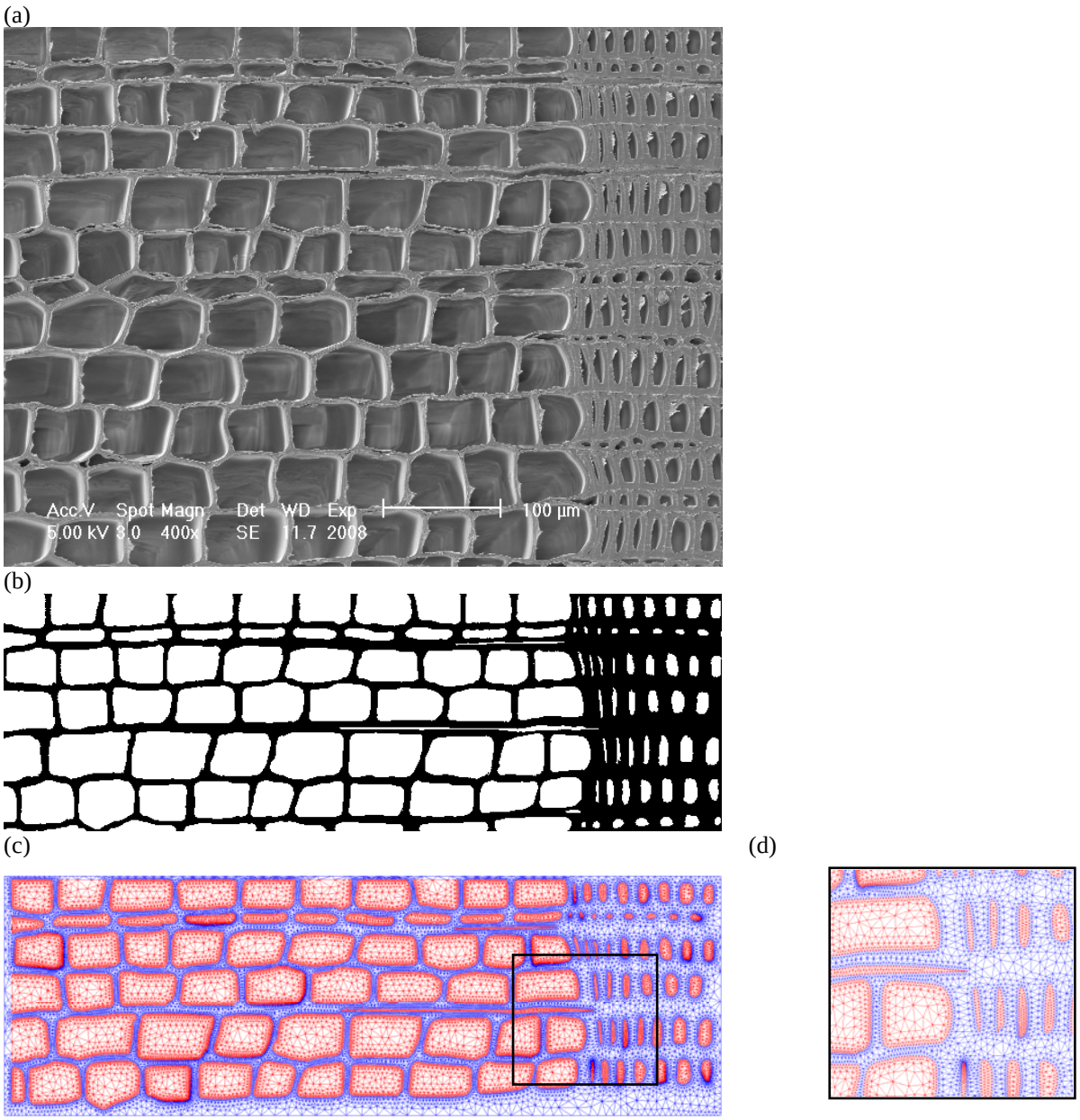

Figure 1: (a) Scanning Electron Micrograph (SEM) from a part of a growth ring. (b) Binary representation of the cell wall and lumen. (c) Finite element mesh. (d) Detail of FEM mesh.

$$\delta(\phi) = \frac{Q}{A}\frac{1}{\Delta p_v} \quad or \quad \mu\ (\phi) = \frac{\delta_a\, A\, \Delta p_v}{Q} \tag{5}$$

where A is the cross section traversed by the flow. This process is repeated for different moisture contents (or relative humidities) to obtain the relationship between water vapour resistance factor and relative humidity. Applying the boundary conditions on the perpendicular sides and repeating the flow simulations, the permeability in the perpendicular direction is obtained.

The stationary flow problem is solved applying the finite element method. Therefore, the domain has to be divided in finite elements and the proper material properties have to be attributed to the elements. To generate a mesh of elements representing the geometry of one growth ring, the binary image (Figure 1b) is first exported to an edge detection software (Autotrace) that extracts the boundaries and produce polygons describing the boundaries between lumen and cell wall. The polygonal image is then used as the base for the generation of the mesh using the program Gid. The domain is represented by an unstructured mesh of triangular linear elements (Figure 1c-d). Each lumen is identified as air with a vapour resistance factor equal to 1. The remaining part is identified as cell wall with a vapour resistance factor equal to μ_w. We assume that the water vapour permeability of the wall is isotropic, i.e. the water vapour permeability normal to and along the cell wall is assumed to be equal. The mesh representing a piece of one growth ring is then used to determine the upscaled water vapour resistance factor μ_{gr} of the growth ring solving the stationary flow problem.

The only unknown in the model is the vapour resistance factor of the wall μ_w. The vapour permeability of the wall is determined from measurements, comparing the upscaled water vapour resistance factor for the complete growth ring μ_{gr} with measurement values μ_m. The water vapour permeability was measured using the dry cup/wet cup method at three different relative humidity ranges (Zillig et al. 2007b). The specimens have a size of 100 x 100 x 10 mm³ and include therefore several growth rings. The specimens were selected and cut in such a way that the specimens have a quite uniform and straight growth ring structure. The measured water vapour resistance factors in radial and tangential direction for three given relative humidities are given in table 1. An easy manner to determine the water vapour resistance factor of the wall μ_w is to first calculate the relation between the upscaled water vapour resistance factors for a growth ring μ_{gr} and the water vapour resistance factor of the wall μ_w. Figure 2 shows that an almost linear relationship between μ_{gr} and μ_w for late and early wood is obtained. This linear relationship can now be used to determine the water vapour resistance factors of the wall for the three different relative humidities. The results are given in Table 1.

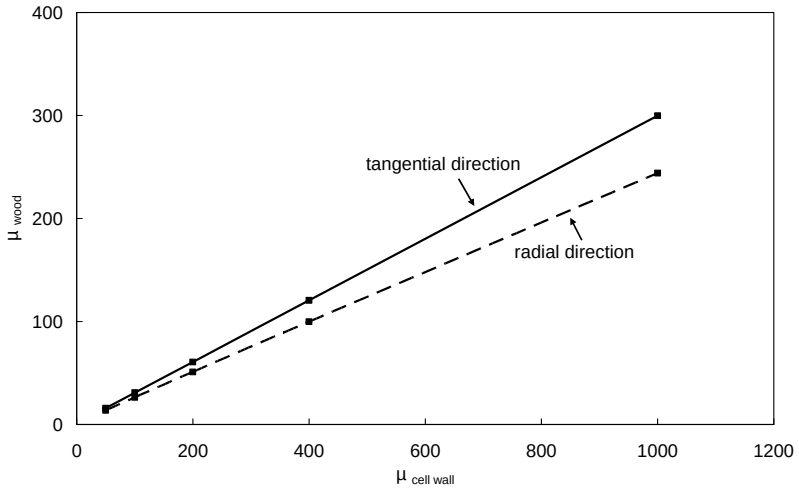

Figure 2: Averaged vapour resistance factor of the total growth ring in radial and tangential direction in dependence of the cell wall vapour resistance factor.

Table 1: Measured and simulated vapor resistance factors for spruce in radial and tangential directions.

	30% RH			62.5% RH			71.5% RH		
	μ_m	μ_w	μ_{gr} (μ_w =1064)	μ_m	μ_w	μ_{gr} (μ_w =252)	μ_m	μ_w	μ_{gr} (μ_w =96)
radial	237	970	260	72	288	63	29	110	25
tangential	341	1138	319	68	224	76	26	84	30

(a)

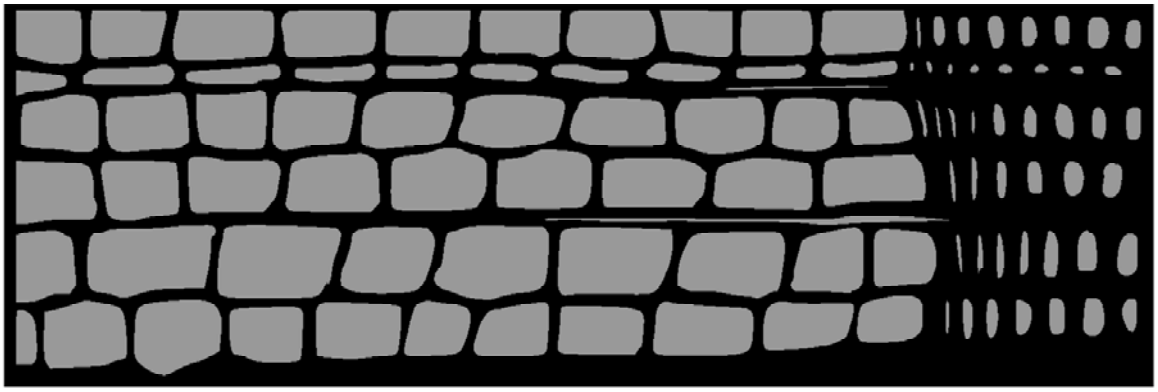

(b)

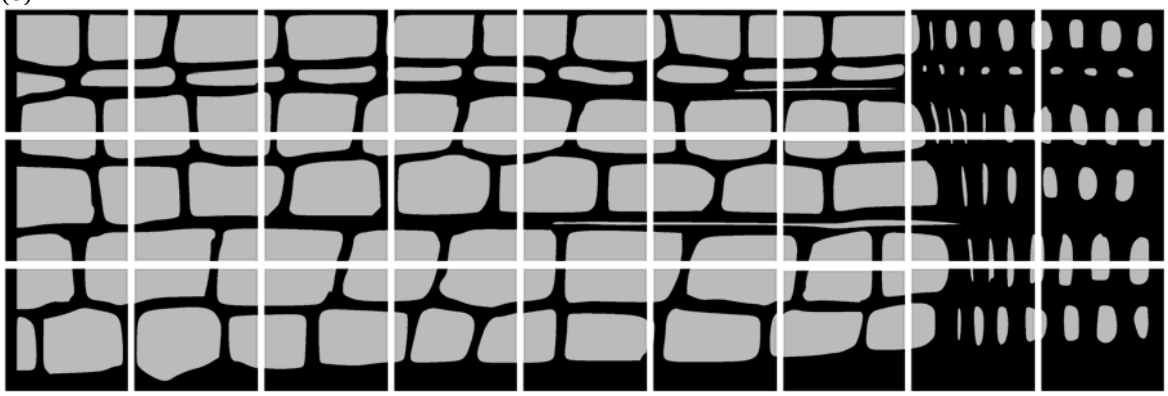

(c)

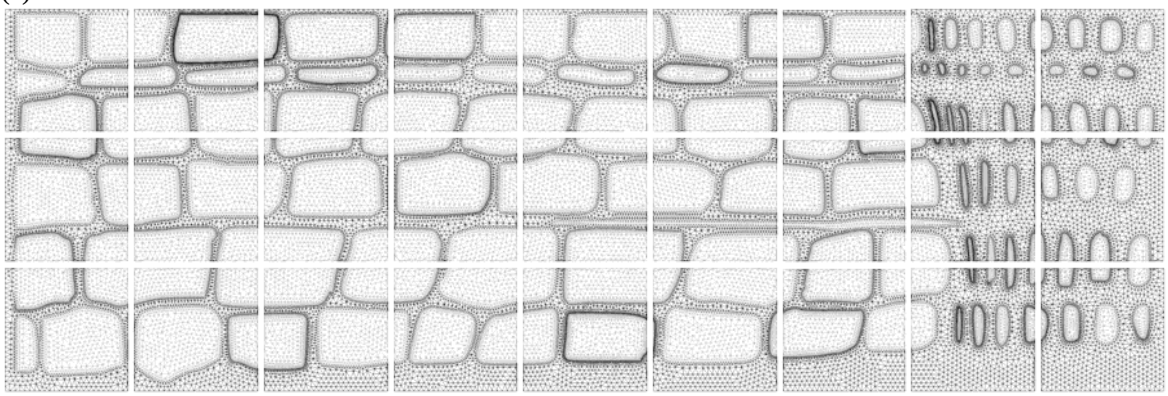

Figure 3: Dividing the full domain in 27 subdomains. (a) Representation of the full computational domain. (b) splitting up into smaller subdomains. (c) Finite element mesh of the different subdomains.

We observe that the determined water vapour resistance factor of the wall μ_w varies highly with relative humidity. The obtained μ_w values for the radial and tangential direction also differ, which contradicts our assumption of isotropy. Therefore, we determine also the isotropic μ_w values (given between brackets in Table 1). With these μ_w values for the wall, the upscaled values μ_{gr} are calculated. These values have to be compared with the measurement values. A reasonable agreement is obtained. We also remark that at low relative humidity the measured μ values for tangential direction are higher than the values for radial direction. At high relative humidity, this observation is opposite. For the upscaled values, the μ_{gr} values for tangential direction are always higher than the values for radial direction. Until now no satisfying explanation was found for this particular experimental observation.

3.3 Local moisture transport properties

The upscaling method also allows to determine the spatial variation of the water vapour transport properties over the growth ring. This is done by dividing the domain into smaller parts and calculating the properties for the different sub-domains. In this example, the domain of 450 x 150 µm was subdivided into 27 square sub-domains with a side length of 50 µm (Figure 3).

First, we determine the variation of the density over the growth ring. Therefore the fraction of the cell wall area to the total area is determined and multiplied by the cell wall density, which is according to Kollmann

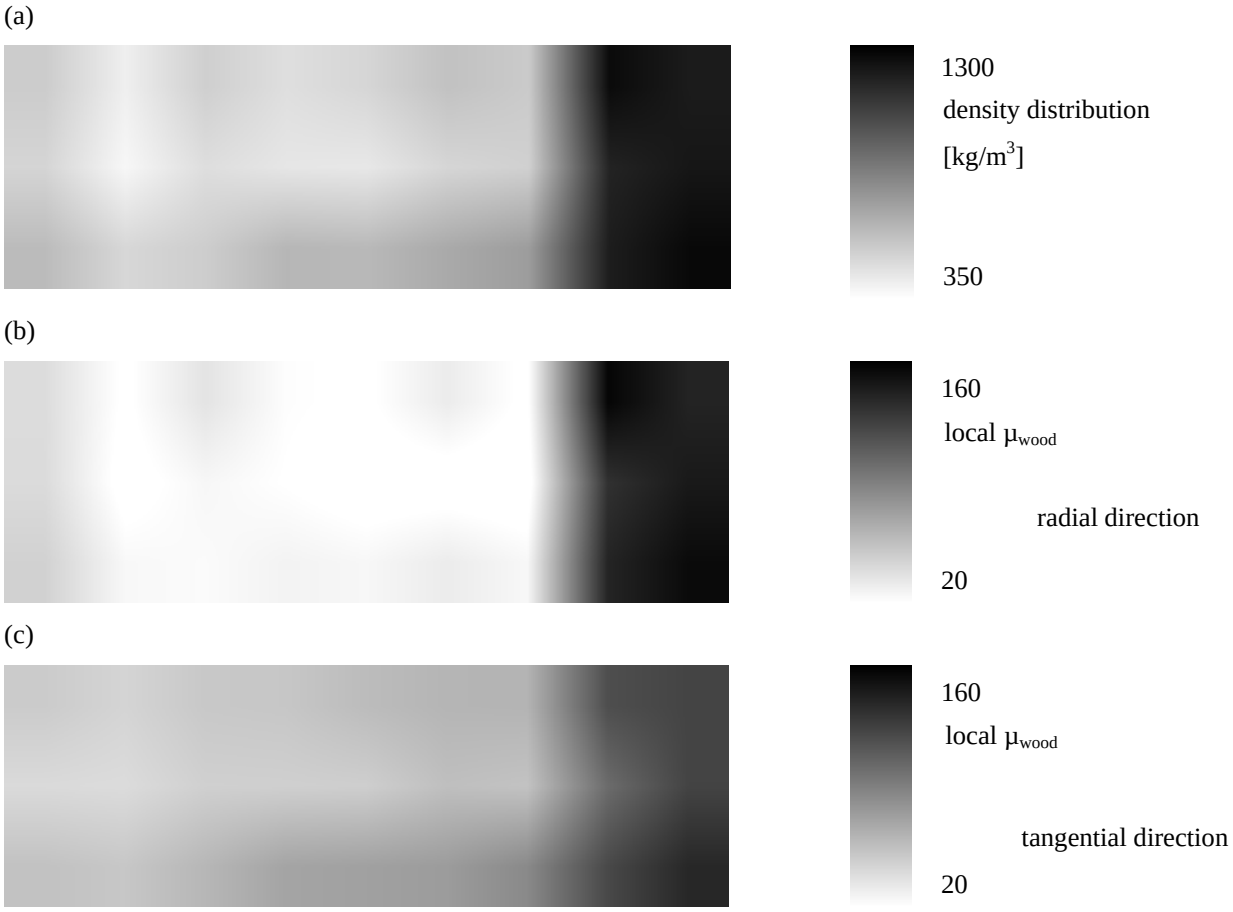

Figure 4: (a) Density distribution. The density varies from 379 kg/m³ in early wood to 1269 kg/m³ in latewood. Location dependent water vapour resistance factor radial direction (b) and in tangential direction (c). The results are shown for a call wall vapour resistance factor of 200.

(1968) 1500 kg/m^3. Figure 4a gives the density distribution. In early wood the average calculated density is 530 ± 170 kg/m^3. The average density of late wood is 1280 ± 50 kg/m³. Limitation of this method is that the density is determined from 2D cross sections and not from real 3D cellular structures. However, due to the low width to length ratio of a wood cell (≈ 2%) the error can be estimated less than 1%. It is remarked that the obtained values are higher than the values obtained in Zillig et al. (2007b), where values were reported of 297 kg/m³ and 888 kg/m³ respectively for early and late wood. The difference may be attributed to the particular SEM section taken in this research.

In a second step, the local water vapour resistance factor is determined solving the stationary flow problem for each sub-domain in radial and tangential direction. In figures 4b-c the distribution of the water vapour resistance factor is shown. The water vapour resistance factor of the wall equals 200. We observe that the μ-values highly differ between early wood and late wood. A steep gradient in µ-value is observed at the border from late wood to early wood. Table 2 gives the average μ values (the maximum and minimum values between brackets) for early and late wood. The following observations can be made: (1) The μ-value for late wood is higher than the value for early wood. For tangential direction the μ-value for late wood is 2.3 times larger than the value for early wood. For the radial direction, the multiplication factor is 5.9. (2) In early wood the μ-value is higher in tangential direction, while in late wood the observation is opposite. (3) The differences in μ-value between radial and tangential direction are higher in early wood than in late wood. (4) In early wood the variances are higher than in late wood.

In figure 5, we give the relation between the density and water vapour resistance factor. We observe that there is a trend showing higher water vapour resistance factors for higher density values. However, some scattering is observed, especially for early wood.

Table 2: Water vapour resistance factors for earlywood and latewood

	µ (-) average (minimum and maximum in brackets)		
	30% RH	62.5% RH	71.5% RH
earlywood			
tangential	281 (206;393)	67 (49; 93)	26 (19; 36)
radial	130 (38; 235)	32 (15; 56)	13 (2; 22)
latewood			
tangential	636 (530; 733)	151 (126; 174)	58 (49; 67)
radial	769 (698; 833)	183 (167; 197)	70 (65; 75)

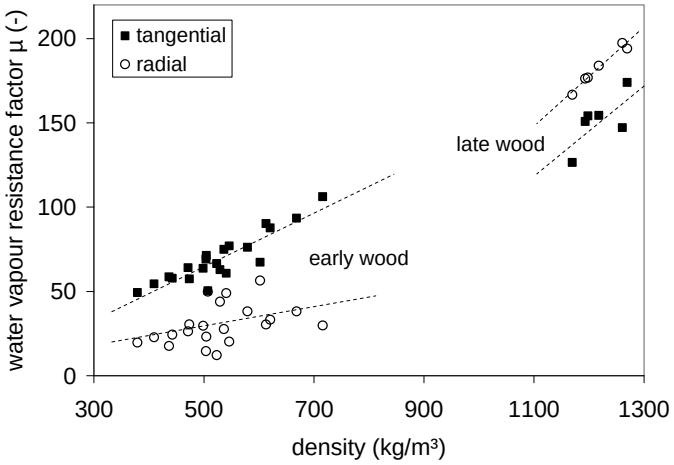

Figure 5: The local water vapour resistance factor in relation of the local density.

4. Conclusions

In this paper we presented an upscaling method in order to determine the water vapour permeability of wood in tangential and radial direction. The method is based on the calculation of stationary water vapour flow on the cellular level. 2D SEM images of the cellular structure are transformed in binary and polygonal edge images, which are meshed into finite elements. The water vapour permeability of the wall is determined comparing upscaled and measured water vapour permeability values. The method allows to determine location dependent density and water vapour permeability. These location dependent material properties can be used in further simulations to model the influence of growth ring structure on the total moisture transport in the wood ignoring the actual geometry of single cells in the growth ring.

5. References

Bertaud, F., Holmbom, B. (2004). Chemical composition of earlywood and latewood in Norway spruce heartwood, sapwood and transition zone wood Wood Science and Technology, 38, 245-256.

Gu H. (2001). Structure based, two-dimensional anisotropic, transient heat conducting model for wood Department Wood Science and Forest Products, Virginia Tech.

Kärenlampi, P. P., Tynjälä, P., Ström, P. (2005). Phase transformations of wood cell wall water J. Wood Sci., 51, 118-123.

Kollmann, F., Côté, W. A. (1968). Principles of wood science and technology. Part 1: Solid wood Springer-Verlag.

Kowalski, S. J. (2003). Thermomechanics of Drying Processes. Springer-Verlag Berlin Heidelberg New York.

Persson K. (2000). Micromechanical modelling of wood and fibre properties Lund University, Department of Mechanics and Materials.

Siau, J. (1995). Wood: Influence of moisture on physical properties, Department of Wood Science and Forest Products, Virginia Polytechnic Institute and State University.

Zillig, W., Janssen, H., Carmeliet, J., Derome, D. (2006). Liquid water transport in wood. 3rd International Building Physics Conference, 27-31.8.2006, Montreal, Canada. Conference Proceedings p. 107 - 114.

Zillig, W., Derome, D., Diepens, J., Carmeliet, J. (2007a). Modelling hysteresis of wood, Proceedings of 12th Symposium for Building Physics, Technische Universität Dresden, Dresden, March 29-31, Vol. 1, pp. 406-413.

Zillig, W., Derome, D., Carmeliet, J., Diepens, J. (2007b), Mesoscopic modeling of vapor transport in wood in tangential and radial direction, Proc. of Building X conference, Proc. Thermal Performance of the Exterior Envelopes of Whole Buildings X, Dec. 2-7, 2007, Clearwater Beach.

Evaluation of Moisture Pins in Wood Claddings

Kristine Nore, Research Fellow,
SINTEF Building and Infrastructure and
Department of Civil and Transport Engineering, Norwegian University of Science and Technology (NTNU)
kristine.nore@sintef.no

Jan Vincent Thue, Professor,
Department of Civil and Transport Engineering, Norwegian University of Science and Technology (NTNU)
jan.thue@ntnu.no

KEYWORDS: Moisture pins; moisture content; measurements; moisture profile; accuracy; wood moisture.

SUMMARY:

The wood moisture content (MC) is vital for the wood performance and durability in external applications. Moisture pins sensors are widely used for measuring the MC of wood materials by measuring the electrical resistance of the material. The pin sensors are durable and respond quickly to changes in the moisture conditions in the wood.

This paper presents a laboratory study of moisture pins used in an extensive field investigation on wood claddings. Attempts were made to use moisture pins for monitoring the moisture profile in the cladding boards. The quality of these measurements is evaluated and compared with gravimetric measurements. The paper also discusses the accuracy of moisture pins measurements.

In order to monitor the wood cladding MC fluctuations resulting from the quick response to the ambient climate, the MC measurements in external applications should be continuous. The laboratory measurements conclude that continuous measurements of the moisture profile was not possible for coated wood cladding.

1. Introduction

This paper presents moisture profile measurements and discusses the accuracy of moisture pins measurements in wood. SINTEF Building and Infrastructure are using wood moisture pins in an extensive field investigation on wooden claddings. The moisture content (MC) fluctuations of treated and untreated wood in external climate are tracked carefully – the importance of measuring these fluctuations is reasoned in this paper. In addition to examining the wood MC in different cladding types and assemblies, we have attempted to measure the moisture profile in the cladding boards. This was in order to study and to verify calculations of moisture transport in the claddings. Laboratory tests measure the moisture profile both gravimetrically and by moisture pins.

In order to achieve durable wood constructions, the MC must be kept below the level of risk for rot. Rot and stain fungi need high MC to be able to decompose the wood substrate. Wood also swells and shrinks according to its MC. Hence, limiting the wood MC is vital for the wood performance and durability in external applications.

MC in wood claddings is usually between 13 and 28 % by weight, depending of its location (Geving et al. 2006). Esping, Salin and Brander (2005) present Swedish requirements for delivery of outer cladding boards, where the MC may not exceed 18 % with a tolerance of ± 2 %. Norwegian delivery requirements for planed timber are 17 % with a tolerance of ± 5 % (NS 3180). A risk for rot is often set to a limit of 20 % MC.

The MC can be found by several methods. Most commonly used is gravimetric, electrical resistance or capacitive measurements. Moisture pins, often of steel, measure the resistance in the wood material. The correlation between resistance and moisture content is used to calculate the wood MC. This measurement method is fast, effective and quite accurate. Moisture pins are widely used in the wood and construction industry, and also when evaluating causes of failures in building constructions that contain wood.

2. Background

The reference method for measuring wood MC is gravimetric measurements (EN 13183-1). This is done by weighing the wet wood material, thereafter drying it at 103 °C, and then weighing the dried material. This is the most exact way to measure the moisture content in wood, but it is time-consuming and often destructive.

Said (2007) presents a literature review on methods of moisture measurements in building envelopes. His opinion is that resistance and voltage methods are most suitable for continuous monitoring of building envelope performance. By voltage measurements he refers to monitoring the surface time-of-wetness (TOW).

There is a correlation between electrical resistance and wood moisture content; when the MC increases the resistance decreases. This correlation is not linear, as seen in Figure 1. The initial mathematical model that describes this correlation was derived in the 1920's (Apneset and Hay, 1992). Resistance measurements must be adjusted according to material temperature, wood density and wood species. Wood species contains different amounts and types of salt, resulting in different conductive properties. Above fibre saturation point the resistance increases slowly, but exact measurements above this point are most often not of interest because the critical risk for rot MC value is exceeded. A relating fact is that the accuracy decreases when the moisture content increases. This is also seen in Figure 1.

EN 13183-2 defines estimation of MC by electrical resistance method – moisture pins. The most exact MC meters measure resistance at the tip of the steel pins, with 2-5 mm not insulated. When the pins are insulated one may measure a moisture profile; the moisture distribution in the material cross section (Apneset and Hay, 1992). The ASTM D 4444-92 presents four special problems that should be considered when doing moisture profile measurements; (1) nonisulated electrodes, (2) nonparabolic gradients, (3) surface moisture on electrode and (4) high surface MC on sample. According to ASTM D 4444-92; "noninsulated pins will bias the reading towards the highest MC in contact with the pins".

The distance between the steel pins are normally about 25 mm, but according to Forsén and Tarvainen (2000) the distance have no significant effect on MC measured. Measuring in the end section of the wood is not correct (EN 13183-2). Forsén and Tarvainen (2000) found that the measured wood MC was not influenced whether the measurements was done perpendicular or parallel to the wood grain. In general, measurements parallel to the grain is recommended.

NT BUILD 420 is a standard for measuring MC using wood probes with embedded electrodes, some with thermocouple integrated. They are meant for continuous measurements, but may have a delay and larger tolerances due to the surface transfers between the dowel and the material of interest.

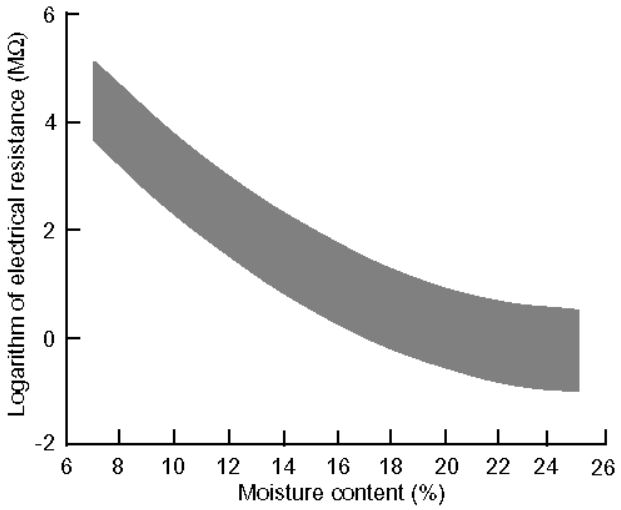

FIG. 1: Wood Moisture Content (MC) versus the logarithm of electrical resistance measured at 27°C. The shaded area includes the 90 percentile (U.S. FPL, 1982).

TABLE 1: Systematic error and rest error, in % MC, at different MC levels (Forsén and Tarvainen, 2000).

	10 % MC	15 % MC	20 % MC
Systematic error	1.4	2.2	2.5
Rest error	0.1	0.4	1.0

Forsén and Tarvainen (2000) and ASTM D 444-92 state that wood density has no influence on moisture readings, but according to NT BUILD 302 the moisture content is read too low in fast grown wood, due to higher resistance in less wood substrate. Measurements on impregnated wood increase the MC reading about 2 – 4 % (Esping, Salin and Brander 2005). ASTM D 4444-92 also reports that chemicals and adhesives, even with small concentrations of salt, may cause abnormal readings – usually higher.

Forsén and Tarvainen (2000) state that resistance measurements are most accurate within a MC range of 8-20 %, while Apneset and Hay (1992) report the range of 7-25 % MC as reliable. Gravimetric control measurements of wood moisture pins were done in the previous investigation at the Voll test house (Geving and Uvsløkk, 2000). The moisture pins corresponded well to gravimetric measurements in the range 10 - 18 % MC, and satisfactory in the span 18 – 25 % MC.

The standards ASTM D 4444-92 and NT BUILD 302 both present the relative error of moisture pins within 7-25 % MC range, after temperature and species are corrected. They state that the error of isolated measurements is 7 % in a 95 % confidence interval (0.5 - 2 % MC). Esping, Salin and Brander (2005), however, reduce the accuracy to 15 % in a 95% confidence interval (1 - 4 % MC). If the tolerance must be below 1 % MC one may increase the number of measurements to five (Apneset and Hay, 1992).

Forsén and Tarvainen (2000) differentiate between systematic and rest error. Systematic error gives the same value at every reading and includes hysteresis, design of moisture sensors, measuring in the end section, wrong measurement calculation, wrong temperature, and wood impregnate. The rest error is variable even when measurements are done exactly the same way and includes inaccuracy in the display, uncertainty in the calibration, variation in the calibration resistance, uncertainty in the preparing of the calculation curve, variation of the electrical resistance of the wood, different measurement depths, and the variation of the moisture profile in the wood. Table 1 gives the systematic and rest error of hand held wood MC meters.

3. Method

Different wood claddings have been mounted on a test house at the field station Voll in Trondheim. Different cladding assemblies, material quality (growth rate) and surface treatments are investigated. The project is described in Geving et al. (2006), and holds 102 moisture pins sensors in total. The wood is Norway spruce (*Picea abies L. Karst*) with two densities; fast grown, 400 kg/m^3 and slow grown, 460 kg/m^3. All moisture pins sensors are positioned to measure resistance perpendicular to the grain. The distance between the electrodes is 25 mm. Most MC sensors are measuring full depth MC_{FD}, see Figure 2. This means that the entire steel pins are pressed 16 mm into the wood.

Assessing the moisture movement in the wood cladding boards was a significant part of the cladding investigation. Local MC measurements were intended when moisture pins were placed in different depths of the claddings. Figure 2 shows the measurement assembly with the MC_L moisture pins in three depths. These pins are insulated with heat-shrunken tubing, except for a length of 3 mm at the tip. The pins measuring the MC_{FD} were noninsulated in full length.

The steel pins used are 2 mm in diameter. Every MC sensor is set in a predrilled hole of 1.9 mm in diameter for the measuring contact area and 2.5 mm in diameter where the insulated parts of the pins are lowered into the wood. At the field investigation, all measurement sensors are read every 10th minute and an average hourly value is stored. The cladding experiment has continued since January 2004.

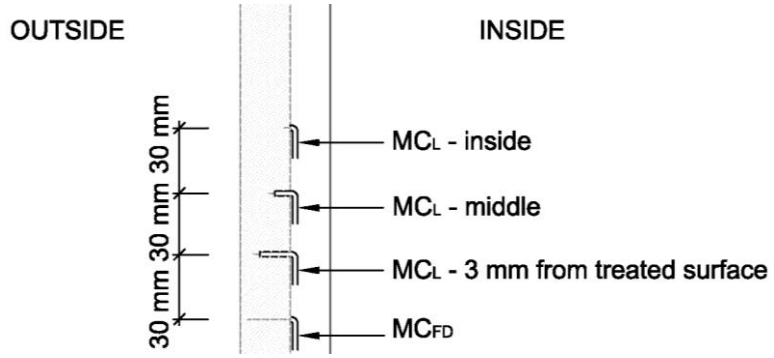

FIG. 2: The set up of the MC measurements. MC_L pins have 3 mm active tip, MC_{FD} are noninsulated full length. Temperature is measured at the inner surface of the cladding board. The cladding board thickness is 19 mm and the outside is coated. A 23 mm air gap separates the cladding from the back wall, which is traditional insulated timber frame.

In this project, wood MC is monitored by measuring resistance as described in EN 13183-2. At the test house the multiplexer measure with 2.7 volt DC. For system control five supplementary reference MC sensors are logged. The hand held moisture meters used in the laboratory measure with 2.7 volt DC. They are read when stabilized, within 1-5 sec. At the continuous field investigation measurements the current is switched in each measurement to avoid polarization of the poles, in what follows from the electrolysis of the water and wood fluids. When the current is switched and MC value is read immediately, the dielectric constant of the wood is not affecting the measurements.

In order to ensure measurements quality, a gravimetric study of the wood moisture pins mounted at the test façade was carried out in October 2006. Gravimetric measurements were in this case a destructive method, stripping down instrumented boards from one test cladding section. The two instrumented boards, from the same full length board, of fast grown wood, primed and coated with alkyd paint. The s_d value of the alkyd coating on fast grown wood was 2.5 m. The boards had full instrumentation with both MC_{FD} and MC_L sensors. The cladding boards (585 mm long) were removed from the wall and cut into four pieces. Two of these four pieces were split into outer, middle and inner part. The paint was scraped off. All board pieces were weighed directly after they were stripped down, and again after drying. The two end section pieces of each test cladding board were used for measuring the average MC. In this way, the split parts used to measure the moisture profile had no original end grained wood.

To study whether continuous moisture profile measurements are possible, new and identical cladding boards were instrumented for the laboratory tests. The cladding boards were conditioned in two relative humidities (RH), 50 % and 75 %, for eight weeks, making sure no moisture profiles were present. No untreated cladding boards were studied; consequently the effect of the surface treatment was not explored.

4. Results from Field Study of Moisture Pins

With the large amount of MC data from the continuous time series, collected for four years, the systematic error is minimal; implying that the variations found in one measurement sensor is true variations. Correlating the measurement series to the ambient climate gives explicit comparison for the direct response. The measurements for one typical moisture pins sensor for ten days, one month and three years are presented in Figure 3, showing hourly, twenty-four hour averaged and monthly averaged values.

Studying the resistance sensor data in Figure 3a, we find that the hourly data variations during a twenty-four hour period may reach 2 % MC. During a month the averaged twenty-four hours values in Figure 3b show a span of about 4 % MC. The span of the 3 year period with averaged monthly values, shown in Figure 3c, reaches about 6 % MC. Continuous hourly measurements are useful to avoid the errors of twenty-four hours fluctuations in nonconditioned investigations.

When using continuously measured data to compare different wood cladding designs, the data variation, e.g. the linear regression trend, gives high quality data to differentiate the cladding designs.

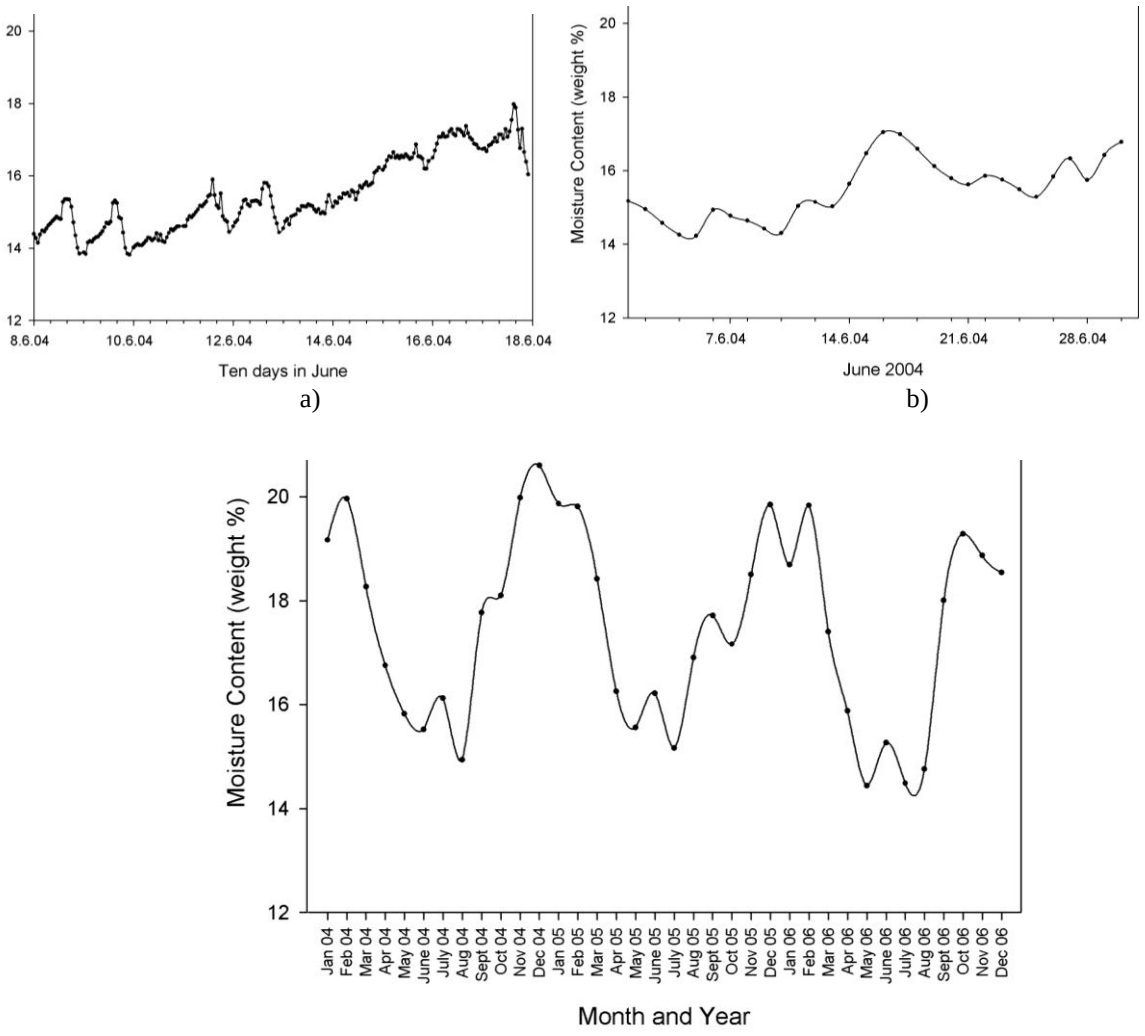

FIG. 3: MC fluctuations of one randomly chosen resistance sensor. a) Hourly values given for a ten day period. b) Twenty-four hours averaged values given for one month. c) Monthly averaged values given for three years.

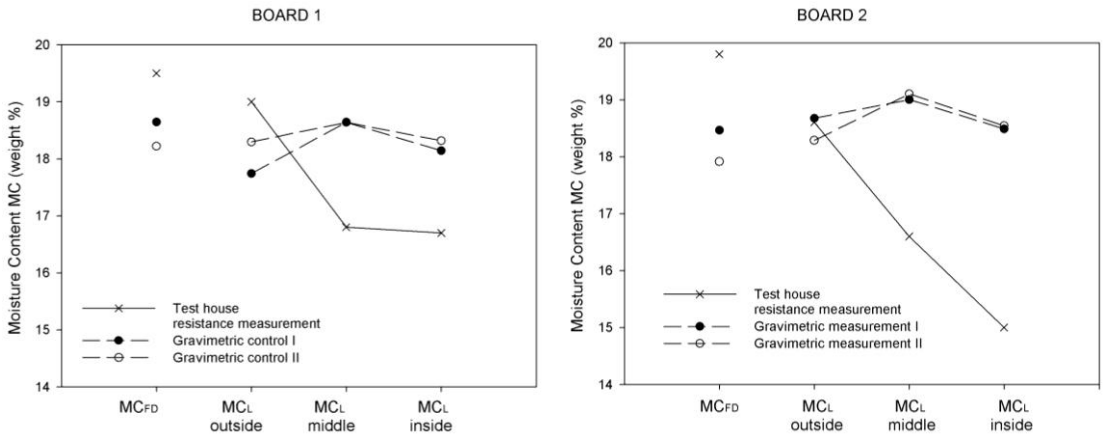

FIG. 4: Gravimetric and electrical resistance measurements of claddings (fast grown bards with alkyd paint). Resistance measurements; wettest part close to coated side. Gravimetric measurement; wettest part is in middle of the board. MC_{FD} sensor and, MC_L sensor corresponds to Figure 2.

The results revealed that the moisture profile measured with moisture pins did not correspond to gravimetric moisture profile measurements. This is seen Figure 4. The readings from the moisture pins gave the apparent moisture profile; the outer part wetter than the inner part, indicating a moisture transport through the claddings from the wetted outside to the ventilated and dry inside of the cladding boards. The gravimetric measurements however, showed wetter middle parts of the boards. 25 hours had passed since last rain fall when the instrumented boards were stripped down. The moisture distributions found by the gravimetric measurements are more accurate and reliable. The drying out through the coating layer is considerable even with an s_d value of 2.5 m. The board pieces used to measure the average MC might also have dried out through the end sections; providing the low gravimetric MC_{FD} in board 2.

Figure 4 shows the highest MC_L value in the outer part, but the MC_{FD} measurement value is always higher. This problem is discussed in the next section.

5. Results from Laboratory Study of Moisture Pins

In the laboratory study the electrical resistance measurements also read a moisture profile in the wood cladding boards, even though no moisture profiles were present – the boards were conditioned and measured in controlled environment. One should have read identical MCs for each RH and not the span of about 3 % at 50 % RH and 4 % at 75 % RH, as shown in Figure 5. The deviation increases with higher RH, this corresponds to Figure 1.

Figure 5 also indicates a difference in the reading of slow and fast grown wood. The fast grown wood gives slightly lower MC. This supports the theory of Apneset and Hay (1992) mentioned in section 2; the wood density does influence the moisture readings, presenting too low MC values for less dense wood. However the calibration curve may not be correct for both densities, which means that the measured MC could be correct. This aspect should be studied in future work.

Both the field and laboratory results present the highest MC values for the MC_{FD} pins. They exceed the outer part pins which have the highest MC_L electrode values. Assessing the nonisolated pins as parallel couplings may explain this behaviour. In an electrical field, all paths will contribute to the conductive capacity. Consequently, the MC_{FD} sensor, with the noninsulated pins, providing the largest contact area and the largest electrical field, will always give a higher MC value than the highest MC_L. This is illustrated in Figure 6. The MC_{FD} measurements might even exceed the highest actual MC, shown in Figure 5. This is not equal to the ASTM D 4444-92 statement; that the MC might approach the highest MC in contact with the pins.

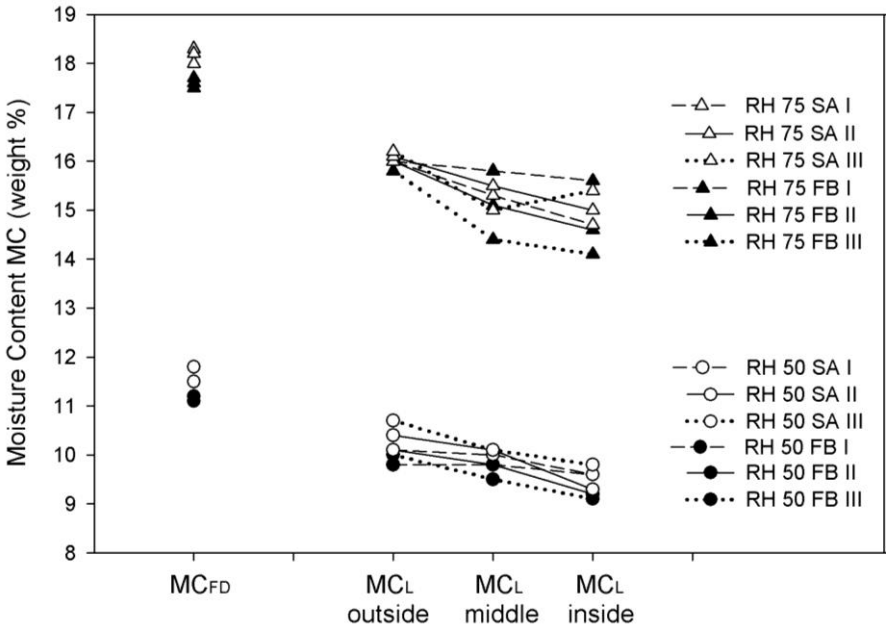

FIG. 5: Electrical resistance measurements of wood claddings conditioned in the laboratory. Six cladding samples are tested in total. SA – Slow grown with alkyd based paint, FB – Fast grown with acryl based paint. MC_{FD} sensor and MC_L sensor corresponds to Figure 2.

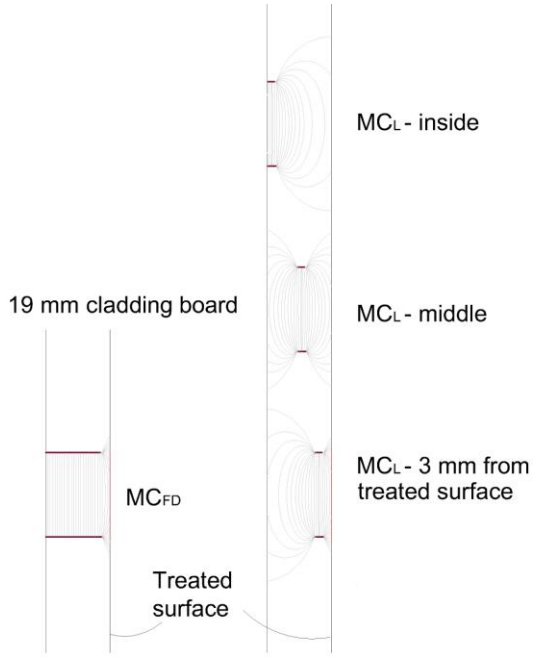

FIG. 6: Electrical field lines in the four moisture pins assemblies.

The electrical field analogy may also explain the apparent moisture profile measurements seen in Figure 5. The electrical fields in the three depths are different, see Figure 6. The inner pins, mounted on the back side of the cladding have the smallest electrical field, and the middle pins have the largest. The pins closest to the treated surface may have a short circuiting due to adhesives in the primer or paint, which provides the highest MC_L measurement. Corresponding conclusions have not been found in literature studied by the authors.

Cladding thickness is usually not more than 23 mm. This is probably not enough to measure full electrical fields at different depths.

6. Conclusions

Using electrical resistance is an effective way to read the moisture content (MC) in wood materials, but unfortunately not very accurate for scientific purposes. The gravimetric control measurements did not validate the resistance moisture profile measurements. Measuring the moisture profile with moisture pins in coated wood claddings is not recommended.

The tests demonstrate that errors that may deflect moisture pins measurements are:

- differences in contact area; length of the electrode and density of wood;
- distance to the surface;
- surface treatment.

From the literature it is also well known that errors may be caused by:

- moisture distribution;
- amount of wood extractives;
- nature of material, homogenous or with abnormal wood structure (e.g. twigs or reaction wood).

7. Recommendations for a better approach

To improve resistance MC measurements MC meters should be operated by qualified personnel and corresponding ambient climate data must be measured. Twenty-four hours fluctuations in external applications are relatively large. Randomly collected data gives low data output, e.g. making one measurement a day.

Monitoring and averaging the MC over a period of time provides an improved conception of the moisture fluctuation in the test boards.

The influence of wood density and surface treatments on electrical resistance MC measurements should be approached in further studies. The behaviour of moisture pins in wood based materials should also be considered according to the findings of this work.

It might be possible to measure continuous moisture profile in wood by resistance MC measurements. Test pieces must be calibrated prior to the experiment. Calibration may be done by measuring the moisture profiles of the test samples conditioned in at least three climates (e.g. 50, 70 and 90 % RH) in order to find correction factors.

8. Acknowledgements

This paper has been written within the NBI Research & Development program "Climate 2000 –Building Constructions in a More Severe Climate" (2000 – 2006) with the strategic institute project "Impact of climate change on the built environment". The authors gratefully acknowledge all construction industry partners and the Research Council of Norway.

9. References

Apneseth, T. and Hay, M. (1992). Test of hand held electircal moisture meters (In Norwegian). Work report. NTI Norwegian Wood Technology Institute. Oslo.

ASTM D 4444-92 (2003). Standard Test Methods for Use and Calibration of Hand-Held Moisture Meters. American Society for Testing and Materials, ASTM International, West Conshohocken, PA, United States.

EN 13183-1 (2002). Moisture content of a piece of sawn timber - Part 1: Determination by oven dry method. European Committee for Standardization. Brussels.

EN 13183-2 (2002). Moisture content of a piece of sawn timber - Part 2: Estimation by electrical resistance method. European Committee for Standardization. Brussels.

Esping, B., Salin, J.G. and Brander, P. (2005). Moisture in wood for the building construction industry – moisture properties, demands, use and measurements. (In Swedish). SP INFO 2005:24, SP Trätek.

Forsén, H. and Tarvainen, V. (2000). Accuracy and functionality of hand held wood moisture content meters. Technical Reesearch Centre of Finland, VTT Publications 420.

Geving, S. and Uvsløkk, S. (2000). Moisture condition in timber frame roofs and wall sturctures. Project report 273. Norwegian Building Research Institute, Trondheim.

Geving, S., Erichsen, T.H, Nore, K. and Time, B. (2006). Hygothermal conditions in wooden claddings – Test house measurements. Project report 407. Norwegian Building Research Institute. Trondheim.

NS 3180. (1976). Quality specifications for planed timber. Pronorm, Norway.

NT BUILD 302 Building materials, wood: Moisture content. Approved 1986-09. Helsingfors Finland.

NT BUILD 420 Building materials, wood: Moisture content. Approved 1993-05. Helsingfors Finland.

Said, M. N. (2007). Measurement methods of moisture in building envelopes – a literature review. International Journal of Architectural Heritage. Vol 1, no.3. pp. 293-310.

U.S. FPL (Forest Product Laboratory) (1982). Wood Engineering Handbook. Englewood Cliffs, NJ: Prentice Hall, Inc.

Measurement and modeling of drying for pellet production

Peter Bengtsson, PhD student,
School of Technology and Design, Växjö University;
peter.bengtsson@vxu.se

Johan Claesson, Professor,
Civil and Environmental Engineering, Chalmers University of Technology;
johan.claesson@chalmers.se

KEYWORDS: *wood, moisture, porous material, drying with warm air, finite difference method.*

SUMMARY:
This paper describes a simulation model of drying of wood particles. The model is based on coupled moisture and heat balance equations and solved by using the finite-difference method. There are balances for absorbed water in the wood, water vapor, air and heat; and a Darcian equation for the flow of humid air. The developed model predicts the drying course for varying drying conditions and materials; in this report it is applied to sawdust drying. The simulation shows fair agreement with the experimental data, though factors such as the intrinsic mass transfer coefficient for the evaporation and the thermal conductivity for the air and wood mixture are possible to optimize further. Predictions of drying times, moisture content and temperature in the material and bed pressure drop are obtained with the model. As in the experiments, the model shows a quit thin drying zone characterized by large temperature gradients. These gradients require a very fine division in cells in the numerical calculations to properly represent the coupled processes. A typical calculation of a drying process during a few hours with 100 cells requires around 10 min computer time on an ordinary PC.

1. Introduction

Since the energy crises of the 1970s, the use of oil and coal as a heating source for small houses has continuously declined in favor of non-fossil wood fuels. One of the main wood fuels is pellets made of residuals from the wood industry. Wood pellet are a compact and CO_2-neutral fuel, often considered to be user-friendly and convenient. However, the raw material of mainly sawdust, wood chips or bark contains a considerable amount of moisture that must be removed to achieve pelletization. Besides this, more energy can be utilized in the combustion process, since a better combustion is achieved. The fuel quality also becomes more homogenous, considered advantageous for the end-user. The removal of moisture by heating is an energy demanding and often time-consuming process. In this paper, the drying of wood particles is investigated both experimentally and theoretically. The focus is on the theoretical approach to modeling the drying process and comparing the modeling results with the experimental data.

The applied drying method (batch drying), commonly used in the wood fuel industry, may utilize low temperature waste heat from available industrial processes. This makes the method very interesting. The drying method is characterized by wood particles located in a batch exposed to a drying air flow. The drying air enters the bottom of a drying chamber and passes through the bed of particles, where an exchange of moisture from the wet material to the air takes place. This exchange is essentially limited to a finite zone called the drying zone. At the lower boundary of the drying zone, the air humidity starts to increase from being in equilibrium with the dried material. At the upper boundary, the moisture content reaches equilibrium with the air (FIG. 1). When drying begins, the drying zone is in the bottom of the bed. As drying progresses, the zone moves upwards until the drying is considered complete. Both the progression and the extension of the drying zone are quit important in the design of full-scale batch dryers. The rate of progression determines the drying times and the size of the dryer. The drying zone extension strongly limits the possibility to saturate the drying air and to utilize the heat energy throughout the drying.

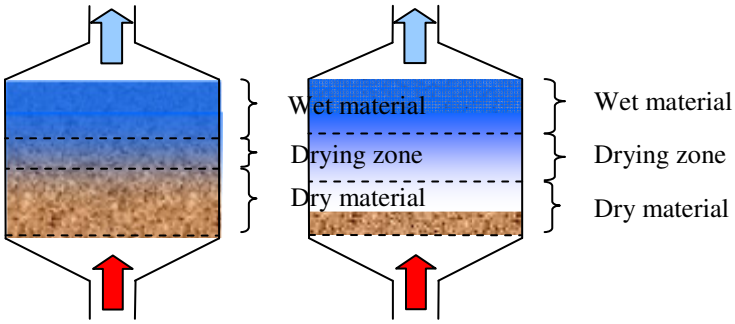

FIG. 1 Drying of wood particles in a batch is characterized by a limited drying zone where the actual drying takes place.

To understand this complex drying process involving simultaneous heat and mass transfer, mathematical modeling of the process is usually applied. Traditionally, these models only consider external heat and mass transfer and neglected the heat and moisture transfer inside the product. The models explain the total moisture transport by convection and assume that during the total drying process, all heat transferred to the product is used to vaporize water. These types of models are reported in chemical engineering books (McCabe and Smith, 1956) and food engineering books (Singh and Heldman, 2001). However, when modeling the drying of biological products such as grain and wood, the internal interaction between moisture and product must be considered. Deomano (2001) stated that both the conditions inside the dryer and the transport mechanism within a single piece of material to be dried must be well understood to obtain an accurate model of a dryer.

The moisture transport within a single wood particle is often described by two different drying periods. Initially, because the wood surface is covered with a layer of water, there is a constant-rate drying period. As the surface starts to dry, a falling-rate drying period is then applied to describe the moisture transport. In this work, a drying equation with a lumped transfer coefficient describes the moisture transport from the wood into the air.

In the literature, at least three different types of batch drying models are presented, namely logarithmic (Hukill, 1954), heat and mass balance (Boyce, 1965) and partial differential equation (p.d.e.) (Bakker-Arkema, et al., 1967; Spencer, 1969; Laws and Parry, 1983; Ratti and Mujumdar, 1995; Wang and Chen, 1999; Sitompul, et al., 2003). Because both logarithmic and heat and mass balance models have shown poor accuracy and applicability (Parry, 1985), p.d.e. models are now used in the development and understanding of the drying process. The above-mentioned works, like most other work on batch drying, treat grains or solid particles in general. Since the biofuels discussed in this work have both similar properties and are dried with the same technique, they may be simulated similarly. However, in the literature, p.d.e models of drying biofuels in batches are rare. Saastamoinen and Impola, (1997) simulated the drying process with p.d.e., coupling a single particle model with a heat and moisture transfer model and solving it numerically. Their model was described as having potential to dimension large-scale dryers. Other works thoroughly discuss p.d.e. modeling of single-wood-particles drying (Kayihan and Stanish, 1984; Johansson, et al., 1997).

2. Procedure and material

The drying equipment used in this study is a stationary bed dryer to dry a batch of biomass. The experimental equipment consists of three main components: a centrifugal fan, an electrical heater and a drying chamber. The fan and heater deliver a maximum of 900 m^3/h of air with a temperature of approximately 90˚C. The drying chamber may be charged with a maximum 0.25 m^3 biofuels. The drying equipment has one inlet for fresh outdoor air, one outlet for moist air and a circulation pipe.

The drying runs begin with determination of the weight and moisture content of the biomass load. Temperature sensors (s1, s2 and s3) are placed at three different levels to determine the drying zone progression through the bed. Sensor s1 is located close to the bed bottom, s2 in the middle of the bed and s3 close to the top of the bed. The bed is pre-heated until it reaches the wet-bulb temperature of the drying air. During the experiments, the airflow and air temperature are kept constant. The humidity of the air entering the batch is automatically controlled. It is kept constant as long as the circulating air contains an adequate amount of water vapor.

The porous material studied consisted of sawdust with a moisture content of 107% (calculated on dry basis).

3. Mathematical modeling

3.1 Formulation of model

The developed and proposed model of the drying process in the porous wood material is a one-dimensional model for coupled moisture and heat balance equations. The pressure drop through the bed is accounted for. Three phases are considered in the porous material: The solid phase consisting of the dry wood particles, the liquid phase consisting of free (and absorbed) water in the wood cells and the gas phase formed by humid air between the particles.

A key point is to mathematically describe the evaporation (and condensation) between the solid wood particles and the humid air in the pores. Let c_s (kg·m^{-3}) denote the equilibrium water vapor concentration for solid particles at the temperature T (˚C) and moisture content u (kg$_{water}$·kg$_{solid}^{-1}$). Thus

$$\phi = \frac{c_s}{c_{sat}(T)}, \qquad \phi = \phi_{sorp}(u) \quad \Rightarrow \quad c_s(u,T) = c_{sat}(T)\cdot\phi_{sorp}(u), \tag{1}$$

Here, ϕ is the relative humidity, $c_{sat}(T)$ the saturated water vapor content at temperature T, and $\phi = \phi_{sorp}(u)$ the inverse of the sorption isotherm $u = u_{sorp}(\phi)$. The sorption isotherm is extended above the fiber saturation point to account for the high initial wood humidity: $\phi = 1$ for $u > u_{fsp}$. Let $G(x,t)$ (kg·m^{-3}·s^{-1}) denote the rate evaporation per unit volume and c_v (kg·m^{-3}) the water vapor concentration in the pores. The evaporation is zero in equilibrium $c_v = c_s$. A reasonable first-order description is

$$G(x,t) = \beta\cdot(c_s - c_v). \tag{2}$$

Here, β (s^{-1}) is a lumped parameter for the water vapor transfer from wood particles to pore gas. It has to be determined by fitting to experiments.

There is a flow of humid air through the porous bed of wet particles. The convective mass flow of dry air q_a and vapor q_v (kg·m^{-2}·s^{-1}) through the bed are related to the volumetric flux V_g (m^3·m^{-2}·s^{-1}) by

$$q_a = V_g c_a, \qquad q_v = V_g c_v. \tag{3}$$

To describe the drying process, three balance equations are set up for liquid water, energy and water vapor. The balance for *liquid water* is

$$\rho_s(1-n_g)\frac{\partial u}{\partial t} = -\beta\cdot(c_s - c_v), \qquad c_s = c_s(u,T). \tag{4}$$

Here, n_g is the porosity of the packed bed and ρ_s is the wood density (kg·m^{-3}). The balance for *heat or enthalpy* is

$$\begin{aligned} &c_{tot}\cdot\frac{\partial T}{\partial t} + h_{ev}(T)\cdot\beta(c_s - c_v) = \frac{\partial}{\partial x}\left(\lambda\frac{\partial T}{\partial x}\right) - c_{pa}\frac{\partial T}{\partial x}\cdot q_a - c_{pv}\frac{\partial T}{\partial x}\cdot q_v, \\ &c_{tot} = c_{ps}(1-n_g)\rho_s + c_{pw}(1-n_g)\rho_s u + c_{pa}n_g c_a + c_{pv}n_g c_v \end{aligned} \tag{5}$$

In this equation, the first term on the left-hand side is the change in heat content with a total heat capacity c_{tot} and the second term is the evaporation heat. The first term on the right-hand side is due to heat conduction. The following two terms are due to the convective heat flow of air and water vapor. Here, λ is the thermal conductivity (W·m^{-1}·K^{-1}), and c_{pa} and c_{pv} are the heat capacities for air and water vapor (J·kg^{-1}·K^{-1}). This equation and the mathematics of the whole model are presented in more detail in Bengtsson and Claesson (2008). The balance equation for *water vapor* is

$$\frac{\partial q_v}{\partial x} = \beta \cdot (c_s - c_v)\,. \tag{6}$$

Here, the term $\partial(n_g v_g)/\partial t$, which represents the very small changes in water vapor content in the gas phase in the pores, is neglected. There is also a mass balance equation for the air component of the humid air. The term $\partial(n_g v_a)/\partial t$ is neglected. This means that the air flow is equal to the inlet air flow: $q_a(x,t) = q_{a0}$. The final differential equation is Darcy's law to describe the gas flow through the porous material:

$$\frac{\partial P}{\partial x} = -\frac{V_g}{K}. \tag{7}$$

Here, K ($m^2 \cdot s^{-1} \cdot Pa^{-1}$) is a hydraulic conductivity coefficient for gas flow through the porous bed, and $\partial P / \partial x$ is the pressure gradient ($Pa \cdot m^{-1}$).

The model now involves four differential equations (4), (5), (6) and (7) for water content u, temperature T, water vapor flux q_v and pressure P, respectively. The equations involve these four variables and the additional variables q_a, c_a, c_v and V_g. These additional variables are obtained from requirement of constant air flow $q_a = q_{a0}$, from (3) and the general gas law:

$$q_a = q_{a0}, \qquad c_a V_g = q_{a0}, \qquad c_v V_g = q_v, \qquad \frac{P}{R(273.15+T)} = \frac{c_a}{M_a} + \frac{c_v}{M_v}. \tag{8}$$

The set of differential equations (4)-(7) is of a special character. Equation (4) involves a derivative in time (and not in x), while (6) and (7) involve the derivate in x (and not in t). This influences strongly the numerical solution.

3.2 Initial and boundary conditions

The boundary conditions at the inlet are:

$$T(0,t) = T_0, \quad \phi(0,t) = \phi_0, \quad V_g(0,t) = V_{g0}, \quad P(0,t) = P_0, \qquad t > 0. \tag{9}$$

At the outlet, the heat equation requires a boundary condition for the temperature:

$$\frac{\partial T}{\partial x} = 0\,, \qquad x = L\,. \tag{10}$$

Equations (4) and (5) have time derivatives, i.e. initial values must be specified. The initial conditions in the bed are:

$$T(x,0) = T_{\text{init}}, \qquad u(x,0) = u_{\text{init}}, \qquad 0 < x < L. \tag{11}$$

3.3 Numerical solution

The four differential equations (4), (5), (6) and (7) and the relations in (8) constitute the actual simulation model. An analytic solution is impossible; therefore, an explicit finite difference method for the numerical solution is applied. The biomass bed is divided into elements of thickness Δx. Consider now a time step when u_n and T_n are known. In particular, this is the case at the initial time step. Using (1) and the relations in (8), we may express the right-hand sides of (6) and (7) as funtions of u, T, q_v and P. The two equations are integrated numerically in x from cell to cell starting with given values at x=0. We get $q_{v,n}$ and P_n, and the other variables, for all cells at the considered time step. Then the values of u and T at the next time step are calculated from (4) and (5). These calculations are repeated for time step after time step. A Mathcad code was developed to carry out the iterative calculation. The numerical procedures and calculations are described in more detail in Bengtsson and Claesson (2008).

4. Results

4.1 Numerical results

A drying simulation of a bed of sawdust ($L = 0.15$ m) serves to illustrate the performance of the developed model. Experimentally measured values used in the simulation were as follows:

$$u_{init} = 1.07\,,\ T_{init} = 43\,,\ T_0 = 74\,,\ \phi_0 = 0.21\,,\ V_{g0} = 0.28\,.$$

The cell thickness is $\Delta x = 0.001$ m. A time step of $\Delta t = 0.5$ s was found to be numerically stable and selected. The computer calculation time was approximately 10 minutes in this particular case. Temperature T, moisture u, evaporation G and pressure profiles ΔP were calculated and presented here for different times (20, 40, 60 and 80 minutes). The model predicts at each time step the mentioned properties at each depth of the bed.

The simulated bed temperatures are shown in FIG. 2a. It can be observed that a sudden temperature change is characteristic for all plots and essentially characterizes the drying process. For example, after 20 minutes of drying (solid line), approximately 0.03 m of the bed has reached T_0 . At 0.04 m into the bed the temperature is still T_{init}. This limited zone of temperature change is the drying zone where the evaporation takes place. The drying zone successively moves through the bed and after 80 minutes it reaches 0.12 m into the bed (dashed-dotted line).

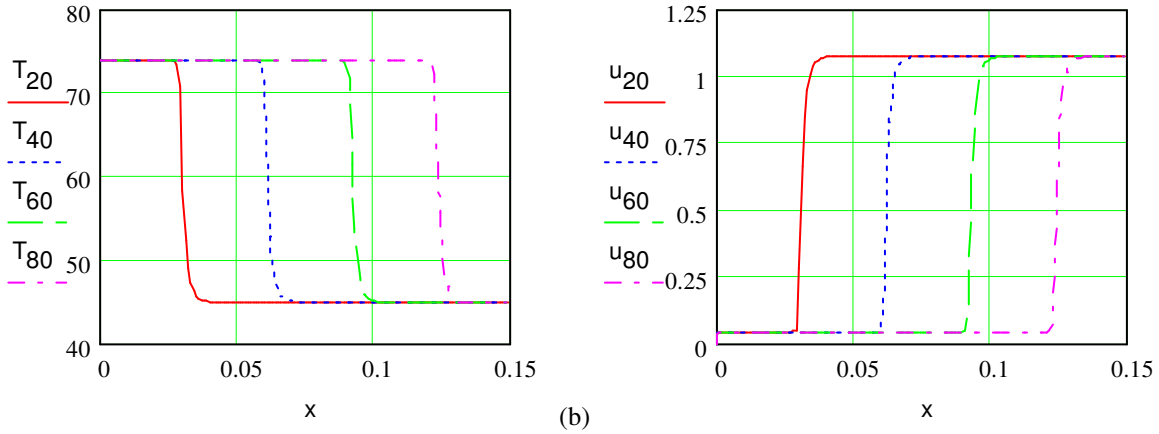

FIG. 2 Simulated temperatures (a) and moisture contents (b) through the bed at different times of drying.

In FIG. 2*b* the moisture content in the bed is shown. After 20 minutes (solid line), approximately 0.03 m of the bed bottom is almost dry and a moisture content of 4.5% is attained, i.e. the moisture content in equilibrium with the drying air humidity. Further drying of the bed bottom with the same air humidity has no influence on the moisture content. FIG. 3 shows the simulated flow of vapor, qv (a) and the rate of evaporation, G (b) through the bed. Note the small decrease in the vapor flow curve taking place downstream after 20 minutes of drying, which indicates a small condensation (FIG. 3a). The rate of evaporation clearly highlights the extension of the drying zone and the intensity of the evaporation. In this particular case, which actually simulates a thin bed, the extension of the drying zone appears to remain constant through the drying.

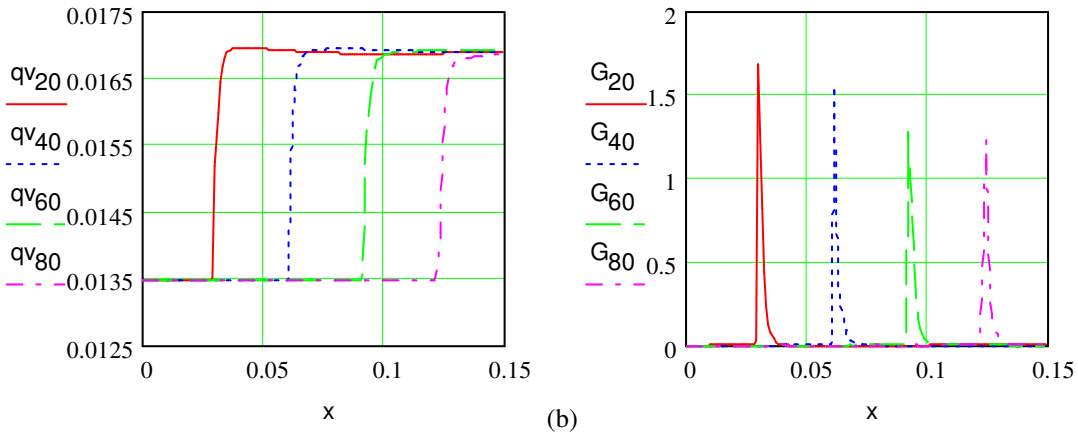

FIG. 3 Simulated flows of vapor (a) and the rate of evaporation (b).

In FIG. 4a the water vapor concentration c_v in the pores is shown. It increases as expected in the drying zone. Together with the volumetric gas flux (FIG. 4b) it determines the flow of vapor (FIG. 3a). Observe the sudden decrease (some 5%) in volumetric air flux which is a consequence of the lower gas temperature above the drying zone.

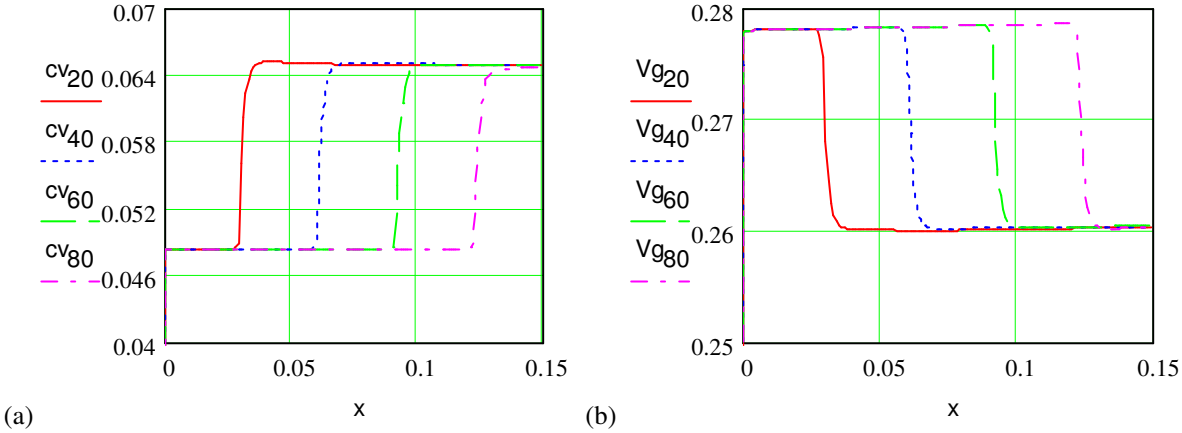

FIG. 4 The water vapor concentration (a) and the volumetric gas flux (b).

The pressure drop across the bed is shown in FIG. 5. It is dependent on the bed height, the drying air velocity and the permeability or conductivity *K*.

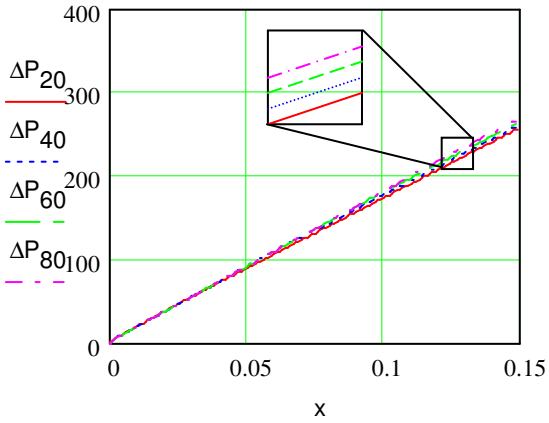

FIG. 5 Pressure drop in the bed at different times.

It should be noted that a constant value for the conductivity is used. Equation 7 shows that P or ΔP corresponds to an integral of V_g, figure 4b. This explains the slight increase of ΔP for increased time t.

4.2 Comparison of numerical results with experiment

The initial and boundary values used in Section 4.1 to illustrate the performance of the model were taken from a sawdust drying experiment performed in the described dryer. In this section, the same drying experiment serves to demonstrate the applicability of the drying model by comparing the experimental result with the result from the numerical model. FIG. 6 shows the temperatures measured by the three sensors (s1, s2 and s3) through the total drying period (dotted lines) and compares them with the simulated temperatures (solid lines). A first observed deviation between the measured and simulated temperatures is initially found where the experimental air temperature is higher. However, the deviation is more inclined to be an experimental source of error and caused by difficulties in controlling the heat effect and settling of the air temperature.

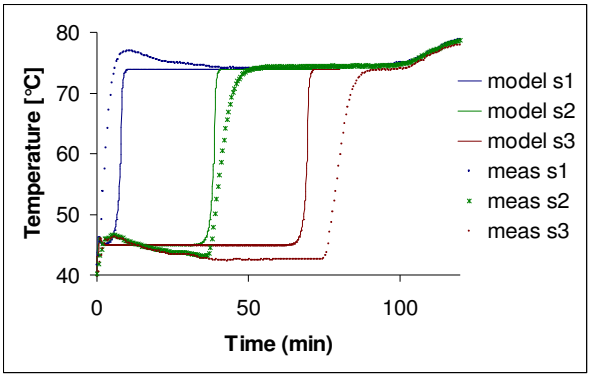

FIG. 6 Comparison between measured and modeled bed temperatures in the sawdust drying experiments.

The model in its present form does not consider varying inlet air temperatures. The modeled drying time scale fits the experimental time scale reasonably well. The drying experiment was considered complete after approximately 110 minutes, when the relative humidity in the air leaving the dryer was below 25%. In the simulation this occurred after approximately 80 minutes. The model predicts shorter drying times. However, fitting of neither the drying coefficient β nor the heat conductivity λ is not yet made.

5. Conclusions

A numerical model to simulate the batch drying of wood particles is developed and presented. The model describes the drying process with fundamental physical properties in coupled moisture and heat balance equations. The model differentiates between moisture in air phase and solid phase, while temperature is equal in both phases. By using the finite-difference method to solve the equation system, the following main conclusions can be drawn:

- The model describes the drying characteristics well, and quantities such as temperature, moisture content and bed pressure drop are determined properly compared to measured data of sawdust drying.
- Due to the large temperature gradients found in the drying zone, the bed must be divided into many thin cells which affects the required computer time for the numerical solution.
- The model requires an intrinsic mass transfer coefficient for the evaporation, and the thermal conductivity for the air and wood mixture. These key parameters are difficult to determine. However, they may be adjusted experimentally to fit other drying conditions or fuels with different properties. The modification $\beta = \beta(u)$ is easy to incorporate in the presented model.

The model may be further developed. Neither the temperature dependence for the sorption isotherm nor the temperature fluctuations of the drying air are considered in the model. These can be easily incorporated. Other important considerations concern the complex internal moisture transport. For larger particles, i.e. wood chips and bark, the mass transfer coefficient may be an inadequate approximation of the internal moisture transfer.

6. References

Bengtsson P. and Claesson J. Modeling of convective drying of permeable materials. Detailed report. To be published July 2008 in Reports, School of industrial engineering, Växjö University, Växjö, Sweden.

Bakker-Arkema F.W., Bickert W.G. and Patterson R.J. (1967). Simultaneous heat and mass transfer during the cooling of a deep bed of biological products under varying inlet air conditions. *Journal of agricultural Engineering Research,* 12**,** 297-307.

Boyce D.S. (1965). Grain moisture and temperature changes with position and time during through drying. *Journal of agricultural engineering research,* 10**,** 331-341.

Deomano E.C. (2001). Mechanism of flake drying and its correlation to quality. Blacksburg, Virginia, Virginia Polytechnic Institute and State University.

Hukill W.V. (1954). Drying of grain. IN Anderson J.A. and Alcock A.W. (Eds.) *Storage of cereal grains and their products.* St. Paul, Minnesota, American association of cereal Chemists.

Johansson A., Fyhr C. and Rasmuson A. (1997). High temperature convective drying of wood chips with air and superheated steam. *International Journal of Heat and Mass Transfer,* 40**,** 2843-2858.

Kayihan F. and Stanish M.A. (1984). Wood particle drying a mathematical model with experimental evaluation. *Drying 84***,** 330-347.

Laws N. and Parry J.L. (1983). Mathematical modelling of heat and mass transfer in agricultural grain drying. *Proceedings of the Royal Society of London.*

McCabe W.L. and Smith J.C. (1956). *Unit operations of chemical engineering,* New York, McGraw-Hill.

Parry J.L. (1985). Mathematical modelling and computer simulation of heat and mass transfer in agricultural grain drying: A review. *Journal of Agricultural Engineering Research,* 32**,** 1-29.

Ratti C. and Mujumdar A.S. (1995). Simulation of Packed-Bed Drying of Foodstuffs with Air-Flow Reversal. *Journal of Food Engineering,* 26**,** 259-271.

Saastamoinen J. and Impola R. (1997). Drying of biomass particles in fixed and moving beds. *Drying Technology,* 15**,** 1919-1929.

Singh R.P. and Heldman D.R. (2001). *Introduction to food engineering,* Amsterdam, Academic Press.

Sitompul J.P., Istadi I. and Sumardiono S. (2003). Modelling and simulation of momentum, heat, and mass transfer in a deep-bed grain dryer. *Drying Technology,* 21**,** 217-229.

Spencer H.B. (1969). A mathematical simulation of grain drying. *Journal of agricultural Engineering Research,* 14**,** 226-235.

Wang Z.H. and Chen G. (1999). Heat and mass transfer in fixed-bed drying. *Chemical Engineering Science,* 54**,** 4233-4243.

Behaviour and Optimization of Environmental Sensitive Layered Systems

Janis Brauns, Professor,
Department of Structural Engineering, Latvia University of Agriculture;
Janis.Brauns@llu.lv

Karlis Rocens, Professor,
Institute of Building and Reconstruction, Riga Technical University;
Rocensk@latnet.lv

KEYWORDS*: Composite materials, environmental exposure, hygrothermal deformation, wood composites.*

SUMMARY*:*
The article discusses analytical methods for estimation of hygromechanical properties and the behaviour of composite materials under unilateral environmental exposure. An advanced graphite-epoxy composite plate, a densified wooden strand board and plywood with different configuration have been examined. It is determined that midplane strains, curvatures and warping at nonsymmetric moisture distribution depend on the moisture content profile, composite type, configuration, and stacking sequence of layers. The optimum configuration for hygrothermal response may not coincide with that for mechanical properties. Sensitivity of a certain configuration of laminate and moisture profiles is an effective means for evaluating the viscoelastic (viscoplastic) stress relaxation in a hygrothermal environment.

1. Introduction

Composite materials are constructed by bonding together several structural elements to form a common structure. The properties and orientation of the elements have to be chosen such that the composite is able to meet the design requirements of strength and stiffness. However, the behaviour of material under various environmental conditions has to be taken into account as well.

The use of advanced high-strength structural composites in aerospace systems and in other applications has expanded rapidly and significant quantities are in production. Due to industrialization of building process and production of inexpensive and effective building materials the utilization of wood and other raw materials is taking place. Accordingly suitable structural models are needed for predicting the hygrothermomechanical properties (Geimer, 1982; Vital et al., 1980) and for the optimum formation of composite materials by taking into account the properties of components and technological process (Rocens, 1983; Brauns and Rocens, 1994a).

In structural elements, composite panels can be affected by unilateral environmental exposure (Brauns and Rocens, 1994a,b; Pipes et al., 1976; Environmental effects…, 1981; Advanced composite materials…, 1978). In general case, the character of swelling and thermal deformation of a composite with moisture or temperature is nonlinear. This study is devoted to the estimation of the mechanical properties and behaviour of different layered systems under nonsymmetric environmental effect. The main purpose is to determine the effect of unilateral environment depending on composite configuration. The estimation is performed in linear region of environment-induced strains assuming on ideal bond between the layers. The numerical analysis was accomplished taking into account the changes in moisture content at the given level of temperature.

The hygrothermal deformation of a unidirectional element of composites in the transverse direction is much higher than in the longitudinal direction and distinctive oriented layers or fibers prohibit free deformation, nonsymmetric residual stresses develop in composite laminates. These environmental stresses can lead to the warping of a composite and initiation of micro cracks, especially under transient conditions, and further degrade the strength properties of composites. The temperature change and moisture absorption affect likewise the mechanical properties of the composite while the dimensional change can influence the performance of the

structural element which can fail by buckling due to restrained expansion. Thus, hygrothermal behaviour affects not only the dimensional stability but also the safety of structures.

2. Heat conduction and moisture diffusion in composites

Considering a composite of thickness *h* as a system of elementary layers with parallel location of layers with respect to the midplane, a Cartesian coordinate system with axis $\{x_i\}$ is introduced (Fig. 1). The hygrothermomechanical properties of elementary layers are determined from the properties of the components by using analytical methods (Tsai and Hahn, 1980), or are found experimentally. The individual coordinate system $\{x_i'\}$ $(i = 1, 2, 3)$ is associated with the principal directions $\varphi^{(k)}$ of orthotropic elementary layers.

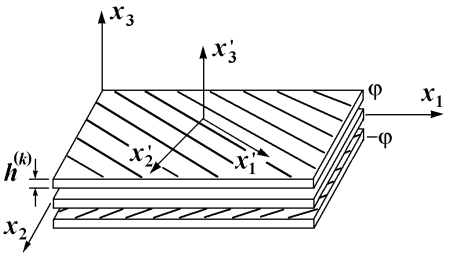

FIG. 1: Multilayer model of wooden composite.

The hygrothermomechanical behaviour of layered media under environmental effects depends on the thermal conductivity and moisture diffusion properties of elementary layer. In the case of thermal exposure the heat conductivities λ_{ij}^T in an arbitrary coordinate system can be expressed in terms of those in the symmetry axes of the layer are given by

$$\lambda_{11}^T = l_1^2\lambda_{11}'^T + l_2^2\lambda_{22}'^T; \qquad \lambda_{12}^T = l_1 l_2\left(\lambda_{11}'^T - \lambda_{22}'^T\right); \qquad \lambda_{22}^T = l_2^2\lambda_{11}'^T + l_1^2\lambda_{22}'^T, \tag{1}$$

where $l_1 = \cos\varphi$ and $l_2 = \sin\varphi$. In the direction $x_3 \equiv x_3'$, the heat conductivity is $\lambda_{33}^T \equiv \lambda_{33}'^T$.

In the case of moisture diffusion, the relation between moisture flux q_i^W and moisture concentration gradient is expressed in terms of the moisture diffusion coefficient λ_{ij}^W so that

$$q_i^W = -\lambda_{ij}^W \frac{\partial W}{\partial x_j}. \tag{2}$$

Note that moisture content *W* represents the amount of moisture as a fraction of the dry mass of the composite.

In practice, very important is one-dimensional diffusion through the element thickness, i.e., in the x_3 direction. Maintaining the temperature and moisture concentration on both surfaces of the material at equilibrium values, as linear approximation for the temperature distribution across the thickness with time *t* the Fourier equation can be used:

$$\frac{\lambda_{33}^T}{\rho C}\frac{\partial^2 T}{\partial x_3^2} = \frac{\partial T}{\partial t}, \tag{3}$$

where ρ and *C* are the mass density of the composite and the specific heat, respectively. Similarly, the Fick equation is applicable to the moisture diffusion

$$\lambda_{33}^W \frac{\partial^2 W}{\partial x_3^2} = \frac{\partial W}{\partial t}. \tag{4}$$

The thermal diffusivity $\lambda^T/(\rho C)$ in Eq. (3) and the moisture diffusion coefficient λ^W in Eq. (4) are measures of the rate at which the temperature and moisture concentration change within the material. These parameters, in general, depend on the temperature and moisture concentration. However, over the range of temperature and

moisture concentration prevailing in applications of composites, the thermal diffusivity is about 10^6 times higher than the moisture diffusion coefficient. As a result, the temperature will reach the given level long before the moisture concentration.

In many cases, the moisture absorption and desorbtion are prevented on one surface of the composite, while the other one is exposed to the environment. Since the moisture diffusion is through the thickness of the composite, in case of large structural elements it does not depend on the structure of layers. The moisture absorption through the thickness of material can be described by exact solution of Eq. (4) given in (Crank, 1956; Jost, 1960). Note, however, that nonsymmetric deformation (warpage) and buckling, due to restrained linear expansion, is sensitive to configuration of layered materials and to certain moisture profiles. Consequently, methods of predicting how various configuration parameters affect the dimensional stability of board are needed. Moreover, the dimensional change of the structural element can influence the performance of the material that results in degradation of the strength properties and decreases the safety of a structure.

Since, in the case of structural elements of finite width, the diffusivity considerably depends on the layer orientation for sufficiently large or short time periods, some approximations for the moisture distribution profile can be used. In the subsequent analysis, parabolic, hyperbolic, and linear moisture distribution has been chosen.

3. Stress-strain relationships including environmental effects

Composite materials deform when they absorb the moisture or when the temperature changes. To determine the resulting strain we assume that the material is elastic and the response of the material does not depend on the history of environmental conditions but only on its initial and final state. Since the order of application of various changes is immaterial, it is assumed that temperature is changed first, followed by moisture absorption.

The final axial strains ε_i' in the unidirectional element are the sum of three types of strain induced by the temperature change, moisture absorption and applied stresses σ_j, respectively

$$\varepsilon_i'(T,W,\sigma_j) = \varepsilon_i'^{T}(T,\sigma_j) + \varepsilon_i'^{W}(T,\sigma_j) + S_{ij}'(T,W)\sigma_j', \tag{5}$$

where S_{ij}' are the compliances of the unidirectional element. Thermal and moisture deformation are the nonlinear functions of T and W, respectively (Environmental effects…, 1981; Advanced composite materials…, 1978). To calculate strains $\varepsilon_i'^{T}$ and $\varepsilon_i'^{W}$, specific thermal strain $\alpha_i'(T)$ and specific swelling $k_i'(W)$ of the element can be used:

$$\varepsilon_i'^{T}(T) = \alpha_i'(T)(T - T_0); \qquad \varepsilon_i'^{W}(W) = k_i'(W)(W - W_0), \tag{6}$$

where T_0 and W_0 are initial temperature and moisture content, respectively. The specific strains denote free expansion of the element when the temperature or moisture content changes per one unit.

Within the composite, the deformation of one layer is constrained by the other with different orientation, and hence environmental stresses arise in each layer. In the general case, the stresses in the elementary layers are different and the stress state of a composite is inhomogeneous. The static equivalent system of average force stresses σ_j and couple stresses μ_j acting on a unit volume of material has been used (Koiter, 1964; Mindlin, 1964). By applying matrix notations, the following constitutive relations for the midplane strains ε_i^0 and the curvatures κ_i are given by

$$\begin{bmatrix} \boldsymbol{\varepsilon}^0(T,W,t) \\ \boldsymbol{\kappa}(T,W,t) \end{bmatrix} = \begin{bmatrix} \boldsymbol{\alpha}(T,W,t) & \boldsymbol{\beta}(T,W,t) \\ \boldsymbol{\beta}^{\mathrm{T}}(T,W,t) & \boldsymbol{\delta}(T,W,t) \end{bmatrix} \cdot \begin{bmatrix} \boldsymbol{\sigma}(T,W,t) \\ \boldsymbol{\mu}(T,W,t) \end{bmatrix}. \tag{7}$$

In Eq (7), the tensor indices are omitted and T denotes transposition. The compliance components α_{ij}, β_{ij}, δ_{ij} $(i, j = 1,...,6)$ depend on the temperature and moisture content. The force and couple stresses in the unit volume of the composite are calculated by averaging:

$$\sigma_j(T,W,t) = \int_{-h/2}^{h/2} \tilde{\sigma}_j^{(k)}(T,W,t)dx_m \; ; \tag{8}$$

$$\mu_j(T,W,t) = \int_{-h/2}^{h/2} x_m \tilde{\sigma}_j^{(k)}(T,W,t)dx_m \; , \tag{9}$$

where $m = 1$ or 2 or 3; $m \neq j$.

The stresses $\tilde{\sigma}_j^{(k)}$ in kth elementary layer in the coordinate system $\{x_i\}$ can be determined by using the variation in temperature of the material or moisture content of the material starting from their initial values and the specific environmental stresses $\tilde{r}_j(W)$ or $\tilde{r}_j(T)$. For some type of composites produced by compression, for example, wooden composites, the stiffness properties also depend on the initial partial density $\hat{\rho}_*$. The analysis is performed at fixed temperature. In this particular case, when $T = \text{const}$ and $W \neq \text{const}$ at a fixed time moment, the stresses in the layers can be found as

$$\left\{\tilde{\sigma}_j(W)_{|\hat{\rho}_*}\right\}^{(k)} = \left\{\tilde{r}_j(W)_{|\hat{\rho}_*}\right\}^{(k)}(W - W_0) \, . \tag{10}$$

The matrix of the specific environmental stresses $\left\{\tilde{r}_j\right\}^{(k)}$ of the layers in the coordinate system $\{x_i\}$ can be represented as

$$\left\{\tilde{r}_j(W)_{|\hat{\rho}_*}\right\}^{(k)} = [g_{ij}]\left\{r_i'(W)_{|\hat{\rho}_*}\right\}^{(k)} \, , \tag{11}$$

where $[g_{ij}]$ is the stress transformation matrix (Tsai and Hahn, 1980). The specific constraining stresses $[r_j']$ in (11) and specific moisture strains $[k_i']$ are associated with the layer stiffness A_{ij}', and for the plane stress state are given by

$$\left\{r_j'(W)_{|\hat{\rho}_*}\right\} = [A_{ij}'(W)_{|\hat{\rho}_*}]\left\{k_i'(W)_{|\hat{\rho}_*}\right\}. \tag{12}$$

For the general case, the compliance matrices in (7) can be represented in terms of the general stiffness of the composite:

$$\boldsymbol{\alpha}(W)_{|\hat{\rho}_*} = \mathbf{S}(W)_{|\hat{\rho}_*} + \mathbf{S}(W)_{|\hat{\rho}_*}\mathbf{B}(W)_{|\hat{\rho}_*}\mathbf{C}(W)_{|\hat{\rho}_*}\mathbf{B}(W)_{|\hat{\rho}_*}\mathbf{S}(W)_{|\hat{\rho}_*} \; ; \tag{13}$$

$$\boldsymbol{\beta}(W)_{|\hat{\rho}_*} = -\mathbf{S}(W)_{|\hat{\rho}_*}\mathbf{B}(W)_{|\hat{\rho}_*}\mathbf{C}(W)_{|\hat{\rho}_*} \, , \tag{14}$$

where

$$\mathbf{C}(W)_{|\hat{\rho}_*} = \left[\mathbf{D}(W)_{|\hat{\rho}_*} - \mathbf{B}(W)_{|\hat{\rho}_*}\mathbf{S}(W)_{|\hat{\rho}_*}\mathbf{B}(W)_{|\hat{\rho}_*}\right]^{-1} . \tag{15}$$

The components of the stiffness of the laminate are evaluated by integration:

$$\left[A_{ij}(W)_{|\hat{\rho}_*}, B_{ij}(W)_{|\hat{\rho}_*}, D_{ij}(W)_{|\hat{\rho}_*}\right] = \int_{-h/2}^{h/2} \tilde{A}_{ij}^{(k)}(W)_{|\hat{\rho}_*}\left[1, x_3, x_3^2\right]dx_3 \, . \tag{16}$$

In Eq. (16), the stiffness matrix $\left[\tilde{A}_{ij}\right]^{(k)}$ of the elementary layer in the coordinate system $\{x_i\}$ can be determined by using the transformation formula. The compliance matrix in Eqs (13) – (15) is $[S_{ij}] = [A_{ij}]^{-1}$. The multilayer model based on the laminate analogy (Halpin et al., 1971) is used to determine the stiffness in Eq. (16) for the high filled wooden strand board (WSB) with short-fiber volume fraction of about 90...95% and more.

4. Numerical results and discussion

In the discussion of hygrothermoelastic behaviour of layered composites, the temperature and the moisture concentration are assumed to be nonuniform over the thickness of material. Since the order of application of various changes is immaterial, conceptually it is imagined that the temperature is changed first and is fixed, while the moisture changes with time and with the coordinate x_3 in the thickness direction. To determine the environmental midplane strains and curvatures, the Eqs (7) – (9) are used. Two types of composites are examined: an advanced graphite-epoxy composite (AS/E) plate and a densified aspen WSB.

By using the properties of unidirectional layer with infinite fibers or short-length flakes, the displacement vector in Eq (7) of the structural behaviour is determined. One way to assess warpage is to fix the laminate at one corner and determine the lateral displacement at the diagonally opposite corner (Fig. 2). This structural behaviour can be predicted by the following equation for a rectangular flat laminate

$$w = 1/2(a^2\kappa_1 + b^2\kappa_2 + 2ab\kappa_6), \tag{17}$$

where w is the corner displacement, a and b are the side dimensions, and κ_i is the curvature determined from Eq. (7). The ratio w/a obtained for the square laminate $a = b = 25$ cm for four laminate configurations from an AS/E composite in the case of three different moisture profiles at moisture content difference $\Delta W = 0.6\%$ are summarized in Fig. 3. Note that the linear (L), parabolic (P) and hyperbolic (H) moisture profiles induce approximately the same warpage for configurations $[(\pm\varphi)_2]_S$ but the differences can be substantial for configurations $[\varphi/0/-\varphi]_S$. The variation of the corner displacement as a function of ply angle is shown in Fig. 4 for the laminates with parabolic moisture profiles. Note that the warpage for configuration $[(\pm\varphi)_2]_S$ is greater and varies regularly with orientation compared with the configuration $[\varphi/0/-\varphi]_S$.

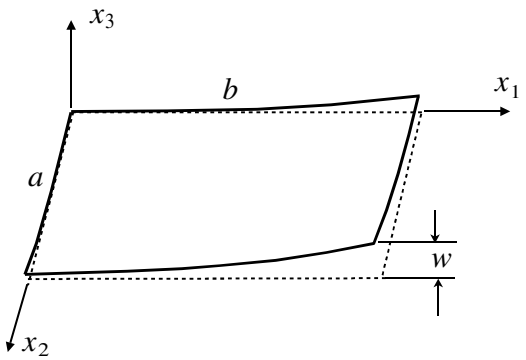

FIG. 2: Corner displacement of a composite plate induced by nonsymmetric moisture distribution.

Due to warpage induced by nonuniform moisture distribution, the corner displacement can be substantial. In numerical analysis, the moisture concentration difference was 0,6%, which corresponds to the linear region of the moisture-induced strain. The displacement depends on the moisture distribution type and composite configuration. Note that the corner displacements exceeding 2,5 cm is probably beyond the limits of linear structural analysis. The hygrostresses in the plies of laminates in the transverse direction and interlaminar shear reach magnitudes, which are comparable to ply strengths. In the elastic analysis, the warpage of the AS/E laminate is large. Sensivity to a certain configuration of the laminate and moisture profiles is an effective means for evaluating the stress relaxation in hygrothermal environment. Note that the corner displacement ratio depends on the composite configuration and increases with the number of the ±45° layers while the mechanical load is the dominant source of the shear stress in the ±45° plies responsible for the shear stiffness.

Analysis of the AS/E composite with the above-mentioned nonsymmetric moisture distribution is performed by using the following experimental characteristics of a unidirectional dry ply at room temperature: $E_1' = 138$, $E_2' = 9.65$, $G_{12}' = 4.21$ GPa; $\nu_{21}' = 0.30$; $k_1' = 0.01$, $k_2' = 0.45$ %. Note that the hygromechanical properties of the AS/E composite change with the moisture content, including specific swelling deformation k_2'. In order to take into account the moisture-caused changes, the reduction factors were used in the calculation.

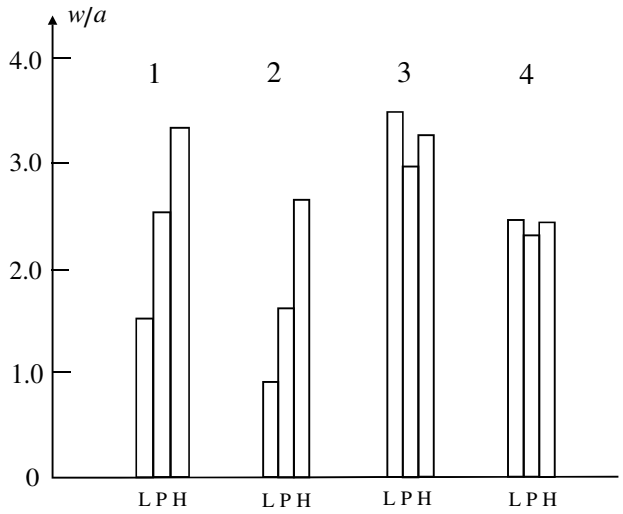

FIG. 3: Predicted warpage induced by nonsymmetric moisture content in AS/E laminates: 1 – $[30/0/–30/0]_S$; 2 – $[45/0/–45/0]_S$; 3 – $[(\pm30)_2]_S$; 4 – $[(\pm45)_2]_S$.

Composition boards, such as flake boards and plywood, change in dimension as the moisture content varies. Since the dimensional stability of the composition boards is critical in most applications, the maximum allowable dimensional change in such products is limited by standards. Consequently, methods of predicting how various processing parameters affect the dimensional stability of the board are needed.

The elementary layers of the composite with short-length components consist of previously calculated elements with the properties determined with regard to pressing during the fabrication of the material and considering the statistical length distribution of flakes as well as incomplete bonding. The technical characteristics of a densified orthotropic layer with unidirectionally oriented short-length aspen flakes at $W_0 = 6\%$ and $\hat{\rho}_* = 750$ kg/m^3 are as follows: $E_1' = 4.8$, $E_2' = 0.53$, $G_{12}' = 0{,}77$ GPa, $\nu_{21}' = 0{,}22$. Nonlinear dependences of the mechanical properties on moisture were taken into account. The specific moisture strains at the given initial conditions are $k_1' = 0{,}01$ and $k_2' = 0{,}25$ %, while the dependencies of these strains on the moisture are based on experimental data.

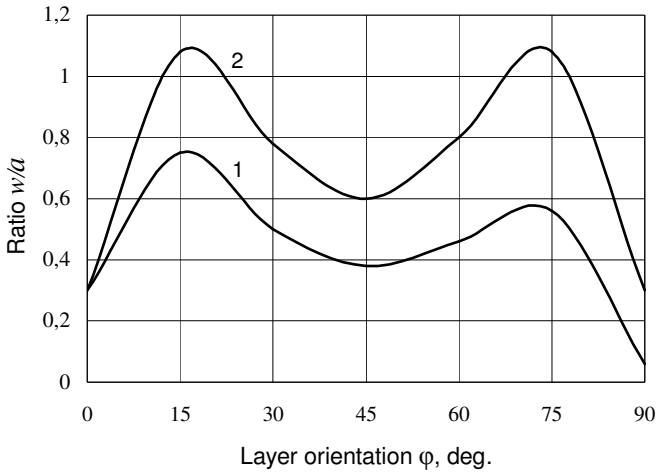

FIG. 4: Predicted warpage induced by 0,6% *nonsymmetric moisture distribution in AS/E laminates* (*parabolic profile*): 1 – $[\varphi,0,-\varphi,0]_S$; 2 – $[(\varphi,-\varphi)_2]_S$.

In the production process of wooden composites, the variation of the properties of wood by means of increasing the volume fraction of cell wall is realized by compressing the wood perpendicular to the grain, i.e., flattening its

cavities. For the wood with a decreased void volume resulting from compression, compliance of wood in the direction of pressing (axis x_3) appears to be higher in comparison with natural wood. Accordingly, unless complete flattening of the vessels is reached, a decrease of the cell-wall material resisting the action of the stresses σ_3 is taking place. The fraction of the cell-wall material of the layer resisting the action of the stresses σ_1' and σ_2' increases, decreasing the compliance in the directions x_1' and x_2'. Plastic, or unrecoverable, deformation is the major part of deformation of the wood that occurs during the hot pressing. When moistening, plastic deformation becomes recoverable and there is a large difference between swelling of the densified wood in the direction of pressing and in the transversal x_2' direction. According to reconstituted wood structure, the specific moisture strain of the densified wood in comparison with the customary wood increases nonlinearly when moisture content grows in the direction of pressing, but decreases in the transversal direction.

By using a multilayer model for the composite with short-length wooden flakes, the total binder volume is distributed in separate layers proportionally to the volume of flakes. To illustrate the effect of flake alignment on moisture deformation, we consider laminates with different orientation of the principal axes of the elementary layers with respect to, e.g., machine direction (x_1). For any laminate, the average orientation angle of fibers (disregarding its sign) relative to the x_1 axis is labeled $\overline{\varphi}$ and the relative alignment ξ is defined as

$$\xi = \left[(45^\circ - \overline{\varphi}) / 45^\circ\right] \cdot 100\% \,. \tag{18}$$

The model of the board used consists of 12 elementary layers, which form a symmetric or nonsymmetric structure. Effect of a nonsymmetric nonlinear distribution of the moisture content of nonsymmetric and antisymmetric structure on warpage was studied. The warpage of the board with antisymmetric structure is essentially higher.

In the case of plywood, the technical characteristics of densified birch veneer used in the analysis are: modulii of elasticity E_1 = 16.5 and E_2 = 0.7 GPa; shear modulii G_{12} = 0.9, G_{13} = 1.5 and G_{23} = 0.3 GPa; Poisson's coefficients ν_{21} = 0.45, ν_{31} = 0.34 and ν_{32} = 0.30. The corrections for moisture change of the elasticity and shear modulii, respectively, are: α_1 = 250, α_2 = 25, α_{12} = 25, α_{13} = 30, and α_{23} = 20 MPa. The specific moisture strains at given initial conditions are: β_1 = 0.00003, β_2 = 0.002, β_3 = 0.003 $(\%)^{-1}$. The partial density of plywood is 660 kg/m^3.

The relationship between expansion (ε_i), thickness swelling (ε_3) and alignment for an increase of moisture content of 12% is shown in Fig. 4. The preferable boards are with relative flake alignment ξ = 0 – 40%. Fig. 4 also shows relationships between alignment and specific reaction F^* in bending and critical stress σ_1^{cr} in compression of a hinged square board.

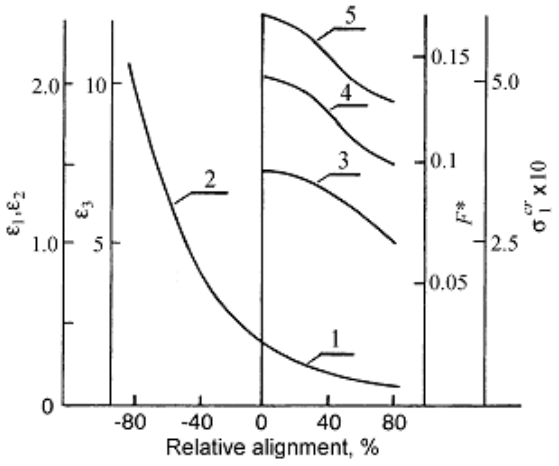

FIG. 4: Effect of flake alignment on swelling and mechanical properties of flakeboard: 1 – ε_1; 2 – ε_2; 3 – ε_3; 4 – F^* (kN); 5 – σ_1^{cr} (MPa).

Conclusions

The following main conclusions can be drawn from the present study:

1. The midplane strains, curvatures and warping of an advanced graphite-epoxy composite plate and a wooden strand board of different configurations densified in technological pressing with nonsymmetric moisture distribution (linear, parabolic and hyperbolic) taking into account the nonlinear swelling properties are determined.
2. Hygrostrains depend on the moisture content and profile, laminate configuration, composite type as well as the ply stiffness, and should be calculated basing on the precise stacking sequence, while thermal deformation in angle-ply laminates, except wooden composites with densified orthotropic layers, can be predicted by using the equivalence principle between the hygro and thermal expansions.
3. The optimum configuration for the hygrothermal behaviour may not coincide with that for the mechanical properties and, for every type of loading, composite materials with an appropriate structure should be used. Sensitivity of a certain configuration of laminate and moisture profiles is an effective means for evaluating the viscoelastic (viscoplastic) stress relaxation in a hygrothermal environment.

References

Advanced composite materials – environmental effects (1978), ASTM STP 658 (Vinson J. R., editor), American Society for Testing and Materials, Philadelphia, 289 p.

Brauns J.A. and Rocens K.A. (1994a). Nonlinear moisture deformation of a composite with a densified reinforcement, *Mech. Compos. Mat*., Vol. 30, No 3, p. 314-320.

Brauns J.A. and Rocens K.A. (1994b). Hygromechanics of composites with unsymmetric structure, *Mech. Compos. Mat*., Vol. 30, No 6, p. 601-607.

Crank J. (1956), The Mathematics of Diffusion, Clarendon Press, Oxford, 347 p.

Environmental effects on composite materials (1981) (Springer G. S., editor), Technomic, Westport, 203 p.

Geimer R.L. (1982). Dimensional stability of flakeboards as affected by board specific gravity and flake alignment, *Forest Prod. J*., Vol. 32, No. 8, p. 44-52.

Halpin J.C., Jerine K. and Whitney J.M. (1971). The laminate analogy for 2 and 3 dimensional composite materials, *J. Compos. Mat*. Vol. 5, No. 1, p. 36-49.

Jost W. (1960). Diffusion in Solids, Liquids, Gases, Academic Press, New York, 558 p.

Koiter W.T. (1964). Couple-stresses in the theory of elasticity, *Proc. Koninkl. Ned. Akad. von Wetenschappen*, Vol. 67, No. 1, 17-44.

Mindlin R.D. (1964). Microstructure in linear elasticity, *Arch. Rat. Mech. Anal*., Vol. 16, No. 1, p. 51-78.

Pipes R.B., Vinson J.R. and Chou T.W. (1976). On the hygrothermal response of laminated composite systems, *J. Compos. Mat.* Vol. 10, No. 2, p. 129-148.

Rocens K.A. (1983). Macrostructure theory of modification of wood properties, *J. Appl. Polym. Sci. Appl. Polym. Symp*., Vol. 37, p. 923-941.

Tsai S.W. and Hahn H.T. (1980). Introduction to composite materials, Technomic Publ. Co., Westport, 457 p.

Vital B.R., Wilson J.B. and Kanarek P.H. (1980). Parameters affecting dimensional stability of flakebord and particleboard, *Forest Prod. J*., Vol. 30, No 1, p. 23-29.

Comparison of small- and large-scale wall assembly specimens exposed to similar experimental conditions

Dominique Derome, Ph.D.
Empa, Swiss Federal Labaratories for Materials Testing and Research, Laboratory for Building Technologies, Überlandstrasse 129, CH-8600, Dübendorf

Saba Saneinejad
Concordia University, Department of Building, Civil and Environmental Engineering, Montreal, Canada H3G 1M8

Jan Carmeliet, Ph.D.
Chair of Building Physics, Swiss Federal Institute of Technology ETHZ Zürich, ETH-Hönggerberg, CH-8093 Zürich, Empa, Swiss Federal Labaratories for Materials Testing and Research, Laboratory for Building Technologies, Überlandstrasse 129, CH-8600, Dübendorf

Achilles Karagiozis, Ph.D.
Oak Ridge National Laboratory, Tennessee, USA

KEYWORDS: *vapour flow, high thermal gradient, moisture accumulation, small- and large-scale testing*

***SUMMARY*:**

It is known that solar driven vapour transport inward to vapour open constructions such as wood frame walls with a vapour tight finishing at the inside may occur and may lead to an undesired wetting of wooden elements and gypsum board. Although the origin of this inward vapour transport may be well understood, the quantification of the moisture damage risks remains not well understood, since the effect of material properties and climate on the two-dimensional hygrothermal behaviour of the walls is not yet adequately addressed.

Therefore, a research project, subsidized by ASHRAE TC4.4, studies solar-driven inward vapour flow combining small- and large-scale wall assemblies tests under comparable conditions. The objective of the tests were to produce precise measurements on wetting and drying behavior of internal parts of the back wall, when a wetted masonry cladding is loaded under cyclic temperature loading. The specimens were composed of: brick veneer, weather resistive membrane (spun-bonded polyolefin), oriented-strand board (OSB) sheathing, glass fiber insulation, gypsum board and interior finish (acrylic paint or vinyl wall covering). It is found that, due to the temperature gradient, an important vapour flow is generated to the back wall, wetting the OSB sheathing, mineral wool and gypsum board. The vapour permeance of the interior finishing determines the wetting of the gypsum board: a vapour tight vinyl wall covering leads to significant wetting of the gypsum board and very low drying rates during drying. The moisture contents in the gypsum board are compared.

1. Introduction

Situations such as heating of the wet masonry due to solar radiation can induce inward water vapour flow, especially when the interior space is air-conditioned at lower temperature. These water vapour flows can be important and lead to moisture accumulation in the back wall. Sustained exposure to high moisture content may lead to the development of mould and rot growth, corrosion of fasteners and reduction of the thermal insulation value. The occurrence of inward moisture flow due to solar radiation is more prevalent in mixed and hot climates, but may also be observed during the summer in cold climates.

The phenomenon of cyclic vapour flow driven by solar radiation and the influence of the wall composition on the hygrothermal performance and durability of wall systems subjected to such flow are not yet fully understood. The ASHRAE T.C. 4.4 committee identified this need, and a research project was initiated to

develop fundamental understanding of the impact of solar-driven moisture flow. Small- and large-scale experimental work was performed in the laboratory and controlled conditions setups for various wall assemblies. The third experimental component of this project was field testing of four assemblies, in Charleston, South Carolina. The results from the three experimental parts will be used to validate computer models, which will be subsequently used to simulate more variations of assembly constructions and environmental loading conditions. This paper presents the small- and large-scale experimental setups and reports on the results for various wall assemblies for this ASHRAE funded project

2. Small-scale experimental work

2.1 Experimental procedure

A small-scale testing setup was developed and built to test simultaneously eight 400 mm x 400 mm specimens. In this paper, we present only the general experimental procedure. More details can be found in Carmeliet et al. (2007) and Deckers (2007). The wall composition is typical for North American low-rise residences, insulated with fiberglass insulation between the studs. An air cavity is present between the brick veneer and the back wall. An exterior sheathing of oriented-strand board (OSB) is used. Two types of weather resistive barriers (WRB) on the OSB are considered: spun-bonded polyolefin (SBPO) and building paper (BP). On the gypsum board, two different finishings are used: a two-layer acrylic paint and a vinyl wall covering (VWC).

At the beginning of the test, 1.5 liter of water is spread over the masonry leading to an average moisture content of 110 kg/m³, which is half of the capillary saturation moisture content. The experiment is divided into two periods: a wetting period and a drying period. During the wetting period, the masonry remains covered with an aluminum plate, sealed with a gasket, preventing drying of the masonry towards the outdoor environment. The drying period starts after 17 days by removing the aluminum plates from the specimens, allowing drying both towards the indoor and outdoor environment.

The indoor and outdoor conditions aim at representing summer conditions in Charleston, South Carolina, including solar radiation on the outside cladding and conditioned air at the indoor side. Two test conditions are considered: constant outside temperature loading and cyclic temperature loading. For the constant loading experiment, the outside temperature is 40ºC and an outside relative humidity (RH) of 10 %. For the cyclic loading an outdoor temperature loading of 40ºC during 8 hours is followed by 16 hours at 21ºC. The outdoor relative humidity varies between 10 % RH at high temperature and 50 % RH at low temperature following the temperature loading. A constant temperature of 18ºC and 50% RH is used as the indoor climate.

The moisture content of the different parts of the wall is determined by gravimetry. The three parts - brick veneer, sheathing (OSB + WRB), insulation (+ eventually wooden stud) & gypsum board (+ interior finishing) are weighed individually.

2.2 Results

Some test results of the small-scale experiments are presented in Figure 1. A more detailed discussion of the experimental results is given in Carmeliet et al. (2007). We observe generally that the inward water vapour transport due to the thermal gradient leads to an important wetting of OSB and gypsum board.

Comparing Figures 1a and 1b (note the difference in moisture content range on the y-axis), we observe that the moisture uptake by the gypsum board covered with the vapour tight VWC is much higher than the uptake of moisture by the gypsum board with vapour open paint. In the case of VWC finishing and constant loading conditions, the gypsum board shows very low drying rates. We further observe that during cyclic loading the wetting of gypsum board is reduced: the moisture content of the gypsum board remains lower than the ones observed for the constant conditions. The maxima of moisture content of the gypsum board with vinyl wall covering and paint in the constant loading case are respectively 230 versus 50 kg/m³, or a ratio of 4.6 to 1. In the cyclic loading case, the maxima are respectively 81 versus 13 kg/m³, or a ratio of 6.4 to 1. This difference in ratio's may be attribute to the fact that the drying is delayed in the cyclic loading. Note that a maximum of 81 and 13 kg/m³ for gypsum board with paint finishing still refers to a RH of respectively 98% and 86%, which is above the limit for moisture damage.

In Figure 1c, we observe that the moisture uptake by OSB first increases fast and attains a maximum at the end of the wetting period. The maximum for constant loading conditions equals 150 kg/m³, which refers to a RH value of 98 % and is above the limit for moisture damage. The moisture content of OSB in the wetting period during cyclic loading remains lower compared to the constant boundary conditions. However, we also observe that the moment at which drying of the OSB starts is delayed and the rate of drying is slower, resulting in higher final moisture contents. This means that, during cyclic loading, the wetting and also the drying potential reduces and the materials may remain, on average, for a longer time at higher moisture content levels.

We also observe that the moisture behavior of OSB and gypsum board does not depend much on the type of WRB in either the constant or cyclic loading case. Walls with SBPO show somewhat lower moisture contents of OSB and gypsum board than walls where building paper is used.

In Figure 1d, we observe that the decrease of moisture content of masonry during the wetting period is slower for cyclic conditions compared to the constant boundary conditions. The reduction of the thermal loading also leads to a slower drying of the masonry during the drying phase.

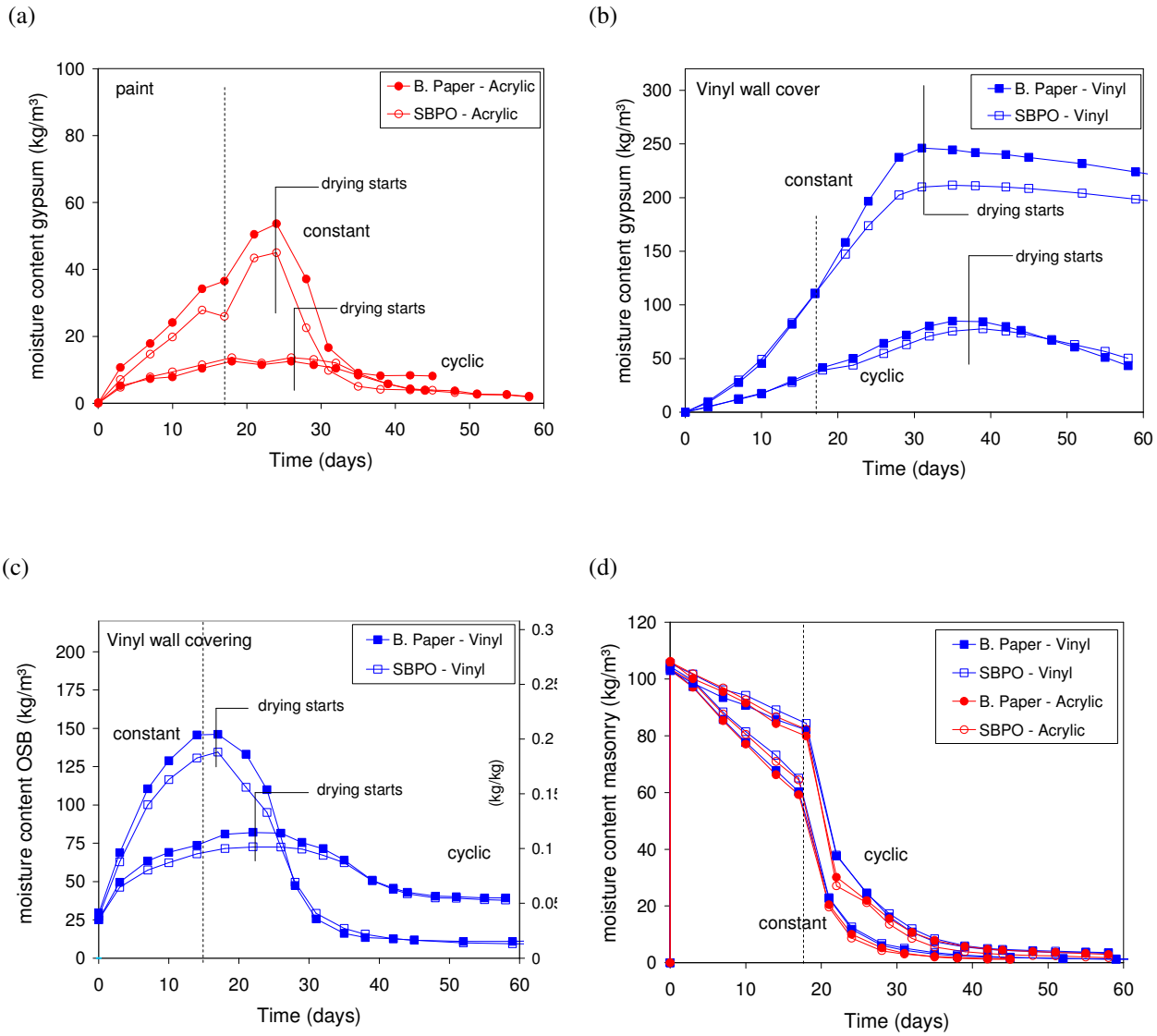

Figure 1. Comparison of moisture content evolution for constant with cyclic loading conditions: (a-b) Moisture content of gypsum board for paint and VWC finishing; (c) Moisture content of OSB for the VWC finishing; (d) Moisture content of masonry for all variants.

3. Large-scale experimental procedures

3.1 Test setup and boundary conditions

Three large-scale tests involved specimens 1.2m wide by 2.4m high. The specimens used for this experiment were typical of North-American wood-frame construction. The specimens were constructed of two main parts. The cladding was 90mm clay brick, mounted in a frame hung in front of an insulated back-wall. The air cavity of 25 mm was not vented. The back-wall consisted of 38mm x 89mm wood studs with fiberglass insulation, enclosed with either OSB sheathing (9 mm) or Extruded Polystyrene Insulation (XPS) (38mm) on the exterior and gypsum board (12 mm) on the interior side. The weather resistive barrier (WRB) of spun-bonded polyolefin covered the exterior face of the OSB. The interior finish on the gypsum board consisted of vinyl wall covering (VWC) or paint.

Figure 2a-c shows the overall test setup; a complete description is found in Edelstein (2007). The specimens were wetted and then exposed to high climatic cycles simulating rain and sun. The interior face of the specimen was exposed to indoor air conditions maintained in the air-conditioned highly insultated test hut. The exterior condition (rain and sun) were reproduced using a wetting and a heating system. To wet the cladding, a spraying apparatus consisted of nozzles mounted on a moveable rack in a manner to ensure uniform wetting of the brick wall. Solar radiation was simulated using 40 heat lamps of 175 Watts placed inside a reflective box. The lamps were positioned and dimmed in a way to ensure uniform heating of the entire brick wall to minimum of 50°C.

The loading of this experiment consisted of alternating periods of wetting and drying. The brick wall was daily wetted to 50% saturation during the wetting phase. The wall was then subjected to 8 hours of radiation. Drying continued for the next 16 hours without radiation. The daily wetting/drying cycles were repeated until a significant amount of moisture was observed within the back-wall. At this point, wetting was stopped and daily drying cycles (8 hours with radiation and 16 hours without) were repeated until the specimen was nearly back to its initial dry state, thus the different wetting and drying phase length for the three different tests.

(a) (b) (c)

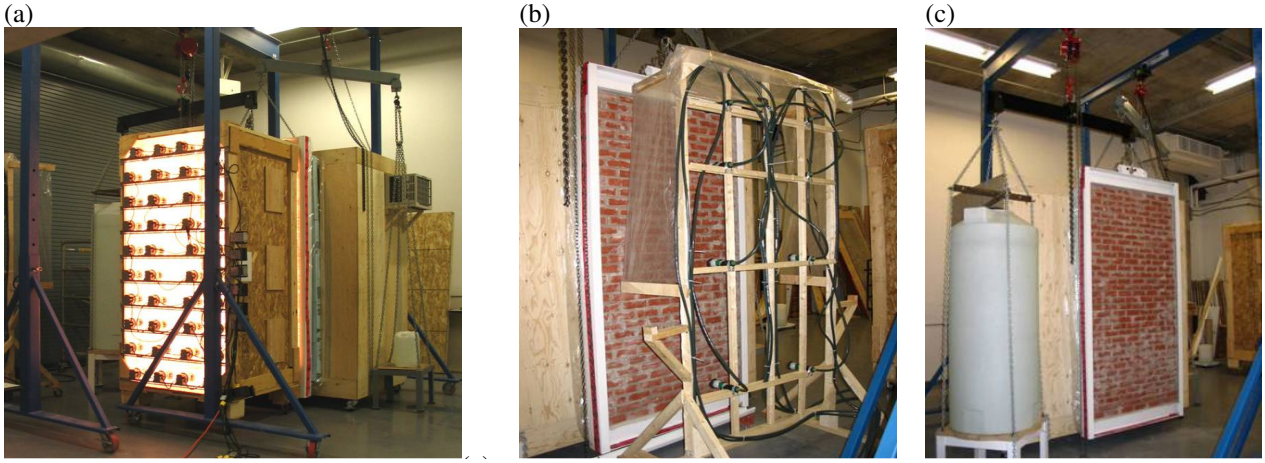

Figure 2. Experimental set-up: (a) Overall view of test,(b) Spraying apparatus,(c) Weighing apparatus.

3.2 Monitoring and instrumentation

The brick frame and the back wall were separately and continuously weighed during the test using a weighing system. Each weighing system was suspended from a gantry crane and consisted of a friction-free leaver arm supporting at one end a specimen and, at its other end, a counter-weight. A load cell was anchored between the counter-weight and the floor and measured any mass change of the specimen during the test period. Different parts of the weighing system can be seen in Figure 2(c). In addition to this continuous monitoring, small gravimetric samples of gypsum board and wood stud were also monitored periodically. Six gypsum board gravimetric specimens of 150mm x 150mm and 3 wood stud specimens of 12.5mm x 12.5mm x 38 mm were taken from the top, middle and bottom of the large-scale specimens. Figure 3(a) shows the locations of the samples. Combined relative humidity and temperature sensors were installed at various positions in the large-scale specimen and additional thermocouples were placed at various layers and various heights of the specimen

for continuous monitoring. Figure 3(b) shows the locations of the relative humidity probes, thermocouples and moisture pins.

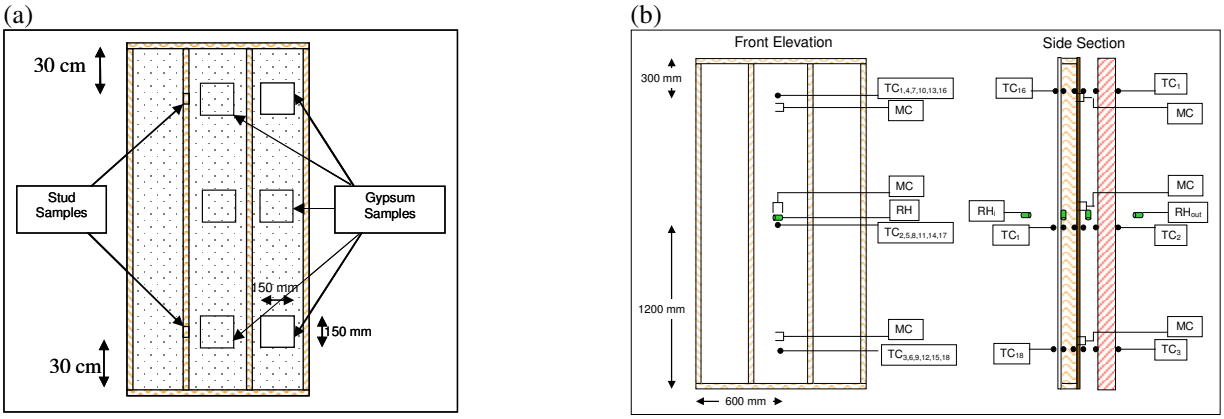

Figure 3 Monitoring lay-out (a) Location of gravimetric samples, (b) Instrumentation for electronic instrumentation.

3.3 Results

3.3.1 Wall with brick cladding and vinyl wall covering finishing

The moisture content evolution in the different components of this wall is shown in Figure 4(a) The cyclic wetting and drying phase for this specimen was continued for 19 days and followed by 23 days of drying. The rapid decrease of mass of the brick wall can be clearly observed. The figure also includes the moisture content of the gypsum taken at three heights in the wall. The moisture content of the gypsum samples increase during the wetting phase and even for a few days after the drying phase starts. It can be seen that the moisture content in the specimen increases with the height. This could be explained by existence of possible convection loops or stack effects in the insulation cavity in contact with the gypsum board. Finally, Figure 4 (a) also included the moisture content of the back wall in kg/m^2. It can be observed that the moisture gain of the back wall follows an evolution similar to the one of the gypsum board, although it should be kept in mind that the back wall mass also includes the moisture absorbed by the wood frame and the OSB.

Figure 4(b) shows the vapour pressure difference between air cavity and insulation cavity, and between insulation cavity and inside the hut. During the wetting phase, the vapour pressure is higher in the cavity and lower inside, highlighting the inward vapour flow. Vapour tight VWC on the interior side of gypsum board however prevents vapour to be transferred to inside and leads to high relative humidity in the gypsum board. The VWC resulted in moisture build up and development of mould on the backside of the VWC. After the start of the drying period, the vapour pressure in the cavity is still higher than in the insulation for about a week, after which the vapour pressure of the cavity falls below that of the insulation.

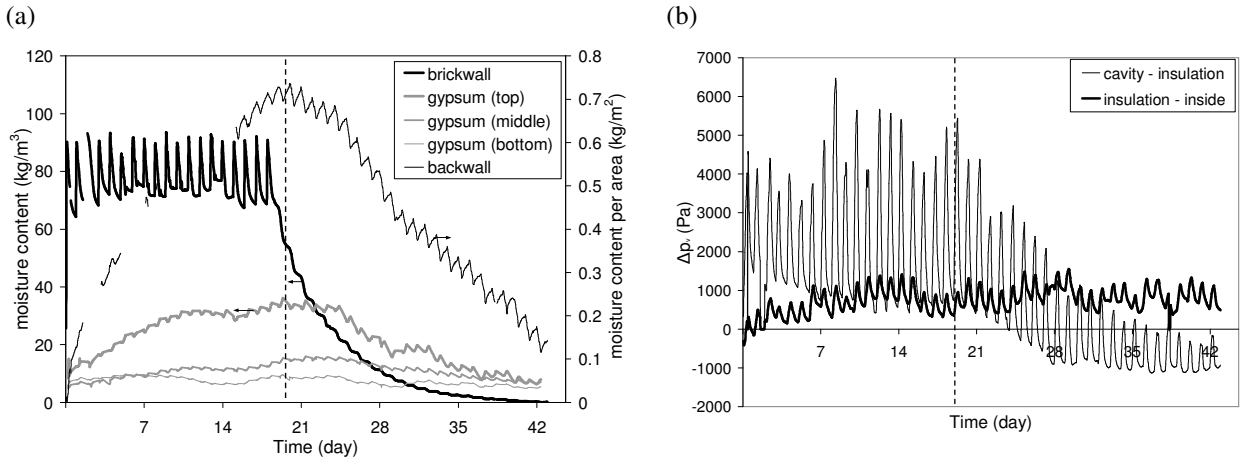

Figure 4 Wall brick veneer and VWC: (a) Moisture content evolution, (b) Vapour pressure differences.

3.3.2 Wall with brick cladding and painted gypsum

In this test, the brick wall was wetted daily for 14 days and dried for 6 days. No moisture content increase was observed in the gypsum gravimetric samples, which is due to the high vapour permeability of the paint on the interior gypsum board, as shown on Figure 5(a). The moisture content monitoring of the back-wall shows some increase of moisture content which could be the moisture absorbed by the OSB. Studying the vapour pressure differences shows that moisture does not accumulate in the insulation and is able to dry towards the inside within hours as shown in Figure 5(b). This is due to the vapour permeable paint on the gypsum board.

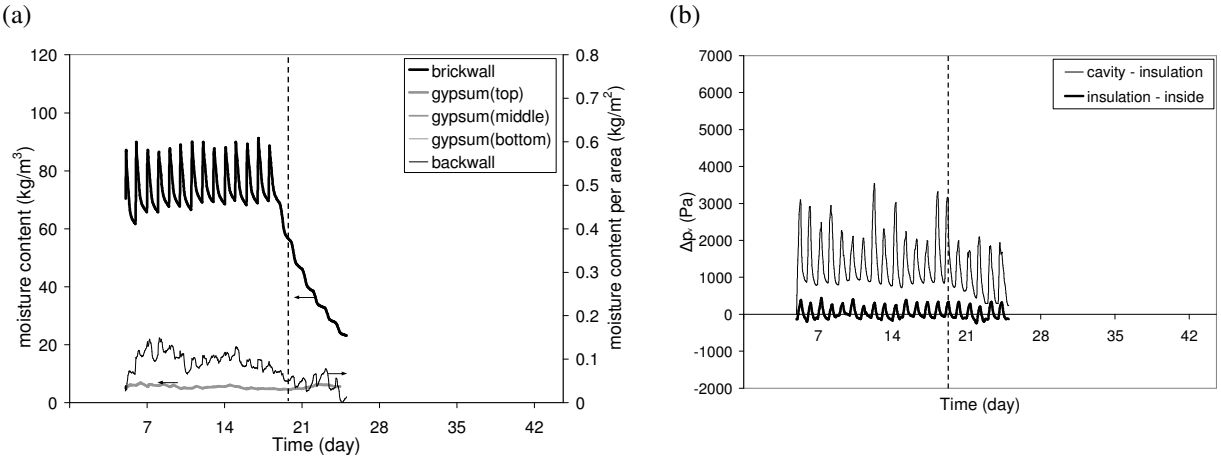

Figure 5 Wall brick veneer with painted gypsum: (a) Moisture content evolution, (b) Vapour pressure differences

3.3.3 Brick wall with XPS sheathing and VWC

Figure 6(a) shows the moisture content of the gypsum gravimetric samples, which increases from the bottom sample to the top sample due to the possible convection loop in the insulation. Looking at the behavior of the back wall, we can see that its moisture content increases rapidly during the 11 days of the wetting phase and even continues to increase during the 10 days of drying phase. In fact, the back wall does not start drying during the test. This increase of the moisture content of the back-wall cannot all be explained by the increase in the moisture content of the gypsum gravimetric samples. It is possible that some moisture, condensed or was transported due to the high vapour pressure gradient into the XPS. Figure 6(b) is incomplete due to the difficulty of monitoring air saturated with moisture. Very high vapour gradients were measured. , after 10 days of drying, the vapour pressure in the cavity starts to be lower than the vapour pressure in the insulation for a few hours daily. The slow drying of the assembly is due to the the presence of the VWC.

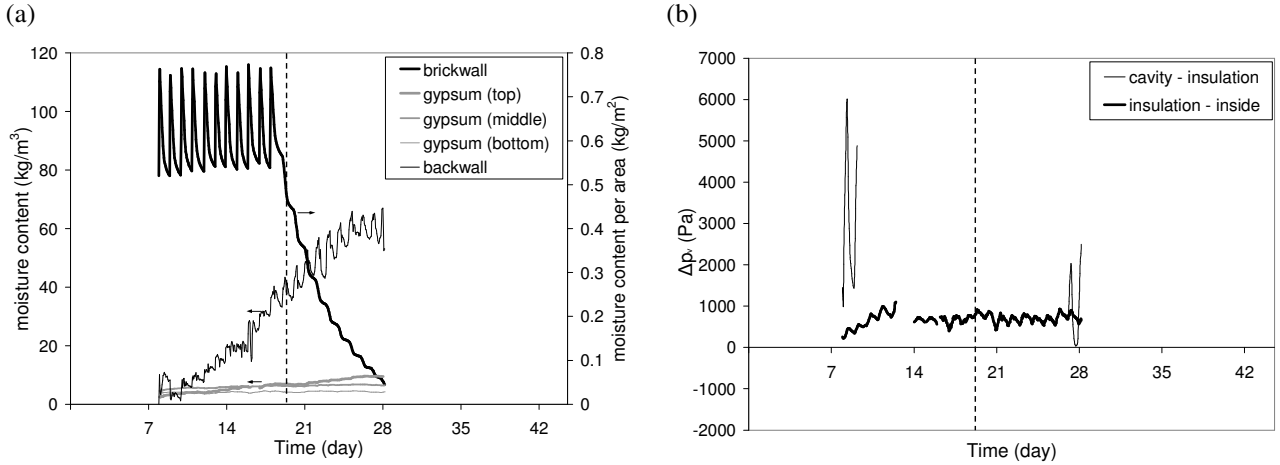

Figure 6 Wall brick veneer with XPS sheathing and VWC (a) Moisture content evolution, (b) Vapour pressure differences.

3.3.4 Comparison

The behaviour of the brick wall is almost identical in the three tests and seems independent of the inner wall components. The bahavior of the gypsum board is quite different in the three tests. Figure 7 shows the moisture content in the gypsum board gravimetric samples for all three tested assemblies. We can see that the gypsum moisture content in the wall with OSB on the exterior and VWC on the interior is the highest moisture content amongst all walls, due to the vapour tight VWC on the interior which does not allow moisture to dry out of the gypsum board. Gypsum board moisture content in the wall 4 with XPS on the exterior and WVC on the interior, drops down significantly comparing to the previous wall. The XPS sheathing reduces the inward moisture flow, resulting in less moisture reaching the gypsum board. Nevertheless, the higher amount of gypsum moisture content in wall with XPS comparing to wall with painted gypsum is due to the presence of the VWC.

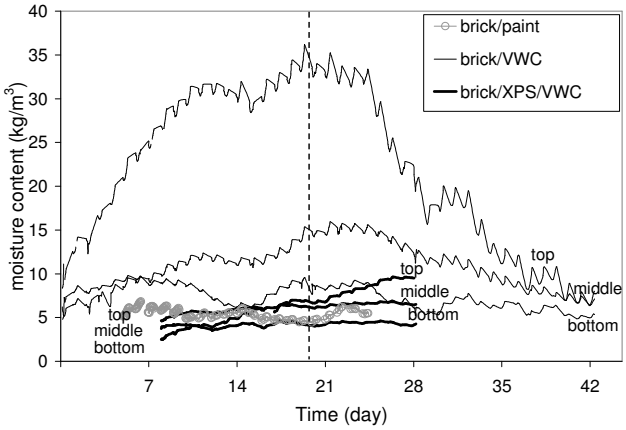

Figure 7 Moisture content of the gypsum board gravimetric samples in the three tests.

4. Discussion

The small scale tests were designed to validate heat and moisture transport simulation models under very controlled loading and boundary conditions: (1) the masonry was initially wetted; (2) during the wetting phase, the specimen were not allowed to dry to the outside, in order to exclude uncertainties in the boundary conditions for the drying of the masonry; (3) controlled constant and cyclic temperature and RH conditions for the outside environment; (4) small specimen size with horizontal cavity in order to exclude possible influence of air transport.

The large scale experiments were designed to include more realistic conditions: (1) story-high vertical non ventilated cavity; (2) repeated wetting by artifical rain and drying by solar radiation; (3) story-high walls including studs, sill plate and top plate (3D effects).

All measurements showed the existence and nature of the vapour flow due to a thermal gradient, and the possible wetting of the back wall materials depending on the moisture transport properties. The wetting of gypsum board was found to be highly sensitive to the vapour permeability of the finishing. However, differences were observed between the small- and large-scale tests: (1) the moisture contents in the large-scale tests were generally lower; (2) the wetting of the wall components was larger at the top of the walls. These differences may be explained by thermal and moisture stack effects and possible air transport in the cavity and insulation in the large scale tests.

The experimental behaviour of the small scale tests was modelled using a heat /moisture simulation model (Deckers 2007). Good agreement was observed between measurement and simulation for constant and cyclic conditions. It was found that due to the important wetting of OSB and WRB, the moisture transport properties of these materials have to be accurately determined at high moisture content for attaining a good agreement.

5. Conclusions

This paper presents experimental results from the small- and large-scale tests of the ASHRAE-1235 project on solar-driven vapour transport in wood frame walls. The objective of the tests is to produce precise measurements on wetting and drying behavior of internal parts of the back wall, when a wetted masonry cladding is loaded under cyclic temperature loading. The walls are constructed according to typical North American construction practices, with vapour open mineral wool as insulation material between the studs.

The small-scale tests show that, due to the temperature gradient, an important vapour flow is generated to the back wall, wetting the OSB, mineral wool and gypsum board. Moisture uptake by the gypsum board covered with the vapour tight vinyl wall covering is much higher than the uptake of moisture by the gypsum board with vapour open paint. A vapour open paint finishing reduces the moisture content of the gypsum board up to a factor of 4 to 6. In the (severe) tests with constant boundary conditions, the moisture content of OSB and gypsum board are too high in all cases producing moisture related problems. In the cyclic loading with vapour open paint, which is the less severe case, the maximum moisture content for gypsum board is still 13 kg/m³ and for OSB 80 kg/m³ which respectively equals to relative humidity of 86% and 90%. The large-scale tests on three specimens consisted in cycles where wetting was repeated daily. The tests result in similar moisture content evolutions of the brick cladding and the gypsum boards as found in the small-scale tests. The large-scale tests highlight the role of VWC in the moisture uptake by the gypsum board. The variant of the XPS sheathing illustrates clearly the high vapour pressure gradient found across the sheathing, resulting in a slow but steady moisture update in the gypsum board.

We showed that, even with vapour open interior finishing and more moderate thermal loading, problems may arise and wall compositions have to be optimized. In further progress of the project, the experimental results, including the presented small-scale and large-scale tests and the field measurements, will be simulated and the simulation models will be validated and used for further analysis under different yearly climatic loading.

Acknowledgements

We would like to acknowledgement the work and involvement of the following M.A.Sc Students: Nele Deckers and Marijke De Meulenaer of the K.U.Leuven, Jason Edelstein of Concordia University. Also, the support and help of Wolfgang Zillig, PhD student and Paul Verbeek and Wim Bertels, technicians, all at KUL was deeply appreciated.

6. References

Carmeliet, J., Karagiozis, A., Derome, D. (2007) “Cyclic temperature gradient driven moisture transport in walls with wetted masonry cladding”, Proceedings of Thermal Performance of the Exterior Envelopes of Whole Buildings X Conference, DOE/ORNL/ASHRAE/BETEC/ABAA, December 2-7, Clearwater Beach, FL, U.S.A., ASHRAE, 9 p.

Deckers, N. (2007) Moisture problems in lightweight structures in warm, humid climates, Master thesis, Laboratory of Building Physics, Katholieke Universiteit Leuven, Leuven, 129 p.

Edelstein, J. (2007) Solar-driven vapor transport in lightweight walls in a hot and humid climate, M.A.Sc. thesis (Building), CBS, DBCE, Concordia University.

Simulation of drying of wood-frame walls submitted to water infiltration

Constance Thivierge, Eng., M.Sc. student,
FPInnovations, Building systems department;
constance.thivierge@qc.forintek.ca

Dominique Derome, Arch., Eng., PhD, Senior Scientist,
Empa, Swiss Federal Labaratories for Materials Testing and Research, Laboratory for Building Technologies, Überlandstrasse 129,CH-8600, Dübendorf

Jan Carmeliet, PhD, Professor,
Chair of Building Physics, Swiss Federal Institute of Technology ETHZ Zürich, ETH-Hönggerberg, CH-8093 Zürich, Empa, Swiss Federal Labaratories for Materials Testing and Research, Laboratory for Building Technologies, Überlandstrasse 129, CH-8600, Dübendorf

KEYWORDS: *wood-frame walls, building envelope, wetting, drying, simulation, laboratory tests.*

SUMMARY:
This paper presents the first steps in validating the hygrothermal simulation of the drying performance of different wood frame wall configurations submitted to water infiltration in the stud cavity. As rain can be the most important potential source of moisture in wall assemblies, an experimental investigation was previously undertaken at Concordia University to compare the wetting and drying potential of 15 different wood-frames walls subjected to water insertion in the stud cavity within a large Environmental Chamber. The moisture distribution in each wall was monitored using moisture content probes and gravimetric measurement and the conditions (exterior and interior) were controlled to reproduce August through November weather conditions for Montreal. The moisture load consisted in a wetted sill plate inserted into the wall assembly.

Simulations are needed to be performed to studying in more details the drying of wood sill and the moisture redistribution and drying in the rest of the wall assembly. As a first step of validation, simulation results of one wall assembly, taking into account proper boundary conditions and appropriate material properties, are compared with the measured results. It is found that initial moisture content distribution, not only moisture content, in the wood sill should be taken into account in the simulation.

1. Introduction

Characterization of the wetting/drying process in wood-framed building envelopes submitted to water penetration is especially relevant where environmental conditions are less forgiving. Examples of major building failures in such types of climate have occurred over the last years, in Vancouver, Seattle, and North Carolina for example (Barrett 1998, Karagiozis and Desjarlais 2003). Combined with environmental conditions, factors like faulty or inappropriate wall design and detailing, and deficient construction can lead to major structural failures, lower performance and health problems of occupants related to the presence of fungi products. The evaluation and characterization of the wetting and drying processes of walls subjected to rain penetration are challenging since the amount of water involved, its location in the envelope, and the time it takes to dry are often not known.

The paper presents the first steps towards validation of simulation to reproduce the behavior of the walls subjected to water infiltration, as documented experimentally in a previous test. Simulations will be needed to to study in more details the drying of wood sill and the moisture redistribution and drying in the rest of the wall assembly. As a first step of validation, simulation results of one wall assembly, taking into account proper boundary conditions and appropriate material properties, are compared with the measured results.

2. Experimental Methodology and Setup

The experimental program to document the performance of wall assemblies under specific climatic loadings including rain infiltration has been reported in Derome et al (2007) and Desmarais et al (2007), and more information on the development of the test procedure is found in Teasdale-St-Hilaire and Derome (2006). The main objective of this test was to document the behavior of different wall systems in which the bottom plate had been wetted due to rain infiltration.

The wall systems components and the environmental conditions were based on Montreal's common construction practices and weather. The wetting load consisted in the insertion of a wetted bottom plate insert at the bottom of each wall at the beginning of each of the four imposed sets of climatic conditions, representing the months of August to November.

2.1 Description of specimens

The construction of the wall specimens was typical of the residential wood-frame construction found in the Montreal region. A set of 15 wall systems was studied to cover all possible combinations. Their composition consisted from outside in:

- Exterior cladding (stucco on building paper or wood cladding on furring and spun bonded polyolefin)
- Sheathing (oriented-strand board (OSB), plywood or fiberboard)
- 2x6 inches wood studs with glass fiber insulation
- Gypsum board (with polyethylene sheet or low-permeance paint)

The wall specimens were installed in a test hut built within an Environmental Chamber where the indoor and outdoor air temperature and relative humidity were controlled.

2.2 Loading conditions

Initially, the inside conditions of the environmental chamber and the inside space of the test hut were set at 21ºC and 60% for some homogenization of the moisture content of the wood and wood-based components for a period of 3 weeks before the start of the test.

The outdoor conditions of the test were determined using selected moisture conditions of a 10% worst year from a 30-year Montreal weather data (methodology presented in Candanedo *et al* 2006) and average Montreal weather data (Teasdale St-Hilaire 2006). For November, the air temperature and relative humidity were kept constant at 2°C and 80%. The conditions are shown in Table 1.

TABLE 1: Exterior Conditions

	$T_{min\ mean}$ [°C]	T_{mean} [°C]	$T_{max\ mean}$ [°C]	$RH_{mean\ at\ 6am}$ [%]	RH_{mean} [%]	$RH_{mean\ at\ 3pm}$ [%]
August	14.7	19.7	24.7	86	75	58
September	8.6	13.6	18.6	87	77	62
October	2	7	12	84	72	62
November	2	2	2	80	80	80

The typical interior conditions values (temperature and RH) for the months of August through November were set as 21°C for the temperature (without variation) and 50% for the relative humidity. These conditions were set within the test hut while the exterior conditions were reproduced in the environmental chamber.

2.3 Wetting load – Wetted bottom plate insert

During the 4 month-period of testing, a wetted bottom plate inserted at the bottom of each wall was replaced four times, i.e. each time the climatic conditions were changed. The bottom plate inserts were cut from longer pieces of lumber that had been immersed in water for 4 weeks. Each piece of lumber was sealed with paraffin wax on 3 sides: both ends and one wide surface (the surface to be seated in the wall).

2.4 Monitoring procedure

The monitoring protocol combined electronic and gravimetric measurements. Thermocouples , relative humidity sensors , moisture content probes , and gravimetric samples (referred to SH) were located on the sheathing and in the studs. The electronic and gravimetric monitoring grids were symmetrical along the central axis of each specimen to provide equivalent locations in the specimens for both types of readings. The gravimetric samples were located within the wall cavity on the inside face of the exterior sheathing. Data were acquired on a regular basis during the duration of testing and provided reliable measurements that were used to establish moisture variation and distribution in relation with the different climatic conditions imposed.

Electronic monitoring

In terms of electronic equipment, the following sensors were installed in each wall specimen: 12 moisture content probes, 16 Type T thermocouples, and 2 relative humidity sensors. All the sensors and controls were linked to a Data Acquisition Systems (DAS). Readings were taken automatically every 10 minutes for the complete duration of the test. Calibration of the thermocouples was done through a thermistor reading and verification with a steady-state homogeneous chamber temperature. Calibration of relative humidity sensors at the end of test was done using a dew-point hygrometer at two relative humidities. Calibration of the moisture content probe readings was done using sorption data for each wood-based material being monitored.

Gravimetric monitoring

The gravimetric analysis involved the regular weighing of sheathing and bottom plate insert samples during the test and their drying at the end of the test to determine their exact moisture content. Eighteen gravimetric sheathing samples (eleven of 2.8 cm and seven of 4.1 cm in diameter) were used in each wall. The wetted bottom plate inserts were monitored using the methodology described below. Figure 1 illustrates the gravimetric monitoring. For the whole duration of the test, all gravimetric measurements for the sheathing and wetted inserts were made weekly (on the same day), including on the first day of each climatic period, for a total of four times per climatic period.

For the bottom plate inserts, a 1 cm thick piece was cut from one end. The cut face was waxed and the bottom plate insert put back into the wall with a dummy to replace the lost volume. The 1 cm portion was then used to determine the moisture content distribution across the bottom plate by cutting slices with a microtome.

FIG. 1: Example of sill plate and sheathing gravimetry samples.

3. Modelling and Simulation

The simulations of the hygrothermal behaviour of the tested walls is required for a more detailed study of the moisture content distribution with the different walls, the role of boundary conditions and material properties and

also to extent the study to a full year of conditions (as the test was limited to 4 months). This paper presents initial steps in validation. For simulation, a heat, air and moisture transport model developed with the finite element method was used. Boundary conditions based on the experimental program and appropriate material properties were used.

The basic equations of the model are as follow for moisture transport (liquid and vapour):

$$\frac{\partial w}{\partial p_c}\frac{\partial p_c}{\partial t} = -\nabla^T (g_{m,l} + g_{m,v}) \quad (1)$$

$$g_{m,l} = -K_l \nabla p_c \quad (2)$$

$$g_{m,v} = -\frac{\delta_v p_v}{\rho_l R T}\nabla p_c - \frac{\delta_v p_v}{\rho_l R T^2}(\rho_l L_v + p_c(T\gamma - 1))\nabla T \quad (3)$$

And for heat transport :

$$(c_0\rho_0 + c_l w)\frac{\partial T}{\partial t} + \left(c_l T \frac{\partial w}{\partial p_c}\right)\frac{\partial p_c}{\partial t} = -\nabla^T (g_{h,c} + g_{h,a}) \quad (4)$$

$$g_{h,c} = -\lambda \nabla T \quad (5)$$

$$g_{h,m} = (c_l T) g_l + (c_v T + L_v) g_v \quad (6)$$

With the following nomenclature:

c : specific heat (J/kg·K)
K : permeability (s) (based on a capillary pressure gradient)
δ: permeability (s) (based of a vapour pressure gradient)
g : flux (kg/m^2·s ou W/m^2)
L: heat of evaporation (J/kg)
p_c : capillary pressure (Pa)
p_v : vapour pressure (Pa)
R : gaz constant
w : moisture content (kg/m^3)
T : temperature (K)
t : time (s)
ρ : density (kg/m^3)
λ : heat conductivity (W/m·K)

In this first step of validation, one wall was used for simulation. The wall is referred to as OSB/wood (wall 23) and consists of a wood cladding, an OSB sheathing, 2 by 6 inches wood studs filled with fibreglass insulation and a painted gypsum. The original sample was 600 mm wide by 2 400 mm high. The simulation is done in two dimensions, with the domain representing a vertical section through the wall assembly. Figure 2a represents the vertical section and the different components.

Figure 2b displays the mesh grid of 502 cells grouped in the 12 zones shown on Figures 2a. The material properties are attributed to each zone as well as the initial capillary pressure and temperature. A Matlab application was developed to produce the input data in terms of connectivity matrix and material properties and initial conditions assignments. Several material properties were taken from Kumaran M. K. and al. (2002). The initial moisture content was taken from sorption curves at equilibrium with 60% for all materials except the wood sill plate. The moisture content of the sill plate, after 30 days of wetting, was 52%MC. This was implemented uniformly as the initial moisture content of the sill plate for the simulation.

The results of the period of November were selected for the first of validation of the model. Thus, for the boundary conditions, the exterior conditions were constant with outside temperature of 2°C and relative humidity of 75%, left of the wall as depicted on Figure 2. The interior conditions were set at 21°C and 50% RH. The top and bottom boundaries were adiabatic.

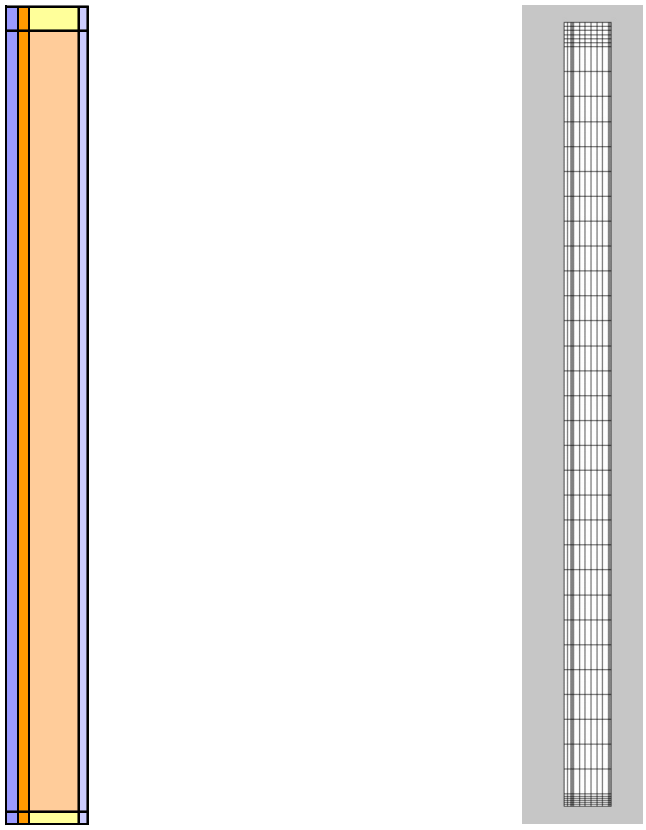

(a) (b)

FIG. 2a. Geometry of the zones of the vertical section of the wall assemblies and, b. Calculation grid.

4. Results

The steps of validation of the simulation consisited in verifying, (a) the drying of the inserted wetted plate versus time and (b) the moisture content distribution over the sheathing area.

Figure 3 compares the experimental and simulation results in terms of moisture content in the sill plate for the month of test. As mentioned above, during the experiment, the sill plate was shortened once a week, and this sample was then sliced with a microtome to establish the moisture gradient across the plate. The dots of Figure 3 represent the experimental moisture content at 6mm from the top surface of the plate. The line represents the simulation results at the same location. The rate of drying of the exeperimental and simulation data is similar, althought the simulation data do not capture the apparent plateau in drying. The simulation started with a uniform moisture content in the sill plate. However, the sill plate after being submerged for four weeks demonstrated a gradient of moisture content from the start of the test. The surface of the inserted plate was actually wet when it was inserted in the wall cavity and this state was not reflected in the initial conditions used for the zone of the bottom plate. Therefore, this moisture gradient will be implemented in the next phase of the work.

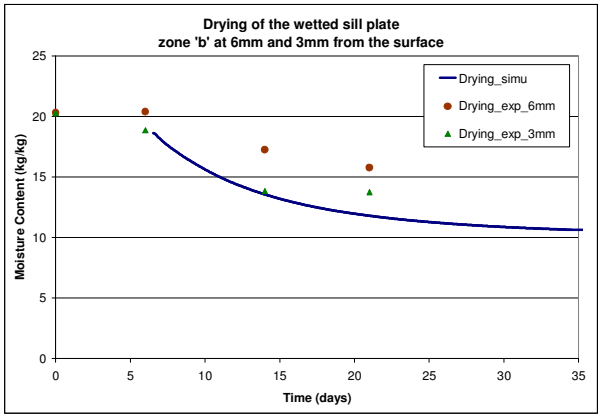

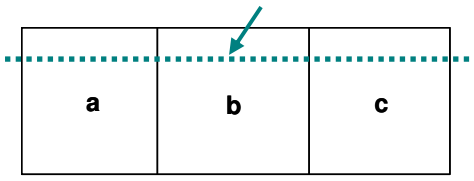

Location of the compared results

FIG. 3: Drying curves obtained from experimental gravimetry and simulation for the inserted wetted plate of wall 23 in section 'b' at 3 and 6 mm from the surface (blue line level).

Next, the simulations versus experimental results for the moisture distribution on the surface of the sheathing were compared. In the test, there were 18 gravimetry samples, located at different levels, on the exterior sheathing for all 15 wall assemblies evaluated. Four (4) of those 18 samples were selected as references to evaluate the accuracy of the moisture content distribution values obtained from simulation for a 30 days period, i.e. SH5, 7, 17 and 18. The gravimetry samples were located at the bottom of the wall (as shown in Figure 4) next to the inserted plate. Given the vapour pressure difference across the assembly, and the low permeability of OSB, a general moisture uptake of the OSB is expected. In addition, the redistribution of the moisture from the sill plate may influence more at the bottom of the wall. Figure 4 presents the experimental results at four locations (encircled at bottom of wall) in solid lines and the simulation results at the same two heights in dash lines. The rate of moisture uptake during the two first weeks is similar for the test and simulation results. However the decrease in rate of moisture uptake noticeable from the second half of the test is not captured by the simulation. The fact that the model is not considering the air gap between the cladding and the sheathing, which acts as a venting space in real life, is reflected in the linearity of the simulated values. The experimental moisture values tend to decrease slightly after the third week of experiment due to the fact that there is some moisture evaporation in the system. The presence of the air gap at the exterior surface of the sheathing has certainly an influence on the behaviour of the system. More simulation work will be to reflect this phenomenon.

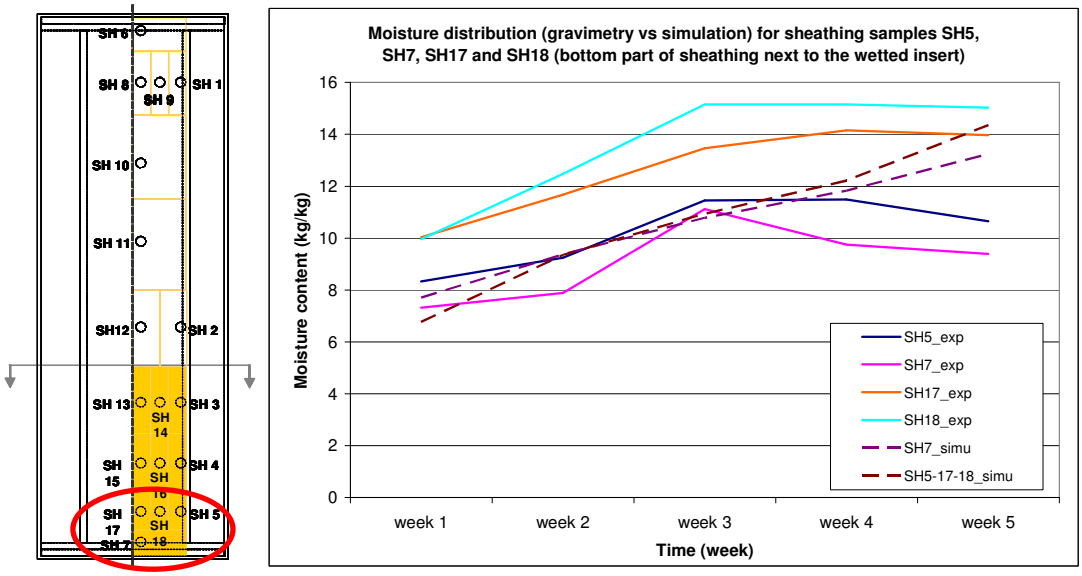

FIG. 4: Gravimetry and simulation comparison for moisture distribution on the sheathing.

Finally, the moisture content distribution versus time in the whole assembly is considered. Figure 5 shows the experimental moisture distribution observed on the inside surface of the sheathing at the end of the November phase and provide, for comparison, the calculated moisture saturation in the assembly at the time steps 0 (day 1) and 30 (after 30 days). The main difference between step 0 and 30 is the moisture intake observe in the cavity of the wall. Step 30 presents a lighter blue inside the cavity and on the sheathing surface. These observations were expected since the experimental program (Figure 5 (a)) presented the same trends.

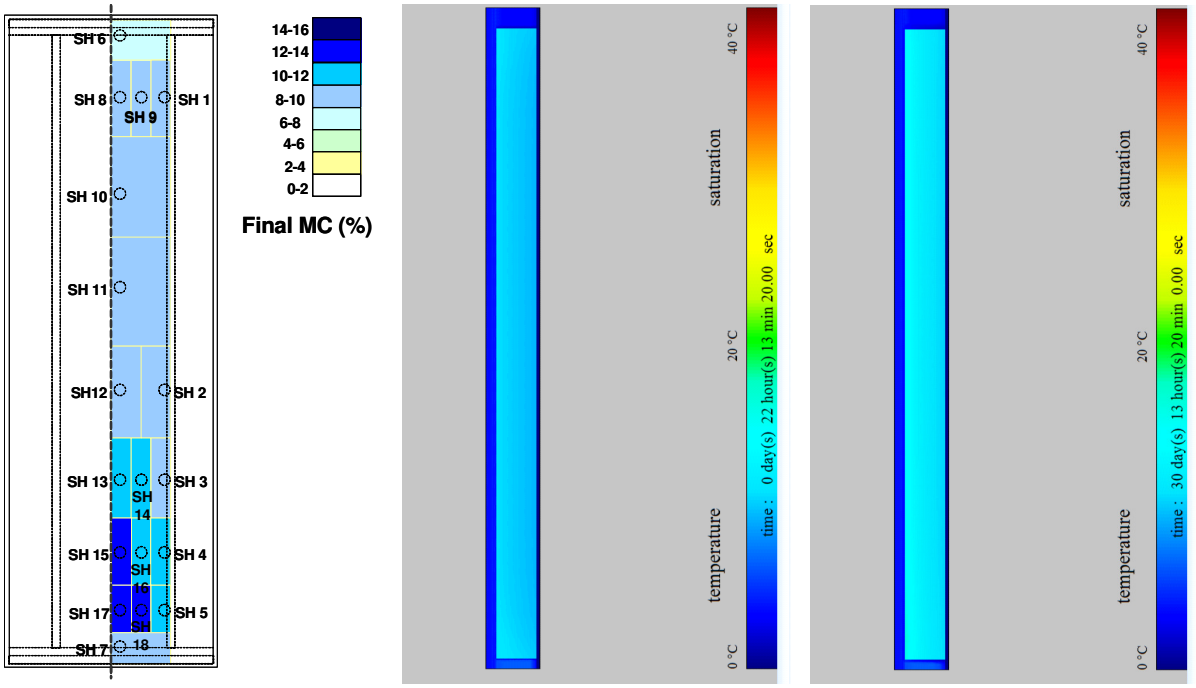

(a) (b) (c)

FIG. 5: Gravimetry results at end of test(a) and simulation results at start (b) and end(c) for moisture content on the sheathing for wall 23 (OSB/wood).

5. Conclusions

This paper presents the first steps in validating the hygrothermal simulation of the drying performance of different wood frame wall configurations submitted to water infiltration in the stud cavity. The results from an experimental investigation to compare the wetting and drying potential of 15 different wood-frames walls subjected to water insertion in the stud cavity were used. The moisture distribution in each wall was monitored using moisture content probes and gravimetric measurement and the boundary conditions were in an environmental chamber. The moisture load consisted in a wetted sill plate inserted into the wall assembly.

As simulations are needed to be performed to study the drying of the wood sill and the moisture redistribution and drying in the rest of the wall assembly, this paper presented the first steps towards validation of the simulation. At this point of the study, simulation results are showing good correlation in terms of (a) rate of drying of the inserted wetted plate and (b) rate of moisture uptake in the sheathing. It was found that initial moisture content distribution, not only moisture content, in the wood sill should be taken into account in the simulation. The next step will then be to refine the initial conditions to reflect the moisture gradient present in the bottom sill plate and to validate the impact of the different materials in relation with the trends that were observe through the analysis of experimental program results.

6. Acknowledgements

The model tool used for the simulation is HAMFEM as described in Janssen H., Blocken B., and Carmeliet J. Conservative modelling of the moisture and heat transfert in building components under atmospheric excitation, *International journal of heat and mass transfer*, 50 (2007) 1128-1140.

7. References

Barrett, D. 1998. The renewal of trust in residential construction. Commission of enquiry into the quality of condominium construction in British Columbia. Report submitted to the Lieutenant Governor in Council of the Government of British Columbia. June. http://www.qp.gov.bc.ca/condo/ Website accessed December 20, 2003.

Candanedo, L., Derome, D., Ge, H., Fazio, P. (2006) "Analysis of Montreal 30-year weather data to select loading conditions for large-scale tests on wall panel systems", Proceedings of Third International Building Physics Conference, Research in Building Physics and Building Engineering, Concordia University, Montreal, Canada, Aug. 27-31, Taylor & Francis/Balkema, pp. 959-966.

Carmeliet, J., Karagiozis, A., Derome, D. (2007) "Cyclic temperature gradient driven moisture transport in walls with wetted masonry cladding", Proceedings of Thermal Performance of the Exterior Envelopes of Whole Buildings X Conference, DOE/ORNL/ASHRAE/BETEC/ABAA, December 2-7, Clearwater Beach, FL, U.S.A., ASHRAE, 9 p.

Derome, D., Desmarais, G., Thivierge, C. (2007) "Large-scale experimental investigation of wood-frame walls exposed to simulated rain penetration in a cold climate", Proceedings of Thermal Performance of the Exterior Envelopes of Whole Buildings X Conference, DOE/ORNL/ASHRAE/BETEC/ABAA, December 2-7, Clearwater Beach, FL, U.S.A., ASHRAE, 9 p.

Desmarais, G., Thivierge, C. Derome, D. (2007) "Water distribution patterns in cladded walls subjected to rain penetration", Proceedings of the 11th Canadian Conference on Building Science and Technology, NBEC Canada, Banff, Alberta, March 21-23, pp. 31-41.

Karagiozis, A. and Desjarlais, A. 2003. What influences the hygrothermal performance of stucco walls in Seattle. 9th Conference on Building Science and Technology, Vancouver, B.C. February 27-28, pp. 32-44.

Kumaran M. K. and al. (2002). A thermal and moisture transport property database for common building and insulating materials, Final report from ASHRAE research project 1018-RP.

Teasdale-St-Hilaire, A. and Derome, D. (2006) "Methodology and application of simulated wind-driven rain infiltration in building envelope experimental testing", ASHRAE Transactions, ASHRAE, Atlanta, Vol. 112, Issue 2, pp. 656-670, 15 p.

Zillig, W., Derome, D., Carmeliet, J., Diepens, J. (2007) "Mesoscopic modelling of vapour transport inwood in tangential an radial direction", Proceedings of Thermal Performance of the Exterior Envelopes of Whole Buildings X Conference, DOE/ORNL/ASHRAE/BETEC/ ABAA, December 2-7, Clearwater Beach, FL, U.S.A., ASHRAE, 7 p.

Determining moisture evacuation profiles and drying capacity of building envelope panels of various configurations

Arslan Alturkistani, Ph.D.,
Building Envelope Performance laboratory, Centre for Building Studies, Department of Building Civil and Environmental Engineering, Concordia University;
arslanza@hotmail.com

Paul Fazio, Professor,
Building Envelope Performance laboratory (BEPL), Centre for Building Studies (CBS), Department of Building Civil and Environmental Engineering (BCEE), Concordia University;
fazio@alcor.concordia.ca http://www.bcee.concordia.ca/index.php/Dr._P._Fazio

Jiwu Rao, Researcher,
BEPL, CBS, BCEE, Concordia University;
raojw@alcor.concordia.ca

KEYWORDS: *Building envelope performance, full-scale lab testing, evacuation profile, drying capacity.*

SUMMARY:

In site situations where rain water penetrates into the stud cavity of the building envelope and concentrates at the bottom, the wet bottom plate becomes a moisture loading source. This moisture evaporates creating a vapor pressure profile that decreases with height and causes a corresponding absorption-evacuation mass profile through the sheathing. Such profiles were observed during an experiment designed to develop a test method to compare the relative performance of different wall configurations. In this experiment 31 wall assemblies were subjected to steady-state climatic loadings and uniform moisture loading consisting of water trays on load cells at the bottom plate within the stud cavities of the wall assemblies. In this paper, a new method is used to develop evacuation profiles due to evaporation of moisture sources in stud cavities of building envelope panels of various configurations. This method takes into account the vapor-pressure-vs.-height and vapor-mass-vs.-height profiles.

1. Introduction

Rain penetration into the stud cavity has caused costly damage to building envelope systems; to limit this damage several studies have been undertaken, e.g. Barrett (1998), Beaulieu et al. (2002), Brown et al. (2003) and Lang et al. (1999). Field surveys have shown that the ingress of rainwater into the building envelope occurs primarily at the interface details between different components, such as window-wall details, deck perimeters, balconies and walkways (Ricketts and Lovatt, 1996). Irrespective of how the rainwater penetrates the building envelope, leaks follow unpredictable routes and generally concentrate at the bottom plate. The resulting situation is a wet envelope that needs to dry out. The envelope that will dry faster will risk less damage. The research presented in this paper was undertaken to investigate the relative capacity of different wall systems to evacuate moisture in the stud cavity with the aim of improving building envelope design.

Researchers have adopted different methodologies to experimentally study the wetting and drying of building envelopes. In some experiments, water was introduced into the building envelope to mimic site situations and at the same time expect uniform distribution of moisture. This objective has remained elusive, since there is no typical established site situation that researchers can mimic or a standard method of investigation.

In experimental studies, water intrusion and subsequent drying are usually investigated separately. The intrusion processes are evaluated with test setups based on or derived from the rain penetration test of ASTM E331 (ASTM, 2000). For example, water was introduced between the siding and building paper to observe the extent of lateral migration of water behind the sidings (Tsongas et al. 1998). From experimental results, qualitative or quantitative relations may be obtained to relate the amount of rain water with envelope and (simulated) weather parameters, such as, defect characteristics, rain intensity, and wind parameters. In these experiments, water is applied to the envelope to simulate intruding water. The amount of water is calculated or estimated from the

qualitative or quantitative relations and the target set for the experiments concerning envelope (defects) and weather parameters.

Several water injection methods have been employed by existing studies. Water was introduced into the stud space at the top center interior face of the sheathing to represent water leakage from a window defect located in the windowsill (Teasdale-St-Hilaire et al. 2003). Controlled amounts of water were inserted through a series of point sources on a horizontal line at the top of the stud cavity, by using a clear vinyl tube with holes drilled at equal intervals (Lang et al. 1999). Other injection approaches aimed at having a more even distribution of moisture content in the wall components. For example, in the wetting system of Schumacher et al. (2003), two layers of thick, highly adsorptive papers were stapled to the sheathing and water was introduced onto the sheathing through a thin plastic tube sandwiched between the paper layers.

Immersion is another wetting method and aims to establish uniform distribution of moisture content in component(s) (Hazleden & Morris 2001; Maref et al. 2004). A portion of the wall was immersed in water to achieve specific levels of moisture content in the components before the wall panels were completed and tested. The complete outer face of the sheathing was immersed in a large water tank, and then stabilized to ensure that the MC throughout the sheathing component reached equilibrium in Maref et al. (2004).

The experiment reported in this paper is based on the premise that water penetrating into the stud cavity will run off the different components and finally concentrate at the bottom of the cavity. In this process, while some of the water leaks out of the building envelope, much remains in or on the bottom plate turning this plate into a significant moisture source to be dried out. The drying process contributes to moisture absorption in the surrounding materials especially the sheathing (Fazio et al. 2006). An important component of this drying process involves first the evaporation of the water, followed by absorption of the water vapor by the various components of the building envelope, and finally evacuation of the moisture to the exterior of the stud cavity.

This new experimental method was designed (Fazio et al. 2007) to develop an alternative methodology for evaluating and comparing the drying capacities of different building envelope systems. In a previous publication of this investigation (Alturkistani et al. 2008), the drying capacities of different building configurations were estimated by a mapping calculation method using moisture content readings obtained from gravimetric samples. This method yields the drying capacity for a wall configuration based on the relation between the source (evaporation) and the vapor diffusing out of the stud cavity (evacuation) for the whole assembly. In this paper the concept of envelope permeance is proposed to describe and quantify the inherent drying potential of the wall configuration in which leakage is controlled.

2. In-cavity evaporation experiment

Thirty-one full-size wall assemblies with different wall configurations were subjected to the same moisture loading conditions and to the same steady-state climatic conditions for extended periods of time in order to evaluate and compare the performance of the different configurations. Uniform moisture loading in the wall assemblies was provided by placing a water tray on a load cell at the bottom of the stud cavity of each wall assembly (Fig. 1). This method is intended to measure the response of the different wall configurations in the process of drying moisture from a source at the bottom plate in the stud cavity. The amounts of water evaporation from the trays were monitored during testing, along with extensive measurements of temperatures,

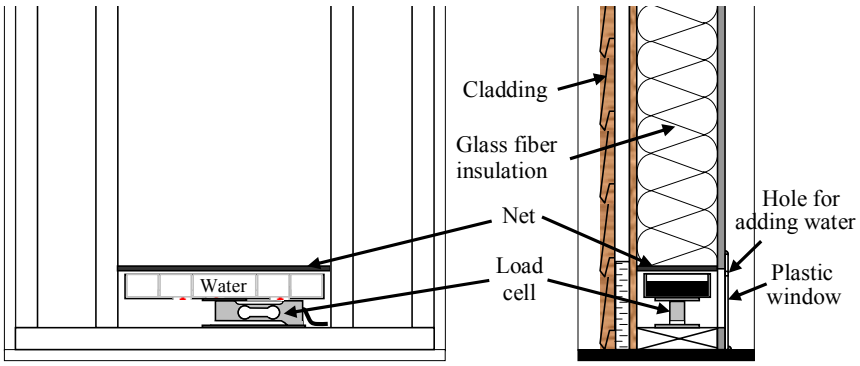

FIG. 1: Moisture source in the stud cavity provided by a water tray on a load cell

relative humidity, and moisture contents by resistive electronic meters and gravimetric samples (Fazio et al., 2006a, 2006b).

Steady-state climatic loading conditions are often used in experimental studies (Maref et al. 2004; Ojanen et al. 2002) to better understand the effect of other parameters; understanding the behavior of systems under static loads before moving to dynamic loads is a common practice in engineering investigations. In this paper, data for test period 2 were used for analysis. Test period 2 lasted for 16 weeks with exterior temperature of 8 ºC, relative humidity of 76% and 2/3 water tray filled; for the interior conditions, the temperature was set at 21ºC and the relative humidity at 35%. Weather data of October was used to determine the outdoor test conditions, since the month of October provides the worst conditions for drying potential; and the year 1977 was selected as the reference year, since October of that year was the 10% worst year during 31 years between 1972 - 2002 in terms of drying potential (Candanedo et al. 2006).

2.1.Evaporation, evacuation and drying capacity

Drying capacity is related to the capacity of a building envelope to evacuate moisture out of the stud cavity and it can serve as an indicator to compare the performance of different envelope system configurations. The envelope system with a greater drying capacity is less likely to undergo moisture damage (Fazio et al. 2007). In this test setup, the water evaporated from the water tray (evaporation) equals the sum of the moisture absorbed by different materials surrounding the stud cavity and the water vapor leaving the stud cavity to either the indoor or outdoor environment that is the "evacuation". Therefore, the drying capacity is defined as the ratio of the evacuation to the total evaporation. It captures the capacity of an envelope to remove internal moisture and, therefore, it can indicate the drying capacity of this envelope (Alturkistani et al. 2008).

2.2.Vapor pressure profiles

Vapor pressures were calculated based on the relative humidity and temperature values measured by two RH sensors at 406mm and 1,829mm from the bottom in the stud cavity of each wall assembly. The vapor pressures were mainly the result of the evaporation from the moisture loading source at the bottom of the cavity.

To obtain the vapor pressure profile in respect to height, a third location is taken at just above the water level of the water tray at a height of 114mm from the base of the assembly. At this point, it is assumed that a near saturation condition of 98% relative humidity is sustained. The fitting curves for the relative humidity profiles inside the stud cavities vs. heights were plotted for the wall assemblies with vapor barriers. Accordingly, the fitting curves for the vapor pressure difference between the stud cavity and outdoor vs. height were then plotted for the wall assemblies with vapor barriers. Figure 2 shows the vapor pressure difference profile for wall

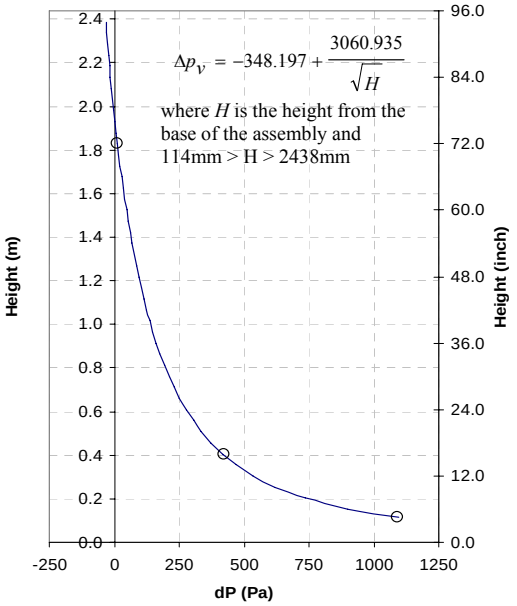

FIG. 2: Vapor pressure difference profile for wall assembly 6 (OSB, stucco, and vapor barrier)

assembly 6 (OSB sheathing, stucco cladding, and vapor barrier). The moisture loading source at the bottom of the cavity creates a nonlinear vapor-pressure difference profile with maximum value at the bottom of the cavity and minimum value at the top of the cavity.

3. Vapor evacuation

Permeance of building envelope layers is used to describe the rates of vapor diffusions under the vapor pressure differential between the two sides. When the envelope permeance, M (ng/Pa·s·m²) is known over a given period of time, θ (s), and under a constant vapor pressure differential, the mass of vapor transport, W (ng), can be calculated from the Fick's law of diffusion:

$$W = M \cdot A \cdot \theta \cdot (p_1 - p_2) \qquad (1)$$

where p_1 and p_2 are the vapor pressures on the two sides of the layer(s) (Pa). In this equation the vapor pressures are typically assumed to be constant in the planes perpendicular to the wall depth. Thus, the vapor pressures at the bottom and top of the stud cavity (along the plane coincident to the inner sheathing surface) are considered to be the same; i.e., the permeance is the same per unit area of the panel.

This condition was found not to be true in the investigation reported in this paper, where the moisture source was located at the bottom plate in the stud cavity. This moisture source gave rise to nonlinear RH and vapor pressure profiles, which varied from a maximum value at the bottom of the cavity to a minimum at the top of the cavity. Since permeance varies with RH, the permeance of the sheathing can be expected to vary in accordance with the RH and vapor pressure profiles. These variables need to be incorporated in the calculation of the amount of water diffusing (evacuation) through the outer layers of the assembly to the outdoor, including the sheathing, weather barrier, and cladding. The vapor diffusion through the drywall side of the stud cavity is assumed to be negligible for wall assemblies having vapor barriers. This calculation method is referred to herein as the Calculated Evacuation Method (CEM).

4. Moisture content and permeance

In the CEM the evacuation of vapor through the outer layers depends mainly on the vapor pressure difference and on the permeance, which in turn varies with moisture content. The moisture content of the materials in the wall assemblies were monitored by gravimetric samples that are cut outs from the sheathing and stud materials. There are 25 gravimetric samples in each wall assembly: 7 samples in the wood studs (5 in the vertical stud, 1 in the top plate and 1 in the bottom plate) and 18 samples in the sheathing material. This moisture content changes with height (Figure 3) and depends on the vapor pressure difference between the inside of the stud cavity and the outdoor.

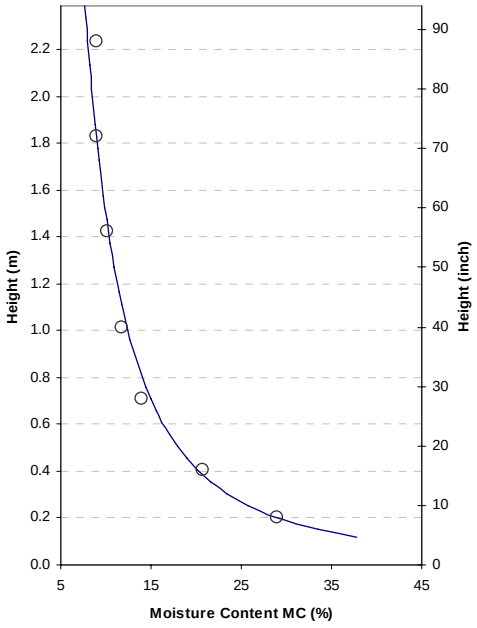

FIG. 3: Moisture content vs. height profile for wall assembly 6 (OSB, stucco, and vapor barrier) for period 2

5. Evacuation zones

The sheathing was divided into four zones of different sizes along the height (Figure 4). The calculated evacuated vapor mass for each zone, W_{di} (g), is obtained by rewriting Eqn. 1 as follows:

$$W_{di} = M_{pi} \cdot A_i \cdot \theta \cdot \Delta p_{ci} \qquad (2)$$

where

W_{di} = mass of the evacuated moisture passing through the outer layers in a specific zone, ng
M_{pi} = permeance of outer layers for a zone from material properties, ng/Pa·s·m²
Ai = zone area, m²
θ = time, s
Δp_{ci} = vapor pressure difference between the vapor pressure in the stud cavity as a function of height corresponding to the zone and the outdoor vapor pressure, Pa, and,

i = 1 to 4 zones.

Since the vapor pressure difference across a zone, Δp_{ci}, for Eq. 2 changes with height, as illustrated in the example of Figure 2, the average Δp_{ci} for the zone is calculated by integrating the vapor pressure difference over that zone.

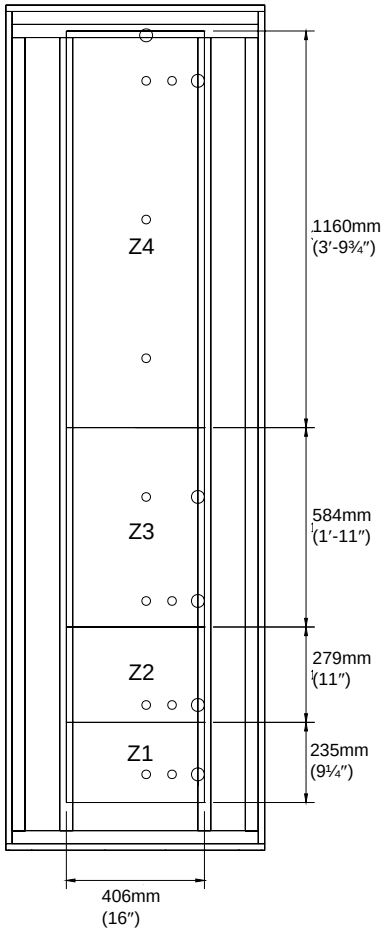

FIG. 4: Sheathing permeance zones and locations of gravimetric samples

6. Results and discussion

Of the 31 assemblies under testing, there were 12 duplicates. The two wall assemblies of each duplicate had the same configurations and were placed on the same relative location of the test rooms, one on the first floor and the other the second. Therefore, these two duplicate assemblies are expected to have the same or similar performance. Table 1 shows the total evacuated vapor mass during period 2 for different wall assemblies having vapor barriers using the CEM. The results are arranged to facilitate the comparisons between duplicate assemblies, in two adjacent rows with the same text shading. The difference in the evacuation values for the duplicate assemblies is attributed to the small variance in the evaporation rates experienced in the test, but, since the drying capacity is the real performance measure that takes into account both, the evaporation and evacuation, the drying capacity percentages is to be examined.

Table 1 also shows the drying capacities of the different configurations. Except for wall assemblies 9 and 21 (fiberboard, vapor barrier and wood siding) that were a special case, it can be observed that duplicate assemblies have the same moisture drying capacity to the exterior, within 10 % margin in one case and 7 % in another case and less than 3 % in the other three cases. These margins can be attributed to experimental errors as well as on the different initial moisture content of the different materials. The bar chart in Figure 5 shows graphically the relative drying performance of the different wall configurations, good agreements between duplicate wall assemblies are observed.

Since there is an air cavity behind the wood siding, the evacuation values for the wall assemblies cladded with wood siding represent the vapor mass that passes through the sheathing and weather resistive membrane and thus dry out by the air circulation in the cavity. As for the wall assemblies cladded with stucco, since there is no air cavity between the sheathing and the cladding, the evacuating vapor mass has to pass through the cladding in addition to the sheathing and the weather resistive membrane. Therefore, the drying capacities for the wall assemblies configured with stucco cladding were much lower than the wood siding assemblies and this is attributed to the vapor absorption in the stucco.

For wall assemblies (9 & 21) with fiberboard, vapor barrier, and wood siding, the evacuation values calculated by the CEM were relatively high, showing drying capacity percentages exceeding 100%. These high values indicate that the evacuation capacity of these wall assemblies is higher than the evaporation amount generated in the cavity, unlike the other wall assemblies where the evaporation amount has exceeded the capacity. This high evacuation capacity for wall assemblies 9 and 21 is attributed to the relatively high water vapor permeability properties of the fiberboard compared to OSB and plywood.

It should be noted that these evacuation values are highly sensitive to the permeability property data used. In the calculations undertaken for the sheathing materials, the permeability values were taken from the material property database generated by Wu et al. (2007) for the materials used in this study. As for the other materials, the permeability values were taken from Kumaran (2002).

TABLE 1: Total evacuated vapor mass by the Calculation Evacuation Method (CEM) and drying capacity for different wall configurations

Assembly #	Configuration (all with VB)	Evacuation Capacity W (g)	Evaporation (g)	Drying capacity %
5	OSB-wood siding-vb	322	640	50
17		255	593	43
6	OSB-stucco-vb	104	783	13
18		69	542	13
7	plywood-wood siding-vb	505	624	81
19		458	642	71
8	plywood-stucco-vb	154	982	16
20		94	603	16
9	fiberboard-wood siding-vb	1206	1022	118
21		1096	849	129
10	fiberboard-stucco-vb	146	829	18
22		118	759	16

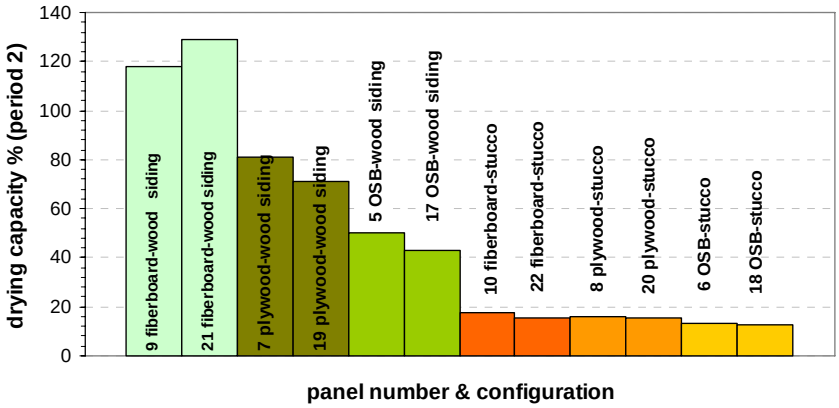

FIG. 5: drying capacities for the duplicate wall assemblies.

7. Conclusions

The water tray method served as in-cavity moisture loading for a large scale test carried out in an environmental chamber to study the relative drying capacity of 31 wall panels using water trays to provide moisture load at the bottom plate. This method generated an effective experimental scenario to evaluate the relative drying performance of building envelope systems of different configurations.

When water penetrates the outer layers and enters the stud cavity of a building envelope system, it runs down and concentrates at the bottom plate. Eventually it evaporates and creates a vapor pressure profile in the stud cavity that decreases nonlinearly with the height, with a maximum value at the bottom plate and a minimum value at the top plate. Since diffusion is driven by the vapor pressure difference, the evacuation of the water vapor through the sheathing is also nonlinear.

The Calculation Evacuation Method (CEM) is introduced to calculate the evacuation through the outer layers of the building envelope including the sheathing, weather barrier, and cladding. The CEM takes into account the nonlinear profile with height of the absorbed vapor mass as well as the vapor pressure profile, and yields a nonlinear evacuation moisture flow profile with maximum value at the base and minimum value at the top of the panel. The relative drying capacities for the different configurations were determined based on the relative quantities of "evacuation" diffusing out of the sheathing to the total measured evaporation from the water source inside the cavity. Similarities in the drying capacity percentages of six pairs of duplicated wall panels show that the water tray test method can provide reasonably repeatable results to warrant further study and use.

Acknowledgement

This study was funded by the Natural Sciences and Engineering Research Council (NSERC) of Canada and wood industry partners.

References

Alturkistani A., Fazio P., Rao J. and Mao Q. (2008). A new test method to determine the relative drying capacity of building envelope panels of various configurations, Accepted by *Building and Environment.*

ASTM. (2000). E331-00. Standard test method for water penetration of exterior windows, curtain walls, and doors by uniform static air pressure difference, *American Society for Testing and Materials*, 04 (11): 51-54.

Barrett D. (1998), *The renewal of trust in residential construction: an inquiry into the quality of condominium construction in British Columbia*, Government of the Province of British Columbia.

Beaulieu P., Bomberg, M., Cornick S., Dalgliesh A., Desmarais G., Djebbar R., Kumaran K., Lacasse M., Lackey J., Maref W., Mukhopadhyaya P., Nofal M., Normandin N., Nicholls M., O'Connor T., Quirt J., Rousseau M., Said M., Swinton M., Tariku F., and van Reenen D. (2002). "Final report from Task 8 of MEWS project (T8-03): hygrothermal response of exterior wall systems to climate loading: methodology

and interpretation of results for Stucco, EIFS, Masonry and Siding clad wood-frame walls." *Research Report* 118, National Research Council of Canada, Institute for Research in Construction, Ottawa, RR-118, Nov., 184 pp.

Brown W., Chouinard K., Lawton M., Patenaude A., Vlooswyk J. (2003). "Field experience with moisture management – putting principles into practice", *BSI 2003 Proceedings of the Seminar Series*, 15 Locations across Canada, Oct. 2003-Jan. 2004, pp. 1-21

Candanedo L., Derome D. and Fazio P. (2006). Analysis of Montreal 30-year weather data to select loading conditions for large-scale tests on wall panel systems, *Proceedings of the Third International Conference in Building Physics (IBPC3): Research in Building Physics and Building Engineering*, Montreal, August 27-31, 959-966.

Fazio P., Mao Q., Ge H., Alturkistani A. and Rao J. (2007). Test method to measure the relative capacity of wall panels to evacuate moisture from their stud cavity, *Journal of Architectural Engineering,* 13(4): 194-204.

Fazio P., Mao Q., Alturkistani A., Vera S. and Rao, J. (2006[a]). Establishing a uniform and measurable moisture source to evaluate the drying capacity of building envelope systems, *Research in Building Physics and Building Engineering: Proceedings of the Third International Conference in Building Physics (IBPC3)*, Montreal, August 27-31, 369-377.

Fazio P., Rao J., Alturkistani A. and Ge H. (2006b). Large scale experimental investigation of the relative drying capacity of building envelope panels of various configurations, *Proceedings of the Third International Conference in building Physics (IBPC3): Research in Building Physics and Building Engineering*, Montreal, August 27-31. 361-368.

Hazleden D. and Morris P. (2001). The influence of design on drying of wood-frame walls under controlled conditions, *Performance of Exterior Envelopes of Whole Buildings VIII: Integration of Building Envelopes, Conference Proceedings, ASHRAE*, Clearwater Beach, Florida, Dec. 2-7, 18.

Kumaran M. (2002). A thermal and moisture transport property database for common building and insulating materials, *Final report from ASHRAE research project 1018-RP*, IRC/NRC, Ottawa, Toronto.

Lang A., Lawton M. and Brown W. (1999). *Stucco-clad wall drying experiment*, Canadian Mortgage and Housing Corporation, Research Report no. 5972204.00, Vancouver, B.C.

Maref W., Lacasse M. and Booth D. (2004). Large-scale laboratory measurements and benchmarking of an advanced hygrothermal model, *CIB Conference*, Toronto, Ontario, May 2-7, 1-10.

Ojanen T., Salonvaara M. and Simonson C. (2002). Integration of simplified drying tests and numerical simulation in moisture performance analysis of the building envelope, *6th Symposium on Building Physics in the Nordic Countries*, June 17, Trondheim, Norway.

Ricketts D. and Lovatt J. (1996). Survey of building envelope failures in the costal climate of British Columbia, *Canadian Mortgage and Housing Corporation*, Vancouver, B.C. 43.

Schumacher C., Shi X., Davidovic D., Burnett E. and Straube J. (2003). Ventilation drying in wall systems, *Research in Building Physics*: *Proceedings of the Second International Building Physics Conference,* A.A. Balkema Publishers, Leuven, Belgium, September 14-18, 479-486.

Teasdale-St-Hilaire A., Derome D. and Fazio P. (2003). Development of an experimental methodology for the simulation of wetting due to rain infiltration for building envelope testing, *Proceedings of the 2nd International Building Physics Conference*, Balkema Publishers, Leuven, Belgium, September 14-18, 455-462.

Tsongas G., Govan D. and McGillis J. (1998). Field observations and laboratory tests of water migration in walls with shiplap hardboard siding, *Thermal Envelopes VII/Moisture—Practices*, 469-483.

Wu Y., Kumaran M. and Fazio P. (2007). Moisture buffering capacities of five North American building materials, Accepted by the *Journal of Testing and Evaluation.*

Investigations on the Durability of Load-Bearing, Directly Rendered, External Sheathings of Wood-Framed Houses

Britta Rosenau, Dipl.-Ing.
Universität Rostock until September 2007, from Oktober 2007 Eternit AG
brosenau@gmx.de

Georg-Wilhelm Mainka, Prof. em. Dr.-Ing.
Universität Rostock
gm009@uni-rostock.de

KEYWORDS: wood-framed house, sheathing, plaster / stucco, mechanical properties, hygro-thermal properties, hygro-thermal calculations, experiments.

SUMMARY:
This paper describes tests on natural sized, directly rendered walls with different sheathing and plaster / coating materials as well as hygro-thermal, mould growth and mechanical calculations.

It is shown that it is possible to build functioning load-bearing, directly rendered, external walls of wood framed houses regarding resistance against very severe climate changes and high mechanical loads. The sheathing materials are distinguished between moisture sensitive and insensitive. Moisture sensitive sheathing materials require a water drainage plane in the area on their outside surface. Moisture insensitive sheathing materials do not need a water drainage plane. In any event, a water-repellent plaster is to be used.

Only the behaviour of the wall construction against the risk of mould growth inside of the outside sheathing could not be satisfactorily solved.

1. Introduction

Several years ago German companies built wood-framed houses with directly-rendered external sheathings. After some time, the exterior walls of many of these houses exhibited large deformations and cracks. As a result, the industry mostly discontinued building with such types of construction. Now the German building industry has old and new sheathing products on the market that are available for directly rendered, exterior walls.

Exterior walls must be resistant to changes in temperature, solar radiation, driving rain and dampness. Additionally, these walls need to bear a variety of loads, for example: the vertical load of the construction itself, snow, traffic, and loads resulting from wind load moment, as well as horizontal wind load. Note: Insulation materials between rendering and sheathing as used in ETICS are not part of this work.

For a long-term durability of directly-rendered, external sheathings of wood framed houses it is necessary to know the possible damages as follows:

- Large vault / bending of the sheathing;
- Failure of the bonding between the sheathing and the rendering;
- Fungal attack in the construction materials;
- Cracks in the rendering due to hygro-thermal impact, allowing penetration of rain;
- Cracks in the rendering at nailed joints of the sheathing caused by horizontal loads.

To understand the material and construction behaviour, Rosenau B. (2008) conducted tests on natural sized walls under combinations of extreme hygro-thermal conditions and mechanical loads relative to cracks. During the tests the air temperature and humidity, the lateral expansion and the bending of the sheathing were measured.

Based on the received data, hygro-thermal calculations on the moisture behaviour and the risk of mould growth in the construction, as well as mechanical calculations on the load bearing capacity compared to the experiments of natural sized walls, were realized .

2. Wall construction and material combination

The natural sized walls consist of five vertical timber studs, a horizontal timber sole plate and a double timber top plate. The size of the studs and plates is 60 mm x 140 mm. The on-centre distance timber of the studs is 625 mm. The boards are 1250 mm wide and 1750 mm high. They are attached to the studs and plates by staples. The spacing of the staples is 75mm along the margin and 150 mm in the vertical centre of the boards.

FIG. 1 shows the frontal view of the wall construction with mechanical loads, possible displacement of the sheathing boards and cracks.

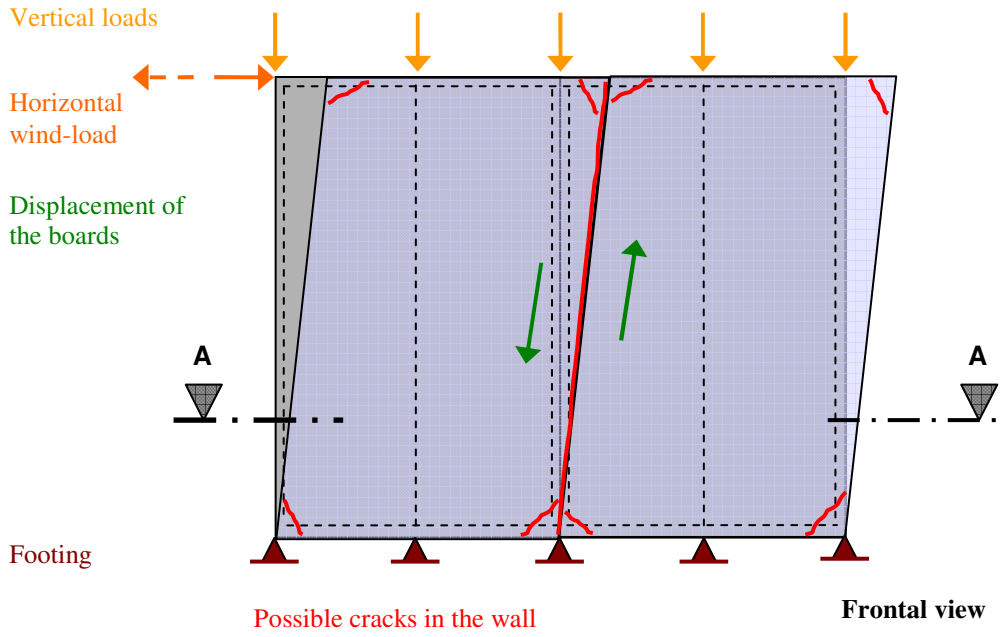

FIG. 1: Wall construction – frontal view

FIG. 2 shows the wall construction in the horizontal section view.

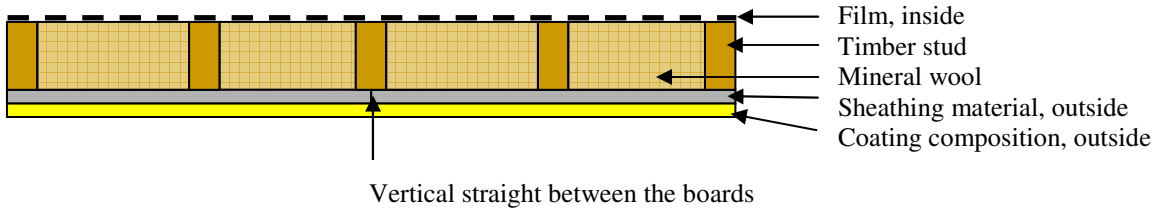

FIG. 2: Wall construction – horizontal section view

TABLE. 1 describes three types of tapes which were used over the vertical straight joints between the sheathing boards

TABLE. 1: Tapes over the vertical straight joints

Sheathing materials	Tapes over the vertical straight joints
Cement-bound particle board	Very flexible fabric strip with thin, grey rubber in the middle, stuck on
Gypsum-fibre board	Very flexible fabric strip with thin, grey rubber in the middle, stuck on
Mineral light-weight board	Adhesive fabric strip with a thin layer of glue on top, stuck on
OSB-board	Adhesive, elastic, flexible polyvinyl chloride strip, 24 mm wide

TABLE. 2 describes the coating compositions of the walls.

TABLE. 2: Coating compositions of the walls

Sheathing boards Material Thickness [mm]	Coating compositions Thickness [mm]	materials
Cement-bound particle board 12 mm	4.5	light-weight, water-repellent, mineral mortar with fabric 9 mm x 6 mm
	15.0	water-repellent, mineral, fibre reinforced plaster with light-weight, mineral components with fabric 6,5 mm x 7 mm
		Pigmented, mineral plaster primer
	1.0	Water-repellent, mineral noble-plaster / top coat
		Mineral-organic façade paint
Gypsum-fibre board 15 mm	1.0	one-component, long-therm flexible, paintable sealing with fabric 4 mm x 4 mm *water drainage plane in the area*
	4.5	light-weight, water-repellent, mineral mortar with fabric 9 mm x 6 mm
	1.7	water-repellent, mineral-organic noble-plaster / top coat
		Mineral-organic façade paint
Mineral light-weight board 15 mm	8.0	Water-repellent , mineral, light-weight mortar with fabric 4 mm x 4 mm
		Pigmented, mineral plaster primer
	1.0	Water-repellent, mineral noble-plaster / top coat
		Mineral-organic façade paint
OSB-board 15 mm	3.5	Rubber based coat *water drainage plane in the area*
		Primer
		Top coat

3. Experiments on natural sized walls

3.1 Natural sized walls under hygro-thermal loads

The construction of natural sized walls is described in section 2. The film inside the walls had a relative water vapour resistance (that of 1 m air) between s_d = 0.5 m (wet cup) and s_d = 5.0 m (dry cup).

TABLE. 3 describes the climate cycles of the wall tests according to ETAG 004. For the tests, the heat-rain-cycles were divided into two parts because of the possible higher water absorption of the test walls after the heat-cold-cycles.

During the tests the wall surfaces were examined for cracks, flaws or other damages. The bending of the sheathing boards relative to the studs and relative to the steel frame as well as the lateral expansion of the boards were measured. The relative humidity and the air temperature in the climate chamber at outside and inside conditions, in the wall between the sheathing boards and the mineral wool, and between the mineral wool and the film were also measured

During the climate chamber test the wall with cement-bound particle boards failed. The plaster / stucco tore in the area of the fabric from the sheathing boards. The walls with gypsum-fibre boards, mineral light-weight boards and OSB-boards resisted without any damages.

FIG. 3 shows the bending and the lateral expansion during the climate tests for the cement-bond particle boards, *FIG. 4* of the gypsum-fibre boards, *FIG. 5* of the mineral light-weight boards and *FIG. 6* of the OSB-boards.

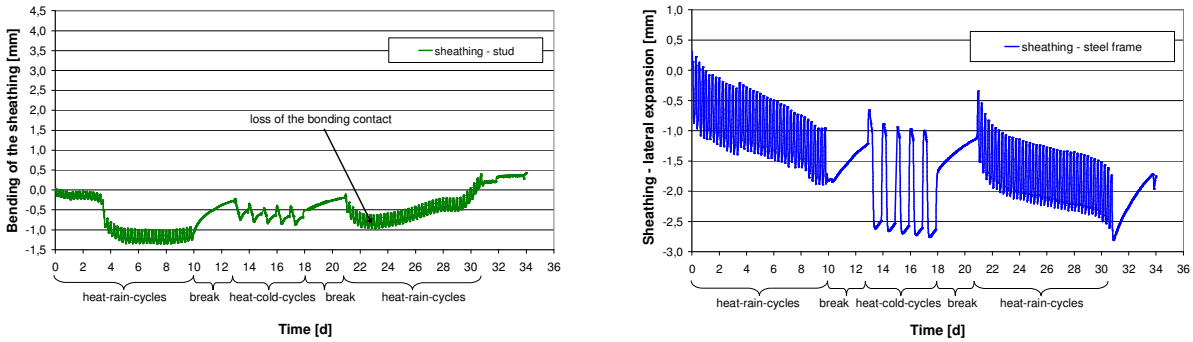

FIG. 3: Wall with cement-bond particle board – bending and lateral expansion

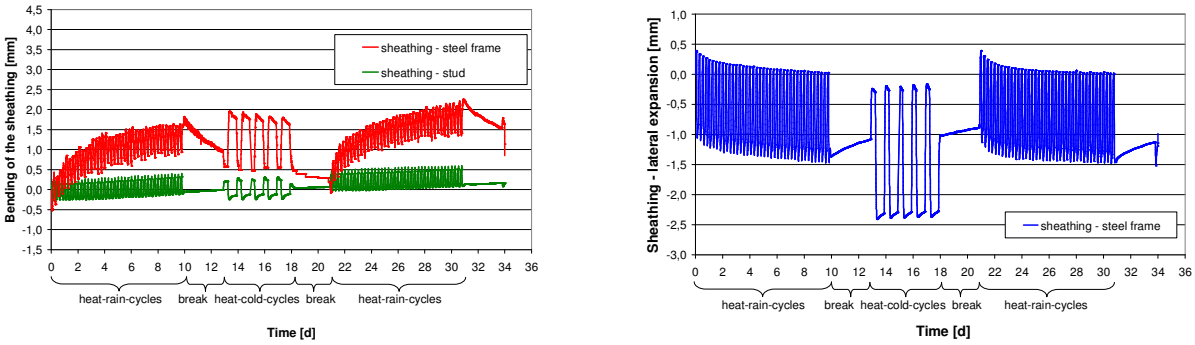

FIG. 4: Wall with gypsum-fibre boards – bending and lateral expansion

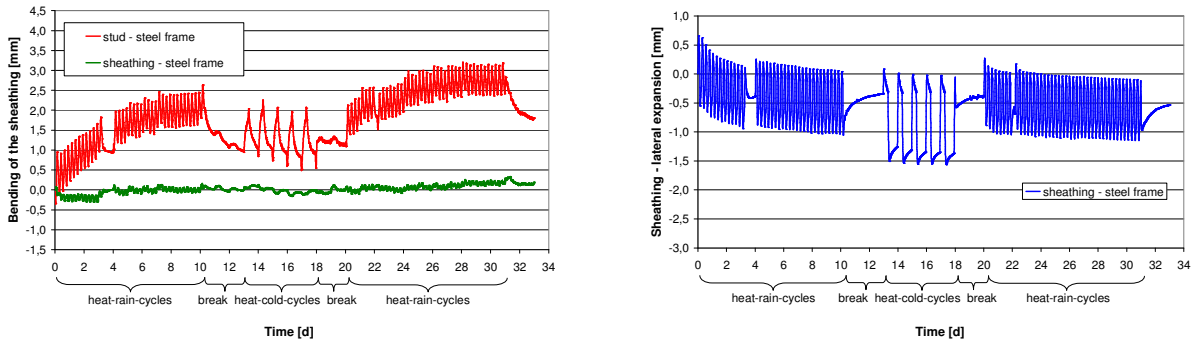

FIG. 5: Wall with mineral light-weight boards – bending and lateral expansion

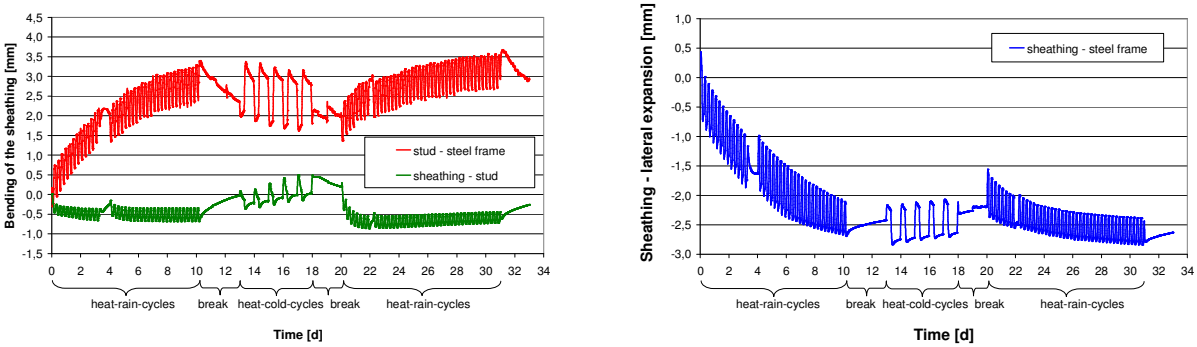

FIG. 6: Wall with OSB-boards – bending and lateral expansion

TABLE. 3: Climate cycles for test walls according to ETAG 004

	Period of time				Climate conditions
	t [h]	∑ t [h]	cycles	t [d]	
Heat-rain-cycles	1	6	40	10	Heating up θ_{Se} to + 70°C
	2				θ_{Se} = + 70°C
	1				Raining θ_W = +15°C
	2				Draining break
Break	> 48	48		2	θ_{Se} = + 20°C, $\phi_L \geq$ 50 % rH
Heat-cold-cycles	1	24	5	5	Heating up θ_{Se} to + 50°C
	7				θ_{Se} = + 50°C
	2				Cooling down θ_{Se} to - 20°C
	14				θ_{Se} = - 20°C
Break	> 48	48		2	θ_{Se} = + 20°C, $\phi_L \geq$ 50 % rH
Heat-rain-cycles	1	6	40	10	Heating up θ_{Se} to + 70°C
	2				θ_{Se} = + 70°C
	1				Raining θ_W = +15°C
	2				Draining break
			∑ t = 29 days		

The high bending deformations between the sheathing boards / studs and the steel frame are results of drying out of the wooden studs outside during the tests. *TABLE. 4* shows the largest deformations of the test walls under hygro-thermal loads.

TABLE. 4: Largest deformations of the test walls under hygro-thermal loads, hygric expansion of the boards

Wall with:	Cement-bond particle board	Gypsum-fibre board	Mineral light-weight board	OSB-board
Bending of the sheathing relative to the stud [mm]	-1.8	+0.4	+0.20	-0.70
Bending of the stud relative to the steel frame [mm]		+1.5	+2.75	+3.25
Lateral expansion of the sheathing [mm/m]	-0.8	-0.3	-0.26	-1.04

The highest bending of the sheathing boards relative to the studs shows the wall with cement-bond particle board which failed during the climate test. The maximal measured bending is more than twice the value of the other walls. The bending of the OSB-board relative to the studs is smaller than 1 mm and because of the very flexible coating, no damage was observed.

Strips over the sheathing joints were always used for the tested walls to moderate the expansion of the sheathing in this point of the construction. The wall with OSB-boards had the highest lateral expansion of the sheathing. The use of a 24 mm wide strip with a non load bearing bonding contact to the OSB-board worked very well in combination with the very flexible coating as a movement distributing area. The measured relatively small lateral expansions of the gypsum-fibre boards and the mineral light-weight boards in combination with a joint strip are not significant.

3.2 Natural sized walls under mechanical loads

A specific steel frame to bear the natural sized walls under mechanical loads was constructed for the use in the climate chamber. *FIG. 7* shows a wall in the frame under mechanical loads. The wall is attached to the steel frame with four bolts through the horizontal timber sole plate. On the double timber top plate four pairs of pulleys enable the lateral displacement and prevent the tip of the wall head.

With vertical presses it is possible to put a vertical load of 10 kN on top of every stud to simulate the loads of a real building. The wind load was simulated by a horizontal press on the double timber top plate. This load changed in direction six times and had load steps of mostly 6 kN until the failure of the wall or the maximum load of 40 kN in each direction was achieved.

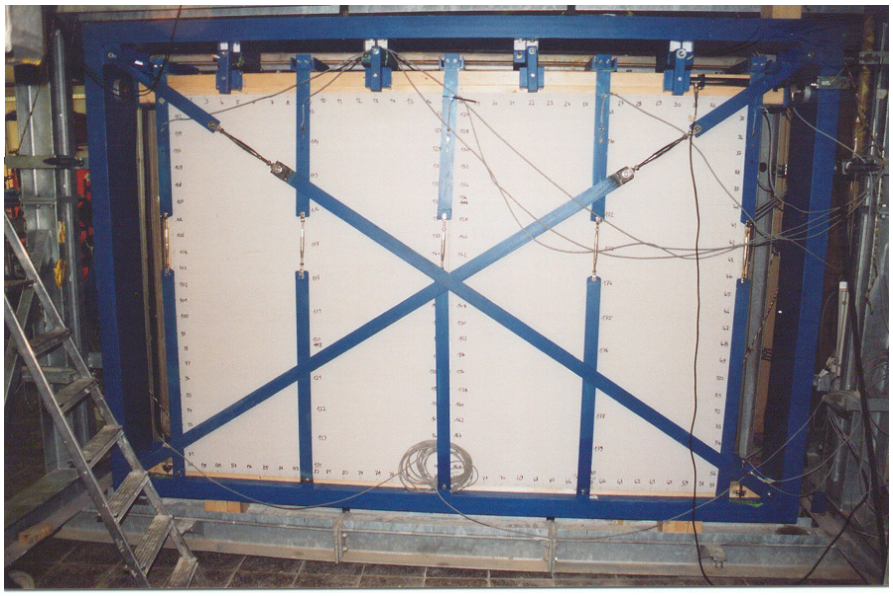

FIG. 7: Steel frame for natural sized walls under mechanical loads

The mechanical tests of walls were made without rendering (one wall for every sheathing material) and with rendering after successfully resisting the climate test. These walls have the same construction as in the climate test, but without the mineral wool and the film.

The walls without coating were 14 days in a climate of 20°C / 65% rH. The directly rendered walls after the climate test did not get any special conditioning. They stood in the ambient climate of the lab.

FIG. 8 shows the forces and the corresponding displacements on the wall heads and in the straight joints. *TABLE. 5* explains the short names in *FIG. 8* and gives the adhesive tension strength between the sheathing boards and the rendering after the climate tests.

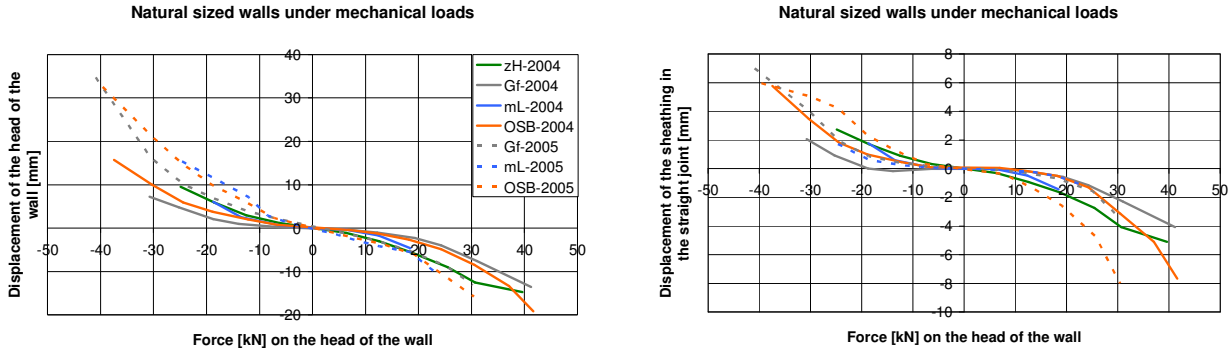

FIG. 8: Natural sized walls – forces and displacements

The displacements of the walls with rendering compared to the walls without rendering under the same load are nearly twice the value. A possible reason for this behaviour is:

- The studs and plates dried out during the climate test and the clamp cored / hole became bigger.

TABLE. 5: Short names of the walls explained, adhesive tension strength and test age

Short name	Sheathing	Rendering	Adhesive tension strength	Test age
zH-2004	Cement-bond particle board	no		
Gf-2004	Gypsum-fibre board	no		
mL-2004	Mineral light-weight board	no		
OSB-2004	OSB-board	no		
Gf-2005	Gypsum-fibre board	yes	0.26 N/mm^2	1.5 years
mL-2005	Mineral light-weight board	yes	0.23 N/mm^2	1.5 years
OSB-2005	OSB-board	yes	0.95 N/mm^2	1.0 years

4. Calculations on natural sized walls

4.1 Mechanical calculations of walls

Mechanical calculations of walls without rendering were made according to the procedure of ***Schulze 1998***. The calculations on the point of failure and the mechanical tests have a good agreement.

TABLE. 6 shows the loads on the point of failure in the experiments and calculations, the measured displacements on the head of the wall and between the two sheathing boards. It also contains the calculated maximally safe load.

TABLE. 6: Loads and displacements on the point of failure and calculated maximally safe load

Short name	Point of failure				Calculated maximally safe load	Safety factor
	Load on the head of the wall		Measured displacements			
	Calculated	Measured	Head of the wall	Between the two sheathing boards		
	[kN]	[kN]	[mm]	[mm]	[kN]	
zH-2004	30	30	26.4	8.6	8.8	3.4
Gf-2004	23	30	15.8	4.8	8.8	2.6
mL-2004	8	12	5.0	1.3	8.0	1.0
OSB-2004	95	>42	>30.0	>12.0	8.8	10.8
Gf-2005	23	30	30.5	8.5	8.8	2.6
mL-2005	8	12	13.1	0.5	8.0	1.0
OSB-2005	95	>40	>40.0	>14.0	8.8	10.8

The calculated and measured load at the head of the wall on the point of failure is the load where the sheathing develops cracks. The displacements in the wall may be as large as possible.

The calculated maximum safe load considers the displacement of the wall due to the maximum load on the staples. Only for the wall with the mineral light-weight board is the safe load for the staples not relevant. Here is realized the point of failure in the board, as observed by cracking, before the staples displace too much.

4.2 Hygro-thermal calculations of walls with rendering

The hygro-thermal calculations were realized with the program ***WUFI 4.0*** and ***WUFI-BIO 2.0***.

The measured parameters of the used sheathing and rendering materials (not part of this paper) were put into ***WUFI 4.0***. The hygro-thermal tests of the walls were calculated with the measured climate data on both sides of the wall. The calculated relative humidity and air temperature were compared with the measured climate conditions on the point between the sheathing and the mineral wool. To get the right results with the calculations it was necessary to switch off the liquid water transport.

For the calculations on walls under climate conditions of Holzkirchen (Germany) the models got an OSB- and a gypsum-fibre board on the inside. The resistance of the water vapour permeability of the inside film changed. The calculations ran over a minimum of three years. The climate data in the mineral wool directly on the outside sheathing were used as input data for the simulation of a possible risk for mould growth in the construction with ***WUFI-BIO 2.0***. *TABLE. 7* shows the results of the calculations.

TABLE. 7: Calculation results – risk of mould growth in the construction inside of the outside sheathing

Wall with: Film, inside: s_d [m]	Cement-bond particle board	Gypsum-fibre board	Mineral light-weight board	OSB-board
100 m	in question	in question	in question	in question
50 m	in question	in question	in question	in question
25 m	in question	yes	in question	yes
5 m	yes	yes	yes	yes
0,5 m	yes	yes	yes	yes

The risk of mould growth in the construction can not be excluded. The water vapour resistance of the film should be $s_d \geq 25$ m. Films with a water vapour resistance $s_d \leq 25$ m should not be used.

Please note: ***WUFI-BIO 2.0*** was develop for simulations of the inner surfaces of building components. Here it is used for calculations inside constructions! For the safety of constructions the simulation results show earlier mould growth than it would be naturally occur.

5. Conclusions and recommendations

The walls with gypsum-fibre, mineral light-weight and OSB-boards worked well under hygro-thermal loads. Only the wall with cement-bond particle board failed. The explanation of this behaviour is, that moisture sensitive gypsum-fibre and OSB-boards got a water drainage plane in the area on their outside surfaces – opposite to the also moisture sensitive cement-bond particle boards. The hygric movements of the cement-bond particle boards were so extreme that the plaster tore in the area of the fabric from the sheathing. The mineral light-weight board is moisture insensitive and does not need a water drainage plane.

Sheathings for load-bearing, directly rendered, external walls should be insensitive to moisture. A moisture sensitive sheathing should only be used in combination with a water drainage plane in the area. The rendering of the sheathings should always be water-repellent. Over the straight joint of the sheathings a strip should be used to separate the rendering from the sheathing or to stabilize the straight joint. In the rendering, only fabrics which don't separate the rendering two-dimensionally, may be used.

The natural sized walls under mechanical loads worked very well in the tests. The test results are in agreement with the calculations. The measured adhesive tension strengths are enough for a durable bonding contact between the sheathing and the plaster.

The risk of mould growth in the construction can not be excluded. For this topic further research is necessary. But films with a water vapour resistance $s_d \leq 25$ m should not be used.

6. References

ETAG 004 (2000). Guideline for European technical approval of external thermal insulation composite systems with rendering, *European Organisation for Technical Approval (EOTA)*, Brussels, Belgium.

Rosenau B. (2008). Untersuchungen zur Gebrauchstauglichkeit von mittragenden, direkt beschichteten Beplankungen bei Außenwänden im Holztafel-/Holzrahmenbau, Phd-thesis submited 15. December 2007 at the University of Rostock, Germany, so far unpublished

Schulze H. (1998). Holzbau – Wände, Decken, Dächer; Konstruktion, Bauphysik, Holzschutz, 2. Edition, *Teubner publishing company*, Stuttgart / Leipzig, Germany.

WUFI 4.0. and WUFI-BIO 2.0. Software, *Fraunhofer Institut für Bauphysik*, Holzkirchen, Germany.

A Comparative Analysis of Hygrothermal Behavior in Wood Construction Walls from Two Different Geographical Perspectives in the USA

Kennard G. Larson, Prof. Dr.
University of Nebraska at Kearney, USA
larsonk@unk.edu

Georg-Wilhelm Mainka, Prof. Dr.-Ing.
Universität Rostock, Germany
georg-wilhelm.mainka@uni-rostock.de

Katrin Riesner, Dr.-Ing.
R & M Shiptechnologies GmbH, Rostock, Germany
katrin.riesner@shiptec.info

Robert Erikson, Dr.
University of Wyoming, Laramie, USA
erikson@uwyo.edu

KEYWORDS: wood-framed house, sheathing, fiberglass insulation, air barriers, moisture barriers, vapor barriers, hygro-thermal properties, hygro-thermal calculations, experiments.

SUMMARY:
In winter of 2006, in Kearney, Nebraska, (Northern U.S.A. latitude 40° 44' N, elevation 652 meters above sea level) numerous climatic data were collected for a 12 week period from January to March. Daily, at 20 minute intervals, data were recorded for nine variables which included numerous temperature readings at various locations in the living space (room), the wall cavity, and the exterior natural air space. In addition to temperature, atmospheric pressure and relative humidity levels were also recorded.

Similarly, in Fall of 2004, data were collected at 30 minute intervals for a 12 week period in a structure located in Laramie, Wyoming, (Northern U.S.A. latitude 41° 3' N, elevation 2193 meters above sea level). The collection of these data allowed the researchers to perform numerous calculations of temperature, relative humidity and dew points at various locations within the wall construction. These data were ultimately further compared for hygrothermal behavior with WUFI, the PC program developed by IBP/ORNL, for calculating coupled heat and moisture transfer in building components.

1. Introduction

Moisture problems in buildings are considered one of the single, largest factors limiting the service life of a building in the United States (Lstiburek, 1991). The goals of this research effort were to determine

- the hygrothermal activity in exterior walls of wood framed construction, and
- to what extent geographical elevation above sea level impacts the climatic and hygrothermal behavior in similarly designed and constructed buildings, and
- if there is a preferred position/location of various types of vapor barriers, i.e. on the interior or exterior surface of the wood frame, and
- which of the tested vapor barrier materials, if any, provides an adequate level of moisture control with capability to discourage the development of mold or fungus growth within the structure.

2. Test Structures

2.1 Location

The test structures studied for this research were residential, single-family homes typical of the Midwest region in the United States. The Energy Efficient Building Association (EEBA) classifies this region as a "Heating Climate" region (Lstiburek, 1991) and recommends various moisture control methods for these regions. Test Structure 1 (later referenced as the *Kearney Project*) was located in Kearney, Nebraska, (Northern U.S.A. latitude 40° 44' N, elevation 652 meters above sea level) as shown in *FIG 1*. Test Structure 2 (later referenced as the *Laramie Project*) was located in Laramie, Wyoming, (Northern U.S.A. latitude 41° 3' N, elevation 2193 meters above sea level) as shown in *FIG 2*. EEBA does not differentiate for elevation values above sea level.

FIG. 1 Test Structure 1 in Kearney, Nebraska

FIG. 2 Test Structure 2 in Laramie, Wyoming

2.2 Wall Construction and Material Combinations

As is typical in most North American wood frame construction, the structural nature of the exterior wall frames of the Test Structures were constructed with "2X4" (38mm X 90mm) or "2X6" wood studs spaced at 16 inches (406mm) "on-center", a horizontal "2X4"or "2X6" wood sole (bottom) plate, and two (double) "2X4" or "2X6" wood top plates. *Table 1* describes, from exterior to interior, the layers of the construction and compares the materials of Test Structures 1 and 2. It also describes the thicknesses of various building components. It is noted that in both test structures, the tested walls were in a North facing orientation.

The materials utilized in the construction of the walls of both test structures were identical with the following exceptions: 1) a kraft paper vapor barrier and hardboard siding were employed in the Kearney project and in lieu of these, a non-permeable polyethylene vapor and a fiber cement siding in the Laramie project, respectively.

FIG. 3 and 4(below) illustrate these differences at the location of the measurements.

Layer	Kearney		Laramie	
exterior	t [mm]	material	t [mm]	material
paint		prepaint		1 coat latex primer 2 coats latex topcoat
siding	10	"lapped" hardboard "Masonite Colorlok"	10	"lapped" fiber cement "Hardiboard"
wind and water barrier		"Tyvek" (58 Perm)		"Tyvek" (58 Perm)
external sheathing	13	OSB	13	OSB
insulation	89	R-11 Fibre glass batt	135	R-19 Fibre glass batt
vapor barrier		kraft paper	0,15	PE-foil (6 mil)
Internal sheathing	13	gypsum board (drywall)	13	gypsum board (drywall)
paint		1 coat latex primer 1 coat latex topcoat		none
interior				

Table 1: Sizes and Materials of Structural Components of the Test Structures

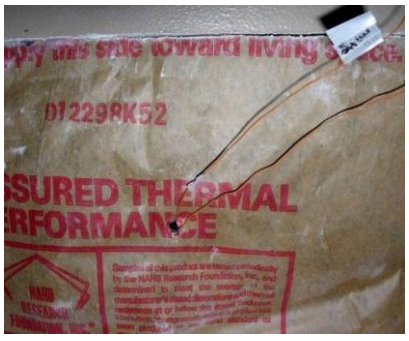

FIG. 3 Kraft paper vapor barrier

FIG. 4 Polyethylene vapor barrier

3. Measurements

3.1 Time, Dates and Location of Measurements within the Structure

For the Kearney project, the climatic data were collected for a 12 week period from January to March, 2006. For the Laramie project, the climatic data was collected for a 12 week period in the Fall of 2004. For consistency, the measuring instruments were arranged in identical fashion in both structures as illustrated in *FIG. 5 and FIG. 6.* Care was taken to insure that the same distances from reference surfaces were maintained. In both projects, duplicate measurements were taken in several locations as a control measure for accuracy.

FIG. 5: Data logger and sensor locations in the Kearney wall

FIG. 6: Sensor locations in the Laramie wall

FIG. 7 and FIG. 8 illustrate location details and various positions of the sensors relative to the interior and exterior of the structure. The exterior temperature/moisture sensor is visible in *FIG. 7* while the Ahlborn data-logger, interior temperature/moisture sensor and air pressure sensor is visible in *FIG. 8.*

FIG. 7: Location of exterior climate sensor

FIG. 8: Location of interior climate sensor

3.2 Recording and Measuring Equipment

The recording and measuring equipment used in both Test Structures was provided by Ahlborn Mess-und Regelungstechnik GmbH in Holzkirchen, Germany. The ALMEMO data-logger model 2590-9 recording instrument allows logging of up to nine data inputs on channels 00 through 08. The data-logger was calibrated to record at 20 minute intervals in the Kearney project and 30 minute intervals in the Laramie project. A typical display of the data-logger is observed in *FIG. 9* following.

FIG. 9 Ahlborn Data-logger

The data-sensors located throughout the construction included four PT100/condensator combination sensors (temperature *and* relative humidity), four thermocouple temperature sensors (bi-metallic), and one atmospheric pressure sensor. *TABLE 2* describes which sensors were connected to respective channels, the variable that the sensor measured, the units of measurement, and the location of the sensors.

TABLE 2: Figure code, assigned channels, sensor types, measured values, units, and location of sensors

Figure Code	Meas. Channel	Sensor Type Temp	RH	Measured Values	Units	Location
i	M04	PT 100	Cond.	temperature + rel. humidity	°c %	air interior
i1	M00	Th. Coup.		temperature	°c	air interior
i/e 0,0	M01	Th. Coup.		temperature	°c	outside of the int. sheathing
i/e 0,4 / 0,5	M02	Th. Coup.		temperature	°c	insulation 60 / 80 % from int. sheathing
i/e 0,6 / 0,8	M03	Th. Coup.		temperature	°c	insulation 40 / 50 % from int. sheathing
i/e 1,0	M05	PT 100	Cond.	temperature + rel. humidity	°c %	inside ext. sheathing 150mm from ceiling
i/e 1,0 35	M06	PT 100	Cond.	temperature + rel. humidity	°c %	inside ext. sheathing 350mm from ceiling
e	M07	PT 100	Cond.	temperature + rel. humidity	°c %	air exterior
pA	M08			air pressure	haPa	interior

The "Figure Code" in *TABLE 2* identifies the "daily mean" values in the figures to follow.

3.3 Measurement Results

FIG. 10 and FIG. 11 illustrate the daily mean temperatures for the Kearney and Laramie project, respectively. *FIG. 12 and FIG. 13* illustrate the relative humidity and air pressure for Kearney and Laramie, respectively. The critical consideration for mold potential is the interior surface of the exterior OSB sheathing (light blue, i/e 1,0). These measurements are shown in the temperature diagram with their time-step values correlated with those for relative humidity. Air pressure is presented in *FIG. 12* and *13* compared with the sea level average at 1000 haPa.

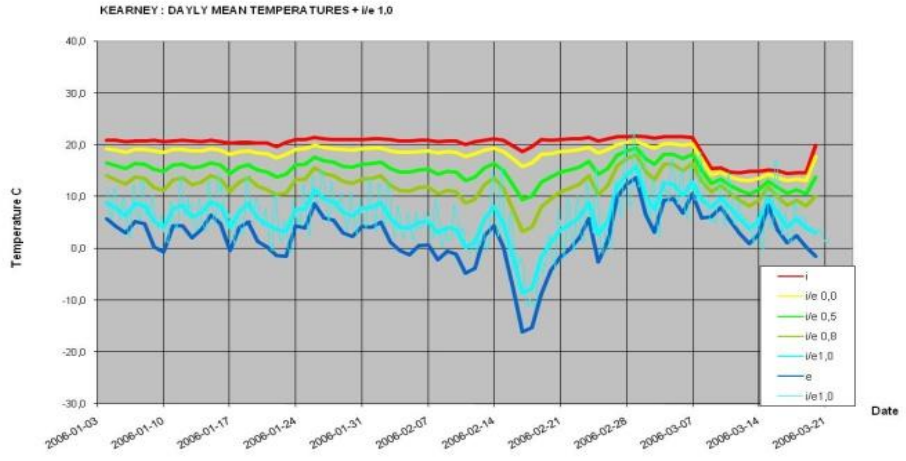

FIG. 10: Kearney daily mean temperatures and inside OSB 1/3 h values

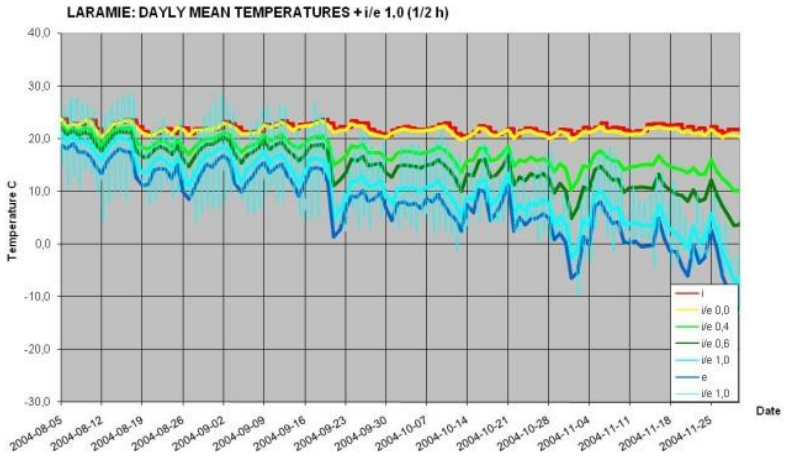

FIG. 11: Laramie daily mean temperatures and inside OSB ½ h values

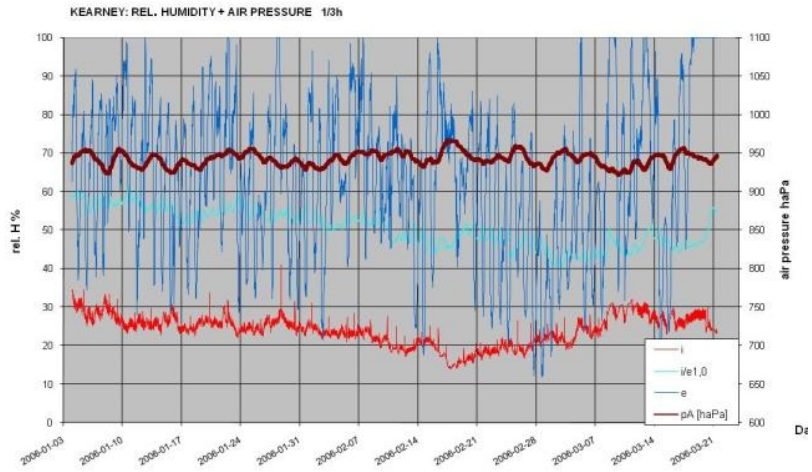

FIG. 12: Kearney relative humidity and air pressure

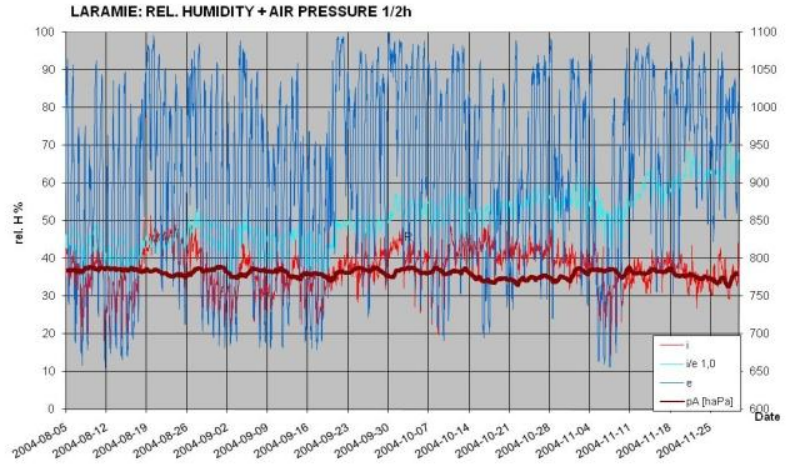

FIG. 13: Laramie relative humidity and air pressure

3.4 Discussion of Results

As would be expected, *FIG. 10 and 12*, demonstrate that low relative humidity (RH) levels were correlated to lower temperatures in the Kearney project. *FIG. 10* illustrates average daily temperatures for increasingly closer distances to the outside atmosphere. *FIG. 12* illustrates that while the extremes in RH (dark blue) in the exterior atmosphere were great, the RH within the wall construction (light blue), specifically on the inside surface of the OSB sheathing, was generally between 50% and 60% RH. With this low level of RH, no condensation would be expected, and therefore no expectation for the development of mold. A further observation is the relatively low RH within the living space of the room. It is likely that the lack of air tightness of the structure would explain this phenomenon by which moisture would escape via the high air exchange rate of the structure. Hagentoft, E, 1996, concluded similar results regarding air leakage carrying moist air into the construction that leads to unacceptably high values even for moderate indoor moisture levels.

The low RH rates in the Laramie project at the interior surface of the OSB sheathing are attributed to the low air pressure (av. 750 haPa) at the relatively high elevation (2193 meters) above sea level. The low pressure would lead to a high evaporation rate resulting in the low RH levels measured. But of special note is the increase of the RH from 40% in Fall to 70 % at the beginning of Winter. This would explain the acceptance of the non-permeable vapor barrier at the much higher elevation without a concern for moisture trapping.

4. Simulation with WUFI

4.1 Objective: To Determine the Risk of Mold Growth under Variable Conditions

Inherent in the study was the consideration of four variables:

- types of vapor barrier materials,
- influence of the location/position of the vapor barrier within the construction,
- warm climatic versus cold climatic conditions, and
- the Kearney project (low elevation) compared to the Laramie project (high elevation).

4.2 Program WUFI

The program WUFI, the software for calculation of transient heat and moisture transport, was used for the simulation studies of the defined variables. WUFI allows the simulations under cold weather or warm weather climatic data. WUFI also allows a convenient mode for changing materials as well as location of materials within the structure and also allows easy selection of various geographical climatic data.

4.3 Construction Data, Variations

Four vapor barrier material scenarios were considered as follows: tests were conducted on three common types of vapor barriers including kraft paper, polyethylene film (PE), and “intelligent” film (PA), as well as a test using no vapor barrier. The two locations or positions of the vapor barriers that were tested are as follows: directly under the interior sheathing (gypsum board) or on the interior surface of the OSB sheathing. A “cold” Test Reference Year (TRY) was calculated for Laramie, but for Kearney, both a cold TRY, as well as a warm TRY, were calculated.

4.4 Climate Data

While there were no measured climate data available for one year, and while there does not exist a TRY or climatic data for Kearney or Laramie in WUFI (North American version), there were climate data available in WUFI for Omaha, Nebraska and Casper, Wyoming, respectively. These available climate data were deemed adequate since Omaha and Casper represent a more severe climate for potential mold growth than either Kearney or Laramie, respectively. Due to climatization, the indoor climate was designed at a temperature 20°C and a relative humidity of 30% and 50%.

4.5 Results of Calculation

The results of the calculation are presented in two steps:

- representative, time-dependent diagrams in *FIG. 14* to *FIG. 16* for one TRY according to the parameters of the measurements. Two monitor positions were installed to record the temperature and the relative humidity at the exterior (position 3: red) and interior (position 4: blue) sides of the insulation.

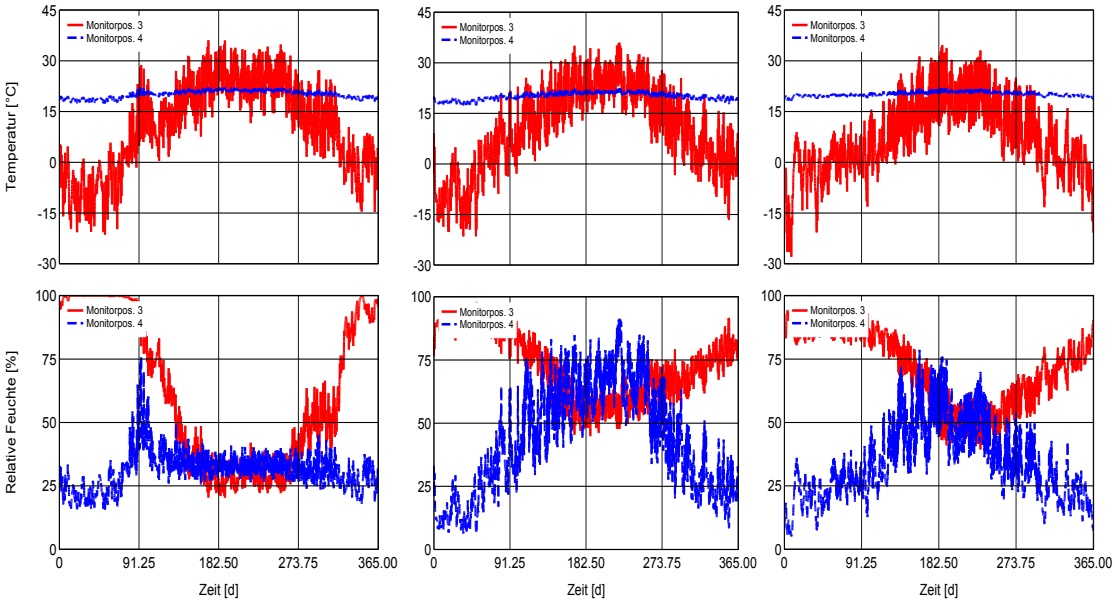

FIG. 14: Kearney warm TRY VB: kraft paper, indoor RH 30%

FIG. 15: Kearney cold TRY VB: PE-foil, indoor RH 50%

FIG. 16: Laramie cold TRY VB: PE-foil, indoor RH 50%

- compilation of the results of the WUFI simulation studies is shown in *TABLE 3*. It represents the results of 24 simulations adjusted for the variables selected for the study. Numeric data in the table are indicative of the units in kilograms of water per square meter (kg/m^2) that could be expected on the interior surface of the OSB sheathing, dependent of the variables. An assumption is made that values of less than 1 kg/m^2 would be of little concern for the risk of mold development and for the risk of condensed water flowing down. Units greater than 1 kg/m^2 are indicated in **red** color and are consider significant.

Table 3: WUFI Simulations for the potential of mold growth in the Kearney and Laramie projects

Mineral Wool		**Water Content (kg/m^2)**		**Omaha**	Kearney	Insulation		**Casper**	Laramie	Insulation	
		end calc.		298 m	652 m	4"	8,9 mm	1612 m	2293 m	6"	12,5 mm
		maximum	Start calc.:	0,16				0,24			
		VaporBarrier	Interior	none	kraft p.	PE	PA	none	kraft p.	PE	PA
TestReferenceYear	warm	exterior VB:	none	*0,18*	*0,17*	*0,04*	*0,05*	*0,62*	*0,5*	*0,06*	*0,06*
			(Tyvek)	**1,63**	**0,96**	**0,16**	**0,16**	**0,79**	**0,6**	**0,24**	**0,24**
	cold	interior VB:	none	*0,19*	*0,17*	*0,04*	*0,03*	*0,53*	*0,43*	*0,05*	*0,06*
			(Tyvek)	**1,96**	**0,96**	**0,16**	**0,16**	**1,1**	**0,78**	**0,24**	**0,24**
			kraft	*0,19*	*0,17*	*0,04*	*0,05*	*0,53*	*0,43*	*0,05*	*0,06*
			paper	**1,96**	**0,97**	**0,16**	**0,16**	**1,1**	**0,78**	**0,24**	**0,24**

4.6 Discussion of Results

FIG. 14 demonstrates that in Kearney during the heating season (Winter) the RH may increase up to 100% at the inside of the OSB, therefore the risk of mold growth is high. On the other hand, in Summer, with high external temperatures and high relative humidity values, there is no risk due to the relatively vapor-open kraft paper. *FIG. 15* demonstrates that a vapor barrier of PE-foil allows the RH in Summer to increase, but at a non-risk level. However, winter conditions still pose a slight risk of mold growth. *FIG. 6* shows similar tendencies for Laramie, but with minimal risk. This appears to be compatible with Lstiburek, 1991, when recommending a maximum 35% RH at 70 degrees F (20 C) during heating periods and when using PE foil as a vapor retarder.

TABLE 3: illustrates that in Laramie, Wyoming, there is little chance of mold development, regardless of the type of vapor barrier or whether a vapor barrier is even used. On the other hand, it is apparent that while the type of vapor barrier used in the Kearney climate is of little consequence, the total absence of a vapor barrier would be a genuine concern for mold risk. Regardless of the location of the vapor barrier and regardless of the climate data (cold or warm), the values were well above the acceptable limit of 1 kg/m^2 ranging from 1,63 kg/m^2 in the warm climate study to1,96 kg/m^2 in the cold climate study. Similarly, Levin, P., and Gudmundsson, K., 1999, concluded that when moisture loads are low, perhaps a vapor barrier is not necessary. On the other hand, indoor moisture conditions exceeding 2 g/m^3, will cause condensation on the inside of the inside of the external sheathing and high relative humidity in the insulation. This poses a significant potential for mold growth and/or structural damage due to degradation of the materials.

5. Comparison of Results and Conclusions

Comparing the results of the WUFI simulations over one TRY, the measured data show similar tendencies and values for the investigated time of measurement.

It becomes quite apparent that the issue of mold growth and its consequential negative effect on structural damage to wood members as well as the impact on poor indoor air quality is dependent on geographic location, elevation, and the use of vapor barriers. It would appear that the issue of mold risk is minimal at high elevations (such as Laramie) due to the rapid evaporation of moisture as a result of low atmospheric air pressure. It is apparent that a kraft paper vapor barrier (a minimal financial investment) is adequate to control condensation within the walls of structures in geographic locations similar to Kearney, Nebraska. On the other hand, to not include a vapor barrier, would pose a significant potential for mold growth in the Kearney climate. In any case, a vapor barrier at the inside of the insulation using foils that are open to vapor diffusion is recommended. To conclude, in winter the temperatures in the Midwest U.S. are similar to Scandinavia. On the other hand, a tropical climate exists in summer, very much unlike Scandinavia. Thus, the question of the location of the vapor barrier could not be directly correlated to previous studies from Scandinavia, some of which are cited in this paper.

6. References

WUFI 4.0 (2005) Software for calculation of transient heat and moisture transport, Fraunhofer Institut für Bauphysik, Holzkirchen Germany

AHLBORN Version 5-Handbuch: Mess- und Regelungstechnik GmbH, 4th edition, 2003, Holzkirchen Germany

Lstiburek, J, 1991, *Moisture Control Handbook in New, Low-Rise Residential Construction*, U.S. Department of Energy, Conservation and Renewable Energy

Levin, P, and Gudmundsson, K., 1999, *Moisture in Constructions with Loose-Fill Insulation and No Vapour Barrier*, Nordic Journal of Building Physics Vol. 2, 1999-2000

Hagentoft, C-E. 1996, Moisture *Conditions in a North Facing Wall with Cellulose Loose Fill Insulation: Constructions with and without Vapor Retarder and Air Leakage*, Journal of Thermal Envelope and Building Science. Vol. 19, pp. 228-243

Moisture Performance Assessment of Wood-frame Exterior Building Envelope Construction in China

Phalguni Mukhopadhyaya, Dr,
Institute for Research in Construction, NRC Canada, Ottawa, Ontario, Canada.
phalguni.mukhopadhyaya@nrc-cnrc.gc.ca, www.nrc.ca

David van Reenen, Mr,
Institute for Research in Construction, NRC Canada, Ottawa, Ontario, Canada.
david.vanreenen@nrc-cnrc.gc.ca, www.nrc.ca

Kumar Kumaran, Dr,
Institute for Research in Construction, NRC Canada, Ottawa, Ontario, Canada.
kumar.kumaran@nrc-cnrc.gc.ca, www.nrc.ca

Curt Copeland, Mr,
Special Advisor and Building Specialist, Canada Wood Group and Council of Forest Industries, Canada
curt@lakecable.ca, www.cofi.org

Paul J. Newman, Mr,
Executive Director, Market Access and Trade, Council of Forest Industries, Canada, and Canada Wood
newman@cofi.org, www.cofi.org

Ramez El Khanagry, Mr,
Graduate Student, Carleton University, Canada
ramez.elkhanagry@nrc-cnrc.gc.ca, www.carleton.ca

Ehab Zalok, Dr,
Professor, Carleton University, Canada
ehab_zalok@carleton.ca, www.carleton.ca

KEYWORDS: *wood-frame, exterior building envelopes, Shanghai (China), hygrothermal.*

SUMMARY:
This paper presents some of the results from a research project that investigates the hygrothermal (i.e. thermal and moisture) performance of the Canadian wood-frame exterior building envelope construction practices in the cities of Shanghai and Beijing (China) and Taichung (Taiwan). This study has been done using a two-dimensional hygrothermal simulation tool, hygIRC-2D. In this paper, four exterior walls and two roof constructions are exposed to the exterior climatic conditions of Shanghai. The first set of simulations is conducted with wall constructions that have no air leakage. Thereafter, two wall constructions are also simulated with various levels of air leakage through the wall assembly. The outputs from the simulations have been analyzed with the help of a moisture response indicator called RHT index. Simulation results indicate the relative performances and suitability of the different wall and roof assemblies in Shanghai. The results of this study, including those presented in this paper, have helped to develop moisture and thermal (i.e. hygrothermal) design guidelines for Canadian style wood-frame building envelope construction in China.

1. Introduction

In Canada and other parts of North America, traditional wood frame exterior building envelope construction is widely used and its ability to manage the exterior and interior moisture and thermal (i.e. hygrothermal) loads is well known from the field performance observations over the years. However, this type of building envelope construction is not traditionally used in China. Currently, Canada Wood, an association of Canadian forest industry partners including the Council of Forest Industries (COFI), is working with various levels of government and the construction sector in China to improve quality design and construction of wood-frame

buildings, including the building envelope. COFI leads in Asia on behalf of Canada Wood. The ultimate objective is to develop growing and sustained markets for Canadian wood products in Asia, particularly China. However, quality assurance is not possible without knowing the consequences and the ability of the wood frame building envelope assemblies to manage the hygrothermal loads in the climatic conditions of China. This long-term performance issue becomes even harder to resolve when there is no comprehensive field performance data, as in this case.

In the absence of any credible field performance data, the National Research Council (NRC) of Canada and Canada Wood initiated a joint research project to investigate the long-term performance of alternative designs of wood-frame building envelope assemblies (walls and roofs) in Shanghai and Beijing (China) and Taichung (Taiwan) using a hygrothermal simulation tool, *hygIRC-2D*. In recent years hygrothermal simulation tools have been widely used for the evaluation of the thermal and moisture response of the building envelopes (*Mukhopadhyaya et. al.2003; Djebbar et. al. 2002, Vinha 2007*). The benchmarked two-dimensional hygrothermal simulation tool, *hygIRC-2D* (*Maref et al. 2002; Hagentoft et al. 2004*), was developed at the Institute for Research in Construction of the National Research Council Canada. Some of the simulation results for Shanghai are presented in the following sections.

1.1 Research objectives and scope

The purpose of this study is to evaluate the hygrothermal performance of alternative wood-frame building envelope designs in Shanghai (China) using the hygrothermal simulation tool *hygIRC-2D*. The numerical simulations were done on four types of exterior walls and two types of unvented roof assemblies. Initially, the roof and wall constructions were simulated assuming no air leakage through the assemblies. Subsequently, simulations with air leakage were conducted on two of the wall constructions under three assumptions of air leakage. As a result, the effects of vapour diffusion could be assessed independently of air leakage. Varying the rates of air leakage helps explain the relationship between air leakage rates and hygrothermal response.

2. . Simulation tool *hygIRC-2D*

The hygrothermal simulation tool used in this study is a computer aided numerical model, *hygIRC-2D*, that can predict the moisture response of building envelopes (*Hens 1996*). *hygIRC-2D* is continuously evolving as a research tool, developed by a group of researchers at the Institute for Research in Construction (IRC) of the National Research Council (NRC), Canada. Interested readers can refer to the publications by *Karagiozis (1997)* and *Djebbar et al., (2002)* for further details. These documents outline the formulation of the combined heat, air and moisture transport equations used in *hygIRC-2D* and the techniques used to solve them numerically. The reliability of *hygIRC-2D* outputs has been established through laboratory measurements and benchmarking exercises (*Maref et al. 2002; Hagentoft et al. 2004*). The effective use of *hygIRC-2D* to analyze and obtain meaningful results, however, demands a proper physical understanding of the problem, an appropriate definition of input parameters and the ability to judiciously interpret the outputs from the simulation tool (*Mukhopadhyaya and Kumaran, 2001; Mukhopadhyaya et al. 2001; Kumaran et al. 2003*).

2.1 Basic inputs and assumptions for modeling

2.1.1 Construction details

Several different wall and roof designs (Figure 1) were evaluated to compare their hygrothermal performance. Canada Wood submitted these designs, with construction details, to the IRC researchers for hygrothermal performance evaluation under Shanghai weather conditions. As mentioned earlier, simulations were first conducted with no air leakage. These include the following exterior wall designs: (i) Wall 1 – Classic cold weather wall; (ii) Wall 2 – Super E® wall; (iii) Wall 3 – Low-cost wall; (iv) Wall 4 – All climate wall; and roof designs: (v) Roof 1 – unvented truss roof with XPS and glass fibre insulation; (vi) Roof 2 – unvented truss roof with spray-on foam insulation.

2.1.2 Air leakage

To understand the effects of imperfect air barriers in the wall constructions, air leakage was introduced in the Super E® and low cost walls. An air leakage path was created through each of the wall assemblies. The air would enter/exit, depending on the nature of indoor and outdoor pressure, along a crack at the exterior top of the

wood-framed wall and then travel through the insulation cavity and exit/enter at the interior bottom of the wall (Figure 2). The size of the crack was varied to simulate various levels of air leakage. This size was based on the normalized leakage area (NLA), which is the area of the crack in cm^2 divided by the area of the wall in m^2. Three levels of air leakage were examined: 0.3, 0.7, and 1.5 NLA.

The following wall and roof constructions were examined with air leakage:

- Wall 2 – Super E® Wall – 0.3, 0.7, and 1.5 NLA
- Wall 3 – Low cost wall – 0.3, 0.7, and 1.5 NLA

2.1.3 Material properties

hygIRC-2D simulation requires eight sets of material properties. These properties are air permeability, thermal conductivity, dry density, heat capacity, sorption characteristics, suction pressure, liquid diffusivity and water vapour permeability. These materials properties were obtained from the IRC/NRC's hygrothermal materials properties database (*Kumaran et al (2002); Kumaran et al (2004); Mukhopadhyaya et al (2004)*) and were determined in the IRC's Thermal Insulation and Moisture Performance Laboratory.

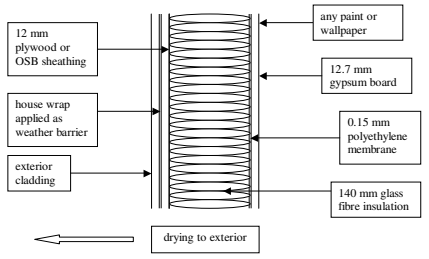

Wall 1-classic cold weather

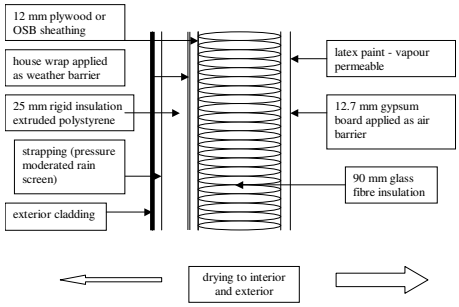

Wall 2- Super E®

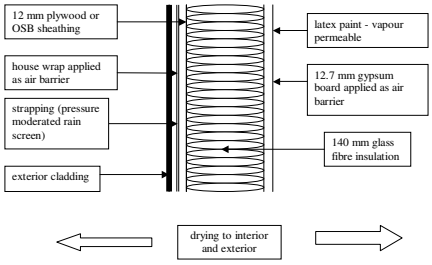

Wall 3-low cost

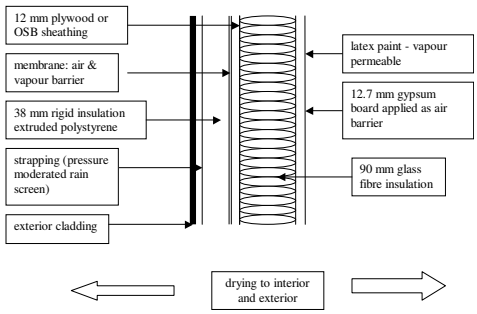

Wall 4-all climate

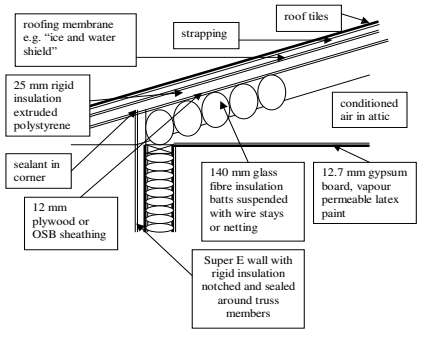

Roof 1-unvented: XPS and glass fibre insulation

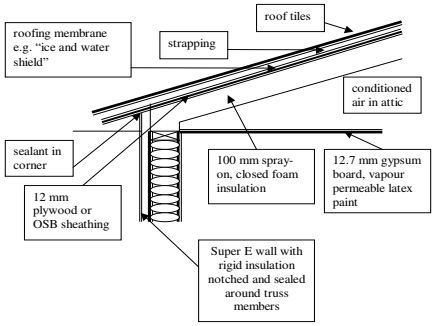

Roof 2-unvented: spray-on foam insulation

FIG 1: Walls and roofs construction details.

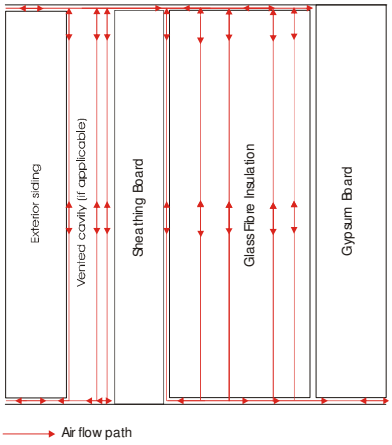

FIG 2: Schematic airflow path.

2.1.4 Environmental conditions

Hourly recorded Shanghai weather data was used as outdoor/external boundary conditions. *hygIRC-2D* requires the following hourly recorded weather components: temperature, relative humidity, wind velocity, wind direction, rainfall, solar radiation and cloud index. Weather data for the year 2003 was obtained from the weather bureau of China. Table 1 provides general climatic conditions for Shanghai.

TABLE 1: Climate+ summary of Shanghai

HDD18	1691	Extreme Mean Maximum	37° C
CDD26	164	RH Mean Coldest Month	75%
Mean Annual Temperature	16° C	RH Mean Hottest Month	83%
Extreme Minimum Temperature	-10° C	Annual Precipitation	119 cm
Extreme Maximum Temperature	39° C	Mean for Dominant Wind	3.8 m/s
Extreme Mean Minimum Temperature	-7° C	Maximum Depth of Frost	8 cm

+ Based on data from 1951 to 1980

The indoor conditions (temperature and relative humidity) used in the simulations were for a controlled indoor environment based on summer and winter seasons, identified according to the criteria specified in the 'Specifications to National (Canada) Energy Code for Houses, (*Swinton and Sander, 1994*)'. If the monthly average outdoor temperature was below 11 °C it was considered winter. If the monthly average temperature was above 11 °C it was considered summer. Indoor conditions in Shanghai were developed based on conversations with building science professionals who had knowledge of building practises in China. In the summer the indoor conditions were 25 °C temperature and 65% relative humidity. In the winter the indoor conditions were 18 °C temperature and 40% relative humidity.

3. Simulation results

A significant amount of data was generated by *hygIRC-2D* simulations and subsequently post-processed for the detailed evaluation of the hygrothermal response of the building envelopes (*Mukhopadhyaya and van Reenen 2007*). For relative comparison of hygrothermal performance of the building envelope assembly, a novel hygrothermal performance indicator was used in this study as described in the following paragraphs.

3.1 RHT index – hygrothermal performance indicator

It is widely accepted that building materials are subject to deterioration under the combined effects of temperature and moisture. The most deleterious conditions are those in which moderate or high temperature is coupled with high humidity for extended periods *(Nofal and Morris 2003)*. This study uses a novel long-term hygrothermal response indicator, called the RHT index, derived from the relative humidity (RH) and temperature (T) conditions inside the building envelope cross section over a period of time for any specific area of the cross-section. The RHT index is an indicator used to quantify and compare the hygrothermal response of the wall assembly. This index captures the duration of moisture and thermal conditions coexisting above threshold RH

and T levels. RH and T are given linear weight in the RHT index. It is to be noted that for many materials this may not always be the case when assessing their long-term performance while subjected to varying and elevated moisture conditions. A different weighting for RH and T can be determined only through controlled long-term experiments. The RHT index as defined in this study is:

$$Cumulative\ RHT=\sum(RH-RH_X)\times(T-T_X) \quad (1)$$

for RH>RH_X% and T>T_X°C at every hour of the simulation.

Where, RH_X and T_X are the threshold values for relative humidity and temperature respectively.

In this set of simulations two sets of threshold levels were used. The first set was with an RH of 80% at 0 °C temperature, hereafter referred as RHT80. The second set was with an RH of 95% at 0 °C temperature, hereafter referred as RHT95. The cumulative RHT was a summation done on an hourly basis for the final two years of the simulation.

During any time step when either or both RH ≤ RH_X % and T ≤ T_X °C, the RHT value for that time step is zero. A schematic diagram for the generation of RHT index value is shown in Figure 3. The results presented in the following section use the cumulative two-year RHT index as a single-value hygrothermal response indicator. A higher value of RHT index indicates a greater potential for moisture-related deterioration. It is to be noted here that two different walls with similar cumulative RHT values can still have very different hygrothermal responses. At the same time, climates or conditions that seem intuitively to be quite different can produce similar cumulative RHT values. It is also to be mentioned here that the threshold RHT index value that borders a safe and unsafe hygrothermal design of a wall system is yet to be defined. IRC researchers will work on this issue in the coming days.

4. Discussion

Computer simulations for each assembly design were subsequently processed to produce the following graphical displays: (i) RHT Analysis for 80% RH and 0°C; (ii) RHT Analysis for 95% RH and 0°C; (iii) moisture accumulation in each product or material component over the review period; (iv) total moisture and moisture content (%) in the wood components over the review period; (v) temperature and relative humidity in the wood components over the review period. Because it is impossible to present all the analytical information in this paper, only brief discussion on significant observations is presented in the following paragraphs. Readers may wish to refer to the publication (*Mukhopadhyaya and van Reenen 2007*) for the entire information.

4.1 Walls with no air leakage

The hygrothermal simulations of the wall assemblies with *hygIRC-2D* indicate that *Wall 1* (classic cold weather) has an area of intense hygrothermal loading (*i.e.* higher RHT index values) along the interior side of the poly sheet (Figure 4). The moisture contents in the top and bottom plates are higher than the other three wall types. The maximum moisture content in the bottom plate reaches a value of approximately 21% and remains at this level for several months during the summer (Figure 5). The other wall cross-sections remain near 15 % moisture content, reaching a maximum of 17%. The higher RHT values and moisture content in the top and bottom plates indicate a higher potential of moisture related damage to this *Wall 1* cross-section.

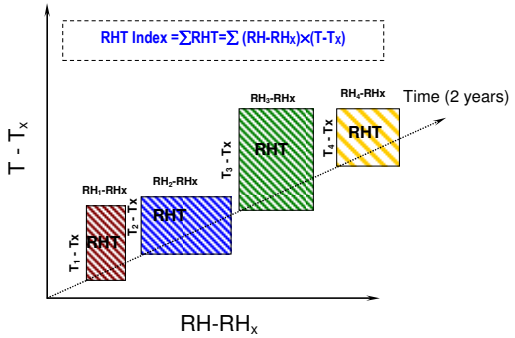

FIG 3: Schematic diagram to explain RHT Index calculation.

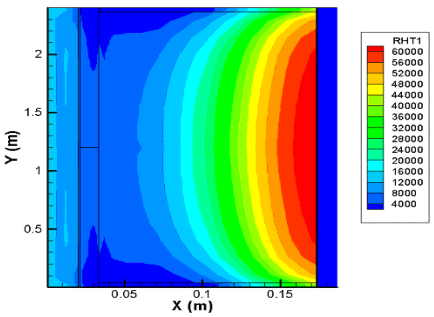

FIG. 4: Wall 1 - RHT analysis for 80% RH and 0 °C

4.2 Roofs

Two unvented roofs (Figure 1) examined here are *Roof 1* (traditional truss with rigid, XPS foam over and glass fibre insulation under sheathing) and *Roof 2* (traditional truss with spray-on foam insulation under sheathing). The hygrothermal analyses, using *hygIRC-2D*, compares the two roofs. Whilst the highest values of RHT indices in both roofs are in the roof tiles, roof 2 shows a higher RHT index in the area of the plywood sheathing and immediately below the sheathing (Figures 6 and 7).

When looking at the total moisture content in the two roofs, *Roof 2* has a higher total value of moisture accumulation for most of the year under consideration (Figures 8 and 9). *Roof 2* shows significantly higher moisture content in the wood components of the roof, i.e., plywood sheathing and upper truss chords (Figures 10 and 11). The plywood, moisture content in *Roof 1* generally varies between 8% and 14% while in *Roof 2* it is approximately 5% higher for most of the year, (Figure 10). An estimate of the moisture content in the truss chords was derived from the relative humidity in the insulated space (Figure 11).

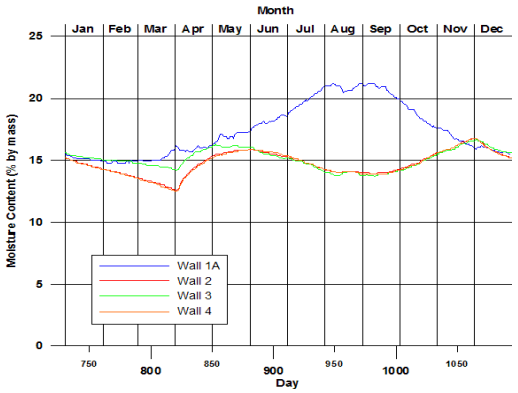

FIG. 5: Average moisture content in bottom plate

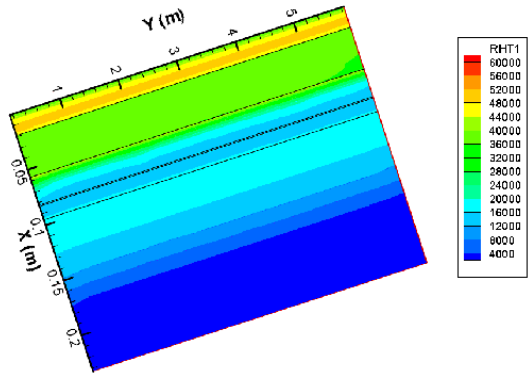

FIG. 6: Roof 1 - RHT analysis for 80% RH and 0°C

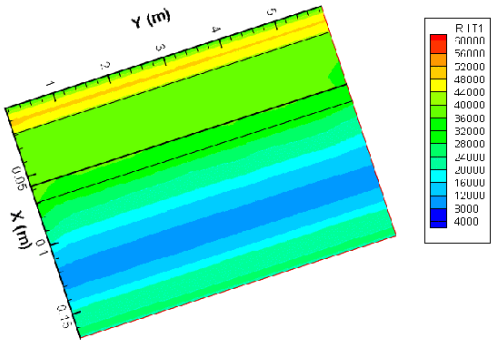

FIG. 7: Roof 2 - RHT analysis for 80% RH and 0°C

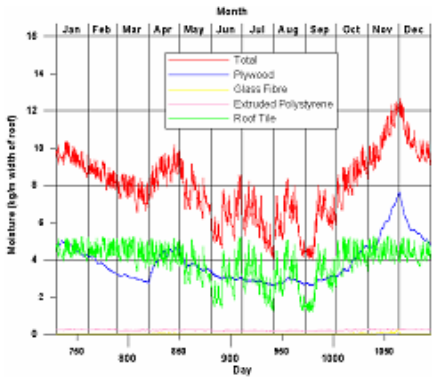

FIG. 8: Moisture accumulation in components of roof 1

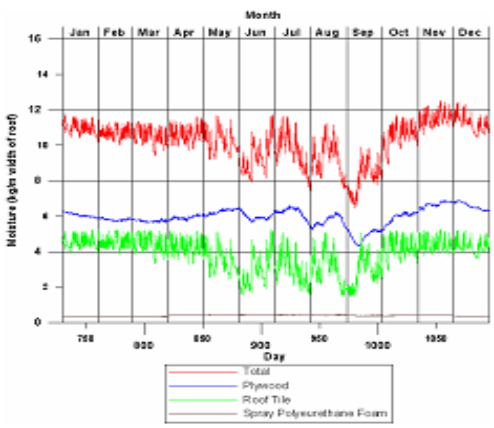

FIG. 9: Moisture accumulation in components of roof 2

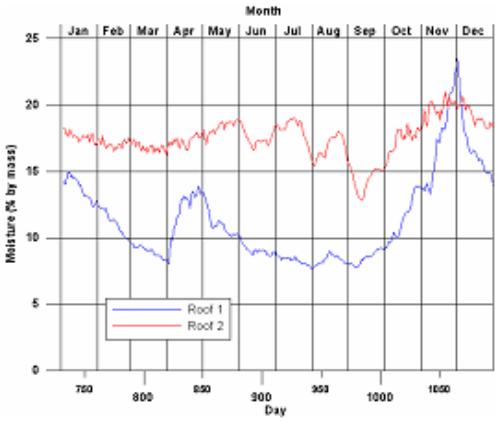

FIG. 10: Roofs-average moisture content in plywood

4.3 Walls with air leakage

Three levels of air leakage (0.3, 0.7, and 1.5 NLA) were examined on *Wall 2* and *Wall 3*. The RHT analyses from hygrothermal simulations show interesting results for *Wall 3* (Figures 12, 13 and 14). There is an area of high hygrothermal loading (i.e. high RHT index) on the interior side of the bottom plate for all three levels of leakage. This area of high hygrothermal loading becomes larger as the level of the air leakage increases. The moisture content in the bottom plate reaches the highest level, and increases with more air leakage (Figure 15).

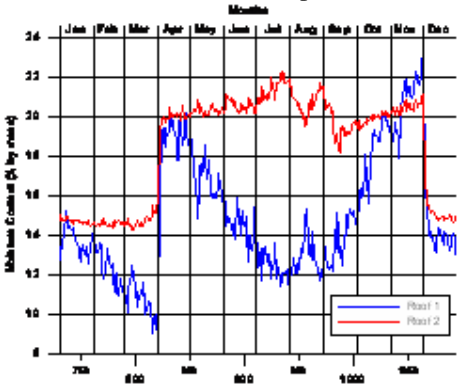

FIG. 11: Roofs - estimate of moisture content in rafters

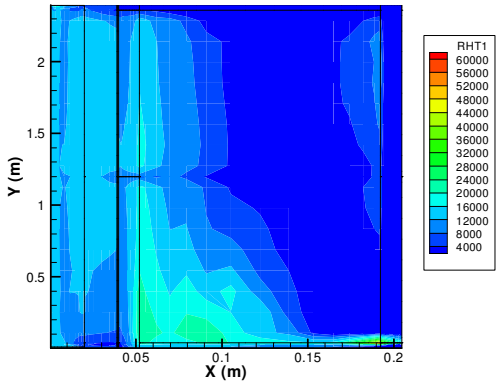

FIG. 12: Wall 3 - 0.3 NLA

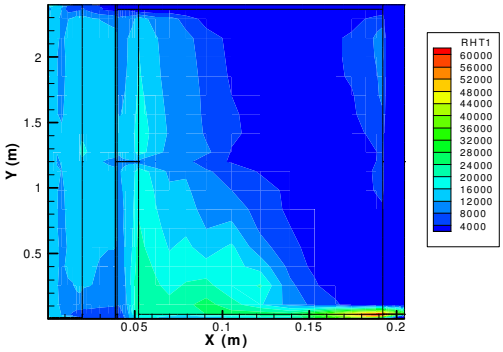

FIG. 13: Wall 3 - 0.7 NLA

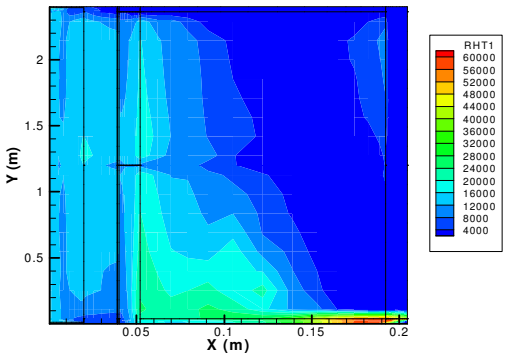

FIG. 14: Wall 3 - 1.5 NLA

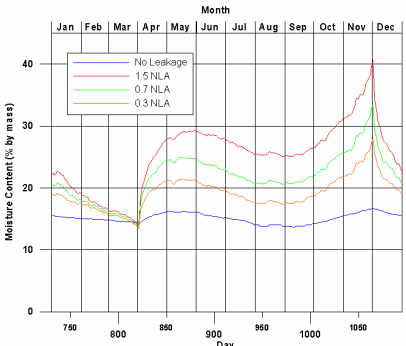

FIG. 15: Wall 3 - Average moisture content in bottom plate

5. Conclusions

- Under conditions with no air leakage, the hygrothermal simulation with *hygIRC-2D* indicates that the classic cold weather wall, as constructed in Canada, has the highest intensity of overall hygrothermal response.
- Air leakage condition has been simulated in both the Super E® wall, and the low cost wall. These simulations show increasing the air leakage through the wall assembly results in higher levels of moisture in the bottom plate.

- The unvented roof simulations show that roof tile is the most vulnerable to high temperatures and moisture levels. The roof with rigid, XPS foam over and glass fibre insulation under the sheathing has resulted in lower moisture contents in the wood components of the construction.

6. References

Djebbar, R., Kumaran, M.K., Van Reenen, D. and Tariku, F. (2002). Hygrothermal Modelling of Building Envelope Retrofit Measures in Multi-unit Residential and Commercial Office Buildings. IRC/NRC, *National Research Council*, Ottawa, Canada, Client Final Report B-1110.3, pp. 187.

Hagentoft, C-E., Adan, O., Adl-Zarrabi, B., Becker, R.; Brocken, H., Carmeliet, J., Djebbar, R., Funk, M., Grunewald, J., Hens, H., Kumaran, M.K., Roels, S., Kalagasidis, A.S., Shamir, D. (2004). Assessment Method of Numerical Prediction Models for Combined Heat, Air and Moisture Transfer in Building Components: Benchmarks for One-dimensional Cases. *Journal of Thermal Envelope and Building Science*, v. 27, no. 4, April 2004, pp. 327-352.

Hens, H. (1996). Heat, air and moisture transport, Final Report, Vol. 1, Task 1: Modelling, *International Energy Agency*, Annex 24, Laboratorium Bouwfysica, K. U.-Leuven, Belgium.

Karagiozis, A. (1997). Analysis of the Hygrothermal Behaviour of Residential High-rise Building Components. Client Report A-3052.4, IRC/NRC, *National Research Council Canada*, Ottawa.

Kumaran, K., Lackey, J., Normandin, N., Tariku, F and van Reenen, D. (2004). A Thermal and Moisture Transport Property Database for Common Building and Insulating Materials, Final Report from *ASHRAE Research Project 1018-RP*, pp. 1-229.

Kumaran, K., Lackey, J., Normandin, N., van Reenen, D. and Tariku, F. (2002). Summary report from Task 3 of MEWS project. Institute for Research in Construction, *National Research Council*, Ottawa, Canada, (NRCC-45369), pp. 1-68.

Kumaran M. K., Mukhopadhyaya P., Cornick S. M., Lacasse, M. A., Maref W., Rousseau M., Nofal M., Quirt J. D. & Dalgliesh W. A. (2003). An Integrated Methodology to Develop Moisture Management Strategies for Exterior Wall Systems. *9th Conference on Building Science and Technology*, Vancouver, Canada, pp. 16.

Maref, W., Kumaran, M. K., Lacasse, M. A. Swinton, M. C. and van Reenen, D. (2002). Advanced Hygrothermal Model hygIRC: Laboratory Measurements and Benchmarking. *12th International Heat Transfer Conference*, Grenoble, France, pp. 1-6.

Mukhopadhyaya, P., Lackey J., Normandin N., Tariku F., and van Reenen, D. (2004). Hygrothermal Performance of Building Envelope Retrofit Options: Task 1 - A Thermal and Moisture Transport Property Database, IRC/NRC, *National Research Council Canada*, Ottawa, Client Final Report, pp. 1-37, (B-1137.5).

Mukhopadhyaya, P. and Kumaran, M. K. (2001). Prediction of Moisture Response of Wood Frame Walls Using IRC's Advanced Hygrothermal Model (hygIRC). *2nd Annual Conference on Durability and Disaster Mitigation in Wood-Frame Housing*, pp. 221-226.

Mukhopadhyaya, P. Kumaran, M. K. van Reenen, D. and Tariku F. (2001). Influence of Sheathing Membrane and Vapour Barrier on Hygrothermal Response of Stucco Walls, *International Conference on Building Envelope Systems and Technologies (ICBEST)*, Vol. 1, pp. 269-274.

Mukhopadhyaya, P., Kumaran, K., Rousseau, M., Tariku, F. van Reenen, D., and Dalgliesh, W.A. (2003). Application of Hygrothermal Analyses to Optimise Exterior Wall Design, *Research in Building Physics*, Sept. 14-18, Lueven, Belgium, pp. 417-426.

Mukhopadhyaya, P., and van Reenen, D. (2007). Assessment of Moisture Performance of Wood-frame Walls in China and Taiwan, IRC/NRC, *National Research Council Canada*, Ottawa, Client Final Report, pp. 1-176, (B1083.1).

Nofal, M. and Morris, P.I. (2003). Criteria for Unacceptable Damage on Wood Systems, *Japan-Canada Conference on Building Envelope*, Vancouver, Canada, 6/4/2003, pp. 1-14.

Swinton, M.C.; Sander, D.M., 1994. "Trade-off Compliance for Houses: Specifications for Calculation Procedures for Demonstrating Compliance to the National Energy Code for Houses using Trade-offs", pp. 46, March 01,(NRCC-39861).

Vinha, J. 2007, Hygrothermal Performance of Timber-Framed External Walls in Finnish Climatic Conditions: A Method for Determining the sufficient Water Vapour Resistance of the Interior Lining of a Wall Assembly, Ph.D. Thesis, Tampere University of Technology.